

# 食品暨化妝品安全研究中心

2020年09月01日~2021年08月31日

## 論文集(中)



**長庚科技大學**  
CHANG GUNG UNIVERSITY OF SCIENCE AND TECHNOLOGY



**CHANG GUNG UNIVERSITY OF SCIENCE AND TECHNOLOGY**

長庚科技大學  
食品暨化妝品安全研究中心  
2020 年 09 月 01 日~2021 年 08 月 31 日

論文集

目 錄

(中冊)

| 序號 | 期刊論文  | 學校主要<br>負責教師 | 頁<br>碼 |
|----|---|--------------|--------|
| 34 | Yamazoe, E., Fang, J. Y., & Tahara, K. (2021). Oral mucus-penetrating PEGylated liposomes to improve drug absorption: Differences in the interaction mechanisms of a mucoadhesive liposome. <i>International Journal of Pharmaceutics</i> , 593: 120148. doi: 10.1016/j.ijpharm.2020.120148 | 方嘉佑          | 476    |
| 35 | Malla, P., Chen, G. C., Liao, H. P., Liu, C. H., & Wu, W. C. (2021). Label-free parathyroid hormone immunosensor using nanocomposite modified carbon electrode. <i>Journal of Electroanalytical Chemistry</i> , 880: 114917. doi: 10.1016/j.jelechem.2020.114917                            | 劉繼賢          | 485    |
| 36 | Prabowo, B. A., Purwidyantri, A., Liu, B., Lai, H. C., & Liu, K. C. (2020). Gold nanoparticle-assisted plasmonic enhancement for DNA detection on a graphene-based portable surface plasmon resonance sensor. <i>Nanotechnology</i> , 32(9): 095503. doi: 10.1088/1361-6528/abcd62          | 賴信志          | 496    |



- |    |  |     |     |
|----|--|-----|-----|
| 37 | Chi, W. C., Kuo, L. M., Yang, S. N., Lee, Y. T., Wen, Z. H., Tsui, K. H., Hwang, T. L., Zhang, Y. L., & Sung, P. J. (2021). Briarenols O and P: Novel briaranes from a cultured octocoral <i>Briareum excavatum</i> (Briareidae). <i>Phytochemistry Letters</i> , 41: 134-138. doi: 10.1016/j.phytol.2020.09.012                       | 黃聰龍 | 506 |
| 38 | Lee, T. L., Lee, M. H., Chen, Y. C., Lee, Y. C., Lai, T. C., Lin, H. Y. H., Hsu, L. F., Sung, H. C., Lee, C. W., & Chen, Y. L. (2020). Vitamin D attenuates ischemia/reperfusion-induced cardiac injury by reducing mitochondrial fission and mitophagy. <i>Frontiers in Pharmacology</i> , 11: 604700. doi: 10.3389/fphar.2020.604700 | 李江文 | 511 |
| 39 | Chang, H. C., Wang, S. W., Chen, C. Y., Hwang, T. L., Cheng, M. J., Sung, P. J., Liao, K. W., & Chen, J. J. (2020). Secoiridoid glucosides and anti-inflammatory constituents from the stem bark of <i>Fraxinus chinensis</i> . <i>Molecules (Basel, Switzerland)</i> , 25(24): 5911. doi: 10.3390/molecules25245911                   | 黃聰龍 | 528 |
| 40 | Kuo, P. C., Tai, S. H., Hung, C. C., Hwang, T. L., Kuo, L. M., Lam, S. H., Cheng, K. C., Kuo, D. H., Hung, H. Y., & Wu, T. S. (2021). Antiinflammatory triterpenoids from the fruiting bodies of <i>Fomitopsis pinicola</i> . <i>Bioorganic Chemistry</i> , 108: 104562. doi: 10.1016/j.bioorg.2020.104562                             | 黃聰龍 | 547 |

- 41    Chen, Y. H., Chang, Y. C., Chen, Y. H.,  
Zheng, L. G., Huang, P. C., Huynh, T. H.,  
Peng, B. R., Chen, Y. Y., Wu, Y. J., Fang, L.  
S., Su, J. H., Hsu, C. M., & Sung, P. J. (2020).  
Natural products from octocorals of the genus  
*Dendronephthya* (family nephtheidae).  
*Molecules (Basel, Switzerland)*, 25(24): 5957.  
doi: 10.3390/molecules25245957  
張佑嘉            558
  
- 42    Cheng, M. H., Chiu, C. H., Chen, C. T., Chou,  
H. H., Pao, L. H., & Wan, G. H. (2021).  
Sources and components of volatile organic  
compounds in breast surgery operating rooms.  
*Ecotoxicology and Environmental Safety*, 209:  
111855. doi: 10.1016/j.ecoenv.2020.111855  
邱群惠            584  
鮑力恒
  
- 43    Lee, T. L., Lai, T. C., Lin, S. R., Lin, S. W.,  
Chen, Y. C., Pu, C. M., Lee, I. T., Tsai, J. S.,  
Lee, C. W., & Chen, Y. L. (2021).  
Conditioned medium from adipose-derived  
stem cells attenuates  
ischemia/reperfusion-induced cardiac injury  
through the  
microRNA-221/222/PUMA/ETS-1 pathway.  
*Theranostics*, 11(7): 3131-3149. doi:  
10.7150/THNO.52677  
李江文            592
  
- 44    Lam, S. H., Jian, S. D., Hwang, T. L., Chen,  
P. J., Hung, H. Y., Kuo, P. C., & Wu, T. S.  
(2021). A new dimeric protoberberine  
alkaloid and other compounds from the tubers  
of *Tinospora dentata*. *Natural Product  
Research*, 35(1): 17-24. doi:  
10.1080/14786419.2019.1611809  
黃聰龍            611

- 45    Chen, H. Y., Ting, Y., Kuo, H. C., Hsieh, C. W., Hsu, H. Y., Wu, C. N., & Cheng, K. C. (2021). Enzymatic degradation of ginkgolic acids by laccase immobilized on core/shell Fe<sub>3</sub>O<sub>4</sub>/nylon composite nanoparticles using novel coaxial electrospraying process. *International Journal of Biological Macromolecules*, 172: 270-280. doi: 10.1016/j.ijbiomac.2021.01.004

郭星君      619
- 46    Kumari, M., Liu, C. H., Wu, W. C., & Wang, C. C. (2021). Gene delivery using layer-by-layer functionalized multi-walled carbon nanotubes: Design, characterization, cell line evaluation. *Journal of Materials Science*, 56(11): 7022-7033. doi: 10.1007/s10853-020-05648-6

劉繼賢      630
- 47    Tai, C. J., Huang, C. Y., Ahmed, A. F., Orfali, R. S., Alarif, W. M., Huang, Y. M., Wang, Y. H., Hwang, T. L., & Sheu, J. H. (2021). An anti-inflammatory 2, 4-Cyclized-3, 4-Secospongian Diterpenoid and furanoterpene-related metabolites of a marine sponge *Spongia* sp. from the Red Sea. *Marine Drugs*, 19(1): 38. doi: 10.3390/md19010038

黃聰龍      642
- 48    Jheng, J. R., Chen, Y. S., & Horng, J. T. (2021). Regulation of the proteostasis network during enterovirus infection: A feedforward mechanism for EV-A71 and EV-D68. *Antiviral Research*, 188: 105019. doi: 10.1016/j.antiviral.2021.105019

洪錦堂      655

- 49 Lee, W. R., Hsiao, C. Y., Huang, T. H., Sung, C. T., Wang, P. W., Cheng, W. T., & Fang, J. Y. (2021). Low-fluence laser-facilitated platelet-rich plasma permeation for treating MRSA-infected wound and photoaging of the skin. *International Journal of Pharmaceutics*, 595: 120242. doi: 10.1016/j.ijpharm.2021.120242 蕭千祐 670  
方嘉佑
- 50 Tang, W. F., Tsai, H. P., Chang, Y. H., Chang, T. Y., Hsieh, C. F., Lin, C. Y., Lin, G. H., Chen, Y. L., Jheng, J. R., Liu, P. C., Yang, C. M., Chin, Y. F., Chen, C. C., Kau, J. H., Hung, Y. J., Hsieh, P. S., & Horng, J. T. (2021). Perilla (*Perilla frutescens*) leaf extract inhibits SARS-CoV-2 via direct virus inactivation. *Biomedical Journal*, 44(3): 293-303. doi: 10.1016/j.bj.2021.01.005 洪錦堂 683
- 51 Liu, C. C., Yang, Y. H., Hsiao, Y. C., Wang, P. J., Liu, J. C., Liu, C. H., Hsieh, W. C., Lin, C. C., & Yu, J. S. (2021). Rapid and efficient enrichment of snake venoms from human plasma using a strong cation exchange tip column to improve snakebite diagnosis. *Toxins*, 13(2): 140. doi: 10.3390/toxins13020140 余兆松 694

- 52 Liao, C. C., Yu, H. P., Yang, S. C., Alalaiwe, A., Dai, Y. S., Liu, F. C., & Fang, J. Y. (2021). Multifunctional lipid-based nanocarriers with antibacterial and anti-inflammatory activities for treating MRSA bacteremia in mice. *Journal of Nanobiotechnology*, 19(1): 1-18. doi: 10.1186/s12951-021-00789-5 方嘉佑 711
- 53 Lin, Y. C., Fang, Y. P., Hung, C. F., Yu, H. P., Alalaiwe, A., Wu, Z. Y., & Fang, J. Y. (2021). Multifunctional TiO<sub>2</sub>/SBA-15 mesoporous silica hybrids loaded with organic sunscreens for skin application: The role in photoprotection and pollutant adsorption with reduced sunscreen permeation. *Colloids and Surfaces B: Biointerfaces*, 202: 111658. doi: 10.1016/j.colsurfb.2021.111658 方嘉佑 729
- 54 Li, M. L., Shih, S. R., Tolbert, B. S., & Brewer, G. (2021). Enterovirus A71 vaccines. *Vaccines*, 9(3): 199. doi: 10.3390/vaccines9030199 施信如 741
- 55 Wei, H. T., Hsu, J. W., Huang, K. L., Bai, Y. M., Su, T. P., Li, C. T., Lin, W. C., Tsai, S. J., Pan, T. L., Chen, T. J., & Chen, M. H. (2021). Timing of the diagnoses of attention deficit hyperactivity disorder and autism spectrum disorder in Taiwan. *Journal of Autism and Developmental Disorders*, 51(3): 790-797. doi: 10.1007/s10803-018-3655-1 潘台龍 751

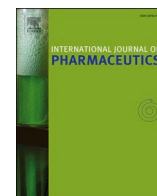
- |    |   |            |     |
|----|---|------------|-----|
| 56 | Tung, S. Y., Lee, K. C., Lee, K. F., Yang, Y. L., Huang, W. S., Lee, L. Y., Chen, W. P., Chen, C. C., Teng, C. C., Shen, C. H., Hsieh, M. C., Huang, C. Y., Sheen, J. M., & Kuo, H. C. (2021). Apoptotic mechanisms of gastric cancer cells induced by isolated erinacine S through epigenetic histone H3 methylation of FasL and TRAIL. <i>Food and Function</i> , 12(8): 3455-3468. doi: 10.1039/d0fo03089a | 郭星君        | 759 |
| 57 | Lin, Z. C., Hwang, T. L., Huang, T. H., Tahara, K., Trousil, J., & Fang, J. Y. (2021). Monovalent antibody-conjugated lipid-polymer nanohybrids for active targeting to desmoglein 3 of keratinocytes to attenuate psoriasiform inflammation. <i>Theranostics</i> , 11(10): 4567-4584. doi: 10.7150/thno.56995  | 黃聰龍<br>方嘉佑 | 773 |
| 58 | Hung, Y. T., Lee, Y. T., Inbaraj, B. S., Sridhar, K., & Chen, B. H. (2021). Analysis and formation of polycyclic aromatic hydrocarbons and cholesterol oxidation products in thin slices of dried pork during processing. <i>Food Chemistry</i> , 353: 129474. doi: 10.1016/j.foodchem.2021.129474  | 李昱宗        | 791 |
| 59 | Lai, H. C., Lin, T. L., Chen, T. W., Kuo, Y. L., Chang, C. J., Wu, T. R., Shu, C. C., Tsai, Y. H., Swift, S., & Lu, C. C. (2021). Gut microbiota modulates COPD pathogenesis: Role of anti-inflammatory <i>Parabacteroides goldsteinii</i> lipopolysaccharide. <i>Gut</i> , 2021: 1-13. doi: 10.1136/gutjnl-2020-322599   | 賴信志        | 802 |



- |    |   |     |     |
|----|---|-----|-----|
| 60 | Pan, T. L., Bai, Y. M., Cheng, C. M., Tsai, S. J., Tsai, C. F., Su, T. P., Li, C. T., Lin, W. C., Chen, T. J., Liang, C. S., & Chen, M. H. (2021). Atopic dermatitis and dementia risk: A nationwide longitudinal study. <i>Annals of Allergy, Asthma and Immunology</i> , 127(2): 200-205. doi: 10.1016/j.anai.2021.03.001 | 潘台龍 | 815 |
| 61 | Huang, W. C., Huang, T. H., Yeh, K. W., Chen, Y. L., Shen, S. C., & Liou, C. J. (2021). Ginsenoside Rg3 ameliorates allergic airway inflammation and oxidative stress in mice. <i>Journal of Ginseng Research</i> , 45(6): 654-664. doi: 10.1016/j.jgr.2021.03.002  | 黃文忠 | 821 |
| 62 | Dash, B. S., Jose, G., Lu, Y. J., & Chen, J. P. (2021). Functionalized reduced graphene oxide as a versatile tool for cancer therapy. <i>International Journal of Molecular Sciences</i> , 22(6): 2989. doi: 10.3390/ijms22062989   | 陳志平 | 832 |
| 63 | Lin, M. H., Hung, C. F., Sung, H. C., Yang, S. C., Yu, H. P., & Fang, J. Y. (2021). The bioactivities of resveratrol and its naturally occurring derivatives on skin. <i>Journal of Food and Drug Analysis</i> , 29(1): 15-38. doi: 10.38212/2224-6614.1151   | 方嘉佑 | 854 |

- |    |   |                |     |
|----|---|----------------|-----|
| 64 | Huang, S. Y., Kung, Y. A., Huang, P. N., Chang, S. Y., Gong, Y. N., Han, Y. J., Chiang, H. J., Liu, K. T., Lee, K. M., Chang, C. Y., Chang, C. C., Huang, C. G., & Shih, S. R. (2021). Stability of SARS-CoV-2 spike G614 variant surpasses that of the D614 variant after cold storage. <i>MSphere</i> , 6(2): 1-8. doi: 10.1128/mSphere.00104-21    | 施信如            | 878 |
| 65 | Liao, P. J., Lin, Y. C., Ting, M. K., Wu, I. W., Chen, S. W., Yang, N. I., & Hsu, K. H. (2021). Adverse body measurements are superior to sarcopenia-associated measurements in predicting chronic diseases. <i>Scientific Reports</i> , 11(1): 7749. doi: 10.1038/s41598-021-85316-0   | 許光宏            | 886 |
| 66 | Chiu, C. H., Chen, C. T., Cheng, M. H., Pao, L. H., Wang, C., & Wan, G. H. (2021). Use of urinary hippuric acid and <i>o</i> -/ <i>p</i> -/ <i>m</i> -methyl hippuric acid to evaluate surgical smoke exposure in operating room healthcare personnel. <i>Ecotoxicology and Environmental Safety</i> , 217: 112231. doi: 10.1016/j.ecoenv.2021.112231 | 邱群惠<br><br>鮑力恒 | 895 |
| 67 | Kuo, P. C., Li, Y. C., Kusuma, A. M., Tzen, J. T. C., Hwang, T. L., Ye, G. H., Yang, M. L., Wang, S. Y. (2021). Anti-inflammatory principles from the needles of <i>Pinus taiwanensis</i> Hayata and in silico studies of their potential anti-aging effects. <i>Antioxidants</i> , 10(4): 598. doi: 10.3390/antiox10040598                           | 黃聰龍            | 902 |

- 68 Nirmal, G. R., Lin, Z. C., Tsai, M. J., Yang, S. C., Alalaiwe, A., & Fang, J. Y. (2021). Photothermal treatment by PLGA–gold nanorod–isatin nanocomplexes under near-infrared irradiation for alleviating psoriasiform hyperproliferation. *Journal of Controlled Release*, 333: 487-499. doi: 10.1016/j.jconrel.2021.04.005 方嘉佑 916
- 69 Stremoukhov, O., Koshovyi, O., Komisarenko, M., Kireyev, I., Gudzenko, A., Korinek, M., Hwang, T. L., Chen, M. H., & Mykhailenko, O. (2021). Phytochemical research and anti-inflammatory activity of the dry extracts from northern highbush blueberry leaves. *ScienceRise: Pharmaceutical Science*, 30(2): 40-48. doi: 10.15587/2519-4852.2021.230288 黃聰龍 929
- 70 Peng, C. C., Huang, T. Y., Huang, C. Y., Hwang, T. L., & Sheu, J. H. (2021). Cherbonolides M and N from a Formosan soft coral *Sarcophyton cherbonnieri*. *Marine Drugs*, 19(5): 260. doi: 10.3390/md19050260 黃聰龍 938
- 71 Wu, S. J., Huang, W. C., Yu, M. C., Chen, Y. L., Shen, S. C., Yeh, K. W., & Liou, C. J. (2021). Tomatidine ameliorates obesity-induced nonalcoholic fatty liver disease in mice. *Journal of Nutritional Biochemistry*, 91: 108602. doi: 10.1016/j.jnutbio.2021.108602 黃文忠 948



# Oral mucus-penetrating PEGylated liposomes to improve drug absorption: Differences in the interaction mechanisms of a mucoadhesive liposome

Eriko Yamazoe<sup>a</sup>, Jia-You Fang<sup>b,c,d,e</sup>, Kohei Tahara<sup>a,\*</sup>

<sup>a</sup> Laboratory of Pharmaceutical Engineering, Gifu Pharmaceutical University, Gifu, Japan

<sup>b</sup> Graduate Institute of Natural Products, Chang Gung University, Kweishan, Taoyuan, Taiwan

<sup>c</sup> Chinese Herbal Medicine Research Team, Healthy Aging Research Center, Chang Gung University, Kweishan, Taoyuan, Taiwan

<sup>d</sup> Research Center for Food and Cosmetic Safety and Research Center for Chinese Herbal Medicine, Chang Gung University of Science and Technology, Kweishan, Taoyuan, Taiwan

<sup>e</sup> Department of Anesthesiology, Chang Gung Memorial Hospital, Kweishan, Taoyuan, Taiwan

## ARTICLE INFO

### Keywords:

PEG  
Liposome  
Mucus penetrating  
Oral  
Peptide

## ABSTRACT

We investigated the feasibility of densely polyethylene glycol (PEG2000)-modified liposomes as mucus-penetrating particles (MPPs) for oral delivery of systemically absorbed peptides. The oral absorption of MPPs and mucoadhesive liposomes modified with glycol chitosan (GCS) was compared. In an *in vitro* artificial mucus model, the densely PEGylated liposomes showed mucus permeability. Intracellular uptake of liposomes was evaluated in a Caco-2 and mucus-secreting Caco-2/HT29 co-culture. Intracellular uptake of MPPs was unaffected by mucus in the co-culture system, whereas the cellular uptake of GCS-liposomes was lower with a mucus layer than in Caco-2 alone. Rat *in vivo* oral absorption of liposomes was evaluated by using fluorescein isothiocyanate dextran (FD) as a model peptide drug. Oral absorption was higher for densely PEGylated than for unmodified liposomes and was PEG-concentration dependent, but excessive PEGylation decreased FD blood concentration. PEGylated liposomes incorporating spermine (SPM) as an absorption enhancer were then designed and showed the highest *in vivo* absorption of FD of all tested formulations. The pharmacological effects of the oral liposomes were evaluated by using elcatonin and did not correlate with FD oral absorption. The non-PEGylated SPM liposomes showed the highest pharmacological effect, suggesting the need for drug-specific optimization of liposomal components and surface modifiers.

## 1. Introduction

Peptides and protein-based medicines, which are generally administered by injection, have low enzyme stability and hydrophilic properties, making it difficult for them to achieve sufficient bioavailability by oral administration because of their low mucosal and membrane permeability (Drucker, 2020). Drug carriers, such as liposomes, emulsions, and polymeric nanoparticles, loaded with biologics have long been used in attempts to improve the oral absorption of peptide and protein drugs, which are generally unstable in the gastrointestinal (GI) tract and have poor epithelial cell permeability (Niu et al., 2016; Renukuntla et al., 2013).

Many studies, including those by our group, have used submicron-sized liposomes of approximately 100 nm as oral drug carriers to improve the absorption of peptides and protein-based drugs, such as

insulin, after oral administration (Cao et al., 2019; Tahara, 2020; Tahara et al., 2018). Downsizing of the drug carrier particles to the nanometer range is accompanied by an increase in the specific surface area of the particles, which improves their interaction with mucus and mucous membranes in the GI tract. However, the oral liposomal system has not yet been put to practical use. In the GI tract, which undergoes repeated dynamic peristaltic movements, oral liposomes would be rapidly excreted from the body, which would not allow sufficient residence time for drug absorption of liposomes in the GI tract (Takeuchi et al., 2001).

We have attempted to design surface-modified liposomes with mucoadhesive polymers (mucoadhesive liposome) to confer a mucoadhesive ability to improve oral absorption of liposomes in the GI tract. Biodegradable/cationic chitosan (CS) derivatives were employed as liposomal surface modifiers with mucosal adhesion (Tahara et al., 2018). CS modification increased the residence time of liposomes in the

\* Corresponding author at: Gifu Pharmaceutical University, 1-25-4 Daigaku-nishi, Gifu 501-1196, Japan.

E-mail address: [tahara@gifu-pu.ac.jp](mailto:tahara@gifu-pu.ac.jp) (K. Tahara).

<https://doi.org/10.1016/j.ijpharm.2020.120148>

Received 4 August 2020; Received in revised form 13 November 2020; Accepted 1 December 2020

Available online 5 December 2020

0378-5173/© 2020 Elsevier B.V. All rights reserved.

GI tract, resulting in improved drug absorption. Although mucoadhesive liposomes can provide long-term retention in the mucosal layer of the GI tract, a drug-loaded liposome can potentially still be eliminated during the repeated mucus turnover before the liposomes permeate through the mucosal layer and reach epithelial cells (Ponchel et al., 1997).

Reportedly, polyethylene glycol (PEG) densely modified nanoparticles as drug carriers can act as mucus-penetrating particles (MPPs) (Ensign et al., 2012; Lai et al., 2009; Liu et al., 2015). MPPs have been developed by mimicking the ability of virus particles with sufficient surface area to rapidly diffuse into the mucosal layer. The mucosal layer in the GI epithelium comprises a dense network of mucin fibers with pores of several hundred nanometers in diameter. Therefore, nano-sized drug carriers are relatively easier to pass through the pores of the mucosal layer than micro-sized ones and have an advantage in mucus permeation (Netsomboon and Bernkop-Schnurch, 2016). To develop nanoparticles with more efficient mucus permeability, it is important to ensure the mobility and diffusivity of the particles in mucus by minimizing the interaction as much as possible between the particles and components of mucus, such as mucin (Liu et al., 2015).

MPPs with excellent mucus permeability can be designed by surface modification using PEG with a relatively low molecular weight (MW 2000) of high-density nanoparticles (approximately  $\geq 5\%$ ) (Wang et al., 2008). The rate of permeation in vaginal mucus has been reported to be significantly higher for high-density PEG-modified (PEGylated) nanoparticles than for unmodified nanoparticles (Huckaby and Lai, 2018; Joraholmen et al., 2017). However, few reports have examined the drug absorption of oral MPPs (Zhou et al., 2019). It is necessary to determine if MPPs are fully partitioned into the GI mucosa because the GI tract is a much more highly peristaltic tissue than other mucosal tissues, such as vaginal or lung mucosa (Alp and Aydogan, 2020; Joraholmen et al., 2017).

The study aim was to determine if high-density PEGylated liposomes, designed as oral drug carriers for peptide drugs, function as MPPs and to measure their absorption characteristics after oral administration. To improve absorption, liposomes incorporating spermine (SPM), a commonly used oral absorption enhancer (Sugita et al., 2007), into lipid bilayers were prepared and densely modified with PEG to impart mucosal permeability. The differences in the absorption mechanisms of MPPs and mucoadhesive particles were investigated by evaluating the oral absorption of mucoadhesive liposomes with glycol chitosan (GCS) as a surface modifier (Netsomboon and Bernkop-Schnurch, 2016; Tahara et al., 2018). Two fluorescein isothiocyanate dextrans (FDs) with different molecular weights and elcatonin were used as models for peptide drugs.

## 2. Material and methods

### 2.1. Materials

Distearoylphosphatidylcholine (DSPC) and 1,2-distearoyl-*sn*-glycero-3-phosphoethanolamine-N-[methoxy (polyethylene glycol)-2000] (MPEG-DSPE) was purchased from NOF (Tokyo, Japan). Cholesterol (Chol), dicetyl phosphate (DCP), SPM, GCS, and FDs with different molecular weights (FD4: average MW3000–5000 and FD10: average MW10,000) were purchased from Sigma-Aldrich (St Louis, MO). Elcatonin was kindly provided by Asahi Kasei (Tokyo, Japan). 1, 1'-Dioctadecyl-3, 3', 3' methyl indocarbocyanine perchlorate (DiI) was purchased from Lambda Probes & Diagnostics (Graz, Austria). Coumarin-6 (C6) was purchased from MP Biomedicals LLC (CA, USA). Nile Red were purchased from Tokyo Chemical Industry Co., Ltd. (Tokyo, Japan). Dulbecco's modified Eagle's medium (DMEM), fetal bovine serum (FBS), non-essential amino acid solution (NEAA), penicillin-streptomycin, L-glutamine, and Hanks' balanced salt solution were purchased from Thermo Fisher Scientific (MA, USA). 2-(N-morpholino) ethanesulfonic acid were purchased from Nacalai Tesque (Kyoto, Japan).

### 2.2. Preparation of surface-modified liposomes

Liposomes were prepared using thin film hydration. DSPC, Chol, and SPM dissolved in chloroform were dried in a rotary evaporator to form a thin lipid film (Murata et al., 2012). Fluorescence-labeled liposomes were generated by dissolving dye (DiI or C6 or Nile Red) into a lipid solution. Usable films were obtained by drying in a vacuum oven overnight to ensure complete removal of the solvent. Subsequently, the lipid films were hydrated at 70 °C by vortex mixing with 16 g/L of FD solution or 160 µg/mL elcatonin solution in distilled water. Submicron-sized liposomes were prepared by using an extruder (LipoFast™-Pneumatic; Avestin, Inc., Ottawa, Canada) with a size-controlled polycarbonate membrane (0.1-µm membrane filter pore size). Extrusion was performed 41 times under nitrogen pressure (200 psi). The resulting vesicles were frozen and thawed three times by using a freezer and a water bath maintained at 40 °C. MPEG-DSPE solution in distilled water and GCS solution in acetate buffer (100 mM, pH 4.4) were used for surface modification to liposomes (Murata et al., 2012). An aliquot of the liposomal suspension was mixed with the same volume of the polymer solution of the different concentrations (0–15% w/v for MPEG-DSPE or 0.3% w/v for GCS as a final concentration). The mixed liposomal suspension with the MPEG-DSPE solution was incubated at 60 °C for 60 min. The final DSPC and FD concentrations in the resulting liposomal suspensions were 20 mM and 8 g/L, respectively.

### 2.3. Characterization of liposomes

Particle sizes and zeta potentials of the liposomes were measured by using a Zetasizer Nano ZS instrument (Malvern, Worcestershire, UK). Liposome samples were diluted 250-fold with distilled water before measuring particle size with a Zetasizer. Free model drug was separated from liposomes using ultracentrifugation (231,000g, 47 min) at 4 °C to determine the entrapment efficiency of FD or elcatonin. FD concentrations in the supernatants were then determined using a fluorescence spectrophotometer (POLARstar Galaxy, BMG Labtech, Ortenberg, Germany) with excitation and emission wavelengths of 485 and 530 nm, respectively. Elcatonin concentrations in supernatants were determined using the Micro BCA protein assay kit (Bio-Rad, CA, USA). The entrapment efficiencies of elcatonin and hydrophobic fluorescence dye in each liposome were around 100% (Murata et al., 2012; Tahara et al., 2018).

### 2.4. Mucin particle method

The mucin particle method was used to evaluate the interaction between mucin and PEG/GCS as surface modifiers, as previously described (Thongborisute and Takeuchi, 2008). The detailed procedure of the mucin particle method is described in the Supplementary Methods. Briefly, a mucin suspension was prepared by filtering a mucin-concentrated suspension. Equal volumes of the mucin suspension and polymer solution were mixed on a vortex mixer. The mixtures were incubated at 37 °C for 1 h. The turbidity of the mixture was measured by UV-Vis spectrophotometry (model UV-1800; Shimadzu, Kyoto, Japan) at 500 nm.

### 2.5. Evaluation of mucus interaction with liposomes in an artificial mucus model

The interaction between liposomes and mucus was evaluated in an *in vitro* artificial mucus model, as described in a previous report (Yang et al., 2011). Details of the preparation of the artificial mucus are described in the Supplementary Methods. One milliliter of a 10% gelatin solution dissolved in hot water was added to screw-cap vials (φ27 mm) and then hardened at 4 °C. One milliliter of the artificial mucus solution was placed statically on top of the gelatin gel layer. Then, 250 µL of the FD4-loaded liposomes labeled with Nile Red was added on top of the mucosal layer, and the behavior of the dye was observed from the top

and side of the vial.

## 2.6. Cell culture

Caco-2 and HT29-MTX E12 cells (American Type Culture Collection, Manassas, VA) were cultured in 75-cm<sup>2</sup> flasks with DMEM supplemented with 10% (v/v) FBS, 1% (v/v) NEAA, 1% (v/v) L-glutamine, and 1% (v/v) penicillin–streptomycin at 37 °C in an atmosphere of 5% CO<sub>2</sub>.

## 2.7. Cellular uptake by confocal laser scanning microscope

Aliquots of Caco-2 and Caco-2/HT29-MTX co-culture (75:25 ratio) were added to Lab-Tek® II Chamber Slides (Nalgen Nunc International, Rochester, NY, USA) at a density of  $3.125 \times 10^4$  cells/well and cultured for 22 days (Akbari et al., 2017). The cells were then washed, and C6-labeled liposomal suspension in serum-free DMEM was added followed by incubation at 37 °C for 1 h. Subsequently, the liposomal suspensions were removed, and the cell layers were washed three times with phosphate-buffered saline (PBS). After nuclei staining by Hoechst 33342, the cells were washed three times in ice-cold PBS and cell monolayers were fixed with 0.5 mL of 4% paraformaldehyde solution for 1 h. After another wash with PBS, the fixed cells were observed by using a confocal laser scanning microscope (CLSM; LSM-700; Carl Zeiss, Jena, Germany).

## 2.8. Cellular uptake by flow cytometry

Caco-2 cells and Caco-2/HT29-MTX (75:25 ratio) were seeded into 24-well plates at a density of  $5.0 \times 10^4$  cells/well and cultured for 21 days. After incubation, the culture media were removed, and C6-labeled liposomes in serum-free DMEM were added and incubated at 37 °C for 1 h. Subsequently, the liposomal suspensions were removed, and the cells were washed three times with PBS. The cells were then trypsinized and collected by centrifugation. The cell pellets were suspended in fresh PBS. Finally, C6-labeled liposomes that interacted with cells were assayed by using a FACSVerse flow cytometer (BD Biosciences, San Jose, CA) with an excitation wavelength of 488 nm and bandpass filters of 527/32 nm (for FITC detection), and data were analyzed using BD FACSuite software.

## 2.9. Animal experiments

All experiments were approved and monitored by the Institutional Animal Care and Use Committee of Gifu Pharmaceutical University (Approval number: 2018–024 and 2019–075) and performed under Japanese legislation on animal studies. Male Wistar rats (8–9 weeks old, SLC, Japan) were used in all *in vivo* studies. Before the experiment, the rats were fasted for 24 h and supplied with water *ad libitum*.

## 2.10. In vivo evaluation of oral FD4/FD10 formulations

Intragastric tubes were used to orally administer FD4/FD10-loaded liposomes to rats. The liposomal suspension administered (1 mL/rat) contained 20 mM lipids and 8.0 mg/mL FD. A 0.35-mL aliquot of blood was collected from the jugular vein before and 0.5, 1, 2, 4, and 6 h after administration. From the collected blood, blood cells were separated by centrifugation to obtain plasma. For quantification of FD in plasma, the sample was added to a 96-well microplate, and the fluorescence intensity was measured by using a 96-well plate reader (POLARstar Galaxy; Cary, NC, USA; Ex: 485 nm; Em: 530 nm).

The distribution of DiI-labeled liposomes and FD4 in the intestinal tract was observed by fluorescence microscopy. After 1 h of oral administration, the small intestine as a whole tissue was removed and opened along the mesenteric border. Once the intestine was opened, exposing the lumen, it was then transferred to a tube containing cold PBS and shaken for washing. The opened intestine was mounted onto a

glass-bottomed base dish with the luminal side up. The DiI-labeled liposomes and FD4 localization in the luminal side of the intestine were observed by fluorescence microscopy (BZ-9000; Keyence, Osaka, Japan).

## 2.11. In vivo pharmacological effect of oral elcatonin

The oral absorption of elcatonin from the different formulations was evaluated by measuring the blood calcium level (Murata et al., 2012). The samples were orally administered to rats (1 mL/rat) at a calcitonin dose of 500 IU/kg. Blood was collected from the jugular vein over 24 h, and the plasma was separated for determination of calcium concentration using the Calcium E test (Wako, Japan). The areas above the blood calcium level curves (AAC) were calculated for estimation of the relative pharmacological efficacy.

## 2.12. Statistical analysis

Statistical comparisons were made by performing Student's *t*-test or one-way ANOVA followed by Scheffe's test. Values of *p* < 0.05 were considered to be indicative of statistical significance.

# 3. Results and discussion

## 3.1. Characterization of surface-modified liposomes

In this study, we focused on PEGylated liposomes based on DSPC/Chol as drug carriers for hydrophilic high-molecular-weight drugs to improve oral absorption in the GI tract by imparting mucus-penetrating properties by high-density PEG surface modification. DSPC liposomes are stable in acidic solutions (pH 2.0), diluted bile and pancreatin solutions, as previously described (Aramaki et al., 1993). DSPC liposomes protected encapsulated peptides against digestive enzymes (Thongborisute et al., 2006). DSPC liposomes, as peptide drug carriers, also increased oral bioavailability of calcitonin (Takeuchi et al., 2005). Therefore, DSPC liposomes were selected in this study. A representative mucoadhesive liposome with GCS modification was also prepared to compare with the MPPs. SPM, an absorption enhancer, was incorporated into the DSPC liposome as a core particle to improve the oral absorption of FD or peptide drugs (Makhlof et al., 2011; Sugita et al., 2007). The characteristics and abbreviations of the different DSPC/Chol-based liposomes prepared in this study are shown in Table 1. Reportedly, it is necessary to modify the nanoparticles with a PEG concentration of ≥5 mol% to provide them with mucus permeability (Wang et al., 2008). The unmodified liposome showed a particle size of approximately 100 nm, and the particle size was slightly larger for the PEGylated liposomes than for the unmodified liposomes. The zeta potential was neutral in the unmodified liposomes and negative in the PEGylated liposomes because of the phosphate group of MPEG-DSPE, indicating a concentration-dependent decrease in the zeta potential. However, the zeta potential of 15% PEG did not decrease relative to that of 10% PEG, suggesting that the MPEG-DSPE on the liposome surface reached saturation and some free MPEG-DSPE molecules were present. The zeta potential of liposomes containing cationic SPM, a versatile absorption promoter, was positively shifted relative to that of unmodified liposomes; the zeta potential was negatively shifted in PEG-modified SPM liposomes, in which SPM liposomes were modified with MPEG-DSPE. Mucoadhesive liposomes were prepared with GCS as a surface modifier, and DCP was incorporated into DSPC/Chol liposomes to give the core liposomes a negative charge (Tahara et al., 2018). A mixture was prepared of negatively charged DCP liposomes and a cationic GCS solution modified by electrostatic interaction. GCS modification caused the liposomes to aggregate, and the particle size was increased to approximately 800 nm. GCS-modified DCP liposomes containing SPM showed particle properties similar to those without SPM. The loading efficiencies of FD4 and FD10 in liposomes were approximately 20–30%.



**Table 1**

Characteristics of FD4 loaded liposomes formulated with different surface properties and lipid compositions. Data are presented as means  $\pm$  SD (SD; n = 3–4).

| Abbreviation | Surface modifiers | Liposomal composition (Molar ratio)    | Average particle size (nm) | Polydispersity | Zeta potential (mV) |
|--------------|-------------------|--|----------------------------|----------------|---------------------|
| Unmodified   | —                 | DSPC/Chol = 8/1                        | 109.0 $\pm$ 8.8            | 0.18 $\pm$ 0.1 | 0.2 $\pm$ 2.5       |
| 3% PEG       | PEG               | DSPC/Chol/MPEG-DSPE = 7.73/1/0.27      | 117.0 $\pm$ 8.5            | 0.10 $\pm$ 0.0 | −34.5 $\pm$ 9.4     |
| 7% PEG       | PEG               | DSPC/Chol/ MPEG-DSPE = 7.37/1/0.63     | 134.0 $\pm$ 4.9            | 0.11 $\pm$ 0.0 | −51.1 $\pm$ 0.6     |
| 10% PEG      | PEG               | DSPC/Chol/ MPEG-DSPE = 7.1/1/0.9       | 126.6 $\pm$ 7.3            | 0.12 $\pm$ 0.0 | −53.0 $\pm$ 1.7     |
| 15% PEG      | PEG               | DSPC/Chol/ MPEG-DSPE = 6.65/1/1.35     | 127.0 $\pm$ 1.4            | 0.14 $\pm$ 0.0 | −48.4 $\pm$ 2.7     |
| SPM          | —                 | DSPC/Chol/SPM = 8/1/2                  | 118.4 $\pm$ 10.5           | 0.11 $\pm$ 0.1 | 34.3 $\pm$ 2.1      |
| PEG-SPM      | PEG               | DSPC/Chol/SPM/ MPEG-DSPE = 7.1/1/2/0.9 | 113.4 $\pm$ 7.2            | 0.12 $\pm$ 0.0 | −9.9 $\pm$ 0.9      |
| GCS          | GCS               | DSPC/Chol/DCP = 8/1/0.5                | 843.8 $\pm$ 177.5          | 0.24 $\pm$ 0.0 | 46.0 $\pm$ 1.7      |
| GCS-SPM      | GCS               | DSPC/Chol/DCP/SPM = 8/1/0.5/2          | 796.7 $\pm$ 97.3           | 0.46 $\pm$ 0.1 | 31.1 $\pm$ 10.0     |

PEG, Polyethylene glycol; DSPC, 1,2-Distearoyl-*sn*-glycero-3-phosphocholine; Chol, Cholesterol; DCP, Dicyetyl phosphate; SPM, Spermine; GCS, Glycol chitosan.

### 3.2. Mucus-penetrating and mucoadhesive properties

To confirm the interaction of the surface modifiers used in this study (PEG and GCS) with mucin, the mucoadhesive properties were confirmed by the mucin particle method (Thongborisute and Takeuchi, 2008). After mixing the mucin suspension with the polymer solution, the turbidity was generally increased in mucin-adherent polymers because of the agglomeration of mucin particles. Fig. 1 shows the turbidity representing the interaction with the mucin suspension at a polymer concentration of 0.3% (w/v). The turbidity of the PEG solution was negligible even when the mucin concentration was increased, suggesting that PEG and mucin do not interact. The mixture of GCS solution and mucin suspension showed significantly higher turbidity, confirming that GCS has mucoadhesive properties.

Using an artificial mucus model (Yang et al., 2011), the mucus adhesion and mucus permeability of FD4-loaded GCS and PEGylated liposomes were visually evaluated, respectively (Fig. 2). Nile Red-labeled liposomes were incubated with artificial mucus on the gelatin layer in the vial. By capturing the snap of the top or side of the vial after the addition of liposomes, dye migration shown by Nile Red, which represents the liposome itself, and FD4 of the model drug were monitored in the artificial mucus. Hydrophobic fluorescent dyes are reported not to leak from liposomes during *in vitro* release studies (Li et al., 2016; Tahara et al., 2018). In the unmodified liposomes, a portion of the liposomes (Nile Red dye) gradually diffused through the artificial mucosal layer over 24 h, but most of the liposomes remained in the upper part of the mucosal layer. In the GCS-modified liposomes with mucosal adhesiveness, the liposomes hardly moved in the mucosal layer and remained at the initial site of addition after 24 h. Unlike the unmodified and GCS-

modified liposomes, the PEGylated liposomes reached the bottom of the artificial mucosal layer after 24 h, indicating that 10% PEG liposomes had mucus permeability. In all liposomes assessed in this study, the FD4-derived dye, unencapsulated or released from the liposomes, spread into the mucosal layer after 6 h and permeated into the agarose gel layer after 24 h. Fluorescence intensity of FD4 that reached the gelatin gel layer after 6 and 24 h showed 10% PEG > Unmodified > GCS, confirming the mucus permeability for 10% PEG and retention of the artificial mucus layer for GCS (Supplementary Fig. 1).

The mechanism of mucus permeability of the dense 10% PEG-modified liposomes was suggested to occur via the diffusion of the liposomes covered with the brush-like conformation of PEG chains through the pores of the mucin network without being tightly adsorbed to the artificial mucus (Yu et al., 2015). The dense brush conformation on the surface of MPPs formed a dynamic hydration layer and flexible PEG chains on the surface of the nanoparticles, forming an effective shield against mucus and exhibiting the mucus-penetrating property.

### 3.3. Cellular uptake of surface-modified liposomes by Caco-2 and Caco-2/HT29-MTX co-culture

Caco-2 cloned from human colon cancer cells differentiates under general culture conditions to form a cell layer with tight junctions with a polarity that distinguishes the intestinal and plasma sides. Caco-2 is a mucus-free cell model, whereas HT29-MTX comprises differentiated cup cells with mucus-secreting properties (Akbari et al., 2017). Thus, the Caco-2/HT29-MTX co-culture system closely mimics the intestinal epithelium, including the presence of a mucosal layer. Intracellular uptake of liposomes labeled with C6 in Caco-2 and Caco-2/HT29-MTX co-cultures was evaluated by CLSM and flow cytometry. Alcian Blue staining confirmed the absence of mucus in Caco-2 cells and presence of a mucosal layer on the cell surface of the co-culture system (Supplementary Fig. 2) (Akbari et al., 2017). MTS cytotoxic studies showed that liposomes were non-toxic in both Caco-2 and Caco-2/HT29-MTX co-cultures within the lipid concentration range used in this study (Supplementary Fig. 3).

Fig. 3a shows the results of intracellular uptake of different C6-labeled liposomes by flow cytometry. Intracellular uptake was significantly higher for PEGylated liposomes than for unmodified liposomes. Significant differences in cellular uptake among the three liposomal formulations were observed but are not marked in Fig. 3a. Dispersibility was slightly better for PEG-modified liposomes than for unmodified liposomes (Table 1), which may have resulted in increased intracellular uptake. The uptake of unmodified and PEG-modified liposomes was unchanged in both Caco-2 cells and the co-culture system. On the other hand, the uptake of GCS-modified liposomes was lower than that of unmodified liposomes, and the uptake of GCS-modified liposomes was significantly lower in the co-culture system than in Caco-2 cells. Uptake into epithelial cells via endocytosis is reduced for larger particle sizes (Tahara et al., 2009). The intracellular uptake of GCS-modified liposomes may have been reduced relative to that of unmodified liposomes because of the increased particle size caused by aggregation (Table 1).

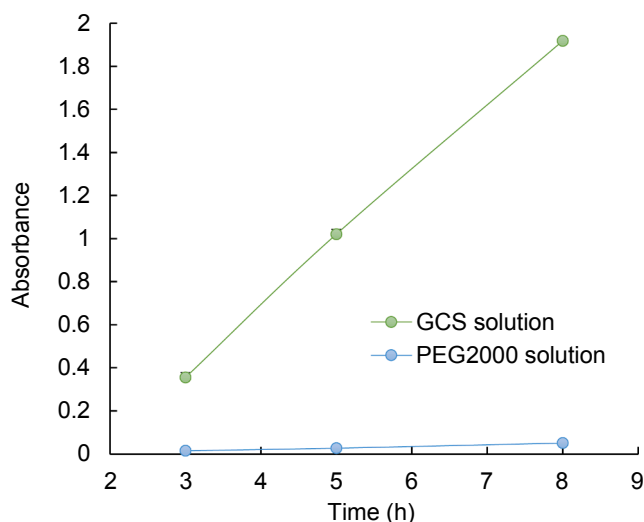


**Fig. 1.** Turbidity as a function of mucoadhesive strength tendency between GCS and PEG2000 solutions and the different concentrations of mucin by a mucin particle method. Symbols represent means  $\pm$  SDs (n = 3).

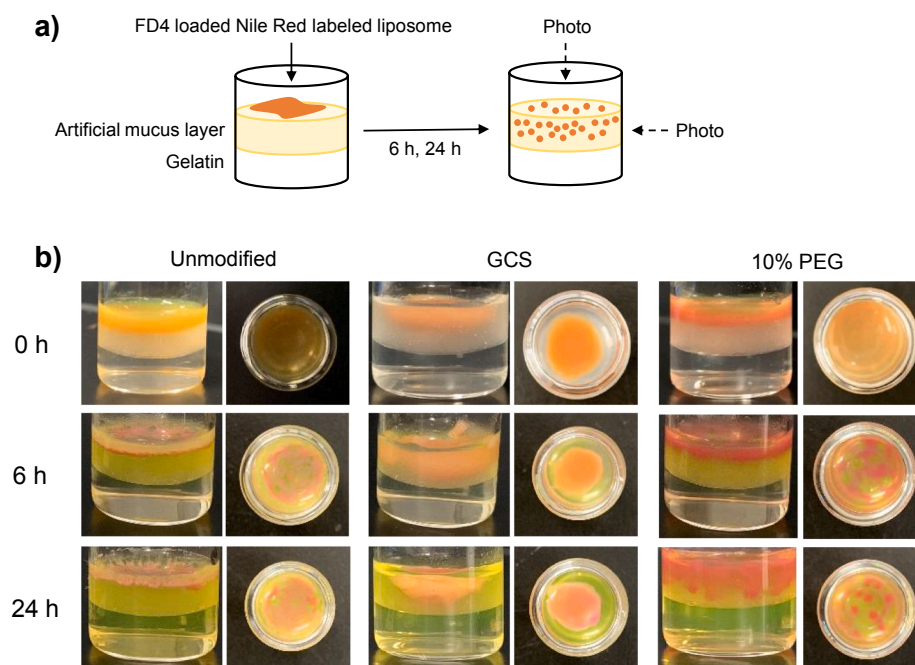


**Fig. 2.** Mucus interaction with the different liposomes in an artificial mucus model. (a) Shown is a schematic of the experimental procedure for visual inspection of Nile Red (liposomal marker) and FD4 (model drug) penetration in an artificial mucus model. (b) Photos of artificial mucus/gelatin layer in a vial to observe penetration of FD4-loaded liposomes labeled with Nile Red into artificial mucus.

#### a) Cellular uptake

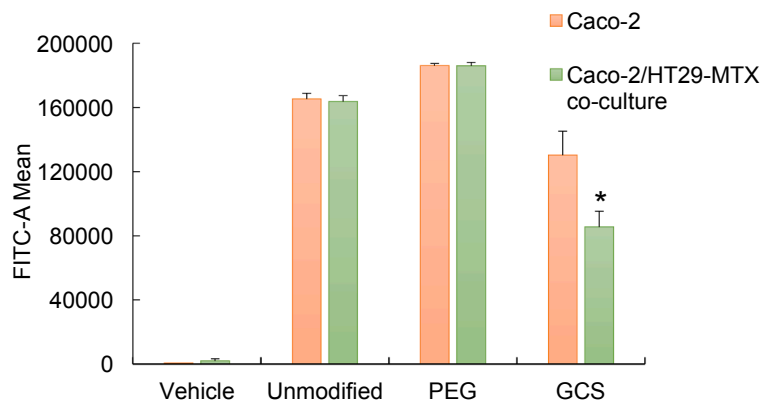
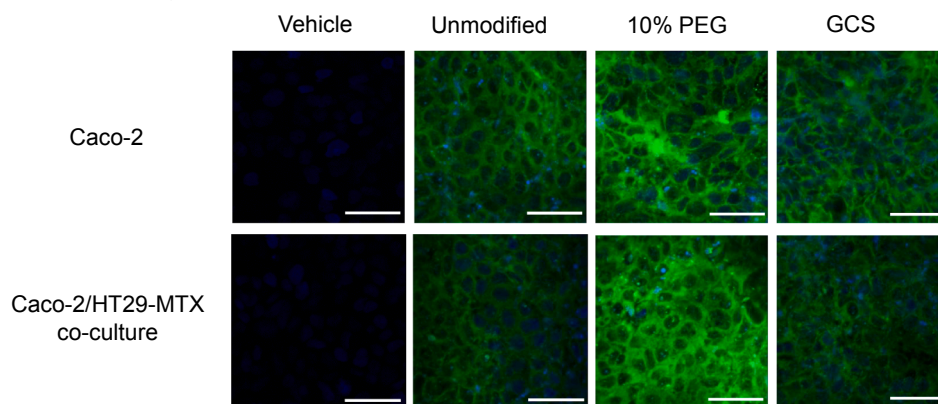


**Fig. 3.** Effect of surface properties of liposomes on liposomal interaction with Caco-2 and Caco-2/HT29 co-culture cells. (a) Mean fluorescence intensity of the cells measured by flow cytometry for cellular uptake of C6-labeled liposomes in Caco-2 and Caco-2/HT29 co-culture cells. Data are shown as means  $\pm$  SD ( $n = 4$  except for the vehicle data of Caco-2 with  $n = 1$ ); \* $p < 0.05$  compared with Caco-2. (b) CLSM images of Caco-2 and Caco-2/HT29 co-culture cells following 1 h of uptake of different liposomal preparations containing C6. Nuclei were stained by Hoechst 33342. Scale bar is 50  $\mu$ m.

#### b) CLSM images



The intracellular uptake of GCS-modified liposomes was reduced in the presence of mucus in the co-culture system. The GCS-modified liposomes attached to the mucosal layer on the cell surface may have been removed along with the mucus by washing the cells.

Fig. 3b shows the results of CLSM observation of cells taken up with C6 liposomes. The nuclei of the cells were stained by using Hoechst 33342. The fluorescence of C6 observed in the cells was greater in the order of PEG > Unmodified > GCS modification and correlated with the flow cytometric results (Fig. 3a).

### 3.4. Effect of liposomal surface modifiers on FD4 oral absorption

To compare the oral absorption of PEGylated SPM liposomes as MMPs and mucoadhesive GCS-modified SPM liposomes, the blood concentration profiles of the FD4-encapsulated liposomes administered orally to rats were evaluated. FD4 is released from liposomes in conditions that simulate the pH at the drug absorption site in the duodenum and ileum of the small intestine (Thongborisute, 2007). We confirmed in other experiments that oral absorption of GCS-SPM liposomes is higher than absorption of unmodified SPM liposomes and GCS liposomes without SPM (manuscript in preparation). As shown in Fig. 4a, blood concentrations were higher in PEG-modified liposomes than in GCS-modified liposomes. However, the average particle size of aggregated GCS-modified liposomes (769.7 nm) was larger than that of PEG-modified liposomes, as shown in Table 1. Several reports have stated that the size of oral nanoparticles affected oral bioavailability and that larger drug carriers had lower bioavailability than smaller ones (Desai et al., 1996; Ong et al., 2016; Shakweh et al., 2005). The large specific surface area of nanoparticles facilitates interaction with mucus and mucous membranes of the GI tract, and increases systemic drug absorption. However, as particle size increases through aggregation, interaction with the mucosa is reduced, resulting in low bioavailability (Takeuchi et al., 2001). The FD4 absorption by GCS-modified liposomes is expected to be higher by optimizing the GCS concentration and other factors to create a surface modification method that prevents particle aggregation.

Pharmacokinetics parameters were calculated from the blood concentration profiles of FD4 by using a moment analysis method, and the parameters of the mean residence time (MRT) of GCS-SPM were

compared with that of PEG-SPM (Supplementary Table 1). The MRT was longer for GCS-SPM than for PEG-SPM, although the AUC value was much lower for GCS than for PEG. The results suggested that GCS-modified liposomes adhered to the mucosa and remained more persistently in the GI tract than MMPs.

To investigate the behavior of liposomes and FD4 in the gastrointestinal tract, small-intestinal tissue sections were observed by fluorescence microscopy (Fig. 4b), rats were orally administered FD4-loaded liposomes labeled with DiI, and the small intestines were excised. The luminal side of the small intestine was observed under a fluorescence microscope. In both liposomes, FD4 fluorescence was observed on the surface of the small intestine. DiI fluorescence was observed throughout the villi, but in the case of PEGylated liposomes, slight fluorescence was also observed at locations near the Peyer's patch. Differences in particle size distribution between PEG- and GCS-modified liposomes are likely to affect their localization around the Peyer's patch (Shakweh et al., 2005).

### 3.5. Effect of MPEG-DSPE concentration in liposomes on oral absorption

The mucus permeability of PEGylated liposomes is greatly affected by the concentration of PEG modification. Therefore, we orally administered 3%, 7%, 10%, and 15% PEGylated FD4-encapsulated liposomes to rats and compared the changes in blood FD4 concentrations (Fig. 5). Although FD4 was barely absorbed by oral administration of FD4 solution, FD4 inclusion in liposomes (unmodified liposomes) increased the blood concentration of FD4. In the case of high-density PEG-modified liposomes, there may be free MPEG-DSPE that is not incorporated into the liposome. The mixture of MPEG-DSPE solution and FD4 solution was almost the same as the oral absorption of the FD4 solution, indicating that free MPEG-DSPE did not affect the absorption of FD4.

Blood levels of FD4 were higher in PEG-modified liposomes than in unmodified liposomes. As the concentration of MPEG-DSPE in liposomes increased, the blood concentration of FD4 increased, but the blood concentration was lower in 15% PEG than in 10% PEG.

The reduction in mucus-penetrating properties because of excessive PEG modification was consistent with the finding in a report about PEG-modified poly(anhydride) nanoparticles (Inchaurrega et al., 2015). It has been reported that the PEG chains on the surface of nanoparticles can be brush-shaped or mushroom-shaped (Huckaby and Lai, 2018). The

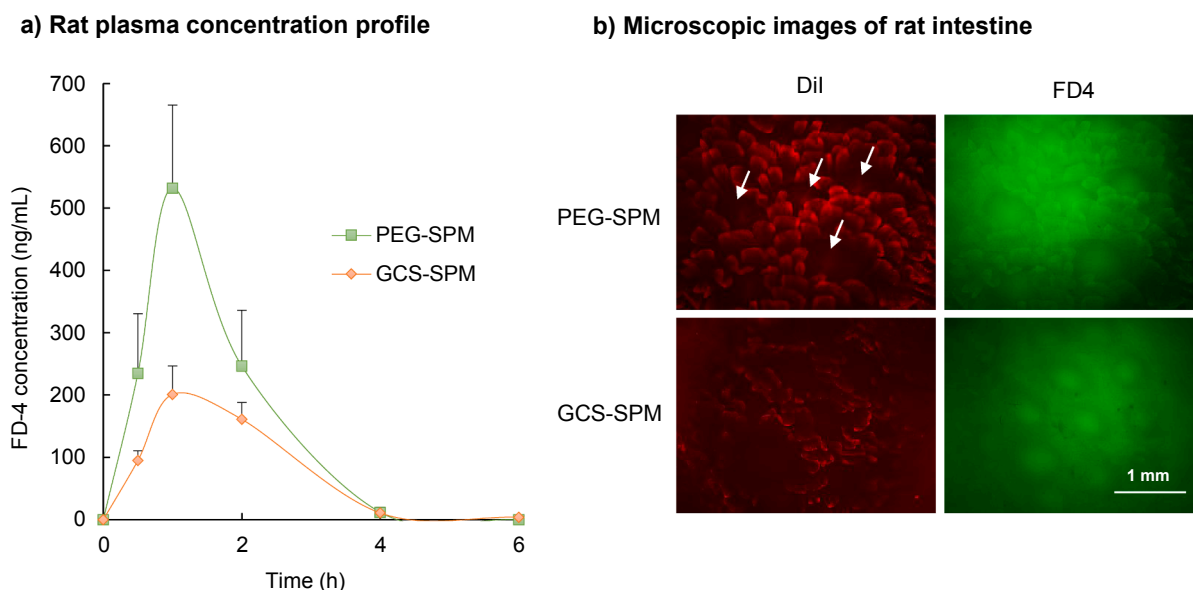


**Fig. 4.** Comparison of FD4 absorption in rats between orally administered mucoadhesive liposomes (GCS) and mucus-penetrating liposomes (PEG) incorporating SPM. (a) Plasma concentration–time profiles of FD4 in rats after oral administration of GCS-SPM and PEG-SPM formulations. Symbols are expressed as the means  $\pm$  SEM ( $n = 5-7$ ). (b) Fluorescence microscopic images of rat intestinal tissues (lumen side) obtained 1 h after oral administration of FD4-loaded GCS-SPM and PEG-SPM liposomes labeled with DiI. White arrows indicate the DiI present on the Peyer's patches.

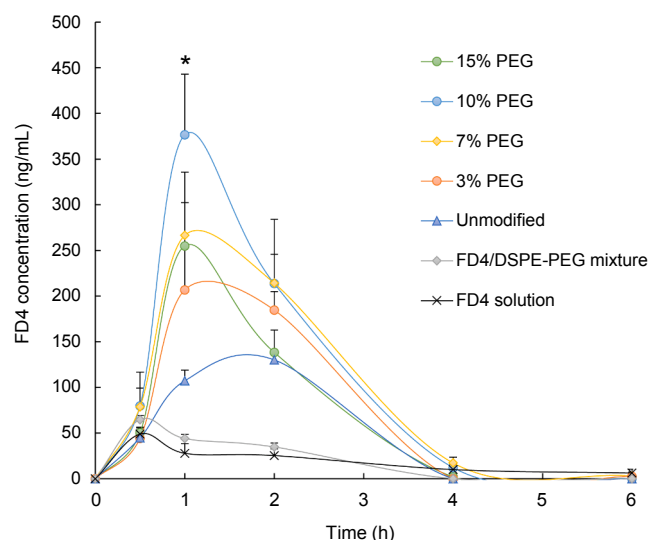


**Fig. 5.** Effect of MPEG-DSPE concentrations in liposomes as MPPs shown by FD4 plasma concentration–time profiles in rats after oral administration of different PEGylated liposomes. Symbols are expressed as the means  $\pm$  SEM ( $n = 4$ –5). \* $p < 0.05$  compared with Unmodified.

dense-brush conformation exhibits mucus permeability because of the formation of a dynamic hydration layer on the surface of the nanoparticles and the relative flexibility of the PEG chains. An excessively dense MPEG-DSPE coating would result in a less flexible surface polymer layer of liposome with entanglements between PEG chains that would cause their interaction with components of the mucosal layer (Inchaurraga et al., 2015). Another possibility is that excessive PEG may limit mucus permeability would be de-PEGylation caused by stealth liposomes formed by free MPEG-DSPE that can form micelles (Paolino et al., 2017). In any case, further investigation will be needed to elucidate the mechanisms of these potential effects.

The application of mucus-permeable PEG-modified liposomes for vaginal administration is reported (Yu et al., 2015). The authors suggest that liposomes modified with 7% PEG or higher are coated with brush-like PEG chains and form an effective shield against mucus, whereas liposomes with less than 5% PEG are covered with mushroom-like PEG

chains, suggesting that they are less effective at shielding. In Fig. 5, the highest blood levels were found at 10% PEG, despite the similar particle size and zeta potential of 7% PEG and 10% PEG (Table 1). For vaginal administration, 7% PEG modification was sufficient to confer mucus permeability, whereas for oral administration, higher concentrations of PEG are necessary because oral liposomes are diluted by gastrointestinal juices. Optimizing PEG concentration would be important based on route of administration.

### 3.6. Effect of spermine incorporated into liposomes on oral absorption

SPM generally acts as an activator of extracellular calcium-sensing receptors, causing phosphorylation of myosin light chains following an increase in intracellular calcium levels that then leads to tight junction opening in the epithelial cell layer (Sugita et al., 2007). However, orally administered absorption enhancers, such as SPM, are subjected to the dilution effect of GI fluid, resulting in the spread of the enhancer molecules over a large surface. Moreover, enzymatic degradation of peptide drugs could further limit the usefulness of orally administered absorption enhancers. Makhlof et al. demonstrated that these drawbacks of absorption enhancers could be overcome by immobilizing the enhancer in a nanoparticulate system (Makhlof et al., 2011).

To increase the bioavailability of PEGylated liposomes for oral MMPs, PEGylated liposomes incorporating SPM, a known absorption promoter, (Makhlof et al., 2011; Sugita et al., 2007) were orally administered to rats and blood levels of FD4 or FD10 were evaluated in this study. Fig. 6 shows the blood concentration of FD4 or FD10 in rats after oral administration. FD4 or FD10 solutions, unmodified liposomes, SPM liposomes, PEG-modified liposomes, and PEG-modified SPM liposomes were used. The modified concentration of PEG was 10% with the highest concentration of FD4 in the blood as shown in Fig. 5. The blood levels of FD4 were in the order of PEG-SPM > PEG > SPM > Unmodified > FD4 solution. Incorporation of SPM into liposomes increased the blood levels of FD4. Orally administered liposomes, incorporating SPM, reach the vicinity of mucosal epithelium in the GI tract, and SPM in the liposomes interacts with the mucosal epithelium. This interaction may have triggered the opening of tight junctions and enhanced the absorption of FD4 released from the liposomes by the intercellular route. SPM liposomes with dense 10% PEG modification showed the highest blood levels of FD among the liposomal formulations evaluated in Fig. 6 due to synergistic effects on enhancing absorption via the intercellular

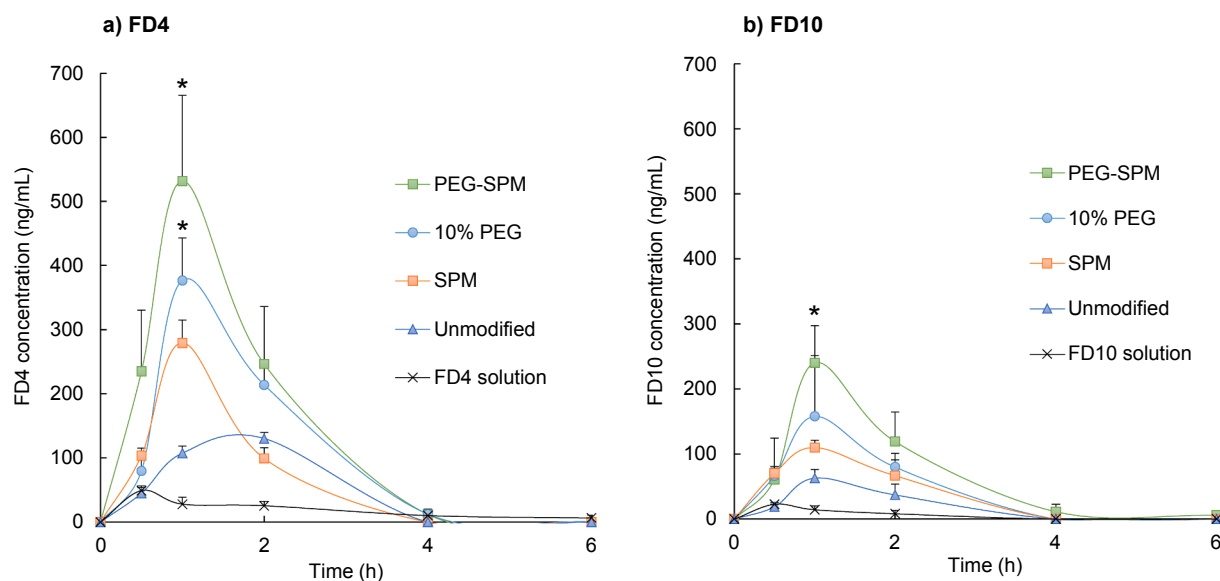


**Fig. 6.** Effects of SPM incorporated into liposomes and of the molecular weight of FD in (a) FD4 and (b) FD10 shown by plasma concentration–time profiles in rats after oral administration of different liposomal formulations. Symbols are expressed as the means  $\pm$  SEM ( $n = 3$ –7). \* $p < 0.05$  compared with Unmodified.



route by SPM and mucus permeability by dense PEG chains. Blood concentrations of the FD10 formulation were in the order of PEG-SPM > PEG > SPM > Unmodified > FD10 solution, with the same absorption pattern as that of FD4. The inclusion of SPM in PEG-modified liposomes improved the oral absorption of FD10.

The maximum blood concentration of FD10 was approximately one-half that of FD4 irrespective of formulations, indicating that the absorption of oral liposomes was affected by the molecular weight of the drug. Molecular weight-dependent oral absorption of FD also has been reported when the cell-penetrating peptides were used as a drug carrier (Kamei et al., 2016). Similar to the results of the present study, the smaller the molecular weight of FD, the greater the oral absorption. Assuming that the liposome itself passes through the GI epithelial cells and transfers to the blood vessels by the intracellular route, oral absorption of drug-loaded liposomes would be unaffected by the drug's molecular weight. Thus, the drug absorption mechanism of oral liposomes would be that the drugs released from liposomes in the vicinity of mucosal epithelial cells are absorbed by passive diffusion through epithelial cells.

### 3.7. Pharmacological effect of elcatonin-loaded PEGylated liposomes by oral administration

As shown in Fig. 6, in the case of FD4/FD10, the oral absorption of PEGylated liposomes incorporating SPM was the most effective for improving the bioavailability among the liposome preparations evaluated in this paper. Iwanaga et al. demonstrated that PEG-modified liposomes enhance peptide stability in the GI tract by protecting drugs against digestion by bile salts in the intestinal fluid (Iwanaga et al., 1997). PEGylated SPM liposomes are expected to improve the stability in the GI tract and increase the pharmacological effect by the mucus permeability and absorption promotion effect of SPM. The pharmacological effects of oral liposomes were evaluated by using elcatonin as a model drug. Elcatonin solution, unmodified liposomes, SPM liposomes, PEG liposomes, and SPM-containing PEGylated liposomes were administered orally to rats to evaluate blood calcium concentration changes. Fig. 7a shows the blood calcium concentration profile, and Fig. 7b shows the results of calculating the AAC from blood calcium concentration. The pharmacological effect of oral elcatonin was greater for SPM > 10% PEG > PEG-SPM > Unmodified > Elcatonin solution, which was different from the case of FD4/FD10 in which PEG-SPM was the most

absorbable (Fig. 6). Polypeptide hormones, such as elcatonin, are more strongly affected by degradative enzymes in the GI tract than FD4/FD10. In the case of elcatonin, it has been reported that nanoparticles incorporating SPM showed partial protection of the substrate against trypsin degradation (Makhlof et al., 2011). The SPM used in this study may have an inhibitory effect on the enzymatic degradation of elcatonin in the GI tract. It was reported that as similar polypeptide hormones, the plasma concentration of salmon calcitonin was not predictive of its clinical therapeutic effect (Fan et al., 2014). Moreover, there is a non-linear relationship between serum calcium and the concentrations in plasma of salmon calcitonin (Miyazaki et al., 2003). There may be inconsistencies in the blood levels of elcatonin (calcitonin from eels) and the calcium level reduction in our experimental results (Fig. 7), as in previous reports of salmon calcitonin.

The results of the *in vivo* oral FD4/FD10 absorption experiments (Fig. 6) show that oral PEGylated liposomes were permeable in the GI mucosa and helped improve absorption of FD4/FD10. However, there was no correlation between FD4/FD10 absorption and the pharmacological effect of elcatonin in oral liposomes, suggesting that the design of oral liposomal formulations should account not only for the GI behavior of liposomes but also for the characteristics of the peptide drug itself, such as the stability, absorption properties, and mechanism of action.

## 4. Conclusions

In this study, we attempted to improve the oral absorption of macromolecular drugs, such as peptides, by loading them into densely PEGylated liposomes with mucus permeability. The permeability of oral liposomes in mucus was improved by dense modification with PEG, although excessive PEG decreased systemic absorption of FD4. The mucus interaction and absorption mechanism of PEGylated liposomes in the GI tract was different from that of GCS-modified liposomes, which show mucosal adhesion. The oral absorption of FD4/FD10 was improved by incorporating SPM, an absorption enhancer, into 10% PEGylated liposomes. The pharmacological effects of different types of oral liposomal formulations were evaluated by using elcatonin as a model peptide drug, but they did not correlate with the blood concentration pattern of FD4/FD10.

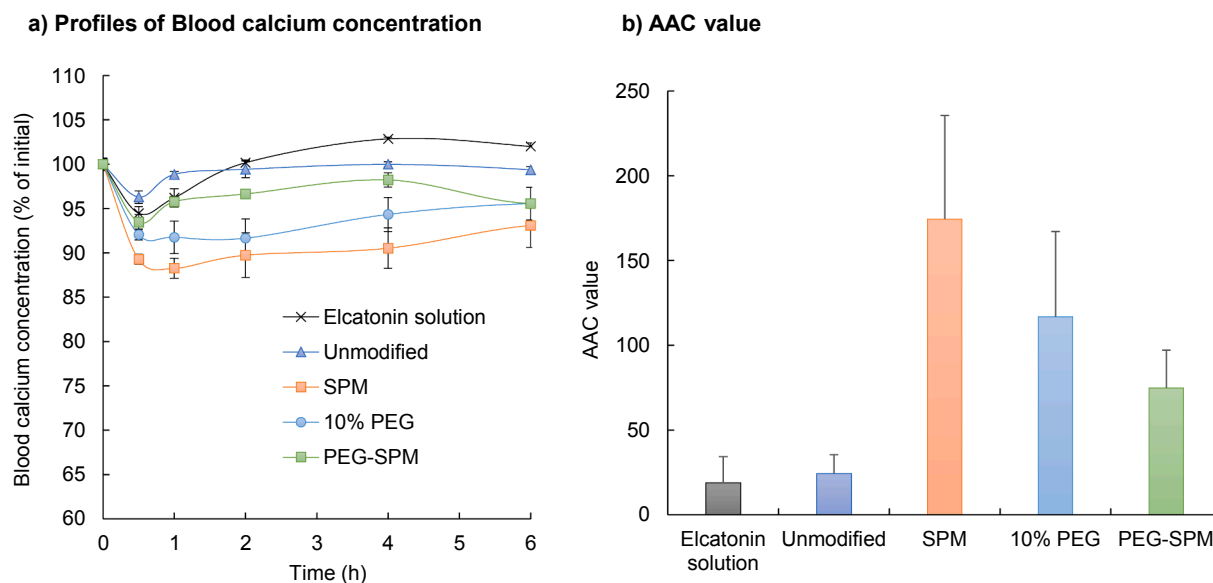


Fig. 7. (a) Plasma calcium level profiles after oral administration of elcatonin-loaded liposomes. Values represent the mean  $\pm$  SEM ( $n = 4-5$ ). (b) Area above the blood calcium concentration-time curves (AAC) after oral administration of elcatonin-loaded liposomes in rats. Data represent the mean  $\pm$  SEM ( $n = 4-5$ ).

## CRediT authorship contribution statement

**Eriko Yamazoe:** Investigation, Formal analysis, Writing - original draft. **Jia-You Fang:** Writing - review & editing. **Kohei Tahara:** Supervision, Conceptualization, Writing - review & editing, Project administration, Funding acquisition.

## Declaration of Competing Interest

The authors declare that they have no known competing financial interests or personal relationships that could have appeared to influence the work reported in this paper.

## Acknowledgments

This work was supported by a research grant from the Nakatomi Foundation, the Mochida Memorial Foundation, and JSPS KAKENHI Grant Number 18K06753.

## Appendix A. Supplementary material

Supplementary data to this article can be found online at <https://doi.org/10.1016/j.ijpharm.2020.120148>.

## References

- Akbari, A., Lavasanifar, A., Wu, J., 2017. Interaction of cruciferin-based nanoparticles with Caco-2 cells and Caco-2/HT29-MTX co-cultures. *Acta Biomater.* 64, 249–258. <https://doi.org/10.1016/j.actbio.2017.10.017>.
- Alp, G., Aydogan, N., 2020. Lipid-based mucus penetrating nanoparticles and their biophysical interactions with pulmonary mucus layer. *Eur. J. Pharm. Biopharm.* 149, 45–57. <https://doi.org/10.1016/j.ejpb.2020.01.017>.
- Aramaki, Y., Tomizawa, H., Hara, T., Yachi, K., Kikuchi, H., Tsuchiya, S., 1993. Stability of liposomes in vitro and their uptake by rat Peyer's patches following oral administration. *Pharm. Res.* 10, 1228–1231. <https://doi.org/10.1023/A:1018936806278>.
- Cao, S.J., Xu, S., Wang, H.M., Ling, Y., Dong, J., Xia, R.D., Sun, X.H., 2019. Nanoparticles: oral delivery for protein and peptide drugs. *AAPS PharmSciTech* 20, 190. <https://doi.org/10.1208/s12249-019-1325-z>.
- Desai, M.P., Labhasetwar, V., Amidon, G.L., Levy, R.J., 1996. Gastrointestinal uptake of biodegradable microparticles: effect of particle size. *Pharm. Res.* 13, 1838–1845. <https://doi.org/10.1023/a:1016085108889>.
- Drucker, D.J., 2020. Advances in oral peptide therapeutics. *Nat. Rev. Drug Discovery* 19, 277–289. <https://doi.org/10.1038/s41573-019-0053-0>.
- Ensign, L.M., Cone, R., Hanes, J., 2012. Oral drug delivery with polymeric nanoparticles: the gastrointestinal mucus barriers. *Adv. Drug Del. Rev.* 64, 557–570. <https://doi.org/10.1016/j.addr.2011.12.009>.
- Fan, T., Chen, C., Guo, H., Xu, J., Zhang, J., Zhu, X., Yang, Y., Zhou, Z., Li, L., Huang, Y., 2014. Design and evaluation of solid lipid nanoparticles modified with peptide ligand for oral delivery of protein drugs. *Eur. J. Pharm. Biopharm.* 88, 518–528. <https://doi.org/10.1016/j.ejpb.2014.06.011>.
- Huckaby, J.T., Lai, S.K., 2018. PEGylation for enhancing nanoparticle diffusion in mucus. *Adv. Drug Del. Rev.* 124, 125–139. <https://doi.org/10.1016/j.addr.2017.08.010>.
- Inchaurraga, L., Martin-Arbella, N., Zabaleta, V., Quincoces, G., Penuelas, I., Irache, J.M., 2015. In vivo study of the mucus-permeating properties of PEG-coated nanoparticles following oral administration. *Eur. J. Pharm. Biopharm.* 97, 280–289. <https://doi.org/10.1016/j.ejpb.2014.12.021>.
- Iwanaga, K., Ono, S., Narioka, K., Morimoto, K., Kakemi, M., Yamashita, S., Nango, M., Oku, N., 1997. Oral delivery of insulin by using surface coating liposomes. *Int. J. Pharm.* 157, 73–80. [https://doi.org/10.1016/s0378-5173\(97\)00237-8](https://doi.org/10.1016/s0378-5173(97)00237-8).
- Joraholmen, M.W., Basnet, P., Acharya, G., Skalko-Basnet, N., 2017. PEGylated liposomes for topical vaginal therapy improve delivery of interferon alpha. *Eur. J. Pharm. Biopharm.* 113, 132–139. <https://doi.org/10.1016/j.ejpb.2016.12.029>.
- Kamei, N., Bech Nielsen, E.J., Nakakubo, T., Aoyama, Y., Rahbek, U.L., Pedersen, B.L., Takeda-Morishita, M., 2016. Applicability and limitations of cell-penetrating peptides in noncovalent mucosal drug or carrier delivery systems. *J. Pharm. Sci.* 105, 747–753. <https://doi.org/10.1016/j.xphs.2015.11.010>.
- Lai, S.K., Wang, Y.Y., Hanes, J., 2009. Mucus-penetrating nanoparticles for drug and gene delivery to mucosal tissues. *Adv. Drug Del. Rev.* 61, 158–171. <https://doi.org/10.1016/j.addr.2008.11.002>.
- Li, H., Guissi, N.E.I., Su, Z., Ping, Q., Sun, M., 2016. Effects of surface hydrophilic properties of PEG-based mucus-penetrating nanostructured lipid carriers on oral drug delivery. *RSC Adv.* 6, 84164–84176. <https://doi.org/10.1039/c6ra18724b>.
- Liu, M., Zhang, J., Shan, W., Huang, Y., 2015. Developments of mucus penetrating nanoparticles. *Asian J. Pharm. Sci.* 10, 275–282. <https://doi.org/10.1016/j.ajps.2014.12.007>.
- Makhlof, A., Werle, M., Tozuka, Y., Takeuchi, H., 2011. A mucoadhesive nanoparticulate system for the simultaneous delivery of macromolecules and permeation enhancers to the intestinal mucosa. *J. Controlled Release.* 149, 81–88. <https://doi.org/10.1016/j.jconrel.2010.02.001>.
- Miyazaki, M., Nakade, S., Iwanaga, K., Morimoto, K., Kakemi, M., 2003. Estimation of bioavailability of salmon calcitonin from the hypocalcemic effect in rats (I): pharmacokinetic-pharmacodynamic modeling based on the endogenous Ca regulatory system. *Drug Metab. Pharmacokinet.* 18, 350–357. <https://doi.org/10.2133/dmpk.18.350>.
- Murata, M., Nakano, K., Tahara, K., Tozuka, Y., Takeuchi, H., 2012. Pulmonary delivery of elcatonin using surface-modified liposomes to improve systemic absorption: polyvinyl alcohol with a hydrophobic anchor and chitosan oligosaccharide as effective surface modifiers. *Eur. J. Pharm. Biopharm.* 80, 340–346. <https://doi.org/10.1016/j.ejpb.2011.10.011>.
- Netsomboon, K., Bernkop-Schnurch, A., 2016. Mucoadhesive vs. mucopenetrating particulate drug delivery. *Eur. J. Pharm. Biopharm.* 98, 76–89. <https://doi.org/10.1016/j.ejpb.2015.11.003>.
- Niu, Z., Conejos-Sanchez, I., Griffin, B.T., O'Driscoll, C.M., Alonso, M.J., 2016. Lipid-based nanocarriers for oral peptide delivery. *Adv. Drug Del. Rev.* 106, 337–354. <https://doi.org/10.1016/j.addr.2016.04.001>.
- Ong, S.G., Ming, L.C., Lee, K.S., Yuen, K.H., 2016. Influence of the encapsulation efficiency and size of liposome on the oral bioavailability of griseofulvin-loaded liposomes. *Pharmaceutics* 8. <https://doi.org/10.3390/pharmaceutics8030025>.
- Paolino, D., Accolla, M.L., Cilurzo, F., Cristiano, M.C., Cosco, D., Castelli, F., Sarpietro, M.G., Fresta, M., Celia, C., 2017. Interaction between PEG lipid and DSPC/ DSPC phospholipids: an insight of PEGylation degree and kinetics of de-PEGylation. *Colloids Surf. B Biointerfaces* 155, 266–275. <https://doi.org/10.1016/j.colsurfb.2017.04.018>.
- Ponchel, G., Montisci, M.-J., Dembri, A., Durrer, C., Duchène, D., 1997. Mucoadhesion of colloidal particulate systems in the gastro-intestinal tract. *Eur. J. Pharm. Biopharm.* 44, 25–31. [https://doi.org/10.1016/S0939-6411\(97\)00098-2](https://doi.org/10.1016/S0939-6411(97)00098-2).
- Renunkuntla, J., Vadlapudi, A.D., Patel, A., Boddu, S.H., Mitra, A.K., 2013. Approaches for enhancing oral bioavailability of peptides and proteins. *Int. J. Pharm.* 447, 75–93. <https://doi.org/10.1016/j.ijpharm.2013.02.030>.
- Shakweh, M., Besnard, M., Nicolas, V., Fattal, E., 2005. Poly (lactide-co-glycolide) particles of different physicochemical properties and their uptake by peyer's patches in mice. *Eur. J. Pharm. Biopharm.* 61, 1–13. <https://doi.org/10.1016/j.ejpb.2005.04.006>.
- Sugita, Y., Takao, K., Toyama, Y., Shirahata, A., 2007. Enhancement of intestinal absorption of macromolecules by spermine in rats. *Amino Acids* 33, 253–260. <https://doi.org/10.1007/s00726-007-0532-1>.
- Tahara, K., 2020. Pharmaceutical formulation and manufacturing using particle/powder technology for personalized medicines. *Adv. Powder Technol.* 31, 387–392. <https://doi.org/10.1016/j.apt.2019.10.031>.
- Tahara, K., Nishio, M., Takeuchi, H., 2018. Evaluation of liposomal behavior in the gastrointestinal tract after oral administration using real-time in vivo imaging. *Drug Dev. Ind. Pharm.* 44, 608–614. <https://doi.org/10.1080/03639045.2017.1405972>.
- Tahara, K., Sakai, T., Yamamoto, H., Takeuchi, H., Hirashima, N., Kawashima, Y., 2009. Improved cellular uptake of chitosan-modified PLGA nanospheres by A549 cells. *Int. J. Pharm.* 382, 198–204. <https://doi.org/10.1016/j.ijpharm.2009.07.023>.
- Takeuchi, H., Matsui, Y., Sugihara, H., Yamamoto, H., Kawashima, Y., 2005. Effectiveness of submicron-sized, chitosan-coated liposomes in oral administration of peptide drugs. *Int. J. Pharm.* 303, 160–170. <https://doi.org/10.1016/j.ijpharm.2005.06.028>.
- Takeuchi, H., Yamamoto, H., Kawashima, Y., 2001. Mucoadhesive nanoparticulate systems for peptide drug delivery. *Adv. Drug Del. Rev.* 47, 39–54. [https://doi.org/10.1016/S0169-409X\(00\)00120-4](https://doi.org/10.1016/S0169-409X(00)00120-4).
- Thongborisute, J., 2007. Studies on polymer-coated liposomes for oral peptide drug delivery. Gifu Pharmaceutical University, Ph.D. Thesis. <https://doi.org/https://ci.nii.ac.jp/naid/500000387008>.
- Thongborisute, J., Takeuchi, H., 2008. Evaluation of mucoadhesiveness of polymers by BIACORE method and mucin-particle method. *Int. J. Pharm.* 354, 204–209. <https://doi.org/10.1016/j.ijpharm.2007.12.001>.
- Thongborisute, J., Tsuruta, A., Kawabata, Y., Takeuchi, H., 2006. The effect of particle structure of chitosan-coated liposomes and type of chitosan on oral delivery of calcitonin. *J. Drug Target.* 14, 147–154. <https://doi.org/10.1080/10611860600648346>.
- Wang, Y.Y., Lai, S.K., Suk, J.S., Pace, A., Cone, R., Hanes, J., 2008. Addressing the PEG mucoadhesivity paradox to engineer nanoparticles that “slip” through the human mucus barrier. *Angew. Chem. Int. Ed. Engl.* 47, 9726–9729. <https://doi.org/10.1002/anie.200803526>.
- Yang, Y., Tsifanskyy, M.D., Shin, S., Lin, Q., Yeo, Y., 2011. Mannitol-guided delivery of Ciprofloxacin in artificial cystic fibrosis mucus model. *Biotechnol. Bioeng.* 108, 1441–1449. <https://doi.org/10.1002/bit.23046>.
- Yu, T., Chan, K.W., Anonuevo, A., Song, X., Schuster, B.S., Chattopadhyay, S., Xu, Q., Oskolkov, N., Patel, H., Ensign, L.M., van Zijl, P.C., McMahon, M.T., Hanes, J., 2015. Liposome-based mucus-penetrating particles (MPP) for mucosal therapeutics: demonstration of diamagnetic chemical exchange saturation transfer (diaCEST) magnetic resonance imaging (MRI). *Nanomedicine* 11, 401–405. <https://doi.org/10.1016/j.nano.2014.09.019>.
- Zhou, X., Liu, Y., Huang, Y., Ma, Y., Lv, J., Xiao, B., 2019. Mucus-penetrating polymeric nanoparticles for oral delivery of curcumin to inflamed colon tissue. *J. Drug Delivery Sci. Technol.* 52, 157–164. <https://doi.org/10.1016/j.jddst.2019.04.030>.





# Label-free parathyroid hormone immunosensor using nanocomposite modified carbon electrode

Pravanjan Malla<sup>a</sup>, Guan-Cheng Chen<sup>a</sup>, Hao-Ping Liao<sup>a</sup>, Chi-Hsien Liu<sup>a,b,c,d,\*</sup>, Wei-Chi Wu<sup>d,e</sup>

<sup>a</sup> Department of Chemical and Materials Engineering, Chang Gung University, 259, Wen-Hwa First Road, Kwei-Shan, Tao-Yuan 333, Taiwan

<sup>b</sup> Research Center for Chinese Herbal Medicine and Research Center for Food and Cosmetic Safety, College of Human Ecology, Chang Gung University of Science and Technology, 261, Wen-Hwa First Road, Taoyuan, Taiwan

<sup>c</sup> Department of Chemical Engineering, Ming Chi University of Technology, 84, Gung-Juan Road, New Taipei City, Taiwan

<sup>d</sup> Department of Ophthalmology, Chang Gung Memorial Hospital, Linkou, 5, Fu-Hsing Street, Taoyuan, Taiwan

<sup>e</sup> College of Medicine, Chang Gung University, 259, Wen-Hwa First Road, Taoyuan, Taiwan

## ARTICLE INFO

### Article history:

Received 28 October 2020

Received in revised form 2 December 2020

Accepted 3 December 2020

Available online 08 December 2020

### Keywords:

Gold nanoparticles

Multi-walled carbon nanotube

Screen-printed electrode

Antibody

Parathyroid hormone

## ABSTRACT

An immunosensor based on screen-printed carbon electrode (SPCE) was explored to detect human parathyroid hormone (PTH). The SPCEs that were modified with nanocomposite containing gold nanoparticle (AuNP) and multi-walled carbon nanotube (MWCNT) were successfully prepared using electrochemical deposition. With these SPCEs, we explored the fabrication of a novel, disposable and sensitive immunosensor comprising nanocomposite, antibody, and horseradish peroxidase. The nanocomposite such as AuNP and MWCNT not only provided a large surface area for antibody immobilization, but it also enhanced the electrochemical signal on the modified SPCE. The nanocomposite modified SPCE was characterized in detail. The label-free impedimetric and amperometric measurements were not affected by interference from the components presented in serum. This PTH immunosensor showed the detection limit of 0.033 and 0.092 pg/mL for impedimetric and amperometric methods. We provided a quick analysis of PTH in serum, which can potentially be used as the electrochemical immunosensing platform for point-of-care testing.

## 1. Introduction

Parathyroid hormone (PTH) measurement is routinely used by physicians to diagnose and monitor patients with hyperparathyroidism, hypoparathyroidism or chronic kidney disease (CKD) [1]. PTH is important in maintaining calcium-phosphorus homeostasis, and it plays a vital role in regulating bone remodeling processes. A high PTH level in CKD patients will be related to their bone loss as well as elevated risks of cardiovascular and cerebrovascular diseases [2]. Monitoring the PTH level is essential for early diagnosis and therapeutic evaluation. Different methods such as enzyme linked immunosorbent assay (ELISA), magnetic immunoassay [3], electrochemiluminescence immunoassays [4], and liquid chromatography-mass spectrometric assay [5] have been used to detect PTH concentration. PTH radioimmunoassay has evolved into a highly sensitive and relatively fast test. PTH measurement is increasingly used in routine clinical practice since the availability of automated radioimmunoassay with excellent analytical performance in large hospitals [6]. However, the drawbacks of the radioimmunoassay include the potential hazard of isotopes, the need for trained personnel, and expensive instruments.

Point-of-care testing provides quick and low-cost assay, and it improves patient outcomes in near-patient settings with easy-to-use devices [7]. For example, biosensors constitute an outstanding alternative for fast, low-cost, efficient, and user-friendly analysis that can be mass produced. [8]. Screen-printed carbon electrodes (SPCEs) have been successfully applied in the on-site detection of various analytes in patients. Disposable SPCEs consist of paper or plastic plates on which the counter, reference, and working electrodes are printed using screen-printing technology. Amperometric, potentiometric, and conductometric signals have been used in SPCE's detection [9]. SPCEs enable the rapid sensing of bio-analytes using only a small volume of sample and minor treatment steps. One of the SPCE applications is the glucose monitoring of diabetic people based on enzyme-conjugated disposable electrodes [10]. The working electrode is the main platform for quantifying the analyte using the antibody-antigen affinity and electrochemical transduction. The properties of working electrodes, including surface topology, functional groups, and conjugation chemistry affect the detection sensitivity [11].

Nanomaterials have been incorporated in electrochemical sensors for food, biological and environmental analysis to improve the surface properties and detection performance [12–15]. The SPCEs combined with

\* Corresponding author at: Department of Chemical and Materials Engineering, Chang Gung University, 259, Wen-Hwa First Road, Kwei-Shan, Tao-Yuan 333, Taiwan.  
E-mail address: [CHL@mail.cgu.edu.tw](mailto:CHL@mail.cgu.edu.tw). (C.-H. Liu).

different nanoparticles significantly enhance electrochemical signal for analytes with ultra-trace quantities [16,17]. Additionally, phosphors having strong photoluminescence can be applied to chemiluminescence assay [18,19]. For example, quantum dots have been applied to enhance sensitivity of theophylline using SPCE [20]. Nanomaterials can also improve the performance of immunosensor via the increased surface area, enhanced electron transfer, analyte accessibility, and supply of functional groups [21–23]. Nanomaterial-modified surfaces can provide a good affinity for detection moiety like antibodies, and they can increase the sensitivity and specificity of biomarker testing. Nanocomposites on the SPCE could enhance electrochemical properties such as fast electron transfer, anti-fouling, and fast labeling, and this can elevate sensing performance [24]. The electrochemical advantages of multi-walled carbon nanotubes (MWCNT) such as excellent electron transfer, chemical stability, high mechanical strength, and large specific surface, make them suitable for use in sensor modification. Gold nanoparticle (AuNP) is being used for fabricating nanocomposites and enhancing sensitivity in electrochemical sensors because of excellent surface and conductivity properties. The affinity energy of AuS bond for thiols groups on antibody toward gold has been estimated around  $126 \text{ KJ mol}^{-1}$  [25]. Therefore, AuNP-MWCNT nanocomposites are synthesized to increase the binding of antibodies on electrode surfaces and to elevate the specific PTH recognition in this study. The surface features of every layer on SPCE have been characterized by Raman spectroscopy, scanning electron microscopy (SEM), transmission electron microscopy (TEM), and Fourier-transform infrared spectroscopy (FTIR). The PTH detection of this immunosensor has been compared using electrochemical impedance spectroscopy (EIS) and cyclic voltammetry (CV).

## 2. Experimental

### 2.1. Reagents and materials

Potassium ferricyanide ( $\text{K}_3\text{Fe}(\text{CN})_6$ ), sodium phosphate dibasic ( $\text{Na}_2\text{HPO}_4$ , 99%), sodium phosphate monobasic ( $\text{NaH}_2\text{PO}_4$ ), gold (III) chloride trihydrate ( $\text{HAuCl}_4$ , 99%), bovine serum albumin, glucose, ovalbumin, gelatin, insulin, human immunoglobulin, lysozyme, human serum, and vitamin C were purchased from Sigma-Aldrich (St. Louis, MO, USA). Fetal bovine serum was purchased from Life Technologies (Grand Island, NY, USA) and glycerol from J.T. Baker (Phillipsburg, NJ, USA). Carboxylated MWCNT (10–30  $\mu\text{m}$ , UniRegion, Taipei, Taiwan) was used in this study. Polyclonal rabbit anti human PTH antibody (AB14493), and human PTH (AB51234) were from Abcam (MA, USA). The disposable SPCE (TE-100) consisted of carbon working electrode, counter electrode and silver pseudo-reference electrode was purchased from Zensor (Taichung, Taiwan). PTH ELISA kit (SEK13192) was obtained from Sino Biological (Beijing, China). Phosphate buffer solution (PBS, 0.1 M and pH 7.0) was used in this study. All reagents were used without further purification. All solutions were prepared using  $18.2 \text{ M}\Omega/\text{cm}$  ultrapure water (Rephile, Taoyuan, Taiwan).

### 2.2. Apparatus

TEM (JM-1011, JEOL, Tokyo, Japan) and Zeta Sizer® Nano ZS 90 (Malvern, Worcestershire, UK) were used to assess size and morphology of nanocomposite. The carbon coated copper grid (CF200-Cu, Electron Microscopy Science, PA, USA) was used to load the nanomaterials for TEM analysis. Surface functionalization of SPCE was characterization by using Fourier transform infrared spectroscopy (FTIR, Alpha, Bruker, Germany). The IR spectra were recorded in the range of  $500\text{--}4000 \text{ cm}^{-1}$  with a resolution of  $2 \text{ cm}^{-1}$  at room temperature using attenuated total reflection device. To determine the hydrophobicity of the surfaces on the modified SPCE, the contact angle analyzer (Phoenix mini, Surface Electro Optics, Republic of Korea) was performed at room temperature using the sessile drop method with ultrapure water droplets. The contact angle was measure by

placing 5  $\mu\text{L}$  of water droplets on the surface of the electrode and analyzing the angle at the air–liquid–solid interface using Young's equation. The average contact angle value was obtained from measurements at three different points on the same SPCE and using three different SPCEs. The spectra of the samples were then processed by Bruker Opus software. The surfaces of SPCEs were investigated using a metallurgical microscope (Leica, DM2700M, Wetzlar, Germany). The elemental analysis was investigated using a scanning electron microscope (HITACHI S-4700, Tokyo, Japan) equipped with an energy dispersive spectrometer (Bruker, XFlash Detector 5030, Berlin, Germany). The D and G bands of carbon on the surfaces of SPCEs were analyzed by Raman mapping system (UninanoTech, Yongin, South Korea). The electrochemical properties of the SPCE were analyzed using ACIP 100 Electrochemical Simulator purchased from Zensor (Taichung, Taiwan).

### 2.3. Preparation of SPCE with MWCNT-AuNP nanocomposite

A nanocomposite surface on the working electrode (3 mm diameter) of SPCE was modified in a single step using the controlled-potential electrodeposition. SPCE was washed with deionized water twice in an ultrasonic bath for 10 s, then  $100 \mu\text{L}$  of 10 mM  $\text{HAuCl}_4$  solution containing 50  $\mu\text{g/mL}$  MWCNT was loaded for the nanocomposite preparation. The controlled-potential and duration of the electrodeposition was set at  $-200 \text{ mV}$  and 300 s, respectively. After washed with ultrapure water twice, the MWCNT-AuNP modified SPCE was ready for the antibody immobilization.

### 2.4. Immunosensor fabrication and PTH assay procedure

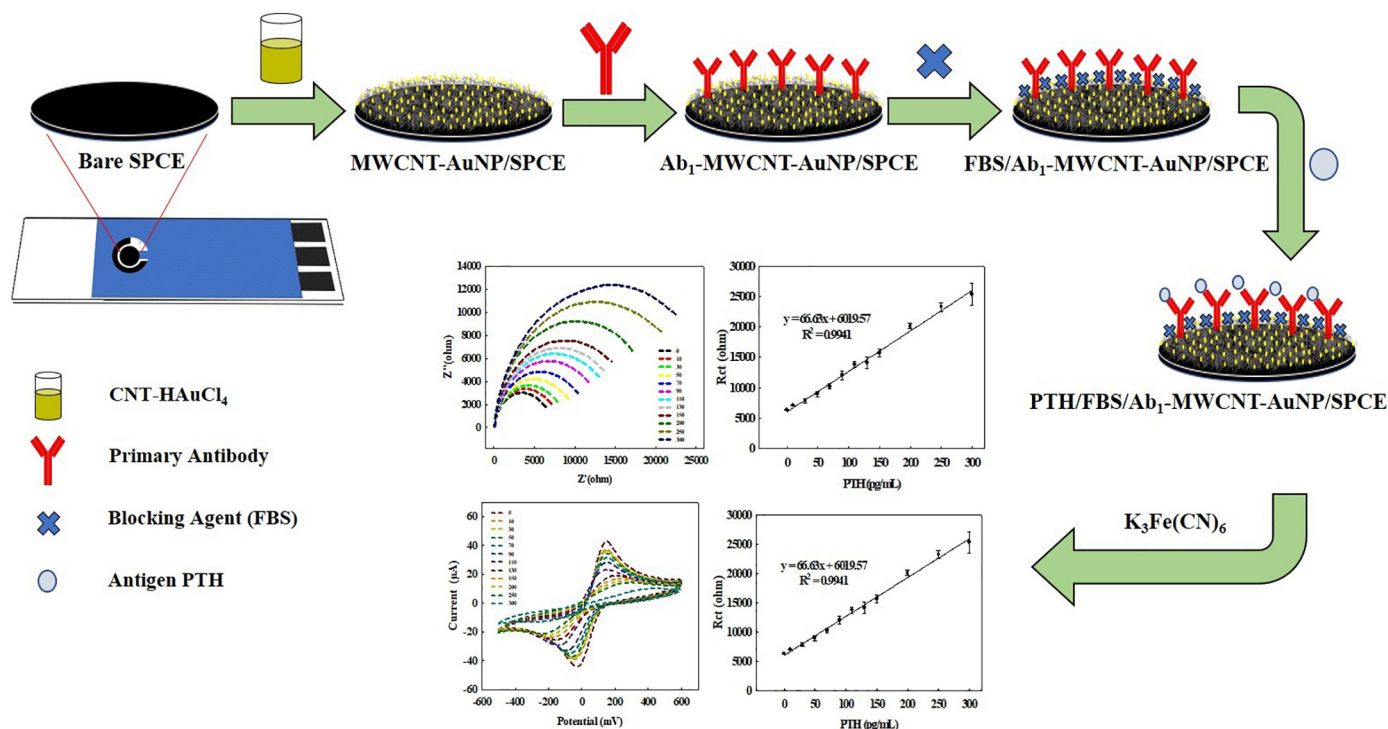
After  $1000\times$  dilution, 30  $\mu\text{L}$  of polyclonal rabbit anti human PTH antibody (stock: 110  $\mu\text{g/mL}$ ) was coated on the MWCNT-AuNP modified electrode and incubated at  $4^\circ\text{C}$  for 30 min. The thiol group of anti-human PTH antibody could adsorb on AuNP in the nanocomposite surface via thiol–gold interaction. The working electrode was washed with deionized water twice and blocked with 30  $\mu\text{L}$  of fetal bovine serum (FBS) solution for 30 min at  $4^\circ\text{C}$ . After twice washing, the PTH immunosensor was stored at the  $4^\circ\text{C}$  condition prior to use. All the antibodies were dissolved in 10% glycerol in PBS to make it viscous and easy to load on electrode surface. The fabrication of this immunosensor is shown in Scheme 1. The step-by-step modification of the electrode was characterized through the microscale morphology and electrochemical properties. Human serum spiked with PTH was used to evaluate the performance of PTH immunosensor. The PTH sample was loaded onto electrodes and kept at  $4^\circ\text{C}$  for 30 min. Electrodes were rinsed with water before EIS and CV techniques were applied to obtain the effects of PTH dosage on electrochemical signals using 100  $\mu\text{L}$  of ferricyanide in PBS. The ELISA assay was performed according to the manufacture's protocol. The claimed detection range was within 0–300  $\text{pg/mL}$ .

### 2.5. Characterization of SPCE electrochemical properties

#### 2.5.1. Measurement of electron transfer rate constant ( $K_s$ ) by CV and EIS

To evaluate the electrochemical properties of the electrodes, the electron transfer rate constant ( $K_s$ ,  $\text{cm/s}$ ) of the SPCEs were estimated by both CV and EIS using 3 mM ferricyanide in PBS. CV scanning was performed over a potential range from  $-500$  to  $+600 \text{ mV}$  at different scan rates varying from 10 to  $100 \text{ mV s}^{-1}$  using 3 mM ferricyanide in PBS. The oxidation and reduction peak currents in CV from different electrode surfaces can be theoretically attributed to electron transfer rates or charge transfer resistances [26]. Therefore, CV was firstly used in the investigation of the peak currents of redox probe and then EIS was utilized for the characterization of the stepwise changes of the surfaces of the biosensor by interpreting the charge transfer resistances. The calculation of  $K_s$  by CV data was based on the Nicholson method as shown in Eqs. (1) and (2) [27].

$$\Psi = (-0.6288 + 0.021\Delta E_p)/(1 - 0.017\Delta E_p) \quad (1)$$



**Scheme 1.** Schematic diagram showing the fabrication process and immuno-electrochemical reaction on the PTH immunosensor.

$$\Psi = Ks[\pi D n v F / (R T)]^{-1/2} \quad (2)$$

where  $\Psi$ , a dynamic parameter, is a function of potential difference ( $\Delta E_p$ );  $D$  is the diffusion coefficient;  $n$  is the number of electrons transferred in the reaction;  $F$  is the Faraday constant;  $v$  is the scanning rate;  $R$  is the gas constant; and  $T$  is the temperature in Kelvin.

Recently, the estimation of  $K_s$  using charge transfer resistance ( $R_{CT}$ ) has been recently reported by using the EIS technology [28]. In Eq. (3),  $K_s$  is related to the quantities like  $R_{ct}$ , surface area, and the concentration of ferricyanide as the following Eq. (3).

$$K_s = R T / (n^2 F^2 A R_{ct} C) \quad (3)$$

where  $C$  is the concentration of ferricyanide ( $\text{mol cm}^{-3}$ );  $A$  is the microscopic area of the electrode ( $\text{cm}^2$ );  $n$  is the number of the electrons involved in the reaction;  $F$  is Faraday's constant ( $96,485 \text{ C mol}^{-1}$ );  $R$  is universal gas constant ( $8.314 \text{ J mol}^{-1} \text{ K}^{-1}$ );  $T$  is the absolute temperature.

### 2.5.2. Calculation of effective surface area

CV data was used to estimate the effective surface area from the linear slope of the peak current ( $I_p$ ) versus square root of scan rate ( $v^{1/2}$ ) applying the Randles-Sevcik equation for a reversible electrochemical process under the diffusion control [29].

$$I_p = 0.4463 (n^3 F^3 v D_0 / RT)^{1/2} A C \quad (4)$$

where  $I_p$  refers to the peak current;  $D_0$  is the diffusion coefficient ( $7.0 \times 10^{-6} \text{ cm}^2 \text{ s}^{-1}$ );  $C$  is the concentration of ferricyanide ( $\text{mol cm}^{-3}$ );  $v$  is the scan rate ( $\text{Vs}^{-1}$ ). By using the slope of  $I_p$  vs.  $v^{1/2}$ , the effective surface area ( $A$ ,  $\text{cm}^2$ ) of the SPCE could be calculated.

### 2.5.3. Impedance analysis by EIS

SPCE's impedance was measured using sinusoidal excitation signal (amplitude 100 mV, initial potential 50 mV, and frequency range from 1 to 1000 Hz) in EIS and 3 mM ferricyanide in PBS. Nyquist plot typically represents a semicircle region and a linear region. The semicircle diameter at higher frequencies corresponds to the charge transfer process and the linear

part at lower frequencies corresponds to the diffusion process. The Randles equivalent circuit was further chosen to fit the impedance data in the EIS experiments using Zsimpwin software (Amertek, TN, USA).

### 2.5.4. EIS estimation of association constant between PTH and antibody

The change in  $R_{ct}$  can be related to the complex formation of antigen and antibody on the electrode surface [30]. The association constant ( $K_a$ ) can be estimated using Eq. (6), where  $\theta$  represents the occupied ratio of the binding sites by PTH.  $R_{ct}(\text{Co})$  and  $R_{ct}(\text{Ci})$  charge transfer resistance without PTH and with tested concentration of PTH, respectively.

$$\theta = 1 - (R_{ct}(\text{Co}) / (R_{ct}(\text{Ci}))) \quad (5)$$

In Langmuir isotherm,  $\theta$  can be related to association constant and PTH concentration using Eq. (6).

$$\theta = K_a \times C / (1 + K_a \times C) \quad (6)$$

where  $K_a$  is related to the equilibrium between PTH and anti-PTH antibody on SPCE and  $C$  is the concentration of PTH in serum. On rearrangement and combination Eqs. (5), (6), we obtain Eq. (7).

$$K_a \times C = ((R_{ct}(\text{Ci}) - R_{ct}(\text{Co})) / (R_{ct}(\text{Co}) - \Delta R_{ct}(\text{Ci})) / (R_{ct}(\text{Co}))) \quad (7)$$

### 2.6. Statistical analysis

Repeatability of the developed sensor was investigated by three SPCEs. The mean and standard deviation (SD) of measurements were calculated by Analysis Toolpak in Microsoft Excel to evaluate the reproducibility of the biosensor. Statistical analysis of the comparison between the electrochemical measurements was performed using an unpaired Student's  $t$ -test. A 0.05 level of probability was taken as the level of significance. The data are expressed as mean  $\pm$  standard deviation from three repeats ( $n = 3$ ). LOD was calculated using the following equation:  $\text{LOD} = 3 \times \text{SD}/m$ ; where  $m$  is the slope of the calibration curve, and SD is from the peak currents of



lowest PTH concentration (three runs). Similarly, LOQ was calculated by equation:  $LOQ = 10 \times SD/m$  [31].

### 3. Results and discussion

#### 3.1. Characterization of prepared SPCEs

##### 3.1.1. Microscopic surface characterization by FE-SEM

The microscopic images of the surfaces of the modified SPCEs revealed the topological and morphological characteristics. Fig. 1(A–C) depicts the micro-scale images of the SPCE surfaces. The graphite flake in bare SPCEs was covered with AuNP and fibrous MWCNT after nanocomposite coating using FE-SEM. A typical flake-like surface was observed in the case of bare SPCE in Fig. 1(A), while for the AuNP SPCE, AuNP were uniformly dispersed in Fig. 1(B). When MWCNT was mixed with HAuCl<sub>4</sub> solution and coated on the electrode surface, the FE-SEM image in Fig. 1(C) showed a uniform coverage of AuNP with the porous structure of MWCNT.

This AuNP supplied the binding site of the antibodies, and it increased the active area for electron transfer on the electrode surface. Both electrode surfaces were homogenous before and after nanocomposite modification, as indicated by the metallurgical microscope (Fig. S1(A–C)). Adding AuNP to MWCNT/SPCE decreased the carbon content from 47 to 7%. Au content of AuNP/SPCE decreased from 93 to 53% as compared to AuNP-MWCNT/SPCE by means of the energy dispersive spectrometer. The golden and porous layer could be found in the electrodes modified with AuNP and MWCNT-AuNP. This suggested that the electrodes exhibited a larger electro-active surface and faster electron transfer rates compared to the bare SPCEs. The nanocomposite offered a better solid-liquid interface than the original graphitic particles on the bare SPCE. To confirm such modification at the sensor surface, the corresponding FTIR spectra (Fig. S2) at bare SPCE, SPCE/AuNP, and AuNP-MWCNT/SPCE were analyzed. The FTIR results confirmed that the surfaces of the immunosensor contained the covalent amide bonds from the antibody. Our IR spectrum was similar to that of the immune-SPCE for thyroid stimulating hormone assay reported by Saxena and Srivastava [32].

Contact angle measurement revealed the difference of hydrophobic property between the bare SPCE and modified SPCEs (Table 1). However,

the nanocomposite modification lightly enhanced the hydrophilicity as the contact angle decreased (Fig. S1 (D–F)). After the introduction of antibodies on the electrode surface, the contact angle could be decreased further, from 88° to 63°. The antibody layer increased the hydrophilicity of SPCE surface. Nanocomposites of MWCNT and AuNP have been reported for SPCE modification to improve the sensitivity and selectivity for breast cancer biomarker and pesticide detection [33,34]. However, this nanocomposite has not been applied to PTH immunosensing. The nanocomposite on the modified SPCE was carefully characterized by SEM, FTIR, Raman, and metallurgical microscope in the next section.

##### 3.1.2. Transmission electron microscope and Raman spectroscopy

To prove that AuNP could be synthesized in-situ on the MWCNT from the HAuCl<sub>4</sub> solution, the solution from the working electrode after 300-s electrodeposition was analyzed by TEM and Nanosizer. In the micrograph of Figs. 1(C) and 2(B), many nanoparticles on the MWCNTs were observed indicating the successful in-situ deposition of AuNP. The MWCNTs in Fig. 2(B) provided a large surface area for PTH sensing and the transfer of redox probes. The size distribution of AuNP, which was electrochemically synthesized in-situ, was analyzed by the dynamic light-scattering technology. The average size of AuNP was around 18 nm, which was similar to the TEM image (Fig. 2(C)). Combined with SEM results, we confirmed that spherical AuNP with narrow size distribution was successfully coated on the SPCE surface after electrodeposition. A root-like structure of AuNP loaded MWCNT was observed (Fig. 2(B)). This simultaneous deposition created a strong interaction between the MWCNTs and AuNP, which could contribute to the high electrochemical activity on the modified SPCEs [35].

The Raman spectra of bare SPCE, AuNP/SPCE, and MWCNT-AuNP/SPCE were shown in Fig. 2(D). The bare SPCE containing graphite represented the typical Raman spectrum. G-band located at  $1576\text{ cm}^{-1}$  was a result of in-plane vibrations of carbon atoms bonded with  $sp^2$  orbital. The peak, appearing at  $1347\text{ cm}^{-1}$ , is known as the D-band. It is due to out-of-plane vibrations attributed to the vibrations of  $sp^3$  carbon atoms [36]. The D/G ratio of AuNP/SPCE (0.86) was slightly lower than the ratio obtained from bare SPCE (0.88) and MWCNT-AuNP/SPCE (0.92). AuNP might hinder in-plane vibrations of  $sp^2$  carbon. The D-band shifted to higher wavenumber  $1363\text{ cm}^{-1}$ , whereas the G-band remained at  $1576\text{ cm}^{-1}$  in

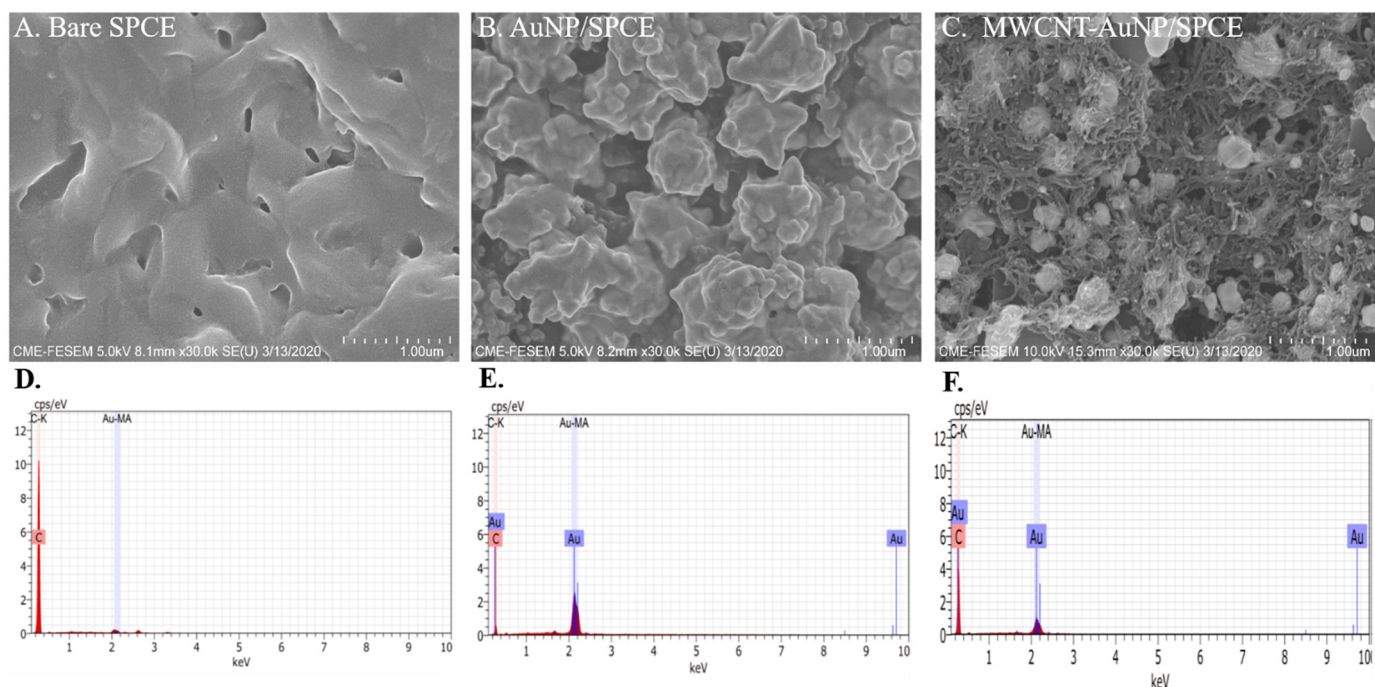
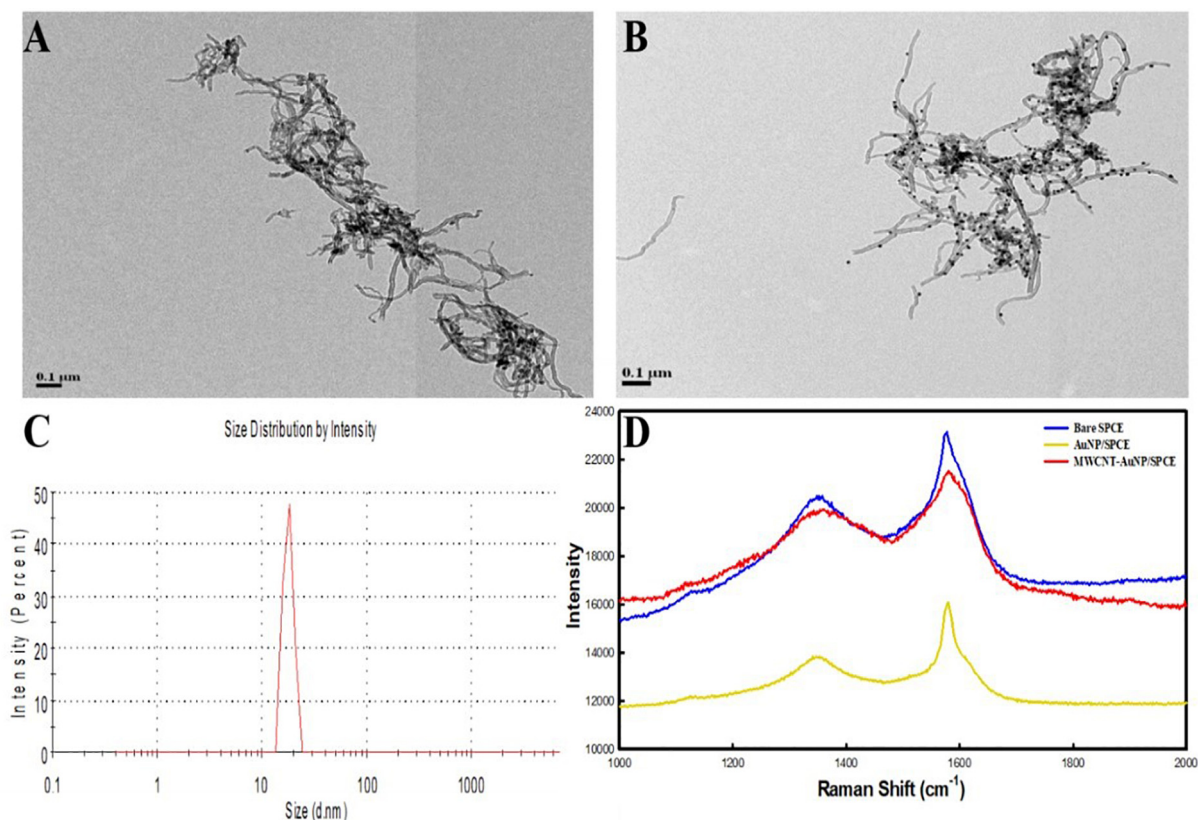


Fig. 1. FE-SEM image of bare and modified SPCEs: (A) Bare, (B) AuNP/SPCE, (C) MWCNT-AuNP/SPCE, with 1.0  $\mu\text{m}$  scale bar. Energy dispersive X-Ray spectroscopy results from the samples: (D) Bare SPCE, (E) AuNP/SPCE, (F) MWCNT-AuNP/SPCE.

**Table 1**Electrochemical and physicochemical characteristics of the modified SPCEs<sup>a</sup>.

| SPCE            | Contact angle | Ks by CV (cm/s) | Ks by EIS (cm/s) | E <sub>1/2</sub> (mV) | ΔE <sub>p</sub> (mV) | I <sub>pa</sub> (μA) | Area (cm <sup>2</sup> ) |
|-----------------|---------------|-----------------|------------------|-----------------------|----------------------|----------------------|-------------------------|
| Bare SPCE       | 127.8 ± 1.7   | 0.00089         | 0.00067          | 55.3 ± 3.0            | 128 ± 6.5            | 29.9 ± 0.4           | 0.067 ± 0.0075          |
| AuNP/SPCE       | 106.1 ± 1.8   | 0.00163         | 0.00401          | 63 ± 8.6              | 101 ± 5.5            | 36.8 ± 1.5           | 0.140 ± 0.0055          |
| MWCNT-AuNP/SPCE | 88.7 ± 4.1    | 0.00368         | 0.00379          | 53 ± 14.6             | 105 ± 1.1            | 38.1 ± 0.8           | 0.145 ± 0.0030          |

<sup>a</sup> E<sub>1/2</sub>: formal potential, I<sub>p</sub>: peak current, ΔE<sub>p</sub>: peak to peak separation, Area: working electrode surface area calculated by Randles-Sevcik Eq. (4). The electrochemical properties were referred to pseudo reference Ag electrode. The result represents mean ± standard deviation from three repeats (*n* = 3).



**Fig. 2.** TEM images of nanocomposites in-situ synthesized on SPCE. (A) MWCNT, (B) MWCNT- AuNP, (C) the size distribution of the prepared AuNP on SPCE using the deposition potential of  $-200$  mV for 300 s. (D) Raman spectra of bare SPCE, AuNP/SPCE, MWCNT-AuNP/SPCE. The scale bar was 100 nm.

two cases of AuNP modified SPCEs. The band shift of D-band in Raman spectra has been reported because of the p-doping effects imposed by the AuNP [37]. Our Raman results also demonstrated the successful MWCNT localization on the working electrode. In Supplementary Information, the amount of MWCNT and the concentration of auric acid during the in-situ electrodeposition were optimized using the chronoamperometric method. Effects of H<sub>2</sub>AuCl<sub>4</sub> (2–20 mM), MWCNT (10–100 μg/mL), and deposition potential ( $-150 \sim -300$  mV) on the performance of peak current are shown in Figs. S3 and S4. Finally, 50 μg/mL of MWCNT, 10 mM of H<sub>2</sub>AuCl<sub>4</sub>, and  $-200$  mV deposition potential were chosen for the deposition of MWCNT-AuNP nanocomposite on the working electrodes.

### 3.2. Electrochemical characterization of SPCE modification

Fig. 3(A) shows voltammograms and peak current of nanocomposite-modified SPCE at different scanning rates. The peak shape of the CV shows a reversible electrochemical reaction in which the rate of reaction is governed by the diffusion of ferricyanide on a planar electrode surface [38]. The scan rate of voltammetry was applied to evaluate the charge transfer process involved at the electrode-electrolyte interface of MWCNT-AuNP/SPCE. The peak currents were plotted against the square root of scan rates in Fig. 3(B). This reversible voltammogram indicated

that the fast kinetics of electron transfer on the electrode can maintain the cyclic balance of redox reaction. Peak current was linearly proportional to the square root of the scan rate from 10 to 100 mV s<sup>-1</sup>. The corresponding linear regression equations were found to be  $I_{pa}$  (anodic peak current) =  $3.50v^{1/2} - 0.68$  ( $R^2 = 0.993$ ) and  $I_{pc}$  (cathodic-peak current) =  $-3.59v^{1/2} + 0.27$  ( $R^2 = 0.992$ ). The linear relationship between current and the square root of scan rate clearly suggested the involvement of the diffusion-controlled process at the interface. The electrochemical behavior of SPCE, AuNP/SPCE, and MWCNT-AuNP/SPCE was also characterized by linear sweep voltammetry. A clear oxidative peak was found at  $+108$  mV. The modified SPCEs had higher peak currents compared to the bare SPCEs in Fig. 3(C, D). The symmetric CV pattern and the linearity of the current-scanning rate indicated a successful modification of the modified SPCE.

The electrochemical properties of the bare and modified SPCEs, such as electron transfer rate constant, peak current, the effective surface area, contact angle, and their standard deviation were summarized in Table 1. The maximal redox peaks in the voltammogram were applied to calculate  $I_{pa}$ ,  $I_{pc}$ , peak-to-peak separation ( $\Delta E_p$ ), and formal potential ( $E_{1/2}$ ). The effective surface area of different SPCEs was determined by applying the Randles-Sevcik equation and assuming the same diffusion coefficient. The Ks was estimated using the Nicholson and EIS methods [39]. Our EIS- and CV-determined Ks values were similar to the previous report by

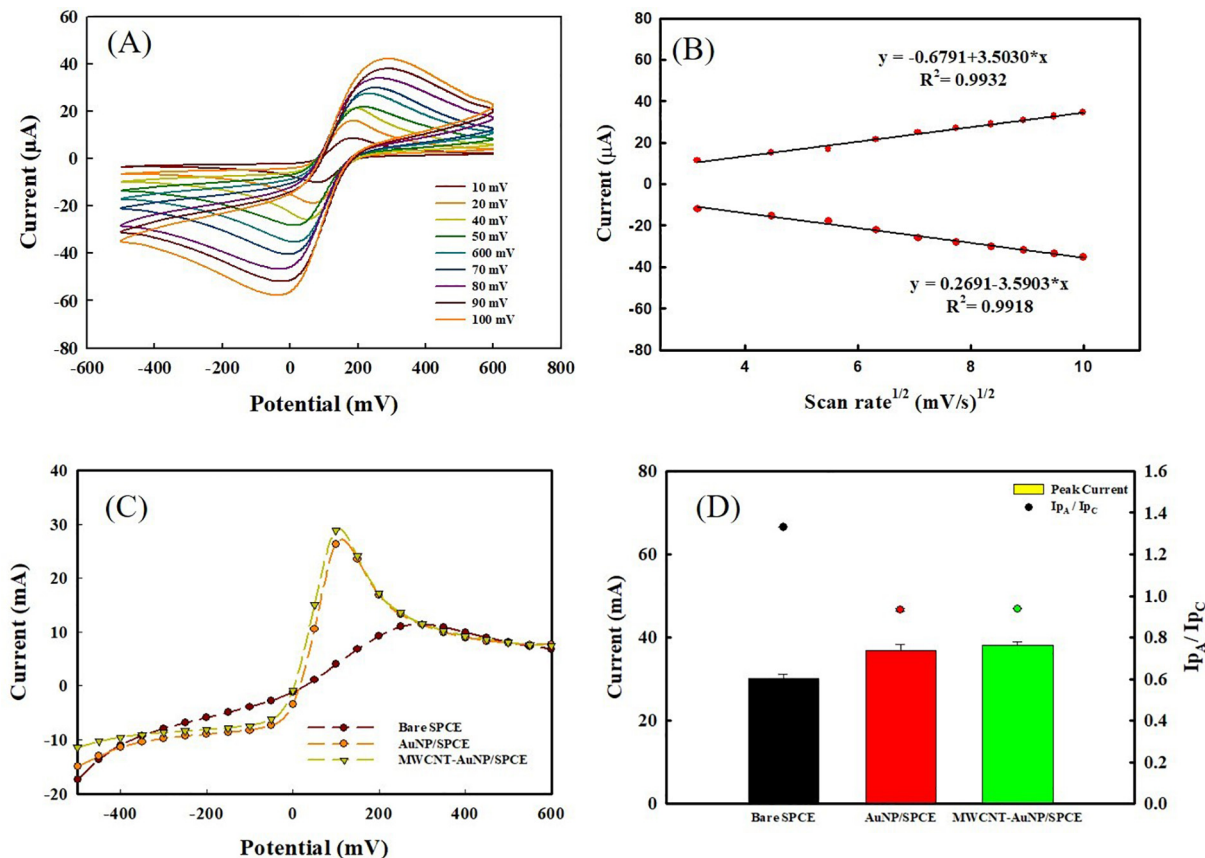


Fig. 3. (A) Cyclic voltammograms of MWCNT-AuNP/SPCE measured in potential window of  $-500$  to  $+600$  mV vs. Ag pseudo-reference electrode at different scan rates (from inner to outer): 10, 20, 30, 40, 50, 60, 70, 80, 90, 100 mV s<sup>-1</sup>. (B) Effect of scan rate on the anodic and cathodic peak current. (C) Linear sweep voltammograms (LSV) of bare SPCE, AuNP/SPCE, MWCNT-AuNP/SPCE. (D) Peak current and I<sub>pA</sub>/I<sub>pC</sub> ratio of different SPCEs by LSV using 3 mM ferricyanide in PBS.

Randviir [28]. The increased rate constants using both CV and EIS confirmed that the nanocomposite surface could significantly increase the effective surface area and electron transfer between the redox probe and electrode surface. After the deposition with nanomaterials (AuNP and MWCNT-AuNP),  $\Delta E_p$  decreased and the peak current increased. The

modified electrode surface was relatively conductive and capable of transferring greater amounts of redox probes compared to the bare SPCEs. The result of the ratio I<sub>pC</sub>/I<sub>pA</sub> closer to 1 identified the reversible current-potential behavior of ferricyanide redox reaction on the SPCE using the CV method [40].

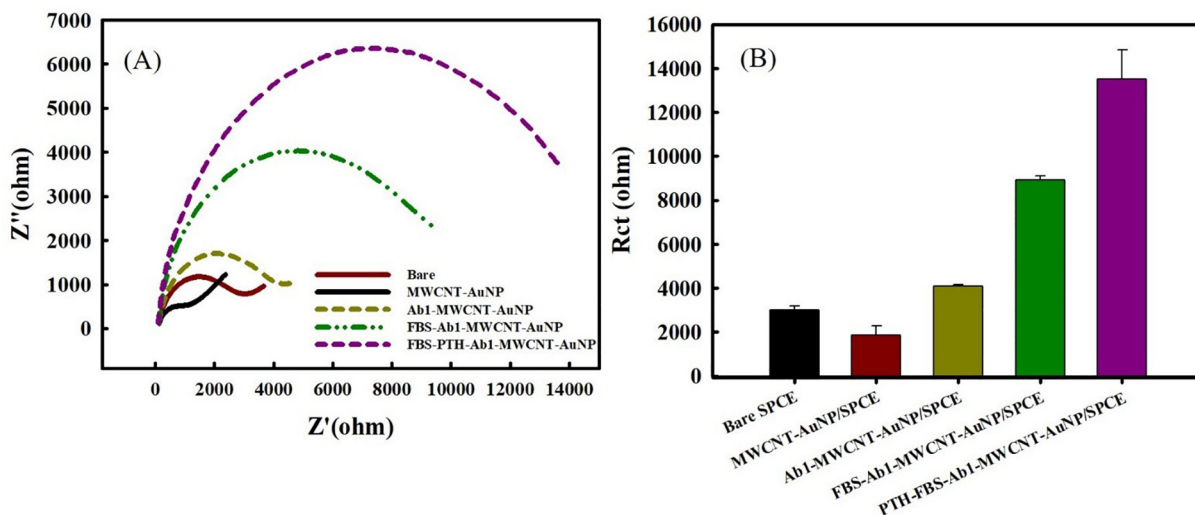


Fig. 4. (A) Impedance results of different modified SPCEs using 3 mM ferricyanide in PBS. EIS was run with amplitude 100 mV with amplitude 100 mV, frequency range 1–1000 Hz, initial potential 50 mV. (B) Histogram of charge transfer resistance of different SPCEs including bare SPCE, MWCNT-AuNP/SPCE, Ab1-MWCNT-AuNP/SPCE, FBS-Ab1-MWCNT-AuNP/SPCE, PTH-FBS-Ab1-MWCNT-AuNP/SPCE. Human serum spiked with 100 pg/mL of PTH was used. Error bar represents the standard deviation from three repeats ( $n = 3$ ).



### 3.3. EIS characterization of modified SPCEs

EIS is well established for characterizing the charge transfer process occurring at the electrode-solution interfaces and for understanding the features of the electrode surface [24]. Nyquist plot derived from EIS spectra can be used to investigate the change in resistance and capacitance of the interface, thus providing insights into the effects of surface modification. Nyquist plot usually includes a semicircle that corresponds to the electron-transfer process, and the diameter of the semicircle corresponds to  $R_{ct}$  [41]. The impedance data of the modified SPCEs were regressed by Zsimpwin to obtain the  $R_{ct}$ , the uncompensated solution resistance ( $R_s$ ), and the double-layer capacitance ( $C_{dl}$ ) using the equivalent circuit (Fig. 4). The  $R_s$  and  $C_{dl}$  values from the modified SPCEs were similar suggesting these parameters were not affected by the nanocomposite deposition and antibody immobilization (Table S1). However,  $R_{ct}$  was significantly influenced by the insulating feature of the antibody and PTH antigen at the electrode-electrolyte interface. The magnitude of  $R_{ct}$  slightly decreased by coating AuNP-MWCNT. The results also confirmed that MWCNT/AuNP nanocomposite was deposited successfully onto the SPCE surface. Upon primary antibody coating, the  $R_{ct}$  values increased, and the covalent attachment of anti-PTH on the electrode surface generated a protein layer. This detection layer hindered interfacial electron transfer, and sequentially increased  $R_{ct}$ . The blocking of the free active surface at the MWCNT/AuNP layer by FBS resulted in a further increase of  $R_{ct}$ , due to the coverage of serum proteins on the modified electrode surface. The impedance results had small relative standard deviation ( $RSD < 10\%$ ), revealing the robustness and repeatability of the SPCE modification process. The parameters of  $R_{ct}$ ,  $R_s$ , and  $C_{dl}$  of SPCEs could successfully represent the impedance environment of this immunosensor. The increased hindrance to the electron transfer process was attributed to the increasing thickness of

the immuno-complex formed on SPCE surfaces. Another two involved mechanisms may be attributed to the blocking of redox reaction and the hamper of electron tunneling by the immuno-complex layer [24].

### 3.4. Effects of capture antibody concentration on PTH detection

The biosensor response is significantly affected by capture antibody density on the electrode when applying the impedimetric and amperometric assays [42]. To establish the effect of capture-antibody loading on the response of the present MWCNT-AuNP/SPCE, antibody dilutions were utilized for the coating of biosensors. For this purpose, 100 pg/mL of PTH standard solutions were separately analyzed by biosensors immobilized with different antibody solutions (55–1110 ng/mL).  $R_{ct}$  values declined from 29,935 to 13,134  $\Omega$  when the antibodies increased from 55 to 1110 ng/mL. In Fig. 5A, the highest  $R_{ct}$  was obtained with 1110 ng/mL of antibody. Higher concentrations of antibodies resulted in a thicker detection layer of anti-PTH antibody, which eventually hindering electron transfer. Hence, considering PTH responsibility and sensitivity, an optimized antibody concentration of 110 ng/mL was chosen to perform further experiments. Another optimized parameter was the coating duration for anti-PTH antibody. The optimum incubation period was studied using 110 ng/mL of anti-PTH antibody. The charge transfer resistances increased with the increasing duration from 15 to 60 min. The 30-min incubation was enough for the antibody immobilization on the SPCEs (Fig. 5C). Prolonging incubation period up to 60 min resulted in an increase in the charge transfer resistance [43]. Incubation duration longer than 60 min was not favored because of drying of anti-PTH antibody solution on the electrode surface. The incubation period were around 30–60 min for antigen-antibody interaction in literature [26]. According to the results, we immobilized antibody on the working electrode using a 30-min duration.

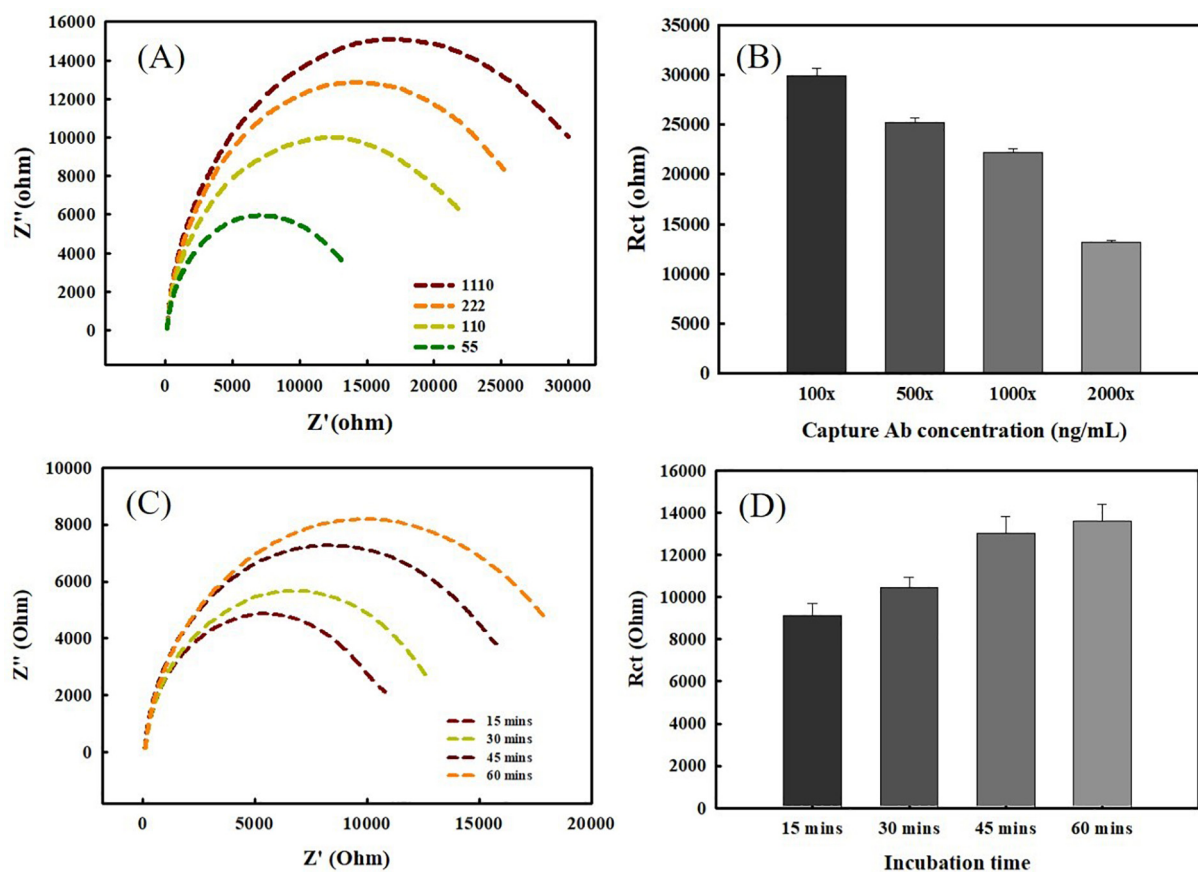


Fig. 5. Effect of capture antibody loading on the biosensor EIS (A) and  $R_{ct}$  signal (B). Effect of coating duration on EIS (C) and  $R_{ct}$  signal (D) using 110 ng/mL antibody. Different antibody dilutions (1110, 222, 110, 55 ng/mL) were used to immobilize the SPCE surface. The impedance spectra were obtained using 100 pg/mL PTH concentration in all these experiments. Error bar represents the standard deviation from three repeats ( $n = 3$ ).

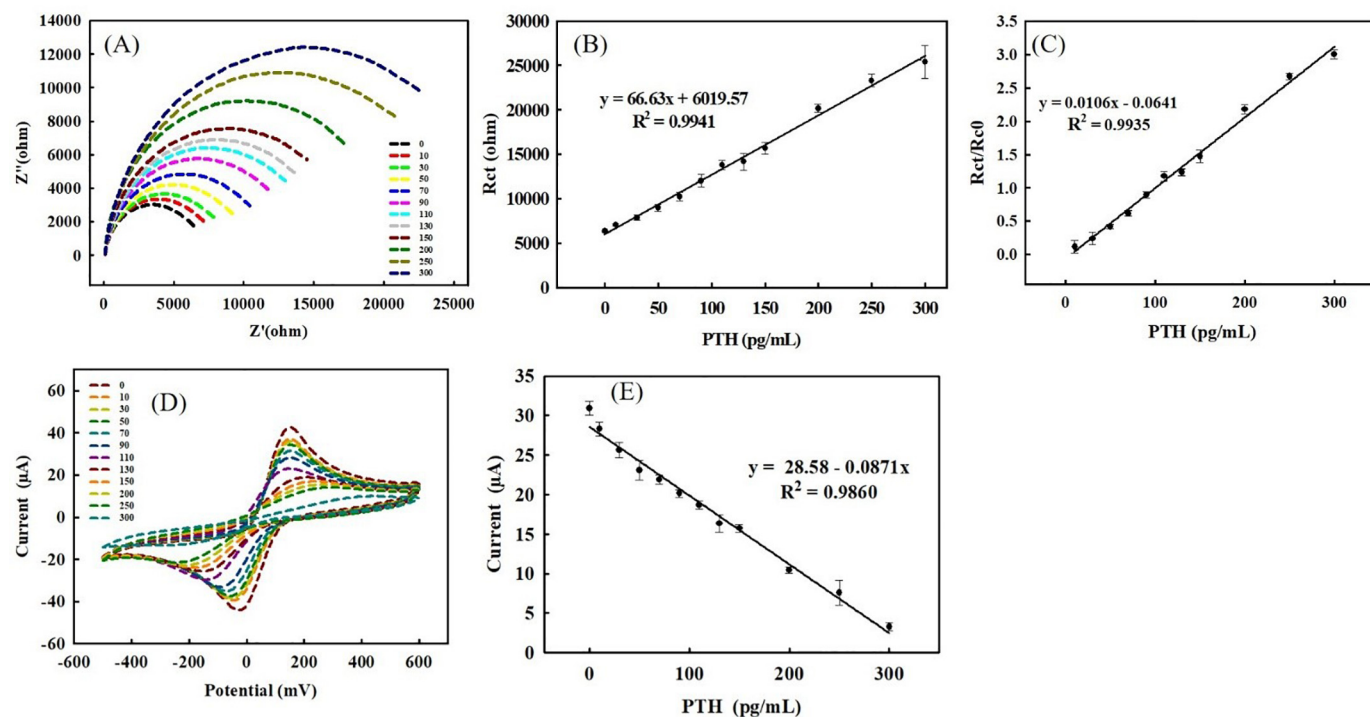


Fig. 6. Impedance spectra and standard curve of PTH dosage (0–300 pg/mL) in human serum (A), (B) and using the immunosensors. Impedance results for measurement of the association constant using human serum spiked with PTH (C). Cyclic voltammetry current signal and standard curve of PTH dosage (0–300 pg/mL) in human serum (D), (E). The EIS and CV signal obtained by placing 100  $\mu$ L of 3 mM potassium ferricyanide in PBS. EIS was run with amplitude 100 mV, frequency range 1–1000 Hz, and initial potential 50 mV and CV run with potential range (–0.5–0.6 V) with 50 mV  $s^{-1}$  scan rate. Error bar represents the standard deviation from three repeats ( $n = 3$ ).

### 3.5. PTH detection using nanocomposite modified immunosensor

#### 3.5.1. Estimation of association constant between the antibody and PTH antigen on SPCE

In order to understand PTH capture by immobilized antibody on SPCE, the association constant ( $K_a$ ) for the binding between PTH and the antibody was determined using EIS and the Langmuir isotherm assumption. The assumptions include monolayer adsorption and equal binding energy for all binding sites [30]. Using Eq. (7), the slope in Fig. 6(C) represented the  $K_a$  value i.e.  $[\Delta R_{ct}(Ci)/(R_{ct}(Co))] = -0.0641 + 0.0106 C_{PTH}$  (pg/mL).  $K_a$  was found to be 0.0106 pg/mL $^{-1}$  and 0.10 pM $^{-1}$  based on PTH molecular weight (9400 Da). These low association constants indicated that the antibody immobilized on the MWCNT-AuNP/SPCE retained the high capture ability for the target PTH. The advantages of EIS technique for the characterization of antigen-antibody affinity are as follows [24]. Nondestructive and label-free assay for the immuno-complex is obtained by applying the small amplitude perturbation to collect the impedance information on the electrode surface. Our results indicated that the minute changes of

immuno-complex on the electrode can be rapidly and sensitively monitored by the EIS method.

#### 3.5.2. PTH detection using EIS method

In order to assess the practical potential of this developed immunosensor, PTH spiked in human serum was used in this study. Since PTH is around 100 pg/mL in the physiological condition [44], the PTH dose range (1–300 pg/mL) was tested in this study. Commercial ELISA kit was used as the reference method. We performed a dose-dependent experiment using EIS to evaluate the developed immunosensor. Fig. 6(A) and (B) show the EIS responses of the developed immunosensor at PTH spiked serum samples. The impedance increased with the increasing PTH concentration. This gradual increment of the Rct was contributed by the formation of immuno-complex that insulated against charge transfer [43]. EIS immunosensing is based on the immuno-complex of antigen and antibody formed on the electrode surfaces, which acts as mediator- and electron-transfer blocking layer. Finally, the flow of current toward the electrode was hindered and the resistance was elevated [45]. The Rct of the immunosensors had a linear relationship with PTH dosage (1–300 pg/mL) spiked in the serum as indicated in Table 2. A calibration curve (Fig. 6B) shows a linear relationship in the range 1–300 pg/mL. The regression equation is expressed as follows:  $R_{ct} = 6019.57 + 66.63 C_{PTH}$ , and the limit of detection (LOD) was 0.033 pg/mL based on the results of three repetitions. LOD was calculated using the following equation:  $LOD = 3 SD m^{-1}$ ; where  $m$  is the slope of the calibration curve, and SD is from the peak currents of lowest PTH concentration (three runs) [46].

#### 3.5.3. PTH detection using the CV method

The linear concentration range, sensitivity, and detection limit of the developed PTH immunosensors were determined using the CV method as compared to the EIS method. The reductive peak current of the immunosensor decreased with increasing PTH concentration (Fig. 6(D) and the peak current versus PTH concentration was shown in Fig. 6(E). The linear regression equation for spiked serum samples and the LOD were  $I_p =$

Table 2

Recovery of this impedimetric and amperometric immunosensor versus ELISA in actual sample<sup>a</sup>.

| PTH spiked (pg/mL) | EIS found (pg/mL) | EIS recovery (%) | CV found (pg/mL) | CV recovery (%) | ELISA found (pg/mL) | ELISA recovery (%) |
|--------------------|-------------------|------------------|------------------|-----------------|---------------------|--------------------|
| 10                 | 8.01              | 80.1             | 8.86             | 88.66           | 15.62               | 156.19             |
| 50                 | 44.96             | 89.92            | 47.13            | 94.25           | 40.38               | 80.76              |
| 150                | 142.79            | 95.19            | 142.07           | 94.71           | 164.43              | 109.62             |
| 200                | 208.01            | 104.00           | 213.80           | 106.90          | 216.33              | 108.17             |
| 250                | 253.66            | 101.46           | 221.33           | 88.53           | 253.95              | 101.58             |
| 300                | 284.41            | 94.80            | 328.51           | 109.50          | 293.95              | 97.98              |

<sup>a</sup> The data are expressed as mean  $\pm$  standard deviation from three repeats ( $n = 3$ ).

**Table 3**

Comparison of the proposed PTH immunosensor performance with the previous methods.

| Nanomaterials                        | Range (pg/mL)                     | LOD (pg/mL) | Relative SD (%) | Method            | Reference |
|--------------------------------------|-----------------------------------|-------------|-----------------|-------------------|-----------|
| Au/MOH/APTES/Anti-PTH/BSA            | 10–60                             | 7.65        | 2.94            | EIS               | [49]      |
| ITO/CPTMS/Anti-PTH/BSA/PTH           | 0.00005–0.15                      | 0.000026    | 2.59            | CV, EIS           | [50]      |
| PAMAM                                | 0.01–0.06                         | 0.00143     | 1.74            | EIS               | [51]      |
| Dopamine                             | 50–8000                           | 0.017       | 5.76            | CV, EIS           | [52]      |
| Nanostructured Au-Pt                 | 1–10,000                          | 0.36        | 8               | EIS, DPV          | [8]       |
| Au/MHL/EPI/EA/GLT/Anti-PTH           | 0.1–0.6                           | 0.001       | 8               | DPV               | [53]      |
| MoS <sub>2</sub> -graphene composite | 1–50                              | 5           | 5.5             | EIS               | [54]      |
| 4-Nitroso-1-naphthol                 | 10 <sup>-1</sup> –10 <sup>8</sup> | 0.1         | –               | Chrono-coulometry | [55]      |
| MWCNT-AuNP Nanocomposite             | 1–10 <sup>5</sup> pg/mL           | 0.092       | 1.37%           | CV                | This work |
|                                      | 1–10 <sup>5</sup> pg/mL           | 0.033       | 3.46%           | EIS               | This work |

28.58–0.087 C<sub>PTH</sub> and 0.092 pg/mL, respectively. The developed immunosensor has great potential for fast PTH detection. The immunological detection using the amperometric method can be summarized as the following events [11]. The redox mediator is released or adsorbed onto the interacting liquid-electrode interface which results in electron transfer to or from the electrodes. The electron transfer then induces a current flow between the working and the counter electrode. The antibody-antigen complex formed on the electrode hinders electron transfer of ferricyanide and its amperometric current in CV.

The calculated LOD values for EIS and CV were 0.033 and 0.092 pg/mL in PTH spiked serum. Recovery results using EIS, CV, and the commercial ELISA methods are shown in Table 2. The recovery values were 80–104% using EIS, 88–109% using CV, and 80–156% using ELISA. These results demonstrate that the developed immunosensors had good recovery and accuracy as compared to the traditional ELISA method. The comparison of the different electrochemical immunosensors for PTH is summarized in Table 3 [8,48–54]. These published immunosensors adopt the EIS, DPV, and CV methods to amplify the signals. The coating materials and immobilization protocols used in these electrodes contribute to the sensitivity and accuracy in the assay. Our proposed SPCE immunosensor could detect PTH in serum using both EIS and CV methods with a fast and reliable performance. This biosensor has the advantages such as fast, low-cost, sensitive, and on-site testing.

### 3.6. Interference assay and storage stability of the immunosensor

To study the selectivity of the fabricated SPCE, human serum spiked with 100 pg/mL of PTH was evaluated in presence of potentially interfering compounds such as insulin, lysozyme, vitamin c, immunoglobulin, serum

albumin, and ovalbumin at the concentration of 1 g/L. The results were statistically compared by performing the one-tailed *t*-test at 5% significant level. No significant interference was observed from the tested compounds (Fig. 7). PTH sensing was not affected by the tested proteins and small molecules. The electrochemical response of immunosensors can be affected by the storage temperature and duration [27]. The fabricated immunosensors were stored in the refrigerator at 4 °C for 36 days and the PTH sensing activity was assessed every 7-day interval. The storage stability of the fabricated immunosensors was evaluated based on the peak current of CV and Rct of EIS using the 100 pg/mL of PTH at the first day as 100%. Under the 4 °C storage after 36 days, the PTH sensing ability was maintained as indicated in Fig. 8. Most of the results after the storage were similar to the day-1 measurement. The relative standard deviations of all measurements were within 8% for both CV and EIS. After 36 days, the antibody activity on SPCEs could be retained for PTH measurements, suggesting that the sensor had good stability (Fig. 8). Glassy carbon electrode has been applied for biomarker detection since their low background current and wide potential window [47,48]. However, this kind of electrode is expensive and pre-polish treatment is needed. The developed immunosensor offers portable and stable detection for the PTH immunoassay. We reported a facile SPCE modification to achieve low cost, high sensitivity, fast detection, and low sample requirement for PTH immunoassay using both amperometric and impedimetric methods.

## 4. Conclusion

A immunosensor for PTH was fabricated based on SPCEs modified by the nanocomposite of AuNP and MWCNT. The nanocomposite was successfully in-situ electrodeposited on the working electrode of SPCE. The

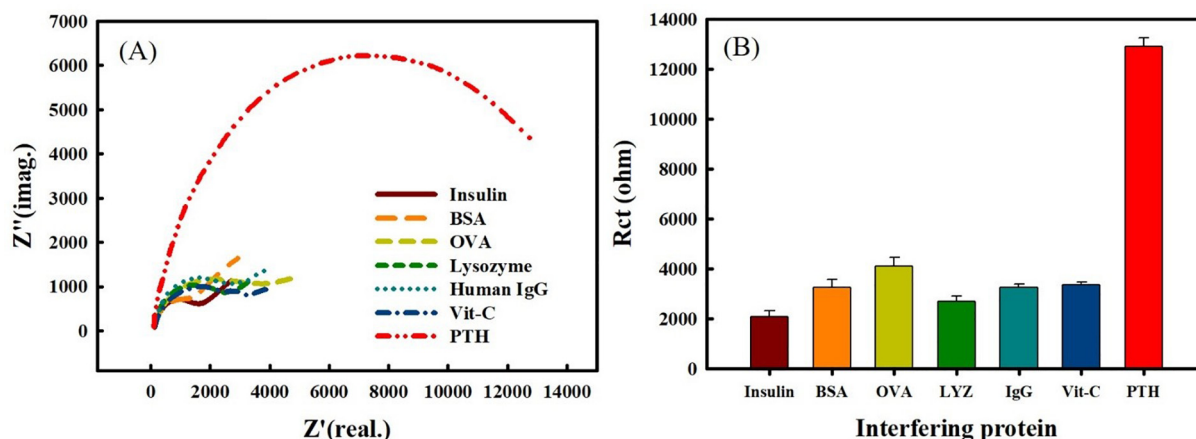
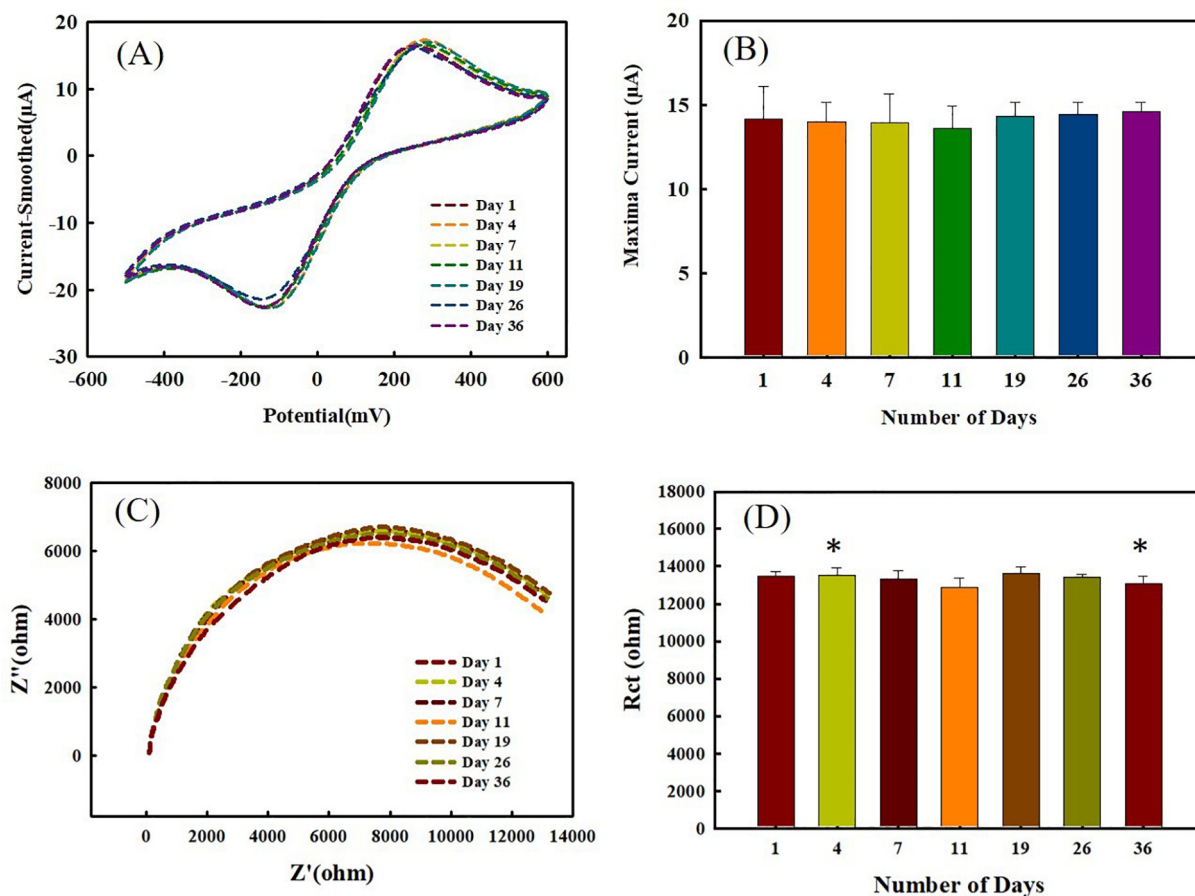


Fig. 7. (A) Impedance spectra of immunosensor under interfering compounds at 1 mg/mL, (B) histogram showing the relative Rct value. EIS was run with amplitude 100 mV, frequency range 1–1000 Hz, and initial potential 50 mV. The PTH concentration in the interference test was 100 pg/mL. Error bar represents the standard deviation from three repeats (*n* = 3).



**Fig. 8.** Stability test using fabricated immunosensor after 36-day storage: (A) CV signal, (B) relative maximal current. The current of Day-0 SPCE was represented as 100%. (C) EIS signal, (D) relative Rct. The Rct of Day-0 SPCE was represented as 100%. CV was performed over  $-500 \sim +600$  mV at  $50$  to  $100$  mV s $^{-1}$  using  $3$  mM ferricyanide in PBS. EIS signal was obtained by placing  $100$   $\mu$ L of  $3$  mM ferricyanide in PBS. EIS was run with amplitude  $100$  mV, frequency range  $1$ – $1000$  Hz, and initial potential  $50$  mV. The tested PTH concentration was  $100$  pg/mL. \* indicated significantly different compared to Day-1 result at  $5\%$  level using one-tailed  $t$ -test. The peak current ( $14.15 \pm 1.96$   $\mu$ A) of Day-1 SPCE was represented as  $100\%$  for CV signal. The Rct ( $13,496 \pm 251$   $\Omega$ ) of Day-1 SPCE was represented as  $100\%$  for EIS signal. Error bar represents the standard deviation from three repeats ( $n = 3$ ).

nanocomposite had advantages such as a large surface area for antibody immobilization and a connected network for fast electron transport. The facile immobilization enabled the formation of a sensing layer which provided excellent reproducibility and stability. The impedimetric and amperometric measurements were not affected by interference from protein components presented in serum. We provided the quick analysis of PTH in serum, which can be used as the label-free immunosensor platform for point-of-care testing. The nanocomposite-based biosensor showed good stability and reproducibility, fast detection, as well as a lower detection limit in human serum PTH samples.

#### Declaration of Competing Interest

The authors declare that they have no conflict of interest.

#### Acknowledgements

We express gratitude to Ministry of Science and Technology (MOST 108-2221-E-182-039), Chang Gung University (BMRP 758) and Chang Gung Memorial Hospital (2J0161, 2H0072, 2H0073) for funding and supporting this research. We appreciate the critical comments from Prof. Purnendu Parhi at Ravenshaw University, India.

#### Appendix A. Supplementary data

Supplementary data to this article can be found online at <https://doi.org/10.1016/j.jelechem.2020.114917>.

#### References

- [1] K. Tan, L. Ong, S.K. Sethi, S. Saw, Comparison of the Elecsys PTH(1-84) assay with four contemporary second generation intact PTH assays and association with other biomarkers in chronic kidney disease patients, *Clin. Biochem.* 46 (9) (2013) 781–786.
- [2] M. Li, F. Lv, Z. Zhang, W. Deng, Y. Li, Z. Deng, Y. Jiang, O. Wang, X. Xing, L. Xu, W. Xia, Establishment of a normal reference value of parathyroid hormone in a large healthy Chinese population and evaluation of its relation to bone turnover and bone mineral density, *Osteoporos. Int.* 27 (5) (2016) 1907–1916.
- [3] W.U. Dittmer, P. de Kievit, M.W.J. Prins, J.L.M. Vissers, M.E.C. Mersch, M.F.W.C. Martens, Sensitive and rapid immunoassay for parathyroid hormone using magnetic particle labels and magnetic actuation, *J. Immunol. Methods* 338 (1–2) (2008) 40–46.
- [4] H. Schmidt-Gayk, E. Spanuth, J. Kötting, R. Bartl, D. Felsenberg, J. Pfeilschifter, F. Raue, J. Roth, Performance evaluation of automated assays for  $\beta$ -CrossLaps, N-MID-Osteocalcin and intact parathyroid hormone (BRIOROSE Multicenter Study), *Clin. Chem. Lab. Med.* 42 (1) (2004) 90–95.
- [5] R. MacNeill, R. Stromeyer, B. Urbanowicz, V. Acharya, M. Moussallie, LC-MS/MS quantification of parathyroid hormone fragment 1-34 in human plasma, *Bioanalysis* 5 (4) (2013) 415–422.
- [6] S.E. Rodgers, J.I. Lew, The parathyroid hormone assay, *Endocr. Pract.* 17 (Suppl. 1) (2011) 2–6.



- [7] L.S. Chen, R.J. Singh, Niche point-of-care endocrine testing—reviews of intraoperative parathyroid hormone and cortisol monitoring, *Crit. Rev. Clin. Lab. Sci.* 55 (2) (2018) 115–128.
- [8] A.K. Yagati, A. Go, S.G. Chavan, C. Baek, M.H. Lee, J. Min, Nanostructured Au-Pt hybrid disk electrodes for enhanced parathyroid hormone detection in human serum, *Bioelectrochemistry* 128 (2019) 165–174.
- [9] R.A.S. Couto, J.L.F.C. Lima, M.B. Quinaz, Recent developments, characteristics and potential applications of screen-printed electrodes in pharmaceutical and biological analysis, *Talanta* 146 (2016) 801–814.
- [10] R.O. Kadara, N. Jenkinson, C.E. Banks, Characterisation of commercially available electrochemical sensing platforms, *Sensors Actuators B Chem.* 138 (2) (2009) 556–562.
- [11] K.K. Mistry, K. Layek, A. Mahapatra, C. RoyChaudhuri, H. Saha, A review on amperometric-type immunosensors based on screen-printed electrodes, *Analyst* 139 (10) (2014) 2289–2311.
- [12] H. Beitollahi, F. Garkani Nejad, S. Tajik, S. Jahani, P. Biparva, Voltammetric determination of amitriptyline based on graphite screen printed electrode modified with a copper oxide nanoparticles, *Int. J. Nano Dimens.* 8 (3) (2017) 197–205.
- [13] S. Tajik, M.A. Taher, New method for microextraction of ultra trace quantities of gold in real samples using ultrasound-assisted emulsification of solidified floating organic droplets, *Microchim. Acta* 173 (1–2) (2011) 249–257.
- [14] M.M. Motaghi, H. Beitollahi, S. Tajik, R. Hosseinzadeh, Nanostructure electrochemical sensor for voltammetric determination of vitamin C in the presence of vitamin B6: application to real sample analysis, *Int. J. Electrochem. Sci.* 11 (9) (2016) 7849–7860.
- [15] M.R. Ganjali, H. Beitollahi, R. Zaimbashi, S. Tajik, M. Rezapour, B. Larijani, Voltammetric determination of dopamine using glassy carbon electrode modified with ZnO/Al<sub>2</sub>O<sub>3</sub> nanocomposite, *Int. J. Electrochem. Sci.* 13 (3) (2018) 2519–2529.
- [16] H. Beitollahi, H. Mahmoudi Moghaddam, S. Tajik, Voltammetric determination of bisphenol A in water and juice using a lanthanum (III)-doped cobalt (II,III) nanocube modified carbon screen-printed electrode, *Anal. Lett.* 52 (9) (2019) 1432–1444.
- [17] H. Mahmoudi-Moghaddam, S. Tajik, H. Beitollahi, Highly sensitive electrochemical sensor based on La<sup>3+</sup>-doped Co<sub>3</sub>O<sub>4</sub> nanocubes for determination of Sudan I content in food samples, *Food Chem.* 286 (2019) 191–196.
- [18] J. Li, R. Pang, Z. Yu, L. Liu, H. Wu, H. Li, L. Jiang, S. Zhang, J. Feng, C. Li, Preparation and luminescence properties of orange-red Ba<sub>3</sub>Y<sub>4</sub>O<sub>9</sub>:Sm<sup>3+</sup> phosphors, *J. Rare Earths* 36 (7) (2018) 680–684.
- [19] Z. Long, J. Zhou, J. Qiu, Q. Wang, D. Zhou, X. Xu, X. Yu, H. Wu, Z. Li, Thermally stable photoluminescence and long persistent luminescence of Ca<sub>3</sub>Ga<sub>4</sub>O<sub>9</sub>:Tb<sup>3+</sup>/Zn<sup>2+</sup>, *J. Rare Earths* 36 (7) (2018) 675–679.
- [20] M.R. Ganjali, Z. Dourandish, H. Beitollahi, S. Tajik, L. Hajiaghbabaei, B. Larijani, Highly sensitive determination of theophylline based on graphene quantum dots modified electrode, *Int. J. Electrochem. Sci.* 13 (3) (2018) 2448–2461.
- [21] A. Adumitrăchioaie, M. Tertiș, M. Suciu, F. Graur, C. Cristea, A novel immunosensing platform for serotonin detection in complex real samples based on graphene oxide and chitosan, *Electrochim. Acta* 311 (2019) 50–61.
- [22] A. Baradoke, B. Jose, R. Pauliukaite, R.J. Forster, Properties of anti-CA125 antibody layers on screen-printed carbon electrodes modified by gold and platinum nanostructures, *Electrochim. Acta* 306 (2019) 299–306.
- [23] J. Upan, P. Banet, P.H. Aubert, K. Ounnunkad, J. Jakmunee, Sequential injection-differential pulse voltammetric immunosensor for hepatitis B surface antigen using the modified screen-printed carbon electrode, *Electrochim. Acta* 349 (2020).
- [24] J. Muñoz, R. Montes, M. Baeza, Trends in electrochemical impedance spectroscopy involving nanocomposite transducers: characterization, architecture surface and biosensing, *TrAC - Trends Anal. Chem.* 97 (2017) 201–215.
- [25] S. Sharma, J. Zapatero-Rodríguez, R. Saxena, R. O'Kennedy, S. Srivastava, Ultrasensitive direct impedimetric immunosensor for detection of serum HER2, *Biosens. Bioelectron.* 106 (2018) 78–85.
- [26] B. Özcan, B. Demirbakan, G. Yeşiller, M.K. Sezginçtürk, Introducing a new method for evaluation of the interaction between an antigen and an antibody: single frequency impedance analysis for biosensing systems, *Talanta* 125 (2014) 7–13.
- [27] X. He, S.J. Chang, K. Settu, C.J. Chen, J.T. Liu, An anti-HCT-interference glucose sensor based on a fiber paper-based screen-printed carbon electrode, *Sensors Actuators B Chem.* 297 (2019).
- [28] E.P. Randviir, A cross examination of electron transfer rate constants for carbon screen-printed electrodes using electrochemical impedance spectroscopy and cyclic voltammetry, *Electrochim. Acta* 286 (2018) 179–186.
- [29] H. Hosseini, H. Ahmar, A. Dehghani, A. Bagheri, A.R. Fakhari, M.M. Amini, Au-SH-SiO<sub>2</sub> nanoparticles supported on metal-organic framework (Au-SH-SiO<sub>2</sub>@Cu-MOF) as a sensor for electrocatalytic oxidation and determination of hydrazine, *Electrochim. Acta* 88 (2013) 301–309.
- [30] S.K. Arya, G. Chormokur, M. Venugopal, S. Bhansali, Dithiobis(succinimidyl propionate) modified gold microarray electrode based electrochemical immunosensor for ultrasensitive detection of cortisol, *Biosens. Bioelectron.* 25 (10) (2010) 2296–2301.
- [31] Ü. Şengül, Comparing determination methods of detection and quantification limits for aflatoxin analysis in hazelnut, *J. Food Drug Anal.* 24 (1) (2016) 56–62.
- [32] R. Saxena, S. Srivastava, An insight into impedimetric immunosensor and its electrical equivalent circuit, *Sensors Actuators B Chem.* 297 (2019).
- [33] M. Freitas, H.P.A. Nows, C. Delerue-Matos, Electrochemical sensing platforms for HER2-ECD breast cancer biomarker detection, *Electroanalysis* 31 (1) (2019) 121–128.
- [34] Q.T. Hua, N. Ruecha, Y. Hiruta, D. Citterio, Disposable electrochemical biosensor based on surface-modified screen-printed electrodes for organophosphorus pesticide analysis, *Anal. Methods* 11 (27) (2019) 3439–3445.
- [35] W. Wu, Inorganic nanomaterials for printed electronics: a review, *Nanoscale* 9 (22) (2017) 7342–7372.
- [36] Y. Wang, Y. Qu, G. Liu, X. Hou, Y. Huang, W. Wu, K. Wu, C. Li, Electrochemical immunoassay for the prostate specific antigen using a reduced graphene oxide functionalized with a high molecular-weight silk peptide, *Microchim. Acta* 182 (11–12) (2015) 2061–2067.
- [37] S. Singh, S.K. Tuteja, D. Sillu, A. Deep, C.R. Suri, Gold nanoparticles-reduced graphene oxide based electrochemical immunosensor for the cardiac biomarker myoglobin, *Microchim. Acta* 183 (5) (2016) 1729–1738.
- [38] A.J. Bard, L.R. Faulkner, *Electrochemical Methods: Fundamentals and Applications*, 2nd edition Wiley, 2000.
- [39] P. Panjul-Bolado, D. Hernández-Santos, P.J. Lamas-Ardiansa, A. Martín-Pernía, A. Costa-García, Electrochemical characterization of screen-printed and conventional carbon paste electrodes, *Electrochim. Acta* 53 (10) (2008) 3635–3642.
- [40] K.F. Chan, H.N. Lim, N. Shams, S. Jayabal, A. Pandikumar, N.M. Huang, Fabrication of graphene/gold-modified screen-printed electrode for detection of carcinoembryonic antigen, *Mater. Sci. Eng. C* 58 (2016) 666–674.
- [41] R.C.B. Marques, S. Viswanathan, H.P.A. Nows, C. Delerue-Matos, M.B. González-García, Electrochemical immunosensor for the analysis of the breast cancer biomarker HER2 ECD, *Talanta* 129 (2014) 594–599.
- [42] F.S. Felix, L. Angnes, Electrochemical immunosensors – a powerful tool for analytical applications, *Biosens. Bioelectron.* 102 (2018) 470–478.
- [43] K. Mahato, B. Purohit, A. Kumar, P. Chandra, Clinically comparable impedimetric immunosensor for serum alkaline phosphatase detection based on electrochemically engineered Au-nano-Dendroids and graphene oxide nanocomposite, *Biosens. Bioelectron.* 148 (2020).
- [44] J.C. Souberbielle, F. Brazier, M.L. Pickett, C. Cormier, S. Minisola, E. Cavalier, How the reference values for serum parathyroid hormone concentration are (or should be) established? *J. Endocrinol. Investig.* 40 (3) (2017) 241–256.
- [45] C. Kokkinos, A. Economou, M.I. Prodromidis, Electrochemical immunosensors: critical survey of different architectures and transduction strategies, *TrAC - Trends Anal. Chem.* 79 (2016) 88–105.
- [46] A. Muhammad, R. Hajian, N.A. Yusof, N. Shams, J. Abdullah, P.M. Woi, H. Garmestani, A screen printed carbon electrode modified with carbon nanotubes and gold nanoparticles as a sensitive electrochemical sensor for determination of thiamphenicol residue in milk, *RSC Adv.* 8 (5) (2018) 2714–2722.
- [47] S. Oluketuyi, E. Mazzeza, J. Zavašnik, K. Pungjunun, K. Kalcher, A. de Marco, E. Mehmeti, Electrochemical immunosensor functionalized with nanobodies for the detection of the toxic microalgae *Alexandrium minutum* using glassy carbon electrode modified with gold nanoparticles, *Biosens. Bioelectron.* 154 (2020).
- [48] P. Shi, R. Xie, P. Wang, Y. Lei, B. Chen, S. Li, Y. Wu, X. Lin, H. Yao, Non-covalent modification of glassy carbon electrode with isoorientin and application to alpha-fetoprotein detection by fabricating an immunosensor, *Sensors Actuators B Chem.* 305 (2020).
- [49] Ç. Sayikli Şimşek, M. Nur Sonuç Karaboğa, M.K. Sezginçtürk, A new immobilization procedure for development of an electrochemical immunosensor for parathyroid hormone detection based on gold electrodes modified with 6-mercaptophexanol and silane, *Talanta* 144 (2015) 210–218.
- [50] İ. Uludağ, M.K. Sezgi Ntürk, An ultrasensitive electrochemical immunosensor platform based on disposable ITO electrode modified by 3-CPTMS for early detection of parathyroid hormone, *Turk. J. Chem.* 43 (6) (2019) 1697–1710.
- [51] H.M. Özcan, M.K. Sezginçtürk, Detection of parathyroid hormone using an electrochemical impedance biosensor based on PAMAM dendrimers, *Biotechnol. Prog.* 31 (3) (2015) 815–822.
- [52] S. Li, Y. Liu, Q. Ma, A novel polydopamine electrochemiluminescence organic nanoparticle-based biosensor for parathyroid hormone detection, *Talanta* 202 (2019) 540–545.
- [53] H.M. Özcan, K. Yıldız, C. Çakar, T. Aydın, E. Asav, A. Sağiroğlu, M.K. Sezginçtürk, Ultrasensitive impedimetric biosensor fabricated by a new immobilisation technique for parathyroid hormone, *Appl. Biochem. Biotechnol.* 176 (5) (2015) 1251–1262.
- [54] H.U. Kim, H.Y. Kim, A. Kulkarni, C. Ahn, Y. Jin, Y. Kim, K.N. Lee, M.H. Lee, T. Kim, A sensitive electrochemical sensor for in vitro detection of parathyroid hormone based on a MoS<sub>2</sub>-graphene composite, *Sci. Rep.* 6 (2016).
- [55] A. Bhatia, P. Nandhakumar, G. Kim, J. Kim, N.S. Lee, Y.H. Yoon, H. Yang, Ultrasensitive detection of parathyroid hormone through fast silver deposition induced by enzymatic Nitroreduction and redox cycling, *ACS Sensors* 4 (6) (2019) 1641–1647.

# Gold nanoparticle-assisted plasmonic enhancement for DNA detection on a graphene-based portable surface plasmon resonance sensor

Brilliant Adhi Prabowo<sup>1,2,3,\*</sup> , Agnes Purwidyantri<sup>1,4</sup> , Bei Liu<sup>2</sup> ,  
Hsin-Chih Lai<sup>5,6,7</sup> and Kou-Chen Liu<sup>2,8,9,10,\*</sup> 

<sup>1</sup> International Iberian Nanotechnology Laboratory, Braga 4715-330, Portugal

<sup>2</sup> Department of Electronics Engineering, Chang Gung University, Taoyuan 33302, Taiwan

<sup>3</sup> Research Center for Electronics and Telecommunications, Indonesian Institute of Sciences, Bandung 40135, Indonesia

<sup>4</sup> Research Unit for Clean Technology, Indonesian Institute of Sciences, Bandung 40135, Indonesia

<sup>5</sup> Department of Medical Biotechnology and Laboratory Science, Chang Gung University, Taoyuan 33302, Taiwan

<sup>6</sup> Research Center for Industry of Human Ecology and Graduate Institute of Health Industry Technology, Chang Gung University of Science and Technology, Taoyuan 33302, Taiwan

<sup>7</sup> Department of Laboratory Medicine, Chang Gung Memorial Hospital, Taoyuan 33305, Taiwan

<sup>8</sup> Center for Biomedical Engineering, Chang Gung University, Taoyuan 33302, Taiwan

<sup>9</sup> Division of Pediatric Infectious Disease, Department of Pediatrics, Chang Gung Memorial Hospital, Taoyuan 33305, Taiwan

<sup>10</sup> Department of Materials Engineering, Ming Chi University of Technology, New Taipei City 24301, Taiwan

E-mail: [brilliant.prabowo@inl.int](mailto:brilliant.prabowo@inl.int) and [jacobliu@gap.cgu.edu.tw](mailto:jacobliu@gap.cgu.edu.tw)

Received 22 September 2020, revised 28 October 2020

Accepted for publication 24 November 2020

Published 10 December 2020



## Abstract

The impact of different gold nanoparticle (GNP) structures on plasmonic enhancement for DNA detection is investigated on a few-layer graphene (FLG) surface plasmon resonance (SPR) sensor. Two distinct structures of gold nano-urchins (GNu) and gold nanorods (GNr) were used to bind the uniquely designed single-stranded probe DNA (ssDNA) of *Mycobacterium tuberculosis* complex DNA. The two types of GNP-ssDNA mixture were adsorbed onto the FLG-coated SPR sensor through the  $\pi$ - $\pi$  stacking force between the ssDNA and the graphene layer. In the presence of complementary single-stranded DNA, the hybridization process took place and gradually removed the probes from the graphene surface. From SPR sensor preparation, the annealing process of the Au layer of the SPR sensor effectively enhanced the FLG coverage leading to a higher load of the probe DNA onto the sensing interface. The FLG was shown to be effective in providing a larger surface area for biomolecular capture due to its roughness. Carried out in the DNA hybridization study with the SPR sensor, GNu, with its rough and spiky structures, significantly reinforced the overall DNA hybridization signal compared with GNr with smooth surfaces, especially in capturing the probe DNA. The DNA hybridization detection assisted by GNu reached the femtomolar range limit of detection. An optical simulation validated the extreme plasmonic field enhancement at the tip of the GNu spicules. The overall integrated approach of the graphene-based SPR sensor and GNu-assisted DNA detection provided the proof-of-concept for the possibility of tuberculosis disease

screening using a low-cost and

\* Authors to whom any correspondence should be addressed.

portable system to be potentially applied in remote or third-world countries.

Supplementary material for this article is available [online](#)

Keywords: DNA, biosensor, *Mycobacterium tuberculosis*, gold nano-urchins, gold nanorods, surface plasmon resonance

(Some figures may appear in colour only in the online journal)

## 1. Introduction

The world-shattering Coronavirus disease (COVID-19) pandemic has been an important reminder of the urgent need for rapid screening and diagnostic methods of respiratory and airborne pathogen infection [1–3]. Another major threat from the respiratory disease class is tuberculosis (TB) infection, which typically spreads in poor and developing countries [4]. The morbidity and mortality rate of TB was predicted to increase significantly as a consequence of the reallocation of resources during the COVID-19 pandemic worldwide [5, 6]. The *Mycobacterium tuberculosis* complex (MTBC) is considered to be the pathogenic species causing the TB disease. It has been declared to bring out deadly effects that have infected almost a quarter of the world population, predominantly in the low-to-middle income countries in Africa, Asia, South America, and Eastern Europe [3, 4]. Unfortunately, the human-to-human airborne transmission of this bacterium makes it hard to be tested in a rapid diagnostic or screening protocol. One of the well-known DNA sequence biomarkers of MTBC is the fragment IS6110, which is stable for decades from the mutation genetic part, and extremely specific to the MTBC species. This fragment exists in several copies in different locations of the MTBC genomic profile. This versatility has made this sequence a favorable biomarker for polymerase chain reaction (PCR) and sequence-based screening diagnostics.

PCR, as the golden standard for quantification of the pathogen through specific nucleic acid amplification, is still regarded as indirect, laborious, and expensive. These drawbacks have been the main challenges for low-to-middle income countries to perform routine and extensive PCR tests in society [1, 7]. Additionally, the typical bench-top PCR system is far from being portable, limiting its application for TB cases, which are most likely to occur in remote and harsh sites. Biosensor technology has long been spotlighted to provide an alternative to the time-consuming standard diagnostic methods, and its growth has been momentarily accelerated by the current pandemic situation toward the realization of next-generation diagnostic methods. Among the myriads of disease biomarkers, the preference of the nucleic acid biomarker from the antigen is highly advantageous because its base-pairing hybridization is highly specific and robust [8] and easy to be functionalized with nanoparticles (NPs) and other surfaces [9]. On the other hand, the detection of serology biomarkers requires complicated purification–separation protocols due to the complex protein matrices in blood or bodily fluids [10, 11].

In the application of DNA on a biosensor, the uniform surface coverage by probe DNA molecules is essential to achieve an overall inherent biorecognition signal after hybridization with the target. The interfacial engineering for biomolecular captures, such as via cross-linking agents [12], electrostatic attraction [13], NP-assisted capture [14], and many other methods has been crucially developed to achieve the best sensing device performance. Gowtham *et al* reported the mechanism of physical absorption of nucleobases onto graphene and carbon nanotubes. Adenine (A), thymine (T), cytosine (C), and guanine (G) interaction between the graphene layer was dominated by the molecular polarizability, which played a vital role in the attractive dispersion force between these materials [15]. The orientation of the binding was reported to be almost parallel to the graphene layer with a separation distance of around 3.5 Å, and it indicated the interaction characteristic for the  $\pi$ - $\pi$  stacking mechanism [15, 16]. Aptamer binding on graphene was also studied for application in  $\alpha$ -thrombin monitoring. The aptamer probes were functionalized by the amine or sulfide group and adsorbed on the graphene surface by the  $\pi$ - $\pi$  stacking force mechanism. Subsequently, the presence of the  $\alpha$ -thrombins attracted the labeled aptamer from the graphene surface due to a massive covalent bond between the amino or sulfide group and the  $\alpha$ -thrombin [17]. In addition, nanomolar and sub-nanomolar range detection of DNA hybridization by the use of graphene for surface-assisted adsorption of the DNA strand were also reported [18, 19].

The utilization of solution-based graphene such as graphene oxide (GO) for capturing the DNA strands via the  $\pi$ - $\pi$  interaction was highly regarded as a simple and low-cost approach to initialize biomolecular recognition on the sensor's interface [20–22]. A significant challenge in working with solution-based graphene is transferring it onto another solid substrate, such as a gold (Au) layer, typically used in the surface plasmon resonance (SPR) sensing setup. Song *et al* recommended the improvement of Au {111} crystallization on the surface to enhance the adsorption energy of the graphene onto the Au layer [23]. Another method emphasized the high possibility for colloidal graphene on a Au SPR chip through metal–carbon bonding with a considerably high uniform coverage rate [20]. The application of deformed multi-layer graphene for effective biomolecular capture was also studied by Hwang *et al*, who successfully created electronic hotspots from the capture of DNA on the crumpled graphene layer [24].

Among the metallic NP clusters, gold NPs (GNPs) have gained significant attention and have been combined with DNA in a number of sensing platforms, including

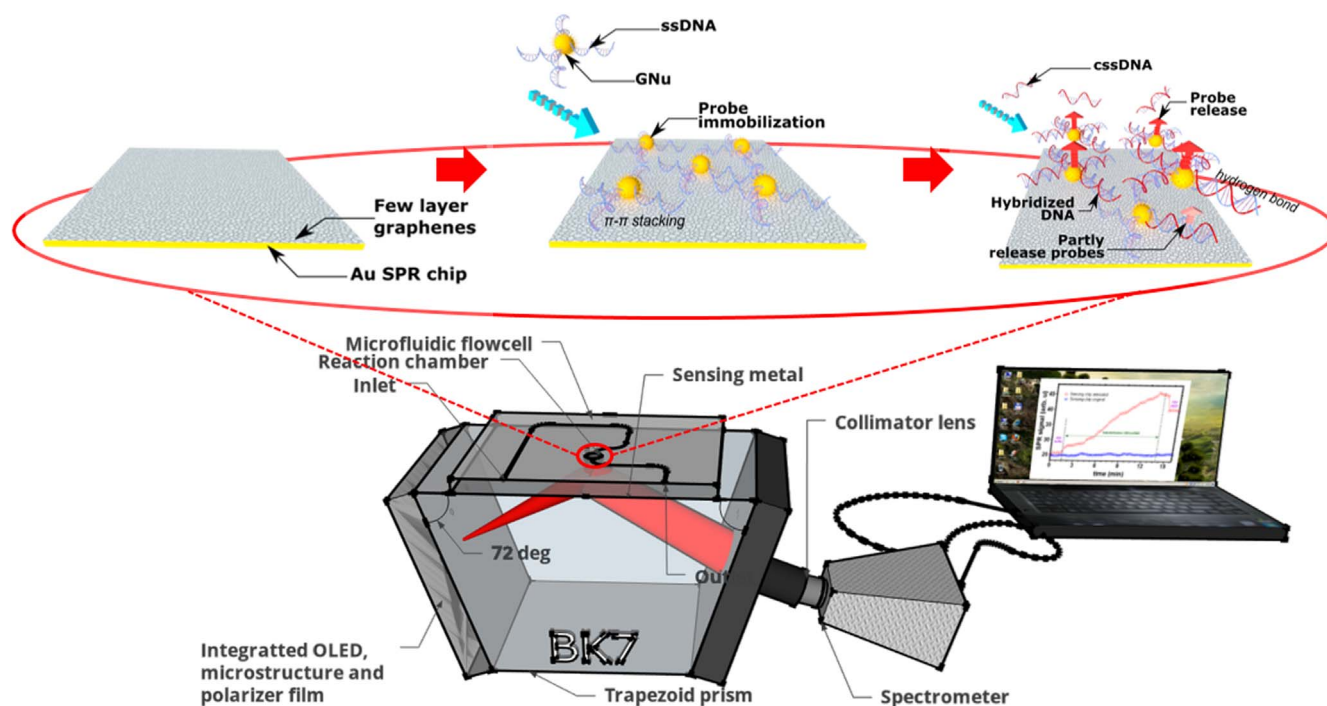


**Figure 1.** Experimental configuration of DNA hybridization on a graphene-based SPR sensor.

electrochemical, transistor-based, and optical sensors, due to their high bio-affinity, chemical and physical stability, surface area-to-volume ratio, and excellent optical features [25–31]. Specifically, the plasmonic enhancement from GNPs has been applied in a variety of optical sensing setups, such as in SPR, photoluminescence, and surface-enhanced Raman spectroscopy biosensors, showing ultrasensitive DNA or aptamer detection [20, 32–35]. The plasmonic coupling is predominantly defined by the nature, size, shape, structure, composition, and aspect ratio of the NPs and the environment dielectric constant and inter-spatial arrangement within the NPs on a solid surface [36]. Some studies have reported a remarkable electric field enhancement of branched GNPs with protruding spikes and sharp tips useful in the biosensing configuration [37, 38].

In this article, we present the proof-of-concept of the MTBC screening method, using few-layer graphene (FLG) on an SPR sensing system. The biorecognition signal from DNA was assisted by the tagging of probe DNA with GNPs with two distinct structures, gold nano-urchins (GNu) or gold nanorods (GNr), to be adsorbed onto the FLG layer via  $\pi$ - $\pi$  stacking. The hybridization event with the target DNA was checked through the release of the gold nanostructure-tagged probe from the sensing interface. The plasmonic activity from both gold nanostructures was compared, and it was noted that GNu provided the most significant enhancement with an impressive limit of detection (LOD). The proposed work combined both the ease of solution-based graphene integration onto the portable SPR chip and facile detection methods for nucleic acid-based TB detection. Typically, experimental works associated with infectious diseases are carried out in a high biosafety level laboratory which highly restricts the circulation of equipments from and to the laboratory.

Therefore, biosensor technology can be a potential approach to eliminate contamination, particularly the modular biosensing technology with the feature of component disposability.

## 2. Materials and method

The primary platform of the portable SPR biosensor utilizing an organic light source in this experiment was described in our previous reports and is depicted in figure 1 [39]. Modular-based instruments and their portability offer an advantage for the real detection scheme of MTBC, which commonly occurs in remote areas or third-world countries. The disposability of the modular component is beneficial for handling the toxicity of the samples.

### 2.1. Material and instruments

Graphene powder and its dispersion solution were purchased from Angstrom Materials Inc. (Ohio, USA). GNu with 70 nm size and GNr with an aspect ratio of 2.5 were bought from NanoSeedz (Hong Kong, PRC). DNA sequences were purchased from Purigo Biotechnology Co. (Taipei, Taiwan). The DNA probe and target sequences were derived from the MTBC DNA fragment IS6110. The single-stranded (ssDNA) probe sequence used in this study was SH-CGTGCGGCTA TTACGAGGAC TCCACGCTGG (30 mers). The sequence of the complementary ssDNA (cssDNA) target was CCGAT AATGCTCCTG AGGTGCGACC (25 mers). In comparison, the sequence of mismatched single-stranded DNA (mssDNA) utilized in the specificity test was ACAGC ATTGCGCGTT CAGACACCGC (25 mers). The target DNA strand was designed with shorter sequences (5 mers shorter) to



accommodate the spacing activity in the probe DNA. A phosphate-buffered saline (PBS) tablet from Sigma Aldrich (Missouri, USA) was employed to produce the PBS buffer solution. NaCl,  $K_2HPO_4$ , and  $KH_2PO_4$  for the salt buffer solution were purchased from Sigma Aldrich (Missouri, USA). The RAMaker system from Protrustech. Co, Ltd. (Tainan City, Taiwan) was applied to perform Raman spectroscopy with a charge-coupled device camera system coupled with an Olympus microscope body. The collimation of light excitation was performed by a 100X objective lens (NA 0.5). The laser power source was 100 mW, the exposure time was 2 s, and the accumulation number was 3. The electron microscopy images were obtained from a field-emission scanning electron microscope (FESEM) with the instrument series of JSM-7500F (JEOL Co., Tokyo, Japan), and transmission electron microscopes (TEM) with the instrument type of JEOL JEM-1230 and JEOL JEM-2100 PLUS (JEOL Co., Tokyo, Japan). Finite-difference time-domain (FDTD) simulation was performed by Lumerical (Pennsylvania, USA).

## 2.2. Sensing chip preparation

A gold sensing chip was prepared and produced based on the protocol explained in our previous report [40]. Next, the chip was annealed in a baking chamber at 300 °C for 30 min with a very slow ramp-up of the temperature, followed by an immediate quenching process by exposing it to  $N_2$  gas at 20 °C. The quenching ramp-down temperature should be carefully handled to avoid substrate cracks. The annealing–quenching step is critical for improving Au {111} crystallization [23, 41]. The dispersant solution of graphene was diluted in deionized water to reach a 1% concentration. To prepare the FLG solution, graphene powder was then dispersed in 1% of the dispersant solution until reaching a concentration of  $0.1\text{ mg ml}^{-1}$  before ultrasonic treatment for 20 min. Subsequently, the FLG solution was dropped onto the sensing surface and baked at 80 °C (the boiling temperature point of the solution was avoided) until the sensing layer was dry.

## 2.3. DNA immobilization and detection

In this study, the ssDNA probe was tagged with the GNu before adsorption onto the sensing membrane. First, 70 nM GNu solution was centrifuged and suspended in PBS solution with a rotation speed of 700 x g for 30 min. The GNu solution was then mixed with the ssDNA in PBS until a final concentration of 100 nM ssDNA was reached. This mixed solution was kept at room temperature for 20–24 hours to allow effective covalent binding between the GNu and ssDNA probe. The target DNA was prepared through a serial dilution using the salt buffer to complete a series of concentrations from 100 fM to 100 nM. The salt buffer for target dilution was prepared by mixing 1 M  $K_2HPO_4$  and 1 M  $KH_2PO_4$  in a 1 M NaCl solution. For GNr-assisted DNA detection, similar stages were applied by replacing the GNu with GNr solution.

## 3. Results and discussion

### 3.1. FLG deposition on Au SPR chip

The deposition of graphene was notably pivotal in interfacing DNA oligonucleotides onto the SPR sensing system. We observed that the drop-casting deposition of the FLG solution onto the Au sensing chip of the portable SPR sensor favorably resulted in graphene with a few-layer structure. In figure S1(a), available online at [stacks.iop.org/NANO/32/095503/mmedia](https://stacks.iop.org/NANO/32/095503/mmedia), the optical microscopy figure shows uniform coverage of FLG on the Au layer, indicated by the homogeneous transparent color spread onto the surface with tiny clumped particles over it. The surface morphologies visualized by FESEM in figure S2 demonstrate the FLG on top of the Au chip, indicated by some visible creases on the surface in contrast to the Au layer without graphene on top. The FLG structure is typically found in the drop-casting method as a result of the graphene film wrinkling due to the surface tension of water when evaporation takes place during the drying protocol [42]. It is noteworthy that the wrinkled structure of graphene is ascribed to the defects and holes in the lattice of tetrahedral  $sp^3$  hybridized carbon atoms, providing extra bonds that finally form atomically rough graphene sheets as compared to pristine graphene [43, 44]. Raman detection of the FLG film in figure S2 presents a substantial uniformity of graphene coverage with very similar spectral features taken at three different sites. Graphene fingerprint peaks were observed, such as visible 2D ( $\sim 2680\text{ cm}^{-1}$ ), considerably sharp G ( $\sim 1571\text{ cm}^{-1}$ ), and intense D ( $\sim 1340\text{ cm}^{-1}$ ) peaks, ascribed to the phonons coupling with two opposite wave vectors,  $sp^2$  carbon and  $sp^3$  carbon, respectively [45]. The lower intensity of the 2D compared with the G peak indicates FLG formation [46, 47], and the highly pronounced D peak (defects), as well as the small 2D peak, is attributed to the defects due to the removal of oxygen in the basal plane [45, 48]. The rough graphene sheet would be beneficial in trapping the probe due to the high surface area in the next stage of surface functionalization. This FLG solution drop-casting method holds a potency for a straightforward and brief process for graphene-based SPR biosensor development.

### 3.2. Absorption profiles of GNu and GNr

The architectural building block of gold nanostructures greatly determines its optical properties. The TEM image in figure 2 inset shows that the GNu consists of poly-branch tips with an approximate tip-to-tip diameter of around 70–80 nm. The absorption spectra of GNu and GNr in the PBS medium are demonstrated in figure 2. GNu absorption appears optimally at around 601 nm wavelength. In the presence of ssDNA on the GNu following the preparation of the probe, the absorption peak was shifted to  $\sim 619\text{ nm}$  wavelength. This finding is in good accordance with that of Rotz *et al* 2015, who reported a similar range of wavelength shifts in a gold nanostar spectrum after DNA conjugation with good maintenance of colloidal stability [49]. In contrast, as seen in the TEM image in figure 2 inset, the dimension of GNr has a

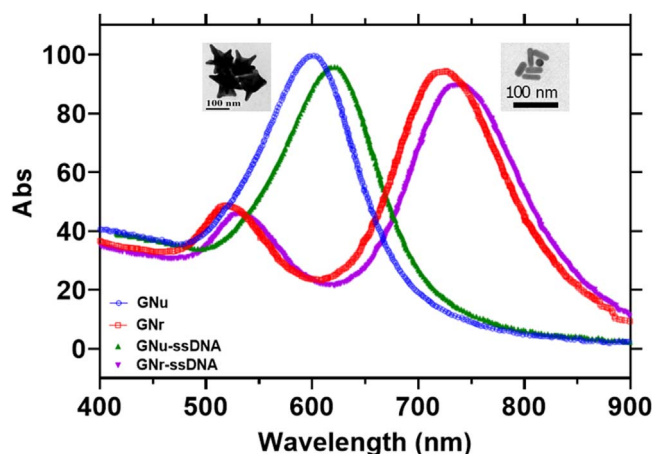
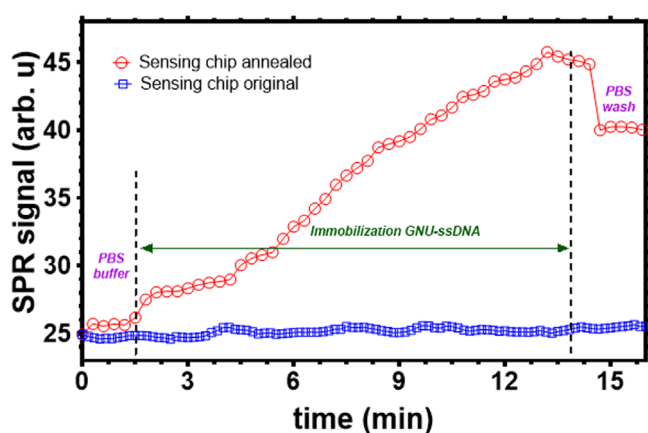
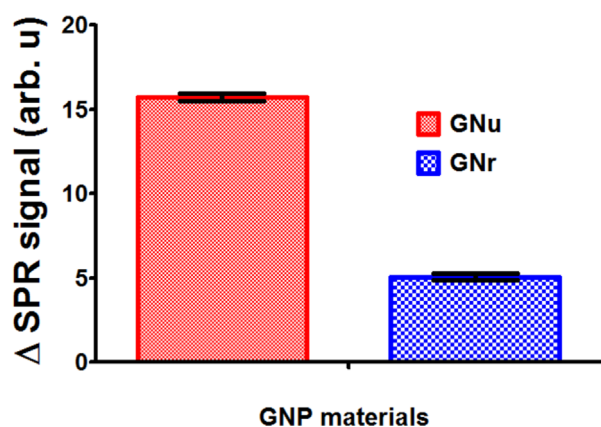


**Figure 2.** UV/vis absorption spectra of GNu and GNr in the absence and presence of ssDNA probe.

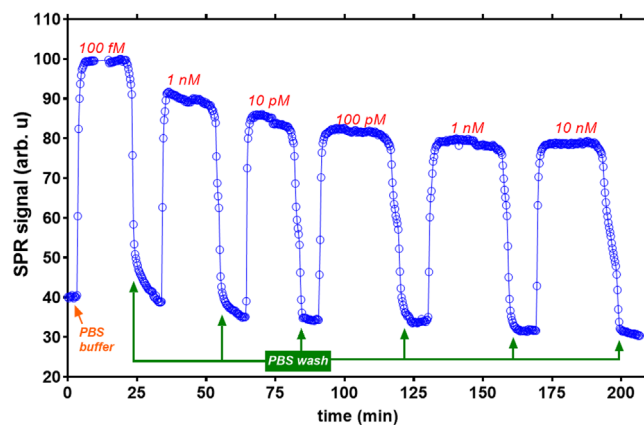


(a)

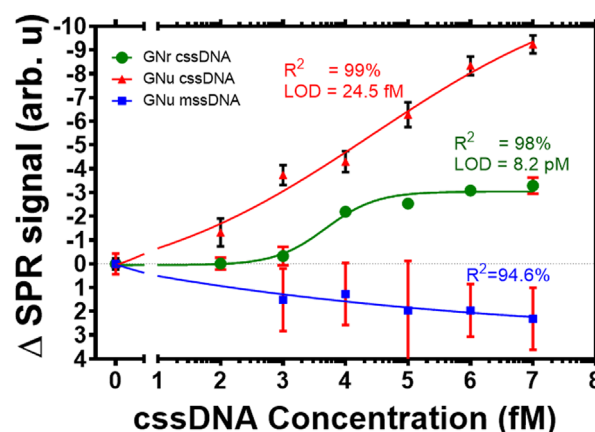


(b)

**Figure 3.** (a) The real-time measured SPR signal comparison of GNu probe immobilization on the FLG layers deposited on the Au chip with and without annealing treatment. (b) The comparison of SPR signal level from GNu-ssDNA and GNr-ssDNA probe immobilization on the FLG layer deposited on an annealed Au SPR chip.



(a)



(b)

**Figure 4.** (a) Real-time SPR sensor measurement of the series concentrations of cssDNA target hybridization with GNu-ssDNA probe. (b) The calibration plots showing the cssDNA target hybridization with GNu-ssDNA and GNr-ssDNA probes, and the specificity test from the hybridization of non-complementary mssDNA and GNu-ssDNA probe.

length of  $\sim 40$  nm and a rod thickness of about 10 nm. GNr absorption showed two major peaks, with the maximum peak at 724 nm wavelength and the minimum one at 522 nm. These peaks emerged as a consequence of the dual orientations of the GNr, which has longitudinal and transverse peaks [50, 51]. In the presence of ssDNA, the minor and major peaks were blue-shifted to 531 nm and 734 nm wavelength, respectively, indicating a successful formation of the ssDNA and GNr nanoprobe complex.

### 3.3. Annealing–quenching protocol of Au sensing chip and GNP effects on SPR signal enhancement

The annealing and quenching step of the Au SPR sensing chip before graphene solution deposition was an attempt to enhance the Au {111} orientation on the surface [41]. Higher-temperature annealing was suggested to obtain highly ordered Au {111}. However, considering that the melting point of the BK7 substrate is around 350 °C, the annealing point in our experiment was set to 300 °C. Moreover, the quenching step with the exposure of the substrate to the cold N<sub>2</sub> gas was

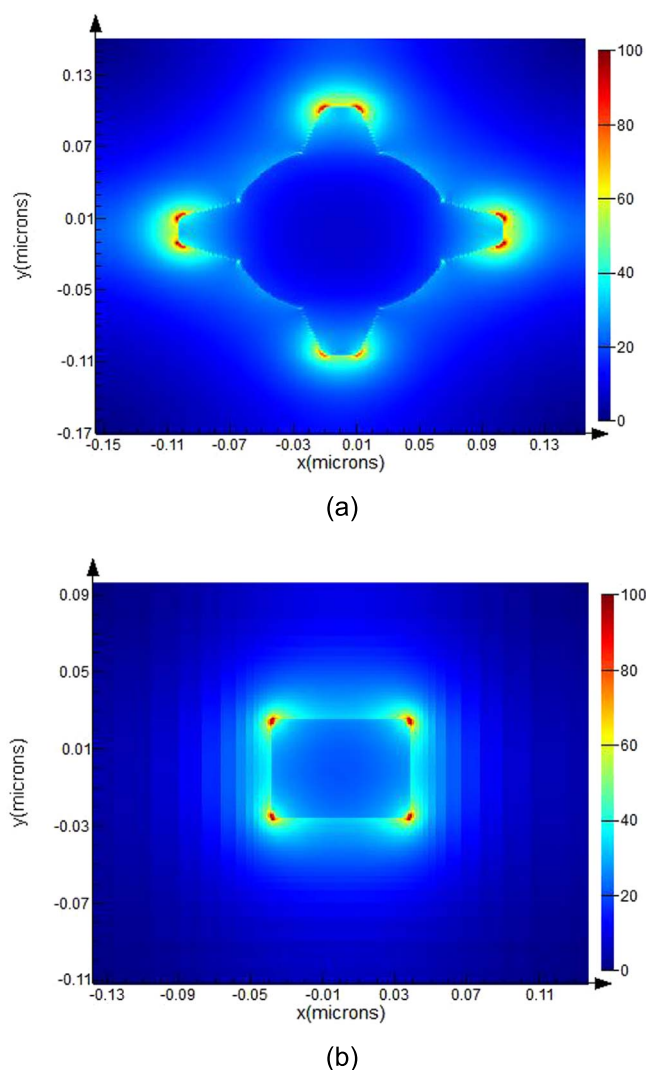


**Figure 5.** The FDTD simulation of plasmonic distribution on GNu and GNr.

conducted to avoid substrate cracks, which easily occur in quenching techniques with cool liquid immersion. Song *et al* reported that Au {111} film exhibited better binding absorption for graphene solution [23]. For the comparison purpose, we measured the probe immobilization on the FLG-covered Au SPR chip in the presence and absence of the annealing–quenching protocol, as displayed in figure 3(a). The strong absorption and homogeneous coverage of the FLG film on the Au SPR sensing chip were assisted by the annealing–quenching protocols, which, in comparison to the non-treated Au chip, dramatically amplified the SPR signal after the immobilization of the GNP-DNA matrix via the  $\pi$ - $\pi$  stacking force between graphene and ssDNA. The  $\pi$ - $\pi$  stacking force exists in the mechanism of ssDNA immobilization since both graphene and ssDNA share identical characteristics as electron-rich materials [16, 23]. It is also essential to note the topological impact of the uniform FLG coverage on the Au sensing chip for probe capture. Pertaining to the convection–diffusion reaction during the FLG drop-casting on the Au chip, the convection-triggered evaporation of liquid and surface roughness of the graphene layer could

enable molecular absorption, facilitating DNA transfer to the graphene interface, which in turn cuts off the diffusion time and yields high-sensitivity detection [24].

On the other hand, in the Au SPR chip without the annealing–quenching step, the probe immobilization stage yielded a negligible SPR signal. This is indicative of the poor FLG sheet coverage on the Au chip. The FLG degradation was plausibly caused by buffer streaming in the reaction chamber, creating the lack of Au {111} orientation with higher energy absorption of the graphene layer. This outcome is in a linear agreement with the report of Song *et al* [23]. The morphology of Au film in the presence and absence of annealing is depicted in figure S3.

#### 3.4. Probe immobilization

GNRs with a length of  $\sim 40$ – $60$  nm and aspect ratio 2.5 were applied to compare the SPR signal enhancement in the GNu-assisted probe immobilization stage. The SPR signal levels are presented in figure 3(b). The GNu-ssDNA achieves a three times higher SPR signal enhancement than the GNr-ssDNA probe's signal. This phenomenon is closely linked with the plasmonic absorption behavior of GNu and GNr, which likely occurs in different wavelength regions. The plasmonic absorption of GNu is observed to be in the range of 600–620 nm, which is correlated to the intensity peak of the OLED light source in this experiment. Contrarily, the maximum plasmonic absorption of GNr was observed in the wavelength range of 720–750 nm, where the intensity of the OLED light source had dropped below the full-width at half maximum [39]. As displayed in figure 3(b), the GNu in this study successfully provided around three times higher enhancement in the SPR signal than the GNr.

#### 3.5. Detection of cssDNA target

Probe DNA immobilization is pivotal in the overall study. In GNr-assisted DNA detection (figures S4(a) and 3(b)), the SPR signal from the GNr was indicative of probe DNA immobilization. However, compared to the GNu-assisted one shown in figures 3(a) and (b), the GNr signal is extremely low since the saturation level was achieved very rapidly within the low range level of the SPR signal (figure S4(a)). In the detection of a series of cssDNA concentrations, the SPR sensor detected the degradation of the signal level after the washing step by PBS solution in both GNr- and GNu-assisted DNA detection (figures S4(b) and 4(a)), respectively. It is also notable that in both approaches, the SPR signal dramatically leaped as the cssDNA target was injected into the reaction chamber due to the immediate change in the refractive index value resulting from the salt buffer from the target dilution. The DNA binding affinity is greatly affected by the ionic strength [52], and salt mainly shows interactions with the negatively charged phosphate molecules [53]. The contrast was seen in the SPR signals after the PBS wash in GNu-assisted DNA detection, which shows more pronounced signal reduction trends as a higher cssDNA concentration was injected into the sensing chamber (figure 4(a)). The drop of



**Table 1.** Performance comparisons of our work with other SPR-based DNA detection studies.

| No  | Sensing platform          | Remarkable technique  | Detection target  | LOD       | References |
|-----|---------------------------|---|-------------------|-----------|------------|
| 1.  | Fiber optic SPR           | SAM-PEG surface chemistry binds the streptavidin for signal enhancement | DNA-protein       | 2 nM      | [59]       |
| 2.  | SPR                       | DNA-templated polyaniline deposition                                    | DNA-PNA           | 5 nM      | [60]       |
| 3.  | SPR imaging               | Signal enhancement by colloidal GNP                                     | DNA hybridization | 10 pM     | [61]       |
| 4.  | SPR imaging               | Signal enhancement by GNP   | MicroRNAs         | 10 fM     | [62]       |
|     | Laboratory SPR            | GO, signal enhancement by GNP   | DNA hybridization | 10 fM     | [20]       |
| 6.  | Commercial SPR Sensia     | Graphene, signal enhancement by Au nanostar                             | DNA hybridization | 0.5 fM    | [32]       |
| 7.  | Localized SPR             | Au nanoisland, signal enhancement by Au nanostar                        | DNA hybridization | 0.2–40 nM | [63]       |
| 8.  | Localized SPR             | Doxorubicin-modified GNPs for signal enhancement                        | DNA hybridization | 600 pM    | [64]       |
| 9.  | Commercial SPR Bia-core X | Signal enhancement by streptavidin                                      | MicroRNA          | 17 pM     | [65]       |
| 10. | Commercial SPR Bia-core X | Signal enhancement by super-sandwich assembly and streptavidin          | MicroRNA          | 9 pM      | [66]       |
| 11. | Laboratory SPR            | Surface-anchored rolling circle and GNP amplification                   | TB DNA            | 5 pM      | [67]       |
| 12. | Modular and portable SPR  | Few graphene layers, signal enhancement by GNu                          | TB DNA            | 24.5 fM   | This work  |

the SPR signal below the reference signal level (negative  $\Delta$ SPR signal) implies the release of ssDNA probes from the graphene surface by a stronger hydrogen bond force during DNA hybridization [54] than the  $\pi$ - $\pi$  stacking force between graphene and probe DNA [55–57]. The removal of the probe is related to the different binding energies, where the DNA hybridization binding energy was estimated at around  $65.7 \text{ kcal mol}^{-1}$  (equivalent to 2.85 eV) [35], while the  $\pi$ - $\pi$  stacking force between the ssDNA and the graphene surface is only approximately 0.49 to 0.61 eV [7, 36]. The removal of the ssDNA and the GNPs away from the sensing area resulted in a significant drop in the plasmonic field, represented by the negative  $\Delta$ SPR signal. This, by the nature, structure, and morphology of the GNPs, was much stronger in GNu than GNR in providing plasmonic effects. This phenomenon leads to a susceptible sensing method with negative signals.

Figure 4(b) demonstrates the calibration plots from the level signal after PBS washing protocols in the real-time dynamic measurement from GNu- and GNR-assisted DNA detection (figures 4(a) and S4(b)). GNu-assisted DNA detection yields a trendline with a correlation coefficient of 99% and an estimated LOD based on the International Union of Pure and Applied Chemistry (IUPAC) definition using confidence level 3. It means the LOD was calculated by the estimation of the concentration (the  $x$ -axis), when the signal level reaches three times the standard deviation (SD) of the reference measurement, in correlation to the dose–response standard curve. The SD of the reference measurement was 0.23, and consequently a calculated LOD of  $\sim 24.5 \text{ fM}$  cssDNA was achieved, significantly lower than that estimated in the GNR SPR signal shown by 8.2 pM of cssDNA.

The calibration plot from the specificity test performed using non-complementary mssDNA target hybridization with the GNu-cssDNA probe is displayed in figure 4(b). In this test, the hydrogen bond of the DNA hybridization was assumed not to exist, and hence the mssDNA strands were accumulated in the graphene layer due to the  $\pi$ - $\pi$  stacking

force. This mechanism produced a slight shifting of the delta SPR signals to the positive signal [58], which opposed the results from the specific binding of hybridized DNA. The combined calibration plots clearly distinguished the GNu paramount characteristics in providing SPR signal enhancement for both highly sensitive and specific detection of DNA hybridization. The plasmonic field enhancement characteristics of GNu and GNR simulated in FDTD are presented in figure 5. GNu showed prominent hotspots in every tip of its spicules, while the GNR hotspots were likely distributed at the edge of its diameter. The robust plasmonic profile of GNu in the simulation affirms the findings on its UV–vis absorption behavior shown in figure 2. It is important to note two crucial contributions of GNu in DNA detection using our constructed SPR sensor. One, the surface roughness effects on the GNu facilitate higher probe DNA binding sites, as proven by the larger shift in the UV–vis absorption outcomes than in the GNR bonded-probe DNA. Two, the sharp spicules and rough morphology of the GNu exhibit a drastic improvement of the SPR signals compared with the smooth-surfaced GNR, as shown in the FDTD simulation.

Comparing with reported studies in related fields in table 1, it is indicated that our modular and portable sensor using a graphene-based SPR sensor combined with GNu-assisted DNA detection shows excellent advantages in terms of simplicity, portability, and specificity. The detection limit in our proposed study is highly comparable to that of the commercial SPR and laboratory SPR, as well as the SPR imaging system, indicating a promising technique for DNA detection at a low concentration.

#### 4. Conclusion

A proof-of-concept of the DNA hybridization of MTBC, assisted by the plasmonic field from GNu, has been presented in a portable graphene-based SPR sensor. The drop-casting of

an FLG solution on the Au chip of the SPR sensor has paved the way for simple, time-saving, and low-cost sensor production. The high accuracy of detection performed in this study, reflected by the low detection limit and high specificity in DNA detection, offers new insights for early screening methods of bacterial infections such as TB in a rapid a low-cost manner with portable sensors, with the possibility of application in remote areas or third-world countries as well as in pandemic scenarios.

## Acknowledgments

The authors wholeheartedly thank the Taiwan Ministry of Science and Technology for the research grant under contract number MOST 109-2221-E-182-021-MY3; MOST 109-2221-E-182-063-MY3; MOST 108-2218-E-182-004; and Chang Gung Memorial Hospital for CMPRD2G0152. Brilliant Adhi Prabowo acknowledges Chang Gung University for the research visit grant under BMRP741.

## ORCID iDs

Briliant Adhi Prabowo  <https://orcid.org/0000-0002-7543-5143>

Agnes Purwidyantri  <https://orcid.org/0000-0002-4457-2778>

Bei Liu  <https://orcid.org/0000-0002-9468-3548>

Kou-Chen Liu  <https://orcid.org/0000-0002-3294-3148>

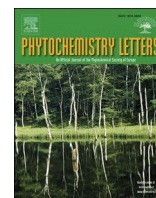
## References

- [1] Udugama B, Kadhiresan P, Kozlowski H N, Malekjahani A, Osborne M, Li V Y C, Chen H, Mubareka S, Gubbay J B and Chan W C W 2020 Diagnosing COVID-19: the disease and tools for detection *ACS Nano* **14** 3822–35
- [2] Ling W 2020 C-reactive protein levels in the early stage of COVID-19 *Médecine Mal. Infect.* **50** 332–4
- [3] WHO 2019 Country Profiles for 30 High TB Burden Countries, *Global Tuberculosis Report 202–97* [https://www.who.int/docs/default-source/documents/tuberculosis/annex-3-global-tb-report-2019-regional-and-global-profiles.pdf?sfvrsn=7f989e9f\\_2](https://www.who.int/docs/default-source/documents/tuberculosis/annex-3-global-tb-report-2019-regional-and-global-profiles.pdf?sfvrsn=7f989e9f_2)
- [4] WHO 2019 *Global Tuberculosis Report* <https://apps.who.int/iris/bitstream/handle/10665/329368/9789241565714-eng.pdf?ua=1>
- [5] Glaziou P 2020 Predicted impact of the COVID-19 pandemic on global tuberculosis deaths in 2020 *MedRxiv.* (<https://doi.org/10.1101/2020.04.28.20079582>)
- [6] WHO 2020 Tuberculosis and COVID-19: considerations for tuberculosis care 1–11 <https://www.who.int/docs/default-source/documents/tuberculosis/infonote-tb-covid-19.pdf>
- [7] Ward M P, Li X and Tian K 2020 Novel coronavirus 2019, an emerging public health emergency *Transbound. Emerg. Dis.* **67** 469–70
- [8] Liu X, Li X, Gao X, Ge L, Sun X and Li F 2019 A universal paper-based electrochemical sensor for zero-background assay of diverse biomarkers *ACS Appl. Mater. Interfaces* **11** 15381–8
- [9] Xu X, Ji J, Chen P, Wu J, Jin Y, Zhang L and Du S 2020 Salt-induced gold nanoparticles aggregation lights up fluorescence of DNA-silver nanoclusters to monitor dual cancer markers carcinoembryonic antigen and carbohydrate antigen 125 *Anal. Chim. Acta* **1125** 41–9
- [10] Chen C, Zhou S, Cai Y and Tang F 2017 Nucleic acid aptamer application in diagnosis and therapy of colorectal cancer based on cell-SELEX technology *Npj Precis. Oncol.* **1** 1–7
- [11] Yan M, Bai W, Zhu C, Huang Y, Yan J and Chen A 2016 Design of nuclease-based target recycling signal amplification in aptasensors *Biosens. Bioelectron.* **77** 613–23
- [12] Xu L, Wang R, Kelso L C, Ying Y and Li Y 2016 A target-responsive and size-dependent hydrogel aptasensor embedded with QD fluorescent reporters for rapid detection of avian influenza virus H5N1 *Sensors Actuators, B Chem.* **234** 98–108
- [13] Zhang H, Qiao B, Guo Q, Jiang J, Cai C and Shen J 2020 A facile and label-free electrochemical aptasensor for tumour-derived extracellular vesicle detection based on the target-induced proximity hybridization of split aptamers *Analyst* **145** 3557–63
- [14] Liu G, Feng D-Q, Li Z and Feng Y 2019 Target-activatable gold nanoparticle-based aptasensing for protein biomarkers using stimuli-responsive aggregation *Talanta* **192** 112–7
- [15] Gowtham S, Scheicher R H, Ahuja R, Pandey R and Karna S P 2007 Physisorption of nucleobases on graphene: density-functional calculations *Phys. Rev. B—Condens. Matter Mater. Phys.* **76** 2–5
- [16] Varghese N, Mogera U, Govindaraj A, Das A, Maiti P K, Sood A K and Rao C N R 2009 Binding of DNA nucleobases and nucleosides with graphene *Chem. Phys. Chem.* **10** 206–10
- [17] Wang L, Zhu C, Han L, Jin L, Zhou M and Dong S 2011 Label-free, regenerative and sensitive surface plasmon resonance and electrochemical aptasensors based on graphene *Chem. Commun. (Camb).* **47** 7794–6
- [18] Šířová H and Homola J 2013 Surface plasmon resonance sensing of nucleic acids: a review *Anal. Chim. Acta* **773** 9–23
- [19] Prabowo B A, Chang Y-F F, Lai H-C C, Alom A, Pal P, Lee Y-Y Y, Chiu N-F F, Hatanaka K, Su L-C C and Liu K-C C 2018 Rapid screening of *Mycobacterium tuberculosis* complex (MTBC) in clinical samples by a modular portable biosensor *Sensors Actuators B. Chem.* **254** 742–8
- [20] Xue T, Cui X, Guan W, Wang Q, Liu C, Wang H, Qi K, Singh D J and Zheng W 2014 Surface plasmon resonance technique for directly probing the interaction of DNA and graphene oxide and ultra-sensitive biosensing *Biosens. Bioelectron.* **58** 374–9
- [21] Wang Y, Li Z, Weber T J, Hu D, Lin C-T, Li J and Lin Y 2013 *In situ* live cell sensing of multiple nucleotides exploiting DNA/RNA aptamers and graphene oxide nanosheets *Anal. Chem.* **85** 6775–82
- [22] Han B *et al* 2018 Direct laser scribing of AgNPs@RGO biochip as a reusable SERS sensor for DNA detection *Sensors Actuators, B Chem.* **270** 500–7
- [23] Song B, Li D, Qi W, Elstner M, Fan C and Fang H 2010 Graphene on Au(111): a highly conductive material with excellent adsorption properties for high-resolution bio/nanodetection and identification *Chem. Phys. Chem.* **11** 585–9
- [24] Hwang M T *et al* 2020 Ultrasensitive detection of nucleic acids using deformed graphene channel field effect biosensors *Nat. Commun.* **11** 1543
- [25] Purwidyantri A, Chen C-H, Hwang B-J, Luo J-D, Chiou C-C C-C, Tian Y-C, Lin C-Y, Cheng C-H and Lai C-S C-S 2016 Spin-coated Au-nanohole arrays

- engineered by nanosphere lithography for a *Staphylococcus aureus* 16S rRNA electrochemical sensor *Biosens. Bioelectron.* **77** 1086–94
- [26] Qiu G, Ng S P and Wu C M L 2015 Differential phase-detecting localized surface plasmon resonance sensor with self-assembly gold nano-islands *Opt. Lett.* **40** 1924–7
- [27] Long Y-T and Jing C 2014 *Localized Surface Plasmon Resonance Based Nanobiosensors 1* (Berlin Heidelberg: Springer-Verlag) (<https://doi.org/10.1007/978-3-642-54795-9>)
- [28] Rasheed P A and Sandhyarani N 2015 A highly sensitive DNA sensor for attomolar detection of the BRCA1 gene: signal amplification with gold nanoparticle clusters *Analyst* **140** 2713–8
- [29] Ding J, Zhang K, Xu W and Su Z 2015 Self-assembly of gold nanoparticles on gold core-induced polypyrrole nanohybrids for electrochemical sensor of dopamine *Nano.* **10** 1550115
- [30] Szunerits S, Spadavecchia J and Boukherroub R 2014 Surface plasmon resonance: signal amplification using colloidal gold nanoparticles for enhanced sensitivity *Rev. Anal. Chem* **33** 153–164.
- [31] Hong X and Hall E. a. H. 2012 Contribution of gold nanoparticles to the signal amplification in surface plasmon resonance *Analyst* **137** 4712
- [32] Zagorodko O, Spadavecchia J, Serrano A Y, Larroulet I and Pesquera A 2014 Highly sensitive detection of DNA hybridization on commercialized graphene-coated surface plasmon resonance interfaces *Anal. Chem.* **86** 11211–6
- [33] Purwidyantri A, Hsu C-H H, Yang C-M M, Prabowo B A, Tian Y-C C and Lai C-S S 2019 Plasmonic nanomaterial structuring for SERS enhancement *RSC Adv.* **9** 4982–92
- [34] Purwidyantri A, Karina M, Hsu C-H, Srikanth Y, Prabowo B A and Lai C-S 2020 Facile bacterial cellulose nanofibrillation for the development of plasmonic paper sensor *ACS Biomater. Sci. Eng.* **6** 3122–31
- [35] Gupta A K, Hsu C-H, Purwidyantri A, Prabowo B A, Chiu K-P, Chen C-H, Tian Y-C and Lai C-S 2020 ZnO-Nanorod processed PC-SET as the light-harvesting model for plasmontronic fluorescence Sensor *Sensors Actuators B Chem.* **307** 127597
- [36] Anker J N, Hall W P, Lyandres O, Shah N C, Zhao J and Van R P 2008 Dwyne, Biosensing with plasmonic nanosensors *Nat. Mater.* **7** 442–53
- [37] Shao L, Susha A S, Cheung L S, Sau T K, Rogach A L and Wang J 2012 Plasmonic properties of single multipiked gold nanostars: correlating modeling with experiments *Langmuir* **28** 8979–84
- [38] Cui Q, Xia B, Mitzscherling S, Masic A, Li L, Bargheer M and Möhwald H 2015 Preparation of gold nanostars and their study in selective catalytic reactions *Colloids Surfaces A Physicochem. Eng. Asp.* **465** 20–5
- [39] Prabowo B A, Su L-C, Chang Y, Lai H, Chiu N-F and Liu K-C 2016 Performance of white organic light-emitting diode for portable optical biosensor *Sens. Actuators B* **222** 1058–65
- [40] Prabowo B A, Alom A, Secario M K, Masim F C P, Lai H C, Hatanaka K and Liu K C 2016 Graphene-based portable SPR sensor for the detection of *Mycobacterium tuberculosis* DNA strain *Procedia Eng.* **168** 541–5
- [41] Uosaki K, Shen Y and Kondo T 1995 Preparation of a highly ordered Au (111) phase on a polycrystalline gold substrate by vacuum deposition and its characterization by XRD, GISXRD, STM/AFM, and electrochemical measurements *J. Phys. Chem.* **99** 14117–22
- [42] Chong W S, Gan S X, Al-Tuwir H M, Chong W Y, Lim C S and Ahmad H 2020 Nanolitre solution drop-casting for selective area graphene oxide coating on planar surfaces *Mater. Chem. Phys.* **249** 122970
- [43] Bagri A, Mattevi C, Acik M, Chabal Y J, Chhowalla M and Shenoy V B 2010 Structural evolution during the reduction of chemically derived graphene oxide *Nat. Chem.* **2** 581–7
- [44] Lerf A, He H, Forster M and Klinowski J 1998 Structure of graphite oxide revisited *J. Phys. Chem. B* **102** 4477–82
- [45] Ferrari A C and Basko D M 2013 Raman spectroscopy as a versatile tool for studying the properties of graphene *Nat. Nanotechnol.* **8** 235–46
- [46] Li Z, Xu Y, Cao B, Qi L, He S, Wang C, Zhang J, Wang J and Xu K 2016 Raman spectra investigation of the defects of chemical vapor deposited multilayer graphene and modified by oxygen plasma treatment *Superlattices Microstruct.* **99** 125–30
- [47] Calizo I, Bejenari I, Rahman M, Liu G and Balandin A A 2009 Ultraviolet Raman microscopy of single and multilayer graphene *J. Appl. Phys.* **106** 043509
- [48] Song N-J, Chen C-M, Lu C, Liu Z, Kong Q-Q and Cai R 2014 Thermally reduced graphene oxide films as flexible lateral heat spreaders *J. Mater. Chem. A* **2** 16563–8
- [49] Rotz M W, Culver K S B, Parigi G, MacRenaris K W, Luchinat C, Odom T W and Meade T J 2015 High relaxivity Gd(III)–DNA gold nanostars: investigation of shape effects on proton relaxation *ACS Nano.* **9** 3385–96
- [50] Mahmoud M A 2014 Controlling the orientations of gold nanorods inside highly packed 2D arrays *Phys. Chem. Chem. Phys.* **16** 26153–62
- [51] Wawra S E, Pflug L, Thajudeen T, Krysch C, Stingl M and Peukert W 2018 Determination of the two-dimensional distributions of gold nanorods by multiwavelength analytical ultracentrifugation *Nat. Commun.* **9** 4898
- [52] De Costa N T S and Heemstra J M 2013 Evaluating the effect of ionic strength on duplex stability for PNA having negatively or positively charged side chains *PLoS One* **8** e58670
- [53] Hooyberghs J, Van Hummelen P and Carlon E 2009 The effects of mismatches on hybridization in DNA microarrays: Determination of nearest neighbor parameters *Nucleic Acids Res.* **37** e53
- [54] Natsume T, Ishikawa Y, Dedachi K, Tsukamoto T and Kurita N 2007 Hybridization energies of double strands composed of DNA, RNA, PNA and LNA *Chem. Phys. Lett.* **434** 133–8
- [55] Xie B P, Qiu G H, Hu P P, Liang Z, Liang Y M, Sun B, Bai L P, Jiang Z H and Chen J X 2018 Simultaneous detection of Dengue and Zika virus RNA sequences with a three-dimensional Cu-based zwitterionic metal–organic framework, comparison of single and synchronous fluorescence analysis *Sensors Actuators, B Chem.* **254** 1133–40
- [56] Ma Y, Wang Y, Luo Y, Duan H, Li D, Xu H and Fodjo E K 2018 Rapid and sensitive on-site detection of pesticide residues in fruits and vegetables using screen-printed paper-based SERS swabs *Anal. Methods* **10** 4655–64
- [57] Oliveira Brett A M and Chiorcea A M 2003 Atomic force microscopy of DNA immobilized onto a highly oriented pyrolytic graphite electrode surface *Langmuir* **19** 3830–9
- [58] Chen T, Li M and Liu J 2018  $\pi$ – $\pi$  stacking interaction: a nondestructive and facile means in material engineering for bioapplications *Cryst. Growth Des.* **18** 2765–83
- [59] Pollet J, Delpont F, Janssen K P F, Jans K, Maes G, Pfeiffer H, Wevers M and Lammertyn J 2009 Fiber optic SPR biosensing of DNA hybridization and DNA–protein interactions *Biosens. Bioelectron.* **25** 864–9
- [60] Su X, Teh H F, Aung K M M, Zong Y and Gao Z 2008 Femtomol SPR detection of DNA–PNA hybridization with the assistance of DNA-guided polyaniline deposition *Biosens. Bioelectron.* **23** 1715–20
- [61] He L, Musick M D, Nicewarner S R, Salinas F G, Benkovic S J, Natan M J and Keating C D 2000 Colloidal

- Au-enhanced surface plasmon resonance for ultrasensitive detection of DNA hybridization *J. Am. Chem. Soc.* **122** 9071–7
- [62] Fang S, Lee H J, Wark A W and Corn R M 2006 Attomole microarray detection of microRNAs by nanoparticle-amplified SPR imaging measurements of surface polyadenylation reactions *J. Am. Chem. Soc.* **128** 14044–6
- [63] Spadavecchia J, Barras A, Lyskawa J, Woisel P, Laure W, Pradier C-M, Boukherroub R and Szunerits S 2013 Approach for plasmonic based DNA sensing: amplification of the wavelength shift and simultaneous detection of the plasmon modes of gold nanostructures *Anal. Chem.* **85** 3288–96
- [64] Spadavecchia J, Perumal R, Barras A, Lyskawa J, Woisel P, Laure W, Pradier C-M, Boukherroub R and Szunerits S 2014 Amplified plasmonic detection of DNA hybridization using doxorubicin-capped gold particles *Analyst* **139** 157–64
- [65] Zhang D, Yan Y, Cheng W, Zhang W, Li Y, Ju H and Ding S 2013 Streptavidin-enhanced surface plasmon resonance biosensor for highly sensitive and specific detection of microRNA *Microchim. Acta* **180** 397–403
- [66] Ding X, Yan Y, Li S, Zhang Y, Cheng W, Cheng Q and Ding S 2015 Surface plasmon resonance biosensor for highly sensitive detection of microRNA based on DNA super-sandwich assemblies and streptavidin signal amplification *Anal. Chim. Acta* **874** 59–65
- [67] Xiang Y, Deng K, Xia H, Yao C, Chen Q, Zhang L, Liu Z and Fu W 2013 Isothermal detection of multiple point mutations by a surface plasmon resonance biosensor with Au nanoparticles enhanced surface-anchored rolling circle amplification *Biosens. Bioelectron.* **49** 442–9





## Briarenols O and P: Novel briaranes from a cultured octocoral *Briareum excavatum* (Briareidae)

Wei-Chiung Chi<sup>a,1</sup>, Liang-Mou Kuo<sup>b,c,1</sup>, San-Nan Yang<sup>d,e</sup>, Yi-Ting Lee<sup>f</sup>, Zhi-Hong Wen<sup>f,g</sup>, Kuan-Hao Tsui<sup>h,i</sup>, Tsong-Long Hwang<sup>j,k,l,m</sup>, Yi-Lin Zhang<sup>n,o,\*</sup>, Ping-Jyun Sung<sup>f,n,o,p,q,\*</sup>

<sup>a</sup> Department of Food Science, National Quemoy University, Kinmen 892009, Taiwan

<sup>b</sup> Department of General Surgery, Chang Gung Memorial Hospital at Chia-Yi, Chiayi, 613016, Taiwan

<sup>c</sup> School of Medicine, College of Medicine, Chang Gung University, Taoyuan, 333323, Taiwan

<sup>d</sup> School of Medicine, College of Medicine, I-SHOU University, Kaohsiung 824005, Taiwan

<sup>e</sup> Department of Pediatrics, E-DA Hospital, Kaohsiung 824410, Taiwan

<sup>f</sup> Department of Marine Biotechnology and Resources, National Sun Yat-sen University, Kaohsiung 804201, Taiwan

<sup>g</sup> Institute of BioPharmaceutical Sciences, National Sun Yat-sen University, Kaohsiung 804201, Taiwan

<sup>h</sup> Department of Obstetrics and Gynecology, Kaohsiung Veterans General Hospital, Kaohsiung 813779, Taiwan

<sup>i</sup> Department of Pharmacy and Master Program, College of Pharmacy and Health Care, Tajen University, Pingtung 907391, Taiwan

<sup>j</sup> Research Center for Chinese Herbal Medicine, Research Center for Food and Cosmetic Safety, Graduate Institute of Healthy Industry Technology, College of Human Ecology, Chang Gung University of Science and Technology, Taoyuan 333324, Taiwan

<sup>k</sup> Graduate Institute of Natural Products, College of Medicine, Chang Gung University, Taoyuan 333323, Taiwan

<sup>l</sup> Chinese Herbal Medicine Research Team, Healthy Aging Research Center, Chang Gung University, Taoyuan 333323, Taiwan

<sup>m</sup> Department of Anaesthesiology, Chang Gung Memorial Hospital, Taoyuan 333423, Taiwan

<sup>n</sup> Graduate Institute of Marine Biology, National Dong Hwa University, Pingtung 944401, Taiwan

<sup>o</sup> National Museum of Marine Biology and Aquarium, Pingtung 944401, Taiwan

<sup>p</sup> Chinese Medicine Research and Development Center, China Medical University Hospital, Taichung 404394, Taiwan

<sup>q</sup> Graduate Institute of Natural Products, Kaohsiung Medical University, Kaohsiung 807378, Taiwan

### ARTICLE INFO

#### Keywords:

*Briareum excavatum*  
Briarane  
Briarenol  
iNOS

### ABSTRACT

Two new 3,8-cyclized cembranoids, briarenols O (1) and P (2), featuring with briarane carbon skeleton have been isolated from a cultured octocoral *Briareum excavatum*. The structures of 1 and 2 were established by spectroscopic methods and 1 was found to be a rare 2-ketobriarane. Briarane 1 enhanced the generation of inducible nitric oxide synthase (iNOS) from RAW 264.7 stimulated by lipopolysaccharides (LPS).

### 1. Introduction

Octocorals belonging to the genus *Briareum* (family Briareidae, order Alcyonacea, class Anthozoa, phylum Cnidaria) (Bayer, 1981; Benayahu et al., 2004; Miyazaki and Reimer, 2014; Samimi-Namin and van Ofwegen, 2016) played the most important flagship-species to produce briarane-type natural products and the compounds of this type have been reported to exhibit interesting bioactivities, such as anti-inflammatory activity (Su et al., 2017; Wei et al., 2013). Most of the pharmaceutical-potentially coral reef organisms are claimed to be endangered species. In order to protect natural population and habits for these target marine organisms from over exploitation and stable

supporting bioactive material for further study (Yan, 2004), a cultured *B. excavatum* (Fig. 1) was studied for its chemical constituents related to briaranes. We reported herein the structures of two new isolates, briarenols O (1) and P (2) (Fig. 1). A pro-inflammatory assay was subjected to evaluate the activity of these two isolates on the release of inducible nitric oxide synthase (iNOS) from RAW 264.7 macrophage cells.

### 2. Results and discussion

Briarenol O (1), [ $\alpha$ ]<sub>D</sub> +21 (c 0.3, CHCl<sub>3</sub>), was obtained as an amorphous solid and had a molecular formula C<sub>23</sub>H<sub>28</sub>O<sub>9</sub> from high resolution

\* Corresponding authors at: National Museum of Marine Biology and Aquarium, Pingtung 944401, Taiwan.

E-mail address: [pjsung@nmmba.gov.tw](mailto:pjsung@nmmba.gov.tw) (P.-J. Sung).

<sup>1</sup> These authors contributed equally to this work.

<https://doi.org/10.1016/j.phytol.2020.09.012>

Received 22 May 2020; Received in revised form 31 July 2020; Accepted 4 September 2020

Available online 10 December 2020

1874-3900/© 2020 Phytochemical Society of Europe. Published by Elsevier Ltd. All rights reserved.

electrospray ionization mass spectroscopy (HRESIMS) at  $m/z$  471.16241  $[M + Na]^+$  (calcd for  $C_{23}H_{28}O_9Na$ , 471.16255) with ten indices of hydrogen deficiency (IHDs). The IR spectrum showed that it contained hydroxy ( $\nu_{\max}$  3436  $\text{cm}^{-1}$ ),  $\gamma$ -lactone ( $\nu_{\max}$  1782  $\text{cm}^{-1}$ ), ester carbonyl ( $\nu_{\max}$  1743  $\text{cm}^{-1}$ ),  $\alpha,\beta$ -unsaturated ester and ketonic carbonyls ( $\nu_{\max}$  1716  $\text{cm}^{-1}$ ) and  $\alpha,\beta$ -unsaturated ketonic carbonyl ( $\nu_{\max}$  1677  $\text{cm}^{-1}$ ) groups. From the  $^{13}\text{C}$  NMR spectrum (Table 1), heteronuclear single quantum coherence (HSQC) and heteronuclear multiple bond correlation (HMBC) spectra, **1** was found to possess a ketone ( $\delta_C$  209.1, C-2), an  $\alpha,\beta$ -unsaturated ketone ( $\delta_C$  200.9, C-12; 126.7, CH-13; 150.8, CH-14), an  $\alpha,\beta$ -unsaturated ester ( $\delta_C$  166.3, C-16; 122.9, C-5; 135.2, CH-6), a  $\gamma$ -lactone moiety ( $\delta_C$  175.1, C-19) and an acetoxy ( $\delta_C$  170.6, acetate carbonyl; 21.0, acetate methyl) functionalities. On the basis of above unsaturation data, **1** was concluded to be a diterpenoid possessing three rings. From the  $^1\text{H}$ – $^1\text{H}$  correlation spectroscopy (COSY) experiment of **1** (Fig. 2), the proton separate spin systems sequences from H<sub>2</sub>-3/H<sub>2</sub>-4, H-6/H-7, H-9/H-10/H-11, H-13/H-14, H-11/H<sub>3</sub>-20 and H-17/H<sub>3</sub>-18 were established. These data, together with the  $^2J$ - or  $^3J$ - $^1\text{H}$ – $^{13}\text{C}$  long-range correlations between H-10, H-13, H-14/C-1; H-14/C-2; H-3 $\beta$ , H-6/C-4; H-9/C-7; H-9/C-8; H-9, H-14/C-10; and H-14/C-12, observed in an HMBC experiment, established the major carbon skeleton of **1** (Fig. 2). The ring junction C-15 methyl group was positioned at C-1 from the HMBC correlations between H<sub>3</sub>-15/C-1, C-2, C-10 and C-14. The 2-keto group was elucidated by the HMBC correlations between H-14, H<sub>3</sub>-15 and the ketone carbonyl ( $\delta_C$  209.1, C-2). The methyl esterified carboxyl group at C-5 was supported by the HMBC spectrum with correlations of  $\delta_H$  6.84 (H-6) and 3.81 (H<sub>3</sub>, s, –OMe) with  $\delta_C$  166.3 (C-16). Furthermore, the acetate ester at C-9 was established by a correlation between H-9 ( $\delta_H$  5.34) and the acetate carbonyl ( $\delta_C$  170.6, ester carbonyl) observed in the HMBC spectrum. Eight of the nine oxygen atoms in the molecular formula could be accounted for the presence of a ketone, an  $\alpha,\beta$ -unsaturated ester, an  $\alpha,\beta$ -unsaturated ketone, a  $\gamma$ -lactone and an ester group. Thus, the remaining one oxygen atom had to be positioned at C-8, an oxygen-bearing quaternary carbon at  $\delta_C$  82.9, as a hydroxy group, although no HMBC correlation was observed between OH-8 ( $\delta_H$  2.64) to any carbon. These findings, together with a COSY correlation between H-17/H<sub>3</sub>-18 and the HMBC correlations between H-17/C-8, C-19; and H<sub>3</sub>-18/C-8, C-17, C-19, were used to establish the molecular framework of **1**.

The configurations of Me-15 and H-10 in naturally occurring briarane analogues were previously assigned  $\beta$ - and  $\alpha$ -orientation, respectively (Su et al., 2017). In the nuclear Overhauser effect spectroscopy (NOESY) experiment of **1** (Fig. 2), one of the C-3 methylene protons ( $\delta_H$  2.44) exhibited a correlation with H-10, suggesting that this proton is  $\alpha$ -oriented, and the proton at  $\delta_H$  2.60 is H-3 $\beta$ . Correlations observed between one of the C-4 methylene protons ( $\delta_H$  2.47) with H-3 $\beta$  and H-7, reflected the  $\beta$ -orientation of H-7. A correlation between H-7 and H-17 supported a  $\beta$ -orientation of H-17 in the  $\gamma$ -lactone moiety. H-9 was found to show correlations with H-11, H-17, H<sub>3</sub>-18 and H<sub>3</sub>-20. From a consideration of

**Table 1**  
 $^1\text{H}$  and  $^{13}\text{C}$  NMR data for briaranes **1** and **2**.

| Position             | <b>1</b>                          |                                   | <b>2</b>                          |                                   |
|----------------------|-----------------------------------|-----------------------------------|-----------------------------------|-----------------------------------|
|                      | $\delta_H$ (J in Hz) <sup>a</sup> | $\delta_C$ , Mult. <sup>b,c</sup> | $\delta_H$ (J in Hz) <sup>d</sup> | $\delta_C$ , Mult. <sup>c,e</sup> |
| 1                    |                                   | 52.7, C                           |                                   | 40.0, C                           |
| 2                    |                                   | 209.1, C                          | 5.13 d (9.6)                      | 77.5, CH                          |
| 3 $\alpha$           | 2.44 m                            | 36.6, CH <sub>2</sub>             | 5.65 dd (11.4, 9.6)               | 131.2, CH                         |
| $\beta$              | 2.60 ddd (14.0, 14.0, 1.2)        |                                   |                                   |                                   |
| 4 $\alpha$           | 3.09 ddd (14.0, 14.0, 0.8)        | 23.6, CH <sub>2</sub>             | 6.39 d (11.4)                     | 128.1, CH                         |
| $\beta$              | 2.47 m                            |                                   |                                   |                                   |
| 5                    |                                   | 122.9, C                          |                                   | n.o. <sup>f</sup>                 |
| 6                    | 6.84 d (9.2)                      | 135.2, CH                         | 5.85 d (8.4)                      | 125.1, CH                         |
| 7                    | 5.16 d (9.2)                      | 77.6, CH                          | 5.07 d (8.4)                      | 78.7, CH                          |
| 8                    |                                   | 82.9, C                           |                                   | 81.3, C                           |
| 9                    | 5.34 d (9.2)                      | 67.3, CH                          | 5.18 d (6.6)                      | 69.4, CH                          |
| 10                   | 3.25 dd (9.2, 5.2)                | 36.9, CH                          | 1.98 dd (6.6, 1.8)                | 36.9, CH                          |
| 11                   | 3.18 qd (7.6, 5.2)                | 43.3, CH                          | 2.05 qdd (7.2, 4.2, 1.8)          | 37.7, CH                          |
| 12                   |                                   | 200.9, C                          | 4.75 d (4.2)                      | 71.6, CH                          |
| 13                   | 6.03 d (10.4)                     | 126.7, CH                         | 3.16 d (3.6)                      | 56.8, CH                          |
| 14                   | 6.36 d (10.4)                     | 150.8, CH                         | 3.01 d (3.6)                      | 62.0, CH                          |
| 15                   | 1.25 s                            | 15.4, CH <sub>3</sub>             | 1.22 s                            | 16.0, CH <sub>3</sub>             |
| 16a                  |                                   | 166.3, C                          | 4.70 d (12.6)                     | 45.5, CH <sub>2</sub>             |
| b                    |                                   |                                   | 4.45 d (12.6)                     |                                   |
| 17                   | 2.43 q (7.2)                      | 42.6, CH                          | 2.33 q (7.2)                      | 43.2, CH                          |
| 18                   | 1.24 d (7.2)                      | 6.4, CH <sub>3</sub>              | 1.17 d (7.2)                      | 6.4, CH <sub>3</sub>              |
| 19                   |                                   | 175.1, C                          |                                   | 175.0, C                          |
| 20                   | 1.30 d (7.6)                      | 14.1, CH <sub>3</sub>             | 1.04 d (7.2)                      | 9.5, CH <sub>3</sub>              |
| OH-8                 | 2.64 s                            |                                   | 3.49 d (6.0)                      |                                   |
| OAc-2                |                                   |                                   |                                   | 169.0, C                          |
|                      |                                   |                                   | 2.05 s                            | 21.0, CH <sub>3</sub>             |
| OAc-9                | 2.21 s                            | 170.6, C                          | 2.19 s                            | 169.4, C                          |
|                      |                                   | 21.0, CH <sub>3</sub>             |                                   | 21.8, CH <sub>3</sub>             |
| OAc-12               |                                   |                                   | 2.12 s                            | 169.9, C                          |
| OCH <sub>3</sub> -16 | 3.81 s                            | 52.9, CH <sub>3</sub>             |                                   | 21.1, CH <sub>3</sub>             |

<sup>a</sup> Spectra recorded at 400 MHz in CDCl<sub>3</sub> at 25 °C.

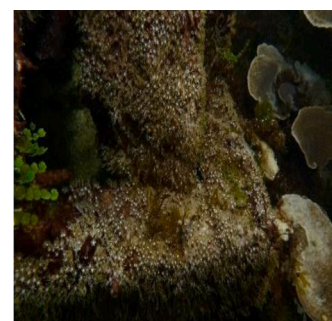
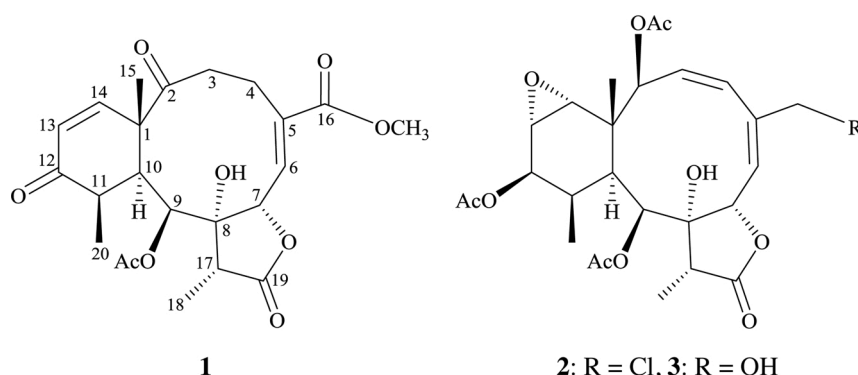
<sup>b</sup> Spectra recorded at 100 MHz in CDCl<sub>3</sub> at 25 °C.

<sup>c</sup> Due to the absence of signals, the  $^{13}\text{C}$  chemical shifts were assigned by the assistance of HSQC and HMBC spectra.

<sup>d</sup> Spectra recorded at 600 MHz in CDCl<sub>3</sub> at 25 °C.

<sup>e</sup> Spectra recorded at 150 MHz in CDCl<sub>3</sub> at 25 °C.

<sup>f</sup> n.o. = not observed.



*B. excavatum*

**Fig. 1.** The structures of briarenols O (**1**), P (**2**), briarenolide Q (**3**) and a picture of *B. excavatum*.

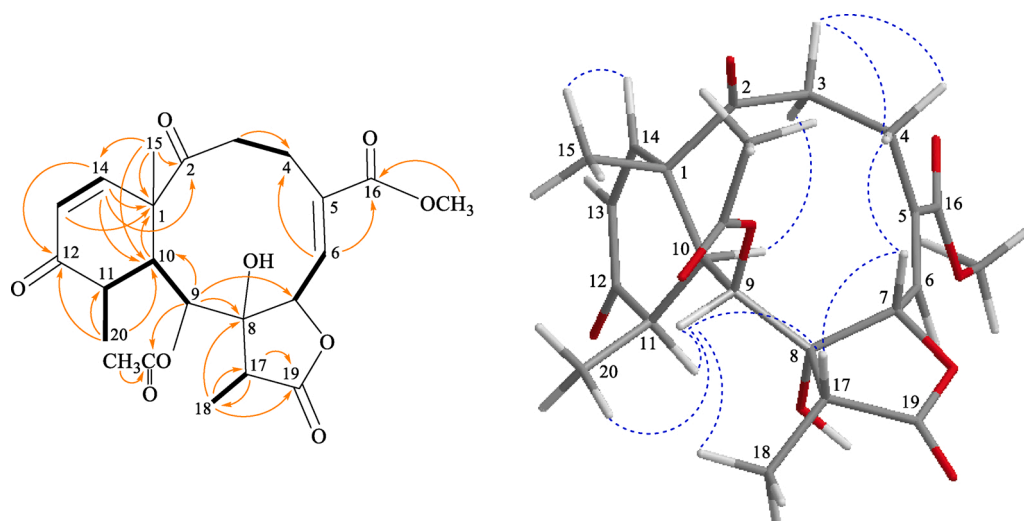


Fig. 2. The COSY (—) correlations, selective HMBC correlations (↪) and protons with key NOESY (····) correlations of **1**.

molecular model, H-9 was found to be reasonably close to H-11, H-17, H<sub>3</sub>-18 and H<sub>3</sub>-20, thus, H-9 should be placed on the  $\alpha$  face. The *cis* geometry of the C-13/14 double bond was indicated by a 10.4 Hz coupling constant between H-13 and H-14 and further supporting by a correlation between these two olefin protons. However, excepting the correlations between H-9/H-11, H-9/H<sub>3</sub>-20 and H-11/H<sub>3</sub>-20, no NOE response was observed between H<sub>3</sub>-20, H-11, OH-8 and the other protons in the NOESY experiment, so the stereochemistry of Me-20 at C-11 and hydroxy group at C-8 cannot be determined by this method.

Previous study showed that the  $^{13}\text{C}$  NMR value of C-8 resonates at  $\delta_{\text{C}}$  82.9 in an 8 $\alpha$ -hydroxy briarane analogue, juncin Z, with an identical moiety as that of **1** (Qi et al., 2006). Based on the  $^{13}\text{C}$  chemical shift of C-8 ( $\delta_{\text{C}}$  82.9), the configuration of C-8 stereogenic center in **1** was  $\alpha$ -oriented. Furthermore, by comparison of the NMR data of Me-20 in **1** ( $\delta_{\text{H}}$  1.30, d,  $J$  = 7.6 Hz;  $\delta_{\text{C}}$  14.1) with those of known briaranes, briareolate ester I ( $\delta_{\text{H}}$  0.98, d,  $J$  = 7.0 Hz;  $\delta_{\text{C}}$  12.5) (Mootoo et al., 1996) and ptilosarcenone ( $\delta_{\text{H}}$  1.30, d,  $J$  = 7 Hz;  $\delta_{\text{C}}$  14.89) (Hendrickson and Cardellina II, 1986; Wratten et al., 1977) (Fig. 3), suggested that the Me-20 at C-11 in **1** should be  $\beta$ -oriented.

Additionally, as briaranes **1** and **2** were isolated along with a known briarane, excavatolide C, from the same target organism, *B. excavatum* (Sheu et al., 1998), and the absolute configuration of this compound was determined by a single-crystal X-ray diffraction analysis (Huynh et al., 2020). Therefore, it is reasonable on biogenetic grounds to assume that briaranes **1** and **2** had the same absolute stereochemistry as that of excavatolide C. In addition, it was rarely found that an esterified carboxyl group in briarane-type diterpenoids (Chang et al., 2012;

Dookran et al., 1993; Kwak et al., 2002; Liaw et al., 2013; Qi et al., 2006; Sung et al., 2009; Taglialatela-Scafati et al., 2003; Wratten and Faulkner, 1979). To the best of our knowledge, briarenol O (**1**) is the second 2-ketobriarane analogue (Hong et al., 2012).

Briarane **2** (briarenol P) was found to have a molecular formula of  $\text{C}_{26}\text{H}_{33}\text{ClO}_{10}$  based on its HRESIMS at  $m/z$  563.16544 [ $\text{M} + \text{Na}$ ] $^{+}$  (calcd for  $\text{C}_{26}\text{H}_{33}\text{ClO}_{10}\text{Na}$ , 563.16545). Its absorption peaks in the IR spectrum showed ester carbonyl,  $\gamma$ -lactone and broad OH stretching at 1740, 1780 and 3463  $\text{cm}^{-1}$ , respectively. The  $^{13}\text{C}$  NMR spectrum indicated that three esters and a  $\gamma$ -lactone were present, as carbonyl resonances were observed at  $\delta_{\text{C}}$  169.0, 169.4, 169.9, and 175.0 (Table 1). It was observed that the spectroscopic data of **2** resembled those of a known briarane, briarenolide Q (**3**) (Fig. 1) (Su et al., 2016). The NMR spectra revealed that the signals corresponding to the 16-hydroxy group in **3** ( $\delta_{\text{H}}$  4.58, 1H, d,  $J$  = 16.0 Hz; 4.33, 1H, d,  $J$  = 16.0 Hz;  $\delta_{\text{C}}$  63.4) were replaced by those of a chlorine atom in **2** ( $\delta_{\text{H}}$  4.70, 1H, d,  $J$  = 12.6 Hz; 4.45, 1H, d,  $J$  = 12.6 Hz;  $\delta_{\text{C}}$  44.5). Therefore, briarenol P (**2**) was assigned as having a structure with the same stereochemistry as **3** because of the stereogenic carbons that **2** has in common with **3**.

The effects of briaranes **1** and **2** on the release of iNOS from LPS-stimulated RAW 264.7 macrophage cells were assessed (Fig. 4). It is interesting to note that **1** at 10  $\mu\text{M}$  enhanced the release of iNOS to 119.67 %, as compared to results of the cells stimulated with LPS only, and cells treated with dexamethasone (10  $\mu\text{M}$ ) were used as a positive control.

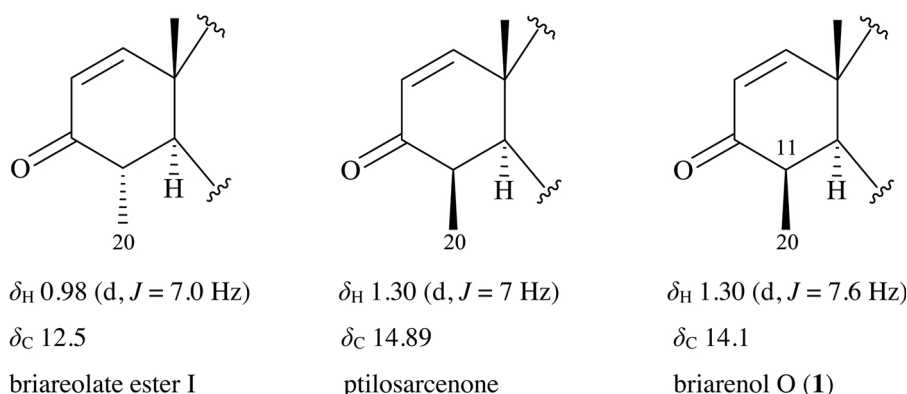
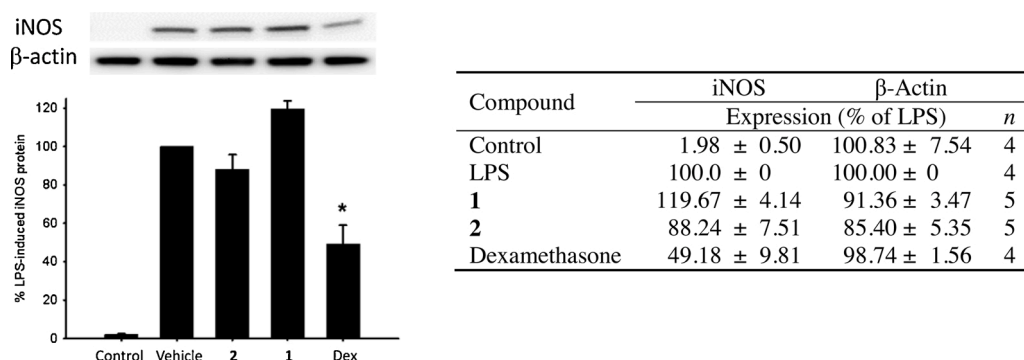


Fig. 3. The  $^1\text{H}$  and  $^{13}\text{C}$  NMR data of Me-20 of briareolate ester I, ptilosarcenone and briarenol O (**1**).



**Fig. 4.** Western blotting showed that briarane **1** enhanced the expression of iNOS. Data were normalized to the cells treated with LPS only, and cells treated with dexamethasone (10  $\mu$ M) were used as a positive control. Data are presented as the mean  $\pm$  SEM ( $n = 4-5$ ). \* Significantly different from cells treated with LPS ( $p < 0.05$ ).

### 3. Experimental

#### 3.1. General

Optical rotations were measured using a JASCO P-1010 digital polarimeter. IR spectra were measured on a Thermo Scientific Nicolet iS5 FT-IR spectrophotometer. NMR spectra were recorded on a 600 or a 400 MHz Jeol ECZ NMR spectrometers using the residual  $\text{CHCl}_3$  signal ( $\delta_{\text{H}}$  7.26 ppm) and  $\text{CDCl}_3$  ( $\delta_{\text{C}}$  77.1 ppm) as internal references for  $^1\text{H}$  and  $^{13}\text{C}$  NMR, respectively. ESIMS and HRESIMS were obtained from the Bruker mass spectrometer with 7 Tesla magnets (model: Solarix FTMS system). Column chromatography was carried out with silica gel (230–400 mesh, Merck). TLC was performed on plates precoated with Kieselgel 60 F<sub>254</sub> (0.25-mm-thick, Merck), then sprayed with 10 %  $\text{H}_2\text{SO}_4$  solution followed by heating to visualize the spots. NP-HPLC was performed using a system comprised of a Hitachi L-7100 pump and a Rheodyne 7725i injection port. RP-HPLC was performed using a system comprised of a Hitachi L-2130 pump, a Hitachi L-2455 photodiode array detector, and a Rheodyne 7725i injection port. A preparative normal-phase column (YMC-Pack SIL, S-5  $\mu\text{m}$ , 250 mm  $\times$  20 mm, Sigma-Aldrich) was used for NP-HPLC. A preparative reverse-phase column (Luna, 5  $\mu\text{m}$ , C18(2) 100 Å, AXIA Packed, 250 mm  $\times$  21.2 mm, Phenomenex) was used for RP-HPLC.

#### 3.2. Animal material

Specimens of *B. excavatum* used for this study were collected from the culturing tank in the NMMBA at April 2016. A voucher specimen was deposited in the NMMBA (voucher no.: NMMBA- TW-GC-2016-031). Identification of the species of this organism was performed by comparison as described in previous studies (Bayer, 1981; Benayahu et al., 2004; Miyazaki and Reimer, 2014; Samimi-Namin and van Ofwegen, 2016).

#### 3.3. Extraction and isolation

Sliced bodies (wet/dry weight = 3980/1860 g) of the coral specimen were prepared and extracted with a mixture of MeOH and  $\text{CH}_2\text{Cl}_2$  (1:1) to give a crude extract (104 g). The extract was then applied to a silica gel column chromatograph (Si C.C.) and eluted with gradients of hexanes/EtOAc (stepwise from 50:1 to 1:2; volume ratio) to furnish fractions A–L. Fractions H and I were combined (19.0 g) and separated on Si C.C. using hexanes/EtOAc (stepwise from 50:1 to pure EtOAc) to obtain fractions H1–H8. Fraction H6 was chromatographed with Si C.C. using hexanes/EtOAc/acetone to obtain fractions H6A–H6K. Fraction H6E was separated by Si C.C. using a mixture of  $\text{CH}_2\text{Cl}_2$  and acetone (4:1) to obtain fractions H6E1–H6E6. Fraction H6E2 was repurified by NP-HPLC using a mixture of  $\text{CH}_2\text{Cl}_2$  and acetone (8:1; at a flow rate

=2.0 mL/min) to yield fractions H6E2A–H6E2E). Fraction H6E2A was separated by RP-HPLC using a mixture of MeOH and  $\text{H}_2\text{O}$  (70:30; at a flow rate =4.0 mL/min) to afford **2** (0.2 mg). Fraction H6E2D was purified by RP-HPLC using a mixture of MeOH and  $\text{H}_2\text{O}$  (60:40; at a flow rate =4.0 mL/min) to afford **1** (0.8 mg).

#### 3.4. Briarenol O (**1**)

Amorphous powder;  $[\alpha]_{\text{D}}^{25} +21$  (c 0.3,  $\text{CHCl}_3$ ); IR (KBr)  $\nu_{\text{max}}$  3436, 1782, 1743, 1716, 1677  $\text{cm}^{-1}$ ;  $^1\text{H}$  (400 MHz,  $\text{CDCl}_3$ ) and  $^{13}\text{C}$  (100 MHz,  $\text{CDCl}_3$ ) NMR data, see Table 1. ESIMS:  $m/z$  471  $[\text{M} + \text{Na}]^+$ , HRESIMS:  $m/z$  471.16241  $[\text{M} + \text{Na}]^+$  (calcd for  $\text{C}_{23}\text{H}_{28}\text{O}_9\text{Na}$ , 471.16255).

#### 3.5. Briarenol P (**2**)

Amorphous powder;  $[\alpha]_{\text{D}}^{25} +17$  (c 0.07,  $\text{CHCl}_3$ ); IR (KBr)  $\nu_{\text{max}}$  3463, 1780, 1740  $\text{cm}^{-1}$ ;  $^1\text{H}$  (600 MHz,  $\text{CDCl}_3$ ) and  $^{13}\text{C}$  (150 MHz,  $\text{CDCl}_3$ ) NMR data, see Table 1. ESIMS:  $m/z$  563  $[\text{M} + \text{Na}]^+$ , 565  $[\text{M} + 2 + \text{Na}]^+$ , HRESIMS:  $m/z$  563.16544  $[\text{M} + \text{Na}]^+$  (calcd for  $\text{C}_{26}\text{H}_{33}\text{ClO}_{10}\text{Na}$ , 563.16545).

#### 3.6. In vitro inflammatory assay

Murine RAW 264.7 macrophages were obtained from the American Type Culture Collection (ATCC; No. TIB-71). Inflammation in macrophages was induced by incubating them for 16 h in a medium containing only LPS (0.01  $\mu\text{g}/\text{mL}$ ) without compounds. For the inflammatory activity assay, compounds (10  $\mu\text{M}$ ) were added to the cells 5 min before LPS challenge. The cells were then washed with ice cold phosphate-buffered saline (PBS), lysed in ice-cold lysis buffer (50 mM Tris, pH 7.5, 150 mM NaCl, 1 % Triton X-100, 100  $\mu\text{g}/\text{mL}$  phenylmethylsulfonyl fluoride, 1  $\mu\text{g}/\text{mL}$  aprotinin), and then centrifuged at 20,000  $\times g$  for 30 min at 4°C. The supernatant was decanted from the pellet and retained for Western blot analysis of pro-inflammation inducible nitric oxide synthase (iNOS) protein expression. Protein concentrations were determined using the detergent compatible (DC) protein assay kit (Bio-Rad, Hercules, CA, USA). Western blotting was performed according to the method described in a previous study (Chen et al., 2016). An equal volume of sample buffer (2 % 2-mercaptoethanol, 2 % sodium dodecyl sulfate (SDS), 0.1 % bromophenol blue, 10 % glycerol, and 50 mM Tris-HCl (pH 7.2)) was added to the samples, and the protein lysates were loaded onto a 10 % SDS-polyacrylamide gel. Electrophoresis was carried out at 150 V for 90 min. After electrophoresis, gels were transferred overnight at 4°C in transfer buffer (380 mM glycine, 50 mM Tris-HCl, 1 % SDS and 20 % methanol) onto a polyvinylidene difluoride membrane (PVDF; Immobilon-P, Millipore Corp. (0.45  $\mu\text{m}$  pore size)). The PVDF membrane was first blocked with 5 % non-fat dry milk in Tris-buffered saline containing 0.1 % Tween (TTBS; 20 mM Tris-HCl, 0.1



% Tween 20, and 137 mM NaCl (pH 7.4)) and incubated overnight at 4 °C with the primary antibodies for iNOS and  $\beta$ -actin proteins. Anti-iNOS antibody was purchased from Cayman Chemical Company (Ann Arbor, MI, USA). A horseradish peroxidase-conjugated secondary antibody was used for detection. It was obtained from Jackson ImmunoResearch Laboratories (West Grove, PA, USA). The bound antibodies were detected by chemiluminescence (Millipore Corp.). The images were obtained using the UVP BioChem Imaging System, and the LabWorks 4.0 software (UVP, Upland, CA, USA) was used to quantify the relative densities.

### Declaration of Competing Interest

The authors declare that they have no known competing financial interests or personal relationships that could have appeared to influence the work reported in this paper.

### Acknowledgments

This research was supported by grants from the National Museum of Marine Biology and Aquarium; the National Dong Hwa University; and the Ministry of Science and Technology, Taiwan (Grant Nos: MOST 106-2320-B-291-001-MY3, 107-2320-B-291-001-MY3 and 107-2320-B-182A-004-MY2), Taiwan, awarded to Liang-Mou Kuo and Ping-Jyun Sung.

### Appendix A. Supplementary data

Supplementary material related to this article can be found, in the online version, at doi:<https://doi.org/10.1016/j.phytol.2020.09.012>.

### References

- Bayer, F.M., 1981. Key to the genera of octocorallia exclusive of Pennatulacea (Coelenterate: Anthozoa), with diagnoses of new taxa. *Proc. Biol. Soc. Wash.* 94, 902–947.
- Benayahu, Y., Jeng, M.-S., Perkol-Finkel, S., Dai, C.-F., 2004. Soft corals (Octocorallia: Alcyonacea) from Southern Taiwan. II. Species diversity and distributional patterns. *Zool. Stud.* 43, 548–560.
- Chang, J.-Y., Liaw, C.-C., Fazary, A.E., Hwang, T.-L., Shen, Y.-C., 2012. New briarane diterpenoids from the gorgonian coral *Junceella juncea*. *Mar. Drugs* 10, 1321–1330.
- Chen, C.-H., Chen, N.-F., Feng, C.-W., Cheng, S.-Y., Hung, H.-C., Tsui, K.-H., Hsu, C.-H., Sung, P.-J., Chen, W.-F., Wen, Z.-H., 2016. A coral-derived compound improves functional recovery after spinal cord injury through its antiapoptotic and anti-inflammatory effects. *Mar. Drugs* 14, 160.
- Dookran, R., Maharaj, D., Mootoo, B.S., Ramsewak, R., McLean, S., Reynolds, W.F., Tinto, W.F., 1993. Diterpenes from the gorgonian coral *Erythropodium caribaeorum* from the Southern Caribbean. *J. Nat. Prod.* 56, 1051–1056.
- Hendrickson, R.L., Cardellina II, J.H., 1986. Structure and stereochemistry of insecticidal diterpenes from the sea pen *Ptilosarcus gurneyi*. *Tetrahedron* 42, 6565–6570.
- Hong, P.-H., Su, Y.-D., Lin, N.-C., Chen, Y.-H., Kuo, Y.-H., Hwang, T.-L., Wang, W.-H., Chen, J.-J., Sheu, J.-H., Sung, P.-J., 2012. Briarenolide E: the first 2-ketobriarane diterpenoid from an octocoral *Briareum* sp. (Briareidae). *Tetrahedron Lett.* 53, 1710–1712.
- Huynh, T.H., Lee, G.-H., Fang, L.-S., Sheu, J.-H., Sung, P.-J., 2020. Briarenols F–H: new polyoxygenated briarane diterpenoids produced by the octocoral *Briareum excavatum*. *Tetrahedron Lett.* 61, 151826.
- Kwak, J.H., Schmitz, F.J., William, G.C., 2002. Milolides G–M, new briarane diterpenoids from the Western Pacific octocoral *Briareum stechei*. *J. Nat. Prod.* 65, 704–708.
- Liaw, C.-C., Lin, Y.-C., Lin, Y.-S., Chen, C.-H., Hwang, T.-L., Shen, Y.-C., 2013. Four new briarane diterpenoids from Taiwanese gorgonian *Junceella fragilis*. *Mar. Drugs* 11, 2042–2053.
- Miyazaki, Y., Reimer, J.D., 2014. Morphological and genetic diversity of *Briareum* (Anthozoa: Octocorallia) from the Ryukyu Archipelago. *Japan. Zool. Sci.* 31, 692–702.
- Mootoo, B.S., Ramsewak, R., Sharma, R., Tinto, W.F., Lough, A.J., McLean, S., Reynolds, W.F., Yang, J.P., Yu, M., 1996. Further briareolate esters and briareolides from the Caribbean gorgonian octocoral *Briareum asbestinum*. *Tetrahedron* 52, 9953–9962.
- Qi, S.H., Zhang, S., Qian, P.Y., Xiao, Z.H., Li, M.Y., 2006. Ten new antifouling briarane diterpenoids from the South China Sea gorgonian *Junceella juncea*. *Tetrahedron* 62, 9123–9130.
- Samimi-Namin, K., van Ofwegen, L.P., 2016. Overview of the genus *Briareum* (Cnidaria, Octocorallia, Briareidae) in the Indo-Pacific, with the description of a new species. *Zookeys* 557, 1–44.
- Sheu, J.-H., Sung, P.-J., Cheng, M.-C., Liu, H.-Y., Fang, L.-S., Duh, C.-Y., Chiang, M.Y., 1998. Novel cytotoxic diterpenes, excavatolides A–E, isolated from the Formosan gorgonian *Briareum excavatum*. *J. Nat. Prod.* 61, 602–608.
- Su, Y.-D., Wen, Z.-H., Wu, Y.-C., Fang, L.-S., Chen, Y.-H., Chang, Y.-C., Sheu, J.-H., Sung, P.-J., 2016. Briarenolides M–T, new briarane diterpenoids from a Formosan octocoral *Briareum* sp. *Tetrahedron* 72, 944–951.
- Su, Y.-D., Su, J.-H., Hwang, T.-L., Wen, Z.-H., Sheu, J.-H., Wu, Y.-C., Sung, P.-J., 2017. Briarane diterpenoids isolated from octocorals between 2014 and 2016. *Mar. Drugs* 15, 44 and previous review articles in this series.
- Sung, P.-J., Wang, S.-H., Chiang, M.Y., Su, Y.-D., Chang, Y.-C., Hu, W.-P., Tai, C.-Y., Liu, C.-Y., 2009. Discovery of new chlorinated briaranes from *Junceella fragilis*. *Bull. Chem. Soc. Jpn.* 82, 1426–1432.
- Tagliatela-Scafati, O., Craig, K.S., Rebérioux, D., Roberge, M., Andersen, R.J., 2003. Briarane, erythran, and aquarian diterpenoids from the Caribbean gorgonian *Erythropodium caribaeorum*. *Eur. J. Org. Chem.* 2003, 3515–3523.
- Wei, W.-C., Sung, P.-J., Duh, C.-Y., Chen, B.-W., Sheu, J.-H., Yang, N.-S., 2013. Anti-inflammatory activities of natural products isolated from soft corals of Taiwan between 2008 and 2012. *Mar. Drugs* 11, 4083–4126.
- Wratten, S.J., Faulkner, D.J., 1979. Some diterpenes from the sea pen *Stylatula* sp. *Tetrahedron* 35, 1907–1912.
- Wratten, S.J., Fenical, W., Faulkner, D.J., Wekell, J.C., 1977. Ptilosarcone, the toxin from the sea pen *Ptilosarcus gurneyi*. *Tetrahedron Lett.* 18, 1559–1562.
- Yan, H.-Y., 2004. Harvesting drugs from the seas and how Taiwan could contribute to this effort. *Changhua J. Med.* 9, 1–6.



# Vitamin D Attenuates Ischemia/Reperfusion-Induced Cardiac Injury by Reducing Mitochondrial Fission and Mitophagy

Tzu-Lin Lee<sup>1</sup>, Ming-Hsueh Lee<sup>2,3</sup>, Yu-Chen Chen<sup>1</sup>, Yi-Chieh Lee<sup>1</sup>, Tsai-Chun Lai<sup>1</sup>, Hugo You-Hsien Lin<sup>4</sup>, Lee-Fen Hsu<sup>2,3</sup>, Hsin-Ching Sung<sup>5,6</sup>, Chiang-Wen Lee<sup>7,8,9\*</sup> and Yuh-Lien Chen<sup>1\*</sup>

## OPEN ACCESS

### Edited by:

Naufal Zagidullin,  
Bashkir State Medical University,  
Russia

### Reviewed by:

Jun Ren,  
University of Washington,  
United States  
Yundai Chen,  
Chinese PLA General Hospital,  
China  
Huang Weijian,  
First Affiliated Hospital of Wenzhou  
Medical University, China

### \*Correspondence:

Chiang-Wen Lee  
cwlee@mail.cgu.edu.tw  
Yuh-Lien Chen  
ylchen@ntu.edu.tw

### Specialty section:

This article was submitted to  
Cardiovascular and Smooth Muscle  
Pharmacology,  
a section of the journal  
Frontiers in Pharmacology

**Received:** 10 September 2020

**Accepted:** 16 November 2020

**Published:** 10 December 2020

### Citation:

Lee T-L, Lee M-H, Chen Y-C, Lee Y-C,  
Lai T-C, Lin H-Y, Hsu L-F, Sung H-C,  
Lee C-W and Chen Y-L (2020) Vitamin  
D Attenuates Ischemia/Reperfusion-  
Induced Cardiac Injury by Reducing  
Mitochondrial Fission and Mitophagy.  
Front. Pharmacol. 11:604700.  
doi: 10.3389/fphar.2020.604700

<sup>1</sup>Department of Anatomy and Cell Biology, College of Medicine, National Taiwan University, Taipei, Taiwan, <sup>2</sup>Division of Neurosurgery, Department of Surgery, Chang Gung Memorial Hospital, Chiayi, Taiwan, <sup>3</sup>Department of Respiratory Care, Chang Gung University of Science and Technology, Chiayi, Taiwan, <sup>4</sup>Division of Nephrology, Department of Internal Medicine, Kaohsiung Medical University Hospital, Kaohsiung, Taiwan, <sup>5</sup>Department of Anatomy, College of Medicine, Chang Gung University, Taoyuan, Taiwan, <sup>6</sup>Aesthetic Medical Center, Department of Dermatology, Chang Gung Memorial Hospital, Taoyuan, Taiwan, <sup>7</sup>Department of Nursing, Division of Basic Medical Sciences, and Chronic Diseases and Health Promotion Research Center, Chang Gung University of Science and Technology, Chiayi, Taiwan, <sup>8</sup>Research Center for Industry of Human Ecology and Research Center for Chinese Herbal Medicine, Chang Gung University of Science and Technology, Taoyuan, Taiwan, <sup>9</sup>Department of Orthopaedic Surgery, Chang Gung Memorial Hospital, Chiayi, Taiwan

Myocardial infarction is the leading cause of morbidity and mortality worldwide. Although myocardial reperfusion after ischemia (I/R) is an effective method to save ischemic myocardium, it can cause adverse reactions, including increased oxidative stress and cardiomyocyte apoptosis. Mitochondrial fission and mitophagy are essential factors for mitochondrial quality control, but whether they play key roles in cardiac I/R injury remains unknown. New pharmacological or molecular interventions to alleviate reperfusion injury are currently considered desirable therapies. Vitamin D<sub>3</sub> (Vit D<sub>3</sub>) regulates cardiovascular function, but its physiological role in I/R-exposed hearts, especially its effects on mitochondrial homeostasis, remains unclear. An *in vitro* hypoxia/reoxygenation (H/R) model was established in H9c2 cells to simulate myocardial I/R injury. H/R treatment significantly reduced H9c2 cell viability, increased apoptosis, and activated caspase 3. In addition, H/R treatment increased mitochondrial fission, as manifested by increased expression of phosphorylated dynein-related protein 1 (p-Drp1) and mitochondrial fission factor (Mff) as well as increased mitochondrial translocation of Drp1. Treatment with the mitochondrial reactive oxygen species scavenger MitoTEMPO increased cell viability and decreased mitochondrial fission. H/R conditions elicited excessive mitophagy, as indicated by increased expression of BCL2-interacting protein 3 (BNIP3) and light chain (LC3BII/I) and increased formation of autolysosomes. In contrast, Vit D<sub>3</sub> reversed these effects. In a mouse model of I/R, apoptosis, mitochondrial fission, and mitophagy were induced. Vit D<sub>3</sub> treatment mitigated apoptosis, mitochondrial fission, mitophagy, and myocardial ultrastructural abnormalities. The results indicate that Vit D<sub>3</sub> exerts cardioprotective effects against I/R cardiac injury by protecting mitochondrial structural and functional integrity and reducing mitophagy.

**Keywords:** cardiac ischemia/reperfusion, mitochondrial fission, vitamin D3, apoptosis, mitophagy

## INTRODUCTION

The World Health Organization (WHO) reports that acute myocardial infarction is the leading cause of morbidity and mortality in many regions of the world (Roth et al., 2017). Timely reperfusion is the most effective approach to save ischemic myocardium. However, reperfusion can induce ischemia-reperfusion (I/R) injury. I/R injury is a multifactorial pathophysiological process that causes cell damage during hypoxia, and the damage becomes more severe when oxygen is re-delivered into the tissue (Rossello et al., 2018). In addition, I/R causes a series of adverse events, such as excessive reactive oxygen species (ROS) production, calcium overload, inflammatory responses, increased apoptosis, and mitochondrial dysfunction, all of which lead to myocardial cell death and accelerate myocardial damage (Yellon and Hausenloy, 2007). Despite the clinical importance of I/R injury, bedside treatments that inhibit I/R are still limited, mainly due to the complex mechanisms that contribute to I/R. New pharmacological or molecular interventions that alleviate reperfusion injury are highly desirable for current reperfusion therapy (Baehr et al., 2019; Yu et al., 2019).

Oxidative stress is a result of increased ROS levels. ROS are produced by mitochondria due to aerobic metabolism during I/R (Chouchani et al., 2014). The cytotoxicity of ROS is associated with the rapid modification of cellular components, including the reduced ability to produce ATP (Navarro and Boveris, 2007). Excessive production of ROS causes toxicity by disrupting the electron transport chain and interfering with mitochondrial permeability transition pores, leading to apoptosis or necrosis (Hausenloy and Yellon, 2013). Although studies have shown that ROS play a key role in heart tissue damage, there is currently no effective treatment. Further research may provide new insights into the clinical treatment of I/R.

Maintaining mitochondrial function and integrity plays a crucial role in normal cell physiology, especially in cardiomyocytes with high energy requirements (Hall et al., 2014). In addition to producing ATP, mitochondria are also the major source of ROS, which can trigger oxidative stress and affect cell fate (Vasquez-Trincado et al., 2016). Therefore, strict quality control mechanisms are required to maintain healthy mitochondria. These quality control mechanisms primarily include mitochondrial dynamics, fission and fusion, and mitophagy. Mitochondrial fission is usually the separation of damaged components from the original mitochondrion, resulting in one functional mitochondrion and another impaired mitochondrion (Westermann, 2010). Mitochondrial fission involves a cytoplasmic protein, dynein-related protein 1 (p-Drp1), that binds to mitochondrial fission factor (Mff) and localizes to the mitochondrial outer membrane, forming a complex that allows mitochondrial fission. However, oxidative stress causes excessive mitochondrial fission, leading to mitochondrial structural changes and dysfunction, as well as cellular damage. In addition to mitochondrial fission, mitophagy, which is a selective form of autophagy, is another specific mechanism by which dysfunctional or impaired mitochondria are degraded and recycled; mitophagy maintains

healthy mitochondrial populations and mitochondrial quality (Ni et al., 2015). Mitochondria that are isolated by mitochondrial fission are cleared by mitophagy, and mitophagy plays a crucial role in maintaining mitochondrial homeostasis (Mao and Klionsky, 2013; Zhou et al., 2020). Mitophagy can maintain energy metabolism in the body to a certain extent and reduce damage caused by external stimuli, thereby protecting the human body; under normal conditions, cellular mitophagy is low (Ravikumar et al., 2010). However, excessive mitophagy can lead to cellular injury (Yang et al., 2019). This observation suggests that mitophagy is regulated by receptor-mediated mitophagy (Schiattarella and Hill, 2016; Bravo-San Pedro et al., 2017). BCL2/adenovirus E1B 19-kDa protein-interacting protein 3 (BNIP3) is localized to the mitochondrial outer membrane and is a receptor-related factor required for mitochondrial elimination. BNIP3 interacts with the LC3 protein family through its cytosol-directed LIR motif, thus mediating mitophagy. However, the role of BNIP3 and LC3B and the role of mitophagy during I/R injury are unclear.

Patients suffering from cardiovascular diseases are frequently deficient in vitamin D (Dibaba, 2019). Previous reports have shown that vitamin D<sub>3</sub> metabolites [including 25-hydroxyvitamin D<sub>3</sub> (25(OH)D<sub>3</sub>) and 1 $\alpha$ ,25-dihydroxyvitamin D<sub>3</sub> (1 $\alpha$ ,25(OH)<sub>2</sub>D<sub>3</sub>)] affect the uptake of calcium and phosphorus, the growth of cells, and the expression of many genes in skeletal muscle cells and cultured myoblast cell lines (Alfawaz et al., 2014; Tao et al., 2015). Low serum levels of 25(OH)D<sub>3</sub> in patients can cause a significantly higher risk of death from heart failure (Liu et al., 2016). Vitamin D is closely associated with cardiac hypertrophy and fibrosis and with atherosclerosis development (Artaza et al., 2009; Gardner et al., 2013). Supplementation with a high dose of vitamin D (25(OH)D<sub>3</sub>, 4000 IU/day) for 12 months can improve the left ventricular ejection fraction and reverse left ventricular remodeling in patients with heart failure and vitamin D deficiency (25(OH)D<sub>3</sub> < 20 ng/ml) (Witte et al., 2016). Although there is evidence that vitamin D is associated with heart disease, little information is available regarding 25-hydroxyvitamin D<sub>3</sub> (Vit D) and I/R. In addition, the role of mitophagy during Vit D treatment in preventing I/R injury remains unclear. Using I/R-exposed mice and H/R-treated cells, we will 1) examine the levels of apoptosis and ROS, 2) elucidate the role of Drp-1 and Mff in mitochondrial dynamics, and 3) identify the role of BNIP3 and LC3B in mitophagy during the progression of mitochondrial dysfunction in I/R-exposed mice treated with Vit D.

## MATERIALS AND METHODS

### Cell Culture and Hypoxia/Reoxygenation Procedure

H9c2 cells, which are rat embryonic ventricular cardiomyocytes, were obtained from American Type Culture Collection (ATCC, VA, USA). The H9c2 cells were cultured in Dulbecco's modified Eagle's medium (Gibco, MA, USA) containing 10% fetal bovine serum [Biological Industries (BI), CT, USA] and supplemented



with 1% penicillin/streptomycin/amphotericin B and 2 mM L-glutamine (BI). The cells were maintained in a humidified incubator at 37°C in 5% CO<sub>2</sub> and 95% air.

H9c2 cells were pretreated for 4 h with or without 100 nM 25-hydroxyvitamin D<sub>3</sub> (Vit D) (Cayman, UM, USA) or 10 nM MitoTEMPO (Santa Cruz, TX, USA). In addition, to evaluate the effect of mitochondrial fission or autophagy on mitophagy, H9c2 cells were pretreated for 4 h with or without the mitochondrial fission inhibitor, Mdivi-1 (10 μM) or the autophagy inhibitor, bafilomycin A1 (10 μM) (Cayman). Hypoxia and reoxygenation (H/R) was carried out based on a previously described method (Yao et al., 2019). In brief, the hypoxic cell culture medium lacked serum. The H9c2 cells were then incubated for 6 h at 37°C in an anaerobic chamber under hypoxic conditions (1% O<sub>2</sub>). The cells were then transferred to a conventional incubator for 12 h. The corresponding control cells were incubated under normoxic conditions for the same duration.

### Cell Viability Assay

The cytotoxic effects of H/R and Vit D were assessed by 3-(4,5-dimethylthiazol-2-yl)-2,5-diphenyltetrazolium bromide (MTT) (Bionovas, ON, CA). After various treatments, MTT solution was added at a final concentration of 0.5 mg/ml and incubated for 4 h in 5% CO<sub>2</sub> at 37°C. The MTT-containing media were then removed, and the formazan crystals were dissolved by adding dimethyl sulfoxide (DMSO, 150 μL/well), followed by incubation for 15 min with mild shaking at room temperature (RT). The optical density was measured spectrophotometrically at 550 nm using a microplate reader (Biotek, VT, USA). The cell viability was expressed relative to that of the control.

### Terminal Deoxynucleotidyl Transferase dUTP Nick-End Labeling (TUNEL) Staining

A TUNEL apoptosis assay was used to detect DNA fragmentation using an *in situ* cell death detection kit (Roche, CA, USA) according to the manufacturer's instructions. Briefly, H9c2 cells were fixed in 4% paraformaldehyde for 20 min after H/R stimulation for the indicated time points. The samples were then incubated with the TUNEL reagent in a dark, humidified chamber at 37°C for 1 h. As a negative control, cells and tissues were treated only with the labeling solution. Nuclear counterstaining with 4',6-diamidino-2-phenylindole (DAPI) (Southern Biotech, AL, USA) was performed, and the stained cells were examined using a fluorescence microscope (Leica, Wetzlar, Germany). The number of TUNEL-positive nuclei was counted under a high-power field in six different non-overlapping fields from each slide.

### Annexin V/Propidium Iodide Assay

Apoptotic and necrotic cells were quantified by annexin V-FITC binding and propidium iodide (PI) uptake (BioLegend, CA, USA) according to the provided protocols. Briefly, after the cells were treated as indicated, the cells were harvested, resuspended in 100 μL binding buffer containing 2.5 μL FITC-annexin V and 5 μL PI solution (100 μg/ml), and incubated for 15 min in the

dark at 4°C. The cellular fluorescence was measured using a FACSCalibur flow cytometer (BD, NJ, USA). The cells that were considered viable were negative for both dyes, while the cells that were in the early phase of apoptosis were annexin V-positive and PI-negative, the cells that were in late phase of apoptosis were annexin V/PI-positive, and the cells that were in necrosis annexin V-negative and PI-positive.

### Western Blot Analysis and Co-immunoprecipitation

Western blot was performed as previously described (Pu et al., 2017). Cardiac tissues and cells were homogenized in RIPA lysis buffer [50 mM Tris, pH 7.4, 150 mM NaCl, 1% NP-40, 0.5% sodium deoxycholate, 0.1% sodium dodecyl sulfate (SDS)]. Samples with equal amounts of protein (20 μg) were electrophoresed in an SDS-polyacrylamide gel and transferred to polyvinylidene fluoride (PVDF) membranes (Millipore, MA, USA). These membranes were probed overnight at 4°C with the following primary antibodies: caspase 3, cytochrome c, p-Drp1, Mff, and LC3B, which were purchased from Cell Signaling (MA, USA), HIF-1α and Bax, which were purchased from GeneTex (Hsinchu city, Taiwan), Bcl-2, which was purchased from BD, and BNIP3, which was purchased from Aviva Systems Biology (CA, USA). Then, the membranes were incubated with a horseradish peroxidase-conjugated goat anti-mouse or anti-rabbit IgG secondary antibody (Jackson, PA, USA). The bound antibodies were detected using enhanced chemiluminescence (ECL) (Merck, NJ, USA). The intensity of the bands was quantified using ImageJ software (NIH, MD, USA). β-actin (Abcam, MA, USA) was used as the internal standard.

For co-immunoprecipitation, cells were collected and lysed with lysis buffer. The supernatant fractions were collected and incubated with 1 μg of the appropriate antibody and precipitated overnight with protein A/G Sepharose beads (G-Bioscience, MO, USA) at 4°C. The beads were washed 3 times with wash buffer by centrifugation at 2,500 g at 4°C. The precipitated proteins were collected by centrifugation at 2,500 g for 5 min. The immunoprecipitated proteins were separated by SDS-PAGE and subjected to Western blot as described above. The primary antibodies were as follows: Drp1 (Cell Signaling) and LC3B antibodies. The precipitation purity was also evaluated with Mff and BNIP3 antibodies.

### Analysis of Mitochondrial Reactive Oxygen Species and Cellular Reactive Oxygen Species Levels

The levels of mitochondrial ROS were detected using the mitochondrial superoxide indicator MitoSox Red (Invitrogen, MA, USA). H9c2 cells were treated with 1 μM MitoSox Red for 15 min at 37°C. Fluorescent images were captured using a fluorescence microscope. TO-PRO-3 (100 nM, Thermo, MA, USA), a dead cell indicator, was added before MitoSox Red analysis by an LSRFortessa flow cytometer (BD). 2',7'-Dichlorodihydrofluorescein diacetate (DCFH-DA) (Thermo) and dihydroethidium (DHE) (Invitrogen) were used to detect

the levels of intracellular oxidative free radicals and superoxide anions, respectively. Cardiomyocytes on coverslips were treated with or without H/R and then incubated with serum-free medium containing DCFH-DA (10  $\mu$ M) in the dark at 37 °C for 30 min. After incubation, the conversion of DCFH-DA to the fluorescent product DCF was detected by fluorescence microscopy, and 5  $\mu$ L PI solution (100  $\mu$ g/ml) was added before DCFH-DA analysis by flow cytometry. In addition, cardiomyocytes were incubated in serum-free medium containing DHE (5  $\mu$ M) for 15 min at 37 °C. Superoxide anions oxidize DHE, yielding ethidium, which emits red fluorescence at 535 nm, and images were captured by fluorescence microscopy. DiOC<sub>6</sub>(3) (90 nM, Thermo), a lipophilic dye that is selective for the mitochondria of live cells, was added before DHE analysis by flow cytometry.

### Determination of Mitochondrial Membrane Potential ( $\Delta\psi$ M)

5,5',6,6'-Tetrachloro-1,1',3,3'-tetraethylbenzimidazolyl-carbocyanine iodide (JC-1, BD) was used to analyze changes in mitochondrial transmembrane potential. After the various treatments, the cells were incubated with JC-1 (2  $\mu$ M) at 37 °C for 30 min in the dark. JC-1 monomers emit green fluorescence and indicate the dissipation of the  $\Delta\psi$ M, whereas JC-1 aggregates emit red and indicate an intact  $\Delta\psi$ M. Cell fluorescence was monitored using an LSM 510 confocal microscope (Zeiss, Oberkochen, Germany) and a FACSCalibur flow cytometer.

### Adenosine Triphosphate Determination

The levels of cellular ATP were evaluated using an ATP assay kit (Molecular Probe, OR, USA). The cells were lysed and then centrifuged (12,000 g) for 5 min at 4 °C. Subsequently, the supernatants were collected, and the ATP levels were analyzed. The ATP working reagent was added to the 96-well plate for 5 min, and 20  $\mu$ L of each sample was also added to each well. The ATP levels were measured using a microplate luminometer (Berthold, Bad Wildbad, Germany) and calculated according to standard ATP curves.

### Acridine Orange Staining

Cells were briefly washed with PBS and incubated with 1  $\mu$ g/ml acridine orange hydrochloride solution (Invitrogen) in PBS for 20 min at RT. Then, the cells were analyzed using confocal microscopy and flow cytometry. The acidic autophagic vacuoles emitted bright red fluorescence, while green fluorescence was observed in the cytoplasm and nucleus.

### Double Immunofluorescence Staining

After the indicated treatments, H9c2 cells on sterilized coverslips were washed with PBS, fixed with 4% paraformaldehyde for 15 min at RT, and then permeabilized with 0.1% Triton X-100 for 10 min at RT. After washing with PBS, the cells were blocked with 3% bovine serum albumin (BSA) (Novagen, Darmstadt, Germany) in PBS for 1 h at RT. The cells were incubated with primary anti-Drp1 (Cell Signaling) or anti-LC3B (Cell Signaling) (1:250 dilution in PBS containing 1% BSA) antibodies overnight at 4 °C. After

washing three times with PBS, the cells were incubated with anti-rabbit Alexa Fluor® 488 (Invitrogen) (1:250 dilution in PBS containing 1% BSA) for 1 h at RT. After washing three times with PBS, the cells were incubated with COX IV (Thermo) (1:250 dilution in PBS containing 1% BSA) overnight at 4 °C. After washing three times with PBS, the cells were incubated with anti-mouse Alexa Fluor® 647 (Invitrogen) antibodies for 1 h at RT. The cells were then counterstained with 1  $\mu$ g/ml DAPI for 3 min. Analysis and photomicrography were performed using an LSM 510 inverted confocal microscope.

### Mitochondria Isolation Assay

A mitochondria isolation kit (Thermo) was used to prepare mitochondrial and cytoplasmic fractions from whole H9c2 cell lysates. The experimental procedures were performed according to the manufacturer's instructions. The mitochondrial and cytoplasmic fractions were stored at -80 °C for further studies.

### Mitochondrial Morphology

Mitochondrial morphology was observed using MitoTracker staining (Invitrogen). After the different treatments, cardiomyocytes were incubated with 400 nM MitoTracker for 1 h at 37 °C in the dark. Visualization was performed using a total internal reflection fluorescence microscope (TIRF, Zeiss) along with DIC optics and epifluorescence illumination, and the length of mitochondria was measured with ImageJ software. The length of more than 50 mitochondria per cell was measured, and measurements were collected from 20 cells. Three replicates were performed for each biological sample.

### Animal Model

Adult male C57BL/6 mice (~25 g) were obtained from National Taiwan University and housed at 25 °C  $\pm$  5 °C with 12-h light/dark cycles. All the animal experiments were performed in accordance with the National Institutes of Health guidelines for the use of laboratory animals and approved by the Taiwan University Animal Ethics Committee. The mice were randomly divided into the following groups: sham surgery, I/R, I/R + Vit D, and Vit D. One week before the surgery, Vit D was dissolved in PBS and intraperitoneally administered 3 times at 30 ng/mouse every 2 days. The sham group received PBS injections on the same schedule. The pharmacological dose was selected based on previous reports (Bodyak et al., 2007; Bae et al., 2011). In addition, bafilomycin (2.5 mg/kg) was intraperitoneally administered 1 day before I/R operation to inhibit the occurrence of autophagy. Myocardial I/R injury was performed according to the previously described method (Yang et al., 2017). Briefly, a mouse was anesthetized with 2% isoflurane, and the heart was manually exposed through a small incision without the need for intubation. Ischemia was induced by ligating the left anterior descending coronary artery (LAD) using an 8-0 nylon suture with a section of PE-10 tubing placed over the LAD at a position 1 mm from the tip of the normally positioned left atrium. After occlusion for 30 min, reperfusion was initiated by releasing the ligature and removing the PE-10

tubing. After reperfusion for 3 h, the heart was removed and immediately placed in ice-cold PBS. Hearts exhibiting infarcts involving the anterior and apical regions were rapidly frozen and stored in liquid nitrogen (N<sub>2</sub>) for Western blot analysis. In some cases, an entire cross-section was fixed with 4% paraformaldehyde solution for haematoxylin and eosin staining and immunohistochemistry.

## Electron Microscopy

Cells and hearts from all the groups were imaged by transmission electron microscopy (TEM) to observe mitochondrial ultrastructure and mitophagy. The samples were immediately fixed with 2% glutaraldehyde and 2% paraformaldehyde in 0.1 M PBS at 4 °C overnight. After washing with PBS, the samples were postfixed with 2% osmium tetroxide. The fixed samples were dehydrated in a graded alcohol series and embedded in epoxy resin. Ultrathin sections were double-stained with uranyl acetate and lead citrate and then examined with a Hitachi H700 electron microscope (Hitachi, Tokyo, JP).

## Statistical Analysis

The data are presented as the mean ± standard error of the mean (SEM) from at least three independent experiments. One-way analysis of variance (ANOVA) was performed between groups, followed by Dunnett's post hoc test.  $p < 0.05$  indicated statistical significance.

## RESULTS

### Vit D Reduces Apoptotic Cell Death After Hypoxia/Reoxygenation Injury *in vitro*

To evaluate whether Vit D pretreatment improves myocardial cell damage under I/R conditions, H9c2 cells were pretreated with Vit D or PBS and then subjected to H/R *in vitro* to simulate the physiological stress experienced by cardiomyocytes during ischemic infarct. Various concentrations of Vit D were used to treat H9c2 cells for 24 h, and the cell viability, which was evaluated by MTT assay, was not reduced (data not shown). Then, H9c2 cells were incubated with or without 100 nM Vit D for 4 h, exposed to hypoxic conditions for 6 h and treated with reoxygenation for 12 h under normoxic conditions (H/R). The MTT assay showed that H/R treatment significantly decreased H9c2 cell viability, while Vit D pretreatment reduced this effect (Figure 1A). Apoptotic cells were detected using the TUNEL assay and annexin V-FITC/PI staining assay. As shown by TUNEL analysis, H/R treatment significantly increased apoptosis, whereas Vit D pretreatment significantly decreased apoptosis (Figures 1B,C). H/R increased the annexin V-positive apoptotic cell populations (annexin V positive/PI positive and annexin V positive/PI negative), whereas Vit D pretreatment significantly decreased these cell populations (Figures 1D,E). To further confirm that the effects of Vit D on apoptosis are due to its antioxidant activity, MitoTEMPO, a mitochondrial ROS scavenger, was used, and its effect on H/R-induced apoptosis was evaluated. Similar to Vit D, the flow cytometry results indicated that MitoTEMPO

also reduced apoptosis in H/R-treated cardiomyocytes (Figures 1D,E). Cleaved caspase three is considered an indicator of apoptosis. Compared to the control, H/R treatment significantly increased the cleaved caspase three levels, while Vit D decreased the levels of cleaved caspase 3 (Figures 1F,G). The expression balance of the BCL-2 families, including pro-apoptotic proteins (such as Bax) and anti-apoptotic proteins (such as Bcl-2), determines cell fate (Siddiqui et al., 2015). We detected the levels of Bcl-2 and Bax expression using Western blot (Figures 1F,G). H/R treatment significantly increased the level of the Bax/Bcl-2 ratio, while Vit D pretreatment decreased it.

### Vit D Inhibits Reactive Oxygen Species Production in Hypoxia/Reoxygenation-Treated Cardiomyocytes

To investigate whether Vit D can affect mitochondrial ROS production in cardiomyocytes under H/R conditions, MitoSox Red was used to detect mitochondrial ROS. The results showed that H/R treatment significantly increased the production of mitochondrial ROS, while Vit D pretreatment decreased this effect (Figure 2A). Similar to pretreatment with Vit D, treatment with MitoTEMPO, a mitochondria-specific ROS scavenger, significantly decreased the mitochondrial ROS production in viable cells (MitoSox Red-positive and TO-PRO-3-negative) after H/R injury (Figures 2B,C). In addition, the cytoplasmic superoxide anion and H<sub>2</sub>O<sub>2</sub> levels were detected using fluorescent protein-based redox probes, namely, DCFH-DA and DHE, respectively. H/R treatment significantly increased the cellular production of cytoplasmic superoxide anions and H<sub>2</sub>O<sub>2</sub>, as determined by fluorescence microscopy, while Vit D pretreatment reversed these effects (Figures 2D,G). In addition, H/R treatment increased the production of cytoplasmic superoxide anions in viable cells (PI-negative and DCFH-DA-positive), as shown by flow cytometry, while Vit D significantly decreased it (Figures 2E,F). Interestingly, the Vit D-treated group had lower DCFH-DA levels than the control group, and the H/R + Vit D group also had lower DCFH-DA levels than the control group. Additionally, the DHE overlay showed that H/R increased cytoplasmic H<sub>2</sub>O<sub>2</sub>, while Vit D decreased cytoplasmic H<sub>2</sub>O<sub>2</sub> (Figure 2H). H/R increased the cytoplasmic H<sub>2</sub>O<sub>2</sub> in viable cells (DHE-positive and DiOC<sub>6</sub>(3)-positive), as shown by flow cytometry, whereas Vit D decreased it (Figure 2I). These results indicate that Vit D is an effective antioxidant in cardiomyocytes.

### Vit D Attenuates the Hypoxia/Reoxygenation-Induced Reduction in the Mitochondrial Membrane Potential ( $\Delta\Psi_m$ ) and ATP Levels

The  $\Delta\Psi_m$  and ATP levels serve as critical parameters for cell apoptosis and mitochondrial function. In most cardiomyocytes, H/R induced marked changes in terms of a shift in fluorescence

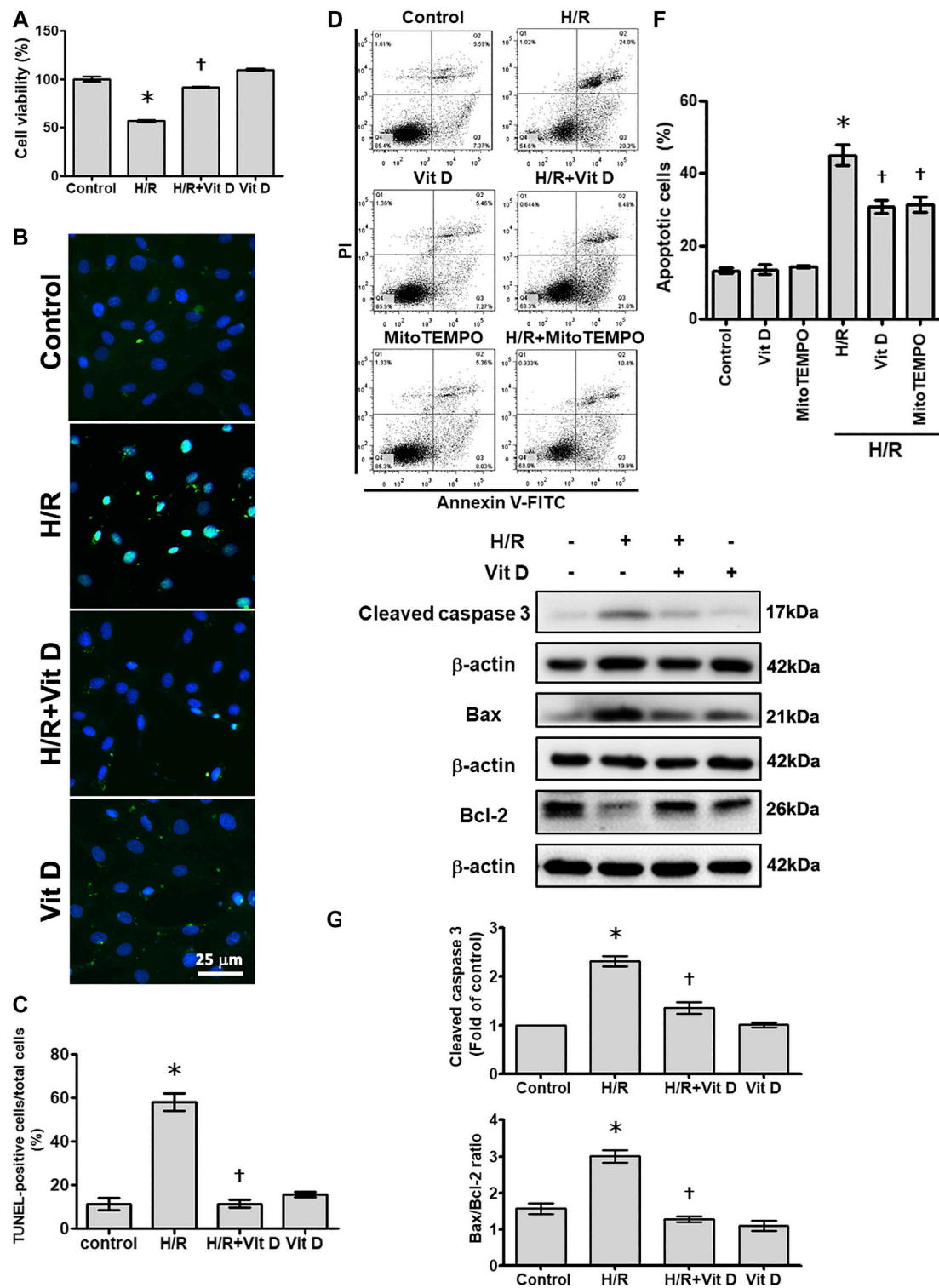


**FIGURE 1** | Vitamin D<sub>3</sub> (25-OH) reduced apoptotic cell death following H/R injury. H9c2 cells were incubated with or without 100 nM Vit D for 4 h and then exposed to hypoxic conditions for 6 h. The cells were then exposed to normoxic conditions for another 12 h. **(A)** Cell viability was measured by MTT assay. (n = 3) **(B and C)** Assessment and calculation of apoptosis by TUNEL assay. The merged images show that apoptotic cells and nuclei appear green and blue, respectively. Scale bar = 25  $\mu$ m. (n = 4) **(D and E)** Representative images and flow cytometric analysis of the percentage of apoptotic H9c2 cells in the H/R model with or without pretreatment with Vit D or MitoTEMPO by annexin V/PI staining. (n = 4) **(F and G)** The levels of cleaved caspase 3, Bax, and Bcl-2 expression were analyzed by Western blot. The ratio of Bax to Bcl-2 reflects the apoptotic activity (n = 3). \* $p$  < 0.05 vs. control, † $p$  < 0.05 vs. H/R.



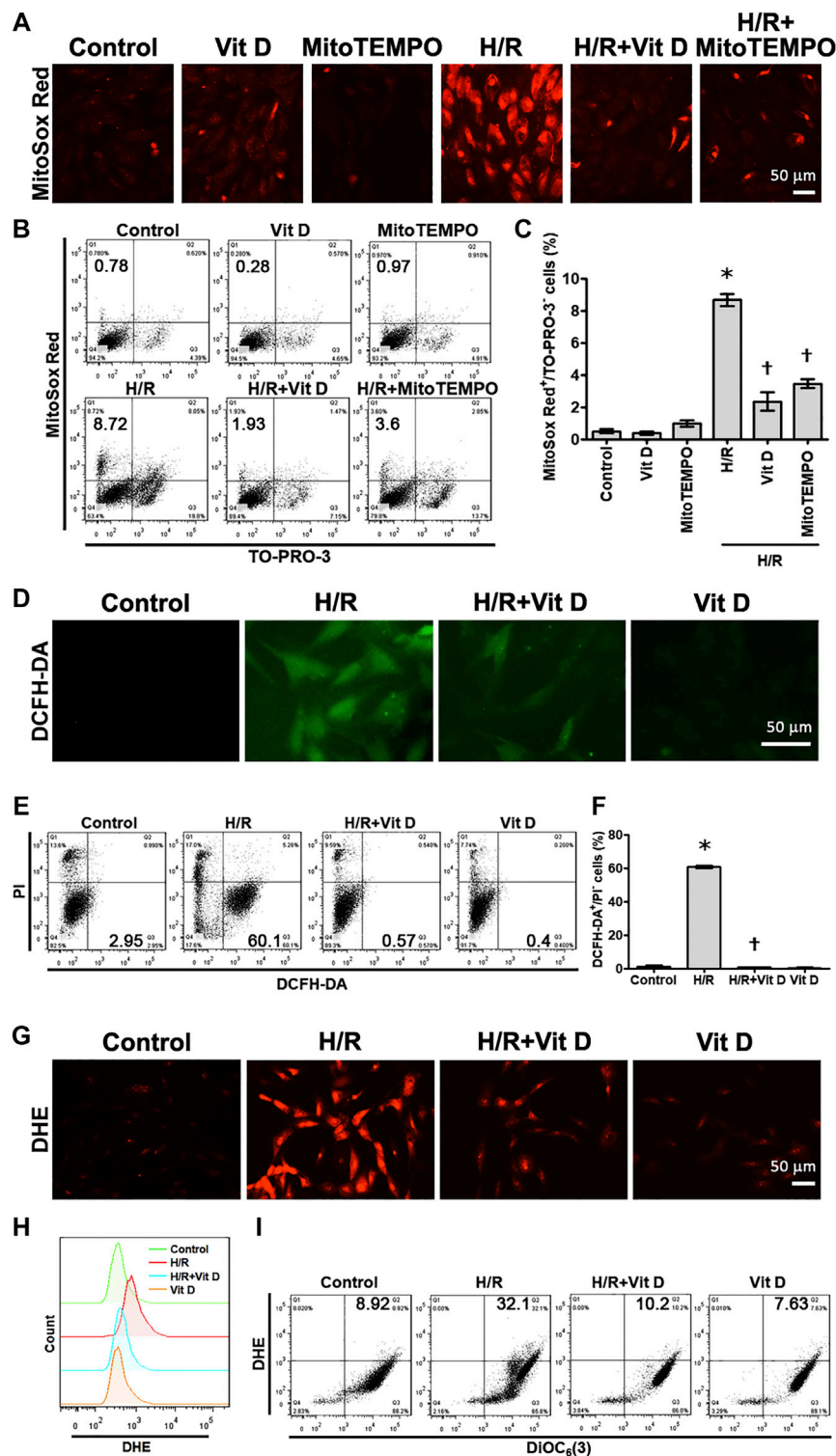


**FIGURE 2 |** Vit D inhibited ROS production in H/R-treated cardiomyocytes. Cardiomyocytes were incubated with or without 100 nM Vit D for 4 h and then exposed to hypoxia for 6 h. The cells were then exposed to normoxia for another 12 h (**A and B, C**) MitoSox Red was used to detect mitochondrial ROS by fluorescence microscopy. MitoSox Red/TO-PRO-3 staining was used to distinguish viable cells producing mitochondrial ROS (MitoSox Red-positive/TO-PRO-3-negative) by flow cytometry. (**D and E, F**) DCFH-DA was used to detect cytoplasmic H<sub>2</sub>O<sub>2</sub> by fluorescence microscopy. DCFH-DA/PI staining was used to examine viable cells with cytoplasmic H<sub>2</sub>O<sub>2</sub> (DCFH-DA-positive/PI-negative) by flow cytometry. (**G**) DHE was used to detect cellular superoxide anions by fluorescence microscopy. (**H**) DHE fluorescence displayed by overlay signals using flow cytometry. (**I**) DHE/DiOC<sub>6</sub>(3) staining was used to detect viable cells with cellular superoxide anions (DHE-positive/DiOC<sub>6</sub>(3)-positive) by flow cytometry. Scale bar = 50  $\mu$ m. (n = 3, \*p < 0.05 vs. control, †p < 0.05 vs. H/R).



emission from red to green, as shown by the JC-1 assay; this shift indicated  $\Delta\Psi_m$  dissipation. The emission of green fluorescence by cardiomyocytes pretreated with Vit D was reduced, and the distribution pattern was similar to that of the control group. In addition, the results of JC-1 analysis by flow cytometry revealed that H/R treatment increased the populations of cells with low  $\Delta\Psi_m$  (JC-1 green positive and red negative), whereas Vit D reversed this effect (**Figures 3A–C**). The ATP content was decreased after H/R injury, while Vit D treatment protected cardiomyocytes from this H/R-induced effect (**Figure 3D**). The ATP concentration of the H/R + Vit D group was higher than that of the control group. The dissipation of  $\Delta\Psi_m$  can lead to mitochondria-dependent apoptosis. In addition, H/R induced the expression of cytochrome c, a marker of mitochondrial apoptosis, whereas this upregulation of cytochrome c was reduced by Vit D pretreatment (**Figures 3E,F**). These results indicate that the protective effect of exogenous Vit D on cardiomyocytes occurs via the modulation of mitochondrial function.

### Vit D Protects Mitochondria by Reducing Mitochondrial Fission

Mitochondria are highly dynamic organelles that undergo fission and fusion, and these processes are closely related to mitochondria function and ROS production (Westermann, 2010). MitoTracker was used to examine the effects of Vit D on the mitochondrial morphology in H/R-treated cardiomyocytes. The results showed that the length of the mitochondria in H/R-treated cells was significantly shorter than that in control-treated cells, and Vit D reversed this effect (**Figures 4A,B**). To further investigate how Vit D regulates mitochondrial fission, p-Drp1 and Mff, two regulatory proteins associated with mitochondrial fission, were examined. Our results showed that H/R treatment increased the expression of p-Drp1 and Mff, whereas the expression of these proteins was decreased by Vit D (**Figures 4C–E**). To further confirm the effects of mitochondrial ROS on mitochondrial fission after H/R injury, we examined the expression of p-Drp1 and Mff in Mito TEMPO and H/R-treated cardiomyocytes. We found that MitoTEMPO reduced the expression of both p-Drp1 and Mff (**Figures 4F–H**). Next, we investigated whether Drp1 interacts with Mff. We found that Drp1 was co-immunoprecipitated with Mff following H/R treatment, while Vit D decreased the interaction (**Figure 4I**). Our results suggest that the protective effect of Vit D against H/R-induced mitochondrial fission is attributed to its antioxidant capacity.

### Vit D Reduces Mitophagy in Cardiomyocytes

It has been reported that mitophagy plays a regulatory role in apoptosis (Yusman et al., 2002). Acridine orange (AO) staining was used to detect autophagic vacuoles. H/R-treated cells exhibited increased autophagosome formation, which was inhibited when cells were pretreated with Vit D; these results indicated that Vit D reduced the accumulation of

autophagosomes (**Figure 5A**). In addition, the results of AO analysis by flow cytometry suggested that H/R injury significantly increased the population of cells undergoing autophagy (AO green positive and red positive), while Vit D decreased this population. AO green and red fluorescence overlay showed that H/R treatment enhanced AO staining, whereas Vit D reduced AO staining (**Figure 5B**). To investigate how Vit D affects mitophagy, we analyzed the expression of BNIP3 and the conversion of LC3I to LC3II by Western blot. The results showed that H/R increased BNIP3 expression and the LC3II/LC3I ratio. Nevertheless, Vit D reduced the expression of both BNIP3 and LC3BII (**Figures 5C–E**). To further confirm the effects of mitochondrial ROS on mitophagy after H/R injury, we examined the expression of BNIP3 and the conversion of LC3I to LC3II in MitoTEMPO and H/R-treated cardiomyocytes. We found that MitoTEMPO reduced the expression of both BNIP3 and LC3BII/LC3BI ratio (**Figures 5F–H**). Next, we investigated whether BNIP3 interacts with LC3B. Strong interactions between BNIP3 and LC3B were observed in H/R-treated cardiomyocytes, and the addition of Vit D markedly inhibited this interaction (**Figure 5I**). Taken together, these results indicate that Vit D can attenuate H/R-induced mitophagy by reducing mitochondrial ROS production.

### Vit D Reduces Mitochondrial Translocation of Drp1, Mff, BNIP3, and LC3B After Hypoxia/Reoxygenation Treatment

We then further evaluated the mitochondrial translocation of Drp1, Mff, BNIP3, and LC3B in response to H/R treatment. H/R treatment induced a significant increase in Drp1, Mff, BNIP3 and LC3B translocation to the mitochondria. However, Vit D treatment reduced the translocation of these proteins (**Figure 6A**). Using double immunofluorescence staining, we further investigated changes in the mitochondria undergoing mitophagy. We observed that co-localization of COX IV (a mitochondrial marker) with Drp1 or LC3B was more clearly present in the H/R group than in the control group, while Vit D pretreatment reduced these phenomena (**Figures 6B,C**). Transmission electron microscopy images showed that Vit D reduced the presence of autophagic vacuoles in H/R-treated cardiomyocytes (**Figure 6D**). To further evaluate the effect of the mitochondrial fission on H/R-induced mitophagy, we performed the treatment of mitochondrial fission inhibitor (Mdivi-1) on the expression of mitophagy-related proteins in H/R-treated H9c2 cells. Cells with Mdivi-1 treatment significantly reduced the levels of H/R-induced BNIP3 and LC3BII/LC3BI ratio expression (**Figure 6E,F**). These results indicated that mitochondrial fission was involved in H/R-induced mitophagy. Furthermore, we examined the effects of Vit D on H/R-induced cardiomyocyte injury via mitophagy, we performed the effect of bafilomycin A1, an autophagy inhibitor, on the expression of mitophagy-related proteins. Cells with bafilomycin A1 treatment significantly reduced H/R-induced BNIP3 and LC3BII/LC3BI expression (**Figures 6G,H**).

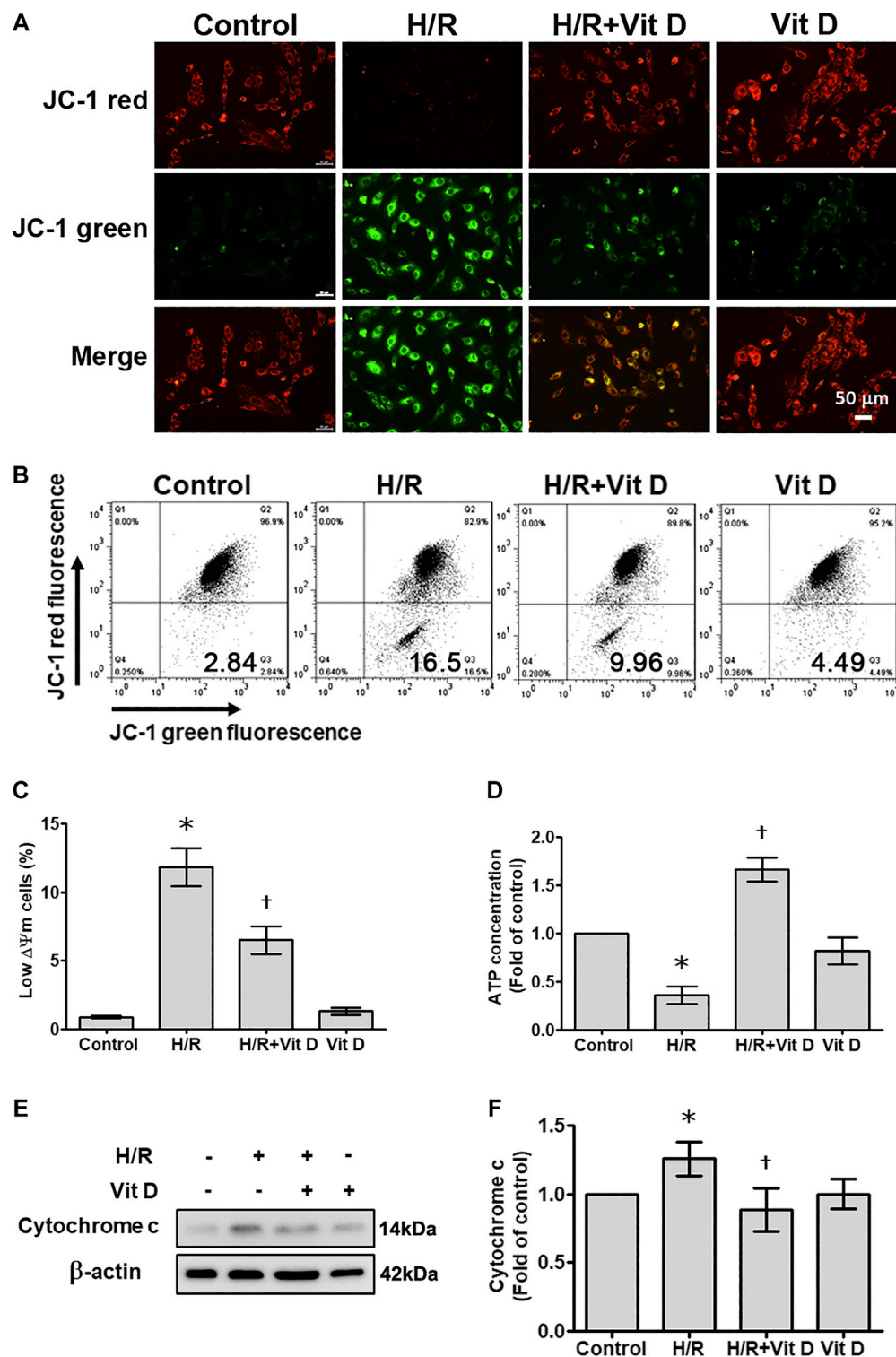


**FIGURE 3** | Vit D restored the mitochondrial membrane potential and ATP production that were decreased by H/R. Cardiomyocytes were incubated with or without 100 nM Vit D for 4 h and then exposed to hypoxia for 6 h. The cells were then exposed to normoxia for another 12 h. **(A)** Representative fluorescence images of JC-1 staining show the change in high mitochondrial membrane potential (red) and low mitochondrial membrane potential (green), which is an early event of apoptosis. H/R treatment increased green fluorescence, whereas Vit D decreased green fluorescence. Scale bar = 50  $\mu$ m. **(B and C)** Flow cytometric patterns and quantitative analysis of cardiomyocytes stained with JC-1. Cell population with low  $\Delta\Psi_m$  according to JC-1 staining (green positive and red negative) ( $n = 4$ ). **(D)** ATP levels were decreased after H/R injury, but ATP levels were restored by Vit D treatment. **(E)** The expression of cytochrome c was detected by Western blot. ( $n = 3$ ). \* $p < 0.05$  vs. control, † $p < 0.05$  vs. H/R.

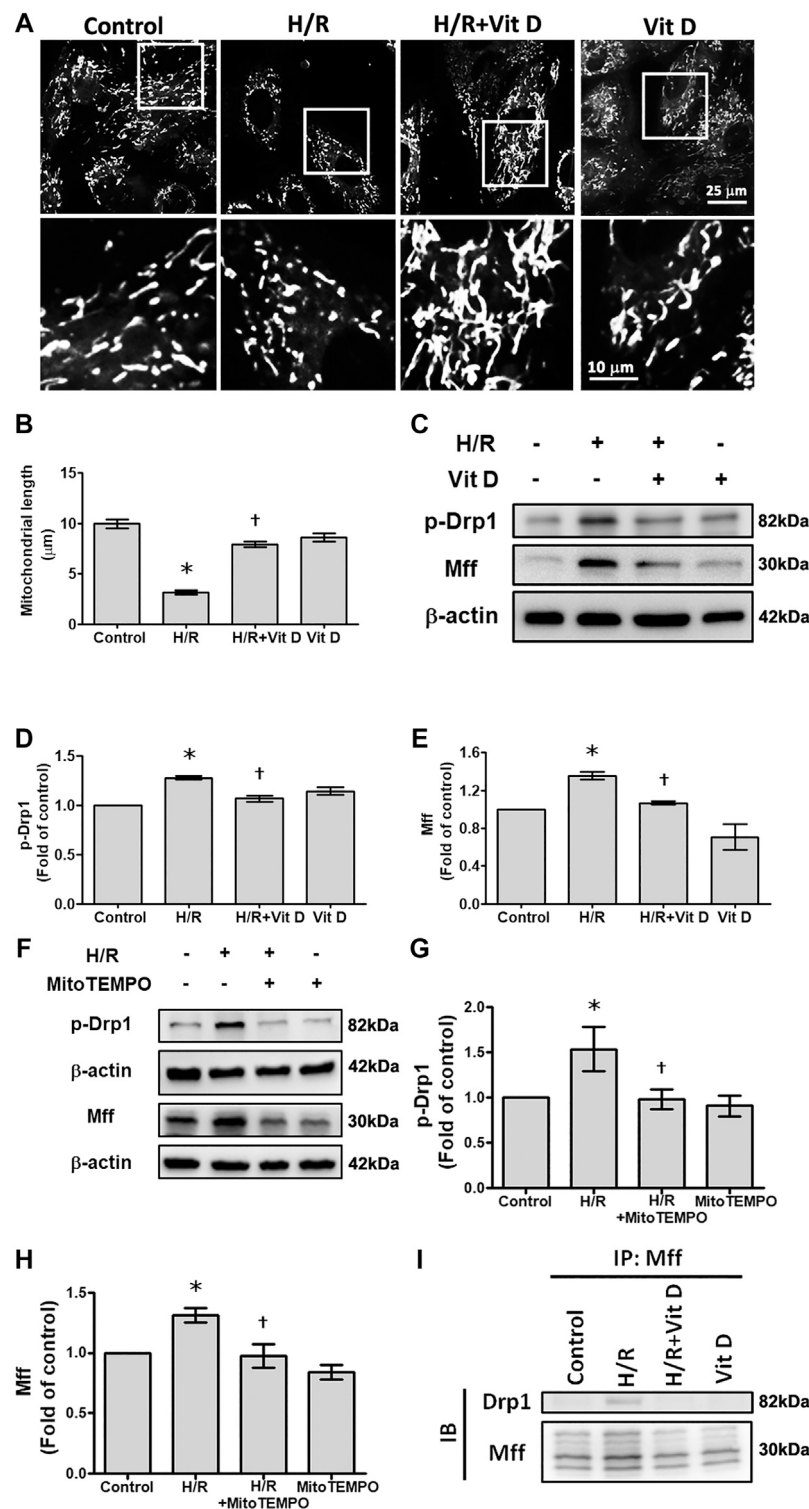


**FIGURE 4 |** Vit D reduced mitochondrial fission in H/R-treated cardiomyocytes. **(A and B)** The mitochondrial morphology in cardiomyocytes was measured by the MitoTracker assay. Scale bar = 25 or 10  $\mu\text{m}$ , as indicated in the panel. **(C–E)** Mitochondrial fission-associated regulatory factors p-Drp1 and Mff were detected by Western blot ( $n = 5$ ). **(F–H)** Measurement of the effect of MitoTEMPO treatment on the expression of p-Drp1 and Mff by Western blot ( $n = 3$ ). **(I)** Measurement of the interaction of Drp1 and Mff by co-immunoprecipitation. The indicated cultured cells were immunoprecipitated with anti-Drp1 antibodies followed by immunoblotting with anti-Mff antibodies. \* $p < 0.05$  vs. control, † $p < 0.05$  vs. H/R.

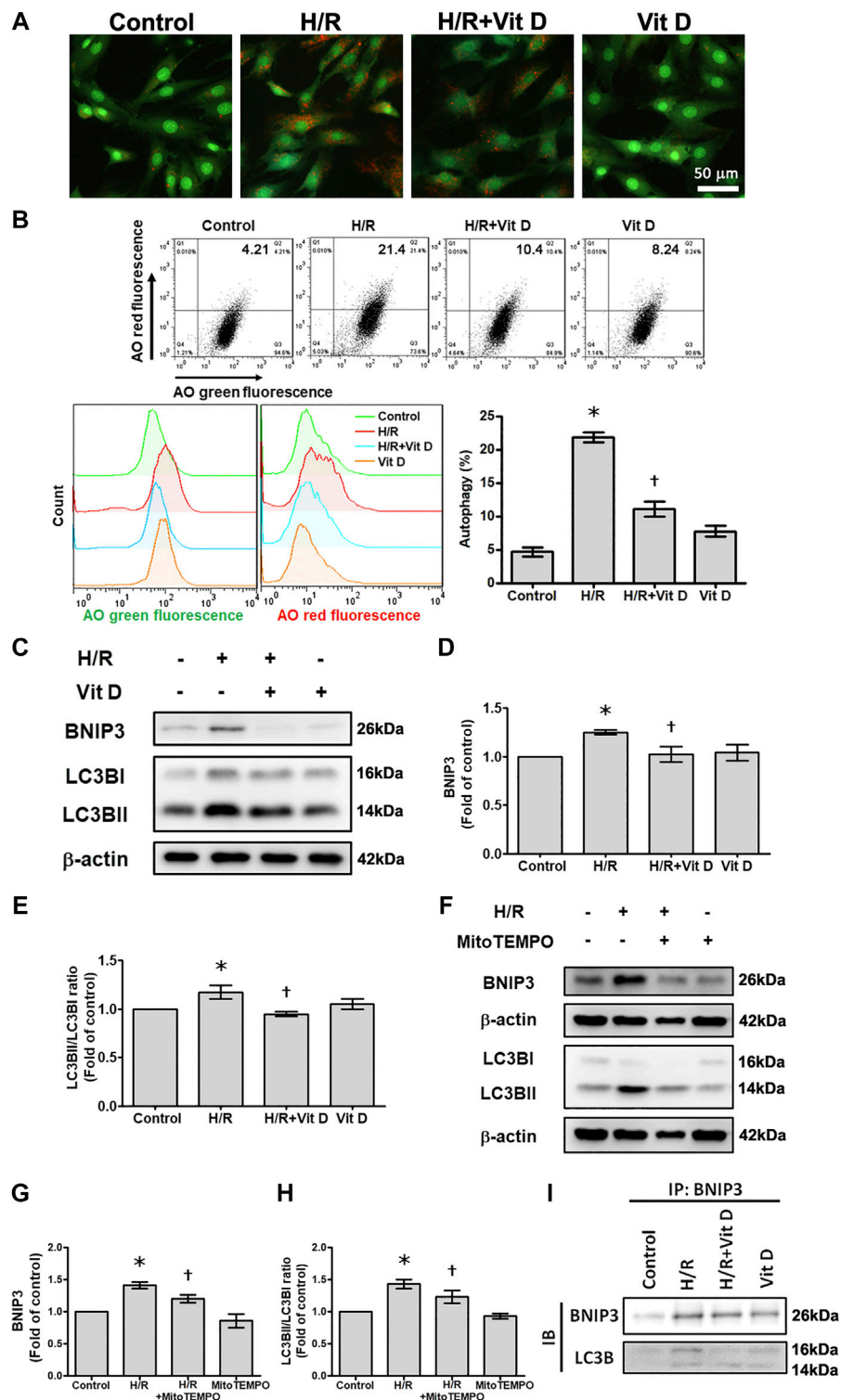


**FIGURE 5 |** Vit D attenuated H/R-induced mitophagy in cardiomyocytes. **(A)** Cells were stained with acridine orange (AO) solution and observed under a fluorescence microscope to examine the changes in the acidic compartments of the cells. Scale bar = 50  $\mu$ m. **(B)** Cells were stained with AO solution and analyzed by flow cytometry. AO green and red overlay fluorescence showed that H/R enhanced AO staining, whereas Vit D reduced it. The bar graph shows the percentages of cells undergoing autophagy (AO red positive and green positive) ( $n = 3$ ). **(C–E)** Expression of BNIP3 and LC3BII/I was examined by Western blot ( $n = 5$ ). **(F–H)** Measurement of the effects of MitoTEMPO on the expression of BNIP3 and LC3BII/I by Western blot ( $n = 5$ ). **(I)** Measurement of the interaction of BNIP3 and LC3BII/I by co-immunoprecipitation. The indicated cultured cells were immunoprecipitated with anti-BNIP3 antibodies followed by immunoblotting with anti-LC3B antibodies. \* $p < 0.05$  vs. control, † $p < 0.05$  vs. H/R.



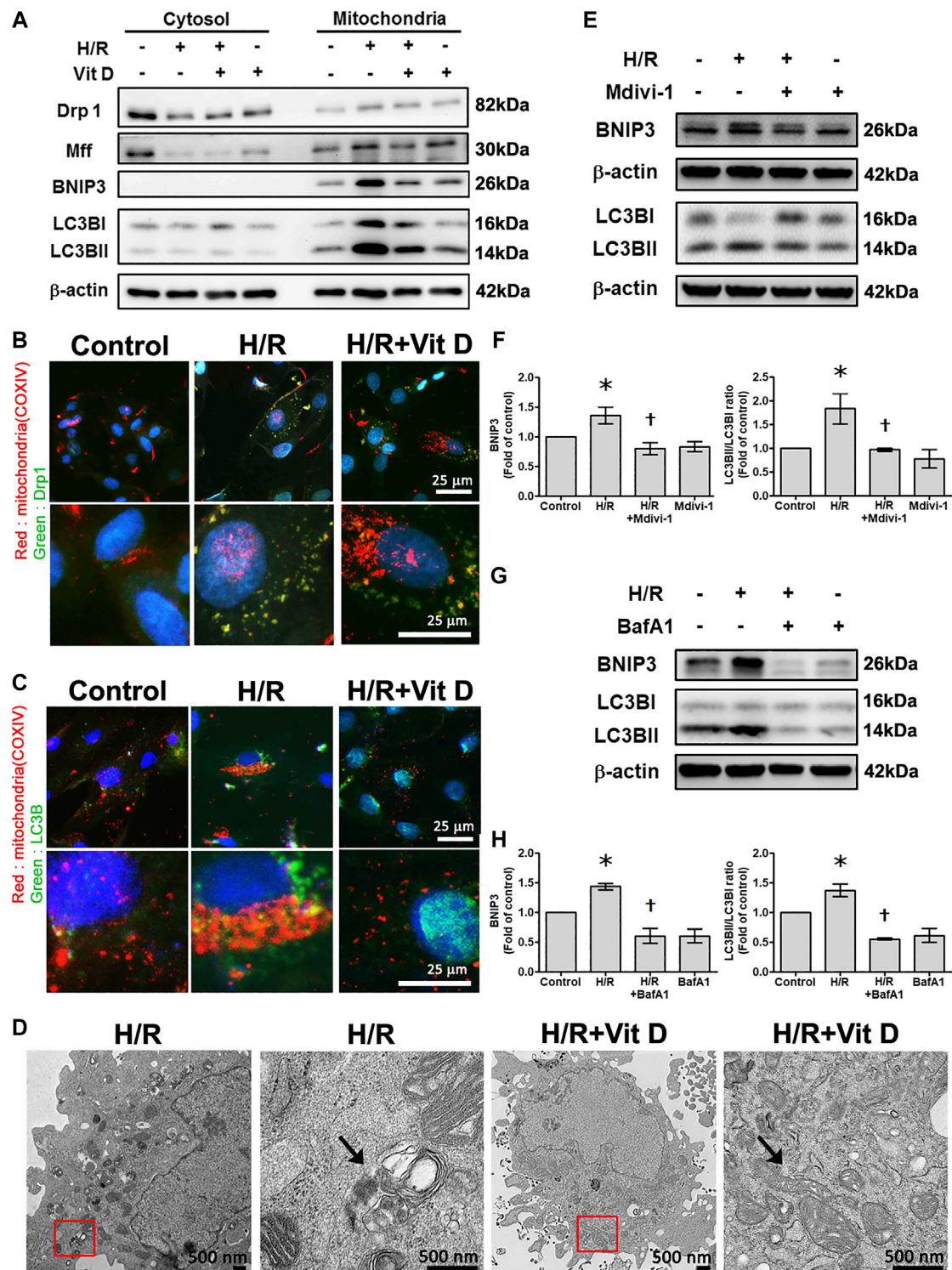


**FIGURE 6** | Vit D reduced the translocation of mitochondrial fission-associated proteins (Drp1 and Mff) and mitophagy-associated proteins (BNIP3 and LC3B) in H/R-treated cardiomyocytes. **(A)** Mitochondrial translocation of Drp1, Mff, BNIP3, and LC3B in response to H/R treatment. H/R treatment induced a significant increase in Drp1, Mff, BNIP3 and LC3B translocation to mitochondria. Vit D treatment reduced this translocation. **(B and C)** Co-localization of COX IV (a mitochondrial marker) and Drp1 or LC3B was examined by dual immunofluorescence staining. The co-localization was increased in the H/R group compared to the control group, while Vit D treatment reduced this effect. Scale bar = 25  $\mu$ m. **(D)** TEM showed that autophagic vacuoles (arrow) were present in the H/R-treated cells, and Vit D reduced the presence of autophagic vacuoles. The right panels are the magnification of the region enclosed in the red box. Scale bar = 500 nm. **(E and F)** The effect of Mdivi-1 (an inhibitor of mitochondrial fission) on the expression levels of BNIP3 and LC3BII/LC3BI ratio were analyzed by Western blot. LC3BII/LC3BI ratios reflect the autophagy activity (n = 3). **(G and H)** The effects of bafilomycin A1, an autophagy inhibitor, on the expression levels of BNIP3 and LC3BII/LC3BI ratio were analyzed by Western blot (n = 3). \*p < 0.05 vs. control, †p < 0.05 vs. H/R.



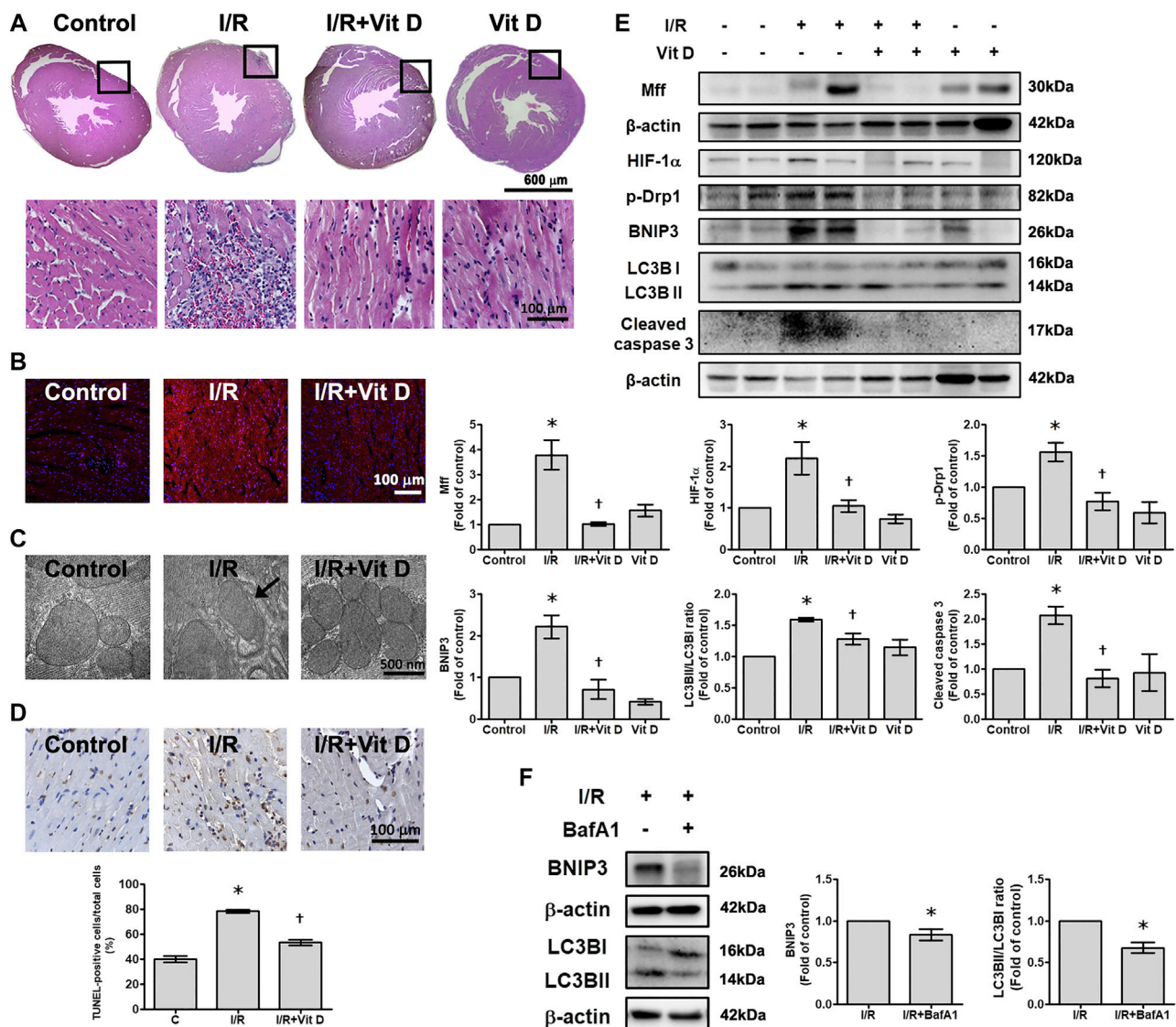


**FIGURE 7 |** Vit D reduced I/R-induced cardiac injury. **(A)** Transverse sections of cardiac morphology were observed by haematoxylin and eosin staining. I/R induced more inflammatory cell infiltration into cardiac tissue than the control, while Vit D ameliorated this inflammatory infiltration. Scale bar = 600  $\mu$ m or 100  $\mu$ m, as indicated in the panel. **(B)** The production of superoxide anions was assessed by DHE staining. Scale bar = 100  $\mu$ m. **(C)** Representative ultrastructural images were observed by TEM. Mitophagy was present in the I/R-treated cardiomyocytes. The control and Vit D treatment groups exhibited intact mitochondrial structures with well-arranged cristae. Scale bar = 500 nm. **(D)** Myocardial apoptosis was identified and quantified by TUNEL assay (TUNEL: brown; nuclei: blue; scale bar = 100  $\mu$ m). **(E)** The protein levels of HIF-1 $\alpha$ , Drp1, Mff, BNIP3, LC3B, and cleaved caspase three were determined by Western blot. Vit D treatment significantly reduced the levels of these proteins in the I/R-treated mice. **(F)** The effect of bafilomycin A1, an autophagy inhibitor, on the levels of BNIP3 and LC3BII/I expression in I/R-treated mice ( $n = 3$ ). \* $p < 0.05$  vs. control, † $p < 0.05$  vs. I/R.

## Vit D Preserves Mitochondrial Membrane Integrity and Ultrastructure in Mouse Hearts After Ischemia/Reperfusion Injury

Compared with sham surgery, I/R induced the infiltration of inflammatory cells into the infarct zone of cardiac tissues, and Vit D ameliorated this inflammatory infiltration (Figure 7A). I/R increased the intracellular levels of superoxide anions, as shown by DHE staining, while Vit D decreased the intercellular levels of superoxide anions in the heart after I/R injury (Figure 7B).

Ultrastructure images were examined by TEM. The mice administered Vit D treatment showed complete mitochondrial structures with well-aligned cristae (Figure 7C). I/R treatment significantly increased the number of apoptotic cells, while Vit D pretreatment reduced the effect (Figure 7D). The levels of HIF-1 $\alpha$ , Mff, p-Drp 1, BNIP3, LC3B and cleaved caspase three in the I/R-treated mice were significantly elevated compared to those in the control-treated mice. Furthermore, Vit D treatment significantly reduced the levels of these proteins during I/R damage (Figure 7E). Furthermore, we examine the effects of Vit D on I/R-induced

mitophagy, we performed the effect of bafilomycin A1 on the expression of mitophagy-related proteins. Mice with bafilomycin A1 treatment significantly reduced I/R-induced BNIP3 and LC3BII/I expression (**Figure 7F**).

## DISCUSSION

The important findings we report are that exogenous Vit D treatment can 1) reduce cardiomyocyte apoptosis and ROS production; 2) increase mitochondrial membrane potential; 3) reduce mitochondrial fission via decreased Drp1 and Mff expression; and 4) reduce mitophagy by reducing the H/R-induced expression of BNIP3 and LC3B. Vit D exerts a protective effect on mitochondrial physiology and morphology and on the expression of key mitochondrial proteins. To the best of our knowledge, this study is one of few studies to show that Drp1/Mff is required for mitochondrial fission and that BNIP3/LC3B is associated with mitophagy; these findings further elucidate the mechanisms of cardiac I/R injury and the effective protection provided by Vit D.

Vit D exerts a wide range of physiological and cytoprotective functions in biological systems. Human skeletal muscle cells treated with  $1\alpha,25$ -dihydroxyvitamin  $D_3$  exhibited an increased mitochondrial oxygen consumption rate and mitochondrial volume (Ryan et al., 2016).  $25(OH)D_3$  and  $1\alpha,25(OH)_2D_3$  affected calcium and phosphorus absorption, gene expression, proliferation, and differentiation in skeletal muscle cells (Birge and Haddad, 1975; Girgis et al., 2014). Vit D depletion exacerbated hypertension and cardiac damage (Andersen et al., 2015). As reported in the literature, Vit D can alleviate  $H_2O_2$ -mediated endothelial cell stress-mediated injury in a dose- and time-dependent manner by reducing anionic superoxide production and apoptosis (Polidoro et al., 2013). Vit D prevents the inflammatory responses observed in endothelial cells and db/db mice exposed to diabetic conditions (Einbinder et al., 2016). Vit D helps reduce diabetic cardiomyopathy not only by improving blood glucose and insulin levels but also by downregulating advanced glycation end product formation and hexosamine pathways in heart tissues (Derakhshanian et al., 2019). Activation of the Vit D receptor prevents myocardial reperfusion injury by inhibiting apoptosis and modulating autophagy (Yao et al., 2015). In accordance with these findings, in the present study, Vit D significantly attenuated I/R-induced cardiac apoptosis *in vivo* and *in vitro*.

During the pathogenesis of myocardial I/R injury, oxidative stress is increased and contributes to the regulation of cardiomyocyte apoptosis (Chen and Zweier, 2014; Zhou et al., 2015). Vit D, an antioxidant vitamin, is essential in regulating the biochemical pathways that lead to proper heart function (Liu et al., 2018). Consistent with these findings, we demonstrated that H/R treatment increased ROS production. Furthermore, Vit D reduced cytoplasmic and mitochondrial ROS production. Mitochondria are the main source of ROS, and excessive ROS production severely accelerates mitochondrial abnormalities and mitochondrial membrane injury (Bliksoen et al., 2015; Ong et al.,

2015). Importantly, we demonstrated that the specific mitochondrial ROS scavenger MitoTEMPO has the same effect on ROS production as Vit D, indicating that in H/R-treated cardiomyocytes, cytoplasmic ROS are mainly derived from mitochondrial ROS. Therefore, we concluded that the antioxidant effects of Vit D may be attributed to the removal of excess mitochondrial ROS. Cardiomyocytes treated with H/R exhibited mitochondrial dysfunction, as evidenced not only by the decrease in both ATP production and mitochondrial membrane potential but also by the increase in ROS production in the present study. These H/R-induced functional and structural defects in mitochondria are associated with mitochondria-dependent apoptotic events, including caspase three activation and chromosomal DNA fragmentation. Importantly, we demonstrated that Vit D prevents H/R-induced cardiac apoptosis by restoring mitochondrial function and regulating intracellular redox status.

Mitochondria are essential for cardiomyocyte survival and death (Yang et al., 2018). Healthy mitochondria produce ATP energy that drives biological processes, while damaged mitochondria produce pathological ROS (Tang et al., 2015). To prevent cell death and maintain mitochondrial function, damaged mitochondria may undergo fission and degradation. Oxidative stress regulates mitochondrial fission events (Kroemer et al., 2007). Mitochondrial fission usually results in the separation of components from an original mitochondrion, producing one healthy mitochondrion and another impaired mitochondrion with reduced membrane potential (Youle and van der Bliek, 2012). However, oxidative stress may lead to excessive mitochondrial fission, resulting in mitochondrial structural changes and dysfunction as well as cellular damage (Reddy, 2014). MitoTracker and transmission electron microscopy revealed mitochondrial rupture or smaller mitochondria in H/R-treated cardiomyocytes, indicating that mitochondrial fission was increased and that Vit D improved this effect. The effect of MitoTEMPO on mitochondrial morphology was identical to that of Vit D, suggesting that the effect of Vit D on mitochondrial fission could be attributed to its antioxidant activity. In addition, mitochondrial fission is regulated by proteins including Drp1 and Mff (Westermann, 2010; Jin et al., 2018; Jin et al., 2020). Drp1 is a cytosolic guanosine triphosphatase that plays an important role in translocation and oligomerization in mitochondrial outer membranes during mitochondrial fission (Hall et al., 2014). Overexpression of a dominant-negative form of Drp1 inhibits cytochrome c release and caspase three activation in H9c2 cells treated with high glucose (Yu et al., 2008). The levels of the Dynamin two and Drp1 proteins were significantly increased when cardiomyocytes were exposed to  $30 \mu M H_2O_2$  (Gao et al., 2016). It is known that the inhibition of Drp1 can reduce the death of cardiomyocytes (Ong et al., 2010). I/R injury increased ROS production and mitochondrial fission in cardiac microvascular endothelial cells (Zhou et al., 2019; Wang et al., 2020). Our study showed that H/R treatment could upregulate the expression of p-Drp1 and Mff, while Vit D could reverse this effect. Furthermore, in this study, when mice were exposed to I/R, apoptosis, caspase three activity, and mitochondrial fission-associated protein levels exhibited the

same trends as those observed *in vitro*. Our data suggested that Vit D can inhibit mitochondrial fission, thereby protecting the heart from I/R injury.

Autophagy is a lysosome-dependent cellular catabolic process that is accompanied by LC3B transformation and BNIP3 expression; autophagy results in the timely clearance of damaged cellular components (Yang and Klionsky, 2010). Maintaining a balance between mitophagy, a selective form of autophagy, and mitochondrial production is critical for maintaining healthy cells (Livingston et al., 2019). Experiments over the years have shown different results, and the effects of mitophagy on diseases associated with organ ischemia is a controversial topic (Andres et al., 2015; Li et al., 2016; Zhou et al., 2018a; Zhou et al., 2018b; Zhang et al., 2018; Wu et al., 2019). Different cell types, animal species, and I/R models can yield to contradictory results. In our study, H/R treatment significantly increased mitophagy by increasing the LC3 -II B/LC3B -I levels and BNIP3 expression compared with the sham operation. In addition, using acridine orange staining and transmission electron microscopy, we observed that H/R significantly induced autophagosome formation. Furthermore, we showed by immunocytochemistry and confocal microscopy analysis that COX IV-labelled mitochondria colocalized with LC3B-labelled autophagosomes, indicating the presence of mitophagy in H/R-treated cardiomyocytes. These features of mitophagy are significantly activated by H/R injury in cardiomyocytes and can be further attenuated by Vit D treatment or MitoTEMPO treatment or Mdivi-1 treatment. H/R damage to cardiomyocytes significantly activates these characteristics of mitochondria, which can be reduced by Vit D treatment or MitoTEMPO treatment or Mdivi-1 treatment. This study describes a new mechanism by which Vit D exerts cardioprotective effects by reducing mitophagy-mediated cell death under I/R conditions. The inhibitory effect of Vit D on ROS production may be due in part to decreased mitophagy. Furthermore, when mice were exposed to I/R, the levels of mitophagy-associated proteins showed the same trends as those observed *in vitro*. In summary, these results suggested that a decrease in mitophagy is associated with the cardioprotective effects of Vit D during cardiac I/R injury.

## REFERENCES

- Alfawaz, H., Tamim, H., Alharbi, S., Aljaser, S., and Tamimi, W. (2014). Vitamin D status among patients visiting a tertiary care center in Riyadh, Saudi Arabia: a retrospective review of 3475 cases. *BMC Publ. Health* 14, 159. doi:10.1186/1471-2458-14-159
- Andersen, L. B., Przybyl, L., Haase, N., Von Versen-Hoynck, F., Qadri, F., Jorgensen, J. S., et al. (2015). Vitamin D depletion aggravates hypertension and target-organ damage. *J Am Heart Assoc* 4. doi:10.1161/jaha.114.001417
- Andres, A. M., Stotland, A., Queliconi, B. B., and Gottlieb, R. A. (2015). A time to reap, a time to sow: mitophagy and biogenesis in cardiac pathophysiology. *J. Mol. Cell. Cardiol.* 78, 62–72. doi:10.1016/j.yjmcc.2014.10.003
- Artaza, J. N., Mehrotra, R., and Norris, K. C. (2009). Vitamin D and the cardiovascular system. *Clin. J. Am. Soc. Nephrol.* 4, 1515–1522. doi:10.2215/cjn.02260409
- Bae, S., Yalamarti, B., Ke, Q., Choudhury, S., Yu, H., Karumanchi, S. A., et al. (2011). Preventing progression of cardiac hypertrophy and development of

Taken together, our current study shows that Vit D prevents H/R-induced apoptosis by inhibiting oxidative stress and regulating mitochondrial function. Vit D inhibits H/R-induced mitochondrial fission and mitophagy by inhibiting Drp1/Mff and BNIP3/LC3B, respectively. After describing the mechanisms of Vit D-mediated protection, this study provides new opportunities for treating H/R-induced cardiac damage.

## DATA AVAILABILITY STATEMENT

The original contributions presented in the study are included in the article/Supplementary Material, further inquiries can be directed to the corresponding authors.

## ETHICS STATEMENT

The animal study was reviewed and approved by National Institutes of Health guidelines for the use of laboratory animals and approved by the Taiwan University Animal Ethics Committee.

## AUTHOR CONTRIBUTIONS

TLL and MHL contributed equally as first authors. TLL, YCC, YCL, and TCL performed the experiments. MHL, YHL, LFH, and HCS contributed to the data analysis. CWL and YLC conceived and coordinated the study and wrote the manuscript. All the authors approved the final version to be published.

## FUNDING

This research was supported in part by research grants from the Ministry of Science and Technology of Taiwan (MOST 108-2320-B002-065-MY3), Chang Gung Medical Research Program Foundation (CMRPG6J0221, 22, 23), and Kaohsiung Medical University Hospital (kmtth-105-054).

heart failure by paricalcitol therapy in rats. *Cardiovasc. Res.* 91, 632–639. doi:10.1093/cvr/cvr133

- Baehr, A., Klymiuk, N., and Kupatt, C. (2019). Evaluating novel targets of ischemia reperfusion injury in pig models. *Int. J. Mol. Sci.* 20. doi:10.3390/ijms20194749
- Birge, S. J., and Haddad, J. G. (1975). 25-hydroxycholecalciferol stimulation of muscle metabolism. *J. Clin. Invest.* 56, 1100–1107. doi:10.1172/jci108184
- Bliksoen, M., Baysa, A., Eide, L., Björås, M., Suganthan, R., Vaage, J., et al. (2015). Mitochondrial DNA damage and repair during ischemia-reperfusion injury of the heart. *J. Mol. Cell. Cardiol.* 78, 9–22. doi:10.1016/j.yjmcc.2014.11.010
- Bodyak, N., Ayus, J. C., Achinger, S., Shivalingappa, V., Ke, Q., Chen, Y. S., et al. (2007). Activated vitamin D attenuates left ventricular abnormalities induced by dietary sodium in Dahl salt-sensitive animals. *Proc. Natl. Acad. Sci. USA.* 104, 16810–16815. doi:10.1073/pnas.0611202104
- Bravo-San Pedro, J. M., Kroemer, G., and Galluzzi, L. (2017). Autophagy and mitophagy in cardiovascular disease. *Circ. Res.* 120, 1812–1824. doi:10.1161/circresaha.117.311082
- Chen, Y. R., and Zweier, J. L. (2014). Cardiac mitochondria and reactive oxygen species generation. *Circ. Res.* 114, 524–537. doi:10.1161/circresaha.114.300559



- Chouchani, E. T., Pell, V. R., Gaude, E., Aksentijevic, D., Sundier, S. Y., Robb, E. L., et al. (2014). Ischaemic accumulation of succinate controls reperfusion injury through mitochondrial ROS. *Nature* 515, 431–435. doi:10.1038/nature13909
- Derakhshanian, H., Djazayeri, A., Javanbakht, M. H., Eshraghian, M. R., Mirshafiei, A., Jahanabadi, S., et al. (2019). Vitamin D downregulates key genes of diabetes complications in cardiomyocyte. *J. Cell. Physiol.* 234, 21352–21358. doi:10.1002/jcp.28743
- Dibaba, D. T. (2019). Effect of vitamin D supplementation on serum lipid profiles: a systematic review and meta-analysis. *Nutr. Rev.* 77 (12), 890–902. doi:10.1093/nutrit/nuz037
- Einbinder, Y., Ohana, M., Benchetrit, S., Zehavi, T., Nacasch, N., Bernheim, J., et al. Zitman-Gal, T. (2016). Glucagon-like peptide-1 and vitamin D: anti-inflammatory response in diabetic kidney disease in db/db mice and in cultured endothelial cells. *Diabetes Metab Res Rev* 32, 805–815. doi:10.1002/dmrr.2801
- Gao, D., Yang, J., Wu, Y., Wang, Q., Wang, Q., Lai, E. Y., et al. (2016). Targeting Dynamin 2 as a novel pathway to inhibit cardiomyocyte apoptosis following oxidative stress. *Cell. Physiol. Biochem.* 39, 2121–2134. doi:10.1159/000447908
- Gardner, D. G., Chen, S., and Glenn, D. J. (2013). Vitamin D and the heart. *Am. J. Physiol. Regul. Integr. Comp. Physiol.* 305, R969–R977. doi:10.1152/ajpregu.00322.2013
- Girgis, C. M., Clifton-Bligh, R. J., Mokbel, N., Cheng, K., and Gunton, J. E. (2014). Vitamin D signaling regulates proliferation, differentiation, and myotube size in C2C12 skeletal muscle cells. *Endocrinology* 155, 347–357. doi:10.1210/en.2013-1205
- Hall, A. R., Burke, N., Dongworth, R. K., and Hausenloy, D. J. (2014). Mitochondrial fusion and fission proteins: novel therapeutic targets for combating cardiovascular disease. *Br. J. Pharmacol.* 171, 1890–1906. doi:10.1111/bph.12516
- Hausenloy, D. J., and Yellon, D. M. (2013). Myocardial ischemia-reperfusion injury: a neglected therapeutic target. *J. Clin. Invest.* 123, 92–100. doi:10.1172/jci62874
- Jin, Q., Li, R., Hu, N., Xin, T., Zhu, P., Hu, S., et al. (2018). DUSP1 alleviates cardiac ischemia/reperfusion injury by suppressing the Mff-required mitochondrial fission and Bnip3-related mitophagy via the JNK pathways. *Redox Biol.* 14, 576–587. doi:10.1016/j.redox.2017.11.004
- Jin, J. Y., Wei, X. X., Zhi, X. L., Wang, X. H., and Meng, D. (2020). Drp1-dependent mitochondrial fission in cardiovascular disease. *Acta Pharmacol. Sin.* 0, 1–10. doi:10.1038/s41401-020-00518-y
- Kroemer, G., Galluzzi, L., and Brenner, C. (2007). Mitochondrial membrane permeabilization in cell death. *Physiol. Rev.* 87, 99–163. doi:10.1152/physrev.00013.2006
- Li, Q., Yu, P., Zeng, Q., Luo, B., Cai, S., Hui, K., et al. (2016). Neuroprotective effect of hydrogen-rich saline in global cerebral ischemia/reperfusion rats: up-regulated tregs and down-regulated miR-21, miR-210 and NF-kappaB expression. *Neurochem. Res.* 41, 2655–2665. doi:10.1007/s11064-016-1978-x
- Liu, M., Li, X., Sun, R., Zeng, Y. I., Chen, S., and Zhang, P. (2016). Vitamin D nutritional status and the risk for cardiovascular disease. *Exp Ther Med* 11, 1189–1193. doi:10.3892/etm.2016.3047
- Liu, Z., Ren, Z., Zhang, J., Chuang, C. C., Kandaswamy, E., Zhou, T., et al. (2018). Role of ROS and nutritional antioxidants in human diseases. *Front. Physiol.* 9, 477. doi:10.3389/fphys.2018.00477
- Livingston, M. J., Wang, J., Zhou, J., Wu, G., Ganley, I. G., Hill, J. A., et al. (2019). Clearance of damaged mitochondria via mitophagy is important to the protective effect of ischemic preconditioning in kidneys. *Autophagy* 15, 2142–2162. doi:10.1080/15548627.2019.1615822
- Mao, K., and Klionsky, D. J. (2013). Mitochondrial fission facilitates mitophagy in *saccharomyces cerevisiae*. *Autophagy* 9, 1900–1901. doi:10.4161/auto.25804
- Navarro, A., and Boveris, A. (2007). The mitochondrial energy transduction system and the aging process. *Am. J. Physiol. Cell Physiol.* 292, C670–C686. doi:10.1152/ajpcell.00213.2006
- Ni, H. M., Williams, J. A., and Ding, W. X. (2015). Mitochondrial dynamics and mitochondrial quality control. *Redox Biol* 4, 6–13. doi:10.1016/j.redox.2014.11.006
- Ong, S. B., Subrayan, S., Lim, S. Y., Yellon, D. M., Davidson, S. M., and Hausenloy, D. J. (2010). Inhibiting mitochondrial fission protects the heart against ischemia/reperfusion injury. *Circulation* 121, 2012–2022. doi:10.1161/circulationaha.109.906610
- Ong, S. B., Samangouei, P., Kalkhoran, S. B., and Hausenloy, D. J. (2015). The mitochondrial permeability transition pore and its role in myocardial ischemia reperfusion injury. *J. Mol. Cell. Cardiol.* 78, 23–34. doi:10.1016/j.jmcc.2014.11.005
- Polidoro, L., Properzi, G., Marampon, F., Gravina, G. L., Festuccia, C., Di Cesare, E., et al. (2013). Vitamin D protects human endothelial cells from H<sub>2</sub>O<sub>2</sub> oxidant injury through the Mek/Erk-Sirt1 axis activation. *J. Cardiovasc Transl Res* 6, 221–231. doi:10.1007/s12265-012-9436-x
- Pu, C. M., Liu, C. W., Liang, C. J., Yen, Y. H., Chen, S. H., Jiang-Shieh, Y. F., et al. (2017). Adipose-derived stem cells protect skin flaps against ischemia/reperfusion injury via IL-6 expression. *J. Invest. Dermatol.* 137, 1353–1362. doi:10.1016/j.jid.2016.12.030
- Ravikumar, B., Moreau, K., Jahreiss, L., Puri, C., and Rubinsztein, D. C. (2010). Plasma membrane contributes to the formation of pre-autophagosomal structures. *Nat. Cell Biol.* 12, 747–757. doi:10.1038/ncb2078
- Reddy, P. H. (2014). Inhibitors of mitochondrial fission as a therapeutic strategy for diseases with oxidative stress and mitochondrial dysfunction. *J. Alzheimers Dis.* 40, 245–256. doi:10.3233/jad-132060
- Rossello, X., He, Z., and Yellon, D. M. (2018). Myocardial infarct size reduction provided by local and remote ischaemic preconditioning: references values from the Hatter Cardiovascular Institute. *Cardiovasc. Drugs Ther.* 32, 127–133. doi:10.1007/s10557-018-6788-8
- Roth, G. A., Johnson, C., Abajobir, A., Abd-Allah, F., Abera, S. F., Abyu, G., et al. (2017). Global, regional, and national burden of cardiovascular diseases for 10 causes, 1990 to 2015. *J. Am. Coll. Cardiol.* 70, 1–25. doi:10.1016/j.jacc.2017.04.052
- Ryan, Z. C., Craig, T. A., Folmes, C. D., Wang, X., Lanza, I. R., Schaible, N. S., et al. (2016). 1 $\alpha$ ,25-Dihydroxyvitamin D<sub>3</sub> regulates mitochondrial oxygen consumption and dynamics in human skeletal muscle cells. *J. Biol. Chem.* 291, 1514–1528. doi:10.1074/jbc.M115.684399
- Schiattarella, G. G., and Hill, J. A. (2016). Therapeutic targeting of autophagy in cardiovascular disease. *J. Mol. Cell. Cardiol.* 95, 86–93. doi:10.1016/j.jmcc.2015.11.019
- Siddiqui, W. A., Ahad, A., and Ahsan, H. (2015). The mystery of BCL2 family: Bcl-2 proteins and apoptosis: an update. *Arch. Toxicol.* 89, 289–317. doi:10.1007/s00204-014-1448-7
- Tang, Y., Liu, J., and Long, J. (2015). Phosphatase and tensin homolog-induced putative kinase 1 and Parkin in diabetic heart: role of mitophagy. *J. Diabetes Investig.* 6, 250–255. doi:10.1111/jdi.12302
- Tao, R. X., Zhou, Q. F., Xu, Z. W., Hao, J. H., Huang, K., Mou, Z., et al. (2015). Inverse correlation between vitamin D and C-reactive protein in newborns. *Nutrients* 7, 9218–9228. doi:10.3390/nu7115468
- Vasquez-Trincado, C., Garcia-Carvajal, I., Pennanen, C., Parra, V., Hill, J. A., Rothermel, B. A., et al. (2016). Mitochondrial dynamics, mitophagy and cardiovascular disease. *J. Physiol* 594, 509–525. doi:10.1113/jp271301
- Wang, J., Toan, S., and Zhou, H. (2020). New insights into the role of mitochondria in cardiac microvascular ischemia/reperfusion injury. *Angiogenesis* 23, 299–314. doi:10.1007/s10456-020-09720-2
- Westermann, B. (2010). Mitochondrial fusion and fission in cell life and death. *Nat. Rev. Mol. Cell Biol.* 11, 872–884. doi:10.1038/nrm3013
- Witte, K. K., Byrom, R., Gierula, J., Paton, M. F., Jamil, H. A., Lowry, J. E., et al. (2016). Effects of vitamin D on cardiac function in patients with chronic HF: the VINDICATE study. *J. Am. Coll. Cardiol.* 67, 2593–2603. doi:10.1016/j.jacc.2016.03.058
- Wu, H., Ye, M., Liu, D., Yang, J., Ding, J. W., Zhang, J., et al. (2019). UCP2 protect the heart from myocardial ischemia/reperfusion injury via induction of mitochondrial autophagy. *J. Cell. Biochem.* 120, 15455–15466. doi:10.1002/jcb.28812
- Yang, Z., and Klionsky, D. J. (2010). Mammalian autophagy: core molecular machinery and signaling regulation. *Curr. Opin. Cell Biol.* 22, 124–131. doi:10.1016/j.ccb.2009.11.014
- Yang, Y., Zhao, L., and Ma, J. (2017). Penehyclidine hydrochloride preconditioning provides cardiac protection in a rat model of myocardial ischemia/reperfusion injury via the mechanism of mitochondrial dynamics mechanism. *Eur. J. Pharmacol.* 813, 130–139. doi:10.1016/j.ejphar.2017.07.031
- Yang, F., Li, T., Dong, Z., and Mi, R. (2018). MicroRNA-410 is involved in mitophagy after cardiac ischemia/reperfusion injury by targeting high-mobility group box 1 protein. *J. Cell. Biochem.* 119, 2427–2439. doi:10.1002/jcb.26405
- Yang, M., Linn, B. S., Zhang, Y., and Ren, J. (2019). Mitophagy and mitochondrial integrity in cardiac ischemia-reperfusion injury. *Biochim. Biophys. Acta (BBA) - Mol. Basis Dis.* 1865, 2293–2302. doi:10.1016/j.bbdis.2019.05.007

- Yao, T., Ying, X., Zhao, Y., Yuan, A., He, Q., Tong, H., et al. (2015). Vitamin D receptor activation protects against myocardial reperfusion injury through inhibition of apoptosis and modulation of autophagy. *Antioxidants Redox Signal.* 22, 633–650. doi:10.1089/ars.2014.5887
- Yao, L., Chen, H., Wu, Q., and Xie, K. (2019). Hydrogen-rich saline alleviates inflammation and apoptosis in myocardial I/R injury via PINK-mediated autophagy. *Int. J. Mol. Med.* 44, 1048–1062. doi:10.3892/ijmm.2019.4264
- Yellon, D. M., and Hausenloy, D. J. (2007). Myocardial reperfusion injury. *N. Engl. J. Med.* 357, 1121–1135. doi:10.1056/NEJMr071667
- Youle, R. J., and Van Der Bliek, A. M. (2012). Mitochondrial fission, fusion, and stress. *Science* 337, 1062–1065. doi:10.1126/science.1219855
- Yu, T., Sheu, S. S., Robotham, J. L., and Yoon, Y. (2008). Mitochondrial fission mediates high glucose-induced cell death through elevated production of reactive oxygen species. *Cardiovasc. Res.* 79, 341–351. doi:10.1093/cvr/cvn104
- Yu, L. M., Dong, X., Zhang, J., Li, Z., Xue, X. D., Wu, H. J., et al. (2019). Naringenin attenuates myocardial ischemia-reperfusion injury via cGMP-PKG/alpha signaling and *in vivo* and *in vitro* studies. *Oxid Med Cell Longev* 2019, 7670854. doi:10.1155/2019/7670854
- Yusman, M. G., Toyokawa, T., Odley, A., Lynch, R. A., Wu, G., Colbert, M. C., et al. (2002). Mitochondrial death protein Nix is induced in cardiac hypertrophy and triggers apoptotic cardiomyopathy. *Nat. Med.* 8, 725–730. doi:10.1038/nm719
- Zhang, W., Chen, C., Wang, J., Liu, L., He, Y., and Chen, Q. (2018). Mitophagy in cardiomyocytes and in platelets: a major mechanism of cardioprotection against ischemia/reperfusion injury. *Physiology* 33, 86–98. doi:10.1152/physiol.00030.2017
- Zhou, T., Chuang, C. C., and Zuo, L. (2015). Molecular characterization of reactive oxygen species in myocardial ischemia-reperfusion injury. *BioMed Res. Int.* 2015, 864946. doi:10.1155/2015/864946
- Zhou, H., Wang, J., Zhu, P., Zhu, H., Toan, S., Hu, S., et al. (2018a). NR4A1 aggravates the cardiac microvascular ischemia reperfusion injury through suppressing FUNDC1-mediated mitophagy and promoting Mff-required mitochondrial fission by CK2α. *Basic Res. Cardiol.* 113, 23. doi:10.1007/s00395-018-0682-1
- Zhou, H., Zhu, P., Wang, J., Zhu, H., Ren, J., and Chen, Y. (2018b). Pathogenesis of cardiac ischemia reperfusion injury is associated with CK2α-disturbed mitochondrial homeostasis via suppression of FUNDC1-related mitophagy. *Cell Death Differ.* 25, 1080–1093. doi:10.1038/s41418-018-0086-7
- Zhou, H., Wang, J., Hu, S., Zhu, H., Toan, S., and Ren, J. (2019). B11 alleviates cardiac microvascular ischemia-reperfusion injury via modifying mitochondrial fission and inhibiting XO/ROS/F-actin pathways. *J. Cell. Physiol.* 234, 5056–5069. doi:10.1002/jcp.27308
- Zhou, H., Toan, S., Zhu, P., Wang, J., Ren, J., and Zhang, Y. (2020). DNA-PKcs promotes cardiac ischemia reperfusion injury through mitigating BI-1-governed mitochondrial homeostasis. *Basic Res. Cardiol.* 115, 11. doi:10.1007/s00395-019-0773-7






**Conflict of Interest:** The authors declare that the research was conducted in the absence of any commercial or financial relationships that could be construed as a potential conflict of interest.

Copyright © 2020 Lee, Lee, Chen, Lee, Lai, Lin, Hsu, Sung, Lee and Chen. This is an open-access article distributed under the terms of the Creative Commons Attribution License (CC BY). The use, distribution or reproduction in other forums is permitted, provided the original author(s) and the copyright owner(s) are credited and that the original publication in this journal is cited, in accordance with accepted academic practice. No use, distribution or reproduction is permitted which does not comply with these terms.



## Article

# Secoiridoid Glucosides and Anti-Inflammatory Constituents from the Stem Bark of *Fraxinus chinensis*

Hao-Chiun Chang <sup>1,2,†</sup> , Shih-Wei Wang <sup>3,4,†</sup> , Chin-Yen Chen <sup>5</sup>, Tsong-Long Hwang <sup>6,7,8</sup> ,  
Ming-Jen Cheng <sup>9</sup>, Ping-Jyun Sung <sup>4,10</sup> , Kuang-Wen Liao <sup>2,11</sup> and Jih-Jung Chen <sup>12,13,\*</sup> 

<sup>1</sup> Department of Orthopaedics, MacKay Memorial Hospital, Taipei 10449, Taiwan; Changhaochiun@gmail.com

<sup>2</sup> Ph.D. Degree Program of Biomedical Science and Engineering, National Chiao Tung University, Hsinchu City 30068, Taiwan; liaonms@g2.nctu.edu.tw

<sup>3</sup> Department of Medicine, MacKay Medical College, New Taipei City 25242, Taiwan; shihwei@mmc.edu.tw

<sup>4</sup> Graduate Institute of Natural Products, Kaohsiung Medical University, Kaohsiung 80708, Taiwan; pjsung@nmmba.gov.tw

<sup>5</sup> Graduate Institute of Pharmaceutical Technology, Tajen University, Pingtung 90741, Taiwan; jjc8506674@gmail.com

<sup>6</sup> Graduate Institute of Natural Products, School of Traditional Chinese Medicine, College of Medicine, Chang Gung University, Taoyuan 33303, Taiwan; htl@mail.cgu.edu.tw

<sup>7</sup> Research Center for Food and Cosmetic Safety, Graduate Institute of Health Industry Technology, College of Human Ecology, Chang Gung University of Science and Technology, Taoyuan 33303, Taiwan

<sup>8</sup> Department of Anesthesiology, Chang Gung Memorial Hospital, Taoyuan 333, Taiwan

<sup>9</sup> Bioresource Collection and Research Center (BCRC), Food Industry Research and Development Institute (FIRDI), Hsinchu 30062, Taiwan; cmj@firdi.org.tw

<sup>10</sup> National Museum of Marine Biology and Aquarium, Pingtung 94450, Taiwan

<sup>11</sup> Institute of Molecular Medicine and Bioengineering, National Chiao Tung University, Hsinchu City 30068, Taiwan

<sup>12</sup> Faculty of Pharmacy, School of Pharmaceutical Sciences, National Yang-Ming University, Taipei 11221, Taiwan

<sup>13</sup> Department of Medical Research, China Medical University Hospital, China Medical University, Taichung 40402, Taiwan

\* Correspondence: chenjj@ym.edu.tw; Tel.: +886-2-2826-7195

† These authors contributed equally to this manuscript.

Academic Editor: Phurpa Wangchuk

Received: 14 November 2020; Accepted: 9 December 2020; Published: 14 December 2020



**Abstract:** Qin Pi (*Fraxinus chinensis* Roxb.) is commercially used in healthcare products for the improvement of intestinal function and gouty arthritis in many countries. Three new secoiridoid glucosides, (8E)-4''-O-methyliligstroside (1), (8E)-4''-O-methyldemethyliligstroside (2), and 3'',4''-di-O-methyl-demethyloleuropein (3), have been isolated from the stem bark of *Fraxinus chinensis*, together with 23 known compounds (4–26). The structures of the new compounds were established by spectroscopic analyses (1D, 2D NMR, IR, UV, and HRESIMS). Among the isolated compounds, (8E)-4''-O-methyliligstroside (1), (8E)-4''-O-methyldemethyliligstroside (2), 3'',4''-di-O-methyldemethyloleuropein (3), oleuropein (6), aesculetin (9), isoscopoletin (11), aesculetin dimethyl ester (12), fraxetin (14), tyrosol (21), 4-hydroxyphenethyl acetate (22), and (+)-pinorelinol (24) exhibited inhibition ( $IC_{50} \leq 7.65 \mu\text{g/mL}$ ) of superoxide anion generation by human neutrophils in response to formyl-L-methionyl-L-leucyl-L-phenylalanine/cytochalasin B (fMLP/CB). Compounds 1, 9, 11, 14, 21, and 22 inhibited fMLP/CB-induced elastase release with  $IC_{50} \leq 3.23 \mu\text{g/mL}$ . In addition, compounds 2, 9, 11, 14, and 21 showed potent inhibition with  $IC_{50}$  values  $\leq 27.11 \mu\text{M}$ , against lipopolysaccharide (LPS)-induced nitric oxide (NO) generation. The well-known proinflammatory cytokines, tumor necrosis factor-alpha (TNF- $\alpha$ ) and interleukin 6 (IL-6), were also inhibited by compounds 1, 9, and 14. Compounds 1, 9, and 14 displayed an anti-inflammatory effect against NO, TNF- $\alpha$ , and IL-6 through the inhibition of activation of MAPKs and I $\kappa$ B $\alpha$  in LPS-activated

macrophages. In addition, compounds **1**, **9**, and **14** stimulated anti-inflammatory M2 phenotype by elevating the expression of arginase 1 and Krüppel-like factor 4 (KLF4). The above results suggested that compounds **1**, **9**, and **14** could be considered as potential compounds for further development of NO production-targeted anti-inflammatory agents.

**Keywords:** *Fraxinus chinensis*; Oleaceae; stem bark; secoiridoid; anti-inflammatory activity

## 1. Introduction

*Fraxinus chinensis* Roxb. (Oleaceae) is a deciduous tree distributed in China, Japan, Korea, Russia, and Vietnam [1]. Its stem bark, called “Qin Pi”, is used as a health food or herbal supplement for improving intestinal function in Asia and America. The Oleaceae family is a rich source of secoiridoid glucosides [2]. A number of secoiridoid glucosides [2–6], coumarins [5,6], phenylpropenoids [5,6], lignans [6], and benzofuran derivatives [6] have been reported from the genus *Fraxinus*. These derivatives have been reported to exhibit several biological activities, such as antidiabetic [4], anti-inflammatory [4], immunosuppressive [4], anticancer [4], and quinone reductase-inducing activities [6]. *F. chinensis* has been found to be an active material by screening for anti-inflammatory effect of many natural sources. Three new secoiridoid glucosides, (8*E*)-4''-*O*-methylligstroside (**1**), (8*E*)-4''-*O*-methyldemethylligstroside (**2**), and 3'',4''-di-*O*-methyldemethyleuropein (**3**), and 23 known compounds (**4–26**) have been isolated and confirmed from the stem bark of *F. chinensis*. This report depicts the structural elucidation of three new compounds **1–3** and the inhibitory activities of all isolated compounds against fMLP/CB-induced O<sub>2</sub><sup>•−</sup> and elastase release and against LPS-induced NO generation.

## 2. Results and Discussion

### 2.1. Isolation and Structural Elucidation

Separation of the EtOAc-soluble fraction of an MeOH extract of stem bark of *F. chinensis* by silica gel chromatography and preparative thin-layer chromatography (TLC) afforded three new (**1–3**) and 23 known compounds (**4–26**) (Figure 1).

Compound **1** was obtained as yellowish oil and the molecular formula was determined to be C<sub>26</sub>H<sub>34</sub>O<sub>12</sub> by ESI-MS [*m/z* 561 [M + Na]<sup>+</sup>] (Figure S1) and HR-ESI-MS [*m/z* 561.1950 [M + Na]<sup>+</sup> (calcd for C<sub>26</sub>H<sub>34</sub>NaO<sub>12</sub>, 561.1948)] (Figure S2). The IR spectrum showed the presence of hydroxyl (3402 cm<sup>−1</sup>) and carbonyl (1727 and 1709 cm<sup>−1</sup>) groups. Analysis of the <sup>1</sup>H (Table 1 and Figure S3) and <sup>13</sup>C NMR (Table 2 and Figure S4) data of **1** revealed signals for a 4-methoxyphenethoxy group [ $\delta_{\text{H}}$  2.85 (2H, t, *J* = 7.0 Hz, H- $\beta$ ), 3.76 (3H, s, OMe-4''), 4.12, 4.24 (each 1H, each dt, *J* = 10.5, 7.0 Hz, H- $\alpha$ ), 6.85 (2H, d, *J* = 9.0 Hz, H-3'' and H-5''), 7.15 (2H, d, *J* = 9.0 Hz, H-2'' and H-6'');  $\delta_{\text{C}}$  35.2 (C- $\beta$ ), 55.9 (OMe-4''), 67.0 (C- $\alpha$ ), 115.1 (C-3'' and C-5''), 131.2 (C-2'' and C-6''), 131.5 (C-1''), 160.0 (C-4'')], a secoiridoid moiety [ $\delta_{\text{H}}$  1.62 (3H, dd, *J* = 7.0, 1.0 Hz, H-10), 2.44 (1H, dd, *J* = 14.0, 9.5 Hz, H-6), 2.69 (1H, dd, *J* = 14.0, 5.0 Hz, H-6), 3.71 (3H, s, OMe-11), 3.95 (1H, dd, *J* = 9.5, 5.0 Hz, H-5), 5.92 (1H, br s, H-1), 6.06 (1H, br q, *J* = 7.0 Hz, H-8), 7.51 (1H, s, H-3);  $\delta_{\text{C}}$  13.7 (C-10), 32.0 (C-5), 41.3 (C-6), 52.1 (CH<sub>3</sub>OCO-4), 95.3 (C-1), 109.5 (C-4), 125.1 (C-8), 130.5 (C-9), 155.3 (C-3), 168.9 (CH<sub>3</sub>OCO-4), 173.4 (C-7)], and a  $\beta$ -glucose moiety [ $\delta_{\text{H}}$  3.28–3.36 (3H, m, H-2', H-4', and H-5'), 3.42 (1H, dd, *J* = 8.5, 8.5 Hz, H-3'), 3.66 (1H, dd, *J* = 12.0, 5.5 Hz, H-6'), 3.88 (1H, dd, *J* = 12.0, 1.5 Hz, H-6'), 4.80 (1H, d, *J* = 7.5 Hz, H-1');  $\delta_{\text{C}}$  62.9 (C-6'), 71.7 (C-4'), 74.9 (C-2'), 78.1 (C-3'), 78.6 (C-5'), 101.0 (C-1')]. These data were nearly identical with those of (8*E*)-ligstroside (**5**) [7], except that a methoxy group [ $\delta_{\text{H}}$  3.76 (3H, s);  $\delta_{\text{C}}$  55.9] at C-4'' of **1** replaced the 4''-hydroxy group of (8*E*)-ligstroside (**5**) [7]. This was supported by NOESY correlations between OMe-4'' ( $\delta_{\text{H}}$  3.76) and H-3''/H-5'' ( $\delta_{\text{H}}$  6.85) and by HMBC correlation between OMe-4'' ( $\delta_{\text{H}}$  3.76) and C-4'' ( $\delta_{\text{C}}$  160.0) (Figure 2). The *E*-configuration at C-8 was confirmed by NOESY

correlation between H-5 and H-10. In the NOESY spectrum, H-1 ( $\delta$  5.92) had the correlation with H-6 ( $\delta$  2.44) and had no correlation with H-5 ( $\delta$  3.95), which indicated the relative configurations of H-1 and H-5 as  $\alpha$  and  $\beta$ , respectively. The position of each substituent was supported by NOESY correlations (Figure 2) between H-1 ( $\delta$  5.92)/H-6 ( $\delta$  2.44), H-1 ( $\delta$  5.92)/H-8 ( $\delta$  6.06), H-5 ( $\delta$  3.95)/H-10 ( $\delta$  1.62), H-1' ( $\delta$  4.80)/H-3' ( $\delta$  3.42), H- $\beta$  ( $\delta$  2.85)/H-2'' ( $\delta$  7.15), and H-3'' ( $\delta$  6.85)/OMe-4'' ( $\delta$  3.76) and by HMBC correlation (Figure 2) between H-1 ( $\delta$  5.92)/C-8 ( $\delta$  125.1), H-1 ( $\delta$  5.92)/C-1' ( $\delta$  101.0), H-3 ( $\delta$  7.51)/C-1 ( $\delta$  95.3), H-3 ( $\delta$  7.51)/C-5 ( $\delta$  32.0), H-5 ( $\delta$  3.95)/C-7 ( $\delta$  173.4), H-5 ( $\delta$  3.95)/C-11 ( $\delta$  168.9), H-10 ( $\delta$  1.62)/C-9 ( $\delta$  130.5), OMe-11 ( $\delta$  3.71)/C-11 ( $\delta$  168.9), H- $\alpha$  ( $\delta$  4.12)/C-7 ( $\delta$  173.4), H- $\alpha$  ( $\delta$  4.12)/C-1'' ( $\delta$  131.5), H- $\beta$  ( $\delta$  2.85)/C-2'',6'' ( $\delta$  131.2), H-3'',5'' ( $\delta$  6.85)/C-1'' ( $\delta$  131.5), and OMe-4'' ( $\delta$  3.76)/C-4'' ( $\delta$  160.0). The full assignment of  $^1\text{H}$  and  $^{13}\text{C}$  NMR resonances was supported by DEPT (Figure S5),  $^1\text{H}$ - $^1\text{H}$  COSY (Figure S6), NOESY (Figure S7), HMBC (Figure S8), and HSQC (Figure S9) spectral analyses. According to the above data, the structure of **1** was elucidated as (8*E*)-4''-*O*-methyligstroside.

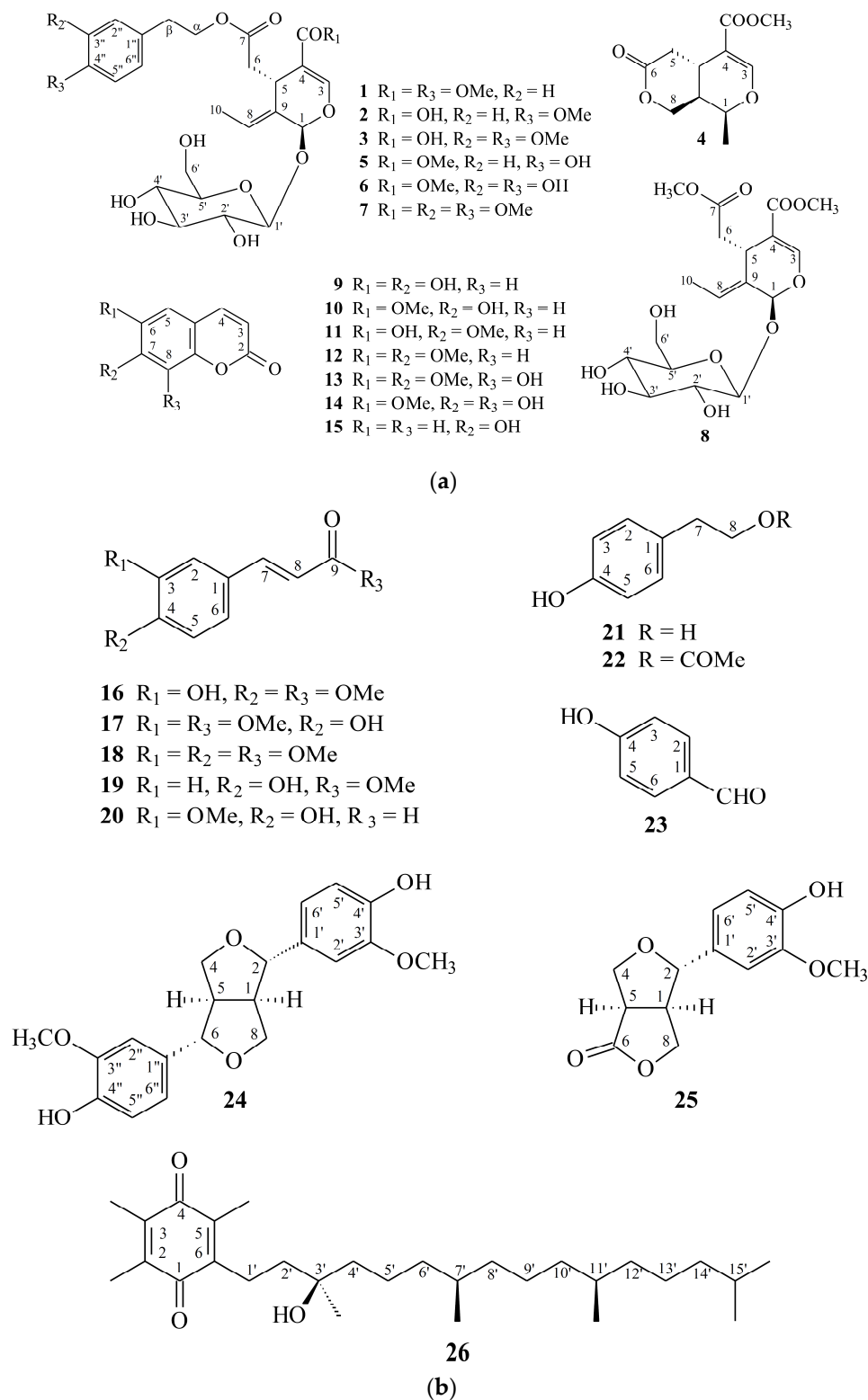
**Table 1.**  $^1\text{H}$ -NMR data for compounds **1–3** ( $\delta$  in ppm, *J* in Hz).

| Position | <b>1</b> <sup>a</sup> | <b>2</b> <sup>a</sup> | <b>3</b> <sup>a</sup> |
|----------|-----------------------|-----------------------|-----------------------|
| 1        | 5.92 br s             | 5.87 br s             | 5.86 br s             |
| 3        | 7.51 s                | 7.39 s                | 7.38 s                |
| 5        | 3.95 dd (9.5, 5.0)    | 4.01 dd (9.5, 5.0)    | 4.00 dd (9.5, 4.5)    |
| 6        | 2.44 dd (14.0, 9.5)   | 2.41 dd (14.0, 9.5)   | 2.41 dd (14.0, 9.5)   |
|          | 2.69 dd (14.0, 5.0)   | 2.79 dd (14.0, 4.5)   | 2.80 dd (14.0, 4.5)   |
| 8        | 6.06 br q (7.0)       | 6.05 br q (7.0)       | 6.06 br q (7.0)       |
| 10       | 1.62 dd (7.0, 1.0)    | 1.66 dd (7.0, 1.0)    | 1.66 dd (7.0, 1.0)    |
| $\alpha$ | 4.12 dt (10.5, 7.0)   | 4.11 dt (10.5, 7.0)   | 4.15 dt (10.5, 7.0)   |
|          | 4.24 dt (10.5, 7.0)   | 4.23 dt (10.5, 7.0)   | 4.27 dt (10.5, 7.0)   |
| $\beta$  | 2.85 t (7.0)          | 2.85 t (7.0)          | 2.86 t (7.0)          |
| 1'       | 4.80 d (7.5)          | 4.80 d (8.0)          | 4.80 d (8.0)          |
| 2'       | 3.28–3.36 m           | 3.29–3.35 m           | 3.28–3.36 m           |
| 3'       | 3.42 dd (8.5, 8.5)    | 3.41 dd (9.0, 8.5)    | 3.41 dd (8.5, 8.5)    |
| 4'       | 3.28–3.36 m           | 3.29–3.35 m           | 3.28–3.36 m           |
| 5'       | 3.28–3.36 m           | 3.29–3.35 m           | 3.28–3.36 m           |
| 6'       | 3.66 dd (12.0, 5.5)   | 3.67 dd (12.0, 5.5)   | 3.66 dd (12.0, 5.5)   |
|          | 3.88 dd (12.0, 1.5)   | 3.88 dd (12.0, 1.5)   | 3.88 dd (12.0, 1.5)   |
| 2''      | 7.15 d (9.0)          | 7.15 d (9.0)          | 6.86 d (2.0)          |
| 3''      | 6.85 d (9.0)          | 6.85 d (9.0)          |                       |
| 5''      | 6.85 d (9.0)          | 6.85 d (9.0)          | 6.88 d (8.5)          |
| 6''      | 7.15 d (9.0)          | 7.15 d (9.0)          | 6.79 dd (8.5, 2.0)    |
| OMe-11   | 3.71 s                |                       |                       |
| OMe-3''  |                       |                       | 3.82 s                |
| OMe-4''  | 3.76 s                | 3.76 s                | 3.80 s                |

<sup>a</sup> Measured in CD<sub>3</sub>OD at 500 MHz.

Compound **2** was obtained as amorphous powder. The ESI-MS (Figure S10) afforded a sodium adduct ion  $[\text{M} + \text{Na}]^+$  at  $m/z$  547, implying a molecular formula of C<sub>25</sub>H<sub>32</sub>O<sub>12</sub>, which was confirmed by the HR-ESI-MS mass spectrum ( $m/z$  547.1787  $[\text{M} + \text{Na}]^+$ , calcd for C<sub>25</sub>H<sub>32</sub>O<sub>12</sub>Na, 547.1791) (Figure S11). The presence of hydroxyl (3334 cm<sup>−1</sup>) and carbonyl (1728 and 1707 cm<sup>−1</sup>) groups were evident from the IR spectrum. The  $^1\text{H}$  (Table 1 and Figure S12) and  $^{13}\text{C}$  NMR (Table 2 and Figure S13) data of **2** were very similar to those of demethyligstroside [3], except that a methoxy group [ $\delta$  3.76 (3H, s)] at C-4'' in **2** replaced the 4''-hydroxy group of demethyligstroside [3]. This was supported by NOESY correlations between OMe-4'' ( $\delta$  3.76) and H-3''/H-5'' ( $\delta$  6.85) and by HMBC correlation between OMe-4'' ( $\delta$  3.76) and C-4'' ( $\delta$  160.0) (Figure 3). The relative configuration of **2** was assigned by NOESY spectrum, which showed correlation between H-1 ( $\delta$  5.87) and H-6 ( $\delta$  2.41), suggesting that H-5 was on the  $\beta$  configuration, and H-1 was on the  $\alpha$  configuration. The *E*-configuration at C-8 was confirmed by NOESY correlation between H-5 and H-10. The full assignment of  $^1\text{H}$  and  $^{13}\text{C}$  NMR resonances

was supported by DEPT (Figure S14),  $^1\text{H}$ - $^1\text{H}$  COSY (Figure S15), NOESY (Figure 3 and Figure S16), HMBC (Figure 3 and Figure S17), and HSQC (Figure S18) spectral analyses. Thus, the structure of 2 was established as shown in Figure 1, and named (8*E*)-4''-*O*-methyl demethyliligstroside.

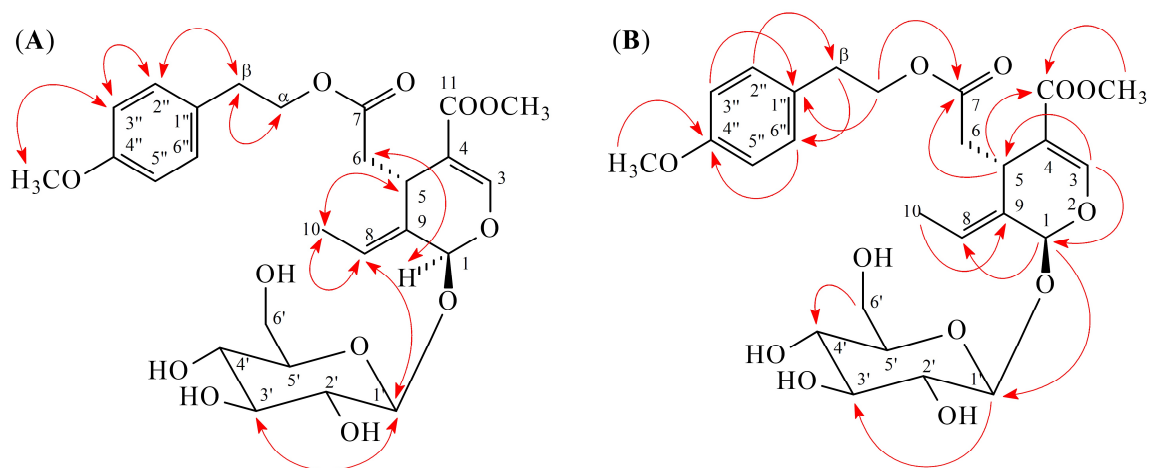


**Figure 1.** The chemical structures of compounds 1–15 (a) and 16–26 (b) isolated from *F. chinensis*.



**Table 2.**  $^{13}\text{C}$ -NMR data for compounds 1–3 ( $\delta$  in ppm).

| Position | 1 <sup>a</sup> | 2 <sup>a</sup> | 3 <sup>a</sup> |
|----------|----------------|----------------|----------------|
| 1        | 95.3           | 95.0           | 95.3           |
| 3        | 155.3          | 152.8          | 155.3          |
| 4        | 109.5          | 110.2          | 109.5          |
| 5        | 32.0           | 31.9           | 32.0           |
| 6        | 41.3           | 41.3           | 41.4           |
| 7        | 173.4          | 173.3          | 173.4          |
| 8        | 125.1          | 124.6          | 125.0          |
| 9        | 130.5          | 130.7          | 130.6          |
| 10       | 13.7           | 13.6           | 13.7           |
| 11       | 168.9          | 171.0          | 168.8          |
| $\alpha$ | 67.0           | 66.9           | 66.9           |
| $\beta$  | 35.2           | 35.2           | 35.7           |
| 1'       | 101.0          | 101.0          | 101.0          |
| 2'       | 74.9           | 74.9           | 74.9           |
| 3'       | 78.1           | 78.1           | 78.1           |
| 4'       | 71.7           | 71.6           | 71.6           |
| 5'       | 78.6           | 78.6           | 78.6           |
| 6'       | 62.9           | 62.9           | 62.9           |
| 1''      | 131.5          | 131.5          | 132.4          |
| 2''      | 131.2          | 131.2          | 114.1          |
| 3''      | 115.1          | 115.1          | 150.5          |
| 4''      | 160.0          | 160.0          | 149.3          |
| 5''      | 115.1          | 115.1          | 113.4          |
| 6''      | 131.2          | 131.2          | 122.6          |
| OMe-11   | 52.1           |                |                |
| OMe-3''  |                |                | 56.7           |
| OMe-4''  | 55.9           | 55.9           | 56.7           |

<sup>a</sup> Measured in  $\text{CD}_3\text{OD}$  at 125 MHz.**Figure 2.** Key NOESY (A) and HMBC (B) correlations of 1.

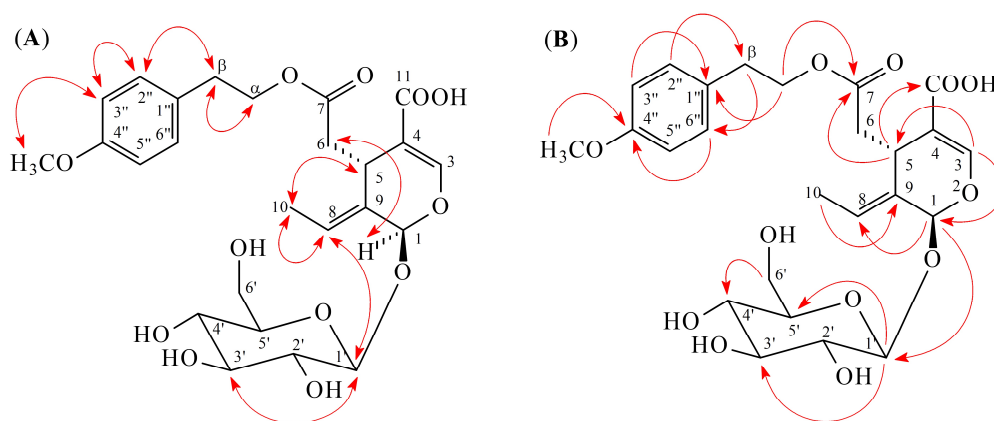


Figure 3. Key NOESY (A) and HMBC (B) correlations of **2**.

Compound **3** was isolated as amorphous powder. Its molecular formula,  $C_{26}H_{34}O_{13}$ , was determined on the basis of the positive ESI-MS at  $m/z$  577  $[M + Na]^+$  (Figure S19) and HR-ESI-MS at  $m/z$  577.1892  $[M + Na]^+$  (calcd 577.1897) (Figure S20) and was supported by the  $^1H$ ,  $^{13}C$ , and DEPT NMR data. The IR absorption bands of **3** revealed the presence of hydroxyl ( $3350\text{ cm}^{-1}$ ) and carbonyl ( $1721$  and  $1698\text{ cm}^{-1}$ ) functions. The  $^1H$  (Table 1 and Figure S21) and  $^{13}C$  NMR (Table 2 and Figure S22) data of **3** were similar to those of **2**, except that a 3,4-dimethoxyphenyl group [ $\delta_H$  3.80 (3H, s, OMe-4''), 3.82 (3H, s, OMe-3''), 6.79 (1H, dd,  $J = 8.5, 2.0\text{ Hz}$ , H-6''), 6.86 (1H, d,  $J = 2.0\text{ Hz}$ , H-2''), 6.88 (1H, d,  $J = 8.5\text{ Hz}$ , H-5'');  $\delta_C$  56.7 (OMe-3''), 56.7 (OMe-4''), 113.3 (C-5''), 114.1 (C-2''), 122.6 (C-6''), 132.5 (C-1''), 149.3 (C-4''), 150.5 (C-3'')] at C- $\beta$  in **3** replaced the 4-methoxyphenyl group at C- $\beta$  of **2**. This was supported by NOESY correlations between Ome-3'' ( $\delta_H$  3.82) and H-2'' ( $\delta_H$  6.86) and by HMBC correlation between OMe-3'' ( $\delta_H$  3.82) and C-3'' ( $\delta_C$  150.5) (Figure 4). The relative configuration of **3** was assumed to be the same as that of **2** based on the NOESY correlation between H-1 ( $\delta_H$  5.86) and H-6 ( $\delta_H$  2.41). The *E*-configuration at C-8 was confirmed by NOESY correlation between H-5 and H-10. The full assignment of  $^1H$  and  $^{13}C$  NMR resonances was further confirmed by DEPT (Figure S23),  $^1H$ - $^1H$  COSY (Figure S24), NOESY (Figure 4 and Figure S25), HMBC (Figure 4 and Figure S26), and HSQC (Figure S27) data. Consequently, the structure of compound **3** was established as 3'',4''-di-*O*-methyldemethyleuropein.

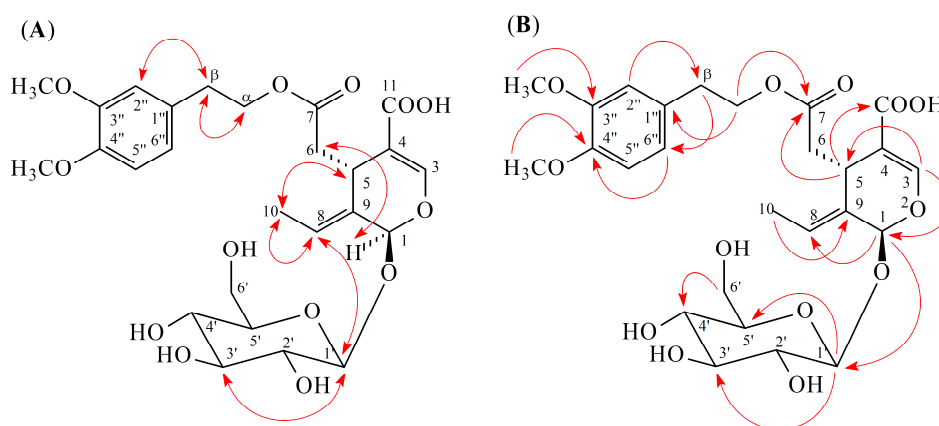


Figure 4. Key NOESY (A) and HMBC (B) correlations of **3**.

## 2.2. Structure Identification of the Known Isolates

The known isolates were readily identified by a comparison of their physical and spectroscopic data (UV, IR,  $^1H$  NMR,  $[\alpha]_D$ , and MS) with those of authentic samples or literature values. They include a pyran derivative, fraxilatone (**4**) [8], four secoiridoids, (*E*)-ligstroside (**5**) [7,9], oleuropein (**6**) [9],

(8*E*)-3'',4''-di-*O*-methyloleuropein (7) [10], and oleoside methyl ester (8) [11], seven coumarins, aesculetin (9) [12], scopoletin (10) [12,13], isoscopoletin (11) [12,14], aesculetin dimethyl ester (12) [12,15], fraxidin (13) [16,17], fraxetin (14) [18], and umbelliferone (15) [19], five phenylpropanoids, methyl isoferulate (16) [20], methyl ferulate (17) [21], methyl 3,4-dimethoxycinnamate (18) [22], methyl (*E*)-*p*-coumarate (19) [23], and (*E*)-ferulaldehyde (20) [24], two phenylethanoids, tyrosol (21) [25] and 4-hydroxyphenethyl acetate (22) [26], a benzenoid, *p*-hydroxybenzaldehyde (23) [27], two lignans, (+)-pinoresinol (24) [28] and (+)-salicifoliol (25) [29], and a  $\alpha$ -tocopheranoid:  $\alpha$ -tocopheryl quinone (26) [30].

### 2.3. Biological Studies

Reactive oxygen species (ROS) (e.g., hydrogen peroxide and superoxide anion ( $O_2^{\bullet-}$ )) and granule proteases (e.g., elastase, proteinase-3, and cathepsin G) produced by human neutrophils are involved in the pathogenesis of a variety of inflammatory diseases [31–33]. The effects on neutrophil proinflammatory responses of isolated compounds from the stem bark of *F. chinensis* were evaluated by suppressing fMLP/CB-induced superoxide radical anion ( $O_2^{\bullet-}$ ) generation and elastase release by human neutrophils. The inhibitory activity data on human neutrophil proinflammatory responses are shown in Table 3. Diphenyleneiodonium and phenylmethylsulfonyl fluoride were used as positive controls for  $O_2^{\bullet-}$  generation and elastase release, respectively. From the results of our biological tests, the following conclusions can be drawn: (a) (8*E*)-4''-*O*-methyliligstroside (1), (8*E*)-4''-*O*-methyldemethyliligstroside (2), 3'',4''-di-*O*-methyldemethyloleuropein (3), oleuropein (6), aesculetin (9), isoscopoletin (11), aesculetin dimethyl ester (12), fraxetin (14), tyrosol (21), 4-hydroxyphenethyl acetate (22), and (+)-pinoresinol (24) showed potent inhibition ( $IC_{50} \leq 7.65 \mu\text{g/mL}$ ) of  $O_2^{\bullet-}$  generation by neutrophils in response to fMLP/CB; (b) (8*E*)-4''-*O*-methyliligstroside (1), aesculetin (9), isoscopoletin (11), fraxetin (14), tyrosol (21), and 4-hydroxyphenethyl acetate (22) displayed potent inhibition ( $IC_{50} \leq 3.23 \mu\text{g/mL}$ ) against fMLP-induced elastase release; (c) secoiridoid glucoside, (8*E*)-4''-*O*-methyliligstroside (1) (with 4''-methoxy group) displayed more effective inhibition than its analogue, (8*E*)-ligstroside (5) (with 4''-hydroxy group) against fMLP-induced  $O_2^{\bullet-}$  generation and elastase release; (d) among the 6,7-disubstituted coumarin derivatives, aesculetin (9) (with 6,7-dihydroxy groups) exhibited more effective inhibition than its analogues, scopoletin (10) (with 7-hydroxy-6-methoxy groups), isoscopoletin (11) (with 6-hydroxy-7-methoxy groups), and aesculetin dimethyl ester (12) (with 6,7-dimethoxy groups) against fMLP-induced  $O_2^{\bullet-}$  generation; (e) among the 6,7,8-trisubstituted coumarin derivatives, fraxetin (14) (with 7,8-dihydroxy-6-methoxy groups) displayed more effective inhibition than its analogue, fraxidin (13) (with 8-hydroxy-6,7-dimethoxy groups) against fMLP-induced  $O_2^{\bullet-}$  generation and elastase release; (f) (8*E*)-4''-*O*-methyliligstroside (1) and fraxetin (14) were the most effective among the isolated compounds, with  $IC_{50}$  values of  $0.08 \pm 0.01$  and  $0.50 \pm 0.10 \mu\text{g/mL}$ , respectively, against fMLP-induced  $O_2^{\bullet-}$  generation and elastase release.

Nitric oxide (NO) is a mediator in the inflammatory response involved in host defense. The anti-inflammatory effects of the compounds isolated from the stem bark of *F. chinensis* were also evaluated by suppressing lipopolysaccharide (LPS)-induced NO generation in macrophage cell line RAW264.7. The inhibitory activity data of the isolates 1–26 on NO generation by macrophages are shown in Table 4. Quercetin was used as the positive control. From the results of our anti-inflammatory assays, the following conclusions can be drawn: (a) (8*E*)-4''-*O*-methyldemethyliligstroside (2), aesculetin (9), isoscopoletin (11), fraxetin (14), and tyrosol (21) showed potent inhibition with  $IC_{50}$  values  $\leq 27.11 \mu\text{M}$ , against lipopolysaccharide (LPS)-induced nitric oxide (NO) generation; (b) secoiridoid glucoside, (8*E*)-4''-*O*-methyliligstroside (1) (with 4''-methoxy group) displayed more effective inhibition than its analogue, (8*E*)-ligstroside (5) (with 4''-hydroxy group) against LPS-induced NO generation; (c) among the 6,7-disubstituted coumarin derivatives, aesculetin (9) (with 6,7-dihydroxy groups) and isoscopoletin (11) (with 6-hydroxy-7-methoxy groups) exhibited more effective inhibition than their analogues, scopoletin (10) (with 7-hydroxy-6-methoxy groups) and aesculetin dimethyl ester (12)

(with 6,7-dimethoxy groups) against LPS-induced NO generation; (d) among the 6,7,8-trisubstituted coumarin derivatives, fraxetin (**14**) (with 7,8-dihydroxy-6-methoxy groups) displayed more effective inhibition than its analogue, fraxidin (**13**) (with 8-hydroxy-6,7-dimethoxy groups) against LPS-induced NO generation; (e) (8E)-4''-O-Methylglistroside (**1**), aesculetin (**9**), and fraxetin (**14**) are the most effective among the isolated compounds, with IC<sub>50</sub> values of 12.38 ± 0.86, 9.36 ± 0.25, and 10.11 ± 0.47 µM, respectively, against LPS-induced NO production; (e) cytotoxic effects were tested using MTT experiment. The high cell viability (95, 98, and 97 %, respectively) of compounds **1**, **9**, and **14** at 50 µM showed that their inhibitory activities against LPS-induced NO generation did not arise from their cytotoxicities.

**Table 3.** Inhibitory effects of compounds **1–26** from the stem bark of *F. chinensis* on superoxide radical anion generation and elastase release by human neutrophils in response to fMet-Leu-Phe/cytochalasin B<sup>a</sup>.

| Compounds  | Superoxide Anion  | Elastase           |
|--|---|--------------------|
|  | IC <sub>50</sub> [µg/mL] <sup>b</sup> or (Inh %) <sup>c</sup> |                    |
| (8E)-4''-O-Methylglistroside ( <b>1</b> )          | 0.08 ± 0.01 ***   | 2.57 ± 0.76 ***    |
| (8E)-4''-O-Methyldemethylglistroside ( <b>2</b> )  | 2.66 ± 0.33 ***   | (42.92 ± 4.45) *** |
| 3'',4''-Di-O-methyldemethyloleuropein ( <b>3</b> ) | 5.22 ± 2.34 ***   | (33.78 ± 1.64) *** |
| Olenoside A ( <b>4</b> )                           | (8.67 ± 1.62) **  | (19.87 ± 2.94) **  |
| (8E)-Ligstroside ( <b>5</b> )                      | (1.30 ± 1.88)   | (26.58 ± 3.94) **  |
| Oleuropein ( <b>6</b> )                            | 2.90 ± 0.46   | (23.76 ± 0.50) *** |
| (8E)-3'',4''-Di-O-methyloleuropein ( <b>7</b> )    | (11.34 ± 6.05) *  | (32.73 ± 4.35) **  |
| Jaspolyside methyl ester ( <b>8</b> )              | (14.39 ± 3.28) *  | (20.54 ± 2.24) *** |
| Esculetin ( <b>9</b> )                             | 0.17 ± 0.03   | 2.41 ± 0.60        |
| Copoletin ( <b>10</b> )                            | (−0.91 ± 1.16)  | (8.98 ± 1.68) **   |
| Soscopoletin ( <b>11</b> )                         | 5.20 ± 1.52   | 3.23 ± 0.68        |
| Esculetin dimethyl ester ( <b>12</b> )             | 7.65 ± 1.62   | (8.95 ± 2.94) *    |
| Raxidin ( <b>13</b> )                              | (8.95 ± 2.94) *   | (12.14 ± 1.91) **  |
| Raxetin ( <b>14</b> )                              | 0.19 ± 0.01   | 0.50 ± 0.10        |
| Umbelliferone ( <b>15</b> )                        | (3.38 ± 1.99)   | (27.92 ± 4.88)     |
| Methyl isoferulate ( <b>16</b> )                   | (9.03 ± 1.65) **  | (−2.76 ± 0.84) *   |
| Methyl ferulate ( <b>17</b> )                      | (23.02 ± 4.18) **   | (24.12 ± 4.58) **  |
| Methyl 3,4-dimethoxycinnamate ( <b>18</b> )        | (42.90 ± 3.97) ***  | (7.05 ± 0.68) ***  |
| Methyl (E)-p-coumarate ( <b>19</b> )               | (8.01 ± 0.66) ***   | (20.30 ± 3.37) **  |
| (E)-Ferulaldehyde ( <b>20</b> )                    | (31.40 ± 7.95) **   | (38.61 ± 3.64) *** |
| Tyrosol ( <b>21</b> )                              | 4.93 ± 0.19   | 2.64 ± 0.22        |
| 4-Hydroxyphenethyl acetate ( <b>22</b> )           | 2.50 ± 0.35   | 3.03 ± 0.48        |
| p-Hydroxybenzaldehyde ( <b>23</b> )                | (16.16 ± 2.03) **   | (24.35 ± 4.45) **  |
| (+)-Pinoresinol ( <b>24</b> )                      | 2.01 ± 0.38   | (42.37 ± 2.06) *** |
| (+)-Salicifolol ( <b>25</b> )                      | (3.70 ± 2.59)   | (9.14 ± 1.58) **   |
| α-Tocopheryl quinone ( <b>26</b> )                 | (17.88 ± 2.82) **   | (11.35 ± 4.41)     |
| Diphenyleneiodonium (DPI) <sup>d</sup>             | 0.52 ± 0.19 ***   | –                  |
| Phenylmethylsulfonyl fluoride (PMSF) <sup>d</sup>  | –   | 34.4 ± 5.1 ***     |

<sup>a</sup> Results are displayed as mean ± SEM (*n* = 3) of three independent experiments. <sup>b</sup> Concentration necessary for 50% inhibition (IC<sub>50</sub>). If IC<sub>50</sub> value of tested compound was <10 µg/mL, it was presented as IC<sub>50</sub> [µg/mL]. <sup>c</sup> Percentage of inhibition (Inh %) at 10 µg/mL. If IC<sub>50</sub> value of tested compound was ≥10 µg/mL, it was displayed as Inh % at 10 µg/mL. <sup>d</sup> DPI and PMSF were employed as positive controls for superoxide anion (O<sub>2</sub><sup>•−</sup>) production and elastase release, respectively. \* *p* < 0.05 compared with the control. \*\* *p* < 0.01 compared with the control. \*\*\* *p* < 0.001 compared with the control.

The results of enzyme-linked immunosorbent assay (ELISA) showed that (8E)-4''-O-methylglistroside (**1**), aesculetin (**9**), and fraxetin (**14**) obviously suppressed TNF-α and IL-6 production in a concentration-dependent manner in RAW264.7 macrophages (Figure 5). Andrographolide was used as positive control. The action mechanisms of **1**, **9**, and **14** in macrophages were further investigated. Mitogen-activated protein kinases (MAPKs) and IκBα are the downstream signaling of LPS in macrophage cell line RAW264.7. Compounds **1**, **9**, and **14** (10 µM) caused a significant reduction of the phosphorylation of MAPKs and IκBα in LPS-induced macrophages (Figure 6).



Notably, phosphorylation of JNK caused by LPS was most significantly inhibited by these compounds. These results suggest that the anti-inflammatory effects of compounds **1**, **9**, and **14** are through the inhibition of activation of MAPKs and I $\kappa$ B $\alpha$  in LPS-activated macrophages.

**Table 4.** Inhibitory effects of compounds **1–26** from the stem bark of *F. chinensis* on nitric oxide (NO) generation by RAW264.7 murine macrophages in response to lipopolysaccharide (LPS).

| Compounds  | IC <sub>50</sub> [ $\mu$ M] <sup>a</sup> |
|--|--|
| (8E)-4''-O-Methylglistroside ( <b>1</b> )          | 12.38 $\pm$ 0.86 *                       |
| (8E)-4''-O-Methyldemethylglistroside ( <b>2</b> )  | 24.72 $\pm$ 1.25 **                      |
| 3'',4''-Di-O-methyldemethyloleuropein ( <b>3</b> ) | 37.14 $\pm$ 2.51 *                       |
| Olenoside A ( <b>4</b> )                           | >100                                     |
| (8E)-Ligstroside ( <b>5</b> )                      | 42.78 $\pm$ 3.23 *                       |
| Oleuropein ( <b>6</b> )                            | 40.02 $\pm$ 2.69 *                       |
| (8E)-3'',4''-Di-O-methyloleuropein ( <b>7</b> )    | 53.44 $\pm$ 4.19                         |
| Jaspolyside methyl ester ( <b>8</b> )              | 65.82 $\pm$ 5.64                         |
| Esculetin ( <b>9</b> )                             | 9.36 $\pm$ 0.25 **                       |
| Copoletin ( <b>10</b> )                            | 53.05 $\pm$ 3.63 *                       |
| Soscopoletin ( <b>11</b> )                         | 15.36 $\pm$ 0.81 *                       |
| Esculetin dimethyl ester ( <b>12</b> )             | 31.80 $\pm$ 2.17 *                       |
| Raxidin ( <b>13</b> )                              | 50.62 $\pm$ 3.08 *                       |
| Raxetin ( <b>14</b> )                              | 10.11 $\pm$ 0.47 *                       |
| Umbelliferone ( <b>15</b> )                        | 48.24 $\pm$ 3.22                         |
| Methyl isoferulate ( <b>16</b> )                   | >100                                     |
| Methyl ferulate ( <b>17</b> )                      | >100                                     |
| Methyl 3,4-dimethoxycinnamate ( <b>18</b> )        | 75.84 $\pm$ 6.28                         |
| Methyl (E)-p-coumarate ( <b>19</b> )               | >100                                     |
| (E)-Ferulaldehyde ( <b>20</b> )                    | 67.38 $\pm$ 4.09                         |
| Tyrosol ( <b>21</b> )                              | 27.11 $\pm$ 1.87 *                       |
| 4-Hydroxyphenethyl acetate ( <b>22</b> )           | 35.36 $\pm$ 2.54 *                       |
| p-Hydroxybenzaldehyde ( <b>23</b> )                | 55.13 $\pm$ 4.25                         |
| (+)-Pinoresinol ( <b>24</b> )                      | 41.69 $\pm$ 3.02 *                       |
| (+)-Salicifoliol ( <b>25</b> )                     | >100                                     |
| $\alpha$ -Tocopheryl quinone ( <b>26</b> )         | >100                                     |
| Quercetin <sup>b</sup>                             | 33.95 $\pm$ 2.34 *                       |

<sup>a</sup> The IC<sub>50</sub> values were calculated from the slope of the dose–response curves (SigmaPlot). Values are expressed as mean  $\pm$  SEM ( $n = 4$ ) of three independent experiments. \*  $p < 0.05$ , \*\*  $p < 0.01$  compared with the control. <sup>b</sup> Quercetin was used as a positive control.

M2-polarized macrophages are important for tissue repair [34]. Arginase 1 is an important M2 marker that connects Krüppel-like factor 4 (KLF4) to the biologic processes involved in M2 polarization [35]. High levels of arginase-1 can compete with iNOS for arginine and reduce NO production [36]. In addition, KLF4, which is one of the major members of the KLF family, was shown to induce M2 macrophage phenotype, whereas it reduced M1 macrophage expression [37]. We further examined whether compounds **1**, **9**, and **14** enhanced the expression level of M2 macrophages. The result showed that expression levels of arginase-1 and KLF4 were both induced by treatment with compounds **1**, **9**, and **14** (Figure 7). These results suggested that compounds **1**, **9**, and **14** promoted the expression of macrophage M2 markers, arginase-1 and KLF4, and exhibited the anti-inflammatory activity. We can also draw a schematic diagram that shows how compounds **1**, **9**, and **14** influence the polarization of M1 and M2 macrophages (Figure 8).

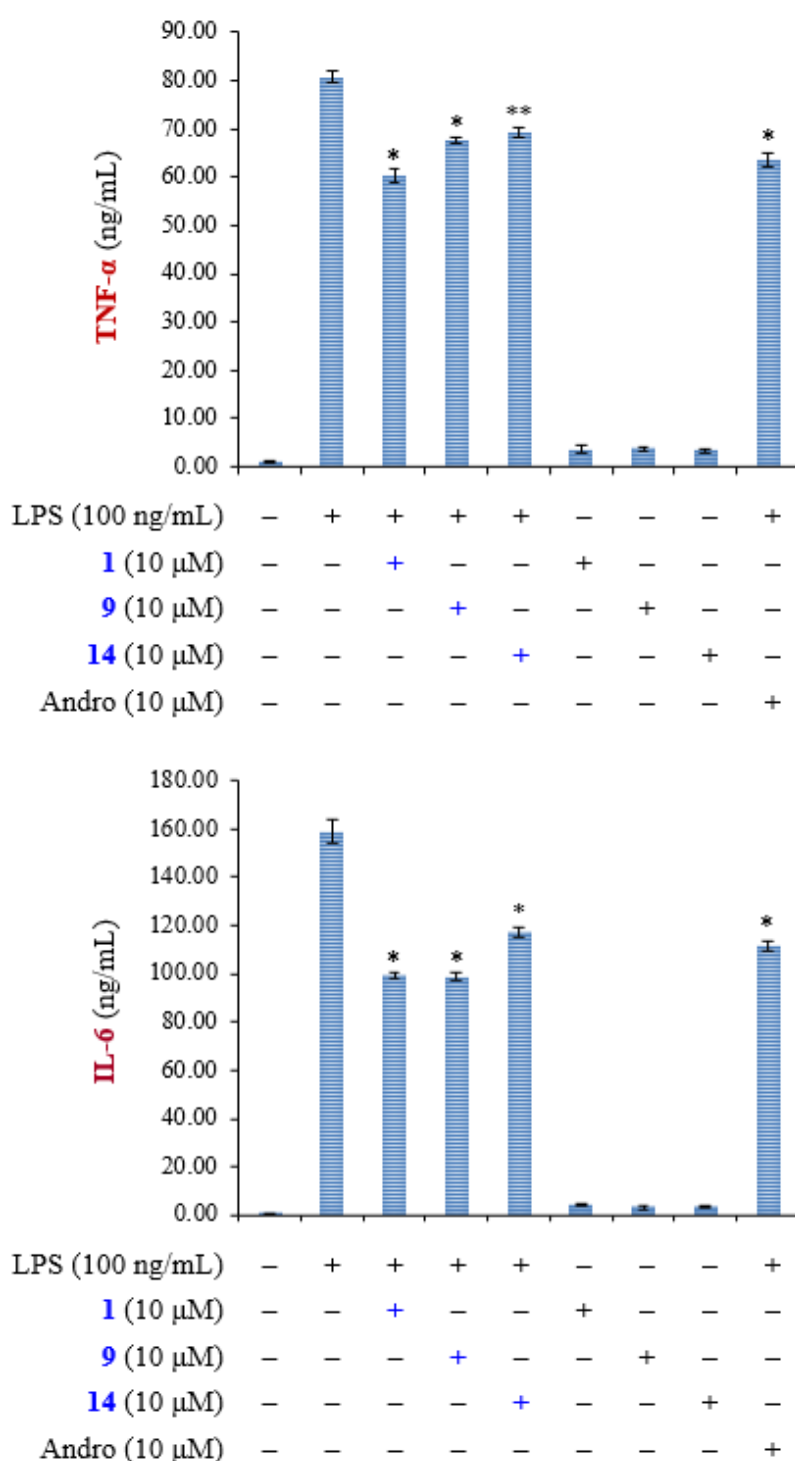


**Figure 5.** Compounds **1**, **9**, and **14** suppress the production of proinflammatory cytokines TNF- $\alpha$  and IL-6 in LPS-stimulated RAW 264.7 macrophages. Andrographolide (Andro) was used as positive control. Results are displayed as mean  $\pm$  SEM ( $n = 3$ ) of three independent experiments. “+” means treatment with LPS or compound. “−” means no treatment with LPS or compound. Asterisks indicate significant differences (\*  $p < 0.05$ , \*\*  $p < 0.01$ ) compared with the control.

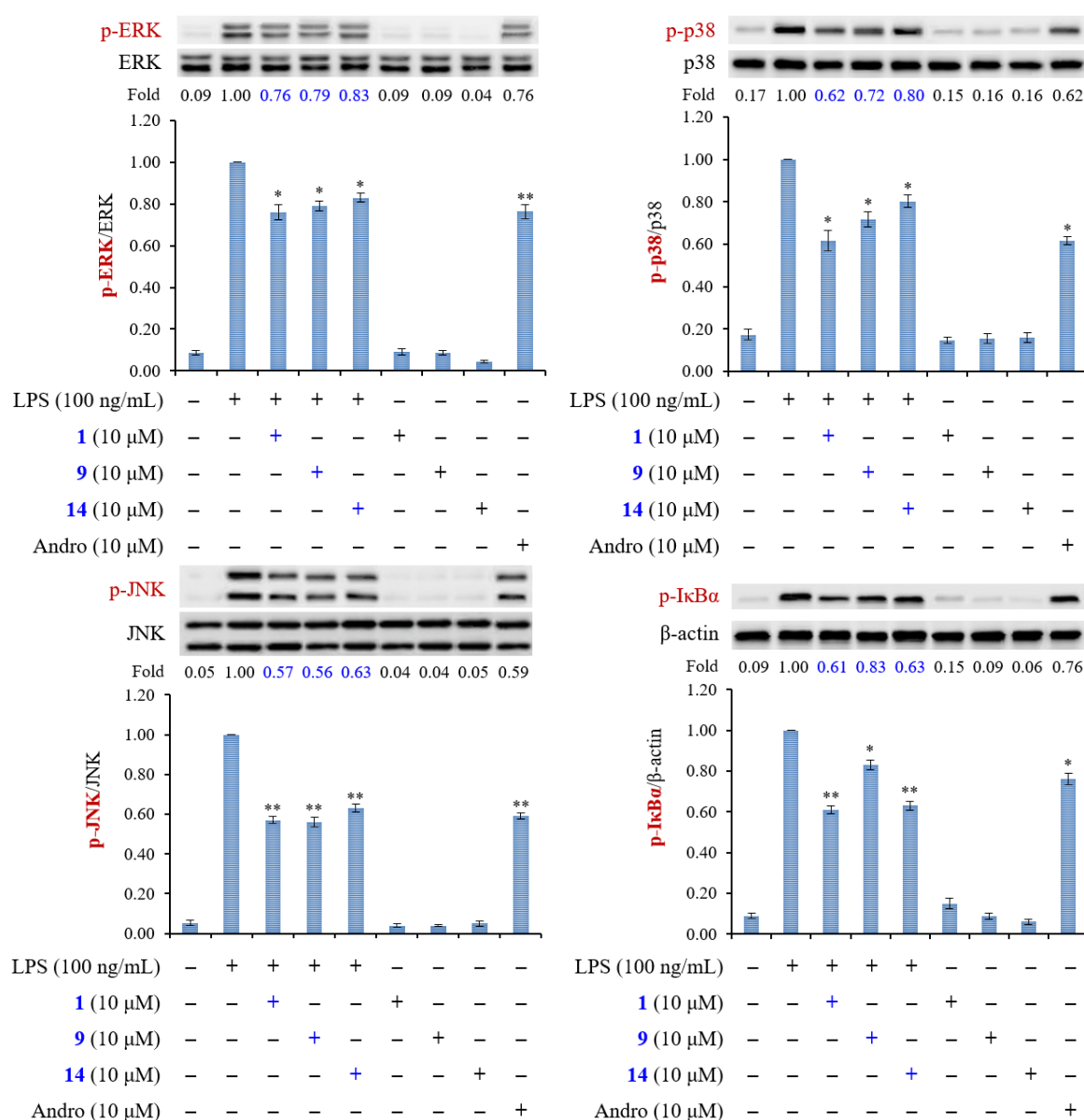


**Figure 6.** Compounds **1**, **9**, and **14** inhibit the phosphorylation of MAPKs and IκBα in LPS-activated macrophages. RAW264.7 cells were pretreated with **1**, **9**, and **14** (10 μM) for 6 h, and then stimulated with LPS for 15 min. Phosphorylation of MAPKs and IκBα was analyzed by immunoblotting. Densitometric analysis of all samples was normalized to the corresponding total protein or β-actin. Andrographolide (Andro) was used as positive control. Results are displayed as mean ± SEM of three independent experiments. “+” means treatment with LPS or compound. “−” means no treatment with LPS or compound. Asterisks indicate significant differences (\*  $p < 0.05$  and \*\*  $p < 0.01$ ) compared with the control.

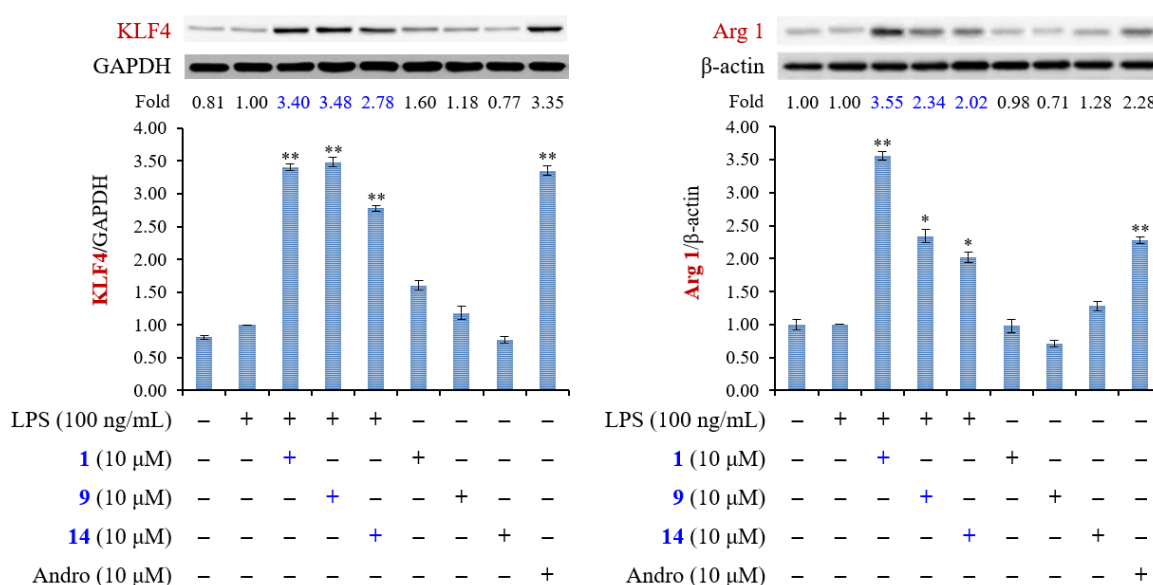


**Figure 7.** The effect of compounds **1**, **9**, and **14** on M2 polarized macrophages in LPS-stimulated RAW264.7 macrophages. RAW264.7 cells were pretreated with **1**, **9**, and **14** (10 μM) for 6 h, and then stimulated with LPS for 20 h. Expression of KLF4 and arginase 1 (Arg 1) were determined by Western blot analysis. Andrographolide (Andro) was used as positive control. The data were expressed as mean ± SEM of three independent experiments. “+” means treatment with LPS or compound. “−” means no treatment with LPS or compound. Asterisks indicate significant differences (\*  $p < 0.05$  and \*\*  $p < 0.01$ ) compared with the control.

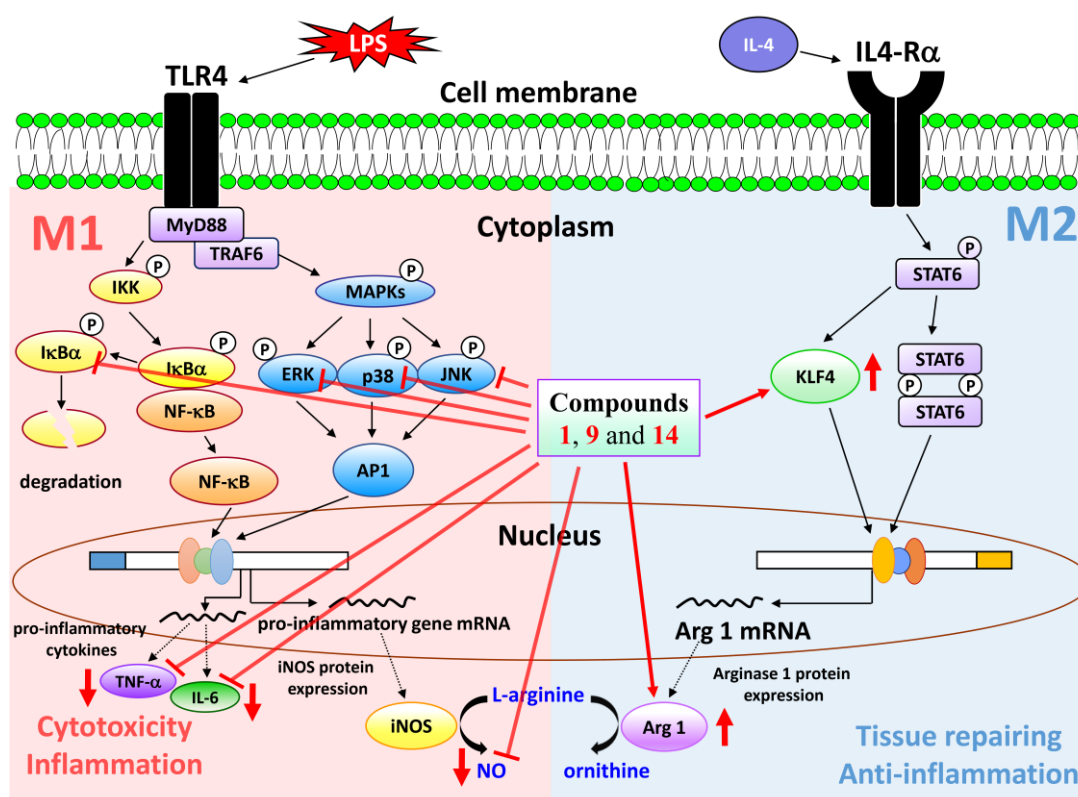


**Figure 8.** Schematic diagram for anti-inflammatory action of compounds **1**, **9**, and **14** in LPS-induced RAW264.7 macrophages.



### 3. Materials and Methods

#### 3.1. General Procedures

Melting points were determined on a Yanaco micro-melting point apparatus (Yanaco, Tokyo, Japan) and are uncorrected. Optical rotations were measured using a Jasco DIP-370 polarimeter (Jasco, Easton, MD, USA) in  $\text{CHCl}_3$ . Ultraviolet (UV) spectra were obtained on a Jasco UV-240 spectrophotometer (Jasco, Easton, MD, USA). Infrared (IR) spectra (neat or KBr) were recorded on a Perkin Elmer 2000 FT-IR spectrometer (PerkinElmer, Waltham, MA, USA). Nuclear magnetic resonance (NMR) spectra, including correlation spectroscopy (COSY), nuclear Overhauser effect spectrometry (NOESY), rotating frame nuclear Overhauser effect spectrometry (ROESY), heteronuclear multiple-bond correlation (HMBC), and heteronuclear single-quantum coherence (HSQC) experiments, were acquired using a Varian Inova 500 spectrometer operating at 500 MHz ( $^1\text{H}$ ) and 125 MHz ( $^{13}\text{C}$ ), respectively, with chemical shifts given in ppm ( $\delta$ ) using tetramethylsilane (TMS) as an internal standard. Electrospray ionization (ESI) and high-resolution electrospray ionization (HRESI) mass spectra were recorded on a Bruker APEX II mass spectrometer (Bruker, Bremen, Germany). Silica gel (70–230, 230–400 mesh) (Merck, Darmstadt, Germany) was used for column chromatography (CC). Silica gel 60 F-254 (Merck, Darmstadt, Germany) was used for thin-layer chromatography (TLC) and preparative thin-layer chromatography (PTLC).

#### 3.2. Plant Material

The stem bark of *F. chinensis* was collected from Pingtung County, Taiwan, in April 2011 and identified by Prof. J. J. Chen. A voucher specimen (FC 201104) was deposited in the Faculty of Pharmacy, National Yang-Ming University, Taipei, Taiwan.

#### 3.3. Extraction and Isolation

The dried stem bark (4.0 kg) of *F. chinensis* was pulverized and extracted three times with MeOH ( $\geq 99\%$ , 20 L each) for three days at room temperature. The MeOH extract was concentrated under reduced pressure at 35 °C, and the residue (384 g) was partitioned between EtOAc ( $\geq 99.5\%$ ) and  $\text{H}_2\text{O}$  ( $\geq 99.5\%$ ) (1:1) to provide the EtOAc-soluble fraction (fraction A; 180 g). Fraction A (180 g) was purified by column chromatography (CC) (10 × 72 cm, 7.2 kg of silica gel, 70–230 mesh;  $\text{CH}_2\text{Cl}_2$  ( $\geq 99\%$ )/MeOH gradient) to afford 10 fractions: A1 (5 L,  $\text{CH}_2\text{Cl}_2$ ), A2 (6 L,  $\text{CH}_2\text{Cl}_2/\text{MeOH}$ , 90:1), A3 (9 L,  $\text{CH}_2\text{Cl}_2/\text{MeOH}$ , 80:1), A4 (6 L,  $\text{CH}_2\text{Cl}_2/\text{MeOH}$ , 60:1), A5 (5 L,  $\text{CH}_2\text{Cl}_2/\text{MeOH}$ , 50:1), A6 (10 L,  $\text{CH}_2\text{Cl}_2/\text{MeOH}$ , 40:1), A7 (5 L,  $\text{CH}_2\text{Cl}_2/\text{MeOH}$ , 20:1), A8 (3 L,  $\text{CH}_2\text{Cl}_2/\text{MeOH}$ , 10:1), A9 (4 L,  $\text{CH}_2\text{Cl}_2/\text{MeOH}$ , 1:1), and A10 (2 L, MeOH). Fraction A1 (12.5 g) was subjected to CC (5 × 45 cm, 500 g of silica gel, 230–400 mesh; *n*-hexane/acetone ( $\geq 99\%$ ) 20:1–0:1, 500 mL fractions) to give eight subfractions: A1-1–A1-8. Part (56 mg) of fraction A1-1 was further purified by preparative TLC (silica gel; *n*-hexane (99%)/EtOAc 2:1) to afford 4-hydroxyphenethyl acetate (**22**) (6.6 mg) ( $R_f = 0.78$ ). Part (38 mg) of fraction A1-2 was further purified by preparative TLC (silica gel; *n*-hexane/EtOAc, 1:1) to obtain *p*-hydroxybenzaldehyde (**23**) (4.2 mg) ( $R_f = 0.90$ ). Part (76 mg) of fraction A1-3 was further purified by preparative TLC (silica gel; *n*-hexane/EtOAc, 3:1) to afford (*E*)-ferulaldehyde (**20**) (6.6 mg) ( $R_f = 0.25$ ). Part (105 mg) of fraction A1-5 was further purified by preparative TLC (silica gel;  $\text{CH}_2\text{Cl}_2/\text{EtOAc}$ , 8:1) to yield (+)-pinoresinol (**24**) (5.5 mg) ( $R_f = 0.32$ ) and (+)-salicifoliol (**25**) (5.6 mg) ( $R_f = 0.26$ ). Part (55 mg) of fraction A1-8 was purified by preparative TLC (silica gel;  $\text{CH}_2\text{Cl}_2/\text{acetone}$ , 30:1) to obtain  $\alpha$ -tocopheryl quinone (**26**) (2.4 mg) ( $R_f = 0.73$ ). Fraction A3 (19.8 g) was subjected to CC (5 × 70 cm, 895 g of silica gel, 230–400 mesh; *n*-hexane/EtOAc 10:1–0:1, 300 mL fractions) to give 10 subfractions: A3-1–A3-10. Part (69 mg) of fraction A3-1 was further purified by preparative TLC (silica gel; *n*-hexane/acetone, 1:1) to afford isoscopoletin (**11**) (2.8 mg) ( $R_f = 0.81$ ). Part (125 mg) of fraction A3-3 was further purified by preparative TLC (silica gel;  $\text{CH}_2\text{Cl}_2/\text{MeOH}$ , 25:1) to obtain olenoside A (**4**) (7.9 mg) ( $R_f = 0.70$ ) and umbelliferone (**15**) (3.7 mg) ( $R_f = 0.70$ ). Part (71 mg) of fraction A3-4 was further purified by preparative TLC (silica gel;  $\text{CH}_2\text{Cl}_2/\text{MeOH}$ , 25:1) to afford fraxidin (**13**) (5.2 mg) ( $R_f = 0.41$ ). Part (33 mg)

of fraction A3-8 was further purified by preparative TLC (silica gel; CH<sub>2</sub>Cl<sub>2</sub>/acetone, 6:1) to yield tyrosol (**21**) (4.9 mg) ( $R_f = 0.52$ ). Part (92 mg) of fraction A3-10 was purified by preparative TLC (silica gel; *n*-hexane/acetone, 1:2) to obtain fraxetin (**14**) (15.9 mg) ( $R_f = 0.30$ ). Fraction A4 (16.7 g) was subjected to CC (5 × 60 cm, 755 g of silica gel, 230–400 mesh; CH<sub>2</sub>Cl<sub>2</sub>/acetone 10:1–0:1, 1.2 L-fractions) to give eight subfractions: A4-1–A4-8. Part (290 mg) of fraction A4-2 was purified by CC (silica gel, *n*-hexane/acetone 3:2) to afford four subfractions (each 1.2 L, A4-2-1–A4-2-4). Part (43 mg) of fraction A4-2-3 was further purified by preparative TLC (silica gel; CH<sub>2</sub>Cl<sub>2</sub>/acetone 15:1) to obtain scopoletin (**10**) (3.1 mg) ( $R_f = 0.39$ ). Part (61 mg) of fraction A4-3 was further purified by preparative TLC (silica gel; CH<sub>2</sub>Cl<sub>2</sub>/acetone, 5:1) to afford aesculetin (**9**) (7.6 mg) ( $R_f = 0.46$ ). Fraction A6 (27.4 g) was subjected to CC (7 × 60 cm, 1.3 kg of silica gel, 230–400 mesh; CH<sub>2</sub>Cl<sub>2</sub>/EtOAc 10:1–0:1, 1 L-fractions) to give 11 subfractions: A6-1–A6-11. Part (61 mg) of fraction A6-1 was further purified by preparative TLC (silica gel; *n*-hexane/acetone, 5:1) to afford methyl 3,4-dimethoxycinnamate (**18**) (4.3 mg) ( $R_f = 0.68$ ). Part (210 mg) of fraction A6-2 was purified by CC (silica gel, *n*-hexane/acetone 5:1) to afford five subfractions (each 250 mL, A6-2-1–A6-2-5). Part (28 mg) of fraction A6-2-2 was further purified by preparative TLC (silica gel; *n*-hexane/EtOAc, 2:1) to afford methyl ferulate (**17**) (5.7 mg) ( $R_f = 0.70$ ). Part (54 mg) of fraction A6-3 was further purified by preparative TLC (silica gel; CH<sub>2</sub>Cl<sub>2</sub>/EtOAc, 6:1) to yield methyl isoferulate (**16**) (4.2 mg) ( $R_f = 0.38$ ). Part (56 mg) of fraction A6-4 was purified by preparative TLC (silica gel; *n*-hexane/EtOAc, 2:1) to obtain aesculetin dimethyl ester (**12**) (4.7 mg) ( $R_f = 0.71$ ) and methyl (*E*)-*p*-coumarate (**19**) (3.9 mg) ( $R_f = 0.73$ ). Part (38 mg) of fraction A6-7 was further purified by preparative TLC (silica gel; CHCl<sub>3</sub> (≥99%)/MeOH, 8:1) to afford oleoside methyl ester (**8**) (5.7 mg) ( $R_f = 0.19$ ). Fraction A9 (17.3 g) was subjected to CC (5 × 60 cm, 780 g of silica gel, 230–400 mesh; CH<sub>2</sub>Cl<sub>2</sub>/MeOH 7:1–0:1, 500 mL fractions) to give 13 subfractions: A9-1–A9-13. Part (75 mg) of fraction A9-4 was further purified by preparative TLC (silica gel; CHCl<sub>3</sub>/MeOH, 7:1) to afford (8*E*)-4''-*O*-methyliligstroside (**1**) (15.7 mg) ( $R_f = 0.66$ ). Part (63 mg) of fraction A9-5 was further purified by preparative TLC (silica gel; CHCl<sub>3</sub>/MeOH, 5:1) to yield (8*E*)-3'',4''-di-*O*-methyloleuropein (**7**) (7.4 mg) ( $R_f = 0.53$ ). Part (108 mg) of fraction A9-7 was purified by CC (silica gel, CHCl<sub>3</sub>/MeOH, 3:1) to afford three subfractions (each 150 mL, A9-7-1–A9-7-3). Fraction A9-7-1 (63 mg) was further purified by preparative TLC (silica gel; CHCl<sub>3</sub>/MeOH, 4:1) to obtain 3'',4''-di-*O*-methyl demethyloleuropein (**3**) (6.1 mg) ( $R_f = 0.61$ ). Fraction A9-7-2 (28 mg) was further purified by preparative TLC (silica gel; CHCl<sub>3</sub>/MeOH, 4:1) to afford (8*E*)-4''-*O*-methyl demethyliligstroside (**2**) (7.2 mg) ( $R_f = 0.55$ ). Fraction A10 (36.8 g) was subjected to silica gel column chromatography (10 × 55 cm, 230–400 mesh) with CH<sub>2</sub>Cl<sub>2</sub>/MeOH, 7:1 to give 14 fractions (each 1.5 L). Part (115 mg) of fraction 10-4 was purified further by preparative TLC (silica gel, CHCl<sub>3</sub>/MeOH, 7:1) to afford (8*E*)-ligstroside (**5**) (12.3 mg) ( $R_f = 0.65$ ). Part (132 mg) of fraction 10-5 was purified further by preparative TLC (silica gel, CH<sub>2</sub>Cl<sub>2</sub>/acetone, 1:2) to yield oleuropein (**6**) (14.6 mg) ( $R_f = 0.35$ ).

(8*E*)-4''-*O*-Methyliligstroside (**1**): yellowish oil;  $[\alpha]_D^{25}$ : −182.2 (*c* 0.2, MOH); UV (MeOH):  $\lambda_{\max}$  (log  $\epsilon$ ) = 238 (4.05), 276 (3.82), 283 (3.81), 318 (3.76) nm; IR (neat):  $\nu_{\max}$  = 3402 (OH), 1727 (C=O), 1708 (C=O) cm<sup>−1</sup>; ESI-MS:  $m/z$  = 561 [M + Na]<sup>+</sup>; HR-ESI-MS:  $m/z$  = 561.1950 [M + Na]<sup>+</sup> (calcd. for C<sub>26</sub>H<sub>34</sub>O<sub>12</sub>Na: 561.1948). <sup>1</sup>H and <sup>13</sup>C NMR spectroscopic data, see Table 1.

(8*E*)-4''-*O*-Methyl demethyliligstroside (**2**): yellowish oil;  $[\alpha]_D^{25}$ : −181.5 (*c* 0.25, MOH); UV (MeOH):  $\lambda_{\max}$  (log  $\epsilon$ ) = 225 (4.04), 276 (3.80), 282 (3.79), 317 (3.73) nm; IR (neat):  $\nu_{\max}$  = 3334 (OH), 1728 (C=O), 1707 (C=O) cm<sup>−1</sup>; ESI-MS:  $m/z$  = 547 [M + Na]<sup>+</sup>; HR-ESI-MS:  $m/z$  = 547.1787 [M + Na]<sup>+</sup> (calcd. for C<sub>25</sub>H<sub>32</sub>O<sub>12</sub>Na: 547.1791). <sup>1</sup>H and <sup>13</sup>C NMR spectroscopic data, see Table 1.

3'',4''-Di-*O*-methyl demethyloleuropein (**3**): amorphous powder;  $[\alpha]_D^{25}$ : −155.2 (*c* 0.22, MOH); UV (MeOH):  $\lambda_{\max}$  (log  $\epsilon$ ) = 226 (4.24), 277 (3.40) nm; IR (neat):  $\nu_{\max}$  = 3350 (OH), 1721 (C=O), 1698 (C=O) cm<sup>−1</sup>; ESI-MS:  $m/z$  = 577 [M + Na]<sup>+</sup>; HR-ESI-MS:  $m/z$  = 577.1892 [M + Na]<sup>+</sup> (calcd. for C<sub>26</sub>H<sub>34</sub>O<sub>13</sub>Na: 577.1897). <sup>1</sup>H and <sup>13</sup>C NMR spectroscopic data, see Table 1.

### 3.4. Biological Assay

The activity of the isolated compounds on neutrophil and macrophage proinflammatory response was evaluated by monitoring the inhibition of all isolated compounds against fMLP/CB-induced  $O_2^{\bullet-}$  and elastase release and against LPS-induced NO generation in a concentration-dependent manner.

#### 3.4.1. Mensuration of Human Neutrophils

Human neutrophils from venous blood of adult, healthy volunteers (20–27 years old) were isolated by a standard pattern of dextran sedimentation before centrifugation in a Ficoll Hypaque gradient and hypotonic lysis of erythrocytes [38]. Purified neutrophils having >98% viable cells, as detected by the trypan blue exclusion method [39], were resuspended in a calcium ( $Ca^{2+}$ )-free HBSS buffer at pH 7.4 and were kept at 4 °C prior to use.

#### 3.4.2. Mensuration of Superoxide Anion ( $O_2^{\bullet-}$ ) Generation

The assay for measurement of  $O_2^{\bullet-}$  generation was based on the SOD-inhibitable reduction of ferricytochrome *c* [40,41]. In short, after supplementation with 1 mM  $Ca^{2+}$  and 0.5 mg/mL ferricytochrome *c*, neutrophils ( $6 \times 10^5$ /mL) were equilibrated at 37 °C for 2 min and incubated with varied concentrations (10–0.01 µg/mL) of DMSO (as control) or tested compounds 1–26 for 5 min. Cells were incubated with cytochalasin B (1 µg/mL) for 3 min before the activation with 100 nM formyl-L-methionyl-L-leucyl-L-phenylalanine for 10 min. Changes in absorbance with the reduction of ferricytochrome *c* at 550 nm were constantly detected in a double-beam, six-cell positioner spectrophotometer with continuous stirring (Hitachi U-3010, Tokyo, Japan). Calculations were founded on differences in the reactions with and without SOD (100 U/mL) divided by the extinction coefficient for the reduction of ferricytochrome *c* ( $\epsilon = 21.1$ /mM/10 mm).

#### 3.4.3. Measurement of Elastase Release

Degranulation of azurophilic granules was measured by determining elastase release as reported previously [41,42]. Assays were carried out applying MeO-Suc-Ala-Ala-Pro-Val-*p*-nitroanilide as elastase substrate. In brief, after supplementation with MeO-Suc-Ala-Ala-Pro-Val-*p*-nitroanilide (100 µM), neutrophils ( $6 \times 10^5$ /mL) were equilibrated at 37 °C for 2 min and incubated with tested compounds for 5 min. Cells were treated with fMLP (100 nM)/CB (0.5 µg/mL), and the changes in absorbance at 405 nm were detected constantly in order to measure elastase release. The results were displayed as the percent of elastase release in the fMLP/CB-activated, drug-free control system.

#### 3.4.4. Determination of NO Production

NO production was indirectly assessed by measuring the nitrite levels in the cultured media and serum determined by a colorimetric method based on the Griess reaction. RAW264.7 cells were pretreated with compounds for 1 h, and then stimulated with LPS (100 ng/mL) for 20 h at 37 °C. Then, cells were dispensed into 96-well plates, and 100 µL of each supernatant was mixed with the same volume of Griess reagent (1% sulfanilamide, 0.1% naphthylethylenediamine dihydrochloride, and 5% phosphoric acid) and incubated at room temperature for 10 min; the absorbance was measured at 540 nm with a Micro-Reader (Molecular Devices). By using sodium nitrite to generate a standard curve, the concentration of nitrite was measured from absorbance at 540 nm [43].

#### 3.4.5. Cell Viability Assay

Cells ( $4 \times 10^5$ ) were cultured in 96-well plates containing DMEM supplemented with 10% FBS for one day to become nearly confluent. Then, cells were cultured with compounds 1–26 in the presence of 100 ng/mL LPS (lipopolysaccharide) for 24 h. After that, the cells were washed twice with DPBS and incubated with 100 µL of 0.5 mg/mL MTT for 2 h at 37 °C testing for cell viability. The medium was then

discarded and 100  $\mu$ L dimethyl sulfoxide (DMSO) was added. After 30 min incubation, absorbance at 570 nm was read using a microplate reader (Molecular Devices, Sunnyvale, CA, USA) [44].

#### 3.4.6. Enzyme-Linked Immunosorbent Assay

RAW264.7 cells ( $4 \times 10^5$  cells in 96-well plates) were pretreated with compounds **1**, **9**, **14**, or vehicle (0.05% DMSO) for 1 h and then stimulated with LPS (100 ng/mL) for 20 h. Supernatants were collected and analyzed for production of TNF- $\alpha$  and IL-6 by using appropriate ELISA kits (R&D, MN, USA) in accordance with the manufacturer's instructions.

#### 3.4.7. Western Blot

Western blot analysis followed as previously described with slight changes [45]. Cells ( $1.0 \times 10^6$ ) were seeded into 6 cm dishes and grown until 80–85% confluent. RAW264.7 cells were pretreated with **1**, **9**, and **14** (10  $\mu$ M) for 6 h, and then stimulated with LPS (100 ng/mL) for 15 min (for detecting p-I $\kappa$ B $\alpha$ , p-ERK, p-JNK, and p-p38) or 20 h (for detecting arginase 1 and KLF4) at 37  $^{\circ}$ C. Cultured medium was removed and cells were washed with ice-cold PBS. After RIPA buffer (Cell Signaling, MA, USA) was added, cells were scraped off the plate and transferred to the Eppendorf on ice immediately. The proteins were quantified using the BCA protein assay. Cells were preserved at  $-80^{\circ}$ C overnight and then centrifuged (15,000  $\times$  rpm, 30 min, 4  $^{\circ}$ C). Equal amounts of protein samples (25  $\mu$ g) and prestained protein marker were loaded onto SDS-PAGE. After being stacked at 80 V and separated at 100 V, the proteins were transferred onto the polyvinylidene fluoride (PVDF) membranes at 350 mA. The PVDF membranes were blocked with 5% (*w/v*) of BSA with Tris-buffered saline (TBST) containing 0.1% (*v/v*) Tween 20 at room temperature for 1 h and washed three times with TBST for 15 min each time. Primary antibodies were incubated with the membranes overnight, shaking at 4  $^{\circ}$ C. Then, each membrane was washed with TBST and incubated with horseradish peroxidase (HRP)-conjugated secondary antibodies at room temperature for 1 h while shaking. Finally, each membrane was developed using an ECL detection kit, and the images were visualized by ImageQuant LAS 4000mini (GE Healthcare, MA, USA). Images were quantified using Image J version 1.48 (NIH, Bethesda, MD, USA).

#### 3.4.8. Statistical Analysis

Results are expressed as the mean  $\pm$  SEM, and comparisons were made using Tukey's HSD test. A probability of 0.05 or less was considered significant. The software SigmaPlot was used for the statistical analysis.

### 4. Conclusions

Twenty-six compounds, including three undescribed secoiridoid glucosides, (8*E*)-4''-*O*-methylligstroside (**1**), (8*E*)-4''-*O*-methyldemethylligstroside (**2**), and 3''4''-di-*O*-methyldemethyl-oleuropein (**3**), were isolated from stem bark of *F. chinensis*. The structures of these isolates were elucidated according to spectroscopic data. The effects on neutrophil proinflammatory responses of isolates were evaluated by suppressing fMLP/CB-induced  $O_2^{\bullet-}$  generation and elastase release by human neutrophils. The results of anti-inflammatory assays show that compounds **1**, **9**, **11**, **14**, **21**, and **22** can obviously inhibit fMLP-induced  $O_2^{\bullet-}$  generation and/or elastase release. (8*E*)-4''-*O*-Methylligstroside (**1**) and fraxetin (**14**) were the most effective among the isolated compounds, with  $IC_{50}$  values of  $0.08 \pm 0.01$  and  $0.50 \pm 0.10$   $\mu$ g/mL, respectively, against fMLP-induced  $O_2^{\bullet-}$  generation and elastase release. Furthermore, compounds **9** and **14** showed potent inhibition with  $IC_{50}$  values of  $9.36 \pm 0.25$  and  $10.11 \pm 0.47$   $\mu$ M, respectively, against LPS-induced NO generation. Compounds **1**, **9**, and **14** suppressed LPS-induced NO, TNF- $\alpha$ , and IL-6 generation via blocking the phosphorylation of MAPKs and degradation of I $\kappa$ B $\alpha$ . In addition, compounds **1**, **9**, and **14** stimulated anti-inflammatory M2 phenotype by elevating the expression of arginase 1 and KLF4. In conclusion, compounds **1**, **9**, and **14** interfered with multiple intracellular targets. Our research indicates *F. chinensis* and its constituents (especially **1**,



9, and 14) may deserve further investigation as potential candidates for the treatment or prevention of various inflammatory diseases.

**Supplementary Materials:** Supplementary materials are available online, Figures S1–S9: ESIMS, HRESIMS, 1D, and 2D NMR spectra for (8E)-4''-O-methyliligstroside (1), Figures S10–S18: ESIMS, HRESIMS, 1D, and 2D NMR spectra for (8E)-4''-O-methyldemethyliligstroside (2), Figures S19–S27: ESIMS, HRESIMS, 1D, and 2D NMR spectra for 3'',4''-di-O-methyl-demethyleuropein (3).

**Author Contributions:** H.-C.C., S.-W.W., T.-L.H., M.-J.C., P.-J.S., and K.-W.L. performed the bioassay and analyzed the data. C.-Y.C. conducted the isolation and structure elucidation of the constituents. J.-J.C. planned, designed, and organized all of the research of this study and the preparation of the manuscript. All authors have read and agreed to the published version of the manuscript.

**Funding:** This research was supported by grants from the Ministry of Science and Technology, Taiwan (No. MOST 106-2320-B-010-033-MY3 and MOST 109-2320-B-010-029-MY3), awarded to Prof. J.-J. Chen.

**Conflicts of Interest:** The authors declare no conflict of interest.

## References

- Wei, Z.; Green, S.P. *Fraxinus chinensis* in *Flora of China*; Science Press: Beijing, China, 1996; Volume 15, p. 277.
- Huang, Y.L.; Oppong, M.B.; Guo, Y.; Wang, L.Z.; Fang, S.M.; Deng, Y.R.; Gao, X.M. The Oleaceae family: A source of secoiridoids with multiple biological activities. *Fitoterapia* **2019**, *136*, 104155. [[CrossRef](#)] [[PubMed](#)]
- Takenaka, Y.; Tanahashi, T.; Shintaku, M.; Sakai, T.; Nagakura, N.; Parida. Secoiridoid glucosides from *Fraxinus americana*. *Phytochemistry* **2000**, *55*, 275–284. [[CrossRef](#)]
- Xiao, K.; Song, Q.H.; Zhang, S.W.; Xuan, L.J. Water-soluble constituents of the root barks of *Fraxinus rhynchophylla* (Chinese drug Qinpi). *J. Asian Nat. Prod. Res.* **2008**, *10*, 205–210. [[CrossRef](#)] [[PubMed](#)]
- Zhang, D.M.; Wnag, L.L.; Li, J.; Hu, L.H. Two new coumarins from *Fraxinus chinensis* Roxb. *J. Integr. Plant Biol.* **2007**, *31*, 1277–1280.
- Wang, L.J.; Sun, F.; Zhang, X.Y.; Ma, Z.J.; Cheng, L. A secoiridoid with quinone reductase inducing activity from *Cortex fraxini*. *Fitoterapia* **2010**, *81*, 834–837. [[CrossRef](#)] [[PubMed](#)]
- Lee, D.G.; Choi, J.S.; Yeon, S.W.; Cui, E.J.; Park, H.J.; Yoo, J.S.; Chung, I.S.; Baek, N.L. Secoiridoid glycoside from the flowers of *Osmanthus fragrans* var. *aurantiacus* Makino inhibited the activity of  $\beta$ -secretase. *J. Korean Soc. Appl. Biol. Chem.* **2010**, *53*, 371–374. [[CrossRef](#)]
- Darmak, N.; Allouche, N.; Hamdi, B.; Litaudon, M.; Darmak, M. New secoiridoid from olive mill wastewater. *Nat. Prod. Res.* **2012**, *26*, 125–131. [[CrossRef](#)]
- Tanahashi, T.; Takenaka, Y.; Nagakura, N. Two dimeric secoiridoid glycosides from *Jasminum polyanthum*. *Phytochemistry* **1996**, *41*, 1341–1345. [[CrossRef](#)]
- He, Z.D.; But, P.H.; Chan, T.W.; Dong, H.; Xu, H.X.; Lau, C.P.; Sun, H.D. Antioxidative glucosides from the fruits of *Ligustrum lucidum*. *Chem. Pharm. Bull.* **2001**, *49*, 780–784. [[CrossRef](#)]
- Shen, Y.C.; Lin, S.L.; Hsieh, P.W.; Chein, C.C. Secoiridoid glycosides from *Jasminum polyanthum*. *J. Chin. Chem. Soc.* **1996**, *43*, 171–176. [[CrossRef](#)]
- Tsukamoto, H.; Hisada, S.; Nishibe, S.; Roux, D.G.; Rourke, J.P. Coumarin from *Olea Africana* and *Olea capensis*. *Phytochemistry* **1984**, *23*, 699–700. [[CrossRef](#)]
- Wu, T.S.; Shi, L.S.; Wang, J.J.; Iou, S.C.; Chang, H.C.; Chen, Y.P.; Kuo, Y.H.; Chang, Y.L.; Teng, C.M. Cytotoxic and antiplatelet aggregation principles of *Ruta graveolens*. *J. Chin. Chem. Soc.* **2003**, *50*, 171–178. [[CrossRef](#)]
- Lee, C.K.; Lee, P.H.; Kuo, Y.H. The chemical constituents from the aril of *Cassia fistula* L. *J. Chin. Chem. Soc.* **2001**, *48*, 1053–1058. [[CrossRef](#)]
- Yu, H.J.; Chen, C.C.; Shieh, B.J. The constituents from the leaves of *Magnolia coco*. *J. Nat. Prod.* **1998**, *61*, 1017–1019. [[CrossRef](#)]
- Kaufmann, F.; Lam, J. Chemical constituents of the genus of *Dahlia* II. The isolation of two new aromatic compounds: Naringenin trimethylether and fraxedin. *Acta Chem. Scand.* **1967**, *21*, 311–313. [[CrossRef](#)]
- Aiyelaagbe, J.B.; Gloer, J.B. Japodic acid, a novel aliphatic acid from *Jatropha podagrica* Hook. *Rec. Nat. Prod.* **2008**, *2*, 100–106.

18. Kumar, S.; Ray, A.B.; Konno, C.; Oshima, Y.; Hikino, H. Cleomiscosin D, a coumarinolignan from seeds of *Cleome Viscosa*. *Phytochemistry* **1988**, *27*, 636–638. [\[CrossRef\]](#)
19. Weight, E.S.; Razdan, T.K.; Qadni, B.; Harkar, S. Chromones and coumarin from *Skimmia larueola*. *Phytochemistry* **1982**, *26*, 2063–2069. [\[CrossRef\]](#)
20. Rose, B.R.; Kaustuv, B. Anullmann ether reaction involving an alkynyl substrate: A convergent route to a combretastatin intermediate. *Synth. Commun.* **1995**, *25*, 3187–3197.
21. Lee, T.H.; Chiou, J.L.; Lee, C.K.; Kuo, Y.H. Separation and determination of chemical constituents in the root of *Rhus javanica* L. var. *roxburghiana*. *J. Chin. Chem. Soc.* **2005**, *52*, 833–841. [\[CrossRef\]](#)
22. Bowden, B.F.; Camie, R.C.; Parnell, J.C. Constituents of the fruit of *Pseudopanax arboreun* (Araliaceae). *Aust. J. Chem.* **1975**, *28*, 91–107. [\[CrossRef\]](#)
23. Gopalakrishnan, S.; Subbarao, G.V.; Nakahara, K.; Yoshihashi, T.; Ito, O.; Maeda, I.; Ono, H.; Yoshida, M. Nitrification inhibitors from root tissues of *Brachiaria humidicola*, a tropical grass. *J. Agric. Food. Chem.* **2007**, *55*, 1385–1388. [\[CrossRef\]](#) [\[PubMed\]](#)
24. Barakat, H.H.; Nawwar, M.A.M.; Buddrust, J.; Linscheid, M. Niloticol, a phenolic glyceride and two phenolic aldehydes from the roots of *Tamarix nilotica*. *Phytochemistry* **1987**, *26*, 1837–1838. [\[CrossRef\]](#)
25. Xu, Q.M.; Liu, Y.L.; Li, X.R.; Feng, Y.L.; Yang, S.L. Two new phenylglycol derivatives isolated from *Syringa reticulata* var. *mandshurica* and their antifungal activities. *Chem. Pharm. Bull.* **2009**, *57*, 863–866. [\[CrossRef\]](#)
26. Assia, I.; Bouaziz, M.; Ghamgui, H.; Kamoun, A.; Miled, N.; Sayadi, S.; Gargouri, Y. Optimization of lipase-catalyzed synthesis of acetylated tyrosol by response surface methodology. *J. Agric. Food Chem.* **2007**, *55*, 10298–10305. [\[CrossRef\]](#)
27. Chiang, C.Y.; Leu, Y.L.; Chan, Y.Y.; Wu, T.S. Sodium aristolochates from the flowers and fruits of *Aristolochia zollingeriana*. *J. Chin. Chem. Soc.* **1998**, *45*, 93–97. [\[CrossRef\]](#)
28. El-Hassan, A.; El-Sayed, M.; Hamed, A.I.; Rhee, I.K.; Ahmed, A.A.; Zeller, K.P.; Verpoorte, R. Bioactive constituents of *Leptadenia arborea*. *Fitoterapia* **2003**, *74*, 184–187. [\[CrossRef\]](#)
29. Marchand, P.A.; Zajick, J.; Lewis, N.G. Oxygen insertion in *Sesamum indicum* furanofuran lignans. Diastereoselective syntheses of enzyme substrate analogues. *Can. J. Chem.* **1997**, *75*, 840–849. [\[CrossRef\]](#)
30. Chang, M.H.; Wang, G.J.; Kuo, Y.H.; Lee, C.K. The low polar constituents from *Bidens pilosa* L. var. *minor* (Blume) Sherff. *J. Chin. Chem. Soc.* **2000**, *47*, 1131–1136. [\[CrossRef\]](#)
31. Borregaard, N. The human neutrophil. Function and dysfunction. *Eur. J. Haematol.* **1998**, *41*, 401–413. [\[CrossRef\]](#)
32. Roos, D.; van Bruggen, R.; Meischl, C. Oxidative killing of microbes by neutrophils. *Microbes Infect.* **2003**, *5*, 1307–1315. [\[CrossRef\]](#) [\[PubMed\]](#)
33. Witko-Sarsat, V.; Rieu, P.; Descamps-Latscha, B.; Lesavre, P.; Halbwachs-Mecarelli, L. Neutrophils: Molecules, functions and pathophysiological aspects. *Lab. Investig.* **2000**, *80*, 617–653. [\[CrossRef\]](#) [\[PubMed\]](#)
34. Benoit, M.; Desnues, B.; Mege, J.L. Macrophage polarization in bacterial infections. *J. Immunol. Res.* **2008**, *181*, 3733–3739. [\[CrossRef\]](#) [\[PubMed\]](#)
35. Pauleau, A.L.; Rutschman, R.; Lang, R.; Pernis, A.; Watowich, S.S.; Murray, P.J. Enhancer-mediated control of macrophage-specific arginase I expression. *J. Immunol.* **2004**, *172*, 7565–7573. [\[CrossRef\]](#) [\[PubMed\]](#)
36. Yang, Z.; Ming, X.F. Functions of arginase isoforms in macrophage inflammatory responses: Impact on cardiovascular diseases and metabolic disorders. *Front. Immunol.* **2014**, *5*, 533. [\[CrossRef\]](#)
37. Liao, X.; Sharma, N.; Kapadia, F.; Zhou, G.; Lu, Y.; Hong, H.; Paruchuri, K.; Mahabeleshwar, G.H.; Dalmas, E.; Venteclef, N.; et al. Krüppel-like factor 4 regulates macrophage polarization. *J. Clin. Investig.* **2011**, *121*, 2736–2749. [\[CrossRef\]](#)
38. Boyum, A. Isolation of mononuclear cells and granulocytes from human blood. Isolation of mononuclear cells by one centrifugation, and of granulocytes by combining centrifugation and sedimentation at 1 g. *Scand. J. Clin. Lab. Investig.* **1968**, *97*, 77–89.
39. Jauregui, H.O.; Hayner, N.T.; Driscoll, J.L.; Williams-Holland, R.; Lipsky, M.H.; Galletti, P.M. Trypan blue dye uptake and lactate dehydrogenase in adult rat hepatocytes-freshly isolated cells, cell suspensions, and primary monolayer cultures. *In Vitro* **1981**, *17*, 1100–1110. [\[CrossRef\]](#)
40. Babior, B.M.; Kipnes, R.S.; Curnutte, J.T. Biological defense mechanisms. The production by leukocytes of superoxide, a potential bactericidal agent. *J. Clin. Investig.* **1973**, *52*, 741–744. [\[CrossRef\]](#)

41. Hwang, T.L.; Leu, Y.L.; Kao, S.H.; Tang, M.C.; Chang, H.L. Viscolin, a new chalcone from *Viscum coloratum*, inhibits human neutrophil superoxide anion and elastase release via a cAMP-dependent pathway. *Free Radic. Biol. Med.* **2006**, *41*, 1433–1441. [[CrossRef](#)]
42. Chen, J.J.; Ting, C.W.; Wu, Y.C.; Hwang, T.L.; Cheng, M.J.; Sung, P.J.; Wang, T.C.; Chen, J.F. New labdane-type diterpenoids and anti-inflammatory constituents from *Hedychium Coronarium*. *Int. J. Mol. Sci.* **2013**, *14*, 13063–13077. [[CrossRef](#)] [[PubMed](#)]
43. Johansson, M.; Köpcke, B.; Anke, H.; Sterner, O. Biologically active secondary metabolites from the ascomycete A111-95. 2. Structure elucidation. *J. Antibiot.* **2002**, *55*, 104–106. [[CrossRef](#)] [[PubMed](#)]
44. Mosmann, T. Rapid colorimetric assay for cellular growth and survival: Application to proliferation and cytotoxicity assays. *J. Immunol. Methods* **1983**, *65*, 55–63. [[CrossRef](#)]
45. Lai, J.L.; Liu, Y.H.; Liu, C.; Qi, M.P.; Liu, R.N.; Zhu, X.F.; Zhou, Q.G.; Chen, Y.Y.; Guo, A.Z.; Hu, C.M. Indirubin inhibits LPS-induced inflammation via TLR4 abrogation mediated by the NF- $\kappa$ B and MAPK signaling pathways. *Inflammation* **2017**, *40*, 1–12. [[CrossRef](#)] [[PubMed](#)]

**Sample Availability:** Samples of the compounds are available from the authors.

**Publisher's Note:** MDPI stays neutral with regard to jurisdictional claims in published maps and institutional affiliations.



© 2020 by the authors. Licensee MDPI, Basel, Switzerland. This article is an open access article distributed under the terms and conditions of the Creative Commons Attribution (CC BY) license (<http://creativecommons.org/licenses/by/4.0/>).



## Antiinflammatory triterpenoids from the fruiting bodies of *Fomitopsis pinicola*

Ping-Chung Kuo<sup>a,1</sup>, Shih-Huang Tai<sup>b,1</sup>, Ching-Che Hung<sup>c</sup>, Tsong-Long Hwang<sup>d,e,f</sup>,  
Liang-Mou Kuo<sup>g,h</sup>, Sio Hong Lam<sup>a</sup>, Kun-Ching Cheng<sup>i</sup>, Daih-Huang Kuo<sup>j</sup>, Hsin-Yi Hung<sup>a,\*</sup>,  
Tian-Shung Wu<sup>a,j,\*</sup>

<sup>a</sup> School of Pharmacy, College of Medicine, National Cheng Kung University, Tainan 70101, Taiwan

<sup>b</sup> Departments of Surgery and Anesthesiology, and Institute of Biomedical Engineering, National Cheng Kung University, Medical Center and Medical School, Tainan 701, Taiwan

<sup>c</sup> Department of Chemistry, National Cheng Kung University, Tainan 70101, Taiwan

<sup>d</sup> Graduate Institute of Natural Products, College of Medicine, Chinese Herbal Medicine Research Team, Healthy Aging Research Center, Chang Gung University, Taoyuan 333, Taiwan

<sup>e</sup> Department of Anesthesiology, Chang Gung Memorial Hospital, Taoyuan 333, Taiwan

<sup>f</sup> Research Center for Chinese Herbal Medicine, Research Center for Industry of Human Ecology, Graduate Institute of Health Industry Technology, College of Human Ecology, Chang Gung University of Science and Technology, Taoyuan 333, Taiwan

<sup>g</sup> Department of General Surgery, Chang Gung Memorial Hospital at Chia-Yi, 613, Taiwan

<sup>h</sup> School of Medicine, College of Medicine, Chang Gung University, Taoyuan 333, Taiwan

<sup>i</sup> Taiwan Sugar Research Institute, Tainan 70176, Taiwan

<sup>j</sup> Department of Pharmacy, College of Pharmacy and Health Care, Tajen University, Pingtung 907, Taiwan

### ARTICLE INFO

#### Keywords:

*Fomitopsis pinicola*  
Fomitopsidaceae  
Triterpenoid  
Antiinflammatory

### ABSTRACT

Twelve undescribed lanostane-type triterpenes, and twenty-two known triterpenes were isolated and identified from a medicinal bracket fungus *Fomitopsis pinicola* (Sw.) P. Karst. The structures of these compounds were determined by spectroscopic and spectrometric analyses. The antiinflammatory potential of thirty-two triterpene compounds was evaluated using neutrophils as an assay model, and pinicolasin J was the most potent inhibitor of superoxide anion generation and elastase release, with IC<sub>50</sub> values of 1.81 ± 0.44 and 2.50 ± 0.64 μM, respectively. This study provides scientific insight into the nutritional supplement value and medicinal development of *Fomitopsis pinicola*.

### 1. Introduction

*Fomitopsis pinicola* (Sw.) P. Karst (Fomitopsidaceae), widely distributed in East Asia and Central Europe, is a type of red-banded polypore growing on decaying logs including *Abies* and *Betula* species [1]. *F. pinicola* was traditionally used for the treatment of headache, nausea, liver problems, hemorrhage, and inflammation [2]. Modern pharmacological studies demonstrated that the chloroform extract of *F. pinicola* possesses antitumor activities, and alkaline extracts are rich in polysaccharides with antihyperglycemic effects [3–6]. The reported principle compounds purified from *F. pinicola* were mostly classified as steroids and triterpenoids [2]. Minor compounds included diterpenoids, sesquiterpenoids, and coumarins [2]. The lanostanoid derivatives had

antimicrobial activity against *Bacillus subtilis* in a TLC bioassay [7]. Moreover, twelve glycosidic triterpenes demonstrated to have antiinflammatory activity mediated by cyclooxygenase-2 inhibition. Among them, fomitocide E had the IC<sub>50</sub> value of 0.15 μM, while clinically used NSAID indomethacin had the IC<sub>50</sub> of 0.6 μM [8]. Moreover, ergosterol identified in the chloroform extract was shown to have proapoptotic characteristics and inhibited the migration of SW-480 cells [9]. In 2019, thirty-five lanostane-type triterpenoids were evaluated their cytotoxicity against five cancer cell lines. Five most potent compounds were cytotoxic with the IC<sub>50</sub> values ranging from 3.92 to 28.51 μM [10]. Our previous study reported isolation of twelve sesquiterpenoids with herbertainoid-like structure from the titled fungi, and the most effective compound demonstrated significant inhibition of superoxide anion

\* Corresponding authors at: School of Pharmacy, College of Medicine, National Cheng Kung University, Tainan, Taiwan.

E-mail addresses: [z10308005@email.ncku.edu.tw](mailto:z10308005@email.ncku.edu.tw) (H.-Y. Hung), [tswu@mail.ncku.edu.tw](mailto:tswu@mail.ncku.edu.tw) (T.-S. Wu).

<sup>1</sup> The authors contributed equally to this work.



generation and elastase release with the  $IC_{50}$  values of  $0.81 \pm 0.15$  and  $0.74 \pm 0.12$   $\mu$ M, respectively [11]. Neutrophils are important immune cells predominantly involved in innate immunity. Upon invasion of the microorganisms, acute inflammation is initiated, and reactive oxygen species (ROS) and lysosomal enzymes (e.g., elastase) are released from neutrophils to kill the microorganisms. If neutrophils persist beyond the acute inflammation phase, chronic inflammation may develop leading to various diseases [12]. Therefore, to continue the identification of antiinflammatory agents for drug discovery, we re-investigated the triterpenoids from *F. pinicola* and examined superoxide anion generation and elastase release from human neutrophils for discovering more antiinflammatory natural leads. Bioassay-guided fractionation of the ethanol extract of *F. pinicola* resulted in the identification of thirty-four triterpenoids. Among them, twelve previously undescribed triterpenoids were characterized using IR, 1D, and 2D NMR spectroscopic analyses as well as MS spectrometric data.

## 2. Material and methods

### 2.1. General experimental procedures

Optical rotations were measured using a JASCO P-2000 digital polarimeter. UV spectra were recorded at room temperature using a U-0080-D UV-Vis spectrophotometer. IR spectra were obtained with a PerkinElmer FT-IR Spectrum RX I spectrophotometer.  $^1H$  and  $^{13}C$  NMR spectra were recorded on a Bruker AV III 400 NMR spectrometer. Chemical shifts are shown in  $\delta$  values (ppm) with tetramethylsilane as an internal standard. The ESIMS and HRESIMS were recorded using a Bruker APEX II FT-MS spectrometer (positive-ion mode). ECD spectra were obtained on a JASCO J-720 spectrometer. Column chromatography (CC) was performed on silica (70–230 mesh and 230–400 mesh, Merck) and Diaion HP-20 (Mitsubishi) gels. High-performance liquid chromatography (HPLC) was performed on a Shimadzu LC-20AT series pump system equipped with a Shimadzu SPD-20A UV-Vis detector and a SIL-10AF autosampling system at ambient temperature using a RP-18 column (Ascentis C18, 5  $\mu$ m, 20 mm  $\times$  25 cm).

### 2.2. Fungus material

The fruiting bodies of *Fomitopsis pinicola* (Sw.) P. Karst (Fomitopsideaceae) were collected in July 2012 at Qilai Mountain in Hualien, Taiwan. The fungus material was identified by Prof. Jin-Bin Wu, Institute of Pharmaceutical Chemistry and Department of Pharmacy, China Medical University, Taichung, Taiwan. A voucher specimen (TSWU-20130711) was deposited in the School of Pharmacy, National Cheng Kung University, Tainan, Taiwan.

### 2.3. Extraction and isolation

The fresh fruiting bodies (13.7 kg) were cut into small pieces and refluxed with ethanol for 8 h three times by Jen Li biotech company. The ethanol was removed and evaporated in vacuo to yield 3320 g dried extract. The ethanol extract (1 kg) was subjected to column chromatography on Diaion HP-20 with a step gradient of water-methanol to give 6 fractions (FP-1 ~ FP-6). Ethanol extract (10 g) separated under the same conditions was used in the bioassay testing. Fraction FP-6 (500 g) was fractionated by silica gel chromatography (IPA-acetone = 15:1) to give 11 fractions. Fr. FP-6-2 was subjected to another silica gel chromatography eluted with hexane-acetone (15:1) to give 12 fractions. FP-6-2-10 was subjected to silica gel chromatography and eluted with hexane-acetone (3:1) to yield 7 fractions. Then, fraction FP-6-2-10-1 was further purified by semipreparative HPLC (MeOH-H<sub>2</sub>O-HCOOH = 67:33:0.1) using an Ascentis C18 column to obtain pinicolasin E (**5**, 2.6 mg), pinicolasin G (**7**, 3.1 mg), pinicolasin H (**8**, 1.9 mg), pinicolasin K (**11**, 6.9 mg), pinicolasin M (**13**, 1.8 mg), and fomipinic acid D (**18**, 16.7 mg). Fraction FP-6-2-10-2 was also purified by semipreparative HPLC

eluted with MeOH-H<sub>2</sub>O-HCOOH (77:23: 0.1) to yield pinicolasin D (**4**, 36.6 mg), pinicolasin L (**12**, 10.1 mg), fomipinic acid D (**18**, 4.5 mg), 3 $\beta$ -acetoxy-15 $\alpha$ -hydroxylanosta-8,24-dien-21-oic acid (**19**, 6.5 mg), and 3 $\alpha$ -pachimic acid (**28**, 41.0 mg). Fraction FP-6-2-10-3 was fractionated by semipreparative HPLC eluted with MeOH-H<sub>2</sub>O-HCOOH (67:33:0.1) to yield pinicolasin D (**4**, 25.2 mg), pinicolasin I (**9**, 2.9 mg), fomipinic acid C (**17**, 19.1 mg), piptolinic acid D (**24**, 17.3 mg), pachymic acid (**29**, 4.5 mg), 3-epidehydropachymic acid (**30**, 21.9 mg), polyporenic acid C (**33**, 14.8 mg), and daedaleanic acid A (**34**, 1.8 mg). Fraction FP-6-2-10-5 was further purified by semipreparative HPLC eluted with MeOH-H<sub>2</sub>O-HCOOH (80:20: 0.1) to yield 3 $\beta$ -acetyl-16 $\alpha$ -hydroxy-trametenolic acid (**20**, 3.4 mg), and polyporenic acid C (**33**, 1.7 mg).

Fraction FP-6-2-10-3 was purified by silica gel CC eluted with DCM-MeOH (69:1) to get 9 subfractions, and subfraction 5 was purified by semipreparative HPLC eluted with CH<sub>3</sub>CN-H<sub>2</sub>O-HCOOH (53:47:0.1) to yield pinicolasin B (**2**, 17.4 mg), pinicolasin C (**3**, 1.5 mg), pinicolasin F (**6**, 19.6 mg), pinicolasin J (**10**, 5.2 mg), pinicolic acid E (**21**, 20.1 mg), 16 $\alpha$ -hydroxy-3-oxolanosta-7,9(11),24-trien-21-oic acid (**22**, 26.1 mg), and polyporenic acid C (**33**, 14.8 mg). Additionally, subfraction 7 was subjected to semipreparative HPLC eluted with MeOH-H<sub>2</sub>O-HCOOH (70:30: 0.1%) to obtain pinicolasin A (**1**, 3.1 mg), 16 $\alpha$ -hydroxy-trametenolic acid (**15**, 1.9 mg), 16 $\alpha$ -hydroxy-3-oxolanosta-7,9(11),24-trien-21-oic acid (**22**, 2.1 mg), 6 $\alpha$ ,16 $\alpha$ -dihydroxy-3-oxolanosta-7,9(11),24-trien-21-oic acid (**23**, 5.5 mg), 3 $\alpha$ ,16 $\alpha$ -hydroxy-lanosta-7,9(11),24-trien-21-oic acid (**25**, 3.8 mg), tumulosic acid (**27**, 9.6 mg), 6 $\alpha$ -hydroxypolyporenic acid C (**32**, 8.9 mg), and polyporenic acid C (**33**, 14.8 mg).

#### 2.3.1. Pinicolasin A (**1**)

Colorless powder;  $[\alpha]_D^{25} + 0.4$  (c 0.07, MeOH); UV (MeOH)  $\lambda_{max}$  (log  $\epsilon$ ) 324 (0.8), 211 (1.2) nm; ECD (MeOH) (Mol. CD) 324 (−1.2), 273 (1.6), 222 (2.4) nm; IR (KBr)  $\nu_{max}$  3731, 2928, 2873, 1699, 1455, 1377, 1260, 1020, 756  $cm^{-1}$ ;  $^1H$  and  $^{13}C$  NMR, see Table 1; HRESIMS  $m/z$  491.3130 ( $[M+Na]^+$  calcd for C<sub>30</sub>H<sub>44</sub>O<sub>4</sub>Na, 491.3131).

#### 2.3.2. Pinicolasin B (**2**)

Colorless powder;  $[\alpha]_D^{25} - 2.3$  (c 0.1, MeOH); UV (MeOH)  $\lambda_{max}$  (log  $\epsilon$ ) 324 (0.3), 208 (0.8) nm; ECD (MeOH) (Mol. CD) 362 (0.5), 272 (1.4), 208 (2.5) nm; IR (KBr)  $\nu_{max}$  3378, 2963, 2873, 1731, 1715, 1567, 1415, 1248, 1031, 755  $cm^{-1}$ ;  $^1H$  and  $^{13}C$  NMR, see Table 1; HRESIMS  $m/z$  489.2976 ( $[M+Na]^+$  calcd for C<sub>30</sub>H<sub>42</sub>O<sub>4</sub>Na, 489.2975).

#### 2.3.3. Pinicolasin C (**3**)

Colorless powder;  $[\alpha]_D^{25} - 37.3$  (c 0.05, MeOH); UV (MeOH)  $\lambda_{max}$  (log  $\epsilon$ ) 208 (0.9) nm; ECD (MeOH) (Mol. CD) 309 (−1.4), 213 (2.7) nm; IR (KBr)  $\nu_{max}$  3518, 2928, 2851, 1731, 1616, 1434, 1379, 1028, 755  $cm^{-1}$ ;  $^1H$  and  $^{13}C$  NMR, see Table 1; HRESIMS  $m/z$  493.3291 ( $[M+Na]^+$  calcd for C<sub>30</sub>H<sub>46</sub>O<sub>4</sub>Na, 493.3288).

#### 2.3.4. Pinicolasin D (**4**)

Colorless powder;  $[\alpha]_D^{25} + 5.4$  (c 0.08, MeOH); UV (MeOH)  $\lambda_{max}$  (log  $\epsilon$ ) 211 (1.3) nm; ECD (MeOH) (Mol. CD) 211 (1.6) nm; IR (KBr)  $\nu_{max}$  3688, 2946, 1716, 1601, 1425, 1373, 1254, 1182, 757  $cm^{-1}$ ;  $^1H$  and  $^{13}C$  NMR, see Table 1; HRESIMS  $m/z$  537.3551 ( $[M+Na]^+$  calcd for C<sub>32</sub>H<sub>50</sub>O<sub>5</sub>Na, 537.3551).

#### 2.3.5. Pinicolasin E (**5**)

Colorless powder;  $[\alpha]_D^{25} - 24.5$  (c 0.09, MeOH); UV (MeOH)  $\lambda_{max}$  (log  $\epsilon$ ) 210 (1.2) nm; ECD (MeOH) (Mol. CD) 307 (−3.3) nm; IR (KBr)  $\nu_{max}$  3699, 2948, 1734, 1607, 1449, 1372, 1247, 1032, 755  $cm^{-1}$ ;  $^1H$  and  $^{13}C$  NMR, see Table 1; HRESIMS  $m/z$  535.3395 ( $[M+Na]^+$  calcd for C<sub>32</sub>H<sub>48</sub>O<sub>5</sub>Na, 535.3394).

#### 2.3.6. Pinicolasin F (**6**)

Colorless powder;  $[\alpha]_D^{25} - 2.4$  (c 0.3, MeOH); UV (MeOH)  $\lambda_{max}$  (log  $\epsilon$ ) 208 (1.1) nm; ECD (MeOH) (Mol. CD) 222 (0.7) nm; IR (KBr)  $\nu_{max}$

**Table 1**

<sup>1</sup>H and <sup>13</sup>C NMR Spectroscopic Data of Compounds 1–7 [ $\delta$  (multi., *J* in Hz) in ppm; <sup>a</sup> <sup>1</sup>H and <sup>13</sup>C NMR data were measured in CD<sub>3</sub>OD at 400 and 100 MHz. <sup>b</sup> <sup>1</sup>H and <sup>13</sup>C NMR data were measured in CDCl<sub>3</sub> at 400 and 100 MHz]

|                     | 1 <sup>a</sup> |  | 2 <sup>a</sup> |  | 3 <sup>a</sup>  |  | 4 <sup>b</sup>  |                                     | 5 <sup>b</sup>  |  | 6 <sup>b</sup>  |  | 7 <sup>a</sup> |  |
|---------------------|----------------|--|----------------|--|-----------------|--|-----------------|-------------------------------------|-----------------|--|-----------------|--|----------------|--|
| position            | δ <sub>C</sub> | δ <sub>H</sub>                           | δ <sub>C</sub> | δ <sub>H</sub>                         | δ <sub>C</sub>  | δ <sub>H</sub>                         | δ <sub>C</sub>  | δ <sub>H</sub>                      | δ <sub>C</sub>  | δ <sub>H</sub>                         | δ <sub>C</sub>  | δ <sub>H</sub>                               | δ <sub>C</sub> | δ <sub>H</sub>                         |
| 1                   | 36.9           | 2.02 (m)<br>1.41(br<br>dd, 13.8,<br>3.6) | 36.7           | 2.06 (m)<br>1.41 (m)                   | 36.8            | 1.78 (dd,<br>12.4, 3.7)<br>1.25 (m)    | 30.8            | 1.40 (m)                            | 35.1            | 1.72 (m)<br>1.32 (m)                   | 32.1            | 1.51 (m)                                     | 30.4           | 1.72 (m)<br>1.64 (m)                   |
| 2                   | 28.5           | 1.92 (m)<br>1.74 (m)                     | 28.4           | 1.92 (m)<br>1.76 (dd,<br>12.6, 4.0)    | 28.5            | 2.08 (m)<br>1.63 (dd,<br>8.0, 3.4)     | 23.3            | 1.85 (m)<br>1.63 (d,<br>6.2)        | 24.0            | 1.70 (m)<br>1.66 (m)                   | 24.3            | 1.91 (m)<br>1.64 (m)                         | 23.1           | 1.92 (m)<br>1.76 (t, 3.3)              |
| 3                   | 77.6           | 3.21 (dd,<br>11.9, 4.3)                  | 77.6           | 3.23 (dd,<br>12.1, 4.4)                | 79.7            | 3.17 (dd,<br>8.2, 8.0)                 | 77.8            | 4.66 (t,<br>2.9)                    | 80.6            | 4.50 (dd,<br>11.6, 4.3)                | 79.9            | 4.68 (t,<br>2.9)                             | 77.9           | 4.69 (t, 2.4)                          |
| 4                   | 42.9           | –  | 43.0           | –                                      | 40.1            | –                                      | 36.7            | –                                   | 37.8            | –                                      | 37.9            | –  | 36.5           | –                                      |
| 5                   | 153.0          | –  | 154.1          | –                                      | 51.9            | 1.08 (m)                               | 51.1            | 1.43 (t,<br>2.9)                    | 50.3            | 1.16 (dd,<br>10.4, 1.7)                | 46.9            | 1.54 (d,<br>13.7)                            | 44.2           | 1.51 (dd,<br>10.0, 5.8)                |
| 6                   | 119.7          | 6.02 (d,<br>6.8)                         | 119.6          | 6.07 (d,<br>7.0)                       | 19.4            | 1.75 (m)<br>1.58 (m)                   | 17.9            | 1.47 (m)                            | 17.9            | 1.70 (d,<br>3.4)                       | 19.2            | 1.58 (m)                                     | 22.8           | 2.09 (m)                               |
| 7                   | 117.4          | 5.56 (d,<br>6.8)                         | 118.6          | 5.62 (d,<br>7.0)                       | 27.2            | 1.97 (m)                               | 26.5            | 2.24 (m)<br>2.13 (m)                | 26.8            | 1.99 (d,<br>6.9)                       | 27.4            | 2.06 (m)                                     | 115.5          | 5.50 (t, 3.5)                          |
| 8                   | 141.7          | –  | 139.2          | –                                      | 133.2           | –                                      | 132.9           | –                                   | 131.6           | –                                      | 135.9           | –  | 139.4          | –                                      |
| 9                   | 147.8          | –  | 148.3          | –                                      | 137.5           | –                                      | 135.4           | –                                   | 135.8           | –                                      | 135.9           | –  | 146.1          | –                                      |
| 10                  | 42.1           | –  | 42.4           | –                                      | 38.5            | –                                      | 36.9            | –                                   | 37.1            | –                                      | 38.2            | –  | 37.5           | –                                      |
| 11                  | 121.4          | 5.47 (s)                                 | 121.4          | 5.59 (s)                               | 28.1            | 2.04 (m)                               | 20.6            | 2.04 (m)<br>1.90 (m)                | 20.1            | 2.03 (m)                               | 21.6            | 2.04 (m)                                     | 122.2          | 5.40 (d, 6.1)                          |
| 12                  | 37.7           | 2.21 (m)<br>1.97 (m)                     | 37.1           | 2.70 (m)<br>2.16 (m)                   | 29.8            | 1.98 (m)<br>1.64 (m)                   | 29.5            | 1.82 (m)<br>1.36 (dd,<br>12.9, 4.7) | 28.6            | 1.54 (d,<br>11.3)                      | 30.3            | 1.78 (d,<br>9.4)<br>1.46 (m)                 | 35.0           | 2.46 (m)<br>2.01 (d, 5.4)              |
| 13                  | 45.7           | –  | 43.7           | –                                      | 44.7            | –                                      | 44.9            | –                                   | 43.5            | –                                      | 47.0            | –  | 42.5           | –                                      |
| 14                  | 49.6           | –  | 45.1           | –                                      | 45.3            | –                                      | 51.4            | –                                   | 44.0            | –                                      | 49.5            | –  | 44.3           | –                                      |
| 15                  | 44.3           | 2.20 (d,<br>9.4)<br>1.53 (d,<br>13.3)    | 47.2           | 2.16 (d,<br>18.2)<br>2.36 (d,<br>18.2) | 47.5            | 2.39 (d,<br>18.5)<br>1.90 (d,<br>18.5) | 73.3            | 4.24 (dd,<br>9.8, 5.7)              | 46.3            | 2.34 (d,<br>18.4)<br>1.94 (d,<br>18.4) | 43.7            | 2.19 (dd,<br>13.7, 8.6)<br>1.28 (d,<br>13.0) | 46.4           | 2.40 (d,<br>18.8)<br>2.13 (d,<br>18.4) |
| 16                  | 77.9           | 4.06 (t,<br>7.4)                         | 219.3          | 2.63 (d,<br>10.5)                      | 220.5           | –                                      | 38.0            | 1.96 (t,<br>6.4)<br>1.77 (m)        | 218.0           | –                                      | 77.8            | 4.03 (t,<br>7.2)                             | 217.2          | –                                      |
| 17                  | 57.6           | 2.15 (m)                                 | 58.5           | 2.63 (d,<br>10.5)                      | 58.7            | 2.55 (d,<br>9.9)                       | 45.8            | 2.23 (m)                            | 57.0            | 2.56 (t,<br>9.7)                       | 57.5            | 2.03 (m)                                     | 57.0           | 2.62 (t, 10.0)                         |
| 18                  | 17.8           | 0.70 (s)                                 | 17.2           | 0.80 (s)                               | 17.4            | 0.88 (s)                               | 16.3            | 0.80 (s)                            | 19.1            | 0.85 (s)                               | 17.9            | 0.78 (s)                                     | 16.6           | 0.73 (s)                               |
| 19                  | 36.0           | 1.26 (s)                                 | 36.2           | 1.31 (s)                               | 19.6            | 1.03 (s)                               | 18.8            | 0.98 (s)                            | 16.5            | 1.01 (s)                               | 19.5            | 1.03 (s)                                     | 22.5           | 1.02 (s)                               |
| 20                  | 49.4           | 2.40 (m)                                 | 49.9           | 2.42 (m)                               | 49.6            | 2.55 (d,<br>9.9)                       | 47.2            | 2.22 (m)                            | 43.6            | 2.55 (m)                               | 48.8            | 2.37 (td,<br>8.7, 3.1)                       | 43.3           | 2.57<br>(dd,10.2,<br>3.2)              |
| 21                  | 180.0          | –  | 181.4          | –                                      | 179.6           | –                                      | 181.7           | –                                   | 179.1           | –                                      | 180.7           | –  | 179.3          | –                                      |
| 22                  | 33.5           | 1.89 (m)<br>1.64 (m)                     | 32.7           | 2.43 (m)<br>1.50 (m)                   | 32.5            | 2.42 (m)<br>1.54 (m)                   | 32.4            | 1.53 (m)                            | 30.8            | 2.45 (m)<br>1.62 (m)                   | 33.5            | 1.83 (dd,<br>13.1, 2.9)<br>1.64 (m)          | 30.9           | 2.49 (m)                               |
| 23                  | 27.5           | 2.07 (m)<br>1.97 (m)                     | 27.3           | 2.00 (dd,<br>11.9, 3.9)                | 21.3            | 1.97 (m)                               | 25.8            | 1.96 (t,<br>6.4)                    | 25.9            | 1.99 (d,<br>7.0)                       | 27.3            | 2.08 (m)<br>1.94 (t,<br>8.0)                 | 25.9           | 2.03 (d, 9.7)<br>1.64 (m)              |
| 24                  | 125.5          | 5.15 (t,<br>7.0)                         | 125.2          | 5.14 (t,<br>6.6)                       | 125.2           | 5.13 (t,<br>7.4)                       | 123.3           | 5.08 (t,<br>7.0)                    | 123.6           | 5.12 (t,<br>5.8)                       | 125.3           | 5.15 (t,<br>6.5)                             | 123.3          | 5.14 (t, 7.0)                          |
| 25                  | 132.6          | –  | 132.9          | –                                      | 132.8           | –                                      | 132.5           | –                                   | 132.3           | –                                      | 132.8           | –  | 132.4          | –                                      |
| 26                  | 17.9           | 1.61 (s)                                 | 17.9           | 1.61 (s)                               | 17.8            | 1.60 (s)                               | 17.7            | 1.58 (s)                            | 17.7            | 1.59 (s)                               | 17.9            | 1.60 (s)                                     | 17.7           | 1.53 (s)                               |
| 27                  | 26.0           | 1.67 (s)                                 | 26.1           | 1.68 (s)                               | 26.0            | 1.68 (s)                               | 25.7            | 1.68 (s)                            | 25.7            | 1.67 (s)                               | 26.0            | 1.68 (s)                                     | 25.7           | 1.68 (s)                               |
| 28                  | 28.2           | 1.19 (s)                                 | 28.2           | 1.21 (s)                               | 28.7            | 0.99 (s)                               | 27.5            | 0.86 (s)                            | 27.9            | 0.89 (s)                               | 28.5            | 0.90 (s)                                     | 27.8           | 0.89 (s)                               |
| 29                  | 25.9           | 1.14 (s)                                 | 26.0           | 1.15 (s)                               | 16.2            | 0.82 (s)                               | 21.8            | 0.91 (s)                            | 17.0            | 0.89 (s)                               | 22.4            | 0.95 (s)                                     | 22.4           | 1.00 (s)                               |
| 30                  | 26.5           | 1.09 (s)                                 | 26.2           | 1.08 (s)                               | 25.3            | 1.09 (s)                               | 17.0            | 0.98(s)                             | 25.0            | 1.07 (s)                               | 25.6            | 1.14 (s)                                     | 25.7           | 1.11 (s)                               |
| 31                  |                |  |                |  |                 |  |                 |                                     |                 |  |                 |  |                |  |
| 1'                  |                |  |                |  |                 |  | 170.8           | –                                   | 171.1           | –                                      | 172.4           |  | 170.8          | –                                      |
| 2'                  |                |  |                |  |                 |  | 21.3            | 2.07 (s)                            | 21.3            | 2.06 (s)                               | 46.0            | 2.70 (m)                                     | 21.3           | 2.05 (s)                               |
| 3'                  |                |  |                |  |                 |  |                 |                                     |                 |  | 70.9            | –  |                |  |
| 4'                  |                |  |                |  |                 |  |                 |                                     |                 |  | 28.1            | 1.37 (s)                                     |                |  |
| 5'                  |                |  |                |  |                 |  |                 |                                     |                 |  | 46.6            | 2.71 (m)                                     |                |  |
| 6'                  |                |  |                |  |                 |  |                 |                                     |                 |  | 173.2           | –  |                |  |
| 6'-OCH <sub>3</sub> |                |  |                |  |                 |  |                 |                                     |                 |  | 52.1            | 3.66 (s)                                     |                |  |
|                     |                |  |                |  |                 |  |                 |                                     |                 |  |                 |  |                |  |
|                     | 8 <sup>b</sup> |  | 9 <sup>b</sup> |  | 10 <sup>b</sup> |  | 11 <sup>a</sup> |                                     | 12 <sup>b</sup> |  | 13 <sup>b</sup> |  |                |  |
| position            | δ <sub>C</sub> | δ <sub>H</sub>                           | δ <sub>C</sub> | δ <sub>H</sub>                         | δ <sub>C</sub>  | δ <sub>H</sub>                         | δ <sub>C</sub>  | δ <sub>H</sub>                      | δ <sub>C</sub>  | δ <sub>H</sub>                         | δ <sub>C</sub>  | δ <sub>H</sub>                               | δ <sub>C</sub> | δ <sub>H</sub>                         |
| 1                   | 35.2           | 1.99 (m)<br>1.52 (m)                     | 30.6           | 1.62 (dd, 5.0,<br>3.0)<br>1.58 (m)     | 31.9            | 1.76 (m)<br>1.72 (m)                   | 30.2            | 1.44 (m)                            | 30.8            | 1.64 (m)<br>1.39 (m)                   | 30.4            | 1.70 (m)<br>1.64 (m)                         |                |  |
| 2                   | 24.1           | 1.74 (m)                                 | 23.1           |  | 24.1            |  | 26.5            |                                     | 23.3            |  | 23.0            |  |                |  |

(continued on next page)

Table 1 (continued)

| position            | 8 <sup>b</sup> |                      | 9 <sup>b</sup> |                      | 10 <sup>b</sup> |                      | 11 <sup>a</sup> |                      | 12 <sup>b</sup> |                     | 13 <sup>b</sup> |                      |
|---------------------|----------------|----------------------|----------------|----------------------|-----------------|----------------------|-----------------|----------------------|-----------------|---------------------|-----------------|----------------------|
|                     | $\delta_C$     | $\delta_H$           | $\delta_C$     | $\delta_H$           | $\delta_C$      | $\delta_H$           | $\delta_C$      | $\delta_H$           | $\delta_C$      | $\delta_H$          | $\delta_C$      | $\delta_H$           |
|                     |                |                      |                | 1.90 (m)             |                 | 2.08 (m)             |                 | 1.85 (m)             |                 | 1.82 (m)            |                 | 1.91 (m)             |
|                     |                |                      |                | 1.73 (m)             |                 | 1.72 (m)             |                 | 1.65 (m)             |                 | 1.62 (m)            |                 | 1.72 (m)             |
| 3                   | 80.5           | 4.52 (dd, 11.3, 4.9) | 78.0           | 4.67 (t, 2.8)        | 80.0            | 4.70 (t, 2.5)        | 77.8            | 4.67 (t, 2.6)        | 77.8            | 4.66 (br s)         | 77.9            | 4.69 (t, 2.9)        |
| 4                   | 37.5           | –                    | 36.5           | –                    | 37.7            | –                    | 36.7            | –                    | 36.7            | –                   | 36.5            | –                    |
| 5                   | 49.2           | 1.21 (dd, 10.9, 4.6) | 44.0           | 1.48 (dd, 11.4, 4.1) | 45.8            | 1.54 (d, 13.7)       | 45.2            | 1.50 (m)             | 45.1            | 1.41 (m)            | 44.2            | 1.52 (dd, 9.8, 6.1)  |
| 6                   | 22.8           | 2.12 (m)             | 22.7           | 2.09 (m)             | 24.0            | 1.55 (t, 7.5)        | 17.8            | 1.64 (m)             | 17.9            | 1.62 (m)            | 22.8            | 2.07 (m)             |
| 7                   | 122.1          | 5.48 (d, 2.2)        | 121.5          | 5.85 (d, 5.4)        | 121.8           | 5.50 (t, 5.1)        | 23.2            | 1.46 (t, 2.3)        | 26.5            | 1.47 (m)            | 122.2           | 5.50 (t, 4.0)        |
| 8                   | 139.5          | –                    | 140.5          | –                    | 143.5           | –                    | 131.3           | 1.95 (m)             | 132.9           | 2.14 (m)            | 139.4           | –                    |
| 9                   | 145.9          | –                    | 146.0          | –                    | 147.1           | –                    | 136.0           | –                    | 135.4           | –                   | 146.1           | –                    |
| 10                  | 37.6           | –                    | 37.3           | –                    | 38.6            | –                    | 37.1            | –                    | 36.9            | –                   | 37.5            | –                    |
| 11                  | 116.0          | 5.39 (d, 5.2)        | 115.5          | 5.29 (d, 6.5)        | 117.2           | 5.37 (d, 4.6)        | 20.1            | 2.10 (m)             | 20.6            | 2.03 (d, 8.2)       | 115.5           | 5.41 (d, 6.3)        |
| 12                  | 34.9           | 2.47 (m)             | 36.1           | 2.26 (m)             | 36.9            | 2.26 (m)             | 28.7            | 2.03 (d, 7.9)        | 29.4            | 1.95 (m)            | 34.9            | 2.44 (d, 17.7)       |
| 13                  | 42.4           | –                    | 44.3           | –                    | 45.7            | –                    | 43.5            | 1.56 (dd, 11.9, 7.2) | 44.9            | 1.25 (s)            | 42.5            | 1.99 (dd, 17.7, 6.4) |
| 14                  | 44.2           | –                    | 51.7           | –                    | 50.0            | –                    | 44.0            | –                    | 51.5            | –                   | 44.3            | –                    |
| 15                  | 46.4           | 2.39 (d, 13.1)       | 74.4           | 4.31 (dd, 9.8, 5.8)  | 44.5            | 2.20 (dd, 13.6, 7.4) | 46.3            | 2.35 (d, 18.2)       | 73.3            | 4.25 (dd, 9.7, 5.7) | 46.4            | 2.37 (d, 18.3)       |
| 16                  | 217.2          | –                    | 38.8           | 1.98 (m)             | 77.6            | 4.03 (t, 7.0)        | 217.9           | 1.96 (d, 18.2)       | 38.0            | 1.95 (m)            | 217.2           | –                    |
| 17                  | 57.0           | 2.61 (t, 10.1)       | 45.6           | 1.79 (d, 5.8)        | 57.7            | 2.15 (m)             | 57.1            | 1.48 (d, 13.6)       | 45.7            | 1.78 (m)            | 56.9            | 2.12 (dd, 10.6, 6.0) |
| 18                  | 16.6           | 0.72 (s)             | 16.2           | 2.26 (m)             | 17.7            | 0.64 (s)             | 17.0            | 4.03 (t, 7.0)        | 16.6            | 0.81 (s)            | 16.6            | 0.75 (s)             |
| 19                  | 22.7           | 1.01 (s)             | 17.3           | 0.69 (s)             | 22.9            | 1.03 (s)             | 18.8            | 4.03 (t, 7.0)        | 18.8            | 0.98 (s)            | 22.5            | 0.97 (s)             |
| 20                  | 43.3           | 2.56 (dd, 10.1, 2.9) | 46.9           | 0.98 (s)             | 48.6            | 2.38 (td, 9.9, 2.1)  | 43.7            | 2.56 (td, 9.7, 2.8)  | 47.1            | 2.25 (m)            | 43.3            | 2.65 (t, 10.0)       |
| 21                  | 178.7          | –                    | 180.2          | –                    | 180.5           | –                    | 179.9           | 2.65 (m)             | 180.6           | –                   | 178.3           | –                    |
| 22                  | 30.8           | 2.45 (m)             | 32.5           | 1.54 (m)             | 33.4            | 1.85 (m)             | 29.3            | 2.65 (m)             | 30.9            | 1.66 (m)            | 29.4            | 1.74 (m)             |
| 23                  | 25.9           | 2.05 (m)             | 25.8           | 1.68 (m)             | 27.4            | 1.68 (m)             | 32.0            | 1.73 (m)             | 31.8            | 1.87 (d, 7.9)       | 32.0            | 2.01 (d, 6.4)        |
| 24                  | 123.3          | 5.13 (t, 7.5)        | 123.2          | 1.98 (m)             | 125.2           | 1.96 (m)             | 154.7           | 2.04 (t, 7.7)        | 154.9           | –                   | 154.7           | –                    |
| 25                  | 132.4          | –                    | 132.5          | 5.08 (t, 6.6)        | 132.8           | 5.15 (t, 6.2)        | 33.6            | –                    | 33.8            | –                   | 33.6            | –                    |
| 26                  | 17.7           | 1.59 (s)             | 17.7           | –                    | 17.9            | –                    | 21.9            | 2.26 (sep, 2.6)      | 21.8            | 2.20                | 21.7            | 2.27 (sep, 6.5)      |
| 27                  | 25.7           | 1.68 (s)             | 25.7           | 1.58 (s)             | 26.0            | 1.60 (m)             | 21.8            | 1.01 (d, 5.4)        | 21.8            | 1.00 (d, 6.5)       | 21.7            | 1.02 (d, 2.2)        |
| 28                  | 28.0           | 0.89 (s)             | 27.8           | 1.68 (s)             | 28.7            | 1.68 (s)             | 21.8            | 1.03 (d, 5.2)        | 21.8            | 1.02 (d, 6.3)       | 21.8            | 1.03 (d, 1.9)        |
| 29                  | 16.9           | 0.96 (s)             | 22.6           | 0.87 (s)             | 28.7            | 0.91 (s)             | 27.5            | 0.87 (s)             | 27.5            | 0.86 (s)            | 27.8            | 0.89 (s)             |
| 30                  | 25.8           | 1.06 (s)             | 22.5           | 0.98 (s)             | 23.2            | 1.03 (s)             | 21.7            | 0.92 (s)             | 21.7            | 0.91 (s)            | 22.4            | 1.00 (s)             |
| 31                  |                |                      |                | 0.99 (s)             | 26.7            | 1.10 (s)             | 25.0            | 1.13 (s)             | 17.0            | 0.99 (s)            | 26.0            | 1.12 (s)             |
| 1'                  | 171.0          | –                    | 170.9          | –                    | 172.4           | –                    | 107.1           | 4.77 (s)             | 107.0           | 4.77 (s)            | 107.2           | 4.78 (s)             |
| 2'                  | 21.3           | 2.07 (s)             | 21.3           | 2.04 (s)             | 46.0            | 2.69 (m)             | 21.3            | 4.74 (s)             | 21.4            | 4.67 (s)            | 21.3            | 4.75 (s)             |
| 3'                  |                |                      |                |                      | 70.9            | –                    |                 |                      |                 |                     |                 |                      |
| 4'                  |                |                      |                |                      | 28.2            | 1.35 (s)             |                 |                      |                 |                     |                 |                      |
| 5'                  |                |                      |                |                      | 46.5            | 2.68 (m)             |                 |                      |                 |                     |                 |                      |
| 6'                  |                |                      |                |                      | 173.2           | –                    |                 |                      |                 |                     |                 |                      |
| 6'-OCH <sub>3</sub> |                |                      |                |                      | 52.1            | 3.64 (s)             |                 |                      |                 |                     |                 |                      |

<sup>1</sup>H and <sup>13</sup>C NMR Spectroscopic Data of Compounds 8–13 [ $\delta$  (multi.,  $J$  in Hz) in ppm; <sup>a</sup> <sup>1</sup>H and <sup>13</sup>C NMR data were measured in CD<sub>3</sub>OD at 400 and 100 MHz. <sup>b</sup> <sup>1</sup>H and <sup>13</sup>C NMR data were measured in CDCl<sub>3</sub> at 400 and 100 MHz]

3507, 2954, 1725, 1602, 1443, 1375, 1353, 1210, 1013, 756 cm<sup>-1</sup>; <sup>1</sup>H and <sup>13</sup>C NMR, see Table 1; HRESIMS  $m/z$  653.4025 ([M+Na]<sup>+</sup> calcd for C<sub>37</sub>H<sub>58</sub>O<sub>8</sub>Na, 653.4024).

### 2.3.7. Pinicolasin G (7)

Colorless powder; [ $\alpha$ ]<sub>D</sub><sup>25</sup> – 46.9 (c 0.1, MeOH); UV (MeOH)  $\lambda_{\max}$  (log  $\epsilon$ ) 241 (1.6), 207 (0.8) nm; ECD (MeOH) (Mol. CD) 224 (1.5) nm; IR (KBr)  $\nu_{\max}$  3447, 2936, 1729, 1597, 1441, 1377, 1248, 1184, 755 cm<sup>-1</sup>; <sup>1</sup>H and <sup>13</sup>C NMR, see Table 1; HRESIMS  $m/z$  533.3236 ([M+Na]<sup>+</sup> calcd for C<sub>32</sub>H<sub>46</sub>O<sub>5</sub>Na, 533.3237).

### 2.3.8. Pinicolasin H (8)

Colorless powder; [ $\alpha$ ]<sub>D</sub><sup>25</sup> – 18.6 (c 0.06, MeOH); UV (MeOH)  $\lambda_{\max}$

(log  $\epsilon$ ) 241 (1.7), 208 (1.1) nm; ECD (MeOH) (Mol. CD) 305 (–2.0), 235 (0.5) nm; IR (KBr)  $\nu_{\max}$  3445, 2934, 1732, 1596, 1448, 1374, 1247, 1032, 754 cm<sup>-1</sup>; <sup>1</sup>H and <sup>13</sup>C NMR, see Table 2; HRESIMS  $m/z$  533.3238 ([M+Na]<sup>+</sup> calcd for C<sub>32</sub>H<sub>46</sub>O<sub>5</sub>Na, 533.3238).

### 2.3.9. Pinicolasin I (9)

Colorless powder; [ $\alpha$ ]<sub>D</sub><sup>25</sup> + 26.3 (c 0.06, MeOH); UV (MeOH)  $\lambda_{\max}$  (log  $\epsilon$ ) 242 (1.3), 208 (0.8) nm; ECD (MeOH) (Mol. CD) 232 (1.7) nm; IR (KBr)  $\nu_{\max}$  3445, 2948, 1715, 1681, 1647, 1456, 1376, 1248, 1033, 756 cm<sup>-1</sup>; <sup>1</sup>H and <sup>13</sup>C NMR, see Table 2; HRESIMS  $m/z$  535.3392 ([M+Na]<sup>+</sup> calcd for C<sub>32</sub>H<sub>48</sub>O<sub>5</sub>Na, 535.3394).

**Table 2**

Inhibitory Effects of Isolated Compounds on Superoxide Anion Generation and Elastase Release in Human Neutrophils in Response to fMLP/CB.

| Compound  | IC <sub>50</sub> (μM) <sup>a</sup> |                  |
|-----------|------------------------------------|------------------|
|           | Superoxide anion generation        | Elastase release |
| 1         | 4.32 ± 0.22                        | >10              |
| 2         | >10                                | >10              |
| 4         | >10                                | >10              |
| 5         | 2.25 ± 0.22                        | 2.87 ± 0.27      |
| 6         | 4.77 ± 0.97                        | 6.66 ± 0.30      |
| 7         | 2.42 ± 0.08                        | 2.67 ± 0.34      |
| 8         | 4.05 ± 1.03                        | 4.84 ± 0.82      |
| 9         | >10                                | >10              |
| 10        | 1.81 ± 0.44                        | 2.50 ± 0.64      |
| 11        | 4.61 ± 0.51                        | 3.51 ± 0.45      |
| 12        | >10                                | >10              |
| 14        | 4.97 ± 0.56                        | 6.40 ± 1.11      |
| 15        | >10                                | >10              |
| 16        | 2.13 ± 0.41                        | 2.83 ± 0.59      |
| 17        | 5.20 ± 1.69                        | 6.74 ± 0.30      |
| 18        | 2.57 ± 0.78                        | 3.30 ± 1.06      |
| 19        | 6.87 ± 0.58                        | >10              |
| 20        | 4.15 ± 0.29                        | 2.46 ± 0.31      |
| 21        | >10                                | >10              |
| 22        | >10                                | >10              |
| 23        | >10                                | >10              |
| 24        | 6.03 ± 0.61                        | >10              |
| 25        | 4.38 ± 0.86                        | 5.86 ± 1.53      |
| 26        | >10                                | >10              |
| 27        | >10                                | >10              |
| 28        | >10                                | 4.73 ± 1.00      |
| 29        | 6.11 ± 1.20                        | >10              |
| 30        | >10                                | 5.38 ± 1.44      |
| 31        | >10                                | >10              |
| 32        | >10                                | >10              |
| 33        | >10                                | >10              |
| 34        | 2.86 ± 0.62                        | 3.42 ± 0.66      |
| Genistein | 1.62 ± 0.14                        | 35.95 ± 1.53     |

<sup>a</sup> Concentration corresponding to 50% inhibition. The results are presented as the mean ± SEM (n = 3–5).

### 2.3.10. Pinicolasin J (10)

Colorless powder;  $[\alpha]_D^{25} - 2.4$  (c 0.3, MeOH); UV (MeOH)  $\lambda_{\max}$  (log  $\epsilon$ ) 239 (1.9), 212 (1.3) nm; ECD (MeOH) (Mol. CD) 219 (3.3) nm; IR (KBr)  $\nu_{\max}$  3495, 2949, 2885, 1737, 1714, 1441, 1377, 1206, 1029, 756  $\text{cm}^{-1}$ ;  $^1\text{H}$  and  $^{13}\text{C}$  NMR, see Table 2; HRESIMS  $m/z$  651.3870  $[\text{M}+\text{Na}]^+$  calcd for  $\text{C}_{37}\text{H}_{56}\text{O}_8\text{Na}$ , 651.3867).

### 2.3.11. Pinicolasin K (11)

Colorless powder;  $[\alpha]_D^{25} - 64.6$  (c 0.1, MeOH); ECD (MeOH) (Mol. CD) 306 (−4.8) nm; IR (KBr)  $\nu_{\max}$  3700, 2953, 1733, 1609, 1453, 1375, 1247, 1182, 755  $\text{cm}^{-1}$ ;  $^1\text{H}$  and  $^{13}\text{C}$  NMR, see Table 2; HRESIMS  $m/z$  549.3549  $[\text{M}+\text{Na}]^+$  calcd for  $\text{C}_{33}\text{H}_{50}\text{O}_5\text{Na}$ , 549.3550).

### 2.3.12. Pinicolasin L (12)

Colorless powder;  $[\alpha]_D^{25} + 0.3$  (c 0.3, MeOH); IR (KBr)  $\nu_{\max}$  3687, 2949, 1716, 1454, 1375, 1250, 1180, 1054, 755  $\text{cm}^{-1}$ ;  $^1\text{H}$  and  $^{13}\text{C}$  NMR, see Table 2; HRESIMS  $m/z$  551.3709  $[\text{M}+\text{Na}]^+$  calcd for  $\text{C}_{33}\text{H}_{52}\text{O}_5\text{Na}$ , 551.3707).

### 2.3.13. Pinicolasin M (13)

Colorless powder;  $[\alpha]_D^{25} - 31.3$  (c 0.06, MeOH); UV (MeOH)  $\lambda_{\max}$  (log  $\epsilon$ ) 242 (0.8), 205 (0.4) nm; ECD (MeOH) (Mol. CD) 305 (−3.1), 228 (1.5) nm; IR (KBr)  $\nu_{\max}$  3701, 2957, 2883, 1733, 1607, 1376, 1246, 1182, 757  $\text{cm}^{-1}$ ;  $^1\text{H}$  and  $^{13}\text{C}$  NMR, see Table 2; HRESIMS  $m/z$  547.3395  $[\text{M}+\text{Na}]^+$  calcd for  $\text{C}_{33}\text{H}_{48}\text{O}_5\text{Na}$ , 547.3394).

## 2.4. Human neutrophil preparation

A standard method of dextran sedimentation was used to isolate

neutrophils prior to centrifugation on a Ficoll Hypaque gradient and hypotonic lysis of erythrocytes. Whole blood of healthy donors (20–30 years of age) was withdrawn by venipuncture; the protocol was approved by Chang Gung Memorial Hospital (IRB protocol number: 102-1595A3) review board. Before use, purified neutrophils were maintained at 4 °C in a  $\text{Ca}^{2+}$ -free Hank's balanced salt solution (HBSS) at pH 7.4. [13]

## 2.5. Superoxide anion generation measurement

Reduction of ferricytochrome *c* be inhibited by superoxide dismutase (SOD) was used to develop the superoxide anion generation assay. Each test compound or an equal volume of vehicle (0.1% DMSO, negative control) was incubated for 5 min with neutrophils ( $6 \times 10^5$  cells/mL) equilibrated in the presence of 0.5 mg/mL ferricytochrome *c* and 1 mM  $\text{Ca}^{2+}$  at 37 °C for 2 min. Cells were initially incubated with cytochalasin B (CB, 1 μg/mL) for 3 min; then, neutrophils were activated by *N*-formyl-L-methionyl-L-leucyl-L-phenylalanine (fMLF, 100 nM). The changes in absorbance due to reduction of ferricytochrome *c* at 550 nm were continuously monitored in a double-beam spectrophotometer equipped with a six cell positioning system (Hitachi U-3010, Tokyo, Japan) under constant stirring. Calculations were based on the differences in the reduction with and without SOD (100 U/mL) divided by the extinction coefficient for the reduction of ferricytochrome *c* ( $\epsilon = 21.1/\text{mM}/10 \text{ mm}$ ). Genistein was used as a positive control [13].

## 2.6. Elastase release assay

Degranulation of azurophilic granules was determined by elastase release as described previously. MeO-Suc-Ala-Ala-Pro-Val-*p*-nitroanilide was used as the elastase substrate. Neutrophils ( $6 \times 10^5$  cells/mL) equilibrated in the presence of MeO-Suc-Ala-Ala-Pro-Val-*p*-nitroanilide (100 μM) at 37 °C for 2 min were incubated with the test compounds or an equal volume of the vehicle (0.1% DMSO, negative control) for 5 min. Cells were activated by 100 nM fMLF and 0.5 μg/mL CB, and changes in absorbance at 405 nm were continuously monitored to measure elastase release. The results are expressed as the percentage of elastase release relative to the values detected in the fMLF/CB-activated drug-free control system. Genistein was used as a positive control [13].

## 2.7. Statistical analysis

The results are expressed as the mean ± SEM. Calculations of 50% inhibitory concentrations (IC<sub>50</sub>) were performed using a computer (PHARM/PCS v.4.2). Statistical comparison between the groups was performed using the Student's *t* test. Values of *p* less than 0.05 were considered statistically significant.

## 3. Results and discussion

The fruiting bodies of *F. pinicola* were extracted with ethanol, and the resulting crude extract was subjected to column chromatography, preparative TLC, and HPLC to afford twelve previously undescribed triterpenoids (1–4, 6–13, Fig. 1) and twenty-two known compounds. The structures of 1–13 were determined as described below.

Compound 1 was isolated as colorless powder with a pseudomolecular formula  $\text{C}_{30}\text{H}_{44}\text{O}_4\text{Na}$  on the basis of HRESIMS  $[\text{M}+\text{Na}]^+$ ,  $m/z$  491.3130. Its  $^1\text{H}$  NMR spectrum revealed seven methyl singlets at  $\delta_{\text{H}}$  0.70 (s), 1.09 (s), 1.14 (s), 1.19 (s), 1.26 (s), 1.61 (s), and 1.67 (s), three conjugated double bond proton signals at  $\delta_{\text{H}}$  5.47 (br s), 5.56 (d,  $J = 6.8$  Hz), and 6.02 (d,  $J = 6.8$  Hz), one olefinic proton at  $\delta_{\text{H}}$  5.15 (t,  $J = 7.0$  Hz), and two oxygenated methines at  $\delta_{\text{H}}$  3.21 (dd,  $J = 11.9, 4.3$  Hz) and 4.06 (t,  $J = 7.4$  Hz). In its  $^{13}\text{C}$  and DEPT-135 NMR spectra, thirty carbons were observed including seven methyls, six methylenes, eight olefinic carbons, two oxygenated methines, and one carboxylic acid. In the HMBC spectral analysis of 1 (Fig. 2), conjugated tri-ene system was



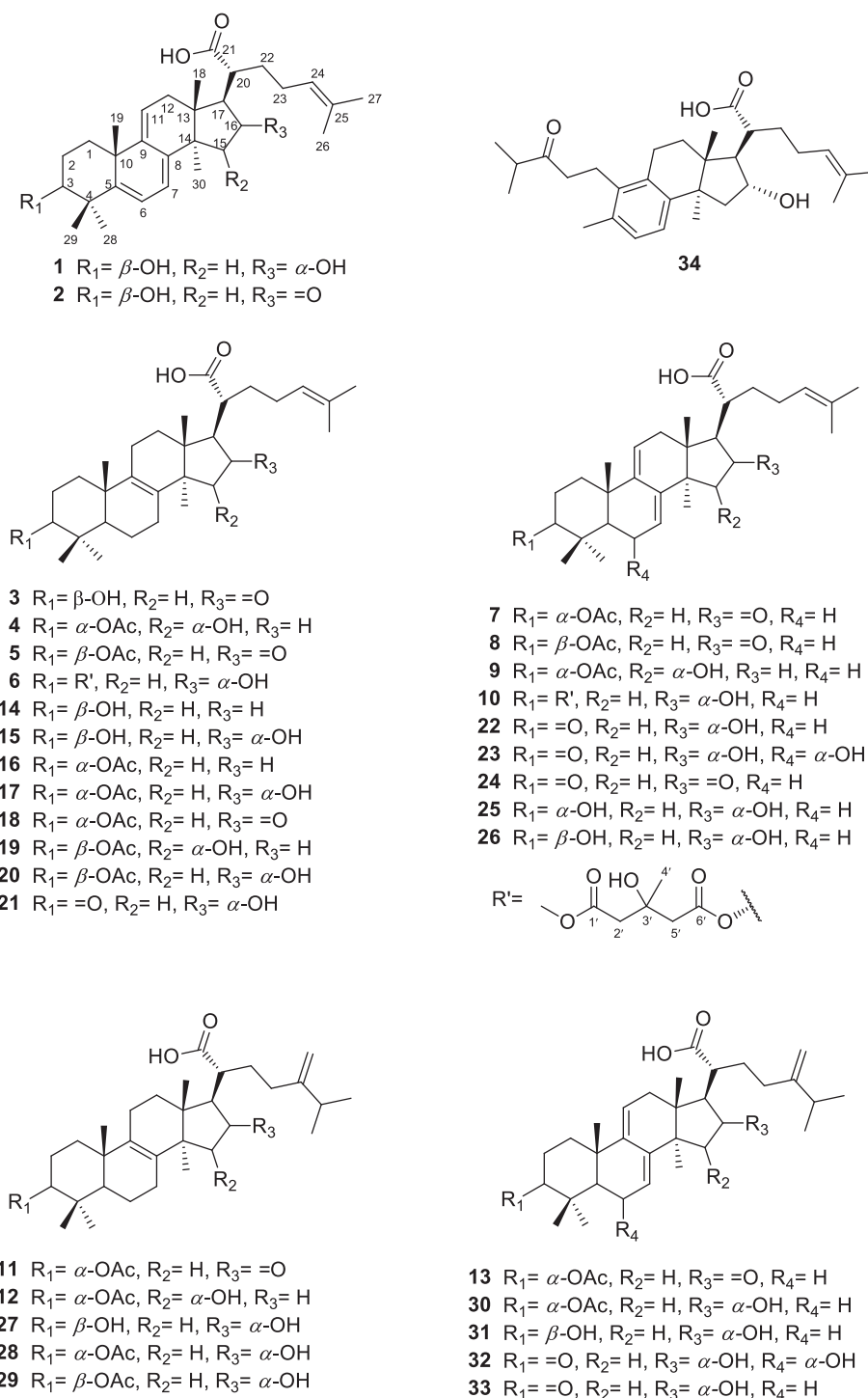


Fig. 1. Structures of triterpenes (1–34) isolated from *Fomitopsis pinicola*.

proposed according to the observed correlations of H-6 ( $\delta_{\text{H}}$  6.02, d,  $J = 6.8$  Hz) to C-4 ( $\delta_{\text{C}}$  42.9), C-8 ( $\delta_{\text{C}}$  141.7), and C-10 ( $\delta_{\text{C}}$  42.1); H-7 ( $\delta_{\text{H}}$  5.56, d,  $J = 6.8$  Hz) to C-5 ( $\delta_{\text{C}}$  153.0), C-9 ( $\delta_{\text{C}}$  147.8), and C-14 ( $\delta_{\text{C}}$  49.6); and H-11 ( $\delta_{\text{H}}$  5.47, br s) to C-7 ( $\delta_{\text{C}}$  117.4). Another carbon–carbon double bond was assigned to  $\Delta^{24,25}$  due to HMBC correlations of H-24 ( $\delta_{\text{H}}$  5.15, t,  $J = 7.0$  Hz) to C-26 ( $\delta_{\text{C}}$  17.9), and H-26 ( $\delta_{\text{H}}$  1.61, s)/H-27 ( $\delta_{\text{H}}$  1.67, s) to C-24 ( $\delta_{\text{C}}$  125.5) and C-25 ( $\delta_{\text{C}}$  132.6). Moreover, a lanostane type triterpene skeleton was constructed based on other HMBC correlations from H-18 ( $\delta_{\text{H}}$  0.70, s) to C-12 ( $\delta_{\text{C}}$  37.7), C-13 ( $\delta_{\text{C}}$  45.7), and C-14 ( $\delta_{\text{C}}$  49.6); from H-19 ( $\delta_{\text{H}}$  1.26, s) to C-1 ( $\delta_{\text{C}}$  36.9), C-5 ( $\delta_{\text{C}}$  153.0), C-9 ( $\delta_{\text{C}}$  147.8), and C-10

( $\delta_{\text{C}}$  42.1); from H-28 ( $\delta_{\text{H}}$  1.19, s)/H-29 ( $\delta_{\text{H}}$  1.14, s) to C-3 ( $\delta_{\text{C}}$  77.6), C-4 ( $\delta_{\text{C}}$  42.9), and C-5 ( $\delta_{\text{C}}$  153.0); and from H-30 ( $\delta_{\text{H}}$  1.09, s) to C-8 ( $\delta_{\text{C}}$  141.7), C-13 ( $\delta_{\text{C}}$  45.7), C-14 ( $\delta_{\text{C}}$  49.6), C-15 ( $\delta_{\text{C}}$  44.3), respectively. Two oxygenated methines at  $\delta_{\text{H}}$  3.21 (dd,  $J = 11.9$ , 4.3 Hz) and 4.06 (t,  $J = 7.4$  Hz) were proposed to be at C-3 and C-16 according to their HMBC correlations [H-3/C-1 ( $\delta_{\text{C}}$  36.9); H-16/C-14 ( $\delta_{\text{C}}$  49.6)]. Further, combining with COSY correlation of H-2 ( $\delta_{\text{H}}$  1.92, 1.74)/H-3 ( $\delta_{\text{H}}$  3.21), H-6 ( $\delta_{\text{H}}$  6.02)/H-7 ( $\delta_{\text{H}}$  5.56), H-11 ( $\delta_{\text{H}}$  5.47)/H-12 ( $\delta_{\text{H}}$  1.97), H-16 ( $\delta_{\text{H}}$  4.06)/H-17 ( $\delta_{\text{H}}$  2.15), H-17 ( $\delta_{\text{H}}$  2.15)/H-20 ( $\delta_{\text{H}}$  2.40), H-20 ( $\delta_{\text{H}}$  2.40)/H-22 ( $\delta_{\text{H}}$  1.89), and H-23 ( $\delta_{\text{H}}$  2.07, 1.97)/H-24 ( $\delta_{\text{H}}$  5.15), the structure of

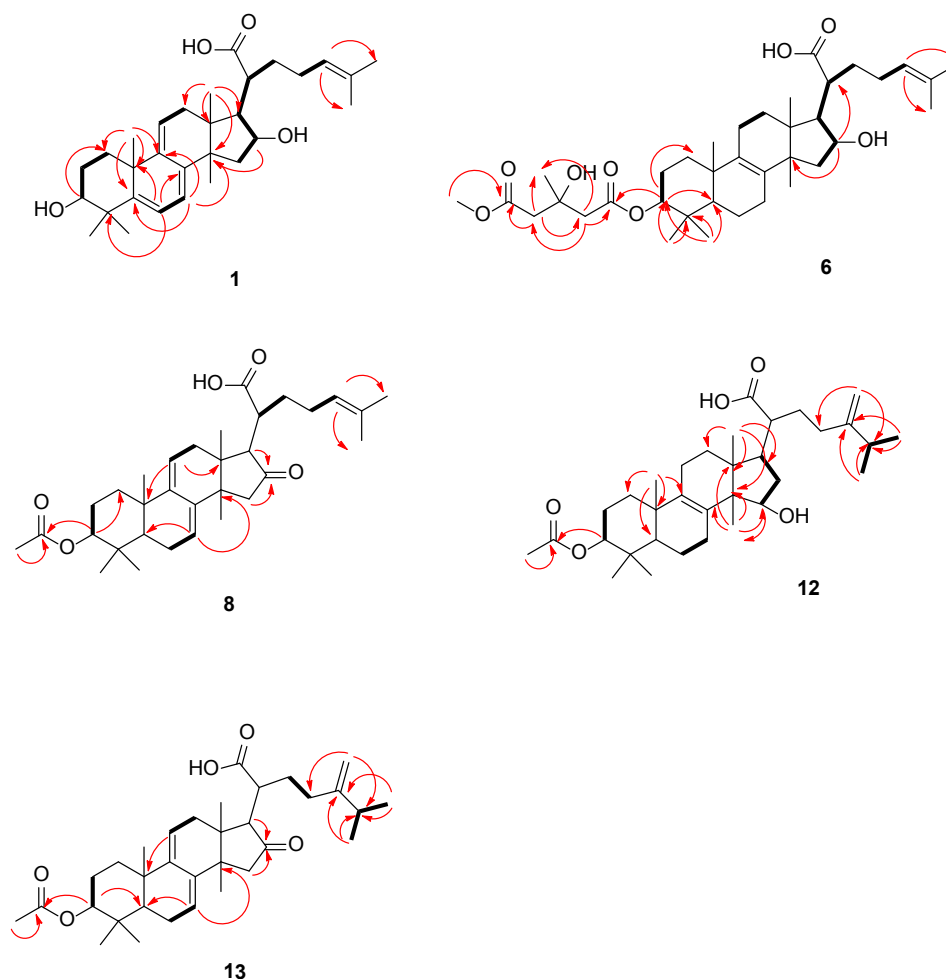


Fig. 2. Key HMBC (→,  $^1\text{H} \rightarrow ^{13}\text{C}$ ) and COSY (↔) correlation of **1**, **6**, **8**, **12**, and **13**.

3,16-dihydroxy-lanosta-5,7,9 (11),24-tetraen-21-oic acid skeleton was built. An  $\alpha$  (axial) orientation of H-3 ( $\delta_{\text{H}}$  3.21, dd,  $J = 11.9, 4.3$  Hz) was indicated by its large vicinal coupling constant values. The data of the literature indicate that H-3 can be in  $\alpha$  orientation if the proton splitting pattern is a doublet of doublet ( $J = 11\text{--}12$  and  $3\text{--}4$  Hz) or a triplet ( $J = 7\text{--}8$  Hz) [14–17], while H-3 is in  $\beta$  orientation with smaller coupling constant (both  $J = 3\text{--}4$  Hz). [18] NOE effects between H-3 and H-28<sub>eq</sub> also supported the H-3 $\alpha$  orientation. Moreover, the NOE correlations of H-18<sub>ax</sub>/H-16 and H-18<sub>ax</sub>/H-20 indicated the stereochemistry of substitutions at C-13, -16, and -20 to be  $\beta$ ,  $\alpha$ , and  $\alpha$ , respectively, as shown in Fig. 3 [19–21]. Further, NOESY correlation between H-16 and H-22 ( $\delta_{\text{H}}$  1.89) could partially support 20R configuration. Other 2D spectral experimental data confirmed the structure of **1** to be 3 $\beta$ ,16 $\alpha$ -dihydroxy-lanosta-5,7,9,24-tetraen-21-oic acid, and the compound was named trivially as pinicolasin A.

Pinicolasin B (**2**), also a colorless powder, had a pseudomolecular formula  $\text{C}_{30}\text{H}_{42}\text{O}_4\text{Na}$  on the basis of HRESIMS ( $[\text{M}+\text{Na}]^+$ ,  $m/z$  489.2976). The IR spectrum of **2** had absorption peaks at 3378 (OH), 1731 (ketone), and 1715 (carboxylic acid)  $\text{cm}^{-1}$ . The  $^1\text{H}$ ,  $^{13}\text{C}$ , and 2D NMR spectra of **2** were very similar to those of **1**. The minor differences included the lack of one oxygenated proton signal ( $\delta_{\text{H}}$  4.06, H-16) in **1** and the presence of a quaternary carbonyl carbon ( $\delta_{\text{C}}$  219.3) in **2**. According to the HMBC spectral analysis, this quaternary carbon was assigned to be C-16 based on the correlations of H-15 ( $\delta_{\text{H}}$  2.16 and 2.36) and H-17 ( $\delta_{\text{H}}$  2.63) with C-16. Moreover, similar to **1**, conjugated tri-ene system was observed based on HMBC correlations of H-6 ( $\delta_{\text{H}}$  6.07, d,  $J = 7.0$  Hz) to C-4 ( $\delta_{\text{C}}$  43.0), C-8 ( $\delta_{\text{C}}$  139.2), and C-10 ( $\delta_{\text{C}}$  42.4); H-7 ( $\delta_{\text{H}}$  5.62, d,  $J = 7.0$  Hz) to C-5 ( $\delta_{\text{C}}$  154.1), C-9 ( $\delta_{\text{C}}$  148.3), and C-14 ( $\delta_{\text{C}}$  45.1); and H-

11 ( $\delta_{\text{H}}$  5.59, s) to C-7 ( $\delta_{\text{C}}$  118.6). Large vicinal coupling constant values of H-3 ( $\delta_{\text{H}}$  3.23, dd,  $J = 12.1, 4.4$  Hz) implied a  $\alpha$  (axial) orientation. In the NOESY spectrum of **2**, NOE correlations were observed between H-3 ( $\delta_{\text{H}}$  3.23)/H-28<sub>eq</sub> ( $\delta_{\text{H}}$  1.21) and H-17 $\alpha$  ( $\delta_{\text{H}}$  2.63)/H-30 ( $\delta_{\text{H}}$  1.08) thus confirming the structure of **2** as 3 $\beta$ -hydroxy-16-oxo-lanosta-5,7,9,24-tetraen-21-oic acid.

The molecular formula of **3** was  $\text{C}_{30}\text{H}_{46}\text{O}_4$  on the basis of HRESIMS analytical data ( $[\text{M}+\text{Na}]^+$ ,  $m/z$  493.3291). Its IR spectrum showed absorption peaks at 3518 (OH), 1731 (ketone), and 1715 (carboxylic acid)  $\text{cm}^{-1}$ . Comparison of the  $^1\text{H}$  NMR spectra of **2** and **3** indicated that three conjugate double bond proton signals disappeared, and only one olefinic proton at  $\delta_{\text{H}}$  5.13 (t) was present in **3**. Furthermore,  $^{13}\text{C}$  NMR spectrum had four olefinic carbons ( $\delta_{\text{C}}$  125.2, 132.8, 133.2, and 137.5); these two double bonds were assigned to be C-24/C-25 and C-8/C-9, respectively, according to their HMBC correlations of H-19 ( $\delta_{\text{H}}$  1.03)/C-9 ( $\delta_{\text{C}}$  137.5), H-30 ( $\delta_{\text{H}}$  1.09)/C-8 ( $\delta_{\text{C}}$  133.2), and H-27 ( $\delta_{\text{H}}$  1.68)/C-24 ( $\delta_{\text{C}}$  125.2) and C-25 ( $\delta_{\text{C}}$  132.8). Additionally, a carbonyl carbon ( $\delta_{\text{C}}$  220.5) was assigned to be at C-16 due to the HMBC correlations from H-15 ( $\delta_{\text{H}}$  2.39, 1.90) to C-16 ( $\delta_{\text{C}}$  220.5) and H-30 ( $\delta_{\text{H}}$  1.09) to C-15 ( $\delta_{\text{C}}$  47.5). Moreover, the configuration of H-3 was assigned to be  $\alpha$  according to the coupling pattern (t,  $J = 7.3$  Hz). NOESY spectra of **3** also supported  $\alpha$  orientation of H-3 based on the NOE correlation between H-3 ( $\delta_{\text{H}}$  3.17) and H-28<sub>eq</sub> ( $\delta_{\text{H}}$  0.99). The structure of **3** was built as 3 $\beta$ -hydroxy-16-oxo-lanosta-8,24-dien-21-oic acid, and this compound was named pinicolasin C.

The molecular formula of pinicolasin D (**4**) was  $\text{C}_{32}\text{H}_{50}\text{O}_5$  on the basis of HRESIMS analytical data ( $[\text{M}+\text{Na}]^+$ ,  $m/z$  537.3551). The  $^1\text{H}$  and  $^{13}\text{C}$  NMR spectra of **4** are very similar to those of **3** except that C-15 carbonyl in **3** was absent and an oxygenated methine ( $\delta_{\text{H}}$  4.24) was

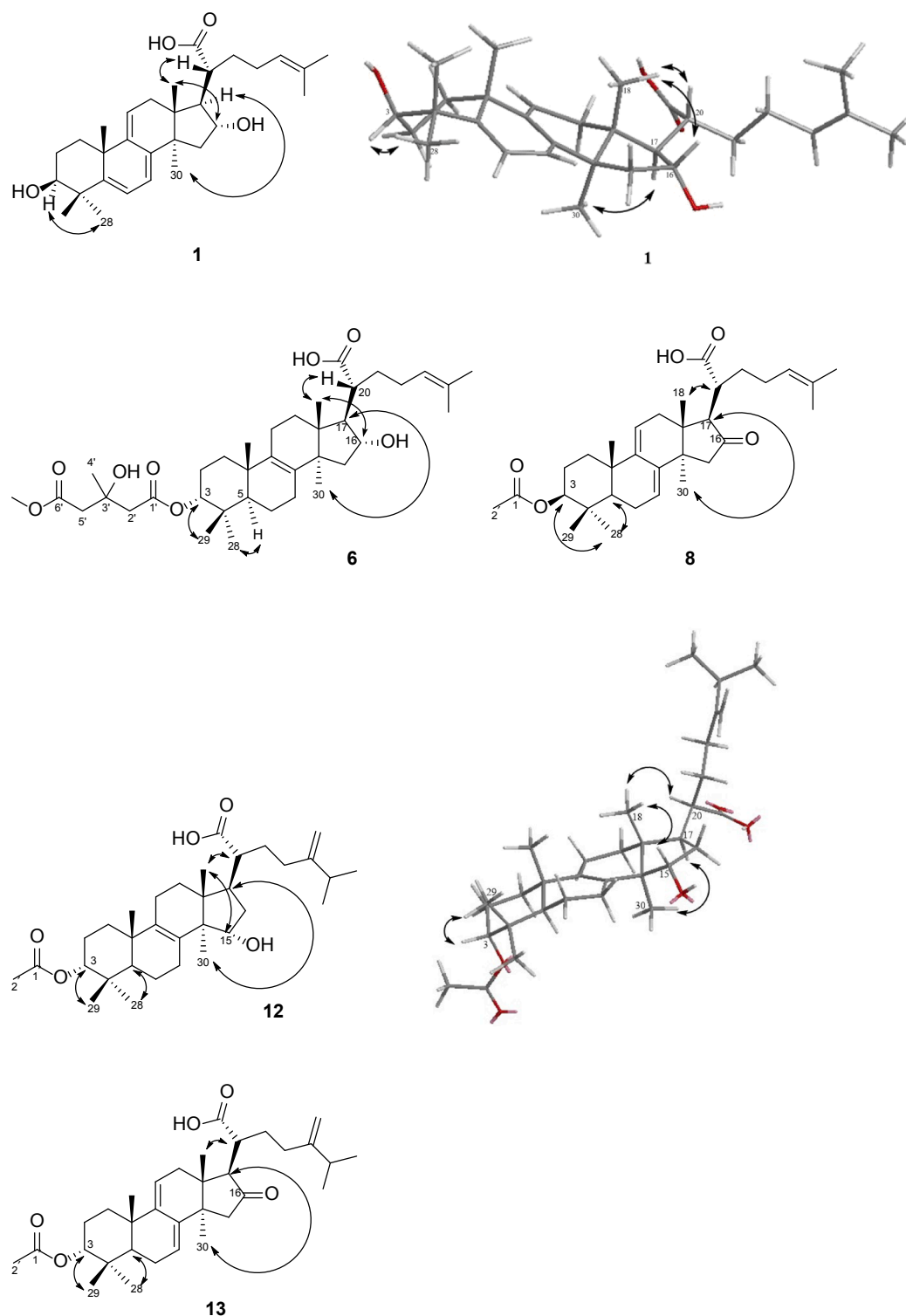


Fig. 3. Key NOESY ( $\leftrightarrow$ ,  $^1\text{H} \rightarrow ^1\text{H}$ ) correlation of **1**, **6**, **8**, **12**, and **13**.

present. This methine was assigned to be H-15 based on the HMBC correlation from H-15 ( $\delta_{\text{H}}$  4.24) to C-30 ( $\delta_{\text{C}}$  17.0). Moreover, an acetyl group was detected ( $\delta_{\text{H}}$  2.07,  $\delta_{\text{C}}$  21.3 and  $\delta_{\text{C}}$  170.8) and was connected to the C-3 hydroxyl group according to the HMBC spectral analysis in which H-3 ( $\delta_{\text{H}}$  4.66) correlated with C-1' ( $\delta_{\text{C}}$  170.8), thus confirming a 3-acetoxy-15-hydroxy-lanosta-8,24-dien-21-oic acid structure [22]. The orientation of H-3 was assigned to be  $\beta$  according to the typical chemical shift (C-3 at  $\delta_{\text{C}}$  77.8) and coupling pattern (br s). Moreover, OH-15 was

in  $\alpha$  orientation based on the NOE effect between H-15 $\beta$  ( $\delta_{\text{H}}$  4.24) and H-18 $_{\text{ax}}$  ( $\delta_{\text{H}}$  0.80). Thus, the structure of **4** was determined to be 3 $\alpha$ -acetoxy-15 $\alpha$ -hydroxy-lanosta-8,24-dien-21-oic acid.

The HRESIMS spectrum of pinicolasin E (**5**) had an  $[\text{M}+\text{Na}]^+$  ion peak at  $m/z$  535.3395 consistent with a pseudomolecular formula of  $\text{C}_{32}\text{H}_{48}\text{O}_5\text{Na}$ . Detailed analysis of  $^1\text{H}$  and  $^{13}\text{C}$  spectra indicated the presence of acetoxy signals of  $\delta_{\text{H}}$  2.06,  $\delta_{\text{C}}$  21.3, and  $\delta_{\text{C}}$  171.1, two olefinic signals of  $\delta_{\text{C}}$  123.6, 131.6, 132.3, and 135.8, and one additional carbonyl

signal of 217.2. The HMBC spectrum of **5** confirmed that the acetoxy was at C-3 position and two olefinic signals was proposed to be  $\Delta^{8,9}$  and  $\Delta^{24,25}$  based on the observed HMBC correlations of H-19 ( $\delta_{\text{H}}$  1.01) to C-9 ( $\delta_{\text{C}}$  135.8) and C-10 ( $\delta_{\text{C}}$  37.1); H-7 ( $\delta_{\text{H}}$  1.99) to C-8 ( $\delta_{\text{C}}$  131.6); H-30 ( $\delta_{\text{H}}$  1.07) to C-8 ( $\delta_{\text{C}}$  131.6); H-24 ( $\delta_{\text{H}}$  5.13) to C-26 ( $\delta_{\text{C}}$  17.8) and C-27 ( $\delta_{\text{C}}$  26.0); H-26 ( $\delta_{\text{H}}$  1.60) to C-24 ( $\delta_{\text{C}}$  125.2); and H-27 ( $\delta_{\text{H}}$  1.68) to C-24 ( $\delta_{\text{C}}$  125.2). In addition, the carbonyl is located at C-16 based on correlations of H-15 ( $\delta_{\text{H}}$  1.94, 2.34) and H-17 ( $\delta_{\text{H}}$  2.56) with C-16 ( $\delta_{\text{C}}$  217.2), suggesting a 3-acetoxy-16-oxo-lanosta-8,24-dien-21-oic acid skeleton. Moreover, the orientation of H-3 was assigned to be  $\alpha$  according to the typical shift of C-3 ( $\delta_{\text{C}}$  80.6) and coupling constants (dd,  $J = 11.6, 4.3$  Hz). Therefore, the structure of **5** was established as 3 $\beta$ -acetoxy-16-oxo-lanosta-8,24-dien-21-oic acid. This compound has just been reported as Formipinic acid **6** [20].

Pinicolasin F (**6**) had a pseudomolecular formula of  $\text{C}_{37}\text{H}_{58}\text{O}_8\text{Na}$  on the basis of HRESIMS ( $[\text{M}+\text{Na}]^+$ ,  $m/z$  653.4025). Comparison of the  $^1\text{H}$  and  $^{13}\text{C}$  spectra of **6** with those of **4** indicated the presence of a 4-carboxymethyl-3-hydroxy-3-methylbutanoyloxy substitution based on the proton signals of H-2' ( $\delta_{\text{H}}$  2.70, m), H-4' ( $\delta_{\text{H}}$  1.37, s), H-5' ( $\delta_{\text{H}}$  2.71, m), and OMe-6' ( $\delta_{\text{H}}$  3.66, s), and also on the carbon signals of C-1' ( $\delta_{\text{C}}$  172.4), C-2' ( $\delta_{\text{C}}$  46.0), C-3' ( $\delta_{\text{C}}$  70.9), C-4' ( $\delta_{\text{C}}$  28.1), C-5' ( $\delta_{\text{C}}$  46.6), C-6' ( $\delta_{\text{C}}$  173.2), and OMe-6' ( $\delta_{\text{C}}$  52.1) [10]. Its HMBC spectrum showed correlations of H-3 ( $\delta_{\text{H}}$  4.68) with C-1' ( $\delta_{\text{C}}$  172.4), H-2' with C-1'/C-4'/C-5', H-4' with C-2'/C-3'/C-5', H-5' with C-2'/C-4'/C-6', and OMe-6' with C-6' supporting C-3 substitution pattern. Furthermore, an oxygenated methine ( $\delta_{\text{H}}$  4.03) was assigned to be at C-16 according to the HMBC correlations from H-16 ( $\delta_{\text{H}}$  4.03) to C-14 ( $\delta_{\text{C}}$  49.5) and C-20 ( $\delta_{\text{C}}$  48.8). Finally, NOESY spectrum of **6** showed correlations of H-3 $\beta$  ( $\delta_{\text{H}}$  4.68) with H-29 $_{\text{ax}}$  ( $\delta_{\text{H}}$  0.95) and H-16 $\beta$  ( $\delta_{\text{H}}$  4.03) with H-18 $_{\text{ax}}$  ( $\delta_{\text{H}}$  0.78) methyl the structure of **6** as 3 $\alpha$ -[4'-carboxymethyl-3'-hydroxy-3'-methylbutanoyloxy]-16 $\alpha$ -hydroxy-lanosta-8,24-dien-21-oic acid.

The molecular formula of **7** was determined as  $\text{C}_{32}\text{H}_{46}\text{O}_5$  according to its HRESIMS analytical data ( $[\text{M}+\text{Na}]^+$ ,  $m/z$  533.3236). Its IR spectrum had absorption peaks at 3447 (OH), 1729 (ketone), and 1597 (conjugate double bonds)  $\text{cm}^{-1}$ . The conjugate double bond was assigned to C-7/C-8/C-9/C-11 based on the proton signals of H-7 ( $\delta_{\text{H}}$  5.50, t,  $J = 3.5$  Hz) and H-11 ( $\delta_{\text{H}}$  5.40, d,  $J = 6.1$  Hz) and carbon signals of C-7 ( $\delta_{\text{C}}$  115.5), C-8 ( $\delta_{\text{C}}$  139.4), C-9 ( $\delta_{\text{C}}$  146.1) and C-11 ( $\delta_{\text{C}}$  122.2), respectively. Moreover, HMBC spectrum of **7** confirmed the assignment based on the correlations of H-7 ( $\delta_{\text{H}}$  5.50)/C-5 ( $\delta_{\text{C}}$  44.2) and C-14 ( $\delta_{\text{C}}$  44.3), H-11 ( $\delta_{\text{H}}$  5.40)/C-10 ( $\delta_{\text{C}}$  37.5), and C-13 ( $\delta_{\text{C}}$  42.5), H-19 ( $\delta_{\text{H}}$  1.02)/C-9 ( $\delta_{\text{C}}$  146.1), and H-30 ( $\delta_{\text{H}}$  1.11)/C-8 ( $\delta_{\text{C}}$  139.4). In addition, 3-acetoxy substitution was assigned based on the chemical shifts of H-2' ( $\delta_{\text{H}}$  2.05, s), C-1' ( $\delta_{\text{C}}$  170.8), and C-2' ( $\delta_{\text{C}}$  21.3), and also by the HMBC correlations from H-2' to C-1', and from H-3 to C-1'. Furthermore, H-3 $\beta$  ( $\delta_{\text{H}}$  4.69, t,  $J = 2.4$  Hz) with smaller coupling constant had NOE correlation with H-29 $_{\text{ax}}$  ( $\delta_{\text{H}}$  1.00) in the NOESY spectrum indicating 3-acetoxy to be in  $\alpha$  orientation [23]. Another carbonyl group was assigned to be at C-16 based on the HMBC correlations of H-15 ( $\delta_{\text{H}}$  2.16, 2.40) and H-17 ( $\delta_{\text{H}}$  2.62) with C-16 ( $\delta_{\text{C}}$  217.2). Therefore, the structure of **7** was constructed as 3 $\alpha$ -acetoxy-16-oxo-lanosta-7,9 (11),24-trien-21-oic acid, and it was assigned a trivial name pinicolasin G.

The molecular formula of **8** was also determined as  $\text{C}_{32}\text{H}_{46}\text{O}_5$ , which was the same as that of **7**, indicating that **8** was an isomer of **7**. The 1D NMR signals of **8** were also very similar to those of **7**. The majority of the difference was the H-3 signal ( $\delta_{\text{H}}$  4.52, dd,  $J = 11.3, 4.9$  Hz;  $\delta_{\text{C}}$  80.5) on A ring. A previous study indicated the splitting pattern of H-3 $\alpha$  to be a doublet of doublet ( $J = 11$ –12 and 3–4 Hz) or a triplet ( $J = 7$ –8 Hz), and the chemical shift of C-3 carbon was at  $\delta_{\text{C}}$  75–78 ppm. [10] Additionally, H-3 $\alpha$  had correlation with H-28 $_{\text{eq}}$  ( $\delta_{\text{H}}$  0.89) in its NOESY spectrum. Moreover, HMBC spectrum of **8** revealed structure of 3-acetoxy-16-oxo-lanosta-7,9 (11),24-trien-21-oic acid according to correlations of H-3 ( $\delta_{\text{H}}$  4.52)/C-1 ( $\delta_{\text{C}}$  35.2)/C-5 ( $\delta_{\text{C}}$  49.2) and C-1' ( $\delta_{\text{C}}$  171.0), H-7 ( $\delta_{\text{H}}$  5.48)/C-5 ( $\delta_{\text{C}}$  49.2) and C-14 ( $\delta_{\text{C}}$  44.2), H-11 ( $\delta_{\text{H}}$  5.39)/C-10 ( $\delta_{\text{C}}$  37.6), and C-13 ( $\delta_{\text{C}}$  42.4), H-18 ( $\delta_{\text{H}}$  0.72)/C-12 ( $\delta_{\text{C}}$  34.9)/C-13 ( $\delta_{\text{C}}$  42.4) /C-14 ( $\delta_{\text{C}}$  44.2) and C-17 ( $\delta_{\text{C}}$  57.0), H-19 ( $\delta_{\text{H}}$  1.02)/C-1 ( $\delta_{\text{C}}$  35.2)/C-5 ( $\delta_{\text{C}}$  49.2)/C-9 ( $\delta_{\text{C}}$

146.1) and C-10 ( $\delta_{\text{C}}$  37.6), H-24 ( $\delta_{\text{H}}$  5.13)/C-26 ( $\delta_{\text{C}}$  17.7)/C-27 ( $\delta_{\text{C}}$  25.7), H-26 ( $\delta_{\text{H}}$  1.59) and H-27 ( $\delta_{\text{H}}$  1.68)/C-24 ( $\delta_{\text{C}}$  123.3) and C-25 ( $\delta_{\text{C}}$  132.4), H-28 ( $\delta_{\text{H}}$  0.89) and H-29 ( $\delta_{\text{H}}$  0.96)/C-3 ( $\delta_{\text{C}}$  80.5)/C-4 ( $\delta_{\text{C}}$  37.5) and C-5 ( $\delta_{\text{C}}$  49.2), H-30 ( $\delta_{\text{H}}$  1.11)/C-8 ( $\delta_{\text{C}}$  139.4)/C-13 ( $\delta_{\text{C}}$  42.4) and C-14 ( $\delta_{\text{C}}$  44.2) and H-2' ( $\delta_{\text{H}}$  2.07)/C-1' ( $\delta_{\text{C}}$  171.0). Therefore, **8** was established as 3 $\beta$ -acetoxy-16-oxo-lanosta-7,9 (11),24-trien-21-oic acid, and was named as pinicolasin H.

Pinicolasin I (**9**) has a molecular formula of  $\text{C}_{32}\text{H}_{48}\text{O}_5$  based on the sodiated pseudomolecular ion peak at  $m/z$  535.3392 ( $[\text{M}+\text{Na}]^+$ ) in the HRESIMS analysis. Comparison of  $^1\text{H}$  and  $^{13}\text{C}$  NMR spectra of **9** with those of **7** indicated that the majority of the signals were similar except the presence of an oxygenated methine ( $\delta_{\text{H}}$  4.31, dd,  $J = 9.8, 5.8$  Hz;  $\delta_{\text{C}}$  74.4) and the disappearance of a carbonyl signal ( $\delta_{\text{C}}$  217.2). Therefore, a skeleton of 3-acetoxy-hydroxy-lanosta-7,9 (11),24-trien-21-oic acid was confirmed [24]. The position of the additional hydroxyl group was assigned at C-15 based on HMBC correlations of H-15 ( $\delta_{\text{H}}$  4.31) with C-8 ( $\delta_{\text{C}}$  140.5) and C-30 ( $\delta_{\text{C}}$  22.5). In addition, H-15 had an NOE effect with H-18 $_{\text{ax}}$  ( $\delta_{\text{H}}$  0.69) indicating the  $\beta$  orientation of H-15. The orientation of H-3 was assigned to be  $\beta$  via the chemical shift of C-3 ( $\delta_{\text{C}}$  78.0) and the splitting pattern of H-3 (t,  $J = 2.8$  Hz). Moreover, NOE effect of H-3 ( $\delta_{\text{H}}$  4.67) with H-29 $_{\text{ax}}$  ( $\delta_{\text{H}}$  0.98) also confirmed the  $\beta$  orientation of H-3. Thus, the structure of **9** was concluded to be 3 $\alpha$ -acetoxy-15 $\alpha$ -hydroxy-lanosta-7,9 (11),24-trien-21-oic acid.

Pinicolasin J (**10**) was purified as a white powder with a molecular formula of  $\text{C}_{37}\text{H}_{56}\text{O}_8$  on the basis of HRESIMS analytical data ( $[\text{M}+\text{Na}]^+$ ,  $m/z$  651.3870). detailed analysis of its  $^1\text{H}$  and  $^{13}\text{C}$  NMR spectra revealed a lanosta-7,9,24-trien-21-oic acid skeleton [25] and the same side chain, 4-carboxymethyl-3-hydroxy-3-methylbutanoyl as that in **6** was observed based on the proton signals at  $\delta_{\text{H}}$  2.69 (d,  $J = 2.8$  Hz), 1.35 (s), 2.68 (d,  $J = 4.3$  Hz), and 3.64 (s) and the carbon signals at  $\delta_{\text{C}}$  172.4, 46.0, 70.9, 28.2, 46.5, 173.2, and 52.1 [10]. HMBC spectral analysis confirmed the linkage via H-3 with C-1'/C-2', H-2' with C-4'/C-5', H-5' with C-2'/C-4'/C-6', OMe-6' with C-6', and H-4' with C-2'/C-3'/C-5', respectively. Moreover, H-3 $\beta$  ( $\delta_{\text{H}}$  4.70, t,  $J = 2.5$  Hz) with smaller coupling constant had NOE correlation with H-29 $_{\text{ax}}$  ( $\delta_{\text{H}}$  1.03) in the NOESY spectrum indicating the  $\alpha$  linkage of the side chain [10]. Additionally, 16 $\alpha$ -hydroxy substitution was assigned based on the HMBC correlations from H-16 ( $\delta_{\text{H}}$  4.03, t,  $J = 7.0$  Hz) to C-14 ( $\delta_{\text{C}}$  50.0) and C-20 ( $\delta_{\text{C}}$  48.6), and the observed NOE effect between H-16 and H-18 $_{\text{ax}}$  ( $\delta_{\text{H}}$  0.64). Thus, the structure of **10** was confirmed as 3 $\alpha$ -[4'-carboxymethyl-3'-hydroxy-3'-methylbutanoyloxy]-16 $\alpha$ -hydroxy-lanosta-7,9 (11),24-trien-21-oic acid.

The molecular formula of **11** was assigned as  $\text{C}_{33}\text{H}_{50}\text{O}_5$  based on the HRESIMS analytical data ( $[\text{M}+\text{Na}]^+$ ,  $m/z$  549.3549). Its  $^1\text{H}$  and  $^{13}\text{C}$  NMR spectra had the typical acetoxy signals at  $\delta_{\text{H}}$  2.07 and  $\delta_{\text{C}}$  170.8, 21.3. The remaining signals consisted of seven methylenes, ten methylenes including a terminal methylene ( $\delta_{\text{H}}$  4.77, s;  $\delta_{\text{H}}$  4.74, s;  $\delta_{\text{C}}$  107.1), five methines including one oxygenated signal ( $\delta_{\text{H}}$  4.67, t,  $J = 2.6$  Hz), and nine quaternary carbons including two carbonyl signals ( $\delta_{\text{C}}$  217.9 and 179.9). Analysis of the terminal methylene revealed a lanostane-type  $\text{C}_{31}$  triterpenoid basic skeleton based on the HMBC correlations of H-31 ( $\delta_{\text{H}}$  4.77 and 4.74) with C-23 ( $\delta_{\text{C}}$  32.0), C-24 ( $\delta_{\text{C}}$  154.7), C-25 ( $\delta_{\text{C}}$  33.6) [10,26]. Moreover, C-16 carbonyl was determined according to the HMBC correlations of H-15 ( $\delta_{\text{H}}$  1.96, 2.35)/C-16 ( $\delta_{\text{C}}$  217.9) and H-17 ( $\delta_{\text{H}}$  2.60, t,  $J = 9.7$  Hz)/C-16. Additionally, the chemical shift and splitting pattern of H-3 ( $\delta_{\text{H}}$  4.67, t,  $J = 2.6$  Hz) and C-3 ( $\delta_{\text{C}}$  77.8) indicated the  $\beta$  orientation of H-3. Therefore, **11** was confirmed as 3 $\alpha$ -acetoxy-16-oxo-lanosta-8,24 (31)-dien-21-oic acid.

Pinicolasin L (**12**) had a molecular formula of  $\text{C}_{33}\text{H}_{52}\text{O}_5$  deduced from HRESIMS pseudomolecular ion peak at  $m/z$  551.3709. Its  $^1\text{H}$  and  $^{13}\text{C}$  NMR had the signals characteristic for a lanostane-type  $\text{C}_{31}$  triterpenoid [10,26]. Comparison of its spectra with those of **11** revealed the presence of one additional hydroxyl in **12** and disappearance of the carbonyl signal detected in **11** confirming a skeleton of 3-acetoxy-hydroxy-lanosta-8,24(31)-dien-21-oic acid. The hydroxyl functionality was determined to be at C-15 based on the HMBC correlation from H-15

( $\delta_{\text{H}}$  4.25) to C-30 ( $\delta_{\text{C}}$  17.0), and H-15 was in the  $\beta$  orientation due to the NOE effect of H-15/H-18<sub>ax</sub> ( $\delta_{\text{H}}$  0.81). Furthermore, NOE effect was detected between H-3 ( $\delta_{\text{H}}$  4.66) and H-29<sub>ax</sub> ( $\delta_{\text{H}}$  0.91) indicating the  $\beta$  orientation of H-3. Moreover, the NOE correlations of H-18<sub>ax</sub>/H-15 and H-18<sub>ax</sub>/H-20 indicated the orientation of substitutions at C-13, -15, and -20 to be  $\beta$ ,  $\alpha$ , and  $\alpha$ , respectively, as shown in Fig. 3. Consequently, the structure of **12** was confirmed as 3 $\alpha$ -acetoxy-15 $\alpha$ -hydroxy-lanostan-8,24(31)-dien-21-oic acid.

The HRESIMS analytical data of **13** ( $[\text{M}+\text{Na}]^+$ ,  $m/z$  547.3395) established its molecular formula as C<sub>33</sub>H<sub>48</sub>O<sub>5</sub>. Its IR spectra had absorption peaks at 3701 (OH), 1733 (carbonyl) and 1607 (conjugated double bonds) cm<sup>-1</sup>. Based on the <sup>1</sup>H and <sup>13</sup>C NMR signals of  $\delta_{\text{H}}$  4.78 (1H, s),  $\delta_{\text{H}}$  4.75 (1H, s), and  $\delta_{\text{C}}$  107.2 and comparison of its spectra with those of **12** and **7**, a lanostane-type C<sub>31</sub> triterpenoid skeleton was confirmed [10,26]. Combination of the IR and NMR spectral signals of  $\delta_{\text{H}}$  5.50 (1H, t,  $J$  = 4.0 Hz) and 5.41 (1H, d,  $J$  = 6.3 Hz) and four olefinic carbons ( $\delta_{\text{C}}$  122.2, 139.4, 146.1 and 111.5),  $\Delta^{7,8}$  and  $\Delta^{9,11}$  were assigned. Detailed HMBC analytical results also supported this assignment via the correlations from H-7( $\delta_{\text{H}}$  5.50) to C-5 ( $\delta_{\text{C}}$  44.2) and C-14 ( $\delta_{\text{C}}$  44.3); from H-11 ( $\delta_{\text{H}}$  5.41) to C-10 ( $\delta_{\text{C}}$  37.5) and C-13 ( $\delta_{\text{C}}$  42.5); from H-19 ( $\delta_{\text{H}}$  0.97) to C-9 ( $\delta_{\text{C}}$  146.1); and from H-30 ( $\delta_{\text{H}}$  1.12) to C-8 ( $\delta_{\text{C}}$  139.4), respectively. Moreover, a typical 3-acetoxy group and a C-16 carbonyl group were detected by 2D-NMR experimental analysis. Its NOESY spectrum had a correlation between H-3 $\beta$  ( $\delta_{\text{H}}$  4.69, t,  $J$  = 2.9 Hz) and H-29<sub>ax</sub> ( $\delta_{\text{H}}$  1.00) supporting a 3 $\alpha$ -acetoxy substitution. Thus, **13** was confirmed as 3 $\alpha$ -acetoxy-16-oxo-lanosta-7,9,24(31)-trien-21-oic acid, and was trivially named as pinicolasin M.

In addition to these thirteen undescribed triterpenoids, twenty-one known constituents were identified, including trametenolic acid **B** (**14**), 16 $\alpha$ -hydroxytrametenolic acid (**15**), 3 $\alpha$ -acetoxy-lanosta-8,24-dien-21-oic acid (**16**), fomipinic acid **C** (**17**), 3 $\alpha$ -acetoxy-16-oxolanosta-8,24-dien-21-oic acid (**18**), 3 $\beta$ -acetoxy-15 $\alpha$ -hydroxy-lanosta-8,24-dien-21-oic acid (**19**), 3 $\beta$ -acetyl-16 $\alpha$ -hydroxytrametenolic acid (**20**), pinicolinic acid **E** (**21**), 16 $\alpha$ -hydroxy-3-oxolanosta-7,9(11),24-trien-21-oic acid (**22**), 6 $\alpha$ ,16 $\alpha$ -dihydroxy-3-oxolanosta-7,9(11),24-trien-21-oic acid (**23**), pipitolinic acid **D** (**24**), 3 $\alpha$ ,16 $\alpha$ -dihydroxy-lanosta-7,9(11),24-trien-21-oic acid (**25**), 3 $\beta$ ,16 $\alpha$ -dihydroxy-lanosta-7,9(11),24-trien-21-oic acid (**26**), tumulosic acid (**27**), 3 $\alpha$ -pachymic acid (**28**), pachymic acid (**29**), 3-*epi*-dehydro-pachymic acid (**30**), dehydrotumulosic acid (**31**), 6 $\alpha$ -hydroxy-poly-porenic acid **C** (**32**), poly-porenic acid **C** (**33**) and daedalenic acid **A** (**34**) (references are provided in Supporting Information). The anti-inflammatory activities of the thirty-two compounds isolated in sufficient quantity were evaluated in a human neutrophil cell model to test their inhibition of the production of superoxide anion and elastase in human neutrophils activated with *N*-formyl-L-methionyl-L-leucyl-L-phenylalanine/cytochalasin B (fMLF/CB). Compound **10** with a 4-carboxymethyl-3-hydroxy-3-methyl-butanoyl side chain had the most potent antiinflammatory activity with the IC<sub>50</sub> of 1.81  $\pm$  0.44  $\mu\text{M}$  for inhibition of superoxide anion generation and the IC<sub>50</sub> of 2.50  $\pm$  0.64  $\mu\text{M}$  for inhibition of elastase release. Compound **6** with the same side chain also demonstrated good inhibition of superoxide anion generation with the IC<sub>50</sub> of 4.77  $\pm$  0.97  $\mu\text{M}$  and inhibition of elastase release with the IC<sub>50</sub> of 6.66  $\pm$  0.30  $\mu\text{M}$  for; the reference compound was genistein (IC<sub>50</sub> 1.62  $\pm$  0.14  $\mu\text{M}$  for superoxide anion generation and IC<sub>50</sub> of 35.95  $\pm$  1.53  $\mu\text{M}$  for inhibition of elastase release). Generally, C-3 carbonyl-bearing compounds had inferior antiinflammatory activity. Differences in the receptor-binding mode or different mechanisms of action may account for these results because no clear structure-activity relationship was observed.

#### 4. Conclusions

Thus, a total of thirty-four triterpenoids, including twelve undescribed compounds, were isolated from *Fomitopsis pinicola* (Sw.) P. Karst. Their structures were characterized by spectroscopic and spectrometric analyses as C<sub>30</sub> or C<sub>31</sub> lanostane-type triterpenoids. Antiinflammatory

activity of thirty-two purified compounds was tested using superoxide anion generation and elastase release as biomarkers. Compound **10** with a 4-carboxymethyl-3-hydroxy-3-methyl-butanoyl side chain had the most potent antiinflammatory activity for inhibition of superoxide anion generation and elastase release. Among all the tested isolates, compounds with C-3 carbonyl had inferior antiinflammatory activity and compounds with a 4-carboxymethyl-3-hydroxy-3-methyl-butanoyl side chain had good antiinflammatory activity. This study provides evidence supporting the use of *Fomitopsis pinicola* in nutritional supplements and as a lead in drug discovery.

#### Declaration of Competing Interest

The authors declare that they have no known competing financial interests or personal relationships that could have appeared to influence the work reported in this paper.

#### Acknowledgements

This study was sponsored by the Ministry of Science and Technology, Taiwan. Authors are thankful to Chang Gung Memorial Hospital (CMRPD1B0281~3, CMRPF1D0442~3, CMRPF 1F0011~3, CMRPF1F0061~3 and BMRP450 granted to T.-L.H.) for the partial financial support of the present study. Thanks Dr. He-Ping Chen at School of Pharmaceutical Sciences, South-Central University for Nationalities for correcting some mistakes.

#### Appendix A. Supplementary material

Supplementary data to this article can be found online at <https://doi.org/10.1016/j.bioorg.2020.104562>.

#### References



- [1] J.-E. Haight, G.A. Laursen, J.A. Glaeser, D.L. Taylor, Phylogeny of *Fomitopsis pinicola*: a species complex, *Mycologia* 108 (2016) 925–938.
- [2] U. Grienke, M. Zöll, U. Peintner, J.M. Rollinger, European medicinal polypores – a modern view on traditional uses, *J. Ethnopharmacol.* 154 (2014) 564–583.
- [3] D. Choi, S.-S. Park, J.-L. Ding, W.-S. Cha, Effects of *Fomitopsis pinicola* extracts on antioxidant and antitumor activities, *Biotechnol. Bioprocess Eng.* 12 (2007) 516–524.
- [4] S.I. Lee, J.S. Kim, S.H. Oh, K.Y. Park, H.G. Lee, S.D. Kim, Antihyperglycemic effect of *Fomitopsis pinicola* extracts in streptozotocin-induced diabetic rats, *J. Med. Food* 11 (2008) 518–524.
- [5] W.-S. Cha, J.-L. Ding, H.-J. Shin, J.-S. Kim, Y.-S. Kim, D. Choi, H.-D. Lee, H.-B. Kang, C.-W. Lee, Effect of *Fomitopsis pinicola* extract on blood glucose and lipid metabolism in diabetic rats, *Korean J. Chem. Eng.* 26 (2009) 1696–1699.
- [6] K.S. Bishop, Characterisation of extracts and anti-cancer activities of *Fomitopsis pinicola*, *Nutrients* 12 (2020) 609–619.
- [7] A.C. Keller, M.P. Maillard, K. Hostettmann, Antimicrobial steroids from the fungus *Fomitopsis pinicola*, *Phytochemistry* 41 (1996) 1041–1046.
- [8] K. Yoshikawa, M. Inoue, Y. Matsumoto, C. Sakakibara, H. Miyatake, H. Matsumoto, S. Arihara, Lanostane triterpenoids and triterpene glycosides from the fruit body of *Fomitopsis pinicola* and their inhibitory activity against COX-1 and COX-2, *J. Nat. Prod.* 68 (2005) 69–73.
- [9] Y. Wang, X. Cheng, P. Wang, L. Wang, J. Fan, X. Wang, Q. Liu, Investigating migration inhibition and apoptotic effects of *Fomitopsis pinicola* chloroform extract on human colorectal cancer SW-480 cells, *PLoS one* 9 (2014), e101303.
- [10] X.R. Peng, H.G. Su, J.H. Liu, Y.J. Huang, X.Z. Yang, Z.R. Li, L. Zhou, M.H. Qiu, C30 and C31 triterpenoids and triterpene sugar esters with cytotoxic activities from edible mushroom *Fomitopsis pinicola* (Sw. Ex Fr.) Krast, *J. Agric. Food Chem.* 67 (2019) 10330–10341.
- [11] S.-H. Tai, P.-C. Kuo, C.-C. Hung, Y.-H. Lin, T.-L. Hwang, S.H. Lam, D.-H. Kuo, J.-B. Wu, H.-Y. Hung, T.-S. Wu, Bioassay-guided purification of sesquiterpenoids from the fruiting bodies of *Fomitopsis pinicola* and their anti-inflammatory activity, *RSC Adv.* 9 (2019) 34184–34195.
- [12] K.M. Pietrosimone, P. Liu, Contributions of neutrophils to the adaptive immune response in autoimmune disease, *World J. Transl. Med.* 4 (2015) 60–68.
- [13] S.C. Yang, P.J. Chung, C.M. Ho, C.Y. Kuo, M.F. Hung, Y.T. Huang, W.Y. Chang, Y. W. Chang, K.H. Chan, T.L. Hwang, Propofol inhibits superoxide production, elastase release, and chemotaxis in formyl peptide-activated human neutrophils by blocking formyl peptide receptor 1, *J. Immunol.* 190 (2013) 6511–6519.
- [14] T. Kamo, M. Asanoma, H. Shibata, M. Hirota, Anti-inflammatory lanostane-type triterpene acids from *Piptoporus betulinus*, *J. Nat. Prod.* 66 (2003) 1104–1106.



- [15] Z. Tohtahon, J.J. Xue, J.X. Han, Y.S. Liu, H.M. Hua, T. Yuan, Cytotoxic lanostane triterpenoids from the fruiting bodies of *Piptoporus betulinus*, *Phytochemistry* 143 (2017) 98–103.
- [16] L. Zhou, Y.C. Zhang, L.A. Gapter, H. Ling, R. Agarwal, K.Y. Ng, Cytotoxic and anti-oxidant activities of lanostane-type triterpenes isolated from *Poria cocos*, *Chem. Pharm. Bull. (Tokyo)* 56 (2008) 1459–1462.
- [17] T. Akihisa, T. Hori, H. Suzuki, T. Sakoh, 24 $\beta$ -Methyl-5 $\alpha$ -cholest-9(11)en-3 $\beta$ -ol, two 24 $\beta$ -alkyl- $\Delta^{5,7,9(11)}$ -sterols and other 24 $\beta$ -alkylsterols from *Chlorella vulgaris*, *Phytochemistry* 31 (1992) 1769–1772.
- [18] T. Akihisa, W.C.M.C. Kokke, J.A. Krause, D.S. Eggleston, S. Katayama, Y. Kimura, T. Tamura, 5-Dehydrokarounidiol [D:C-Friedo-oleana-5,7,9(11)-triene-3 $\alpha$ ,29-diol], a novel triterpene from *Trichosanthes kirilowii* Maxim, *Chem. Pharm. Bull.* 40 (1992) 3280–3283.
- [19] M. Uklya, T. Akihisa, H. Tokuda, M. Hirano, M. Oshikubo, Y. Nobukuni, Y. Kimura, T. Tai, S. Kondo, H. Nishino, Inhibition of tumor-promoting effects by poricoic acids G and H and Other lanostane-type triterpenes and cytotoxic activity of poricoic acids A and G from *Poria cocos*, *J. Nat. Prod.* 65 (2002) 462–465.
- [20] J. Zhang, B. Chen, J. Liang, J. Han, L. Zhou, R. Zhao, H. Liu, H. Dai, Lanostane triterpenoids with PTP1B inhibitory and glucose-uptake stimulatory activities from mushroom *Fomitopsis pinicola* collected in North America, *J. Agric. Food Chem.* 68 (2020) 10036–10049.
- [21] I. Sofrenić, B. Andelković, N. Todorović, T. Stanojković, L. Vujisić, M. Novaković, S. Milosavljević, V. Tešević, Cytotoxic triterpenoids and triterpene sugar esters from the medicinal mushroom *Fomitopsis betulina*, *Phytochemistry* 181 (2021), 112580.
- [22] Y.-M. Ying, W.-G. Shan, L.-W. Zhang, Y. Chen, Z.-J. Zhan, Lanostane triterpenes from *Ceriporia lacerate* HS-ZJUT-C13A, a fungal endophyte of *Huperzia serrata*, *Helvetica Chimica Acta* 96 (2013) 2092–2097.
- [23] M. Hirotani, I. Asaka, C. Ino, T. Furuya, M. Shiro, Ganoderic acid derivatives and ergosta-4,7,22-triene-3,6-dione form *Ganoderma lucidum*, *Phytochemistry* 26 (1987) 2797–2803.
- [24] T. Tai, T. Shingu, T. Kikuchi, Y. Tezuka, A. Akahori, Isolation of lanostane-type triterpene acids having an acetoxyl group from sclerotia of *Poria cocos*, *Phytochemistry* 40 (1995) 225–231.
- [25] K.H. Lai, M.C. Lu, Y.C. Du, M. El-Shazly, T.Y. Wu, Y.M. Hsu, A. Henz, J.C. Yang, A. Backlund, F.R. Chang, Y.C. Wu, Cytotoxic lanostanoids from *Poria cocos*, *J. Nat. Prod.* 79 (2016) 2805–2813.
- [26] T. Shingu, T. Tai, A. Akahori, A lanostane triterpenoid from *Poria cocos*, *Phytochemistry* 31 (1992) 2548–2549.

Review

# Natural Products from Octocorals of the Genus *Dendronephthya* (Family Nephtheidae)

Yung-Husan Chen <sup>1</sup>, Yu-Chia Chang <sup>2</sup>, Yu-Hsin Chen <sup>3</sup>, Li-Guo Zheng <sup>3,4</sup>, Pin-Chang Huang <sup>3,4</sup>, Thanh-Hao Huynh <sup>3,5</sup>, Bo-Rong Peng <sup>3,4,6</sup>, You-Ying Chen <sup>3,5</sup>, Yu-Jen Wu <sup>7</sup>, Lee-Shing Fang <sup>5,8,9</sup>, Jui-Hsin Su <sup>3,10</sup>, Chang-Min Hsu <sup>11,\*</sup> and Ping-Jyun Sung <sup>3,5,10,12,13,\*</sup>

<sup>1</sup> Department of Pharmacy, Xiamen Medical College, Xiamen 361023, Fujian, China; cyxuan@xmmc.edu.cn

<sup>2</sup> Research Center for Chinese Herbal Medicine, Graduate Institute of Healthy Industry Technology, College of Human Ecology, Chang Gung University of Science and Technology, Taoyuan 333324, Taiwan; ycchang03@mail.cgu.edu.tw

<sup>3</sup> National Museum of Marine Biology and Aquarium, Pingtung 944401, Taiwan; kb5634@yahoo.com.tw (Y.-H.C.); t0919928409@gmail.com (L.-G.Z.); foter25632@gmail.com (P.-C.H.); haohuynh0108@gmail.com (T.-H.H.); pengpojung@gmail.com (B.-R.P.); zoeblack0108@gmail.com (Y.-Y.C.); x2219@nmmba.gov.tw (J.-H.S.)

<sup>4</sup> Doctoral Degree Program in Marine Biotechnology, National Sun Yat-sen University, Kaohsiung 804201, Taiwan

<sup>5</sup> Department of Marine Biotechnology and Resources, National Sun Yat-sen University, Kaohsiung 804201, Taiwan; lsfang@csu.edu.tw

<sup>6</sup> Doctoral Degree Program in Marine Biotechnology, Academia Sinica, Taipei 115201, Taiwan

<sup>7</sup> Department of Food Science and Nutrition, Meiho University, Pingtung 912009, Taiwan; x00002180@meiho.edu.tw

<sup>8</sup> Center for Environmental Toxin and Emerging-Contaminant Research, Cheng Shiu University, Kaohsiung 833301, Taiwan

<sup>9</sup> Super Micro Mass Research and Technology Center, Cheng Shiu University, Kaohsiung 833301, Taiwan

<sup>10</sup> Graduate Institute of Marine Biology, National Dong Hwa University, Pingtung 944401, Taiwan

<sup>11</sup> Department of Immunology & Rheumatology, Antai Medical Care Corporation Antai Tian-Sheng Memorial Hospital, Pingtung 928004, Taiwan

<sup>12</sup> Chinese Medicine Research and Development Center, China Medical University Hospital, Taichung 404394, Taiwan

<sup>13</sup> Graduate Institute of Natural Products, Kaohsiung Medical University, Kaohsiung 807378, Taiwan

\* Correspondence: a094250@mail.tsm.org.tw (C.-M.H.); pjsung@nmmba.gov.tw (P.-J.S.); Tel.: +886-8-882-5037 (P.-J.S.); Fax: +886-8-882-5087 (P.-J.S.)

Received: 24 November 2020; Accepted: 15 December 2020; Published: 16 December 2020



**Abstract:** In this review, 170 natural substances, including steroid, diterpenoid, sesquiterpenoid, peptide, prostaglandin, base, chlorolipid, bicyclic lactone, amide, piperazine, polyketide, glycerol, benzoic acid, glycyrrhetyl amino acid, hexitol, pentanoic acid, aminoethyl ester, octadecanone, alkaloid, and a 53-kD allergenic component from octocorals belonging to genus *Dendronephthya*, were listed. Some of these compounds displayed potential bioactivities.

**Keywords:** octocoral; *Dendronephthya*; steroid; natural compound

## 1. Introduction

Octocorals of the genus *Dendronephthya* (phylum Cnidaria, class Anthozoa, subclass Octocorallia, order Alcyonacea, suborder Alcyoniina, family Nephtheidae) [1], distributed in the Indo-Pacific Ocean, have been investigated. Since the initial study in 1999 discovered four antifouling *seco*-steroids, isogosterones A–D (1–4), from an octocoral *Dendronephthya* sp. collected off the Izu Peninsula, Japan [2]

(Figure 1), subsequent studies over the past two decades have yielded a series of interesting secondary metabolites, particularly steroid metabolites. In this article, different types of compounds isolated from *Dendronephthya* spp., were summarized.

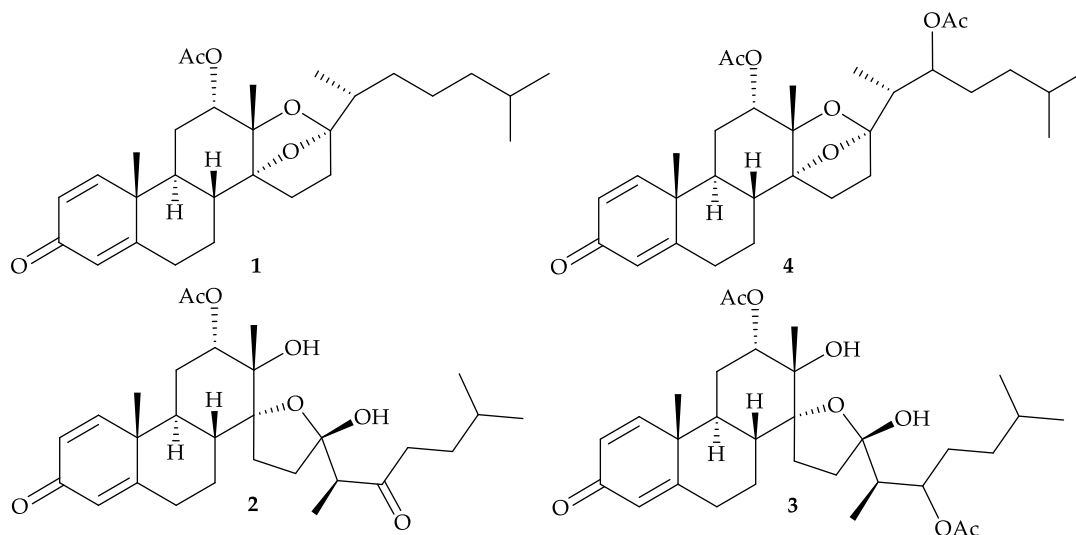


Figure 1. Structures of isogosterones A–D (1–4).

## 2. *Dendronephthya gigantea* (Verrill, 1864)

The *Dendronephthya* genus includes one common species, *D. gigantea*. Yoshikawa and colleagues isolated five polyhydroxylated sterols, including two new metabolites, dendronesterols A (5) and B (6), along with three known analogues, (22*E*,24*S*)-24-methyl-cholesta-7,22-diene-3 $\beta$ ,5 $\alpha$ ,6 $\beta$ ,9 $\alpha$ -tetrol (7) [3], (22*E*)-cholesta-7,22-diene-3 $\beta$ ,5 $\alpha$ ,6 $\beta$ ,9 $\alpha$ -tetrol (8) [3], and (22*E*)-24-norcholesta-7,22-diene-3 $\beta$ ,5 $\alpha$ ,6 $\beta$ -triol (9) [4,5] (Figure 2), from *D. gigantea* collected off the coast of Tokushima, Japan [6]. The study also established the structures of new sterols 5 and 6 by spectroscopic methods. A cytotoxic assay showed that sterol 6 had an IC<sub>50</sub> value of 5.2  $\mu$ g/mL in the treatment of L1210 (mouse lymphocytic leukemia) cells [6].

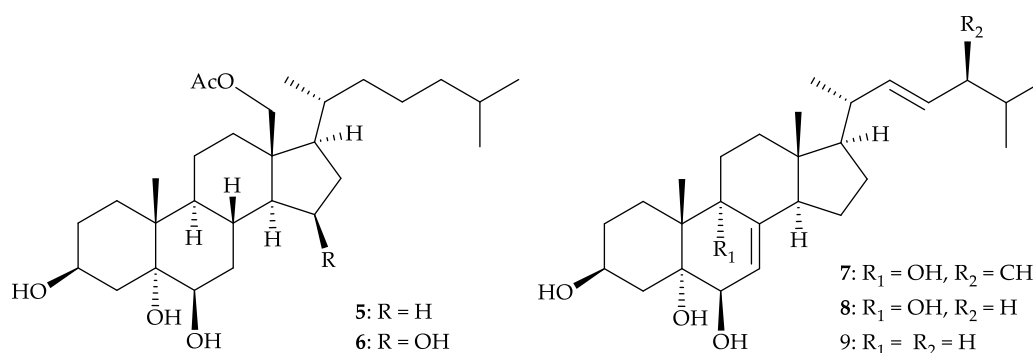
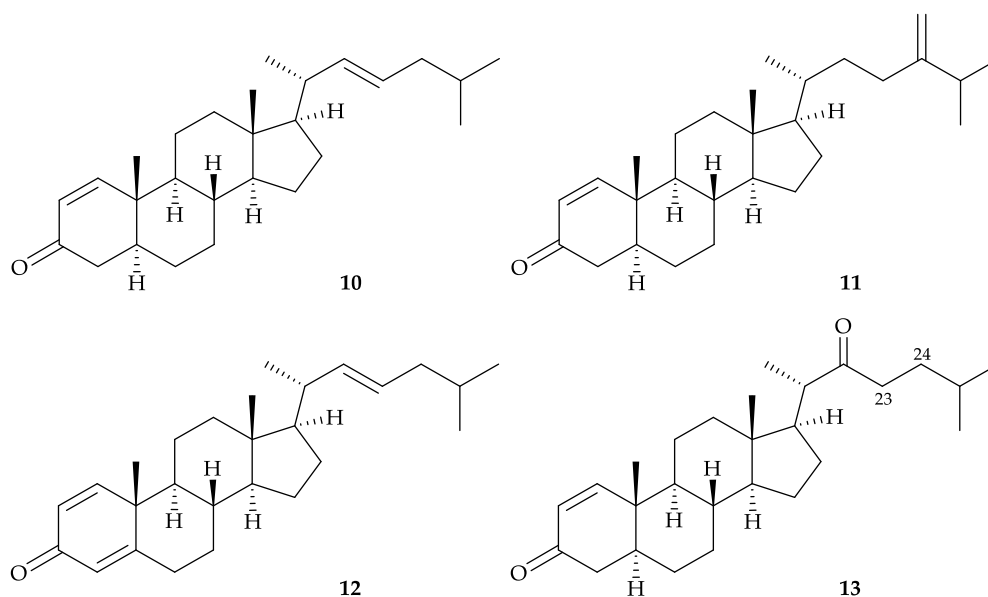


Figure 2. Structures of dendronesterols A (5) and B (6), (22*E*,24*S*)-24-methyl-cholesta-7,22-diene-3 $\beta$ ,5 $\alpha$ ,6 $\beta$ ,9 $\alpha$ -tetrol (7), (22*E*)-cholesta-7,22-diene-3 $\beta$ ,5 $\alpha$ ,6 $\beta$ ,9 $\alpha$ -tetrol (8), and (22*E*)-24-norcholesta-7,22-diene-3 $\beta$ ,5 $\alpha$ ,6 $\beta$ -triol (9).

In 2004, three new steroids, dendronesterones A–C (10–12), along with a known steroid, cholest-1-ene-3,22-dione (13) [7], were isolated from *D. gigantea*, collected at Green Island, off Taiwan [8] (Figure 3). Structures of steroids 10–13 were established by spectroscopic methods, and the <sup>1</sup>H and <sup>13</sup>C chemical shifts at C-23 and C-24 in steroid 13 were revised in this study. In the cytotoxic testing, steroids 10 and 13 had ED<sub>50</sub> values of 9.84 and 8.93  $\mu$ M, respectively, in the treatment of P-388

(mouse lymphoma) cells, and **13** was cytotoxic toward HT-29 (human colorectal adenocarcinoma) cells with an ED<sub>50</sub> value of 9.03  $\mu$ M [8].



**Figure 3.** Structures of dendronesterones A–C (**10–12**) and cholest-1-ene-3,22-dione (**13**).

Furthermore, two known metabolites, including a monoalkyl glycerol ether ( $\pm$ )-1-nonadecyloxy-2,3-propanediol (**14**) [9], a ceramide, (2*S*,3*R*,4*E*,8*E*)-*N*-hexadecanoyl-2-amino-4,8-octadecadiene-1,3-diol (**15**) [10–14], as well as two bases, thymine (**16**) and uracil (**17**), (Figure 4), were isolated from the organic extract of *D. gigantea*, collected in the area of Jeju Island, Korea [15]. The structures of metabolites **14–17** were established by spectroscopic methods and by comparison of their physical and spectral data with those of literature values and glycerol **14** was found to be cytotoxic toward A549 (human lung epithelial carcinoma), HT-29, HT-1080 (human connective tissue epithelial fibrosarcoma), and SNU-638 (human gastric adenocarcinoma) cells with IC<sub>50</sub> values of 15.1, 14.5, 13.7, and 15.5  $\mu$ g/mL, respectively [15]. Glycerol **14** was not optically active ( $[\alpha]_D^{25}$  0.00 (*c* 0.134, MeOH)), indicating that this compound is a racemic mixture. Thus, the stereogenic center C-2 in **14** was not determined [15]. Sphingolipid **15** showed cytotoxicity against human peripheral blood mononuclear cells (PBMC) with an ED<sub>50</sub> of 20  $\mu$ g/mL [13].

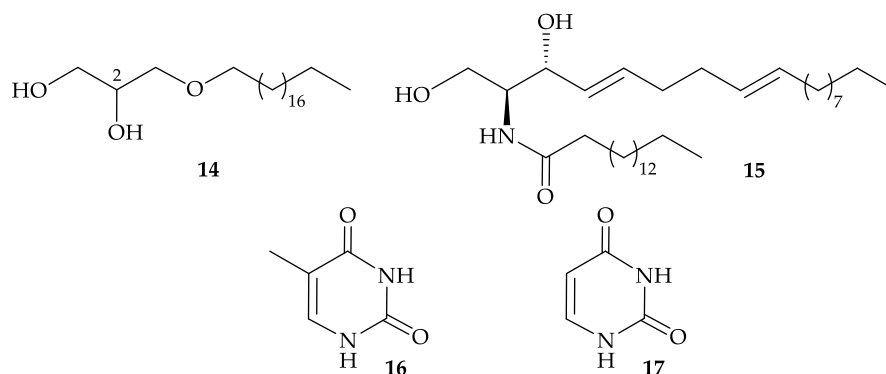


**Figure 4.** Structures of ( $\pm$ )-1-nonadecyloxy-2,3-propanediol (**14**) and (2*S*,3*R*,4*E*,8*E*)-*N*-hexadecanoyl-2-amino-4,8-octadecadiene-1,3-diol (**15**), thymine (**16**), and uracil (**17**).

Eight well known secondary metabolites, including (2*S*,3*R*,4*E*,8*E*)-*N*-hexadecanoyl-2-amino-4,8-octadecadiene-1,3-diol (**15**) [10–14] (Figure 4), (2*S*,3*R*,4*E*)-*N*-hexadecanoyl-2-amino-4-octadecane-1,3-

diol (**18**) [10,16], *N*-phenethylacetamide (**19**) [17–21], cyclo-(Leu-Pro) (**20**), cyclo-(Ala-Pro) (**21**), cyclo-(Val-Pro) (**22**) [22], 2,4-dichlorobenzonic acid (**23**) [23], thymidine (**24**) [24–32], 2'-deoxyuridine (**25**) [27–30,32,33], and cholesterol (**26**) [30] (Figure 5), were isolated from *D. gigantea*, collected from the South China Sea [34]. The structures of compounds **15** and **18–26** were elucidated by spectral data and by comparison with the spectral and physical data of other known compounds [34].

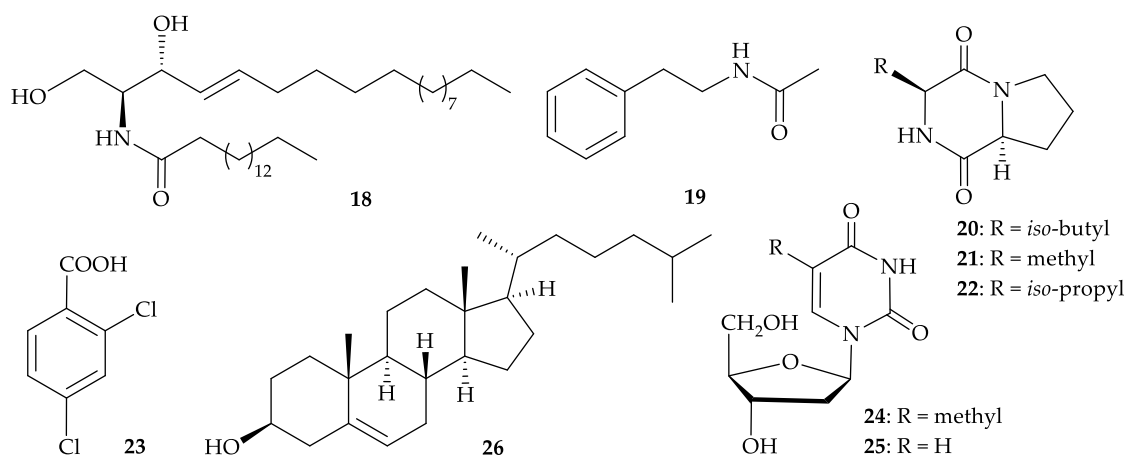


**Figure 5.** Structures of (2*S*,3*R*,4*E*)-*N*-hexadecanoyl-2-amino-4-octadecane-1,3-diol (**18**), *N*-phenethylacetamide (**19**), cyclo-(Leu-Pro) (**20**), cyclo-(Ala-Pro) (**21**), cyclo-(Val-Pro) (**22**), 2,4-dichlorobenzonic acid (**23**), thymidine (**24**), 2'-deoxyuridine (**25**), and cholesterol (**26**).

In 2012, six steroids, including three new compounds, 3-oxocholest-1,22-dien-12 $\beta$ -ol (**27**), 3-oxocholest-1,4-dien-20 $\beta$ -ol (**28**), 3-oxocholest-1,4-dien-12 $\beta$ -ol (**29**), along with three known analogues, (20*S*)-20-hydroxyergosta-1,4,24-trien-3-one (**30**) [35], 5 $\alpha$ ,8 $\alpha$ -epidioxycholesta-6,22-dien-3 $\beta$ -ol (**31**) [36], and 5-cholestene-3 $\beta$ ,12 $\beta$ -diol (**32**) [37] (Figure 6), were isolated from *D. gigantea*, collected near Geo-Je Island, South Korea [38]. The structures for steroids **27–32** were established by spectroscopic methods. Steroids **27–31** displayed inhibitory activity against farnesoid X-activated receptor (FXR) with IC<sub>50</sub>'s 14, 15, 100, 22, and 61  $\mu$ M, respectively, and were not cytotoxic toward the CV-1 cells (*Cercopithecus aethiops*, African green monkey kidney cells) [38].

In 2017, Jeon and Lee's group reported the isolation of a mixture consisting nine 3 $\beta$ -hydroxy- $\Delta^5$ -steroidal congeners, including 26,27-dinorergosta-5,22-dien-3 $\beta$ -ol (**33**) [39], cholesta-5,22-dien-3 $\beta$ -ol (including 22-*trans* form **34** and 22-*cis* form **35**) [40], cholest-5-en-3 $\beta$ -ol (= cholesterol) (**26**) [30] (Figure 5), ergosta-5,22-dien-3 $\beta$ -ol (**36**) [41], stigmasta-5,24-dien-3 $\beta$ -ol (= fucosterol) (**37**) [42–48], stigmasta-5,22-dien-3 $\beta$ -ol (**38**) [48], stigmasta-5-en-3 $\beta$ -ol (**39**) [48], and 22,23-methylenecholesterol (**40**) [49] (Figure 7), from *D. gigantea* collected from Jeju Island, South Korea [50]. The structures for all sterols **26** and **33–40** were determined by GC-MS/MS analysis. In lipopolysaccharides (LPS)-stimulated RAW cells, this mixture inhibited nitric oxide (NO) and prostaglandin E<sub>2</sub> (PGE<sub>2</sub>) production via the downregulation of inducible nitric oxide synthase (iNOS) and cyclooxygenase-2 (COX-2) inflammatory mediators. This sterol-rich mixture also suppressed the expression of proinflammatory cytokines, including tumor necrosis factor- $\alpha$  (TNF- $\alpha$ ), interleukin 1 $\beta$  (IL-1 $\beta$ ), and interleukin 6 (IL-6). The anti-inflammatory effects of this sterol-rich mixture was confirmed in an LPS-stimulated in vivo zebrafish model by the downregulation of iNOS and COX-2 expression, inhibition of NO and reactive oxygen species (ROS) levels, and increased cytoprotective effects against LPS-induced toxicity [50]. Furthermore, this sterol-rich fraction was found to exhibit cytotoxicity toward HL-60 (human acute promyelocytic leukemia) and MCF-7 (Michigan Cancer Foundation-7, human invasive ductal carcinoma) cells with IC<sub>50</sub> values of 13.59 and 29.41  $\mu$ g/mL [51], and one of the mixtures, stigmasta-5-en-3 $\beta$ -ol (**39**), displayed cytotoxicity on HL-60 and MCF-7 cells with IC<sub>50</sub> values of 37.82 and 45.17  $\mu$ g/mL, respectively [52].



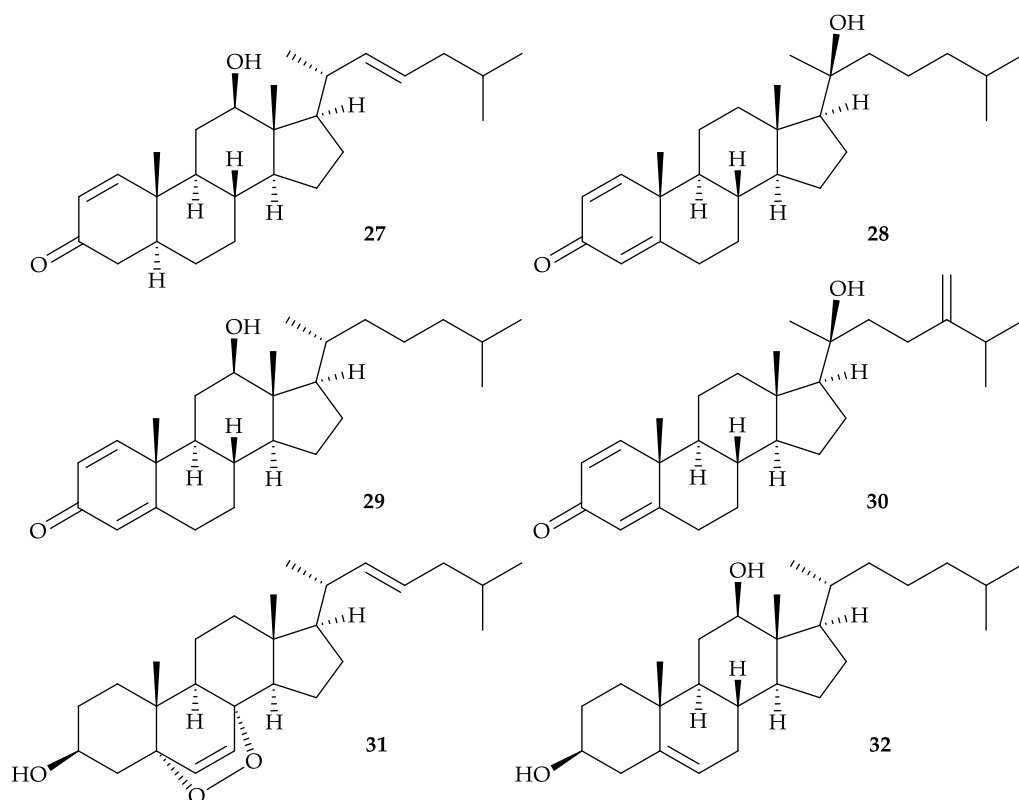


**Figure 6.** Structures of 3-oxocholest-1,22-dien-12 $\beta$ -ol (27), 3-oxocholest-1,4-dien-20 $\beta$ -ol (28), 3-oxo-cholest-1,4-dien-12 $\beta$ -ol (29), (20S)-20-hydroxyergosta-1,4,24-trien-3-one (30), 5 $\alpha$ ,8 $\alpha$ -epidioxycholesta-6,22-dien-3 $\beta$ -ol (31), and 5-cholestene-3 $\beta$ ,12 $\beta$ -diol (32).

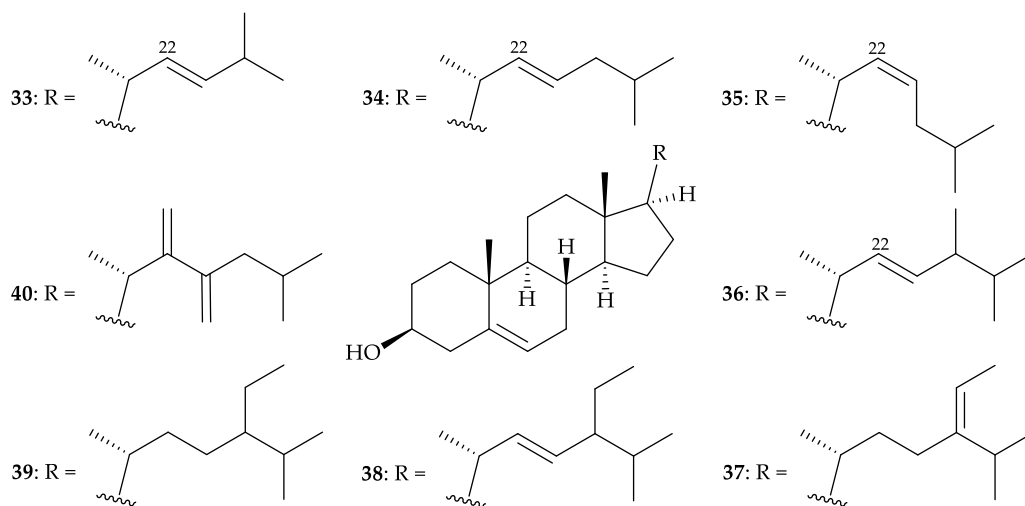


**Figure 7.** Structures of 26,27-dinorergosta-5,22-dien-3 $\beta$ -ol (33), cholesta-5,22-dien-3 $\beta$ -ol (including 22-*trans* form 34 and 22-*cis* form 35), ergosta-5,22-dien-3 $\beta$ -ol (36), stigmasta-5,24-dien-3 $\beta$ -ol (= fucosterol) (37), stigmasta-5,22-dien-3 $\beta$ -ol (38), stigmasta-5-en-3 $\beta$ -ol (39), and 22,23-methylene-cholesterol (40).

Fifteen steroids, including four new compounds, 7-dehydroerectasteroid F (41), 11 $\alpha$ -acetoxyarmatinol A (42), 22,23-didehydroarmatinol A (43), and 3-O-acetylhyrtiosterol (44), as well as 11 known steroids, 24-methylene-5-cholesten-3 $\beta$ ,7 $\beta$ -diol (45) [53], 24-methylene-5-cholesten-3 $\beta$ ,19-diol (= litosterol) (46) [54], 24-methylene-5-cholesten-3 $\beta$ ,19-diol-7 $\beta$ -monoacetate (47) [55], 5,6-epoxylitosterol (48) [54], armatinol A (49) [56], hyrtiosterol (50) [57,58], (2 $\beta$ ,3 $\beta$ ,4 $\alpha$ ,5 $\alpha$ ,8 $\beta$ ,11 $\beta$ )-4-

methylergost-24-ene-2,3,8,11-tetrol (**51**) [58], and erectasteroids C–F (**52–55**) [59] (Figure 8), were isolated from *D. gigantea*, collected from the inner coral reef of Meishan, Hainan Province, China [60]. The structures of new steroids **41–43** were elucidated by comprehensive spectroscopic analysis and steroid **41** was found to show protection against hydrogen-peroxide ( $H_2O_2$ )-induced oxidative damage in neuron-like PC-12 (rat adrenal gland pheochromocytoma) cells by promoting nuclear translocation of nuclear factor erythroid 2-related factor 2 (Nrf2) and enhancing the expression of heme oxygenase-1 (HO-1) [60].

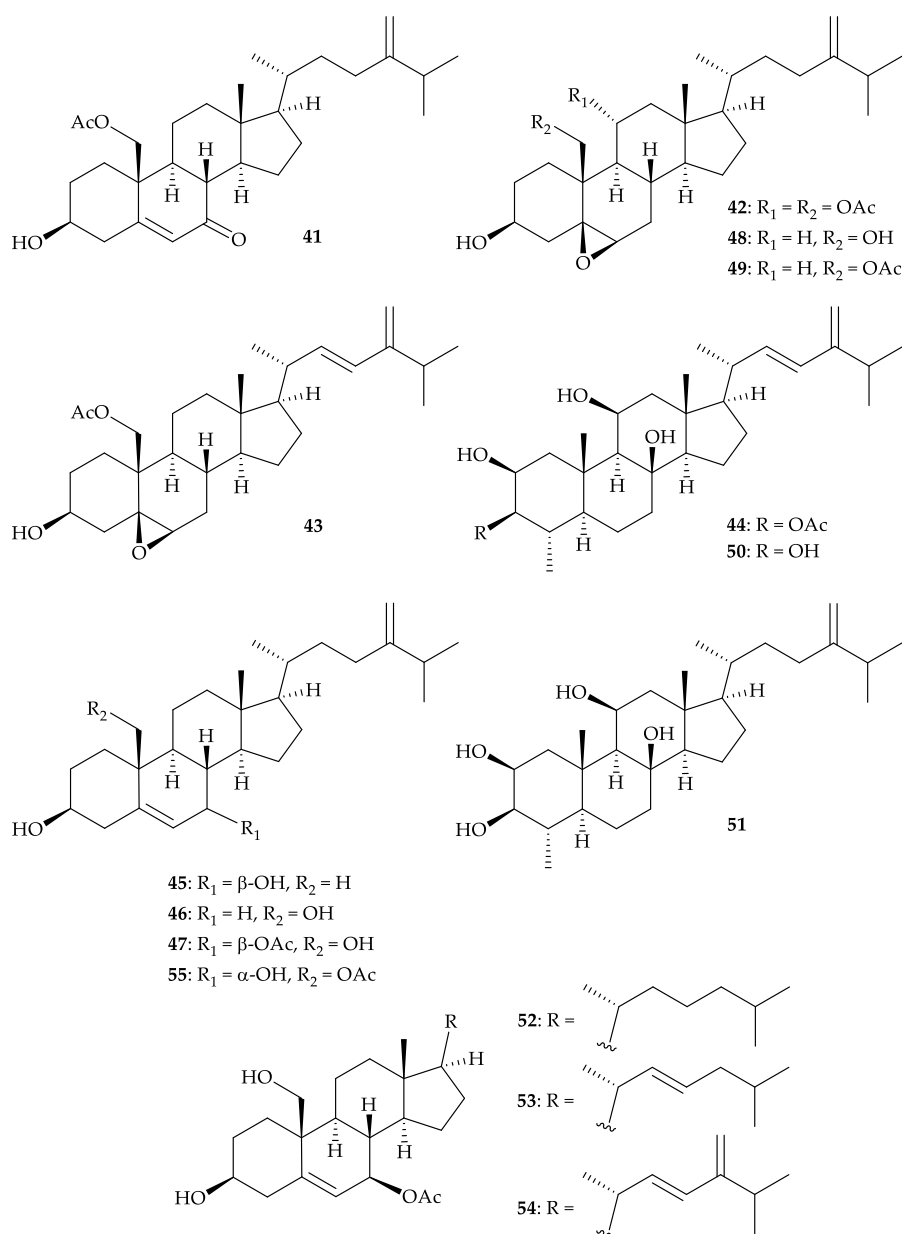


**Figure 8.** Structures of 7-dehydroerectasteroid F (**41**), 11 $\alpha$ -acetoxymartinol A (**42**), 22,23-didehydroarmatinol A (**43**), 3-O-acetylhyrtiosterol (**44**), 24-methylene-5-cholesten-3 $\beta$ ,7 $\beta$ -diol (**45**), 24-methylene-5-cholesten-3 $\beta$ ,19-diol (**46**), 24-methylene-5-cholesten-3 $\beta$ ,19-diol-7 $\beta$ -monoacetate (**47**), 5,6-epoxylitosterol (**48**), armatinol A (**49**), hyrtiosterol (**50**), (2 $\beta$ ,3 $\beta$ ,4 $\alpha$ ,5 $\alpha$ ,8 $\beta$ ,11 $\beta$ )-4-methylergost-24(28)-ene-2,3,8,11-tetrol (**51**), and erectasteroids C–F (**52–55**).

### 3. *Dendronephthya griffini* (Roxas, 1933)

Ten new steroids, griffinisterones A–I (**56–64**) and griffinipregnane (**65**) (Figure 9), were obtained from *D. griffini* specimens collected by a bottom trawl net at depths from 200 to 100 m at Taiwan Strait in December 2004 [61,62]. The structures of steroids **56–65** were determined by spectroscopic methods and the configuration of griffinisterone A (**56**) was further confirmed by a single-crystal X-ray diffraction analysis [61,62]. The absolute stereochemistry of griffinisterone E (**60**) was determined by the application of a modified phenylglycine methyl ester (PGME) method [61]. Anti-inflammatory assays revealed that griffinisterones A–D (**56–59**), F–H (**61–63**), and griffinipregnane (**65**), reduced the levels of iNOS protein to 49.7, 48.9, 8.1, 29.8, 13.4, 6.5, 15.4, and 59.6%, respectively, at a concentration of 10  $\mu$ M [61,62]. At the same concentration, griffinisterones F (**61**), G (**62**), and griffinipregnane (**65**), reduced the levels of COX-2 protein to 61.7, 31.5, and 52.3%, respectively [62].

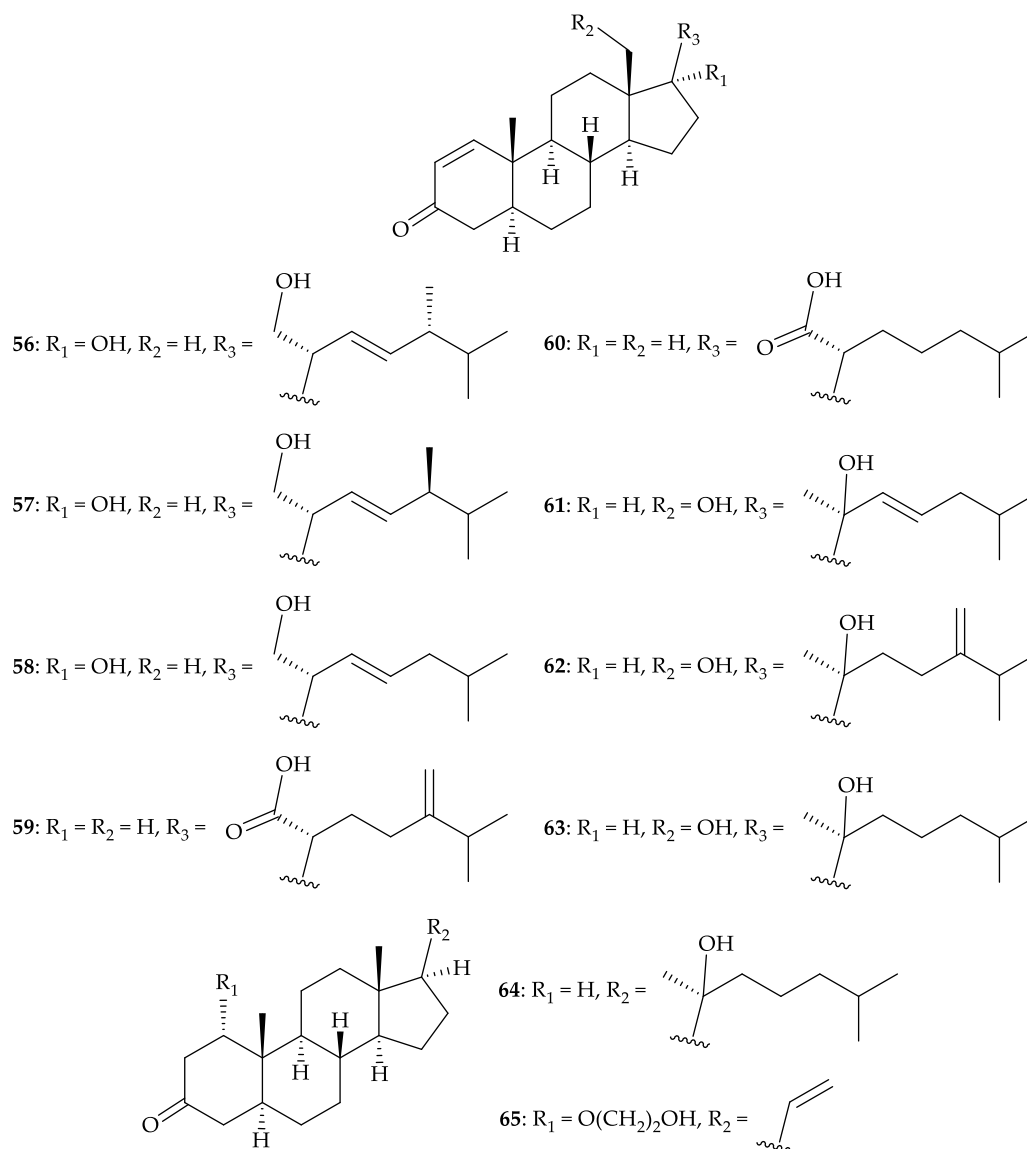


Figure 9. Structures of griffinisterones A–I (**56–64**) and griffinipregnane (**65**).

Furthermore, two new interesting polychlorolipids, (2*R*,3*S*,4*R*,5*S*,6*S*,7*R*)-2,3,5,6,7-pentachloropentadec-14-en-4-yl hydrogen sulfate (**66**), (2*R*,3*S*,4*R*,5*S*,6*S*,7*R*)-2,3,5,6,7-pentachloropentadec-14-en-4-ol (**67**), and a new natural substance, (2*R*,3*S*,4*R*,5*S*,6*S*,7*R*,*E*)-2,3,5,6,7,15-hexachloropentadec-

14-en-4-ol (**68**) [63,64], along with a known analogue, chlorosulfolipid (**69**) [63,64] (Figure 10), were obtained from *D. griffini* [65]. The structures of chlorolipids **66–69** were determined by extensive spectroscopic analysis and by comparison of the NMR data with those of known compounds. It was found that chlorolipid **68** has been prepared from the hydrolysis of **69** [63] and by a total synthesis of racemic **68** [64]. Chlorolipid **68** was isolated for the first time from a natural source and the compounds of this type was isolated for the first time from the soft corals [65].

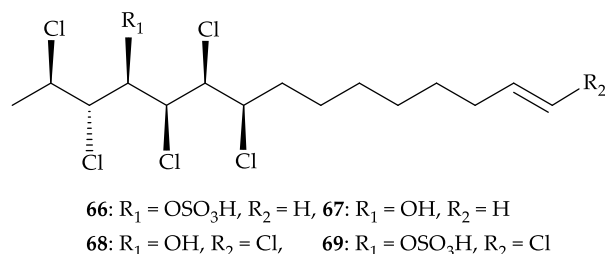


Figure 10. Structures of polychlorolipids **66–69**.

#### 4. *Dendronephthya hemprichi* (Klunzinger, 1877)

Chemical investigation of the extract of *D. hemprichi*, collected from the Red Sea, Egypt, delivered a novel glycyrrhetyl amino acid, dendrophen (**70**), a new sterol, dendrotriol (**71**), along with the well-known metabolites, cholesterol (**26**) [30] (Figure 4) and hexitol (**72**) [66]. The structures of new compounds **70** and **71** were established by spectroscopic methods, although the stereochemistry for C-24 stereogenic center in **71** was not determined [66]. Furthermore, chromatography separation of the low-polarity components of *D. hemprichi* extract afforded 4-oxo-pentanoic acid (**73**), 2-methyl-acrylic acid 2-diethylaminoethyl ester (**74**), juniper camphor (**75**), and 2-octadecanone (**76**) (Figure 11) [66].

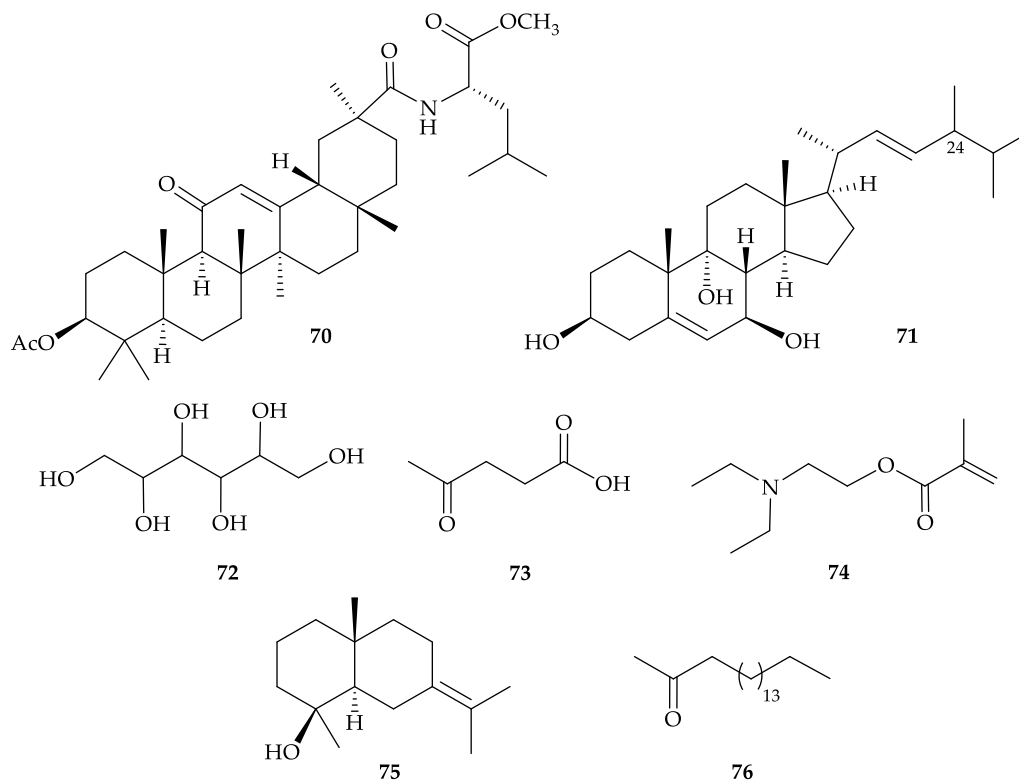
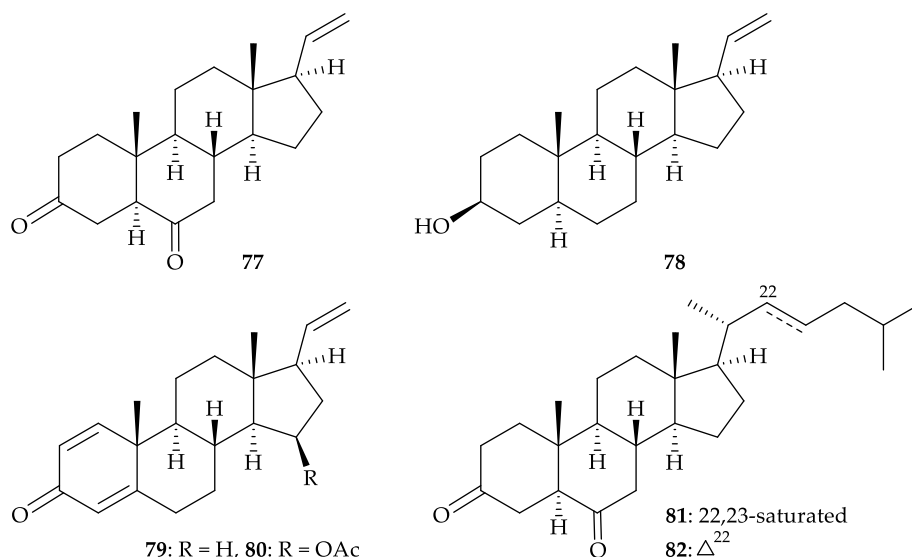


Figure 11. Structures of dendrophen (**70**), dendrotriol (**71**), hexitol (**72**), 4-oxo-pentanoic acid (**73**), 2-methyl-acrylic acid 2-diethylaminoethyl ester (**74**), juniper camphor (**75**), and 2-octadecanone (**76**).

### 5. *Dendronephthya mucronata* (Pütter, 1900)

A new pregnane-type steroid 5 $\alpha$ -pregn-20-en-3,6-dione (**77**), along with five known steroids, 5 $\alpha$ -pregn-20-en-3 $\beta$ -ol (**78**) [67–69], 1,4,20-pregnatrien-3-one (**79**) [70–74], 15 $\beta$ -acetoxypregna-1,4,20-trien-3-one (**80**) [73,75], 5 $\alpha$ -cholestan-3,6-dione (**81**) [76–78], and 5 $\alpha$ -cholest-22-en-3,6-dione (**82**) [79], (Figure 12), were isolated from *D. mucronata* collected from waters off Phu Quoc Islands, Kien Giang, Vietnam in 2018 [80]. The structure of new steroid **77** was elucidated by spectroscopic method. Steroids **78** and **81** showed moderate inhibitory effects on LPS-induced NO formation in RAW264.7 murine macrophage cells with IC<sub>50</sub> values of 30.15 and 35.97  $\mu$ M, respectively.



**Figure 12.** Structures of 5 $\alpha$ -pregn-20-en-3,6-dione (**77**), 5 $\alpha$ -pregn-20-en-3 $\beta$ -ol (**78**), 1,4,20-pregnatrien-3-one (**79**), 15 $\beta$ -acetoxypregna-1,4,20-trien-3-one (**80**), 5 $\alpha$ -cholestan-3,6-dione (**81**), and 5 $\alpha$ -cholest-22-en-3,6-dione (**82**).

Furthermore, three new bicyclo lactones, dendronephthyones A–C (**83–85**), along with a known analogue, suberosanone B (**86**) [81] (Figure 13), were isolated from the methanol extract of the same target material *D. mucronata* [82]. Structures of lactones **83–86** were established by spectroscopic methods and these four compounds exhibited cytotoxicity toward HeLa (human papillomavirus-related endocervical adenocarcinoma) cells with IC<sub>50</sub> values of 32.48, 30.12, 35.45, and 14.45  $\mu$ M, respectively [82].

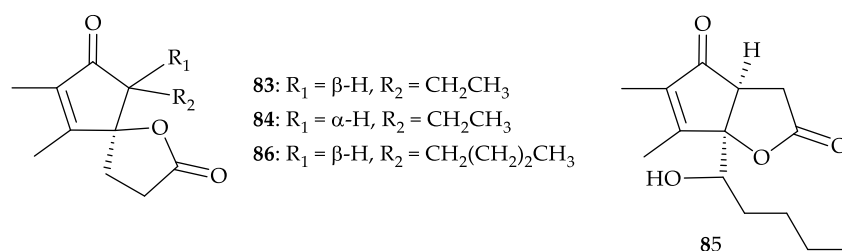


**Figure 13.** Structures of dendronephthyones A–C (**83–85**) and suberosanone B (**86**).

### 6. *Dendronephthya nipponica* (Utinomi, 1952)

A red soft-coral *D. nipponica* cause spiny lobster fisherman living along the coast of Miyazaki Prefecture, Japan to develop occupational allergies. In order to understand the allergic mechanism, a new 53-kD allergenic component (Den n 1) (**87**) was purified and the N-terminal amino of this allergen component was determined and identified as Asp-Asp-Ile-Asn-Arg-Tyr-Ala-Phe-Asp-Asn-Lys-Ile-Asn-Asp-Lys-Leu-Phe-Asp-His-Trp-Gln-Ser [83].



### 7. *Dendronephthya puetteri* (Kükenthal, 1905)

In 2018, Jeon's group reported the isolation of a  $3\beta$ -hydroxy- $\Delta^5$ -steroidal congener, consisting of six sterols, cholesterol (26) [30] (Figure 4), cholesta-5,22-dien- $3\beta$ -ol (34) [40], ergosta-5,22-dien- $3\beta$ -ol (36) [41], stigmasta-5-en- $3\beta$ -ol (39) [48], 22,23-methylenecholesterol (40) [49] (Figure 7), and cholesta-5,24-dien- $3\beta$ -ol (88) [84] (Figure 14), from *D. puetteri*, collected from the Jeju Island, South Korea [85]. The structures for all sterols 26, 34, 36, 39, 40, and 88 were determined by GC-MS/MS analysis [85]. In lipopolysaccharides (LPS)-stimulated RAW264.7 cells, this mixture inhibited nitric oxide (NO) production with an  $IC_{50}$  value of 6.54  $\mu$ g/mL. Moreover, this congener reduced the level of  $PGE_2$ , TNF- $\alpha$ , IL-1 $\beta$ , and IL-6. The anti-inflammatory effects of this sterol-rich mixture was confirmed in an LPS-stimulated in vivo zebrafish model by the downregulation of NO, iNOS, COX-2, ROS production and cell death [85,86], and this sterol rich congener showed cytotoxicity toward HL-60 and MCF-7 cells with  $IC_{50}$  values of 25.27 and 22.81  $\mu$ g/mL, respectively [87].

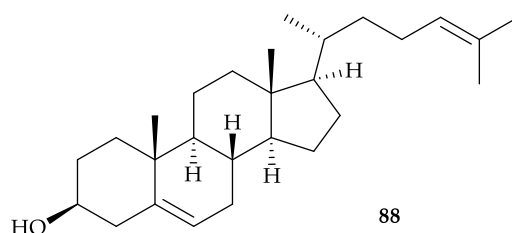


Figure 14. Structure of cholesta-5,24-dien- $3\beta$ -ol (88).

### 8. *Dendronephthya rubeola* (Henderson, 1909)

Four new acetoxycapnellenes,  $2\alpha,8\beta,13$ -triacetoxycapnell-9-ene- $10\alpha$ -ol (89),  $3\alpha,8\beta,14$ -triacetoxycapnell-9-ene- $10\alpha$ -ol (90),  $3\alpha,14$ -diacetoxycapnell-9-ene- $8\beta,10\alpha$ -diol (91),  $3\alpha,8\beta$ -diacetoxycapnell-9-ene- $10\alpha$ -ol (92), and the first epoxyprecapnellene,  $3\alpha,4\alpha$ -epoxyprecapnell-10-ene (93), as well as two known analogues, capnell-9-ene- $8\beta,10\alpha$ -diol (94) [88,89] and  $8\beta$ -acetoxycapnell-9-ene- $10\alpha$ -ol (95) [88,90] (Figure 15), were obtained from *D. rubeola*, collected from the waters near Bali, Indonesia [91]. Structures of 89–95 were established by spectroscopic methods. Compounds 94 and 95 displayed antiproliferative activity against L-929 (murine connective tissue fibroblasts) ( $GI_{50}$  = 6.8, 20.9  $\mu$ M) [91]; 94 displayed cytotoxicity toward HL-60, K-562 (human chronic myelogenous leukemia), G-402 (human renal leiomyoblastoma), MCF-7, HT-115 (human colon carcinoma), and A-2780 (human ovarian endometrioid adenocarcinoma) cells with  $IC_{50}$  values of 51, 0.7, 42–51, 93, 63, and 9.7  $\mu$ M, respectively [89]. Compounds 94 and 95 also showed cytotoxicity toward HeLa cells ( $CC_{50}$  = 7.6, 9.4  $\mu$ M) [91]. It is interesting to note that compound 94 (capnell-9-ene- $8\beta,10\alpha$ -diol) inhibited the interaction of oncogenic transcription factor Myc (a family of regulator genes and proto-oncogenes that code for transcription factors) with its partner protein Max (inhibition = 77%) in yeast [91].

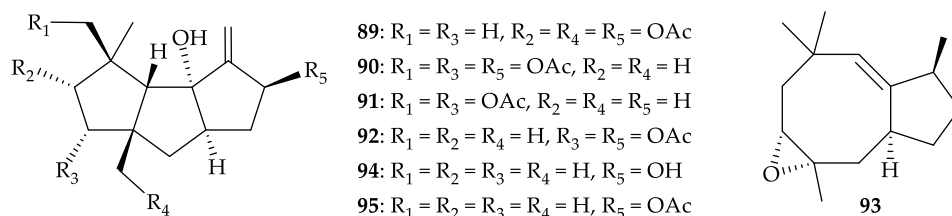
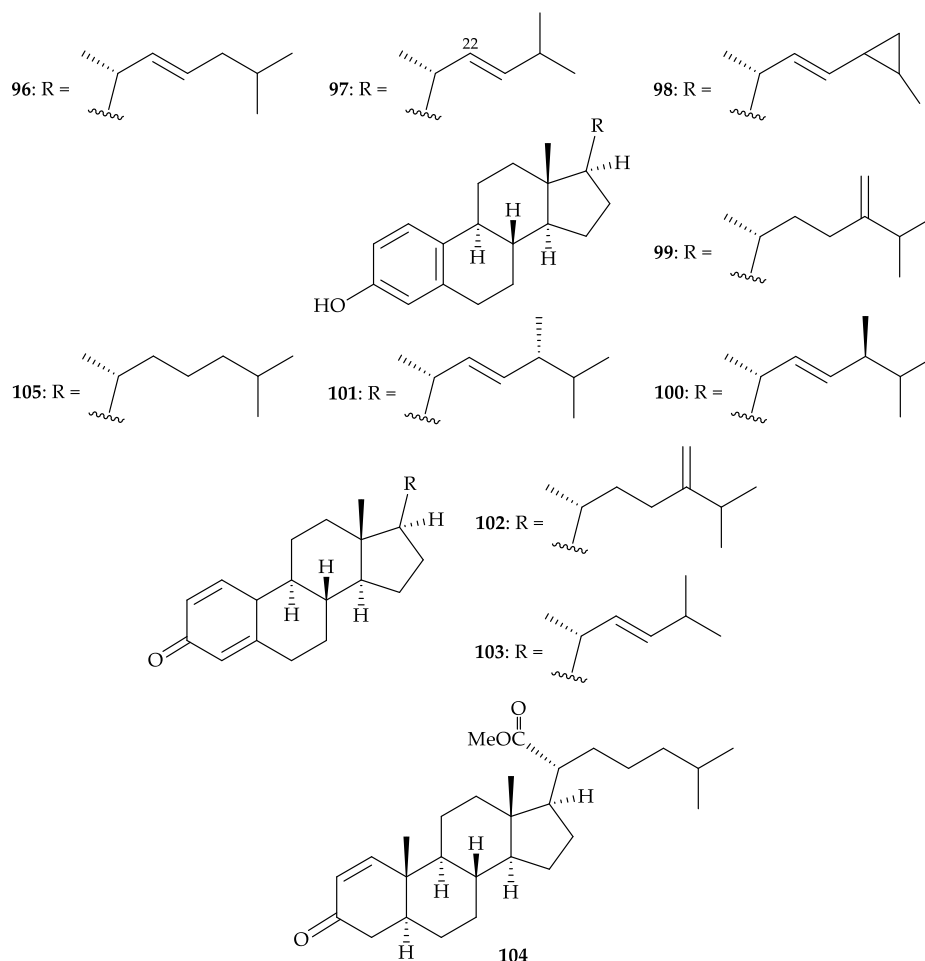


Figure 15. Structures of  $2\alpha,8\beta,13$ -triacetoxycapnell-9-ene- $10\alpha$ -ol (89),  $3\alpha,8\beta,14$ -triacetoxycapnell-9-ene- $10\alpha$ -ol (90),  $3\alpha,14$ -diacetoxycapnell-9-ene- $8\beta,10\alpha$ -diol (91),  $3\alpha,8\beta$ -diacetoxycapnell-9-ene- $10\alpha$ -ol (92),  $3\alpha,4\alpha$ -epoxyprecapnell-10-ene (93), capnell-9-ene- $8\beta,10\alpha$ -diol (94), and  $8\beta$ -acetoxycapnell-9-ene- $10\alpha$ -ol (95).

### 9. *Dendronephthya studeri* (Ridley, 1884)

Eleven steroids, including eight new metabolites, (22*E*)-19-norcholesta-1,3,5,22-tetraen-3-ol (**96**), (22*E*)-19,24-dinorcholesta-1,3,5,22-tetraen-3-ol (**97**), (22*E*)-24,26-cyclo-19-norcholesta-1,3,5,22-tetraen-3-ol (**98**), 24-methylene-19-norcholesta-1,3,5,22-tetraen-3-ol (**99**), (22*E*,24*S*)-24-methyl-19-norcholesta-1,3,5,22-tetraen-3-ol (**100**), (22*E*,24*R*)-24-methyl-19-norcholesta-1,3,5,22-tetraen-3-ol (**101**), 24-methylenecholesta-1,4,22-trien-3-one (**102**), and (22*E*)-24-cholesta-1,4,22-trien-3-one (**103**), which all were found to be characterized by either the presence of an aromatic ring or a cross-conjugated dienone system in ring A, as well as three known steroids, methyl spongoate (**104**) [92], 19-norcholesta-1,3,5-trien-3-ol (**105**) [93,94], and dendronesterone C (**12**) (Figure 3) [8], were obtained from *D. studeri*, collected off the coast of Xiaodong Sea, Hainan Province, China [95] (Figure 16). Structures of isolates **12** and **96–105** were established by spectroscopic analysis and by comparison of their NMR data with those reported in the literature. Steroid **104** exhibited cytotoxicity against BEL-7402 (human papillomavirus-related endocervical adenocarcinoma), A-549, HT-29, and P-388 cells with IC<sub>50</sub> values of 0.14, 5, 5, and 3.8 µg/mL [92].



**Figure 16.** Structures of (22*E*)-19-norcholesta-1,3,5,22-tetraen-3-ol (**96**), (22*E*)-19,24-dinorcholesta-1,3,5,22-tetraen-3-ol (**97**), (22*E*)-24,26-cyclo-19-norcholesta-1,3,5,22-tetraen-3-ol (**98**), 24-methylene-19-norcholesta-1,3,5,22-tetraen-3-ol (**99**), (22*E*,24*S*)-24-methyl-19-norcholesta-1,3,5,22-tetraen-3-ol (**100**), (22*E*,24*R*)-24-methyl-19-norcholesta-1,3,5,22-tetraen-3-ol (**101**), 24-methylenecholesta-1,4,22-trien-3-one (**102**), (22*E*)-24-cholesta-1,4,22-trien-3-one (**103**), methyl spongoate (**104**), and 19-norcholesta-1,3,5-trien-3-ol (**105**).

### 10. *Dendronephthya* spp.

*Dendronephthya* is a genus of octocoral belonging to the family Nephtheidae and there are over 250 described species in this genus. In 1990, Katrich and colleagues identified the correlation between the number of particular phospholipids (PhLs) and prostaglandins (PGs) that influenced the prostaglandin-like activities of the extracts from (1) *Dendronephthya* sp., collected in the region of the Great Barrier Reef, Australia and (2) *Dendronephthya* sp., collected in Vietnam [96].

An acetone extract from *Dendronephthya* sp., collected in 1990, off the Chichi-jima and Haha-jima Islands in the Ogasawara Islands, Japan, showed a high level of antifouling activity against the blue mussel *Mytilus edulis* [97]. Purification of the extract gave mixtures of sterols and fatty acids as active components. In the sterol mixture, there are several sterols, (24*S*)-24-methylcholesta-5(*E*),22-dien-3 $\beta$ -ol (= pincsterol) or (24*R*)-24-methylcholesta-5(*E*),22-dien-3 $\beta$ -ol (= brassicasterol) (**106**) [98], cholesterol (**26**) [30] (Figure 5),  $\beta$ -sitosterol (stigmasta-5-en-3 $\beta$ -ol) (**39**) [48], and  $\beta$ -cholestanol (5 $\alpha$ -cholestan-3 $\beta$ -ol) (**107**) [99] were identified and sterol **39** in this study [97] was found to contain 35% of a 24*S* epimer (clionasterol) (**108**) [100,101] (Figure 17). Sterol **39** had the highest antifouling activity among sterols **26**, **39**, and **107** [97]. Moreover, a fatty acid mixture, showing the presence of saturated and unsaturated fatty acids with a chain length of C<sub>12</sub> to C<sub>22</sub>, being rich in C<sub>16</sub> and C<sub>18</sub> acids as active constituents in antifouling activity [97].

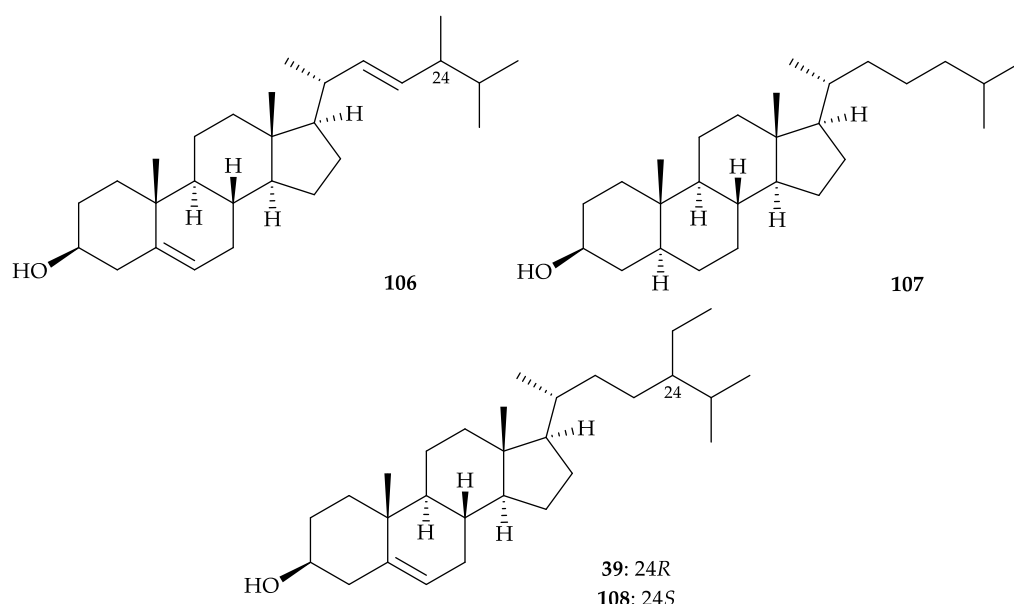


**Figure 17.** Structures of pincsterol (24*S*), brassicasterol (24*R*) (**106**),  $\beta$ -cholestanol (**107**),  $\beta$ -sitosterol (**39**), and clionasterol (**108**).

Kawamata et al. isolated an antifouling substance, trigonelline (**109**) (Figure 18), from *Dendronephthya* sp. collected at Chichijima Island in the Ogasawara Islands [102]. The structure of **109** was elucidated by spectroscopic methods and this compound showed the same level of settling-inhibitory activity against the acorn barnacle *Balanus amphitrite* larvae as CuSO<sub>4</sub> [102,103].

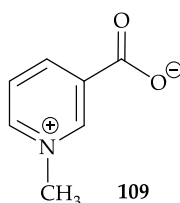


**Figure 18.** Structure of trigonelline (**109**).

In 1999, the ethanol extract of two soft coral specimens *Dendronephthya* (Roxasia) sp. and *Dendronephthya* (Morchellana) sp., collected off the Gopalpur coast, Bay of Bengal, were found to display attachment inhibitory activity against the settlement of cyprids of barnacle *Balanus amphitrite* [104], and the extract was claimed to contain natural non-toxic antifouling agents, although no natural products was reported to be active components.

Research by a group in Japan identified four new antifouling *seco*-steroids, isogosterones A–D (1–4) (Figure 1) from an octocoral identified as *Dendronethphyia* sp. collected off the Izu Peninsula, Japan [2], and their structures were elucidated on the basis of spectroscopic data. This is the first time to isolate naturally occurring 13,17-secosteroids. It is interesting to note that secosteroids 3 and 4 were interconvertible in  $\text{CHCl}_3$  and 3 was detected as the hydrolyzed product of 4 [2]. These four secosteroids displayed activity to inhibit the settlement of *B. amphitrite* cyprid larvae with an  $\text{EC}_{50}$  values of 2.2  $\mu\text{g/mL}$

Furthermore, a new steroid, methyl 3-oxochola-4,22-dien-24-oate (110) (Figure 19) [105], from *Dendronephthya* sp. collected off the Kii Peninsula, Japan, and determined its structure using spectroscopic methods [105]. Steroid 110 was lethal to cyprids of *B. amphitrite* at 100  $\mu\text{g/mL}$  ( $\text{LD}_{100}$ ) but did not inhibit larval settlement of *B. amphitrite* [105].

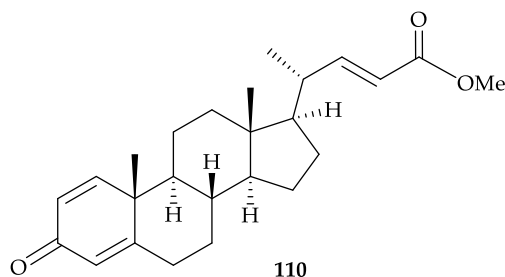


Figure 19. Structure of methyl 3-oxochola-4,22-dien-24-oate (110).

Four new brominated oxylipins, (4*S*,5*E*,7*Z*,12*R*,14*Z*,17*Z*)-4-hydroxy-17,18-didehydrobromovulone-3 (111), (4*S*,5*E*,7*Z*,12*R*,14*Z*,17*Z*)-4-( $\alpha$ -D-glucopyranosyloxy)-17,18-didehydrobromovulone-3 (112), (4*R*,5*E*,7*Z*,12*R*,14*Z*,17*Z*)-4-hydroxy-17,18-didehydrobromovulone-3 (113), and (4*R*,5*E*,7*Z*,12*R*,14*Z*,17*Z*)-4-( $\beta$ -D-glucopyranosyloxy)-17,18-didehydrobromovulone-3 (114), (Figure 20) were isolated from *Dendronephthya* spp. (red variety—for compounds 111 and 112; yellow variety—for compounds 113 and 114) collected in the Gulf of Aqaba in the Red Sea (Eilat, Israel) [106]. The structures, including the absolute configurations of oxylipins 111–114, were determined by spectroscopic and chemical methods. All the isolates showed significant inhibition of the growth of crown gall tumors on potato disks inoculated with *Agrobacterium tumefaciens* and gave positive responses in a brine shrimp toxicity toward *Artemia salina*; these compounds showed antibacterial activity against the Gram-(+) bacteria *Staphylococcus aureus* and *Bacillus subtilis* [106].

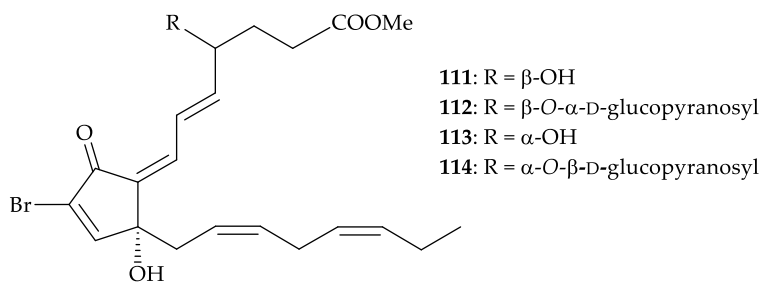
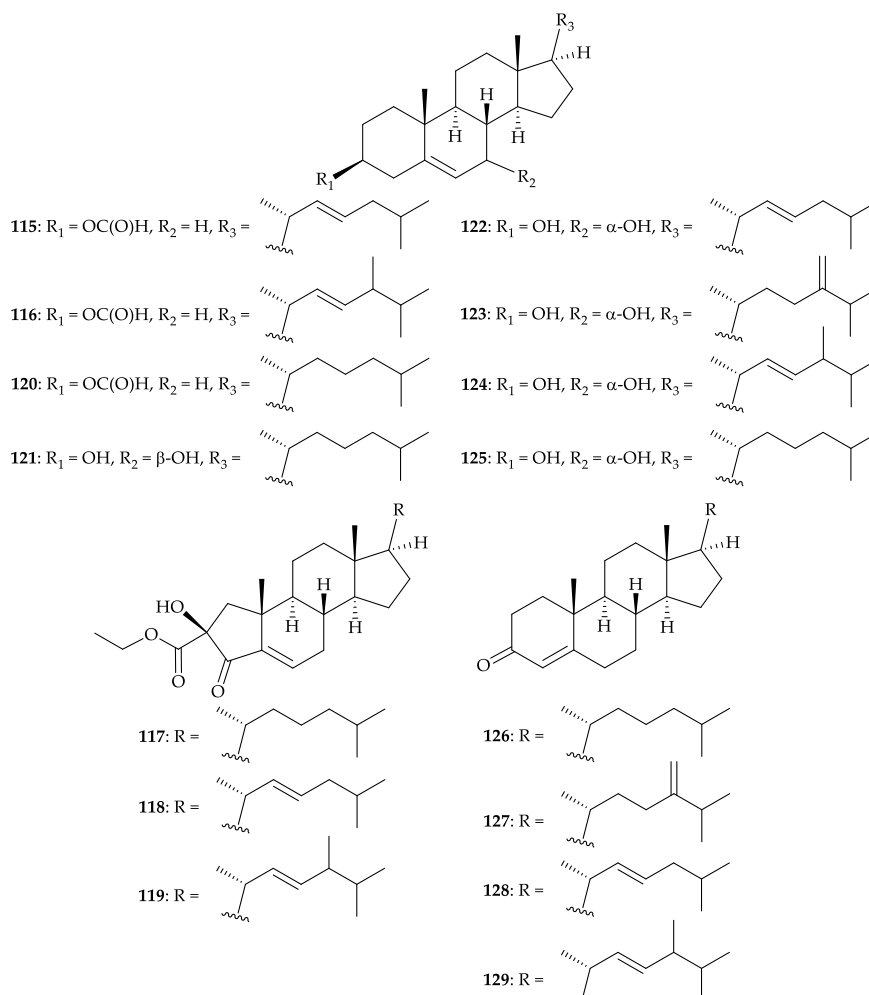


Figure 20. Structures of oxylipins 112–114.

Fifteen steroids, including five new compounds, (22*E*)-3-O- $\beta$ -formylcholest-5,22-diene (115), (22*E*)-3-O- $\beta$ -formyl-24-methyl-cholest-5,22-diene (116), 2-ethoxycarbonyl-2- $\beta$ -hydroxy-A-nor-

cholest-5-ene-4-one (117), (22*E*)-2-ethoxycarbonyl-2- $\beta$ -hydroxy-A-nor-cholest-5,22-diene-4-one (118), (22*E*)-2-ethoxycarbonyl-2- $\beta$ -hydroxy-24-methyl-A-nor-cholest-5,22-diene-4-one (119), a new natural steroid, 3- $\beta$ -formyloxycholest-5-ene (120) [107], as well as nine known steroids, 3 $\beta$ ,7 $\beta$ -dihydroxycholest-5-ene (121) [108,109], (22*E*)-3 $\beta$ ,7 $\alpha$ -dihydroxycholest-5,22-diene (122) [110], 3 $\beta$ ,7 $\alpha$ -dihydroxy-24-methylenecholest-5-ene (123) [109], 3 $\beta$ ,7 $\alpha$ -dihydroxy-24-methylcholest-5,22-diene (124) [110], 3 $\beta$ ,7 $\alpha$ -dihydroxycholest-5-ene (125) [110–112], cholest-4-ene-3-one (126) [113–115], 24-methylenecholest-4-ene-3-one (127) [116,117], (22*E*)-cholest-4,22-dien-3-one (128) [116], and (22*E*)-24-methylcholest-4,22-dien-3-one (129) [118] (Figure 21), were isolated from the soft coral *Dendronephthya* sp. collected off coral reef in Sanya, Hainan Province, South China Sea of People's Republic of China [119]. The structures of steroids 115–129 were elucidated by spectroscopic methods and by comparison of their spectroscopic data with those reported previously. However, the configuration of Me-28 at stereogenic center C-24 in steroids 116, 119, 124, and 129 were not determined in this study. Steroids 115, 116, and 120 belonging to 3-*O*-formylated cholesterol analogues and steroids 117–119 are unique ring A-contracted steroids [119].



**Figure 21.** Structures of (22*E*)-3-*O*- $\beta$ -formylcholest-5,22-diene (115), (22*E*)-3-*O*- $\beta$ -formyl-24-methylcholest-5,22-diene (116), 2-ethoxycarbonyl-2- $\beta$ -hydroxy-A-nor-cholest-5-ene-4-one (117), (22*E*)-2-ethoxycarbonyl-2- $\beta$ -hydroxy-A-nor-cholest-5,22-diene-4-one (118), (22*E*)-2-ethoxycarbonyl-2- $\beta$ -hydroxy-24-methyl-A-nor-cholest-5,22-diene-4-one (119), 3- $\beta$ -formyloxycholest-5-ene (120), 3 $\beta$ ,7 $\beta$ -dihydroxycholest-5-ene (121), (22*E*)-3 $\beta$ ,7 $\alpha$ -dihydroxycholest-5,22-diene (122), 3 $\beta$ ,7 $\alpha$ -dihydroxy-24-methylenecholest-5-ene (123), 3 $\beta$ ,7 $\alpha$ -dihydroxy-24-methylcholest-5,22-diene (124), 3 $\beta$ ,7 $\alpha$ -dihydroxycholest-5-ene (125), cholest-4-ene-3-one (126), 24-methylenecholest-4-ene-3-one (127), (22*E*)-cholest-4,22-dien-3-one (128), and (22*E*)-24-methylcholest-4,22-dien-3-one (129).



A chemical examination of a soft coral identified as *Dendronephthya* sp., collected from the inner coral reef in Sanya Bay, Hainan Island of China, resulted in the isolation of 20 cembrane-type diterpenoids [120], including 15 new metabolites, dendronpholides C–F (**130–133**), I–R (**134–143**), and (–)-sandensolide (**144**) (an enantiomer of sandensolide) [120–124], along with five known compounds, 11-episinulariolide (**145**) [125–130], and sinulaflexiolides E, F, J, K (**146–149**) [128] (Figure 22). The structures of all isolates **130–149** were determined through spectroscopic methods and by comparison with those reported in literature [120]. Cembranoid dendronpholides C (**130**), J (**135**), and sinulaflexiolide E (**146**) showed cytotoxicity toward BGC-823 (human papillomavirus-related endocervical adenocarcinoma) cells with IC<sub>50</sub> values of 0.05, 0.20, 0.02 µg/mL, respectively, whereas the other compounds were not active. A comparison of the cytotoxic data between **130** and **144** revealed that the methyl ester functionality plays a crucial role in the inhibition of BGC-823 cells compared to the ε-lactone functionality. This is the first report of cembrane-type diterpenoids from the soft corals belonging to the genus *Dendronephthya* [120].

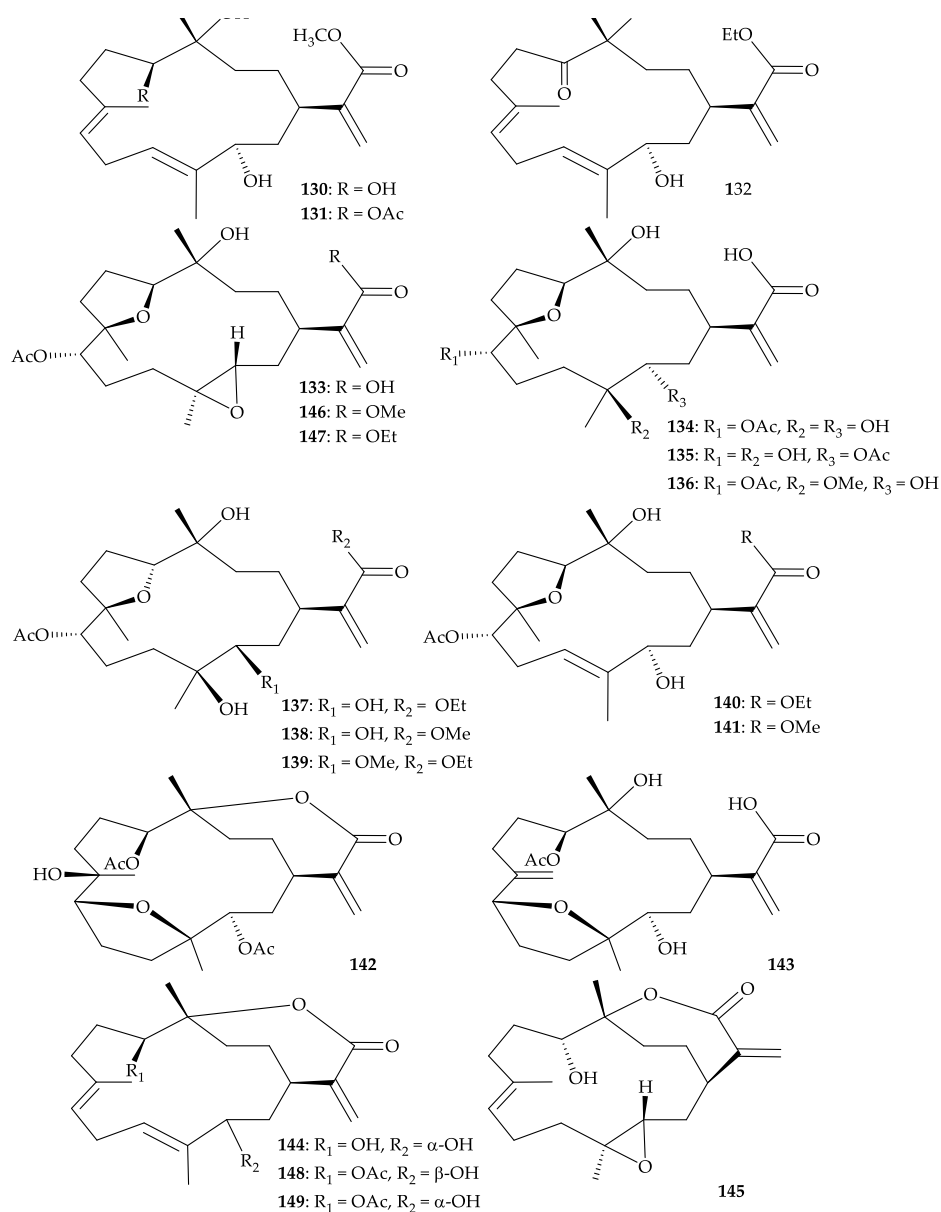


**Figure 22.** Structures of dendronpholides C–F (**130–133**), I–R (**134–143**), (–)-sandensolide (**144**), 11-episinulariolide (**145**) and sinulaflexiolides E, F, J, K (**146–149**).

In 2010, two tetrahydroxylated sterols, including a new compound, 23-nor-ergost-24-ene-3 $\beta$ ,5 $\alpha$ ,6 $\beta$ ,7 $\beta$ -tetrol (**150**) and a known analogue, ergost-24-ene-3 $\beta$ ,6 $\beta$ ,9 $\alpha$ ,19 $\beta$ -tetrol (**151**) [131], were isolated from *Dendronephthya* sp. collected from Naozhou Islands of the South China Sea [132] (Figure 23). The structures of sterols **150** and **151** were identified by spectroscopic methods [132]. Sterol **150** showed cytotoxicity toward the BEL-7402, MCG (human plasma cell myeloma), MCF, LoVo (human colorectal adenocarcinoma), and Hep G2 (human hepatocellular carcinoma) cells with IC<sub>50</sub> values of 32.2, 20.5, 2.0, 5.5, and 18.6  $\mu$ g/mL, respectively, and sterol **151** was cytotoxic against MCG and LoVo cells (IC<sub>50</sub> = 22.0, 13.8  $\mu$ g/mL), respectively [132].

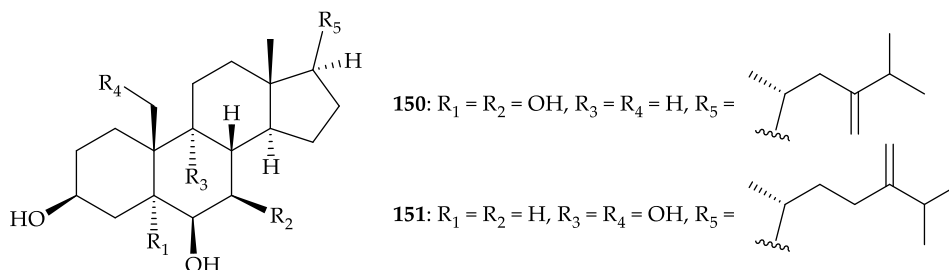


**Figure 23.** Structures of 23-nor-ergost-24-ene-3 $\beta$ ,5 $\alpha$ ,6 $\beta$ ,7 $\beta$ -tetrol (**150**) and ergost-24-ene-3 $\beta$ ,6 $\beta$ ,9 $\alpha$ ,19 $\beta$ -tetrol (**151**).

Three new ylangene-type sesquiterpenoids, dendronephthols A–C (**152–154**) (Figure 24), together with two known steroids, dendronesterone A (**10**) [8] (Figure 3) and cholesterol (**26**) [30] (Figure 5), were isolated from a Red Sea soft coral *Dendronephthya* sp., collected near the coast of Hurghada, Egypt [133]. The structures of new sesquiterpenoids **152–154** were established by spectroscopic methods and **152** and **154** were found to be cytotoxic against L5178Y (mouse lymphoma) cells with ED<sub>50</sub> values of 8.4 and 6.8  $\mu$ g/mL, respectively [133].

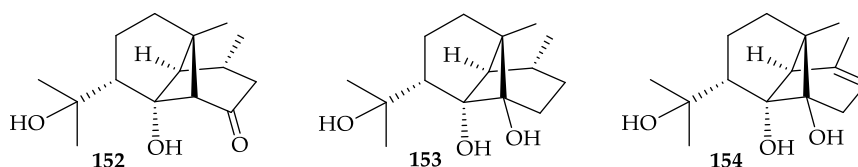


**Figure 24.** Structures of dendronephthols A–C (**152–154**).

Furthermore, two new steroids, dendronesterones D (**155**) and E (**156**), featuring with 1,4-dienone moiety, together with three known steroids, methyl 3-oxochola-4,22-dien-24-oate (**110**) [105] (Figure 19), 5 $\alpha$ ,8 $\alpha$ -epidioxy-24(S)-methylcholesta-6,22-dien-3 $\beta$ -ol (**157**), and 5 $\alpha$ ,8 $\alpha$ -epidioxy-24(S)-methylcholesta-6,9,22-trien-3 $\beta$ -ol (**158**) [36,134], were isolated from an octocoral *Dendronephthya* sp., collected off the northeast coast of Taiwan [135] (Figure 25). The structures of new steroids **155** and **156** were elucidated by using spectroscopic methods and **155** was found to suppress the expression of inducible nitric oxide synthase (iNOS) and cyclooxygenase-2 (COX-2) to 24.2 and 70.4% at a concentration of 10  $\mu$ M [135].

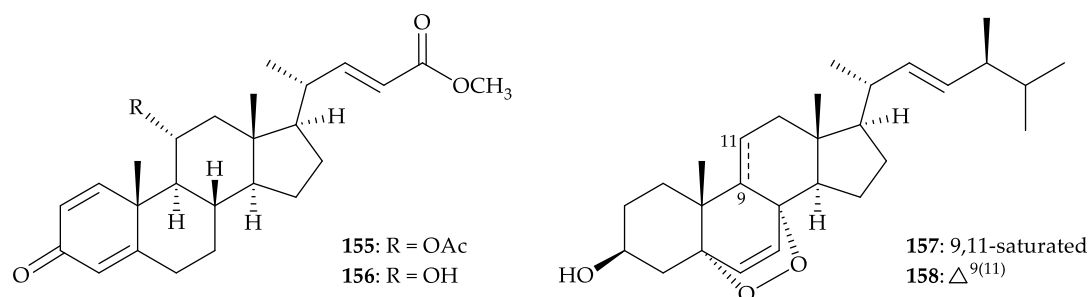


**Figure 25.** Structures of dendronesterones D (155) and E (156), 5α,8α-epidioxy-24(S)-methylcholesta-6,22-dien-3β-ol (157), and 5α,8α-epidioxy-24(S)-methylcholesta-6,9,22-trien-3β-ol (158).

Two new 2,5-piperazinedione derivatives, janthinolides A (159) and B (160), as well as a new natural product, deoxymycelianamide (161) [136,137], and two known metabolites, griseofulvin (162) [138–142], and dechlorogriseofulvin (163) [142–144], were isolated from the fermentation broths of the endophytic fungus *Penicillium janthinellum*, isolated from a soft coral identified as *Dendronephthya* sp., collected in the South China Sea [145]. The structures of metabolites 159–163 were determined by spectroscopic data analysis and compound 162 displayed inhibitory concentration at 2.75 and 20 µg/mL against the fungal pathogen *Alternaria solani* and ascomycetous pathogen *Pyricularia oryzae*, respectively [145] (Figure 26).

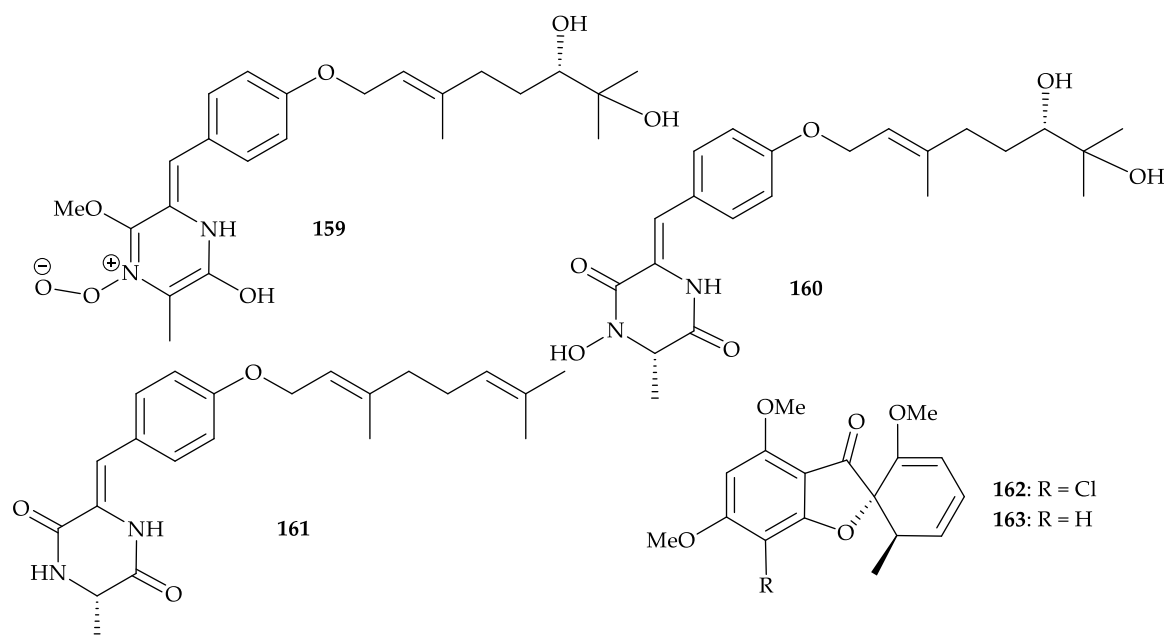


**Figure 26.** Structures of janthinolides A (159), B (160), deoxymycelianamide (161), griseofulvin (162), and dechlorogriseofulvin (163).

Moreover, seven isoechinulin-type alkaloids, neoechinulin A (164) [146–154], preechinulin (165) [155,156], isoechinulin A (166) [149,157], tardioxopiperazine A (167) [158], varicolorin L (168) [159], dihydroxyisoechinulin A (169) [160], and L-alanyl-L-tryptophan anhydride (170) [161] (Figure 27), were isolated from the fermentation broths of an endophytic fungus *Nigrospora oryzae* isolated from a soft coral identified as *Dendronephthya* sp. collected in the South China Sea [162]. The structures of 164–170 were determined by their spectroscopic data and by comparison with those reported in the literature. In the antifouling activity against the larval settlement of barnacle *Balanus amphitrite*, compound 166 showed activity with an IC<sub>50</sub> value of 5.92 µg/mL [162].

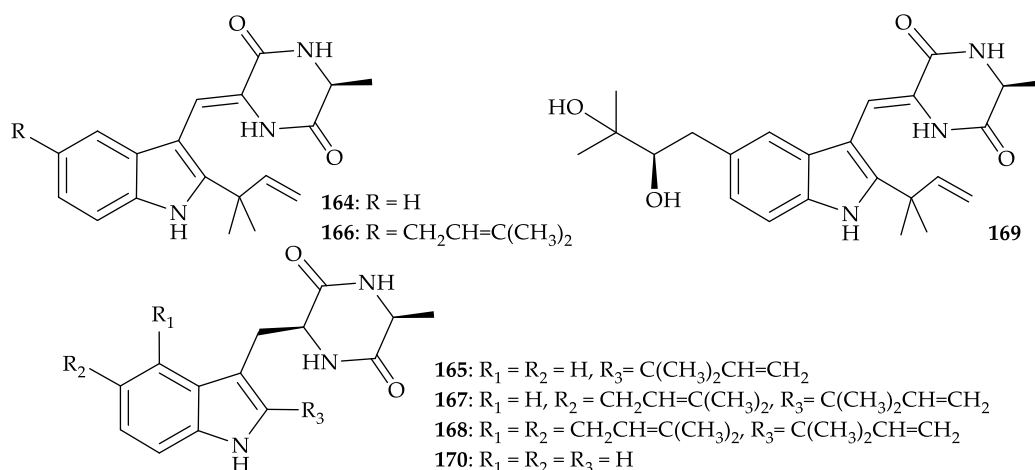


**Figure 27.** Structures of neoechinulin A (164), preechinulin (165), isoechinulin A (166), tardioxopiperazine A (167), varicolorin L (168), dihydroxyisoechinulin A (169), and L-alanyl-L-tryptophan anhydride (170).

## 11. Conclusions

Ever since the *seco*-steroids, isogosterones A–D (1–4) were obtained from a specimen of the octocoral *Dendronephthya* collected off the Izu Peninsula, Japan [2], 170 interesting secondary metabolites, including 96 steroids (56.47%), 20 cembranes (11.76%), 11 sesquiterpenoids (6.47%), 11 amides (6.47%), 4 chlorolipids (2.35%), 4 bicyclic lactones (2.35%), 4 prostaglandins (2.35%), 4 bases (2.35%), 3 peptides (1.76%), 2 polyketides (1.18%), 2 ceramides (1.18%), 1 glycerol (0.59%), 1 glycyrrhetyl amino acid (0.59%), 1 benzoic acid (0.59%), 1 trigonelline (0.59%), 1 hexitol (0.59%), 1 pentanoic acid (0.59%), 1 octadecanone (0.59%), 1 aminoethyl ester (0.59%), and a 53-KD allergenic component (0.59%), were produced by *Dendronephthya* spp., and extensive biomedical activities, especially in cytotoxicity and anti-inflammatory activity, were related to these natural substances (Figure 28).

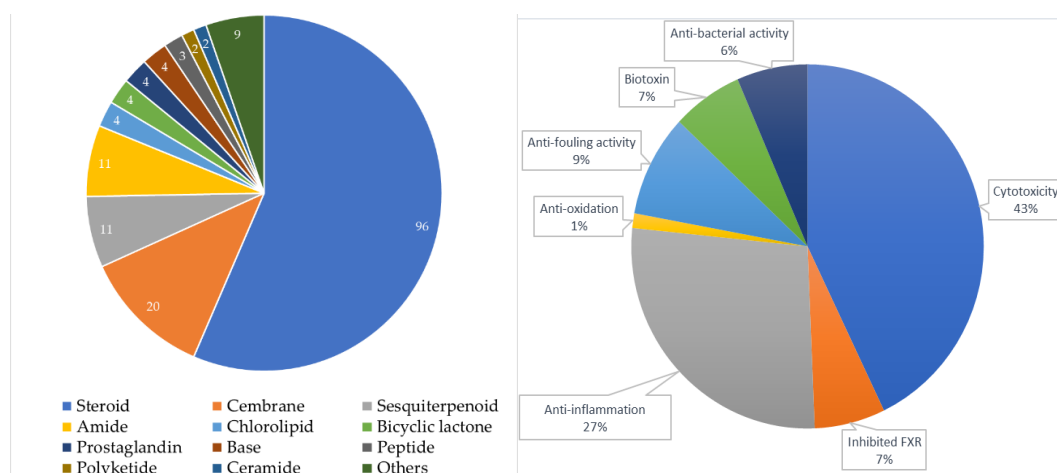


**Figure 28.** Biomedical activities of natural products from *Dendronephthya* spp.

All the secondary metabolites from *Dendronephthya* spp., reported between 1999 and 2019 were obtained from the octocorals distributed in the Indo-Pacific Ocean and Red Sea. As more than 56% of the compounds obtained from the *Dendronephthya* genus are steroids, based on above findings, these results suggest that continuing the investigation of new steroid analogues with the potential bioactivities from this marine organism are worthwhile for further development. The octocoral *Dendronephthya* sp. had been transplanted to culturing tanks located in the National Museum of Marine

Biology and Aquarium, Taiwan, for the extraction of additional natural products to establish a stable supply of bioactive material.

**Author Contributions:** Y.-H.C. (Yung-Husan Chen), C.-M.H., and P.-J.S. contributed in terms of writing the manuscript. Y.-C.C., Y.-H.C. (Yu-Hsin Chen), L.-G.Z., P.-C.H., T.-H.H., B.-R.P., Y.-Y.C., Y.-J.W., L.-S.F., and J.-H.S., conceived and designed the format of the manuscript. All authors have read and agreed to the published version of the manuscript.

**Funding:** This research was supported by grants from the National Museum of Marine Biology and Aquarium; the Ministry of Science and Technology (Grant Nos. MOST 109-2320-B-276-002-MY3, 107-2320-B-291-001-MY3, 109-2320-B-291-001-MY3), Taiwan, awarded to Yu-Jen Wu and Ping-Jyun Sung.

**Conflicts of Interest:** The authors declare no conflict of interest.

## References

- Dai, C.-F.; Chin, C.-H. *Octocoral Fauna of Kenting National Park*, 1st ed.; Kenting National Park Headquarters: Kenting Pingtung, Taiwan, 2019; pp. 54, 382–405.
- Tomono, Y.; Hirota, H.; Fusetani, N. Isogosterones A–D, antifouling 13,17-secosteroids from an octocoral *Dendronephthya* sp. *J. Org. Chem.* **1999**, *64*, 2272–2275. [[CrossRef](#)]
- Migliuolo, A.; Notaro, G.; Piccialli, V.; Sica, D. New tetrahydroxylated sterols from the marine sponge *Spongia officinalis*. *J. Nat. Prod.* **1990**, *53*, 1414–1424. [[CrossRef](#)]
- Piccialli, V.; Sica, D. Four new trihydroxylated sterols from the sponge *Spongionella gracilis*. *J. Nat. Prod.* **1987**, *50*, 915–920. [[CrossRef](#)]
- Cafieri, F.; Fattorusso, E.; Gavagnin, M.; Santacroce, C. 3 $\beta$ ,5 $\alpha$ ,6 $\beta$ -Trihydroxysterols from the Mediterranean bryozoan *Myriapora truncata*. *J. Nat. Prod.* **1985**, *48*, 944–947. [[CrossRef](#)]
- Yoshikawa, K.; Kanekuni, S.; Hanahusa, M.; Arihara, S.; Ohta, T. Polyhydroxylated sterols from the octocoral *Dendronephthya gigantea*. *J. Nat. Prod.* **2000**, *63*, 670–672. [[CrossRef](#)]
- Seo, Y.; Jung, J.H.; Rho, J.-R.; Shin, J.; Song, J.-I. Isolation of novel bioactive steroids from the soft coral *Alcyonium gracillimum*. *Tetrahedron* **1995**, *51*, 2497–2506. [[CrossRef](#)]
- Duh, C.-Y.; El-Gamal, A.A.H.; Song, P.-Y.; Wang, S.-K.; Dai, C.-F. Steroids and sesquiterpenoids from the soft corals *Dendronephthya gigantea* and *Lemnalia cervicorni*. *J. Nat. Prod.* **2004**, *67*, 1650–1653. [[CrossRef](#)]
- Quijano, L.; Cruz, F.; Navarrete, I.; Gómez, P.; Rios, T. Alkyl glycerol monoethers in the marine sponge *Desmapsamma anchorata*. *Lipids* **1994**, *29*, 731–734. [[CrossRef](#)]
- Shin, J.; Seo, Y. Isolation of new ceramides from the gorgonian *Acabaria undulata*. *J. Nat. Prod.* **1995**, *58*, 948–953. [[CrossRef](#)]
- Subrahmanyam, C.; Kulatheeswaran, R.; Venkateswara Rao, C. New spingosines from two soft corals of the Andaman & Nicobar Islands. *Indian J. Chem.* **1996**, *35B*, 578–580.
- Liang, L.; Deng, S.; Wu, H. Studies on the chemical constituents of the soft coral *Lobophytum* sp. from South China Sea. *Chin. J. Mar. Drugs* **2000**, *19*, 5–7.
- Muralidhar, P.; Kumar, M.M.; Krishna, N.; Rao, C.B.; Rao, D.V. New sphingolipids and a sterol from a *Lobophytum* species of the Indian Ocean. *Chem. Pharm. Bull.* **2005**, *53*, 168–171. [[CrossRef](#)] [[PubMed](#)]
- Zhou, G.-X.; Huang, M.-Y.; Shi, J.-G. Ceramides and cerebrosides from *Bugula neritina*. *Chin. J. Mar. Drugs* **2005**, *24*, 37–40.
- Han, A.-R.; Song, J.-I.; Jang, D.S.; Min, H.-Y.; Lee, S.K.; Seo, E.-K. Cytotoxic constituents of the octocoral *Dendronephthya gigantea*. *Arch. Pharm. Res.* **2005**, *28*, 290–293. [[CrossRef](#)]
- Marinetti, G.V.; Stotz, E. The isolation of *N*-stearyl- and *N*-palmitylsphingosines from beef spleen. *J. Am. Chem. Soc.* **1957**, *79*, 145–146. [[CrossRef](#)]
- Llinarés, J.; Elguero, J.; Faure, R.; Vincent, E.-J. Carbon-13 NMR studies of nitrogen compounds. I—Substituent effects of amino, acetamido, diacetamido, ammonium and trimethylammonium groups. *Org. Magn. Res.* **1980**, *14*, 20–24. [[CrossRef](#)]
- Maskey, R.P.; Asolkar, R.N.; Kapaun, E.; Wagner-Döbler, I.; Laatsch, H. Phytotoxic arylethylamides from limnic bacteria using a screening with microalgae. *J. Antibiotics* **2002**, *55*, 643–649. [[CrossRef](#)]
- Zhao, P.-J.; Wang, H.-X.; Li, G.-H.; Li, H.-D.; Liu, J.; Shen, Y.-M. Secondary metabolites from endophytic *Streptomyces* sp. Lz531. *Chem. Biodivers.* **2007**, *4*, 899–904. [[CrossRef](#)]



20. Han, W.-J.; Lu, X.-L.; Xu, Q.-Z.; Liu, X.-Y.; Jiao, B.-H. Isolation, identification and biological characterization of secondary metabolites produced by a marine *Bacillus subtilis*. *Acad. J. Second Mil. Med. Univ.* **2008**, *29*, 1234–1238. [[CrossRef](#)]
21. Wu, H.-H.; Tian, L.; Chen, G.; Xu, N.; Wang, Y.-N.; Sun, S.; Pei, Y.-H. Six compounds from marine fungus Y26-02. *J. Asian Nat. Prod. Res.* **2009**, *11*, 748–751. [[CrossRef](#)]
22. Gautschi, M.; Schmid, J.P.; Peppard, T.L.; Ryan, T.P.; Tuorto, R.M.; Yang, X. Chemical characterization of diketopiperazines in beer. *J. Agric. Food Chem.* **1997**, *45*, 3183–3189. [[CrossRef](#)]
23. Wright, A.D.; Papendorf, O.; König, G.M. Ambigol C and 2,4-dichlorobenzoic acid, natural products produced by the terrestrial cyanobacterium *Fischcherella ambigua*. *J. Nat. Prod.* **2005**, *68*, 459–461. [[CrossRef](#)] [[PubMed](#)]
24. Levene, P.A.; Tipson, R. Stuart. The ring structure of thymidine. *Science* **1935**, *81*, 98. [[CrossRef](#)] [[PubMed](#)]
25. Ericson, L.-E.; Widoff, E.; Bánhidi, Z.G. Studies of growth factors for *Streptococcus faecalis* occurring in marine algae. *Acta Chem. Scand.* **1953**, *7*, 974–979. [[CrossRef](#)]
26. Jones, A.J.; Grant, D.M.; Winkley, M.W.; Robins, R.K. Carbon-13 magnetic resonance. XVII. Pyrimidine and purine nucleosides. *J. Am. Chem. Soc.* **1970**, *92*, 4079–4087. [[CrossRef](#)] [[PubMed](#)]
27. Komori, T.; Sanechika, Y.; Ito, Y.; Matsuo, J.; Nohara, T.; Kawasaki, T. Biologically active glycosides from Asteroidea, I-Structures of a new cerebroside mixture and of two nucleosides from the starfish *Acanthaster planci*. *Liebigs Ann. Chem.* **1980**, *1980*, 653–668. [[CrossRef](#)]
28. Deng, S.; Wu, J.; Li, F.; Peng, S.; Chen, J.; Liu, X.; Zhong, H. Studies on the activity constituent of sponge from South China Sea *Gelliodes spinosella* Thiele (I). *Guangzhou Chem.* **1993**, *1*, 37–41.
29. Xiao, D.; Deng, S.; Wu, H. A study on chemical constituents of the South China Sea marine sponge *Pachychalina* sp. *Nat. Prod. Res. Devel.* **1997**, *9*, 1–4.
30. Shao, Z.-Y.; Guo, Y.-W.; Yu, J.-L.; Zhu, D.-Y. Studied on chemical constitution of *Dysidea* sp. from South China Sea. *Nat. Prod. Res. Dev.* **2004**, *16*, 19–22.
31. Wang, B.; Dong, J.; Zhou, X.; Lee, K.J.; Huang, R.; Zhang, S.; Liu, Y. Nucleosides from the marine sponge *Haliclona* sp. *Z. Naturforsch. C* **2009**, *64*, 143–148. [[CrossRef](#)]
32. Huang, R.-M.; Chen, Y.-N.; Zeng, Z.; Gao, C.-H.; Su, X.; Peng, Y. Marine nucleosides: Structure, bioactivity, synthesis and biosynthesis. *Mar. Drugs* **2014**, *12*, 5817–5838. [[CrossRef](#)]
33. Huang, R.; Zhou, X.; Peng, Y.; Yang, X.; Xu, T.; Liu, Y. Nucleosides from the marine sponge *Callyspongia* sp. *Chem. Nat. Comp.* **2011**, *46*, 1010–1011. [[CrossRef](#)]
34. Wang, Y.-L.; Liao, X.-J.; Xu, S.-H. Study on chemical constituents of soft coral *Dendronephthya gigantea* from the South China Sea. *Chin. Pharm. J.* **2009**, *44*, 740–742.
35. Mellado, G.G.; Zubía, E.; Ortega, M.J.; López-González, P.J. Steroids from the Antarctic octocoral *Anthomastus bathyproctus*. *J. Nat. Prod.* **2005**, *68*, 1111–1115. [[CrossRef](#)] [[PubMed](#)]
36. Gunatilaka, A.A.L.; Gopichand, Y.; Schmitz, F.J.; Djerassi, C. Minor and trace sterols in marine invertebrates. 26. Isolation and structure elucidation of nine new 5 $\alpha$ ,8 $\alpha$ -epidioxy sterols from four marine organisms. *J. Org. Chem.* **1981**, *46*, 3860–3866. [[CrossRef](#)]
37. Swell, L.; Gustafsson, J.; Schwartz, C.C.; Halloran, L.G.; Danielsson, H.; Vlahcevic, Z.R. An in vivo evaluation of the quantitative significance of several potential pathways to cholic and chenodeoxycholic acids from cholesterol in man. *J. Lipid Res.* **1980**, *21*, 455–466.
38. Shin, K.; Chin, J.; Hahn, D.; Lee, J.; Hwang, H.; Won, D.H.; Ham, J.; Choi, H.; Kang, E.; Kim, H.; et al. Sterols from a soft coral, *Dendronephthya gigantea* as farnesoid X-activated receptor antagonists. *Steroids* **2012**, *77*, 355–359. [[CrossRef](#)]
39. Smith, A.G.; Goad, L.J. Sterol biosynthesis by the sea urchin *Echinus esculentus*. *Biochem. J.* **1974**, *142*, 421–427. [[CrossRef](#)]
40. Idler, D.R.; Wiseman, P. Identification of 22-*cis*-cholesta-5,22-dien-3 $\beta$ -ol and other scallop sterols by gas-liquid chromatography and mass spectrometry. *Comp. Biochem. Physiol.* **1971**, *38A*, 581–590. [[CrossRef](#)]
41. Byju, K.; Anuradha, V.; Vasundhara, G.; Nair, S.M.; Kumar, N.C. In vitro and in silico studies on the anticancer and apoptosis-inducing activities of the sterols identified from the soft coral, *Subergorgia reticulata*. *Pharmacogn. Mag.* **2014**, *10*, S65–S71.
42. Heilbron, I.M.; Phipers, R.F.; Wright, H.R. Chemistry of the brown algae. *Nature* **1934**, *133*, 419. [[CrossRef](#)]
43. Heilbron, I.; Phipers, R.F.; Wright, H.R. The chemistry of the the algae. Part I. The algae sterol fucosterol. *J. Chem. Soc.* **1934**, 1572–1576. [[CrossRef](#)]

44. Nes, W.R.; Castle, M.; McClanahan, J.L.; Settine, J.M. Confirmation of the structure of fucosterol by nuclear magnetic resonance spectroscopy (1). *Steroids* **1966**, *8*, 655–657. [[CrossRef](#)]
45. Patterson, G.W. The distribution of sterols in algae. *Lipids* **1971**, *6*, 120–127. [[CrossRef](#)]
46. Sheu, J.-H.; Sung, P.-J. Isolation of 24-hydroperoxy-24-vinylcholesterol and fucosterol from the brown alga *Turbinaria conoides*. *J. Chin. Chem. Soc.* **1991**, *38*, 501–503. [[CrossRef](#)]
47. Sheu, J.-H.; Wang, G.-H.; Sung, P.-J.; Chiu, Y.-H.; Duh, C.-Y. Cytotoxic sterols from the Formosan brown alga *Turbinaria ornata*. *Planta Med.* **1997**, *63*, 571–572. [[CrossRef](#)]
48. Ribeiro, S.M.; Cassiano, K.M.; Cavalcanti, D.N.; Teixeira, V.L.; Pereira, R.C. Isolated and synergistic effects of chemical and structural defenses of two species of *Tethya* (Porifera: Demospongiae). *J. Sea Res.* **2012**, *68*, 57–62. [[CrossRef](#)]
49. Padhan, S.K.; Mishra, P.M.; Baliarsingh, S.; Sree, A.; Panigrahi, M. Fatty acid profile and sterol composition of the marine sponge *Petrosia testudinaria*. *Chem. Nat. Comp.* **2015**, *51*, 323–325. [[CrossRef](#)]
50. Shanura Fernando, I.P.; Asanka Sanjeewa, K.K.; Kim, H.-S.; Kim, S.-Y.; Lee, S.-H.; Lee, W.W.; Jeon, Y.-J. Identification of sterols from the soft coral *Dendronephthya gigantea* and their anti-inflammatory potential. *Environ. Toxicol. Pharmacol.* **2017**, *55*, 37–43. [[CrossRef](#)]
51. Shanura Fernando, I.P.; Asanka Sanjeewa, K.K.; Kim, H.-S.; Wang, L.; Lee, W.W.; Jeon, Y.-J. Apoptotic and antiproliferative properties of 3 $\beta$ -hydroxy- $\Delta^5$ -steroidal congeners from a partially purified column fraction of *Dendronephthya gigantea* against HL-60 and MCF-7 cancer cells. *J. Appl. Toxicol.* **2018**, *38*, 527–536. [[CrossRef](#)]
52. Shanura Fernando, I.P.; Asanka Sanjeewa, K.K.; Ann, Y.-S.; Ko, C.-I.; Lee, S.-H.; Lee, W.W.; Jeon, Y.-J. Apoptotic and antiproliferative properties of stigmast-5-en-3-ol from *Dendronephthya gigantea* on human leukemia HL-60 and human breast cancer MCF-7 cells. *Toxicol. in Vitro* **2018**, *52*, 297–305. [[CrossRef](#)] [[PubMed](#)]
53. Findlay, J.A.; Patil, A.D. Novel sterols from the finger sponge *Haliclona oculata*. *Can. J. Chem.* **1985**, *63*, 2406–2410. [[CrossRef](#)]
54. Ighchi, K.; Saitoh, S.; Yamada, Y. Novel 19-oxygenated sterols from the Okinawan soft coral *Litophyton viridis*. *Chem. Pharm. Bull.* **1989**, *37*, 2553–2554. [[CrossRef](#)]
55. Bortolotto, M.; Braekman, J.C.; Daloze, D.; Losman, D.; Tursch, B. Chemical studies of marine invertebrates. XXIII. A novel polyhydroxylated sterol from the soft coral *Litophyton viridis* (Coelenterata, Octocorallia, Alcyonacea). *Steroids* **1976**, *28*, 461–466. [[CrossRef](#)]
56. El-Gamal, A.A.H.; Wang, S.-K.; Dai, C.-F.; Duh, C.-Y. New nardosinanes and 19-oxygenated ergosterols from the soft coral *Nephthea armata* collected in Taiwan. *J. Nat. Prod.* **2004**, *67*, 1455–1458. [[CrossRef](#)]
57. Youssef, D.T.A.; Singab, A.N.B.; van Soest, R.W.M.; Fusetani, N. Hyrtiosenolides A and B, two new sesquiterpenes  $\gamma$ -methoxybutenolides and a new sterol from a Red Sea sponge *Hyrtios* species. *J. Nat. Prod.* **2004**, *67*, 1736–1739. [[CrossRef](#)]
58. Jia, R.; Guo, Y.-W.; Mollo, E.; Gavagnin, M.; Cimino, G. Two new polyhydroxylated steroids from the Hainan soft coral *Sinularia* sp. *Helv. Chim. Acta* **2006**, *89*, 1330–1336. [[CrossRef](#)]
59. Cheng, S.-Y.; Dai, C.-F.; Duh, C.-Y. New 4-methylated and 19-oxygenated steroids from the Formosan soft coral *Nephthea erecta*. *Steroids* **2007**, *72*, 653–659. [[CrossRef](#)]
60. Wu, J.; Xi, Y.; Huang, L.; Li, G.; Mao, Q.; Fang, C.; Shan, T.; Jiang, W.; Zhao, M.; He, W.; et al. A steroid-type antioxidant targeting the Keap1/Nrf2/ARE signaling pathway from the soft coral *Dendronephthya gigantea*. *J. Nat. Prod.* **2018**, *81*, 2567–2575. [[CrossRef](#)]
61. Chao, C.-H.; Wen, Z.-H.; Chen, I.-M.; Su, J.-H.; Huang, H.-C.; Chiang, M.Y.; Sheu, J.-H. Anti-inflammatory steroids from the octocoral *Dendronephthya griffini*. *Tetrahedron* **2008**, *64*, 3554–3560. [[CrossRef](#)]
62. Chao, C.-H.; Wen, Z.-H.; Su, J.-H.; Chen, I.-M.; Huang, H.-C.; Dai, C.-F.; Sheu, J.-H. Further study on anti-inflammatory oxygenated steroids from the octocoral *Dendronephthya griffini*. *Steroids* **2008**, *73*, 1353–1358. [[CrossRef](#)] [[PubMed](#)]
63. Ciminiello, P.; Fattorusso, E.; Forino, M.; Di Rosa, M.; Ianaro, A.; Poletti, R. Structural elucidation of a new cytotoxin isolated from mussels of the Adriatic Sea. *J. Org. Chem.* **2001**, *66*, 578–582. [[CrossRef](#)] [[PubMed](#)]
64. Nilewski, C.; Geisser, R.W.; Carreira, E.M. Total synthesis of a chlorosulfolipid cytotoxin associated with seafood poisoning. *Nature* **2009**, *457*, 573–577. [[CrossRef](#)] [[PubMed](#)]
65. Chao, C.-H.; Huang, H.-C.; Wang, G.-H.; Wen, Z.-H.; Wang, W.-H.; Chen, I.-M.; Sheu, J.-H. Chlorosulfolipids and the corresponding alcohols from the octocoral *Dendronephthya griffini*. *Chem. Pharm. Bull.* **2010**, *58*, 944–946. [[CrossRef](#)]

66. Shaaban, M.; Shaaban, K.A.; Abd-Alla, H.I.; Hanna, A.G.; Laatsch, H. Dendrophene, a novel glycyrrhetyl aminon acid from *Dendronephthya hemprichi*. *Z. Naturforsch.* **2011**, *66b*, 425–432. [\[CrossRef\]](#)
67. Schow, S.R.; McMorris, T.C. Synthesis of 5 $\alpha$ -pregna-1,20-dien-3-one. *Steroids* **1977**, *30*, 389–392. [\[CrossRef\]](#)
68. Lorenzo, M.; Cueto, M.; D'Croz, L.; Maté, J.L.; San-Martín, A.; Darias, J. Muriceanol, a 24-epoxide sterol link in the carbon flux toward side-chain dealkylation of sterols. *Eur. J. Org. Chem.* **2006**, *2006*, 582–585. [\[CrossRef\]](#)
69. Ioannou, E.; Abdel-Razik, A.F.; Alexi, X.; Vagias, C.; Alexis, M.N.; Roussis, V. Pregnanes with antiproliferative activity from the gorgonian *Eunicella cavolini*. *Tetrahedron* **2008**, *64*, 11797–11801. [\[CrossRef\]](#)
70. Higgs, M.D.; Faulkner, D.J. 5 $\alpha$ -Pregna-1,20-dien-3-one and related compounds from a soft coral. *Steroids* **1977**, *30*, 379–388. [\[CrossRef\]](#)
71. Kingston, J.F.; Gregory, B.; Fallis, A.G. Pregna-1,4,20-triene-3-one, a novel marine steroid from the sea raspberry *Gersemia rubiformis*. *Tetrahedron Lett.* **1977**, *18*, 4261–4264. [\[CrossRef\]](#)
72. Kingston, J.F.; Gregory, B.; Fallis, A.G. Marine natural products. Novel C<sub>21</sub>  $\Delta^{20}$  pregnanes from the sea raspberry (*Gersemia rubiformis*). *J. Chem. Soc. Perkin Trans. I* **1979**, 2064–2068. [\[CrossRef\]](#)
73. Ciavatta, M.L.; Lopez Gresa, M.P.; Manzo, E.; Gavagnin, M.; Wahidulla, S.; Cimino, G. New C<sub>21</sub>  $\Delta^{20}$  pregnanes, inhibitors of mitochondrial respiratory chain, from Indopacific octocoral *Carijoo* sp. *Tetrahedron Lett.* **2004**, *45*, 7745–7748. [\[CrossRef\]](#)
74. Yan, X.-H.; Jia, R.; Shen, X.; Guo, Y.-W. A new dolabellane diterpenoid from the Hainan soft coral *Spongodes* sp. *Nat. Prod. Res.* **2007**, *21*, 897–902. [\[CrossRef\]](#) [\[PubMed\]](#)
75. Nam, N.H.; Huong, N.T.; Hanh, T.T.H.; Thanh, N.V.; Cuong, N.X.; Thung, D.C.; Kiem, P.V.; Minh, C.V. Pregnane steroids from the Vietnamese octocoral *Carijoo riisei*. *Nat. Prod. Res.* **2017**, *31*, 2435–2440.
76. Nussim, M.; Mazur, Y.; Sondheimer, F. The hydration of unsaturated steroids by the Brown Hydroboration Reaction. I. Monounsaturated steroids. *J. Org. Chem.* **1964**, *29*, 1120–1131. [\[CrossRef\]](#)
77. Wahidulla, S.; D'Souza, L.; Patel, J. 5 $\alpha$ -Cholestane-3,6-dione from the red alga *Acanthophora spicifera*. *Phytochemistry* **1987**, *26*, 2864–2865. [\[CrossRef\]](#)
78. Wijnberg, J.B.P.A.; de Groot, A. Synthesis and <sup>13</sup>C-NMR analysis of 5 $\alpha$ - and 5 $\beta$ -cholestane-3,6-dione. *Steroids* **1989**, *54*, 333–344. [\[CrossRef\]](#)
79. Gosavi, K.; Moses Babu, J.; Mathur, H.H.; Bhadbhade, M. Isolation and X-ray structure of a new 3,6-diketo steroid from red alga *Hypnea musciformis*. *Chem. Lett.* **1995**, *24*, 519–520. [\[CrossRef\]](#)
80. Ngoc, N.T.; Hanh, T.T.H.; Cuong, N.X.; Nam, N.H.; Thung, D.C.; Ivanchina, N.V.; Dang, N.H.; Kicha, A.A.; Kiem, P.V.; Minh, C.V. Steroids from *Dendronephthya mucronata* and their inhibitory effects on lipopolysaccharide-induced NO formation in RAW264.7 cells. *Chem. Nat. Comp.* **2019**, *55*, 1090–1093. [\[CrossRef\]](#)
81. Zhang, J.; Liang, Y.; Li, L.-C.; Xu, S.-H. Suberosanones A–C, new metabolites possessing cyclopentenone system from the South China Sea gorgonian coral *Subergorgia suberosa*. *Helv. Chim. Acta* **2014**, *97*, 128–136. [\[CrossRef\]](#)
82. Ngoc, N.T.; Hanh, T.T.H.; Nguyen, H.D.; Quang, T.H.; Cuong, N.X.; Nam, N.H.; Thung, D.C.; Ngai, N.D.; Kiem, P.V.; Minh, C.V. Bicyclic lactones from the octocoral *Dendronephthya mucronata*. *Nat. Prod. Res.* **2019**, *1–5*. [\[CrossRef\]](#) [\[PubMed\]](#)
83. Onizuka, R.; Kamiya, H.; Muramoto, K.; Goto, R.; Inoue, K.; Kumamoto, K.; Nakajima, Y.; Iida, S.; Ishigami, F. Purification of the major allergen of red soft coral (*Dendronephthya nipponica*). *Int. Arch. Allergy Immunol.* **2001**, *125*, 135–143. [\[CrossRef\]](#) [\[PubMed\]](#)
84. Wilson, W.K.; Sumpter, R.M.; Warren, J.J.; Rogers, P.S.; Ruan, B.; Schroepfer, G.J., Jr. Analysis of unsaturated C<sub>27</sub> sterols by nuclear magnetic resonance spectroscopy. *J. Lipid Res.* **1996**, *37*, 1529–1555. [\[PubMed\]](#)
85. Fernando, I.P.S.; Lee, W.W.; Jayawardena, T.U.; Kang, M.-C.; Ann, Y.-S.; Ko, C.-I.; Park, Y.J.; Jeon, Y.-J. 3 $\beta$ -Hydroxy- $\Delta^5$ -steroidal congeners from a column fraction of *Dendronephthya puetteri* attenuate LPS-induced inflammatory responses in RAW 264.7 macrophages and zebrafish embryo model. *RSC Adv.* **2018**, *8*, 18626–18634. [\[CrossRef\]](#)
86. Kim, E.-A.; Ding, Y.; Yang, H.-W.; Heo, S.-J.; Lee, S.-H. Soft coral *Dendronephthya puetteri* extract ameliorates inflammations by suppressing inflammatory mediators and oxidative stress in LPS-stimulated zebrafish. *Int. J. Mol. Sci.* **2018**, *19*, 2695. [\[CrossRef\]](#)
87. Jayawardena, T.U.; Lee, W.W.; Fernando, I.P.S.; Sanjeewa, K.K.A.; Wang, L.; Lee, T.-G.; Park, Y.J.; Ko, C.-I.; Jeon, Y.-J. Antiproliferative and apoptosis-inducing potential of 3 $\beta$ -hydroxy- $\Delta^5$ -steroidal congeners purified from the soft coral *Dendronephthya puetteri*. *J. Oceanol. Limnol.* **2019**, *37*, 1382–1392. [\[CrossRef\]](#)

88. Sheikh, Y.M.; Singy, G.; Kaisin, M.; Eggert, H.; Djerassi, C.; Tursch, B.; Daloze, D.; Braekman, J.C. Chemical studies of marine invertebrates—XIV. Four representatives of a novel sesquiterpene class—the capnellane skeleton. *Tetrahedron* **1976**, *32*, 1171–1178. [[CrossRef](#)]
89. Morris, L.A.; Jaspars, M.; Adamson, K.; Woods, S.; Wallace, H.M. The capnellenes revisited: New structures and new biological activity. *Tetrahedron* **1998**, *54*, 12953–12958. [[CrossRef](#)]
90. Kaisin, M.; Braekman, J.C.; Daloze, D.; Tursch, B. Novel acetoxycapnellenes from the alcyonacean *Capnella imbricata*. *Tetrahedron* **1985**, *41*, 1067–1072. [[CrossRef](#)]
91. Grote, D.; Hänel, F.; Dahse, H.-M.; Seifert, K. Capnellenes from the soft coral *Dendronephthya rubeola*. *Chem. Biodivers.* **2007**, *4*, 1683–1693. [[CrossRef](#)]
92. Yan, X.-H.; Lin, L.-P.; Ding, J.; Guo, Y.-W. Methyl spongoate, a cytotoxic steroid from the Sanya soft coral *Spongodes* sp. *Bioorg. Med. Chem. Lett.* **2007**, *17*, 2661–2663. [[CrossRef](#)] [[PubMed](#)]
93. Suginome, H.; Senboku, H.; Yamada, S. A new aromatization of ring-A of steroids. Synthesis of estrone. *Tetrahedron Lett.* **1988**, *20*, 79–80. [[CrossRef](#)]
94. Kočovský, P.; Baines, R.S. Stereoelectronically controlled, thallium(III)-mediated C-19 degradation of 19-hydroxy steroids. An expedient route to estrone and its congeners via 19-nor-10 $\beta$ -hydroxy intermediates. *J. Org. Chem.* **1994**, *59*, 5439–5444. [[CrossRef](#)]
95. Yan, X.-H.; Liu, H.-L.; Huang, H.; Li, X.-B.; Guo, Y.-W. Steroids with aromatic A-rings from the Hainan soft coral *Dendronephthya studeri* Ridley. *J. Nat. Prod.* **2011**, *74*, 175–180. [[CrossRef](#)] [[PubMed](#)]
96. Katrich, E.M.; Isai, S.V.; Mishchenko, T.Y. Phospholipid composition of prostaglandin extracts of some marine invertebrates with different degrees of prostaglandin-like activity. *Chem. Nat. Comp.* **1990**, *26*, 264–267. [[CrossRef](#)]
97. Mizobuchi, S.; Shimidzu, N.; Katsuoka, M.; Adachi, K.; Miki, W. Antifouling substances against the mussel in an octocoral *Dendronephthya* sp. *Nippon Suisan Gakk.* **1993**, *59*, 1195–1199. [[CrossRef](#)]
98. Matsumoto, T.; Shimizu, N.; Shigemoto, T.; Itoh, T.; Iida, T.; Nishioka, A. Isoaltion of 22-dehydro- campesterol from the seeds of *Brassica juncea*. *Phytochemistry* **1983**, *22*, 789–790. [[CrossRef](#)]
99. Weldon, P.J.; Flachsbarth, B.; Schulz, S. Natural products from the integument of nonavian reptiles. *Nat. Prod. Rep.* **2008**, *25*, 738–756. [[CrossRef](#)]
100. Dzeha, T.; Jaspars, M.; Tabudravu, J. Clionasterol, a triterpenoid from the Kenyan marine green macroalga *Halimeda macroloba*. *West. Indian Ocean J. Mar. Sci.* **2003**, *2*, 157–161.
101. Gallo, C.; Landi, S.; d’Ippolito, G.; Nuzzo, G.; Manzo, E.; Sardo, A.; Fontana, A. Diatoms synthesize sterols by inclusion of animal and fungal genes in the plant pathway. *Sci. Rep.* **2020**, *10*, 4204. [[CrossRef](#)]
102. Kawamata, M.; Kon-ya, K.; Miki, W. Trigonelline, an antifouling substance isolated from an octocoral *Dendronephthya* sp. *Fish. Sci.* **1994**, *60*, 485–486. [[CrossRef](#)]
103. Miki, W.; Kon-ya, K.; Mizobuchi, S. Biofouling and marine biotechnology: New antifoulants from marine invertebrates. *J. Mar. Biotechnol.* **1996**, *4*, 117–120.
104. Wilsanand, V.; Wagh, A.B.; Bapuji, M. Antifouling activities of marine sedentary invertebrates on some macrofoulers. *Indian J. Mar. Sci.* **1999**, *28*, 280–284.
105. Tomono, Y.; Hirota, H.; Imahara, Y.; Fusetani, N. Four new steroids from two octocorals. *J. Nat. Prod.* **1999**, *62*, 1538–1541. [[CrossRef](#)] [[PubMed](#)]
106. Řezanka, T.; Dembitsky, V.M. Brominated oxylipins and oxylipin glycosides from Red Sea corals. *Eur. J. Org. Chem.* **2003**, 309–316. [[CrossRef](#)]
107. Kang, B.K.; Chung, M.J.; Park, Y.J. The crystal and molecular structure of cholesteryl formate. *Bull. Korean Chem. Soc.* **1985**, *6*, 333–337.
108. Teng, J.I.; Kulig, M.J.; Smith, L.L.; Kan, G.; van Lier, J.E. Sterol metabolism. XX. Cholesterol 7 $\beta$ -hydroperoxide. *J. Org. Chem.* **1973**, *38*, 119–123. [[CrossRef](#)]
109. de Riccardis, F.; Minale, L.; Iorizzi, M.; Debitus, C.; Lévi, C. Marine sterols. Side-chain-oxygenated sterols, possibly of abiotic origin, from the New Caledonian sponge *Stelodoryx chlorophylla*. *J. Nat. Prod.* **1993**, *56*, 282–287. [[CrossRef](#)]
110. Notaro, G.; Piccialli, V.; Sica, D. New steroidal hydroxyketones and closely related diols from the marine sponge *Cliona copiosa*. *J. Nat. Prod.* **1992**, *55*, 1588–1594. [[CrossRef](#)]
111. Shoppee, C.W.; Newman, B.C. Steroids. Part XXX. Some properties of the cholest-5-ene-3 $\beta$ ,7 $\xi$ -diols and their esters. *J. Chem. Soc. (C)* **1968**, *8*, 981–983. [[CrossRef](#)]



112. Kumar, V.; Amann, A.; Ourisson, G.; Luu, B. Stereospecific syntheses of 7 $\beta$ - and 7 $\alpha$ -hydroxycholesterols. *Synth. Commun.* **1987**, *17*, 1279–1286. [\[CrossRef\]](#)
113. Rizvi, S.Q.A.; Williams, J.R. Synthesis and carbon-13 nuclear magnetic resonance studies of  $\Delta^5$  and saturated 4,4-disubstituted 3-ketosteroids. *J. Org. Chem.* **1981**, *46*, 1127–1132. [\[CrossRef\]](#)
114. Parish, E.J.; Honda, H.; Chitrakorn, S.; Livant, P. A facile chemical synthesis of cholest-4-en-3-one. Carbon-13 nuclear magnetic resonance spectral properties of cholest-4-en-3-one and cholest-5-en-3-one. *Lipids* **1991**, *26*, 675–677. [\[CrossRef\]](#)
115. Wu, K.; Li, W.; Song, J.; Li, T. Production, purification, and identification of cholest-4-en-3-one produced by cholesterol oxidase from *Rhodococcus* sp. in aqueous/organic biphasic system. *Biochem. Insights* **2015**, *8*(S1), 1–8.
116. Sheikh, Y.M.; Djerassi, C. Steroids from sponges. *Tetrahedron* **1974**, *30*, 4095–4103. [\[CrossRef\]](#)
117. Guella, G.; Mancini, I.; Pietra, F. Isolation of ergosta-4,24-dien-3-one from both Astrophorida demosponges and Subantarctic hexactinellides. *Comp. Biochem. Physiol.* **1988**, *90B*, 113–115. [\[CrossRef\]](#)
118. Wright, J.L.C.; McInnes, A.G.; Shimizu, S.; Smith, D.G.; Walter, J.A.; Idler, D.; Khalil, W. Identification of C-24 alkyl epimers of marine sterols by  $^{13}\text{C}$  nuclear magnetic resonance spectroscopy. *Can. J. Chem.* **1978**, *56*, 1898–1903.
119. Li, G.; Deng, Z.; Guan, H.; van Ofwegen, L.; Proksch, P.; Lin, W. Steroids from the soft coral *Dendronephthya* sp. *Steroids* **2005**, *70*, 13–18. [\[CrossRef\]](#)
120. Ma, A.; Deng, Z.; van Ofwegen, L.; Bayer, M.; Proksch, P.; Lin, W. Dendronpholides A–R, cembranoid diterpenes from the Chinese soft coral *Dendronephthya* sp. *J. Nat. Prod.* **2008**, *71*, 1152–1160, (Correction in *J. Nat. Prod.* **2010**, *73*, 1026). [\[CrossRef\]](#)
121. Anjaneyulu, A.S.R.; Rao, G.V.; Sagar, K.S.; Kumar, K.R.; Mohan, K.C. Sandensolide: A new dihydroxycembranolide from the soft coral, *Sinularia sandensis* Verseveldt of the Indian Ocean. *Nat. Prod. Lett.* **1995**, *7*, 183–190. [\[CrossRef\]](#)
122. Anjaneyulu, A.S.R.; Sagar, K.S.; Rao, G.V. New cembranoid lactones from the Indian Ocean soft coral *Sinularia flexibilis*. *J. Nat. Prod.* **1997**, *60*, 9–12. [\[CrossRef\]](#)
123. Hu, L.-C.; Su, J.-H.; Chiang, M.Y.-N.; Lu, M.-C.; Hwang, T.-L.; Chen, Y.-H.; Hu, W.-P.; Lin, N.-C.; Wang, W.-H.; Fang, L.-S.; et al. Flexibilins A–C, new cembrane-type diterpenoids from the Formosan soft coral, *Sinularia flexibilis*. *Mar. Drugs* **2013**, *11*, 1999–2012. [\[CrossRef\]](#)
124. Chen, C.-T.; Kao, C.L.; Li, H.-T.; Chen, C.-Y. Chemical constituents of cultured soft coral *Sinularia flexibilis*. *Chem. Nat. Comp.* **2018**, *54*, 168–169. [\[CrossRef\]](#)
125. Tursch, B.; Braekman, J.C.; Daloze, D.; Herin, M.; Karlsson, R.; Losman, D. Chemical studies of marine invertebrates—XI. Sinulariolide, a new cembranolide diterpene from the soft coral *Sinularia flexibilis* (Coelenterata, Octocorallia, Alcyonacea). *Tetrahedron* **1975**, *31*, 129–133. [\[CrossRef\]](#)
126. Kazlauskas, R.; Murphy, P.T.; Wells, R.J.; Schönholzer, P.; Coll, J.C. Cembranoid constituents from an Australian collection of the soft coral *Sinularia flexibilis*. *Aust. J. Chem.* **1978**, *31*, 1817–1824. [\[CrossRef\]](#)
127. Mori, K.; Suzuki, S.; Iguchi, K.; Yamada, Y. 8,11-Epoxy bridged cembranolide diterpene from the soft coral *Sinularia flexibilis*. *Chem. Lett.* **1983**, *12*, 1515–1516. [\[CrossRef\]](#)
128. Wen, T.; Ding, Y.; Deng, Z.; van Ofwegen, L.; Proksch, P.; Lin, W. Sinulaflexiolides A–K, cembrane-type diterpenoids from the Chinese soft coral *Sinularia flexibilis*. *J. Nat. Prod.* **2008**, *71*, 1133–1144. [\[CrossRef\]](#)
129. Michalek, K.; Bowden, B.F. A natural algacide from soft coral *Sinularia flexibilis* (Coelenterata, Octocorallia, Alcyonacea). *J. Chem. Ecol.* **1997**, *23*, 259–273. [\[CrossRef\]](#)
130. Lo, K.-L.; Khalil, A.T.; Kuo, Y.-H.; Shen, Y.-C. Sinuladiterpenes A–F, new cembrane diterpenes from *Sinularia flexibilis*. *Chem. Biodivers.* **2009**, *6*, 2227–2235. [\[CrossRef\]](#)
131. Xu, S.H.; Zeng, L.M. The identification of two new sterols from marine organism. *Chin. Chem. Lett.* **2000**, *11*, 531–534.
132. Liao, X.; Xu, S.; Lin, H. Isolation and identification of two tetrahydroxylated sterols with cytotoxic activity. *Chin. J. Org. Chem.* **2010**, *30*, 749–752.
133. Elkhayat, E.S.; Ibrahim, S.R.M.; Fouad, M.A.; Mohamed, G.A. Dendronephthols A–C, new sesquiterpenoids from the Red Sea soft coral *Dendronephthya* sp. *Tetrahedron* **2014**, *70*, 3822–3825. [\[CrossRef\]](#)
134. Ioannou, E.; Abdel-Razik, A.F.; Zervou, M.; Christofidis, D.; Alexi, X.; Vagias, C.; Alexis, M.N.; Roussis, V. 5 $\alpha$ ,8 $\alpha$ -Epidioxysterols from the gorgonian *Eunicella cavolini* and the ascidian *Trididemnum inarmatum*: Isolation and evaluation of their antiproliferative activity. *Steroids* **2009**, *74*, 73–80. [\[CrossRef\]](#)



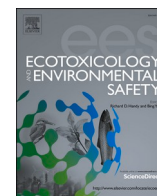
135. Huynh, T.-H.; Chen, P.-C.; Yang, S.-N.; Lin, F.-Y.; Su, T.-P.; Chen, L.-Y.; Peng, B.-R.; Hu, C.-C.; Chen, Y.-Y.; Wen, Z.-H.; et al. New 1,4-dienonesteroids from the octocoral *Dendronephthya* sp. *Mar. Drugs* **2019**, *17*, 530. [\[CrossRef\]](#)
136. Gallina, C.; Remeo, A.; Tortorella, V.; D'Agnolo, G. Racemic deoxymycelianamide. *Chem. Ind.* **1966**, *30*, 1300–1301.
137. Gallina, C.; Remeo, A.; Tortorella, V.; D'Agnolo, G. Synthesis of racemic deoxymycelianamide. *Ann. Chim.* **1968**, *58*, 280–285.
138. Birch, A.J.; Donovan, F.W. Studies in relation to biosynthesis. I. Some possible routes to derivatives of orcinol and phloroglucinol. *Aust. J. Chem.* **1953**, *6*, 360–368. [\[CrossRef\]](#)
139. Birch, A.J.; Massy-Westropp, R.A.; Rickards, R.W.; Smith, H. Studies in relation to biosynthesis. Part XIII. Griseofulvin. *J. Chem. Soc.* **1958**, 360–365. [\[CrossRef\]](#)
140. Tanabe, M.; Detre, G. The use of  $^{13}\text{C}$ -labeled acetate in biosynthetic studies. *J. Am. Chem. Soc.* **1966**, *88*, 4515–4517. [\[CrossRef\]](#)
141. Harris, C.M.; Roberson, J.S.; Harris, T.M. Biosynthesis of griseofulvin. *J. Am. Chem. Soc.* **1976**, *98*, 5380–5386. [\[CrossRef\]](#)
142. Cole, R.J.; Kirksey, J.W.; Holaday, C.E. Detection of griseofulvin and dechlorogriseofulvin by thin-layer chromatography and gas-liquid chromatography. *Appl. Microbiol.* **1970**, *19*, 106–108. [\[CrossRef\]](#)
143. Jarvis, B.B.; Zhou, Y.; Jiang, J.; Wang, S.; Sorenson, W.G.; Hintikka, E.-L.; Nikulin, M.; Parikka, P.; Etzel, R.A.; Dearborn, D.G. Toxigenic molds in water-damaged buildings: Dechlorogriseofulvins from *Memnoniella echinata*. *J. Nat. Prod.* **1996**, *59*, 553–554. [\[CrossRef\]](#)
144. MacMillan, J. Griseofulvin. Part VII. Dechlorogriseofulvin. *J. Chem. Soc.* **1953**, 1697–1702. [\[CrossRef\]](#)
145. Xue, C.; Li, T.; Deng, Z.; Fu, H.; Lin, W. Janthinolide A-B, two new 2,5-piperazinedione derivatives from the endophytic *Penicillium janthinellum* isolated from the soft coral *Dendronephthya* sp. *Pharmazie* **2006**, *61*, 1041–1044. [\[CrossRef\]](#)
146. Itokawa, H.; Akita, Y.; Yamazaki, M. The indole derivatives isolated from the oil cakes of *Camellia* seeds. On the relation to the components of the fungus infecting the oil cakes. *Yakugaku Zasshi* **1973**, *93*, 1251–1252. [\[CrossRef\]](#)
147. Casnati, G.; Pochini, P.; Ungaro, R. Neoechinulin: A new isoprenyl-indole metabolite from *Aspergillus amstelodami*. *Gazz. Chim. Ital.* **1973**, *103*, 141–151.
148. Dossena, A.; Marchelli, R.; Pochini, A. New metabolites of *Aspergillus amstelodami* related to the biogenesis of neoechinulin. *J. Chem. Soc. Chem. Comm.* **1974**, 771–772. [\[CrossRef\]](#)
149. Nagasawa, H.; Isogai, A.; Ikeda, K.; Sato, S.; Murakoshi, S.; Suzuki, A.; Tamura, S. Isolation and structure elucidation of a new indole metabolite from *Aspergillus ruber*. *Agric. Biol. Chem.* **1975**, *39*, 1901–1902. [\[CrossRef\]](#)
150. Cardillo, R.; Fuganti, C.; Ghiringhelli, D.; Grasselli, P.; Gatti, G. Stereochemical course of the  $\alpha,\beta$ -desaturation of L-tryptophan in the biosynthesis of cryptoechinuline A in *Aspergillus amstelodami*. *J. Chem. Soc. Chem. Comm.* **1975**, 778–779. [\[CrossRef\]](#)
151. Marchelli, R.; Dossena, A.; Casnati, G. Biosynthesis of neoechinulin by *Aspergillus amstelodami* from cyclo-L-[U- $^{14}\text{C}$ ]alanyl-L-[5,7- $^3\text{H}_2$ ]tryptophyl. *J. Chem. Soc. Chem. Comm.* **1975**, 779–780. [\[CrossRef\]](#)
152. Marchelli, R.; Dossena, A.; Pochini, A.; Dradi, E. The structures of five new dihydropeptides related to neoechinulin, isolated from *Aspergillus amstelodami*. *J. Chem. Soc. Perkin Trans. I* **1977**, 713–717. [\[CrossRef\]](#)
153. Yagi, R.; Doi, M. Isolation of an antioxidative substance produced by *Aspergillus repens*. *Biosci. Biotechnol. Biochem.* **1999**, *63*, 932–933. [\[CrossRef\]](#)
154. Li, Y.; Li, X.; Kim, S.-K.; Kang, J.S.; Choi, H.D.; Rho, J.R.; Son, B.W. Golmaenone, a new diketopiperazine alkaloid from the marine-derived fungus *Aspergillus* sp. *Chem. Pharm. Bull.* **2004**, *52*, 375–376. [\[CrossRef\]](#)
155. Stipanovic, R.D.; Schroeder, H.W. Preechinulin, a metabolite of *Aspergillus chevalieri*. *Trans. Br. Mycol. Soc.* **1976**, *66*, 178–179. [\[CrossRef\]](#)
156. Hamasaki, T.; Nagayama, K.; Hatsuda, Y. Structure of a new metabolite from *Aspergillus chevalieri*. *Agric. Biol. Chem.* **1976**, *40*, 203–205. [\[CrossRef\]](#)
157. Nagasawa, H.; Isogai, A.; Suzuki, A.; Tamura, S. Structures of isoechinulins A, B and C, new indole metabolites from *Aspergillus ruber*. *Tetrahedron Lett.* **1976**, *17*, 1601–1604. [\[CrossRef\]](#)
158. Fujimoto, H.; Fujimaki, T.; Okuyama, E.; Yamazaki, M. Immunomodulatory constituents from an Ascomycete, *Microascus tardifaciens*. *Chem. Pharm. Bull.* **1999**, *47*, 1426–1432. [\[CrossRef\]](#)
159. Wang, W.-L.; Lu, Z.-Y.; Tao, H.-W.; Zhu, T.-J.; Fang, Y.-C.; Gu, Q.-Q.; Zhu, W.-M. Isoechinulin-type alkaloids, varicolorins A–L, from halotolerant *Aspergillus varicolor*. *J. Nat. Prod.* **2007**, *70*, 1558–1564. [\[CrossRef\]](#)

160. Li, Y.; Li, X.; Kang, J.S.; Choi, H.D.; Son, B.W. New radical scavenging and ultraviolet-a protecting prenylated dioxopiperazine alkaloid related to isoechinulin A from a marine isolate of the fungus *Aspergillus*. *J. Antibiot.* **2004**, *57*, 337–340. [[CrossRef](#)]
161. Hamasaki, T.; Nagayama, K.; Hatsuda, Y. A new metabolite, L-alanyl-L-tryptophan anhydride from *Aspergillus chevalieri*. *Agric. Biol. Chem.* **1976**, *40*, 2487. [[CrossRef](#)]
162. Sun, X.-P.; Xu, Y.; Cao, F.; Xu, R.-F.; Zhang, X.-L.; Wang, C.-Y. Isoechinulin-type alkaloids from a soft coral-derived fungus *Nigrospora oryzae*. *Chem. Nat. Comp.* **2014**, *50*, 1153–1155. [[CrossRef](#)]

**Publisher’s Note:** MDPI stays neutral with regard to jurisdictional claims in published maps and institutional affiliations.



© 2020 by the authors. Licensee MDPI, Basel, Switzerland. This article is an open access article distributed under the terms and conditions of the Creative Commons Attribution (CC BY) license (<http://creativecommons.org/licenses/by/4.0/>).



## Sources and components of volatile organic compounds in breast surgery operating rooms

Ming-Huei Cheng<sup>a,b,1</sup>, Chun-Hui Chiu<sup>c,d,1</sup>, Chi-Tsung Chen<sup>e</sup>, Hsu-Huan Chou<sup>e,f</sup>,  
Li-Heng Pao<sup>c,g</sup>, Gwo-Hwa Wan<sup>h,i,j,k,\*</sup>

<sup>a</sup> Department of Plastic and Reconstruction Surgery, Chang Gung Memorial Hospital, Taoyuan, Taiwan

<sup>b</sup> College of Medicine, Chang Gung University, Taoyuan, Taiwan

<sup>c</sup> Graduate Institute of Health Industry and Technology, Research Center for Chinese Herbal Medicine, Research Center for Food and Cosmetic Safety, College of Human Ecology, Chang Gung University of Science and Technology, Taoyuan, Taiwan

<sup>d</sup> Department of Traditional Chinese Medicine, Keelung Chang Gung Memorial Hospital, Keelung, Taiwan

<sup>e</sup> Graduate Institute of Clinical Medical Sciences, College of Medicine, Chang Gung University, Taoyuan, Taiwan

<sup>f</sup> Department of General Surgery, Linkou Chang Gung Memorial Hospital, Taoyuan, Taiwan

<sup>g</sup> Department of Gastroenterology and Hepatology, Linkou Chang Gung Memorial Hospital, Taoyuan, Taiwan

<sup>h</sup> Department of Respiratory Therapy, College of Medicine, Chang Gung University, Taoyuan, Taiwan

<sup>i</sup> Department of Respiratory Care, Chang Gung University of Science and Technology, Chiayi, Taiwan

<sup>j</sup> Department of Obstetrics and Gynaecology, Taipei Chang Gung Memorial Hospital, Taipei, Taiwan

<sup>k</sup> Center for Environmental Sustainability and Human Health, Ming Chi University of Technology, Taishan, New Taipei, Taiwan

### ARTICLE INFO

Edited by: Dr G Liu

#### Keywords:

Surgical smoke

Breast surgery

Electrosurgical units

Electrocautery power

Volatile organic compounds

### ABSTRACT

**Objectives:** The composition and concentration distribution of volatile organic compounds (VOCs) in surgical smoke had seldomly been reported. This study aimed to investigate the profile of VOCs and their concentration in surgical smoke from breast surgery during electrocautery in different tissues, electrosurgical units, and electrocautery powers.

**Methods:** Thirty-eight surgical smoke samples from 23 patients performed breast surgery were collected using evacuated stainless steel canisters. The concentrations of 87 VOCs in surgical smoke samples were analyzed by gas chromatography-mass spectrometry. The human tissues, electrosurgical units, and electrocautery power were recorded.

**Results:** The median level of total VOCs concentrations in surgical smoke samples from mammary glands (total VOCs: 9953.5 ppb; benzene: 222.7 ppb; 1,3-butadiene: 856.2 ppb; vinyl chloride: 3.1 ppb) using conventional electrosurgical knives were significantly higher than that from other tissues (total VOCs: 365.7–4266.8 ppb,  $P < 0.05$ ; benzene: 26.4–112 ppb,  $P < 0.05$ ; 1,3-butadiene: 15.6–384 ppb,  $P < 0.05$ ; vinyl chloride: 0.6–1.8 ppb,  $P < 0.05$ ) using different electrosurgical units. A high methanol concentration was found in surgical smoke generated during breast surgery (641.4–4452.5 ppb) using different electrosurgical units. An electrocautery power of  $\geq 27.5$  watts used for skin tissues produced a higher VOCs concentration (2905.8 ppb).

**Conclusions:** The surgical smoke samples collected from mammary glands using conventional electrosurgical knives had high VOCs concentrations. The carcinogens (including benzene, 1,3-butadiene, and vinyl chloride) and methanol were found in the surgical smoke samples from different electrosurgical units. The type of electrosurgical unit and electrocautery power used affected VOCs concentrations in surgical smoke.

### 1. Introduction

An electrosurgical machine utilizes tissue resistance to the flow of

current from the electrode to convert electrical energy into heat. Tissue heating may not completely be achieved during electrosurgical procedures and often accompany by surgical smoke with an unpleasant

\* Correspondence to: Department of Respiratory Therapy, College of Medicine, Chang Gung University, Wen-Hwa 1st Road, Kwei-Shan, Taoyuan, Taiwan.

E-mail addresses: [minghuei@cgmh.org.tw](mailto:minghuei@cgmh.org.tw) (M.-H. Cheng), [chchiu@mail.cgust.edu.tw](mailto:chchiu@mail.cgust.edu.tw) (C.-H. Chiu), [jackson08036@gmail.com](mailto:jackson08036@gmail.com) (C.-T. Chen), [b9002009@cgmh.org.tw](mailto:b9002009@cgmh.org.tw) (H.-H. Chou), [paoh@mail.cgust.edu.tw](mailto:paoh@mail.cgust.edu.tw) (L.-H. Pao), [ghwan@mail.cgu.edu.tw](mailto:ghwan@mail.cgu.edu.tw) (G.-H. Wan).

<sup>1</sup> The author was equally contributed with the first author.

<https://doi.org/10.1016/j.ecoenv.2020.111855>

Received 30 September 2020; Received in revised form 15 December 2020; Accepted 21 December 2020

Available online 29 December 2020

0147-6513/© 2020 The Authors.

Published by Elsevier Inc.

This is an open access article under the CC BY-NC-ND license

(<http://creativecommons.org/licenses/by-nc-nd/4.0/>).

odor (Massarweh et al., 2006). Surgical smoke is mainly composed of 95% water vapor, 5% suspended particles, bioaerosols, and chemical gases (Ulmer, 2008). Hill et al. (2012) indicated that the average daily diathermy activation time was 12 min and 43 s for surgery, and the surgical smoke production per day is equivalent to smoking 27–30 cigarettes per day.

Three factors such as human tissue, type of surgery, and electrosurgical unit influence the concentration and composition of VOCs. The increase in electrocautery power was not related to the changes in the concentrations of 1,3-butadiene, benzene, and furfural in surgical smoke (Kocher et al., 2019). A Brazil study showed that the components of VOCs in surgical smoke produced when electrocoagulating subcutaneous tissue, pork meat, and liver tissue of pigs were different (Kalil et al., 2016). The concentrations of toluene, ethylbenzene, and xylene produced from verruca extraction surgery were higher than those produced from pilonidal sinus removal surgery and abdominal surgery (Al Sahaf et al., 2007). In addition to styrene, the mean concentrations of benzene, ethylbenzene, toluene, heptane, and methylpropene produced from electrocautery was significantly higher than those from the ultrasonic knife (Fitzgerald et al., 2012). The National Institute for Occupational Safety and Health study indicated that the most common components in surgical smoke were ethanol and isopropyl alcohol; other pollutants, including acetaldehyde, acetone, acetonitrile, benzene, hexane, styrene, and toluene, were also found (Lee et al., 2018). Additionally, the electrocautery time was positively associated with the VOC concentration in the air inside the operating rooms (ORs) (Liang et al., 2020).

The United States Occupational Safety and Health Administration (OSHA) estimated that 500,000 health care personnel in ORs were exposed to surgical smoke each year (Occupational Safety and Health Administration OSHA, 2008). A few studies have investigated the health hazards associated with surgical smoke exposure. An *in vitro* study found that surgical smoke exposure can cause apoptosis in 40% of human small airway epithelial cells and 20% of mice macrophages as well as increase the concentration of lactate dehydrogenase in both cell types, causing impairment in the cell membrane structure (Sisler et al., 2018). Moreover, a questionnaire-based study found that the risk of severe persistent asthma in OR nurses was 2.48 times higher than that in the administrative nurse after adjusting for age, body mass index, and smoking history (Le Moual et al., 2013). The risk of lung cancer in OR nurses who worked for over 15 years was 0.58-fold higher than that in nurses who worked in other units of the hospital when adjusted for age, smoking history, secondhand smoke exposure, and fruit and vegetable intake. The working year had no association with the incidence of lung cancer in OR nurses (Gates et al., 2007).

To date, only a few studies have evaluated the composition and change of VOC concentration in surgical smoke under different electrocautery conditions. Therefore, this study aimed to evaluate the profile of VOCs and their concentration distribution in surgical smoke during breast surgery.

## 2. Materials and methods

### 2.1. Surgical smoke sampling and analysis

The breast surgery ORs were located on the second floor of an 11-story medical building in Linkuo Chang Gung Memorial Hospital in northern Taiwan. The breast surgery ORs were categorized as ISO 14644–1 class 7 (ISO International Organization for Standardization, 2015) and measured room volumes of 110–140 m<sup>3</sup>. Each OR was equipped with high-efficiency particulate air (HEPA) H14 filters, which were changed annually, in the central ceiling of the ORs. The ventilation rate of ORs was 20–22 air changes per hour (ACH) throughout the day and around 85% of the total circulating airflow was returned through four return air vents to the supply air system. The breast surgery ORs were kept at 19–23 °C of set indoor temperature and 55–65% of set relative humidity (RH). Additionally, the OR personnel usually included

one surgeon, two scrubbing nurses, one circulating nurse, and one anesthesia nurse.

Altogether, 38 surgical smoke samples from 23 patients were collected during breast surgery (partial mastectomy, simple mastectomy, sentinel lymph node dissection, and breast reconstruction surgery) including breast skin (n = 8), breast adipose tissues (n = 6), mammary glands (n = 10), breast tumors (n = 3), abdominal skin (n = 2), and abdominal adipose tissues (n = 3) using conventional electrosurgical knives as well as breast adipose tissues (n = 3) and mammary glands (n = 3) using pulsed electron avalanche knives (PEAK). Additionally, this study collected 3 air samples during disinfection from patients to evaluate the VOC concentrations in alcohol-based disinfectants.

The surgical smoke samples were collected from the start of cauterization of a particular site. A grab sampling technique was used with a 6 liter of evacuated canister for 30 s followed by the NIOSH sampling method (LeBouf et al., 2012). During the sampling period, the sampling head was placed at 2–3 cm to the surgical site, and the information such as electrosurgical unit, electrocautery power, electrocautery tissue, and indoor thermal-hygrometric conditions of the ORs were recorded. The gas chromatography–mass spectrometry analysis of 87 VOCs in surgical smoke samples was performed using the NIEA A715.15B standard method of Taiwan's Environmental Analysis Laboratory (Environmental Analytical Laboratory (EAL), 2014). The analytical system included an Agilent 6890 series gas chromatograph with HP7673 autosampler, split/splitless injector, MSD detector and DB-1 column (60 m x 0.32 mm x 3.0 µm, Agilent, USA). The parameters were set as follows: oven temperature at 35 °C for 5 min and raised at rates of 10 °C/min to 200 °C, high-purity helium gas flow rate was 2.0 mL/min in constant flow mode, inlet temperature was 125 °C, split ratio was 0.2:1. The temperatures of the interface and the ion source were set at 230 °C and mass scan range was 30–280 m/z. All MS data for analytes were collected by ChemStation software. To achieve the quality control and assurance of the analytical data, a standard gas sample (1 ppmv, Linde Spectra Environmental Gases, USA) was prepared and a calibration curve (1–80 ppbv) of 87 VOCs was analyzed for each experiment. All the data of 87 VOCs in standard gas samples and surgical smoke samples from patients were blank-corrected to account for background signal. Additionally, ten percent of the steel canisters were sampled for blank analysis to ensure data quality. The relative difference in duplicate measurements of the samples was below 25%, and the recovery rate of samples ranged between 70% and 130% in this study.

### 2.2. Statistical methods

This study used the SPSS version 25.0 (SPSS, Chicago, Illinois, USA) for statistical analysis. The figures were graphed using the GraphPad Prism 7.0 software (GraphPad Software, Inc., San Diego, CA, USA). The significance level was set at 0.05. The Kruskal-Wallis test and Mann-Whitney *U* test were used to analyze the changes in VOC concentration in surgical smoke samples in different electrocautery tissues, electrosurgical units, and electrocautery power.

This study combined the VOC data from breast skin with that from abdominal skin and defined as subcutaneous tissues. In addition, VOC data from breast and abdominal adipose tissues were pooled and defined as adipose tissues.

## 3. Results

During the skin disinfection procedure performed in surgical patients, 23 VOCs were detected in the air samples, indicating that methanol (24.9 ppb) had the highest mean concentration, followed by acetone (12.6 ppb), isopropylbenzene (4.0 ppb), toluene (3.1 ppb), and propane (1.7 ppb) (Fig. 1). Other VOCs included 2-butanone, chloromethane, (*p,m*)-xylene, alpha-methyl styrene, n-undecane, dichlorodifluoromethane, chlorodifluoromethane, n-dodecane, methylene chloride, o-xylene, benzene, trichlorofluoromethane, ethylbenzene, 1,3-

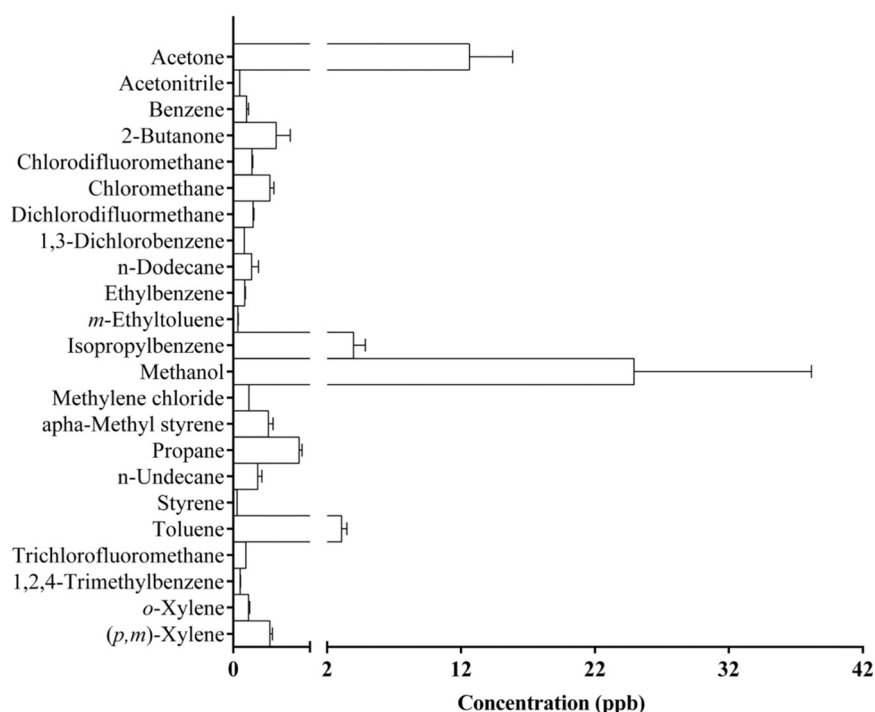


Fig. 1. VOC concentration distribution in background air samples during the skin disinfection procedure. Data were represented as mean and standard error of the mean.

dichlorobenzene, 1,2,4-trimethylbenzene, acetonitrile, m-ethyltoluene, and styrene.

The thermal-hygroscopic characteristics of the breast surgery ORs were 18.50–22.95 °C and 41.63–56.46%. The median VOC concentration in surgical smoke samples from mammary glands (9953.5 ppb) was significantly higher than that from breast subcutaneous tissues (2024.4 ppb,  $P < 0.001$ ), breast adipose tissues (1865.9 ppb,  $P = 0.001$ ), and breast tumors (1308.8 ppb,  $P = 0.011$ ) using conventional electrosurgical knives as well as that from breast adipose tissues (365.8 ppb,  $P = 0.011$ ) and mammary glands (4266.8 ppb,  $P = 0.011$ ) using PEAK (Fig. 2).

The mean methanol concentration (1182.9 ppb) in surgical smoke samples from breast subcutaneous tissues using conventional electrosurgical knives was the highest, followed by acetonitrile (264.7 ppb), propane (225.7 ppb), 1,3-butadiene (170.7 ppb), acrolein (82.5 ppb), acrylonitrile (77.4 ppb), acetone (65.69 ppb), 1-hexene (56.7 ppb), and

benzene (52.15 ppb) (Table 1). The mean methanol concentration (1088.1 ppb) in surgical smoke samples from breast adipose tissues using conventional electrosurgical knives was the highest, followed by 1,3-butadiene (313.1 ppb), propane (265.5 ppb), acetonitrile (174.1 ppb), acrolein (146.7 ppb), acetone (129.5 ppb), 1-hexene (105.4 ppb), acrylonitrile (77.4 ppb), and benzene (74.1 ppb). Moreover, the mean methanol concentration (4304.6 ppb) in surgical smoke samples from mammary glands using conventional electrosurgical knives was the highest, followed by acetonitrile (1665.4 ppb), propane (1228.2 ppb), 1,3-butadiene (1002.8 ppb), acrylonitrile (549.6 ppb), acrolein (509.4 ppb), acetone (316.1 ppb), 1-hexene (268.4 ppb), benzene (242.5 ppb), and trans-2-butadiene (130.0 ppb). The composition of VOCs in the surgical smoke samples from breast tumor using conventional electrosurgical knives mainly included methanol (736.7 ppb), acetonitrile (258.4 ppb), propane (88.9 ppb), acetone (83.1 ppb), acrylonitrile (68.7 ppb), acrolein (39.7 ppb), benzene (31.6 ppb), 1,3-butadiene (26.8 ppb),

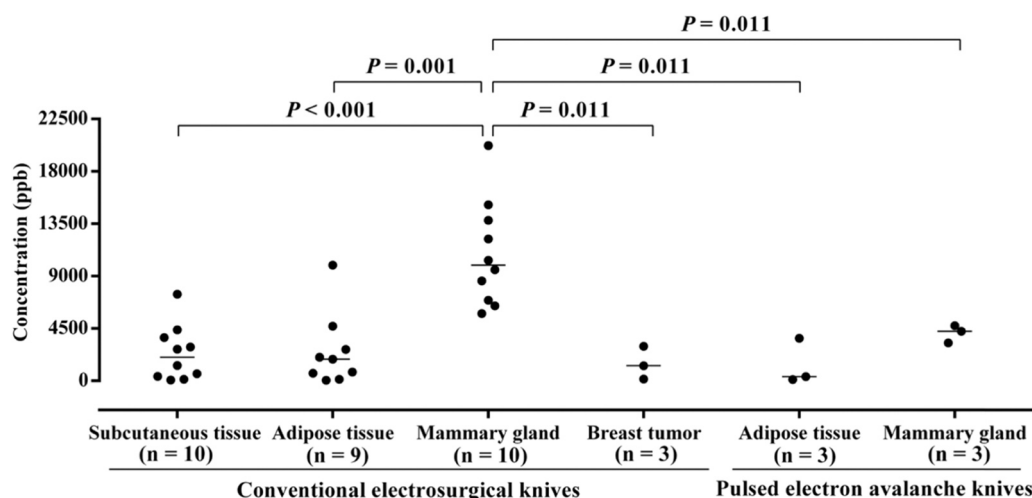


Fig. 2. 87 VOCs concentrations in surgical smoke samples from breast surgeries using electrosurgical knives and PEAK. PEAK: pulsed electron avalanche knives.



**Table 1**  
Concentration distribution of VOCs in surgical smoke samples from different tissues using two electrosurgical units.

| IARC group | Compounds (ppb)                         | Electrosurgical knives                 |                                  |                        | PEAK knives          |                                  |                       |        |           |        |           |
|------------|---|--|----------------------------------|------------------------|----------------------|----------------------------------|-----------------------|--------|-----------|--------|-----------|
|            |   | Breast subcutaneous tissue<br>(n = 10) | Breast adipose tissue<br>(n = 9) | Mammary gland (n = 10) | Breast tumor (n = 3) | Breast adipose tissue<br>(n = 3) | Mammary gland (n = 3) |        |           |        |           |
| 3          | (p,m)-Xylene                            | 2.29                                   | (1.27)§                          | 4.98                   | (1.39)               | 1.82                             | (1.23)§               | 2.53   | (0.78)§   | 3.86   | (1.93)    |
| 3          | 1,1,1-Trichloroethane                   | —                                      | —                                | —                      | —                    | —                                | —                     | —      | —         | —      | —         |
| 2B         | 1,1,2,2-Tetrachloroethane               | —                                      | —                                | —                      | —                    | —                                | —                     | —      | —         | —      | —         |
|            | 1,1,2-Trichloro-1,2,2-trifluoroethane   | —                                      | —                                | —                      | —                    | —                                | —                     | —      | —         | —      | —         |
| 3          | 1,1,2-Trichloroethane                   | —                                      | —                                | —                      | —                    | —                                | —                     | —      | —         | —      | —         |
|            | 1,1-Dichloroethane                      | 1.32                                   | (a)                              | —                      | —                    | —                                | —                     | —      | —         | —      | —         |
|            | 1,1-Dichloroethene                      | 0.26                                   | (a)                              | —                      | —                    | —                                | —                     | —      | —         | —      | —         |
|            | 1,2,3-trimethylbenzene                  | 0.14                                   | (0.01)                           | 0.13                   | (0.02)               | 0.11                             | (a)                   | 0.19   | (a)       | —      | —         |
|            | 1,2,4-Trichlorobenzene                  | —                                      | —                                | 0.66                   | (0.02)               | —                                | —                     | —      | —         | —      | —         |
|            | 1,2,4-Trimethylbenzene                  | 0.30                                   | (0.09)§                          | 0.40                   | (0.07)               | 0.23                             | (0.11)§               | 0.30   | (0.18)§   | 0.22   | (0.04)§   |
|            | 1,2-Dibromoethane                       | —                                      | —                                | —                      | —                    | —                                | —                     | —      | —         | —      | —         |
|            | 1,2-Dichloro-1,1,2,2,-tetrafluoroethane | —                                      | —                                | —                      | —                    | —                                | —                     | —      | —         | —      | —         |
|            | 1,2-Dichlorobenzene                     | —                                      | —                                | —                      | —                    | —                                | —                     | —      | —         | —      | —         |
| 2B         | 1,2-Dichloroethane                      | 0.20                                   | (0.08)                           | 0.42                   | (0.01)†              | 0.15                             | (a)                   | 0.49   | (0.44)    | 0.27   | (a)       |
| 1          | 1,2-Dichloropropane                     | —                                      | —                                | —                      | —                    | —                                | —                     | —      | —         | —      | —         |
|            | 1,3,5-Trimethylbenzene                  | 0.23                                   | (0.19)                           | 0.28                   | (0.29)               | 0.11                             | (a)                   | 0.13   | (a)       | —      | —         |
| 1          | 1,3-Butadiene                           | 170.73                                 | (184.84)§                        | 1002.75                | (459.69)             | 26.75                            | (30.44)§              | 194.23 | (128.84)§ | 418.27 | (172.77)§ |
|            | 1,3-Dichlorobenzene                     | —                                      | —                                | —                      | —                    | —                                | —                     | —      | —         | —      | —         |
|            | 1,4-Dichlorobenzene                     | —                                      | —                                | —                      | —                    | —                                | —                     | 0.14   | (a)       | —      | —         |
|            | 1-Hexene                                | 56.70                                  | (64.05)§                         | 268.40                 | (98.66)              | 23.36                            | (27.67)§              | 56.16  | (48.62)§  | 88.82  | (25.61)§  |
|            | 2,2,4-Trimethylpentane                  | 0.19                                   | (0.04)                           | —                      | —                    | —                                | —                     | —      | —         | —      | —         |
|            | 2,3-Dimethylpentane                     | 0.33                                   | (a)                              | —                      | (a)                  | —                                | —                     | —      | —         | —      | —         |
|            | 2,4-Dimethylpentane                     | —                                      | —                                | —                      | —                    | —                                | —                     | —      | —         | —      | —         |
|            | 2-Butanone                              | 12.17                                  | (8.98)§                          | 47.31                  | (20.76)              | 12.35                            | (13.74)§              | 17.47  | (20.89)§  | 28.38  | (11.98)§  |
|            | 2-Methylheptane                         | 1.16                                   | (0.73)§                          | 2.93                   | (1.54)               | 1.31                             | (a)                   | 0.17   | (0.06)§   | 1.04   | (0.14)§   |
|            | 2-Methylhexane                          | 2.77                                   | (1.71)§                          | 7.87                   | (1.53)               | 0.94                             | (a)                   | 1.29   | (0.78)§   | 3.82   | (0.79)§   |
|            | 2-Methylpentane                         | 0.70                                   | (0.50)§                          | 2.23                   | (0.43)               | 0.79                             | (0.50)§               | 0.93   | (0.70)§   | 1.29   | (a)       |
|            | 3-Chloro-1-Propene                      | —                                      | —                                | —                      | —                    | —                                | —                     | 0.17   | (a)       | —      | —         |
|            | 3-Methylheptane                         | 0.61                                   | (0.21)§                          | 1.34                   | (0.67)               | 0.27                             | (a)                   | 0.64   | (a)       | —      | —         |
|            | 3-Methylpentane                         | 0.56                                   | (0.53)                           | 0.28                   | (a)                  | —                                | —                     | 5.52   | (a)       | 1.26   | (a)       |
|            | 4-Methyl-2-Pentanone                    | 0.37                                   | (a)                              | 0.79                   | (0.52)               | 0.45                             | (0.23)§               | 0.36   | (a)       | —      | —         |
|            | Acetone                                 | 65.69                                  | (66.69)§                         | 316.12                 | (249.58)             | 83.06                            | (66.70)§              | 70.02  | (42.24)§  | 126.43 | (49.55)§  |
|            | Acetonitrile                            | 264.74                                 | (388.96)§                        | 1665.37                | (1234.65)            | 258.42                           | (281.97)§             | 162.46 | (119.28)§ | 566.50 | (86.53)§  |
| 3          | Acrolein                                | 82.45                                  | (90.81)§                         | 509.39                 | (218.51)             | 39.72                            | (51.42)§              | 100.24 | (63.91)§  | 156.03 | (66.22)§  |
| 2B         | Acrylonitrile                           | 77.44                                  | (97.11)§                         | 549.58                 | (399.65)             | 68.72                            | (72.56)§              | 48.96  | (27.96)§  | 183.87 | (66.60)§  |
| 1          | Apha-Methyl styrene                     | 1.24                                   | (0.35)                           | 1.14                   | (0.38)               | 0.71                             | (0.11)                | 0.92   | (0.40)    | 0.41   | (0.29)    |
| 1          | Benzene                                 | 52.15                                  | (64.82)§                         | 242.53                 | (95.73)              | 31.62                            | (29.10)§              | 43.60  | (24.23)§  | 120.60 | (17.20)†§ |
| 2 A        | Benzyl chloride                         | 0.67                                   | (a)                              | 0.45                   | (0.28)               | —                                | —                     | —      | —         | 0.17   | (a)       |
| 2B         | Bromodichloromethane                    | —                                      | —                                | —                      | —                    | —                                | —                     | —      | —         | —      | —         |
|            | Bromomethane                            | —                                      | —                                | 0.20                   | (0.06)               | —                                | —                     | —      | —         | —      | —         |
| 2B         | Carbon tetrachloride                    | 0.11                                   | (a)                              | 0.19                   | (a)                  | —                                | —                     | —      | —         | —      | —         |
|            | Chlorobenzene                           | 1.44                                   | (a)                              | 0.32                   | (0.01)               | 5.36                             | (a)                   | —      | —         | —      | —         |
| 3          | Chlorodifluoromethane                   | 0.53                                   | (0.14)                           | 0.49                   | (0.12)               | 0.42                             | (0.20)                | 0.56   | (0.14)    | 0.68   | (0.32)    |
| 3          | Chloroethane                            | 1.44                                   | (1.01)                           | 2.17                   | (0.79)               | 0.71                             | (a)                   | —      | —         | 1.28   | (0.77)    |
| 2B         | Chloroform                              | 0.19                                   | (0.13)                           | —                      | (0.07)               | 0.18                             | (0.08)                | 0.59   | (a)       | 0.35   | (0.03)    |
|            | Chloromethane                           | 18.24                                  | (33.42)§                         | 71.55                  | (47.85)              | 25.30                            | (20.21)§              | 9.46   | (6.20)§   | 28.62  | (7.91)§   |
|            | cis-1,2-Dichloroethene                  | 0.28                                   | (a)                              | —                      | —                    | —                                | —                     | —      | —         | —      | —         |
| 2B         | cis-1,3-Dichloropropene                 | —                                      | —                                | —                      | —                    | —                                | —                     | —      | —         | —      | —         |
|            | cis-2-Butene                            | 26.31                                  | (16.87)§                         | 111.19                 | (38.63)              | 10.78                            | (9.33)§               | 26.30  | (19.14)§  | 32.65  | (12.25)§  |
|            | cis-2-Pentene                           | 10.65                                  | (9.54)§                          | 35.00                  | (12.11)              | 2.86                             | (2.66)§               | 8.38   | (7.20)§   | 10.47  | (3.24)§   |
|            | Cyclohexane                             | 0.36                                   | (a)                              | —                      | —                    | —                                | —                     | 1.23   | (a)       | 0.76   | (a)       |

(continued on next page)

Table 1 (continued)

| IARC group | Compounds (ppb)           | Electrosurgical knives                 |                                  |                        | PEAK knives          |                                  |                             |
|------------|---------------------------|--|----------------------------------|------------------------|----------------------|----------------------------------|-----------------------------|
|            |                           | Breast subcutaneous tissue<br>(n = 10) | Breast adipose tissue<br>(n = 9) | Mammary gland (n = 10) | Breast tumor (n = 3) | Breast adipose tissue<br>(n = 3) | Mammary gland (n = 3)       |
| 2B         | Dibromochloromethane      | –                                      | –                                | –                      | –                    | –                                | –                           |
|            | Dichlorodifluoromethane   | 0.51<br>(0.08)                         | 0.53<br>(0.13)                   | 0.52<br>(0.20)         | 0.50<br>(0.05)       | 0.53<br>(0.30)                   | 0.37<br>(0.07)              |
|            | Ethylbenzene              | 3.78<br>(4.18)                         | 2.72<br>(2.62)                   | 13.64<br>(5.27)        | 4.37<br>(4.34)       | 2.57<br>(1.29)                   | 7.89<br>(5.82) <sup>†</sup> |
| 3          | Heptane                   | 12.36<br>(10.03)                       | 14.06<br>(14.96)                 | 50.63<br>(23.20)       | 8.68<br>(9.13)       | 9.33<br>(7.90)                   | 20.26<br>(9.21)             |
|            | Hexachlorobutadiene       | –                                      | –                                | –                      | –                    | –                                | –                           |
|            | Hexane                    | 10.21<br>(8.97)                        | 14.90<br>(17.44)                 | 39.30<br>(9.08)        | 3.63<br>(2.98)       | 10.02<br>(9.13)                  | 13.50<br>(1.65)             |
|            | Isopentane                | 1.86<br>(0.69)                         | 2.05<br>(1.06)                   | 6.11<br>(8.27)         | –                    | 4.72<br>(4.20)                   | 4.57<br>(a)                 |
|            | Isopropylbenzene          | 4.78<br>(3.18)                         | 5.03<br>(2.00)                   | 3.80<br>(1.00)         | 2.91<br>(1.24)       | 3.97<br>(2.29)                   | 2.67<br>(3.01)              |
|            | m-Diethylbenzene          | –                                      | –                                | –                      | –                    | –                                | –                           |
| 3          | Methanol                  | 1182.94<br>(1368.91)                   | 1088.06<br>(1199.92)             | 4304.60<br>(2176.35)   | 736.73<br>(671.02)   | 950.26<br>(936.34)               | 1806.40<br>(489.52)         |
|            | Methyl methacrylate       | 1.38<br>(0.20)                         | 3.07<br>(2.29)                   | –                      | 0.85<br>(a)          | 3.03<br>(1.92)                   | 4.00<br>(1.29)              |
|            | Methylcyclohexane         | 0.83<br>(0.55)                         | 1.14<br>(1.19)                   | 2.76<br>(0.60)         | 0.57<br>(0.30)       | 1.04<br>(0.92)                   | 1.18<br>(0.42)              |
| 2A         | Methylcyclopentane        | 2.30<br>(1.62)                         | 2.97<br>(2.74)                   | 6.47<br>(1.58)         | 0.73<br>(0.63)       | 1.72<br>(1.41)                   | 2.38<br>(0.21)              |
|            | Methylene chloride        | 0.80<br>(0.58)                         | 0.62<br>(0.24)                   | 0.69<br>(0.29)         | 3.37<br>(a)          | 1.09<br>(0.22)                   | 1.31<br>(0.66)              |
|            | m-Ethyltoluene            | 0.26<br>(0.12)                         | 0.26<br>(0.08)                   | 0.50<br>(0.12)         | 0.28<br>(0.13)       | 0.28<br>(0.14)                   | 0.26<br>(0.04)              |
|            | n-Dodecane                | 0.93<br>(0.48)                         | 0.91<br>(0.31)                   | 1.54<br>(0.73)         | 0.81<br>(0.64)       | 0.57<br>(0.33)                   | 0.47<br>(a)                 |
|            | n-Pentane                 | 16.21<br>(15.33)                       | 29.79<br>(42.68)                 | 81.18<br>(29.99)       | 6.19<br>(5.59)       | 18.79<br>(11.85)                 | 29.60<br>(9.51)             |
|            | n-Propylbenzene           | 0.43<br>(0.31)                         | 0.33<br>(0.21)                   | 1.07<br>(0.43)         | 0.34<br>(0.25)       | 0.29<br>(0.11)                   | 0.44<br>(0.23)              |
|            | n-Undecane                | 1.36<br>(0.47)                         | 1.46<br>(0.81)                   | 2.96<br>(0.68)         | 0.90<br>(0.70)       | 1.29<br>(0.49)                   | 1.08<br>(0.39)              |
|            | Octane                    | 5.99<br>(5.33)                         | 10.57<br>(12.33)                 | 25.90<br>(5.36)        | 1.74<br>(1.38)       | 6.78<br>(6.28)                   | 9.81<br>(0.72)              |
|            | o-Ethyltoluene            | 0.21<br>(0.11)                         | 0.19<br>(0.07)                   | 0.34<br>(0.09)         | 0.24<br>(a)          | 0.21<br>(a)                      | –                           |
| 3          | o-Xylene                  | 0.91<br>(0.51)                         | 0.93<br>(0.46)                   | 2.13<br>(0.45)         | 0.86<br>(0.52)       | 1.07<br>(0.24)                   | 1.35<br>(0.46)              |
|            | p-Diethylbenzene          | –                                      | –                                | –                      | –                    | –                                | –                           |
|            | p-Ethyltoluene            | 0.21<br>(0.11)                         | 0.15<br>(0.02)                   | 0.26<br>(0.09)         | 0.12<br>(a)          | 0.18<br>(0.08)                   | 0.14<br>(a)                 |
| 2A         | Propane                   | 225.70<br>(238.45)                     | 265.50<br>(393.26)               | 1228.15<br>(742.82)    | 88.87<br>(106.61)    | 243.25<br>(241.21)               | 299.21<br>(218.26)          |
|            | Styrene                   | 3.78<br>(4.71)                         | 3.50<br>(3.21)                   | 14.48<br>(5.63)        | 3.80<br>(3.73)       | 2.31<br>(1.28)                   | 6.47<br>(4.41)              |
|            | Tetrachloroethylene       | –                                      | –                                | –                      | –                    | 0.56<br>(a)                      | 0.53<br>(a)                 |
| 3          | Toluene                   | 25.06<br>(22.22)                       | 23.74<br>(23.18)                 | 84.41<br>(42.16)       | 26.67<br>(18.94)     | 23.21<br>(14.68)                 | 40.61<br>(11.65)            |
|            | trans-1,2-Dichloroethene  | –                                      | –                                | –                      | –                    | –                                | 0.26<br>(a)                 |
|            | trans-1,3-Dichloropropene | –                                      | –                                | –                      | –                    | –                                | –                           |
| 2B         | trans-2-Butadiene         | 27.57<br>(20.98)                       | 59.19<br>(74.74)                 | 130.01<br>(46.55)      | 8.93<br>(9.91)       | 31.41<br>(24.34)                 | 38.60<br>(14.91)            |
|            | trans-2-Pentene           | 14.48<br>(12.46)                       | 22.93<br>(26.96)                 | 46.90<br>(17.26)       | 4.01<br>(3.67)       | 10.29<br>(7.10)                  | 16.76<br>(7.39)             |
|            | Trichloroethylene         | –                                      | –                                | –                      | –                    | –                                | –                           |
| 1          | Trichlorofluoromethane    | 0.23<br>(0.01)                         | 0.34<br>(0.08)                   | 0.27<br>(0.10)         | 0.23<br>(a)          | 0.23<br>(a)                      | 0.26<br>(0.06)              |
|            | Vinyl acetate             | 5.96<br>(5.12)                         | 3.11<br>(0.78)                   | 23.08<br>(7.92)        | 4.13<br>(4.90)       | 6.78<br>(4.37)                   | 8.67<br>(3.34) <sup>†</sup> |
|            | Vinyl chloride            | 1.06<br>(0.99)                         | 1.08<br>(0.91)                   | 3.32<br>(1.22)         | 0.69<br>(0.44)       | 0.55<br>(0.34)                   | 1.62<br>(0.39)              |

Data were presented as mean (SD). –: not detected.  
<sup>a</sup> only one air sample was detected.  
<sup>†</sup> compared to breast subcutaneous tissue using electrosurgical knives,  $P < 0.05$ ;  
<sup>‡</sup> compared to breast adipose tissue using electrosurgical knives,  $P < 0.05$ ;  
<sup>§</sup> compared to mammary gland using electrosurgical knives,  $P < 0.05$ .

toluene (26.7 ppb), and chloromethane (25.3 ppb).

The predominant composition of VOCs from breast adipose tissues using PEAK included methanol (950.3 ppb), propane (243.3 ppb), 1,3-butadiene (194.2 ppb), acetonitrile (162.5 ppb), acrolein (100.2 ppb), acetone (70.0 ppb), 1-hexene (56.2 ppb), acrylonitrile (49.0 ppb), and benzene (43.6 ppb) (Table 1). For mammary glands, the mean methanol concentration (1806.4 ppb) was highest, followed by acetonitrile (566.5 ppb), 1,3-butadiene (418.3 ppb), propane (299.2 ppb), acrylonitrile (183.9 ppb), acrolein (156.0 ppb), acetone (126.4 ppb), benzene (120.6 ppb), 1-hexene (88.8 ppb), and toluene (40.6 ppb).

Furthermore, this study evaluated the changes in the concentrations of carcinogenic benzene (IARC group 1) in the surgical smoke samples, indicating that the median concentration of benzene from mammary glands (222.7 ppb) was significantly higher than that from breast subcutaneous tissues (39.1 ppb,  $P < 0.01$ ), breast adipose tissues (39.1 ppb,  $P < 0.01$ ), and breast tumors (26.4 ppb,  $P = 0.011$ ) using conventional electrosurgical knives, as well as that from adipose tissues (45.1 ppb,  $P = 0.011$ ), and mammary glands (112.0 ppb,  $P = 0.018$ ) using PEAK. In addition, the median concentration of benzene in the surgical smoke samples from mammary glands using PEAK was significantly higher than that from breast subcutaneous tissues using conventional electrosurgical knives (39.1 ppb,  $P = 0.043$ ). For 1,3-butadiene (IARC group 1), the median concentration in the surgical smoke samples from mammary glands (856.2 ppb) was significantly higher than that from breast subcutaneous tissues (80.1 ppb,  $P < 0.01$ ), breast adipose tissues (147.3 ppb,  $P < 0.01$ ), and breast tumors (15.6 ppb,  $P = 0.011$ ) using conventional electrosurgical knives as well as that from adipose tissues (210.6 ppb,  $P = 0.011$ ) and mammary glands (384.0 ppb,  $P = 0.028$ ) using PEAK.

With regard to IARC group 2 A, no difference was observed in the median concentrations of benzyl chloride and tetrachloroethylene in the surgical smoke samples from different tissues using conventional electrosurgical knives and PEAK. The median concentrations of IARC group 2B substances, acrylonitrile (440.2 ppb) and vinyl acetate (20.2 ppb) in surgical smoke samples from mammary glands using conventional electrosurgical knives were significantly higher than that from breast subcutaneous tissues (acrylonitrile: 40.3 ppb,  $P < 0.01$ ; vinyl acetate: 5.0 ppb,  $P < 0.01$ ), breast adipose tissues (acrylonitrile: 43.5 ppb,  $P < 0.01$ ; vinyl acetate: 2.9 ppb,  $P < 0.01$ ), and breast tumors (acrylonitrile: 43.2 ppb,  $P = 0.011$ ; vinyl acetate: 2.3 ppb,  $P = 0.017$ ), as well as that from adipose tissues (acrylonitrile: 39.6 ppb,  $P = 0.011$ ; vinyl acetate: 6.8 ppb,  $P = 0.04$ ) and mammary glands (acrylonitrile: 184.0 ppb,  $P = 0.018$ ; vinyl acetate: 8.3 ppb,  $P = 0.017$ ) using PEAK. No differences were observed in the median levels of chloroform and carbon tetrachloride in surgical smoke samples from different breast tissues.

In IARC group 3, the median levels of acrolein (440.2 ppb), toluene (70.2 ppb), and (*p,m*)-xylene (5.1 ppb), and *o*-xylene (2.2 ppb) in surgical smoke samples from mammary glands using conventional electrosurgical knives were significantly higher than that from breast subcutaneous tissues (acrolein: 51.6 ppb, toluene: 20.9 ppb, (*p,m*)-xylene: 1.9 ppb, *o*-xylene: 0.8 ppb,  $P < 0.01$ ), breast adipose tissues (acrolein: 64.7 ppb, toluene: 16.2 ppb, (*p,m*)-xylene: 2.2 ppb, *o*-xylene: 0.8 ppb,  $P < 0.01$ ), and breast tumors (acrolein: 18.2 ppb,  $P = 0.011$ ; toluene: 19.8 ppb,  $P = 0.018$ ; (*p,m*)-xylene: 1.5 ppb,  $P = 0.018$ ; *o*-

xylene: 0.7 ppb,  $P = 0.018$ ), as well as that from breast adipose tissues (acrolein: 116.9 ppb,  $P = 0.011$ ; toluene: 19.0 ppb,  $P = 0.011$ ; (*p,m*)-xylene: 2.4 ppb,  $P = 0.018$ ; *o*-xylene: 1.0 ppb,  $P = 0.018$ ) and mammary glands (acrolein: 118.0 ppb,  $P = 0.011$ ; toluene: 35.0 ppb,  $P = 0.028$ ) using PEAK.

This study further evaluated the concentration distribution of 87 VOCs using conventional electrosurgical knives under different electrocautery power conditions (Table 2). The analytical results show that the median level of 87 VOCs from skin tissues using an electrocautery power of  $\geq 27.5$  watts (2905.8 ppb) was significantly higher than that using an electrocautery power of  $< 27.5$  watts (381.7 ppb). However, no difference was found in the median level of 87 VOCs from adipose tissues and mammary glands under different electrocautery power conditions.

#### 4. Discussion

To the best of our knowledge, this study first attempted to analyze the VOC profile of surgical smoke samples from breast surgeries. The predominant component of air samples collected from the skin disinfection procedure was methanol. The source of methanol in the air samples warrants further evaluation. Moreover, the level of methanol in the surgical smoke samples from different tissues of breast surgeries using conventional electrosurgical knives and PEAK was 29.6-to-172.7-fold higher than that in surgical smoke samples during skin disinfection. Thus, the level of methanol exposure among surgeons and other medical care personnel in ORs should be evaluated. An *in vitro* experiment from NIOSH showed that the surgical smoke samples from five fibroadipose tissues from breast reduction surgeries and one below knee amputation surgery was mainly composed of ethanol (average value: 1200  $\mu\text{g}/\text{m}^3$ ; 37,158 ppb) and isopropanol (average value: 600  $\mu\text{g}/\text{m}^3$ ; 18,579 ppb) (Lee et al., 2018). In this study, ethanol and isopropanol were not included in the standard quantitative analysis of 87 VOCs. However, the semiquantitative analysis showed that the surgical smoke from breast surgery had ethanol (484–917,000 ppb) and isopropanol (11.5–62.6 ppb), which is similar to results of the NIOSH study with high percentages of ethanol (83–90%) and isopropanol (80–86%) (Lee et al., 2018). The above difference in the concentration of two VOCs might be related to the different tissues, air sampling, and electrocautery power conditions.

Methanol can be absorbed through skin contact and inhalation. Exposure to excessive amounts of methanol vapor can suppress the central nervous system and cause optic nerve injury, such as eye irritation, headache, fatigue, and drowsiness. Exposure to 50,000 ppm of methanol causes death within 1–2 h (U.S. Coast Guard, 1999). The US OSHA recommended that the permissible exposure limits - short-term exposure limit and ceiling for methanol should not exceed 250 ppm and 1000 ppm, respectively, to avoid the risk of developing intolerable irritation and chronic or irreversible tissue lesions, prevent accidents, or avoid the reduction in work efficiency (Occupational Safety and Health Administration OSHA, 2020). In this study, the methanol concentration in surgical smoke samples from breast surgeries in the ORs did not exceed the recommended level set by the US OSHA (Occupational Safety and Health Administration OSHA, 2020); the potential toxicity of

**Table 2**

Concentrations of 87 VOCs in surgical smoke from breast surgeries using electrosurgical knives under different electrocautery power conditions.

| ppb            | Skin tissues          |                    | <i>P</i> | Adipose tissues     |                  | <i>P</i> | Mammary glands      |                  | <i>P</i> |
|----------------|-----------------------|--------------------|----------|---------------------|------------------|----------|---------------------|------------------|----------|
|                | $\geq 27.5$ W (n = 5) | $< 27.5$ W (n = 5) |          | $\geq 35$ W (n = 7) | $< 35$ W (n = 5) |          | $\geq 35$ W (n = 5) | $< 35$ W (n = 5) |          |
| Mean           | 3758.8                | 980.4              | 0.047    | 3189.8              | 1729.3           | 0.462    | 12,275.9            | 9529.6           | 0.602    |
| SD             | 2332.2                | 1542.5             |          | 3875.6              | 2185.1           |          | 6120.9              | 1965.8           |          |
| Median         | 2905.8                | 381.7              |          | 1865.9              | 1080.0           |          | 13,809.3            | 9552.8           |          |
| 25 percentiles | 2724.0                | 129.6              |          | 758.0               | 111.7            |          | 6439.1              | 8604.1           |          |
| 75 percentiles | 4387.5                | 606.5              |          | 2701.1              | 2697.4           |          | 15,132.2            | 10,354.2         |          |

Skin tissues included breast and abdominal subcutaneous tissues; Adipose tissues came from breast and abdomen.

methanol for humans, such as headache and vision impairment, should be investigated. The removal of surgical smoke in the operation area using a smoke evacuation system to reduce the exposure risk of medical care personnel is recommended.

A previous study showed that the concentration of 18 VOCs in surgical smoke samples from 20 surgical patients who underwent laparoscopic nephrectomy was 3759–7531  $\mu\text{g}/\text{m}^3$  (977.3–1958.1 ppb) (Choi et al., 2014). Our study indicated the concentration of 87 VOCs in surgical smoke during breast surgeries seemed to be higher than above study. The possible reasons for the concentration difference between studies might be related to the type of surgery, electrocautery power, electrocautery time, sampling period, and the number of VOCs analyzed. In this study, the substances of IARC group 1 detected in the surgical smoke samples from skin tissue, adipose tissue, mammary gland, and tumor in breast surgeries included benzene (26.35–222.65 ppb), 1,3-butadiene (15.55–856.2 ppb), and vinyl chloride (0.55–3.11 ppb). The levels of benzene and 1,3-butadiene in the surgical smoke samples from breast surgeries were higher than those from an *in vitro* study of pig liver tissues (benzene: 6.21 ppb, 1,3-butadiene: 2.45 ppb) and pork tissues (benzene: 19.06 ppb, 1,3-butadiene: 15.4 ppb) in Switzerland (Kocher et al., 2019). Additionally, 1,2-dichloropropane and trichloroethylene were not detected in the surgical smoke samples from breast surgeries in our study. Previous studies have found that exposure to 10 ppm of benzene for 30 years was associated with death from leukemia (Austin et al., 1998). The incidence of lung cancer was also related to the monthly cumulative exposure to benzene and working years (Wong, 1987). Moreover, long-term exposure (6 h/d, 5 d/week, 104 weeks) to 1,3-butadiene was associated with lung tumor growth in female mice (Melnick et al., 1990). Exposure to vinyl chloride (600 ppm, 4 h/d, 5 d/week, 12 months) resulted in liver tumors in male rats (Radake et al., 1981). Therefore, the health risk of exposure to relatively low concentrations of surgical smoke in health care personnel in the ORs during breast surgery warrants further investigation.

With regard to the type of electrosurgical unit, a US study found that the mean level of benzene in surgical smoke samples from laparoscopic surgery using electrosurgical knives (85 ppb) was significantly higher than that using ultrasonic scalpels (1 ppb) (Fitzgerald et al., 2012). Results of our study indicate that the median levels of benzene, styrene, and toluene in the surgical smoke samples from mammary glands using electrosurgical knives were significantly higher than those using PEAK, which might be due to the operation conditions and the materials of electrosurgical units. The surface temperature of PEAK (40–170 °C) was lower than that of a conventional electrosurgical knife (200–350 °C) (Spektor et al., 2016), possibly resulting in lower VOC production from PEAK. Additionally, this study found that the changes in the concentrations of 87 VOCs in the surgical smoke samples from skin tissues in breast surgeries using conventional electrosurgical knives were associated with the electrocautery power setting. Our results differed from those reported in the Switzerland study (Kocher et al., 2019), which indicated that electrocautery power was not associated with the concentrations of VOCs, including 1,3-butadiene, benzene, and furfural. The relationship between electrocautery power and the composition of VOCs in surgical smoke samples should also be evaluated further.

To avoid personal exposure to surgical smoke, effective methods should be adopted, such as using an efficient local smoke evacuation system, increasing the ventilation rate in ORs, and wearing a fit personal protective mask. Controlling the pollution source is the best way to reduce the VOCs exposure in health care personnel. An efficient local smoke evacuation system can be direct to remove the VOCs in surgical smokes during operations. The suction efficiency of a local smoke evacuation system deserves further concerns. According to ASHRAE/ASHRAE 170 standard and Facility Guidelines Institute (FGI) standard, the minimum suggested OR ventilation rate were 20 ACH and 15 ACH, respectively (American Society of Heating Refrigerating and Air-Conditioning Engineers, 2017; Facility Guidelines Institute (FGI), 2018). Until recently, no standard or guideline was established for

exposure of OR health care personnel to VOCs. Additionally, surgical masks have a limited ability to remove the VOCs in surgical smokes. The use of powered air purifying respirators (PAPR) might be alternative personal protective equipment for health care personnel in ORs. Thus, this study recommends that health care settings should regularly monitor the air quality of ORs and maintain the ventilation systems to ensure the health and safety of health care personnel in the ORs.

This study had several limitations. First, the study evaluated the exposure to VOCs using area sampling, not personal sampling, because it was impossible to perform the personal sampling during operations. Second, the operation time of breast surgery ranged from 39 to 807 min in the study, however, the actual cauterization time in patients was not measured. A grab sampling was adopted using an evacuated canister for only 30 s during cauterization period, so that the VOCs exposure of OR health care personnel may be underestimated. Thus, the time of exposure to surgical smoke warrants further evaluation. Third, the surgical smoke samples were collected near the surgical site to avoid interfering with the operations. The analytical results might not directly reflect the actual exposure of VOCs in OR health care personnel in the study.

## 5. Conclusions

The median level of 87 VOCs in the surgical smoke samples from mammary glands using conventional electrosurgical knives was the highest. High levels of methanol and IARC group 1 compounds, including benzene, 1,3-butadiene, and vinyl chloride were found in breast surgeries using conventional electrosurgical knives. The concentration of 87 VOCs was affected by the electrocautery power used in cutting the subcutaneous tissues.

## CRedit authorship contribution statement

**Ming-Huei Cheng:** Conceptualization, Investigation, Writing - review & editing. **Chun-Hui Chiu:** Methodology, Formal analysis, Writing - original draft. **Chi-Tsung Chen:** Investigation, Formal analysis, Writing - original draft. **Hsu-Huan Chou:** Investigation. **Li-Heng Pao:** Project administration, Funding acquisition. **Gwo-Hwa Wan:** Conceptualization, Methodology, Investigation, Writing - original draft, Writing - review & editing, Project administration, Funding acquisition.

## Declaration of Competing Interest

The authors declare that they have no known competing financial interests or personal relationships that could have appeared to influence the work reported in this paper.

## Acknowledgements

The authors would like to thank the Ministry of Science and Technology (107–2314-B-182–054), Chang Gung University of Science and Technology (ZRRPF3H0081), and Chang Gung Medical Foundation (BMRP441), Taiwan, for financially supporting this research. Also, the authors thank Mrs. Chi Wang for her assistance on administration affairs of the operating rooms in this study.

## References

- Al Sahaf, O.S., Vega-Carrascal, I., Cunningham, F.O., McGrath, J.P., Bloomfield, F.J., 2007. Chemical composition of smoke produced by high-frequency electrosurgery. *Ir. J. Med. Sci.* 176, 229–232.
- American Society of Heating Refrigerating and Air-Conditioning Engineers, 2017. ANSI/ASHRAE/ASHE Standard 170-2017: ASHRAE/ASHE Standard Ventilation of Health Care Facilities.
- Austin, H., Delzell, E., Cole, P., 1998. Benzene and leukemia. A review of the literature and a risk assessment. *Am. J. Epidemiol.* 127, 419–439.
- Choi, S.H., Kwon, T.G., Chung, S.K., Kim, T.H., 2014. Surgical smoke may be a biohazard to surgeons performing laparoscopic surgery. *Surg. Endosc.* 28, 2374–2380.

- Environmental Analytical Laboratory (EAL), 2014. Environmental Protection Administration, Taiwan. Analytical method for determining volatile organic compound in air - stainless steel canister / gas chromatography-mass spectrometry (NIEA A715.15B). <https://www.epa.gov.tw/DisplayFile.aspx?FileID=18E7C2F1DB13EBCB>. (Accessed 20 August 2020). [In Chinese].
- Facility Guidelines Institute (FGI), 2018. Status update, edition of the Guidelines for Design and Construction of Health Care Facilities, FGI - Facilities Guidelines Institute. <http://www.fgiguideinlines.org>. (Accessed 10 November 2020).
- Fitzgerald, J.E., Malik, M., Ahmed, I., 2012. A single-blind controlled study of electrocautery and ultrasonic scalpel smoke plumes in laparoscopic surgery. *Surg. Endosc.* 26, 337–342.
- Gates, M.A., Feskanich, D., Speizer, F.E., Hankinson, S.E., 2007. Operating room nursing and lung cancer risk in a cohort of female registered nurses. *Scand. J. Work Environ. Health* 33, 140–147.
- Hill, D.S., O'Neill, J.K., Powell, R.J., Oliver, D.W., 2012. Surgical smoke - a health hazard in the operating theatre: a study to quantify exposure and a survey of the use of smoke extractor systems in UK plastic surgery units. *J. Plast. Reconstr. Aesthet. Surg.* 65, 911–916.
- ISO (International Organization for Standardization), 2015. Cleanrooms and Associated Controlled Environments. Part 1: Classification of Air Cleanliness by Particle Concentration; ISO standard 14644–1:1999. International Organization for Standardization: Geneva, Switzerland.
- Kalil, J., Pessine, F.B., Fidelis, C.H., Menezes, F.H., Palma, P.C., 2016. Analysis of electrocautery generated smoke by chromatographic-mass spectrometry. *Rev. Col. Bras. Cir.* 43, 124–128.
- Kocher, G.J., Sesia, S.B., Lopez-Hilfiker, F., Schmid, R.A., 2019. Surgical smoke: still an underestimated health hazard in the operating theatre. *Eur. J. Cardiothorac. Surg.* 55, 626–631.
- Le Moual, N., Varraso, R., Zock, J.P., Henneberger, P., Speizer, F.E., Kauffmann, F., Camargo, C.A., 2013. Are operating room nurses at higher risk of severe persistent asthma? The Nurses' Health Study. *J. Occup. Environ. Med.* 55, 973–977.
- LeBouf, R.F., Stefaniak, A.B., Virji, M.A., 2012. Validation of evacuated canisters for sampling volatile organic compounds in healthcare settings. *J. Environ. Monit.* 14, 977–983.
- Lee, T., Soo, J.C., LeBouf, R.F., Burns, D., Schwegler-Berry, D., Kashon, M., Bowers, J., Harper, M., 2018. Surgical smoke control with local exhaust ventilation: experimental study. *J. Occup. Environ. Hyg.* 15, 341–350.
- Liang, C.C., Wu, F.J., Chien, T.Y., Lee, S.T., Chen, C.T., Wang, C., Wan, G.H., 2020. Effect of ventilation rate on the optimal air quality of trauma and colorectal operating rooms. *Build. Environ.* 169, 106548.
- Massarweh, N.N., Cosgriff, N., Slakey, D.P., 2006. Electrosurgery: history, principles, and current and future uses. *J. Am. Coll. Surg.* 202, 520–530.
- Melnick, R.L., Huff, J., Chou, B.J., Miller, R.A., 1990. Carcinogenicity of 1,3-butadiene in C57BL/6 x C3H F1 mice at low exposure concentrations. *Cancer Res* 50, 6592–6599.
- Occupational Safety and Health Administration (OSHA), 2008. Laser/Electrosurgery Plume. <https://www.osha.gov/SLTC/laserelectrosurgeryplume/index.html>. (Accessed February 22, 2019).
- Occupational Safety and Health Administration (OSHA), 2020. METHYL ALCOHOL (METHANOL). <http://www.osha.gov/chemicaldata/chemResult.html?RecNo=474>. (Accessed 20 August 2020).
- Radake, M.J., Stemmer, K.L., Bingham, E., 1981. Effect of ethanol on vinyl chloride carcinogenesis. *Environ. Health Perspect.* 41, 59–62.
- Sisler, J.D., Shaffer, J., Soo, J.C., LeBouf, R.F., Harper, M., Qian, Y., Lee, T., 2018. In vitro toxicological evaluation of surgical smoke from human tissue. *J. Occup. Med. Toxicol.* 13, 12.
- Spektor, Z., Kay, D.J., Mandell, D.L., 2016. Prospective comparative study of pulsed-electron avalanche knife (PEAK) and bipolar radiofrequency ablation (coblation) pediatric tonsillectomy and adenoidectomy. *Am. J. Otolaryngol.* 37, 528–533.
- U.S. Coast Guard, 1999. Chemical Hazard Response Information System (CHRIS)-Hazardous Chemical Data. Commandant Instruction 16465.12C. U.S. Government Printing Office, Washington, D.C.
- Ulmer, B.C., 2008. The hazards of surgical smoke. *AORN J.* 87, 721–734.
- Wong, O., 1987. An industry wide mortality study of chemical workers occupationally exposed to benzene. II. Dose response analyses. *Br. J. Ind. Med.* 44, 382–395.



## Research Paper

# Conditioned medium from adipose-derived stem cells attenuates ischemia/reperfusion-induced cardiac injury through the microRNA-221/222/PUMA/ETS-1 pathway

Tzu-Lin Lee<sup>1</sup>, Tsai-Chun Lai<sup>1</sup>, Shu-Rung Lin<sup>2,3</sup>, Shu-Wha Lin<sup>4</sup>, Yu-Chen Chen<sup>1</sup>, Chi-Ming Pu<sup>5,6</sup>, I-Ta Lee<sup>7</sup>, Jaw-Shiun Tsai<sup>8,9</sup>, Chiang-Wen Lee<sup>10,11,12</sup>, Yuh-Lien Chen<sup>1</sup>✉

1. Department of Anatomy and Cell Biology, College of Medicine, National Taiwan University, Taipei, Taiwan.
2. Department of Bioscience Technology, College of Science, Chung-Yuan Christian University, Taoyuan, Taiwan.
3. Center for Nanotechnology and Center for Biomedical Technology, Chung-Yuan Christian University, Taoyuan, Taiwan.
4. Department of Clinical Laboratory Sciences and Medical Biotechnology, College of Medicine, National Taiwan University, Taipei, Taiwan.
5. Department of Anatomy and Cell Biology, College of Medicine, National Taiwan University, Taipei, Taiwan.
6. Division of Plastic Surgery, Department of Surgery, Cathay General Hospital, Taipei, Taiwan.
7. School of Dentistry, College of Oral Medicine, Taipei Medical University, Taipei, Taiwan.
8. Department of Family Medicine, National Taiwan University Hospital, Taipei, Taiwan.
9. Center for Complementary and Integrated Medicine, National Taiwan University Hospital, Taipei, Taiwan.
10. Department of Nursing, Division of Basic Medical Sciences, and Chronic Diseases and Health Promotion Research Center, Chang Gung University of Science and Technology, Chiayi, Taiwan.
11. Research Center for Industry of Human Ecology and Research Center for Chinese Herbal Medicine, Chang Gung University of Science and Technology, Taoyuan, Taiwan.
12. Department of Orthopaedic Surgery, Chang Gung Memorial Hospital, Chiayi, Taiwan.

✉ Corresponding author: Prof. Yuh-Lien Chen, Department of Anatomy and Cell Biology, College of Medicine, National Taiwan University, No. 1, Sec 1, Ren-Ai Road, Taipei 100233, Taiwan, ROC. Tel: 886-2-23123456-88176, E-mail: ylchenv@ntu.edu.tw

© The author(s). This is an open access article distributed under the terms of the Creative Commons Attribution License (<https://creativecommons.org/licenses/by/4.0/>). See <http://ivyspring.com/terms> for full terms and conditions.

Received: 2020.09.01; Accepted: 2020.12.17; Published: 2021.01.01

## Abstract

**Rationale:** Cardiovascular diseases, such as myocardial infarction (MI), are the leading causes of death worldwide. Reperfusion therapy is the common standard treatment for MI. However, myocardial ischemia/reperfusion (I/R) causes cardiomyocyte injury, including apoptosis and fibrosis. We aimed to investigate the effects of conditioned medium from adipose-derived stem cells (ADSC-CM) on apoptosis and fibrosis in I/R-treated hearts and hypoxia/reoxygenation (H/R)-treated cardiomyocytes and the underlying mechanisms.

**Methods:** ADSC-CM was collected from ADSCs. The effects of intramuscular injection of ADSC-CM on cardiac function, cardiac apoptosis, and fibrosis examined by echocardiography, Evans blue/TTC staining, TUNEL assay, and Masson's trichrome staining in I/R-treated mice. We also examined the effects of ADSC-CM on apoptosis and fibrosis in H/R-treated H9c2 cells by annexin V/PI flow cytometry, TUNEL assay, and immunocytochemistry.

**Results:** ADSC-CM treatment significantly reduced heart damage and fibrosis of I/R-treated mice and H/R-treated cardiomyocytes. In addition, the expression of apoptosis-related proteins, such as p53 upregulated modulator of apoptosis (PUMA), p-p53 and B-cell lymphoma 2 (BCL2), as well as the fibrosis-related proteins ETS-1, fibronectin and collagen 3, were significantly reduced by ADSC-CM treatment. Moreover, we demonstrated that ADSC-CM contains a large amount of miR-221/222, which can target and regulate PUMA or ETS-1 protein levels. Furthermore, the knockdown of PUMA and ETS-1 decreased the induction of apoptosis and fibrosis, respectively. MiR-221/222 overexpression achieved similar results. We also observed that cardiac I/R markedly increased apoptosis and fibrosis in miR-221/222 knockout (KO) mice, while ADSC-CM decreased these effects. The increased phosphorylation of p38 and NF-κB not only mediated myocardial apoptosis through the PUMA/p53/BCL2 pathway but also regulated fibrosis through the ETS-1/fibronectin/collagen 3 pathway.

**Conclusions:** Overall, our results show that ADSC-CM attenuates cardiac apoptosis and fibrosis by reducing PUMA and ETS-1 expression, respectively. The protective effect is mediated via the miR-221/222/p38/NF- $\kappa$ B pathway.

Key words: Ischemia/reperfusion injury, ADSC-CM, miR-221/222, apoptosis, fibrosis

## Introduction

Cardiovascular diseases are major health problems and associated with clinical mortality worldwide. The most common cardiovascular disease is myocardial ischemia caused by coronary artery occlusion. An effective treatment of myocardial infarction is reperfusion therapy, which can promote blood restoration to the ischemic myocardium. However, this treatment can cause ischemia/reperfusion (I/R) injury, which leads to secondary and complicated heart damage [1]. Studies have shown that cardiac apoptosis and fibrosis play important roles in the progression of myocardial I/R injury [2, 3]. Cardiomyocyte apoptosis is a rare event in the healthy myocardium. However, this is the earliest and main form of infarcted cardiomyocyte death and is associated with I/R injury [3]. PUMA (p53-upregulated modulator of apoptosis) is the only BH3 protein in the BCL2 family that can rapidly induce apoptosis by increasing p53 levels [2, 4]. In addition, myocardial fibrosis is caused by excessive extracellular matrix deposition (such as collagen) and activation of myofibroblasts in the damaged area, resulting in scar formation and permanent damage to heart function [5]. ETS-1 is an important mediator of cardiac fibrosis induced by angiotensin II [6]. However, the mechanism of I/R-induced injury is unclear, and a satisfactory treatment method is not yet available. Preventing cardiac apoptosis and fibrosis has become the goal of certain therapies that interfere with I/R injury.

The use of mesenchymal stem cells (MSCs) for the treatment of I/R injury seems to have many advantages because these cells are safe, pluripotent and have immunological privilege [7, 8]. Adipose-derived stem cells (ADSCs) have become the preferred cell type for the treatment of I/R injury because they have the following advantages over other types of MSCs: abundance and expansion ability, relatively easy harvest, high MSC frequency, multi-lineage differentiation, and powerful proliferation [7]. There is increasing evidence that ADSC transplantation can improve heart function after myocardial infarction through direct differentiation and paracrine effects [9]. The beneficial effect induced by ADSCs is mainly mediated by a paracrine mechanism, and the direct differentiation of cells plays a minor role [10]. Paracrine products of

ADSCs, including cytokines, growth factors, RNA and microRNAs, may affect cell functions and be delivered to target organs for repair [11]. However, the evidence supporting paracrine mechanisms playing a therapeutic role in apoptosis and fibrosis in I/R injury is unclear. Previous studies have shown that miR-221/222 is involved in pathological cardiovascular mechanisms, including angiogenesis, inflammation, vascular remodeling, fibrosis, cardiac hypertrophy, and apoptosis [12, 13]. Bioinformatics analysis showed that PUMA and ETS-1 are candidate targets of miR-221/222. MiR-221/222 induces cell survival by targeting PUMA in glioblastoma [14]. ETS-1 upregulation mediates angiotensin II-induced cardiac fibrosis [6]. However, the role of miR-221/222 in the heart or during I/R is still unknown, and further research is ongoing. Taking all these factors into consideration, the purpose of this study was to examine whether miR-221/222 participates in the regulation of apoptosis and fibrosis in I/R cardiac injury and H/R-treated cardiomyocytes by targeting PUMA and ETS-1, respectively. Here, we investigated the effects of conditioned medium from adipose-derived stem cells (ADSC-CM) on cardiac apoptosis and fibrosis in I/R-treated mice and H/R-treated H9c2 cells and the underlying mechanisms. The results demonstrated that the cardioprotective effects of ADSC-CM are closely related to reducing apoptosis and fibrosis in I/R-induced cardiac injury through the regulation of miR-221/222.

## Materials and Methods

### *In vivo* myocardial ischemia/reperfusion (I/R) model

The present study used male C57BL/6J wild-type (WT) mice and miR-221/222-knockout (KO) mice aged 8-12 weeks. We generated miR-221/222-KO mice by deleting the X-linked miR-221/222 gene and bred them on a C57BL/6J background for 10 generations. To induce myocardial I/R, the mice were anesthetized with 3% isoflurane. Briefly, the anterior descending branch of the left coronary artery (LAD) was ligated with a 7-0 nylon suture, and a silicone tube (OD 86 mm) was placed 1 mm below the ligation to cause myocardial ischemia. The effectiveness of the occlusion was verified by

whitening of the ventricle at the distal end of the ligation. Then, 25 min after the occlusion, 50  $\mu$ L of ADSC-CM (4  $\mu$ g/mL) was uniformly injected intramuscularly into five locations in the border area of the anterior wall of the left ventricle. After 30 min of occlusion, the silicone tube was removed to allow blood reperfusion. All mice were anesthetized again after 3 h or 3 d of reperfusion, and the chest was reopened. In the sham operation group, the heart was exposed without LAD ligation. Blood samples and the heart were collected for further analysis. All animal experiments were conducted in accordance with the guidelines for animal care of National Taiwan University (IACUC approval no: 20180426) and complied with the Guide for the Care and Use of Laboratory Animals (NIH publication no. 86-23, revised in 1985). To assess the infarct size, the heart was excised and cut into 1 mm thick cross-sections. The heart sections were then incubated with a 1% triphenyltetrazolium chloride (TTC) solution at 37 °C for 10 min. The infarct area was expressed as the percentage of infarct area (pale) to the total area (red) and measured with ImageJ (NIH, MD, USA). In addition, Evans blue/TTC double staining was used to determine area at risk and infarct area. Briefly, the ligature around LAD was retied and 0.2 mL of 2% Evans blue dye was injected into the left ventricle. The heart was quickly excised and cut into 1 mm thick cross-sections, and then stained with 1% TTC solution at 37 °C for 10 min. The Evans blue-stained area (blue), TTC-stained area (red; area at risk), and TTC-negative staining area (pale; infarct myocardium) were photographed and measured with ImageJ.

### Physiological assessment of cardiac function

The effects of I/R and ADSC-CM on cardiac function were recorded and evaluated by echocardiography. Mice were anesthetized with isoflurane (0.5-1.5% in O<sub>2</sub>) and placed on the rail system to maintain the body temperature (37 °C  $\pm$  0.5 °C). Echocardiography was performed with a small animal high-resolution ultrasound system (Prospect, S-Sharp, Taipei, Taiwan) equipped with a 40-MHz single-element transducer. M-mode image was acquired at the level of the papillary muscle of the left ventricle from the long-axis view for evaluation of fractional shortening (FS) and the ejection fraction (EF).

### H9c2 cell culture and *in vitro* hypoxia/reoxygenation (H/R) model

H9c2 cells were originally derived from embryonic rat ventricular cardiomyocytes and were purchased from the American Type Culture

Collection (ATCC, VA, USA). Cardiomyocytes were cultured in Dulbecco's modified Eagle's medium (GIBCO, MA, USA) supplemented with 10% fetal bovine serum (Biological Industries, CT, USA) and 1% penicillin (BI). The cultures were maintained in a humid incubator (95% air and 5% CO<sub>2</sub>) at 37 °C. To simulate myocardial I/R injury *in vivo*, H/R was performed on H9c2 cells. H9c2 cells were exposed to hypoxia for 24 h in a hypoxic incubator (5% CO<sub>2</sub> and 1% O<sub>2</sub> at 37 °C) in which O<sub>2</sub> was replaced with N<sub>2</sub>. After hypoxic exposure, the cells were reoxygenated for 12 h at 37 °C in a normoxic incubator with 95% air and 5% CO<sub>2</sub>.

### Preparation of conditioned medium from adipose-derived stem cells (ADSC-CM)

Human adipose-derived stem cells (ADSCs) were purchased from Lonza (Basel, Switzerland). ADSCs were cultured in DMEM containing 20% FBS and penicillin/streptomycin. The cells that attached to the flask were then cultured, and the medium was changed every two days. Cells between the 3rd and 8th passages were used for all experiments. ADSCs were characterized as positive for CD73, CD90, and CD105 and negative for CD34 and CD45 by immunocytochemistry and flow cytometry. ADSCs have the potential to differentiate into adipocytes, osteoblasts and chondrocytes. To prepare CM from ADSCs, the cells were seeded at  $5 \times 10^5$  cells per 10-cm plate. ADSCs reached 80% confluence and were then placed in serum-free medium for 24 h. The medium was then collected for *in vitro* and *in vivo* experiments. The collected CM was concentrated using Amicon Ultra-15 centrifugal filter units (Millipore, MA, USA). The final concentration of the CM was 4  $\mu$ g/mL. In addition, ADSCs were transfected with miR-221/222 inhibitors for 24 h and the miR-221/222-inhibitors-ADSC-CM was collected to examine the effects of miR-221/222 on the apoptosis and fibrosis of H/R-treated cardiomyocytes.

### Measurement of lactate dehydrogenase

Necrotic cell death was evaluated by measuring LDH activity. The amount of LDH in the serum was determined by the LDH cytotoxicity detection kit (Wako, Osaka, Japan) and then examined by an automatic biochemical analyzer (Hitachi 7070, Tokyo, Japan).

### ROS measurement by dihydroethidium (DHE) staining

DHE is a redox-sensitive probe that is used to measure ROS production. Cryostat sections of cardiac tissues were incubated with 2  $\mu$ M DHE dye (Beyotime Technology) in the dark at 37 °C for 20 min. The

oxidative stress level was examined and observed under a fluorescence microscope. Image-Pro Plus software was used to quantify the red staining, which represented oxidative stress.

### **Terminal deoxyribonucleotidyl transferase-mediated dUTP nick-end labeling (TUNEL) analysis**

According to the manufacturer's instructions, the *in situ* cell death detection kit (Roche, CA, USA) was used to evaluate apoptotic cells in cardiac sections and cultured cardiomyocytes. Nuclei were stained with DAPI for 10 min. Three slides were prepared for each group. The sections were observed with a confocal microscope. The percentage of TUNEL-positive nuclei relative to the total nuclei was determined in five randomly selected 40× fields on each slide in a blinded manner.

### **Western blot**

Heart tissues were homogenized and lysed in RIPA buffer (154 mM NaCl, 0.25% sodium deoxycholate, 1% NP-40, 0.8 mM EDTA, and 65.2 mM Tris base) containing a protease inhibitor cocktail (Genestar Biotechnology, Taiwan). Cells were lysed in RIPA buffer (TOOLS, New Taipei City, Taiwan) containing 1% protease inhibitor (Rockford, Illinois, USA) for 1 h at 4 °C. The proteins in tissue and cell lysates were separated by 10% SDS-PAGE (Invitrogen) and transferred to PVDF membranes. The membranes were blocked with TBST containing 5% skim milk for 1 h. Thereafter, the following primary antibodies were used: anti-PUMA (1:2000 dilution, Cell Signaling), anti-phospho-p53 (1:2000 dilution, Cell Signaling), anti-BCL2 (1:2000 dilution, BD, CA, USA), anti-ETS-1 (1:3000 dilution, Abcam), anti-fibronectin (1:3000 dilution, Abcam), anti-collagen 3 (COL3A1; 1:3000 dilution, Proteintech, IL, USA), anti-phospho-p38 MAPK (1:5000 dilution, Cell Signaling), and anti-phospho-NF-κB p65 (1:5000 dilution, Cell Signaling). The membranes were then incubated with horseradish peroxidase-conjugated goat anti-rabbit IgG antibodies (1: 2000 dilution; Sigma, MO, USA) at RT for 1 h. The bound antibodies were detected with Chemiluminescence Plus reagent (Millipore). The images were visualized by the BioSpectrum 815 imaging system (UVP, Upland, CA, USA), and the intensity of each band was quantified using ImageJ software. An antibody against GAPDH (1: 3000 dilution; Santa Cruz Biotechnology) was used as a loading control.

### **Histological analysis**

All mice were sacrificed, and the hearts were removed. Six hearts were selected from each group for

histological analysis. The heart was cut in half by performing a transverse slice between the atrioventricular sulcus and the apex. The sample was fixed in 4% paraformaldehyde, embedded in paraffin, and cut into 5 µm-thick cross-sections. The morphology of the cross-sections was observed with hematoxylin and eosin (HE) staining. The cross-section of the heart was stained with Masson's trichrome (Sigma) to identify collagen deposition, which is shown in blue. Briefly, the heart sections were incubated with Bouin's solution at 56 °C for 15 min and then washed with tap water. The slides were incubated with Weigert's iron hematoxylin solution, Biebrich scarlet-acid fuchsin solution, phosphomolybdic-phosphotungstic acid solution and aniline blue solution. Finally, the slides were treated with a 1% acetic acid solution, dehydrated, and mounted with mounting solution.

### **Immunostaining**

Heart sections were immersed in 0.01 M sodium citrate for antigen retrieval and treated with 3% H<sub>2</sub>O<sub>2</sub> for 10 min to remove endogenous peroxidase. The sections were then incubated with 10% normal horse serum (NHS) for 1 h, followed by the primary antibodies anti-PUMA (1:200 dilution, Cell Signaling), anti-ETS-1 (1:200 dilution, Abcam), anti-fibronectin (1:50 dilution, Abcam), and anti-collagen 3 (1:50 dilution, Proteintech) overnight at 4 °C. Then, a second antibody specific to the primary antibody was selected and allowed to react at RT for 90 min. The avidin-biotin-peroxidase-complex was incubated for 1 h. Finally, the tissues were stained with DAB (Sigma) color reaction solution and observed with a light microscope. Additionally, after each designated treatment, the H9c2 cells on the coverslip were fixed in 4% paraformaldehyde for 15 min and then permeabilized with 0.1% Triton X-100 for 1 min at RT. The cells were washed again and then blocked for 1 h with 1% bovine serum albumin (BSA, Novagen) in PBS at RT. The cells were incubated with the previously identified antibodies. After being washed 3 times with PBS, the cells were incubated with anti-rabbit 488 (Invitrogen, A27034) at RT for 1 h. The nuclei were counterstained with DAPI for 5 min, and then the cells were observed and photographed under a fluorescence microscope.

### **The assessment of cell death by annexin V/PI double staining**

Annexin V-FITC and PI apoptosis detection kits (BD Biosciences, CA, USA) were used to evaluate cell death. H9c2 cells were harvested, resuspended in 100 µL of binding buffer containing 2.5 µL of FITC and 5 µL of PI (100 µg/mL), and incubated in the dark at 4



°C for 15 min. Flow cytometry was used to assess cell death. These graphs are divided into four regions, corresponding to live cells that are negative for both probes (PI-/FITC-; Q3), PI-negative and annexin-positive apoptotic cells (PI-/FITC+; Q1), PI- and annexin-positive late apoptotic cells (PI+/FITC+; Q2), and PI-positive and annexin-negative necrotic cells (PI+/FITC-; Q4).

### RNA isolation and quantitative reverse transcription PCR (RT-qPCR)

Total RNA was isolated from cells or freshly frozen mouse ventricular tissues by using TRIzol reagent (Thermo Fisher, Waltham, USA) according to the manufacturer's protocol. RNA quantification was performed using a NanoDrop™ 2000 spectrophotometer (Thermo Fisher). For qPCR analysis of miRNA expression, RNA was converted into cDNA by the TaqMan MicroRNA reverse transcription kit (Invitrogen, CA, USA). The expression levels of miR-221 and miR-222 were quantified using commercially available TaqMan MicroRNA assay kits for miR-221 (000524), miR-222 (002276) and RNU6B (001973) and TaqMan™ Universal PCR master mix without UNG in a QuantStudio™ 3 Real-Time PCR System (Applied Biosystems). All reactions were repeated at least three times. The miRNA expression was normalized to the RNU6B control. The fold change in miR-221 and miR-222 expression was quantified by the  $2^{-\Delta\Delta C_t}$  method.

### siRNA transduction

Accell SMARTpool siRNA (Dharmacon, PA, USA) targets and silences ETS-1 or PUMA. A 100  $\mu$ M siRNA stock solution without RNase was prepared and stored at -20 °C. H9c2 cells were cultured in 6-well plates (Costar, DC, USA) at 70-80% confluence for 24 h, and then the medium was replaced with 1  $\mu$ M PUMA or ETS-1 siRNA in Lipofectamine 3000 (Thermo Fisher Scientific). The cells were cultured in an incubator at 37 °C for 48 h. The downregulation of ETS-1 and PUMA was confirmed by Western blotting.

### Transient transfection

To manipulate the function of miR-221/222 in H9c2 cells, H9c2 cells were seeded into 6-well plates at a density of  $3 \times 10^5$  cells per well and transfected with specific miR-221/222 mimics or a duplex RNA inhibitor (Dharmacon, CO, USA), whose sense sequences were the same as or complementary to miR-221/222, to overexpress or knockdown miR-221/222, respectively. Briefly, according to the manufacturer's protocol, H9c2 cells were grown to 70-80% confluence and transfected with miR-221/222 mimics at a concentration of 100 nM/well using

Lipofectamine 3000 reagent (Invitrogen), followed by analysis of ETS-1 and PUMA expression, apoptosis, and fibrosis. Nontargeting sequences were used as negative controls.

Full-length cDNAs encoding rat ETS-1 and PUMA were purchased from Dharmacon. The purified plasmid DNA was diluted in 200  $\mu$ L of DMEM, mixed with Lipofectamine 3000 (Invitrogen) and incubated at RT for 15 min. H9c2 cells were grown to 60 to 70% confluence in 6-well culture plates. The DNA/Lipofectamine 3000 mixture was added to the cells and incubated at 37 °C for 44 h. H9c2 cells transfected with rat ETS-1 or PUMA were used to analyze cell fibrosis or apoptosis, respectively.

*In vivo* transfection was carried out by TurboFect *in vivo* transfection reagent (Thermo), and miR-221/222 mimics or inhibitors (50 pmole) were prepared at a volume of 50  $\mu$ L per the manufacturer's instructions. The *in vivo* transfection process followed the protocol of I/R with ADSC-CM injection. The 50  $\mu$ L mixture of mimics or inhibitors was uniformly injected intramuscularly into five locations in the border area of the anterior wall of the left ventricle.

### Dual-luciferase reporter assay

The wild-type (WT) and mutant (MUT) PUMA 3'-UTR luciferase reporter gene plasmids were produced by Promega (WI, USA). The cells were then cotransfected with miR-NC or miR-221/222 mimics together with the WT or MUT PUMA-3'-UTR reporter plasmid using Lipofectamine 3000 reagent at 37 °C for 48 h. The relative luciferase activity was measured using a dual luciferase assay system (Promega). In addition, the WT and MUT ETS-1 3'-UTR luciferase reporter gene plasmids were produced by Promega. The procedures were similar to those described above.

### Statistical analysis

For each experimental condition, at least three replicates were performed, and the results given are representative of these replicates. The data are expressed as the mean  $\pm$  standard error of the mean (SEM). Differences between 2 groups were calculated using the Student's *t* test. ANOVA followed by Dunnett's post hoc test was used for statistical analysis. A *p*-value less than 0.05 was considered statistically significant.

## Results

### The cardioprotective effects of ADSC-CM are associated with reduced apoptosis and fibrosis in I/R-induced cardiac injury

Echocardiographic analysis was used to examine the effects of ADSC-CM on the cardiac function. M-mode images of three groups were shown in Figure



1A. Compared with the control group, I/R significantly reduced fractional shortening (FS) and ejection fraction (EF). In contrast, ADSC-CM treatment significantly increased FS and EF. Meanwhile, TTC staining was performed to evaluate the infarct area (Figure 1B). The area of myocardial infarction in I/R mice at 3 days was  $26.9 \pm 5.1\%$ . But in mice treated with ADSC-CM, it was significantly smaller ( $6.3 \pm 2.6\%$ ). Compared with the control group, the I/R group showed a significant myocardial infarction area by Evans blue and TTC double staining, while pretreatment with ADSC-CM reduced the myocardial infarction area. In addition, we examined the recruitment of inflammatory cells in the infarcted area at 3 h and 3 d after myocardial infarction (I/R 3 h and I/R 3 d groups, respectively) by H&E staining. Inflammatory cell infiltration was obviously observed in the I/R 3 d group but not the I/R 3 h group. Monocyte infiltration into the infarcted area was reduced by ADSC-CM treatment (Figure 1C). Oxidative stress plays an important role in cardiac damage caused by I/R. Therefore, we examined the effect of ADSC-CM on ROS production. As shown in Figure 1D, DHE-positive cells were clearly observed after I/R induction (I/R 3 h and I/R 3 d groups). ADSC-CM greatly reduced the generation of ROS. LDH release is an indicator of cell damage. As shown in Figure 1E, the release of LDH in plasma was significantly increased in the I/R group. However, ADSC-CM significantly reduced the release of LDH. TUNEL analysis showed that I/R induced a significant increase in apoptosis, while ADSC-CM reduced the level of apoptosis (Figure 1F). In addition, I/R increased collagen deposition, as observed by Masson's trichrome staining, while ADSC-CM reduced collagen deposition (Figure 1G). The immunohistochemistry results showed that I/R induced the expression of fibronectin and collagen 3 (fibrosis markers), while ADSC-CM reduced the expression of these markers (Figure 1H). To further investigate the molecular mechanisms involved, the protein levels of apoptosis markers such as p-p53 and BCL2 and fibrotic markers such as fibronectin and collagen 3 were examined. As shown in Figure 1I, I/R significantly increased the expression of p-p53, fibronectin and collagen 3, while ADSC-CM treatment significantly reduced the expression of these factors.

### **ADSC-CM protected against myocardial I/R injury in mice through miR-221/222**

The expression of miR-221/222 in I/R-injured hearts was significantly downregulated, as shown by RT-qPCR. After injecting ADSC-CM into the myocardium, the expression of miR-221/222 was

significantly increased (Figure 2A). Importantly, ADSC-CM contained a large amount of miR-221/222 compared to H9c2 cells and ADSC lysates (Figure 2B). The miR-221/222 target sites in the 3' untranslated regions (3'-UTRs) of the PUMA and ETS-1 genes were predicted using the "miRanda" target prediction program. Specifically, the 3'-UTRs of PUMA and ETS-1 contain binding sites for miR-221/222. To confirm this prediction, we conducted a PUMA and ETS-1 luciferase assay with constructs containing the miR-221/222 binding sequences of the PUMA and ETS-1, and miR-221/222 mimics resulted in reduced luciferase activity. The relative luciferase activity of PUMA-MUT and ETS-1-MUT were not significantly different (Figure 2C). As shown in Figure 2D, in the control group, PUMA and ETS-1 expression was not observed by immunohistochemistry, while in the I/R treatment group, strong staining was observed in cardiac tissues. In contrast, the administration of ADSC-CM resulted in weakened PUMA and ETS-1 staining in I/R-treated animals. Similarly, Western blotting was used to confirm these results (Figure 2E). Western blot analysis showed that the protein levels of PUMA and ETS-1 were increased in response to I/R induction, while ADSC-CM decreased the expression of these factors.

### **ADSC-CM reduced apoptosis and fibrosis in H9c2 cells stimulated with hypoxia/reoxygenation (H/R)**

Hypoxia/reoxygenation (H/R) is an important factor in the induction of apoptosis and fibrosis [15, 16]. H9c2 cells were pretreated with or without ADSC-CM for 4 h and then placed in serum-free medium. H9c2 cells were incubated at 37 °C for 24 h under 1% O<sub>2</sub> to induce hypoxia. After that, the cells were placed in a normoxic incubator for 12 h. H/R increased ROS production, while ADSC-CM significantly reduced ROS production, as shown by DCFH-DA staining (Figure 3A). H/R increased apoptosis and decreased cell viability compared to those of control cells, as shown by flow cytometry and MTT analysis (Figure 3B). Apoptosis was further assessed by TUNEL assay. Treatment with ADSC-CM significantly decreased H/R-induced apoptosis (Figure 3C). H/R induced the expression of PUMA and ETS-1, and ADSC-CM treatment reduced the expression of these factors, as shown by Western blotting and immunofluorescent staining (Figure 3D). Because ADSC-CM increased miR-221/222 expression in I/R-treated mice, we examined whether miR-221/222 could protect cardiomyocytes from H/R-induced apoptosis and fibrosis.

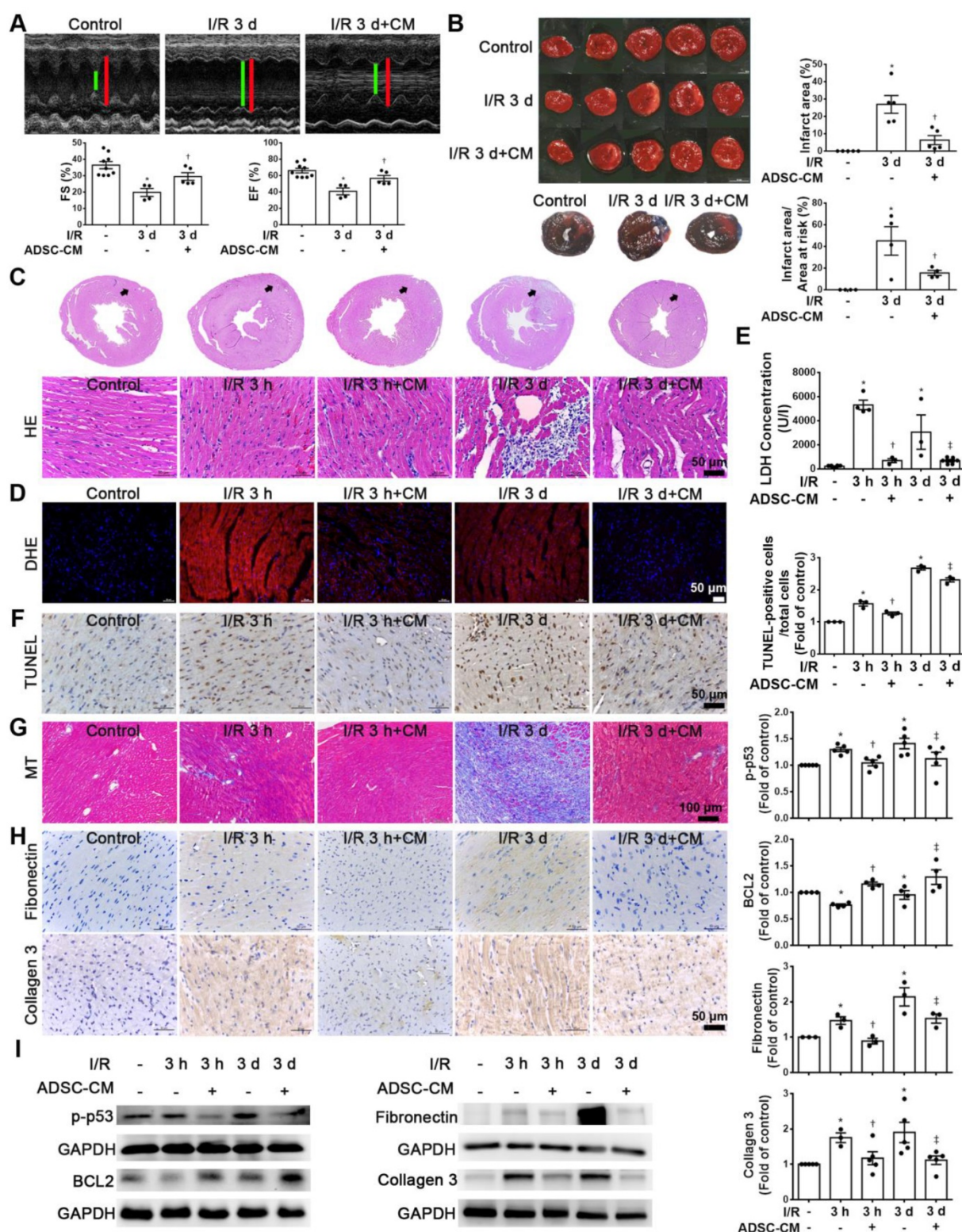


**Figure 1: ADSC-CM treatment reduced I/R-induced cardiac apoptosis and fibrosis.** The left anterior descending coronary artery (LAD) of male C57/B6J mice was ligated for 30 min and then reperused for 3 h (I/R 3 h) or 3 d (I/R 3 d). In ADSC-CM-treated animals, ADSC-CM (4  $\mu$ g/mL) was injected into the anterior wall of the left ventricle. Sham-operated animals underwent the same procedure without occlusion of the LAD. (A) Representative echocardiogram from the control, I/R 3 d, and I/R 3 d+CM mice. Quantitative data of the fractional shortening (FS) and the ejection fraction (EF). (B) The infarct area was determined by TTC staining. The ischemic area showed pale and viable myocardium showed red. Infarct area was quantified as a percentage of total slice area. Infarct area and area at risk quantification by Evans blue and TTC double staining. Graphic representation of the infarct size expressed as percentage of infarct area over area at risk. (C) The morphology of cardiac sections was observed by HE staining (scale bar = 50  $\mu$ m). (D) Measurement of intracellular ROS was performed by DHE staining (scale bar = 50  $\mu$ m). (E) LDH levels in serum were measured by an LDH cytotoxicity detection kit. Myocardial apoptosis was determined and quantified by TUNEL assay (TUNEL-positive cells: brown; nuclei: blue; scale bar = 50  $\mu$ m). (F) The presence of collagen deposition was evaluated by Masson's trichrome (MT) staining (scale bar = 100  $\mu$ m). (G) The expression of fibronectin and collagen 3 was examined by immunohistochemistry (scale bar = 50  $\mu$ m). (H) The expression levels of p-p53, BCL2, fibronectin, and collagen 3 expression were measured by Western blotting. The data are expressed as the mean  $\pm$  SEM (n = 3-5). \*P < 0.05 vs. control,  $\dagger$ P < 0.05 vs. the I/R 3 h group,  $\#$ P < 0.05 vs. the I/R 3 d group.



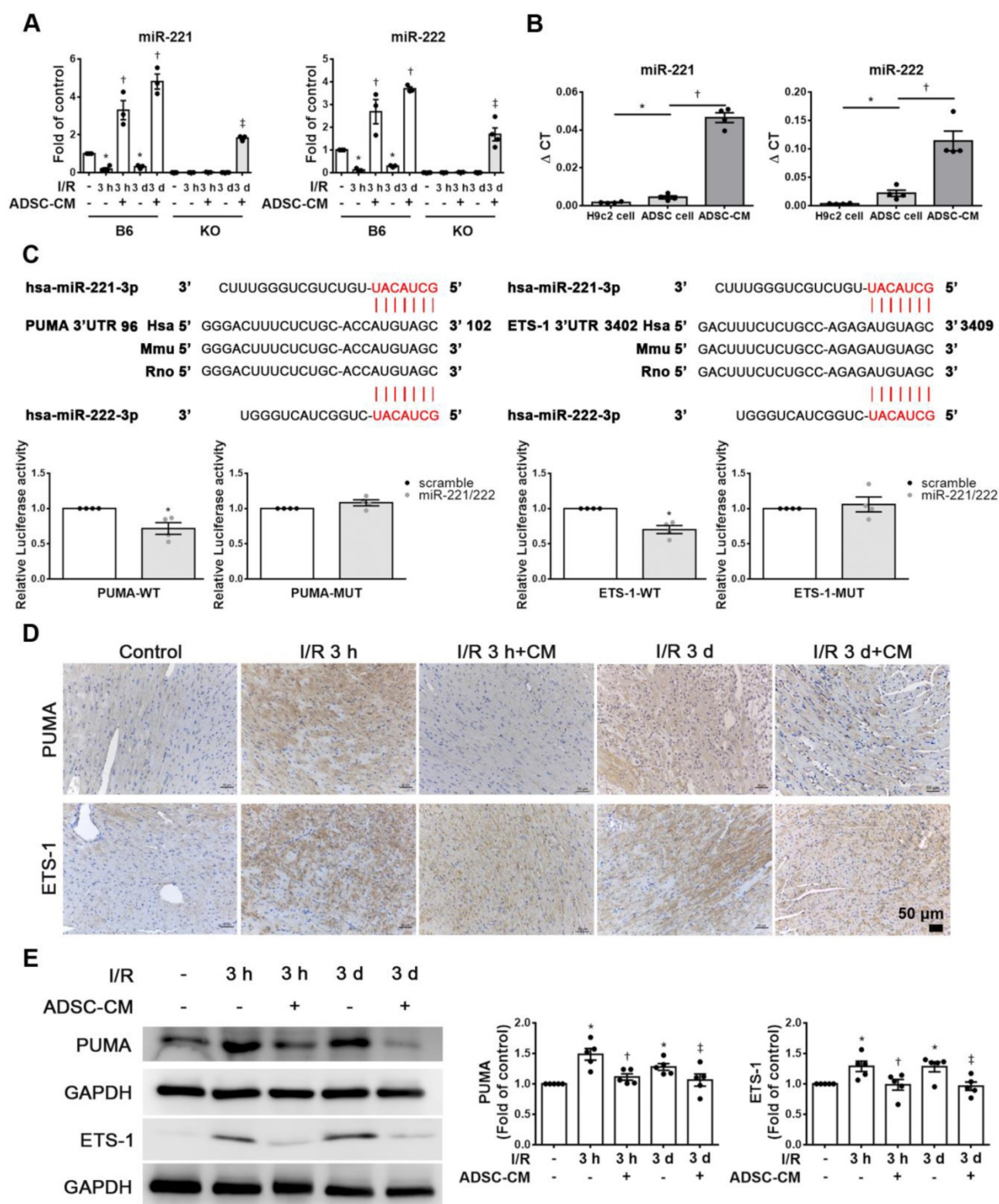


**Figure 2: ADSC-CM protected against myocardial I/R injury in mice through miR-221/222.** (A) The levels of miR-221/222 were measured by RT-qPCR. (B) ADSC-CM contains a large amount of miR-221/222. (C) Nucleotide resolution of the predicted miR-221/222 binding sequence in PUMA and ETS-1. Luciferase activity in H9c2 cells cotransfected with PUMA-WT or PUMA-MUT, ETS-1-WT or ETS-1-MUT and miR-NC mimic or miR-221/222 mimics. (D) The expression of PUMA and ETS-1 in cardiac tissues was determined by immunohistochemistry (scale bar = 50  $\mu$ m). (E) Western blot analysis of PUMA and ETS-1 expression. The data are expressed as the mean  $\pm$  SEM ( $n = 3-5$ ). \* $P < 0.05$  vs. control, † $P < 0.05$  vs. the I/R 3 h group, ‡ $P < 0.05$  vs. the I/R 3 d group or KO control.

The expression of miR-221/222 was significantly downregulated in the H/R treatment group compared with the control group, as shown by

RT-qPCR, while ADSC-CM increased miR-221/222 expression (Figure 3E). To further investigate the molecular mechanisms involved, the protein levels of

apoptosis and fibrosis markers (such as p-p53, BCL2, fibronectin and collagen 3) were examined. As shown in Figure 3F, H/R significantly increased the expression level of p-p53 and decreased the expression level of BCL2, while ADSC-CM reversed these effects. In addition, H/R significantly increased the expression of fibronectin and collagen 3, while ADSC-CM administration markedly reduced the

expression of these factors, as shown by Western blotting and immunofluorescent staining (Figure 3G). Taken together, these data indicate that miR-221/222 is an effective regulator of cardiac apoptosis and fibrosis. The administration of ADSC-CM resulted in decreases in H/R-induced apoptosis and fibrosis through miR-221/222.

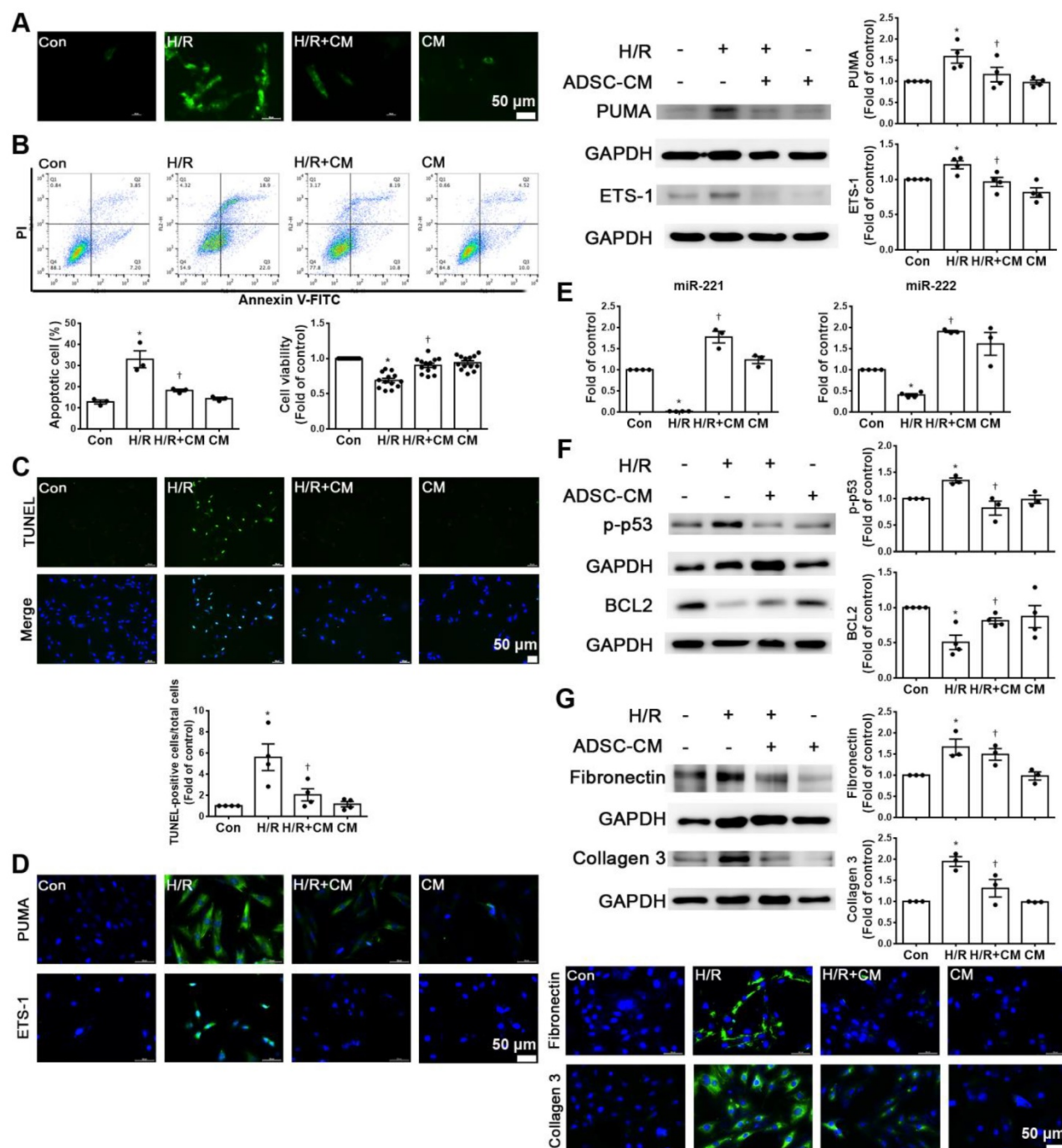


**Figure 3: ADSC-CM attenuated hypoxia/reoxygenation (H/R)-induced apoptosis and fibrosis in H9c2 cells.** Cardiomyocytes were pretreated with or without ADSC-CM for 4 h and then exposed to hypoxia for 24 h. The cells were then exposed to normoxia for another 12 h. (A) DCFH-DA staining was used to examine cytoplasmic  $H_2O_2$  by fluorescence microscopy (scale bar = 50  $\mu$ m). (B) Apoptosis and cell viability were evaluated by flow cytometry with annexin V/PI staining and MTT assays. (C) Apoptosis was examined by TUNEL assay (green: TUNEL-positive nuclei; blue: DAPI-positive nuclei; scale bar = 50  $\mu$ m). (D) The expression levels of PUMA and ETS-1 were examined by immunofluorescent staining and Western blot (scale bar = 50  $\mu$ m). (E) MiR-221/222 levels were measured by RT-qPCR. (F) The levels of apoptosis markers (p-p53 and BCL2) were examined by Western blot. (G) The levels of fibrosis markers (fibronectin and collagen 3) were examined by Western blot and immunofluorescent staining (scale bar = 50  $\mu$ m). The data are expressed as the mean  $\pm$  SEM (n = 3-4). \*P < 0.05 vs. control, †P < 0.05 vs. H/R.

### **MiR-221/222 associated with ADSC-CM reduced apoptosis and fibrosis of H/R-treated H9c2 cells**

To clarify the effects of miR-221/222 on apoptosis and fibrosis, the expression levels of the apoptotic and fibrotic markers PUMA and ETS-1, respectively, in cardiomyocytes transfected with miR-221/222 mimics were measured by Western blot analysis. MiR-221/222 mimics reduced PUMA and p-p53 expression in H/R-treated cardiomyocytes and increased BCL2 expression (Figure 4A). The immunofluorescent staining of PUMA was consistent with the Western blot results (Figure 4B). The transfection of miR-221/222 mimics also significantly reduced H/R-induced apoptosis, as shown by TUNEL analysis and flow cytometry (Figure 4C). Knockdown of PUMA in H9c2 cells exposed to H/R reduced p-p53 and increased BCL2, modulating apoptosis (Figure 4D). TUNEL analysis also confirmed these results (Figure 4E). In addition, miR-221/222 mimics significantly reduced ETS-1 expression in H/R-treated cardiomyocytes, and transfection with miR-221/222 mimics also significantly decreased H/R-induced fibronectin and collagen 3 expression, as shown by Western blot (Figure 4F). The results of immunofluorescent staining of ETS-1 were consistent with the Western blot results (Figure 4G). Knocking down ETS-1 in H9c2 cells exposed to H/R reduced the expression of fibronectin and collagen 3 (Figure 4H).

Enhanced PUMA expression increased p-p53 and decreased BCL2 expression, while transfection of miR-221/222 mimics reversed the effect of PUMA overexpression, as shown by Western blotting (Figure 4I). The TUNEL assay also confirmed this result (Figure 4J). In addition, enhanced ETS-1 expression increased the expression of fibronectin and collagen 3, while transfection of miR-221/222 mimics reversed the effect of ETS-1 overexpression, as shown by Western blot (Figure 4K). Therefore, these results indicate that PUMA and ETS-1 are involved in apoptosis and fibrosis mediated by oxidative stress through the regulation of miR-221/222. Western blot analysis showed that the miR-221/222 inhibitors increased the protein levels of PUMA and ETS-1 in H/R-treated cells treated with ADSC-CM (Figure 4L). Transfection with miR-221/222 inhibitors increased apoptosis compared with that of the H/R+ ADSC-CM group (Figure 4M). The miR-221/222 inhibitors reduced the effects of ADSC-CM on the expression of p-p53, BCL2, fibronectin, and collagen 3 in H/R-treated cells, as shown by Western blot (Figure 4N-O). ADSCs were transfected with miR-221/222 inhibitors, and then the conditioned media were

collected. The levels of miR-221/222 were significantly decreased in miR-221/222 inhibitors-ADSC-CM when compared with those in the ADSC-CM by RT-qPCR (Figure 4P). These conditioned media were used to examine the effects of miR-221/222 on apoptosis and fibrosis of H/R-treated H9c2 cells. The miR-221/222 inhibitors-ADSC-CM increased the levels of PUMA and ETS-1 expression when compared with H/R+ADSC-CM-treated cardiomyocytes (Figure 4Q). The miR-221/222 inhibitors-ADSC-CM also increased p-p53 and decreased BCL2 expression (Figure 4R). Similarly, TUNEL assay was used to confirm these results (Figure 4S). In addition, through Western blot and immunofluorescent staining, ADSC-CM significantly reduced the expression of fibronectin and collagen 3 in H/R-treated cells, while miR-221/222 inhibitors-ADSC-CM increased their expression (Figure 4R, T).

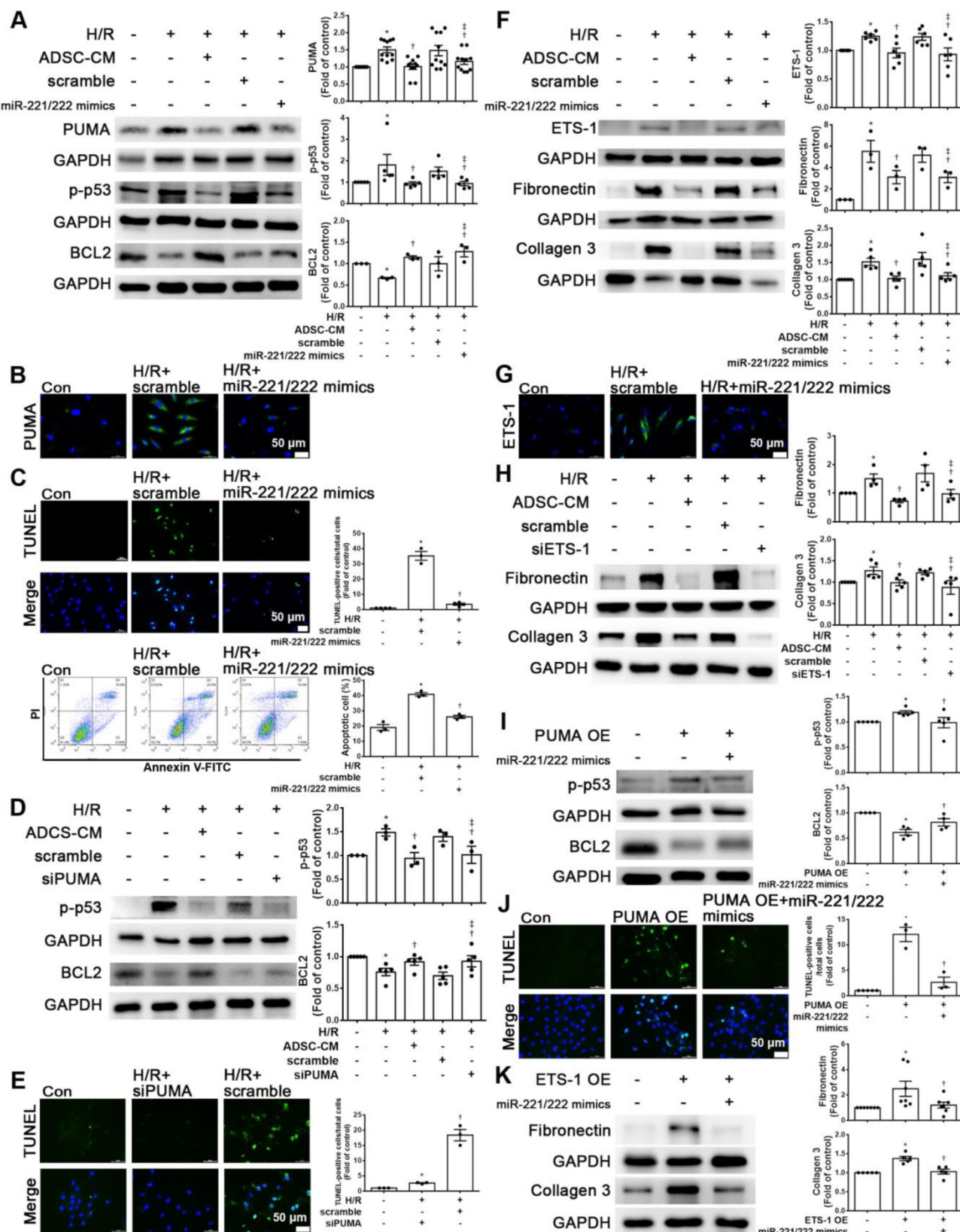
### **ADSC-CM reduced apoptosis and fibrosis in H/R-treated H9c2 cells via the p38 and NF- $\kappa$ B pathways**

Increasing evidence has shown that p-p38 and NF- $\kappa$ B proteins play critical roles in H/R-induced injury [17, 18]. We first examined the phosphorylation levels of p38 and NF- $\kappa$ B p65 in H9c2 cells stimulated with H/R. The phosphorylation levels of p38 and p65 were increased in H/R-treated H9c2 cells compared with control cells, while ADSC-CM treatment reduced the phosphorylation levels, as shown by Western blot (Figure 5A). To determine whether the effect of ADSC-CM on apoptosis and fibrosis in H/R-treated H9c2 cells requires the p38 pathway, the p38 inhibitor SB203580 was used during H/R induction. SB203580 reduced the expression of PUMA, p-p53, ETS-1, fibronectin, and collagen 3 in H/R-treated H9c2 cells while increasing BCL2 expression (Figure 5B-C). To confirm the role of NF- $\kappa$ B p65 in the antiapoptotic and antifibrotic effects on ADSC-treated H9c2 cells, the NF- $\kappa$ B inhibitor Bay 11-7082 was used and reduced the expression of PUMA and p-p53 and increased the expression of BCL2 in H/R-treated H9c2 cells (Figure 5D). In addition, Bay 11-7082 reduced H/R-induced ETS-1, fibronectin, and collagen 3 expression in H9c2 cells (Figure 5E). Transfection of the miR-221/222 mimics significantly reduced the H/R-induced p38 and p65 phosphorylation (Figure 5F). Furthermore, SB203580 reduced NF- $\kappa$ B phosphorylation, while Bay 11-7082 treatment had no significant effect on p38 phosphorylation (Figure 5G). SB203580 and Bay 11-7082 treatment significantly reduced apoptosis, as shown by TUNEL assay (Figure 5H). Consistent with the Western blot results, SB203580 and Bay 11-7082 reduced the expression of fibronectin and collagen 3,



as shown by immunofluorescent staining (Figure 5I). In addition, I/R significantly reduced p-p38 and p-p65 compared to those of control mice, as shown by Western blot, while ADSC-CM reversed these effects

*in vivo* (Figure 5J). Taken together, these findings indicate that ADSC-CM prevents cardiac I/R injury through the p38/NFκB p65 pathway.



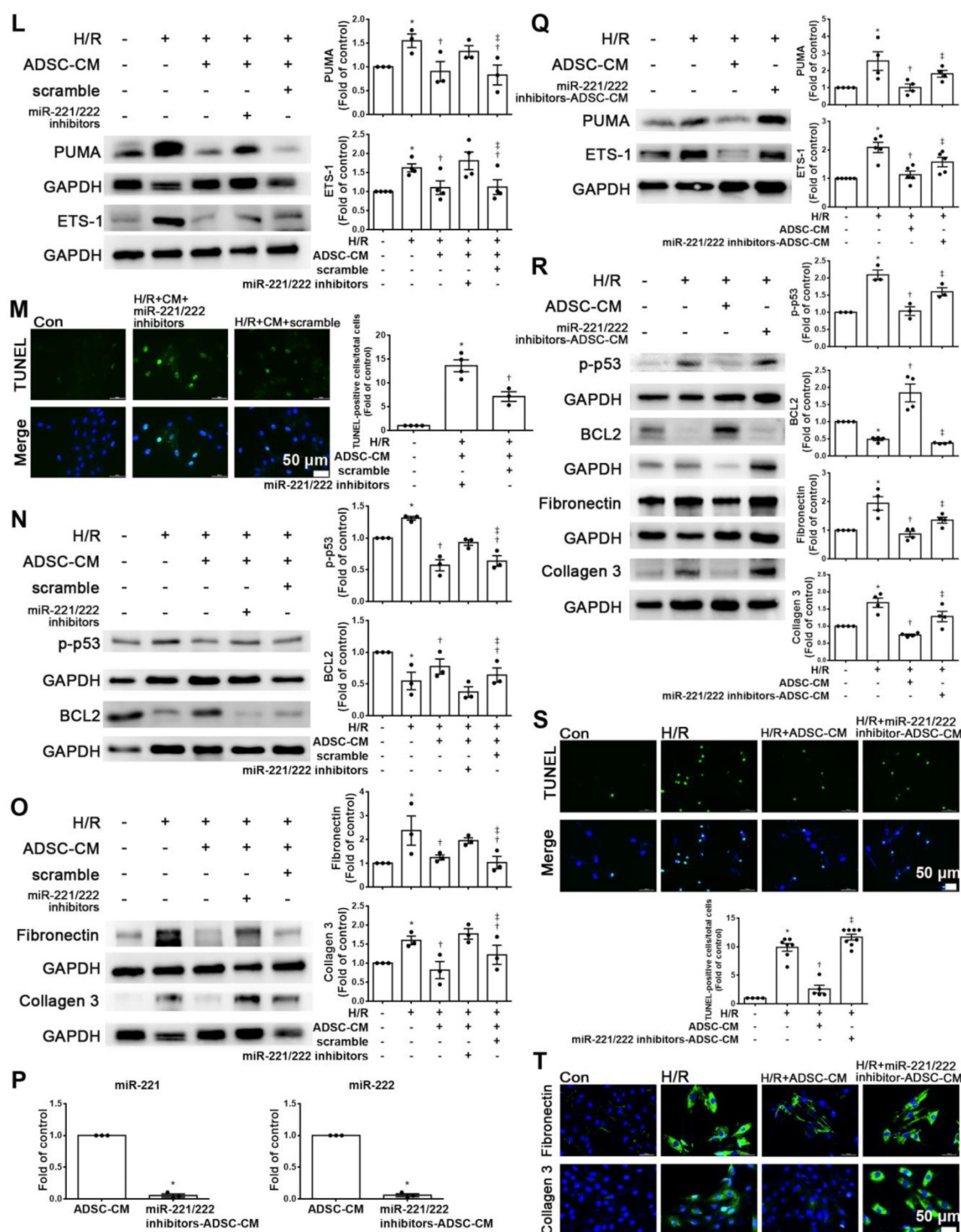


**Figure 4: MiR-221/222 was involved in the ADSC-CM-mediated reduction in H/R-induced apoptosis and fibrosis in H9c2 cells.** (A) Western blot analysis of PUMA, p-p53, and BCL2 expression in cells transfected with miR-221/222 mimics. (B) PUMA expression was examined by immunofluorescent staining (scale bar = 50  $\mu$ m). (C) Transfection with miR-221/222 mimics significantly decreased H/R-induced apoptosis, as examined by TUNEL assay and flow cytometry using annexin V/PI (scale bar = 50  $\mu$ m). (D) Knockdown of PUMA in H9c2 cells exposed to H/R increased BCL2 expression and decreased p-p53, as shown by Western blot. (E) The number of apoptotic H9c2 cells after siPUMA transfection and H/R treatment was examined by TUNEL assay (scale bar = 50  $\mu$ m). (F) Transfection of miR-221/222 mimics significantly reduced ETS-1, fibronectin and collagen 3 expression in H/R-treated H9c2 cells, as shown by Western blot. (G) ETS-1 expression was examined by immunofluorescent staining (scale bar = 50  $\mu$ m). (H) Knockdown of ETS-1 in H9c2 cells exposed to H/R reduced fibronectin and collagen 3 expression, as shown by Western blot. (I) The overexpression of PUMA significantly decreased BCL2 expression and increased p-p53 expression, as shown by Western blot. (J) PUMA-overexpressing cells transfected with miR-221/222 mimics decreased

apoptosis, as shown by TUNEL assay (scale bar = 50  $\mu$ m). (K) ETS-1-overexpressing cells transfected with miR-221/222 mimics decreased fibronectin and collagen 3 expression, as shown by Western blot. (L) ADSC-CM-treated cells treated by H/R and transfected with miR-221/222 inhibitors increased PUMA and ETS-1 expression, as shown by Western blot. (M) ADSC-CM-treated cells exposed to H/R and transfected with miR-221/222 inhibitors increased the number of apoptotic cells, as shown by TUNEL assay (scale bar = 50  $\mu$ m). (N, O) Western blot analysis showed that the miR-221/222 inhibitors increased the protein levels of p-p53, fibronectin and collagen 3. (P) ADSCs were transfected with miR-221/222 inhibitors and then the conditioned media were collected. MiR-221/222 levels were measured by RT-qPCR. (Q, R) MiR-221/222 inhibitors-ADSC-CM was used to examine the effects of miR-221/222 on the expression of PUMA, ETS-1, p-p53, BCL2, fibronectin, and collagen 3 in H/R-treated H9c2 cells. (S) MiR-221/222 inhibitors-ADSC-CM was used to examine the effects of miR-221/222 on cell apoptosis in H/R-treated H9c2 cells, as shown by TUNEL assay (scale bar = 50  $\mu$ m). (T) MiR-221/222 inhibitors-ADSC-CM was used to examine the effects of miR-221/222 on the expression of fibronectin and collagen 3 by immunofluorescent staining (scale bar = 50  $\mu$ m). The data are expressed as the mean  $\pm$  SEM (n = 3-7). \*P < 0.05 vs. control, †P < 0.05 vs. H/R, PUMA-OE, ETS-1-OE, ‡P < 0.05 vs. H/R+scramble, H/R+miR221/222 mimics, H/R+ADSC-CM.

## ADSC-CM protected against myocardial I/R injury in miR-221/222 KO mice

Compared with that of the sham operation group, the serum LDH activity was significantly increased in the I/R group of miR-221/222 KO mice. However, the addition of ADSC-CM significantly reduced LDH levels after I/R induction in miR-221/222 KO mice (Figure 6A). In addition, after I/R induction of miR-221/222 KO mice, TUNEL analysis and Masson's trichrome staining showed that apoptosis and fibrosis were significantly increased, while ADSC-CM treatment reduced apoptosis and fibrosis (Figure 6B-C). After I/R, the expression of PUMA and ETS-1 in miR-221/222 KO mice was significantly increased, as shown by Western blot and immunohistochemistry, and these effects were reduced by ADSC-CM administration (Figure 6D). In addition, the levels of p-p53, fibronectin and collagen 3 expression were upregulated in the I/R group, while ADSC-CM decreased the expression (Figure 6E). Consistent with the results of ADSC-CM treatment, compared with the I/R group, the group transfected with miR-221/222 mimics exhibited significantly reduced apoptosis and fibrosis, as shown by TUNEL analysis and Masson's trichrome staining, respectively (Figure 6F). The protein expression of BCL2 in the I/R group was reduced, while *in vivo* transfection of miR-221/222 mimics increased BCL2 expression (Figure 6G). Moreover, the expression levels of p-p53, fibronectin and collagen 3 were upregulated in the I/R group, while *in vivo* transfection of miR-221/222 mimics reduced the expression of these factors. In addition, the PUMA and ETS-1 levels of the I/R group increased, while the transfection of miR-221/222 mimics reduced the expression of these factors (Figure 6G). Similarly, these results were confirmed by immunohistochemistry (Figure 6H). In contrast, the I/R+ADSC-CM+miR-221/222 inhibitor group did not exhibit decreased apoptosis and fibrosis compared to the I/R group (Figure 6I). The expression of PUMA and ETS-1 was upregulated in the I/R group and was not affected in the I/R+ADSC-CM+miR-221/222 inhibitor group (Figure 6J). Similarly, these data were confirmed by immunohistochemistry (Figure 6K). These findings strongly support that ADSC-CM prevents myocardial I/R injury through miR-221/222

*in vivo*.

## Discussion

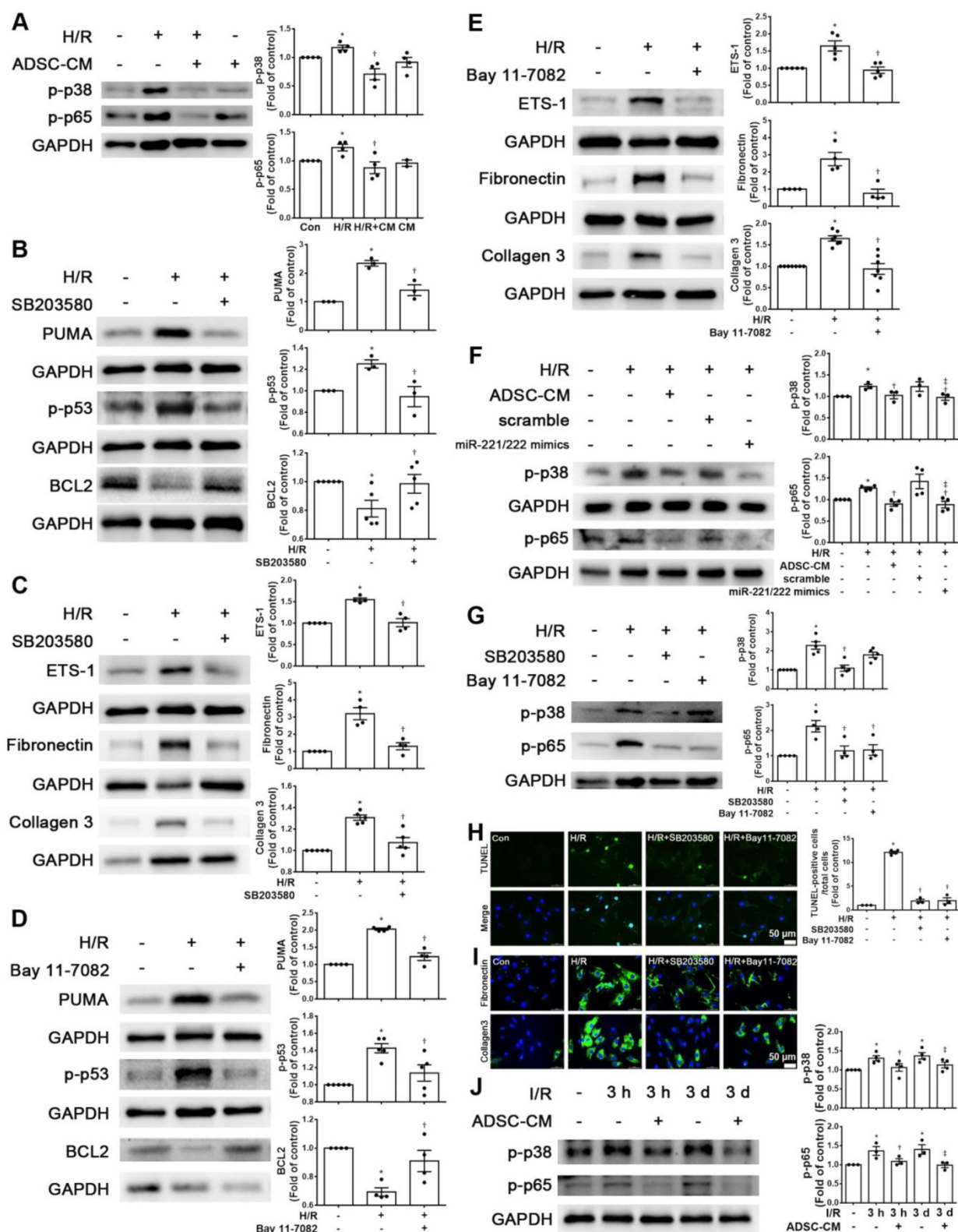
In this study, we demonstrated reductions in miR-221/222 expression levels in I/R-treated hearts and H/R-treated H9c2 cells. In addition, ADSC-CM containing large amounts of miR-221/222 can reduce cardiac apoptosis and fibrosis. MiR-221/222 can target and regulate PUMA or ETS-1 expression levels. Furthermore, miR-221/222 regulates the PUMA/p53/BCL2 pathway to mediate cardiomyocyte apoptosis and the ETS-1/fibronectin/collagen 3 pathway to mediate fibrosis through the p38/NF- $\kappa$ B pathway.

I/R injury leads to heart damage in various ways. Oxidative stress, cell apoptosis, and fibrosis are closely correlated with I/R injury, which may further lead to heart failure [19]. Apoptosis is the most important factor related to the loss of cardiomyocytes during I/R. The level of PUMA expression was very low under normal circumstances, while the expression of PUMA in I/R-treated heart tissues was upregulated [2]. The I/R environment after heart transplantation induces elevated levels of PUMA expression in heart transplant tissues [20]. PUMA has been shown to regulate apoptosis-promoting activity [21, 22]. Therefore, it is reasonable to hypothesize that PUMA is a new therapeutic target for the regulation of apoptosis during cardiac I/R. In addition, ETS-1 upregulation mediates angiotensin II-induced cardiac fibrosis [6]. ETS-1 participates in this process by regulating the expression of fibrotic matrix genes, such as collagen 1, collagen 3, and fibronectin [23]. Consistent with previous observations, we demonstrated that I/R induced increases in oxidative stress, myocardial apoptosis and fibrosis, as shown by DHE staining, TUNEL assay and Masson's trichrome staining, respectively. In addition, we also showed that I/R-treated cardiac tissues and H/R-treated cardiomyocytes exhibited increased expression levels of PUMA and ETS-1. Importantly, we demonstrated that the downregulation of PUMA and ETS-1 expression by the transfection of siPUMA and siETS-1 directly prevented H/R-induced apoptosis and fibrosis. Moreover, conditioned medium from ADSCs decreased the expression of apoptosis- and fibrosis-related proteins. In this study, we



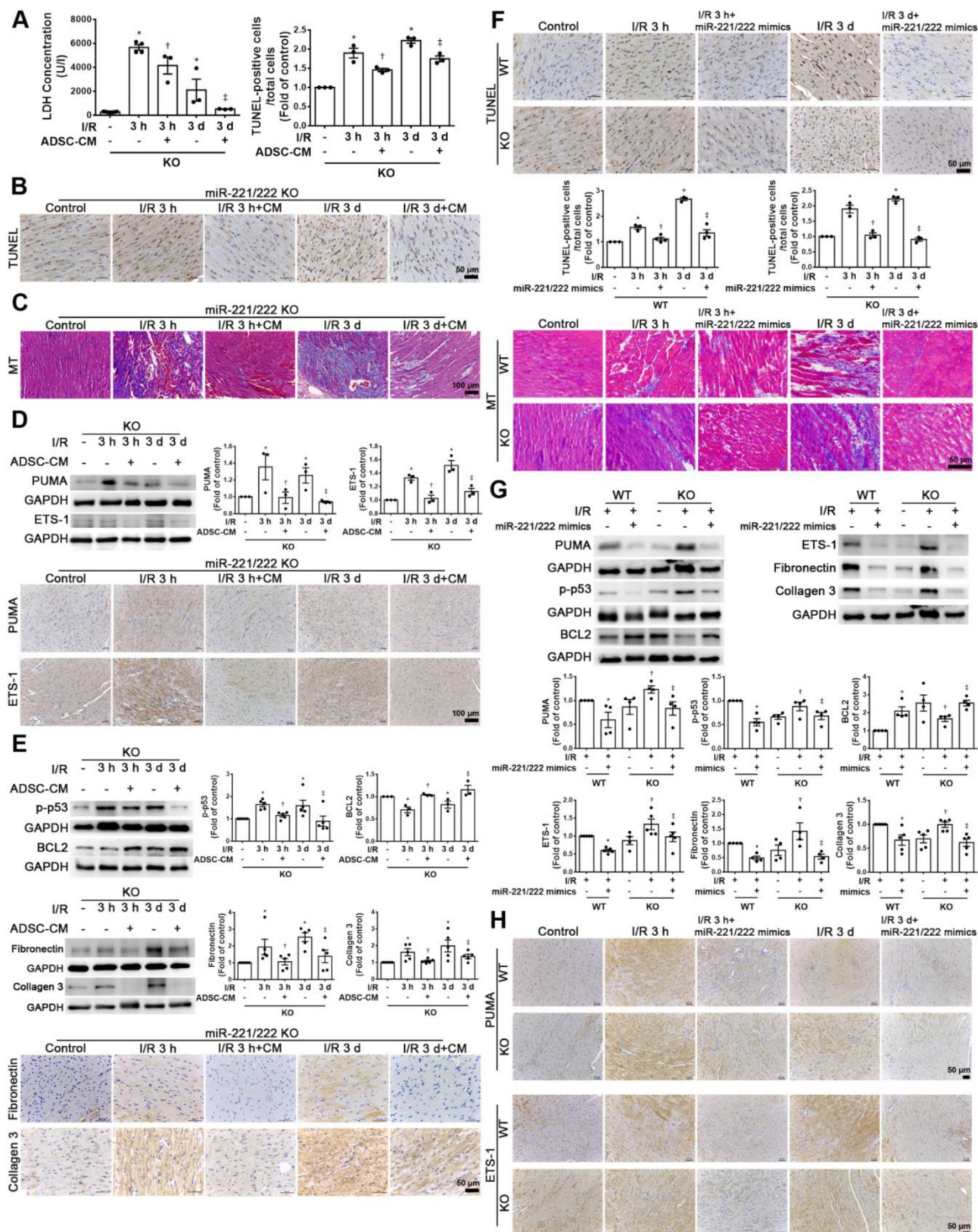
demonstrated that targeting PUMA and ETS-1 has a cardioprotective effect against myocardial I/R injury

by inhibiting apoptosis and fibrosis.



**Figure 5: ADSC-CM reduced apoptosis and fibrosis in H/R-treated H9c2 cells through the p-p38/NFκB p65 pathway.** (A) Cardiomyocytes were pretreated with or without ADSC-CM for 4 h and then exposed to hypoxia for 24 h. The cells were then exposed to normoxia for another 12 h. The phosphorylation levels of p38 and NFκB p65 were examined by Western blot. (B, C) Cells were pretreated with or without SB203580 (10 μM, p38 inhibitor) for 1 h and then induced with H/R. The expression levels of PUMA, p-p53, BCL2, ETS-1, fibronectin, and collagen 3 were examined by Western blot. SB203580 reduced the expression of PUMA, p-p53, ETS-1, fibronectin, and collagen 3, while increasing BCL2 expression in H/R-treated H9c2 cells. (D, E) Cells were pretreated with or without Bay 11-7082 (2.5 μM, NFκB inhibitor) for 1 h and then induced with H/R. Bay 11-7082 reduced the expression of PUMA and p-p53 and increased the expression of BCL2. Bay 11-7082 also significantly reduced H/R-induced ETS-1, fibronectin, and

collagen 3 expression in H9c2 cells. (F) The transfection of miR-221/222 mimics significantly ameliorated I/R-reduced p38 and p65 phosphorylation, as shown by Western blot. (G) The p38 inhibitor reduced the phosphorylation of NF $\kappa$ B, while the NF- $\kappa$ B inhibitor did not affect p38 phosphorylation, as shown by Western blot. (H, I) Treatment with the p38 inhibitor or with the NF $\kappa$ B inhibitor decreased apoptosis and fibrosis, as shown by TUNEL assay and immunofluorescent staining, respectively. (scale bar = 50  $\mu$ m). (J) I/R significantly increased p-p38 and p-p65 compared to those of the control mice, as shown by Western blot, while ADSC-CM reversed these effects *in vivo*. The data are expressed as the mean  $\pm$  SEM (n = 3-7). \*P < 0.05 vs. control,  $\dagger$ P < 0.05 vs. H/R, I/R,  $\#$ P < 0.05 vs. H/R+scramble, H/R+miR221/222 mimics.





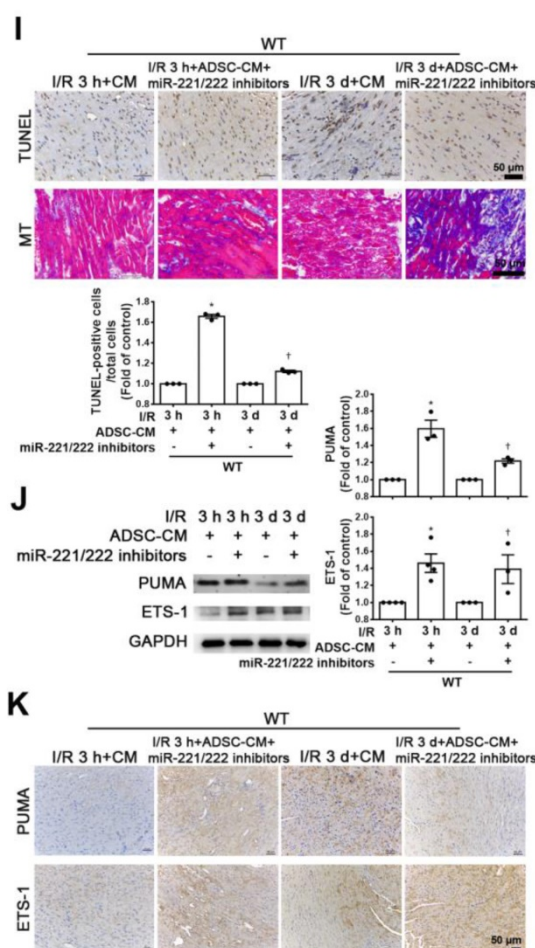


**Figure 6: ADSC-CM ameliorated myocardial I/R injury in miR-221/222 KO mice.** The LAD of miR-221/222 KO mice was occluded for 30 min and then reperused for 3 h or 3 d. In ADSC-CM-treated animals, ADSC-CM (4  $\mu$ g/mL) was injected into the anterior wall of the left ventricle. (A) ADSC-CM significantly inhibited I/R-increased LDH levels. (B, C) The levels of apoptosis and fibrosis were examined by TUNEL assay and Masson's trichrome (MT) staining, respectively (scale bar = 50  $\mu$ m; 100  $\mu$ m). (D) The protein levels of PUMA and ETS-1 were evaluated by Western blot analysis and immunohistochemistry (scale bar = 100  $\mu$ m). (E) The expression levels of p-p53, BCL2, fibronectin and collagen 3 were examined by Western blot and immunohistochemistry (scale bar = 50  $\mu$ m). (F) The effects of the *in vivo* transfection of miR-221/222 mimics on apoptosis and fibrosis were examined by TUNEL assay and Masson's trichrome staining, respectively, in normal mice and miR-221/222 KO mice. (scale bar = 50  $\mu$ m). (G) The effect of the *in vivo* transfection of miR-221/222 mimics treatment on the expression of PUMA, p-p53, BCL2, ETS-1, fibronectin and collagen 3 was measured by Western blot. (H) The effects of the *in vivo* transfection of miR-221/222 mimics treatment on the expression of PUMA and ETS-1 were examined by immunohistochemistry (scale bar = 50  $\mu$ m). (I) The effects of the *in vivo* transfection of miR-221/222 inhibitors on apoptosis and fibrosis were examined by TUNEL assay and Masson's trichrome staining, respectively (scale bar = 50  $\mu$ m). (J, K) The expression of PUMA and ETS-1 in WT mice transfected with miR-221/222 inhibitors was evaluated by Western blot and immunohistochemistry. The data are expressed as the mean  $\pm$  SEM (n = 3-5). \*P < 0.05 vs. control,  $\dagger$ P < 0.05 vs. the I/R 3 h or KO control group,  $\ddagger$ P < 0.05 vs. the I/R 3 d or KO I/R group.

In recent years, MSCs have become a good source of cell therapy because of their easy availability [8]. Compared with other types of MSCs, ADSCs have advantages in the treatment of myocardial infarction, liver fibrosis and oxidative damage [10]. However, low survival rates, poor differentiation efficacy, and the potential carcinogenicity of implanted cells may impair the safety of stem cell-based therapies [24]. Conditioned medium from ADSCs can be optimized by using increased concentrations and/or increasing the injection frequency, which is another method of directly transplanting stem cells [10]. It is expected that the paracrine products secreted from stem cells will be converted into improved therapeutic agents [25, 26]. The therapeutic effect of ADSC transplantation is mainly induced by paracrine-mediated cardioprotection and angiogenesis, while the role of

ADSC differentiation and participation in angiogenesis is small [10]. CM protects prolonged storage grafts from I/R injury [27]. Human ADSC-CM has a therapeutic effect on mouse ischemic stroke models mainly by reducing nerve cell apoptosis and increasing endothelial cell proliferation [24]. Bone marrow mesenchymal stem cell conditioned medium (BMSC-CM) reduced hypoxia-induced cardiomyocyte apoptosis [28]. Our previous study showed that ADSC-CM protected against I/R-induced injury in skin flaps [29]. Several studies have also shown that the injection of microparticles packaged from CM/secretome and coated with cell membranes of mesenchymal stem cells enhance the therapeutic benefits of CM after MI [30-32]. In addition, the previous study reported that cardiac stem cell-derived exosomes conjugated with cardiac

homing peptide alleviated I/R-induced cardiac injury [33]. Another study showed that platelet-targeted delivery of peripheral blood mononuclear cells to the ischemic heart restores cardiac function after I/R injury [34]. The present study showed that ADSC-CM treatment reduced the expression of apoptosis-related proteins, such as PUMA, p-p53, and BCL2, and decreased apoptosis. I/R increased the accumulation of excessive extracellular matrix, which leads to ventricular remodeling and irreversible myocardial fibrosis [35]. In this study, ADSC-CM treatment significantly decreased the expression of ETS-1, fibronectin, and collagen 3, and attenuated cell fibrosis. Therefore, we demonstrated that ADSC-CM administration can play a beneficial role in I/R injury by reducing cardiac apoptosis and fibrosis.

The paracrine products produced by ADSCs include cytokines, growth factors, and miRNAs [11]. In addition, exosomes secreted by most cell types, including mesenchymal stem cells, have beneficial effects on acute ischemia/reperfusion injury and can reduce the adverse remodeling in pigs after chronic MI [36, 37]. A recent study showed that miR-21-5p dysregulation occurs in exosomes derived from heart failure patients, which can inhibit angiogenesis and cardiomyocyte survival [38]. To explore the mechanism by which ADSC-CM protects cardiomyocytes from I/R damage, we studied this miRNA-mediated process. MiRNAs are usually released to recipient cells as key regulators [39]. ADSC-CM reduced cardiomyocyte apoptosis, which may be related to the transfer of miRNAs from the conditioned medium to cardiomyocytes [10]. In this study, we focused on miR-221/222, which is enriched in ADSC-CM, and found that the expression of miR-221/222 in ADSC-CM was closely related to the protective effect of ADSC-CM both *in vitro* and *in vivo*. MiR-221/222 suppresses apoptosis by targeting growth arrest-specific transcript 5 in breast cancer [40]. PUMA has been reported to be the target of miR-221/222 in human epithelial cancers, human glioma cells, and multiple myeloma cells [14, 41, 42]. In addition, miR-221/222 targets ETS-1 in endothelial cells to regulate angiotensin II-induced endothelial inflammation and migration [43]. ETS-1 also plays a role in heart remodeling [6]. MiR-221/222 is involved in ETS-1-regulated fibrosis [44]. Here, we provide the first evidence that the expression levels of miR-221/222 in I/R-treated hearts and H/R-treated cardiomyocytes were decreased, while ADSC-CM increased these levels. The transfection of miR-221/222 mimics decreased I/R-induced cardiac injury. Using luciferase reporter assays, we proved that miR-221/222 of ADSC-CM could directly bind to the 3'-UTRs of PUMA and ETS-1 and inhibit the

expression of PUMA and ETS-1. Moreover, compared with ADSC-CM, anti-miR-221/222 treatment had the opposite effects on PUMA and ETS-1 expression. Therefore, miR-221/222 is thought to inhibit PUMA and ETS-1 through sequence-specific target recognition and subsequently inhibit cardiomyocyte apoptosis and fibrosis. The present study provides evidence that PUMA and ETS-1 are direct targets of miR-221/222, and they act as apoptosis and fibrosis regulators in cardiomyocytes, respectively. MiR-221/222 in ADSC-CM exerts protective effects on I/R-treated hearts and H/R-treated cardiomyocytes both *in vitro* and *in vivo*.

p38 MAPK and NF- $\kappa$ B are frequently activated after cells are exposed to environmental stress, such as I/R-induced cardiac injury [45, 46]. P38/NF- $\kappa$ B has been reported to be a mediator of stress-induced cell death and fibrosis [47, 48]. P-p38/NF- $\kappa$ B participates in inflammation and apoptosis by regulating the expression of many downstream target genes, such as the apoptotic protein PUMA [2, 49, 50]. The activation of NF- $\kappa$ B signaling leads to the upregulation of PUMA during I/R injury in heart transplantation [20]. Inhibitors of p38/NF- $\kappa$ B expression appear to be downstream of PUMA inhibition [51, 52]. Inhibition of p53-PUMA feedback loop activation prevents neuronal apoptosis and inflammatory responses by downregulating the NF- $\kappa$ B pathway in spinal cord I/R injury [52]. In addition, the downstream signaling cascade of p38 MAPK and NF- $\kappa$ B induces ETS-1 expression [53, 54]. Epidermal growth factor-induced ETS-1 regulates the expression of collagen I and III through the p38-MAPK signaling pathway in smooth muscle cells [55]. Furthermore, the activation of NF- $\kappa$ B activates ETS-1 expression [56]. Our previous study showed that activation of p38/NF- $\kappa$ B affects the expression of miR-221/222, thereby increasing ICAM-1 expression and monocyte adhesion in TNF- $\alpha$ -treated endothelial cells [57]. The present study showed that the phosphorylation levels of p38 MAPK and NF- $\kappa$ B p65 in H/R-treated cardiomyocytes and I/R-treated mice were significantly increased compared to those of normal control mice, but ADSC-CM treatment significantly abrogated the increased phosphorylation levels of p38 MAPK/NF $\kappa$ B p65. We also demonstrated that miR-221/222 mimics inhibited I/R-induced p38/NF $\kappa$ B activation. Treatment with SB203580 (a p38 MAPK inhibitor) and Bay 11-7082 (a p65 inhibitor) markedly attenuated the expression of PUMA and ETS-1 in H9c2 cells exposed to the H/R environment. Our work demonstrated a new pathway by which miR-221/222 regulates cardiac apoptosis and fibrosis, namely, the p-p38/NF- $\kappa$ B pathway. We concluded that the protective effects of ADSC-CM

rely on the miR-221/222/PUMA/ETS-1 pathway and p38 MAPK/NFκB signaling pathway.

In summary, this study provides the first evidence from *in vitro* and *in vivo* experiments confirming that the cardioprotective effect of ADSC-CM is mediated by increasing miR-221/222 expression and blocking p38/NF-κB phosphorylation, thus leading to decreased PUMA and ETS-1 expression in the context of ischemic injury. Exploring the active components and functional mechanisms of ADSC-CM is critical for the development of a new type of myocardial ischemia biotherapy. This study clarified the mechanism by which ADSC-CM protects the ischemic myocardium and provided a new method to reduce myocardial ischemic injury.

## Acknowledgments

## Sources of funding

This research was supported by research grants from the Ministry of Science and Technology of Taiwan (MOST 108-2320-B-002-065-MY3), the National Taiwan University Hospital (109-S4728), the Chang Gung University of Science Foundation (ZRRPF3K0111) and the Chang Gung Medical Research Program Foundation (CMRPG6J0221, 22, and 23).

## Competing Interests

The authors have declared that no competing interest exists.

## References

- Hausenloy DJ, Yellon DM. Ischaemic conditioning and reperfusion injury. *Nat Rev Cardiol*. 2016; 13: 193-209.
- Chen L, Zhang D, Yu L, Dong H. Targeting MIAT reduces apoptosis of cardiomyocytes after ischemia/reperfusion injury. *Bioengineered*. 2019; 10: 121-32.
- Liu T, Song D, Dong J, Zhu P, Liu J, Liu W, et al. Current understanding of the pathophysiology of myocardial fibrosis and its quantitative assessment in heart failure. *Front Physiol*. 2017; 8: 238.
- Yang X, Fu J, Wan H, Liu Z, Yu L, Yu B, et al. Protective roles and mechanisms of taurine on myocardial hypoxia/reoxygenation-induced apoptosis. *Acta Cardiol Sin*. 2019; 35: 415-24.
- Lal H, Ahmad F, Zhou J, Yu JE, Vagnozzi RJ, Guo Y, et al. Cardiac fibroblast glycogen synthase kinase-3β regulates ventricular remodeling and dysfunction in ischemic heart. *Circulation*. 2014; 130: 419-30.
- Hao G, Han Z, Meng Z, Wei J, Gao D, Zhang H, et al. Ets-1 upregulation mediates angiotensin II-related cardiac fibrosis. *Int J Clin Exp Pathol*. 2015; 8: 10216-27.
- Kern S, Eichler H, Stoeve J, Klütter H, Bieback K. Comparative analysis of mesenchymal stem cells from bone marrow, umbilical cord blood, or adipose tissue. *Stem Cells*. 2006; 24: 1294-301.
- Williams AR, Hare JM. Mesenchymal stem cells: biology, pathophysiology, translational findings, and therapeutic implications for cardiac disease. *Circ Res*. 2011; 109: 923-40.
- Li TS, Cheng K, Malliaras K, Smith RR, Zhang Y, Sun B, et al. Direct comparison of different stem cell types and subpopulations reveals superior paracrine potency and myocardial repair efficacy with cardiosphere-derived cells. *J Am Coll Cardiol*. 2012; 59: 942-53.
- Yang D, Wang W, Li L, Peng Y, Chen P, Huang H, et al. The relative contribution of paracrine effect versus direct differentiation on adipose-derived stem cell transplantation mediated cardiac repair. *PLoS One*. 2013; 8: e59020.
- Ma T, Sun J, Zhao Z, Lei W, Chen Y, Wang X, et al. A brief review: adipose-derived stem cells and their therapeutic potential in cardiovascular diseases. *Stem Cell Res Ther*. 2017; 8: 124.
- Chistiakov DA, Sobenin IA, Orekhov AN, Bobryshev YV. Human miR-221/222 in physiological and atherosclerotic vascular remodeling. *Biomed Res Int*. 2015; 2015: 354517.
- Corsten MF, Heggermont W, Papageorgiou AP, Deckx S, Tijssma A, Verhesen W, et al. The microRNA-221/-222 cluster balances the antiviral and inflammatory response in viral myocarditis. *Eur Heart J*. 2015; 36: 2909-19.
- Zhang CZ, Zhang JX, Zhang AL, Shi ZD, Han L, Jia ZF, et al. MiR-221 and miR-222 target PUMA to induce cell survival in glioblastoma. *Mol Cancer*. 2010; 9: 229.
- Liu Y, Lu T, Zhang C, Xu J, Xue Z, Busuttil RW, et al. Activation of YAP attenuates hepatic damage and fibrosis in liver ischemia-reperfusion injury. *J Hepatol*. 2019; 71: 719-30.
- Paillard M, Tubbs E, Thiebaut PA, Gomez L, Fauconnier J, Da Silva CC, et al. Depressing mitochondria-reticulum interactions protects cardiomyocytes from lethal hypoxia-reoxygenation injury. *Circulation*. 2013; 128: 1555-65.
- Li X, Xie X, Yu Z, Chen Y, Qu G, Yu H, et al. Bone marrow mesenchymal stem cells-derived conditioned medium protects cardiomyocytes from hypoxia/reoxygenation-induced injury through Notch2/mTOR/autophagy signaling. *J Cell Physiol*. 2019; 234: 18906-16.
- Wang D, Chen T, Liu F. Betulinic acid alleviates myocardial hypoxia/reoxygenation injury via inducing Nrf2/HO-1 and inhibiting p38 and JNK pathways. *Eur J Pharmacol*. 2018; 838: 53-9.
- Neri M, Riezso I, Pascale N, Pomara C, Turillazzi E. Ischemia/reperfusion injury following acute myocardial infarction: a critical issue for clinicians and forensic pathologists. *Mediators Inflamm*. 2017; 2017: 7018393.
- Jing H, Zou G, Hao F, Wang H, Wang S. Hsp27 reduces cold ischemia-reperfusion injury in heart transplantation through regulation of NF-κB and PUMA signaling. *Int J Clin Exp Pathol*. 2018; 11: 281-92.
- Mandl A, Huong Pham L, Toth K, Zambetti G, Erhardt P. Puma deletion delays cardiac dysfunction in murine heart failure models through attenuation of apoptosis. *Circulation*. 2011; 124: 31-9.
- Zhou X, Li J, Marx C, Tolstov Y, Rauch G, Herpel E, et al. Uncoupling of PUMA expression and apoptosis contributes to functional heterogeneity in renal cell carcinoma - prognostic and translational implications. *Transl Oncol*. 2015; 8: 480-6.
- Xu L, Fu M, Chen D, Han W, Ostrowski MC, Grossfeld P, et al. Endothelial-specific deletion of Ets-1 attenuates Angiotensin II-induced cardiac fibrosis via suppression of endothelial-to-mesenchymal transition. *BMB Rep*. 2019; 52: 595-600.
- Cho YJ, Song HS, Bhang S, Lee S, Kang BG, Lee JC, et al. Therapeutic effects of human adipose stem cell-conditioned medium on stroke. *J Neurosci Res*. 2012; 90: 1794-802.
- Ratajczak MZ, Kucia M, Jadczyk T, Greco NJ, Wojakowski W, Tendera M, et al. Pivotal role of paracrine effects in stem cell therapies in regenerative medicine: can we translate stem cell-secreted paracrine factors and microvesicles into better therapeutic strategies? *Leukemia*. 2012; 26: 1166-73.
- Varderdidou-Minasian S, Lorenowicz MJ. Mesenchymal stromal/stem cell-derived extracellular vesicles in tissue repair: challenges and opportunities. *Theranostics*. 2020; 10: 5979-97.
- Korkmaz-Icöz S, Li S, Hüttner R, Ruppert M, Radovits T, Loganathan S, et al. Hypothermic perfusion of donor heart with a preservation solution supplemented by mesenchymal stem cells. *J Heart Lung Transplant*. 2019; 38: 315-26.
- Li W, Li Y, Chu Y, Wu W, Yu Q, Zhu X, et al. PLCE1 promotes myocardial ischemia-reperfusion injury in H/R H9c2 cells and I/R rats by promoting inflammation. *Biosci Rep*. 2019; 39: BSR20181613.
- Pu CM, Liu CW, Liang CJ, Yen YH, Chen SH, Jiang-Shieh YF, et al. Adipose-derived stem cells protect skin flaps against ischemia/reperfusion injury via IL-6 expression. *J Invest Dermatol*. 2017; 137: 1353-62.
- Luo L, Tang J, Nishi K, Yan C, Dinh PU, Cores J, et al. Fabrication of synthetic mesenchymal stem cells for the treatment of acute myocardial infarction in mice. *Circ Res*. 2017; 120: 1768-75.
- Tang J, Shen D, Caranasos TG, Wang Z, Vandergriff AC, Allen TA, et al. Therapeutic microparticles functionalized with biomimetic cardiac stem cell membranes and secretome. *Nat Commun*. 2017; 8: 13724.
- Huang K, Ozpinar EW, Su T, Tang J, Shen D, Qiao L, et al. An off-the-shelf artificial cardiac patch improves cardiac repair after myocardial infarction in rats and pigs. *Sci Transl Med*. 2020; 12: eaa9683.
- Vandergriff A, Huang K, Shen D, Hu S, Hensley MT, Caranasos TG, et al. Targeting regenerative exosomes to myocardial infarction using cardiac homing peptide. *Theranostics*. 2018; 8: 1869-78.
- Ziegler M, Wang X, Lim B, Leitner E, Klingberg F, Ching V, et al. Platelet-targeted delivery of peripheral blood mononuclear cells to the ischemic heart restores cardiac function after ischemia-reperfusion injury. *Theranostics*. 2017; 7: 3192-206.
- Fan D, Takawale A, Lee J, Kassiri Z. Cardiac fibroblasts, fibrosis and extracellular matrix remodeling in heart disease. *Fibrogenesis Tissue Repair*. 2012; 5: 15.
- Gallet R, Dawkins J, Valle J, Simolo E, de Couto G, Middleton R, et al. Exosomes secreted by cardiosphere-derived cells reduce scarring, attenuate adverse remodelling, and improve function in acute and chronic porcine myocardial infarction. *Eur Heart J*. 2017; 38: 201-11.
- Kalra H, Drummen GP, Mathivanan S. Focus on extracellular vesicles: introducing the next small big thing. *Int J Mol Sci*. 2016; 17: 170.

38. Qiao L, Hu S, Liu S, Zhang H, Ma H, Huang K, et al. microRNA-21-5p dysregulation in exosomes derived from heart failure patients impairs regenerative potential. *J Clin Invest*. 2019; 129: 2237-50.
39. Moreno-Moya JM, Vilella F, Simón C. MicroRNA: key gene expression regulators. *Fertil Steril*. 2014; 101: 1516-23.
40. Zong Y, Zhang Y, Sun X, Xu T, Cheng X, Qin Y. miR-221/222 promote tumor growth and suppress apoptosis by targeting lncRNA GAS5 in breast cancer. *Biosci Rep*. 2019; 39: BSR20181859.
41. Zhang C, Zhang J, Zhang A, Wang Y, Han L, You Y, et al. PUMA is a novel target of miR-221/222 in human epithelial cancers. *Int J Oncol*. 2010; 37: 1621-6.
42. Zhao JJ, Chu ZB, Hu Y, Lin J, Wang Z, Jiang M, et al. Targeting the miR-221-222/PUMA/BAK/BAX pathway abrogates dexamethasone resistance in multiple myeloma. *Cancer Res*. 2015; 75: 4384-97.
43. Zhu N, Zhang D, Chen S, Liu X, Lin L, Huang X, et al. Endothelial enriched microRNAs regulate angiotensin II-induced endothelial inflammation and migration. *Atherosclerosis*. 2011; 215: 286-93.
44. Verjans R, Peters T, Beaumont FJ, van Leeuwen R, van Herwaarden T, Verheesen W, et al. MicroRNA-221/222 family counteracts myocardial fibrosis in pressure overload-induced heart failure. *Hypertension*. 2018; 71: 280-8.
45. Gray CB, Suetomi T, Xiang S, Mishra S, Blackwood EA, Glembotski CC, et al. CaMKII $\delta$  subtypes differentially regulate infarct formation following ex vivo myocardial ischemia/reperfusion through NF- $\kappa$ B and TNF- $\alpha$ . *J Mol Cell Cardiol*. 2017; 103: 48-55.
46. Li J, Lang MJ, Mao XB, Tian L, Feng YB. Antiapoptosis and mitochondrial effect of pioglitazone preconditioning in the ischemic/reperfused heart of rat. *Cardiovasc Drugs Ther*. 2008; 22: 283-91.
47. Savira F, Cao L, Wang I, Yang W, Huang K, Hua Y, et al. Apoptosis signal-regulating kinase 1 inhibition attenuates cardiac hypertrophy and cardiorenal fibrosis induced by uremic toxins: Implications for cardiorenal syndrome. *PLoS One*. 2017; 12: e0187459.
48. Yang H, Li N, Song LN, Wang L, Tian C, Tang CS, et al. Activation of NOD1 by DAP contributes to myocardial ischemia/reperfusion injury via multiple signaling pathways. *Apoptosis*. 2015; 20: 512-22.
49. Rudolf K, Cervinka M, Rudolf E. Sulforaphane-induced apoptosis involves p53 and p38 in melanoma cells. *Apoptosis*. 2014; 19: 734-47.
50. Wang P, Qiu W, Dudgeon C, Liu H, Huang C, Zambetti GP, et al. PUMA is directly activated by NF- $\kappa$ B and contributes to TNF- $\alpha$ -induced apoptosis. *Cell Death Differ*. 2009; 16: 1192-202.
51. Dziegielewska B, Brautigan DL, Lerner JM, Dziegielewska J. T-type Ca<sup>2+</sup> channel inhibition induces p53-dependent cell growth arrest and apoptosis through activation of p38-MAPK in colon cancer cells. *Mol Cancer Res*. 2014; 12: 348-58.
52. Li XQ, Yu Q, Chen FS, Tan WF, Zhang ZL, Ma H. Inhibiting aberrant p53-PUMA feedback loop activation attenuates ischaemia reperfusion-induced neuroapoptosis and neuroinflammation in rats by downregulating caspase 3 and the NF- $\kappa$ B cytokine pathway. *J Neuroinflammation*. 2018; 15: 250.
53. Okano K, Hibi A, Miyaoka T, Inoue T, Sugimoto H, Tsuchiya K, et al. Inhibitory effects of the transcription factor Ets-1 on the expression of type I collagen in TGF- $\beta$ 1-stimulated renal epithelial cells. *Mol Cell Biochem*. 2012; 369: 247-54.
54. Zhang Y, Wu J, Ye M, Wang B, Sheng J, Shi B, et al. ETS1 is associated with cisplatin resistance through IKK $\alpha$ /NF- $\kappa$ B pathway in cell line MDA-MB-231. *Cancer Cell Int*. 2018; 18: 86.
55. Rao VH, Rai V, Stoupa S, Agrawal DK. Blockade of Ets-1 attenuates epidermal growth factor-dependent collagen loss in human carotid plaque smooth muscle cells. *Am J Physiol Heart Circ Physiol*. 2015; 309: H1075-86.
56. Li L, Miao X, Ni R, Miao X, Wang L, Gu X, et al. Epithelial-specific ETS-1 (ESE1/ELF3) regulates apoptosis of intestinal epithelial cells in ulcerative colitis via accelerating NF- $\kappa$ B activation. *Immunol Res*. 2015; 62: 198-212.
57. Liu CW, Sung HC, Lin SR, Wu CW, Lee CW, Lee IT, et al. Resveratrol attenuates ICAM-1 expression and monocyte adhesiveness to TNF- $\alpha$ -treated endothelial cells: evidence for an anti-inflammatory cascade mediated by the miR-221/222/AMPK/p38/NF- $\kappa$ B pathway. *Sci Rep*. 2017; 7: 44689.





## A new dimeric protoberberine alkaloid and other compounds from the tubers of *Tinospora dentata*

Sio-Hong Lam<sup>a</sup>, Shu-Duan Jian<sup>b</sup>, Tsong-Long Hwang<sup>c,d,e</sup>, Po-Jen Chen<sup>f</sup>,  
Hsin-Yi Hung<sup>a</sup>, Ping-Chung Kuo<sup>a</sup> and Tian-Shung Wu<sup>a,g</sup>

<sup>a</sup>School of Pharmacy, College of Medicine, National Cheng Kung University, Tainan, Taiwan; <sup>b</sup>Chuang Song Zong Pharmaceutical Co., LTD, Kaohsiung City, Taiwan; <sup>c</sup>Graduate Institute of Natural Products, School of Traditional Chinese Medicine, College of Medicine, Chang Gung University, Taoyuan, Taiwan; <sup>d</sup>Research Center for Chinese Herbal Medicine, Research Center for Food and Cosmetic Safety, Graduate Institute of Health Industry Technology, College of Human Ecology, Chang Gung University of Science and Technology, Taoyuan, Taiwan; <sup>e</sup>Department of Anesthesiology, Chang Gung Memorial Hospital, Taoyuan, Taiwan; <sup>f</sup>Department of Cosmetic Science, Providence University, Taichung, Taiwan; <sup>g</sup>Department of Pharmacy, College of Pharmacy and Health Care, Tajen University, Pingtung, Taiwan

### ABSTRACT

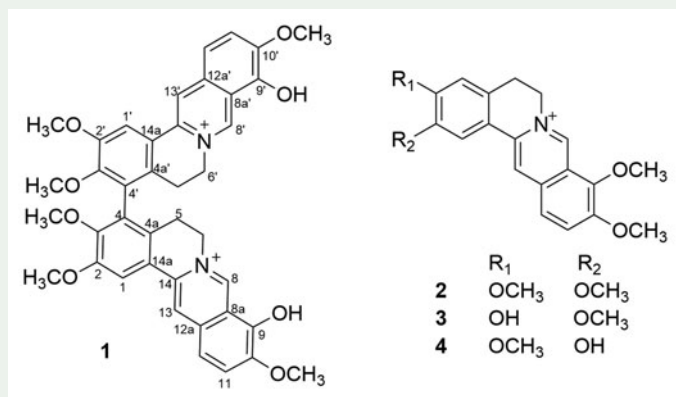
A new dimeric quaternary protoberberine alkaloid, bispalmatrubine (**1**), and thirteen known compounds (**2–14**) were purified from the tubers of *Tinospora dentata*. Their structures were determined by spectroscopic and spectrometric analytical methods. Among the isolates, eight compounds were examined for their *in vitro* anti-inflammatory potential and several tested alkaloids displayed moderate inhibitory effects of *N*-formyl-methionyl-leucyl-phenylalanine/cytochalasin B (fMLP/CB)-induced superoxide anion generation and elastase release.


### ARTICLE HISTORY


Received 18 November 2018  
Accepted 23 April 2019

### KEYWORDS

Menispermaceae; anti-inflammatory; superoxide anion generation; elastase release



**CONTACT** Ping-Chung Kuo  [z10502016@email.ncku.edu.tw](mailto:z10502016@email.ncku.edu.tw)  School of Pharmacy, College of Medicine, National Cheng Kung University, Tainan, 701, Taiwan; Tian-Shung Wu  [tswu@mail.ncku.edu.tw](mailto:tswu@mail.ncku.edu.tw)  School of Pharmacy, College of Medicine, National Cheng Kung University, Tainan, 701, Taiwan and Department of Pharmacy, College of Pharmacy and Health Care Tajen University, Pingtung, 907, Taiwan.

 Supplemental data for this article is available online at <https://doi.org/10.1080/14786419.2019.1611809>.

© 2019 Informa UK Limited, trading as Taylor & Francis Group



## 1. Introduction

*Tinospora*, a genus belonged to Menispermaceae, included more than 20 species all over the world (Editorial Committee of the Flora of Taiwan 1996). This genus is widely used as folk medicine in Southeast Asian countries such as India and Thailand for the treatment of malaria, gout, diabetes, and skin diseases (Krishna et al. 2009). In recent years, there are several important physiological activities reported for this genus, such as antibacterial (Chakraborty et al. 2014), antioxidant (Upadhyay et al. 2010; Mishra et al. 2011), anti-inflammatory (Liu et al. 2010), cytotoxic (Choudhary et al. 2010; Ng et al. 2010) and immunomodulatory activities (More and Pai 2011; Sengupta et al. 2011), especially the most explored hypoglycemic activity (Lam et al. 2012; Ruan et al. 2013). Various chemical constituents including the furanoditerpenoids (Chen 1975; Choudhary et al. 2010), alkaloids (Dong et al. 2010), and lignans (Li et al. 2004) are isolated from this genus. In our continuous ongoing projects on *Tinospora* genus, the stems of *T. crispa* was reported to be rich-in furanoditerpenoids and displayed significant hypoglycemic activity (Lam et al. 2012). The stems of *T. sinensis* exhibited various chemical compositions mainly for lignans and pyrrole alkaloids (Lam et al. 2018). In addition, the reported structure of new compound tinosporide A from *T. sinensis* should be revised as liriodendrin (Zhou et al. 2017). *T. dentata* is the only endemic species of this genus grown in Taiwan (Editorial Committee of the Flora of Taiwan 1996). In Chinese folk medicine, *T. dentata* is used for relieving abdominal pain, diarrhea, phlegm and stomach, and often used for sore throat and cough treatment. However, the chemical composition of this plant is poorly understood and its biological activity so far not yet examined (Chen 1975). Therefore, we wish to study the chemical constituents of *T. dentata* and the characterized compounds could be examined for their inhibition of fMLP/CB-induced superoxide anion generation and elastase release.

## 2. Results and discussion

Reflux of the tubers of *T. dentata* with methanol yielded methanol extract which was fractionated by liquid-liquid partition into ethyl acetate (EtOAc), *n*-butanol (*n*-BuOH), and water (H<sub>2</sub>O) layers. The EtOAc-soluble layer was further partition with 5% HCl to yield the EtOAc fraction (non-alkaloids) and acidic water fraction (alkaloids). Further silica gel column chromatography purification afforded a total of fourteen compounds. Compound **1** was elucidated as a new dimeric protoberberine type alkaloid based on the 1D nuclear magnetic resonance (NMR), 2D NMR and mass spectrometric (MS) analyses. The known compounds **2–14** were identified by comparison of their physical and spectral data with those reported in the literature, including four protoberberine type alkaloids, palmatine (**2**), jatrorrhizine (**3**), columbamine (**4**) (Thuy et al. 2006); three oxoaporphine type alkaloids, homomoschatoline (**5**), lysicamine (**6**) (Skiles et al. 1979), dicentrinone (**7**) (Chen et al. 1997); two diterpenoids, columbin (**8**) (Chen et al. 1973), isocolumbin (**9**) (Overton et al. 1966) (Figure 1); four steroids, a mixture of stigmasterol (**10**) and  $\beta$ -sitosterol (**11**) (Kuo and Li 1997), a mixture of stigmasteryl glycoside (**12**) and  $\beta$ -sitosteryl glycoside (**13**) (Khatun et al. 2012); and one benzenoid, benzoin (**14**) (Pouchert and Campell 1974), respectively.

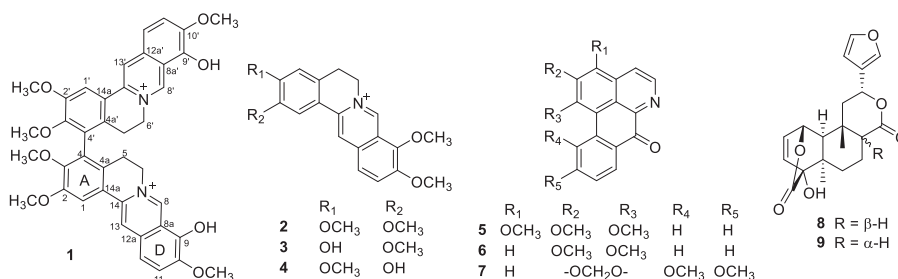


**Figure 1.** Structures of compounds 1–9.

Bispalmatrubine (**1**), obtained as yellowish powder, was positive to the Dragendorff's test and shown strong ultraviolet (UV) absorption maxima at 404, 354 and 263 nm, which was characteristic of a quaternary protoberberine alkaloid (Scott 1964; Shamma 1972). The phenolic nature was evidenced by bathochromic shifts in the presence of base. The <sup>1</sup>H NMR spectra of **1** (Table S1) revealed two typical signals of the berberine skeleton at δ 9.71 (s, 1H, H-8) and 8.88 (s, 1H, H-13). One proton singlet in the aromatic region at δ 7.80 was assigned to H-1 of ring A. In addition, two AB system protons at δ 8.05 (d, 1H, *J* = 9.1 Hz, H-11) and 8.13 (d, 1H, *J* = 9.1 Hz, H-12) indicated the *ortho* coupling of aromatic ring D. In addition, one methylene group (CH<sub>2</sub>-5) at δ 2.85 (1H, m) and δ 3.00 (1H, m) and the down field shifted signals at δ 4.90 (2H, m, CH<sub>2</sub>-6) caused by quaternary ammonium group were also observed. These results indicated that **1** is 2,3,4,9,10-pentasubstituted protoberberine. The heteronuclear multiple bond correlation (HMBC) spectrum showed the key correlations from H-1 to C-2, C-14, C-14b; from H-8 to C-6, C-8a, C-9, C-12a, C-14; from H-11 to C-10, C-12a; from H-12 to C-10, C-13; and from H-13 to C-12a, C-14, respectively (Figure S7). The locations of three methoxy groups were also confirmed by HMBC correlations (Table S1). The significant correlations of H-1/H-13, OMe-2; H-11/H-12, OMe-10; and H-12/H-13, H-1, were observed in the nuclear Overhauser effect spectroscopy (NOESY). The dimer structure was suggested by high resolution electrospray ionization mass spectrometry (HR-ESI-MS) exhibited a *M*/2 ion peak at *m/z* 337.1338 ([*M*/2]<sup>+</sup>, calcd. 337.1309), in which one amu less than that of palmatrubine. In addition, H-4 of palmatrubine was not observed in **1**. There were two possible connection patterns for this dimer, i.e. C-3 to C-3' or C-4 to C-4', and it was clarified that compound **1** exhibited a characteristic mass fragments at *m/z* 191 and *m/z* 529 for a berberine skeleton possessing two *ortho* methoxyl groups in the A ring by retro Diels-Alder reaction (see Figure S10) (Thuy et al. 2006). These experimental data concluded that the dimer was linked through C-4 to C-4' of ring A and it was further evidenced by the C-C linkage carbon signal at δ 122.2 (C-4). Thus, the structure of compound **1** was determined as a palmatrubine dimer and named bispalmatrubine. Bispalmatrubine (**1**) with significant steric restriction between two *ortho*-substituted aryl systems (ring A to A') which will exhibit atropisomerism phenomenon. However, our sample had been run out for the bioassay and several chemical detections. Therefore, we could not determine the atropisomeric features of this compound in the present study. The first known dimeric protoberberine alkaloid, bisjatrorrhizine was isolated from the roots of *Jatrorrhiza palmata* (Menispermaceae) (Carvalho 1972). However, there was no other dimeric

**Table 1.** Effects of purified compounds on superoxide anion generation and elastase release in fMLP/CB-induced human neutrophils.

| Compound               | Superoxide anion   |       |                                    |  |  | Elastase           |       |                       |  |  |
|------------------------|--------------------|-------|------------------------------------|--|--|--------------------|-------|-----------------------|--|--|
|                        | Inh % <sup>a</sup> |       | IC <sub>50</sub> (μM) <sup>b</sup> |  |  | Inh % <sup>a</sup> |       | IC <sub>50</sub> (μM) |  |  |
| <b>1</b>               | 10.5               | ± 2.1 | >10                                |  |  | 13.9               | ± 1.8 | **                    |  |  |
| <b>2</b>               | 2.3                | ± 2.7 | >10                                |  |  | 3.6                | ± 4.1 | >10                   |  |  |
| <b>4</b>               | 3.6                | ± 0.5 | **                                 |  |  | 19.3               | ± 3.6 | **                    |  |  |
| <b>5</b>               | 57.4               | ± 5.0 | ***                                |  |  | −5.9               | ± 2.5 | >10                   |  |  |
| <b>7</b>               | 62.3               | ± 5.3 | ***                                |  |  | 38.7               | ± 5.6 | ***                   |  |  |
| <b>8</b>               | 3.7                | ± 1.8 | >10                                |  |  | −2.4               | ± 5.9 | >10                   |  |  |
| <b>9</b>               | −2.8               | ± 2.7 | >10                                |  |  | −5.8               | ± 7.5 | >10                   |  |  |
| <b>14</b>              | −0.8               | ± 1.7 | >10                                |  |  | −0.6               | ± 5.8 | >10                   |  |  |
| Genistein <sup>c</sup> | 84.7               | ± 4.2 | 1.2 ± 0.1                          |  |  | 42.4               | ± 3.8 | 16.2 ± 3.4            |  |  |

Results are presented as mean ± S.E.M. (n = 3 ~ 4). \*\*  $p < 0.01$ , \*\*\*  $p < 0.001$  compared with control (DMSO). <sup>a</sup>Percentage of inhibition (Inh %) at 10 μM concentration. <sup>b</sup>For compounds **5**, **7**, and genistein, IC<sub>50</sub> values were calculated from a series of different examined concentrations of 1–10 μM (**5** and **7**) and 1–50 μM (genistein), respectively. <sup>c</sup>Genistein was used as a positive control.

protoberberine alkaloid identified from the natural sources. Bispalmatrubine (**1**) represented the second natural appearance of such skeleton also belonged to Menispermaceae family.

For the purpose to study the relationship between chemical compositions and bio-activity of *T. dentata*, eight purified compounds were evaluated for their inhibitory bio-activity of generation for superoxide anion and elastase by human neutrophils in response to fMLP/CB (Table 1) (Yu et al. 2011; Yang et al. 2013). However, most of them did not display effective inhibition at the test concentration (10 μM). Among these, **4** and **7** displayed inhibitions of elastase release with inhibition percentages ranged from 19.3 ± 3.6 to 38.7 ± 5.6%. In addition, compounds **5** and **7** exhibited higher inhibitory percentages (57.4 ± 5.0% and 62.3 ± 5.3%) on superoxide anion generation with IC<sub>50</sub> of 8.4 ± 0.8 μM and 5.0 ± 1.0 μM, respectively (Table 1). However, the new dimer dimeric quaternary protoberberine alkaloid, bispalmatrubine (**1**), exhibited only weak inhibitory activities in this assay. In comparison, genistein, a broad-spectrum tyrosine kinase inhibitor (Duan et al. 2003), was used as a positive control (Leu et al. 2012) and displayed IC<sub>50</sub> of 1.2 ± 0.1 μM and 16.2 ± 3.4 μM towards superoxide anion generation and elastase release.

### 3. Experimental

#### 3.1. General experimental procedures

The UV spectra of isolated compounds were recorded on a Shimadzu UV-260 spectrophotometer (Shimadzu, Kyoto, Japan). The optical rotation and infrared (IR) spectra were measured on a JASCO DIP-360 polarimeter and a JASCO A-302 Infrared Spectrometer (Jasco, Tokyo, Japan), respectively. 1D and 2D NMR spectra were detected on the Bruker Avance III 700 and 400 NMR spectrometers (Bruker, Billerica, MA, US). The HR-ESI-MS were taken on a Bruker Daltonics micrOTOF orthogonal ESI-TOF mass spectrometer (Bruker, Billerica, MA, US). Silica gel was purchased from Merck (70–230 mesh, Darmstadt, Germany). Thin-layer chromatography (TLC) was conducted on Merck precoated silica gel 60 F254 plates (Darmstadt, Germany) and monitoring by

UV light to visualize the spots. GR grade organic solvent: Methanol, chloroform, *n*-butanol, *n*-hexane, ethyl acetate, and acetone (ACS grade) were purchased from Mallinckrodt (St. Louis, MO, USA). CD<sub>3</sub>OD was purchased from Sigma-Aldrich (St. Louis, MO, USA). A double-beam and six-cell positioner spectrophotometer (Hitachi U-3010, Tokyo, Japan) was used to measure superoxide anion generation and elastase release activities.

### 3.2. Plant material

The tubers of *T. dentata* were purchased from the herb store at Pingtung, Taiwan and verified by Prof. Chang-Sheng Kuoh (Department of Biology, National Cheng Kung University, Tainan, Taiwan). A voucher specimen (TSWu 20121016) has been deposited in the Herbarium of School of Pharmacy, National Cheng Kung University, Tainan, Taiwan.

### 3.3 Extraction and isolation

The dried tubers of *T. dentata* (10 kg) were powdered and refluxed with methanol (7 L x 10) to obtain the methanol extract (1.9 kg). Portion of this extract (1 kg) was suspended in distilled water and partitioned with ethyl acetate to yield ethyl acetate (EA)-soluble layer (400 g) and water-soluble layer (600 g). Water-soluble layer was subsequently partition with *n*-butanol (*n*-BuOH) to yield *n*-BuOH layer (200 g). 15 g of *n*-BuOH layer was fractionated on a silica gel column (500 g) with gradient mixtures from 0–5% methanol in chloroform to produce four alkaloids, included bispalmatrubine hydroxide (**1**, 6 mg), palmatine hydroxide (**2**, 875 mg), jatrorrhizine hydroxide (**3**, 97 mg) and columbamine hydroxide (**4**, 214 mg).

A part of EA-soluble layer (100 g) was further partition with 5% HCl aqueous solution (1 L) and divided into EA fraction (60 g, non-alkaloids) and acidic water fraction (40 g, alkaloids). When the EA fraction was concentrated under reduced pressure, a large amount of columbin (**8**, 3.5 g) was recrystallized. EA fraction was further chromatographed directly on silica gel (200 g) and eluted with a gradient of chloroform and methanol to afford columbin (**8**, 1.1 g), isocolumbin (**9**, 2.2 g), a mixture of stigmasterol (**10**) and  $\beta$ -sitosterol (**11**) (40 mg), a mixture of stigmasteryl glycoside (**12**) and  $\beta$ -sitosteryl glycoside (**13**) (25 mg), and benzoin (**14**) (33 mg).

The acidic water fraction was neutralized by ammonia to base and partition with chloroform to yield chloroform layer and basic water layer. The chloroform layer (2 g) was fractionated by silica gel (50 g) column chromatography eluted with gradient mixtures from 0–8% acetone in chloroform and then yielded homomoschatoline (**5**, 120 mg), lysicamine (**6**, 55 mg) and dicentrinone (**7**, 12 mg).

#### 3.3.1. Bispalmatrubine (1)

Yellowish powder; UV (MeOH)  $\lambda_{\max}$  (log  $\epsilon$ ) 205 (4.18), 263 (4.09), 354 (4.03), 404 (3.81) nm; IR (neat)  $\nu_{\max}$  3400, 1635, 1565, 1500, 1460 cm<sup>-1</sup>; <sup>1</sup>H NMR (700 MHz, CD<sub>3</sub>OD)  $\delta$  9.71 (2H, s, H-8 & -8'), 8.88 (2H, s, H-13 & -13'), 8.13 (2H, d, *J* = 9.1 Hz, H-12 & -12'), 8.05 (2H, d, *J* = 9.1 Hz, H-11 & -11'), 7.80 (2H, s, H-1 & -1'), 4.90 (4H, m, H-6 & -6'), 4.20 (6H,

s, OCH<sub>3</sub>-3 & -3'), 4.12 (12H, s, OCH<sub>3</sub>-2, -2', -10, & -10'), 3.00 (2H, m, H-5a & -5'a), 2.86 (2H, m, H-5b & -5'b); <sup>13</sup>C NMR (175 MHz, CD<sub>3</sub>OD) δ 151.9 (C-10 & 10'), 149.5 (C-2 & 2'), 145.9 (C-8 & 8'), 146.0 (C-9 & 9') 145.6 (C-3 & 3'), 140.3 (C-14 & 14'), 135.4 (C-8a & 8a'), 129.9 (C-14a & 14a'), 128.1 (C-12 & 12'), 124.5 (C-11 & 11'), 123.2 (C-12a & 12a'), 122.2 (C-2 & 2'), 121.4 (C-13 & 13'), 119.7 (C-4a & 4a'), 109.5 (C-1 & 1'), 62.5 (OCH<sub>3</sub>-3 & 3'), 57.7 (OCH<sub>3</sub>-10 & 10'), 57.2 (C-6 & 6'), 57.1 (OCH<sub>3</sub>-2 & 2'), 25.6 (C-5 & 5'); ESI-MS *m/z* 359, 353, 337 (100), 191, 169; HR-ESI-MS *m/z* 337.1338 ([M]<sup>2+</sup>, calcd for [C<sub>40</sub>H<sub>38</sub>N<sub>2</sub>O<sub>8</sub>]<sup>2+</sup> 337.1309).

### 3.4. Anti-inflammatory bioactivity examination

The details of the preparation of human neutrophils, measurement of superoxide anion generation and elastase release are provided in the [Supplementary Material](#).

## 4. Conclusion

The traditional use of *T. dentata* is for relieving heat and from the human body, which may be contributed by the anti-inflammatory activities. Some major components isolated in this study had showed moderated inhibitory activity on the superoxide anion generation and elastase release. These components may be one of the reasons to contribute the action for relieving heat of *T. dentata*. Additionally, the discovery of bispal-matrubine (**1**) in Menispermaceae, was valuable as a traditional morphological marker for chemotaxonomic research in the future.

## Disclosure statement

No potential conflict of interest was reported by the authors.

## Funding

This work was supported by the Ministry of Science and Technology (MOST), Taiwan; the authors are also thankful for partial financial support from Chang Gung Memorial Hospital (CMRPD1B0281~3, CMRPF1D0442~3, CMRPF 1F0011~3, CMRPF1F0061~3 and BMRP450 granted to H.-L.H).

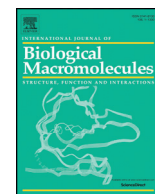
## References

- Carvalhas ML. 1972. Bisjatrorrhizine, a new dimeric protoberberine alkaloid from *Jatrorrhiza pal-mata* (Lam.) Miers. J. J Chem Soc, Perkin Trans 1:3:327–330.
- Chakraborty B, Nath A, Saikia H, Sengupta M. 2014. Bactericidal activity of selected medicinal plants against multidrug resistant bacterial strains from clinical isolates. Asian Pac J Trop Med. 7:S435–S441.
- Chen IS. 1975. The constituents of *Tinospora dentata* Diels. J Chin Chem Soc. 22(3):271–274.
- Chen KS, Wu YC, Teng CM, Ko FN, Wu TS. 1997. Bioactive alkaloids from *Illigera luzonensis*. J Nat Prod. 60(6):645–647.
- Chen YP, Hsü HY, Ruo TI, Iguchi K, Kakisawa H. 1973. Isolation of columbin from *Melothria maderospatana*. Phytochemistry. 12(12):3000.



- Choudhary MI, Ismail M, Shaari K, Abbaskhan A, Sattar SA, Lajis NH. 2010. *cis*-Clerodane-type furanoditerpenoids from *Tinospora crispa*. J Nat Prod. 73(4):541–547.
- Dong LP, Chen CX, Ni W, Xie BB, Li JZ, Liu HY. 2010. A new dinorclerone diterpenoid glycoside from *Tinospora sinensis*. Nat Prod Res. 24(1):13–17.
- Duan W, Kuo IC, Selvarajan S, Chua KY, Bay BH, Fred Wong WS. 2003. Antiinflammatory effects of genistein, a tyrosine kinase inhibitor, on a guinea pig model of asthma. Am J Respir Crit Care Med. 167(2):185–192.
- Editorial Committee of the Flora of Taiwan 1996. Flora of Taiwan, 2nd ed. Taipei, Taiwan, Vol. 2; p. 605.
- Khatun M, Billah M, Quader MA. 2012. Sterols and sterol glucoside from *Phyllanthus* species. Dhaka Univ J Sci. 60(1):5–10.
- Krishna KL, Jigar B, Jagruti P. 2009. Guduchi (*Tinospora cordifolia*): biological and medicinal properties: a review. Internet J. Alternative Med. 6:1–12.
- Kuo YH, Li YC. 1997. Constituents of the bark of *Ficus microcarpa* L. f. J Chin Chem Soc. 44(3): 321–325.
- Lam SH, Ruan CT, Hsieh PH, Su MJ, Lee SS. 2012. Hypoglycemic diterpenoids from *Tinospora crispa*. J Nat Prod. 75(2):153–159.
- Lam SH, Chen PH, Hung HY, Hwang TL, Chiang CC, Thang TD, Kuo PC, Wu TS. 2018. Chemical constituents from the stems of *Tinospora sinensis* and their bioactivity. Molecules. 23(10):2541.
- Leu YL, Hwang TL, Kuo PC, Liou KP, Huang BS, Chen GF. 2012. Constituents from *Vigna vexillata* and their anti-inflammatory activity. Int J Mol Sci. 13(8):9754–9768.
- Li W, Koike K, Liu L, Lin L, Fu X, Chen Y, Nikaido T. 2004. New lignan glucosides from the stems of *Tinospora sinensis*. Chem Pharm Bull. 52(5):638–640.
- Liu X, Hu Z, Shi Q, Zeng H, Shen Y, Jin H, Zhang W. 2010. Anti-inflammatory and anti-nociceptive activities of compounds from *Tinospora sagittata* (Oliv.) Gagnep. Arch Pharm Res. 33(7): 981–987.
- Mishra A, Kumar S, Bhargava A, Sharma B, Pandey AK. 2011. Studies on in vitro antioxidant and antistaphylococcal activities of some important medicinal plants. Cell Mol Biol (Noisy-le-Grand). 57(1):16–25.
- More P, Pai K. 2011. Immunomodulatory effects of *Tinospora cordifolia* (Guduchi) on macrophage activation. Biol Med. 3:134–140.
- Ng KW, Salhimi SM, Majid AM, Chan KL. 2010. Anti-angiogenic and cytotoxicity studies of some medicinal plants. Planta Med. 76(9):935–940.
- Overton KH, Weir NG, Wylie A. 1966. The stereochemistry of the Colombo root bitter principles. J Chem Soc C:1482–1490.
- Pouchert CJ, Campbell JR. 1974. The Aldrich library of NMR spectra. Millwaukee, Wisconsin: Aldrich Chemical. Co. Vol. IV.
- Ruan CT, Lam SH, Lee SS, Su MJ. 2013. Hypoglycemic action of borapetoside A from the plant *Tinospora crispa* in mice. Phytomedicine. 20(8–9):667–675.
- Scott AI. 1964. Interpretation of the ultraviolet spectra of natural compounds. Oxford: Pergamon p. 95.
- Sengupta M, Sharma GD, Chakraborty B. 2011. Effect of aqueous extract of *Tinospora cordifolia* on functions of peritoneal macrophages isolated from CCl<sub>4</sub> intoxicated male albino mice. BMC Complement Altern Med. 11:102
- Shamma M. 1972. The isoquinoline alkaloids. New York: Academic Press.
- Skiles JW, Saa JM, Cava MP. 1979. Splendidine, a new oxoaporphine alkaloid from *Abuta rufescens* Aublet. Can J Chem. 57(13):1642–1646.
- Thuy TT, Franke K, Porzel A, Wessjohann L, Sung TV. 2006. Quaternary protoberberine alkaloids from *Stephania rotunda*. J Chem. 44:259–264.
- Upadhyay AK, Kumar K, Kumar A, Mishra HS. 2010. *Tinospora cordifolia* (Willd.) Hook. f. and Thoms. (*Guduchi*) – validation of the Ayurvedic pharmacology through experimental and clinical studies. Int J Ayurveda Res. 1(2):112–121.
- Yang SC, Chung PJ, Ho CM, Kuo CY, Hung MF, Huang YT, Chang WY, Chang YW, Chan KH, Hwang TL. 2013. Propofol inhibits superoxide production, elastase release, and chemotaxis in

- formyl peptide-activated human neutrophils by blocking formyl peptide receptor 1. *J Immunol.* 190(12):6511–6519.
- Yu HP, Hsieh PW, Chang YJ, Chung PJ, Kuo LM, Hwang TL. 2011. 2-(2-Fluorobenzamido)benzoate ethyl ester (EFB-1) inhibits superoxide production by human neutrophils and attenuates hemorrhagic shock-induced organ dysfunction in rats. *Free Radic Biol Med.* 50(12):1737–1748.
- Zhou D, Wei H, Jiang Z, Li X, Jiao K, Jia X, Hou Y, Li N. 2017. Natural potential neuroinflammatory inhibitors from *Alhagi sparsifolia* Shap. *Bioorg Med Chem Lett.* 27(4):973–978.



# Enzymatic degradation of ginkgolic acids by laccase immobilized on core/shell Fe<sub>3</sub>O<sub>4</sub>/nylon composite nanoparticles using novel coaxial electrospaying process

Hung-Yueh Chen<sup>a,1</sup>, Yuwen Ting<sup>a,1</sup>, Hsing-Chun Kuo<sup>b,c,d,e</sup>, Chang-Wei Hsieh<sup>f</sup>, Hsien-Yi Hsu<sup>g,h</sup>, Chun-Nan Wu<sup>a,\*</sup>, Kuan-Chen Cheng<sup>a,i,j,k,\*</sup>

<sup>a</sup> Graduate Institute of Food Science and Technology, National Taiwan University, Taipei 10617, Taiwan

<sup>b</sup> Chang Gung Memorial Hospital, Chiayi 613, Taiwan

<sup>c</sup> Research Center for Industry of Human Ecology, Chang Gung University of Science and Technology, Taoyuan 33305, Taiwan

<sup>d</sup> Department of Nursing, Division of Basic Medical Sciences, Chang Gung University of Science and Technology, Chiayi 61363, Taiwan

<sup>e</sup> Chronic Diseases and Health Promotion Research Center, Chang Gung University of Science and Technology, Chiayi 61363, Taiwan

<sup>f</sup> Department of Food Science and Biotechnology, National Chung Hsing University, Taichung 145, Taiwan

<sup>g</sup> School of Energy and Environment & Department of Materials Science and Engineering, City University of Hong Kong, Kowloon Tong, Hong Kong, China

<sup>h</sup> Shenzhen Research Institute of City University of Hong Kong, Shenzhen 518057, China

<sup>i</sup> Institute of Biotechnology, National Taiwan University, Taipei 10617, Taiwan

<sup>j</sup> Department of Medical Research, China Medical University Hospital, China Medical University, Taichung 404332, Taiwan

<sup>k</sup> Department of Optometry, Asia University, Taichung 41354, Taiwan

## ARTICLE INFO

### Article history:

Received 17 November 2020

Received in revised form 29 December 2020

Accepted 1 January 2021

Available online 5 January 2021

### Keywords:

Enzyme immobilization

Coaxial electrospaying

Laccase

Ginkgolic acid

Iron oxide

Nylon

## ABSTRACT

Enzyme immobilization can increase enzyme reusability to reduce cost of industrial production. *Ginkgo biloba* leaf extract is commonly used for medical purposes, but it contains ginkgolic acid, which has negative effects on human health. Here, we report a novel approach to solve the problem by degrading the ginkgolic acid with immobilized-laccase, where core/shell composite nanoparticles prepared by coaxial electrospaying might be first applied to enzyme immobilization. The core/shell Fe<sub>3</sub>O<sub>4</sub>/nylon 6,6 composite nanoparticles (FNCNs) were prepared using one-step coaxial electrospaying and can be simply recovered by magnetic force. The glutaraldehyde-treated FNCNs (FNGCNs) were used to immobilize laccase. As a result, thermal stability of the free laccase was significantly improved in the range of 60–90 °C after immobilization. The laccase-immobilized FNGCNs (L-FNGCNs) were applied to degrade the ginkgolic acids, and the rate constants (*k*) and times (*τ*<sub>50</sub>) were ~0.02 min<sup>-1</sup> and lower than 39 min, respectively, showing good catalytic performance. Furthermore, the L-FNGCNs exhibited a relative activity higher than 0.5 after being stored for 21 days or reused for 5 cycles, showing good storage stability and reusability. Therefore, the FNGCNs carrier was a promising enzyme immobilization system and its further development and applications were of interest.

© 2021 Elsevier B.V. All rights reserved.

## 1. Introduction

Enzyme immobilization, which is a technique to separate enzyme from reaction medium, can simplify enzyme recovery and increase enzyme reusability to reduce cost of industrial production [1–4]. It has been widely used in food and pharmaceutical industries for various applications, such as isoflavone aglycone enrichment [5,6], mogrosides deglycosylation [7], lactose-free milk production [8], and detoxification [9,10]. Laccase (*p*-diphenol: oxygen oxidoreductase; EC 1.10.3.2), a

polyphenol oxidase with a molecular weight of 50–90 kDa, is widely distributed in fungi, plants, bacteria, and insects [11]. It is a general-purpose enzyme commonly used for various applications, such as clarifying beverage in food industry [12], and bleaching pulp to reduce use of toxic chemicals in pulp and paper industry [13]. Hence, immobilization of laccase attracts attention and it has been widely studied [12,14–16].

*Ginkgo biloba* (*G. biloba*) leaf extract has been used for medical purposes due to the presence of various bioactive compounds. However, it contains ginkgolic acid, which is considered to be a toxic, allergenic, and mutagenic substance to human health, limiting its practical applications in industry [17]. In the previous study, we first successfully degraded ginkgolic acid from the *G. biloba* leaf extract using a laccase-immobilized electrospun nylon nanofiber mat [18]. The enzymatic

\* Corresponding authors at: 1, Sec 4, Roosevelt Rd., Taipei 10617, Taiwan.

E-mail addresses: [wulalaworld@gmail.com](mailto:wulalaworld@gmail.com) (C.-N. Wu), [kccheng@ntu.edu.tw](mailto:kccheng@ntu.edu.tw)

(K.-C. Cheng).

<sup>1</sup> These authors contributed equally to the work.

degradation method was simple to use, avoided remaining toxic solvent residues, and reduced the cost of water management. Therefore, based on the significant effect, it is of interest to achieve enzymatic degradation of ginkgolic acid by other novel laccase-immobilized carriers, such as magnetic nanomaterials.

It has been widely studied that efficiency of catalytic reaction can be improved by using nanoparticles with large surface area [19–25]. In addition, during immobilization, the amount of immobilized enzyme, enzyme activity, thermal stability, and pH stability are influenced by surface area of the used immobilization carrier. Therefore, to maintain enzyme performance, magnetic nanomaterials, such as iron oxide ( $\text{Fe}_3\text{O}_4$ ) nanoparticles, are potential candidates for effective enzyme immobilization because they have large surface area and can be simply recovered by magnetic force [26–34]. However, sensitivity to pH and oxidation can cause  $\text{Fe}_3\text{O}_4$  to aggregate easily during reaction, resulting in lower dispersibility of  $\text{Fe}_3\text{O}_4$  nanoparticles. When magnetic particles are used as carriers for enzyme immobilization, surface coating is a useful way to reduce attractive forces between the particles, preventing aggregation of the particles [35,36]. In addition,  $\text{Fe}_3\text{O}_4$  nanoparticles have less functional groups on their surfaces to combine enzymes, and thus practical application of  $\text{Fe}_3\text{O}_4$  nanoparticles was limited. To improve these disadvantages, formation of core/shell  $\text{Fe}_3\text{O}_4$ /polymer composite nanoparticles is effective. Several related studies have been reported that the neat or surface-modified  $\text{Fe}_3\text{O}_4$  nanoparticles were coated with chitosan [16,37], cellulose [35], polyacrylic acid [26], polyamidoamine [38], and other polymers.

Coaxial electrospraying is a simple method with desirable engineered properties for production of core/shell composite nanoparticles [39]. Compared with other chemical methods of nanoparticle fabrication, such as spray drying and emulsification, coaxial electrospraying is a more convenient one-step method to fabricate nanoparticles in dried form; furthermore, size and shape of the obtained nanoparticles can be designed by adjusting the experimental conditions [40]. It was reported that the core/shell composite nanoparticles fabricated by coaxial electrospraying can be applied to delivery systems of bioactive compounds in food (such as zein/chitosan [41] and chitosan/alginate [42]) and pharmaceutical (such as ethylcellulose/stearic acid [43] and chitosan/polyvinylpyrrolidone [44]) industries. However, the related studies focused on application of enzyme immobilization are few to date. According to the advantages described above, core/shell composite nanoparticles fabricated by coaxial electrospraying are promising as carriers for enzyme immobilization.

In the present study, coaxial electrospraying was applied to prepare core/shell  $\text{Fe}_3\text{O}_4$ /nylon 6,6 composite nanoparticles. The composite nanoparticles were used to immobilize laccase and then achieve oxidative degradation of ginkgolic acids. The instruments, concepts, procedures, and abbreviations are clearly organized and illustrated in Fig. 1. The  $\text{Fe}_3\text{O}_4$  and nylon 6,6 were used as cores and shells of the composite nanoparticles, respectively, while glutaraldehyde was used as a crosslinker to combine the nylon shells and laccase. Nylon 6,6 is an inexpensive polyamide with high mechanical strength and high thermal stability [45], which is widely used in various industries. Due to these superior properties, nylon 6,6 has been studied for application in enzyme immobilization [15,46], and thus it was used as the shell material in the present study. All the components of the laccase-immobilized composite nanoparticles, including  $\text{Fe}_3\text{O}_4$  [47], nylon 6,6 [48,49], glutaraldehyde [50], and laccase [51] were reported to be biocompatible. Response surface methodology (RSM) is a combination of experimental design and statistical analysis, and has been applied to optimize production processes [42,52,53]. Here, RSM was used to achieve small size of the composite nanoparticles by adjusting experimental conditions, including concentration and flow rate of the nylon solution as well as voltage. Furthermore, with the exception of stability and reusability, size distribution, morphology observation, structure characterization, and degradation performance of the composite nanoparticles before and/or after laccase immobilization were also investigated.

To our best knowledge, this is the first study to prepare core/shell composite nanoparticles with magnetic sensitivity for enzyme immobilization using coaxial electrospraying technique. The one-step technique was convenient and can directly fabricate dry nanoparticles, showing advantages over the conventional methods. The laccase-immobilized composite nanoparticles were expected to be simply recovered by magnetic force as well as exhibit high immobilization and degradation efficiencies. In addition, thermal and storage stability as well as reusability of the laccase were expected to be improved through immobilization on the composite nanoparticles.

## 2. Experimental section

### 2.1. Materials

Iron oxide ( $\text{Fe}_3\text{O}_4$ , particle size 50–100 nm), glutaraldehyde, 2,2'-Azino-bis(3-ethylbenzothiazoline-6-sulfonic acid) diammonium salt (ABTS), and laccase (*p*-diphenol: oxygen oxidoreductase; EC 1.10.3.2) from *Trametes versicolor* were purchased from Sigma-Aldrich (St. Louis, MO, USA). Nylon 6,6 pellets were provided by Keen Crop Company (Tainan, Taiwan). Polyethylene glycol (PEG) 8000 was purchased from Alfa Aesar, Thermo Fisher Scientific (Haverhill, MA, USA). *G. biloba* leaves were purchased from Shun-Yi Chemical (Taichung, Taiwan). Double-distilled water was used.

### 2.2. Optimization of conditions for electrospraying nylon shells

During preparation of the core/shell  $\text{Fe}_3\text{O}_4$ /nylon composite nanoparticles (FNCNs),  $\text{Fe}_3\text{O}_4$  and nylon solutions were simultaneously sprayed from the inner and outer needles, respectively (see Fig. 1). Then, the nylon shells immediately covered the  $\text{Fe}_3\text{O}_4$  cores to form the FNCNs. To minimize sizes of the FNCNs, the optimal conditions for forming the thinnest nylon shells were obtained by electrospraying only the nylon solution with the outer needle to form neat nylon nanoparticles, in the absence of the  $\text{Fe}_3\text{O}_4$  cores (see the dashed frame in Fig. 1b). The smaller neat nylon nanoparticles indicated that the thinner nylon shells and the smaller FNCNs can be obtained under the same conditions when the  $\text{Fe}_3\text{O}_4$  and nylon solutions were simultaneously sprayed. This concept was similar to making Daifuku, a Japanese sweet consisting of mochi (a rice cake, as shell) and red bean paste (as core). When a smaller mochi is stuffed a red bean paste, a smaller Daifuku with a thinner mochi shell is obtained. Hence, before preparing the FNCNs, the optimal conditions for forming the smallest neat nylon nanoparticles using electrospraying were determined by using Box–Behnken design of response surface methodology (RSM) in advance [18].

The effects of concentration of the nylon solution (%  $X_1$ ), applied voltage (kV  $X_2$ ), and flow rate of the nylon solution ( $\text{mL h}^{-1}$   $X_3$ ) on sizes of the neat nylon nanoparticles were investigated. Ranges of the three variables,  $X_1$ ,  $X_2$ , and  $X_3$ , were determined according to the pre-experimental results and shown in Table 1.  $X_1$ ,  $X_2$ , and  $X_3$  were ranged in 1.5–2.5% (2%), 24–26 kV (25 kV), and 2–3  $\text{mL h}^{-1}$  (2.5  $\text{mL h}^{-1}$ ), respectively, where the values in the brackets were the corresponding center points. A three-dimensional RSM model was designed after 20 experiments, and 6 replicates of the center points were employed. According to the experimental results, regression analysis and surface plotting were performed to establish optimum conditions for minimizing sizes of the neat nylon nanoparticles using the Minitab software (version 16, Minitab Inc., State College, PA, USA). A quadratic equation used to design the three-dimensional RSM model is shown as follows:

$$Y = \beta_0 + \sum_{i=1}^3 \beta_i X_i + \sum_{i=1}^3 \beta_{ii} X_i^2 + \sum_{i=1}^3 \sum_{j=1}^3 \beta_{ij} X_i X_j, \quad (1)$$

where  $Y$ ,  $\beta_0$ ,  $\beta_i$ ,  $\beta_{ii}$ , and  $\beta_{ij}$  were the response variable, model constant, linear coefficient, quadratic coefficient, and interaction coefficient, respectively;  $X_i$  and  $X_j$  were the independent variables.

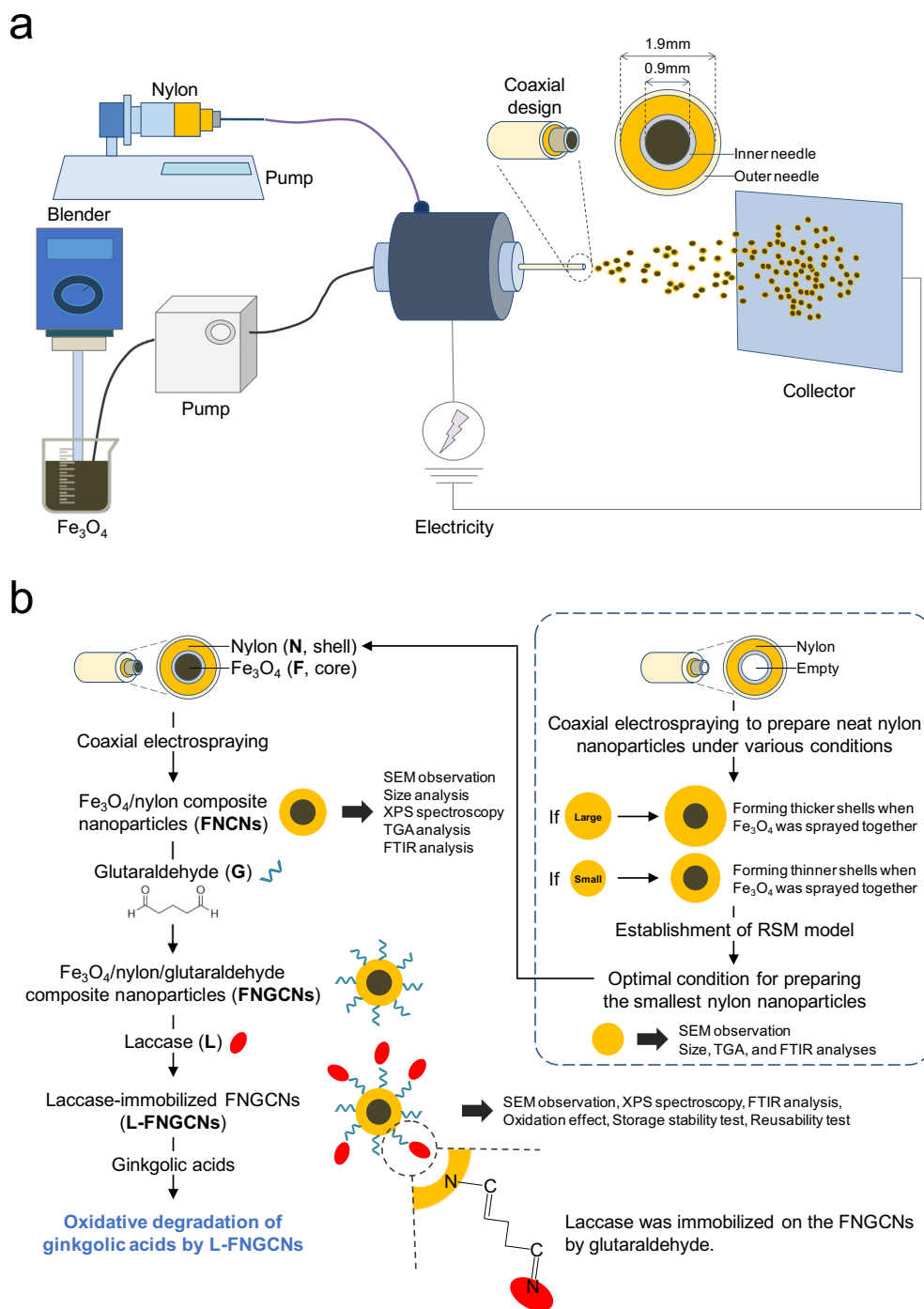


**Fig. 1.** (a) An illustration of the coaxial electrospinning system used to prepare Fe<sub>3</sub>O<sub>4</sub>/nylon composite nanoparticles (FNCNs) with unique core/shell structure. (b) A scheme introducing experimental procedures and abbreviations of the samples in each step. The dashed frame describes optimization of conditions for electrospinning nylon shells. The possible linkage relationship is shown according to the results in Section 3.3.

### 2.3. Preparation of the FNCNs using coaxial electrospinning

Preparation and activation of the nylon pellets were reported in the previous study [5]. In brief, the nylon pellets (40 cm<sup>3</sup>) were submerged in a dimethyl sulfate (DMS) solution (30 mL) at 100 °C for 4 min. After that, the pellets were immediately washed with cold methanol (MeOH) and then immersed in a 10% hexamethylenediamine (HMDA) solution (30 mL) at room temperature for 90 min. The FNCNs were prepared by coaxial electrospinning. As shown in Fig. 1a, the used spray head consisted of two coaxially arranged needles and was connected to a

high voltage supply (15–25 kV). The inner needle was slightly longer than the outer needle and diameters of the former and latter were 0.9 and 1.9 mm, respectively. The distance between the spray head and the baking sheet that served as the collector was 20 cm in all the experiments. According to the optimal conditions of the nylon shells obtained from Section 2.2, a 15.3 g L<sup>-1</sup> nylon solution was used as the shell fluid. The nylon solution was prepared by adding the activated nylon pellets to a formic acid/acetic acid (1:1) solution and stirred at room temperature for 12 h. A 25 g L<sup>-1</sup> Fe<sub>3</sub>O<sub>4</sub>/methanol solution containing 25 g L<sup>-1</sup> polyethylene glycol (PEG) was used as



**Table 1**

The experimental results of Box–Behnken design. The values were used to investigate optimal conditions for forming the smallest neat nylon nanoparticles with the outer needle of the coaxial electrospraying system.

| Run | $X_1$<br>(concentration, %) | $X_2$<br>(voltage, kV) | $X_3$<br>(flow rate, mL h <sup>-1</sup> ) | Average<br>diameter (nm) |
|-----|-----------------------------|------------------------|---|--------------------------|
| 1   | 2                           | 25                     | 2.5                                       | 250.90                   |
| 2   | 2                           | 25                     | 2.5                                       | 162.30                   |
| 3   | 2                           | 26.68                  | 2.5                                       | 149.37                   |
| 4   | 2                           | 25                     | 2.5                                       | 133.40                   |
| 5   | 1.5                         | 24                     | 3   | 126.00                   |
| 6   | 1.5                         | 26                     | 2   | 156.10                   |
| 7   | 2.5                         | 24                     | 3   | 233.60                   |
| 8   | 2                           | 25                     | 3.34                                      | 132.10                   |
| 9   | 1.16                        | 25                     | 2.5                                       | 123.50                   |
| 10  | 2                           | 23.32                  | 2.5                                       | 192.30                   |
| 11  | 2                           | 25                     | 2.5                                       | 134.40                   |
| 12  | 1.5                         | 26                     | 3   | 296.45                   |
| 13  | 2                           | 25                     | 2.5                                       | 158.10                   |
| 14  | 2.5                         | 26                     | 2   | 197.55                   |
| 15  | 1.5                         | 24                     | 2   | 404.05                   |
| 16  | 2                           | 25                     | 1.66                                      | 206.97                   |
| 17  | 2.84                        | 25                     | 2.5                                       | 224.80                   |
| 18  | 2.5                         | 26                     | 3   | 199.20                   |
| 19  | 2.5                         | 24                     | 2   | 191.10                   |
| 20  | 2                           | 25                     | 2.5                                       | 134.40                   |

the core fluid. The shell and core fluids were fed through independent syringe pumps with different flow rates. Sizes of the neat nylon nanoparticles and FNCNs prepared by coaxial electrospraying were measured using a dynamic light scattering (DLS) particle size analyzer (90Plus/BI-MAS, Brookhaven, NY, USA). The measurements were carried out at an incident angle of 90°, a wavelength of 660 nm, and room temperature.

#### 2.4. Laccase immobilization

In the present study, glutaraldehyde was used as a crosslinker to combine the FNCNs and laccase, resulting in laccase immobilization [54]. The FNCNs were treated with a 2.5% glutaraldehyde solution at room temperature for 1 h to form Fe<sub>3</sub>O<sub>4</sub>/nylon/glutaraldehyde composite nanoparticles (FNGCNs). Then, the FNGCNs were washed with water and incubated in a 1 mg mL<sup>-1</sup> laccase solution at 4 °C for 24 h, where the solvent was pH 5.0 citric acid/Na<sub>2</sub>HPO<sub>4</sub> buffer solution. The laccase-immobilized FNGCNs (L-FNGCNs) were washed with the same buffer solution to remove unlinked laccase and then stored at 4 °C. The amount of the laccase on the L-FNGCNs was determined by concentration difference of the laccase solution before and after the immobilization, according to Bradford dye-binding procedure [55]. Before measuring relative activity of the immobilized laccase in the further experiments, an examination was performed in advance. The L-FNGCNs were taken out from the buffer solution and reacted with a 0.5 mM ABTS/citric acid/Na<sub>2</sub>HPO<sub>4</sub> buffer solution (for detail, see Section 2.7) in order to confirm that the laccase was stably immobilized on the nanoparticle surfaces and can exhibit catalytic activity. After that, the ABTS on the L-FNGCNs was removed by centrifugation three times, and then the L-FNGCNs were recovered and directly used to measure relative activity of the immobilized laccase.

#### 2.5. Morphology observation

Scanning electron microscopy (SEM) images of the nanoparticles were observed using an ultra-high resolution scanning electron microscope (SU8200, Hitachi, Tokyo, Japan) at an accelerating voltage of 2.0 kV. The samples were coated with gold using an ion coater (IB-2, Hitachi, Tokyo, Japan) in advance.

#### 2.6. Structure characterization

Covalent bonding between the FNGCNs and laccase was investigated using an X-ray photoelectron spectra (XPS) spectrometer (Theta Probe, Thermo Scientific, UK) with monochromated Al K $\alpha$  radiation at 20.0 eV pass energy. Thermogravimetric analysis (TGA) of the nanoparticles was carried out using a thermogravimetric analyzer (TGA Q50, TA Instruments, New Castle, DE, USA) at 10 °C min<sup>-1</sup> from room temperature to 700 °C in a nitrogen atmosphere. Fourier transform infrared (FTIR) spectrum was measured using a FTIR spectrometer (Spectrum Two, PerkinElmer, Shelton, USA) in absorption mode from 400 to 4000 cm<sup>-1</sup> in wavenumber with a resolution of 4 cm<sup>-1</sup>. The nanoparticle sample (1 mg) was mixed with KBr (100 mg) to prepare a dish and used for measuring a spectrum.

#### 2.7. Determination of optimal reaction conditions for the L-FNGCNs

The method was modified according to Amin et al. [14]. To determine optimal pH value and temperature, relative activities of the free and immobilized laccases were evaluated with a 0.5 mM ABTS/citric acid/Na<sub>2</sub>HPO<sub>4</sub> buffer solution as a substrate. The tested pH values and temperatures were 3, 4, 5, 6, 7, and 8, as well as 30, 40, 50, 60, 70, 80, and 90 °C, respectively. The relative activity was determined by measuring ABTS oxidation at 420 nm with an extinction coefficient of 36,000 mM<sup>-1</sup> cm<sup>-1</sup> using a Multiskan GO microplate spectrophotometer (Thermo Fisher Scientific, Waltham, USA). Before each experiment, catalytic activity of the immobilized laccase was confirmed in advance according to Section 2.4.

#### 2.8. Extraction of ginkgolic acids

The extraction process was modified according to the method reported by Pereira et al. [56]. *G. biloba* leaves (20 g) were extracted by methanol (200 mL) under stirring for 24 h. Then, the mixture was centrifuged at 3000×g for 10 min, and the supernatant was carefully collected and dried under reduced pressure using a rotary evaporator (N-1200A, Eyela, Tokyo, Japan). The dried powder containing ginkgolic acids was dissolved in a citric acid/Na<sub>2</sub>HPO<sub>4</sub> buffer solution (pH 4) and stored at 4 °C.

#### 2.9. HPLC analysis

The analytic process was modified according to Pereira et al. [56]. Resolution of the ginkgolic acid was performed using a high-performance liquid chromatography (HPLC) system containing two LDC pumps (ConstaMetric 3200 and ConstaMetric 3500), a YMC-Pack ODS-AMC C18 column (5  $\mu$ m, 250 × 4.6 mm), and an analytical mixer. The obtained data was analyzed using a SISC chromatography data system (SISC, New Taipei City, Taiwan). Detection was performed by UV absorption at 210 nm. The injection volume and elution rate were 20  $\mu$ L and 1.0 mL min<sup>-1</sup>, respectively. Formic acid aqueous solution (solvent A, 0.1%) and formic acid/acetonitrile solution (solvent B, 0.1%) were used as the eluent.

#### 2.10. Storage stability and reusability

The method was modified according to Ulu et al. [37]. Storage stability and reusability of the L-FNGCNs were determined by measuring relative activities of the immobilized laccase on ABTS using the method and optimal conditions from Section 2.7. After each reaction was carried out, the L-FNGCNs were washed with the citric acid/Na<sub>2</sub>HPO<sub>4</sub> buffer solution to remove the ABTS on the nanoparticle surfaces. For storage stability test, the L-FNGCNs were stored at 4 °C and the reaction was carried out after 0, 2, 4, 6, 10, 14, 21, and 28 days of storage. For reusability test, the reaction was repeated 10 times within 1 day. Before the first

reaction of each test, catalytic activity of the immobilized laccase was confirmed in advance according to Section 2.4.

### 2.11. Statistical analysis

All the experiments were performed at least in triplicate and the obtained data were expressed as mean  $\pm$  stand deviation. Statistical analysis was performed by analysis of variance (ANOVA). The *P*-value was set at 0.05.

## 3. Results and discussion

### 3.1. Optimization of conditions for electrospaying nylon shells

During preparation of the FNCNs using coaxial electrospaying, the thinnest nylon shells were formed on the  $\text{Fe}_3\text{O}_4$  cores under the optimal conditions obtained from Section 2.2, resulting in the smallest FNCNs. After the nylon shells reacted with glutaraldehyde as a crosslinker, the obtained  $\text{Fe}_3\text{O}_4$ /nylon/glutaraldehyde composite nanoparticles (FNGCNs) had the largest specific surface area for enzyme immobilization. Therefore, immobilization efficiency and catalytic activity of laccase could be improved through the coaxial electrospaying system developed in the present study.

Response surface methodology (RSM) was used to determine the optimal conditions for forming the smallest neat nylon nanoparticles in absence of the  $\text{Fe}_3\text{O}_4$  cores by the established electrospaying system. Three important parameters, including concentration of the nylon solution, applied voltage, and flow rate of the nylon solution, were optimized by RSM according to the studies related to nanoparticle production [57]. Experimental design and obtained sizes of the neat nylon nanoparticles were shown in Table 1. These 20 results and Eq. (1) were used to generate a quadratic regression equation (Eq. (2)) of the three-dimensional RSM model as following:

$$Y = 17075.6 - 783.394X_1 - 989.351X_2 - 2850.72X_3 + 61.936X_1^2 + 14.312X_2^2 + 55.4094X_3^2 + 12.3875X_1X_2 + 90.925X_1X_3 + 94.3875X_2X_3 \quad (2)$$

where *Y* was size of the neat nylon nanoparticle (nm), as well as  $X_1$ ,  $X_2$ , and  $X_3$  were concentration (%), voltage (kV), and flow rate ( $\text{mL h}^{-1}$ ), respectively. Relationships of size of the neat nylon nanoparticles between the three parameters were expressed in the forms of surface and contour plots (Fig. 2a–f). As shown in Table 2, lack of fit was not significant ( $P = 0.067 > 0.05$ ), showing accuracy of the RMS model to size of the neat nylon nanoparticles. According to Eq. (2), theoretical smallest size of the neat nylon nanoparticle was determined to be 88.45 nm under the optimal conditions, where the concentration, voltage, and flow rate were 1.53%, 23.32 kV, and  $3.34 \text{ mL h}^{-1}$ , respectively. After that, neat nylon nanoparticles were practically prepared following these optimal conditions and their typical SEM images were shown in Fig. 2g and h. These nanoparticles had smooth surfaces and exhibited good formability. Size distribution of the neat nylon nanoparticles was shown in Fig. 2i and the average diameter was  $98.90 \pm 21.96 \text{ nm}$ , which was close to the theoretical value. Thus, the results proved the practicability of the optimal conditions from the designed RSM model.

### 3.2. Morphology of the FNCNs

Fig. 3 shows size distribution, photographs, and typical SEM images of the FNCNs prepared using the coaxial electrospaying system developed in the present study. Average diameter of the FNCNs was  $376 \pm 102 \text{ nm}$  (Fig. 3a), which was determined by using a DLS particle size analyzer. The FNCNs were well dispersed in water and can be easily separated from water with a magnet (Fig. 3a). It indicates that attractive forces between the magnetic  $\text{Fe}_3\text{O}_4$  cores were well controlled by the nylon shells, avoiding aggregation in water and resulting in easy and

rapid recovery of the FNCNs without excessive loss. For practical application of a nanocarrier, effective recovery process is a critical issue to be considered because it can improve reusability of the nanocarrier to reduce production cost. Therefore, the FNCNs were expected to be a potential nanocarrier showing good reusability after laccase immobilization was carried out.

As described in the Section 3.1, the optimal conditions for forming the thinnest nylon shells were determined by the RSM model. The next step was to prepare the smallest intact FNCNs by controlling flow rate of the  $\text{Fe}_3\text{O}_4$  solution under the optimal conditions of the nylon solution during the coaxial electrospaying process. For the typical SEM images (Fig. 3b–d), the nylon phase was originally smooth but showed wrinkles during observation. With a low flow rate of  $0.06\text{--}0.08 \text{ mL min}^{-1}$  (Fig. 3b), it was primarily the FNCNs with excess nylon phase that were observed; with a high flow rate of up to  $0.11 \text{ mL min}^{-1}$  (Fig. 3c), it was primarily the FNCNs with a lot of nylon nanoparticles (see Fig. 2g) that were observed. These results indicated that flow rate of the  $\text{Fe}_3\text{O}_4$  solution was important for preparation of the FNCNs and the optimal flow rate was in the range of  $0.09\text{--}0.10 \text{ mL min}^{-1}$ . Therefore, a flow rate of  $0.09 \text{ mL min}^{-1}$  for the  $\text{Fe}_3\text{O}_4$  solution was used to prepare the FNCNs (Fig. 3d). These small FNCNs were used for the further experiments and analyses, as well as expected to show good immobilization efficiency and catalytic activity due to their large specific area [58].

### 3.3. Structure characterization

Fig. 4a and b show C1s XPS spectra of the FNCNs and laccase-immobilized FNGCNs (L-FNGCNs), respectively, which were used to investigate surface chemical bonding of both the nanoparticles. Glutaraldehyde was used as a crosslinker to combine the FNCNs and laccase. Before immobilization, the FNCNs showed characteristic signals at 284.6, 286.2, and 288.8 eV, corresponding to C–C, C–N, and C=O of the nylon shells, respectively (Fig. 4a) [59,60]. After immobilization, except for the three original signals, a new signal at 285.8 eV was observed (Fig. 4b), indicating that C=N bonds were formed between the laccase and glutaraldehyde of the FNGCNs [7,61]. According to the results, the laccase was successfully immobilized by the FNGCNs.

Fig. 4c and d show TGA and derivative thermogravimetric analysis (DTG) curves of the neat nylon nanoparticles and FNCNs from room temperature to  $700^\circ\text{C}$ . For Fig. 4c, onset decomposition temperature ( $T_{\text{onset}}$ ) was determined by the intersection point of the two tangent lines for the TGA curve in the corresponding range [62,63]. The  $T_{\text{onset}}$  of the neat nylon nanoparticles and FNCNs were  $\sim 393$  and  $\sim 356^\circ\text{C}$ , respectively. It is attributed to the difference of specific heat ( $\text{Fe}_3\text{O}_4$ :  $104 \text{ J kg}^{-1} \text{ K}^{-1}$  [64]; nylon 6,6:  $2900 \text{ J kg}^{-1} \text{ K}^{-1}$  [65]), resulting in early decomposition of nylon molecules on the interfaces between  $\text{Fe}_3\text{O}_4$  cores and nylon shells. It seems that mechanism of the phenomenon has not yet been reported and is thus worth investigating in the next step. On the other hand, the neat nylon nanoparticles were completely decomposed at  $620^\circ\text{C}$ , while the weight of the FNCNs remained constant at  $\sim 20\%$  when the temperature was higher than  $620^\circ\text{C}$ , indicating that the weight fraction of the  $\text{Fe}_3\text{O}_4$  cores in the FNCNs was  $\sim 20\%$ . DTG curves reveal that the maximums of thermal decomposition rates of the neat nylon nanoparticles and FNCNs occurred at  $\sim 434$  and  $\sim 400^\circ\text{C}$ , respectively, corresponding to the trend of the TGA curves.

Fig. 4e shows FTIR spectra of the neat nylon nanoparticles, FNCNs, and L-FNGCNs from  $400$  to  $4000 \text{ cm}^{-1}$ . For the neat nylon nanoparticles, the peaks at  $\sim 1540$ ,  $\sim 1635$ ,  $\sim 2865$ ,  $\sim 2930$ ,  $\sim 3075$ , and  $\sim 3300 \text{ cm}^{-1}$  correspond to amide II band (N–H in-plane bending, C–N stretching, and C–C stretching), amide I band (C=O stretching, C–N stretching, and C–C–N deformation), symmetric  $\text{CH}_2$  stretching, asymmetric  $\text{CH}_2$  stretching, amide II band (overtone), and N–H stretching, respectively [66]. For the FNCNs, the peak at  $\sim 580 \text{ cm}^{-1}$  corresponds to Fe–O stretching of  $\text{Fe}_3\text{O}_4$ , and the absorption at  $\sim 1635 \text{ cm}^{-1}$  increased due to O–H bending of  $\text{Fe}_3\text{O}_4$  [67]. For the L-FNGCNs, the peak at  $\sim 950 \text{ cm}^{-1}$  was assigned to

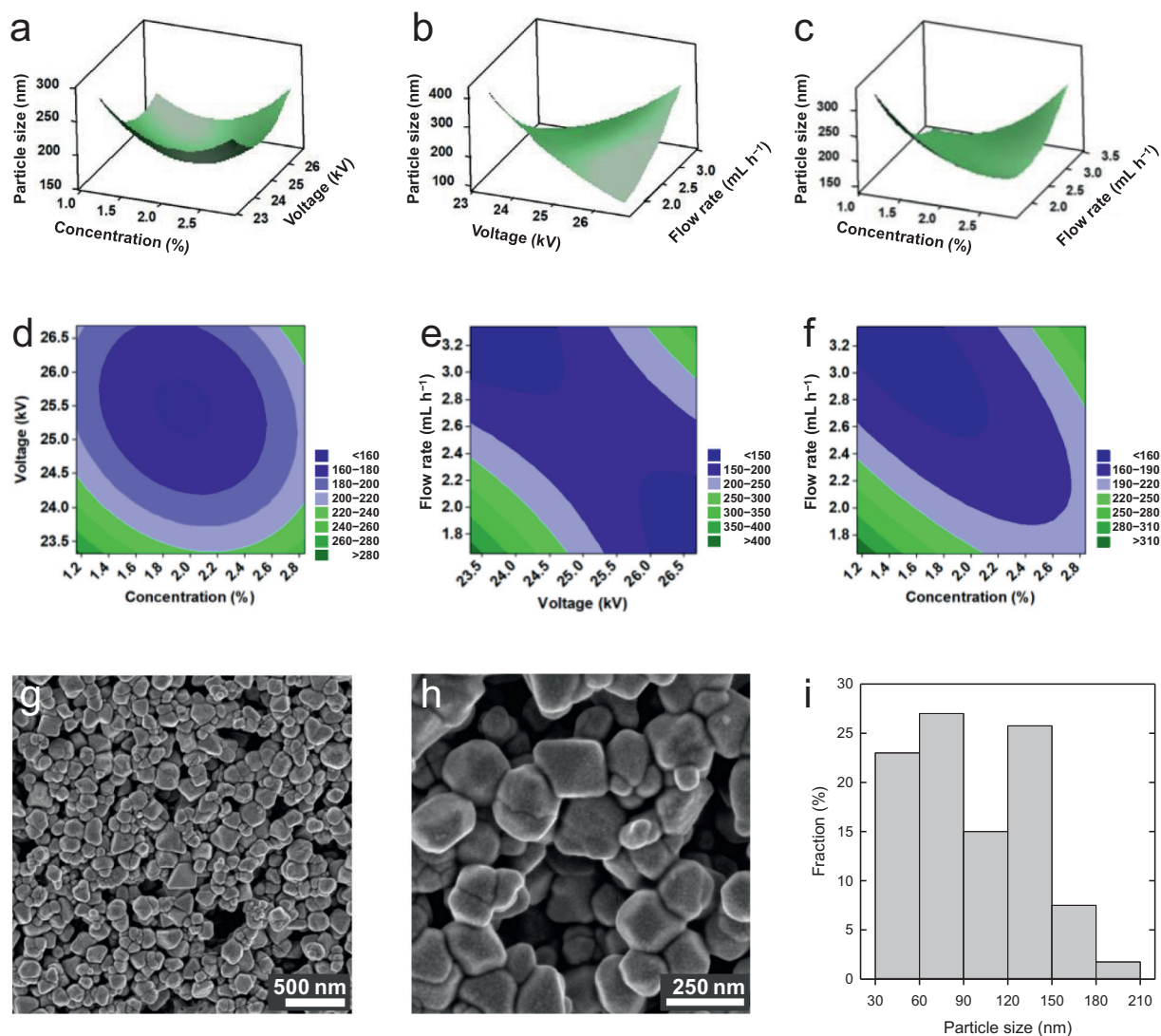


**Fig. 2.** Optimization of conditions for electro spraying nylon shells. Surface plots of concentration vs. voltage (a), voltage vs. flow rate (b), and concentration vs. flow rate (c). Contour plots (d), (e), and (f) correspond to (a), (b), and (c), respectively. Typical SEM images of the neat nylon nanoparticles observed at 30,000 $\times$  (g) and 80,000 $\times$  (h) magnifications. (i) Size distribution of the neat nylon nanoparticles determined using a DLS particle size analyzer.

**Table 2**

Analysis of variance (ANOVA) of the response variables for size of the neat nylon nanoparticles prepared with the outer needle of the coaxial electro spraying system.

| Source <sup>1</sup> | DF | Adj MS   | F-value | P-value |
|---------------------|----|----------|---------|---------|
| Regression          | 9  | 3973.4   | 0.73    | 0.677   |
| Conc                | 1  | 6.2      | 0.00    | 0.974   |
| Vol                 | 1  | 2310.9   | 0.42    | 0.530   |
| FR                  | 1  | 3526.8   | 0.65    | 0.440   |
| Conc                | 1  | 3455.2   | 0.63    | 0.444   |
| Vol                 | 1  | 2951.9   | 0.54    | 0.479   |
| FR                  | 1  | 2765.4   | 0.51    | 0.492   |
| Conc * Vol          | 1  | 306.9    | 0.06    | 0.817   |
| Conc * FR           | 1  | 4133.7   | 0.76    | 0.404   |
| Vol * FR            | 1  | 17,818.0 | 3.27    | 0.101   |
| Residual error      | 10 | 5448.5   |         |         |
| Lack of fit         | 5  | 8845.0   | 4.31    | 0.067   |
| Pure error          | 5  | 2051.9   |         |         |
| Core total          | 19 |          |         |         |

<sup>1</sup> DF = degree of freedom, Adj MS = adjusted mean squares, Conc = concentration (%), Vol = voltage (kV), FR = flow rate (mL h<sup>-1</sup>).

glutaraldehyde and laccase; the peak at  $\sim 1070\text{ cm}^{-1}$  correspond to C–O–C stretching of laccase; the peaks at  $\sim 1390$  and  $\sim 2395\text{ cm}^{-1}$  were assigned to laccase; the absorption at  $\sim 1590\text{ cm}^{-1}$  increased due to C=O stretching of glutaraldehyde and amide II band (C=O of CONH) of laccase; the peak at  $\sim 1715\text{ cm}^{-1}$  correspond to C=O stretching of glutaraldehyde; the broad peak at  $\sim 3415\text{ cm}^{-1}$  correspond to O–H stretching of glutaraldehyde and laccase as well as N–H stretching of laccase [68–70].

According to the results, all the components in each nanoparticle sample were detected in the FTIR spectra. Except for hydrogen bonds, it is considered that the nylon shells and laccase linked with glutaraldehyde mainly by C–N and C=N bonds, respectively [71–73]. The C=N bond between the laccase and glutaraldehyde was already confirmed by the XPS spectra as described above. According to the good results of storage stability and reusability of the L-FNGCNs (see Section 3.6), both the nylon shells and laccase had significant interactions between the glutaraldehyde. Therefore, it is considered that the peaks corresponding to C–N stretching (at  $\sim 1253\text{ cm}^{-1}$ ) [74] and C=N stretching (at  $\sim 1652\text{ cm}^{-1}$ ) [75] were overlapped by the adjacent peaks. A possible linkage relationship between the nylon shells, glutaraldehyde, and laccase was shown in Fig. 1b.



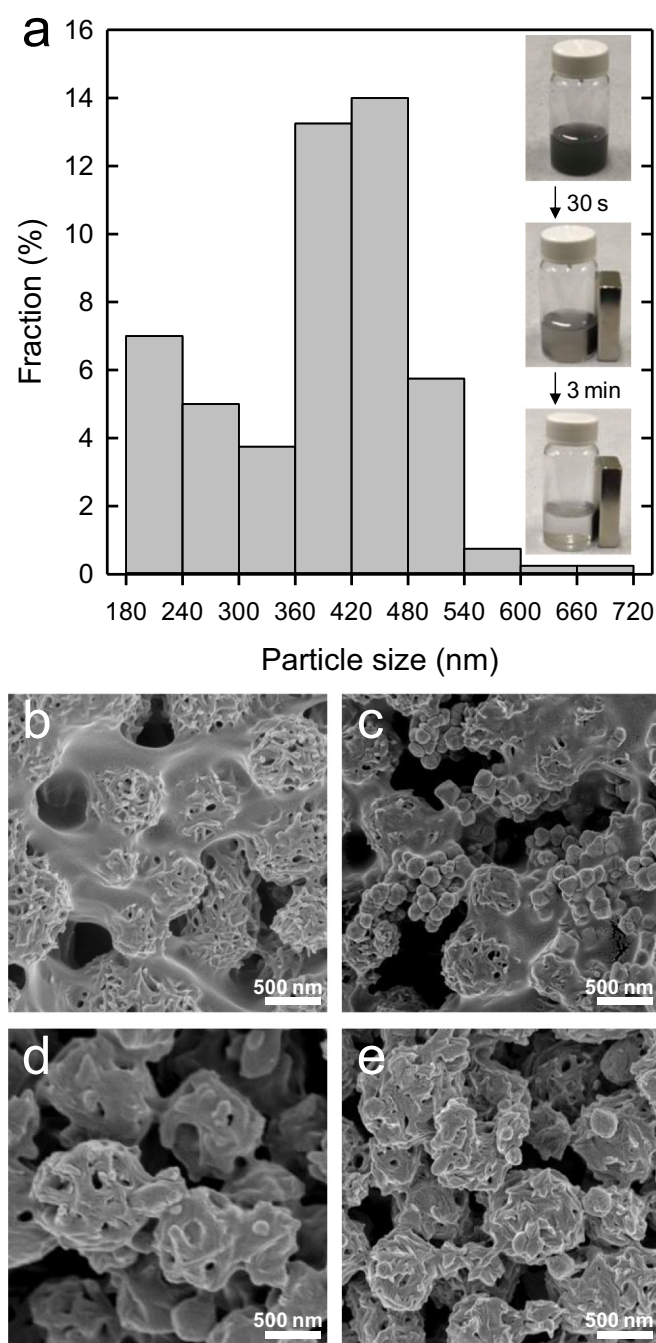


**Fig. 3.** (a) Size distribution of the FNCNs and photographs of the FNCNs recovered with a magnet. Typical SEM images of the FNCNs prepared at  $\text{Fe}_3\text{O}_4$  flow rates of 0.06–0.08 (b), 0.11 (c), and 0.09 (d)  $\text{mL min}^{-1}$ . (e) Typical SEM image of the L-FNCNs, where the FNCNs prepared with  $\text{Fe}_3\text{O}_4$  flow rate of 0.09  $\text{mL min}^{-1}$  were treated with glutaraldehyde and then used to immobilize laccase.

### 3.4. Determination of optimal reaction conditions for the L-FNCNs

Catalytic activity of enzyme was considerably affected by pH value and temperature. In order to find out the optimal reaction conditions for the L-FNCNs, catalytic activity of the immobilized laccase was examined at pH values of 3, 4, 5, 6, 7, and 8, as well as temperatures of 30, 40, 50, 60, 70, 80, and 90 °C. Fig. 5 shows effects of pH value (Fig. 5a) and temperature (Fig. 5b) on relative activities of the free laccase and L-FNCNs. As shown in Fig. 5a, compared with the free

laccase, the L-FNCNs exhibited almost the same relative activities at pH 4 and 5 but lower relative activities at the other pH values. As shown in Fig. 5b, the free laccase and L-FNCNs exhibited the highest relative activities at 30 and 60 °C, respectively. The relative activity of the free laccase decreased with increasing temperature; while that of the L-FNCNs increased with increasing temperature from 30 to 60 °C, plateaued at 70 and 80 °C, and then decreased considerably at 90 °C. It indicates that thermal stability of the free laccase was significantly improved after immobilization on the FNCNs. Change of thermal stability of the laccase is attributed to the configuration of the laccase affected by covalent bonding between the laccase and glutaraldehyde of the FNCNs [14,15]. According to the results, the optimal reaction conditions for the L-FNCNs were determined to be pH 4 and 60 °C. Furthermore, the L-FNCNs showed potential for industrial application due to that an enzyme with higher thermal stability can react at higher temperatures, enhancing bioconversion efficiency and reducing cost of cooling process [76].

### 3.5. Effect of the L-FNCNs on oxidative degradation of the ginkgolic acids

Before evaluating the oxidation effect of the L-FNCNs on the ginkgolic acid, the oxidation effect of the L-FNCNs on ABTS was investigated in advance. Relative activities of the free laccase, laccase-immobilized nylon (coded as L-nylon) nanoparticles, and L-FNCNs on ABTS were measured. Before the immobilization, the neat nylon nanoparticles were treated with glutaraldehyde. The amounts of laccase immobilized on the L-nylon nanoparticles and L-FNCNs were both approximately 60 mg/g nanoparticles. It is noticed that for the laccase-immobilized nanocarriers, oxidation effect of the immobilized laccase were confirmed in advance before measuring the relative activities according to Section 2.4. The optimal reaction conditions of pH 4 and 60 °C were applied and ABTS was used as the substrate to determine relative activities of the free laccase and laccase-immobilized nanocarriers. As shown in Fig. 5c, the L-FNCNs exhibited considerably high relative activity, which was much higher than that of the L-nylon nanoparticles, showing good oxidation effect and corresponding to the result in Fig. 4b. It is attributed to the lack of magnetic sensitivity in the L-nylon nanoparticles, making them difficult to recover after confirming oxidation effect. The decreased amount of the L-nylon nanoparticles deteriorated its oxidation effect, indicating the importance of effective recovery for catalytic performance of an enzyme immobilization carrier. As a result, recovery efficiency of the neat nylon nanoparticles can be significantly improved by forming the core/shell FNCNs using coaxial electrospaying technique.

Kinetic parameters including rate constant ( $k$ ) and time ( $\tau_{50}$  and  $\tau_{100}$ ) of the free laccase, L-FNCNs, and L-nylon nanoparticles were calculated and shown in Table 3. The free laccase exhibited the highest  $k$  value ( $2.49 \pm 0.19 \text{ min}^{-1}$ ) followed by the L-FNCNs ( $0.13 \pm 0.01 \text{ min}^{-1}$ ) and L-nylon nanoparticles ( $0.04 \pm 0.01 \text{ min}^{-1}$ ) in order of decreasing  $k$  value. The parameters  $\tau_{50}$  and  $\tau_{100}$  represent the time needed to oxidize 50% and 100% of the ABTS, respectively. The free laccase exhibited the lowest  $\tau_{50}$  value ( $0.28 \pm 0.00 \text{ min}$ ) followed by the L-FNCNs ( $5.04 \pm 0.28 \text{ min}$ ) and L-nylon nanoparticles ( $16.38 \pm 0.66 \text{ min}$ ) in order of increasing  $\tau_{50}$  value. For  $\tau_{100}$  value, the same trend was observed as follows: free laccase ( $2.38 \pm 0.29 \text{ min}$ ) < L-FNCNs ( $29.54 \pm 4.88 \text{ min}$ ) < L-nylon nanoparticles ( $67.32 \pm 5.48 \text{ min}$ ).

After the oxidation effect of the L-FNCNs on ABTS was confirmed, the oxidation effect of the L-FNCNs on ginkgolic acid was evaluated. The experimental conditions were pH 4 and 60 °C, the same as those for ABTS. In the previous study, we first carried out oxidative degradation of the ginkgolic acids by the free and immobilized laccases, where the latter was immobilized on the electrospun nylon nanofiber mat [18]. The widths of the nanofibers were  $121 \pm 33 \text{ nm}$ , and the area of the mat used for oxidation was  $1 \times 1 \text{ cm}^2$ . According to the results, the L-FNCNs were expected to exhibit effects on oxidative degradation

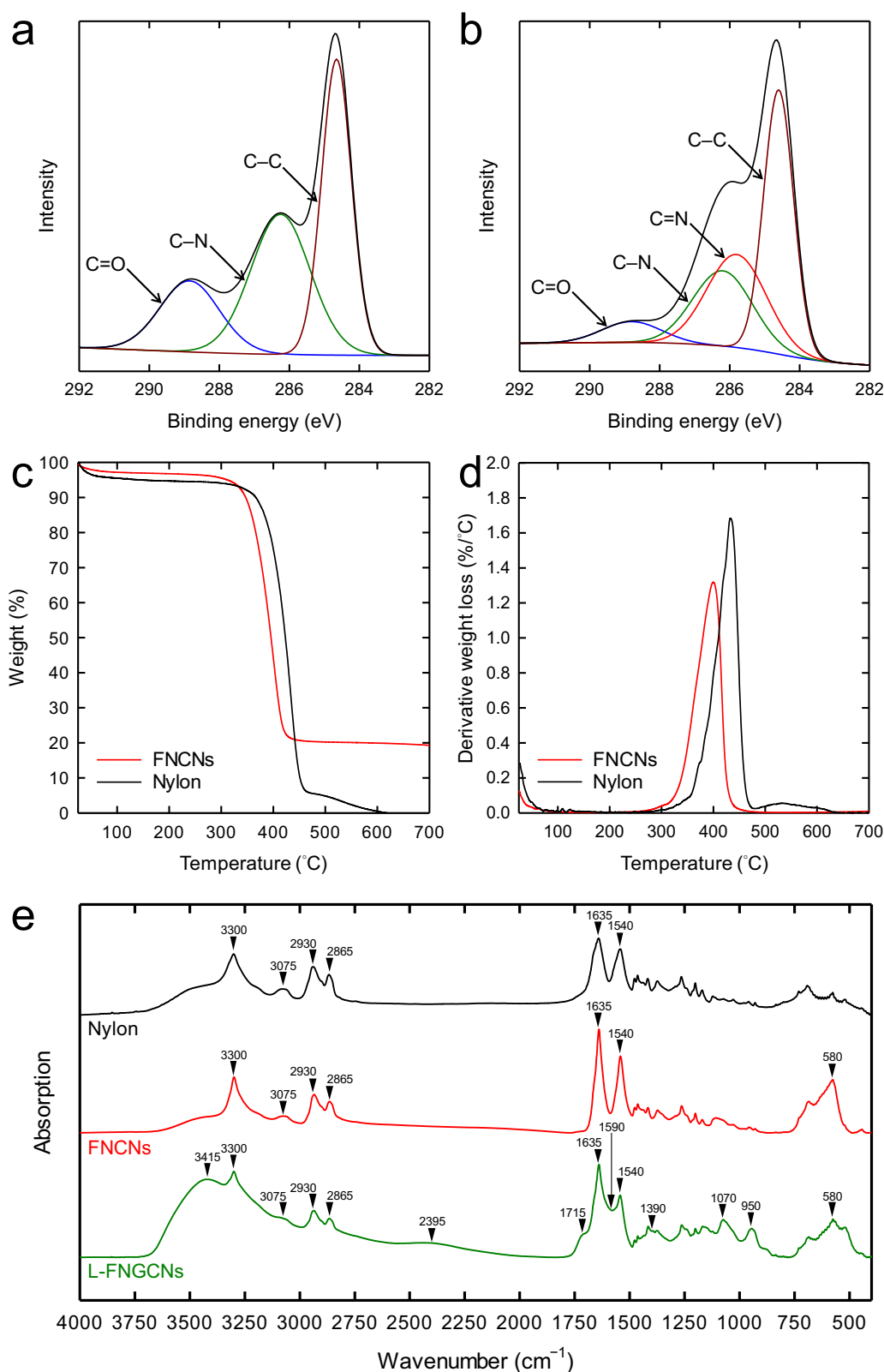


**Fig. 4.** Typical C1s XPS spectra of the (a) FNCNs and (b) L-FNCNs. The characteristic signals at 284.6, 286.2, and 288.8 eV correspond to C–C, C–N, and C=O of the nylon shells, respectively. The characteristic signal at 285.8 eV correspond to C=N formed between the laccase and glutaraldehyde of the FNCNs. TGA (c) and DTG (d) curves of the neat nylon nanoparticles and FNCNs from room temperature to 700 °C. (e) FTIR spectra of the neat nylon nanoparticles, FNCNs, and L-FNCNs.

of the ginkgolic acids, which were obtained from the *G. biloba* leaf extract as described in Section 2.8. As shown in Table 4, the L-FNCNs exhibited significantly positive oxidation effects on the C13:0 and C15:1

ginkgolic acids. The  $k$  values of the C13:0 and C15:1 ginkgolic acids were  $0.022 \pm 0.002$  and  $0.018 \pm 0.001 \text{ min}^{-1}$ , respectively. On the other hand, the  $\tau_{50}$  values of the C13:0 and C15:1 ginkgolic acids were



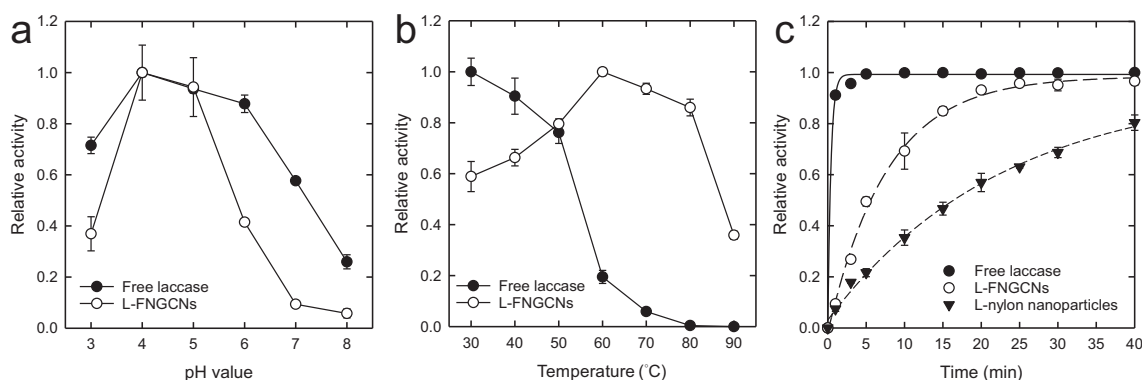


**Fig. 5.** Effects of pH value (a) and temperature (b) on relative activities of the free laccase and L-FNGCNs. The temperature and pH value of (a) and (b) were 50 °C and 4, respectively. According to the results, the optimal reaction conditions for the L-FNGCNs were determined to be pH 4 and 60 °C. (c) Catalytic behavior of the free laccase and different laccase-immobilized nanocarriers under the optimal reaction conditions.

$32.35 \pm 4.00$  and  $38.69 \pm 5.85$  min, respectively. For the  $\tau_{100}$  values, they were both estimated to be higher than 60 min. As a result, for oxidative degradation of the ginkgolic acids, the L-FNGCNs showed better effects than the laccase immobilized on the electrospun nylon nanofiber mat [18]. It is probably due to the morphology of the nanocarriers, which affects the amounts of the immobilized laccases (those on the L-FNGCNs and laccase-immobilized nylon nanofiber mat were 60 and 48 mg/g nanocarrier, respectively) and their reactivities. Compared with the laccase-immobilized nylon nanofiber mat, which had a large and tough structure consisting of the nanofibers overlapped and entangled to each other, the L-FNGCNs were individual spheres and had good mobility in the reaction system, resulting in higher reactivity with the ginkgolic acid molecules.

In conclusion, according to our experimental results, enzyme immobilization by the FNGCNs showed a large immobilization amount, improved thermal stability of the enzyme, and avoided aggregation to allow easy recovery. These advantages resulted in good catalytic performance of the enzyme-immobilized FNGCNs. Furthermore, coaxial electrospinning provides a one-step solution to produce nanoparticles with narrow size distribution, without heating and decreasing the use of water. Hence, coaxial electrospinning has potential for application of enzyme immobilization.

### 3.6. Storage stability and reusability of the L-FNGCNs

Fig. 6 shows storage stability within 28 days (Fig. 6a) and reusability for 10 cycles (Fig. 6b) of the L-FNGCNs. The relative activity to oxidize ABTS was maintained at higher than 0.5 after being stored for 21 days or reused for 5 cycles. This indicated that the laccase was well immobilized on the FNGCNs, which can significantly reduce cost of mass production.

## 4. Conclusions

The core/shell FNCNs for laccase immobilization were successfully developed with  $\text{Fe}_3\text{O}_4$  and nylon solutions using RSM model and one-

step coaxial electrospinning. These FNCNs had an average diameter of  $376 \pm 102$  nm and can be simply recovered by magnetic force. Glutaraldehyde-treated FNCNs (FNGCNs) were used to carry out immobilization, where the glutaraldehyde was a crosslinker to combine the nylon shells and laccase. As a result, thermal stability of the laccase was significantly improved in the range of 60–90 °C after immobilization. Compared with the free laccase, the laccase-immobilized FNGCNs (L-FNGCNs) can react at higher temperatures, enhancing bioconversion efficiency and reducing cost of cooling process. The L-FNGCNs were applied for oxidative degradation of the ginkgolic acids, and the rate constants ( $k$ ) and times ( $\tau_{50}$ ) were  $\sim 0.02 \text{ min}^{-1}$  and lower than 39 min, respectively, showing good catalytic performance. In addition, for the L-FNGCNs, the relative activity to oxidize ABTS was maintained at higher than 0.5 after being stored for 21 days or reused for 5 cycles, showing good storage stability and reusability. The present study might be the first study to date to prepare core/shell composite nanoparticles with magnetic sensitivity for enzyme immobilization and catalytic application using coaxial electrospinning technique. Hence, the preparation, characterization, and application were worthy of reference for the related research fields. Future work is focused on effect of surface modification of the composite nanoparticles on immobilization efficiency and catalytic activity of laccase.

### CRediT authorship contribution statement

**Hung-Yueh Chen:** Perform investigation, data curation, writing original draft, and revision. **Yuwen Ting:** Provide supervision, methodology development, and review & editing of the whole work. **Hsing-Chun Kuo:** Provide resource and funding acquisition of the work. **Chang-Wei Hsieh:** Provide resource and review & editing of the work. **Hsien-Yi Hsu:** Provide supervision, formal analysis, and review & editing of the whole work. **Chun-Nan Wu:** Provide supervision, data curation and review & editing of the whole work. **Kuan-Chen Cheng:** Provide supervision, conceptualization, and review & editing of the whole work.

**Table 3**

Kinetic parameters including rate constant ( $k$ ) and time ( $\tau$ ) of the free laccase, L-FNGCNs, and L-nylon nanoparticles for oxidation of ABTS.

| Kinetic parameter <sup>1</sup> | Free laccase    | L-FNGCNs         | L-nylon nanoparticles |
|--------------------------------|-----------------|------------------|-----------------------|
| $k$ ( $\text{min}^{-1}$ )      | $2.49 \pm 0.19$ | $0.13 \pm 0.01$  | $0.04 \pm 0.01$       |
| $\tau_{50}$ (min)              | $0.28 \pm 0.00$ | $5.04 \pm 0.28$  | $16.38 \pm 0.66$      |
| $\tau_{100}$ (min)             | $2.38 \pm 0.29$ | $29.54 \pm 4.88$ | $67.32 \pm 5.48$      |

<sup>1</sup> The parameters  $\tau_{50}$  and  $\tau_{100}$  represent the time needed to oxidize 50% and 100% of the ABTS, respectively.

**Table 4**

Kinetic parameters including rate constant ( $k$ ) and time ( $\tau$ ) of the L-FNGCNs for oxidation of the ginkgolic acids.

| Kinetic parameter <sup>1</sup> | C13:0 ginkgolic acid | C15:1 ginkgolic acid |
|--------------------------------|----------------------|----------------------|
| $k$ ( $\text{min}^{-1}$ )      | $0.022 \pm 0.002$    | $0.018 \pm 0.001$    |
| $\tau_{50}$ (min)              | $32.35 \pm 4.00$     | $38.69 \pm 5.85$     |
| $\tau_{100}$ (min)             | $>60$                | $>60$                |

<sup>1</sup> The parameters  $\tau_{50}$  and  $\tau_{100}$  represent the time needed to oxidize 50% and 100% of the ginkgolic acids, respectively.

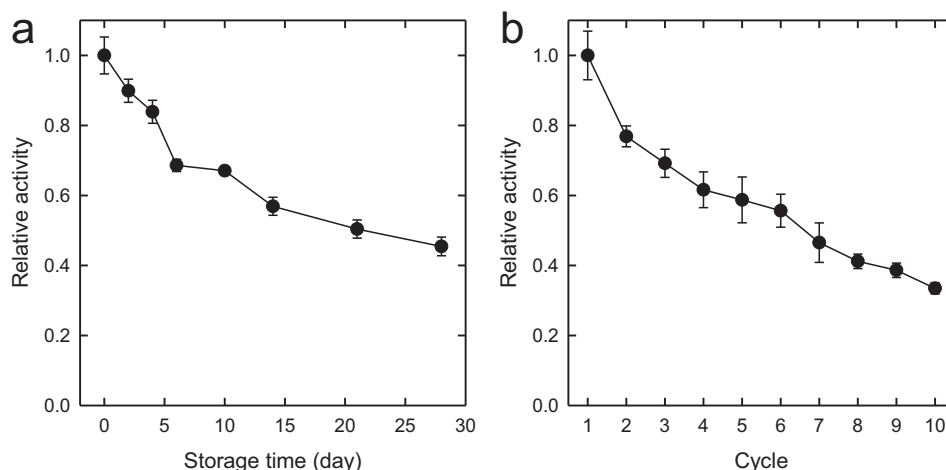


Fig. 6. Storage stability within 28 days (a) and reusability for 10 cycles (b) of the L-FNGCNs, which were evaluated by the relative activity to oxidize ABTS.

### Declaration of competing interest

The authors report no conflicts of interest. The authors alone are responsible for the content and writing of this article.

### Acknowledgments

This study was funded by the Ministry of Science and Technology, Taiwan, under contract numbers MOST 104-2221-E-002-125-MY3, MOST 105-2221-E-002-212-MY3, and MOST 106-2628-E-002-009-MY3. The authors greatly acknowledge the article proofreading by Iris YS Wu who is a native speaker from University of California, Berkeley (Berkeley, CA, USA).

### References

- [1] G. Irena, B. Jolanta, Z. Karolina, Chemical modification of poly(ethylene terephthalate) and immobilization of the selected enzymes on the modified film, *Appl. Surf. Sci.* 225 (2009) 8293–8298, <https://doi.org/10.1016/j.apsusc.2009.05.126>.
- [2] V. Singh, K. Rakshit, S. Rathee, S. Angmo, S. Kaushal, P. Garg, J.H. Chung, R. Sandhir, R.S. Sangwan, N. Singhal, Metallic/bimetallic magnetic nanoparticle functionalization for immobilization of  $\alpha$ -amylase for enhanced reusability in biocatalytic processes, *Bioresour. Technol.* 214 (2016) 528–533, <https://doi.org/10.1016/j.biortech.2016.05.002>.
- [3] R.M. El-Shishtawy, M. Aldahri, Y.Q. Almulaiky, Dual immobilization of  $\alpha$ -amylase and horseradish peroxidase via electrospraying: a proof of concept study, *Int. J. Biol. Macromol.* 163 (2020) 1353–1360, <https://doi.org/10.1016/j.ijbiomac.2020.07.278>.
- [4] W.M. Alshawafi, M. Aldahri, Y.Q. Almulaiky, N. Salah, S.S. Moselhy, I.H. Ibrahim, R.M. El-Shishtawy, S.A. Mohamed, Immobilization of horseradish peroxidase on PMMA nanofibers incorporated with nanodiamond, *Artif. Cells Nanomed. Biotechnol.* 46 (2018) S973–S981, <https://doi.org/10.1080/21691401.2018.1522321>.
- [5] K.-I. Chen, Y.-C. Lo, N.-W. Su, C.-C. Chou, K.-C. Cheng, Enrichment of two isoflavone aglycones in black soymilk by immobilized  $\beta$ -glucosidase on solid carriers, *J. Agric. Food Chem.* 60 (2012) 12540–12546, <https://doi.org/10.1021/jf304405t>.
- [6] K.-I. Chen, Y.-C. Lo, C.-W. Liu, R.-C. Yu, C.-C. Chou, K.-C. Cheng, Enrichment of two isoflavone aglycones in black soymilk by using spent coffee grounds as an immobiliser for  $\beta$ -glucosidase, *Food Chem.* 139 (2013) 79–85, <https://doi.org/10.1016/j.foodchem.2013.01.093>.
- [7] H.-T. Wang, J.-T. Yang, K.-I. Chen, T.-Y. Wang, T.-J. Lu, K.-C. Cheng, Hydrolyzation of mogrosides: immobilized  $\beta$ -glucosidase for mogrosides deglycosylation from Lo Han Kuo, *Food Sci. Nutr.* 7 (2019) 834–843, <https://doi.org/10.1002/fsn3.932>.
- [8] C.-Y. Ko, J.-M. Liu, K.-I. Chen, C.-W. Hsieh, Y.-L. Chu, K.-C. Cheng, Lactose-free milk preparation by immobilized lactase in glass microsphere bed reactor, *Food Biophys* 13 (2018) 353–361, <https://doi.org/10.1007/s11483-018-9541-8>.
- [9] K.I. Chen, C.Y. Chiang, C.Y. Ko, H.Y. Huang, K.C. Cheng, Reduction of phytic acid in soymilk by immobilized phytase system, *J. Food Sci.* 83 (2018) 2963–2969, <https://doi.org/10.1111/1750-3841.14394>.
- [10] X. Li, X. Peng, Q. Wang, H. Zuo, X. Meng, B. Liu, Effective detoxification of patulin from aqueous solutions by immobilized porcine pancreatic lipase, *Food Control* 78 (2017) 48–56, <https://doi.org/10.1016/j.foodcont.2017.02.048>.
- [11] S. Afreen, D. Idrees, R. Khera, M. Amir, M.I. Hassan, S. Mishra, Investigation of the role of central metal ion of *Cyathus bulleri* laccase 1 using guanidinium chloride-induced denaturation, *Int. J. Biol. Macromol.* 132 (2019) 994–1000, <https://doi.org/10.1016/j.ijbiomac.2019.04.014>.
- [12] V. Lettera, C. Pezzella, P. Cicatiello, A. Piscitelli, V.G. Giacobelli, E. Galano, A. Amoresano, G. Sannia, Efficient immobilization of a fungal laccase and its exploitation in fruit juice clarification, *Food Chem.* 196 (2016) 1272–1278, <https://doi.org/10.1016/j.foodchem.2015.10.074>.
- [13] Y. Pei, S. Wang, C. Qin, J. Su, S. Nie, X. Song, Optimization of laccase-aided chlorine dioxide bleaching of bagasse pulp, *BioResources* 11 (2016) 696–712, <https://doi.org/10.15376/biores.11.1.696-712>.
- [14] R. Amin, A. Khorshidi, A.F. Shojaei, S. Rezaei, M.A. Faramarzi, Immobilization of laccase on modified  $\text{Fe}_3\text{O}_4/\text{SiO}_2/\text{Kit-6}$  magnetite nanoparticles for enhanced delignification of olive pomace bio-waste, *Int. J. Biol. Macromol.* 114 (2018) 106–113, <https://doi.org/10.1016/j.ijbiomac.2018.03.086>.
- [15] M.J.F. Jasni, P. Sathishkumar, S. Somambikai, A.R.M. Yusoff, F. Ameen, N.A. Buang, M.R.A. Kadir, Z. Yusop, Fabrication, characterization and application of laccase-nylon 6,6/ $\text{Fe}^{3+}$  composite nanofibrous membrane for 3,30-dimethoxybenzidine detoxification, *Bioprocess Biosyst. Eng.* 40 (2017) 191–200, <https://doi.org/10.1007/s00449-016-1686-6>.
- [16] N.A. Kalkan, S. Aksoy, E.A. Aksoy, N. Hasirci, Preparation of chitosan-coated magnetite nanoparticles and application for immobilization of laccase, *J. Appl. Polym. Sci.* 123 (2011) 707–716, <https://doi.org/10.1002/app.34504>.
- [17] D. Wang, H. Zhu, M. Li, X. Song, H. Yan, J. Yu, X. Wang, An efficient method for the preparative separation and isolation of ginkgolic acids from the sarcotesta of *Ginkgo biloba* L by pH-zone-refining countercurrent chromatography coupled with inner-recycling mode, *Ind. Crop. Prod.* 126 (2018) 69–75, <https://doi.org/10.1016/j.indcrop.2018.09.034>.
- [18] H.-Y. Chen, K.-C. Cheng, R.-J. Hsu, C.-W. Hsieh, H.-T. Wang, Y. Ting, Enzymatic degradation of ginkgolic acid by laccase immobilized on novel electrospun nanofiber mat, *J. Sci. Food Agric.* 100 (2020) 2705–2712, <https://doi.org/10.1002/jsfa.10301>.
- [19] S. Cen, X. Lv, Y. Jiang, A. Fakhri, V.K. Gupta, Synthesis and structure of iron-copper/hollow magnetic/metal-organic framework/coordination sites in a heterogeneous catalyst for a Fenton-based reaction, *Catal. Sci. Technol.* 10 (2020) 6687–6693, <https://doi.org/10.1039/D0CY01027H>.
- [20] M. Yang, F. Lu, T. Zhou, J. Zhao, C. Ding, A. Fakhri, V.K. Gupta, Biosynthesis of nano bimetallic Ag/Pt alloy from *Crocus sativus* L. extract: biological efficacy and catalytic activity, *J. Photochem. Photobiol. B Biol.* 212 (2020) 112025, <https://doi.org/10.1016/j.jphotobiol.2020.112025>.
- [21] J. Zhang, E. Ding, S. Xu, Z. Li, A. Fakhri, V.K. Gupta, Production of metal oxides nanoparticles based on poly-alanine/chitosan/reduced graphene oxide for photocatalysis degradation, anti-pathogenic bacterial and antioxidant studies, *Int. J. Biol. Macromol.* 164 (2020) 1584–1591, <https://doi.org/10.1016/j.ijbiomac.2020.07.291>.
- [22] M. Huang, R. Zhang, Z. Yang, J. Chen, J. Deng, A. Fakhri, V.K. Gupta, Synthesis of  $\text{Co}_3\text{S}_4\text{-SnO}_2/\text{polyvinylpyrrolidone-cellulose}$  heterojunction as highly performance catalyst for photocatalytic and antimicrobial properties under ultra-violet irradiation, *Int. J. Biol. Macromol.* 162 (2020) 220–228, <https://doi.org/10.1016/j.ijbiomac.2020.06.092>.
- [23] H. Wang, G. Li, A. Fakhri, Fabrication and structural of the  $\text{Ag}_2\text{S-MgO/graphene oxide}$  nanocomposites with high photocatalysis and antimicrobial activities, *J. Photochem. Photobiol. B Biol.* 207 (2020), 111882, <https://doi.org/10.1016/j.jphotobiol.2020.111882>.
- [24] G. Wang, A. Fakhri, Preparation of CuS/polyvinyl alcohol-chitosan nanocomposites with photocatalysis activity and antibacterial behavior against G+/G- bacteria, *Int. J. Biol. Macromol.* 155 (2020) 36–41, <https://doi.org/10.1016/j.ijbiomac.2020.03.077>.
- [25] M. Lu, Y. Cui, S. Zhao, A. Fakhri,  $\text{Cr}_2\text{O}_3/\text{cellulose}$  hybrid nanocomposites with unique properties: facile synthesis, photocatalytic, bactericidal and antioxidant application, *J. Photochem. Photobiol. B Biol.* 205 (2020), 111842, <https://doi.org/10.1016/j.jphotobiol.2020.111842>.
- [26] P. Esmailnejad-Ahranjani, M. Kazemine, G. Singh, A. Arpanaei, Study of molecular conformation and activity-related properties of lipase immobilized onto core-shell structured polyacrylic acid-coated magnetic silica nanocomposite particles, *Langmuir* 32 (2016) 3242–3252, <https://doi.org/10.1021/acs.langmuir.5b03614>.

- [27] S.K.S. Patel, S.H. Choi, Y.C. Kang, J.-K. Lee, Eco-friendly composite of Fe<sub>3</sub>O<sub>4</sub>-reduced graphene oxide particles for efficient enzyme immobilization, *ACS Appl. Mater. Interfaces* 9 (2017) 2213–2222, <https://doi.org/10.1021/acsami.6b05165>.
- [28] K.Z. Elwakeel, A.S. Al-Bogami, E. Guibal, 2-Mercaptobenzimidazole derivative of chitosan for silver sorption—contribution of magnetite incorporation and sonication effects on enhanced metal recovery, *Chem. Eng. J.* 403 (2021), 126265, <https://doi.org/10.1016/j.cej.2020.126265>.
- [29] K.Z. Elwakeel, A. Shahat, A.S. Al-Bogami, B. Wijesiri, A. Goonetilleke, The synergistic effect of ultrasound power and magnetite incorporation on the sorption/desorption behavior of Cr(VI) and As(V) oxoanions in an aqueous system, *J. Colloid Interface Sci.* 569 (2020) 76–88, <https://doi.org/10.1016/j.jcis.2020.02.067>.
- [30] K.Z. Elwakeel, A. Shahat, Z.A. Khan, W. Alshitari, E. Guibal, Magnetic metal oxide-organic framework material for ultrasonic-assisted sorption of titan yellow and rose bengal from aqueous solutions, *Chem. Eng. J.* 392 (2020), 123635, <https://doi.org/10.1016/j.cej.2019.123635>.
- [31] M.A. El-Liethy, K.Z. Elwakeel, M.S. Ahmed, Comparison study of Ag(I) and Au(III) loaded on magnetic thiourea-formaldehyde as disinfectants for water pathogenic microorganism's deactivation, *J. Environ. Chem. Eng.* 6 (2018) 4380–4390, doi: <https://doi.org/10.1016/j.jece.2018.06.028>.
- [32] S.A. Mohamed, M.H. Al-Harbi, Y.Q. Almulaiky, I.H. Ibrahim, R.M. El-Shishtawy, Immobilization of horseradish peroxidase on Fe<sub>3</sub>O<sub>4</sub> magnetic nanoparticles, *Electron. J. Biotechnol.* 27 (2017) 84–90, <https://doi.org/10.1016/j.ejbt.2017.03.010>.
- [33] S.A. Mohamed, M.H. Al-Harbi, Y.Q. Almulaiky, I.H. Ibrahim, H.A. Salah, M.O. El-Badry, A.M. Abdel-Aty, A.S. Fahmy, R.M. El-Shishtawy, Immobilization of *Trichoderma harzianum*  $\alpha$ -amylase on PPyAgNp/Fe<sub>3</sub>O<sub>4</sub>-nanocomposite: chemical and physical properties, *Artif. Cells Nanomed. Biotechnol.* 46 (2018) 201–206, <https://doi.org/10.1080/21691401.2018.1453828>.
- [34] W.H. Abdulla, Y.Q. Almulaiky, R.M. El-Shishtawy, Encapsulation of HRP enzyme onto a magnetic Fe<sub>3</sub>O<sub>4</sub> Np-PMMA film via casting with sustainable biocatalytic activity, *Catalysts* 10 (2020), 181, <https://doi.org/10.3390/catal10020181>.
- [35] H. Suo, L. Xu, Y. Xue, X. Qiu, H. Huang, Y. Hu, Ionic liquids-modified cellulose coated magnetic nanoparticles for enzyme immobilization: improvement of catalytic performance, *Carbohydr. Polym.* 234 (2020), 115914, <https://doi.org/10.1016/j.carbpol.2020.115914>.
- [36] Q. Zhang, L. Yu, B. Liu, F. Li, B. Tang, Reduction of nitroarenes by magnetically recoverable nitroreductase immobilized on Fe<sub>3</sub>O<sub>4</sub> nanoparticles, *Sci. Rep.* 10 (2020), 2810, <https://doi.org/10.1038/s41598-020-59754-1>.
- [37] A. Ulu, E. Birhanli, F. Boran, S. Köytepe, O. Yesilada, B. Ateş, Laccase-conjugated thiolated chitosan-Fe<sub>3</sub>O<sub>4</sub> hybrid composite for biocatalytic degradation of organic dyes, *Int. J. Biol. Macromol.* 150 (2020) 871–884, <https://doi.org/10.1016/j.ijbiomac.2020.02.006>.
- [38] M. Demir, M. Şenel, A. Baykal, Reversible immobilization of BSA on Cu-chelated PAMAM dendrimer-modified iron oxide nanoparticles, *Appl. Surf. Sci.* 314 (2014) 697–703, <https://doi.org/10.1016/j.apsusc.2014.07.082>.
- [39] M. Zamani, M.P. Prabhakaran, S. Ramakrishna, Advances in drug delivery via electrospon and electrosprayed nanomaterials, *Int. J. Nanomedicine* 8 (2013) 2997–3017, <https://doi.org/10.2147/IJN.S43575>.
- [40] J.A. Bhushani, C. Anandharamakrishnan, Electrospraying and electrospraying techniques: potential food based applications, *Trends Food Sci. Tech.* 38 (2014) 21–33, <https://doi.org/10.1016/j.tifs.2014.03.004>.
- [41] Y. Baspinar, M. Üstündaş, O. Bayraktar, C. Sezgin, Curcumin and piperine loaded zein-chitosan nanoparticles: development and in-vitro characterisation, *Saudi Pharm. J.* 26 (2018) 323–334, <https://doi.org/10.1016/j.jsps.2018.01.010>.
- [42] S. Tsai, Y. Ting, Synthesis of alginate/chitosan bilayer nanocarrier by CCD-RSM guided co-axial electrospray: a novel and versatile approach, *Food Res. Int.* 116 (2019) 1163–1172, <https://doi.org/10.1016/j.foodres.2018.11.047>.
- [43] M. Eltayeb, E. Stride, M. Edirisinghe, Electrosprayed core-shell polymer-lipid nanoparticles for active component delivery, *Nanotechnology* 24 (2013), 465604, <https://doi.org/10.1088/0957-4484/24/46/465604>.
- [44] Y. Wang, Y. Zhang, B. Wang, Y. Cao, Q. Yu, T. Yin, Fabrication of core-shell micro-nanoparticles for programmable dual drug release by emulsion electrospraying, *J. Nanopart. Res.* 15 (2013) 1726, <https://doi.org/10.1021/jp8052899>.
- [45] M. Yanilmaz, J. Zhu, Y. Lu, Y. Ge, X. Zhang, High-strength, thermally stable nylon 6,6 composite nanofiber separators for lithium-ion batteries, *J. Mater. Sci.* 52 (2017) 5232–5241, <https://doi.org/10.1007/s10853-017-0764-8>.
- [46] D.E. Wong, K.J. Senecal, J.M. Goddard, Immobilization of chymotrypsin on hierarchical nylon 6,6 nanofiber improves enzyme performance, *Colloids Surf. B Biointerfaces* 154 (2017) 270–278, <https://doi.org/10.1016/j.colsurfb.2017.03.033>.
- [47] M. Rasekh, Z. Ahmad, R. Cross, J. Hernández-Gil, J.D.E.T. Wilton-Ely, P.W. Miller, Facile preparation of drug-loaded Trisairon encapsulated Superparamagnetic Iron oxide nanoparticles using coaxial electrospray processing, *Mol. Pharm.* 14 (2017) 2010–2023, <https://doi.org/10.1021/acs.molpharmaceut.7b00109>.
- [48] P.K. Ajikumar, R. Lakshminarayanan, S. Valiyaveetil, Controlled deposition of thin films of calcium carbonate on natural and synthetic templates, *Cryst. Growth Des.* 4 (2003) 331–335, <https://doi.org/10.1021/cg034128e>.
- [49] N. Hassanein, H. Bougherara, A. Amlah, In-vitro evaluation of the bioactivity and the biocompatibility of a novel coated UHMWPE biomaterial for biomedical applications, *J. Mech. Behav. Biomed. Mater.* 101 (2020), 103409, <https://doi.org/10.1016/j.jmbmb.2019.103409>.
- [50] Food and Drug Administration (FDA), Food additive status list, <https://www.fda.gov/food/food-additives-petitions/food-additive-status-list/> 2019. (Accessed 25 December 2020).
- [51] D.S. Brinch, P.B. Pedersen, Toxicological studies on Laccase from *Myceliophthora thermophila* expressed in *Aspergillus oryzae*, *Regul. Toxicol. Pharmacol.* 35 (2002) 296–307, <https://doi.org/10.1006/rtp.2002.1538>.
- [52] K.-D. Hsu, S.-P. Wu, S.-P. Lin, C.-C. Lum, K.-C. Cheng, Enhanced active extracellular polysaccharide production from *Ganoderma formosanum* using computational modeling, *J. Food Drug Anal.* 25 (2017) 804–811, <https://doi.org/10.1016/j.jfda.2016.12.006>.
- [53] S.P. Santoso, C.-C. Chou, S.-P. Lin, F.E. Soetaredjo, S. Ismadij, C.-W. Hsieh, K.-C. Cheng, Enhanced production of bacterial cellulose by *Komactobacter intermedius* using statistical modeling, *Cellulose* 27 (2020) 2497–2509, <https://doi.org/10.1007/s10570-019-02961-5>.
- [54] F.S. Alatawi, N.H. Elsayed, M. Monier, Immobilization of horseradish peroxidase on modified nylon-6 fibers, *ChemistrySelect* 5 (2020) 6841–6850, <https://doi.org/10.1002/slct.202000818>.
- [55] M.M. Bradford, A rapid and sensitive method for the quantitation of microgram quantities of protein utilizing the principle of protein-dye binding, *Anal. Biochem.* 72 (1976) 248–254, [https://doi.org/10.1016/0003-2697\(76\)90527-3](https://doi.org/10.1016/0003-2697(76)90527-3).
- [56] E. Pereira, L. Barros, M. Dueñas, A.L. Antonio, C. Santos-Buelga, I.C.F.R. Ferreira, Gamma irradiation improves the extractability of phenolic compounds in *Ginkgo biloba* L, *Ind. Crop. Prod.* 74 (2015) 144–149, <https://doi.org/10.1016/j.indcrop.2015.04.039>.
- [57] D.N. Nguyen, C. Clasen, G. Van den Mooter, Pharmaceutical applications of Electrospraying, *J. Pharm. Sci.* 105 (2016) 2601–2620, <https://doi.org/10.1016/j.xphs.2016.04.024>.
- [58] M.C.C. Pinto, D.M.G. Freire, J.C. Pinto, Influence of the morphology of Core-Shell supports on the immobilization of lipase B from *Candida antarctica*, *Molecules* 19 (2014) 12509–12530, <https://doi.org/10.3390/molecules190812509>.
- [59] S. Estrada-Flores, A. Martínez-Luévano, P. Bartolo-Pérez, L.A. García-Cerda, T.E. Flores-Guía, E.N. Aguilera-González, Facile synthesis of novel calcium silicate hydratednylon 6/66 nanocomposites by solution mixing method, *RSC Adv.* 8 (2014) 41818–41827, <https://doi.org/10.1039/C8RA07116K>.
- [60] M.K. Khan, J. Luo, Z. Wang, R. Khan, X. Chen, Y. Wan, Alginate dialdehyde meets nylon membrane: a versatile platform for facile and green fabrication of membrane adsorbents, *J. Mater. Chem. B* 6 (2018) 1640–1649, <https://doi.org/10.1039/C7TB02966G>.
- [61] X. Yan, T. Xu, G. Chen, S. Yang, H. Liu, Q. Xue, Preparation and characterization of electrochemically deposited carbon nitride films on silicon substrate, *J. Phys. D: Appl. Phys.* 37 (2004) 907–913, <https://doi.org/10.1088/0022-3727/37/6/015>.
- [62] C.-N. Wu, S.-C. Fuh, S.-P. Lin, Y.-Y. Lin, H.-Y. Chen, J.-M. Liu, K.-C. Cheng, TEMPO-oxidized bacterial cellulose pellicle with silver nanoparticles for wound dressing, *Biomacromolecules* 9 (2018) 544–554, <https://doi.org/10.1021/acs.biomac.7b01660>.
- [63] C.-N. Wu, H.-M. Lai, Novel pH-responsive granules with tunable volumes from oxidized corn starches, *Carbohydr. Polym.* 208 (2019) 201–212, <https://doi.org/10.1016/j.carbpol.2018.12.058>.
- [64] K.P.V.K. Varma, P.S. Kishore, V.D. Prasad, Enhancement of heat transfer using Fe<sub>3</sub>O<sub>4</sub>/water nanofluid with varying cut-radius twisted tape inserts, *Int. J. Appl. Eng. Res.* 12 (2017) 7088–7095, <https://dx.doi.org/10.53762/IJAER/12.18.2017.7088-7095>.
- [65] S. Senthilvelan, R. Gnanamoorthy, Fiber reinforcement in injection molded nylon 6/6 spur gears, *Appl. Compos. Mater.* 13 (2006) 237–248, <https://doi.org/10.1007/s10443-006-9016-9>.
- [66] L.-T. Lim, I.J. Britt, M.A. Tung, Sorption and transport of water vapor in nylon 6,6 film, *Appl. Polym.* 71 (1999) 197–206, [https://doi.org/10.1002/\(SICI\)1097-4628\(19990110\)71:2<197::AID-APP2>3.0.CO;2-J](https://doi.org/10.1002/(SICI)1097-4628(19990110)71:2<197::AID-APP2>3.0.CO;2-J).
- [67] L. Nalbandian, E. Patrikiadou, V. Zaspalis, A. Patrikidou, E. Hatzidaki, C. N. Papandreou, Magnetic nanoparticles in medical diagnostic applications: synthesis, characterization and proteins conjugation, *Curr. Nanosci.* 12 (2016) 455–468, <https://doi.org/10.2174/1573413712666151210230002>.
- [68] T.U. Patro, H.D. Wagner, Influence of graphene oxide incorporation and chemical cross-linking on structure and mechanical properties of layer-by-layer assembled poly(vinyl alcohol)-Laponite free-standing films, *J. Polym. Sci. B Polym. Phys.* 54 (2016) 2377–2387, <https://doi.org/10.1002/polb.24226>.
- [69] C.C.S. Fortes, A.L. Daniel-da-Silva, A.M.R.B. Xavier, A.P.M. Tavares, Optimization of enzyme immobilization on functionalized magnetic nanoparticles for laccase biocatalytic reactions, *Chem. Eng. Process.* 117 (2017) 1–8, <https://doi.org/10.1016/j.cep.2017.03.009>.
- [70] A.I. El-Batal, N.M. ElKenawy, A.S. Yassin, M.A. Amin, Laccase production by *Pleurotus ostreatus* and its application in synthesis of gold nanoparticles, *Biotechnol. Rep.* 5 (2015) 31–39, <https://doi.org/10.1016/j.btre.2014.11.001>.
- [71] O.I. Kalaoglu-Altan, Y. Li, R. McMaster, A. Shaw, Z. Hou, M. Vergaeren, R. Hoogenboom, T.R. Dargaville, K.D. Clerck, Crosslinking of electrospon and bioextruded partially hydrolyzed poly(2-ethyl-2-oxazoline) using glutaraldehyde vapour, *Eur. Polym. J.* 120 (2019), 109218, <https://doi.org/10.1016/j.eurpolymj.2019.109218>.
- [72] R. Xu, R. Tang, Q. Zhou, F. Li, B. Zhang, Enhancement of catalytic activity of immobilized laccase for diclofenac biodegradation by carbon nanotubes, *Chem. Eng. J.* 262 (2015) 88–95, <https://doi.org/10.1016/j.cej.2014.09.072>.
- [73] MCAT review and MCAT prep online, oxygen containing compounds - aldehydes and ketones, <http://mcat-review.org/aldehydes-ketones.php> 2018. (Accessed 25 December 2020).
- [74] H. Wei, S. Chai, N. Hu, Z. Yang, L. Wei, L. Wang, The microwave-assisted solvothermal synthesis of a crystalline two-dimensional covalent organic framework with high CO<sub>2</sub> capacity, *Chem. Commun.* 51 (2015) 12178–12181, <https://doi.org/10.1039/C5CC04680G>.
- [75] P.G. Ingole, N.R. Thakare, K. Kim, H.C. Bajaj, K. Singh, H. Lee, Preparation, characterization and performance evaluation of separation of alcohol using crosslinked membrane materials, *New J. Chem.* 37 (2013) 4018–4024, <https://doi.org/10.1039/C3NJ00952A>.
- [76] A. Varshney, B. Ahmad, G. Rabbani, V. Kumar, S. Yadav, R.H. Khan, Acid-induced unfolding of didecameric keyhole limpet hemocyanin: detection and characterizations of decameric and tetrameric intermediate states, *Amino Acids* 39 (2010) 899–910, <https://doi.org/10.1007/s00726-010-0524-4>.



# Gene delivery using layer-by-layer functionalized multi-walled carbon nanotubes: design, characterization, cell line evaluation

Monika Kumari<sup>1</sup>, Chi-Hsien Liu<sup>1,2,3,4,\*</sup> , Wei-Chi Wu<sup>4,5</sup>, and Chun-Chao Wang<sup>6</sup>

<sup>1</sup> Department of Chemical and Materials Engineering, Chang Gung University, 259, Wen-Hwa First Road, Kwei-Shan, Tao-Yuan 333, Taiwan

<sup>2</sup> Research Center for Chinese Herbal Medicine and Research Center for Food and Cosmetic Safety, College of Human Ecology, Chang Gung University of Science and Technology, 261, Wen-Hwa First Road, Taoyuan, Taiwan

<sup>3</sup> Department of Chemical Engineering, Ming Chi University of Technology, 84, Gung-Juan Road, New Taipei City, Taiwan

<sup>4</sup> Department of Ophthalmology, Chang Gung Memorial Hospital, Linkou, 5, Fu-Hsing Street, Taoyuan, Taiwan

<sup>5</sup> College of Medicine, Chang Gung University, 259, Wen-Hwa First Road, Taoyuan, Taiwan

<sup>6</sup> Institute of Molecular Medicine and Department of Medical Science, National Tsing Hua University, 101, Kuang-Fu Road, Hsinchu, Taiwan

Received: 8 July 2020

Accepted: 3 December 2020

Published online:

15 January 2021

© The Author(s), under exclusive licence to Springer Science+Business Media, LLC part of Springer Nature 2021

## ABSTRACT

Multi-walled carbon nanotubes (MWCNTs) with special nanoneedle structure have emerged as new promising candidates for plasmid and drug delivery. However, the delivery is greatly limited by the high tendency of CNT to form aggregates, the “less dispersion problem,” and CNT cytotoxicity. Here, we described an extensive evaluation of the ability of layer-by-layer modification strategy to reduce CNT size and toxicity, and to shield CNT hydrophobic surfaces. The MWCNTs can be derivatized with carboxylate groups (cMWCNT) and sequentially functionalized with protein, cationic polyethylenimine (PEI), and polysaccharide. The protein coating, characterized by Fourier transform infrared and deconvolution methods, could serve as the hydrophilic, biocompatible matrix and scaffold for sequential conjugation. We found that coated PEI-enhanced electrostatic interactions between plasmid DNA and CNTs. The functionalized cMWCNTs were analyzed by thermogravimetric analysis, dynamic light scattering, and electron microscopy technologies. The conjugation of cMWCNTs–ovalbumin–PEI with oxidized pectin further promoted green fluorescence intensity by balancing the intracellular DNA release and were easier to disperse. Our in-depth study demonstrated that functionalized CNTs can be improved by fine-tuned process parameters of the protein–PEI–polysaccharide modification.

Handling Editor: Christopher Blanford.

Address correspondence to E-mail: CHL@mail.cgu.edu.tw



## Introduction

Recent developments in nucleic acid vehicles enable us to make targeted gene delivery [1–3]. Although viral vectors deliver genetic material with high efficiency, they cause side effects, resulting in cautious clinical use [4]. Non-viral nanomaterials, such as carbon nanotubes (CNTs), are promising alternative tools because of their unique electrical properties and ease of operation and functionalization [5]. CNTs are hollow cylinders and can be classified based on the number of layers of graphene: single-walled carbon nanotubes (SWCNTs) and multi-walled carbon nanotubes (MWCNTs). SWCNTs (with a diameter between 0.4 and 2 nm) were not able to pierce the cell membranes. In contrast, MWCNTs (with a diameter between 10 and 100 nm) are found able to be internalized in cells through direct penetration [6]. In addition, MWCNT modification allows customization to suit their potential as delivery tools in vitro and in vivo [7]. There is a demand to evaluate process parameters to broaden functionalization options for MWCNT delivery vehicles [8–10].

The main problems that limited the biological application of non-functionalized CNTs are their cytotoxicity and low solubility in water [11, 12]. Covalent functionalization, such as oxidation, and chemical conjugation with the cationic polymers (for example, polyethylenimine (PEI)) usually enhance MWCNT solubility; however, these modifications may increase dose-dependent cytotoxicity [13]. Non-covalent methods made MWCNTs less toxic, but damaged the transfection efficiency [14, 15]. The low transfection efficiency and high cytotoxic effect of functionalized MWCNTs restrict MWCNTs as gene delivery vectors [15]. Adopting a nature-inspired route, CNTs have been modified with protein-polysaccharide conjugates [16]. Functionalizing MWCNTs with proteins provide reactive groups and enhanced cell–CNT interaction [17]. Amino-functionalized MWCNT-delivered siRNAs have effectively inhibited the growth of tumor cells in vivo, as compared with clinically approved cationic liposome (DOTAP: cholesterol) [18]. Protein-functionalized MWCNTs have been shown to transfect difficult-to-transfect cells in vitro [19]. Protein-functionalized CNTs coupled with natural polysaccharides are used as basic formula for drug delivery because of their biocompatibility [20–22]. These studies show that

modified MWCNTs are suitable for use in preclinical or in vivo trials; however, each step of the functionalization processes is not yet optimized [23].

Here, we describe the development of layer-by-layer modification, a strategy for engineering of carboxylate MWCNTs (cMWCNTs)-based delivery carrier. The utility of ovalbumin (OVA) could improve biocompatibility, and oxidized pectin could reduce PEI cytotoxicity by decreasing the positive charge density. The functionalized cMWCNTs were carefully characterized by Fourier transform infrared (FTIR), thermogravimetric analysis, zeta potential, and TEM images. Finally, we demonstrate the ability of cMWCNTs–OVA–PEI-oxidized pectin as a delivery vehicle for hard-to-transfect cells.

## Materials and methods

### Materials

MWCNTs, zein, OVA, BSA, trypsin–EDTA, glutaraldehyde, chlorpromazine (CPZ), sodium azide (SA), genistein (Gen), monensin (Mon), PEI, sodium periodate, sodium cyanoborohydride, carbodiimide, pectin, and KBr were purchased from Sigma-Aldrich (St. Louis, MO, USA). Methyl- $\beta$ -cyclodextrin (MCD) was acquired from Wako Pure Chemical Industries, Ltd. (Osaka, Japan). Plasmid expressing green fluorescent protein (GFP-C3, size 4.7 kb) was from Takara Bio (Shiga, Japan) and amplified in *Escherichia coli* strain DH-5 $\alpha$ . The plasmid was purified from the cell pellets using a purification kit (GeneMark, Taipei, Taiwan). Fetal bovine serum (FBS) was purchased from Biological Industries (Haemek, Israel). All reagents were used without further purification.

### Oxidation and functionalization of MWCNTs

#### Oxidation of MWCNTs

The carboxylate MWCNTs (cMWCNTs) were generated based on established protocols [24]. Briefly, 40 mg of MWCNTs was dissolved in 10 mL concentrated H<sub>2</sub>SO<sub>4</sub>/HNO<sub>3</sub> (3:1, v/v) solution and evenly distributed by sonicating for 5 min. The mixture was incubated at 70 °C for 8 h. The mixture was sonicated for 1 min every hour during the incubation. After incubation, the mixture was centrifuged at



12,000 rpm for 5 min and cMWCNTs was washed six times with distilled water to remove excess acid. Finally, the cMWCNTs were dried overnight at 60 °C.

#### *Functionalization of cMWCNTs*

To establish MWCNT functionalization procedure, cMWCNTs were modified with protein, PEI, and then pectin. Briefly, 1 mg of cMWCNTs was dissolved in 500  $\mu$ L of water and sonicated for 5 min. The carboxyl group of cMWCNTs was activated using EDC/NHS linker to generate semi-stable amine-reactive NHS ester. Vortexed for 1 h at room temperature and centrifuged to remove free EDC/NHS. The activated cMWCNTs were mixed with 1 mg proteins (BSA, OVA, or zein) to generate protein-functionalized cMWCNT (cMWCNT–OVA, cMWCNT–BSA, and cMWCNT–zein). Next, protein-functionalized cMWCNTs and PEI were cross-linked with glutaraldehyde. Vortexed for 2 h at room temperature. cMWCNTs–OVA–PEI, cMWCNTs–BSA–PEI, and cMWCNTs–zein–PEI were washed three times with deionized water to remove unconjugated PEI.

#### *Periodate oxidation procedure for pectin*

To prepare oxidized pectin, 2 mg of pectin was dissolved in 500  $\mu$ L of distilled water. Ten mg of sodium periodate was dissolved in 500  $\mu$ L of distilled water. These two solutions were mixed and vortexed for 30 min at room temperature in the dark. Oxidized pectin was washed two times using 50 kDa Vivaspintube to remove the excess  $\text{NaIO}_4$  while maintaining the oxidized pectin in the retentate. The volume of purified oxidized pectin was about 600  $\mu$ L. Oxidized pectin and cMWCNTs–OVA–PEI were mixed in the presence of sodium cyanoborohydride (1 mg/mL) and vortexed for 2 h at room temperature in the dark. The imine bond between PEI amine and oxidized pectin can be further reduced to secondary amine and thus decreases the content of primary amine present on the surface of PEI. The cMWCNTs–OVA–PEI–oxidized pectin was washed three times with deionized water.

#### **Characterization of functionalized cMWCNTs**

The surface property of CNTs was characterized using transmission electron microscopy (TEM). A drop of diluted sample was dispersed onto a 100-mesh copper grid and dried overnight prior to observation. The presence of specific chemical groups of functionalized cMWCNTs was evaluated using Fourier transform infrared spectroscopy (FTIR). The sample spectra were analyzed using Bruker OPUS software. The surface charge of CNTs was tested at pH values from 3 to 11 using ZetaSizer<sup>®</sup> Nano ZS 90.

#### **Plasmid DNA condensation and protection assay**

The condensation of plasmid DNA onto functionalized cMWCNTs was analyzed using agarose gel assay. Briefly, 2–10  $\mu$ g of cMWCNTs–OVA–PEI or cMWCNTs–OVA–PEI–oxidized pectin was mixed with 1  $\mu$ g of DNA. Incubated for 30 min at room temperature. Functionalized cMWCNTs efficiently bound DNA to form the polyplex. The interaction of plasmid DNA with functionalized cMWCNTs was studied with gel electrophoresis in 1% agarose and tris-acetate–EDTA buffer at 80 V for 20 min and was visualized using Gel-Doc EZ Imager (Bio-Rad, Hercules, CA).

#### **GFP gene expression and cell compatibility**

Cells were seeded at 50,000 cells/well on 48-well culture plates. After reaching 80–90% confluence, cells were transfected with 300  $\mu$ L of freshly prepared polyplexes in serum-free DMEM medium and incubated for 6 h at 37 °C. The polyplex mixture was aspirated, and FBS-containing DMEM medium was added. Cells were cultured for 24 h. The cells were washed with PBS and fixed with ethanol/acetic acid solution (0.5 mL 5% acetic acid in 9 mL 95% ethanol) for 5 min at room temperature. The cell nuclei were stained by adding 300  $\mu$ L of Hoechst 33,342 (10 ppm) for 20 min. After cells were washed with PBS, GFP expression and cell viability were studied using IN cell analyzer 1000 at 10  $\times$  magnification. The excitation and emission wavelengths were 480 nm and

525 nm for GFP, and 350 nm and 455 nm for Hoechst 33,342.

The percentage of transfected cells is defined as:

$$\text{Transfect efficiency} = \frac{\text{Number of cells exhibiting both blue and green fluorescence}}{\text{Number of cells exhibiting blue fluorescence}} \times 100$$

The cell viability was analyzed by blue count from the nuclei stained with Hoechst 33,342. Hence, it is defined as:

$$\text{Cell viability} = \frac{\text{Number of cells exhibiting blue fluorescence in treated well}}{\text{Number of cells exhibiting blue fluorescence in control well}} \times 100$$

plasmid DNA [25]. However, our cMWCNTs modified with PEI (cMWCNTs–PEI) were highly toxic and low dispersible in culture medium which impeded

the transfection efficiency (Fig. S1). The protein moieties on CNTs can interact with cellular components, increase biocompatibility, and provide functional groups for further modification [26, 27]. To develop a

## Thermogravimetric analysis

Functionalized cMWCNTs (3–5 mg) were loaded in platinum pans and analyzed using thermogravimetric analyzer (Q50, TA Instruments). The thermal behaviors of the sample are studied in nitrogen under a constant flow rate. The samples were heated to 700 °C at a heating rate of 10 °C/minutes.

## Statistical analysis

All experiments were conducted at least two times measurement in duplicate. Data are reported as mean  $\pm$  standard deviation. Differences between two groups were determined using the two-tailed Student *t* test in Microsoft Excel 2010. Statistically, significant difference was considered when *p* value < 0.05.

## Results and discussion

### Functionalization and characterization of cMWCNTs

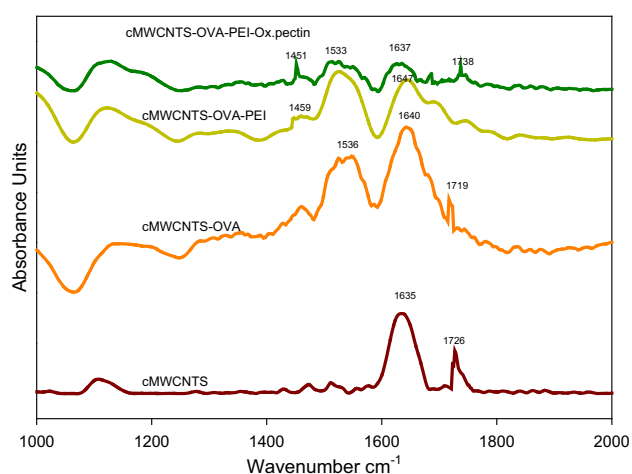
MWCNTs coated with positively charged PEI have been reported to increase the electrostatic affinity to

layer-by-layer MWCNT structure, protein was used to functionalize cMWCNTs via EDC/NHS linker. Then, MWCNTs–protein complexes were covalently conjugated with PEI via glutaraldehyde linker. Three proteins (BSA, OVA, and zein) were used to functionalize cMWCNTs. The protein content on functionalized cMWCNTs using bicinchoninic acid test is shown in Fig. S2. BSA and OVA could found on the cMWCNT surface at 0.6 mg/g level. Our experiment about protein-functionalized cMWCNTs demonstrated that cMWCNTs–OVA–PEI showed the highest level of transfection efficiency of GFP gene expression (Fig. S3). This was due to that protein influenced the cMWCNT solubility and spatial arrangement of residues on protein moiety affected cell endocytosis [28, 29]. The zein-modified cMWCNTs showed the poor dispersion in the medium. OVA, BSA, and zein were structurally different with respect to the amino acid sequence, helix loop arrangement, molecular weight, charge, and solubility. As compared with BSA and zein modification, OVA showed the highest transfection efficiency. Therefore, we chose cMWCNTs–OVA–PEI as our basic platform and conjugated it with oxidized pectin using Schiff base formation and reductive amination to create stable amine linkages.

**Table 1** Characterization of secondary structure for OVA, zein and BSA conjugated on cMWCNTs

| Secondary structure | Percentage |             |      |              |      |             |
|---------------------|------------|-------------|------|--------------|------|-------------|
|                     | OVA        | cMWCNTs–OVA | zein | cMWCNTs–zein | BSA  | cMWCNTs–BSA |
| $\beta$ -Sheet      | 27         | 10.7        | 11.7 | 7.0          | 49.8 | 9.8         |
| $\beta$ -Turn       | 27.6       | 56.3        | 36.1 | 34.6         | 21.9 | 48.6        |
| Helix               | 11.2       | 1.6         | 10.4 | –            | 21   | 8.6         |
| Random coil         | 33.4       | 4.6         | 52.0 | –            | –    | –           |
| Antiparallel sheet  | –          | 25.8        | –    | –            | 7    | 16.3        |
| Indefinite          | –          | –           | –    | 57.8         | 0.3  | 16.2        |

–: not determined

**Figure 1** FTIR spectra of cMWCNTs (red line), cMWCNTs–OVA (orange line), cMWCNTs–OVA–PEI (yellow line), and cMWCNTs–OVA–PEI-oxidized pectin (green line).

We quantified protein secondary structure from Fourier transform infrared (FTIR) spectra of proteins before and after binding to the surface of CNTs. The Amide I region of FTIR spectra ( $1600\text{--}1700\text{ cm}^{-1}$ , Fig. S4) is used for the analysis because it represents the C=O stretching vibration of the peptide backbone [30]. Amide I peak deconvolution showed the secondary structure composition as given in Table 1. When binding to the MWCNTs, a decrease in the  $\beta$ -sheet and  $\alpha$ -helix contents was observed [31]. This result supported the idea that protein molecules unfolded into a loop and wrapped on the cMWCNTs.

### FTIR spectra and TEM images of functionalized cMWCNTs

FTIR spectra were used to qualitatively analyze functional groups on MWCNTs (Fig. 1). Carbonyl stretching frequency (C=O) around  $1726\text{ cm}^{-1}$  and C=C stretching around  $1635\text{ cm}^{-1}$  were present in

cMWCNT data. In cMWCNTs–OVA data, the presence of amide bond formation (new peaks between  $1500$  and  $1600\text{ cm}^{-1}$ ) and decreased intensity of carboxyl group peak ( $1735\text{ cm}^{-1}$ ) provided the evidence of OVA conjugation [32]. In the cMWCNTs–OVA–PEI sample, the presence of the Schiff base bond was found around  $1459\text{ cm}^{-1}$  and decreased intensity of peak between  $1700$  and  $1740\text{ cm}^{-1}$  provided the evidence of PEI conjugation. In cMWCNTs–OVA–PEI-oxidized pectin data, we observed the presence of COOH group of oxidized pectin ( $1738\text{ cm}^{-1}$ ). In particular, Schiff base between the aldehyde of oxidized pectin and the free amine groups induced shift of  $1459\text{ cm}^{-1}$  to  $1451\text{ cm}^{-1}$ , consistent with previous reports [33]. Through transmission electron microscopy (TEM), the morphology and structure of pristine and modified MWCNTs were characterized (Fig. 2). cMWCNTs and cMWCNTs–OVA were shortened, but no surface damage by acid treatment or structural alternation by OVA modification was observed. PEI molecules induced aggregation, which could be reversed by binding of oxidized pectin (Fig. 2d, e). Thus, this work provides a simple yet potent strategy to prepare layer-by-layer functionalized cMWCNTs.

### Thermogravimetric and zeta potential analysis of functionalized cMWCNTs

Thermogravimetric analysis (TGA) is used to quantitatively determine functional groups on the surface of CNTs. CNTs can be heated up to  $700\text{ }^{\circ}\text{C}$ , and any changes in weight loss can be used to characterize the CNT modification. Our study revealed that cMWCNTs are thermally stable up to  $700\text{ }^{\circ}\text{C}$  (Fig. 3).

The TGA curves of the cMWCNTs–OVA–PEI and cMWCNTs–OVA–PEI-oxidized pectin showed the weight loss of  $\sim 70\%$ . This is because that functional

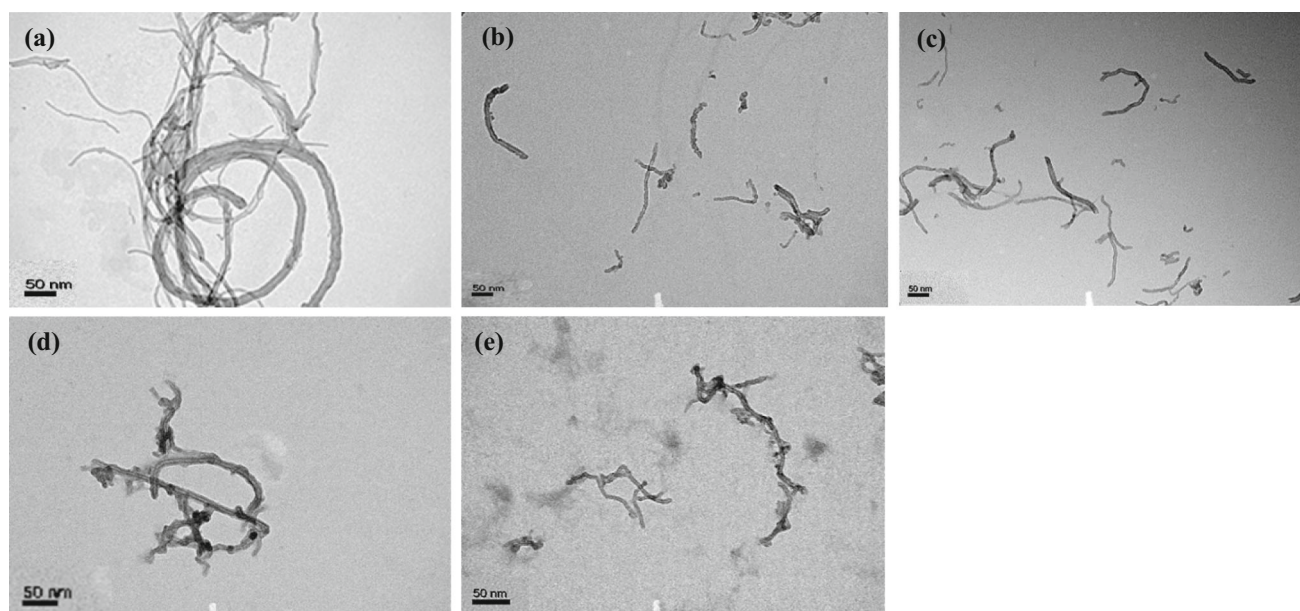


**Figure 2** TEM image of **a** pristine MWCNTs, **b** cMWCNTs, **c** cMWCNTs–OVA, **d** cMWCNTs–OVA–PEI, and **e** cMWCNTs–OVA–PEI-oxidized pectin. The scale bar was 50 nm.

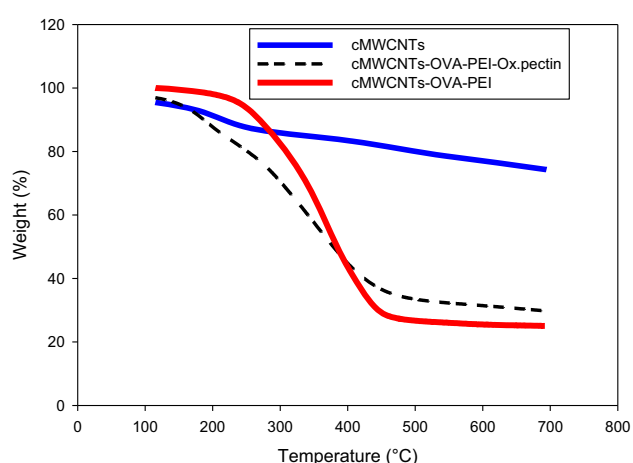


**Figure 3** Thermogravimetric data for cMWCNTs (blue line) and cMWCNT–OVA–PEI (green line), and cMWCNTs–OVA–PEI-oxidized pectin (red line).

groups were expected to decompose at high temperatures [34]. Interestingly, pectin coating thermally stabilized functionalized cMWCNTs. The extent of protein, cationic polymer, and polysaccharide on cMWCNTs was quantified by thermogravimetric analysis. In addition, we determine the size, polydispersity index (PDI), and zeta potential of CNTs. Zeta potentials as a function of pH for MWCNTs are given in Fig. 4a. cMWCNTs and cMWCNTs–OVA had isoelectric points at pH 7. In cMWCNTs–OVA–PEI and cMWCNTs–OVA–PEI-oxidized pectin, the

isoelectric points move to a basic value at pH 9. The modification with PEI increased the surface positive charge, size, and PDI of cMWCNTs–OVA. The further introduction of oxidized pectin decreased the zeta potential and had uniform size distribution. Together, oxidized pectin provided balance charges, which decreased the zeta potential, mildly reduced the DNA binding, and enhanced the DNA release in cells. To assess the binding ability to plasmid DNA, we performed agarose gel retardation assay (Fig. S3c). Both cMWCNTs–OVA–PEI and cMWCNTs–OVA–PEI-oxidized pectin were able to bind plasmid DNA by forming polyplexes that were unable to migrate through the gel. As expected, positive charged cMWCNTs–OVA–PEI showed higher DNA condensation efficacy, which was reflected by the absence of free DNA. The coating of oxidized pectin decreased the net positive charge and mildly reduced the DNA binding via electrostatic interaction. Another purpose of incorporating oxidized pectin onto the surface of modified cMWCNTs–OVA–PEI was to reduce the cMWCNTs aggregation tendency. Previously, primary amine has been reported to disrupt protein kinase C function and PEI itself induced LDH leakage to greater extents compared with other cationic polymers due to high charge density [35]. The excess positive charge of cationic polymer leads to high cytotoxicity toward cells. Therefore, many researchers shield the excess



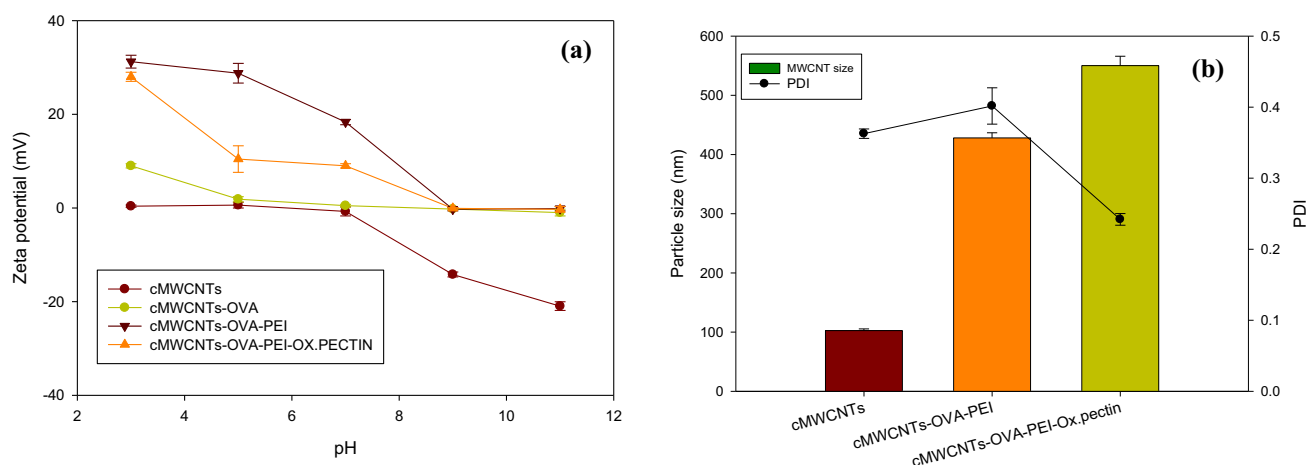


**Figure 4** Physiochemical characterization of functionalized cMWCNTs and non-functionalized cMWCNTs. **a** zeta potential and **b** size and PDI value. The measurements were taken in triplicate and error bar represents the standard deviation.

positive charge of cationic polymer with anionic macromolecules to enhance the cell viability without compromising the transfection efficiency [36, 37].

### Gene delivery, biocompatibility, and internalization mechanism

#### Transfection efficiency

CNT-based delivery systems were generally easy to prepare and were valuable for promoting DNA delivery to hard-to-transfect cells and inducing less cell death. The transfection of CNT is dependent on loading of pDNA, mammalian cell line types, dispersion, and agglomeration behavior, and functional groups on the surface of CNTs [14]. We explored two

functionalized cMWCNTs, cMWCNTs–OVA–PEI and cMWCNTs–OVA–PEI–oxidized pectin, at different weight ratios (6:1 and 8:1) to enhance DNA transfection efficiency. We found that our functionalized cMWCNTs were applicable to three different cell types of different origins, CHO-K1 (derived from Chinese hamster ovary), Caco-2 (derived from human epithelial colorectal adenocarcinoma), and RGC-5 (derived from retinal ganglion cells) (Fig. 5). In addition, increasing CNT/DNA ratio further enhanced the transfection efficiency.

Previous studies had shown that pectin-enhanced cellular uptake of the nanoparticles through receptor-mediated endocytosis [38, 39]. We next tested whether the coated pectin impact DNA delivery of CNTs. We observed that coated oxidized pectin greatly

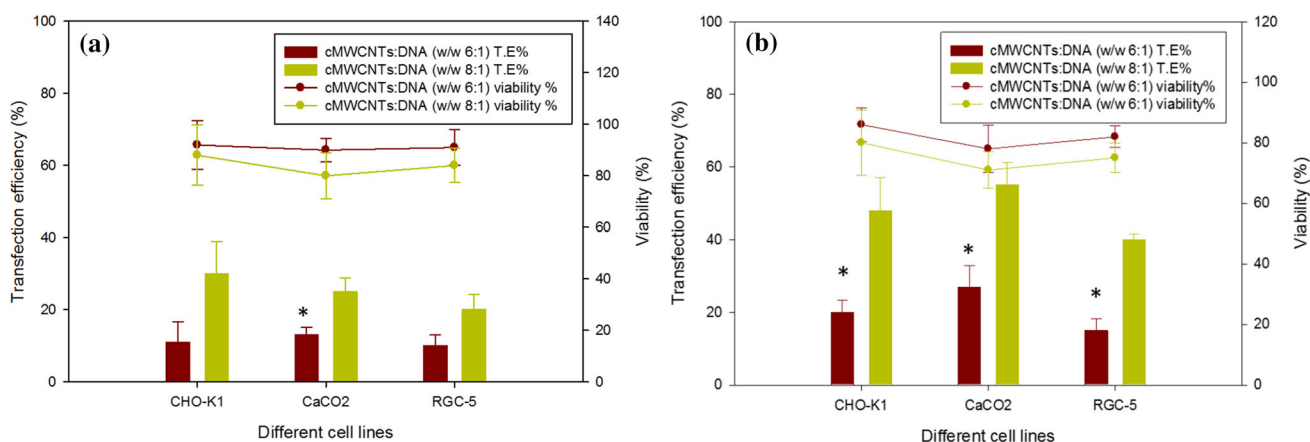


**Figure 5** Transfection efficiency of **a** cMWCNTs–OVA–PEI and **b** cMWCNTs–OVA–PEI–oxidized pectin in three different cell lines. The measurements were taken in triplicate and error bar

represents the standard deviation. Stars (\*) indicate the significant difference as compared with the 8:1 weight ratio of each cell line.



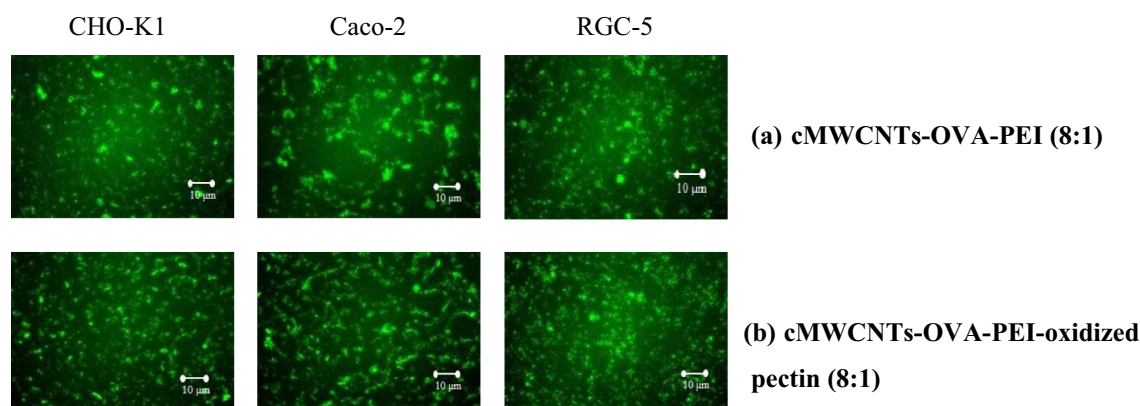


**Figure 6** Fluorescence images of different cell lines (CHO-K1, Caco-2, and RGC-5) transfected at a 8:1 weight ratio of cMWCNT to DNA in serum-free condition. **a** cMWCNTs–OVA–PEI and **b** cMWCNTs–OVA–PEI-oxidized pectin.

enhanced transfection efficiency in three cell lines, and pectin-functionalized MWCNTs were clearly less toxic (Fig. 5), consistent with the previous study [40]. We hypothesized that our suitably functionalized cMWCNTs–OVA–PEI-oxidized pectin may serve as a good platform for gene delivery in difficult-to-transfect cells. To address this, we attached plasmids encoding green fluorescent protein (GFP) to functionalized cMWCNTs via electrostatic interaction and transported the polyplex into the cell. As shown in Fig. 6a, b, cMWCNTs–OVA–PEI/plasmid polyplex caused high levels of GFP expression in a wide range

of mammalian cells. In addition, more GFP expressing cells were found after treatment with pectin-functionalized MWCNTs (cMWCNTs–OVA–PEI-oxidized pectin).

### Cell viability

Previous studies have shown that CNTs in their bare state and free PEI were toxic [41]. We completed additional experiments to directly evaluate the modified CNTs at each reaction step to analyze their toxicity and transfection efficiency. We found that

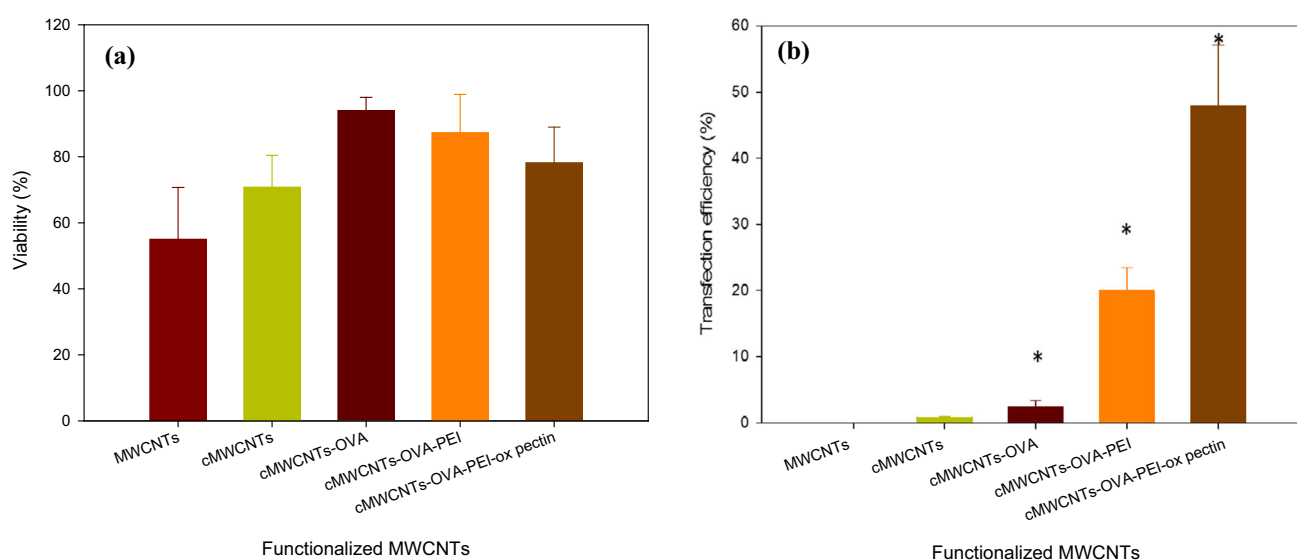


**Figure 7** Biocompatibility and transfection efficiency of functionalized MWCNTs in CHO-K1 cells. **a** Cell viability. **b** Transfection efficiency. The cells treated with polyplexes were prepared by mixing 8 μg of each modified cMWCNTs or pristine MWCNTs with 1 μg of pDNA. The cell viability and transfection

efficiency was analyzed using IN Cell analyzer 1000 microscope. The measurements were taken in triplicate and error bar represents the standard deviation. Stars (\*) indicate the significant difference as compared with control (MWCNTs).

our functionalization strategy reduced CNT toxicity and enabled MWCNTs to transfect the difficult-to-transfect cell lines, CHO-K1 (Fig. 7). As predicted, CNT *in vitro* biocompatibility was increased by OVA, but decreased by PEI. More importantly, optimal transfection was achieved using tailored MWCNTs functionalization with pectin, up to two–threefold higher than using PEI coating alone. The stealth role of the pectin on the modified MWCNTs may contribute to the transfection efficiency without compromising the cell viability.

### Internalization mechanism

If coated pectin directly enhanced CNT/DNA delivery, at least some of the cellular internalization pathways of pectin were responsible for the cellular uptake of pectin-functionalized CNT [14, 42, 43]. The most obvious candidate for such pectin-dependent internalization was endocytosis. Previously, Rejman et al. demonstrated that the particle size range from 200 to 500 nm could be internalized via caveolae dependent pathway, and mainly affected by cholesterol depletion [44]. Katav et al. have reported that the pectin nanoparticles deliver the plasmid DNA via binding to galactose-binding lectins present on the cell surface [40]. To investigate how internalization influences pectin-functionalized CNT uptake, internalization pathways were inhibited individually (Fig. 8). We found that inhibitors of ATPase (sodium azide (SA)), caveolae-mediated endocytosis (genistein (Gen)) and clathrin-mediated endocytosis

(chlorpromazine (CPZ) and monensin (Mon)) all resulted in a slight decrease in CNT internalization in CHO-K1 and Caco-2 cells. Moreover, the cholesterol-depleting agent, methyl- $\beta$ -cyclodextrin (MCD), blocked CNT uptake. This altered CNT uptake is pectin-dependent at least in CHO-K1 cells, suggesting that cholesterol-dependent endocytic processes may be required for pectin-enhanced CNT uptake.

### Conclusion

To serve as carriers for gene delivery, CNTs were often functionalized with biopolymers to improve biocompatibility and conjugated with cationic molecules to interact electrostatically with DNAs (Table 2) [45–47]. The major challenges for using MWCNTs as a gene delivery vector were toxicity and low dispersion that reduces the gene delivery efficiency. The study described here overcame this problem by layer-by-layer modification strategy using OVA, PEI, and oxidized pectin to functionalize MWCNTs. MWCNT modifications were carefully characterized by FTIR, thermogravimetric analysis, zeta potential, and TEM images. We showed that our functionalized MWCNTs could achieve good transfection efficiency and reduce cellular toxicity in multiple hard-to-transfect cell lines. This strategy could expand the toolbox for developing biomedical applications utilizing tailored carbon nanotubes.

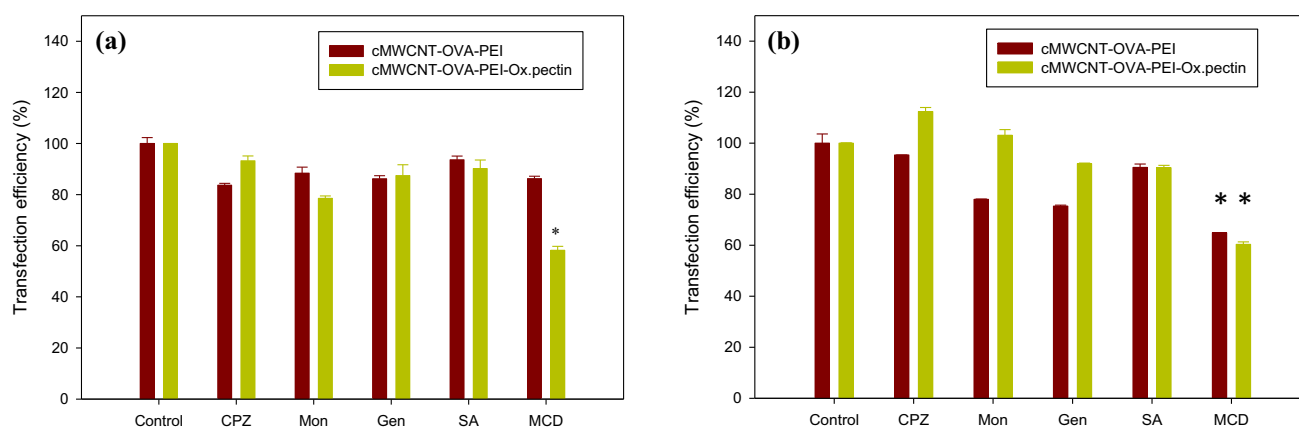


**Figure 8** Effect of endocytic inhibitors on the transfection efficiency of both functionalized cMWCNTs in **a** CHO-K1 and **b** Caco-2 cells. The cells without inhibitor treatment were considered as control and the percentage of transfection

efficiency was calculated by considering the transfection efficiency of control as 100%. The measurements were taken in duplicate and error bar represents standard deviation. Stars (\*) indicate the significant difference as compared with controls.

**Table 2** Literature survey of plasmid DNA delivery using MWCNTs

| Modified MWCNT                 | Animal, tissue or cell type     | Plasmid cargo                   | Transfection efficiency      | Viability | Reference    |
|--------------------------------|---------------------------------|---------------------------------|------------------------------|-----------|--------------|
| PEI–SWCNT by disulfide bond    | Murine neuroblastoma cells      | Luciferase                      | 32%                          | 62%       | [45]         |
| PEI–cholesterol–SWCNT          | HEK293                          | GFP                             | Fourfold over control        | 46%       | [46]         |
| COOH–SWCNT                     | Fish koi muscle                 | Herpesvirus immunogenic protein | 19-fold over plasmid control | –         | [48]         |
| COOH–SWCNT                     | Bovine skin fibroblast cells    | GFP                             | 3.30%                        | 46%       | [19]         |
| Pegylated peptide–SWCNT        | Human lung adenocarcinoma cells | Orange fluorescent protein      | 26%                          | –         | [49]         |
| PEI–phospholipid–SWCNT         | Murine neuroblastoma cells      | eGFP                            | 19-fold over PEI control     | 62%       | [47]         |
| Glycopolymer–SWCNT             | HeLa cells                      | eGFP                            | 22%                          | 65%       | [50]         |
| MWCNTs–OVA–PEI-oxidized pectin | CHO, RGC5, Caco-2 cells         | eGFP                            | > 55%                        | > 80%     | Present work |

–: Not mentioned

## Acknowledgements

We express gratitude to Ministry of Science and Technology (MOST 106-2221-E-182-050, 108-2221-E-182-039), Chang Gung University (BMRP 758), and Chang Gung Memorial Hospital (2J0161, 2H0072, 2H0073) for funding and supporting this research.

## Compliance with ethical standards

**Conflict of interest** The authors declare that they have no conflict of interest.

**Supplementary Information:** The online version contains supplementary material available at (<http://doi.org/10.1007/s10853-020-05648-6>).

## References

- [1] Chen X, Zhang Q, Li J, Yang M, Zhao N, Xu FJ (2018) Rattle-structured rough nanocapsules with in-situ-formed gold nanorod cores for complementary gene/chemo/photothermal therapy. *ACS Nano* 12:5646–5656. <https://doi.org/10.1021/acsnano.8b01440>
- [2] Zhao N, Fan W, Zhao X et al (2020) Polycation-carbon nanohybrids with superior rough hollow morphology for the NIR-II responsive multimodal therapy. *ACS Appl Mater Interfaces* 12:11341–11352. <https://doi.org/10.1021/acsnano.8b01440>
- [3] Feng L, Yang X, Shi X et al (2013) Polyethylene glycol and polyethylenimine dual-functionalized nano-graphene oxide for photothermally enhanced gene delivery. *Small* 9:1989–1997. <https://doi.org/10.1002/sml.201202538>
- [4] Naldini L (2015) Gene therapy returns to centre stage. *Nature* 526:351–360. <https://doi.org/10.1038/nature15818>
- [5] Ibraheem D, Elaissari A, Fessi H (2014) Gene therapy and DNA delivery systems. *Int J Pharm* 459:70–83. <https://doi.org/10.1016/j.ijpharm.2013.11.041>
- [6] Taghavi S, Abnous K, Taghdisi SM, Ramezani M, Alibolandi M (2020) Hybrid carbon-based materials for gene delivery in cancer therapy. *J Control Release* 318:158–175. <https://doi.org/10.1016/j.jconrel.2019.12.030>
- [7] de Menezes BRC, Rodrigues KF, da Silva Fonseca BC, Ribas RG, do Amaral montanheiroThim TLGP (2019) Recent advances in the use of carbon nanotubes as smart biomaterials. *J Mater Chem B* 7:1343–1360. <https://doi.org/10.1039/C8TB02419G>
- [8] Hu Y, Liu S, Li X et al (2018) Facile preparation of bio-compatible poly(l-lactic acid)-modified halloysite nanotubes/poly(ε-caprolactone) porous scaffolds by solvent evaporation of Pickering emulsion templates. *J Mater Sci* 53:14774–14788. <https://doi.org/10.1007/s10853-018-2588-6>
- [9] Liu H, Wang ZG, Liu SL et al (2019) Intracellular pathway of halloysite nanotubes: potential application for antitumor drug delivery. *J Mater Sci* 54:693–704. <https://doi.org/10.1007/s10853-018-2775-5>
- [10] Nasari M, Semnani D, Hadjianfar M, Amanpour S (2020) Poly (ε-caprolactone)/poly (N-vinyl-2-pyrrolidone) core–

- shell nanofibers loaded by multi-walled carbon nanotubes and 5-fluorouracil: an anticancer drug delivery system. *J Mater Sci* 55:10185–10201. <https://doi.org/10.1007/s10853-020-04784-3>
- [11] Bates K, Kostarelos K (2013) Carbon nanotubes as vectors for gene therapy: Past achievements, present challenges and future goals. *Adv Drug Deliv Rev* 65:2023–2033. <https://doi.org/10.1016/j.addr.2013.10.003>
- [12] Alshehri R, Ilyas AM, Hasan A, Arnaout A, Ahmed F, Memic A (2016) Carbon nanotubes in biomedical applications: factors, mechanisms, and remedies of toxicity. *J Med Chem* 59:8149–8167. <https://doi.org/10.1021/acs.jmedchem.5b01770>
- [13] Nunes A, Amsharov N, Guo C et al (2010) Hybrid polymer-grafted multiwalled carbon nanotubes for in vitro gene delivery. *Small* 6:2281–2291. <https://doi.org/10.1002/sml.201000864>
- [14] Liu YZ, Ma D et al (2013) Biocompatible multi-walled carbon nanotube-chitosan-folic acid nanoparticle hybrids as GFP gene delivery materials. *Colloids Surf B Biointerfaces* 111:224–231. <https://doi.org/10.1016/j.colsurfb.2013.06.010>
- [15] Saito N, Haniu H, Usui Y et al (2014) Safe clinical use of carbon nanotubes as innovative biomaterials. *Chem Rev* 114:6040–6079. <https://doi.org/10.1021/cr400341h>
- [16] Katouzian I, Jafari SM (2019) Protein nanotubes as state-of-the-art nanocarriers: Synthesis methods, simulation and applications. *J Control Release* 303:302–318. <https://doi.org/10.1016/j.jconrel.2019.04.026>
- [17] Pantarotto D, Singh R, McCarthy D et al (2004) Functionalized carbon nanotubes for plasmid DNA gene delivery. *Angew Chem Int Ed Engl* 43:5242–5246. <https://doi.org/10.1002/anie.200460437>
- [18] Podesta JE, Al-Jamal KT, Herrero MA et al (2009) Antitumor activity and prolonged survival by carbon-nanotube-mediated therapeutic siRNA silencing in a human lung xenograft model. *Small* 5:1176–1185. <https://doi.org/10.1002/sml.200801572>
- [19] Munk M, De Souza Salomão Zanette R, De Almeida Camargo LS et al (2017) Using carbon nanotubes to deliver genes to hard-to-transfect mammalian primary fibroblast cells. *Biomed Phys Eng Express* 3:045002. <https://doi.org/10.1088/2057-1976/aa7927>
- [20] Naqash F, Masoodi FA, Rather SA, Wani SM, Gani A (2017) Emerging concepts in the nutraceutical and functional properties of pectin—a review. *Carbohydr Polym* 168:227–239. <https://doi.org/10.1016/j.carbpol.2017.03.058>
- [21] Li A, Wu B, Mu C, Lin W (2011) Concomitant degradation in periodate oxidation of carboxymethyl cellulose. *Carbohydr Polym* 84:881–886. <https://doi.org/10.1016/j.carbpol.2010.12.026>
- [22] Hu Q, Luo Y (2018) Recent advances of polysaccharide-based nanoparticles for oral insulin delivery. *Int J Biol Macromol* 120:775–782. <https://doi.org/10.1016/j.ijbiomac.2018.08.152>
- [23] Singh A, Hua Hsu M, Gupta N et al (2020) Derivatized carbon nanotubes for gene therapy in mammalian and plant cells. *ChemPlusChem* 85:466–475. <https://doi.org/10.1002/cplu.201900678>
- [24] Celik E, Liu L, Choi H (2011) Protein fouling behavior of carbon nanotube/polyethersulfone composite membranes during water filtration. *Water Res* 45:5287–5294. <https://doi.org/10.1016/j.watres.2011.07.036>
- [25] Benjaminsen RV, Matthebjerg MA, Henriksen JR, Moghimi SM, Andresen TL (2013) The possible “proton sponge” effect of polyethylenimine (PEI) does not include change in lysosomal pH. *Mol. Ther* 21:149–157. <https://doi.org/10.1038/mt.2012.185>
- [26] Nepal D, Geckeler KE (2007) Proteins and carbon nanotubes: close encounter in water. *Small* 3:1259–1265. <https://doi.org/10.1002/sml.200600511>
- [27] Zhang T, Song X, Kang D et al (2015) Modified bovine serum albumin as an effective charge-reversal platform for simultaneously improving the transfection efficiency and biocompatibility of polyplexes. *J Mater Chem B* 3:4698–4706. <https://doi.org/10.1039/C5TB00548E>
- [28] Zeinabad HA, Zarrabian A, Saboury AA, Alizadeh AM, Falahati M (2016) Interaction of single and multi wall carbon nanotubes with the biological systems: tau protein and PC12 cells as targets. *Sci Rep* 6:26508. <https://doi.org/10.1038/srep26508>
- [29] Hashida Y, Umeyama T, Mihara J et al (2012) Development of a novel composite material with carbon nanotubes assisted by self-assembled peptides designed in conjunction with beta-sheet formation. *J Pharm Sci* 101:3398–3418. <https://doi.org/10.1002/jps.23144>
- [30] Kumari M, Liu C-H, Wu W-C (2018) Protein moiety in oligochitosan modified vector regulates internalization mechanism and gene delivery: polyplex characterization, intracellular trafficking and transfection. *Carbohydr Polym* 202:143–156. <https://doi.org/10.1016/j.carbpol.2018.08.131>
- [31] Yang M, Meng J, Mao X et al (2010) Carbon nanotubes induce secondary structure changes of bovine albumin in aqueous phase. *J Nanosci Nanotechnol* 10:7550–7553. <https://doi.org/10.1166/jnn.2010.2825>
- [32] Krimm S, Bandekar J (1986) Vibrational spectroscopy and conformation of peptides, polypeptides, and proteins. In: Anfinsen CB, Edsall JT, Richards FM (eds) *Advances in Protein Chemistry*. Academic Press, Cambridge
- [33] Chetouani A, Elkolli M, Bounekhel M, Benachour D (2017) Chitosan/oxidized pectin/PVA blend film: mechanical and

- biological properties. *Polym Bull* 74:4297–4310. <https://doi.org/10.1007/s00289-017-1953-y>
- [34] Caoduro C, Kacem R, Boukari K et al (2016) Carbon nanotube-Protamine hybrid: evaluation of DNA cell penetration. *Carbon* 96:742–752. <https://doi.org/10.1016/j.carbon.2015.09.098>
- [35] Jiang HL, Kwon JT, Kim YK et al (2007) Galactosylated chitosan-graft-polyethylenimine as a gene carrier for hepatocyte targeting. *Gene Ther* 14:1389–1398. <https://doi.org/10.1038/sj.gt.3302997>
- [36] Zintchenko A, Philipp A, Dehshahri A, Wagner E (2008) Simple modifications of branched PEI lead to highly efficient siRNA carriers with low toxicity. *Bioconjug Chem* 19:1448–1455. <https://doi.org/10.1021/bc800065f>
- [37] Rezaee M, Gholami L, Gildeh MS, Ramezani M, Kazemi Oskuee R (2019) Charge reduction: an efficient strategy to reduce toxicity and increase the transfection efficiency of high molecular weight polyethylenimine. *J Pharm Investig* 49:105–114. <https://doi.org/10.1007/s40005-018-0388-2>
- [38] Liu L, Fishman ML, Kost J, Hicks KB (2003) Pectin-based systems for colon-specific drug delivery via oral route. *Biomaterials* 24:3333–3343. [https://doi.org/10.1016/S0142-9612\(03\)00213-8](https://doi.org/10.1016/S0142-9612(03)00213-8)
- [39] Salatin S, Yarikhosroushahi A (2017) Overviews on the cellular uptake mechanism of polysaccharide colloidal nanoparticles. *J Cell Mol Med* 21:1668–1686. <https://doi.org/10.1111/jcmm.13110>
- [40] Katav T, Liu L, Traitel T, Goldbart R, Wolfson M, Kost J (2008) Modified pectin-based carrier for gene delivery: cellular barriers in gene delivery course. *J Control Release* 130:183–191. <https://doi.org/10.1016/j.jconrel.2008.06.002>
- [41] Varkouhi AK, Foillard S, Lammers T et al (2011) siRNA delivery with functionalized carbon nanotubes. *Int J Pharm* 416:419–425. <https://doi.org/10.1016/j.ijpharm.2011.02.009>
- [42] Kostarelos K, Lacerda L, Pastorin G et al (2007) Cellular uptake of functionalized carbon nanotubes is independent of functional group and cell type. *Nat Nanotechnol* 2:108–113. <https://doi.org/10.1038/nnano.2006.209>
- [43] Ravelli D, Merli D, Quartarone E, Profumo A, Mustarelli P, Fagnoni M (2013) PEGylated carbon nanotubes: preparation, properties and applications. *RSC Adv* 3:13569–13582. <https://doi.org/10.1039/C3RA40852C>
- [44] Rejman J, Oberle V, Zuhorn IS, Hoekstra D (2004) Size-dependent internalization of particles via the pathways of clathrin- and caveolae-mediated endocytosis. *Biochem J* 377:159–169. <https://doi.org/10.1042/bj20031253>
- [45] Nia AH, Eshghi H, Abnous K, Ramezani M (2017) The intracellular delivery of plasmid DNA using cationic reducible carbon nanotube—Disulfide conjugates of polyethylenimine European. *J Pharm Sci* 100:176–186. <https://doi.org/10.1016/j.ejps.2017.01.014>
- [46] Kong F, Liu F, Li W et al (2016) Smart carbon nanotubes with laser-controlled behavior in gene delivery and therapy through a non-digestive trafficking pathway. *Small* 12:6753–6766. <https://doi.org/10.1002/sml.201601092>
- [47] Behnam B, Shier WT, Nia AH, Abnous K, Ramezani M (2013) Non-covalent functionalization of single-walled carbon nanotubes with modified polyethylenimines for efficient gene delivery. *Int J Pharm* 454:204–215. <https://doi.org/10.1016/j.ijpharm.2013.06.057>
- [48] Hu F, Li Y, Wang Q et al (2020) Carbon nanotube-based DNA vaccine against koi herpesvirus given by intramuscular injection. *Fish Shellfish Immunol* 98:810–818. <https://doi.org/10.1016/j.fsi.2019.11.035>
- [49] Ohta T, Hashida Y, Higuchi Y, Yamashita F, Hashida M (2017) Vitro cellular gene delivery employing a novel composite material of single-walled carbon nanotubes associated with designed peptides with pegylation. *J Pharm Sci* 106:792–802. <https://doi.org/10.1016/j.xphs.2016.10.025>
- [50] Ahmed M, Jiang X, Deng Z, Narain R (2009) Cationic glyco-functionalized single-walled carbon nanotubes as efficient gene delivery vehicles. *Bioconjug Chem* 20:2017–2022. <https://doi.org/10.1021/bc900229v>

**Publisher's Note** Springer Nature remains neutral with regard to jurisdictional claims in published maps and institutional affiliations.



## Article

# An Anti-Inflammatory 2,4-Cyclized-3,4-Secospongian Diterpenoid and Furanoterpene-Related Metabolites of a Marine Sponge *Spongia* sp. from the Red Sea

Chi-Jen Tai <sup>1</sup>, Chiung-Yao Huang <sup>2</sup>, Atallah F. Ahmed <sup>3,4,\*</sup> , Raha S. Orfali <sup>3</sup>, Walied M. Alarif <sup>5</sup>, Yusheng M. Huang <sup>6,7</sup> , Yi-Hsuan Wang <sup>8</sup>, Tsong-Long Hwang <sup>8,9,10</sup>  and Jyh-Horng Sheu <sup>1,2,11,12,\*</sup>

- <sup>1</sup> Doctoral Degree Program in Marine Biotechnology, National Sun Yat-sen University, Kaohsiung 80424, Taiwan; chijentai@g-mail.nsysu.edu.tw
- <sup>2</sup> Department of Marine Biotechnology and Resources, National Sun Yat-sen University, Kaohsiung 80424, Taiwan; betty8575@yahoo.com.tw
- <sup>3</sup> Department of Pharmacognosy, College of Pharmacy, King Saud University, Riyadh 11451, Saudi Arabia; rorfali@ksu.edu.sa
- <sup>4</sup> Department of Pharmacognosy, Faculty of Pharmacy, Mansoura University, Mansoura 35516, Egypt
- <sup>5</sup> Department of Marine Chemistry, Faculty of Marine Sciences, King Abdulaziz University, Jeddah 21589, Saudi Arabia; welaref@kau.edu.sa
- <sup>6</sup> Department of Marine Recreation, National Penghu University of Science and Technology, Magong, Penghu 88046, Taiwan; yusheng@gms.npu.edu.tw
- <sup>7</sup> Tropical Island Sustainable Development Research Center, National Penghu University of Science and Technology, Magong, Penghu 88046, Taiwan
- <sup>8</sup> Graduate Institute of Natural Products, College of Medicine, Chang Gung University, Taoyuan 33302, Taiwan; d0901501@cgu.edu.tw (Y.-H.W.); htl@mail.cgu.edu.tw (T.-L.H.)
- <sup>9</sup> Research Center for Chinese Herbal Medicine, Research Center for Food and Cosmetic Safety, Graduate Institute of Health Industry Technology, College of Human Ecology, Chang Gung University of Science and Technology, Taoyuan 33303, Taiwan
- <sup>10</sup> Department of Anesthesiology, Chang Gung Memorial Hospital, Taoyuan 33305, Taiwan
- <sup>11</sup> Graduate Institute of Natural Products, Kaohsiung Medical University, Kaohsiung 80708, Taiwan
- <sup>12</sup> Department of Medical Research, China Medical University Hospital, China Medical University, Taichung 404333, Taiwan
- \* Correspondence: afahmed@ksu.edu.sa (A.F.A.); sheu@mail.nsysu.edu.tw (J.-H.S.); Tel.: +966-114-677264 (A.F.A.); +886-7-525-2000 (ext. 5030) (J.-H.S.); Fax: +966-114-677245 (A.F.A.); +886-7-525-5020 (J.-H.S.)



**Citation:** Tai, C.-J.; Huang, C.-Y.; Ahmed, A.F.; Orfali, R.S.; Alarif, W.M.; Huang, Y.M.; Wang, Y.-H.; Hwang, T.-L.; Sheu, J.-H. An Anti-Inflammatory 2,4-Cyclized-3,4-Secospongian Diterpenoid and Furanoterpene-Related Metabolites of a Marine Sponge *Spongia* sp. from the Red Sea. *Mar. Drugs* **2021**, *19*, 38. <https://doi.org/10.3390/md19010038>

Received: 16 December 2020

Accepted: 14 January 2021

Published: 16 January 2021

**Publisher's Note:** MDPI stays neutral with regard to jurisdictional claims in published maps and institutional affiliations.



**Copyright:** © 2021 by the authors. Licensee MDPI, Basel, Switzerland. This article is an open access article distributed under the terms and conditions of the Creative Commons Attribution (CC BY) license (<https://creativecommons.org/licenses/by/4.0/>).

**Abstract:** Chemical investigation of a Red Sea *Spongia* sp. led to the isolation of four new compounds, i.e., 17-dehydroxy-sponalactone (**1**), a carboxylic acid, spongiafuranic acid A (**2**), one hydroxamic acid, spongiafuranohydroxamic acid A (**3**), and a furanyl trinor-sesterpenoid 16-*epi*-irciformonin G (**4**), along with three known metabolites (–)-sponalisolide B (**5**), 18-nor-3,17-dihydroxy-spongia-3,13(16),14-trien-2-one (**6**), and cholesta-7-ene-3 $\beta$ ,5 $\alpha$ -diol-6-one (**7**). The biosynthetic pathway for the molecular skeleton of **1** and related compounds was postulated for the first time. Anti-inflammatory activity of these metabolites to inhibit superoxide anion generation and elastase release in *N*-formyl-methionyl-leucyl phenylalanine/cytochalasin B (fMLF/CB)-induced human neutrophil cells and cytotoxicity of these compounds toward three cancer cell lines and one human dermal fibroblast cell line were assayed. Compound **1** was found to significantly reduce the superoxide anion generation and elastase release at a concentration of 10  $\mu$ M, and compound **5** was also found to display strong inhibitory activity against superoxide anion generation at the same concentration. Due to the noncytotoxic activity and the potent inhibitory effect toward the superoxide anion generation and elastase release, **1** and **5** can be considered to be promising anti-inflammatory agents.

**Keywords:** Red Sea sponge; *Spongia*; seco-spongian diterpenoid; isoprenoid-derived amide

## 1. Introduction

Marine sponges have been considered to be an important source for the discovery of structurally diverse bioactive secondary metabolites [1]. Many natural products from sponges have been shown to exhibit a variety of biological activities, such as antimicrobial [2–5], antiviral [6–8], antiprotozoal [8–10], cytotoxic [6,11–13], anti-inflammatory [14–16], antioxidant [4,17,18], immunosuppressive [1,19,20], and antifeedant [21–23]. The genus *Spongia* (Spongidae) has been chemically investigated since 1971 [24] and the studies have led to the discovery of a series of furanoterpenes [24–26], spongian diterpenoids [27–32], scalarane sesterterpenoids [33–35], sesquiterpene quinones [36,37], along with other kinds of metabolites, for example, sterols [38–40] and macrolides [41].

We report, herein, the chemical investigation of an unidentified *Spongia* species inhabiting along the eastern coast of the Red Sea. This study afforded four new natural products including a rare A-ring contracted diterpenoid, 17-dehydroxysponalactone (**1**), a C<sub>12</sub> carboxylic acid, spongiafuranic acid A (**2**); a C<sub>12</sub> hydroxamic acid, spongiafuranohydroxamic acid A (**3**); and a furanyl trinor-sesterterpenoid, 16-*epi*-irciformonin G (**4**); along with three known metabolites, (–)-sponalisolide B (**5**) [42], 18-nor-3,17-dihydroxyspongia-3,13(16),14-trien-2-one (**6**) [43], and cholesta-7-ene-3 $\beta$ ,5 $\alpha$ -diol-6-one (**7**) [40] (Figure 1 and Supplementary Materials Figures S1–S35 for **1**–**5**). Furthermore, in order to discover bioactive lead compounds, assays for the anti-inflammatory activity of the isolated compounds by inhibition of the superoxide anion generation and elastase release in *N*-formyl-methionyl-leucyl phenylalanine/cytochalasin B (fMLF/CB)-induced human neutrophils, and the cytotoxicity of these compounds against three tumor cell lines, murine leukemia (P388), human bile duct carcinoma (HuCCCT), and human colon adenocarcinoma (DLD-1), and a human dermal fibroblast (CCD-966SK) cell line were undertaken. Compounds **1** and **5** were shown to exhibit the promising anti-inflammatory activity.

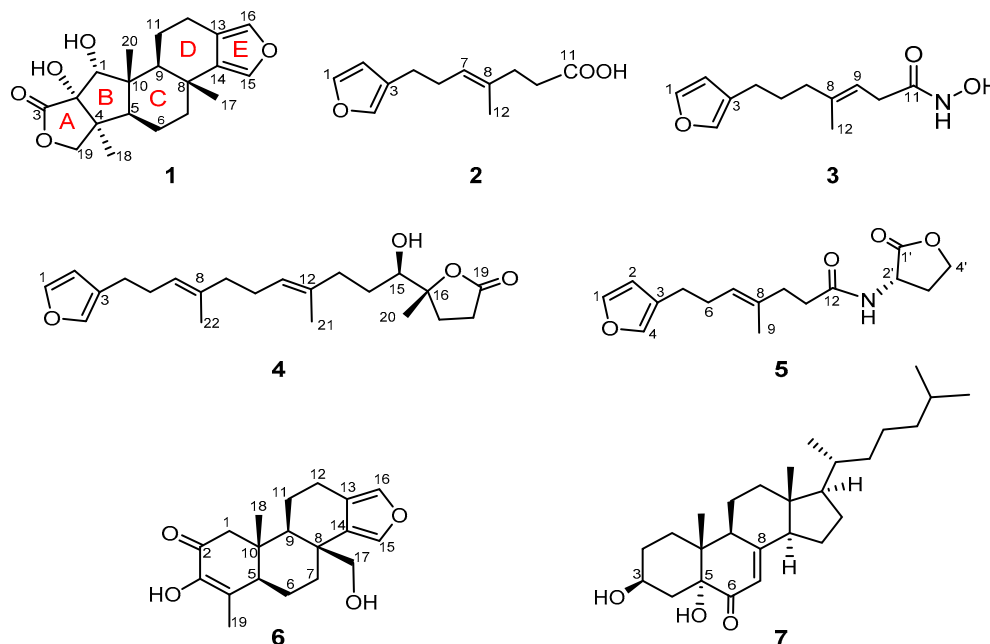


Figure 1. Structures of compounds **1**–**7** isolated from a Red Sea *Spongia* sp.

## 2. Results and Discussion

Compound **1** was obtained as a white powder. Its molecular formula C<sub>20</sub>H<sub>26</sub>O<sub>5</sub> was established by the molecular ion peak at  $m/z$  369.1672 [M + Na]<sup>+</sup> in the HRESIMS, consistent with eight degrees of unsaturation. The IR spectrum showed absorptions of hydroxyl (3455 and 3401 cm<sup>−1</sup>) and lactone carbonyl (1752 cm<sup>−1</sup>) functionalities. The <sup>13</sup>C NMR spectroscopic data of **1** exhibited 20 carbon signals (Table 1), which were assigned by the assistance of DEPT spectrum showing thirteen carbon signals of a diterpene, including

three ring-juncture methyls ( $\delta_C$  26.9, 22.6, and 14.0;  $\delta_H$  1.24, 1.14, and 0.84) and a 3,4-disubstituted furan ring ( $\delta_C$  137.1, CH; 134.8, CH; 136.8, C; and 119.6, C and  $\delta_H$  7.06, 1H, br s and 7.09, 1H, br s) [30,31,35,44]. On the basis of the number of unsaturations, **1** was, thus, suggested to be a pentacyclic 3,4-disubstituted furan diterpenoid. The NMR spectroscopic data of **1** and 2D NMR correlations (Figure 2) were similar to those of the previously described sponalactone (**8**) [30], except that a hydroxymethyl in **8** was replaced by a methyl at C-8 in **1**. Compound **1** also possesses the same B, C, and D rings as **9** [32] (Scheme 1).

**Table 1.**  $^1\text{H}$  and  $^{13}\text{C}$  NMR data (500 and 125 MHz,  $\text{CDCl}_3$ ) for **1**.

| Position | $\delta_H$ , m (J in Hz)        | $\delta_C$ , Type   |
|----------|---------------------------------|---------------------|
| 1        | 3.87, 1H, br s                  | 81.8, CH            |
| 2        | -                               | 83.3, C             |
| 3        | -                               | 180.6, C            |
| 4        | -                               | 47.6, C             |
| 5        | 1.90, 1H, d (11.5)              | 56.0, CH            |
| 6        | 1.63, 1H, br dd (10.5, 10.5)    | 18.3, $\text{CH}_2$ |
|          | 1.66, 1H, m                     |                     |
| 7        | 1.64, 1H, m                     | 40.0, $\text{CH}_2$ |
|          | 2.16, 1H, br d (10.5)           |                     |
| 8        | -                               | 34.4, C             |
| 9        | 1.96, 1H, d (11.5)              | 47.0, CH            |
| 10       | -                               | 46.4, C             |
| 11       | 1.68, 1H, m                     | 20.2, $\text{CH}_2$ |
|          | 1.78, 1H, dq (12.5, 6.5)        |                     |
| 12       | 2.59, 1H, ddd (16.0, 12.5, 6.5) | 19.7, $\text{CH}_2$ |
|          | 2.76, 1H, dd (16.0, 6.0)        |                     |
| 13       | -                               | 119.6, C            |
| 14       | -                               | 136.8, C            |
| 15       | 7.09, 1H, br s                  | 134.8, CH           |
| 16       | 7.06, 1H, br s                  | 137.1, CH           |
| 17       | 1.24, 3H, s                     | 26.9, $\text{CH}_3$ |
| 18       | 1.14, 3H, s                     | 22.6, $\text{CH}_3$ |
| 19       | 3.92, 1H, d (12.0)              | 74.6, $\text{CH}_2$ |
|          | 4.37, 1H, d (12.0)              |                     |
| 20       | 0.84, 3H, s                     | 14.0, $\text{CH}_3$ |

The relative and absolute configurations of **1** were established on the basis of nuclear Overhauser effect (NOE) correlation analysis (Figure 3) and by comparison of the observed NOE correlations with those of the related compounds [30,31], the observed pyridine-induced solvent shifts [45], and biogenetic consideration. The NOESY spectrum of **1** showed NOE correlations of  $\text{H}_3$ -17/ $\text{H}_3$ -20 and H-5/H-9, depicting the  $5R^*, 8R^*, 9S^*, 10R^*$ -configuration. H-1 displayed NOE interactions with the  $\beta$ -oriented  $\text{H}_3$ -20 and H-11 $\alpha$  ( $\delta_H$  1.68, m), indicating the  $\alpha$ -orientation of the H-1. Furthermore, the NOE correlations of H-5/ $\text{H}_3$ -18,  $\text{H}_3$ -18/H-19 $\alpha$  ( $\delta_H$  3.92) and H-19 $\beta$  ( $\delta_H$  4.37)/ $\text{H}_3$ -20 disclosed the  $\alpha$ - and  $\beta$ -orientations of  $\text{H}_3$ -18 and the  $\gamma$ -lactone ring, respectively, and the  $\alpha$ -orientation of the hydroxyl at C-2, accordingly. The analysis of the pyridine-induced deshielding effect of the axial hydroxy groups was also employed to support the configuration of **1**. Therefore, the significant pyridine-induced downfield shifts ( $\Delta\delta = \delta_{\text{CDCl}_3} - \delta_{\text{C}_6\text{D}_5\text{N}}$ ) exerted on H-5 ( $\Delta\delta_H = -0.24$  ppm) could only be approached when 1-OH was axially oriented on the same  $\alpha$ -face of the molecule. Also,  $\text{H}_3$ -18 exhibited pyridine-induced downfield shift ( $\Delta\delta_H = -0.14$  ppm) due to the vicinal effect of 2-OH, which should be *syn* to  $\text{H}_3$ -18 [45]. On the basis of the above findings, we propose that **1** can be derived from an intermediate spongian **9**, which was biosynthesized from the mevalonic acid pathway, after oxygenation of the six-membered ring A and a subsequent ring contraction and formation of a five-membered carbocycle, as illustrated in Scheme 1.

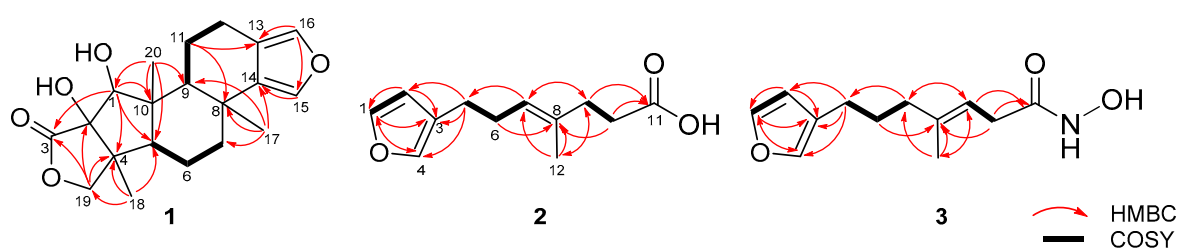
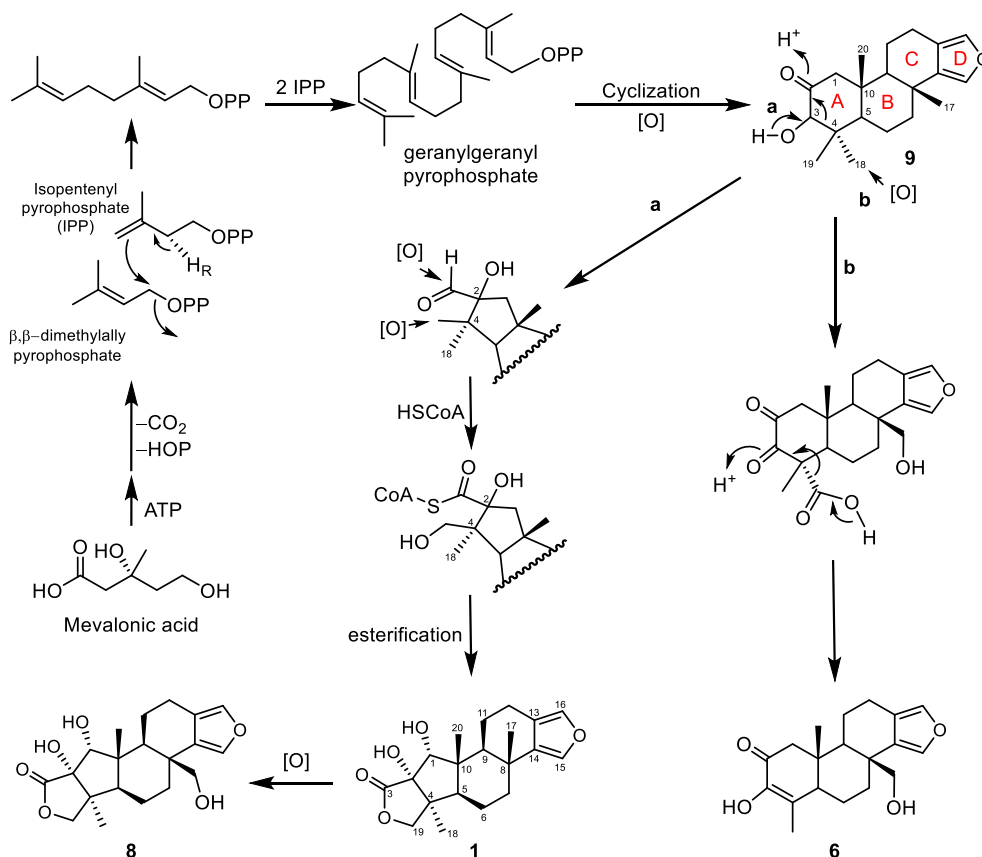


Figure 2. Selected  $^1\text{H}$ - $^1\text{H}$  COSY and HMBC correlations for **1**, **2**, and **3**.



Scheme 1. Plausible biosynthetic pathway of **1**, **6**, and related metabolites.

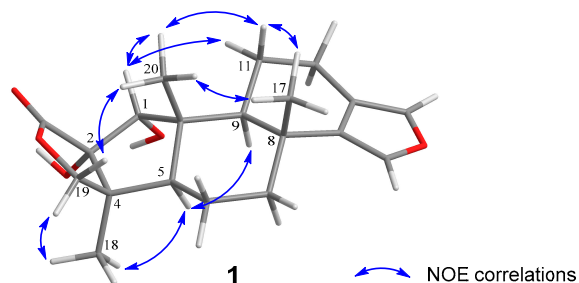


Figure 3. Selected nuclear Overhauser effect (NOE) correlations for **1**.

Metabolite **2** was isolated as a colorless oil. Its molecular formula was determined to be  $\text{C}_{12}\text{H}_{16}\text{O}_3$  from the HREIMS ( $m/z$  231.0992 [ $\text{M} + \text{Na}^+$ ]), indicating the four degrees of unsaturation. The IR spectrum displayed the absorptions of carboxylic acid ( $3105$ – $2857$  and  $1708\text{ cm}^{-1}$ ) and olefin ( $1654\text{ cm}^{-1}$ ). The NMR data (Table 2) showed the presence of a monosubstituted furan ring ( $\delta_{\text{C}}$  142.5, CH; 138.8, CH; 111.0, CH; and 124.7, C;  $\delta_{\text{H}}$  7.34, 7.20, and 6.27, each 1H, s) [24–26,42], a trisubstituted olefin ( $\delta_{\text{C}}$  124.7, CH;  $\delta_{\text{H}}$  5.22, 1H, s), a

methyl ( $\delta_C$  15.9;  $\delta_H$  1.61, 3H, s) and a carbonyl group ( $\delta_C$  180.0, C). Other  $^1H$  NMR signals in the shielded region ( $\delta_H$  2.25–2.47, 8H) were attributable to four methylene groups, as depicted from the COSY (Figure 2) correlations. The methylene protons H<sub>2</sub>-6 ( $\delta_H$  2.25, dt,  $J$  = 7.6, 7.2 Hz, 2H) was found to be further correlated with the olefinic proton ( $\delta_H$  5.22, dd,  $J$  = 7.2, 7.2 Hz, H-7) in **2**. The detailed analysis of HMBC correlations (Figure 2) resolved the carbon positions of the furan ring, olefinic double bond, and the carboxyl group to be at C-1-C-4, C-7/C-8, and C-11, respectively. Furthermore, the methyl group was positioned at C-8. The furanyl H-2 ( $\delta_H$  6.27, s), H-4 ( $\delta_H$  7.20, s), and the olefinic proton H-7 ( $\delta_H$  5.22, dd,  $J$  = 7.2, 7.2 Hz, 2H) displayed HMBC correlations with the  $sp^3$  carbon C-5 ( $\delta_C$  24.8, CH<sub>2</sub>), and H<sub>3</sub>-12 ( $\delta_H$  1.61, s) showed HMBC correlations with C-7 ( $\delta_C$  124.7, CH) and C-9 ( $\delta_C$  34.2, CH<sub>2</sub>), while the signal of H<sub>2</sub>-9 ( $\delta_H$  2.32, dd,  $J$  = 7.6, 7.6 Hz, 2H) was found to be correlated with the carboxyl carbon (C-11,  $\delta_C$  180.0). Moreover, the NOE correlations observed for H<sub>3</sub>-12 with H<sub>2</sub>-6 but not with H-5 and the chemical shift of C-12 ( $\delta_C$  < 20 ppm) assigned the *E*-configuration of the 7,8-double bond [46]. Therefore, **2** was determined to be a furanotrinorsescuiterpenoid carboxylic acid with the structure of (*E*)-7-(furan-3-yl)-4-methylhept-4-enoic acid. The literature search showed that this compound had been prepared as a synthetic intermediate during the total syntheses of the furanosesquiterpenoids and dendrolasins [42,47], however, its NMR data had not been reported. Therefore, this is the first report of **2** as a natural product, with the NMR data assigned and reported for the first time.

**Table 2.**  $^1H$  and  $^{13}C$  NMR data for compounds **2** and **3**.

| #  | <b>2</b>                                    |                         | <b>3</b>                                    |                         |
|----|---|-------------------------|---|-------------------------|
|    | $\delta_H$ , m ( $J$ in Hz)<br><sup>a</sup> | $\delta_C$ <sup>b</sup> | $\delta_H$ , m ( $J$ in Hz)<br><sup>a</sup> | $\delta_C$ <sup>b</sup> |
| 1  | 7.34, 1H, brs                               | 142.5, CH               | 7.35, 1H, brs                               | 142.9, CH               |
| 2  | 6.27, 1H, brs                               | 111.0, CH               | 6.27, 1H, brs                               | 111.2, CH               |
| 3  | -   | 124.7, C                | -   | 125.1, C                |
| 4  | 7.20, 1H, s                                 | 138.8, CH               | 7.21, 1H, s                                 | 139.1, CH               |
| 5  | 2.45, 2H, dt<br>(7.6, 7.6)                  | 24.8, CH <sub>2</sub>   | 2.40, 2H, dt<br>(7.6, 7.6)                  | 24.4, CH <sub>2</sub>   |
| 6  | 2.25, 2H, dt<br>(7.6, 7.2)                  | 28.3, CH <sub>2</sub>   | 2.25, 2H, dt<br>(7.6, 7.6)                  | 28.1, CH <sub>2</sub>   |
| 7  | 5.22, 1H, dd<br>(7.2, 7.2)                  | 124.7, CH               | 2.08, 2H, dd<br>(7.2, 7.6)                  | 39.1, CH <sub>2</sub>   |
| 8  | -   | 133.7, C                | -   | 139.7, C                |
| 9  | 2.32, 2H, dd<br>(7.6, 7.6)                  | 34.2, CH <sub>2</sub>   | 5.34, 1H, dd<br>(6.0, 6.0)                  | 115.5, CH               |
| 10 | 2.47, 2H, m                                 | 32.9, CH <sub>2</sub>   | 3.10, 2H, d (6.8)                           | 33.2, CH <sub>2</sub>   |
| 11 | -   | 180.0, C                | -   | 176.1, C                |
| 12 | 1.61, 3H, s                                 | 15.9, CH <sub>3</sub>   | 1.65, 3H, s                                 | 16.5, CH <sub>3</sub>   |

<sup>a</sup> Spectrum recorded at 400 MHz in CDCl<sub>3</sub>. <sup>b</sup> Spectrum recorded at 100 MHz in CDCl<sub>3</sub>.

Metabolite **3** exhibited almost the same NMR data as those of **2** (Table 2) from C-1 to C-6, with the carbon chemical shifts of the trisubstituted double bond ( $\delta_C$  139.7, C and 115.5, CH;  $\delta_H$  5.34, dd,  $J$  = 6.0, 6.0 Hz, 1H) and the carbonyl group ( $\delta_C$  176.1, C) in **3** showing significant differences of  $\Delta\delta_C$  −6.0, +9.2, and −3.9 ppm as compared with those of the corresponding carbons in **2**, respectively. As illustrated by  $^1H$ - $^1H$  COSY correlations (Figure 2), the double bond has been isomerized from the C-7/C-8 position in **2** to the C-8/C-9 position in **3**. However, the IR spectrum displayed the absorptions of the hydroxyl and NH groups (3407–2858 cm<sup>−1</sup>), carbonyl group (1705 cm<sup>−1</sup>), and olefin (1634 cm<sup>−1</sup>) functionalities. Furthermore, the HREIMS  $m/z$  246.1098 [M + Na]<sup>+</sup> established the molecular formula of **3** to be C<sub>12</sub>H<sub>17</sub>NO<sub>3</sub> and the chemical shift of the carbonyl group (176.1 ppm), showing that a hydroxamic acid moiety [48–51] replaced a carboxylic acid group at C-11 in **3**.



Compound **4** was isolated as a colorless oil,  $[\alpha]_D^{25} +4.4$  (c 0.74,  $\text{CHCl}_3$ ). The ESIMS and NMR spectroscopic data (Table 3) established the molecular formula  $\text{C}_{22}\text{H}_{32}\text{O}_4$  for **4**. The IR absorptions 3432, 1769, and  $1647\text{ cm}^{-1}$  revealed the presence of hydroxyl, carbonyl, and olefin functionalities, respectively. Moreover, it was found that the NMR data of **4** was the same as those of irciformonin G (**10**) [52] in all aspects except for those at positions 17 and 18–20 (Table 4), proposing **4** as an isomer of **10**. By using Mosher's method [53,54], the 15*R* absolute configuration in **4** was established based on the calculated  $\Delta\delta_{\text{H}}$  ( $\delta_{\text{S}} - \delta_{\text{R}}$ ) values of protons neighboring C-15 of (*S*)- and (*R*)- $\alpha$ -methoxy- $\alpha$ -(trifluoromethyl)-phenylacetyl (MTPA) esters **4a** and **4b**, respectively (Figure 4). After the assignment of the 15*R* configuration, the  $^{13}\text{C}$  NMR data of C-15 to C-20 of **4** were further compared with the corresponding data of irciformonin G (**10**), (+)-sponalisolide A (**11**), and 8-*epi*-(+)-sponalisolide A (**12**) [42] of known absolute configurations (Table 4 and Figure 5). The 15*R*,16*R*-configuration of **4** was, thus, confirmed as those of the 7*R*, 8*R* configured **12**, while **10** and **11** possessed the same configurations (*R,S*) at the corresponding asymmetric carbons. From the above findings, compound **4** was, thus, identified as 16-*epi*-irciformonin G.

Table 3.  $^1\text{H}$  and  $^{13}\text{C}$  NMR data for compounds **4**, **5**, and (–)-sponalisolide B.

| <b>4</b> |  |                                  | <b>5</b> |  |                                  | <b>(–)-Sponalisolide B</b>  |                                  |
|----------|--|----------------------------------|----------|--|----------------------------------|---|----------------------------------|
| #        | $\delta_{\text{H}}$ , m (J in Hz) <sup>a</sup> | $\delta_{\text{C}}$ <sup>b</sup> | #        | $\delta_{\text{H}}$ , m (J in Hz) <sup>a</sup>                     | $\delta_{\text{C}}$ <sup>b</sup> | $\delta_{\text{H}}$ , m (J in Hz) <sup>c</sup>                      | $\delta_{\text{C}}$ <sup>d</sup> |
| 1        | 7.34, 1H, brs                                  | 142.5, CH                        | 1        | 7.34, 1H, brs  | 142.6, CH                        | 7.33, 1H, t (1.6)   | 142.7, CH                        |
| 2        | 6.28, 1H, brs                                  | 111.1, CH                        | 2        | 6.27, 1H, brs  | 111.0, CH                        | 6.26, 1H, brs   | 111.1, CH                        |
| 3        | —  | 124.9, C                         | 3        | —  | 124.7, C                         | —   | 124.9, C                         |
| 4        | 7.21, 1H, s                                    | 138.8, CH                        | 4        | 7.20, 1H, s  | 138.8, CH                        | 7.20, 1H, brs   | 139.0, CH                        |
| 5        | 2.45, 2H, t (7.5)                              | 25.0, CH <sub>2</sub>            | 5        | 2.45, 2H, t (7.5)  | 24.8, CH <sub>2</sub>            | 2.44, 2H, dd (7.7, 7.3)   | 24.9, CH <sub>2</sub>            |
| 6        | 2.24, 2H, dt (7.5, 7.0)                        | 28.4, CH <sub>2</sub>            | 6        | 2.25, 2H, dt (7.5, 7.0)  | 28.3, CH <sub>2</sub>            | 2.24, 2H, ddd (14.6, 7.3, 7.0)                                      | 28.5, CH <sub>2</sub>            |
| 7        | 5.16, 1H, t, (6.0)                             | 123.9, CH                        | 7        | 5.23, 1H, t (7.0)  | 125.1, CH                        | 5.22, 1H, t (7.0)   | 125.2, CH                        |
| 8        | —  | 135.5, C                         | 8        | —  | 134.1, C                         | —   | 134.2, C                         |
| 9        | 2.00, 2H, dd, (7.5, 7.0)                       | 39.5, CH <sub>2</sub>            | 9        | 1.61, 3H, s  | 16.0, CH <sub>3</sub>            | 1.60, 3H, s   | 16.1, CH <sub>3</sub>            |
| 10       | 2.08, 2H, m                                    | 26.5, CH <sub>2</sub>            | 10       | 2.35, 2H, m  | 34.7, CH <sub>2</sub>            | 2.33, 2H, m   | 35.1, CH <sub>2</sub>            |
| 11       | 5.17, 1H, t, (6.0)                             | 125.4, CH                        | 11       | 2.34, 2H, m  | 34.9, CH <sub>2</sub>            | 2.33, 2H, m   | 34.9, CH <sub>2</sub>            |
| 12       | —  | 134.3, C                         | 12       | —  | 173.3, C                         | —   | 173.5, C                         |
| 13       | 2.24, 1H, m;<br>2.07, 1H, m                    | 36.2, CH <sub>2</sub>            | 1'       | —  | 175.4, C                         | —   | 175.6, C                         |
| 14       | 1.50, 1H, m;<br>1.58, 1H, m                    | 28.9, CH <sub>2</sub>            | 2'       | 4.50, 1H, ddd, (11.5, 8.5, 5.5)<br>2.86, 1H, ddd, (12.0, 8.5, 6.0) | 49.3, CH                         | 4.52, 1H, ddd, (11.7, 8.6, 5.8)<br>2.82, 1H, ddd, (12.2, 8.6, 5.8); | 49.4, CH                         |
| 15       | 3.51, 1H, br d (10.5)                          | 76.7, CH                         | 3'       | 2.08, 1H, qd, (11.5, 9.0)<br>4.47, t (9.5)                         | 30.7, CH <sub>2</sub>            | 2.08, 1H, qd, (11.7, 9.1)<br>4.45, 1H, t, (9.5);                    | 30.7, CH <sub>2</sub>            |
| 16       | —  | 88.7, C                          | 4'       | 4.27, 1H, ddd, (11.5, 9.5, 6.0)                                    | 66.1, CH <sub>2</sub>            | 4.27, 1H, ddd, (11.3, 9.5, 5.8)                                     | 66.2, CH <sub>2</sub>            |
| 17       | 2.63, 2H, dd (9.0, 7.5)                        | 29.2, CH <sub>2</sub>            | NH       | 6.00 brs   | —                                | 6.16 brs  | —                                |
| 18       | 1.92, 1H, ddd (13.0, 8.0, 8.0);                | 30.6, CH <sub>2</sub>            |          |  |                                  |   |                                  |
| 19       | 2.20, 1H, m                                    | 176.7, C                         |          |  |                                  |   |                                  |
| 20       | —  | 21.3, CH <sub>3</sub>            |          |  |                                  |   |                                  |
| 21       | 1.37, 3H, s                                    | 16.0, CH <sub>3</sub>            |          |  |                                  |   |                                  |
| 22       | 1.61, 3H, s                                    | 15.9, CH <sub>3</sub>            |          |  |                                  |   |                                  |

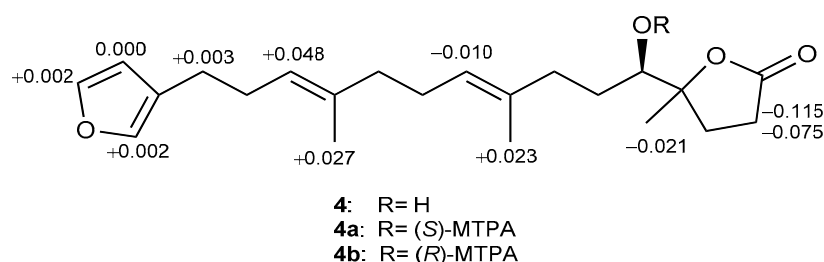
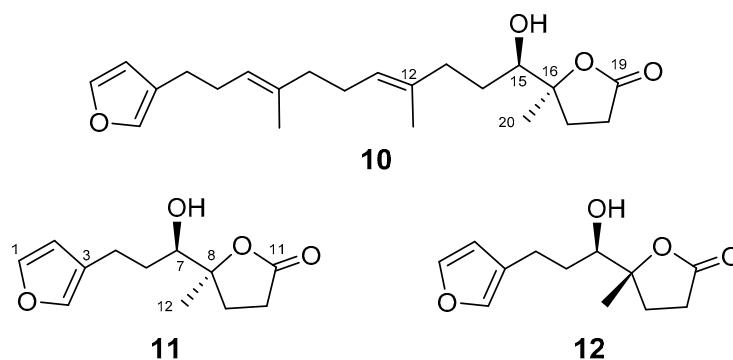
<sup>a</sup> Spectrum recorded at 500 MHz in  $\text{CDCl}_3$ . <sup>b</sup> Spectrum recorded at 125 MHz in  $\text{CDCl}_3$ . <sup>c</sup> Spectrum recorded at 400 MHz in  $\text{CDCl}_3$  [42].

<sup>d</sup> Spectrum recorded at 125 MHz in  $\text{CDCl}_3$  [42].

**Table 4.** Selected  $^{13}\text{C}$  NMR data at C-15–C-20 of **4** and **10** and the correspondent carbons C-7–C-12 of the related compounds **11** and **12**.

|      | <b>4</b> <sup>a</sup> | <b>10</b> (15 <i>R</i> ,16 <i>S</i> ) <sup>b</sup> | C#   | <b>11</b> (7 <i>R</i> ,8 <i>S</i> ) <sup>c</sup> | <b>12</b> (7 <i>R</i> ,8 <i>R</i> ) <sup>c</sup> |
|------|-----------------------|--|------|--|--|
| C-15 | 76.7                  | 75.5   | C-7  | 75.1   | 76.2   |
| C-16 | 88.7                  | 88.9   | C-8  | 88.9   | 88.9   |
| C-17 | 29.2                  | 27.8   | C-9  | 27.6   | 29.2   |
| C-18 | 30.6                  | 29.5   | C-10 | 29.5   | 30.7   |
| C-19 | 176.7                 | 177.3  | C-11 | 177.1  | 176.6  |
| C-20 | 21.3                  | 23.0   | C-12 | 23.1   | 21.4   |

<sup>a</sup> Spectrum recorded at 125 MHz in  $\text{CDCl}_3$ . <sup>b</sup> Spectrum recorded at 75 MHz in  $\text{CDCl}_3$  [52]. <sup>c</sup> Spectrum recorded at 125 MHz in  $\text{CDCl}_3$  [42].

**Figure 4.**  $^1\text{H}$  NMR chemical shift differences  $\Delta\delta$  ( $\delta_S - \delta_R$ ) in ppm for  $\alpha$ -methoxy- $\alpha$ -(trifluoromethyl)-phenylacetyl (MTPA) esters of **4**.**Figure 5.** Structures of known compounds **10–12**.

(–)-Sponalisolide B (**5**) was isolated as a colorless oil,  $[\alpha]_D^{25} -8.5$  ( $c$  0.34,  $\text{CHCl}_3$ ). Through detailed analysis of NMR spectroscopic data (Table 3), in particular two-dimensional (2D) NMR correlations, the structure of **5** was established to be identical to that of the known (–)-sponalisolide B [42]. However, the coupling constants and spin-spin splitting patterns of the proton  $\text{H}_2-6$  ( $\delta_{\text{H}}$  2.25, dt, 2H,  $J = 7.5, 7.0$  Hz at 500 MHz in  $\text{CDCl}_3$ ) were wrongly assigned. We, herein, reanalyzed the spectrum and provided the correct NMR data for **5**.

With the aim of discovering bioactive compounds from these isolates, the cytotoxic activities of the isolated compounds **1–7** against the proliferation of three cancer cell lines including murine leukemia (P388), human bile duct carcinoma (HuCCCT), and human colon adenocarcinoma (DLD-1), and a human dermal fibroblast cell line (CCD-966SK) were evaluated, using the Alamar Blue assay [55,56]. The results indicated that none of the tested metabolites exhibited cytotoxic activity ( $\text{IC}_{50} > 20 \mu\text{g/mL}$ ).

The anti-inflammatory activities of compounds **1–7** on inhibition of superoxide anion ( $\text{O}_2^-$ ) generation and elastase release in the fMLF/CB-stimulated human neutrophils [57–59] were also evaluated. The results (Table 5) showed that **1** exhibited potent activity to inhibit the superoxide anion generation ( $91.38 \pm 2.91\%$ ) and elastase release ( $90.29 \pm 7.71\%$ ) at

10  $\mu\text{M}$ , with the  $\text{IC}_{50}$  values of  $3.37 \pm 0.21$  and  $4.07 \pm 0.60$   $\mu\text{M}$ , respectively. Compound **5** was also found to display significant inhibitory activity against the superoxide anion generation ( $\text{IC}_{50} = 5.31 \pm 1.52$   $\mu\text{M}$ ), and the percentage of inhibition was  $67.12 \pm 6.00\%$  at 10  $\mu\text{M}$ . Due to the noncytotoxic character and the potent activity toward the superoxide anion generation and elastase release, **1** and **5** can be considered to be the promising anti-inflammatory agents.

**Table 5.** Effects of compounds **1–7** on superoxide anion generation and elastase release in *N*-formyl-methionyl-leucyl phenylalanine/cytochalasin B (fMLF/CB)-induced human neutrophils.

| Compound              | Superoxide Anion                                |            |       |            |     | Elastase  |            |       |            |     |
|-----------------------|---|------------|-------|------------|-----|---|------------|-------|------------|-----|
|                       | $\text{IC}_{50}$ ( $\mu\text{M}$ ) <sup>a</sup> |            | Inh % |            |     | $\text{IC}_{50}$ ( $\mu\text{M}$ ) <sup>a</sup> |            | Inh % |            |     |
| 1                     | 3.37  | $\pm$ 0.21 | 91.38 | $\pm$ 2.91 | *** | 4.07  | $\pm$ 0.60 | 90.29 | $\pm$ 7.71 | *** |
| 2                     | — <sup>b</sup>                                  |            | 3.47  | $\pm$ 0.68 | **  | —   |            | 14.03 | $\pm$ 3.28 | *   |
| 3                     | —   |            | 8.85  | $\pm$ 3.73 |     | —   |            | 18.00 | $\pm$ 6.08 | *   |
| 4                     | —   |            | 2.61  | $\pm$ 1.26 |     | —   |            | −1.07 | $\pm$ 7.93 |     |
| 5                     | 5.31  | $\pm$ 1.52 | 67.12 | $\pm$ 6.00 | *** | —   |            | 35.18 | $\pm$ 8.03 | **  |
| 6                     | —   |            | 9.44  | $\pm$ 5.04 |     | —   |            | 19.24 | $\pm$ 3.86 | **  |
| 7                     | —   |            | 12.79 | $\pm$ 6.01 |     | —   |            | 25.87 | $\pm$ 4.18 | **  |
| LY294002 <sup>c</sup> | 1.88  | $\pm$ 0.77 | 90.27 | $\pm$ 3.87 | *** | 2.58  | $\pm$ 0.67 | 77.59 | $\pm$ 2.34 | *** |

Percentage of inhibition (Inh %) at 10  $\mu\text{M}$ . Results are presented as mean  $\pm$  SEM ( $n \geq 3$ ). \*  $p < 0.05$ , \*\*  $p < 0.01$ , \*\*\*  $p < 0.001$  as compared with the control (DMSO). <sup>a</sup> Concentration necessary for 50% inhibition ( $\text{IC}_{50}$ ). <sup>b</sup> The compound is not considered to be anti-inflammatory when  $\text{IC}_{50}$  value is  $>10$   $\mu\text{M}$ . <sup>c</sup> A phosphatidylinositol-3-kinase inhibitor was used as a positive control.

### 3. Materials and Methods

#### 3.1. General Procedures

Measurements of optical rotations and IR spectra were carried out on a JASCO P-1020 polarimeter and FT/IR-4100 infrared spectrophotometer (JASCO Corporation, Tokyo, Japan), respectively. ESIMS and HRESIMS were performed on a Bruker APEX II (Bruker, Bremen, Germany) mass spectrometer. The NMR spectra were recorded on a Varian 400MR FT-NMR at 400 and 100 MHz for  $^1\text{H}$  and  $^{13}\text{C}$ , respectively or a Varian Unity INOVA500 FT-NMR at 500 and 125 MHz for  $^1\text{H}$  and  $^{13}\text{C}$ , respectively (Varian Inc., Palo Alto, CA, USA). Silica gel or reversed-phase (RP-18, 230–400 mesh) silica gel was used for column chromatography and analytical thin-layer chromatography (TLC) analysis (Kieselgel 60 F-254, 0.2 mm, Merck, Darmstadt, Germany), respectively. Isolation and purification of compounds by high-performance liquid chromatography (HPLC) were achieved using an Hitachi L-2455 HPLC apparatus (Hitachi, Tokyo, Japan) equipped with a Supelco C18 column (250  $\times$  21.2 mm, 5  $\mu\text{m}$ , Supelco, Bellefonte, PA, USA).

#### 3.2. Animal Material

The sponge *Spongia* sp. was collected during March 2016, off the Red Sea Coast at Jeddah, Saudi Arabia (21°22'11.08" N, 39°06'56.62" E). A voucher sample (RSS-1) has been deposited at the Department of Pharmacognosy, College of Pharmacy, King Saud University, Saudi Arabia.

#### 3.3. Extraction and Separation

The *Spongia* sp. was collected and freeze-dried. The freeze-dried material (550 g dry wt) was minced and extracted exhaustively with EtOAc/MeOH/ $\text{CH}_2\text{Cl}_2$  (1:1:0.5) (3  $\times$  10 L). The solvent-free extract was suspended in water and partitioned with  $\text{CH}_2\text{Cl}_2$ , EtOAc, and then *n*-BuOH saturated with water to obtain  $\text{CH}_2\text{Cl}_2$  (18.47 g), EtOAc (0.782 g), and *n*-BuOH (1.0 g) fractions. The  $\text{CH}_2\text{Cl}_2$  fraction was chromatographed over silica gel column, using EtOAc in *n*-hexane (0% to 100%, stepwise), to yield 12 fractions (F1–F12). F6 (1.21 g), eluted with *n*-hexane/EtOAc (1:1), was re-chromatographed over a RP-18 column using MeOH in  $\text{H}_2\text{O}$  (50% to 100%, stepwise) to give 15 subfractions (F6-1 to F6-15). F6-5 (83.0 mg), F6-8 (85.2 mg), F6-11 (21.1 mg), and F6-14 (23.5 mg) were purified on RP-18

HPLC separately, using MeOH/H<sub>2</sub>O (1.4:1), CH<sub>3</sub>CN/H<sub>2</sub>O (1:1.7), MeOH/H<sub>2</sub>O (1.5:1), and CH<sub>3</sub>CN/H<sub>2</sub>O (1.6:1), in order, to afford **2** (55.5 mg) from F6-8, **6** (6.2 mg) from F6-5, **1** (10.2 mg) from F6-11, and **4** (7.4 mg) from F6-14. F7 (1.1 g), eluted with *n*-hexane/EtOAc (1:3), was isolated using RP-18 silica gel column chromatography and MeOH in H<sub>2</sub>O (50% to 100%, stepwise) as a mobile phase to result in 20 subfractions (F7-1 to F7-20). F7-4 (16.1 mg) and F7-6 (25.7 mg) were further separated on RP-18 HPLC, using CH<sub>3</sub>CN/H<sub>2</sub>O (1:1.7) and (1:2.5), separately, to afford **3** (4.6 mg) from F7-4, **5** (9.1 mg) and **7** (4.3 mg) from F7-6.

### 3.3.1. 17-Dehydroxysponalactone (**1**)

White powder,  $[\alpha]_D^{25} +27.7$  ( $c = 0.71$ , CHCl<sub>3</sub>); IR (neat)  $\nu_{\max}$  3455, 3401, 2962, 2927, 2864, 1752, 1663, 1455, 1387, 1186, 1150, 1111, 1060, 1019, 890.0, and 757 cm<sup>-1</sup>; <sup>1</sup>H NMR (500 MHz, CDCl<sub>3</sub>); and <sup>13</sup>C (125 MHz, CDCl<sub>3</sub>) data, see Table 1. ESIMS  $m/z$  369 [M + Na]<sup>+</sup>; <sup>1</sup>H NMR (C<sub>5</sub>D<sub>5</sub>N, 400 MHz)  $\delta_H$  7.37 (1H, br s, H-16), 7.26 (1H, br s, H-15), 4.44 (1H, d,  $J = 9.6$  Hz, H-19), 4.30 (1H, br s, H-1), 3.94 (1H, d,  $J = 9.6$  Hz, H-19), 2.66 (1H, m, H-12), 2.60 (1H, m, H-12), 2.26 (1H, m, H-9), 2.14 (1H, d,  $J = 11.5$  Hz, H-5), 2.12 (1H, m, H-7), 1.76 (1H, m, H-11), 1.67 (1H, m, H-6), 1.60 (1H, m, H-11), 1.57 (1H, m, H-6), 1.56 (1H, m, H-7), 1.28 (3H, s, H<sub>3</sub>-18), 1.24 (3H, s, H<sub>3</sub>-17), 0.94 (3H, s, H<sub>3</sub>-20); <sup>13</sup>C NMR (C<sub>5</sub>D<sub>5</sub>N, 100 MHz)  $\delta_C$  181.0 (C, C-3), 138.0 (CH, C-15), 136.0 (C, C-14), 135.7 (CH, C-16), 120.5 (C, C-13), 84.3 (C, C-2), 82.7 (CH, C-1), 74.4 (CH<sub>2</sub>, C-19), 57.0 (CH, C-5), 47.8 (CH, C-9), 47.6 (C, C-4), 47.0 (C, C-10), 40.9 (CH<sub>2</sub>, C-7), 35.1 (C, C-8), 27.4 (CH<sub>3</sub>, C-17), 23.8 (CH<sub>3</sub>, C-18), 20.9 (CH<sub>2</sub>, C-11), 20.4 (CH<sub>2</sub>, C-12), 18.9 (CH<sub>2</sub>, C-6), 14.5 (CH<sub>3</sub>, C-20). HRESIMS  $m/z$  369.1672 [M + Na]<sup>+</sup> (calcd for C<sub>20</sub>H<sub>26</sub>O<sub>5</sub>Na, 369.1673).

### 3.3.2. Spongiafuranic Acid A (**2**)

Colorless oil, IR (neat)  $\nu_{\max}$  3105, 2920, 2918, 2857, 1708, 1654, 1500, 1446, 1386, 1298, 1210, 1163, 1024, and 874 cm<sup>-1</sup>; <sup>1</sup>H NMR (400 MHz, CDCl<sub>3</sub>); and <sup>13</sup>C (100 MHz, CDCl<sub>3</sub>) data, see Table 2. ESIMS  $m/z$  231 [M + Na]<sup>+</sup>. HRESIMS  $m/z$  231.0994 [M + Na]<sup>+</sup> (calcd for C<sub>12</sub>H<sub>16</sub>O<sub>3</sub>Na, 231.0997).

### 3.3.3. Spongiafuranohydroxamic Acid A (**3**)

Colorless oil, IR (neat)  $\nu_{\max}$  3407, 3252, 2918, 2858, 1704, 1634, 1442, 1372, 1298, 1205, 1136, 1027, and 963 cm<sup>-1</sup>; <sup>1</sup>H NMR (400 MHz, CDCl<sub>3</sub>); and <sup>13</sup>C (100 MHz, CDCl<sub>3</sub>) data, see Table 2. ESIMS  $m/z$  246 [M + Na]<sup>+</sup>. HRESIMS  $m/z$  246.1098 [M + Na]<sup>+</sup> (calcd for C<sub>12</sub>H<sub>17</sub>NO<sub>3</sub>Na, 246.1100).

### 3.3.4. 16-Epi-Irciformonin G (**4**)

Colorless oil,  $[\alpha]_D^{25} +4.4$  ( $c = 0.74$ , CHCl<sub>3</sub>); IR (neat)  $\nu_{\max}$  3432, 2920, 2851, 1769, 1647, 1557, 1456, 1384, 1239, 1162, 1089, 944, 874, and 776 cm<sup>-1</sup>; <sup>1</sup>H NMR (500 MHz, CDCl<sub>3</sub>); and <sup>13</sup>C (125 MHz, CDCl<sub>3</sub>) data, see Table 3. ESIMS  $m/z$  383 [M + Na]<sup>+</sup>. HRESIMS  $m/z$  383.2195 [M + Na]<sup>+</sup> (calcd for C<sub>22</sub>H<sub>32</sub>O<sub>4</sub>Na, 383.2198).

### 3.3.5. Preparation of (S)- and (R)-MTPA Esters of **4**

To a solution of **4a** (1 mg, 2.8  $\mu$ M) in pyridine (100  $\mu$ L), *R*-(−)-MTPA-Cl (5  $\mu$ L) was added and left to react overnight at RT. The reaction was ended by addition of water (1.0 mL), and the mixture was further processed, as previously described [53,54], to afford (S)-MTPA ester (**4a**, 1.4 mg, 2.4  $\mu$ M). The correspondent (*R*)-MTPA ester (**4b**, 0.9 mg, 1.6  $\mu$ M) was similarly obtained from the reaction of *S*-(+)-MTPA-Cl with **4**. <sup>1</sup>H NMR (CDCl<sub>3</sub>, 400 MHz) of **4a**:  $\delta_H$  7.340 (1H, br dd,  $J = 1.8, 1.8$  Hz, H-1), 7.208 (1H, br s, H-4), 6.275 (1H, br s, H-2), 5.164 (1H, dd,  $J = 8.0, 8.0$  Hz, H-11), 5.113 (1H, m, H-7), 2.489 (1H, m, H-18a), 2.450 (2H, dd,  $J = 7.6, 7.6$  Hz, H<sub>2</sub>-5), 2.426 (1H, m, H-18a), 1.593 (3H, H<sub>3</sub>-21), 1.559 (3H, H<sub>3</sub>-22), and 1.355 (3H, H<sub>3</sub>-20). <sup>1</sup>H NMR (CDCl<sub>3</sub>, 400 MHz) of **4b**:  $\delta_H$  7.338 (1H, br s, H-1), 7.206 (1H, br s, H-4), 6.275 (1H, br s, H-2), 5.174 (1H, ddd,  $J = 9.2, 9.2, 3.2$  Hz, H-11),

5.065 (1H, br dd,  $J = 7.8, 7.8$  Hz, H-7), 2.563 (1H, m, H-18a), 2.541 (1H, m, H-18a), 2.447 (2H, dd,  $J = 8.0, 8.0$  Hz, H<sub>2</sub>-5), 1.570 (3H, H<sub>3</sub>-21), 1.532 (3H, H<sub>3</sub>-22), and 1.376 (3H, H<sub>3</sub>-20).

### 3.4. In Vitro Bioassays

#### 3.4.1. Anti-Inflammatory Activity

Human neutrophils were isolated from the blood of healthy adult volunteers and enriched by using dextran sedimentation, Ficoll–Hypaque gradient centrifugation, and hypotonic lysis, as described previously [59]. Then, neutrophils were incubated in Ca<sup>2+</sup>-free HBSS buffer (pH 7.4, ice-cold).

#### Superoxide Anion Generation

Neutrophils ( $6 \times 10^5$  cells/mL) incubated (with 0.6 mg/mL ferricytochrome *c* and 1 mM Ca<sup>2+</sup>) in HBSS at 37 °C were treated with DMSO (as control) or tested compound for 5 min. Neutrophils were primed by 1 µg/mL cytochalasin B (CB) for 3 min before being activated by 100 nM fMLF for 10 min. The change of superoxide anion generation was spectrophotometrically measured at 550 nm (U-3010, Hitachi, Tokyo, Japan) [57,58]. LY294002 [2-(4-morpholinyl)-8-phenyl-1(4*H*)-benzopyran-4-one] was used as a positive control.

#### Elastase Release

Neutrophils ( $6 \times 10^5$  cells/mL) incubated (with 100 µM MeO-Suc-Ala-Ala-Pro-Val-*p*-nitroanilide and 1 mM Ca<sup>2+</sup>) in HBSS at 37 °C were treated with DMSO or the tested compound for 5 min. Neutrophils were, then, activated with fMLF (100 nM)/CB (0.5 µg/mL) for 10 min. The change of elastase release was spectrophotometrically measured at 405 nm (U-3010, Hitachi, Tokyo, Japan) [58].

#### 3.4.2. Cytotoxic Activity

P388, HuCCT-1, DLD-1, and CCD-966SK cell lines were purchased from the American Type Culture Collection (ATCC). Cytotoxicities of compounds 1–7 were measured using Almar Blue assay [55,56], with doxorubicin hydrochloride used as a positive control.

#### 3.4.3. Statistical Analysis

Data are displayed as the mean  $\pm$  SEM and comparisons were performed by one-way ANOVA with Dunnett analysis. All results were obtained from more than 3 biological replicates. A *p* value of 0.05 or less was considered to be significant. The software Prism (GraphPad Software, San Diego, CA, USA) was used for the statistical analysis.

## 4. Conclusions

The chemical investigation of dichloromethane-soluble fraction of the organic extract of a Red Sea sponge *Spongia* sp. resulted in the isolation and identification of a rare A-ring contracted secospongian diterpenoid 17-dehydroxysonalactone (1) and three new furano-norterpenoids 2–4. Compound 1 was found to be noncytotoxic but was shown to exhibit potent inhibitory activity against the superoxide anion generation and elastase release in the fMLF/CB-induced neutrophils, and 5 was also found to display strong inhibitory activity against the superoxide anion generation. Therefore, 1 and 5 are the promising candidates for further development of anti-inflammatory agents.

**Supplementary Materials:** HRESIMS, <sup>1</sup>H, <sup>13</sup>C, DEPT, HMQC, COSY, HMBC, and NOESY spectra of new compounds 1–4 are available online at <https://www.mdpi.com/1660-3397/19/1/38/s1>, Figure S1: HRESIMS spectrum of 1, Figure S2: <sup>1</sup>H NMR spectrum of 1 in CDCl<sub>3</sub> at 500 MHz, Figure S3: <sup>13</sup>C NMR spectrum of 1 in CDCl<sub>3</sub> at 125 MHz, Figure S4: HSQC spectrum of 1 in CDCl<sub>3</sub>, Figure S5: <sup>1</sup>H-<sup>1</sup>H COSY spectrum of 1 in CDCl<sub>3</sub>, Figure S6: HMBC spectrum of 1 in CDCl<sub>3</sub>, Figure S7: NOESY spectrum of 1 in CDCl<sub>3</sub>, Figure S8: HRESIMS spectrum of 2, Figure S9: <sup>1</sup>H NMR spectrum of 2 in CDCl<sub>3</sub> at 400 MHz, Figure S10: <sup>13</sup>C NMR spectrum of 2 in CDCl<sub>3</sub> at 100 MHz, Figure S11: HSQC spectrum of 2 in CDCl<sub>3</sub>, Figure S12: <sup>1</sup>H-<sup>1</sup>H COSY spectrum of 2 in CDCl<sub>3</sub>, Figure S13: HMBC spectrum of 2 in CDCl<sub>3</sub>, Figure S14: NOESY spectrum of 2 in CDCl<sub>3</sub>, Figure S15: HRESIMS spectrum



of **3**, Figure S16:  $^1\text{H}$  NMR spectrum of **3** in  $\text{CDCl}_3$  at 400 MHz, Figure S17:  $^{13}\text{C}$  NMR spectrum of **3** in  $\text{CDCl}_3$  at 100 MHz, Figure S18: HSQC spectrum of **3** in  $\text{CDCl}_3$ , Figure S19:  $^1\text{H}$ - $^1\text{H}$  COSY spectrum of **3** in  $\text{CDCl}_3$ , Figure S20: HMBC spectrum of **3** in  $\text{CDCl}_3$ , Figure S21: NOESY spectrum of **3** in  $\text{CDCl}_3$ , Figure S22: HRESIMS spectrum of **4**, Figure S23:  $^1\text{H}$  NMR spectrum of **4** in  $\text{CDCl}_3$  at 500 MHz, Figure S24:  $^{13}\text{C}$  NMR spectrum of **4** in  $\text{CDCl}_3$  at 125 MHz, Figure S25: HSQC spectrum of **4** in  $\text{CDCl}_3$ , Figure S26:  $^1\text{H}$  NMR spectrum of **4** in  $\text{CD}_3\text{OD}$  at 400 MHz, Figure S27:  $^{13}\text{C}$  NMR spectrum of **4** in  $\text{CD}_3\text{OD}$  at 100 MHz, Figure S28: HSQC spectrum of **4** in  $\text{CD}_3\text{OD}$ , Figure S29:  $^1\text{H}$ - $^1\text{H}$  COSY spectrum of **4** in  $\text{CD}_3\text{OD}$ , Figure S30: HMBC spectrum of **4** in  $\text{CD}_3\text{OD}$ , Figure S31: NOESY spectrum of **4** in  $\text{CD}_3\text{OD}$ , Figure S32: HRESIMS spectrum of **5**, Figure S33:  $^1\text{H}$  NMR spectrum of **5** in  $\text{CDCl}_3$  at 500 MHz, Figure S34:  $^{13}\text{C}$  NMR spectrum of **5** in  $\text{CDCl}_3$  at 125 MHz, Figure S35: HSQC spectrum of **5** in  $\text{CDCl}_3$ .

**Author Contributions:** Conceptualization and guiding the experiment, J.-H.S.; investigation, C.-J.T. and A.F.A.; analysis, C.-J.T., C.-Y.H., A.F.A., W.M.A., and R.S.O.; writing—original draft, C.-J.T., A.F.A., and J.-H.S.; writing—review and editing, J.-H.S.; biological activity analyses, C.-J.T., Y.-H.W., and T.-L.H.; collection of the sponge, A.F.A.; species identification of the sponge, Y.M.H. All authors have read and agreed to the published version of the manuscript.

**Funding:** This study was mainly supported by grants from the Ministry of Science and Technology (MOST 104-2320-B-110-001-MY2, 105-2811-M-110-013-, 106-2113-M-110-002-, 107-2320-B-110-001-MY3, and 108-2320-B-110-003-MY2) awarded to J.-H.S. A.F.A. would like to extend appreciation to the Deanship of Scientific Research at King Saud University for further funding this work through research group RG-1440-127.

**Institutional Review Board Statement:** The research protocol was granted approval by the institutional review board of Chang Gung Memorial Hospital (IRB No: 201601307A3, 20161124-20191123; 201902217A3, 20200501-20240630). The study was conducted in accordance with the Declaration of Helsinki.

**Informed Consent Statement:** All subjects gave their informed consent for inclusion before they participated in the study.

**Data Availability Statement:** Data available in a publicly accessible repository.

**Conflicts of Interest:** The authors declare no conflict of interest.

## References

- Carroll, A.R.; Copp, B.R.; Davis, R.A.; Keyzers, R.A.; Prinsep, M.R. Marine natural products. *Nat. Prod. Rep.* **2019**, *36*, 122–173. [\[CrossRef\]](#) [\[PubMed\]](#)
- Keffer, J.L.; Plaza, A.; Bewley, C.A. Motualevic acids A-F, antimicrobial acids from the sponge *Siliquariaspongia* sp. *Org. Lett.* **2009**, *11*, 1087–1090. [\[CrossRef\]](#) [\[PubMed\]](#)
- Hagiwara, K.; Garcia Hernandez, J.E.; Harper, M.K.; Carroll, A.; Motti, C.A.; Awaya, J.; Nguyen, H.Y.; Wright, A.D. Puupehenol, a potent antioxidant antimicrobial meroterpenoid from a Hawaiian deep-water *Dactylospongia* sp. sponge. *J. Nat. Prod.* **2015**, *78*, 325–329. [\[CrossRef\]](#) [\[PubMed\]](#)
- Gotsbacher, M.P.; Karuso, P. New antimicrobial bromotyrosine analogues from the sponge *Pseudoceratina purpurea* and its predator *Tylodina corticalis*. *Mar. Drugs* **2015**, *13*, 1389–1409. [\[CrossRef\]](#) [\[PubMed\]](#)
- Cariello, L.; Zanetti, L.; Cuomo, V.; Vanzanella, F. Antimicrobial activity of avarol, a sesquiterpenoid hydroquinone from the marine sponge, *Dysidea avara*. *Comp. Biochem. Physiol. B.* **1982**, *71*, 281–283. [\[CrossRef\]](#)
- Gong, K.K.; Tang, X.L.; Liu, Y.S.; Li, P.L.; Li, G.Q. Imidazole alkaloids from the South China Sea sponge *Pericharax heteroraphis* and their cytotoxic and antiviral activities. *Molecules* **2016**, *21*, 150. [\[CrossRef\]](#)
- Bastos, J.C.; Kohn, L.K.; Fantinatti-Garboggini, F.; Padilla, M.A.; Flores, E.F.; da Silva, B.P.; de Menezes, C.B.; Arns, C.W. Antiviral activity of *Bacillus* sp. isolated from the marine sponge *Petromica citrina* against bovine viral diarrhea virus, a surrogate model of the hepatitis C virus. *Viruses* **2013**, *5*, 1219–1230. [\[CrossRef\]](#)
- El Sayed, K.A.; Hamann, M.T.; Hashish, N.E.; Shier, W.T.; Kelly, M.; Khan, A.A. Antimalarial, antiviral, and antitoxoplasmosis norsesterterpene peroxide acids from the Red Sea sponge *Diacarnus erythraeanus*. *J. Nat. Prod.* **2001**, *64*, 522–524. [\[CrossRef\]](#)
- Chianese, G.; Silber, J.; Luciano, P.; Merten, C.; Erpenbeck, D.; Topaloglu, B.; Kaiser, M.; Tasdemir, D. Antiprotozoal linear furanosesterterpenoids from the marine sponge *Ircinia oros*. *J. Nat. Prod.* **2017**, *80*, 2566–2571. [\[CrossRef\]](#)
- Regalado, E.L.; Tasdemir, D.; Kaiser, M.; Cachet, N.; Amade, P.; Thomas, O.P. Antiprotozoal steroidal saponins from the marine sponge *Pandaros acanthifolium*. *J. Nat. Prod.* **2010**, *73*, 1404–1410. [\[CrossRef\]](#)
- Qin, G.F.; Tang, X.L.; de Voogd, N.J.; Li, P.L.; Li, G.Q. Cytotoxic components from the Xisha sponge *Fascaplysinopsis reticulata*. *Nat. Prod. Res.* **2018**, 1–7. [\[CrossRef\]](#) [\[PubMed\]](#)

12. Urda, C.; Fernández, R.; Rodríguez, J.; Peérez, M.; Jiménez, C.; Cuevas, C. Daedophamide, a cytotoxic cyclodepsipeptide from a *Daedalopelta* sp. sponge collected in Indonesia. *J. Nat. Prod.* **2017**, *80*, 3054–3059. [\[CrossRef\]](#) [\[PubMed\]](#)
13. Jiao, W.H.; Shi, G.H.; Xu, T.T.; Chen, G.D.; Gu, B.B.; Wang, Z.; Peng, S.; Wang, S.P.; Li, J.; Han, B.N.; et al. Dysiherbols A-C and dysideanone E, cytotoxic and NF- $\kappa$ B inhibitory tetracyclic meroterpenes from a *Dysidea* sp. marine sponge. *J. Nat. Prod.* **2016**, *79*, 406–411. [\[CrossRef\]](#) [\[PubMed\]](#)
14. Gui, Y.H.; Jiao, W.H.; Zhou, M.; Zhang, Y.; Zeng, D.Q.; Zhu, H.R.; Liu, K.C.; Sun, F.; Chen, H.F.; Lin, H.W. Septosones A-C, in vivo anti-inflammatory meroterpenoids with rearranged carbon skeletons from the marine sponge *Dysidea septosa*. *Org. Lett.* **2019**, *21*, 767–770. [\[CrossRef\]](#) [\[PubMed\]](#)
15. Randazzo, A.; Bifulco, G.; Giannini, C.; Bucci, M.; Debitus, C.; Cirino, G.; Gomez-Paloma, L. Halipeptins A and B: Two novel potent anti-inflammatory cyclic depsipeptides from the Vanuatu marine sponge *Haliclona* species. *J. Am. Chem. Soc.* **2001**, *123*, 10870–10876. [\[CrossRef\]](#)
16. Costantino, V.; Fattorusso, E.; Mangoni, A.; Perinu, C.; Cirino, G.; De Gruttola, L.; Roviezzo, F. Tedanol: A potent anti-inflammatory *ent*-pimarane diterpene from the Caribbean sponge *Tedania ignis*. *Bioorg. Med. Chem.* **2009**, *17*, 7542–7547. [\[CrossRef\]](#)
17. Liu, Y.; Ji, H.; Dong, J.; Zhang, S.; Lee, K.J.; Matthew, S. Antioxidant alkaloid from the South China Sea marine sponge *Iotrochota* sp. *Z. Naturforsch. C* **2008**, *63*, 636–638. [\[CrossRef\]](#)
18. Utkina, N.K. Antioxidant activity of zyzzyanones and makaluvamines from the marine sponge *Zyzzya fuliginosa*. *Nat. Prod. Commun.* **2013**, *8*, 1551–1552. [\[CrossRef\]](#)
19. Costantino, V.; Fattorusso, E.; Mangoni, A.; Di Rosa, M.; Ianaro, A. Glycolipids from sponges. VII. Simplexides, novel immuno-suppressive glycolipids from the Caribbean sponge *Plakortis simplex*. *Bioorg. Med. Chem. Lett.* **1999**, *9*, 271–276. [\[CrossRef\]](#)
20. Gunasekera, S.P.; Cranick, S.; Longley, R.E. Immunosuppressive compounds from a deep water marine sponge, *Agelas flabelliformis*. *J. Nat. Prod.* **1989**, *52*, 757–761. [\[CrossRef\]](#)
21. Kubanek, J.; Fenical, W.; Pawlik, J.R. New antifeedant triterpene glycosides from the Caribbean sponge *Erylus formosus*. *Nat. Prod. Lett.* **2001**, *15*, 275–285. [\[CrossRef\]](#) [\[PubMed\]](#)
22. Assmann, M.; van Soest, R.W.; Kock, M. New antifeedant bromopyrrole alkaloid from the Caribbean sponge *Stylissa caribica*. *J. Nat. Prod.* **2001**, *64*, 1345–1347. [\[CrossRef\]](#) [\[PubMed\]](#)
23. Albrizio, S.; Ciminiello, P.; Fattorusso, E.; Magno, S.; Pawlik, J.R. Amphitoxin, a new high molecular weight antifeedant pyridinium salt from the Caribbean sponge *Amphimedon compressa*. *J. Nat. Prod.* **1995**, *58*, 647–652. [\[CrossRef\]](#) [\[PubMed\]](#)
24. Fattorusso, E.; Minale, L.; Sodano, G.; Trivellone, E. Isolation and structure of nitenin and dihydronitenin, new furanoterpenes from *Spongia nitens*. *Tetrahedron* **1971**, *27*, 3909–3917. [\[CrossRef\]](#)
25. Abdjul, D.B.; Yamazaki, H.; Kanno, S.I.; Wewengkang, D.S.; Rotinsulu, H.; Sumilat, D.A.; Ukai, K.; Kapojos, M.M.; Namikoshi, M. Furanoterpenes, new types of protein tyrosine phosphatase 1B inhibitors, from two Indonesian marine sponges, *Ircinia* and *Spongia* spp. *Bioorg. Med. Chem. Lett.* **2017**, *27*, 1159–1161. [\[CrossRef\]](#)
26. Bauvais, C.; Bonneau, N.; Blond, A.; Perez, T.; Bourguet-Kondracki, M.L.; Zirah, S. Furanoterpene diversity and variability in the marine sponge *Spongia officinalis*, from untargeted LC-MS/MS metabolomic profiling to furanolactam derivatives. *Metabolites* **2017**, *7*, 27. [\[CrossRef\]](#)
27. Li, C.J.; Schmitz, F.J.; Kelly-Borges, M. Six new spongian diterpenes from the sponge *Spongia matamata*. *J. Nat. Prod.* **1999**, *62*, 287–290. [\[CrossRef\]](#)
28. Gross, H.; Wright, A.D.; Reinscheid, U.; König, G.M. Three new spongian diterpenes from the Fijian marine sponge *Spongia* sp. *Nat. Prod. Commun.* **2009**, *4*, 315–322. [\[CrossRef\]](#)
29. El-Desoky, A.H.; Kato, H.; Tsukamoto, S. Ceylonins G-I: Spongian diterpenes from the marine sponge *Spongia ceylonensis*. *J. Nat. Prod.* **2017**, *71*, 765–769. [\[CrossRef\]](#)
30. Chen, Q.; Mao, Q.; Bao, M.; Mou, Y.; Fang, C.; Zhao, M.; Jiang, W.; Yu, X.; Wang, C.; Dai, L.; et al. Spongian diterpenes including one with a rearranged skeleton from the marine sponge *Spongia officinalis*. *J. Nat. Prod.* **2019**, *82*, 1714–1718. [\[CrossRef\]](#)
31. Kazlauskas, R.; Murphy, P.T.; Wells, R.J.; Noack, K.; Oberhansli, W.E.; Schonholzer, P. A new series of diterpenes from Australian *Spongia* species. *Aust. J. Chem.* **1979**, *32*, 867–880. [\[CrossRef\]](#)
32. Searle, P.A.; Molinzi, T.F. Scalemic 12-hydroxyambliofuran and 12-acetoxyambliofuran, five tetracyclic furanoditerpenes and a furanosesterterpene from *Spongia* sp. *Tetrahedron* **1994**, *50*, 9893–9908. [\[CrossRef\]](#)
33. Yang, I.; Lee, J.; Lee, J.; Hahn, D.; Chin, J.; Won, D.H.; Ko, J.; Choi, H.; Hong, A.; Nam, S.J.; et al. Scalalactams A-D, scalarane sesterterpenes with a  $\gamma$ -Lactam moiety from a Korean *Spongia* sp. marine sponge. *Molecules* **2018**, *23*, 3187. [\[CrossRef\]](#) [\[PubMed\]](#)
34. Nam, S.J.; Ko, H.; Ju, M.K.; Hwang, H.; Chin, J.; Ham, J.; Lee, B.; Lee, J.; Won, D.H.; Choi, H.; et al. Scalarane sesterterpenes from a marine sponge of the genus *Spongia* and their FXR antagonistic activity. *J. Nat. Prod.* **2007**, *70*, 1691–1695. [\[CrossRef\]](#) [\[PubMed\]](#)
35. Tsukamoto, S.; Miura, S.; van Soest, R.W.M.; Ohta, T. Three new cytotoxic sesterterpenes from a marine sponge *Spongia* sp. *J. Nat. Prod.* **2003**, *66*, 438–440. [\[CrossRef\]](#)
36. Li, J.; Gu, B.B.; Sun, F.; Xu, J.R.; Jiao, W.H.; Yu, H.B.; Han, B.N.; Yang, F.; Zhang, X.C.; Lin, H.W. Sesquiterpene quinones/hydroquinones from the marine sponge *Spongia pertusa* Esper. *J. Nat. Prod.* **2017**, *80*, 1436–1445. [\[CrossRef\]](#)
37. Ito, T.; Nguyen, H.M.; Win, N.N.; Vo, H.Q.; Nguyen, H.T.; Morita, H. Three new sesquiterpene aminoquinones from a Vietnamese *Spongia* sp. and their biological activities. *J. Nat. Prod.* **2018**, *72*, 298–303. [\[CrossRef\]](#)

38. Migliuolo, A.; Piccialli, V.; Sica, D. Two new 9,11-secosterols from the marine sponge *Spongia officinalis*. Synthesis of 9,11-seco-3 $\beta$ ,6 $\alpha$ ,11-trihydroxy-5 $\alpha$ -cholest-7-en-9-one. *Steroids* **1992**, *57*, 344–347. [[CrossRef](#)]
39. Migliuolo, A.; Piccialli, V.; Sica, D.; Giordano, F. New D<sup>8</sup>- and D<sup>8</sup>(14)-5 $\alpha$ ,6 $\alpha$ -epoxysterols from the marine sponge *Spongia officinalis*. *Steroids* **1993**, *58*, 134–140. [[CrossRef](#)]
40. Aiello, A.; Fattorusso, E.; Magno, S.; Menna, M. Isolation of five new 5 $\alpha$ -hydroxy-6-keto-D<sup>7</sup> sterols from the marine sponge *Oscarella lobularis*. *Steroids* **1991**, *56*, 337–340. [[CrossRef](#)]
41. Grassia, A.; Bruno, I.; Debitus, C.; Marzocco, S.; Pinto, A.; Gomez-Paloma, L.; Riccio, R. Spongidepsin, a new cytotoxic macrolide from *Spongia* sp. *Tetrahedron* **2001**, *57*, 6257–6260. [[CrossRef](#)]
42. Sun, D.Y.; Han, G.Y.; Yang, N.N.; Lan, L.F.; Li, X.W.; Guo, Y.W. Racemic trinorsesquiterpenoids from the Beihai sponge *Spongia officinalis*: Structure and biomimetic total synthesis. *Org. Chem. Front.* **2018**, *5*, 1022–1027. [[CrossRef](#)]
43. Parrish, S.M.; Yoshida, W.Y.; Kondratyuk, T.P.; Park, E.J.; Pezzuto, J.M.; Kelly, M.; Williams, P.G. Spongiapyridine and related spongians isolated from an Indonesian *Spongia* sp. *J. Nat. Prod.* **2014**, *77*, 1644–1649. [[CrossRef](#)] [[PubMed](#)]
44. Pech-Puch, D.; Rodriguez, J.; Cautain, B.; Sandoval-Castro, C.A.; Jimenez, C. Cytotoxic furanoditerpenes from the sponge *Spongia tubulifera* collected in the Mexican Caribbean. *Mar. Drugs* **2019**, *17*, 416. [[CrossRef](#)] [[PubMed](#)]
45. Demarco, P.V.; Farkas, E.; Doddrell, D.; Mylari, B.L.; Wenkert, E. Pyridine-induced solvent shifts in the nuclear magnetic resonance spectra of hydroxylic compounds. *J. Am. Chem. Soc.* **1968**, *90*, 5480–5486. [[CrossRef](#)]
46. Kalinowski, H.O.; Berger, S.; Braun, S. *Carbon-13 NMR Spectroscopy*; John Wiley & Sons: Chichester, UK, 1988.
47. Parker, K.A.; Johnson, W.S. Synthesis of dendrolasin. *Tetrahedron Lett.* **1969**, *17*, 1329–1332. [[CrossRef](#)]
48. Brown, D.A.; Glass, W.K.; Mageswaran, R.; Mohammed, S.A. <sup>1</sup>H and <sup>13</sup>C NMR studies of isomerism in hydroxamic acids. *Magn. Reson. Chem.* **1991**, *29*, 40–45. [[CrossRef](#)]
49. Trabulsi, H.; Guillot, R.; Rousseau, G. Preparation of imino lactones by electrophilic cyclization of  $\beta$ ,  $\gamma$ -unsaturated hydroxamates: Formation of 3-cyanoprop-2-en-1-ones through fragmentation reactions. *Eur. J. Org. Chem.* **2010**, *2010*, 5884–5896. [[CrossRef](#)]
50. Tiecco, M.; Testaferri, L.; Marini, F.; Sternativo, S.; Bagnoli, L.; Santi, C.; Temperini, A. A sulfur-containing diselenide as an efficient chiral reagent in asymmetric selenocyclization reactions. *Tetrahedron: Asymmetry* **2001**, *12*, 1493–1502. [[CrossRef](#)]
51. Pretsch, E.; Clerc, T.; Seibl, J.; Simon, W. *Tables of Spectral Data for Structure Determination of Organic Compounds*; Springer-Verlag: Berlin Heidelberg, Germany, 1983.
52. Shen, Y.C.; Shih, P.S.; Lin, Y.S.; Lin, Y.C.; Kuo, Y.H.; Kuo, Y.C.; Khalil, A.T. Irciformonins E–K, C22-trinorsesquiterpenoids from the sponge *Ircinia formosana*. *Helv. Chim. Acta* **2009**, *92*, 2101–2110. [[CrossRef](#)]
53. Ohtani, I.; Kusumi, T.; Kashman, Y.; Kakisawa, H. High-field FT NMR application of Mosher's method. The absolute configurations of marine terpenoids. *J. Am. Chem. Soc.* **1991**, *113*, 4092–4096. [[CrossRef](#)]
54. Huang, H.C.; Ahmed, A.F.; Su, J.H.; Chao, C.H.; Wu, Y.C.; Chiang, M.Y.; Sheu, J.H. Crassolidides A–F, cembranoids with a trans-fused lactone from the soft coral *Sarcophyton crassocaule*. *J. Nat. Prod.* **2006**, *69*, 1554–1559. [[CrossRef](#)] [[PubMed](#)]
55. O'Brien, J.; Wilson, I.; Orton, T.; Pognan, F. Investigation of the Alamar Blue (resazurin) fluorescent dye for the assessment of mammalian cell cytotoxicity. *Eur. J. Biochem.* **2000**, *267*, 5421–5426. [[CrossRef](#)]
56. Nakayama, G.R.; Caton, M.C.; Nova, M.P.; Parandoosh, Z. Assessment of the Alamar Blue assay for cellular growth and viability in vitro. *J. Immunol. Methods* **1997**, *204*, 205–208. [[CrossRef](#)]
57. Yu, H.P.; Hsieh, P.W.; Chang, Y.J.; Chung, P.J.; Kuo, L.M.; Hwang, T.L. 2-(2-Fluorobenzamido)benzoate ethyl ester (EFB-1) inhibits superoxide production by human neutrophils and attenuates hemorrhagic shock-induced organ dysfunction in rats. *Free Radic. Biol. Med.* **2011**, *50*, 1737–1748. [[CrossRef](#)] [[PubMed](#)]
58. Yang, S.C.; Chung, P.J.; Ho, C.M.; Kuo, C.Y.; Hung, M.F.; Huang, Y.T.; Chang, W.Y.; Chang, Y.W.; Chan, K.H.; Hwang, T.L. Propofol inhibits superoxide production, elastase release, and chemotaxis in formyl peptide-activated human neutrophils by blocking formyl peptide receptor 1. *J. Immunol.* **2013**, *190*, 6511–6519. [[CrossRef](#)]
59. Hwang, T.L.; Su, Y.C.; Chang, H.L.; Leu, Y.L.; Chung, P.J.; Kuo, L.M.; Chang, Y.J. Suppression of superoxide anion and elastase release by C18 unsaturated fatty acids in human neutrophils. *J. Lipid Res.* **2009**, *50*, 1395–1408. [[CrossRef](#)]



## Invited Review

## Regulation of the proteostasis network during enterovirus infection: A feedforward mechanism for EV-A71 and EV-D68

Jia-Rong Jheng<sup>a</sup>, Yuan-Siao Chen<sup>a</sup>, Jim-Tong Horng<sup>a,b,c,d,\*</sup><sup>a</sup> Department of Biochemistry and Molecular Biology, College of Medicine, Chang Gung University, Kweishan, Taoyuan, Taiwan<sup>b</sup> Research Center for Industry of Human Ecology and Graduate Institute of Health Industry Technology, Chang Gung University of Science and Technology, Taoyuan, Taiwan<sup>c</sup> Research Center for Emerging Viral Infections, College of Medicine, Chang Gung University, Kweishan, Taoyuan, Taiwan<sup>d</sup> Molecular Infectious Disease Research Center, Chang Gung Memorial Hospital, Chang Gung University College of Medicine, Taoyuan, Taiwan

## ARTICLE INFO

## Keywords:

Antiviral

Enterovirus D68

Enterovirus A71

ER stress

Proteostasis network

Unfolded protein response

## ABSTRACT

The proteostasis network guarantees successful protein synthesis, folding, transportation, and degradation. Mounting evidence has revealed that this network maintains proteome integrity and is linked to cellular physiology, pathology, and virus infection. Human enterovirus A71 (EV-A71) and EV-D68 are suspected causative agents of acute flaccid myelitis, a severe poliomyelitis-like neurologic syndrome with no known cure. In this context, further clarification of the molecular mechanisms underlying EV-A71 and EV-D68 infection is paramount. Here, we summarize the components of the proteostasis network that are intercepted by EV-A71 and EV-D68, as well as antivirals that target this network and may help develop improved antiviral drugs.

## 1. Introduction

The proteostasis network (PN) is an inter-organelle communication network comprising the protein-translation machinery, the trafficking PN, and the protein quality control system – which collectively ensure successful protein synthesis, folding, transportation, and degradation (Hutt and Balch, 2013; Powers et al., 2009) (Fig. 1). Proteostasis is not only key to ensuring normal cellular physiology (Hipp et al., 2019; Jheng et al., 2018a) but also has been intricately linked to virus infection (Marques et al., 2019; Heaton et al., 2016). Viruses may disturb the PN by enhancing or suppressing PN-related protein expression or co-opting PN molecules to facilitate viral replication. In this review, we discuss the molecular mechanisms involved in the pathogenesis of EV-A71 and EV-D68 infections and their potential impact on PN. The background section describes the epidemiology and pathogenesis of EV-A71 and EV-D68 and the components of PN. The mechanisms by which EV-A71 and EV-D68 disturb or co-opt the protein homeostasis system are subsequently discussed. We also summarize the current therapeutic options as well as the limitations in targeting viral protein translation or host PN to outmaneuver both viruses. Finally, an extended discussion on the widespread application of these antivirals is provided.

## 2. Background

## 2.1. Human enterovirus A71 (EV-A71) and EV-D68

EV-A71 and EV-D68 are members of the Picornaviridae family. They share similar features and are closely related to the other two picornaviruses, i.e., poliovirus and coxsackievirus type B3 (CVB3) (Lin et al., 2009a). EV-A71 was initially identified in an infant with encephalitis in 1969 (Schmidt et al., 1974). Large-scale EV-A71 epidemics have occurred in the Asia-Pacific region, including Brunei, Cambodia, China, Malaysia, Singapore, and Vietnam (Puenpa et al., 2019). Human EV-A71 epidemics can cause febrile illness, acute respiratory disease, and occasional neurological complications. Infections generally occur during the warm months of the year and recur annually. EV-D68, an *Enterovirus D* species, was initially isolated in California from children with pneumonia and bronchiolitis in 1962 (Schieble et al., 1967). EV-D68 only caused sporadic infections worldwide until upsurges occurred in Europe, North America, Asia, and Australia as of 2008 (Centers for Disease, 2011; Tokarz et al., 2012; Levy et al., 2015). Over 1000 cases of infection, resulting in 14 deaths, were reported during the 2014 EV-D68 epidemic in the United States (Sejvar et al., 2016). Currently, EV-D68 regularly circulates in the United States and has been linked to severe respiratory disease and acute flaccid myelitis (AFM), which has been associated with poliomyelitis (Lugo and Krogstad, 2016). AFM affects

\* Corresponding author. Department of Biochemistry, Chang Gung University, 259 Wen-Hua 1st Rd., Kweishan, Taoyuan, 333, Taiwan.

E-mail address: [jimtong@mail.cgu.edu.tw](mailto:jimtong@mail.cgu.edu.tw) (J.-T. Horng).<https://doi.org/10.1016/j.antiviral.2021.105019>

Received 13 October 2020; Received in revised form 12 January 2021; Accepted 16 January 2021

Available online 20 January 2021

0166-3542/© 2021 Published by Elsevier B.V.



**Abbreviations**

|        |   |        |   |
|--------|---|--------|---|
| A3G    | APOBEC3G  | NLS    | nuclear-localization signal                               |
| ACBD3  | acyl-coenzyme A binding domain-containing 3                                     | OSBP   | oxysterol-binding protein                                 |
| AFM    | acute flaccid myelitis  | PCBP   | poly(rC)-binding protein                                  |
| AUF1   | AU-rich element RNA-binding factor 1  | PABP   | poly(A)-binding protein                                   |
| BPI    | Bactericidal/permeability-increasing protein                                    | PI4KB  | phosphatidylinositol 4-kinase III $\beta$                 |
| BPIFB6 | Bactericidal/permeability-increasing protein fold-containing family B, member 6 | PI4P   | phosphatidylinositol-4-phosphate                          |
| CNX    | calnexin  | PN     | proteostasis network                                      |
| CRT    | calreticulin  | PTB    | polypyrimidine tract-binding protein                      |
| CVB3   | coxsackievirus type B3  | RTN    | reticulum   |
| eIF3   | eukaryotic initiation factors   | UPR    | unfolded-protein response                                 |
| ERAD   | ER-associated degradation   | TDP    | 1,3,5-Trihydroxy-13,13-dimethyl-2H-pyran [7,6-b] xanthone |
| eRF1   | eukaryotic release factor 1   | TRAM   | translocating chain-associated membrane protein           |
| FBP    | far-upstream element (FUSE)-binding proteins                                    | TRAP   | translocon-associated protein complex                     |
| EV-D68 | human enterovirus D68   | RA     | Rosmarinic acid   |
| EV-A71 | human enterovirus A71   | S1P    | site-1 protease   |
| hnRNP  | heterogeneous nuclear ribonucleoproteins  | Sam68  | 68-kDa Src-associated protein in mitosis                  |
| HSV-1  | herpes simplex virus-1  | SG     | stress granule  |
| IRES   | internal ribosome entry site  | SNAP29 | synaptosome-associated protein of 29 kDa                  |
| ITAF   | IRES-transactivating factor   | STX17  | syntaxin-17   |
| JEV    | Japanese encephalitis virus   | UGGT   | UDP-glucose: glycoprotein glucosyltransferase             |
| miR    | microRNA  | VAMP8  | vesicle-associated membrane protein-8                     |
|        |   | vsRNA  | virus-derived small RNA                                   |
|        |   | XBP1   | X-box binding protein-1                                   |

the spinal cord's gray matter, and thereby weakens the muscles and reflexes of the body. Recent epidemiological studies have shown that both EV-A71 and EV-D68 were the probable causes of the AFM outbreak in the United States after the eradication of poliomyelitis (Adam, 2019).

The complete genome sequences (approximately 7400 nucleotides)

of picornaviruses consist of a 5'-untranslated region (5'-UTR), a 3'-UTR, and a single open-reading frame (Fig. 2). The open-reading frame is approximately 6500 nucleotides long and encodes a polyprotein, which is proteolytically processed by the viral proteases 2A<sup>pro</sup> and 3C<sup>pro</sup> to yield structural proteins (VP1–VP4 from the P1 capsid precursor) and

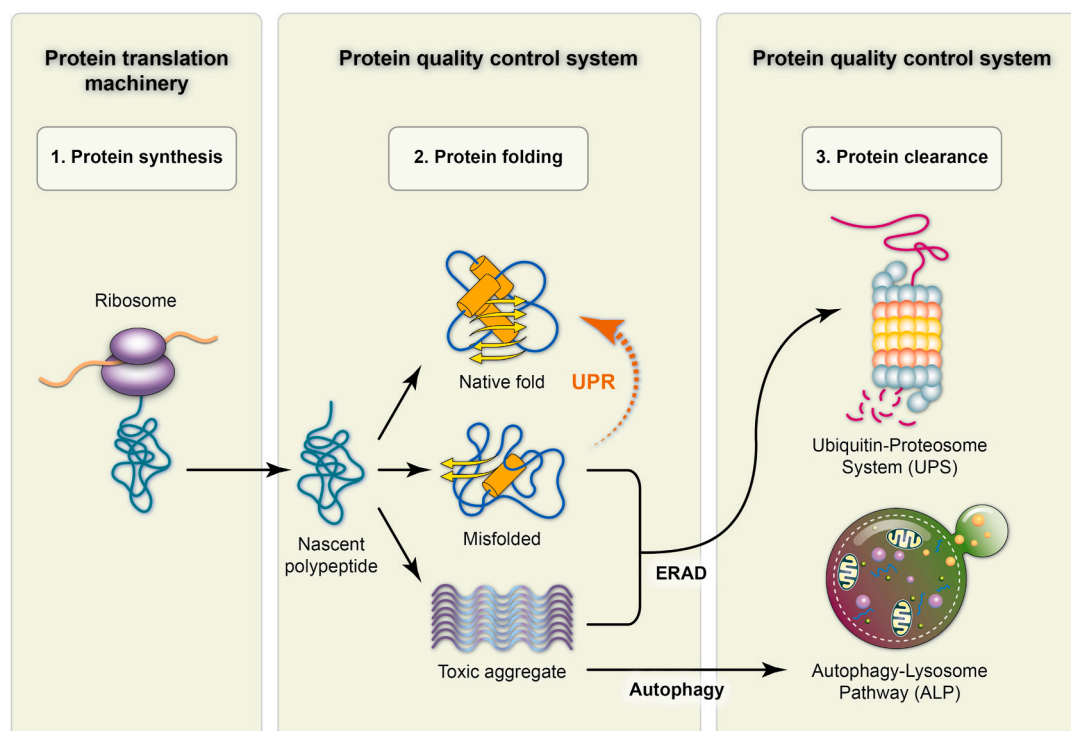


**Fig. 1. Schematic illustration of the proteostasis network (PN).** The PN consists of the protein translation machinery, the ER protein trafficking, and the protein quality system, which together ensure cellular proteostasis by minimizing the accumulation of misfolded or aggregated proteins. It begins with (1) protein synthesis at the ribosomes. (2) Then the nascent polypeptide folds into its functional conformation for trafficking to the transport destination. Misfolded proteins can be recognized and refolded by the UPR. However, proteins with inefficient and inaccurate folding are substrates of (3) ERAD or autophagy, which ultimately degrade them via the UPS or the lysosomal degradation pathway, respectively.



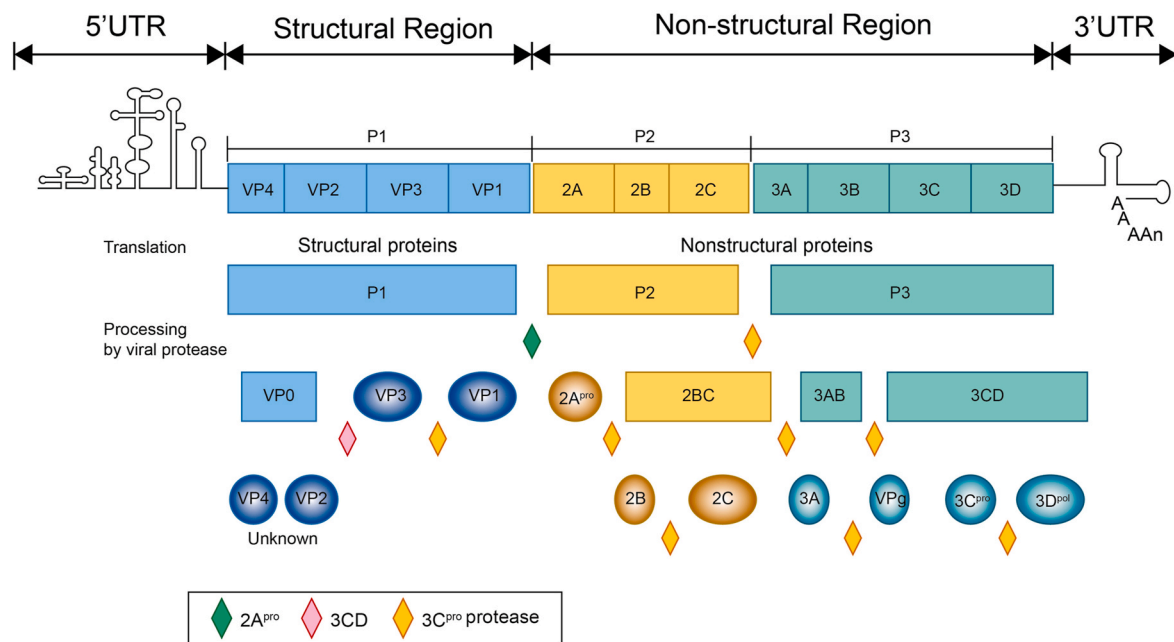


**Fig. 2.** A diagrammatic representation of the enterovirus genome and the respective polyprotein products. The enterovirus genome contains a single open reading frame flanked by 5' and 3' untranslated regions (UTRs). The 5'-UTR contains an internal ribosome entry site (IRES) that is responsible for translation initiation. The polyadenylated 3'-UTR is involved in viral replication and may manipulate protein translation. The polyprotein encoded by the enterovirus genome is proteolytically processed by the viral proteases 2A<sup>pro</sup> and 3C<sup>pro</sup> to yield 11 mature proteins.

non-structural proteins (2A<sup>pro</sup>, 2B, 2C<sup>ATPase</sup>, 3A, 3B, 3C<sup>pro</sup>, and RNA polymerase [3D<sup>pol</sup>] from the P2–P3 precursor). The 5'-UTR of the positive-strand RNA genome forms a cloverleaf structure, which plays a central role in the regulation of viral RNA replication; an internal ribosome entry site (IRES) is responsible for translation initiation. The polyadenylated 3'-UTR is involved in viral replication and can manipulate IRES activity (Dobrikova et al., 2003).

## 2.2. Proteostasis network

### 2.2.1. Protein-translation machinery

Eukaryotic protein synthesis is a highly regulated and complicated process consisting of three phases: initiation, elongation, and termination. Briefly, during the initiation phase, the 40 S ribosome forms a 43S pre-initiation complex with the eukaryotic translation initiation factors (eIF)-GTP-Met-tRNA<sup>Met</sup>. The 43S pre-initiation complex is recruited to the 5' cap of eukaryotic mRNAs by the heterotrimeric eIF4F complex, which is composed of eIF4E, eIF4G, and eIF4A. Subsequently, poly(A)-binding protein (PABP) associates with polyadenylated 3' mRNA and interacts with eIF4G to form the 5'-cap-eIF4E-eIF4G-PABP-poly(A) complex. After eIF4E kinases bind to and phosphorylate eIF4E, the resulting 48S complex scans the mRNA until an optimal start codon is recognized. During the elongation step, aminoacyl-tRNAs are delivered to the ribosome A site and ribosome-catalyzed peptide bonds are formed. Finally, the translation-termination step begins with the recognition of a stop codon by eukaryotic release factor 1 (eRF1), which is part of the eRF1-eRF3-GTP complex. With the help of eRF3 GTPase, the release of the polypeptide is mediated by eRF1-triggered hydrolysis of the polypeptidyl-tRNA. Notably, the switch from cap-dependent to cap-independent/IRES-dependent translation is required when cells face pathophysiological stress conditions, including hypoxia, temperature changes, DNA damage, and virus infection (Martinez-Salas et al., 2013).

### 2.2.2. Trafficking PN

The effective cooperation between membranes and organelles facilitates the accurate modification and transportation of proteins and lipids; importantly, the interplay between proteins and lipid

components impacts the endomembrane system of eukaryotic cells (Echarri and Del Pozo, 2015; Chandra et al., 2009). Most endoplasmic reticulum (ER)-resident and secretory proteins are first co-translationally targeted to the membrane of the ER. After insertion of nascent proteins into the ER with the aid of the Sec61 translocon, a signal peptidase cleaves signal peptides and releases polypeptides from the membrane. The binding of chaperones and folding enzymes protects these unfolded polypeptides from incorrect folding or aggregation, thereby allowing the polypeptide chain to adopt its correct conformation. Proteins that fold correctly are packaged into ER-derived cargo vesicles and are transported to the ER/Golgi-intermediate compartment and to the Golgi complex in a COP II-dependent manner. In contrast, proteins recycled from the cis-Golgi complex to the ER rely on COP I-mediated retrograde trafficking.

### 2.2.3. Protein-quality control system

A dynamic protein equilibrium reflects the balance between protein synthesis and protein degradation. Aberrant proteins, which are continuously produced by abnormal cell functions, are detected and removed to prevent their accumulation; of note, the accumulation of misfolded proteins in the ER under certain physiological conditions and pathological perturbations disturbs proteostasis and causes ER stress. Several specialized mechanisms, including those involved in the unfolded protein response (UPR), ER-associated degradation (ERAD), and autophagy, ensure adequate protein folding and maturation to achieve proteostasis (Moon et al., 2018; Rutkowski and Hegde, 2010).

The UPR consists of three transmembrane ER-resident UPR sensors: the activating transcription factor 6 (ATF6), the inositol-requiring protein 1 (IRE1), and the protein kinase RNA-like ER kinase (PERK) (Fig. 3A) (Walter and Ron, 2011; Hetz, 2012). PERK, IRE1, and ATF6 can bind to the chaperone GRP78/BiP and remain inactive under normal circumstances. Misfolded and unfolded proteins in the ER compete for the binding to GRP78/BiP, which results in the activation of PERK, IRE1, ATF6, and downstream signal-transduction pathways (Otero et al., 2010; Bertolotti et al., 2000). The activated PERK cytosolic domain phosphorylates and activates the eukaryotic initiation factor 2α (eIF2α) at serine 51, which inhibits protein translation and subsequently relieves

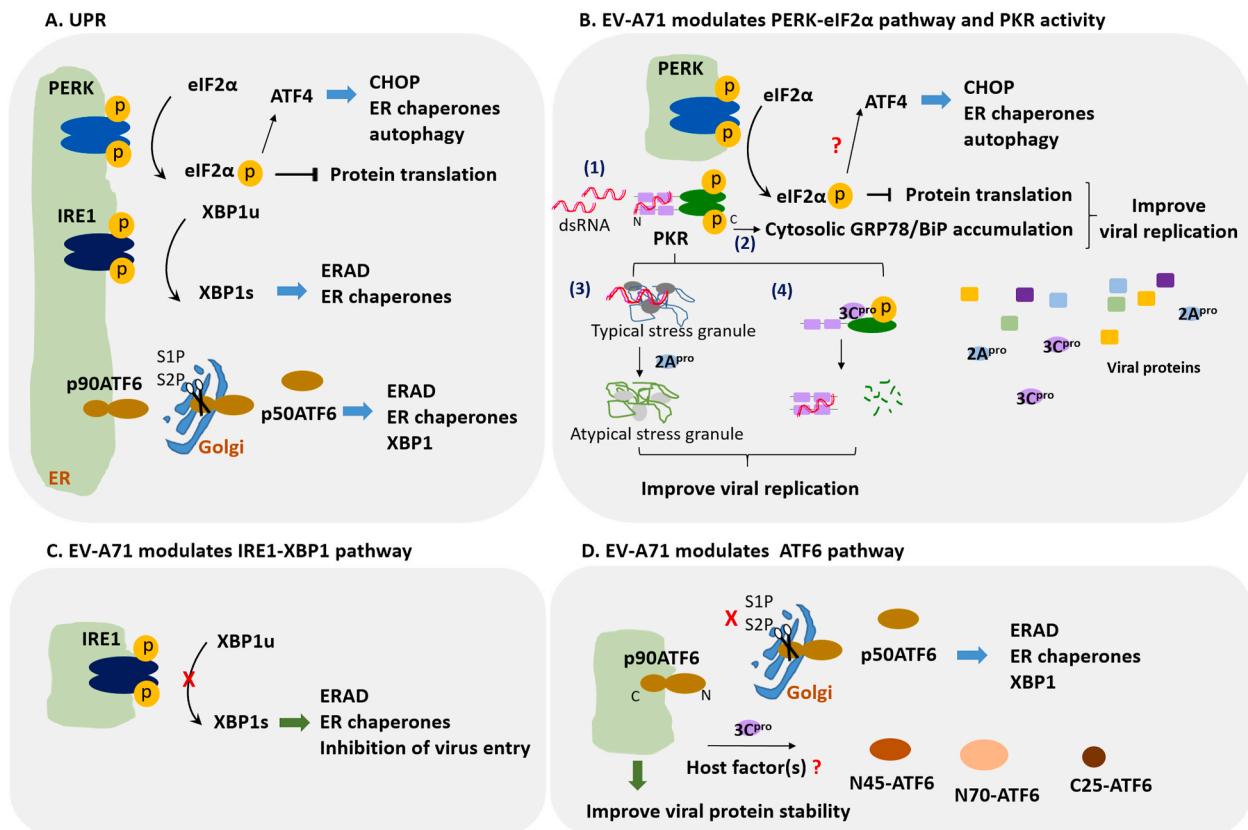


**Fig. 3. Overview of the EV-A71 modulated UPR.** (A) The tripartite arms of the UPR. The three sensors PERK, IRE1, and ATF6 are activated in response to ER stress. Activated PERK phosphorylates eIF2 $\alpha$ , which inhibits global protein synthesis. However, phospho-eIF2 $\alpha$  enhances the translation of ATF4 to induce the expression of chaperones and proteins involved in apoptosis and autophagy regulation. Activated IRE1 $\alpha$  splices XBP1 mRNA (XBP1u) to XBP1s, which encodes the transcription factor XBP1s to positively regulate the expression of chaperones and ERAD-related proteins. Golgi S1P- and S2P-mediated proteolysis activate p90ATF6. The resulting N-terminal p50ATF6 activates the transcription of chaperones, ERAD-related proteins, and UPR-target genes. (B) EV-A71 modulates the PERK-eIF2 $\alpha$  pathway and PKR activity. (B-1) EV-A71 infection activates both PERK and PKR to phosphorylate eIF2 $\alpha$ . (B-2) Activated PKR induces long-lasting ER stress to improve virus replication through the cytoplasmic accumulation of GRP78/BiP. Viral 2A<sup>pro</sup> and 3C<sup>pro</sup> subvert the antiviral action of PKR via different mechanisms. (B-3) 2A<sup>pro</sup> converts dsRNA-trapping typical stress granules into atypical stress granules, which only restrain host mRNA. (B-4) 3C<sup>pro</sup> targets and cleaves PKR to produce an N-terminal PKR fragment containing the dsRNA binding domain, which competes with PKR for dsRNA binding, ensuring viral replication. (C) EV-A71 infection induces the phosphorylation of IRE1 and diminishes the expression of antiviral XBP1s via unknown mechanisms. (D) The p90ATF6 stabilizes viral proteins and is required for EV-A71 replication, especially in the early phase of viral infection. Then, accumulated 3C<sup>pro</sup> and host factors unconventionally cleave the p90ATF6 to produce small fragments with molecular weights of about 25 kDa, 45 kDa, and 70 kDa; the function of the cleavage products is still unclear.

the loading of ER-folding machinery to facilitate the refolding of misfolded and unfolded proteins (Harding et al., 1999). However, several autophagy-related proteins are upregulated by PERK-mediated induction of ATF4 and CHOP, both effectors of the integrated stress response (Deegan et al., 2015; Pakos-Zebrucka et al., 2016). The activated IRE1 cytoplasmic domain, with endoribonuclease activity, cleaves X-box binding protein-1 (XBP-1) mRNA to generate an XBP-1 splice variant (XBP1s) with a translational frameshift (Yoshida et al., 2001; Korennykh et al., 2009). XBP1s activates the expression of UPR-related molecular chaperones, foldases, and ERAD components to relieve ER stress and restore proteostasis (Lee et al., 2003). The activated ATF6 protein translocates into the Golgi apparatus, where it is cleaved by site-1 protease (S1P) and S2P to form the cytosolic p50 fragment, which in turn induces the expression of genes such as CHOP, XBP1, and genes required for ERAD to resolve ER stress (Haze et al., 1999; Yoshida et al., 2000).

ERAD is a multistep process comprising the recognition, translocation, and ubiquitination of misfolded proteins by the cytosolic 26 S proteasome (Vembar and Brodsky, 2008; Brodsky and Wojcikiewicz, 2009). Newly synthesized polypeptides in the ER are immediately conjugated with N-linked oligosaccharides (core glycans), which are recognized and bound by calnexin (CNX) and calreticulin (CRT) to facilitate correct protein folding. ERp57 is a thiol oxidoreductase that interacts with CNX and CRT to facilitate glycoprotein folding (Oliver

et al., 1999). After completion of folding, glucosidase II releases the protein from CNX and CRT by removing the glucose molecule from the core glycan. If the protein is properly folded, it is sequentially released from the ER through the protein secretory pathway. Conversely, if the protein is not correctly folded, it is re-glucosylated by UDP-glucose: glycoprotein glucosyltransferase (UGGT) and re-associated with CNX or CRT for further refolding. If protein folding remains unsuccessful, the mannose of the core glycan is eventually trimmed by ER mannosidase I or ER degradation-enhancing  $\alpha$ -mannosidase-like protein, causing the protein to be recognized by the osteosarcoma 9 protein and subsequently transported to the cytosol for ubiquitin-associated proteasomal degradation (Helenius and Aebi, 2004; Wang et al., 2015; Ferris et al., 2014).

Autophagy – a lysosome-dependent cellular degradation program for long-lived cytoplasmic proteins and damaged organelles (Baiceanu et al., 2016; Parzych and Klionsky, 2014) – is activated in response to cellular stress and plays a key role in the renewal of cellular components (Yang and Klionsky, 2020). Additionally, it is considered the last line of defense to restore proteostasis. When UPR or ERAD are unable to remove misfolded and unfolded proteins, cell damage will eventually occur as a result of partial engulfing of damaged ER by autophagic vesicles (Qi and Chen, 2019).

### 3. How EV-A71 and EV-D68 interfere with PN

#### 3.1. Viral interference with protein translation

Similar to poliovirus and CVB3, EV-A71 and EV-D68 possess a type-1 IRES comprised of domains II to VI and a Yn-Xm-AUG motif at its 3' ends (Thompson and Sarnow, 2003). Translation-initiation factors such as eIF4A, eIF4B, eIF3, eIF2, eIF1A, truncated eIF4G (lacking an N-terminal eIF4E-binding domain), and ITAFs are involved in the internal initiation of translation (Thompson and Sarnow, 2003; Sweeney et al., 2014; Zhang et al., 2015a; White et al., 2011). During EV-A71 infection, the hijacking, cleavage, or modulation of those factors abrogates host cap-dependent translation through mechanisms that disrupt the conformations of circular mRNAs or antagonize new rounds of translation initiation. Cleavage of eIF4Gs (eIF4GI and eIF4G II) by viral 2A<sup>pro</sup> separates the N-terminal eIF4E-binding site on eIF4G from the C-terminal eIF4A- and eIF3-binding sites, thereby abolishing bridges between mRNAs and ribosomes (Hsu et al., 2009). Moreover, cleavage of PABP by 2A<sup>pro</sup> and 3C<sup>pro</sup> impairs ribosome recycling. While eIF4E is dispensable for IRES-dependent translation of EV-A71, viral infection induces microRNA (miR)141-mediated suppression of eIF4E, thereby inhibiting host translation (Ho et al., 2011). Enterovirus infection also induces eIF2 $\alpha$  phosphorylation. Notably, tight binding between phospho-eIF2 $\alpha$  and eIF2B suspends the eIF2 nucleotide recycling. As eIF2 $\alpha$  is required for translational initiation at type-1 IRES (White et al., 2011), EV-A71 infection is expected to initiate an eIF2 $\alpha$ -independent translation. Accordingly, poliovirus-cleaved eIF5B – particularly the resulting N-terminal truncated eIF5B – has been shown to be responsible for type-1 IRES translation in an eIF2 $\alpha$ -independent manner (White et al., 2011). CVB3 infection also induces eIF5B cleavage (de Breyne et al., 2008), raising the possibility that eIF5B plays a role in the gain of type-1 IRES translation following eIF2 $\alpha$  phosphorylation. Moreover, EV-A71-induced eRF1 (otherwise called ETF1) overexpression via downregulation of miR-197 was hypothesized to stabilize the viral RNA to facilitate viral replication (Tang et al., 2019).

Heterogeneous nuclear ribonucleoproteins (hnRNPs) and far-upstream element (FUSE)-binding proteins (FBPs) have been identified as ITAFs. In addition to controlling cellular RNA metabolism and gene expression under normal conditions, these proteins interact with IRESs to modulate mRNA translation when cells are exposed to stress (Martinez-Salas et al., 2013). It is believed that ITAFs modulate IRESs activities via the remodeling of their structures, rendering them capable of binding to ribosomes and initiation factors as well. The ITAFs that promote efficient virus replication include hnRNP A1, poly(rC)-binding protein 1 (PCBP1), PCBP2, hnRNP K, 68-kDa Src-associated protein in mitosis (Sam68), polypyrimidine tract-binding protein (PTB), FBP1, FBP3, and DDX3X, among others. Depletion of each of these ITAFs inhibited EV-A71 IRES activity and viral protein production. Given that protein recognition depends on the RNA sequence and structure, each ITAF appears to have specific targets along the EV-A71 IRES (Table 1). Accordingly, electrophoretic mobility shift assay analysis demonstrated that hnRNP A1 could interact with stem-loops II and VI of the EV-A71 5'-UTR and that hnRNP A2 could take over the function of hnRNP A1 (Lin et al., 2009b). Recently, the combination of nuclear magnetic resonance spectroscopy and small-angle X-ray scattering was used to refine the structure of the stem-loop II domain of EV-A71 in the hnRNP A1-RNA complex, demonstrating that hnRNP A1 altered the structure of stem-loop II to stimulate EV-A71 translation (Tolbert et al., 2017). The cytoplasmic re-localization of hnRNP A1, which is mediated by MINK/p38 MAPK signaling and the downstream molecule Hsp27, is essential for EV-A71 replication (Leong et al., 2015; Dan et al., 2019). PCBP1 interacts with stem-loops I and IV, whereas PCBP2 recognizes stem-loop IV of the EV-A71 IRES and is required for 48 S complex formation on the IRES (Sweeney et al., 2014; Luo et al., 2014). Although PCBP1 and PCBP2 are characterized by similar primary structures with over 80 percent amino acid homology (Ghanem et al., 2014), they have

**Table 1**

ITAFs that regulate IRES-dependent translation of EV-A71.

| ITAFs             | Target region (s)              | References            |
|-------------------|--------------------------------|-----------------------|
| <b>Activator</b>  |                                |                       |
| hnRNP A1          | stem-loops II and VI           | Lin et al. (2009b)    |
| PCBP1             | stem-loops I and IV            | Luo et al. (2014)     |
| PCBP2             | stem-loop IV                   | Sweeney et al. (2014) |
| hnRNP K           | stem-loops I-II and IV         | Lin et al. (2008)     |
| Sam68             | stem-loops IV and V            | Zhang et al. (2015a)  |
| PTB               | stem-loop VI                   | Xi et al. (2019)      |
| FBP1              | spacer region                  | Huang et al. (2011)   |
| FBP3              | the target region is uncertain | Huang et al. (2016)   |
| DDX3X             | stem-loop IV                   | Su et al. (2018)      |
| HuR               | stem-loop II                   | Lin et al. (2015)     |
| Ago2              | stem-loop II                   | Lin et al. (2015)     |
| <b>Suppressor</b> |                                |                       |
| AUF1              | stem-loop II                   | Lin et al. (2014)     |
| FBP2              | stem-loop I-II                 | Lin et al. (2009c)    |
|                   | stem-loop II-III               |                       |
|                   | stem-loop VI- spacer region    |                       |
| A3G               | stem-loop I and II             | Li et al. (2018)      |
| vsRNA1            | stem-loop II                   | Weng et al. (2014)    |

distinct sequence-binding affinities and specificities and, therefore, cannot replace each other functionally (Walter et al., 2002). hnRNP K binds to stem-loops I-II and IV in the 5'-UTR (Lin et al., 2008; Lu and Gao, 2016). Sam68 contains a nuclear-localization signal (NLS) and, thus, is localized in the nucleus (Ishidate et al., 1997).

Previous studies have shown that Sam68 recognizes stem-loops IV and V in the 5'-UTR, and forms complexes with hnRNP K, PCBP2, and PABP (Zhang et al., 2015a; Yang et al., 2002). The role of Sam68 in virus replication was initially proposed by McBride et al. (1996). They identified an interaction between the poliovirus 3D<sup>pol</sup> protein and Sam68 using the yeast two-hybrid system. Cellular fractionation and immunoprecipitation experiments showed the presence of Sam68 and 3D<sup>pol</sup> on poliovirus-induced membranes. It is, however, unclear how Sam68 re-distributes from the nucleus to the cytoplasm. One hypothesis is that viral 3D<sup>pol</sup> may facilitate the cytosolic redistribution of Sam68 since EV-A71 3D<sup>pol</sup> is a nucleocytoplasmic shuttling protein that was previously detected in both cytosolic and nuclear fractions of infected cells (Tang et al., 2016). Alternatively, protein modification or proteolytic processing of nucleoporin proteins or Sam68 may cause Sam68 to re-localize to the cytoplasm (Gustin and Sarnow, 2001). Accordingly, the 3C<sup>pro</sup> protein from foot-and-mouth disease virus (a picornavirus) cleaves and produces a cytosol-localized Sam68 C-terminal truncation mutant (Lawrence et al., 2012). Further investigations are required to clarify the mechanisms underlying the subcellular distribution of Sam68 in virus-infected cells.

PTB is a multifunctional protein originally identified as a splicing regulator (Gil et al., 1991). PTB binds to the 5'-UTR stem-loop VI region via the RNA-binding domains RRM1 and RRM2 (Xi et al., 2019; Lin et al., 2009c). Proteins of the FBP family (FBP1, FBP2, and FBP3) share a high degree of sequence homology and bind to both single-stranded DNA and mRNA to modulate gene expression (Duncan et al., 1994; Davis-Smyth et al., 1996; Kroll et al., 2002). FBP1 and FBP3 positively regulate EV-A71 IRES activity, whereas FBP2 inhibits viral RNA translation (Lin et al., 2009c; Huang et al., 2011, 2016). Interestingly, it has been demonstrated that viral proteinase 2A cleaves FBP1 at Gly-371 and that the resulting product (FBP1<sup>1-371</sup>) contributes additively, together with the full-length FBP1 to IRES-driven translation (Hung et al., 2016). DDX3X, a DEAD-box ATP-dependent RNA helicase can bind to the EV-A71 IRES by itself with no particular sequence preference, as shown via *in vitro* RNA-binding assays. However, in the presence of truncated eIF4G, DDX3X may specifically bind to a region near stem-loop IV to unwind the secondary structure, thereby enabling efficient ribosome entry and scanning (Su et al., 2018). Of note, EV-A71 infection also regulates the expression of some ITAFs that negatively regulate IRES-driven translation. FBP2 interacts with the stem-loop I-II,



stem-loop II-III, and stem-loop VI-spacer regions, thereby impairing the interactions between EV-A71 IRES and other pro-viral ITAFs (Lin et al., 2009c). The coordination of proteasomal activity, autophagy, and caspase activity contributes to EV-A71-induced FBP2 truncation (Chen et al., 2013). Interestingly, the resulting truncated product showed opposite effects on IRES activity. FBP2<sup>1–503</sup> enhanced IRES activity, but FBP2<sup>190–711</sup> negatively regulated EV-A71 translation (Chen et al., 2013). The AU-rich element RNA-binding factor 1 (AUF1) was associated with the AU-rich elements (Marques et al., 2019) in the 3'-UTR of the viral genome and mediated mRNA degradation (Zhang et al., 1993). Studies on poliovirus demonstrated that host-virus interactions can regulate viral IRES activity (Cathcart et al., 2013). The proteolytically active 2A<sup>pro</sup> protein alone is sufficient for the cytoplasmic redistribution of AUF1; there AUF1 directly targets stem-loop IV and impedes viral translation. However, proteolytic cleavage of AUF1 by the viral 3CD<sup>pro</sup> protein releases AUF1 from the IRES, subverting the host antiviral response (Cathcart et al., 2013). Nonetheless, modulation of poliovirus IRES activity by AUF1 is independent of its ARE-binding activity, since the loss of AUF1 does not affect poliovirus replication when the genomic 3'-UTR is absent (Ullmer and Semler, 2018). In contrast, AUF1 binds to stem-loop II (but not to stem-loop IV) of the EV-A71 5'-UTR and competes with hnRNP A1 for IRES association (Lin et al., 2014). Other stem-loop II-targeting proteins such as Ago2 and HuR are not required for AUF1 binding (Lin et al., 2015). However, it is presently unclear whether EV-A71 proteases regulate the cellular localization and activity of AUF1. APOBEC3G (A3G) is a cytidine deaminase that executes RNA/DNA editing (Teng et al., 1993; Petersen-Mahrt et al., 2002). A3G has been implicated in restricting human immunodeficiency virus (Sejvar et al., 2016) replication by inducing extensive G-to-A hypermutations in the nascent viral DNA. In addition, A3G can be found in progeny virions and therefore decreases the infectivity of virus particles. Recent findings have shown that A3G inhibits EV-A71 replication through cytidine deaminase-independent mechanisms (Li et al., 2018; Wang et al., 2019a). A3G binds to the stem-loop I and II regions of the EV-A71 5'-UTR and competes with PCBP1 for IRES binding (Li et al., 2018). However, the incorporation of A3G into nascent virions is controversial. It has been reported that the viral 2C and 3D<sup>pol</sup> proteins can interact with A3G (Li et al., 2018; Wang et al., 2019a). The interaction between 2C and A3G antagonizes A3G through autophagic degradation, whereas the role of 3D<sup>pol</sup> in A3G-dependent suppression of viral infectivity remains unclear.

Non-coding RNAs have recently become classified as ITAFs (Godet et al., 2019). For instance, the P53-inducible long non-coding RNA TRMP suppresses IRES-dependent translation of p27 via competition with p27 mRNA for PTBP1 binding (Yang et al., 2018a). During EV-A71 infection, virus-derived small RNA 1 (vsRNA1) targets stem-loop II of the EV-A71 5'-UTR and inhibits the activity of the IRES (Weng et al., 2014). It is noteworthy that vsRNA1 enhances the association of many ITAFs with the EV-A71 IRES, indicating that viral IRES activity is regulated in a complex manner under certain circumstances (Lin et al., 2015). The sequence and the secondary structure of the IRES determine virulence. Furuse et al. reported that the 5'-UTR of EV-D68 strains exhibit sequence diversity that may alter IRES activity in a cell-line dependent manner (Furuse et al., 2019). Interestingly, recent circulating strains possess mutations in stem-loop IV and coincidentally exhibit higher IRES activity than the prototype EV-D68 Fermon strain (Furuse et al., 2019). Whether the sequence diversity of the 5'-UTR (especially the stem-loop IV region) affects the IRES activity and virulence of EV-D68 requires further investigation.

### 3.2. Viral interference with the targeting of ER-resident and secretory proteins

The eukaryotic translocon comprises multiple copies of the core Sec61αβγ heterotrimer and several associated components, such as oligosaccharyltransferase, the translocon-associated protein complex

(TRAP), and the translocating chain-associated membrane protein (TRAM) (Conti et al., 2015). Few studies have focused on the modulation of the translocon by viruses and the associated effects on viral propagation. The adverse effects of Sec61α perturbation on viral replication and infectivity were recently reported for influenza A virus, dengue virus, and HIV (Heaton et al., 2016). In contrast, short-interfering RNA (siRNA)-mediated depletion of another translocon subunit (Sec61γ) actually increased EV-A71 replication (Murray et al., 2017; van der Sanden et al., 2016). Through proteomic analysis, Kuo et al. found that SSR1 (a member of the TRAP complex) was upregulated in EV-A71-infected cells (Kuo et al., 2015). Further research is needed to decipher the role of SSR1 in the replication of enteroviruses.

### 3.3. Viral interference with the endomembrane system

Viruses lack translational apparatuses required for viral protein production, and therefore effective viral protein synthesis occurs on cytosolic, remodeled membranes, where the viral genome is compartmentalized into a vesicle-like structure designated as the viral replication complex. The endomembrane system is believed to play key roles in EV-A71 and EV-D68 infection. Clathrin and caveolin are required for SCARB2-mediated and PSGL1-mediated virus entry, respectively (Lin et al., 2012, 2013). After entry into host cells, intracellular-membrane remodeling is required for virus infection, which provides a membrane source for the formation of the replication complex and enables nascent virions to exit the host cell. COP I-mediated vesicle transport supports effective viral replication, as the loss of key molecules that constitute COP I coats and participate in COP I-mediated vesicle trafficking was found to inhibit EV-A71 replication (Wang et al., 2012a, 2014). Although COP II-dependent budding of vesicles from the ER was required for the formation of poliovirus-replication complexes (Rust et al., 2001), depletion of the COP II subunit Sec13p, or Sec23p using siRNA did not affect EV-A71 replication (Wang et al., 2012a). However, only a small quantity of Sec13/31 was required for the transportation of small cargos (Townley et al., 2008); therefore, the question as to whether such selective export is sufficient for EV-A71 replication remains unanswered.

ER reticulons (RTNs) are proteins that help modulate ER biogenesis and vesicle trafficking (Pendin et al., 2011; Wakana et al., 2005). The interaction between RTN3 and EV-A71 was first identified using the yeast two-hybrid system (Tang et al., 2007). A highly conserved C-terminal reticulon-homology domain in RTNs is responsible for the interaction with the EV-A71 2C protein. Diminution of the ubiquitously expressed RTN3 protein significantly decreases EV-A71 double-stranded RNA synthesis and protein expression, suggesting its pivotal role in viral replication. In addition, immunoprecipitation experiments demonstrated that RTN3 could also interact with the 2C proteins of poliovirus and coxsackievirus A16, implying that RTN3 is a common factor required for human enterovirus replication (Tang et al., 2007). Accordingly, electron microscopy-based observations of cells infected with EV-A71 or poliovirus demonstrated that a large amount of single- or double-membrane vesicles accumulated near the cell nucleus and some were located adjacent to the swollen ER, suggesting that the ER is a membrane source for the viral-replication complex (Wang et al., 2017a; Suhy et al., 2000). Strikingly, decreased RTN3 expression was observed during the late stage of EV-A71 infection (Tang et al., 2007), which was probably due to virus-induced inhibition of host protein synthesis. Given that RTN3 overexpression can impair retrograde transport (Wakana et al., 2005), RTN3 diminishment might benefit COP I-mediated transportation. Further research is required to elucidate whether the precise control of RTN3 expression in EV-A71-infected cells can provide an optimal environment for viral replication.

Bactericidal/permeability-increasing protein (BPI) fold-containing family B, member 6 (BPIFB6) is another ER-localized protein that contributes to EV-A71 replication via the modulation of vesicle trafficking (Morosky et al., 2016). BPIFB6 is a lipid-binding protein, suggesting that

it coordinates lipid-transfer and -secretory pathways between organelles. BPIFB6-deficient cells show disrupted retrograde and anterograde trafficking and altered Golgi network morphology, leading to ineffective viral replication. The Golgi protein, acyl-coenzyme A binding domain-containing 3 (ACBD3) is an EV-A71 3A-interacting protein required for viral RNA replication (Fan et al., 2010). Both residues 44 (Plaze et al., 2020) and 54 (Kai et al., 2014a) of EV-A71 3A are essential for the EV-A71 3A-ACBD3 interaction, as the substitution of either amino acid abolishes EV-A71 3A-ACBD3-phosphatidylinositol 4-kinase III $\beta$  (PI4KB) complex formation (Lei et al., 2017; Xiao et al., 2017). This complex is localized into the viral RNA-replication site, where the lipid kinase PI4KB catalyzes the production of phosphatidylinositol-4-phosphate (PI4P), thereby modulating the membrane composition and vesicle formation; therefore, the complex serves essential roles in viral replication and virion secretion (De Matteis et al., 2013; Bishe et al., 2012). Consistent with these findings, the ACBD3-PI4KB interaction was previously shown to be crucial for the replication of other enteroviruses, including EV-D68 (Xiao et al., 2017; Lyoo et al., 2019).

### 3.4. Viral interference with the protein-quality control system

The roles of ER stress and UPRs have been highlighted by studies investigating host-virus interactions (Jheng et al., 2014). EV-A71 infection activates both PKR and PERK, whereas the downstream protein eIF2 $\alpha$  is mainly phosphorylated by PKR, but not PERK (Jheng et al., 2010). Both EV-A71 dsRNA and viral proteins can modulate PKR activity (Bou-Nader et al., 2019). With the dexterous manipulation of the PKR by EV-A71 3C<sup>pro</sup>, EV-A71 subverts the antiviral function of PKR. The viral 3C<sup>pro</sup> protein interacts with PKR to mediate PKR phosphorylation and cleavage. The 3C<sup>pro</sup>-induced failure of PKR dimerization abrogates signaling through the PKR-eIF2 $\alpha$  pathway. Additionally, the 3C<sup>pro</sup>--generated short N-terminal PKR fragment promotes EV-A71 replication impacting viral RNA and protein levels, as well as viral titers (Chang et al., 2017). The dsRNA-induced activation of PKR is considered a crucial step of the antiviral immune response. However, dsRNA-mediated PKR activation may contribute to EV-A71 replication via the generation of long-lasting ER stress through the upregulation and cytosolic redistribution of GRP78/BiP (Fig. 3B) (Jheng et al., 2016). Given that PKR drives diverse mechanisms that determine cell fate (Garcia et al., 2006), these results indicate that PKR likely plays other veiled roles in virus replication.

The PKR-eIF2 $\alpha$ -signaling cascade results in typical stress granule (SG) formation where both host mRNAs and viral mRNAs are sequestered, which in principle would result in failed virus replication (White and Lloyd, 2012). Although EV-A71 and EV-D68 induce SG accumulation in infected cells, the viral 2A<sup>pro</sup> protein counteracts the formation of typical adverse SGs (Cheng et al., 2020; Yang et al., 2018b). Yang et al. revealed that EV-A71 2A<sup>pro</sup> transforms typical SGs into atypical SGs containing only host mRNAs, favoring viral translation (Yang et al., 2018b). Likewise, Sanz et al. demonstrated that the PV IRES-dependent translation was fully functional when PV 2A<sup>pro</sup> was present, even when eIF2 $\alpha$  was phosphorylated (Sanz et al., 2013). Notably, although the EV-A71 3C<sup>pro</sup> protein might abolish typical SG formation via the cleavage of PKR or other SG components, the transformation of SGs occurs during the early phase of EV-A71 infection when the protease activity of 2A<sup>pro</sup> is more predominant than that of 3C<sup>pro</sup> (Chang et al., 2017; Yang et al., 2018b). In addition, the SG-targeting antagonist properties of 2A<sup>pro</sup> appear to be conserved among enteroviruses, including EV-A71, CV-A21, and EV-D68 (Visser et al., 2019).

In the IRE1-XBP1 pathway, the expression of spliced XBP1 is hampered in EV-A71-infected cells due to 2A<sup>pro</sup>-mediated global translational shutoff, even though the IRE1 protein is activated (Fig. 3C). Overexpression of spliced XBP1 inhibits virus entry (Jheng et al., 2012). While the mechanisms governing this process require further elucidation, it has been proposed that spliced XBP1 might modulate

protein-expression levels via transcriptional or post-transcriptional control mechanisms (Zhou et al., 2011; He et al., 2010).

Regarding the ATF6 pathway, CVB3-infected cells showed p50ATF6 transcriptional activity, whereas EV-A71-infected cells exhibited no evidence of p50ATF6 expression (Haze et al., 1999; Jheng et al., 2018b). Alternatively, p90ATF6 can be proteolytically processed by both 3C<sup>pro</sup> and host factors during the late stage of viral infection (Fig. 3D) (Jheng et al., 2018b). Viral 3C<sup>pro</sup> cleaves the C-terminal domain of ectopically expressed p90ATF6, whereas host factors cleave the middle region of p90ATF6 to produce a 45-kDa fragment (Jheng et al., 2018b). The cleaved products would likely be readily degraded or unstable in virus-infected cells and, thus, poorly detected by polyclonal antibodies raised against the full-length ATF6 (Jheng et al., 2010). Intriguingly, p90ATF6 may be associated with protein stability, at least considering the precursor of the viral structural protein, VP1. The knockdown of p90ATF6 lowered both the stability of ectopically expressed P1 and the virus titers (Jheng et al., 2018b). Given that the structural protein VP1 influences virulence via the modulation of autophagy (Hu et al., 2017; Liu et al., 2019; Li et al., 2019), these findings plausibly suggest that p90ATF6 serves an autophagy-dependent essential role during early virus infection. Accordingly, it would be interesting to investigate the role of p90ATF6 in the regulation of protein stability and its possible contribution to the PN.

Several studies have suggested a potential mechanism whereby EV-A71 benefits from disturbances in the ERAD process (Wang et al., 2017a; Yan et al., 2020; Huang et al., 2017). EV-A71 inhibits the degradation of ERAD substrates, downregulating ERAD components via the 2A<sup>pro</sup>-induced global translational attenuation and the 3C<sup>pro</sup>-mediated specific cleavage of UBC6e (Wang et al., 2017a). The co-opt of ERAD components, such as UGGT1, AAA-ATPase p97, and N-glycanase NGLY1, by EV-A71 is essential for virus replication. The ER-resident protein UGGT1 is proposed to improve glycoprotein quality control by promoting the reglucosylation of glycoproteins that fail to acquire their native folded conformation (Ferris et al., 2013; Wu et al., 2016). The interaction between EV-A71 3D<sup>pol</sup> and UGGT1 was first identified via immunoprecipitation-coupled mass spectrometry (Huang et al., 2017). UGGT1 facilitates the localization of EV-A71 3D<sup>pol</sup> to the viral replication complex, and consequently viral RNA synthesis. Consistently, mice with the heterozygous disruption of UGGT1 exhibit lower viral pathogenicity than infected wild-type mice. UGGT1 is also essential for EV-D68 dissemination; a decreased virus titer was observed in UGGT1-silenced cells compared with that in control cells transfected with a scrambled siRNA. The proviral roles of p97 and NGLY1 were identified in a human genome-wide RNA interference screen (Wu et al., 2016). p97 is not only an EV-A71 2C-interacting protein that facilitates virus replication (Wang et al., 2017a; Guan et al., 2017) but also participates in viral entry through the VCP-UFD1-nucleolin axis (Wang et al., 2017a; Yan et al., 2020). Considering that p97 and UGGT1 compose a recently discovered checkpoint complex that prevents the transport of functional polypeptides with minor structural defects into the Golgi (Merulla et al., 2015), further investigation is required to determine whether interactions between viral proteins and p97 or UGGT1 interfere with such retention-based quality control.

Following the discovery that cellular autophagy could be induced by poliovirus or CVB3 infection (Taylor and Kirkegaard, 2007; Wong et al., 2008), Huang et al. demonstrated that EV-A71 infection induced autophagy *in vitro* and *in vivo*; moreover, the proviral role of autophagy was demonstrated in cells treated with pharmacological autophagy inhibitors and inducers (Huang et al., 2009). In addition, the viral 2C protein-mediated autophagic degradation of the negative IRES regulator A3G promoted viral translation (Li et al., 2018). Lee et al. further demonstrated that virus-induced autophagy was indispensable for the pathogenesis of EV-A71 in a suckling mouse model (Lee et al., 2014). Unlike CVB3, which induces incomplete autophagy via the blockage of the autophagic flux (Tian et al., 2018), EV-A71 infection enhances acidic autolysosome formation. Vesicle acidification is vital for efficient



EV-A71 replication as viral RNA and protein levels and viral titers were decreased in host cells treated with the autophagic flux inhibitors, bafilomycin A1 and NH<sub>4</sub>Cl (Lee et al., 2014; Lai et al., 2017). Different from EV-A71 VP1 or 2C (which triggers autophagy), the interaction between EV-A71 2BC and the SNARE proteins, syntaxin-17 (STX17) and synaptosome-associated protein of 29 kDa (SNAP29), was found to be responsible for autolysosome formation and active viral replication (Li et al., 2018, 2019; Hu et al., 2017; Liu et al., 2019); the overexpression of 2BC alone did not induce LC3 conversion (Lai et al., 2017). Further research is needed to understand the role of 2BC-SNARE complexes in virion egress.

Autophagy is also obligatory for EV-D68 infection (Corona et al., 2018). Although STX17 expression was increased during the course of infection, EV-D68 3C<sup>pro</sup>-mediated proteolytic cleavage decreased the level of SNAP29. Of note, SNAP29 silencing negatively regulates EV-D68 replication, whereas SNAP29 overexpression facilitates virion exit. However, the enhanced extracellular virus particles' release from cells exogenously overexpressing SNAP29 may not be a result of enhanced

autophagic flux, since only the full STX17-SNAP29-vesicle-associated membrane protein-8 (VAMP8) complex enhanced the flux process.

#### 4. The PN as a therapeutic target against EV-A71 and EV-D68

As previously noted, multiple mechanisms involved in cellular protein homeostasis can enable virus infection. In this section, we provide a summary of the antiviral drugs that have been used to treat EV-A71 and EV-D68 infections in light of their capacity to modulate the PN. The antiviral spectrum and the biological activity of these agents have also been expanded to meet the requirements for drug repurposing in the context of emerging viral diseases (Tables 2-4).

##### 4.1. Inhibition of IRES-dependent translation

Agents that inhibit IRES-mediated translation mainly exert their action through mechanisms that induce a structural RNA change or alter the composition of IRES-associated ITAFs. Amiloride is an FDA-

**Table 2**

Antivirals that target IRES-dependent translation to inhibit EV-A71. The table shows the status of agents in drug development and their antiviral activity against other human viruses.

| Antiviral agents                     | Status      | Comments (target viruses, models, and others)                                | References  |
|--------------------------------------|-------------|--|---|
| DMA-135 (amiloride derivative)       | Preclinical | EV-A71<br>SF268 cells  | Davila-Calderon et al. (2020)   |
| Kaempferol                           | Marketed    | HIV-1 <sup>c</sup><br>In vitro peptide displacement assay                    | Patwardhan et al. (2017)  |
|                                      |             | EV-A71<br>293 S cells; mice  | Dai et al. (2019)   |
|                                      |             | JEV<br>BHK21 cells   | Zhang et al. (2012)   |
|                                      |             | Influenza virus <sup>c</sup><br>MDCK cells; mice                             | Kai et al. (2014a)  |
|                                      |             | MHS cells; mice  | Zhang et al. (2017)   |
| Prunin                               | Preclinical | SARS-CoV <sup>c</sup><br>In vitro voltage-clamp experiments                  | Schwarz et al. (2014)   |
|                                      |             | EV-A71<br>RD cells, SJ cells, mice   | Gunaseelan et al. (2019)  |
|                                      |             | CA6 and CA16,<br>Enterovirus B   |   |
| Apigenin                             | Marketed    | HCV<br>Huh7.5 cells  |   |
|                                      |             | EV-A71<br>293S cells   | Dai et al. (2019)   |
|                                      |             | RD cells; mice   | Zhang et al. (2014)   |
|                                      |             | Influenza virus<br>MDCK cells  | Liu et al. (2008)   |
|                                      |             | HCV <sup>c</sup><br>Huh7-Feo cells <sup>a</sup>                              | Shibata et al. (2014)   |
|                                      |             | Parainfluenza virus<br>Vero cells  | Ozcelik et al. (2011)   |
|                                      |             | HSV-1<br>MDBK cells  | Ozcelik et al. (2011)   |
|                                      |             | Epstein-Barr virus<br>P3HR1, NA and HA cells <sup>b</sup>                    | Wu et al. (2017)  |
| TDP                                  | Preclinical | EV-A71<br>RD cells   | Dan et al. (2019)   |
| Oblongifolin M                       | Preclinical | EV-A71<br>RD cells   | Wang et al. (2016)  |
| CX-6258 (Pim1 kinase inhibitor)      | Preclinical | EV-A71<br>RD and HeLa cells  | Zhou et al. (2019)  |
| Rosmarinic acid                      | Marketed    | EV-A71<br>RD cells; mice   | Hsieh et al. (2020); Lin et al. (2019); Chen et al. (2017); Chung et al. (2015) |
|                                      |             | JEV <sup>c</sup><br>BV-2 cells; mice   | Swarup et al. (2007)  |
| miR-197                              | Preclinical | EV-A71<br>RD cells   | Tang et al. (2016)  |
| IMB-Z (N-phenylbenzamide derivative) | Preclinical | EV-A71<br>Vero cells, H1-HeLa cells, HCT-8 cells, 293 T cells, SK-N-SH cells | Wang et al. (2019a)   |
| Amantadine*                          | Marketed    | EV-A71, EMCV<br>In vitro IRES assay  | Chen et al. (2008)  |
|                                      |             | Influenza virus <sup>c</sup><br>Mice   | Grunert and Hoffmann (1977)   |
| Emetine*                             | Marketed    | EV-A71,<br>RD and Vero cells; mice   | Tang et al. (2020)  |
|                                      |             | EV-D68, CV-A16, CV-B1,<br>RD cells   | Tang et al. (2020)  |
|                                      |             | Echovirus<br>HFF cells   | Mukhopadhyay et al. (2016)  |
|                                      |             | HCMV<br>in vitro reverse transcriptase assay                                 | Chaves Valadao et al. (2015)  |
|                                      |             | HIV <sup>c</sup><br>HEK293 cells   | Yang et al. (2018c)   |
|                                      |             | Zika virus <sup>c</sup><br>Vero-E6 cells; mice                               | Yang et al. (2018c)   |
|                                      |             | Ebola virus <sup>c</sup><br>BHK-21 cells                                     | Shen et al. (2019)  |
|                                      |             | HCoV-OC43 <sup>c</sup><br>LLC-MK2 cells                                      |   |
|                                      |             | HCoV-NL63 <sup>c</sup><br>Vero-E6 cells                                      | Shen et al. (2019)  |
|                                      |             | MERS-CoV <sup>c</sup><br>DBT cells   | Shen et al. (2019)  |
|                                      |             | MHV-A59 <sup>c</sup><br>Vero-E6 cells  | Choy et al. (2020)  |
| Sorafenib*                           | Marketed    | SARS-CoV-2 <sup>c</sup><br>RD, Vero, SK-N-SH cells                           | Gao et al. (2014)   |
|                                      |             | EV-A71<br>HuH7.5 cells   | Himmelsbach et al. (2009)   |
|                                      |             | HCV <sup>c</sup><br>Vero cells   | Lundberg et al. (2018)  |
|                                      |             | Alphaviruses <sup>c</sup>  |   |

\*FDA-approved agent.

<sup>a</sup> Huh7-Feo cells: Huh7 cells harboring an HCV replicon reporter construct.

<sup>b</sup> NA and HA cells: EBV-converted cells obtained via the co-cultivation of rAkata cells with the nasopharyngeal carcinoma cell lines TW01 and HONE-1 cells, respectively.

<sup>c</sup> With different targets and mode-of-action compared to enteroviruses.

**Table 3**

**Antivirals that target the endomembrane system to inhibit EV-A71 and EV-D68.** The table shows the status of agents in drug development and their antiviral activity against other human viruses.

| Antiviral agents | Status      | Comments (target viruses, models, and others)                        |   | References                                      |
|------------------|-------------|--|---|---|
| Enviroxime       | Preclinical | Rhinoviruses, Poliovirus, CA21, CVB3                                 | H1–HeLa cells                               | Heinz and Vance (1995)                          |
|                  |             | EV-A71, EV-D68   | RD cells                                    | Smee et al. (2016)                              |
| GW5074           | Preclinical | EV-A71, Poliovirus   | RD cells<br>Vero cells                      | Arita et al. (2009)                             |
|                  |             | Dengue virus, Zika virus <sup>a</sup> , West Nile virus <sup>a</sup> | Vero cells                                  | Yang et al. (2019)                              |
| T-00127-HEV1     | Preclinical | EV-A71, Poliovirus, CVB3   | RD cells                                    | Arita et al. (2011)                             |
| T-00127-HEV2     | Preclinical | EV-A71, Poliovirus   | RD cells                                    | Arita et al. (2013)                             |
| AN-12-H5         | Preclinical | EV-A71, Poliovirus   | RD cells                                    | Arita et al. (2010)                             |
|                  |             | HCV  | Huh7.5.1 cells                              | Arita et al. (2011)                             |
| Itraconazole*    | Marketed    | EV-A71, CVB3, EMCV   | BGM cells                                   | Strating et al. (2015)                          |
|                  |             | HRV14, HCV, Saffold virus<br>Influenza virus <sup>a</sup>            | HeLa R19 cells<br>A549 and Vero cells; mice | Strating et al. (2015)<br>Schloer et al. (2019) |
| OSW-1            | Preclinical | EV-A71, CVA-21, HRV-2, HRV-14, CVB3                                  | HeLa R19, HAP1, BGM, Vero and MEF cells     | Albulescu et al. (2015)                         |

\*FDA-approved agent.

<sup>a</sup> Different targets and mode-of-action compared to enteroviruses.

approved potassium-sparing diuretic used to treat hypertension, thiazide-induced hypokalemia, and congestive heart failure (Rojas et al., 2017). Interestingly, amiloride has been shown to restrain the replication of HRV2, poliovirus, and CVB3 in virus-infected cells (Harrison et al., 2008; Ogram et al., 2014). However, amiloride treatment induced the generation of a drug-resistant CVB3 strain harboring a mutant 3D<sup>pol</sup> (Harrison et al., 2008). A study further demonstrated that amiloride competes with VPg for the binding to 3D<sup>pol</sup>, causing impaired VPgUpU synthesis and viral RNA replication (Ogram et al., 2014). Currently, an amiloride derivative, DMA-135, was identified via peptide-displacement assays to evaluate ligands targeting the stem-loop II structure of the EV-A71 IRES (Davila-Calderon et al., 2020). Treatment with DMA-135 induced a structural change in the IRES that facilitated AUF1 binding, ultimately repressing translation. Remarkably, DMA-135 and other amiloride-based compounds also target HIV-1-TAR, an RNA element required for HIV gene transcription and translation (Patwardhan et al., 2017). Amantadine is known for its anti-influenza A virus activity by targeting viral M2 proton channel (Grunert and Hoffmann, 1977; Wang et al., 1993); it also shows an inhibitory effect on IRESs of EV-A71 and encephalomyocarditis virus (EMCV) (Chen et al., 2008). Although amantadine is an FDA-approved agent for Influenza A prophylaxis and treatment, the emergence of resistant viruses is the major issue in controlling Influenza A virus infection (Cheng et al., 2009). Amantadine is also used to treat Parkinson's disease (Crosby et al., 2003), and recent studies demonstrated that amantadine might reduce the effects of SARS-CoV-2 infection (Smieszek et al., 2020; Rejdak and Grieb, 2020).

Moreover, several flavonoids exhibit antiviral activity *in vitro* and *in vivo* (Zakaryan et al., 2017; Dai et al., 2019). The altered composition of

**Table 4**

**Antivirals that target the protein-quality control system to inhibit EV-A71.** The table shows the status of agents in drug development and their antiviral activity against other human viruses.

| Antiviral agents | Status      | Comments (target viruses, models, and others) |  | References                             |
|------------------|-------------|---|--|--|
| Resveratrol      | preclinical | EV-A71  | RD cells   | Zhang et al. (2015b); Du et al. (2019) |
|                  |             | Influenza virus <sup>c</sup>                  | MDCK cells; mice   | Palamara et al. (2005)                 |
|                  |             | RSV <sup>c</sup>                              | Hep-2 and 9HTEo Cells                                    | Xie et al. (2012)                      |
|                  |             | HCV (core protein) <sup>c</sup>               | Mice   | Jiang et al. (2012)                    |
|                  |             | HSV <sup>c</sup>                              | Vero and MRC-5 cells; mice                               | Docherty et al. (1999)                 |
|                  |             | HIV <sup>c</sup>                              | MAGI cells <sup>a</sup>                                  | Zhang et al. (2009)                    |
|                  |             | MERS <sup>c</sup>                             | Vero-E6 cells  | Lin et al. (2017a)                     |
| Berberine        | Preclinical | EV-A71  | Vero cells   | Wang et al. (2017b)                    |
|                  |             | Influenza virus <sup>c</sup>                  | MDCK cells   | Wu et al. (2011)                       |
|                  |             |   | A549 cells; mice   | Yan et al. (2018)                      |
|                  |             | HCMV <sup>c</sup>                             | MRC-5 cells  | Hayashi et al. (2007)                  |
|                  |             |   | HFF cells  | Luganini et al., (2019)                |
|                  |             | Alphaviruses <sup>c</sup>                     | BHK-21 cells   | Varghese et al. (2016)                 |
| Chloroquine*     | Marketed    | EV-A71  | RD cells; mice   | Tan et al. (2018)                      |
|                  |             |   | Human NSCs <sup>b</sup> and IMR-32-derived neuronal cell | Lin and Huang (2020)                   |
|                  |             | Zika virus                                    | Vero, MEF and Huh7; mice                                 | Zhang et al. (2019)                    |
|                  |             | SARS-CoV-2                                    | Vero-E6 cells  | Gorshkov et al. (2020)                 |

\*FDA-approved agent.

<sup>a</sup> MAGI (multinuclear activation of galactosidase indicator) cells: a recombinant HeLa-CD4-LTR-β-galactosidase indicator cell line.

<sup>b</sup> Human NSCs: human neural stem cells.

<sup>c</sup> Different targets and mode-of-action compared to enteroviruses.

IRES-associated ITAFs was observed after treatment with the antiviral flavonoids kaempferol, prunin, and apigenin (Tsai et al., 2011; Gunaseelan et al., 2019; Zhang et al., 2014). Kaempferol is known for its anti-cancer, antioxidant, and anti-inflammatory activities (Imran et al., 2019; Wang et al., 2018). Similarly, the RNA-binding properties of kaempferol contribute to protection against infection with the Japanese encephalitis virus (JEV); of note, the biomolecular interactions between kaempferol and viral RNA were proved via *in vitro* isothermal titration calorimetry and electrospray ionization mass spectrometry (Zhang et al., 2012). Additionally, an *in vitro* assay demonstrated that Kaempferol and its derivatives might inhibit SARS-CoV virion egress via the targeting of viral cation-selective channel 3a (Schwarz et al., 2014). Regrettably, no consistent results were obtained in the context of Influenza (Kai et al., 2014b; Dong et al., 2014). The virucide activity of prunin has been demonstrated *in vitro* and *in vivo* (Gunaseelan et al., 2019). Again, mutations that occurred in the viral IRES led to the development of

prunin-resistant EV-A71. Those mutations, located in the stem-loops II and VI of the EV-A71 5'-UTR, might alter the IRES RNA secondary structure and thereby confer acquiring tolerance to altered composition of IRES-associated ITAFs induced by prunin. Prunin also inhibits the replication of hepatitis C virus (HCV), with a different type of IRES from EV-A71 (Gunaseelan et al., 2019), suggesting pruning might act as a potential broad-spectrum IRES inhibitor, and is therefore, worthwhile to study further. Apigenin inhibits EV-A71 IRES activity via the abolishment of the association between viral RNA and hnRNP A1 and A2 proteins (Zhang et al., 2014). With multiple effective bioactive mechanisms, apigenin showed beneficial effects in the context of cancer, behavioral disorders, and metabolic diseases in various clinical trials (Salehi et al., 2019; Wang et al., 2019b). Its antiviral activity against HCV, influenza virus, parainfluenza virus, herpes simplex virus-1 (HSV-1), and Epstein-Barr virus has been examined *in vitro* (Shibata et al., 2014; Liu et al., 2008; Ozcelik et al., 2011; Wu et al., 2017). Based on the toxicology trial results and broad-spectrum antiviral activity, apigenin is thus worthy of further development.

Natural products isolated from Chinese medical herbs can inhibit EV-A71 IRES activity. 1, 3, 5-Trihydroxy-13,13-dimethyl-2H-pyran [7,6-b] xanthone (TDP) and oblongifolin M downregulated the stress-related proteins Hsp27, and ERp57, respectively (Fu et al., 2012; Wang et al., 2016). Decreased Hsp27 expression reduced viral 2A<sup>pro</sup>-mediated eIF4G cleavage and the cytoplasmic translocation of hnRNP A1 (Dan et al., 2019). Likewise, the Pim1 kinase inhibitor CX-6258 impacts EV-A71 replication via the inhibition of viral 2A<sup>pro</sup>-mediated eIF4G cleavage and the cytoplasmic accumulation of AUF1 (Zhou et al., 2019). While the mechanism explaining how ERp57 affected IRES activity remains unclear, its critical roles in the infection of Simian virus 40, influenza virus, and paramyxovirus have been implicated (Schelhaas et al., 2007; Walczak and Tsai, 2011; Piacentini et al., 2018). Rosmarinic acid (RA), an ester of caffeic acid and 3,4-dihydroxyphenyllactic acid found in various herbs such as Danshen (*Salvia miltiorrhiza*) and Lemon balm (*Melissa officinalis*), inhibited EV-A71 infection as demonstrated by *in vitro* and *in vivo* studies (Hsieh et al., 2020; Lin et al., 2019; Chen et al., 2017; Chung et al., 2015). More than to inhibit the interactions between the capsid VP1 protein and cognate sulfated receptors, RA may decrease the IRES activity via the reduction of virus-induced reactive oxygen species and the abrogation of the hnRNP A1 cytoplasmic translocation (Hsieh et al., 2020; Chen et al., 2017). RA also acts as an inhibitor of JEV and Hepatitis B Virus (Tsukamoto et al., 2018; Swarup et al., 2007). Remarkably, RA is related to additional health benefits through various mechanisms such as antioxidant and anti-inflammatory effects (Nunes et al., 2017). Importantly, a randomized controlled trial revealed that the acceptable daily intake (Sejvar et al., 2016) value of RA is 500 mg per day in healthy individuals, substantiating its possible therapeutic antiviral applications (Noguchi-Shinohara et al., 2015).

Other mechanisms that interfere with the nucleocytoplasmic shuttling of ITAFs have been described. Tang et al. found that miR-197 inhibited EV-A71 infection, repressing the expression of the small GTPase, Ran (Tang et al., 2016). miR-197 administration results in reduced IRES activity. Aberrant localization of the viral 3D<sup>pol</sup> protein and the fusion protein 3xGFP-NLS (which has the classical NLS of hnRNP K) was observed in Ran-silenced cells. Therefore, Ran is a logical molecular target for the inhibition of EV-A71 inhibition; compounds that block Ran might therefore have anti-viral properties. Additionally, N-phenylbenzamide derivatives were evaluated as EV-A71 inhibitors (Ji et al., 2013). The A3G agonist properties of IMB-Z have been demonstrated among those derivatives (Wang et al., 2019a). IMB-Z mediated the enhanced cellular expression of A3G; of note, the increased levels of virion-packaged A3G reduced EV-A71 infectivity (Wang et al., 2019a), probably via the disruption of the interaction between the viral IRES and the PCBP1 (Li et al., 2018). Remarkably, A3G impaired the replication of HIV-1 and HCV *in vitro* (Wang et al., 2012b; Zhu et al., 2015), raising the possibility that IMB-Z might protect cells from HIV-1 and HCV infection.

#### 4.2. Inhibition of the endomembrane system

Agents that target phosphoinositide kinases or lipid shuttling have been shown to inhibit enterovirus replication (Arita et al., 2010, 2011; van der Schaar et al., 2013). Enviroxime was initially found to inhibit rhinoviruses in the low nanomolar range (Gilbert et al., 1988). However, controversial results concerning its antiviral activity and adverse side effects on the gastrointestinal system led to the premature termination of the anti-viral trials (Phillipotts et al., 1981, 1983; Hayden and Gwaltney, 1982; Miller et al., 1985). *In vitro* studies revealed that enviroxime also inhibited other enteroviruses and identified viral 3A and 3AB as possible inhibitory targets according to the appearance of middle and C-terminal amino acid substitutions of 3 A in enviroxime-resistant viruses (De Palma et al., 2009; Heinz and Vance, 1995, 1996; Brown-Augsburger et al., 1999). Studies subsequently discovered several antivirals that raise 3A-mutant drug-resistant viruses and collectively defined these agents as enviroxime-like compounds. These agents have been classified into two main categories: one targets PI4KB activity (GW5074 and T-00127-HEV1) and the other targets PI4P-binding proteins (AN-12-H5, T-00127-HEV2, itraconazole, and OSW-1) such as oxysterol-binding protein (OSBP), or OSBP-related protein 4 to interfere with lipid transfer, thereby perturbing the formation of membrane-bounded replication compartments for viral replication (Arita et al., 2009, 2011, 2013; Strating et al., 2015; Yang et al., 2019; Albulescu et al., 2015). Among the enviroxime-like compounds, itraconazole has been approved by the FDA for the treatment of fungal infections in immunocompromised patients (McKinsey et al., 1999). In addition, it may have an anti-influenza and anti-SARS-CoV-2 activity (WHO, 2020; Schloer et al., 2019). Except for enviroxime, the antiviral activity of those compounds against EV-D68 has not been confirmed (Smeets et al., 2016); however, their targeted mechanism is essential in EV-D68 viral replication, indicating their potential anti-EV-D68 efficacy.

#### 4.3. Inhibition of the protein quality control system

Recent studies have shown that agents targeting the protein quality-control system have potential therapeutic effects against viral infection, revealing compounds that protect cells from EV-A71 infection via the targeting of ER stress or autophagy (Jheng et al., 2014; Ahmad et al., 2018). A growing body of cell-based research revealed that resveratrol, a phenolic phytoalexin, can exert antiviral activity against several viruses, including EV-A71, influenza virus, respiratory syncytial virus, HCV, herpes simplex virus, HIV, and MERS-CoV (Abba et al., 2015; Lin et al., 2017a; Jiang et al., 2012; Zhang et al., 2009, 2015b; Palamara et al., 2005; Xie et al., 2012; Docherty et al., 1999, 2005). While *in vitro* evidence showed that resveratrol is a multifunctional compound with several beneficial biological properties (Gambini et al., 2015), its low bioavailability (due to its poor water solubility, chemical instability, and intestinal metabolism) limits its clinical applications (Francioso et al., 2014; Berman et al., 2017). To overcome this issue, micronized resveratrol (SRT501) or resveratrol-functionalized nanoparticles were developed, enhancing the resveratrol bioavailability (Wan et al., 2018; Lin et al., 2017b; Howells et al., 2011). With regard to anti-EVs, a recent *in vitro* study demonstrated that resveratrol-loaded nanoparticles conferred resistance to EV-A71-induced cell injury via the inhibition of both ER stress-signaling pathways and autophagy (Du et al., 2019). However, because of the unacceptable safety profile of resveratrol (or SRT501), further clinical exploration to assess its potential therapeutic uses is needed (Berman et al., 2017; Ramirez-Garza et al., 2018).

Berberine, an isoquinoline alkaloid, is a natural product with beneficial effects in the context of lipid metabolism, and with immunomodulatory, anti-cancer, and anti-viral potential (Yin et al., 2008; Imenshahidi and Hosseinzadeh, 2016). Berberine inhibited the replication of EV-A71 via the downregulation of autophagy and the MEK-ERK-signaling pathway, both of which are required for the propagation of EV-A71 (Wang et al., 2017b). Berberine was also effective

against influenza A infection *in vitro* and in mice (Wu et al., 2011; Yan et al., 2018), as well as against human cytomegalovirus (Hayashi et al., 2007; Laganini et al., 2019), and alphaviruses (Varghese et al., 2016). In terms of common treatments of metabolic diseases, studies compared the effect of berberine to that of metformin, a prescription drug used to treat type 2 diabetes; of note, both agents affect the activity of the key metabolic regulator AMPK and have clinical applications in the treatment of dyslipidemia and inflammation (Di Fusco et al., 2018; Jeong et al., 2009). Berberine has been used to treat metabolic disorders in several trials (Yin et al., 2008; Ming et al., 2018; Lan et al., 2015); intriguingly, both berberine and metformin might be promising compounds for the treatment of COVID-19 (WHO, 2020; Sharma et al. (2020).

Dexamethasone, a glucocorticoid, has been shown to inhibit the infection of cattle foot-and-mouth disease virus, probably through its immunosuppressive activity (Ilott et al., 1997). However, its potential therapeutic use for the treatment of human hand, foot, and mouth disease (HFMD) is controversial. Neurogenic pulmonary edema has been found in patients with severe HFMD and might be correlated with calreticulin surface exposure (Ecto-CRT)-mediated immunogenic cell death and central nervous system damage (Hu et al., 2017; Gardai et al., 2005). Overexpression of EV-A71 VP1 protein in rat brainstem neurons induces Ecto-CRT via the activation of ER stress and autophagy, and the treatment with dexamethasone alleviates VP1-induced ER stress and reduces neuronal cell damage (Hu et al., 2017). However, early treatment with dexamethasone exacerbates enterovirus 71 infection in mice (Shen et al., 2014) and in a mouse model of EV-D68-associated AFM (Hixon et al., 2017). Of note, a clinical trial is ongoing to evaluate the therapeutic effects of dexamethasone in the context of severely ill COVID-19 patients compared with those receiving standard of care (NCT04366739).

Owing to the crucial role of 2C on EV-A71-induced autophagy, it is possible that 2C inhibitors such as guanidine hydrochloride, dibucaine, and pirlindole (Tang et al., 2007; De Palma et al., 2008; Sadeghipour et al., 2012; Ulferts et al., 2013, 2016), might also inhibit EV-A71 replication via the modulation of autophagy. Accordingly, an *in vitro* study revealed that certain enterovirus 2C inhibitors (e.g., fluoxetine and TBZE-029) show viral species-specificity, potentially inhibiting CVB3 and EV-D68, but not EV-A71 (Ulferts et al., 2013).

## 5. Concluding remarks and future perspectives

Viruses can hijack and manipulate the host's protein homeostasis, including translation machinery, the endomembrane system, and the protein quality control system. In this scenario, antivirals that act on the PN offer a promising broad-spectrum therapeutic strategy against different enterovirus species. Sorafenib and chloroquine – two FDA-approved drugs – are among the most promising antivirals. While sorafenib has a multifaceted action against EV-A71 through its anti-IRES activity and its ability to inhibit a wide spectrum of protein kinases required for virus infection (Gao et al., 2014; Whirl-Carrillo et al., 2012; Wong et al., 2005), chloroquine is known to target both endosomal acidification and autophagy (Tan et al., 2018; Al-Bari, 2017). However, in EV-A71- and EV-D68-infected cells, the extent to which PN processes occur in an independent and yet cooperative manner remains unclear. Further investigation will provide a better understanding of the crosstalk that occurs between each branch of the PN during EV-A71 and EV-D68 infection. This knowledge will offer exciting new therapeutic strategies for targeting the host PN to overcome EV-A71 and EV-D68 infection.

## Declaration of competing interest

The authors declare that they have no known competing financial interests or personal relationships that could have appeared to influence the work reported in this paper.

## Acknowledgements

Previous research from our laboratory included in this review was financially supported by the Chang Gung Memorial Hospital (BMRP416, CMRPD1G0301-3, CMRPD1F0581-3, and CMRPD1K0241-2), the Ministry of Science and Technology of Taiwan (106-2320-B-182-004-MY3, 106-2811-B-182-011, 106-2632-B-182-001, 107-2811-B-182-512, 108-2320-B-182-039-, 109-2320-B-182-026 -MY3, 109-2327-B-182-002, and 109-2327-B-182-003-), and the Research Center for Emerging Viral Infections from The Featured Areas Research Center Program within the framework of the Higher Education Sprout Project by the Ministry of Education (MOE) in Taiwan, and the Ministry of Science and Technology, Taiwan (MOST 109-2634-F-182-001-). The authors wish to thank Miss Ingrid Kuo and the Center for Big Data Analytics and Statistics (Grant CLRPG3D0046) at Chang Gung Memorial Hospital for creating the illustrations.

## References

- Abba, Y., et al., 2015. Antiviral activity of resveratrol against human and animal viruses. *Adv Virol* 2015, 184241.
- Adam, D.C., 2019. Report on the 2018 acute flaccid myelitis outbreaks in the USA. *Global Biosecurity* 1 (1), 129–139.
- Ahmad, L., Mostowy, S., Sancho-Shimizu, V., 2018. Autophagy-virus interplay: from cell biology to human disease. *Front Cell Dev Biol* 6, 155.
- Al-Bari, M.A.A., 2017. Targeting endosomal acidification by chloroquine analogs as a promising strategy for the treatment of emerging viral diseases. *Pharmacol Res Perspect* 5 (1), e00293.
- Albulescu, L., et al., 2015. Broad-range inhibition of enterovirus replication by OSW-1, a natural compound targeting OSBP. *Antivir. Res.* 117, 110–114.
- Arita, M., Wakita, T., Shimizu, H., 2009. Cellular kinase inhibitors that suppress enterovirus replication have a conserved target in viral protein 3A similar to that of enviroxime. *J. Gen. Virol.* 90 (Pt 8), 1869–1879.
- Arita, M., et al., 2010. A bifunctional anti-enterovirus compound that inhibits replication and the early stage of enterovirus 71 infection. *J. Gen. Virol.* 91 (Pt 11), 2734–2744.
- Arita, M., et al., 2011. Phosphatidylinositol 4-kinase III beta is a target of enviroxime-like compounds for antipoliavirus activity. *J. Virol.* 85 (5), 2364–2372.
- Arita, M., et al., 2013. Oxysterol-binding protein family I is the target of minor enviroxime-like compounds. *J. Virol.* 87 (8), 4252–4260.
- Baiceanu, A., et al., 2016. Endoplasmic reticulum proteostasis in hepatic steatosis. *Nat. Rev. Endocrinol.* 12 (12), 710–722.
- Berman, A.Y., et al., 2017. The therapeutic potential of resveratrol: a review of clinical trials. *NPJ Precis. Oncol.* 1.
- Bertolotti, A., et al., 2000. Dynamic interaction of BiP and ER stress transducers in the unfolded-protein response. *Nat. Cell Biol.* 2 (6), 326–332.
- Bishe, B., et al., 2012. Role of phosphatidylinositol 4-phosphate (PI4P) and its binding protein GOLPH3 in hepatitis C virus secretion. *J. Biol. Chem.* 287 (33), 27637–27647.
- Bou-Nader, C., et al., 2019. The search for a PKR code-differential regulation of protein kinase R activity by diverse RNA and protein regulators. *RNA* 25 (5), 539–556.
- Brodsky, J.L., Wojcikiewicz, R.J., 2009. Substrate-specific mediators of ER associated degradation (ERAD). *Curr. Opin. Cell Biol.* 21 (4), 516–521.
- Brown-Augsburger, P., et al., 1999. Evidence that enviroxime targets multiple components of the rhinovirus 14 replication complex. *Arch. Virol.* 144 (8), 1569–1585.
- Cathcart, A.L., Rozovics, J.M., Semler, B.L., 2013. Cellular mRNA decay protein AUF1 negatively regulates enterovirus and human rhinovirus infections. *J. Virol.* 87 (19), 10423–10434.
- Centers for Disease, C., 2011. Prevention, Clusters of acute respiratory illness associated with human enterovirus 68–Asia, Europe, and United States, 2008–2010. *MMWR Morb. Mortal. Wkly. Rep.* 60 (38), 1301–1304.
- Chandra, P.P., Ktistakis, N.T., 2009. Lipid-dependent membrane remodeling in protein trafficking. In: Segev, N. (Ed.), *Trafficking inside Cells: Pathways, Mechanisms and Regulation*. Springer, pp. 210–232 chap. 11.
- Chang, Y.H., et al., 2017. dsRNA binding domain of PKR is proteolytically released by enterovirus A71 to facilitate viral replication. *Front. Cell Infect. Microbiol.* 7, 284.
- Chaves Valadao, A.L., et al., 2015. Natural plant alkaloid (emetine) inhibits HIV-1 replication by interfering with reverse transcriptase activity. *Molecules* 20 (6), 11474–11489.
- Chen, Y.J., et al., 2008. Amantadine as a regulator of internal ribosome entry site. *Acta Pharmacol. Sin.* 29 (11), 1327–1333.
- Chen, L.L., et al., 2013. Enterovirus 71 infection cleaves a negative regulator for viral internal ribosomal entry site-driven translation. *J. Virol.* 87 (7), 3828–3838.
- Chen, S.G., et al., 2017. Anti-enterovirus 71 activities of Melissa officinalis extract and its biologically active constituent rosmarinic acid. *Sci. Rep.* 7 (1), 12264.
- Cheng, P.K., et al., 2009. Oseltamivir- and amantadine-resistant influenza viruses A (H1N1). *Emerg. Infect. Dis.* 15 (6), 966–968.
- Cheng, J., et al., 2020. Typical stress granule proteins interact with the 3' untranslated region of enterovirus D68 to inhibit viral replication. *J. Virol.* 94 (7).



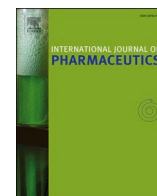
- Choy, K.T., et al., 2020. Remdesivir, lopinavir, emetine, and homoharringtonine inhibit SARS-CoV-2 replication in vitro. *Antivir. Res.* 178, 104786.
- Chung, Y.C., et al., 2015. Magnesium lithospermate B and rosmarinic acid, two compounds present in *Salvia miltiorrhiza*, have potent antiviral activity against enterovirus 71 infections. *Eur. J. Pharmacol.* 755, 127–133.
- Conti, B.J., et al., 2015. Cotranslational stabilization of Sec62/63 within the ER Sec61 translocon is controlled by distinct substrate-driven translocation events. *Mol. Cell* 58 (2), 269–283.
- Corona, A.K., et al., 2018. Enteroviruses remodel autophagic trafficking through regulation of host SNARE proteins to promote virus replication and cell exit. *Cell Rep.* 22 (12), 3304–3314.
- Crosby, N., Deane, K.H., Clarke, C.E., 2003. Amantadine in Parkinson's disease. *Cochrane Database Syst. Rev.* (1), CD003468.
- Dai, W., et al., 2019. Antiviral efficacy of flavonoids against enterovirus 71 infection in vitro and in newborn mice. *Viruses* 11 (7).
- Dan, X., et al., 2019. Hsp27 responds to and facilitates enterovirus A71 replication by enhancing viral internal ribosome entry site-mediated translation. *J. Virol.* 93 (9).
- Davila-Calderon, J., et al., 2020. IRES-targeting small molecule inhibits enterovirus 71 replication via allosteric stabilization of a ternary complex. *Nat. Commun.* 11 (1), 4775.
- Davis-Smyth, T., et al., 1996. The far upstream element-binding proteins comprise an ancient family of single-strand DNA-binding transactivators. *J. Biol. Chem.* 271 (49), 31679–31687.
- de Breyne, S., et al., 2008. Cleavage of eukaryotic initiation factor eIF5B by enterovirus 3C proteases. *Virology* 378 (1), 118–122.
- De Matteis, M.A., Wilson, C., D'Angelo, G., 2013. Phosphatidylinositol-4-phosphate: the Golgi and beyond. *Bioessays* 35 (7), 612–622.
- De Palma, A.M., et al., 2008. The thiazolobenzimidazole TBZE-029 inhibits enterovirus replication by targeting a short region immediately downstream from motif C in the nonstructural protein 2C. *J. Virol.* 82 (10), 4720–4730.
- De Palma, A.M., et al., 2009. Mutations in the nonstructural protein 3A confer resistance to the novel enterovirus replication inhibitor TTP-8307. *Antimicrob. Agents Chemother.* 53 (5), 1850–1857.
- Deegan, S., et al., 2015. A close connection between the PERK and IRE arms of the UPR and the transcriptional regulation of autophagy. *Biochem. Biophys. Res. Commun.* 456 (1), 305–311.
- Di Fusco, D., et al., 2018. Metformin inhibits inflammatory signals in the gut by controlling AMPK and p38 MAP kinase activation. *Clin. Sci. (Lond.)* 132 (11), 1155–1168.
- Dobrikova, E., et al., 2003. Activity of a type 1 picornavirus internal ribosomal entry site is determined by sequences within the 3' nontranslated region. *Proc. Natl. Acad. Sci. U. S. A.* 100 (25), 15125–15130.
- Docherty, J.J., et al., 1999. Resveratrol inhibition of herpes simplex virus replication. *Antivir. Res.* 43 (3), 145–155.
- Docherty, J.J., et al., 2005. Effect of resveratrol on herpes simplex virus vaginal infection in the mouse. *Antivir. Res.* 67 (3), 155–162.
- Dong, W., et al., 2014. A dual character of flavonoids in influenza A virus replication and spread through modulating cell-autonomous immunity by MAPK signaling pathways. *Sci. Rep.* 4, 7237.
- Du, N., et al., 2019. Resveratrol-loaded nanoparticles inhibit enterovirus 71 replication through the oxidative stress-mediated ERS/autophagy pathway. *Int. J. Mol. Med.* 44 (2), 737–749.
- Duncan, R., et al., 1994. A sequence-specific, single-strand binding protein activates the far upstream element of c-myc and defines a new DNA-binding motif. *Genes Dev.* 8 (4), 465–480.
- Echarri, A., Del Pozo, M.A., 2015. Caveolae - mechanosensitive membrane invaginations linked to actin filaments. *J. Cell Sci.* 128 (15), 2747–2758.
- Fan, J., et al., 2010. Acyl-coenzyme A binding domain containing 3 (ACBD3; PAP7; GCP60): an emerging signaling molecule. *Prog. Lipid Res.* 49 (3), 218–234.
- Ferris, S.P., et al., 2013. UDP-glucose:glycoprotein glucosyltransferase (UGGT1) promotes substrate solubility in the endoplasmic reticulum. *Mol. Biol. Cell* 24 (17), 2597–2608.
- Ferris, S.P., Kodali, V.K., Kaufman, R.J., 2014. Glycoprotein folding and quality-control mechanisms in protein-folding diseases. *Dis. Model. Mech.* 7 (3), 331–341.
- Francioso, A., et al., 2014. Chemistry, stability and bioavailability of resveratrol. *Med. Chem.* 10 (3), 237–245.
- Fu, W.M., et al., 2012. Heat shock protein 27 mediates the effect of 1,3,5-trihydroxy-13,13-dimethyl-2H-pyran [7,6-b] xanthone on mitochondrial apoptosis in hepatocellular carcinoma. *J. Proteomics* 75 (15), 4833–4843.
- Furuse, Y., et al., 2019. Evolutionary and functional diversity of the 5' untranslated region of enterovirus D68: increased activity of the internal ribosome entry site of viral strains during the 2010s. *Viruses* 11 (7).
- Gambini, J., et al., 2015. Properties of resveratrol: in vitro and in vivo studies about metabolism, bioavailability, and biological effects in animal models and humans. *Oxid. Med. Cell Longev.* 2015, 837042.
- Gao, M., et al., 2014. The multi-targeted kinase inhibitor sorafenib inhibits enterovirus 71 replication by regulating IRES-dependent translation of viral proteins. *Antivir. Res.* 106, 80–85.
- Garcia, M.A., et al., 2006. Impact of protein kinase PKR in cell biology: from antiviral to antiproliferative action. *Microbiol. Mol. Biol. Rev.* 70 (4), 1032–1060.
- Gardai, S.J., et al., 2005. Cell-surface calreticulin initiates clearance of viable or apoptotic cells through trans-activation of LRP on the phagocyte. *Cell* 123 (2), 321–334.
- Ghanem, L.R., Chatterji, P., Liebhauer, S.A., 2014. Specific enrichment of the RNA-binding proteins PCBP1 and PCBP2 in chief cells of the murine gastric mucosa. *Gene Expr. Patterns* 14 (2), 78–87.
- Gil, A., et al., 1991. Characterization of cDNAs encoding the polypyrimidine tract-binding protein. *Genes Dev.* 5 (7), 1224–1236.
- Gilbert, B.E., et al., 1988. Small particle aerosols of enviroxime-containing liposomes. *Antivir. Res.* 9 (6), 355–365.
- Godet, A.C., et al., 2019. IRES trans-acting factors, key actors of the stress response. *Int. J. Mol. Sci.* 20 (4).
- Gorshkov, K., et al., 2020. The SARS-CoV-2 cytopathic effect is blocked with autophagy modulators. *bioRxiv [Preprint]*. <https://doi.org/10.1101/2020.05.16.091520>, 2020 May 28;2020.05.16.091520, Update in: *ACS Infect. Dis.* 2020 Dec 21; PMID: 32511355; PMCID: PMC7259466.
- Grunert, R.R., Hoffmann, C.E., 1977. Sensitivity of influenza A/New Jersey/8/76 (Hsw1N1) virus to amantadine-HCl. *J. Infect. Dis.* 136 (2), 297–300.
- Guan, H., et al., 2017. Crystal structure of 2C helicase from enterovirus 71. *Sci. Adv.* 3 (4), e1602573.
- Gunaseelan, S., et al., 2019. Prunin suppresses viral IRES activity and is a potential candidate for treating enterovirus A71 infection. *Sci. Transl. Med.* 11 (516).
- Gustin, K.E., Sarnow, P., 2001. Effects of poliovirus infection on nucleocytoplasmic trafficking and nuclear pore complex composition. *EMBO J.* 20 (1–2), 240–249.
- Harding, H.P., Zhang, Y., Ron, D., 1999. Protein translation and folding are coupled by an endoplasmic-reticulum-resident kinase. *Nature* 397 (6716), 271–274.
- Harrison, D.N., et al., 2008. Amiloride derivatives inhibit coxsackievirus B3 RNA replication. *J. Virol.* 82 (3), 1465–1473.
- Hayashi, K., et al., 2007. Antiviral activity of berberine and related compounds against human cytomegalovirus. *Bioorg. Med. Chem. Lett.* 17 (6), 1562–1564.
- Hayden, F.G., Gwaltney Jr., J.M., 1982. Prophylactic activity of intranasal enviroxime against experimentally induced rhinovirus type 39 infection. *Antimicrob. Agents Chemother.* 21 (6), 892–897.
- Haze, K., et al., 1999. Mammalian transcription factor ATF6 is synthesized as a transmembrane protein and activated by proteolysis in response to endoplasmic reticulum stress. *Mol. Biol. Cell* 10 (11), 3787–3799.
- He, Y., et al., 2010. Emerging roles for XBP1, a sUPER transcription factor. *Gene Expr.* 15 (1), 13–25.
- Heaton, N.S., et al., 2016. Targeting viral proteostasis limits influenza virus, HIV, and dengue virus infection. *Immunity* 44 (1), 46–58.
- Heinz, B.A., Vance, L.M., 1995. The antiviral compound enviroxime targets the 3A coding region of rhinovirus and poliovirus. *J. Virol.* 69 (7), 4189–4197.
- Heinz, B.A., Vance, L.M., 1996. Sequence determinants of 3A-mediated resistance to enviroxime in rhinoviruses and enteroviruses. *J. Virol.* 70 (7), 4854–4857.
- Helenius, A., Aebi, M., 2004. Roles of N-linked glycans in the endoplasmic reticulum. *Annu. Rev. Biochem.* 73, 1019–1049.
- Hetz, C., 2012. The unfolded protein response: controlling cell fate decisions under ER stress and beyond. *Nat. Rev. Mol. Cell Biol.* 13 (2), 89–102.
- Himmelsbach, K., et al., 2009. New aspects of an anti-tumour drug: sorafenib efficiently inhibits HCV replication. *Gut* 58 (12), 1644–1653.
- Hipp, M.S., Kasturi, P., Hartl, F.U., 2019. The proteostasis network and its decline in ageing. *Nat. Rev. Mol. Cell Biol.* 20 (7), 421–435.
- Hixon, A.M., Clarke, P., Tyler, K.L., 2017. Evaluating treatment efficacy in a mouse model of enterovirus D68-associated paralytic myelitis. *J. Infect. Dis.* 216 (10), 1245–1253.
- Ho, B.C., et al., 2011. Enterovirus-induced miR-141 contributes to shutoff of host protein translation by targeting the translation initiation factor eIF4E. *Cell Host Microbe* 9 (1), 58–69.
- Howells, L.M., et al., 2011. Phase I randomized, double-blind pilot study of micronized resveratrol (SRT501) in patients with hepatic metastases—safety, pharmacokinetics, and pharmacodynamics. *Canc. Prev. Res.* 4 (9), 1419–1425.
- Hsieh, C.F., et al., 2020. Rosmarinic acid exhibits broad anti-enterovirus A71 activity by inhibiting the interaction between the five-fold axis of capsid VP1 and cognate sulfated receptors. *Emerg. Microb. Infect.* 9 (1), 1194–1205.
- Hsu, Y.Y., et al., 2009. Visualizing and quantifying the differential cleavages of the eukaryotic translation initiation factors eIF4GI and eIF4GII in the enterovirus-infected cell. *Biotechnol. Bioeng.* 104 (6), 1142–1152.
- Hu, D.D., et al., 2017. Glucocorticoids prevent enterovirus 71 capsid protein VP1 induced calreticulin surface exposure by alleviating neuronal ER stress. *Neurotox. Res.* 31 (2), 204–217.
- Huang, S.C., et al., 2009. Enterovirus 71-induced autophagy detected in vitro and in vivo promotes viral replication. *J. Med. Virol.* 81 (7), 1241–1252.
- Huang, P.N., et al., 2011. Far upstream element binding protein 1 binds the internal ribosomal entry site of enterovirus 71 and enhances viral translation and viral growth. *Nucleic Acids Res.* 39 (22), 9633–9648.
- Huang, H.L., et al., 2016. Interactome analysis of the EV71 5' untranslated region in differentiated neuronal cells SH-SY5Y and regulatory role of FBP3 in viral replication. *Proteomics* 16 (17), 2351–2362.
- Huang, P.N., et al., 2017. UGGT1 enhances enterovirus 71 pathogenicity by promoting viral RNA synthesis and viral replication. *PLoS Pathog.* 13 (5), e1006375.
- Hung, C.T., et al., 2016. Additive promotion of viral internal ribosome entry site-mediated translation by far upstream element-binding protein 1 and an enterovirus 71-induced cleavage product. *PLoS Pathog.* 12 (10), e1005959.
- Hutt, D.M., Balch, W.E., 2013. Expanding proteostasis by membrane trafficking networks. *Cold Spring Harb Perspect. Biol.* 5 (7).
- Ilott, M.C., et al., 1997. Dexamethasone inhibits virus production and the secretory IgA response in oesophageal-pharyngeal fluid in cattle persistently infected with foot-and-mouth disease virus. *Epidemiol. Infect.* 118 (2), 181–187.
- Imenshahidi, M., Hosseinzadeh, H., 2016. Berberis vulgaris and berberine: an update review. *Phytother. Res.* 30 (11), 1745–1764.
- Imran, M., et al., 2019. Kaempferol: a key emphasis to its anticancer potential. *Molecules* 24 (12).



- Ishidate, T., et al., 1997. Identification of a novel nuclear localization signal in Sam68. *FEBS Lett.* 409 (2), 237–241.
- Jeong, H.W., et al., 2009. Berberine suppresses proinflammatory responses through AMPK activation in macrophages. *Am. J. Physiol. Endocrinol. Metab.* 296 (4), E955–E964.
- Jheng, J.R., et al., 2010. Endoplasmic reticulum stress is induced and modulated by enterovirus 71. *Cell Microbiol.* 12 (6), 796–813.
- Jheng, J.R., et al., 2012. Inhibition of enterovirus 71 entry by transcription factor XBP1. *Biochem. Biophys. Res. Commun.* 420 (4), 882–887.
- Jheng, J.R., Ho, J.Y., Horng, J.T., 2014. ER stress, autophagy, and RNA viruses. *Front. Microbiol.* 5, 388.
- Jheng, J.R., et al., 2016. Enterovirus 71 induces dsRNA/PKR-dependent cytoplasmic redistribution of GRP78/BiP to promote viral replication. *Emerg. Microb. Infect.* 5, e23.
- Jheng, J.R., et al., 2018a. The double-edged sword of endoplasmic reticulum stress in uremic sarcopenia through myogenesis perturbation. *J. Cachexia Sarcopenia Muscle* 9 (3), 570–584.
- Jheng, J.R., et al., 2018b. A novel role of ER stress signal transducer ATF6 in regulating enterovirus A71 viral protein stability. *J. Biomed. Sci.* 25 (1), 9.
- Ji, X.Y., et al., 2013. Synthesis and antiviral activity of N-phenylbenzamide derivatives, a novel class of enterovirus 71 inhibitors. *Molecules* 18 (3), 3630–3640.
- Jiang, L., et al., 2012. Resveratrol prevents hepatic steatosis induced by hepatitis C virus core protein. *Biotechnol. Lett.* 34 (12), 2205–2212.
- Kai, H., et al., 2014a. In vitro and in vivo anti-influenza virus activities of flavonoids and related compounds as components of Brazilian propolis (AF-08). *J. Funct. Foods* 8, 214–223.
- Kai, H., et al., 2014b. In vitro and in vivo anti-influenza virus activities of flavonoids and related compounds as components of Brazilian propolis (AF-08). *J. Funct. Foods* 8, 214–223.
- Korennykh, A.V., et al., 2009. The unfolded protein response signals through high-order assembly of Ire1. *Nature* 457 (7230), 687–693.
- Kroll, T.T., et al., 2002. A homolog of FBP2/KSRP binds to localized mRNAs in *Xenopus* oocytes. *Development* 129 (24), 5609–5619.
- Kuo, R.L., et al., 2015. Proteomics analysis of EV71-infected cells reveals the involvement of host protein NEDD4L in EV71 replication. *J. Proteome Res.* 14 (4), 1818–1830.
- Lai, J.K.F., et al., 2017. 2BC non-structural protein of enterovirus A71 interacts with SNARE proteins to trigger autolysosome formation. *Viruses* 9 (7).
- Lan, J., et al., 2015. Meta-analysis of the effect and safety of berberine in the treatment of type 2 diabetes mellitus, hyperlipemia and hypertension. *J. Ethnopharmacol.* 161, 69–81.
- Lawrence, P., Schafer, E.A., Rieder, E., 2012. The nuclear protein Sam68 is cleaved by the FMDV 3C protease redistributing Sam68 to the cytoplasm during FMDV infection of host cells. *Virology* 425 (1), 40–52.
- Lee, A.H., Iwakoshi, N.N., Glimcher, L.H., 2003. XBP-1 regulates a subset of endoplasmic reticulum resident chaperone genes in the unfolded protein response. *Mol. Cell Biol.* 23 (21), 7448–7459.
- Lee, Y.R., et al., 2014. Enterovirus 71-induced autophagy increases viral replication and pathogenesis in a suckling mouse model. *J. Biomed. Sci.* 21, 80.
- Lei, X., et al., 2017. The Golgi protein ACBD3 facilitates Enterovirus 71 replication by interacting with 3A. *Sci. Rep.* 7, 44592.
- Leong, S.Y., Ong, B.K., Chu, J.J., 2015. The role of Misshapen NCK-related kinase (MINK), a novel Ste20 family kinase, in the IRES-mediated protein translation of human enterovirus 71. *PLoS Pathog.* 11 (3), e1004686.
- Levy, A., et al., 2015. Enterovirus D68 disease and molecular epidemiology in Australia. *J. Clin. Virol.* 69, 117–121.
- Li, Z., et al., 2018. Enterovirus 71 antagonizes the inhibition of the host intrinsic antiviral factor A3G. *Nucleic Acids Res.* 46 (21), 11514–11527.
- Li, P., et al., 2019. Enterovirus 71 VP1 promotes mouse Schwann cell autophagy via ER stress-mediated PMP22 upregulation. *Int. J. Mol. Med.* 44 (2), 759–767.
- Lin, J.Y., Huang, H.I., 2020. Autophagy is induced and supports virus replication in Enterovirus A71-infected human primary neuronal cells. *Sci. Rep.* 10 (1), 15234.
- Lin, J.Y., et al., 2008. Heterogeneous nuclear ribonuclear protein K interacts with the enterovirus 71 5' untranslated region and participates in virus replication. *J. Gen. Virol.* 89 (Pt 10), 2540–2549.
- Lin, J.-Y., et al., 2009a. Viral and host proteins involved in picornavirus life cycle. *J. Biomed. Sci.* 16 (1), 103.
- Lin, J.Y., et al., 2009b. hnRNP A1 interacts with the 5' untranslated regions of enterovirus 71 and Sindbis virus RNA and is required for viral replication. *J. Virol.* 83 (12), 6106–6114.
- Lin, J.Y., Li, M.L., Shih, S.R., 2009c. Far upstream element binding protein 2 interacts with enterovirus 71 internal ribosomal entry site and negatively regulates viral translation. *Nucleic Acids Res.* 37 (1), 47–59.
- Lin, Y.W., et al., 2012. Human SCARB2-mediated entry and endocytosis of EV71. *PLoS One* 7 (1), e30507.
- Lin, H.Y., et al., 2013. Caveolar endocytosis is required for human PSGL-1-mediated enterovirus 71 infection. *J. Virol.* 87 (16), 9064–9076.
- Lin, J.Y., Li, M.L., Brewer, G., 2014. mRNA decay factor AUF1 binds the internal ribosomal entry site of enterovirus 71 and inhibits virus replication. *PLoS One* 9 (7), e103827.
- Lin, J.Y., Brewer, G., Li, M.L., 2015. HuR and Ago2 bind the internal ribosome entry site of enterovirus 71 and promote virus translation and replication. *PLoS One* 10 (10), e0140291.
- Lin, S.C., et al., 2017a. Effective inhibition of MERS-CoV infection by resveratrol. *BMC Infect. Dis.* 17 (1), 144.
- Lin, Y.F., et al., 2017b. Resveratrol-loaded nanoparticles conjugated with kidney injury molecule-1 as a drug delivery system for potential use in chronic kidney disease. *Nanomedicine* 12 (22), 2741–2756.
- Lin, W.Y., Yu, Y.J., Jinn, T.R., 2019. Evaluation of the virucidal effects of rosmarinic acid against enterovirus 71 infection via in vitro and in vivo study. *Virol. J.* 16 (1), 94.
- Liu, A.L., et al., 2008. Anti-influenza virus activities of flavonoids from the medicinal plant *Elsholtzia rugulosa*. *Planta Med.* 74 (8), 847–851.
- Liu, Z.W., et al., 2019. Enterovirus 71 VP1 protein regulates viral replication in SH-SY5Y cells via the mTOR autophagy signaling pathway. *Viruses* 12 (1).
- Lu, J., Gao, F.H., 2016. Role and molecular mechanism of heterogeneous nuclear ribonucleoprotein K in tumor development and progression. *Biomed. Rep.* 4 (6), 657–663.
- Luganini, A., et al., 2019. The isoquinoline alkaloid berberine inhibits human cytomegalovirus replication by interfering with the viral Immediate Early-2 (IE2) protein transactivating activity. *Antivir. Res.* 164, 52–60.
- Lugo, D., Krogstad, P., 2016. Enteroviruses in the early 21st century: new manifestations and challenges. *Curr. Opin. Pediatr.* 28 (1), 107–113.
- Lundberg, L., et al., 2018. Repurposed FDA-Approved drug sorafenib reduces replication of Venezuelan equine encephalitis virus and other alphaviruses. *Antivir. Res.* 157, 57–67.
- Luo, Z., et al., 2014. PolyC-binding protein 1 interacts with 5'-untranslated region of enterovirus 71 RNA in membrane-associated complex to facilitate viral replication. *PLoS One* 9 (1), e87491.
- Lyoo, H., et al., 2019. ACBD3 is an essential pan-enterovirus host factor that mediates the interaction between viral 3A protein and cellular protein P14KB. *mBio* 10 (1).
- Marques, M., et al., 2019. Cellular proteostasis during influenza A virus infection—friend or foe? *Cells* 8 (3).
- Martinez-Salas, E., et al., 2013. RNA-binding proteins impacting on internal initiation of translation. *Int. J. Mol. Sci.* 14 (11), 21705–21726.
- McBride, A.E., Schlegel, A., Kirkegaard, K., 1996. Human protein Sam68 relocation and interaction with poliovirus RNA polymerase in infected cells. *Proc. Natl. Acad. Sci. U. S. A.* 93 (6), 2296–2301.
- McKinsey, D.S., et al., 1999. Itraconazole prophylaxis for fungal infections in patients with advanced human immunodeficiency virus infection: randomized, placebo-controlled, double-blind study. National Institute of Allergy and Infectious Diseases Mycoses Study Group. *Clin. Infect. Dis.* 28 (5), 1049–1056.
- Merulla, J., Solda, T., Molinari, M., 2015. A novel UGGT1 and p97-dependent checkpoint for native ectodomains with ionizable intramembrane residue. *Mol. Biol. Cell* 26 (8), 1532–1542.
- Miller, F.D., et al., 1985. Controlled trial of enviroxime against natural rhinovirus infections in a community. *Antimicrob. Agents Chemother.* 27 (1), 102–106.
- Ming, J., et al., 2018. Effectiveness and safety of bifidobacteria and berberine in people with hyperglycemia: study protocol for a randomized controlled trial. *Trials* 19 (1), 72.
- Moon, H.W., Han, H.G., Jeon, Y.J., 2018. Protein quality control in the endoplasmic reticulum and cancer. *Int. J. Mol. Sci.* 19 (10).
- Morosky, S., Lennemann, N.J., Coyne, C.B., 2016. BPIFB6 regulates secretory pathway trafficking and enterovirus replication. *J. Virol.* 90 (10), 5098–5107.
- Mukhopadhyay, R., et al., 2016. Efficacy and mechanism of action of low dose emetine against human cytomegalovirus. *PLoS Pathog.* 12 (6), e1005717.
- Murray, J., et al., 2017. A universal mammalian vaccine cell line substrate. *PLoS One* 12 (11), e0188333.
- Noguchi-Shinohara, M., et al., 2015. Pharmacokinetics, safety and tolerability of melissa officinalis extract which contained rosmarinic acid in healthy individuals: a randomized controlled trial. *PLoS One* 10 (5), e0126422.
- Nunes, S., et al., 2017. Therapeutic and nutraceutical potential of rosmarinic acid—Cytoprotective properties and pharmacokinetic profile. *Crit. Rev. Food Sci. Nutr.* 57 (9), 1799–1806.
- Ogram, S.A., et al., 2014. Amiloride inhibits the initiation of Coxsackievirus and poliovirus RNA replication by inhibiting VPg uridylation. *Virology* 464–465, 87–97.
- Oliver, J.D., et al., 1999. ERp57 functions as a subunit of specific complexes formed with the ER lectins calreticulin and calnexin. *Mol. Biol. Cell* 10 (8), 2573–2582.
- Otero, J.H., Lizak, B., Hendershot, L.M., 2010. Life and death of a BiP substrate. *Semin. Cell Dev. Biol.* 21 (5), 472–478.
- Ozelik, B., Kartal, M., Orhan, I., 2011. Cytotoxicity, antiviral and antimicrobial activities of alkaloids, flavonoids, and phenolic acids. *Pharm. Biol.* 49 (4), 396–402.
- Pakos-Zebrucka, K., et al., 2016. The integrated stress response. *EMBO Rep.* 17 (10), 1374–1395.
- Palamara, A.T., et al., 2005. Inhibition of influenza A virus replication by resveratrol. *J. Infect. Dis.* 191 (10), 1719–1729.
- Parzych, K.R., Klionsky, D.J., 2014. An overview of autophagy: morphology, mechanism, and regulation. *Antioxidants Redox Signal.* 20 (3), 460–473.
- Patwardhan, N.N., et al., 2017. Amiloride as a new RNA-binding scaffold with activity against HIV-1 TAR. *Medchemcomm* 8 (5), 1022–1036.
- Pendin, D., McNew, J.A., Daga, A., 2011. Balancing ER dynamics: shaping, bending, severing, and mending membranes. *Curr. Opin. Cell Biol.* 23 (4), 435–442.
- Petersen-Mahrt, S.K., Harris, R.S., Neuberger, M.S., 2002. AID mutates *E. coli* suggesting a DNA deamination mechanism for antibody diversification. *Nature* 418 (6893), 99–103.
- Phillipotts, R.J., et al., 1981. The activity of enviroxime against rhinovirus infection in man. *Lancet* 1 (8234), 1342–1344.
- Phillipotts, R.J., et al., 1983. Therapeutic activity of enviroxime against rhinovirus infection in volunteers. *Antimicrob. Agents Chemother.* 23 (5), 671–675.

- Piacentini, S., et al., 2018. Nitazoxanide inhibits paramyxovirus replication by targeting the Fusion protein folding: role of glycoprotein-specific thiol oxidoreductase ERp57. *Sci. Rep.* 8 (1), 10425.
- Plaze, M., et al., 2020. Inhibition of the Replication of SARS-CoV-2 in Human Cells by the FDA-Approved Drug Chlorpromazine. *bioRxiv*, 2020.05.079608.
- Powers, E.T., et al., 2009. Biological and chemical approaches to diseases of proteostasis deficiency. *Annu. Rev. Biochem.* 78, 959–991.
- Puenpa, J., et al., 2019. The history of enterovirus A71 outbreaks and molecular epidemiology in the asia-pacific region. *J. Biomed. Sci.* 26 (1), 75.
- Qi, Z., Chen, L., 2019. Endoplasmic reticulum stress and autophagy. *Adv. Exp. Med. Biol.* 1206, 167–177.
- Ramirez-Garza, S.L., et al., 2018. Health effects of resveratrol: results from human intervention trials. *Nutrients* 10 (12).
- Rejdak, K., Grieb, P., 2020. Adamantanes might be protective from COVID-19 in patients with neurological diseases: multiple sclerosis, parkinsonism and cognitive impairment. *Mult. Scler. Relat. Disord.* 42, 102163.
- Rojas, E.A., et al., 2017. Amiloride, an old diuretic drug, is a potential therapeutic agent for multiple myeloma. *Clin. Canc. Res.* 23 (21), 6602–6615.
- Rust, R.C., et al., 2001. Cellular COPII proteins are involved in production of the vesicles that form the poliovirus replication complex. *J. Virol.* 75 (20), 9808–9818.
- Rutkowski, D.T., Hegde, R.S., 2010. Regulation of basal cellular physiology by the homeostatic unfolded protein response. *J. Cell Biol.* 189 (5), 783–794.
- Sadeghipour, S., Bek, E.J., McMinn, P.C., 2012. Selection and characterisation of guanidine-resistant mutants of human enterovirus 71. *Virus Res.* 169 (1), 72–79.
- Salehi, B., et al., 2019. The therapeutic potential of apigenin. *Int. J. Mol. Sci.* 20 (6).
- Sanz, M.A., et al., 2013. Phosphorylation of eIF2 $\alpha$  is responsible for the failure of the picornavirus internal ribosome entry site to direct translation from Sindbis virus replicons. *J. Gen. Virol.* 94 (Pt 4), 796–806.
- Schellhaas, M., et al., 2007. Simian Virus 40 depends on ER protein folding and quality control factors for entry into host cells. *Cell* 131 (3), 516–529.
- Schieble, J.H., Fox, V.L., Lennette, E.H., 1967. A probable new human picornavirus associated with respiratory diseases. *Am. J. Epidemiol.* 85 (2), 297–310.
- Schloer, S., et al., 2019. The clinically licensed antifungal drug itraconazole inhibits influenza virus in vitro and in vivo. *Emerg. Microb. Infect.* 8 (1), 80–93.
- Schmidt, N.J., Lennette, E.H., Ho, H.H., 1974. An apparently new enterovirus isolated from patients with disease of the central nervous system. *J. Infect. Dis.* 129 (3), 304–309.
- Schwarz, S., et al., 2014. Kaempferol derivatives as antiviral drugs against the 3a channel protein of coronavirus. *Planta Med.* 80 (2–3), 177–182.
- Sejvar, J.J., et al., 2016. Acute flaccid myelitis in the United States, august–december 2014: results of nationwide surveillance. *Clin. Infect. Dis.* 63 (6), 737–745.
- Sharma, S., Ray, A., Sadasivam, B., 2020. Metformin in COVID-19: a possible role beyond diabetes. *Diabetes Res. Clin. Pract.* 164, 108183.
- Shen, F.H., et al., 2014. Early dexamethasone treatment exacerbates enterovirus 71 infection in mice. *Virology* 464–465, 218–227.
- Shen, L., et al., 2019. High-throughput screening and identification of potent broad-spectrum inhibitors of coronaviruses. *J. Virol.* 93 (12).
- Shibata, C., et al., 2014. The flavonoid apigenin inhibits hepatitis C virus replication by decreasing mature microRNA122 levels. *Virology* 462–463, 42–48.
- Smee, D.F., et al., 2016. Susceptibilities of enterovirus D68, enterovirus 71, and rhinovirus 87 strains to various antiviral compounds. *Antivir. Res.* 131, 61–65.
- Smieszek, S.P., Przychodzen, B.P., Polymeropoulos, M.H., 2020. Amantadine disrupts lysosomal gene expression: a hypothesis for COVID19 treatment. *Int. J. Antimicrob. Agents* 55 (6), 106004.
- Strating, J.R., et al., 2015. Itraconazole inhibits enterovirus replication by targeting the oxysterol-binding protein. *Cell Rep.* 10 (4), 600–615.
- Su, Y.S., et al., 2018. Stimulation of the internal ribosome entry site (IRES)-dependent translation of enterovirus 71 by DDX3X RNA helicase and viral 2A and 3C proteases. *Front. Microbiol.* 9, 1324.
- Suhy, D.A., Giddings Jr., T.H., Kirkegaard, K., 2000. Remodeling the endoplasmic reticulum by poliovirus infection and by individual viral proteins: an autophagy-like origin for virus-induced vesicles. *J. Virol.* 74 (19), 8953–8965.
- Swarup, V., et al., 2007. Antiviral and anti-inflammatory effects of rosmarinic acid in an experimental murine model of Japanese encephalitis. *Antimicrob. Agents Chemother.* 51 (9), 3367–3370.
- Sweeney, T.R., et al., 2014. The mechanism of translation initiation on Type 1 picornavirus IRESs. *EMBO J.* 33 (1), 76–92.
- Tan, Y.W., et al., 2018. An evaluation of chloroquine as a broad-acting antiviral against hand, foot and mouth disease. *Antivir. Res.* 149, 143–149.
- Tang, W.F., et al., 2007. Reticulon 3 binds the 2C protein of enterovirus 71 and is required for viral replication. *J. Biol. Chem.* 282 (8), 5888–5898.
- Tang, W.F., et al., 2016. Host MicroRNA miR-197 plays a negative regulatory role in the enterovirus 71 infectious cycle by targeting the RAN protein. *J. Virol.* 90 (3), 1424–1438.
- Tang, W.F., et al., 2019. Large-scale proteomic identification of targets of cellular miR-197 downregulated by enterovirus A71. *J. Proteome Res.* 18 (1), 449–460.
- Tang, Q., et al., 2020. Emetine protects mice from enterovirus infection by inhibiting viral translation. *Antivir. Res.* 173, 104650.
- Taylor, M.P., Kirkegaard, K., 2007. Modification of cellular autophagy protein LC3 by poliovirus. *J. Virol.* 81 (22), 12543–12553.
- Teng, B., Burant, C.F., Davidson, N.O., 1993. Molecular cloning of an apolipoprotein B messenger RNA editing protein. *Science* 260 (5115), 1816–1819.
- Thompson, S.R., Sarnow, P., 2003. Enterovirus 71 contains a type I IRES element that functions when eukaryotic initiation factor eIF4G is cleaved. *Virology* 315 (1), 259–266.
- Tian, L., et al., 2018. The cytotoxicity of coxsackievirus B3 is associated with a blockage of autophagic flux mediated by reduced syntaxin 17 expression. *Cell Death Dis.* 9 (2), 242.
- Tokarz, R., et al., 2012. Worldwide emergence of multiple clades of enterovirus 68. *J. Gen. Virol.* 93 (Pt 9), 1952–1958.
- Tolbert, M., et al., 2017. HnRNP A1 alters the structure of a conserved enterovirus IRES domain to stimulate viral translation. *J. Mol. Biol.* 429 (19), 2841–2858.
- Townley, A.K., et al., 2008. Efficient coupling of Sec23–Sec24 to Sec13–Sec31 drives COPII-dependent collagen secretion and is essential for normal craniofacial development. *J. Cell Sci.* 121 (Pt 18), 3025–3034.
- Tsai, F.J., et al., 2011. Kaempferol inhibits enterovirus 71 replication and internal ribosome entry site (IRES) activity through FUBP and HNRP proteins. *Food Chem.* 128 (2), 312–322.
- Tsukamoto, Y., et al., 2018. Rosmarinic acid is a novel inhibitor for Hepatitis B virus replication targeting viral epsilon RNA-polymerase interaction. *PLoS One* 13 (5), e0197664.
- Ulferts, R., et al., 2013. Selective serotonin reuptake inhibitor fluoxetine inhibits replication of human enteroviruses B and D by targeting viral protein 2C. *Antimicrob. Agents Chemother.* 57 (4), 1952–1956.
- Ulferts, R., et al., 2016. Screening of a library of FDA-approved drugs identifies several enterovirus replication inhibitors that target viral protein 2C. *Antimicrob. Agents Chemother.* 60 (5), 2627–2638.
- Ullmer, W., Semler, B.L., 2018. Direct and indirect effects on viral translation and RNA replication are required for AUF1 restriction of enterovirus infections in human cells. *mBio* 9 (5).
- van der Sanden, S.M., et al., 2016. Engineering enhanced vaccine cell lines to eradicate vaccine-preventable diseases: the polio end game. *J. Virol.* 90 (4), 1694–1704.
- van der Schaar, H.M., et al., 2013. A novel, broad-spectrum inhibitor of enterovirus replication that targets host cell factor phosphatidylinositol 4-kinase III $\beta$ . *Antimicrob. Agents Chemother.* 57 (10), 4971–4981.
- Varghese, F.S., et al., 2016. Discovery of berberine, abamectin and ivermectin as antivirals against chikungunya and other alphaviruses. *Antivir. Res.* 126, 117–124.
- Vembar, S.S., Brodsky, J.L., 2008. One step at a time: endoplasmic reticulum-associated degradation. *Nat. Rev. Mol. Cell Biol.* 9 (12), 944–957.
- Visser, L.J., et al., 2019. Essential role of enterovirus 2A protease in counteracting stress granule formation and the induction of type I interferon. *J. Virol.* 93 (10).
- Wakana, Y., et al., 2005. Reticulon 3 is involved in membrane trafficking between the endoplasmic reticulum and Golgi. *Biochem. Biophys. Res. Commun.* 334 (4), 1198–1205.
- Walczak, C.P., Tsai, B., 2011. A PDI family network acts distinctly and coordinately with ERp29 to facilitate polyomavirus infection. *J. Virol.* 85 (5), 2386–2396.
- Walter, P., Ron, D., 2011. The unfolded protein response: from stress pathway to homeostatic regulation. *Science* 334 (6059), 1081–1086.
- Walter, B.L., et al., 2002. Distinct poly(rC) binding protein KH domain determinants for poliovirus translation initiation and viral RNA replication. *J. Virol.* 76 (23), 12008–12022.
- Wan, S., et al., 2018. Resveratrol-loaded PLGA nanoparticles: enhanced stability, solubility and bioactivity of resveratrol for non-alcoholic fatty liver disease therapy. *R Soc. Open Sci.* 5 (11), 181457.
- Wang, C., et al., 1993. Ion channel activity of influenza A virus M2 protein: characterization of the amantadine block. *J. Virol.* 67 (9), 5585–5594.
- Wang, J., Wu, Z., Jin, Q., 2012a. COPI is required for enterovirus 71 replication. *PLoS One* 7 (5), e38035.
- Wang, X., et al., 2012b. The cellular antiviral protein APOBEC3G interacts with HIV-1 reverse transcriptase and inhibits its function during viral replication. *J. Virol.* 86 (7), 3777–3786.
- Wang, J., Du, J., Jin, Q., 2014. Class I ADP-ribosylation factors are involved in enterovirus 71 replication. *PLoS One* 9 (6), e99768.
- Wang, Q., Groenendyk, J., Michalak, M., 2015. Glycoprotein quality control and endoplasmic reticulum stress. *Molecules* 20 (8), 13689–13704.
- Wang, M., et al., 2016. Oblongifolin M, an active compound isolated from a Chinese medicinal herb *Garcinia oblongifolia*, potentially inhibits enterovirus 71 reproduction through downregulation of ERp57. *Oncotarget* 7 (8), 8797–8808.
- Wang, T., et al., 2017a. Enterovirus 71 protease 2Apro and 3Cpro differentially inhibit the cellular endoplasmic reticulum-associated degradation (ERAD) pathway via distinct mechanisms, and enterovirus 71 hijacks ERAD component p97 to promote its replication. *PLoS Pathog.* 13 (10), e1006674.
- Wang, H., et al., 2017b. Berberine inhibits enterovirus 71 replication by downregulating the MEK/ERK signaling pathway and autophagy. *Virol. J.* 14 (1), 2.
- Wang, J., et al., 2018. Antitumor, antioxidant and anti-inflammatory activities of kaempferol and its corresponding glycosides and the enzymatic preparation of kaempferol. *PLoS One* 13 (5), e0197563.
- Wang, H., et al., 2019a. APOBEC3G is a restriction factor of EV71 and mediator of IMB-Z antiviral activity. *Antivir. Res.* 165, 23–33.
- Wang, M., et al., 2019b. A review on flavonoid apigenin: dietary intake, ADME, antimicrobial effects, and interactions with human gut microbiota. *BioMed Res. Int.* 2019, 7010467.
- Weng, K.F., et al., 2014. A cytoplasmic RNA virus generates functional viral small RNAs and regulates viral IRES activity in mammalian cells. *Nucleic Acids Res.* 42 (20), 12789–12805.
- Whirl-Carrillo, M., et al., 2012. Pharmacogenomics knowledge for personalized medicine. *Clin. Pharmacol. Ther.* 92 (4), 414–417.
- White, J.P., Lloyd, R.E., 2012. Regulation of stress granules in virus systems. *Trends Microbiol.* 20 (4), 175–183.
- White, J.P., Reineke, L.C., Lloyd, R.E., 2011. Poliovirus switches to an eIF2-independent mode of translation during infection. *J. Virol.* 85 (17), 8884–8893.

- WHO, W.H.O., 2020. WHO R&D blueprint. COVID 19 Exper. Treat.
- Wong, W.R., et al., 2005. Phosphorylation of PI3K/Akt and MAPK/ERK in an early entry step of enterovirus 71. *Life Sci.* 78 (1), 82–90.
- Wong, J., et al., 2008. Autophagosome supports coxsackievirus B3 replication in host cells. *J. Virol.* 82 (18), 9143–9153.
- Wu, Y., et al., 2011. In vivo and in vitro antiviral effects of berberine on influenza virus. *Chin. J. Integr. Med.* 17 (6), 444–452.
- Wu, K.X., et al., 2016. Human genome-wide RNAi screen reveals host factors required for enterovirus 71 replication. *Nat. Commun.* 7, 13150.
- Wu, C.C., et al., 2017. Inhibition of Epstein-Barr virus reactivation by the flavonoid apigenin. *J. Biomed. Sci.* 24 (1), 2.
- Xi, J., et al., 2019. Polypyrimidine tract-binding protein regulates enterovirus 71 translation through interaction with the internal ribosomal entry site. *Virol. Sin.* 34 (1), 66–77.
- Xiao, X., et al., 2017. Enterovirus 3A facilitates viral replication by promoting phosphatidylinositol 4-kinase III $\beta$ -ACBD3 interaction. *J. Virol.* 91 (19).
- Xie, X.H., et al., 2012. Resveratrol inhibits respiratory syncytial virus-induced IL-6 production, decreases viral replication, and downregulates TRIF expression in airway epithelial cells. *Inflammation* 35 (4), 1392–1401.
- Yan, Y.Q., et al., 2018. Anti-influenza activity of berberine improves prognosis by reducing viral replication in mice. *Phytother. Res.* 32 (12), 2560–2567.
- Yan, J., et al., 2020. Involvement of VCP/UFD1/Nucleolin in the viral entry of Enterovirus A species. *Virus Res.* 283, 197974.
- Yang, Y., Klionsky, D.J., 2020. Autophagy and disease: unanswered questions. *Cell Death Differ.* 27 (3), 858–871.
- Yang, J.P., et al., 2002. Functional interaction of Sam68 and heterogeneous nuclear ribonucleoprotein K. *Oncogene* 21 (47), 7187–7194.
- Yang, Y., et al., 2018a. TRMP, a p53-inducible long noncoding RNA, regulates G1/S cell cycle progression by modulating IRES-dependent p27 translation. *Cell Death Dis.* 9 (9), 886.
- Yang, X., et al., 2018b. Picornavirus 2A protease regulates stress granule formation to facilitate viral translation. *PLoS Pathog.* 14 (2), e1006901.
- Yang, S., et al., 2018c. Emetine inhibits Zika and Ebola virus infections through two molecular mechanisms: inhibiting viral replication and decreasing viral entry. *Cell Discov.* 4, 31.
- Yang, S.N.Y., et al., 2019. Novel flavivirus antiviral that targets the host nuclear transport importin  $\alpha$ /beta1 heterodimer. *Cells* 8 (3).
- Yin, J., Xing, H., Ye, J., 2008. Efficacy of berberine in patients with type 2 diabetes mellitus. *Metabolism* 57 (5), 712–717.
- Yoshida, H., et al., 2000. ATF6 activated by proteolysis binds in the presence of NF-Y (CBF) directly to the cis-acting element responsible for the mammalian unfolded protein response. *Mol. Cell Biol.* 20 (18), 6755–6767.
- Yoshida, H., et al., 2001. XBP1 mRNA is induced by ATF6 and spliced by IRE1 in response to ER stress to produce a highly active transcription factor. *Cell* 107 (7), 881–891.
- Zakaryan, H., et al., 2017. Flavonoids: promising natural compounds against viral infections. *Arch. Virol.* 162 (9), 2539–2551.
- Zhang, W., et al., 1993. Purification, characterization, and cDNA cloning of an AU-rich element RNA-binding protein. AUF1. *Mol. Cell Biol.* 13 (12), 7652–7665.
- Zhang, H.S., et al., 2009. Resveratrol inhibited Tat-induced HIV-1 LTR transactivation via NAD(+)-dependent SIRT1 activity. *Life Sci.* 85 (13–14), 484–489.
- Zhang, T., et al., 2012. Anti-Japanese-encephalitis-viral effects of kaempferol and daidzin and their RNA-binding characteristics. *PLoS One* 7 (1), e30259.
- Zhang, W., et al., 2014. Apigenin inhibits enterovirus-71 infection by disrupting viral RNA association with trans-acting factors. *PLoS One* 9 (10), e110429.
- Zhang, H., et al., 2015a. Nuclear protein Sam68 interacts with the enterovirus 71 internal ribosome entry site and positively regulates viral protein translation. *J. Virol.* 89 (19), 10031–10043.
- Zhang, L., et al., 2015b. Resveratrol inhibits enterovirus 71 replication and pro-inflammatory cytokine secretion in rhabdomyosarcoma cells through blocking IKKs/NF-kappaB signaling pathway. *PLoS One* 10 (2), e0116879.
- Zhang, R., et al., 2017. Kaempferol ameliorates H9N2 swine influenza virus-induced acute lung injury by inactivation of TLR4/MyD88-mediated NF-kappaB and MAPK signaling pathways. *Biomed. Pharmacother.* 89, 660–672.
- Zhang, S., et al., 2019. Chloroquine inhibits endosomal viral RNA release and autophagy-dependent viral replication and effectively prevents maternal to fetal transmission of Zika virus. *Antivir. Res.* 169, 104547.
- Zhou, Y., et al., 2011. Regulation of glucose homeostasis through a XBP-1-FoxO1 interaction. *Nat. Med.* 17 (3), 356–365.
- Zhou, F., et al., 2019. Pim1 impacts enterovirus A71 replication and represents a potential target in antiviral therapy. *iScience* 19, 715–727.
- Zhu, Y.P., et al., 2015. Host APOBEC3G protein inhibits HCV replication through direct binding at NS3. *PLoS One* 10 (3), e0121608.



# Low-fluence laser-facilitated platelet-rich plasma permeation for treating MRSA-infected wound and photoaging of the skin

Woan-Ruoh Lee<sup>a,b,1</sup>, Chien-Yu Hsiao<sup>c,d,e,1</sup>, Tse-Hung Huang<sup>d,f,g,h</sup>, Calvin T. Sung<sup>i</sup>,  
Pei-Wen Wang<sup>j</sup>, Wen-Ting Cheng<sup>k</sup>, Jia-You Fang<sup>d,k,l,\*</sup>

<sup>a</sup> Graduate Institute of Medical Sciences, Taipei Medical University, Taipei, Taiwan

<sup>b</sup> Department of Dermatology, Taipei Medical University Shuang Ho Hospital, New Taipei City, Taiwan

<sup>c</sup> Department of Nutrition and Health Sciences, Chang Gung University of Science and Technology, Kweishan, Taoyuan, Taiwan

<sup>d</sup> Research Center for Food and Cosmetic Safety and Research Center for Chinese Herbal Medicine, Chang Gung University of Science and Technology, Kweishan, Taoyuan, Taiwan

<sup>e</sup> Aesthetic Medical Center, Department of Dermatology, Chang Gung Memorial Hospital, Kweishan, Taoyuan, Taiwan

<sup>f</sup> Department of Traditional Chinese Medicine, Chang Gung Memorial Hospital, Keelung, Taiwan

<sup>g</sup> School of Traditional Chinese Medicine, Chang Gung University, Kweishan, Taoyuan, Taiwan

<sup>h</sup> School of Nursing, National Taipei University of Nursing and Health Sciences, Taipei, Taiwan

<sup>i</sup> School of Medicine, University of California, Riverside, USA

<sup>j</sup> Department of Medical Research, China Medical University Hospital, China Medical University, Taichung, Taiwan

<sup>k</sup> Pharmaceutics Laboratory, Graduate Institute of Natural Products, Chang Gung University, Kweishan, Taoyuan, Taiwan

<sup>l</sup> Department of Anesthesiology, Chang Gung Memorial Hospital, Kweishan, Taoyuan, Taiwan

## ARTICLE INFO

### Keywords:

Platelet-rich plasma  
Low-fluence laser  
Topical delivery  
Skin absorption  
Skin infection  
Photoaging

## ABSTRACT

Platelet-rich plasma (PRP) is rich in cytokines and growth factors and is a novel approach for tissue regeneration. It can be used for skin rejuvenation but the large molecular size of the actives limits its topical application. In this study, low-fluence laser-facilitated PRP was delivered to evaluate its effect on absorption through the skin, infection-induced wound, and photoaging. The PRP permeation enhancement was compared for two ablative lasers: fractional (CO<sub>2</sub>) laser and fully-ablative (Er:YAG) laser. In the Franz cell experiment, pig skin was treated with lasers with superficial ablation followed by the application of recombinant cytokines, growth factors, or PRP. The transport of interferon (IFN)- $\gamma$  and tumor necrosis factor (TNF)- $\alpha$  was negligible in intact skin and stratum corneum (SC)-stripped skin. Both lasers significantly elevated skin deposition of IFN- $\gamma$  and TNF- $\alpha$  from PRP, and fully-ablative laser showed a higher penetration enhancement. A similar tendency was found for vascular endothelial growth factor and epidermal growth factor. Er:YAG laser-exposed skin displayed 1.8- and 3.9-fold higher skin deposition of platelet-derived growth factor (PDGF)-BB and transforming growth factor (TGF)- $\beta$ 1 from PRP, respectively. According to the confocal images, both laser interventions led to an extensive and deep distribution of IFN- $\gamma$  and PDGF-BB in the skin. In the in vivo methicillin-resistant *Staphylococcus aureus* (MRSA) infection model, CO<sub>2</sub> laser- and Er:YAG laser-assisted PRP delivery reduced bacterial load from  $1.8 \times 10^6$  to  $5.9 \times 10^5$  and  $1.4 \times 10^4$  colony-forming units, respectively. The open wound induced by MRSA was closed by the laser-assisted PRP penetration. In the mouse photoaging model, elastin and collagen deposition were fully restored by combined PRP and full-ablative laser but not by PRP alone and PRP combined with fractional laser. Laser-facilitated PRP delivery even with a low fluence setting can be considered a promising strategy for treating some dermatological disorders.

\* Corresponding author at: Pharmaceutics Laboratory, Graduate Institute of Natural Products, Chang Gung University, 259 Wen-Hwa 1st Road, Kweishan, Taoyuan 333, Taiwan.

E-mail address: [fajy@mail.cgu.edu.tw](mailto:fajy@mail.cgu.edu.tw) (J.-Y. Fang).

<sup>1</sup> Equal contribution.

<https://doi.org/10.1016/j.ijpharm.2021.120242>

Received 20 October 2020; Received in revised form 22 December 2020; Accepted 4 January 2021

Available online 21 January 2021

0378-5173/© 2021 Elsevier B.V. All rights reserved.



## 1. Introduction

Platelet-rich plasma (PRP) is a fraction of plasma that has abundant cytokines, growth factors, and peptides to enhance wound healing and tissue regeneration (Lang et al., 2018). PRP injection is extensively applied for the repair of cartilage and bone injury (Kennedy et al., 2018; Delgado et al., 2019). PRP application has attracted increasing attention over the past decade for dermatological applications such as treating a wound, scar, alopecia, wrinkle, and vitiligo (Alves et al., 2020; Mercuri et al., 2020). The use of PRP is an inexpensive and readily available therapy in clinical practice for skin rejuvenation and aesthetics (Hesseler and Shyam, 2019). Subcutaneous or intradermal injection is a common administration route for PRP therapy of skin. The patients are subjected to venipuncture at least twice, one for blood drawing and another for autologous PRP injection. Multiple injections result in the risk of bleeding, pain, erythema, bruising, and infection (Abuaf et al., 2016). A large volume of PRP injection also stretches the wound or nidus, leading to the worsening of the injury. Topical PRP delivery may also accelerate the closure of open wounds such as ulcers and traumatic wounds. However, this route is difficult for cosmetic or aesthetic treatment because of the intact or partial barrier function of the skin. The application of PRP injection for skin rejuvenation gets limited due to the adverse effects and patients' compliance (Maisel-Campbell et al., 2020).

For an efficient topical permeation, the active ingredients should facilely pass across the rate-limiting stratum corneum (SC), although penetration is especially challenging for the macromolecules including proteins, DNAs, and vaccines (Lee et al., 2016). The development of novel approaches for topical PRP delivery is crucial. Ablation of the superficial skin layer by the lasers to reduce the permeation barrier is vital to achieving increased and controlled macromolecule delivery (Hsiao et al., 2019; Wenande et al., 2020). Ablative lasers precisely control the ablation depth of skin with less cross-contamination risk than stripping and the use of microneedle (Garvie-Cook et al., 2016). Laser-assisted absorption for topical PRP may be an alternative to the intralesional route for promoting cutaneous distribution and minimizing adverse effects. The objective of this study was to investigate whether the ablative lasers could improve the efficiency of PRP penetration for the treatment of dermatological disorders. There are some commercial devices available to simply prepare PRP. We used Medifuge® with a specified mode for preparing PRP in the present study. The most commonly used lasers to enhance skin penetration are CO<sub>2</sub> and erbium: yttrium–aluminum–garnet (Er:YAG) lasers (Haedersdal et al., 2016). In this study, we used fractional-ablative CO<sub>2</sub> laser and full-ablative Er:YAG laser for assisted PRP delivery. The fractional laser produces an array of microchannels extending through the superficial skin. The migration of the surrounding viable cells facilitates quick epidermal healing of fractional laser-generated holes (Lee et al., 2019). Laser therapy has been used as one of the strategies for skin rejuvenation. Combined PRP and laser therapy evidently improve cutaneous aging (Wang et al., 2020). The laser fluence or energy used for this combined therapy is very high, which may be associated with significant pain and skin damage, as well as an increased patient burden. However, the fluence used for enhanced skin permeation is lower than that for laser therapy and indicates a safe use and fast recovery of the laser-assisted drug delivery.

Methicillin-resistant *Staphylococcus aureus* (MRSA) infection and UVA-induced photoaging in mouse skin were used as disease models in this investigation. MRSA is a common cause of skin infection that is particularly difficult to eradicate. PRP has been reported to display antimicrobial activity including that on MRSA strains (Cieslik-Bielecka et al., 2018; Farghali et al., 2019). Photoaged skin reveals the appearance of increased erythema and wrinkling due to the inflammation and collagen destruction. We examined whether the low-fluence laser treatment could facilitate topical PRP absorption into/across MRSA-infected and UVA-irradiated skins to reduce the bacterial burden and improve photoaging, respectively.

## 2. Materials and methods

### 2.1. Preparation of PRP

The protocol was approved by the Institutional Review Board at Chang Gung Memorial Hospital, and the written informed consent was obtained from all volunteers. The whole blood sample was withdrawn from healthy donors and collected in a tube containing an anticoagulant (heparin), mixed gently, and centrifuged (Medifuge® MF200, Silfradent) using a PRP preparation program according to the manufacturer's instruction (Koyuncu et al., 2020). The tube displayed three layers after centrifugation, a lower density layer containing red blood cells, a thin intermediate layer corresponding to PRP, and the top layer containing platelet-poor plasma (PPP) (Fig. 1A). The platelet amount in PRP and PPP was quantified by the automatic hematology analyzer. The concentrations of interferon (IFN)- $\gamma$ , tumor necrosis factor (TNF)- $\alpha$ , platelet-derived growth factor (PDGF)-BB, transforming growth factor (TGF)- $\beta$ 1, vascular endothelial growth factor (VEGF), and epidermal growth factor (EGF) in PRP were determined using ELISA kits (Abcam).

### 2.2. Laser assembly

A fractional CO<sub>2</sub> laser (Mosaic eCO<sub>2</sub>, Lutronic, Goyang, Korea) used a 10,600 nm wavelength and irradiated a scanning area of  $1.4 \times 1.4$  cm<sup>2</sup>. There were 400 spots in 1 cm<sup>2</sup> to generate a microscopic thermal zone (MTZ). The diameter of each MTZ was 300  $\mu$ m with a fluence of 4 mJ. The full-ablative laser used in this study was of Er:YAG modality (Contour, Sciton, Palo Alto, CA, USA), and emitted a 2,940 nm irradiation over a scanning area of  $1.5 \times 1.5$  cm<sup>2</sup>. A square scanning handpiece with 16 ablation spots was used. The diameter of each spot was 3.5 mm with a 10% overlap. The ablation depth was set to 20  $\mu$ m with a fluence of 5 J/cm<sup>2</sup>. The laser treatment on skin was performed in Taipei Medical University Shuang Ho Hospital.

### 2.3. Animals

The animal experiments were carried out in strict accordance with the recommendation in the Guidelines for the Care and Use of Laboratory Animals of Chang Gung University (CGU107-119). The investigation conducted was fully accredited by the Association for Assessment and Accreditation of Laboratory Animal Care. One-week-old pathogen-free pigs were obtained from Animal Technology Institute Taiwan (Miaoli, Taiwan). Eight-week-old BALB/c and nude mice were purchased from the National Laboratory Animal Center (Taipei, Taiwan).

### 2.4. Laser-treated skin imaging

The pig skin was irradiated by the lasers to observe the skin surface and histology. The microscopic appearance of the skin surface with or without laser treatment was observed using a digital magnifier (Mini Scope-V, M&T Optics) and a light microscope (DMi8, Leica). The skin surface was also visualized by scanning electron microscope (SEM) at a larger magnification. The skin was immersed in paraffin wax and then 5  $\mu$ m thick slices were prepared. The paraffin-embedded skin was stained by hematoxylin and eosin (H&E) for imaging under a light scope.

### 2.5. In vitro PRP permeation

The PRP delivery into/across pig skin was determined through the Franz diffusion cell evaluation platform. The skin with or without laser irradiation was mounted between the donor and receptor chambers. The cellophane tape application was used 20 times to remove the skin surface and obtain SC-stripped skin. The receptor medium (5 mL) was phosphate buffer at pH 7.4 containing 0.01% protease inhibitor. The donor medium (0.5 mL) was the recombinant cytokines or growth factors in saline with 0.01% protease inhibitor. Human PRP in saline (20%)

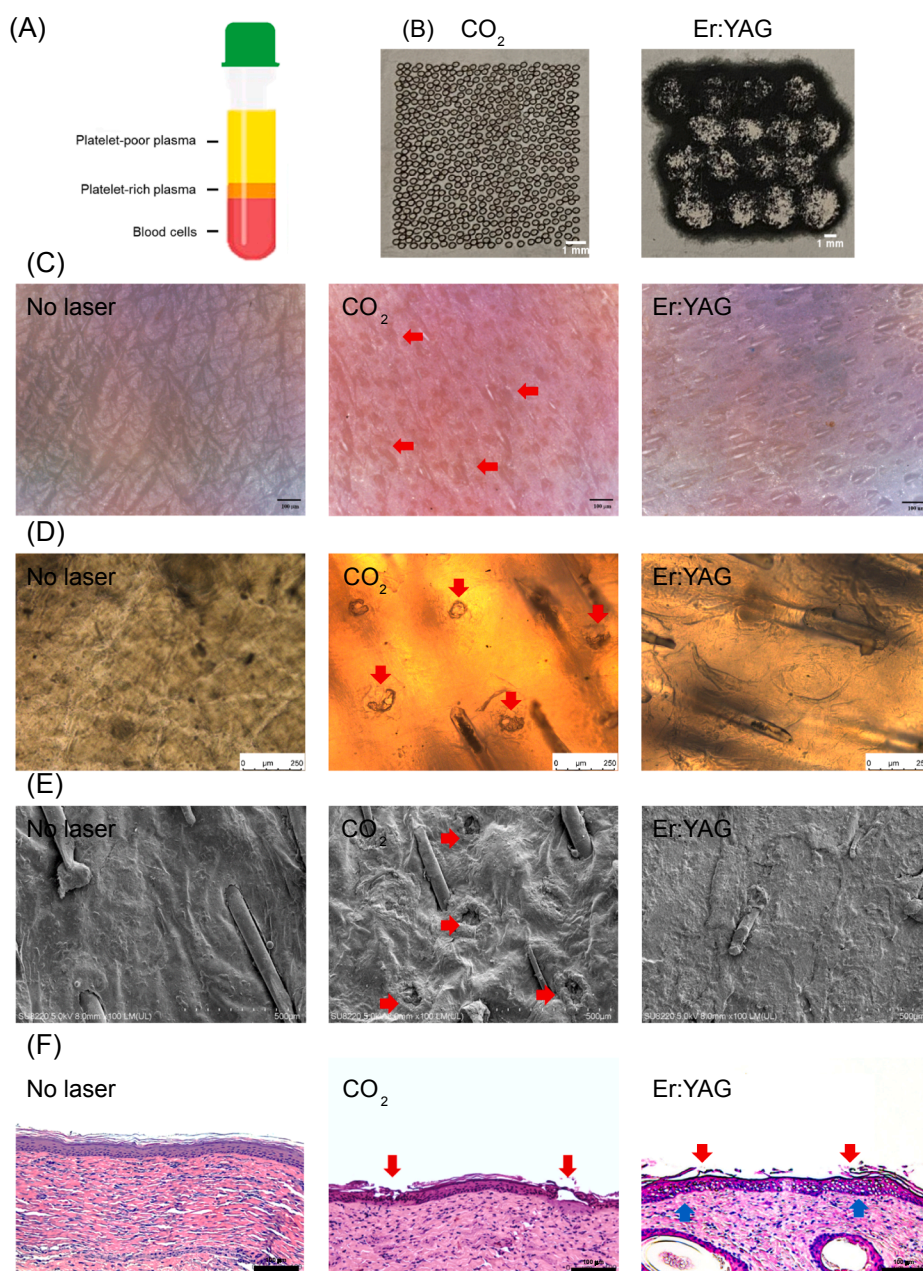


**Fig. 1.** The images of the skin treated by CO<sub>2</sub> laser and Er:YAG laser: (A) the distribution of PRP in the a tube containing anticoagulant (heparin). The tube was centrifuged in a commercial centrifugation system (Medifuge® MF200, Silfradent) with a PRP preparation program according to the manufacturer's instruction; (B) the thermal paper imaging after the treatment of CO<sub>2</sub> laser or Er:YAG laser; (C) the skin surface imaging captured by handheld digital magnifier; (D) the skin surface imaging captured by optical microscopy; and (E) the H&E staining of the skin observed by optical microscopy. The red arrows in the images indicate the micro-pores created by CO<sub>2</sub> laser.

was also loaded in the donor chamber for assessing the skin penetration of cytokines and growth factors. The effective delivery region was 0.785 cm<sup>2</sup>. The stirring rate of the stir bar was kept at 600 rpm at the receptor temperature of 37 °C. Medium (300 µL) from the receptor was withdrawn at determined intervals. The fresh medium was supplied to the receptor chamber to maintain a constant volume of 5 mL. After a 24-h treatment, the skin was removed from the cell to estimate skin deposition. The skin sample was weighed, cut, and homogenized by MagNA Lyser (Roche). The homogenization medium was PBS containing 0.01% protease inhibitor. The homogenate was centrifuged at 10,000 × g and the supernatant was collected. The permeant amount in the receptor and skin reservoir was quantified by ELISA.

## 2.6. The distribution of IFN-γ and PDGF-BB in the skin

We selected IFN-γ and PDGF-BB as the model permeants to visualize the skin distribution after laser treatment. Fluorescein isothiocyanate (FITC)-conjugated IFN-γ and PDGF-BB were purchased from

Elabscience. The pig skin was removed from Franz cell after a 4 h treatment of FITC-IFN-γ and FITC-PDGF-BB at a dose similar to that in PRP (in 20% saline). The permeant concentration mimicked their concentration in PRP. After washing with water, the skin distribution of permeants was monitored by confocal microscopy (TCS SP2, Leica). The skin thickness was optically scanned at 5 µm increments through the z-axis from the skin surface. Images were acquired by summing 15 fragments. The 3D image of the skin was also established.

## 2.7. In vivo PRP permeation

The back skin of the nude mouse was irradiated by laser. The Franz cell donor was fixed on the treated site using cyanoacrylate glue. An aliquot (0.2 mL) of 20% PRP in saline was loaded into the donor chamber. The administration durations were 3 h and 6 h. The animal was sacrificed to excise the treated skin and in vivo skin deposition of cytokines and growth factors was estimated by ELISA after skin extraction using the same technique as that used for in vitro skin

deposition.

## 2.8. Time-response of MRSA inhibition

The MRSA strain used in this experiment was ATCC33591. The eradication of MRSA by PRP within a 24 h period was assessed in 96-well plates. Test bacteria ( $OD_{600} = 0.01$ ) were inoculated with PRP at various platelet concentrations and incubated for 24 h at 37 °C. The absorbance of all wells was measured at 600 nm in an ELISA reader to evaluate MRSA growth in a real-time mode.

## 2.9. Detection of live/dead MRSA

The viability and death of MRSA after PRP treatment were examined. MRSA was grown to  $OD_{600} = 0.1$  and then treated with PRP for 4 h. The MRSA stained by Live/Dead BacLight® kit containing SYTO9 and propidium iodide (PI) was analyzed by flow cytometry and fluorescence microscopy. The detailed procedures have been described earlier (Chou et al., 2019).

## 2.10. MRSA infection in mouse skin

The shaved BALB/c mouse back skin was irradiated by the lasers. Human PRP containing  $7.5 \times 10^6$  platelets/mL was then applied to the back skin with or without laser irradiation. After 24 h, MRSA ( $OD_{600} = 0.15$ ) in PBS (100  $\mu$ L) was subcutaneously injected into the treated site. The microscopic appearance of the skin surface was visualized by a digital magnifier on day 5 post-laser treatment. Skin erythema was analyzed using a CD100 colorimeter (Yokogawa). Transepidermal water loss (TEWL) was measured by TM300 Tewameter (Courage and Khazaka). After sacrificing the mouse, the skin was excised and homogenized by MagNA Lyser to detect the colony-forming unit (CFU) of MRSA using serially diluted homogenate on tryptic soy broth.

## 2.11. UVA-induced photoaging in mouse skin

The nude mouse with or without laser treatment was topically administered with PRP diluted with saline (20%). After 24 h, the mouse back was exposed to UVA (3 J/cm<sup>2</sup>) at 365 nm (Bio-Sun, Vilber Lourmat). The distance between the dorsal surface and UVA light was 9 cm. The mouse was irradiated by UVA every other day for five days. Topical PRP was applied in the days following UVA exposure. The animal was sacrificed after three cycles of UVA irradiation and PRP administration. The image of the dorsal skin was acquired by Mini Scope-V. ELISA was performed to estimate hyaluronan, elastin, and collagen in the skin based on the manufacturer's instructions (Cusabio).

## 2.12. Statistical analysis

All data were reported as the mean and standard error of the mean. Data analysis was conducted using Winks SDA 7 software. Kruskal-Wallis test followed by Dunn's post-hoc test, which was utilized to check statistical significance with  $p < 0.05$  (\*),  $p < 0.01$  (\*\*), and  $p < 0.001$  (\*\*\*) in the figures.

## 3. Results

### 3.1. Concentrations of cytokines and growth factors in PRP

PRP was prepared from the fresh blood of healthy volunteers. We determined the platelet amount and the level of the major cytokines and growth factors in PRP from 20 donors. The platelet concentration within PRP was estimated to be  $9.50 \pm 2.37 \times 10^5$  cells/ $\mu$ L, whereas the concentration of platelets in PPP was  $2.64 \pm 0.73 \times 10^5$  cells/ $\mu$ L. The concentration of proinflammatory cytokines and growth factors in PRP preparation is summarized in Table 1. The most abundant ingredient in

**Table 1**

The concentration of cytokines and growth factors in PRP.

| Ingredient     | Concentration (pg/ml) |
|----------------|-----------------------|
| IFN- $\gamma$  | 2132.82 $\pm$ 36.78   |
| TNF- $\alpha$  | 851.47 $\pm$ 37.74    |
| PDGF-BB        | 3378.29 $\pm$ 242.95  |
| TGF- $\beta$ 1 | 2128.82 $\pm$ 62.83   |
| VEGF           | 59.20 $\pm$ 8.16      |
| EGF            | 275.18 $\pm$ 32.03    |

Each value represents the mean  $\pm$  SEM ( $n = 20$ ).

PRP was PDGF-BB (3378 pg/mL), followed by IFN- $\gamma$  (2133 pg/mL) and TGF- $\beta$ 1 (2129 pg/mL). The limited intersubject variation indicates the reproducibility of different blood donors. The standardization of PRP preparation was thus achieved.

### 3.2. Laser-treated skin imaging

The laser irradiation was done on thermal paper as shown in Fig. 1B. The dots on the thermal paper confirmed the production of fractional MTZ by CO<sub>2</sub> laser. The dot size was about 300  $\mu$ m, which simulated the fractional spot size irradiated by CO<sub>2</sub> laser. The Er:YAG laser spot was larger than that formed by CO<sub>2</sub> laser. There was an overlap between the spots (10%) after scanning the 16 spots to create full ablation. The pig skin surface with or without laser processing was observed using a digital magnifier and optical microscopy (Fig. 1C and 1D). The fractional CO<sub>2</sub> laser showed alignment with the microchannels in the skin (red arrows). The distance between the pores was about 500  $\mu$ m. The fractional poration resulted in the pores with a diameter of nearly 100  $\mu$ m. The pore size was smaller than the spot size of the CO<sub>2</sub> laser. The CO<sub>2</sub> laser irradiation on the skin included the zone of pore formation and the surrounding coagulation area. The skin surface furrows in the control skin were absent after Er:YAG laser treatment, demonstrating the extensive ablation of the superficial layer. The SEM images of non-treated skin revealed roughness and hair shafts on the surface (Fig. 1E). Protruded coagulation was found around the pores produced by the fractional laser (red arrows). The surface roughness was reduced by Er:YAG laser exposure due to the full ablation effect. In contrast, the untreated control, the cross-section of the pig skin exhibited the intact skin structure (Fig. 1F). SC in the intact skin consisted of several layers of combined corneocytes and lipids. CO<sub>2</sub> laser generated microscopic ablation holes through SC and epidermis (red arrows). The depth of the clefts was 40–50  $\mu$ m. The coagulated tissue induced by thermal transport of CO<sub>2</sub> laser was found near the pores. The ablation depth produced by Er:YAG laser was shallower than that of the fractional laser. Fully-ablative laser resulted in superficial thinning reaching the SC with some remnant SC layers (red arrows) and the H&E-stained histology showed few vacuoles in the epidermis (blue arrows) after Er:YAG laser exposure.

### 3.3. Enhanced in vitro skin delivery of recombinant cytokines and growth factors after laser treatments

We first examined the skin delivery of recombinant cytokines and growth factors that were abundant in PRP preparation. In vitro percutaneous absorption was performed using Franz cell. The dose of the recombinant permeants loaded in the donor was the same as their concentration in PRP preparation (20% in saline). The absorption of these permeants was quantified by ELISA. The permeant retained in the skin reservoir (skin deposition) dictates the absorption into the skin, whereas the cumulative amount in receptor chamber simulates the delivery into deeper strata of the skin or circulation in vivo. The left and right panel of Fig. 2A represents skin deposition and the cumulative amount of recombinant IFN- $\gamma$ , respectively. However, the IFN- $\gamma$  amount into and across intact and SC-stripped skins was not detectable by ELISA, indicating a negligible absorption. The laser treatments allowed the



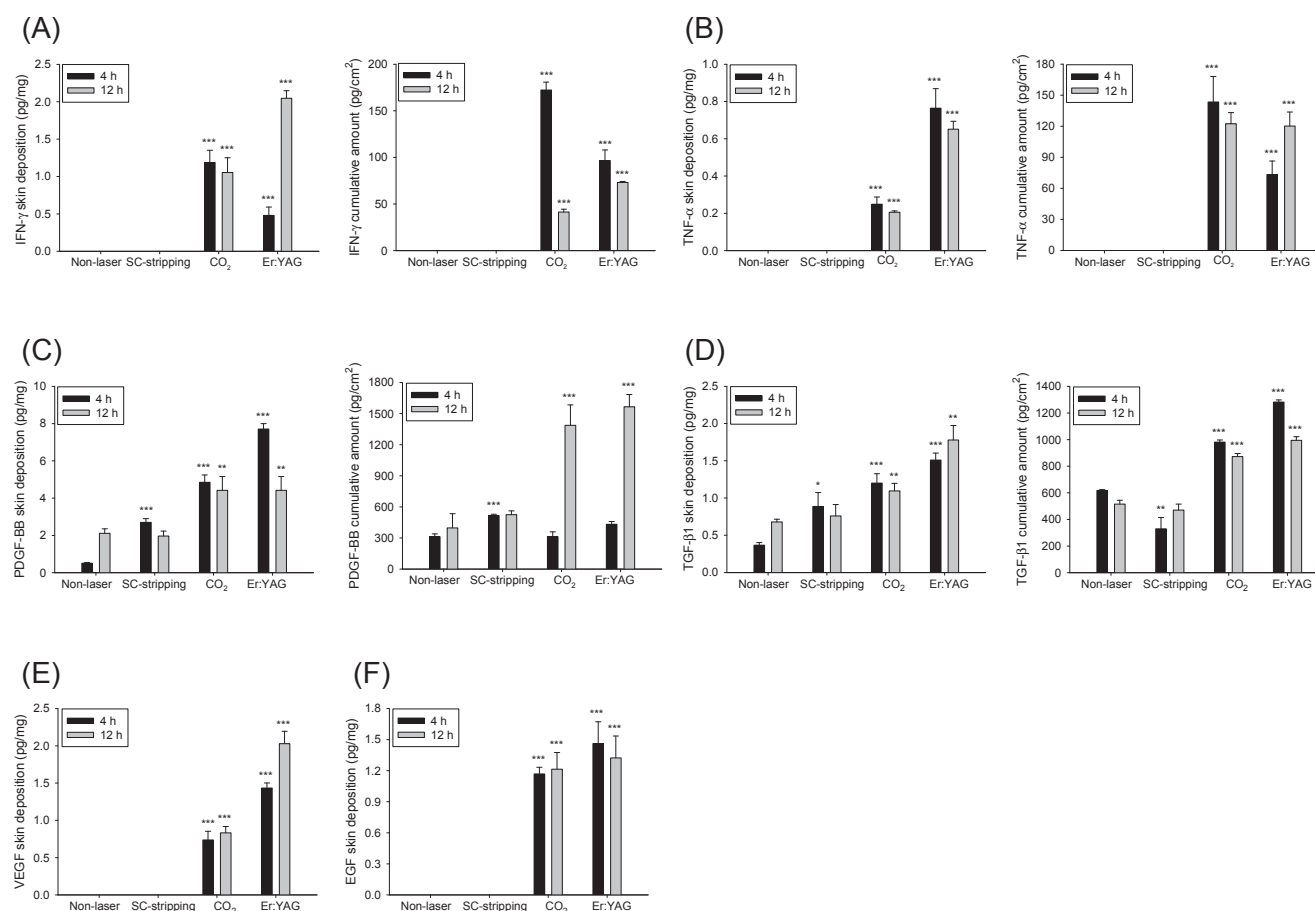


**Fig. 2.** The in vitro pig skin deposition (pg/mg) and cumulative amount (pg/cm<sup>2</sup>) of the recombinant cytokines and growth factors in intact, SC-stripped, and laser-treated skins at 4 h and 12 h: (A) the skin deposition and cumulative amount of IFN- $\gamma$ ; (B) the skin deposition and cumulative amount of TNF- $\alpha$ ; (C) the skin deposition and cumulative amount of PDGF-BB; (D) the skin deposition and cumulative amount of TGF- $\beta$ 1; (E) the skin deposition of VEGF; and (F) the skin deposition of EGF. The data are presented as the mean of 4 experiments  $\pm$  S.E.M. \* $p$  < 0.05, \*\* $p$  < 0.01, \*\*\* $p$  < 0.001 as compared to intact skin.

absorption of pure IFN- $\gamma$  and its skin deposition increased from 0 to 1.3 pg/mg by CO<sub>2</sub> laser treatment. No difference in skin deposition was seen between the different durations of the IFN- $\gamma$  application (4 h versus 12 h). IFN- $\gamma$  accumulation in Er:YAG laser-treated skin increased from 0.5 to 2.0 pg/mg following the increase in the application time from 4 h to 12 h. Contrary to this result, the cumulative amount in the receptor decreased following the increase in application time of both lasers. Like IFN- $\gamma$ , TNF- $\alpha$  manifested no permeation in the intact and SC-stripped skins (Fig. 2B) and the lasers improved TNF- $\alpha$  delivery into skin and receptor. The Er:YAG laser resulted in 3-fold greater skin deposition than that by CO<sub>2</sub> laser. Furthermore, the fractional laser at 4 h showed a higher receptor amount of TNF- $\alpha$  as compared to full-ablative laser, whereas the cumulative amount at 12 h was comparable between both lasers.

Considering the growth factors, PDGF-BB permeation was detectable in the untreated and SC-stripped skins (Fig. 2C). SC stripping increased the skin deposition and cumulative amount of PDGF-BB compared to that in the control skin at 4 h. However, this effect was not observed after a 12 h application. Although both lasers further improved PDGF-BB skin deposition, Er:YAG laser revealed greater enhancement than CO<sub>2</sub> modality. The increase in the cumulative amount in receptor was observed after laser treatment for a 12-h PDGF-BB application but not for a 4 h application. SC stripping promoted TGF- $\beta$ 1 skin deposition by 2.5-fold at 4 h compared with that of the intact skin, whereas the cumulative amount even reduced by stripping at this time point (Fig. 2D). A further increase in TGF- $\beta$ 1 delivery was detected in the laser treatment groups. The fully-ablative laser-treated skin group was more efficient in

enhancing TGF- $\beta$ 1 penetration than fractional laser. Er:YAG laser-assisted TGF- $\beta$ 1 deposition was 4.1- and 2.6-fold higher than that in the intact skin at 4 h and 12 h, respectively. The negligible VEGF uptake in intact and SC-stripped skins could be ameliorated by the lasers (Fig. 2E). Er:YAG laser showed a greater increase in VEGF deposition than that by CO<sub>2</sub> laser. The deposition of VEGF in the skin increased with an increase in the application time. No VEGF was detectable in the receptor medium for all treatment groups. The same phenomenon was observed for EGF delivery into the receptor chamber. A remarkable deposition of EGF in the skin was achieved after laser irradiation (Fig. 2F), and the increase in EGF permeation by fractional laser approximated to that by fully-ablative laser.

### 3.4. The lasers enhance in vitro skin delivery of PRP

The in vitro cutaneous delivery of cytokines and growth factors from PRP was assessed as illustrated in Fig. 3. Like IFN- $\gamma$ , no permeation was detected when non-treated and SC-stripped skins were used as the diffusion barriers (Fig. 3A). A profound penetration into/across laser-treated skin was attained for IFN- $\gamma$ . Longer PRP exposure did not further increase the delivery on skin. A greater IFN- $\gamma$  deposition after Er:YAG laser treatment than that after CO<sub>2</sub> laser was observed. TNF- $\alpha$  concentration in the skin reservoir and receiver chamber was below the detection limit in the intact and SC-stripped skins (Fig. 3B). CO<sub>2</sub> laser and Er:YAG laser delivered 1.0 and 0.9 pg/mg TNF- $\alpha$  into the skin at 4 h, respectively. The lasers similarly facilitated TNF- $\alpha$  deposition in the skin at longer PRP exposure time. Stripping of SC led to reduced PDGF-BB



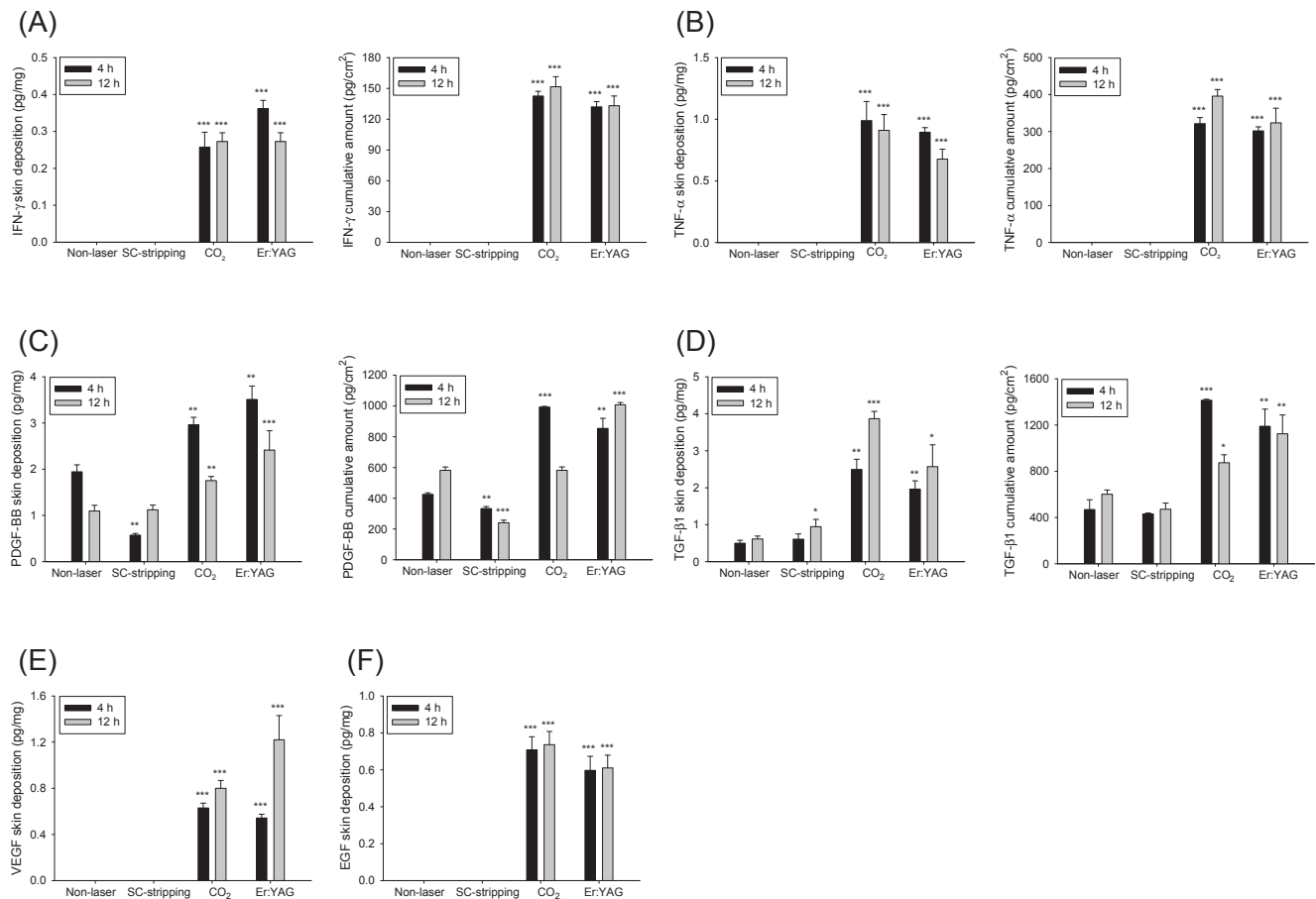


**Fig. 3.** The in vitro pig skin deposition (pg/mg) and cumulative amount (pg/cm<sup>2</sup>) of the PRP-derived cytokines and growth factors in intact, SC-stripped, and laser-treated skins at 4 h and 12 h: (A) the skin deposition and cumulative amount of IFN-γ; (B) the skin deposition and cumulative amount of TNF-α; (C) the skin deposition and cumulative amount of PDGF-BB; (D) the skin deposition and cumulative amount of TGF-β1; (E) the skin deposition of VEGF; and (F) the skin deposition of EGF. The data are presented as the mean of 4 experiments ± S.E.M. \*p < 0.05, \*\*p < 0.01, \*\*\*p < 0.001 as compared to intact skin.

deposition compared to that in the control group at 4 h (Fig. 3C). Laser application delivered significantly increased PDGF-BB deposition into the skin than in the intact skin. The CO<sub>2</sub> and Er:YAG lasers demonstrated 1.5- and 1.8-fold greater PDGF-BB uptake after a PRP exposure for 4 h and with time, improved laser-assisted PDGF-BB deposition was sustained. A 2.3- and 2.0-fold increase in PDGF-BB cumulative amount in the receptor was detected with fractional and fully-ablative lasers at 4 h, respectively.

Compared to intact and SC-stripped skins, PRP-derived TGF-β1 largely deposited in laser-processed skin and increased to 4–6-fold higher level with time than that in the untreated group (Fig. 3D). A similar tendency was observed in the cumulative amount in the receptor. In all treatment groups, negligible VEGF and EGF transport across the skin (receiver chamber) was maintained. Both lasers promoted 0.6 pg/mg VEGF deposition after a 4 h PRP exposure (Fig. 3E). Er:YAG laser represented higher VEGF deposition than CO<sub>2</sub> laser after a 12 h exposure. Irradiation of CO<sub>2</sub> laser or Er:YAG laser on pig skin resulted in an increase in PRP-derived EGF from 0 to 0.6–0.7 pg/mg (Fig. 3F). Laser-facilitated PRP delivery, compared to recombinant permeants, offered lower VEGF and EGF deposition. A similar trend was discovered in the cases of IFN-γ and PDGF-BB. On the other hand, PRP-derived TNF-α and TGF-β1 showed greater or similar delivery on the skin compared to their recombinant forms.

### 3.5. The laser treatments increase skin distribution and penetration depth of IFN-γ and PDGF-BB

The skin distribution was visualized by confocal microscopy in a horizontal scanning mode to see the macromolecule absorption. IFN-γ and PDGF-BB conjugated with FITC were utilized as the representative permeant of cytokines and growth factors, respectively. The left panel of Fig. 4A shows that the skin was scanned at 5 μm increments from the surface to observe IFN-γ distribution in the intact skin. A faint fluorescence was observed throughout all depths of intact skin. The upper right panel is the planar image summing 15 separate sections. A weak fluorescence in the intact skin due to IFN-γ was observed. As shown in the lower right panel of Fig. 4A, the 3D skin structure also represents a negligible IFN-γ deposition. The IFN-γ fluorescence from CO<sub>2</sub> laser-treated skin exceeded that from the control skin (Fig. 4B). CO<sub>2</sub> laser-mediated IFN-γ delivery exhibited significantly stronger fluorescence at the depth of more than 30 μm, suggesting a large distribution in the dermis but not in the epidermis. The merged and 3D images showed an extensive distribution of the permeant. Additionally, the fully-ablative laser also facilitated IFN-γ to the dermis (Fig. 4C). Fluorescence from IFN-γ was distributed in some focal areas with stronger intensity than fractional laser. While PDGF-BB distribution in untreated skin remained low (Fig. 4D), CO<sub>2</sub> laser caused a successful delivery of PDGF-BB into the deeper skin strata (Fig. 4E). We observed a wide and uniform PDGF-BB skin distribution based on the merged image. A stronger PDGF-BB fluorescence was obtained by Er:YAG laser than that by CO<sub>2</sub> laser (Fig. 4F). Dermal fluorescence reached a significantly higher intensity

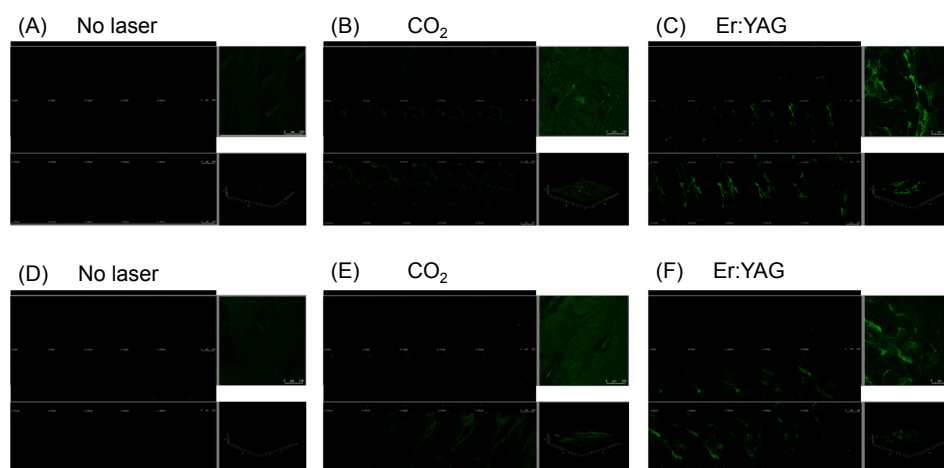


**Fig. 4.** The biodistribution of FITC-conjugated IFN- $\gamma$  and PDGF-BB in the intact, CO<sub>2</sub> laser- or Er:YAG laser-treated pig skin monitored by confocal microscopy: (A) topical application of IFN- $\gamma$  on intact skin; (B) topical application of IFN- $\gamma$  on CO<sub>2</sub> laser-treated skin; (C) topical application of IFN- $\gamma$  on Er:YAG laser-treated skin; (D) topical application of PDGF-BB on intact skin; (E) topical application of PDGF-BB on CO<sub>2</sub> laser-treated skin; and (F) topical application of PDGF-BB on Er:YAG laser-treated skin. The left panel is the 2-D (x-y axis) imaging of the skin with various depths. The upper right panel is the 2-D (x-y axis) imaging of the skin by summing the left panel. The lower right panel is the 3-D (x-y-z axis) imaging of the skin.

than on the epithelium.

### 3.6. The laser treatments enhance in vivo skin delivery of PRP

The in vivo skin deposition of topically applied PRP in mouse skin was examined at 3 h and 6 h post-administration and was assessed in terms of IFN- $\gamma$ , TNF- $\alpha$ , PDGF-BB, and TGF- $\beta$ 1 deposition. The full-ablative laser manifested a stronger capability to enhance IFN- $\gamma$  deposition than fractional laser (Fig. 5A). The in vivo skin deposition of TNF- $\alpha$ , PDGF-BB, and TGF- $\beta$ 1 at 6 h was higher after Er:YAG laser intervention than that after CO<sub>2</sub> laser intervention (Fig. 5B to 5D). Considering these three permeants at 3 h, there was no significant difference between the skin deposition of CO<sub>2</sub> laser- and Er:YAG laser-treated

groups.

### 3.7. PRP eradicates planktonic MRSA

The effect of laser-facilitated PRP delivery was appraised using two dermatological disorder models, MRSA infection and photoaging. We first examined the antibacterial activity of PRP on planktonic MRSA. The time-killing curve provided the data regarding the extent and rate of anti-MRSA potency (Fig. 6A). To test for the antimicrobial activity, the platelet count in PRP was estimated and diluted to different concentrations for testing. We found that MRSA growth inhibition increased with the increase in platelet concentration. The representative flow cytometric profile shows a high survival rate of MRSA in non-treated

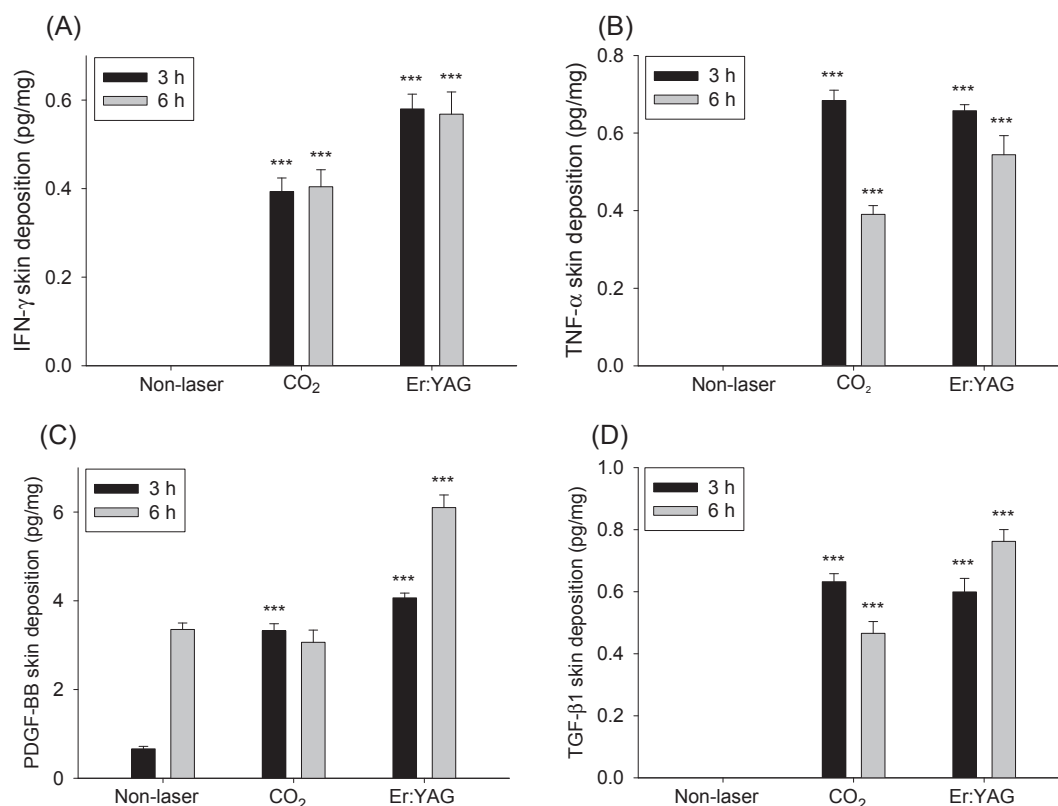


**Fig. 5.** The in vivo nude mouse skin deposition (pg/mg) of the recombinant cytokines and growth factors in intact, SC-stripped, and laser-treated skins at 3 h and 6 h: (A) the skin deposition of IFN- $\gamma$ ; (B) the skin deposition of TNF- $\alpha$ ; (C) the skin deposition of PDGF-BB; and (D) the skin deposition of TGF- $\beta$ 1. The data are presented as the mean of 6 experiments  $\pm$  S.E.M. \*\*\* $p$  < 0.001 as compared to intact skin.

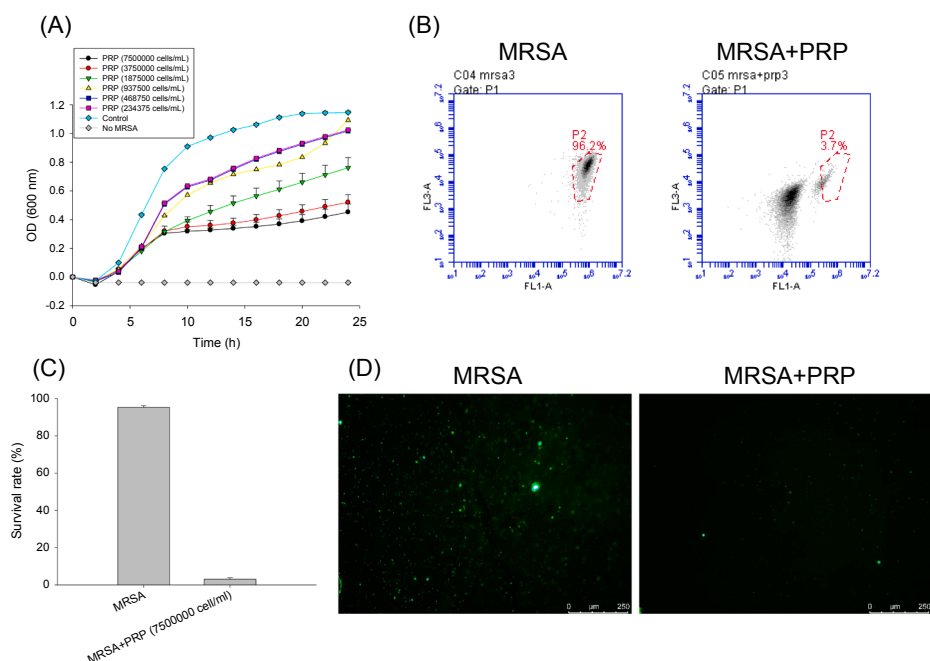


**Fig. 6.** Determination of the antibacterial activity of PRP against planktonic MRSA: (A) time-killing curves of PRP with different platelet concentrations; (B) the flow cytometry histogram; (C) the survival rate of MRSA measured by flow cytometry; and (D) the planktonic live/dead MRSA strains treated by PRP viewed under fluorescence microscopy. The data are presented as the mean of 3 experiments  $\pm$  S.E.M.

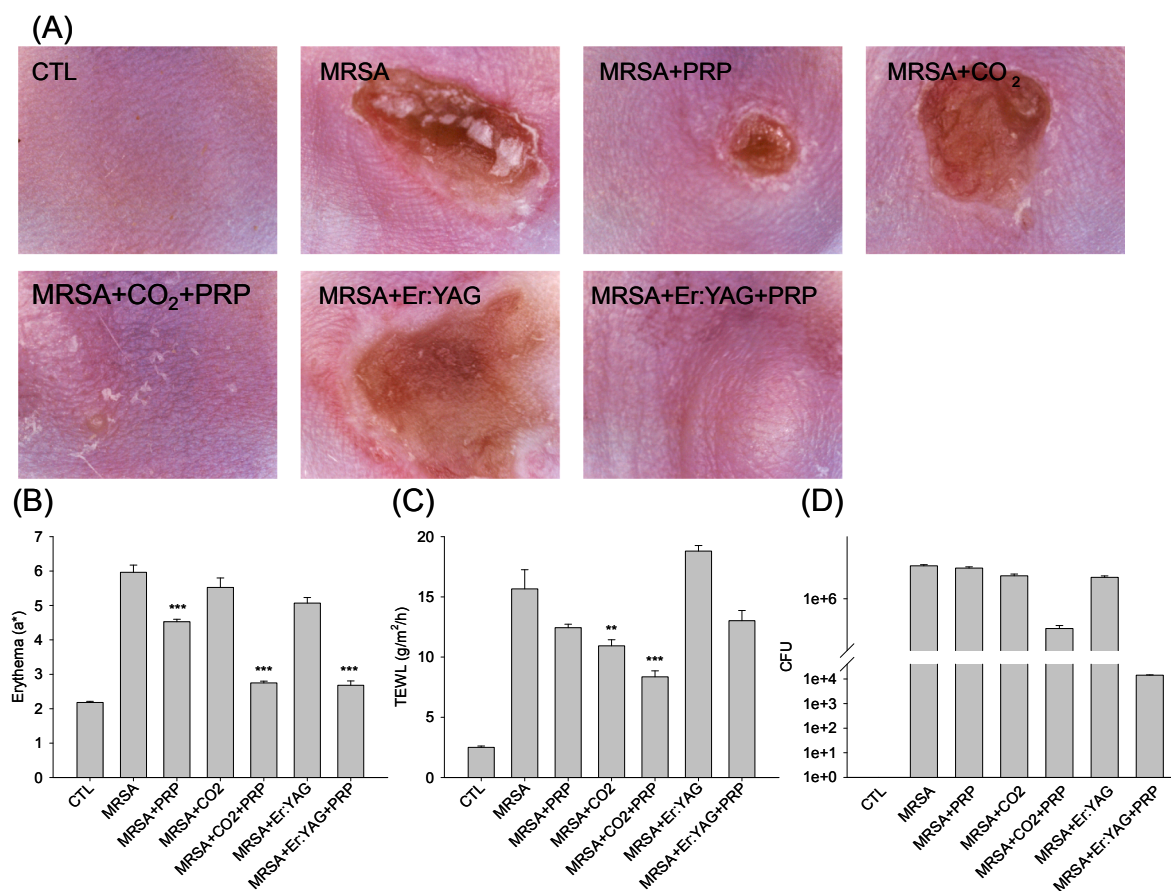


**Fig. 7.** Effect of topical PRP on MRSA-infected wound with and without laser treatment: (A) the skin surface of MRSA-infected mice after treatment of PRP viewed under phenotypic images; (B) skin erythema ( $a^*$ ) of MRSA-infected mice after treatment PRP; (C) TEWL of MRSA-infected mice after treatment PRP; and (D) bacterial burden (CFU) of MRSA-infected mice after treatment PRP. The data are presented as the mean of 6 experiments  $\pm$  S.E.M.  $^{**}p < 0.01$ ,  $^{***}p < 0.001$  as compared to MRSA-infected group without any intervention.

control (the left panel of Fig. 6B), but PRP at  $7.5 \times 10^6$  platelets/mL killed most of MRSA (the right panel of Fig. 6B). The viable MRSA percentage measured from flow cytometry revealed that PRP killed >97% of the microbes (Fig. 6C). The bactericidal effect of PRP was estimated under fluorescence microscopy by visualizing MRSA survival. SYTO9 (green) and PI (red) stained live and dead cells, respectively. In the control, MRSA exhibited a diffuse distribution of live MRSA (the left panel of Fig. 6D), while the green fluorescence indicating live cells was nearly absent in the PRP-treated group (the right panel of Fig. 6D). However, the PI staining did not increase following PRP intervention. This indicated that the major antibacterial activity of PRP may not be membrane disruption because PI could penetrate across the disintegrated membrane to bind DNA.

### 3.8. PRP mitigates in vivo MRSA burden in the skin

The mouse model of cutaneous infection by subcutaneous MRSA was used to evaluate the antibacterial effect of PRP. The abscess revealed an open wound with edema and erythema five days post-MRSA injection (Fig. 7A). Topical PRP alone restricted the nidus size and the combined PRP and lasers further minimized the abscess with no open wound. We expected that some constituents from PRP could penetrate into the intact skin for decreasing MRSA growth. For instance, PDGF-BB could deliver into the intact skin based on in vivo skin deposition data. Slight skin redness was detected after combined PRP and laser treatments as compared to healthy control. Furthermore, laser exposure without PRP delivery did not significantly reduce the lesional region. Here, the erythema ( $a^*$ ) was quantified by colorimetry (Fig. 7B). MRSA injection elevated  $a^*$  from 2 to 6, while the topical PRP significantly decreased  $a^*$  to 4.5. Additionally, both laser-assisted PRP delivery approaches could reduce  $a^*$  by one-half as compared to MRSA treatment without any intervention. Laser treatment alone had no effect on the alleviation of erythema. Then, the barrier function of the skin was analyzed by TEWL (Fig. 7C). MRSA infection caused dysfunction of barrier property for

increasing TEWL from 2.5 to 15.7 g/cm<sup>2</sup>/h. We observed that while PRP alone could not improve pathogen-induced barrier disintegration, TEWL was reduced after CO<sub>2</sub> laser-assisted delivery of PRP. Nevertheless, we did not observe this effect for the Er:YAG laser-assisted PRP permeation. The bacterial count was measured to assess the MRSA burden in the skin (Fig. 7D), and we found that the fractional laser and full-ablative laser were effective in inhibiting MRSA growth. CO<sub>2</sub> laser-assisted PRP delivery achieved a 3-fold reduction in CFU compared with MRSA infection without intervention. A 2-log decrease in CFU in the skin was detected by combined PRP and Er:YAG laser treatment.

### 3.9. Laser-facilitated PRP delivery alleviates skin photoaging

A skin photoaging model was established and treated with PRP alone or combined with PRP and low-fluence laser before UVA irradiation. The microscopic appearance of the skin surface showed a visibly red color with the wrinkling of the UVA-exposed skin (Fig. 8A). Topically applied PRP could not change these signs even after laser intervention. The H&E-stained histology of such skin showed an epidermal thickness increase after UVA exposure, accompanied by hyperkeratosis (Fig. 8B). The hyperplasia and hyperkeratosis were still observed after topical PRP application alone, although the scaling was reduced by laser-assisted PRP delivery. Immune cell infiltration was visible in the lower dermis after combined PRP and lasers treatment. This remarkable infiltration was not detected in the other treatment groups. Our data showed that the hyaluronan level in the mouse skin is reduced after UVA treatment (Fig. 8C). The amount of hyaluronan in the UVA-irradiated mice after PRP treatment with or without lasers was not significantly different from that in the UVA-exposed group without intervention. The elastin in the skin is decreased by UVA irradiation than normal control (Fig. 8D). This reduction could not be recovered by PRP alone or by CO<sub>2</sub> laser-assisted PRP delivery. There was an increase in elastin to baseline control in the Er:YAG laser-assisted PRP delivery group. The total collagen level demonstrated a significant decrease (29% relative to control) after UVA

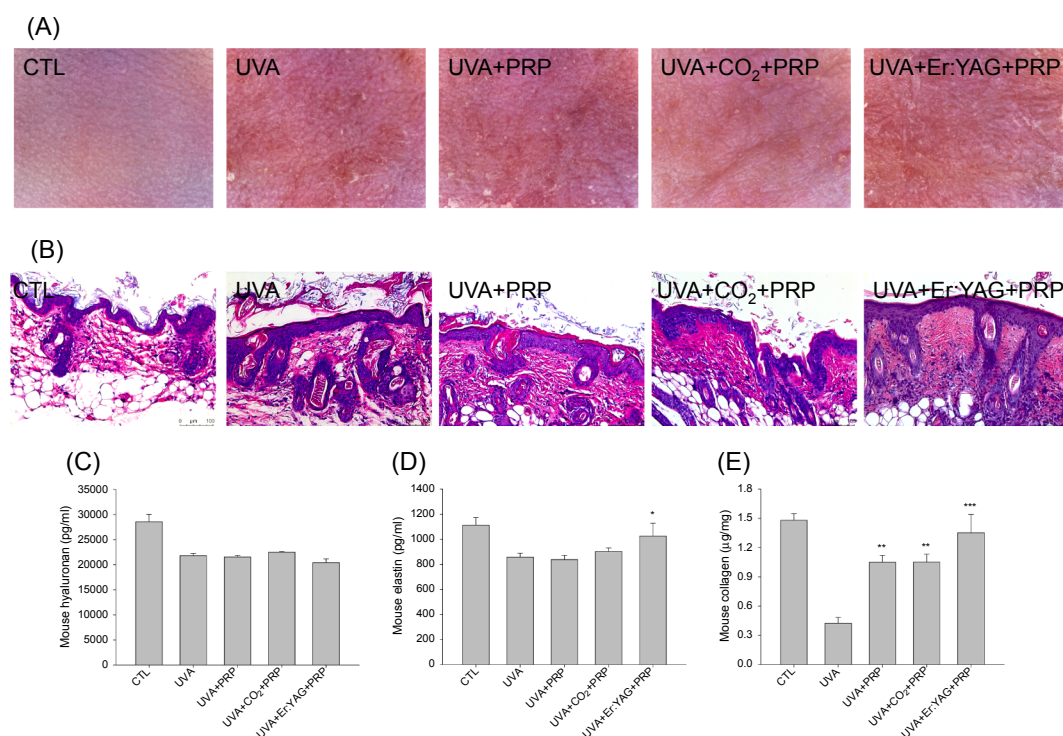


**Fig. 8.** Effect of topical PRP on UVA-induced skin photoaging with and without laser treatment: (A) the skin surface of photoaged mice after treatment of PRP viewed under phenotypic images; (B) the H&E staining of the photoaged skin after treatment of PRP viewed under optical microscopy; (C) hyaluronan amount in skin; (D) elastin amount in skin; and (E) total collagen amount in skin. The data are presented as the mean of 6 experiments  $\pm$  S.E.M. \* $p < 0.05$ , \*\* $p < 0.01$ , \*\*\* $p < 0.001$  as compared to UVA-exposed group without any intervention.



exposure (Fig. 8E). PRP singly or combined with fractional laser partially restored collagen from 0.4 to 1.1  $\mu\text{g}/\text{mg}$ . Nevertheless, there was no significant difference in the collagen amount between PRP alone and CO<sub>2</sub> laser-assisted group. UVA-induced collagen reduction was totally abrogated by Er:YAG laser combined with PRP treatment.

#### 4. Discussion

A common approach to deliver PRP is through repeated injections, which limits the clinical application due to the invasiveness, pain, infection, and misplaced administration. An alternative way of delivering PRP would be a topical application to minimize the side effects. The innate barrier property of the skin is the restrained permeation of PRP. We showed here for the first time that low-fluence laser exposure enhanced PRP absorption in the skin. The lasers provided sufficient ablation depth allowing facile PRP diffusion. PRP combined with laser-assisted delivery was more efficient in treating infected wound and photoaging than PRP alone, and fully-ablative laser showed better performance than fractional-ablative laser. Our data demonstrate the potential of laser-assisted PRP delivery for local therapy instead of conventional administration. The physiological number of platelets in circulation ranges between  $1.5 \times 10^5$  and  $4.0 \times 10^5$  cells/ $\mu\text{L}$ . PRP is the plasma fraction containing a larger platelet amount relative to circulation, basically 3- to 7-fold the concentration of the whole blood (Hessler and Shyam, 2019). In this study, PRP achieved a platelet concentration 2–4 times the baseline amount.

For successful PRP therapy, a 3- to 5-fold increase in growth factors in the nidus is needed (Le et al., 2018). Permeation of the macromolecules in PRP is difficult because of their inability to penetrate SC, resulting in the failure to achieve therapeutic impact. Our result proved that the fractional and full-ablative lasers can improve topical PRP transport into/across the skin within hours. As observed through confocal microscopy, significant enhancement of PRP deposition in the deep skin layer was visualized. The lasers partially ablated the SC barrier to facilitate macromolecule delivery into the skin. However, the total stripping of SC failed to promote PRP permeation. Besides SC, the tight junction in the epidermis also essentially resists and limits macromolecule transport (Bäsler et al., 2016). The fractional CO<sub>2</sub> laser created micropores through SC and epidermis. The remnant SC and epidermis also suffered from thermal effect elicited by CO<sub>2</sub> laser and weakened the barrier function. The photomechanical wave generated by Er:YAG laser enlarges the lacunar space of SC (Lin et al., 2014). We also found few vacuoles inside the epidermis after Er:YAG laser irradiation. This laser disrupted the epidermis to produce a transient route for the delivery of macromolecules. Moreover, tape stripping reduced PDGF-BB uptake in the skin. The first step of topical delivery for many permeants involves partitioning into SC for subsequent diffusion (Hsiao et al., 2019). The loss of SC can decrease the reservoir for drug partitioning, causing a decline in permeation.

The fractional laser generated the micropores of nearly 100  $\mu\text{m}$  diameter, a size sufficient to permit the entrance of macromolecules. Here, only a part of the skin surface was irradiated by fractional laser, leaving most of the skin surface untreated and intact. However, the fractional laser enhanced the permeation of TNF- $\alpha$ , PDGF-BB, and TGF- $\beta$ 1 from PRP to a level comparable to the fully-ablative laser. The microchannels produced by fractional laser showed deeper ablation than superficial peeling by fully-ablative laser. Furthermore, the peripheral region of the microchannels contributed to an effective area for permeant diffusion. The peripheral site of the holes increased the contact surface area for topical PRP delivery. Most of the recombinant macromolecules exhibited better permeation enhancement by Er:YAG laser assistance than by CO<sub>2</sub> laser. The same tendency was observed for PRP-derived IFN- $\gamma$  and VEGF. These observations demonstrate that a large-area superficial ablation is still important to attain a better delivery enhancement even when the ablation depth is very shallow. Like the tape stripping effect, some remnant SC layer produced by Er:YAG

laser was beneficial to be act as the permeant partitioning reservoir for increasing permeation. The CO<sub>2</sub> laser is known to evoke coagulation around the microchannels in the skin (Lee et al., 2014b). This coagulated zone plays a role in impairing drug permeation (Meesters et al., 2018). This effect offsets the facile delivery of macromolecules into the skin.

We found that some growth factors such as PDGF-BB and TGF- $\beta$ 1 could passively penetrate into/across intact skin. Intact SC totally retards the passive diffusion of macromolecules; therefore, hair follicles can be the possible pathway for transport of these permeants (Rancan and Vogt, 2014). Our previous study (Lee et al., 2014a) suggested that Er:YAG laser ablation could affect the structure of hair follicles to induce a preferential drug accumulation in follicles. This effect was not observed after CO<sub>2</sub> laser treatment. This is another reason for the minor enhancement in permeation by CO<sub>2</sub> laser. The confocal images revealed an extensive distribution of the permeants after fractional laser management. This indicates that the permeant diffusion was not only limited in the micropores. We could confirm the lateral entrance of the macromolecules from the laser-created pores. The channels also offered a pathway for the macromolecules to gain an access to deeper strata of the skin via perpendicular delivery. A significant permeant distribution in the dermis was detected by fractional laser-treated skin. Most of the macromolecules in the recombinant form showed better laser-assisted delivery than in their PRP form. It is because that cytokines and growth factors should be released from  $\alpha$ -granules of platelets after reaching the administration site (Samadi et al., 2019). This additional step slows down the diffusion into the skin. An exception in this study was the higher deposition of TNF- $\alpha$  and TGF- $\beta$ 1 in the skin mediated by fractional laser in PRP preparation than the recombinant type. We cannot give an explanation for this with existing results, and further investigation is necessary to elucidate the mechanisms. Our data proves that a low laser fluence is satisfactory in enhancing PRP penetration. The increased permeation followed by the prolonged PRP treatment was observed for most of the cases. However, the reduced permeation after a longer treatment was detected in some cases, e.g. PDGF-BB and TGF- $\beta$ 1 delivery. This could be due to the subsequent delivery of the permeants from skin reservoir to receptor, leading to the decreased skin deposition after a long-term treatment. The possible degradation of the growth factors in skin or receptor was another concern.

In the last decade, there has been a rise in drug resistance in *S. aureus* infection in the skin. Development of novel anti-MRSA agents is urgently needed for treating skin infections. A previous study (Cetinkaya et al., 2018) reported the successful treatment of PRP on infected skin wounds in rats. We confirmed here that PRP was capable of inhibiting MRSA growth in the planktonic form. The ability of PRP to release antimicrobial peptides from  $\alpha$ -granules plays a principal role in the antibacterial activity (Farghali et al., 2019). The other proteins such as cytokines and growth factors also contribute to the antibacterial impact of PRP (Li et al., 2019). For instance, EGF shows the capacity against chronic wound microbiota (de Oliveira et al., 2019). The cytokines induce the expression of antimicrobial peptides in response to bacterial infection (Fernando et al., 2018). Another possibility is the host defense immune system activated by PRP, which increases the expression of immunoglobulin-G Fc receptor and aids navigation towards the chemoattractant N-Met-Leu-Phe (Farghali et al., 2019). Our results reveal that the lasers elicit an efficient PRP delivery to the MRSA-infected site for inhibiting bacterial burden and the subsequent erythema and disintegrated barrier. The fully-ablative modality showed greater improvement than fractional laser. Subcutaneous MRSA injection caused the bacterial accumulation under the skin, therefore, PRP should diffuse across the mouse skin to fulfill the eradication effect. In vitro permeation study verified the ability of the lasers to promote PRP delivery across the skin to the receiver chamber. Bacterial infection extends the inflammation during the healing step and PRP can terminate this inflammation process through some anti-inflammatory cytokines such as IL-4, IL-10, and IFN- $\gamma$  (Woodell-May et al., 2011). Inflammation termination is also mediated by TGF and VEGF (Alves and Grimalt,

2020). These evidences proved the reduction in MRSA-induced inflammation by laser-assisted PRP delivery and the open wound evoked by MRSA could be closed by laser-assisted PRP administration. A high concentration of PDGF-BB and TGF is responsible for wound healing. Both growth factors stimulate chemotaxis, mitogenesis, and stem cell replication at the wound site (Amable et al., 2013). The skin barrier function could be recovered to normal status after CO<sub>2</sub> and Er:YAG laser treatment for 16 h and 1–3 days, respectively (Lee et al., 2012; 2019). We found that the TEWL between MRSA alone and MRSA infection with Er:YAG laser irradiation was approximate, indicating that Er:YAG laser was of no use to treat infection. Nevertheless, the barrier property of the MRSA-infected skin treated with CO<sub>2</sub> laser alone could be partially recovered. The TEWL was determined after a 5-day treatment of the lasers. CO<sub>2</sub> laser may first disrupt the skin and then accelerated wound healing by producing hyperplasia (Filippini et al., 2017). This effect might result in the partial recovery of wound healing. The laser-assisted PRP delivery did not fully recover barrier function disintegrated by MRSA after 5 days. This demonstrates that a 5-day recovery was insufficient to improve the MRSA-induced skin damage although the bacterial load was significantly reduced.

UVA damages the skin to cause thickening, rough texture, wrinkling, and erythema of the skin. Extracellular matrix components such as elastin and collagen are degraded by UVA-generated reactive oxygen species to cause photoaging (Sayama et al., 2010). PRP releases cytokines and growth factors that stimulate dermal fibroblast proliferation, leading to an increase in endogenous hyaluronan, elastin, and collagen levels (de Oliveira et al., 2019; Nicoletti et al., 2019). TNF- $\alpha$  may have either a beneficial or detrimental role in wound healing. However, we expected that TNF- $\alpha$  in PRP could increase wound healing based on its capability to stimulate inflammation and increase macrophage-produced growth factors for reepithelialization (Barrientos et al., 2008). TGF- $\beta$ 1 and VEGF are proven to inhibit matrix metalloproteinases for raising collagen production (Lei et al., 2019). This study showed that laser-facilitated PRP delivery was favorable in improving skin photoaging, and fully-ablative laser represented greater improvement than fractional laser. Once the lasers weakened the SC barrier, PRP facily reached the dermis to exert the bioactivity. The ablative lasers have been recognized as a promising therapy to treat photodamaged skin because of their capability to remodel collagen (Borges et al., 2020). Previous studies have suggested a synergistic effect of topical PRP and fractional CO<sub>2</sub> laser for skin rejuvenation (Hui et al., 2017; Abdel-Maguid et al., 2019). The laser fluence used for obtaining the synergistic effect was very high (42–225 mJ) for achieving skin remodeling. This energy can give the risk of prolonged erythema, edema, and crusting. Although the combined PRP and laser with therapeutic energy can be beneficial in treating skin aging, wider and deeper microchannels created by the high fluence can be filled by interstitial fluid and fibrin to render less effective PRP transport (Maisel-Campbell et al., 2020). The laser used in this study only irradiated at a low fluence of 4 mJ. The adverse effects could be escaped to maintain the photoaging mitigation by laser-assisted PRP delivery.

It was interesting to find immune cell infiltration in the dermis by laser-facilitated PRP absorption in photoaged skin. Wound healing is categorized into three phases: inflammation, proliferation, and remodeling (Chin et al., 2019). Inflammation is involved in the platelet-mediated hemostasis and the release of chemotactic growth factors and can extend for 2–6 days (Abu-Ghname et al., 2019). The growth factors in PRP such as PDGF and VEGF slow down cutaneous aging by acting as chemoattractants for neutrophils and macrophages (Zhang et al., 2018; Lei et al., 2019). The antimicrobial proteins in PRP also create an antimicrobial environment via immune cell recruitment (Hui et al., 2017). Previous studies (Charles-de-Sá et al., 2018, 2020) have confirmed that inflammatory infiltration is advantageous for skin aging therapy. The low-fluence lasers could further increase PRP transport into photoaged skin, leading to a significant immune cell migration as observed in histology. Although the Er:YAG laser was helpful in

recovering elastin and collagen, their levels reduced by photodamage, the UVA-induced wrinkling was still present in the laser-assisted groups. Epidermal hyperplasia is thought to prompt wrinkle formation (Bosset et al., 2002). Epidermal thickening induced by UVA could not be inhibited by laser-assisted delivery in our study. Further improvement is needed by the optimization of PRP dose or laser condition.

Subcutaneous or intradermal injection is a common route of PRP delivery to treat photoaging (Du and Lei, 2020). The use of PRP for rejuvenation of photoaged skin may even need 150 injections per course of treatment (Pavlović and Loubser, 2019). The injection site is predisposed to swelling because of the large administration volume (about 3 mL), resulting in a rough appearance. The operational error by the clinical practitioners is another risk causing complications of PRP injection (Kalyam et al., 2016). These drawbacks can be obviated by less-invasive laser-assisted PRP delivery via topical route. Topical therapy is expected to associate with less pain than injection for increasing patients' compliance. The precise control of laser modality leads to lower interphysician variation than an injection, thus avoiding the possible off-target effect. Low-fluence lasers did not seem to potentiate any skin irritation. We had previously examined the skin barrier function recovery after CO<sub>2</sub> and Er:YAG laser ablation at the fluence similar to the present study (Lee et al., 2012; 2019). The mouse skin could be recovered to baseline control within 16 h and 1–3 days after exposure to CO<sub>2</sub> laser and Er:YAG laser, respectively. Our data signified a more efficient PRP delivery and therapy using a fully-ablative laser than using a fractional laser. Er:YAG laser causes shallower ablation, therefore, treatment using Er:YAG laser is less painful than that by CO<sub>2</sub> laser in a clinical situation (Meesters et al., 2018).

There were some limitations in this study, which need to be addressed. The short duration (five days) for the final examination allowed insight only into the early stage of healing. A five-day period may be insufficient for PRP to improve all skin features affected by infection or photoaging. Additional study with a longer follow-up will be critical to fully understand the effect of laser-facilitated PRP preparation. Importantly, the complex ingredients in PRP preparation also need to be mentioned. It is difficult to elucidate detailed mechanisms of laser-assisted PRP therapy. We employed pig and mouse as the animal models in the present work. The difference between animal and human skin cannot be disregarded. A further clinical study is vital to explore the application of laser-assisted delivery on humans.

## 5. Conclusions

PRP is increasingly popular and demonstrates promising outcomes in the field of dermatological treatments. This investigation evaluated the efficacy of low-fluence lasers for enhancing topical PRP delivery. We found that both fractional and fully-ablative lasers were able to improve the skin permeation of cytokines and growth factors from PRP preparation. This enhancement by the lasers was even higher than that achieved by tape stripping. Increased PRP absorption improved the wound closure produced by MRSA infection and MRSA load also diminished by the laser-facilitated approach. Furthermore, combined PRP and low-fluence lasers were more efficient in recovering elastin and collagen deposition in photoaged mouse skin. The fully-ablative laser was superior to the fractional laser to promote PRP permeation and the subsequent therapeutic efficiency. Our study, therefore, provides a strategy to potentially deliver PRP into the skin by the low-fluence lasers. We anticipate that this new approach of PRP delivery can be applied as an alternative to injections.

## CRedit authorship contribution statement

**Woan-Ruoh Lee:** Conceptualization, Project administration, Writing - original draft. **Chien-Yu Hsiao:** Investigation, Data curation, Methodology. **Tse-Hung Huang:** Project administration, Methodology, Formal analysis. **Calvin T. Sung:** Investigation, Resources. **Pei-Wen**

**Wang:** Formal analysis, Data curation. **Wen-Ting Cheng:** Data curation, Writing - original draft. **Jia-You Fang:** Funding acquisition, Supervision, Writing - review & editing.

## Declaration of Competing Interest

The authors declare that they have no known competing financial interests or personal relationships that could have appeared to influence the work reported in this paper.

## Acknowledgements

The authors are grateful to the financial support from Ministry of Science and Technology of Taiwan (MOST-107-2320-B-182-016-MY3) and Chang Gung Memorial Hospital (CMRPG2G0333).

## References

- Abdel-Maguid, E.M., Awad, S.M., Hassan, Y.S., El-Mokhtar, M.A., El-Deek, H.E.M., Mekki, M.M.A., 2019. Efficacy of stem cell-conditioned medium vs. platelet-rich plasma as an adjuvant to ablative fractional CO<sub>2</sub> laser resurfacing for atrophic post-acne scars: a split-face clinical trial. *J. Dermatol. Treat.* <https://doi.org/10.1080/09546634.2019.1630701>.
- Abuaf, O.K., Yildiz, H., Baloglu, H., Bilgili, M.E., Simsek, H.A., Dogan, B., 2016. Histological evidence of new collagen formulation using platelet rich plasma in skin rejuvenation: a prospective controlled clinical study. *Ann. Dermatol.* 28, 718–724.
- Abu-Ghname, A., Perdanasari, A.T., Davis, M.J., Reece, E.M., 2019. Platelet-rich plasma: principles and applications in plastic surgery. *Semin. Plast. Surg.* 33, 155–161.
- Alves, R., Grimalt, R., 2020. Platelet-rich plasma and its use for cicatricial and non-cicatricial alopecias: a narrative review. *Dermatol. Ther.* 10, 623–633.
- Amable, P.R., Carias, R.B.V., Teixeira, M.V.T., Da Cruz Pacheco, Í., do Amaral, R.J.F.C., Granjeiro, J.M., Borojevic, R., 2013. Platelet-rich plasma preparation for regenerative medicine: optimization and quantification of cytokines and growth factors. *Stem Cell Res. Ther.* 4, 67.
- Barrientos, S., Stojadinovic, O., Golinko, M.S., Brem, H., Tomic-Canic, M., 2008. Growth factors and cytokines in wound healing. *Wound Rep. Reg.* 16, 585–601.
- Bäslar, K., Bergmann, S., Heisig, M., Naegel, A., Zorn-Kruppa, M., Brandner, J.M., 2016. The role of tight junctions in skin barrier function and dermal absorption. *J. Control. Release* 242, 105–118.
- Borges, J., Araújo, L., Cuzzi, T., Martinez, L., Gonzales, Y., Manela-Azulay, M., 2020. Fractional laser resurfacing treats photoaging by promoting neocollagenesis and cutaneous edema. *J. Clin. Aesthet. Dermatol.* 13, 22–27.
- Bosset, S., Barré, P., Chalon, A., Kurfurst, R., Bonté, F., André, P., Perrier, P., Disant, F., Le Varlet, B., Nicolas, J.F., 2002. Skin ageing: clinical and histopathologic study of permanent and reducible wrinkles. *Eur. J. Dermatol.* 12, 247–252.
- Cetinkaya, R.A., Yilmaz, S., Ünlü, A., Petrone, P., Marini, C., Karabulut, E., Urkan, K., Karabacak, M., Uyanik, M., Eker, I., Kilic, A., Gunal, A., 2018. The efficacy of platelet-rich plasma gel in MRSA-related surgical wound infection treatment: an experimental study in an animal model. *Eur. J. Trauma Emerg. Surg.* 44, 859–867.
- Charles-de-Sá, L., Gontijo-de-Amorim, N.F., Sbarbati, A., Benati, D., Bernardi, P., Borojevic, R., Carias, R.B.V., Rigotti, G., 2020. Photoaging skin therapy with PRP and ADSC: a comparative study. *Stem Cells Int.* 2020, 2032359.
- Charles-de-Sá, L., Gontijo-de-Amorim, N.F., Takiya, C.M., Borojevic, R., Benati, D., Bernardi, P., Sbarbati, A., Rigotti, G., 2021. Effect of use of platelet-rich plasma (PRP) in skin with intrinsic aging process. *Aesthet. Surg. J.* 38, 321–328.
- Chin, J.S., Madden, L., Chew, S.Y., Becker, D.L., 2019. Drug therapies and delivery mechanisms to treat perturbed skin wound healing. *Adv. Drug Deliv. Rev.* 149–150, 2–18.
- Chou, W.L., Lee, T.H., Huang, T.H., Wang, P.W., Chen, Y.P., Chen, C.C., Chang, Z.Y., Fang, J.Y., Yang, S.C., 2019. Coenzyme Q<sub>0</sub> from *Antrodia cinnamomea* exhibits drug-resistant bacteria eradication and keratinocyte inflammation mitigation to ameliorate infected atopic dermatitis in mouse. *Front. Pharmacol.* 10, 1445.
- Cieslik-Bielecka, A., Bold, T., Ziolkowski, G., Pierchala, M., Królikowska, A., Reichert, D., 2018. Antibacterial activity of leukocyte- and platelet-rich plasma: an in vitro study. *BioMed Res. Int.* 2018, 9471723.
- Delgado, D., Grate, A., Vincent, H., Bilbao, A.M., Patel, R., Fiz, N., Sampson, S., Sánchez, M., 2019. Current concepts in intraosseous platelet-rich plasma injections for knee osteoarthritis. *J. Clin. Orthop. Trauma* 10, 36–41.
- de Oliveira, B.G.R.B., de Oliveira, F.P., Teixeira, L.A., de Paula, G.R., de Oliveira, B.C., Pires, B.M.F.B., 2019. Epidermal growth factor vs platelet-rich plasma: activity against chronic wound microbiota. *Int. Wound J.* 16, 1408–1415.
- Du, R., Lei, T., 2020. Effects of autologous platelet-rich plasma injections on facial skin rejuvenation. *Exp. Ther. Med.* 19, 3024–3030.
- Farhali, H.A., AbdElkader, N.A., AbuBakr, H.O., Aljuaydi, S.H., Khattab, M.S., Elhelw, R., Elhariri, M., 2019. Antimicrobial action of autologous platelet-rich plasma on MRSA-infected skin wounds in dogs. *Sci. Rep.* 9, 12722.
- Fernando, N., de Silva, R., Handunetti, S.M., Karunanayake, L., De Silva, N.L., de Silva, H.J., Rajapakse, S., Premawansa, S., 2018. Effect of antimicrobial agents on inflammatory cytokines in acute leptospirosis. *Antimicrob. Agents Chemother.* 62, e02312–17.
- Filippini, M., Del Duca, E., Negosanti, F., Bonciani, D., Negosanti, L., Sannino, M., Cannarozzo, G., Nisticò, S.P., 2017. Fractional CO<sub>2</sub> laser: from skin rejuvenation to vulvo-vaginal reshaping. *Photomed. Laser Surg.* 35, 171–175.
- Garvie-Cook, H., Stone, J.M., Yu, F., Guy, R.H., Gordeev, S.N., 2016. Femtosecond pulsed laser ablation to enhance drug delivery across the skin. *J. Biophotonics* 9, 144–154.
- Haedersdal, M., Erlandsson, A.M., Paasch, U., Anderson, R.R., 2016. Translational medicine in the field of ablative fractional laser (AFXL)-assisted drug delivery: a critical review from basics to current clinical status. *J. Am. Acad. Dermatol.* 74, 981–1004.
- Hesseler, M.J., Shyam, N., 2019. Platelet-rich plasma and its utility in medical dermatology: a systematic review. *J. Am. Acad. Dermatol.* 81, 834–846.
- Hsiao, C.Y., Yang, S.C., Alalaiwe, A., Fang, J.Y., 2019. Laser ablation and topical drug delivery: a review of recent advances. *Expert Opin. Drug Deliv.* 16, 937–952.
- Hui, Q., Chang, P., Guo, B., Zhang, Y., Tao, K., 2017. The clinical efficacy of autologous platelet-rich plasma combined with ultra-pulsed fractional CO<sub>2</sub> laser therapy for facial rejuvenation. *Rejuven. Res.* 20, 25–31.
- Kalyam, K., Kavoussi, S.C., Ehrlich, M., Teng, C.C., Chadha, N., Khodadadeh, S., Liu, J., 2016. Irreversible blindness following periorcular autologous platelet-rich plasma skin rejuvenation treatment. *Ophthalm. Plast. Reconstr. Surg.* 33, S12–S16.
- Kennedy, M.L., Whitney, K., Evans, T., LaPrade, R.F., 2018. Platelet-rich plasma and cartilage repair. *Curr. Rev. Musculoskelet. Med.* 11, 573–582.
- Koyuncu, B.Ö., Çelik, K.I., Yüce, M.Ö., Günbay, T., Çömlekçioğlu, M.E., 2020. The role of concentrated growth factor on implant stability: a preliminary study. *J. Stomatol. Oral Maxillofac. Surg.* 121, 363–367.
- Lang, S., Loibl, M., Herrmann, M., 2018. Platelet-rich plasma in tissue engineering: hype and hope. *Eur. Surg. Res.* 59, 265–275.
- Le, A.D.K., Enweze, L., DeBaun, M.R., Dragoo, J.L., 2018. Current clinical recommendation for use of platelet-rich plasma. *Curr. Rev. Musculoskelet. Med.* 11, 624–634.
- Lee, W.R., Hsiao, C.Y., Huang, T.H., Wang, C.L., Alalaiwe, A., Chen, E.L., Fang, J.Y., 2019. Post-irradiation recovery time strongly influences fractional laser-facilitated skin absorption. *Int. J. Pharm.* 564, 48–58.
- Lee, W.R., Shen, S.C., Aljuffali, I.A., Lin, Y.K., Huang, C.W., Fang, J.Y., 2016. Non-ablative fractional laser assists cutaneous delivery of small- and macro-molecules with minimal bacterial infection risk. *Eur. J. Pharm. Sci.* 92, 1–10.
- Lee, W.R., Shen, S.C., Aljuffali, I.A., Li, Y.C., Fang, J.Y., 2014a. Erbium-yttrium-aluminum-garnet laser irradiation ameliorates skin permeation and the follicular delivery of anti-alopecia drugs. *J. Pharm. Sci.* 103, 3542–3552.
- Lee, W.R., Shen, S.C., Al-Suwayeh, S.A., Li, Y.C., Fang, J.Y., 2012. Erbium:YAG laser resurfacing increases skin permeability and the risk of excessive absorption of antibiotics and sunscreens: the influence of skin recovery on drug absorption. *Toxicol. Lett.* 211, 150–158.
- Lee, W.R., Shen, S.C., Chen, W.Y., Aljuffali, I.A., Suen, S.Y., Fang, J.Y., 2014b. Noninvasive delivery of siRNA and plasmid DNA into skin by fractional ablation: erbium:YAG laser versus CO<sub>2</sub> laser. *Eur. J. Pharm. Biopharm.* 86, 315–323.
- Lei, X., Xu, P., Cheng, B., 2019. Problems and solutions for platelet-rich plasma in facial rejuvenation: a systematic review. *Aesthet. Plast. Surg.* 43, 457–469.
- Lin, C.H., Aljuffali, I.A., Fang, J.Y., 2014. Lasers as an approach for promoting drug delivery via skin. *Expert Opin. Drug Deliv.* 11, 599–614.
- Li, T., Ma, Y., Wang, M., Wang, T., Wei, J., Ren, R., He, M., Wang, G., Boey, J., Armstrong, D.G., Deng, W., Chen, B., 2019. Platelet-rich plasma plays an antibacterial, anti-inflammatory and cell proliferation-promoting role in an in vitro model for diabetic infected wounds. *Infect. Drug Resistance* 12, 297–309.
- Maisel-Campbell, A.L., Ismail, A., Reynolds, K.A., Poon, E., Serrano, L., Grushchak, S., Farid, C., West, D.P., Alam, M., 2020. A systematic review of the safety and effectiveness of platelet-rich plasma (PRP) for skin aging. *Arch. Dermatol. Res.* 312, 301–315.
- Meesters, A.A., Nieboer, M.J., Kezic, S., de Rie, M.A., Wolkerstorfer, A., 2018. Parameters in fractional laser assisted delivery of topical anesthetics: role of laser type and laser settings. *Lasers Surg. Med.* 50, 813–818.
- Mercuri, S.R., Vollono, L., Paolino, G., 2020. The usefulness of platelet-rich plasma (PRP) for the treatment of vitiligo: state of the art and review. *Drug Des. Develop. Ther.* 14, 1749–1755.
- Nicoletti, G., Saler, M., Villani, L., Rumolo, A., Tresoldi, M.M., Faga, A., 2019. Platelet rich plasma enhancement of skin regeneration in an ex-vivo human experimental model. *Front. Bioeng. Biotechnol.* 7, 2.
- Pavlović, M.D., Loubser, M.D., 2019. Use of platelet-rich plasma injection for rejuvenation of photoaged facial skin? *JAMA Dermatol.* 155, 755.
- Rancan, F., Vogt, A., 2014. Getting under the skin: what is the potential of the transfollicular route in drug delivery? *Ther. Deliv.* 5, 875–877.
- Samadi, P., Sheykhasan, M., Khoshinani, H.M., 2019. The use of platelet-rich plasma in aesthetic and regenerative medicine: a comprehensive review. *Aesthet. Plast. Surg.* 43, 803–814.
- Sayama, A., Soushin, T., Okada, T., Doi, K., Nakayama, H., 2010. Morphological and biochemical changes during aging and photoaging of the skin of C57BL/6J mice. *J. Toxicol. Pathol.* 23, 133–139.
- Wang, J.V., Schoenberg, E., Saedi, N., Ibrahim, O., 2020. Platelet-rich plasma, collagen peptides, and stem cells for cutaneous rejuvenation. *J. Clin. Aesthet. Dermatol.* 13, 44–49.

- Wenande, E., Anderson, R.R., Haedersdal, M., 2020. Fundamentals of fractional laser-assisted drug delivery: an in-depth guide to experimental methodology and data interpretation. *Adv. Drug Deliv. Rev.* 153, 169–184.
- Woodell-May, J., Matuska, A., Oyster, M., Welch, Z., O'Shaughnessey, K., Hoepfner, J., 2011. Autologous protein solution inhibits MMP-13 production by IL-1 $\beta$  and TNF $\alpha$ -stimulated human articular chondrocytes. *J. Orthop. Res.* 16, 1320–1326.
- Zhang, M., Park, G., Zhou, B., Luo, D., 2018. Applications and efficacy of platelet-rich plasma in dermatology: a clinical review. *J. Cosmet. Dermatol.* 17, 660–665.



Available online at [www.sciencedirect.com](http://www.sciencedirect.com)

ScienceDirect

Biomedical Journal

journal homepage: [www.elsevier.com/locate/bj](http://www.elsevier.com/locate/bj)

## Original Article

# Perilla (*Perilla frutescens*) leaf extract inhibits SARS-CoV-2 via direct virus inactivation

Wen-Fang Tang<sup>a,1</sup>, Hui-Ping Tsai<sup>b,1</sup>, Yu-Hsiu Chang<sup>b,1</sup>,  
Tein-Yao Chang<sup>b,1</sup>, Chung-Fan Hsieh<sup>a</sup>, Chia-Yi Lin<sup>a</sup>, Guan-Hua Lin<sup>a</sup>,  
Yu-Li Chen<sup>d,e</sup>, Jia-Rong Jheng<sup>e</sup>, Ping-Cheng Liu<sup>b</sup>, Chuen-Mi Yang<sup>b</sup>,  
Yuan-Fan Chin<sup>b</sup>, Cheng Cheung Chen<sup>b,c</sup>, Jyh-Hwa Kau<sup>b</sup>, Yi-Jen Hung<sup>b</sup>,  
Po-Shiuan Hsieh<sup>b</sup>, Jim-Tong Horng<sup>a,d,e,f,\*</sup>

<sup>a</sup> Research Center for Emerging Viral Infections, College of Medicine, Chang Gung University, Kweishan, Taoyuan, Taiwan

<sup>b</sup> Institute of Preventive Medicine, National Defense Medical Center, Taipei, Taiwan

<sup>c</sup> Graduate Institute of Medical Science, National Defense Medical Center, Taipei, Taiwan

<sup>d</sup> Research Center for Industry of Human Ecology and Research Center for Chinese Herbal Medicine, Graduate Institute of Health Industry Technology, Chang Gung University of Science and Technology, Taoyuan, Taiwan

<sup>e</sup> Department of Biochemistry and Molecular Biology, College of Medicine, Chang Gung University, Kweishan, Taoyuan, Taiwan

<sup>f</sup> Molecular Infectious Disease Research Center, Chang Gung Memorial Hospital, Chang Gung University College of Medicine, Taoyuan, Taiwan

## ARTICLE INFO

## Article history:

Received 4 November 2020

Accepted 22 January 2021

Available online 28 January 2021

## Keywords:

COVID-19

*Perilla frutescens* (L.) Britt

SARS-CoV-2

Traditional Chinese medicine

Coronavirus

Zisu

## ABSTRACT

**Background:** While severe acute respiratory syndrome coronavirus 2 (SARS-CoV-2) infection presents with mild or no symptoms in most cases, a significant number of patients become critically ill. Remdesivir has been approved for the treatment of coronavirus disease 2019 (COVID-19) in several countries, but its use as monotherapy has not substantially lowered mortality rates. Because agents from traditional Chinese medicine (TCM) have been successfully utilized to treat pandemic and endemic diseases, we designed the current study to identify novel anti-SARS-CoV-2 agents from TCM.

**Methods:** We initially used an antiviral-induced cell death assay to screen a panel of herbal extracts. The inhibition of the viral infection step was investigated through a time-of-drug-addition assay, whereas a plaque reduction assay was carried out to validate the antiviral activity. Direct interaction of the candidate TCM compound with viral particles was assessed using a viral inactivation assay. Finally, the potential synergistic efficacy of remdesivir and the TCM compound was examined with a combination assay.

**Results:** The herbal medicine *Perilla* leaf extract (PLE, approval number 022427 issued by the Ministry of Health and Welfare, Taiwan) had EC<sub>50</sub> of 0.12 ± 0.06 mg/mL against SARS-CoV-2 in Vero E6 cells – with a selectivity index of 40.65. Non-cytotoxic PLE concentrations were

\* Corresponding author. Department of Biochemistry and Molecular Biology, College of Medicine, Chang Gung University, Kweishan, Taoyuan, 333, Taiwan.

E-mail address: [jimtong@mail.cgu.edu.tw](mailto:jimtong@mail.cgu.edu.tw) (J.-T. Horng).

Peer review under responsibility of Chang Gung University.

<sup>1</sup> These authors contributed equally to this work.

<https://doi.org/10.1016/j.bj.2021.01.005>

2319-4170/© 2021 Chang Gung University. Publishing services by Elsevier B.V. This is an open access article under the CC BY-NC-ND license (<http://creativecommons.org/licenses/by-nc-nd/4.0/>).

capable of blocking viral RNA and protein synthesis. In addition, they significantly decreased virus-induced cytokine release and viral protein/RNA levels in the human lung epithelial cell line Calu-3. PLE inhibited viral replication by inactivating the virion and showed additive-to-synergistic efficacy against SARS-CoV-2 when used in combination with remdesivir.

**Conclusion:** Our results demonstrate for the first time that PLE is capable of inhibiting SARS-CoV-2 replication by inactivating the virion. Our data may prompt additional investigation on the clinical usefulness of PLE for preventing or treating COVID-19.

## At a glance of commentary

### Scientific background on the subject

Over the last two decades, respiratory illnesses caused by coronavirus infections have compromised individual health, burdened health-care systems, and caused substantial economic and well-being losses. Unfortunately, effective prevention and treatment have been hampered by the absence of specific pharmacological interventions. In this scenario, new drugs derived from Chinese herbs have been actively researched in the ongoing quest to tackle the COVID-19 pandemic.

### What this study adds to the field

Perilla leaf extract (PLE) inhibits the initial viral entry step by inactivating the SARS-CoV-2 virion. Additionally, it significantly decreases virus-induced cytokine release and viral protein/RNA levels in the human lung epithelial cell line Calu-3. PLE combined with remdesivir shows additive-to-synergistic efficacy against SARS-CoV-2. Altogether, our results provide empirical evidence that PLE may be part of the therapeutic armamentarium against COVID-19.

Severe acute respiratory syndrome coronavirus 2 (SARS-CoV-2) is the causative agent of coronavirus disease 2019 (COVID-19) [1]. SARS-CoV-2 is a positive-sense, single-stranded RNA virus containing a canonical set of four major structural proteins. These include the spike (S), membrane (M), and envelope (E) proteins localized to the membrane envelope and the nucleocapsid (N) protein found in the ribonucleoprotein core. Similar to the SARS-CoV that caused a disease outbreak in 2003, SARS-CoV-2 uses its spike protein to interact with its cellular receptor, angiotensin-converting enzyme 2, for host cell entry [2,3]. Four other human coronaviruses (HCoVs) are typical causative agents of common colds. These include HCoV-OC43 and HCoV-229E that are responsible for  $\leq 30\%$  of all upper respiratory tract infections [4]. While SARS-CoV-2 infection presents with mild to no symptoms in most cases, a significant number of patients become critically ill and require hospitalization and intensive care. As of October 28, 2020, there were >44 million confirmed cases of COVID-19 and

1,172,000 COVID-19-related deaths worldwide. Notably, SARS-CoV-2 infections can elicit cytokine storms characterized by massively increased plasma concentrations of inflammatory cytokines and chemokines (i.e., IL-6, IFN- $\gamma$ , TNF- $\alpha$ , MCP1, and CXCL10) [5–8].

While vaccination programs against SARS-CoV-2 are currently ongoing, the long-term safety of available vaccines remains a major concern. In this scenario, there is an urgent need for both repurposed drugs and agents from traditional Chinese medicine (TCM) to contain the spread of this highly contagious disease.

The repurposed antiviral remdesivir – which was originally developed and administered as an Ebola polymerase inhibitor – is currently the only antiviral agent approved for COVID-19 therapy. While it reduces hospitalization length, it does not significantly lower COVID-19 mortality rates [9]. Agents from TCM have been frequently prescribed to prevent or treat the SARS-CoV outbreak in 2003. Medication records from antiquity disclosed that certain TCMs can be clinically useful to treat respiratory infections. In previous SARS-CoV outbreaks, several provinces in China issued TCM programs based on the principles tonifying *qi*, protecting against external pathogens, dispersing wind, discharging heat, and resolving dampness. The most frequently used herbs – prescribed either separately or in combination – included Radix Astragali (Huangqi), Radix Glycyrrhizae (Gancao), Radix Saposhnikoviae (Fangfeng), Rhizoma Atractylodis Macrocephalae (Baizhu), Lonicerae japonicae Flos (Jinyinhua), and Fructus forsythiae (Lianqiao).

Perilla (*Perilla frutescens* L. Britt) is commonly known as perilla, Korean perilla, beefsteak plant, purple mint, perilla mint, Chinese basil, Zisu (in China), and Shiso (in Japan). Various parts of the perilla plant have different ethnopharmacological effects. While the leaves are used to tonify stomach function, discharge heat, and improve healthy *qi*, and seeds decrease *qi*, resolve phlegm, relieve cough and asthma, and alleviate constipation [10]. In the current study, we investigated the mechanisms underlying the anti-SARS-CoV-2 activity of perilla leaf extract (PLE) using standardized herbal preparations and identified PLE as a virucidal agent that directly inactivates the viral particle.

## Materials and methods

### Cell lines and viruses

Vero E6, human hepatocellular carcinoma (Huh7), human rhabdomyosarcoma (RD), and Calu-3 cells were maintained in Dulbecco's modified Eagle's medium (DMEM, Gibco, BRL, Gaithersburg, MD, USA) supplemented with 10% (w/v) fetal

bovine serum (FBS). Madin–Darby canine kidney (MDCK) cells were cultured in DMEM containing 10% FBS, 2 mM L-glutamine (Gibco), 100 fold dilution nonessential amino acid mixture (Gibco), 100 U/mL penicillin, and 0.1 mg/mL streptomycin (Gibco). Cell lines were obtained from the Chang Gung Memorial Hospital and passages were <25 in all cases. The SARS-CoV-2 strain CDC-4 (CGMH-CGU-01; GISAID accession number EPI\_ISL\_411915 and NCBI accession number MT192759) was provided by the Taiwan Center for Disease Control [11] and amplified in Vero E6 cells. HCoV-229 was obtained from the Research Center for Emerging Viral Infections of the Chang Gung University (Kweishan, Taoyuan, Taiwan) and amplified in Huh7 cells. The viral titer was determined by a plaque assay. SARS-CoV-2 was handled either in a biosafety level three or a biosafety level four laboratory.

### Reagent preparation

PLE (Cat. number 6216; approval number 022427 issued by the Ministry of Health and Welfare, Taiwan) was purchased – along with other herbal powders listed in [Table 1] – from SunTen Pharmaceutical Co. Ltd. (Taipei, Taiwan). The plant name was checked against <http://www.theplantlist.org> and verified by the Brion Research Institute of Taiwan. PLE (25 mg/

mL stock solution) was sterilized using a 0.22-μm filter and maintained in small aliquots at –80 °C. The voucher specimen used in the present study was deposited in the herbarium of the Chang Gung University (Kweishan, Taoyuan, Taiwan). The results of high-performance liquid chromatography analysis are shown in Figure S1. The chromatograms detected the presence of rosmarinic acid – which serves as the constituent marker of PLE according to government guidelines.

### Cytotoxicity and cytopathic effect (CPE) assay

A 96-well tissue culture plate was seeded with Vero E6 cells ( $2 \times 10^4$ /well) and incubated at 37 °C for 16–20 h under 5% CO<sub>2</sub>. Cell viability was measured following incubation with PLE for 72 h and subsequent staining with 5 mg/mL methyl thiazolyl tetrazolium (MTT). Thereafter, the crystal product formazan was dissolved in dimethyl sulfoxide (200 μL/well), and the absorbance (OD<sub>570nm</sub>) of each well was measured using a microplate reader. CC<sub>50</sub> represents the cytotoxicity concentration at which 50% cell death occurs [12]. Live imaging of virus-induced CPE was recorded using CytoSMART Lux2 (Scintica Instrumentation Inc., Maastricht, the Netherlands).

### EC<sub>50</sub> determination

Vero E6 cells ( $2 \times 10^4$ /well) plated in 96-well plates were inoculated with virus at a multiplicity of infection (MOI) of  $2.5 \times 10^{-4}$  plaque forming unit (PFU)/cell (which is equivalent to the 9TCID<sub>50</sub>, i.e., the median tissue culture infective dose). Cells were maintained in E<sub>2</sub> (DMEM containing 2% [v/v] FBS) with different concentrations of PLE. After incubation at 37 °C under 5% CO<sub>2</sub> for 72 h, cell viability was determined using the MTT assay. EC<sub>50</sub> was defined as the PLE concentration required to inhibit 50% CPE. Remdesivir (MedChemExpress, Monmouth Junction, NJ, USA) was the positive control for each

**Table 1** Antiviral activity screening of herbal medicines *in vitro*.

| Herbal extract <sup>a</sup>                          | Final concentration | Antiviral activity <sup>b</sup> | Toxicity |
|--|---------------------|---------------------------------|----------|
| 荊防敗毒散Ching-fang-pai-tu-san                           | 1.25 mg/mL          | –                               | –        |
| 柴葛解肌湯Chai-ge-jie-ji-tang                             | –                   | –                               | –        |
| 川芎茶調散Chuan-xiong-cha-tiao-san                        | 1.25 mg/mL          | –                               | –        |
| 麻杏石甘湯Ma-xing-shi-gan-tang                            | 1.25 mg/mL          | partial                         | –        |
| 葛根湯Ko-Ken Tang                                       | 1.25 mg/mL          | –                               | –        |
| 廣藿香Pogostemon cablin (Blanco) Benth                  | 1.25 mg/mL          | –                               | –        |
| 菊花Chrysanthemi Flos                                  | 1.25 mg/mL          | –                               | –        |
| 黃蘗Phellodendri Cortex                                | 1.25 mg/mL          | –                               | –        |
| 丁香Caryophylli Flos                                   | 1.25 mg/mL          | –                               | +        |
| 紫蘇葉Perillae Folium                                   | 1.25 mg/mL          | +                               | –        |
| 薑黃Curcumae Longae Rhizoma                            | 1.25 mg/mL          | –                               | –        |
| 骨碎補Davallia mariesii Rhizoma (water-butanol extract) | 0.125 mg/mL         | –                               | +        |
| 白芍Paeoniae Alba Radix                                | 0.125 mg/mL         | –                               | +        |
| 苦丁茶Ilex Kaushue                                      | 1.25 mg/mL          | –                               | +        |
| 赤芍Paeoniae Rubra Radix (ethanol extract)             | 0.125 mg/mL         | –                               | –        |
| 牡丹皮Moutan Radicis Cortex                             | 0.125 mg/mL         | –                               | +        |
| 牛筋草Eleusine indica (Goosegrass)                      | 0.125 mg/mL         | –                               | –        |
| 龍牙草Agrimonia pilosa (Hairyvein agrimonia)            | 0.125 mg/mL         | –                               | +        |

<sup>a</sup> Water extract unless otherwise described in parenthesis.

<sup>b</sup> “–” indicates no activity or no cytotoxicity; “+” indicates protection or cytotoxicity.

**Table 2** CC<sub>50</sub> and EC<sub>50</sub> of PLE in various cell lines and viruses.

| Cell line or virus strain | CC <sub>50</sub> (mg/mL) <sup>a</sup> | EC <sub>50</sub> (mg/mL) <sup>b</sup> | SI <sup>c</sup> |
|---------------------------|---------------------------------------|---------------------------------------|-----------------|
| Vero E6                   | 4.64 ± 0.16                           |                                       |                 |
| Calu-3                    | >5                                    |                                       |                 |
| Huh7                      | >1.25                                 |                                       |                 |
| RD                        | 10.92 ± 0.47                          |                                       |                 |
| MDCK                      | 1.73 ± 0.39                           |                                       |                 |
| HCoV-229E                 |                                       | >1.25                                 | –               |
| SARS-CoV-2                |                                       | 0.12 ± 0.06                           | 40.65           |
| EV-A71                    |                                       | 0.04 ± 0.00                           | 280             |
| Influenza A/WSN/1933      |                                       | 1.09 ± 0.37                           | 1.58            |

<sup>a</sup> CC<sub>50</sub>: Drug concentration causing 50% cytotoxicity as determined by the MTT assay. Vero E6, Huh7, RD, and MDCK cells were incubated with PLE for 3 days, whereas Calu-3 cells for 2 days.

<sup>b</sup> EC<sub>50</sub>: Concentration of compounds inhibiting 50% of the cytopathic effects caused by viral infection according to the MTT assay. EC<sub>50</sub> is presented as mean ± standard deviation of two-three independent experiments. HCoV-229E and SARS-CoV-2 were assayed in Huh7 and Vero E6 cells, respectively.

<sup>c</sup> Selectivity index (SI): CC<sub>50</sub>/EC<sub>50</sub>.

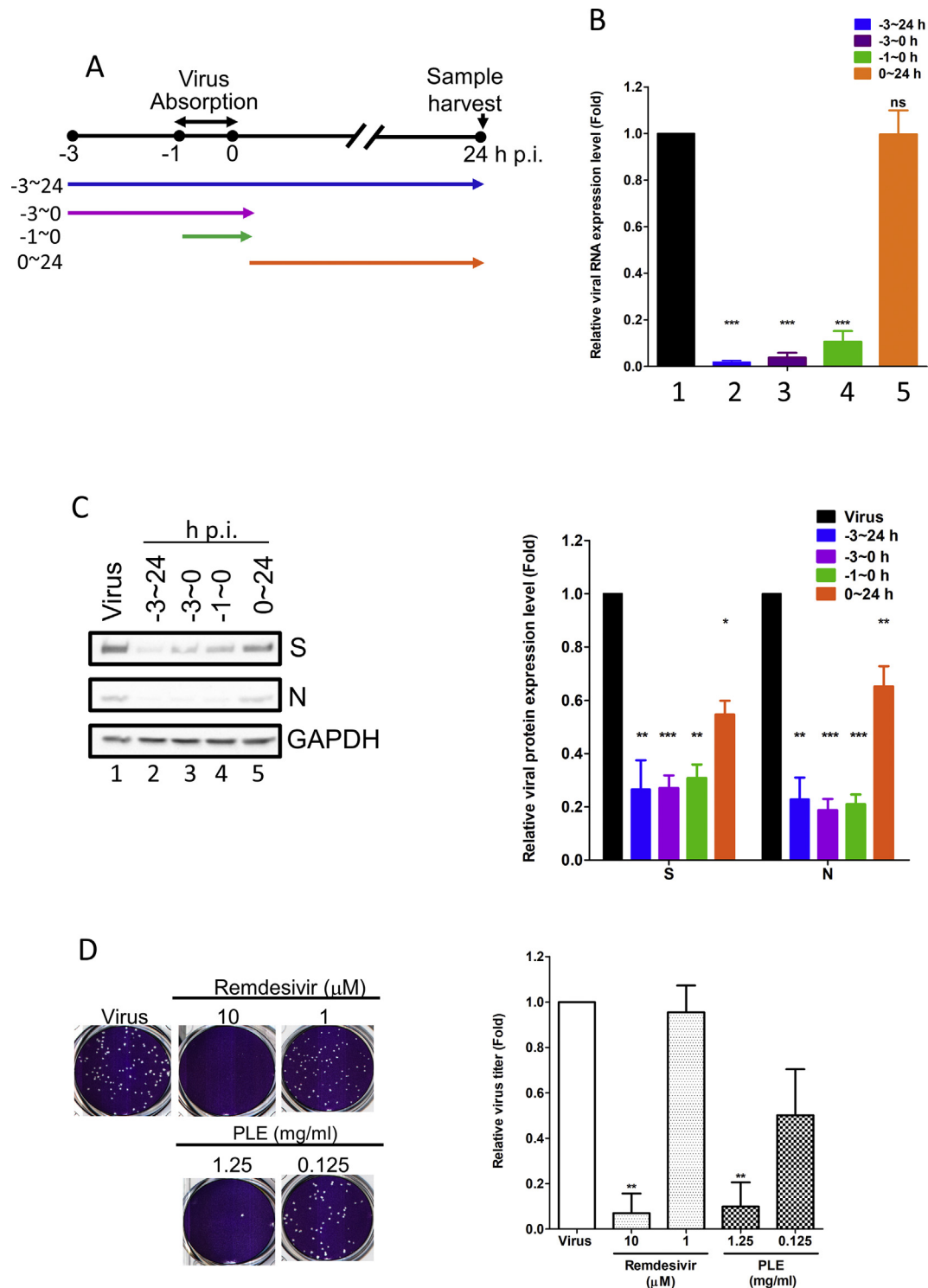


Fig. 1 Treatment with PLE inhibits SARS-CoV-2 at early stages of replication. (A) Schematic representation of the time-of-addition assay. (B–C) Vero E6 cells were infected with SARS-CoV-2 at a MOI of 0.01. Subsequently, PLE (1.25 mg/mL) was added at the following time points: before virus entry (between –3 and 0 h p.i.), during virus adsorption (–1–0 h p.i.), and following virus adsorption (0–24 h p.i.). Infected cells were collectively harvested at 24 h p.i.; viral RNA synthesis and viral protein expression were analyzed with qPCR (B) and western blotting (C), respectively. (B) Expression levels of viral RNA were initially normalized to GAPDH mRNA at each experimental condition. Moreover, the ratio measured in PLE-treated cells was normalized to the RNA level of virus control (arbitrarily set to 1). (C) The intensity of SARS-CoV-2 spike protein (S) and nucleocapsid (N) expression was normalized to GAPDH. Moreover, the ratio measured in PLE-treated cells was normalized to the protein level of virus control (arbitrarily set to 1). N = 3. (D) The results of the plaque reduction assay revealed that SARS-CoV-2 infectivity was diminished after exposure of Vero E6 cells to PLE. SARS-CoV-2 was pre-incubated with various concentrations of PLE or remdesivir before its addition to Vero E6 cells for the plaque assay. The number of plaques was calculated and normalized to that of virus control (arbitrarily set to 1). Data in bar charts are expressed as means  $\pm$  standard error of the mean from at least two independent experiments. \*p < 0.05, \*\*p < 0.01, and \*\*\*p < 0.005; ns = not significant.



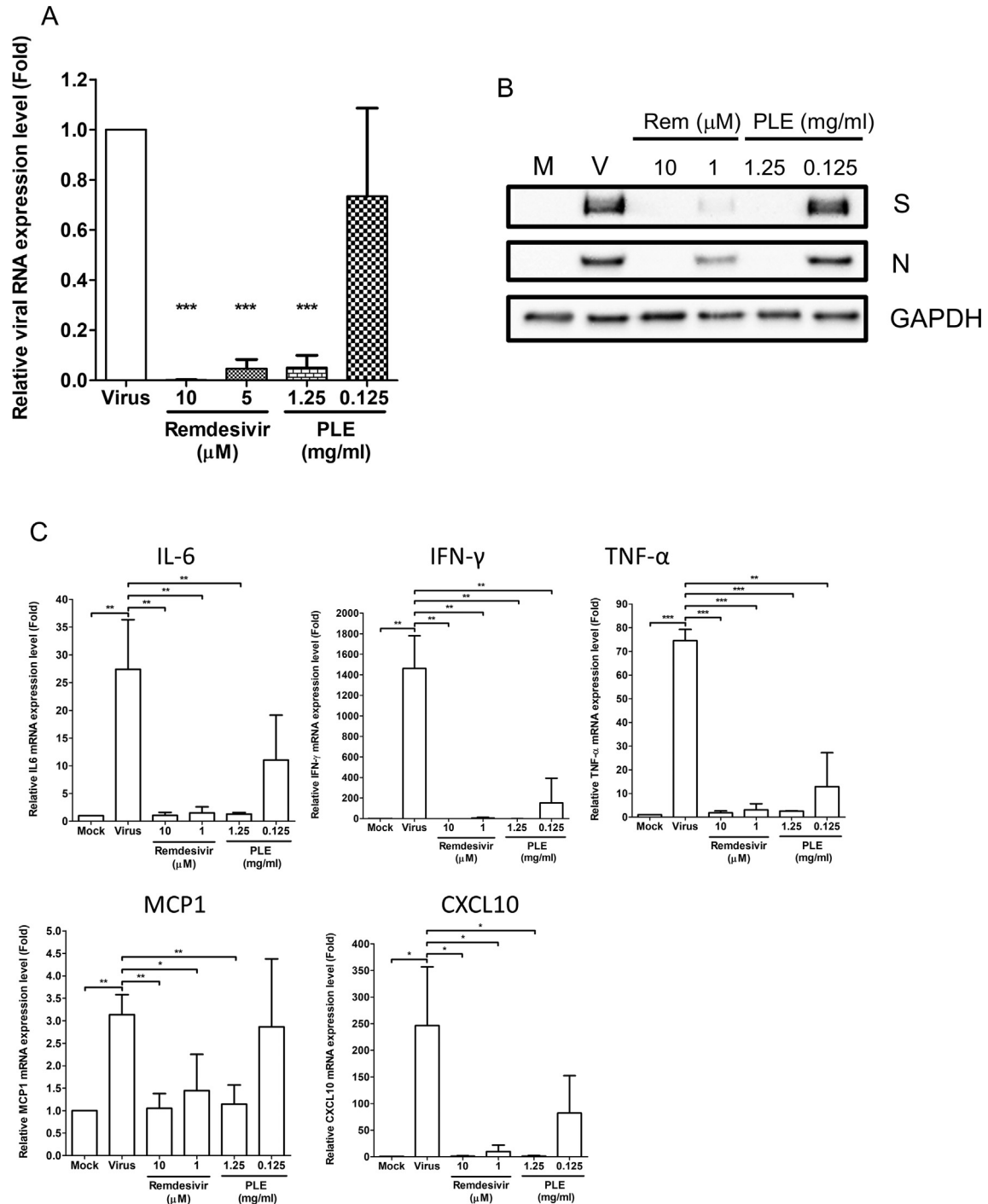
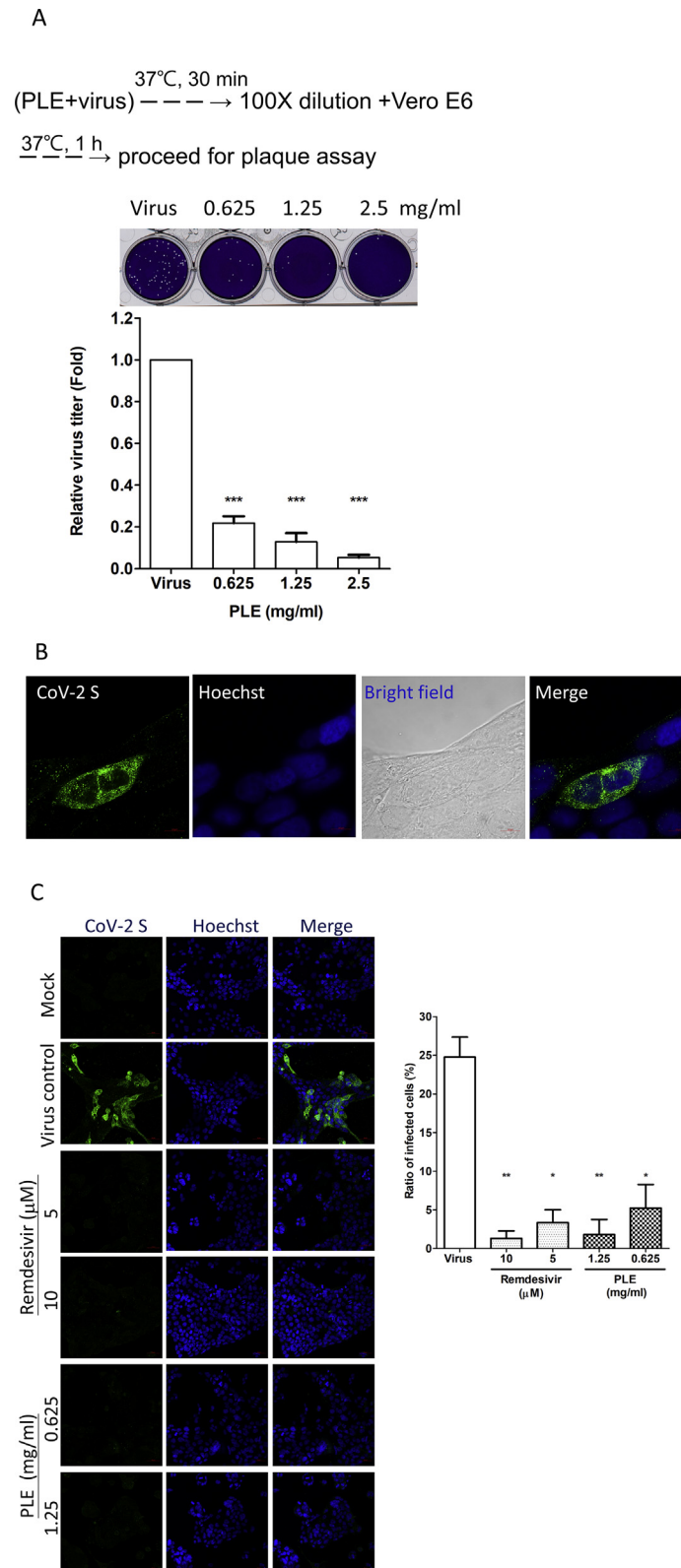


Fig. 2 PLE inhibits SARS-CoV-2 replication in Calu-3 cells. The expression of viral RNA and proteins (A–B) and cytokine mRNA (C) in Calu-3 cells was inhibited by PLE. Calu-3 cells were infected with SARS-CoV-2 in presence of various concentrations of PLE with remdesivir serving as positive control. Upon cell harvesting, RNA and viral protein quantification was performed with qRT-PCR (A) and western blotting (B), respectively. (A, C) Expression levels of viral or cytokine RNA were initially normalized to GAPDH mRNA. Moreover, the ratio measured in PLE-treated cells was normalized to the RNA level of virus control (arbitrarily set to 1). Data are expressed as means  $\pm$  standard error of the mean from at least three independent experiments. \* $p$  < 0.05, \*\* $p$  < 0.01, and \*\*\* $p$  < 0.005.



**Fig. 3** SARS-CoV-2 was inactivated by PLE. (A) The virus stock was pre-treated with increasing concentrations of PLE, and the remaining viral titers were subsequently determined using a plaque assay carried out in Vero E6 cells. The number of plaques for PLE-treated viruses was normalized to that of the virus control (arbitrarily set to 1). Data are expressed as means  $\pm$  standard error of the mean from at least three independent experiments. (B–C) Confocal immunofluorescence microscopy revealed that PLE treatment reduced viral protein synthesis in Calu-3 cells. Cells treated with or without remdesivir and PLE were infected with SARS-CoV-2 at a MOI of 0.01. Cells were harvested at 48 h p.i. for confocal microscopy using the anti-S antibodies as indicated. Fluorescence images of S protein subcellular distribution in SARS-CoV-2-infected Calu-3 cells obtained either in

EC<sub>50</sub> determination. Mock infection was used as negative control.

### Time-of-drug-addition assay

PLE (1.25 mg/mL) was incubated with Vero E6 cells in six-well plates (1 mL/well) between –3 h post-infection (p.i.) and 0 h p.i., between –1 h p.i. and 0 h p.i., between 0 h p.i. and 24 h p.i., and between –3 h and 24 h p.i. at 37 °C. The virus was absorbed to cells between –1 h p.i. and 0 h p.i. at an MOI of 0.01. Cell lysates from each treatment were harvested at 24 h p.i. for quantitative reverse transcription polymerase chain reaction (qRT-PCR) and Western blot analyses.

### Plaque assay and plaque reduction assays

For plaque assay, Vero E6 cells ( $4 \times 10^5$ /well) were inoculated with serially diluted SARS-CoV-2 (0.5 mL/well) in 12-well plates for 1 h at 37 °C under occasional shaking. Cells were washed twice with phosphate-buffered saline. After the addition of 1.4% (v/v) methylcellulose in E<sub>2</sub> (1.5 mL), cells were incubated for 3 days. Upon fixation with 4% (v/v) paraformaldehyde (PFA) for 1 h at room temperature, cells were stained with 0.5% (w/v) crystal violet for 30 min at room temperature. For plaque reduction assay, Vero E6 cells inoculated with SARS-CoV-2 (approximately 90 PFU/well; 0.5 mL/well) in presence of PLE for 1 h at 37 °C under occasional shaking. After washing, 1.5 mL of 1.4% (v/v) methylcellulose in E<sub>2</sub> containing PLE was added to cells – which were subsequently incubated for 3 days.

### RNA extraction and qRT-PCR analysis

Total RNA from Vero E6 or Calu-3 cells was extracted using TRIzol reagent (Thermo Fisher Scientific Inc, MA, USA) according to the manufacturer's instructions. Equal amounts of total RNA were reverse transcribed using the M-MLV reverse transcriptase system (Thermo Fisher Scientific Inc.) using random primers. Subsequently, qRT-PCR was performed with a QuantStudio3 RT-qPCR system (Applied Biosystems, Foster City, CA, USA) using primer pairs specific for the E gene. GAPDH was used as the internal control. The primer sequences are listed in Table S1, and the relative mRNA expression was calculated using the  $2^{-\Delta\Delta C_t}$  method [13].

### Western blot

Cells were harvested, treated with  $3 \times$  sodium dodecyl sulfate (SDS) sample buffer, denatured at 37 °C for 1 h, and subjected to 8% SDS-polyacrylamide gel electrophoresis. Proteins were immunoblotted onto polyvinylidene fluoride membranes and stained with mouse monoclonal anti-spike (GTX632604; GeneTex, Hsinchu, Taiwan, 1: 5000) or mouse monoclonal anti-

nucleocapsid (GTX632269, GeneTex, 1: 2000) antibodies. Mouse monoclonal GAPDH (GTX627408, GeneTex, 1: 5000) was used as the loading control.

### Viral particle inactivation assay

The virus (3000 PFUs) was incubated with increasing PLE concentrations in 500  $\mu$ L DMEM for 30 min at 37 °C and 5% CO<sub>2</sub>. The reaction mixture was diluted 100-fold to reduce the antiviral effect of PLE. After treatment, the residual viral titer was measured using a plaque assay.

### Cytokine analysis

Calu-3 cells ( $5 \times 10^5$ /well) were seeded in six-well plates for 3–4 days before infection with SARS-CoV-2 (MOI = 0.01) for 1 h. The virus was subsequently removed and replaced with E<sub>2</sub>. At 48 h p.i., cells were harvested for qRT-PCR and Western blot analyses. The cytokine primer sequences are shown in Table S1.

### Immunofluorescence assays

Calu-3 cells ( $5 \times 10^5$ /well) were seeded on a coverslip glass, which was set in a six-well plate. After infection with SARS-CoV-2 at a MOI of 0.01, cells were fixed with PFA at 48 h p.i. and stained with anti-spike antibodies (GeneTex). Fluorescence was examined using a confocal microscope (LSM780, Carl Zeiss AG, Oberkochen, Germany).

### Evaluation of PLE activity in combination with remdesivir

Vero E6 cells were seeded in a six-well tissue culture plate. Several dilutions of both remdesivir (concentrations: 0, 2, and 4  $\mu$ M) and PLE (concentrations: 0, 1.25, and 2.5 mg/mL) were subsequently tested in a checkerboard matrix. None of the tested combinations was found to induce cytotoxicity. The inhibitory efficacy was assessed by qRT-PCR at 24 h p.i. To evaluate drug–drug interactions, the combination index was calculated by using Highest Single Agent (HSA) reference model of Synergy Finder, version 2.0 [14]. Interactions between drugs were considered antagonistic, additive, or synergistic when the combination indices were  $< -10$ ,  $-10 \leq \leq 10$ , or  $>10$ , respectively.

### Statistical analysis

Data were analyzed using GraphPad Prism v. 8.0 (GraphPad Software, La Jolla, CA, USA) and presented as means  $\pm$  standard error of the mean. Differences between pairs of means were analyzed using two-sample t-test. All

absence (B) or presence (C) of inhibitors. Magnifications of objective lenses:  $100 \times$  (B) and  $20 \times$  (C). Nuclei were stained with a Hoechst dye. The transmitted light in the bright field revealed the overall morphology of Calu-3 cells. The bar chart in the right panel illustrates the ratios of infected cells under different experimental conditions (magnification of objective lens:  $20 \times$ ). For each condition, the ratio of spike-positive cells was calculated in two independent experiments from  $>200$  cells in randomly selected fields. \* $p < 0.05$ , \*\* $p < 0.01$ , and \*\*\* $p < 0.005$ .

tests were two-sided and *P* value less than 0.05 was considered statistically significant.

## Results

### PLE exhibits anti-SAR-CoV-2 activity in Vero E6 cells

To identify herbal extracts with potential activity against SARS-CoV-2, we performed a primary antiviral screen of a panel of Chinese herbs known to eliminate dampness and reduce heat. To this end, an assay of these materials was carried out to measure the inhibition of virus-induced cell death [Table 1]. PLE had an EC<sub>50</sub> of  $0.12 \pm 0.06$  mg/mL, a CC<sub>50</sub> of  $4.64 \pm 0.16$  mg/mL, and a selectivity index of ~40.65 for SARS-CoV-2 inhibition in Vero E6 cells [Table 2]. PLE was also capable of inhibiting EV-A71 and influenza virus – suggesting a broad-spectrum inhibition capacity against RNA viruses. The antiviral activity was apparently highly specific. No HCoV-229E inhibition was evident at a PLE concentration of  $\leq 1.25$  mg/mL [Table 1]. Remdesivir (positive control) had an EC<sub>50</sub> of  $3.28 \pm 1.78$   $\mu$ M. PLE-mediated protection against virus-induced cell death was monitored in parallel using a live imaging system (Figure S2). Virus-mediated CPE was evident at a MOI of 0.01. The cells aggregated and detached from the dish by 48 h p.i. (Figure S2, left panel). However, PLE (1.25 mg/mL) delayed the onset of CPE (Figure S2, right panel).

### PLE may target the early stage of viral infection cycle

We assessed the time course of drug addition to identify the stage at which PLE inhibits the viral replication cycle [Fig. 1A]. Compared with the mock-treated control, the addition of PLE markedly inhibited viral RNA and protein syntheses at treatment course from –3 h p.i. to 24 h p.i. [lanes 2; Fig. 1B,C]. PLE showed a stronger inhibitory activity when it was added at earlier time points (from –3 h to 0 h p.i. and from –1 h to 0 h p.i.) than when it was added between 0 h p.i. and 24 h p.i. [Fig. 1B,C]. These findings indicate that PLE may play a role in blocking viral entry. PLE treatment inhibited SARS-CoV-2 plaque formation in a dose-dependent manner [Fig. 1D]. In addition, we found that the antiviral activity of PLE (1.25 mg/mL) was similar to that of remdesivir (10  $\mu$ M; positive control) as shown by the extent of inhibition of plaque formation [Fig. 1D]. The foregoing data strongly support the anti-SARS-CoV-2 activity of PLE.

### PLE inhibits virus-induced proinflammatory cytokine expression

The primary targets of SARS-CoV-2 are the epithelial cells in the airways and lungs. Therefore, the antiviral efficiency of PLE was assessed in the human lung alveolar cell line Calu-3, which is highly susceptible to viral infection [15]. As expected, SARS-CoV-2 infection was robust in Calu-3 cells. Viral RNA and protein syntheses were markedly increased by 48 h p.i. but were inhibited by both remdesivir and PLE in a dose-dependent manner [Fig. 2A,B]. Dramatic changes in cytokine levels are associated with COVID-19 progression. For this reason, we examined the effects of PLE on cytokine and

chemokine expression induced by SARS-CoV-2 in Calu-3 cells. The mRNA levels of CXCL10, IL-6, TNF- $\alpha$ , IFN- $\gamma$ , and MCP1 were compared between PLE- and mock-treated Calu3 cells [Fig. 2C]. Relative cytokine/chemokine mRNA levels were increased several fold upon viral infection [Fig. 2C]. Similar to remdesivir, 1.25 mg/mL PLE significantly decreased the relative cytokine/chemokine mRNA levels. The viral protein/RNA synthesis was highly positively correlated with cytokine levels, indicating that cytokine inhibition is closely associated with PLE-mediated reduction in viral replication [Fig. 2A–C].

### PLE inactivates viral particles and blocks their entry into host cells

We observed that PLE inhibited the initial step of viral replication in a time-of-addition assay [Fig. 1]. We thus performed a viral inactivation assay to determine whether PLE can directly target the virion. Viruses subjected to PLE treatment showed significant dose-dependent decrease in their relative titers. Thus, PLE directly targets the virus and has virucidal efficacy [Fig. 3A]. We used immunofluorescence staining to evaluate the reduction in viral protein synthesis in infected cells treated with PLE [Fig. 3B,C]. [Fig. 3B] (bright field) shows Calu-3 cells clustered in a characteristic multinuclear structure. The immunofluorescence foci of the viral spike protein were evenly distributed in the cytoplasm at the site of viral replication. As shown in [Fig. 3C], the intensity of viral spike protein (left panels) and the ratio of infected cells (right panel) were markedly reduced in both remdesivir- and PLE-treated Calu-3 cells. Hoechst staining demonstrated that the observed reduction in immunofluorescent foci was not attributable to the absence of cells. While these morphological data are consistent with the Western blot results shown in [Fig. 2], they corroborate the hypothesis that PLE treatment inhibits viral protein synthesis and viral replication by inhibiting viral entry.

### Synergy between PLE and remdesivir

While remdesivir does not reduce COVID-19-related mortality, clinical trials have shown improvements in terms of recovery time. Hence, it is necessary to combine this drug with other therapeutic agents characterized by different modes of action. We assessed drug–drug interactions between PLE and remdesivir using a cell-based assay. We used qRT-PCR to evaluate the inhibition of viral RNA synthesis by drug combinations [Fig. 4A]. The results of data analysis obtained using SynergyFinder version 2 are presented in [Fig. 4B]. The combination of PLE and remdesivir had a synergistic score of  $14.98 \pm 5.84$ , indicating an additive-to-synergistic effect of PLE when combined with remdesivir [Fig. 4B]. We also used MTT staining to evaluate the inhibitory efficacy on cell viability by drug combinations (Figure S3). A similar additive-to-synergistic effect was evident (synergistic score:  $10.06 \pm 3.76$ ). Taken together, these results provide a strong rationale for clinical trials investigating the potential utility of combinatory PLE and remdesivir treatment.



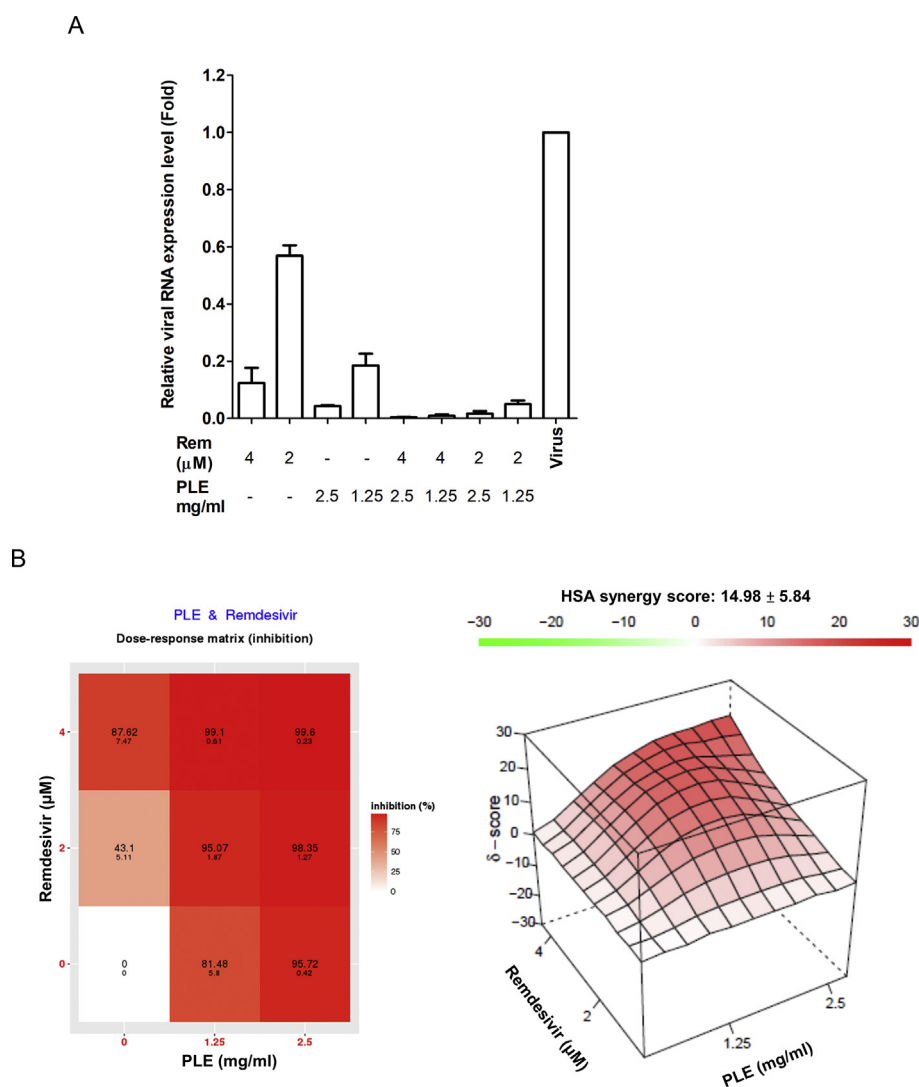


Fig. 4 Antiviral activity of PLE and remdesivir used in combination (A). Vero E6 cells were infected with SARS-CoV-2 with serial dilutions of PLE in combination with remdesivir and subsequently harvested at 24 h p.i. to quantify viral RNA loads by qRT-PCR. Expression levels of viral RNA were initially normalized to GAPDH mRNA. The ratio of drug-treated cells was subsequently normalized to the RNA level of virus control (arbitrarily set to 1). (B) The ratio of drug inhibition elicited by the combination of PLE and remdesivir was calculated with the HSA reference synergy model available in the SynergyFinder software (version 2). The graphs illustrate average results from two independent experiments carried out in duplicate.

## Discussion

COVID-19 has threatened human health on an unprecedented scale owing to the lack of specific anti-viral treatments. Recently, emergency use authorization has been granted to SARS-CoV-2 mRNA vaccines based on new technologies. Both Pfizer and Moderna vaccines – which have been developed on a nucleoside modified mRNA platform – induce immunogenicity to a stabilized membrane anchored spike protein. In addition, Regeneron antibodies (REGN-COV2) consist of an antibody cocktail comprising casirivimab and imdevimab – two monoclonal antibodies that are specifically directed against the spike protein of SARS-CoV-2. Pfizer and Moderna vaccines have been shown to confer a greater than 90 percent

protection. REGN-COV2 induced a significant reduction in viral loads and mitigated clinical symptoms in patients with COVID-19; thus, it might act as a therapeutic substitute for the naturally-occurring immune response. However, the safety and duration of immunity conferred by these vaccines have not yet been fully elucidated. Additionally, children under the age of 12 years, African Americans, and immunocompromised patients were underrepresented in currently available trials. In this scenario, there is an urgent need to identify novel antiviral agents with satisfactory efficacy against this virus. In this study, we empirically demonstrated that PLE has potent anti-SARS-CoV-2 activity. Specifically, our results provide evidence that it blocks viral entry into the host cell by directly inactivating the virion. It also inhibits viral RNA and protein syntheses, as well as virus-induced cytokine production. Viral

entry inhibitors offer several therapeutic advantages. Accordingly, they may directly attenuate or destroy the virus and can be relatively less cytotoxic than agents with other mechanisms of action as they need not permeate the host cell. In addition, they may also display a potential prophylactic efficacy. Intriguingly, PLE can be formulated not only into agonists but also as external preparations such as hand sanitizers and environmental disinfectants.

Health authorities in various provinces of mainland China have officially recommended the use of herbal formulas to control the spread of COVID-19 in the general population. The main functions of these herbal formulas are to strengthen *qi*, expel external pathogens, disperse wind, and discharge heat. To this end, a total of 54 herbs have been listed, and PLE was the sixth most common extract in all formulas [16]. However, the exact role of PLE in such herbal formulations when used for directly targeting the virus remains unknown. The TCM Huoxiang Zhengqi capsules/Shui contain PLE and other herbs have been administered to dissipate cold and eliminate dampness. Few studies have described the use of these capsules to treat patients with COVID-19 during the medical observation period [17–19]. A clinical trial of Huoxiang Zhengqi capsules combined with Western medicines for treating patients with COVID-19 reported an improved therapeutic efficacy [20]. As PLE is a component of this formulation, it might be responsible for its anti-SARS-CoV-2 activity. We tested PLE derived from different batches and commercial suppliers and found that all of them displayed a similar anti-SARS-CoV-2 activity. Taken together, these findings clearly indicate that all of these formulations contain the same pharmacologically active principle(s) and attempts to identify and quantify them are currently ongoing.

Dramatic relative changes in cytokine levels have been observed in patients with severe COVID-19 [5–8]. The occurrence of a hyperinflammatory state and the accumulation of monocytes/macrophages and neutrophils in lung tissues are typical features of severe disease [6]. In this context, anti-inflammatory inhibitors such as IL-1 and IL-6 blockers can be therapeutically useful [21]. Expectedly, we observed elevated levels of different proinflammatory cytokines and chemokines (i.e., TNF- $\alpha$ , IFN- $\gamma$ , IL-6, CCL-2/MCP1, and CXCL10/IP-10) in Calu-3 cells infected with SARS-CoV-2. However, PLE treatment inhibited all of these proinflammatory factors and alleviated the cytokine storm induced by SARS-CoV-2. It is therefore plausible that PLE could act as an anti-inflammatory inhibitor. Nevertheless, this hypothesis requires additional *in vivo* investigations.

Synergistic or additive drug combinations can reduce the required dose of each individual drug, mitigate toxicity and adverse reactions, and enhance overall therapeutic efficacy. The combination of compounds with at least two different antiviral mechanisms may also mitigate the risk of inducing drug-resistant viral mutants [22]. Certain drug combinations administered for treating HIV and HCV infections have shown remarkable therapeutic efficacy. Thus, remdesivir should be combined with other drugs to improve the overall survival rate of patients with COVID-19. Several attempts are currently ongoing to address this issue. Based on laboratory data and the results of a small randomized trial [23], the National Institute of Allergy and Infectious Diseases (USA) conducted the Adaptive COVID-19 Treatment Trial 3 to evaluate the

safety and efficacy of a combination of remdesivir and IFN-1 $\beta$  in hospitalized patients with confirmed SARS-CoV-2 infection and lung involvement. Here, we demonstrate that the combination of PLE and remdesivir showed additive-to-synergistic efficacy against SARS-CoV-2 in Vero-E6 cells. Because PLE has been widely used in Asian countries to treat patients with various viral infections, our findings should prompt additional clinical investigations of this extract as an adjunct to remdesivir in patients with COVID-19.

---

## Conclusion

In this study, we have shown that PLE is capable of preventing SARS-CoV-2 entry into host cells. Our findings may pave the way to the clinical use of this extract for preventing and/or treating COVID-19. Notably, perilla has a widespread distribution and large amounts of its herbal extracts can easily be obtained from intensive farming. While the exact active ingredients of PLE have not been elucidated yet, clinically useful preparations can easily be obtained following standard protocols and formulated in oral supplements or medicated topical products. Finally, the use of PLE can theoretically alleviate the ongoing shortage of prescription drugs such as remdesivir.

---

## Authors' contribution

W.-F. Tang, H.-P. Tsai, Y.-H. Chang, T.-Y. Chang, C.-F. Hsieh, C.-Y. Lin, G.-H. Lin, Y.-L. Chen, J.-R. Jheng, P.-C. Liu, C.-M. Yang, and Y.-F. Chin performed the experiments and conducted data analysis. H.-P. Tsai, Y.-H. Chang, T.-Y. Chang, P.-C. Liu, C.-M. Yang, C.-C. Chen, Y.-F. Chin, J.-H. Kau, Y.-J. Hung, and P.-S. Hsieh were in charge of high-security experiments. W.-F. Tang and J.-T. Horng designed the study, analyzed and interpreted data, and drafted the paper. All authors have read and approved the final manuscript.

---

## Funding

This research was funded by the Chang Gung Memorial Hospital, Taoyuan, Taiwan (BMRP416, CMRPD1G0301-3, CMRPD1F0581-3, and CMRPD1K0241-2), the Ministry of Science and Technology of Taiwan (106-2320-B-182-004-MY3, 106-2811-B-182-011, 106-2632-B-182-001, 107-2811-B-182-512, 108-2320-B-182-039-, 109-2320-B-182-026 -MY3, 109-2327-B-182-002, and 109-2327-B-182-003- to J.-T. Horng and 109-2327-B-016 -002 – to C.-C. Chen), the Research Centre for Emerging Viral Infections from The Featured Areas Research Centre Program within the framework of the Higher Education Sprout Project by the Ministry of Education in Taiwan, and the Ministry of Science and Technology, Taiwan (MOST 109-2634-F-182-001).

---

## Availability of data and materials

The analytical methods and all study materials will be made available upon publication of the study. The original data set

can be obtained from the corresponding author upon reasonable request.

## Ethics approval and consent to participate

Not applicable.

## Conflicts of interest

The authors declare they have no actual or potential competing financial interests.

## Acknowledgements

The authors are grateful to Scintica Instrumentation Inc. for the kind gift of the CytoSMART Lux2 instrument. The authors thank Drs. Shin-Ru Shih, Pei-Wen Hsieh, and Tsong-Long Hwang for their constructive suggestions. We acknowledge the help of Dr. Ming-Chung Lee (Brion Research Institute) in botanical identification experiments. We also indebted to the Institute of Preventive Medicine, National Defense Medical Center, for providing biosafety level three and four laboratory in which SARS-CoV-2 was handled.

## Appendix A. Supplementary data

Supplementary data to this article can be found online at <https://doi.org/10.1016/j.bj.2021.01.005>.

## REFERENCES

- [1] Coronaviridae Study Group of the International Committee on Taxonomy of V. The species Severe acute respiratory syndrome-related coronavirus: classifying 2019-nCoV and naming it SARS-CoV-2. *Nat Microbiol* 2020;5:536–44.
- [2] Hoffmann M, Kleine-Weber H, Schroeder S, Kruger N, Herrler T, Erichsen S, et al. SARS-CoV-2 cell entry depends on ACE2 and TMPRSS2 and is blocked by a clinically proven protease inhibitor. *Cell* 2020;181:271–280 e8.
- [3] Walls AC, Park YJ, Tortorici MA, Wall A, McGuire AT, Veasler D. Structure, function, and antigenicity of the SARS-CoV-2 spike glycoprotein. *Cell* 2020;181:281–292 e6.
- [4] Masters PS, Perlman S. Coronaviridae. In: David M, Knipe PMH, Martin Malcolm A, Griffin Diane E, Lamb Robert A, Bernard Roizman, Straus Stephen E, editors. *Fields virology*. Philadelphia: Lippincott Williams & Wilkins; 2013. p. 825–58.
- [5] Huang C, Wang Y, Li X, Ren L, Zhao J, Hu Y, et al. Clinical features of patients infected with 2019 novel coronavirus in Wuhan, China. *Lancet* 2020;395:497–506.
- [6] Wong CK, Lam CW, Wu AK, Ip WK, Lee NL, Chan IH, et al. Plasma inflammatory cytokines and chemokines in severe acute respiratory syndrome. *Clin Exp Immunol* 2004;136:95–103.
- [7] Wu C, Chen X, Cai Y, Xia J, Zhou X, Xu S, et al. Risk factors associated with acute respiratory distress syndrome and death in patients with coronavirus disease 2019 pneumonia in Wuhan, China. *JAMA Intern Med* 2020;180:934–43.
- [8] Zhou F, Yu T, Du R, Fan G, Liu Y, Liu Z, et al. Clinical course and risk factors for mortality of adult inpatients with COVID-19 in Wuhan, China: a retrospective cohort study. *Lancet* 2020;395:1054–62.
- [9] Rochwerg B, Agarwal A, Zeng L, Leo YS, Appiah JA, Agoritsas T, et al. Remdesivir for severe covid-19: a clinical practice guideline. *BMJ* 2020;370:m2924.
- [10] Ahmed HM. Ethnomedicinal, phytochemical and pharmacological investigations of perilla frutescens (L.) Britt. *Molecules* 2018;24:102.
- [11] Gong YN, Tsao KC, Hsiao MJ, Huang CG, Huang PN, Huang PW, et al. SARS-CoV-2 genomic surveillance in Taiwan revealed novel ORF8-deletion mutant and clade possibly associated with infections in Middle East. *Emerg Microb Infect* 2020;9:1457–66.
- [12] Chang CW, Leu YL, Horng JT. Daphne Genkwa sieb. Et zucc. Water-soluble extracts act on enterovirus 71 by inhibiting viral entry. *Viruses* 2012;4:539–56.
- [13] Livak KJ, Schmittgen TD. Analysis of relative gene expression data using real-time quantitative PCR and the 2<sup>-</sup>(Delta Delta C(T)) method. *Methods* 2001;25:402–8.
- [14] Ianevski A, He L, Aittokallio T, Tang J. SynergyFinder: a web application for analyzing drug combination dose-response matrix data. *Bioinformatics* 2017;33:2413–5.
- [15] Imai M, Iwatsuki-Horimoto K, Hatta M, Loeber S, Halfmann PJ, Nakajima N, et al. Syrian hamsters as a small animal model for SARS-CoV-2 infection and countermeasure development. *Proc Natl Acad Sci U S A* 2020;117:16587–95.
- [16] Luo H, Tang QL, Shang YX, Liang SB, Yang M, Robinson N, et al. Can Chinese medicine be used for prevention of coronavirus disease 2019 (COVID-19)? A review of historical classics, research evidence and current prevention programs. *Chin J Integr Med* 2020;26:243–50.
- [17] Han YY, Zhao MR, Shi B, Song ZH, Zhou SP, He Y. Application of integrative therapy protocols for treatment of coronavirus disease 2019 (COVID-19). *Chin Tradit Herb Drugs* 2020;4:878–82.
- [18] General Office of National Health Committee. Notice on the issuance of guidelines of diagnosis and treatment for 2019-nCoV infected pneumonia, <http://bgs.satcm.gov.cn/zhengcewenjian/2020-02-06/12847.html>; 2000 [accessed 6 February 2020].
- [19] Zhu YG, Deng ZW, Liu LH, Liu XH, Li XZ, Chen WH, et al. Compilation of drug information for the diagnosis and treatment of COVID-19 (version 1). *Cent S Pharm* 2020;18:1–14.
- [20] Xiao M, Tian J, Zhou Y, Xu X, Min X, Lv Y, et al. Efficacy of Huoxiang Zhengqi dropping pills and Lianhua Qingwen granules in treatment of COVID-19: a randomized controlled trial. *Pharmacol Res* 2020;161:105126.
- [21] Lu L, Zhang H, Zhan M, Jiang J, Yin H, Dauphars DJ, et al. Preventing mortality in COVID-19 patients: which cytokine to target in a raging storm? *Front Cell Dev Biol* 2020;8:677.
- [22] Tsiodras S, Mooney JD, Hatzakis A. Role of combination antiviral therapy in pandemic influenza and stockpiling implications. *BMJ* 2007;334:293–4.
- [23] Rahmani H, Davoudi-Monfared E, Nourian A, Khalili H, Hajizadeh N, Jalalabadi NZ, et al. Interferon beta-1b in treatment of severe COVID-19: a randomized clinical trial. *Int Immunopharm* 2020;88:106903.

## Article

# Rapid and Efficient Enrichment of Snake Venoms from Human Plasma Using a Strong Cation Exchange Tip Column to Improve Snakebite Diagnosis

Chien-Chun Liu <sup>1,†</sup> , Ya-Han Yang <sup>2,†</sup>, Yung-Chin Hsiao <sup>1,3</sup>, Po-Jung Wang <sup>1</sup>, Jo-Chuan Liu <sup>4</sup>, Chien-Hsin Liu <sup>5</sup>, Wen-Chin Hsieh <sup>5</sup> , Chih-Chuan Lin <sup>6</sup>  and Jau-Song Yu <sup>1,3,4,7,\*</sup> 

- <sup>1</sup> Molecular Medicine Research Center, Chang Gung University, Taoyuan 333, Taiwan; chienchunliu1016@gmail.com (C.-C.L.); hschin@mail.cgu.edu.tw (Y.-C.H.); mapleleaves730@gmail.com (P.-J.W.)
- <sup>2</sup> School of Medicine, College of Medicine, Chang Gung University, Taoyuan 333, Taiwan; yangyahan8246@gmail.com
- <sup>3</sup> Liver Research Center, Chang Gung Memorial Hospital at Linkou, Taoyuan 333, Taiwan
- <sup>4</sup> Graduate Institute of Biomedical Sciences, College of Medicine, Chang Gung University, Taoyuan 333, Taiwan; Joy6408@gmail.com
- <sup>5</sup> Center for Research, Diagnostics and Vaccine Development of Centers for Disease Control, Ministry of Health and Welfare, Taipei 10050, Taiwan; liuch@cdc.gov.tw (C.-H.L.); vac@cdc.gov.tw (W.-C.H.)
- <sup>6</sup> Department of Emergency Medicine, Chang Gung Memorial Hospital at Linkou, Taoyuan 333, Taiwan; bearuncle@yahoo.com
- <sup>7</sup> Research Center for Food and Cosmetic Safety, College of Human Ecology, Chang Gung University of Science and Technology, Taoyuan 333, Taiwan
- \* Correspondence: yusong@mail.cgu.edu.tw; Tel.: +886-3-211-8800 (ext. 5171); Fax: +886-3-2118891
- † These authors contributed equally to this work.



**Citation:** Liu, C.-C.; Yang, Y.-H.; Hsiao, Y.-C.; Wang, P.-J.; Liu, J.-C.; Liu, C.-H.; Hsieh, W.-C.; Lin, C.-C.; Yu, J.-S. Rapid and Efficient Enrichment of Snake Venoms from Human Plasma Using a Strong Cation Exchange Tip Column to Improve Snakebite Diagnosis. *Toxins* **2021**, *13*, 140. <https://doi.org/10.3390/toxins13020140>

Received: 4 January 2021

Accepted: 11 February 2021

Published: 13 February 2021

**Publisher's Note:** MDPI stays neutral with regard to jurisdictional claims in published maps and institutional affiliations.



**Copyright:** © 2021 by the authors. Licensee MDPI, Basel, Switzerland. This article is an open access article distributed under the terms and conditions of the Creative Commons Attribution (CC BY) license (<https://creativecommons.org/licenses/by/4.0/>).

**Abstract:** Snake envenomation is a serious public health issue in many tropical and subtropical countries. Accurate diagnosis and immediate antivenom treatment are critical for effective management. However, the venom concentration in the victims' plasma is usually low, representing one of the bottlenecks in developing clinically applicable assays for venom detection and snakebite diagnosis. In this study, we attempted to develop a simple method for rapid enrichment of venom proteins from human plasma to facilitate detection. Our experiments showed that several major protein components of both *Naja atra* (*N. atra*) and *Bungarus multicinctus* (*B. multicinctus*) venoms have higher isoelectric point (pI) values relative to high-abundance human plasma proteins and could be separated via strong cation exchange–high-performance liquid chromatography (SCX-HPLC). Based on this principle, we developed an SCX tip column-based protocol for rapid enrichment of *N. atra* and *B. multicinctus* venom proteins from human plasma. Application of liquid chromatography–tandem mass spectrometry (LC-MS/MS) led to the identification of cytotoxin and beta-bungarotoxin as the major proteins enriched by the SCX tip column in each venom sample. The entire process of venom enrichment could be completed within 10–15 min. Combination of this method with our previously developed lateral flow strip assays (rapid test) significantly enhanced the sensitivity of the rapid test, mainly via depletion of the plasma protein background, as well as increase in venom protein concentration. Notably, the SCX tip column-based enrichment method has the potential to efficiently enrich other *Elapidae* snake venoms containing proteins with higher pI values, thereby facilitating venom detection with other assays. This simple and rapid sample preparation method should aid in improving the clinical utility of diagnostic assays for snakebite.

**Keywords:** snakebite; venom; strong cation exchange chromatography; lateral flow strip; clinical diagnostic assay

**Key Contribution:** The SCX tip column developed in our laboratory effectively and rapidly enriched snake venom proteins (cytotoxin and beta-bungarotoxin) from human plasma, supporting its utility in venom detection assays to improve the specificity and sensitivity of snakebite diagnosis.



## 1. Introduction

Snake envenomation is a serious public health issue in many tropical and subtropical countries. According to a recent epidemic study, about 1.8–2.7 million snake envenomation cases occur each year, leading to 81,410–137,880 deaths and 244,230–413,640 amputations or other permanent disabilities [1]. In Taiwan, approximately 1000 snake envenomation cases are reported on an annual basis. Six species of clinically important venomous snakes are found in Taiwan, which include *Trimeresurus stejnegeri*, *Protobothrops mucrosquamatus*, *Naja atra*, *Bungarus multicinctus*, *Deinagkistrodon acutus*, and *Daboia russelli formosensis* [2,3]. Four types of antivenom have been produced to treat snakebites by these native species [4], and, due to the sufficient supply, antivenom is always given for envenoming in Taiwan.

Several clinical challenges need to be overcome for effective management of snakebite. Firstly, victims bitten by different snakes may display similar symptoms, leading to potential misuse of antivenom treatment. Snake venom can cause irreversible damage if patients do not receive the correct treatment [5], highlighting the vital need for accurate diagnosis and immediate intervention. Currently, two main techniques are available for the detection and diagnosis of snake envenomation. The first is enzyme-linked immunosorbent assay (ELISA) with high sensitivity that has been successfully used for clinical diagnosis of snakebite and detection of venom concentrations in patient plasma [6,7]. ELISA is highly sensitive, with a detection limit of up to 1 ng/mL. However, this technique takes more than four hours to complete, which is too time-consuming for snakebites that require immediate treatment. Another common method is the rapid test [8–10], which usually takes 5 to 20 min to generate results, a time-frame more suitable for effective snakebite diagnosis and management. However, this procedure is less sensitive than ELISA, with a detection limit of ~5–10 ng/mL. Even in cases where the venom level in serum/plasma is lower than 10 ng/mL, victims may develop local and/or systemic symptoms. Moreover, since the observed serum/plasma venom protein concentration decreases with time, prediction of clinical severity according to this parameter is a challenge [7]. Difficulties in detection might occur if confronting patients that delayed in seeking medical care or patients with low venom concentration in their plasma. Therefore, the sensitivity of the rapid test should be enhanced in order to improve its clinical utility.

In this study, an SCX tip column-based method was developed to rapidly enrich snake venom proteins from human plasma based on biophysical differences (pI values) between human plasma proteins and main venom proteins. Combination of this method with rapid test increased the sensitivity of the rapid test and enriched signals to facilitate identification of the envenoming species. We propose that the protein enrichment technique developed in this study may be successfully applied to enhance the sensitivity and clinical utility of biological assays for snake venom.

## 2. Results

### 2.1. Differences in pI Values between High-Abundance Human Plasma Proteins and Snake Venom Proteins

To determine the differences in pI values of proteins abundant in human plasma and venom proteins, we calculated pI values of the top 14 abundant proteins in plasma and venom proteins from *B. multicinctus* and *N. atra* using the online software UniProt Compute pI/Mw. As shown in Supplementary Table S1, pI values of the 14 high-abundance proteins in human plasma ranged from 4.6 to 7.2. In contrast, pI values of the major toxic proteins in *B. multicinctus* venom, such as  $\alpha$ -bungarotoxin and  $\beta$ -bungarotoxin, were >7.5, ranging from 7.57 to 10.08. Similarly, pI values of most *N. atra* venom proteins were >8. Only a few components belonging to protein families of phospholipase A<sub>2</sub>, snake venom metalloproteinase, and nerve growth factor have lower pI values (4.9 to 7.68). Our results indicate that the pI values of the majority of venom proteins from *B. multicinctus* and *N. atra* are distinct from those of the top 14 plasma proteins, supporting the feasibility of separating major venom components from human plasma proteins based on their charges.

## 2.2. SCX-HPLC for Separating Venom Proteins from Human Plasma Proteins

To ascertain whether *B. multicinctus* and *N. atra* venom proteins could be efficiently separated from plasma proteins based on charge, human plasma and both snake venom samples were analyzed via SCX-HPLC, respectively. According to chromatography patterns, the major peak of the human plasma proteins appeared within 10 min (Figure 1). In analysis of *N. atra* venom, one dominant peak was eluted within 10 min with a retention time almost equal to that of human plasma, while the retention times of the two other peak signals were near 25 and 45 min, respectively (Figure 1A). In analysis of *B. multicinctus* venom, the two most abundant peaks were observed near 15 min and 45 min apart from the peak before 10 min that co-eluted with the major peak of human plasma proteins (Figure 1B). The results collectively suggest that the charges of high-abundance human plasma proteins are distinct from those of several venom proteins from both *B. multicinctus* and *N. atra*, which should allow efficient separation of proteins from snake venom and human plasma during ion exchange chromatography and allow determination of the ion concentration suitable for isolation of venom proteins from plasma matrix.

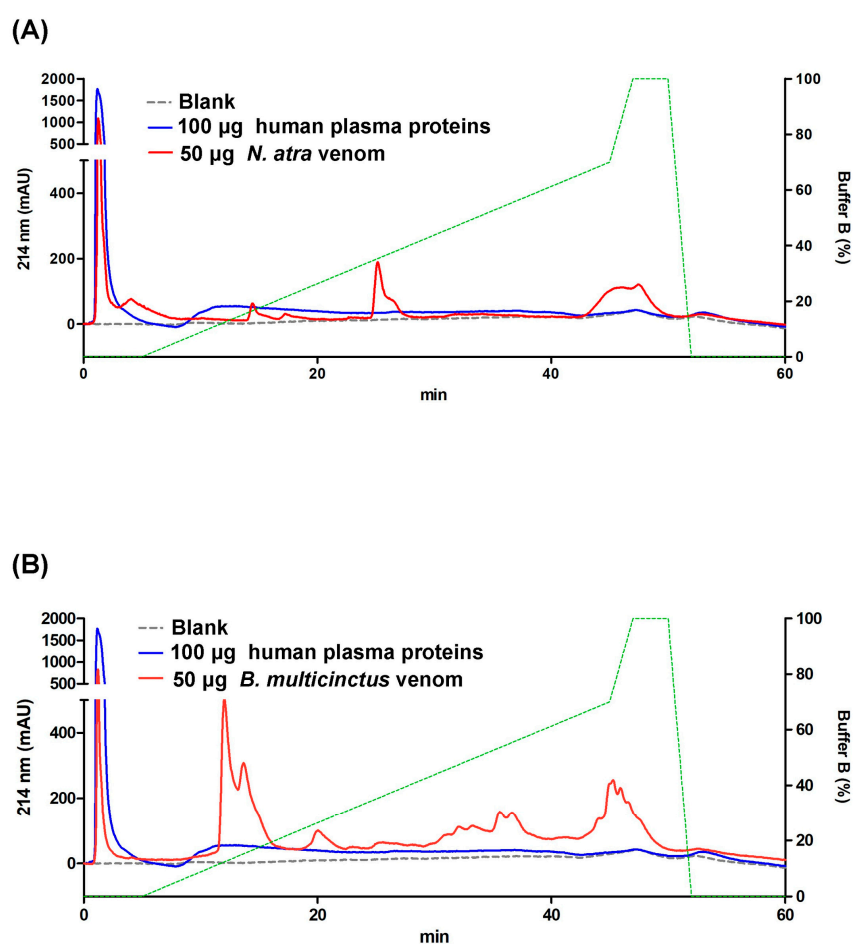


**Figure 1.** Chromatography patterns of human plasma proteins and *Naja atra* and *B. multicinctus* venom proteins analyzed via strong cation exchange–high-performance liquid chromatography (SCX-HPLC). Human plasma proteins (100 µg), *Naja atra* venom proteins (50 µg), and *B. multicinctus* venom proteins (50 µg) were individually analyzed using SCX-HPLC. The overlapping patterns of human plasma proteins with *Naja atra* and *B. multicinctus* venom proteins are shown in (A,B), respectively.

## 2.3. Development of Methodology for Efficient Enrichment of Snake Venom Proteins from Human Plasma

To determine the suitable ion concentration for separating venom proteins from human plasma, snake venom and plasma proteins were captured using a homemade

SCX tip column and eluted stepwise with buffers containing different concentrations of NaCl. Since elution buffers contain high concentrations of salt, each eluted fraction was precipitated with acetone prior to SDS-PAGE. As detected in the gel images, the majority of plasma proteins were not retained with SCX resin and eluted with buffer lacking NaCl (Figure 2). In contrast, most *N. atra* venom proteins were retained in the SCX tip column and eluted as two protein fractions (Figure 3A). The first fraction was eluted with buffers containing 0–40 mM NaCl, and the second with buffers containing 100–300 mM NaCl. When the same experimental conditions were applied to a mixture containing *N. atra* venom and human plasma proteins, the eluted profiles indicated that, as expected, the second fraction of venom proteins eluted with 100–300 mM NaCl was clearly separated from human plasma proteins (Figure 3B).

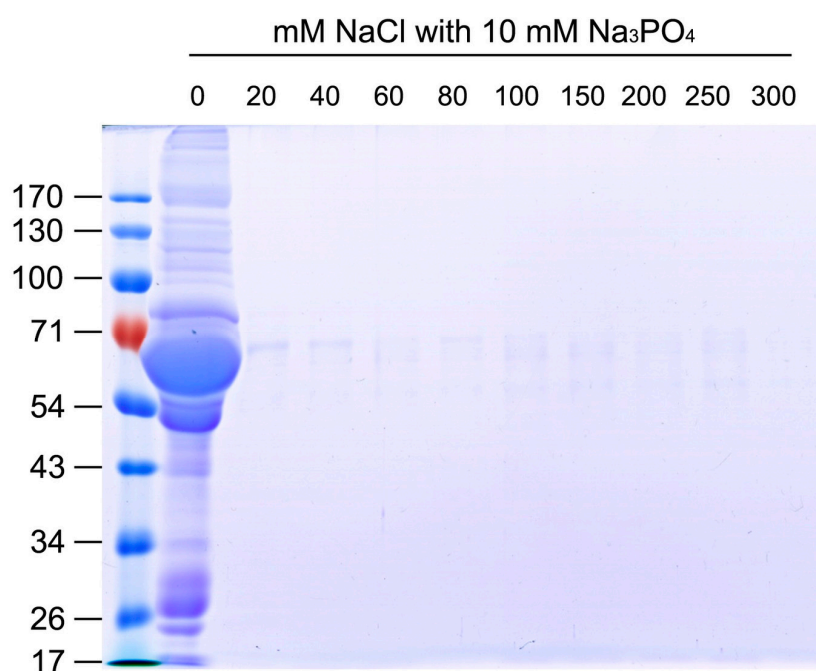


**Figure 2.** Separation of human plasma proteins with SCX tip column. Human plasma proteins (200 µg) were loaded onto the SCX tip column and eluted with buffer containing different NaCl concentrations. Each eluted fraction was precipitated with acetone and analyzed via 10% SDS-PAGE. Protein bands were visualized using Coomassie blue staining.

Upon application of the same experimental design to *B. multicinctus* venom and high-abundance human plasma proteins, similar results were obtained. *B. multicinctus* venom proteins were separated into two groups using the SCX tip column (Figure 4A). The first group of proteins appeared in fractions eluted with 0–60 mM NaCl and the second group with buffer containing 150–250 mM NaCl. Consistent with the above findings, the eluted protein profile clearly showed separation of venom proteins eluted with 150–250 mM NaCl from human plasma proteins (Figure 4B). Overall, these results are in keeping with expectations based on our estimation of pI values of venom proteins from both snakes and abundant proteins from human plasma. Accordingly, buffer containing 80 mM NaCl was utilized as wash buffer for the majority of plasma proteins, and buffer containing 300 mM NaCl was utilized as elution buffer for venom proteins retained in the SCX tip column.

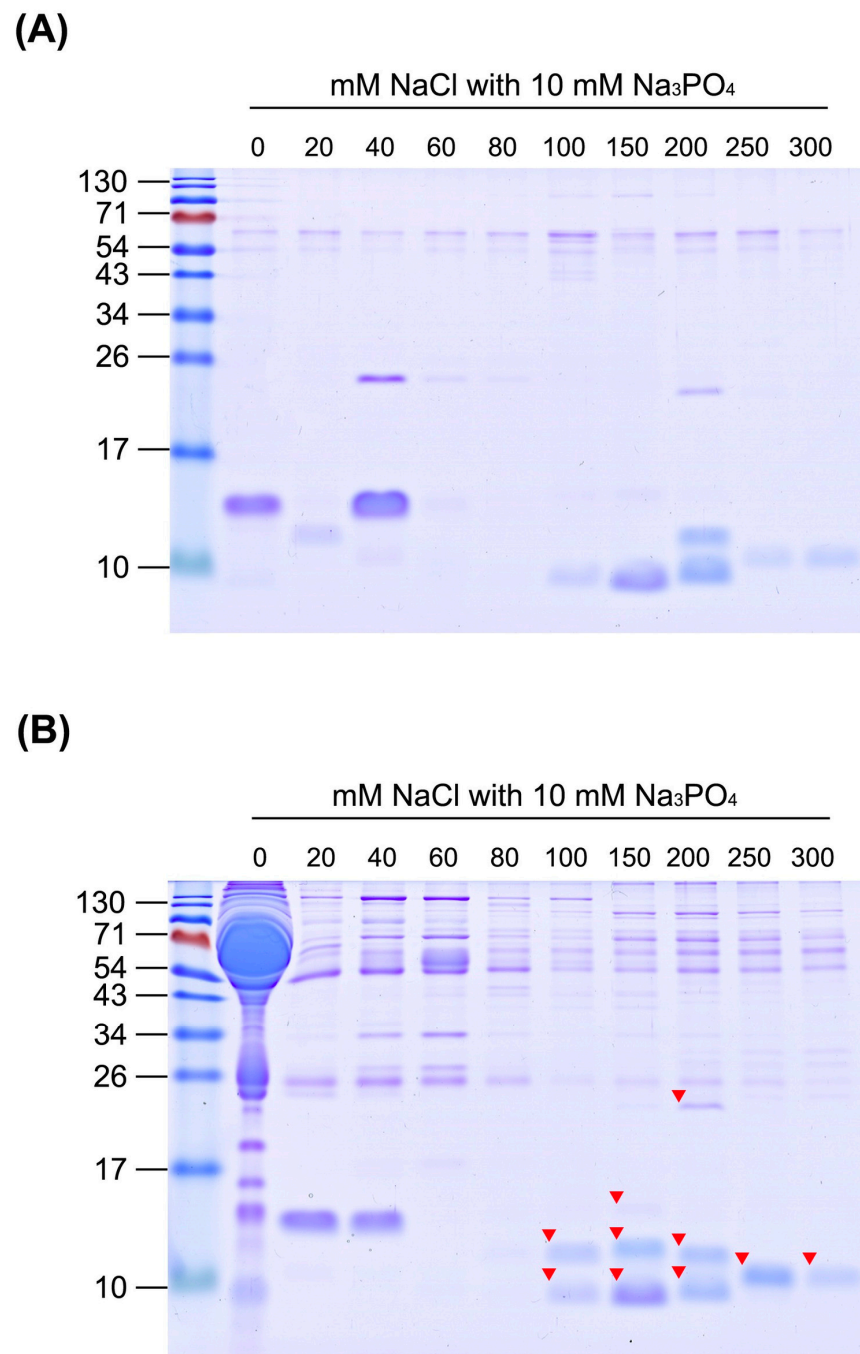


**Figure 3.** Separation of *N. atra* venom proteins from human plasma proteins with SCX tip column. **(A)** *N. atra* venom proteins (25 µg) and **(B)** a mixture containing *N. atra* venom proteins (25 µg) and human plasma proteins (100 µg) were, respectively, loaded onto SCX tip columns and stepwise-eluted with buffers containing different concentrations of NaCl. All eluted fractions were precipitated with acetone and half the precipitate analyzed using 15% SDS-PAGE. Protein bands were visualized via Coomassie blue staining. Arrowheads denote the bands excised for protein identification using liquid chromatography-tandem mass spectrometry (LC-MS/MS).



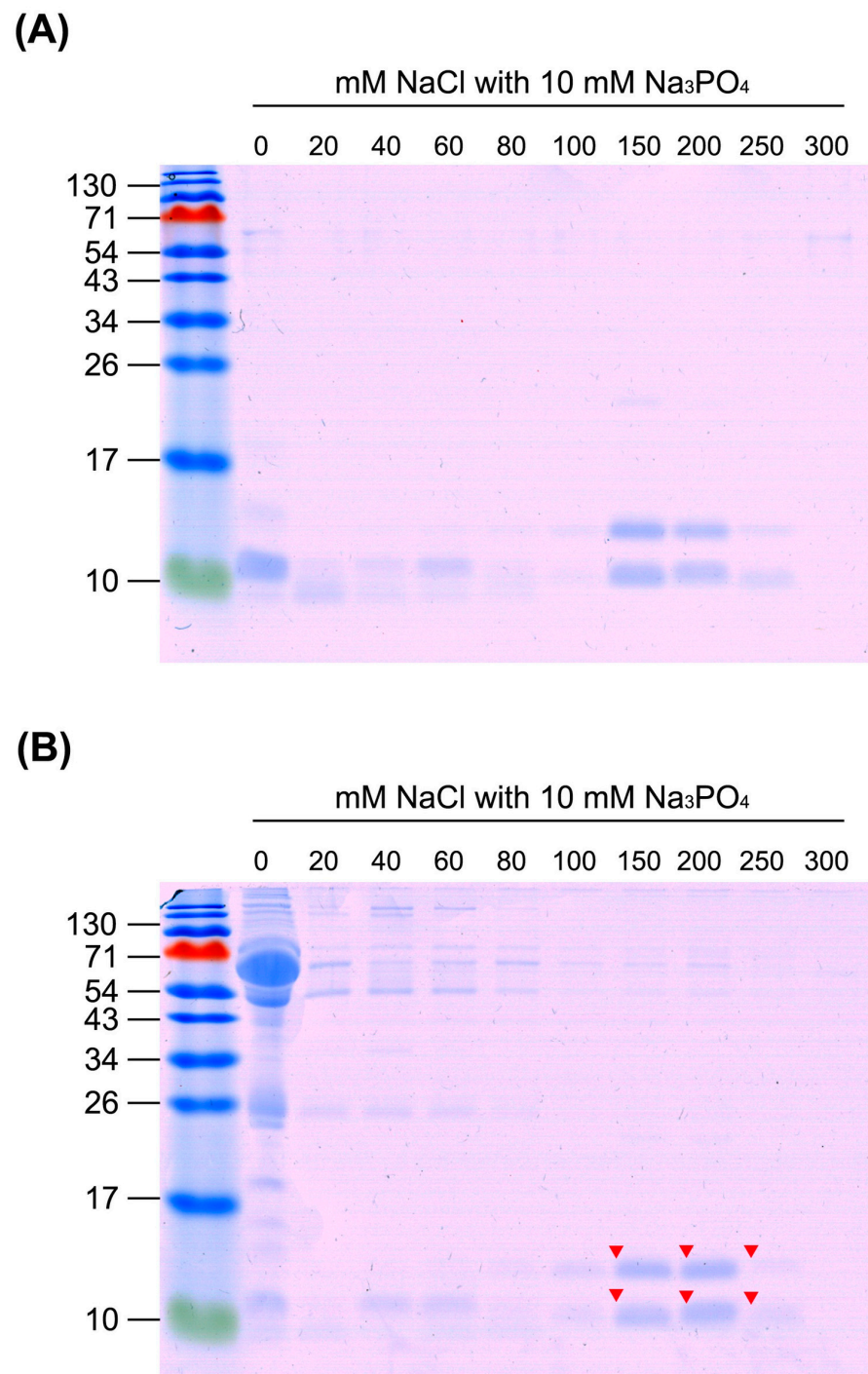


**Figure 4.** Separation of *B. multicinctus* venom proteins from human plasma proteins with the SCX tip column. **(A)** *B. multicinctus* venom proteins (25 µg) and **(B)** a mixture of *B. multicinctus* venom proteins (25 µg) and human plasma proteins (100 µg) were, respectively, loaded onto SCX tip column and stepwise-eluted with buffers containing different concentrations of NaCl. All eluted fractions were precipitated with acetone and half of the precipitate analyzed via 15% SDS-PAGE. Protein bands were visualized with Coomassie blue staining. Arrowheads denote the protein bands excised for protein identification using LC-MS/MS.

#### 2.4. Identification of SCX Tip Column-Enriched Snake Venom Proteins

To determine the identities of enriched venom proteins, marked protein bands on the gel (Figures 3B and 4B) were excised, digested with trypsin, and analyzed via liquid

chromatography-tandem mass spectrometry (LC-MS/MS). Among enriched proteins from *N. atra* venom, bands with lower molecular weight (~10 kDa) were identified as cytotoxins (CTX), probable weak neurotoxin, and long neurotoxin homolog, and those with higher molecular weight (~25 kDa) as the cysteine-rich venom protein natrin (Table 1). In addition, enriched protein from *B. multicinctus* venom was identified as beta-bungarotoxin (BBTX) (Table 1). Since this protein has two chains (A and B) linked via a disulfide bond, two protein bands were evident in reducing SDS-PAGE (Figure 4). According to the intensities of protein bands, CTXs and BBTX were determined as the predominantly enriched proteins from *N. atra* and *B. multicinctus* venom types, respectively.

**Table 1.** Summary of proteins identified in SCX-enriched venom protein samples via LC-MS/MS.

| Species        | Sample   | Accession | Description                          | Coverage (%) <sup>1</sup> | Peptides <sup>2</sup> | PSMs <sup>3</sup> | MW [kDa] | pI  |
|----------------|----------|-----------|--------------------------------------|---------------------------|-----------------------|-------------------|----------|-----|
| <i>N. atra</i> | 100mM-1  | P60304    | Cytotoxin 1                          | 35.8                      | 4                     | 10                | 9.0      | 8.7 |
|                | 100mM-2  | P60304    | Cytotoxin 1                          | 71.6                      | 11                    | 229               | 9.0      | 8.7 |
|                |          | P80245    | Cytotoxin 6                          | 58.0                      | 8                     | 103               | 9.0      | 8.9 |
|                |          | P01442    | Cytotoxin 2                          | 51.9                      | 7                     | 86                | 9.0      | 8.9 |
|                |          | P01443    | Cytotoxin 4                          | 51.9                      | 7                     | 86                | 9.1      | 9.0 |
|                | 150 mM-1 | P60304    | Cytotoxin 1                          | 35.8                      | 5                     | 12                | 9.0      | 8.7 |
|                |          | P80245    | Cytotoxin 6                          | 43.2                      | 5                     | 10                | 9.0      | 8.9 |
|                | 150 mM-2 | O93422    | Long neurotoxin homolog              | 22.1                      | 2                     | 6                 | 9.8      | 8.7 |
|                |          | Q9YGI2    | Probable weak neurotoxin NNAM1       | 22.1                      | 2                     | 6                 | 9.8      | 8.5 |
|                |          | Q9YGI4    | Probable weak neurotoxin NNAM2       | 25.6                      | 2                     | 10                | 9.9      | 8.6 |
|                | 150 mM-3 | P60304    | Cytotoxin 1                          | 71.6                      | 11                    | 356               | 9.0      | 8.7 |
|                |          | P80245    | Cytotoxin 6                          | 71.6                      | 12                    | 164               | 9.0      | 8.9 |
|                |          | P01442    | Cytotoxin 2                          | 59.3                      | 9                     | 124               | 9.0      | 8.9 |
|                |          | P01443    | Cytotoxin 4                          | 59.3                      | 9                     | 124               | 9.1      | 9.0 |
|                | 200 mM-1 | Q7ZZN8    | Cysteine-rich venom protein natrin-2 | 33.6                      | 9                     | 63                | 26.2     | 8.7 |
|                | 200 mM-2 | Q9YGI2    | Probable weak neurotoxin NNAM1       | 36.1                      | 4                     | 99                | 9.8      | 8.5 |
|                |          | O93422    | Long neurotoxin homolog              | 36.1                      | 4                     | 99                | 9.8      | 8.7 |
|                |          | Q9YGI4    | Probable weak neurotoxin NNAM2       | 25.6                      | 2                     | 37                | 9.9      | 8.6 |
|                | 200 mM-3 | P60301    | Cytotoxin 3                          | 60.5                      | 9                     | 178               | 9.0      | 9.0 |
|                |          | P60304    | Cytotoxin 1                          | 65.4                      | 9                     | 161               | 9.0      | 8.7 |
|                |          | P80245    | Cytotoxin 6                          | 58.0                      | 9                     | 115               | 9.0      | 8.9 |
|                | 250 mM-1 | P62375    | Cytotoxin A5                         | 45.8                      | 4                     | 44                | 9.3      | 9.0 |
|                | 300 mM-1 | P62375    | Cytotoxin A5                         | 46.0                      | 6                     | 17                | 9.3      | 9.0 |

Table 1. Cont.

| Species                | Sample   | Accession | Description  | Coverage (%) <sup>1</sup> | Peptides <sup>2</sup> | PSMs <sup>3</sup> | MW [kDa] | pI  |
|------------------------|----------|-----------|--|---------------------------|-----------------------|-------------------|----------|-----|
| <i>B. multicinctus</i> | 150 mM-1 | P00617    | Basic phospholipase A2 beta-bungarotoxin A1 chain                        | 21.1                      | 2                     | 5                 | 16.2     | 7.5 |
|                        | 150 mM-2 | P00987    | Kunitz-type serine protease inhibitor homolog beta-bungarotoxin B1 chain | 28.2                      | 3                     | 17                | 9.6      | 8.7 |
|                        | 200 mM-1 | P00617    | Basic phospholipase A2 beta-bungarotoxin A1 chain                        | 61.9                      | 9                     | 44                | 16.2     | 7.5 |
|                        | 200 mM-2 | P00987    | Kunitz-type serine protease inhibitor homolog beta-bungarotoxin B1 chain | 48.2                      | 5                     | 26                | 9.6      | 8.7 |
|                        | 250 mM-1 | P00617    | Basic phospholipase A2 beta-bungarotoxin A1 chain                        | 53.1                      | 7                     | 17                | 16.2     | 7.5 |
|                        | 250 mM-2 | P00987    | Kunitz-type serine protease inhibitor homolog beta-bungarotoxin B1 chain | 30.6                      | 3                     | 9                 | 9.6      | 8.7 |

<sup>1</sup> Coverage (%): Displays by default the percentage of the protein sequence covered by identified peptides. <sup>2</sup> Peptides: Displays the number of distinct peptide sequences in the protein. <sup>3</sup> PSMs: Displays the total number of identified peptide sequences (peptide spectral matches) for the protein, including those redundantly identified.

### 2.5. Evaluation of Venom Protein Enrichment Efficiency Via the SCX Tip Column

To evaluate the recovery rates of venom proteins, 5 µg BBTX was subjected to SCX tip column enrichment and enriched samples analyzed via SDS-PAGE with Coomassie blue staining. The recovery rate of BBTX during acetone precipitation, which is usually conducted to rapidly remove high salts from eluted fractions for SDS-PAGE analysis, was additionally evaluated. Compared to the amount of input, recovery rate of acetone precipitation was ~98%, and recovery of SCX tip column enrichment in conjunction with acetone precipitation was ~99% (Figure 5A). While small variations are possible due to operational errors, the results clearly suggest a >95% recovery rate via SCX tip column enrichment for BBTX. In addition, enrichment performance remained consistent between each manually prepared SCX tip column (Figure S1).

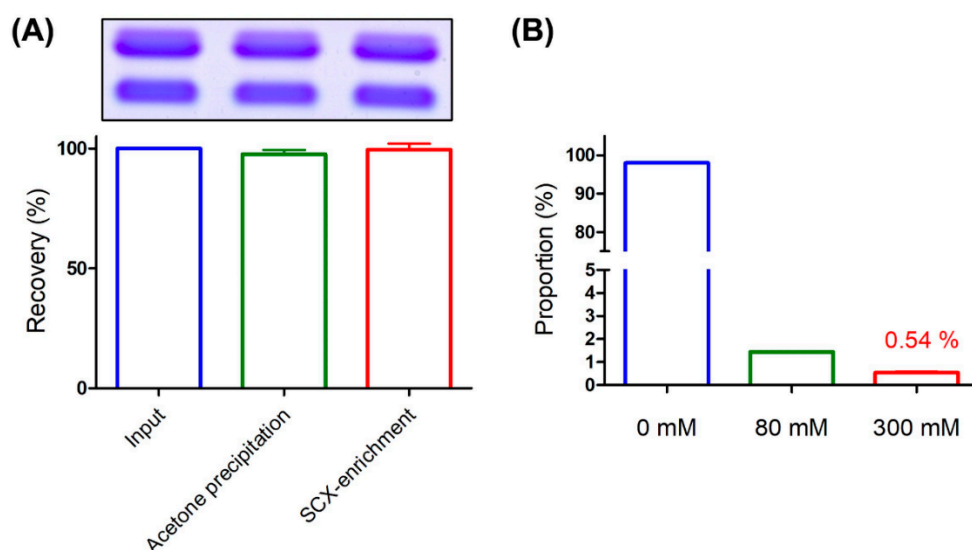


**Figure 5.** Evaluation of venom protein enrichment efficiency with the SCX tip column. **(A)** Purified BBTX (5 µg) was subjected to acetone precipitation and SCX tip column enrichment in conjunction with acetone precipitation. SDS-PAGE with Coomassie blue staining was conducted to evaluate the recovery rate of BBTX by comparing with the amount of input. **(B)** Human plasma (1 mg protein) was captured with a SCX tip column and eluted with 0, 80, and 300 mM NaCl buffer. Each eluted fraction was quantified using BCA and the proportion of plasma proteins in individual fractions calculated. The bar charts depict the average of triplicate results with standard deviation (SD).

To further evaluate the ability to remove background plasma during the enrichment process, human plasma containing 1 mg protein was captured using the SCX tip column and eluted stepwise with buffer containing 0, 80, and 300 mM NaCl (Figure 5B). Each eluted fraction was quantified using the BCA protein assay kit and the proportion of plasma proteins calculated. Our results showed that >95% plasma proteins were depleted upon washing with 0 mM NaCl and only 0.54% remained in the fraction eluted with 300 mM NaCl buffer, clearly indicating that the majority of plasma proteins are efficiently removed with this technique.

## 2.6. Combination of SCX-Tip Column Enrichment with Snakebite Detection Assays

We hypothesized that application of SCX tip column enrichment should facilitate the concentration and purification of venom proteins from clinical samples to aid in the development of efficient bioassays for snakebite detection (Figure 6). To evaluate the feasibility of SCX tip column enrichment, samples prepared by mixing snake venom with human plasma to mimic clinical specimens from snakebite patients were enriched using the SCX tip column and subsequently tested with lateral flow strips developed previously [9] to distinguish between hemorrhagic and neurotoxic snake venoms in Taiwan. A positive signal would appear on the hemorrhagic test line (H line) when the test sample contained *T. stejnegeri* or *P. mucrosquamatus* venom proteins and on the neurotoxic test line (N line) in cases where the test sample contained *B. multicinctus* or *N. atra* venom proteins. The positive signal of the control line signified successful movement of HSS-Ab (hemorrhagic species-specific antibody)- or NSS-Ab (neurotoxic species-specific antibody)-conjugated colloidal gold to the top of the lateral flow strip (i.e., as quality control of the strip). Snake venom was serially diluted with human plasma into four concentrations (50, 10, 5, and 1 ng/mL) and subjected to two different tests. One sample was processed via SCX tip column enrichment before being subjected to the rapid test, and the other was directly examined with the rapid test.



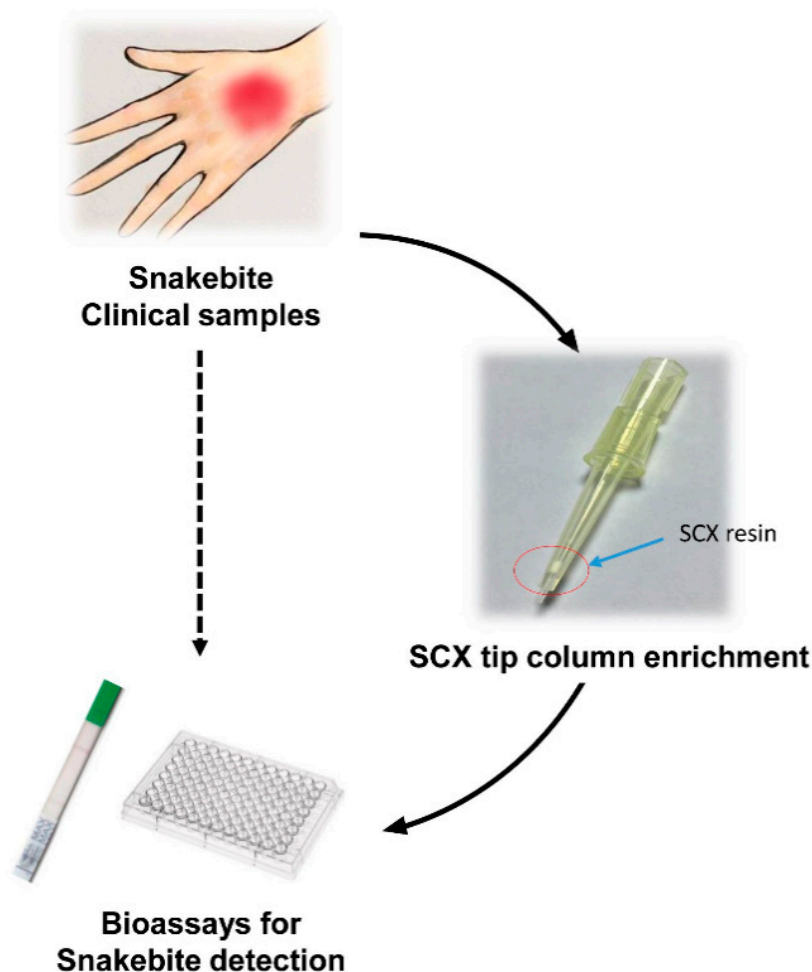


**Figure 6.** Flowchart of hypothetical usage of SCX tip column-based enrichment of venom proteins.

Following SCX tip column enrichment, signals of *B. multicinctus* samples were significantly magnified (Figure 7A). The sample with the lowest concentration (1 ng/mL) still displayed visible bands and detectable signals on the N line compared with the blank control (Figure 7B). The detection limit was enhanced from 5 ng/mL to 1 ng/mL with this process. Consistently, the signal from *N. atra* venom samples was clearer after enrichment (Figure 8A). Following enrichment, the 5 ng/mL sample displayed a visual band on the N line with a relative signal (measured via densitometry analysis) three times higher than that of the blank control and the original sample prior to enrichment. On the other hand, we observed no detectable signal on the N line of the strip with the 1 ng/mL sample before and after SCX tip column enrichment (Figure 8B). These results support our hypothesis that the SCX tip column-based enrichment method developed in this study could successfully increase the sensitivity of lateral flow strip assay for detection of *Elapidae* snake venoms. Furthermore, this device may be further incorporated with other bioassays to improve snakebite diagnosis worldwide.

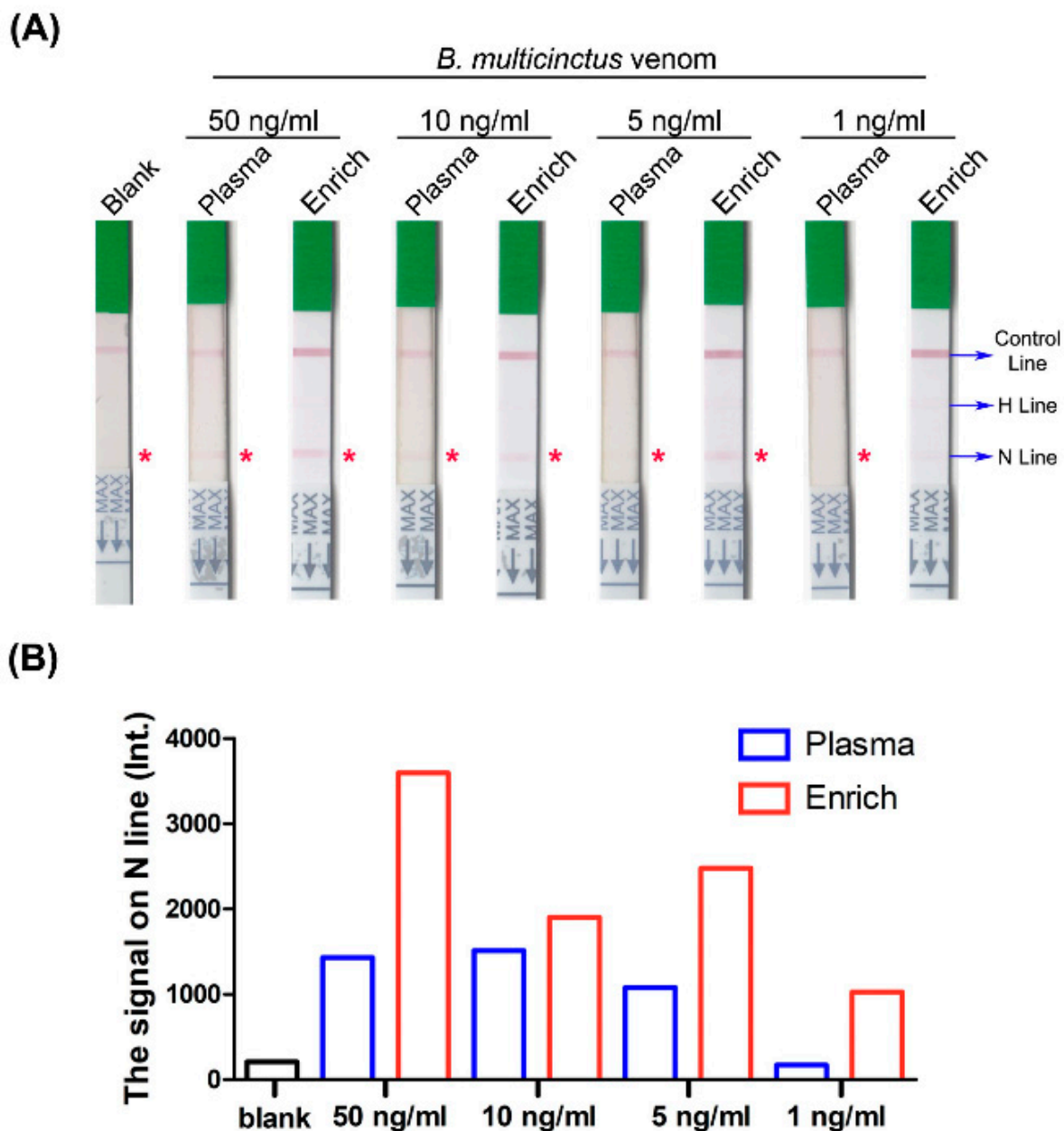


**Figure 7.** Detection of *B. multicinctus* venom proteins in human plasma before and after SCX tip column enrichment via the lateral flow strip assay. **(A)** *B. multicinctus* venom was serially diluted with human plasma into four concentrations, processed with or without SCX tip column enrichment, and tested with lateral flow strips. Blank, plasma sample without venom; Plasma, venom-containing plasma before enrichment; Enrich, venom-containing plasma after enrichment; H line, hemorrhagic test line; N line, neurotoxic test line. The asterisk (\*) denotes the position of N line on each strip. **(B)** Quantification of the signal on the N line via densitometry analysis using ImageJ software.

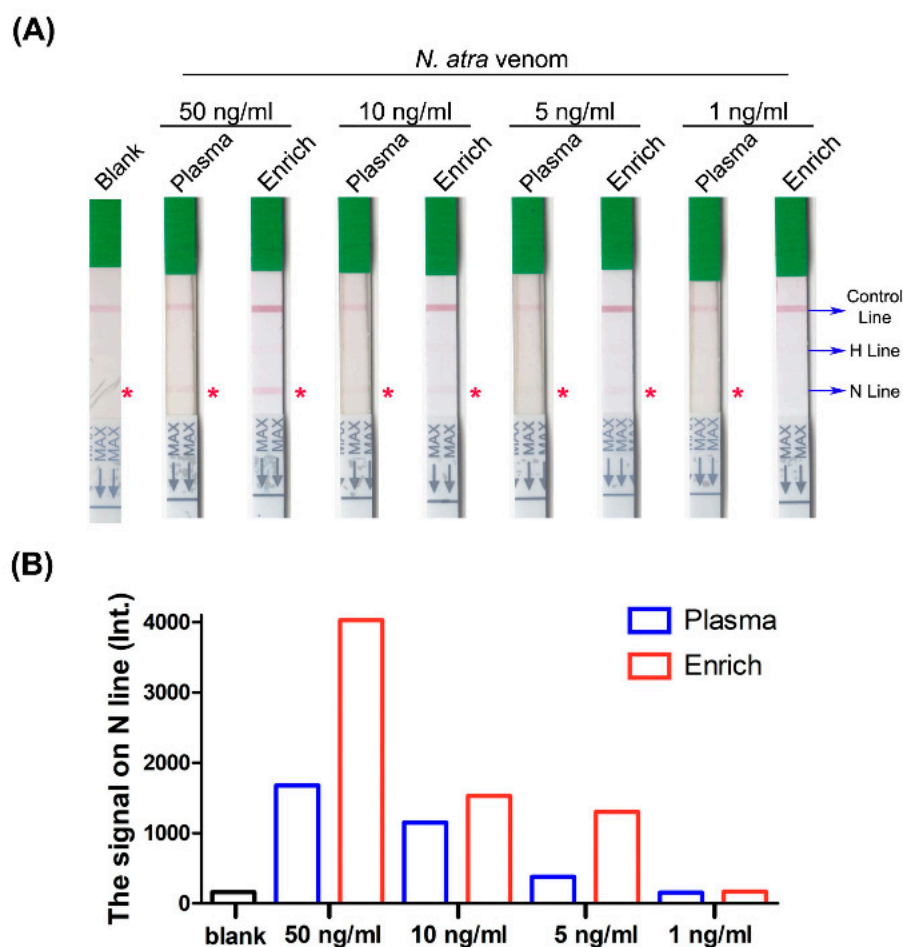


**Figure 8.** Detection of *N. atra* venom proteins in human plasma before and after SCX tip column enrichment with the lateral flow strip assay. (A) *N. atra* venom was serially diluted with human plasma into four concentrations, processed with or without SCX tip column enrichment, and tested with lateral flow strips. Blank, plasma sample without venom; Plasma, venom-containing plasma before enrichment; Enrich, venom-containing plasma after enrichment; H line, hemorrhagic test line; N line, neurotoxic test line. The asterisk (\*) denotes the position of N line on each strip. (B) Quantification of the signal on the N line via densitometry analysis using ImageJ software.

### 3. Discussion

Here, we examined the hypothesis that different isoelectric points (pI values) of plasma proteins and venom proteins could be used for separation via a SCX tip column-based protocol with buffers containing different NaCl concentrations. Our newly developed enrichment method successfully removed >95% plasma protein background and enhanced the detection limit of the lateral strip assay for snake venom proteins.

A number of recent studies have reported one-step purification methods for venom protein enrichment [11–13]. For instance, affinity chromatography-based methods can be effectively used to obtain high-purity (~90%) targeted toxins. However, this procedure is time-consuming, requiring 1–2 h to capture proteins from the matrix [12,13]. Additionally, elution buffers of this methodology usually require extreme pH, necessitating eluted proteins to be processed by buffer exchange or diluted with neutralizing solution before further application. Therefore, the affinity chromatography-based method is appropriate to enrich venom proteins for further pharmacological application or research, but not suitable for combination with bioassays for snake venom detection. Our SCX tip column enrichment method is similar to that of Guan et al. (2018) [11], which is also based on solid-phase extraction (SPE). They used a commercial mixed-mode SPE cartridge to trap

cobrotoxin, a neurotoxin from *Naja* species, which was eluted with 70% ACN buffer. The high concentration of ACN in elution buffer was applied for further LC-MS/MS analysis. However, high levels of organic solvents disrupt antibody-antigen interactions and may not be appropriate for combination with most antibody-based bioassays and biosensors. The SCX tip column-based method developed in this study requires only 5–10 min for target protein enrichment, which is suitable for the immediate diagnostic requirement of snakebite management in an emergency. Moreover, the buffer system used in this enrichment technique does not require extreme pH or high concentrations of organic solvents. The NaCl-based buffer can preserve affinity interactions between antibodies and antigens and is thus more applicable while combining with antibody-based assay platforms. In addition to lateral flow strip assay, SCX tip column enrichment may be efficiently combined with other bioassays or biosensors for snake venom detection, such as ELISA [14], surface plasmon resonance [15,16], and optical biosensors [17], to achieve the goal of early detection with high sensitivity.

In the future, this method can be applied to enrich proteins from other medically significant venom samples to facilitate accurate snakebite diagnosis. According to our preliminary survey, several venom proteins other than *N. atra* and *B. multicinctus* from *Elapidae* snakes have the property of high pI value and may thus be efficiently separated from human plasma via SCX tip column enrichment. For example, *Ophiophagus hannah* venom is mainly composed of 3FTX with a pI value of around 8.5 [18] and *Dendroaspis polylepsis* venom mainly comprises Kunitz-type serine protease inhibitors with a pI value of 9.93 [19]. Both snake venoms are potential candidates for application of our enrichment method. However, this technique has a number of limitations. Our study design is based on the difference in pI values between venom and plasma proteins, and its application may not be appropriate to enrich venom samples whose major protein components have lower pI values than plasma proteins. For instance, the venom of *Bothrops atrox*, a viper from Brazil, is mostly composed of snake venom metalloproteinases with a pI value of around 5.8, which is similar to that of high-abundance human plasma proteins [20], and would therefore not be suitable for protein enrichment using the SCX tip column.

#### 4. Conclusions

In conclusion, we have developed an SCX tip column enrichment method that can be used to rapidly enrich snake venom proteins from human plasma. This technique facilitates removal of >95% of the plasma background, thereby enhancing the venom protein signal on lateral flow strip assays, leading to an increase in the detection limit from 5 ng/mL to 1 ng/mL for *B. multicinctus* venom and 10 ng/mL to 5 ng/mL for *N. atra* venom. Effective concentration of target venom proteins and removal of the background matrix from biological samples by the SCX tip column not only improves the sensitivity of the lateral flow strip assay, but also has the potential to enhance the performance of other snake venom detection assays or biosensors. In addition, target venoms are not limited to Taiwanese cobra and krait. Other *Elapidae* snake venoms containing proteins with higher pI values are expected to be enriched using this easily operable device. Our novel rapid, simple, and cost-effective method should aid in improving the clinical utility of snakebite diagnostic assays.

#### 5. Materials and Methods

##### 5.1. Snake Venom

Lyophilized venom of *N. atra* and *B. multicinctus* was obtained from the Centers for Disease Control, R.O.C. (Taiwan). Purified beta-bungarotoxin was purchased from Biotium (Hayward, CA, USA).

##### 5.2. Strong Cation Exchange High-Performance Liquid Chromatography (SCX-HPLC)

The sample was dissolved in solution A (50 mM Na<sub>3</sub>PO<sub>4</sub>, pH 6.8) and separated via HPLC using a Mono S 4.6/100PE column. The flow rate was set to 1 mL/min and the



column eluted with a linear gradient of solution A and solution B (50 mM Na<sub>3</sub>PO<sub>4</sub>, 1 M NaCl, pH 6.8) as follows: Isocratic (0% solution B for 3 min), followed by linear gradients of 0–70% solution B for 40 min, 70–100% solution B for 2 min, isocratic 100% B for 3 min, linear gradient of 70–0% solution B for 2 min, and subsequent re-equilibration with 0% solution B for 10 min. Peaks were detected by monitoring absorbance at 214 nm.

### 5.3. Separation of Venom and Plasma Proteins Using the Strong Cation Exchange (SCX) Tip Column

The tip column composed of Axygen® 200 µL universal fit pipet tips (Product Number: TR-222-Y, Corning, Arizona, USA) and a glass fiber filter (Product Number: 240-1, Cambridge Technology Inc., Massachusetts, U.S.A) was manually prepared. The detailed process of generating the tip column is presented in Supplemental Figure S2. Each tip column was packed with 20 µL.

SOURCE 30S medium (GE healthcare, IL, USA), washed with 100 µL elution buffer (300 mM NaCl, 10 mM Na<sub>3</sub>PO<sub>4</sub>, pH 7.4, 25% ACN) and equilibrated with 100 µL equilibration buffer (10 mM Na<sub>3</sub>PO<sub>4</sub>, pH 7.4, 25% ACN). Two volumes of wash buffer (80 mM NaCl, 10 mM Na<sub>3</sub>PO<sub>4</sub>, pH 7.4, 25 % ACN) were added to the sample (200 µL buffer to 100 µL sample) and the diluted sample flushed through the SCX tip column twice. The column was subsequently washed with 100 µL of wash buffer three times. Finally, enriched proteins were eluted with 60 µL buffer. Enriched samples were used immediately or stored at −20 °C for further use.

### 5.4. Acetone Precipitation

Protein sample (200 µL) was mixed with 800 µL of 100% acetone and incubated at −20 °C overnight to precipitate proteins. Samples were centrifuged at 16,000× *g* for 10 min at 4 °C. The resulting supernatant was removed and precipitated sample dried using SpeedVac. Dried samples were stored at −20 °C or dissolved in sample buffer for SDS-PAGE.

### 5.5. In-Gel Tryptic Digestion

Selected protein bands were excised from the gel and subjected to in-gel tryptic digestion, as described by Lin et al. [21]. Gel pieces were destained with 40% ACN containing 30 mM ammonium bicarbonate for 15 min. After removal of the solution, the gel was incubated in 25 mM ammonium bicarbonate for 15 min, which was removed, followed by incubation in 100% ACN for 5 min. Following removal of ACN, the gel was reduced with 10 mM dithiothreitol at 56 °C for 45 min. Dithiothreitol was washed off, and the gel alkylated with 55 mM iodoacetamide at room temperature in the dark for 30 min. After washing off iodoacetamide, the gel was incubated in 40% ACN containing 30 mM ammonium bicarbonate for 15 min and finally, 100% ACN for 5 min. ACN was washed off, proteins in the processed gel pieces digested with freshly prepared 20 µg/mL trypsin solution (Promega, Madison, WI, USA) in 25 mM ammonium bicarbonate at 37 °C for 16 h, and extracted with 100% ACN containing 1% TFA. Tryptic peptide extracts were concentrated with SpeedVac and stored at −20 °C before use.

### 5.6. LC-MS/MS Analysis

Each peptide sample was reconstituted with 0.1% formic acid (FA) and analyzed on a nano-LC–LTQ–Orbitrap Hybrid Mass Spectrometer (Thermo Fisher, CA, USA) as described previously [22]. Briefly, samples were loaded across a trap column (Zorbax 300SB-C18, 0.3 × 5 mm; Agilent Technologies, Wilmington, DE, USA) at a flow rate of 0.2 µL/min in HPLC buffer (0.1% FA) and separated on a resolving 10 cm analytical C18 column (inner diameter, 75 µm) using a 15 µm tip (New Objective, Woburn, MA, USA). Peptides were eluted using a linear gradient of 0–10% HPLC elution buffer (99.9% ACN containing 0.1% FA) for 3 min, 10–30% buffer B for 35 min, 30–35% buffer B for 4 min, 35–50% buffer B for 1 min, 50–95% buffer B for 1 min, and 95% buffer B for 8 min, with a flow rate of 0.25 µL/min across the analytical column. The resolution of Orbitrap was 30,000, and the ion signal

of  $(\text{Si}(\text{CH}_3)_2\text{O})_6\text{H}^+$  at 445.120025 ( $m/z$ ) used as a lock mass for internal calibration. One MS scan alternating with six MS/MS scans for the 10 most abundant precursor ions was applied. The  $m/z$  values selected for MS/MS were dynamically excluded for 180 s. For MS scans, the  $m/z$  value of the scan range was 400–2000 Da. For MS/MS scans,  $>1 \times 10^4$  ions accumulated in the ion trap to generate spectra. MS and MS/MS spectra were acquired using one scan with maximum fill times of 1000 and 100 ms, respectively.

#### 5.7. Database Searches and Bioinformatics Analysis

Raw MS data files were analyzed using Proteome Discoverer Software (version 1.3.0.339; Thermo Fisher, San Jose, CA, USA) and searched against the UniProt database (Taxonomy: Other lobe-finned fish and tetrapods) using the MASCOT search engine (version 2.2; Matrix Science, London, UK). The enzyme specificity parameter was set to “trypsin” and one missed cleavage was allowed. Carbamidomethylation of cysteines was set as a static modification, and oxidation of methionine, acetyl (protein N-term), and Gln->pyro-Glu (N-term Q) set as dynamic modifications. The tolerance of MS was 10 ppm, and that of MS/MS was 0.5 Da. The decoy database search approach was assessed for peptide identification and threshold of target false discovery rate (FDR) estimated as  $<0.01$ . Each reported protein ID should have at least two peptides present in the sample, at least one of which is the unique peptide for the reported protein.

#### 5.8. Venom Detection with Lateral Flow Strips

Lateral flow strips for detection of *N. atra* and *B. multicinctus* venom proteins were designed as described previously [9]. Briefly, conjugate pads were saturated with colloidal gold conjugated with HSS-Ab (hemorrhagic species-specific antibodies) or NSS-Ab (neurotoxic species-specific antibodies) and dried at 37 °C for 1 h before assembly. Nitrocellulose membrane was pasted onto the cardboard followed by conjugated and absorbent pads that overlapped each side of the nitrocellulose membrane by about 2 mm. The sample pad was also laid over the absorbent pad and pasted onto the cardboard. The AGISMA RT RP-1000 immuno-strip printer (REGA Biotechnology Inc., Taipei, Taiwan) was used to dispense HSS-Abs and NSS-Abs (2 mg/mL) onto hemorrhagic and neurotoxic test lines (H and N lines), respectively, and goat anti-horse IgG antibody (2 mg/mL) (REGA Biotechnology Inc.) onto the control line on the nitrocellulose membrane. The distance between each line was 5 mm. Strips were prepared and assembled in a low-humidity environment, packaged into an aluminum pouch, and stored at room temperature before use. Mimic snake venom samples were subjected to SCX tip column enrichment and the enriched sample (100–200 µL) subsequently diluted with an equal volume of reaction buffer (100 mM borax, 250 nM polyvinylpyrrolidone (PVP)—40 and 1% Triton X-100) in a microcentrifuge tube. Lateral flow strips were directly soaked in the samples, and the results were recorded after a 15-min reaction. The signal intensity on the neurotoxic test line was quantified via densitometry using ImageJ software [23].

**Supplementary Materials:** The following are available online at <https://www.mdpi.com/2072-6651/13/2/140/s1>, Table S1: pI values of high-abundance human plasma proteins (Top-14) and snake venom proteins. Figure S1: Reproducibility of *B. multicinctus* venom enrichment using different manual SCX-tip columns. *B. multicinctus* venom (20 µg protein) was subjected to venom protein enrichment using three different SCX tip columns. Venom proteins absorbed on each column were eluted by 300 mM NaCl and analyzed by SDS-PAGE, followed by Coomassie blue staining. Figure S2: Procedure of making a tip column. A 200 µL polypropylene tip was cut into 3 segments. Segment-1 (S1) was placed onto segment-3 (S3), and pieces of glass fiber filter inserted into the upper site of S1 to form the tip column.

**Author Contributions:** Conceptualization, C.-C.L. (Chien-Chun Liu) and Y.-H.Y.; methodology, C.-C.L. (Chien-Chun Liu) and Y.-C.H.; formal analysis, Y.-H.Y., P.-J.W. and J.-C.L.; investigation, C.-C.L. (Chien-Chun Liu) and Y.-H.Y.; resources, C.-H.L., W.-C.H. and C.-C.L. (Chih-Chuan Lin); data curation, Y.-C.H. and J.-S.Y.; writing—original draft preparation, C.-C.L. (Chien-Chun Liu) and Y.-H.Y.; writing—review and editing, J.-S.Y.; supervision, J.-S.Y.; project administration, C.-C.L.

(Chien-Chun Liu); funding acquisition, J.-S.Y. All authors have read and agreed to the published version of the manuscript.

**Funding:** This research was funded by the “Molecular Medicine Research Center, Chang Gung University” from The Featured Areas Research Center Program within the framework of the Higher Education Sprout Project by the Ministry of Education (MOE) in Taiwan.

**Institutional Review Board Statement:** Not applicable.

**Informed Consent Statement:** Not applicable.

**Acknowledgments:** We thank Kun-Yi Chien from “Proteomics Core Laboratory, Molecular Medicine Research Center, Chang Gung University” for the excellent assistance with the venom protein identification presented in this investigation.

**Conflicts of Interest:** The authors have no conflict of interest to declare.

## References

- Kasturiratne, A.; Wickremasinghe, A.R.; de Silva, N.; Gunawardena, N.K.; Pathmeswaran, A.; Premaratna, R.; Savioli, L.; Lalloo, D.G.; de Silva, H.J. The global burden of snakebite: A literature analysis and modelling based on regional estimates of envenoming and deaths. *PLoS Med.* **2008**, *5*, e218. [\[CrossRef\]](#) [\[PubMed\]](#)
- Chen, J.C.; Liaw, S.J.; Bullard, M.J.; Chiu, T.F. Treatment of poisonous snakebites in northern Taiwan. *J. Formos Med. Assoc.* **2000**, *99*, 135–139.
- Kuo, T.P.; Wu, C.S. Clinico-pathological studies on snakebites in Taiwan. *Taiwan Yi Xue Hui Za Zhi* **1972**, *71*, 447–466.
- Liau, M.Y.; Huang, R.J. Toxoids and antivenoms of venomous snakes in Taiwan. *J. Toxicol. Toxin Rev.* **1997**, *16*, 163–175.
- Mao, Y.C.; Liu, P.Y.; Chiang, L.C.; Lai, C.S.; Lai, K.L.; Ho, C.H.; Wang, T.H.; Yang, C.C. Naja atra snakebite in Taiwan. *Clin. Toxicol.* **2018**, *56*, 273–280. [\[CrossRef\]](#)
- Huang, Y.P.; Yu, Y.J.; Hung, D.Z. Sandwich enzyme-linked immunosorbent assay for Taiwan cobra venom. *Vet. Hum. Toxicol.* **2002**, *44*, 200–204. [\[PubMed\]](#)
- Hung, D.Z.; Liau, M.Y.; Lin-Shiau, S.Y. The clinical significance of venom detection in patients of cobra snakebite. *Toxicon* **2003**, *41*, 409–415. [\[CrossRef\]](#)
- Hung, D.Z.; Lin, J.H.; Mo, J.F.; Huang, C.F.; Liau, M.Y. Rapid diagnosis of Naja atra snakebites. *Clin. Toxicol.* **2014**, *52*, 187–191. [\[CrossRef\]](#) [\[PubMed\]](#)
- Liu, C.C.; Yu, J.S.; Wang, P.J.; Hsiao, Y.C.; Liu, C.H.; Chen, Y.C.; Lai, P.F.; Hsu, C.P.; Fann, W.C.; Lin, C.C. Development of sandwich ELISA and lateral flow strip assays for diagnosing clinically significant snakebite in Taiwan. *PLoS Negl. Trop. Dis.* **2018**, *12*, e0007014. [\[CrossRef\]](#)
- Pawade, B.S.; Salvi, N.C.; Shaikh, I.K.; Waghmare, A.B.; Jadhav, N.D.; Wagh, V.B.; Pawade, A.S.; Waykar, I.G.; Potnis-Lele, M. Rapid and selective detection of experimental snake envenomation—Use of gold nanoparticle based lateral flow assay. *Toxicon* **2016**, *119*, 299–306. [\[CrossRef\]](#)
- Guan, F.; You, Y.; Li, X.; Robinson, M.A. Detection and confirmation of alpha-cobratoxin in equine plasma by solid-phase extraction and liquid chromatography coupled to mass spectrometry. *J. Chromatogr. A* **2018**, *1533*, 38–48. [\[CrossRef\]](#)
- Timms, M.; Ganio, K.; Steel, R. Extraction of alpha-neurotoxins from equine plasma by receptor based affinity purification. *Drug Test Anal.* **2020**. [\[CrossRef\]](#)
- Saavedra, S.L.; Acosta, G.; Avila, L.; Giudicessi, S.L.; Camperi, S.A.; Albericio, F.; Cascone, O.; Martinez Ceron, M.C. Use of a phosphopeptide as a ligand to purify phospholipase A2 from the venom of Crotalus durissus terrificus by affinity chromatography. *J. Chromatogr. B Analyt. Technol. Biomed. Life Sci.* **2020**, *1146*, 122070. [\[CrossRef\]](#)
- Theakston, R.D.; Laing, G.D. Diagnosis of snakebite and the importance of immunological tests in venom research. *Toxins* **2014**, *6*, 1667–1695. [\[CrossRef\]](#) [\[PubMed\]](#)
- Faure, G.; Copic, A.; Le Porrier, S.; Gubensek, F.; Bon, C.; Krizaj, I. Crotoxin acceptor protein isolated from Torpedo electric organ: Binding properties to crotoxin by surface plasmon resonance. *Toxicon* **2003**, *41*, 509–517. [\[CrossRef\]](#)
- Choudhury, S.N.; Konwar, B.; Kaur, S.; Doley, R.; Mondal, B. Study on Snake Venom Protein-Antibody Interaction by Surface Plasmon Resonance Spectroscopy. *Photonic Sens.* **2018**, *8*, 193–202. [\[CrossRef\]](#)
- Rogers, K.R.; Valdes, J.J.; Eldefrawi, M.E. Effects of receptor concentration, media pH and storage on nicotinic receptor-transmitted signal in a fiber-optic biosensor. *Biosens. Bioelectron.* **1991**, *6*, 1–8. [\[CrossRef\]](#)
- Tan, C.H.; Tan, K.Y.; Fung, S.Y.; Tan, N.H. Venom-gland transcriptome and venom proteome of the Malaysian king cobra (Ophiophagus hannah). *BMC Genom.* **2015**, *16*, 687. [\[CrossRef\]](#)
- Laustsen, A.H.; Lomonte, B.; Lohse, B.; Fernandez, J.; Gutierrez, J.M. Unveiling the nature of black mamba (Dendroaspis polylepis) venom through venomomics and antivenom immunoprofiling: Identification of key toxin targets for antivenom development. *J. Proteom.* **2015**, *119*, 126–142. [\[CrossRef\]](#)

20. Monteiro, W.M.; Contreras-Bernal, J.C.; Bisneto, P.F.; Sachett, J.; Mendonca da Silva, I.; Lacerda, M.; Guimaraes da Costa, A.; Val, F.; Brasileiro, L.; Sartim, M.A.; et al. Bothrops atrox, the most important snake involved in human envenomings in the amazon: How venomomics contributes to the knowledge of snake biology and clinical toxinology. *Toxicon X* **2020**, *6*, 100037. [[CrossRef](#)]
21. Liu, C.C.; You, C.H.; Wang, P.J.; Yu, J.S.; Huang, G.J.; Liu, C.H.; Hsieh, W.C.; Lin, C.C. Analysis of the efficacy of Taiwanese freeze-dried neurotoxic antivenom against Naja kaouthia, Naja siamensis and Ophiophagus hannah through proteomics and animal model approaches. *PLoS Negl. Trop. Dis.* **2017**, *11*, e0006138. [[CrossRef](#)] [[PubMed](#)]
22. Liu, C.C.; Chou, Y.S.; Chen, C.Y.; Liu, K.L.; Huang, G.J.; Yu, J.S.; Wu, C.J.; Liaw, G.W.; Hsieh, C.H.; Chen, C.K. Pathogenesis of local necrosis induced by Naja atra venom: Assessment of the neutralization ability of Taiwanese freeze-dried neurotoxic antivenom in animal models. *PLoS Negl. Trop. Dis.* **2020**, *14*, e0008054. [[CrossRef](#)] [[PubMed](#)]
23. Mendez, R.; Bonilla, F.; Sasa, M.; Dwyer, Q.; Fernandez, J.; Lomonte, B. Proteomic profiling, functional characterization, and immunoneutralization of the venom of Porthidium porrasii, a pitviper endemic to Costa Rica. *Acta Trop.* **2019**, *193*, 113–123. [[CrossRef](#)] [[PubMed](#)]




RESEARCH

Open Access



# Multifunctional lipid-based nanocarriers with antibacterial and anti-inflammatory activities for treating MRSA bacteremia in mice

Chia-Chih Liao<sup>1,2†</sup>, Huang-Ping Yu<sup>1,2†</sup>, Shih-Chun Yang<sup>3</sup>, Ahmed Alalaiwe<sup>4</sup>, You-Shan Dai<sup>5</sup>, Fu-Chao Liu<sup>1,2\*</sup> and Jia-You Fang<sup>1,5,6\*</sup> 

## Abstract

**Background:** Bacteremia-induced sepsis is a leading cause of mortality in intensive care units. To control a bacterial infection, an immune response is required, but this response might contribute to organ failure. Kidneys are one of the main organs affected by bacteremia. Combination therapies with antibacterial and anti-inflammatory effects may be beneficial in treating bacteremia. This study aimed to develop nanostructured lipid carriers (NLCs) loaded with ciprofloxacin and rolipram that exert a combination of anti-methicillin-resistant *Staphylococcus aureus* (MRSA) and anti-inflammatory effects. Retinol was incorporated into the nanoparticles to transport retinol-binding protein 4 (RBP4) to the kidneys, which abundantly express RBP receptors. The NLCs were fabricated by high-shear homogenization and sonication, and neutrophils were used as a model to assess their anti-inflammatory effects. Mice were injected with MRSA to establish a model of bacteremia with organ injury.

**Results:** The mean nanoparticle size and zeta potential of the NLCs were 171 nm and  $-39$  mV, respectively. Ciprofloxacin (0.05%, w/v) and rolipram (0.02%) achieved encapsulation percentages of 88% and 96%, respectively, in the nanosystems. The minimum bactericidal concentration of free ciprofloxacin against MRSA increased from 1.95 to 15.63  $\mu\text{g/ml}$  when combined with rolipram, indicating a possible drug-drug interaction that reduced the antibacterial effect. Nanoparticle inclusion promoted the anti-MRSA activity of ciprofloxacin according to time-kill curves. The NLCs were found to be largely internalized into neutrophils and exhibited superior superoxide anion inhibition than free drugs. Retinol incorporation into the nanocarriers facilitated their efficient targeting to the kidneys. The NLCs significantly mitigated MRSA burden and elastase distribution in the organs of MRSA-infected animals, and the greatest inhibition was observed in the kidneys. Bacterial clearance and neutrophil infiltration suppression attenuated the bacteremia-induced cytokine overexpression, leading to an improvement in the survival rate from 22% to 67%.

**Conclusions:** The dual role of our NLCs endowed them with greater efficacy in treating MRSA bacteremia than that of free drugs.

**Keywords:** Nanostructured lipid carriers, Ciprofloxacin, Rolipram, Bacteremia, Methicillin-resistant *Staphylococcus aureus*, Sepsis

\*Correspondence: ana5189@adm.cgmh.org.tw; fajy@mail.cgu.edu.tw

<sup>†</sup>Chia-Chih Liao and Huang-Ping Yu contributed equally to this work

<sup>1</sup> Department of Anesthesiology, Chang Gung Memorial Hospital, 5 Fuxing Street, Kweishan, Taoyuan 333, Taiwan

<sup>5</sup> Pharmaceuticals Laboratory, Graduate Institute of Natural Products, Chang Gung University, 259 Wen-Hwa 1st Road, Kweishan, Taoyuan 333, Taiwan

Full list of author information is available at the end of the article

## Background

Bacteremia is described as the appearance of pathogenic bacteria in the bloodstream. The most common cause of bacteremia is *Staphylococcus aureus* infection [1]. In the United States, the annual incidence of *S. aureus* bacteremia has been 4.3–38.2 per 100,000 persons, with an



© The Author(s) 2021. This article is licensed under a Creative Commons Attribution 4.0 International License, which permits use, sharing, adaptation, distribution and reproduction in any medium or format, as long as you give appropriate credit to the original author(s) and the source, provide a link to the Creative Commons licence, and indicate if changes were made. The images or other third party material in this article are included in the article's Creative Commons licence, unless indicated otherwise in a credit line to the material. If material is not included in the article's Creative Commons licence and your intended use is not permitted by statutory regulation or exceeds the permitted use, you will need to obtain permission directly from the copyright holder. To view a copy of this licence, visit <http://creativecommons.org/licenses/by/4.0/>. The Creative Commons Public Domain Dedication waiver (<http://creativecommons.org/publicdomain/zero/1.0/>) applies to the data made available in this article, unless otherwise stated in a credit line to the data.

associated mortality of 20%, since the 1990s [2]. Methicillin-resistant *S. aureus* (MRSA) is an additional bacterial burden with a high death rate. The mortality of patients with critical MRSA bacteremia can exceed 60% [3]. Individuals with bacteremia usually experience systemic inflammation due to a proinflammatory cytokine burst by immune cells [4]. Bacteremia, followed by acute inflammation, can lead to sepsis and multiple organ failure. Sepsis is an inflammatory and immune response to infection. The activation of proinflammatory mediators by sepsis contributes to organ damage, especially damage to the heart, lungs, and kidneys. The majority of bacteria identified in sepsis patients are gram-positive pathogens, such as *S. aureus*, with an increasing trend in drug-resistant microbes [5]. Severe septic shock is observed in 38%–40% of patients with *S. aureus* bacteremia [6].

Despite therapeutic innovation, the mortality rate due to bacteremia-induced sepsis is still high [1, 7]. Resistance to first-line antibiotics complicates the treatment of MRSA bacteremia [8]. The poor clinical outcomes highlight the urgent need for developing improved therapy for MRSA bacteremia. In the last decade, nano-based drug delivery systems have been increasingly used to improve antibacterial and anti-inflammatory treatments. The large surface-to-volume ratios and drug loading capacities of nanoparticles contribute to their biological advantages, namely, increased drug solubility, enhanced drug storage stability, improved bioavailability, prolonged half-life, and efficient organ targeting [9]. Nanoparticulate drug delivery is considered beneficial for the encapsulation of active agents against resistant bacteria and inflammatory disorders [10, 11]. Nanostructured lipid carriers (NLCs) are lipid-based nanocarriers that allow increased drug encapsulation because of the imperfect lipid matrix that is composed of lipids in both solid and liquid forms. The use of biodegradable lipids leads to higher tolerability of NLCs than that of polymeric and metallic nanoparticles [12]. There have been no investigation on the application of nanomedicine to treat bacteremia. To date, clinical trials aiming to study anti-inflammatory approaches have failed to improve the outcomes of bacteremia-induced sepsis [13]; therefore, the development of novel therapeutic modalities with antibacterial and anti-inflammatory properties remains a critical issue. A new emerging regimen for inhibiting the inflammatory response is currently being investigated for the treatment of bacteremia-induced sepsis [7]. The use of treatments that combine antibiotics and anti-inflammatory therapies has been proven to reduce mortality in sepsis compared to the use of antibiotics alone [14, 15]. Therefore, this study explored the applicability of intravenous NLCs with combined anti-MRSA and anti-inflammatory activities for the

treatment of bacteremia. To this end, ciprofloxacin and rolipram were both incorporated into NLCs.

The standard therapy for MRSA bacteremia includes the early intravenous administration of antibiotics, such as vancomycin, daptomycin, and teicoplanin [16]. Ciprofloxacin, a broad-spectrum antibiotic belonging to the class of fluoroquinolones, may also be intravenously administered to treat bacteremia [17–19]. To alleviate the inflammation stimulated by bacteremia or sepsis, phosphodiesterase 4 (PDE4) inhibitors have been proven effective in mitigating the cytokine storm induced by bacteria or viruses for the treatment of sepsis-induced organ damage [20–23]. The inhibition of PDE4 is associated with the suppression of immune overactivity via the prevention of cAMP degradation, as PDE4 can decrease cAMP expression to activate the inflammatory response. One representative PDE4 inhibitor is rolipram, which is a novel PDE4 inhibitor. Rolipram improves cardiac and renal function through the inhibition of cytokine overexpression in a rodent model of sepsis [24, 25]. Neutrophils are the most important cell in the host response to bacterial infection [26], and their migration is a fundamental component of the immune response elicited by bacteremia [12]. In this study, primary human neutrophils were used as model cells to examine the anti-inflammatory effect of NLCs. We established an MRSA-infected bacteremia model in rats to assess the inhibitory effect of NLCs on MRSA burden, acute inflammation, and mortality rate. We also monitored the biodistribution of the nanoparticles in various organs.

## Results

### Physicochemical features of NLCs

The particle size, polydispersity index (PDI), and surface charge are important features of nanocarriers that govern their stability and biological performance. As shown in Table 1, the mean diameter of the prepared lipid-based nanoparticles was 171 nm. The NLCs exhibited monodispersity with a PDI of 0.42. The zeta potential of the dual drug-loaded nanoparticles was highly negative at −39 mV. The encapsulation efficiency of the drugs determined

**Table 1 Physicochemical properties of the nanostructured lipid carriers on nanoparticulate size, polydispersity index (PDI) and zeta potential**

| Property             | Value         |
|----------------------|---------------|
| Size (nm)            | 171.40 ± 5.82 |
| Polydispersity index | 0.42 ± 0.04   |
| Zeta potential (mV)  | −38.80 ± 0.61 |

Each value represents the mean ± SEM (n = 3)

by ultracentrifugation showed that the encapsulation percentages of ciprofloxacin and rolipram in the NLCs were  $88.21 \pm 7.0\%$  and  $95.81 \pm 12.24\%$ , respectively. The release of ciprofloxacin and rolipram from the nano-carriers was examined. The obtained profiles of ciprofloxacin release as a function of time indicated an initial burst release from the control vehicle and NLCs (the left panel of Additional file 1: Figure S1). Ciprofloxacin release from the free control reached nearly 100% after 24 h, indicating a fast release. Inclusion in the nanoparticles decreased the release rate of ciprofloxacin. A similar trend was detected in the case of rolipram (the right panel of Additional file 1: Figure S1).

Anti-MRSA activity of NLCs

The capability of the NLCs to inhibit MRSA growth was examined to understand their potential for treating MRSA-induced bacteremia. As shown in Table 2, the minimum bactericidal concentration (MBC) of ciprofloxacin alone was 0.98 µg/ml. Rolipram alone did not exhibit

any anti-MRSA activity. Surprisingly, treatment with the combination of both drugs significantly reduced the anti-MRSA activity of ciprofloxacin. The MBC of ciprofloxacin increased by 8-fold after rolipram intervention. The antimicrobial potency of the NLCs loaded with ciprofloxacin was found to have a MBC between 0.98 and 1.95 µg/ml. Similar to their free forms, the combination of ciprofloxacin and rolipram in the NLCs increased the MBC of ciprofloxacin by 4–8-fold. Time-kill curves provide information regarding the extent and rate of anti-MRSA activity. Figure 1a and b show the time-response MRSA growth inhibition of ciprofloxacin and rolipram at low (0.5 and 0.2 µg/ml) and high doses (1 and 0.4 µg/ml), respectively. The control group was the MRSA population not treated with drugs or nanoparticles. Treatment with rolipram, in both its free and nanoparticulate forms, had no significant influence on MRSA growth compared to the no treatment control. The NLCs without drugs also showed no MRSA inhibition; however, the formulations containing ciprofloxacin markedly suppressed the growth of MRSA. The ciprofloxacin-loaded NLCs were more efficient than free ciprofloxacin in inhibiting bacterial growth. At high doses, free and nanoparticulate ciprofloxacin completely inhibited MRSA growth over 24 h. However, a combination of ciprofloxacin and rolipram in free form weakened the anti-MRSA effect.

**Table 2** The MBC (µg/ml) of ciprofloxacin in free form and nanostructured lipid carriers in the presence or absence of rolipram against MRSA

| Formulation                      | MBC (µg/ml) |
|----------------------------------|-------------|
| Ciprofloxacin in free form       | 0.98        |
| Ciprofloxacin + rolipram         | 7.81        |
| Ciprofloxacin in NLCs            | 0.98–1.95   |
| Ciprofloxacin + rolipram in NLCs | 7.81        |

Each value represents the mean ± SEM (n = 3)

Anti-inflammatory activity of NLCs

Primary neutrophils were used as model cells to examine the anti-inflammatory activity of the NLCs and to confirm the possible activity that mitigates bacteremia-elicited acute inflammation. Prior to assessing inflammation inhibition, a cytotoxicity experiment was performed

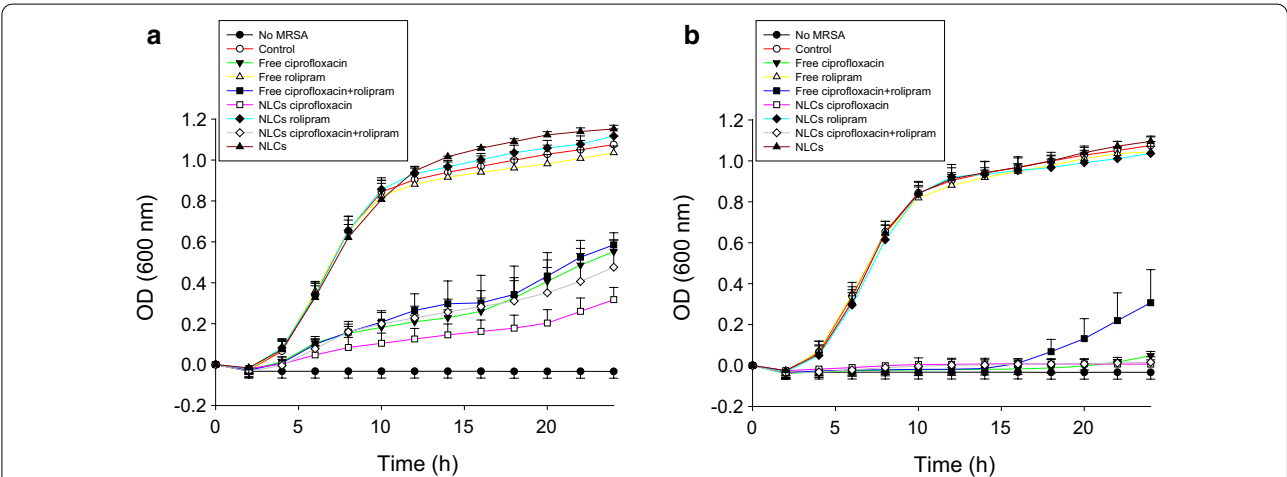


**Fig. 1** Determination of the antibacterial activity of free drugs and NLCs against planktonic drug-resistant MRSA: **a** the time-killing curves of ciprofloxacin (0.5 µg/ml) and rolipram (0.2 µg/ml); and **b** the time-killing curves of ciprofloxacin (1 µg/ml) and rolipram (0.4 µg/ml). All data are expressed as the mean ± SEM (n = 3). MRSA, methicillin-resistant *Staphylococcus aureus*; OD, optical density; SEM, standard error of mean

by measuring lactate dehydrogenase (LDH) leakage, and the results are shown in Fig. 2a. Various concentrations of ciprofloxacin (0.75–75 nM) and/or rolipram (0.3–30 nM) in both free and nanoparticulate forms did not exert cytotoxic effects on neutrophils. Activated neutrophils produce superoxide anions to induce oxidative stress. We observed that ciprofloxacin, in both its free and nanoparticulate forms, failed to suppress extracellular superoxide anion production (Fig. 2b). Rolipram inhibited superoxide anion production in a concentration-dependent manner, and the nanocarrier formulation (59%–88% suppression) showed greater inhibition than the free drug (17%–78% suppression). The inhibition of oxidative stress by rolipram was not a consequence of cytotoxicity since there was no LDH leakage after rolipram treatment. In fact, the incorporation of ciprofloxacin decreased the rolipram-induced superoxide inhibition. Free ciprofloxacin even completely prevented the inhibitory activity of free rolipram.

We next used confocal microscopy to visualize the uptake of the NLCs by human neutrophils. The nuclei were stained with DAPI and emitted a blue signal, as shown in Fig. 2c. Neutrophils treated with low (5  $\mu$ l) and high (10  $\mu$ l) amounts of NLCs emitted increased red fluorescence compared to the nontreated neutrophils. The lipid nanoparticles were predominantly located in the cytoplasm as punctate dots. The distribution of the red fluorescence was comparable between the neutrophils treated with low and high amounts of NLCs. As shown in Fig. 2d, the intracellular fluorescence, as analyzed by flow cytometry, markedly increased by a factor of 2 log after nanoparticle internalization.

#### Biodistribution of NLCs in rats

The distribution of NLCs after injection into the human body is important for understanding possible drug deposition in organs and for achieving effective therapy. To assess the biodistribution of NLCs in peripheral organs after intravenous injection, the lipophilic dye iFluor 790 was loaded into the nanocarriers for near-infrared (NIR) monitoring. We used healthy rats, rather than mice, as the animal model in this biodistribution experiment due to their larger organ size and lower autoNIR signal in organs, which facilitated clearer visualization. Figure 3 shows the qualitative and quantitative analyses of nanoparticle distribution by IVIS. The rats that received no

treatment (blank control) exhibited negligible autoNIR signals in their organs, except for the gastrointestinal tract (Fig. 3a). The NIR signal in the organs before and after receiving free dye was comparable (Fig. 3b), indicating a rapid degradation of the dye in circulation. The intravenously injected NLCs were deposited mainly in the kidneys (Fig. 3c). The NIR signal in the other organs after nanoparticle distribution was comparable to that in the blank control group. The renal distribution of nanoparticles can be affected by retinol; therefore, we reduced the retinol concentration in the NLCs from 0.25–0% and 0.1% to visualize their biodistribution, and we found that the NIR signal was weaker (Fig. 3d and e). The quantification of the NIR intensity indicated a lower accumulation of NLCs without retinol in the kidney than that of the NLCs with retinol (Fig. 3f). After the intravenous injection of the NLCs with different percentages of retinol, there was no significant difference in the NIR intensity in other organs.

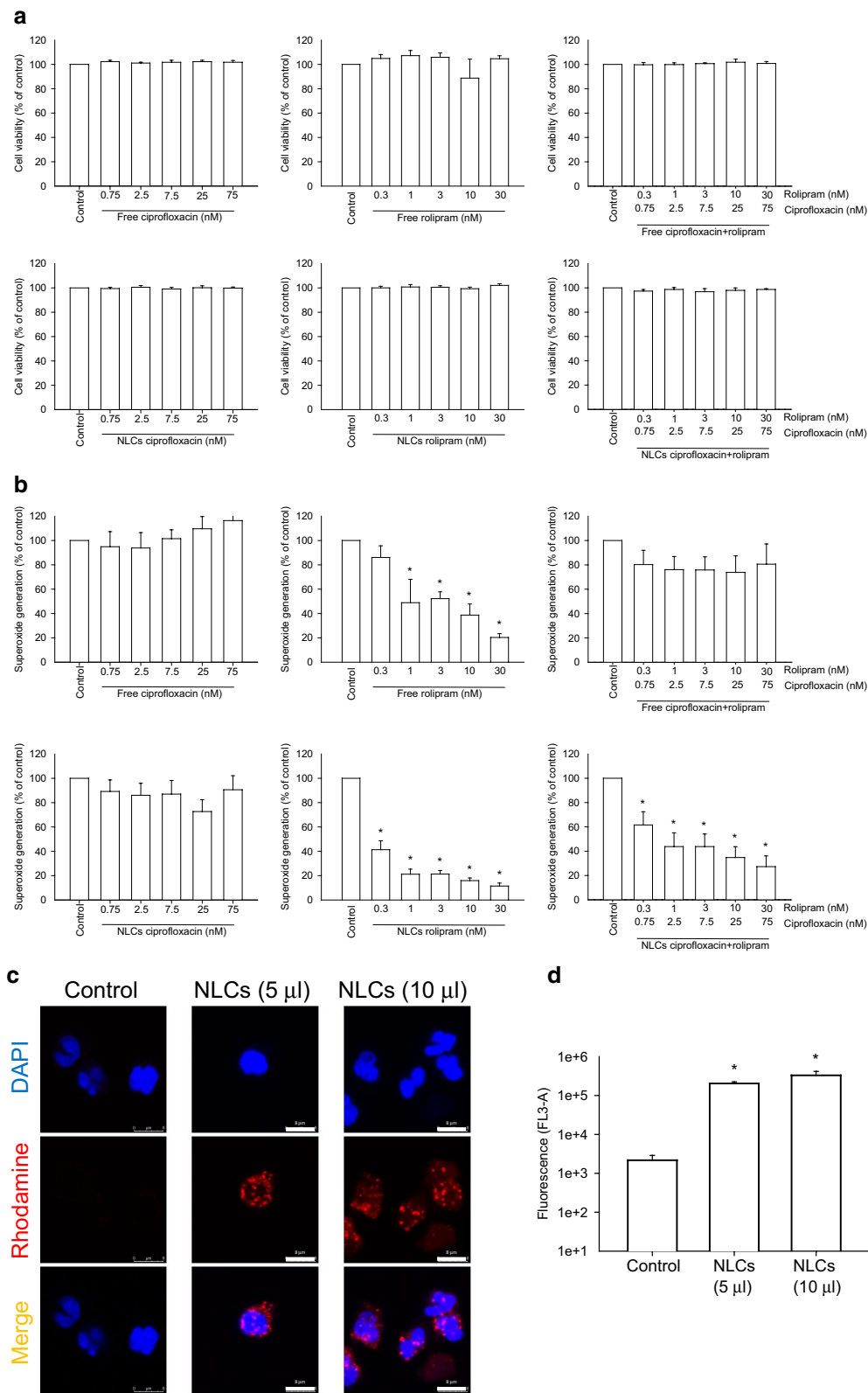
#### Use of NLCs for MRSA bacteremia treatment

To evaluate the protective effects of free drugs and NLCs on MRSA-induced bacteremia in mice, we examined the survival rate of the mice four days after intravenous injection of the drug-loaded formulations. The mice infected with MRSA displayed 22% survival on day four, as shown by the Kaplan-Meier curve in Fig. 4a. Following treatment with the combination of free ciprofloxacin (2.5 mg/kg) and rolipram (1 mg/kg), 41% of the infected mice survived after four days of MRSA intervention. We found an improvement in the survival of the bacteremic mice (67%) that received NLCs containing 0.25% (w/v) retinol, suggesting significant disease remission. The surviving mice were sacrificed to quantify the MRSA accumulation in blood and peripheral organs. No MRSA was detected in the animals that did not receive bacterial injection (control) (Fig. 4b). Four days after injection, MRSA was largely deposited in the blood and organs. The MRSA colony-forming unit (CFU) count was log-transformed in this figure. Neither the free drugs nor the NLCs reduced the MRSA CFU counts in the heart and spleen. Significant inhibition of the MRSA CFU counts in the blood and lungs was observed after treating the mice with the free drugs. The NLCs caused a 1–2 log reduction in the CFU counts in the blood, lungs, liver, and kidneys compared to those in the infected mice without treatment;

(See figure on next page.)

**Fig. 2** Effects of free drugs and NLCs on primary human neutrophils ( $6 \times 10^5$  cells/ml): **a** neutrophil cytotoxicity assay by LDH determination; **b** the measurement of extracellular superoxide production; **c** the uptake of rhodamine 800-loaded NLCs by human neutrophils observed via confocal microscopy; and **d** the fluorescence intensity of rhodamine 800 in the neutrophils analyzed by flow cytometry. All data are expressed as the mean  $\pm$  SEM ( $n = 3$ ). \*  $p < 0.05$  as compared to control group. LDH, lactate dehydrogenase; DAPI, 4',6-diamidino-2-phenylindole





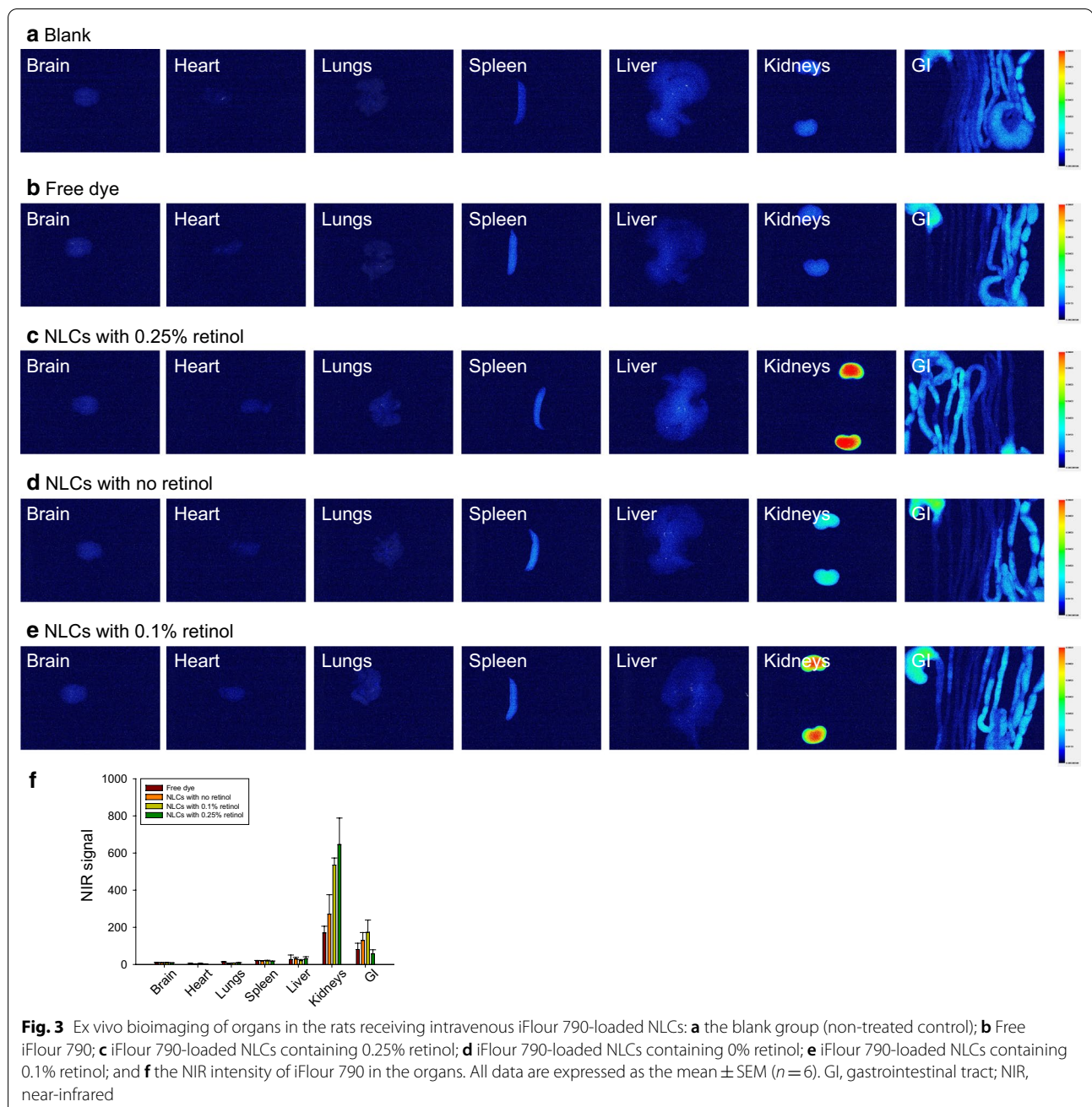
the greatest decrease in the CFU count was observed in the kidneys. Statistical analysis revealed that compared with the free drug control, the nanoparticles led to a significant reduction in MRSA in the liver and kidneys. To explore the anti-inflammatory activity, the excised organs were visualized by *ex vivo* bioimaging to assess the elastase distribution in organs. Elastase is an indicator of activated and infiltrating neutrophils. As shown in Fig. 4c, the elastase signal (bright red color) in all the organs showed an increasing trend in response to MRSA infection. The administration of the combination of ciprofloxacin and rolipram in their free forms decreased the elastase levels in the heart, but this decrease was not observed in the other organs. We observed that the elastase levels in the heart, lungs, spleen, and kidneys were reduced in the group that received the NLCs, but the NLC-treated group did not exhibit a reduction in the elastase level in the liver.

Only a limited number of mice survived long enough to assess the MRSA burden and elastase levels; therefore, we shortened the treatment duration to 40 h for further examination. As shown in Fig. 5a, the MRSA inhibition in the heart and lungs was comparable between the free drug and NLC treatment groups. The bacterial count in the blood, liver, and kidneys was significantly reduced by the NLCs compared with the free drugs. There was a 2-log reduction in the MRSA growth in the blood and kidneys in the NLC group compared to the MRSA group without drug intervention. After the four-day treatment, neither the free drugs nor the NLCs decreased the MRSA accumulation in the spleen. The elastase distribution trends in the mice after 40 h of treatment were consistent with the results of the longer treatment (four days), as shown in Fig. 5b. The NLCs more substantially decreased the elastase levels than the free drugs in the infected mice. Next, we examined whether free drugs or NLCs suppressed proinflammatory cytokine expression in the organs involved in bacteremia. The ELISA results are shown in Fig. 5c–g. The level of IFN- $\gamma$  in the MRSA-infected animals significantly increased compared with that in the healthy control animals (Fig. 5c). The administration of the combination of ciprofloxacin and rolipram in their free and nanoparticulate forms caused comparable inhibition of IFN- $\gamma$ . The administration of NLCs resulted in significantly lower expression of IL-1 $\beta$  in the heart and kidneys (Fig. 5d). This effect was not observed in the group treated with free drugs. Treatment with free drugs and NLCs significantly inhibited the IL-1 $\beta$  overexpression in the lungs and liver to comparable degrees. IL-1 $\beta$  expression in the spleen increased in the free drug-treated mice, but not in the infected mice without drug intervention, compared to the healthy control mice. We could not explain this phenomenon with the existing knowledge. Further study is needed to delineate the possible mechanisms.

MRSA intervention did not have a significant effect on IL-6 expression in the organs, except for the spleen (Fig. 5e). Nevertheless, compared with no drug treatment, the NLCs still exhibited the capability to inhibit IL-6 expression in the lungs and spleen. This result suggests that the protein concentration of IL-17A significantly increased in all organs after MRSA challenge (Fig. 5f). The free drugs were capable of inhibiting IL-17A in the lungs and kidneys. NLC administration further reduced IL-17A production in the lungs, liver, and kidneys by 61%, 52%, and 67%, respectively. The NLCs decreased IL-17A production in the kidneys to the baseline levels observed in the controls. No IL-17A suppression was observed in the heart and spleen of infected mice after treatment with the free drugs or NLCs. TNF- $\alpha$  expression in all the organs increased by 2.1–3.7-fold in the MRSA-infected animals compared to that in the healthy animals (Fig. 5g). The TNF- $\alpha$  levels in the heart and liver were markedly reduced to baseline levels after treatment with both the free drugs and NLCs. The free drugs exerted no effect on the suppression of TNF- $\alpha$  overexpression in the kidneys. Nanocarrier treatment resulted in a 2-fold decrease in the TNF- $\alpha$  levels in the kidneys compared with those observed in the infected group.

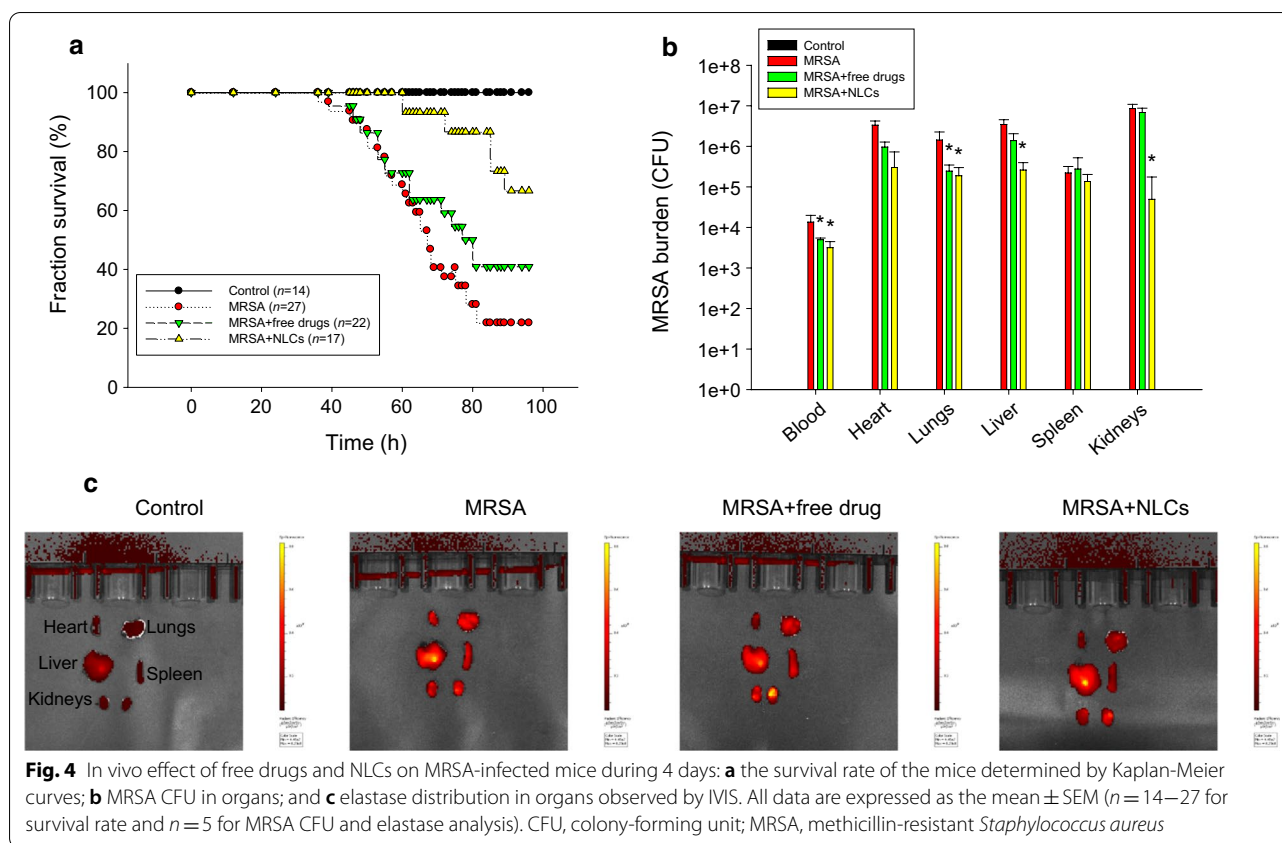
#### Histological observation

Forty hours after MRSA challenge, the mice were sacrificed to observe the histology of the different organs. The histology of the spleen was excluded in this experiment because of the negligible effects of free drug or nanoparticle treatment on the inhibition of MRSA and the suppression of some cytokines. The hearts of the healthy mice showed intact myocytes and cardiac muscle fibers, as shown in Fig. 6. MRSA infection resulted in a large area of cell debris with suppurative inflammation and immune cell infiltration. The area of suppurative inflammation was reduced after free drug and NLC treatment. Hematoxylin and eosin (H&E) staining of the lungs of the infected mice showed interstitial congestion with a loss of lung architecture. Edema and immune cell recruitment in the parenchyma were also observed in the MRSA-infected lungs. Moreover, interstitial thickening with congestion was worsened by free drug administration. The NLCs, however, markedly attenuated the MRSA-induced lung injury with a greater region of preserved pulmonary architecture. The hepatocytes in the liver tissues of the normal mice appeared well organized. Congestion and inflammatory cell infiltration were observed in hepatic tissues after MRSA injection. This was a typical observation of liver infection in the early stage. While congestion could be improved by the free drugs and NLCs, this improvement was limited. H&E staining revealed that the kidney structure consisted mainly of renal tubules and



medulla. The renal tissues in the control mice appeared normal and regular. MRSA challenge induced cell debris accumulation and acute suppurative inflammation in the tissue. Following MRSA intervention, immune cell infiltration and tubule necrosis were also visualized. Following MRSA treatment, the kidney structure was preserved by the injection of the drugs in their free forms. Congestion and immune cell recruitment were reduced by the NLCs compared to those observed in the infected group.

The MRSA distribution in the organs was examined using *S. aureus* Rosenbach antibody immunohistochemistry, as shown in Fig. 7a. There were bacterial clusters in the hearts of the MRSA-treated mice. These clusters were limited by the free and nanoparticulate forms of the drugs. The MRSA distribution in the lungs was also inhibited by the free drugs and NLCs. However, the MRSA distribution in the liver could not be clearly observed in all the groups. This could be due to the minimal aggregation of MRSA in the liver, which makes it



difficult to recognize abscesses in the tissue. The MRSA bacterial clusters in the kidneys were reduced by the NLCs but not by the free forms of the drugs. Ly6G is a biomarker of neutrophil migration into organs that is used to characterize the features of sepsis. We visualized neutrophil accumulation in the heart 40 h after MRSA injection, as shown in Fig. 7b. Neutrophil diffusion was attenuated by the administration of the drugs, and the NLCs demonstrated better performance. On the other hand, the neutrophil infiltration in the lungs and liver caused by MRSA was reduced by the drugs in either their free forms or nanoparticulate forms; however, this reduction was not very significant. Neutrophils expressing Ly6G were clearly detected in the kidneys after MRSA infection. The number of neutrophils was markedly reduced after nanocarrier injection, indicating an efficient alleviation of infection-associated inflammation.

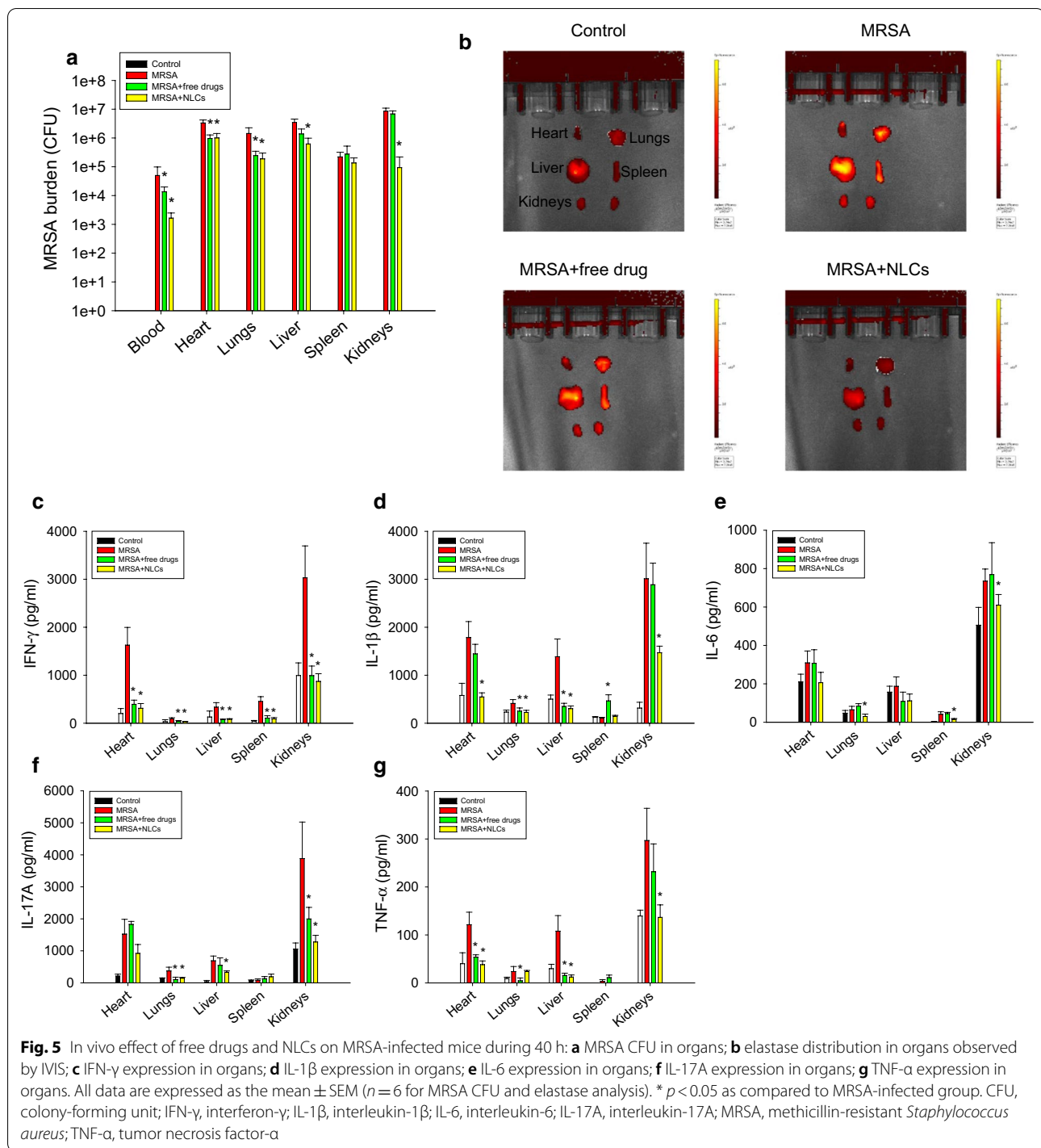
## Discussion

Early initiation of the inhibition of bacterial growth and inflammation is crucial for the treatment of bacteremia and sepsis. The current therapy for mitigating bacteremia-induced sepsis is unsatisfactory for achieving a successful outcome. Improving drug delivery systems is

one of the strategies for enhancing therapeutic efficiency against bacteremia. In our study, we carried out thorough analyses to assess the capability of treating bacteremia with NLCs incorporating both antibacterial and anti-inflammatory drugs. We found that NLCs were more effective in eradicating MRSA than free drugs (Fig. 1). A similar trend was observed for inhibiting superoxide anion production by activated neutrophils (Fig. 2b). Our results demonstrate a large accumulation of intravenously injected NLCs in the kidneys (Fig. 3). This accumulation was beneficial for alleviating the renal dysfunction caused by bacteremia. Intravenous delivery of dual drug-loaded nanocarriers prevented the worsening of sepsis in mice and elevated the survival rate (Fig. 4a). Nanomedicine has been widely used due to its success in eradicating drug-resistant bacteria in vitro or in vivo [27–32]. We focused on the effect of nanocarriers encapsulating two drugs on the treatment of the bacteremia induced by MRSA. We also found that retinol incorporation in NLCs was beneficial for renal targeting in order to treat kidney injury.

The application of high-pressure homogenization and sonication was used to obtain NLCs of small particle size (Table 1). Particle diameters of 10–200 nm are most relevant for exerting biological effects [33]. For lipid-based





nanoparticles, a PDI of  $\leq 0.3$  is considered to be acceptable [34]. Our nanosystems showed a PDI of 0.42, and they can be considered highly polydisperse [35]. Nevertheless, the particle diameter was maintained at low size (171 nm) with a similar PDI in the three batches ( $0.42 \pm 0.04$ ). We therefore concluded that the quality control of the

nanocarriers was adequate. The nanocarriers prepared in the present study fit this criterion. Cationic nanoparticles are associated with hemolysis after intravenous administration [36]; therefore, we designed nanoparticles with a negative surface charge to prevent hemolysis. We incorporated deoxycholic acid into the nanoformulations

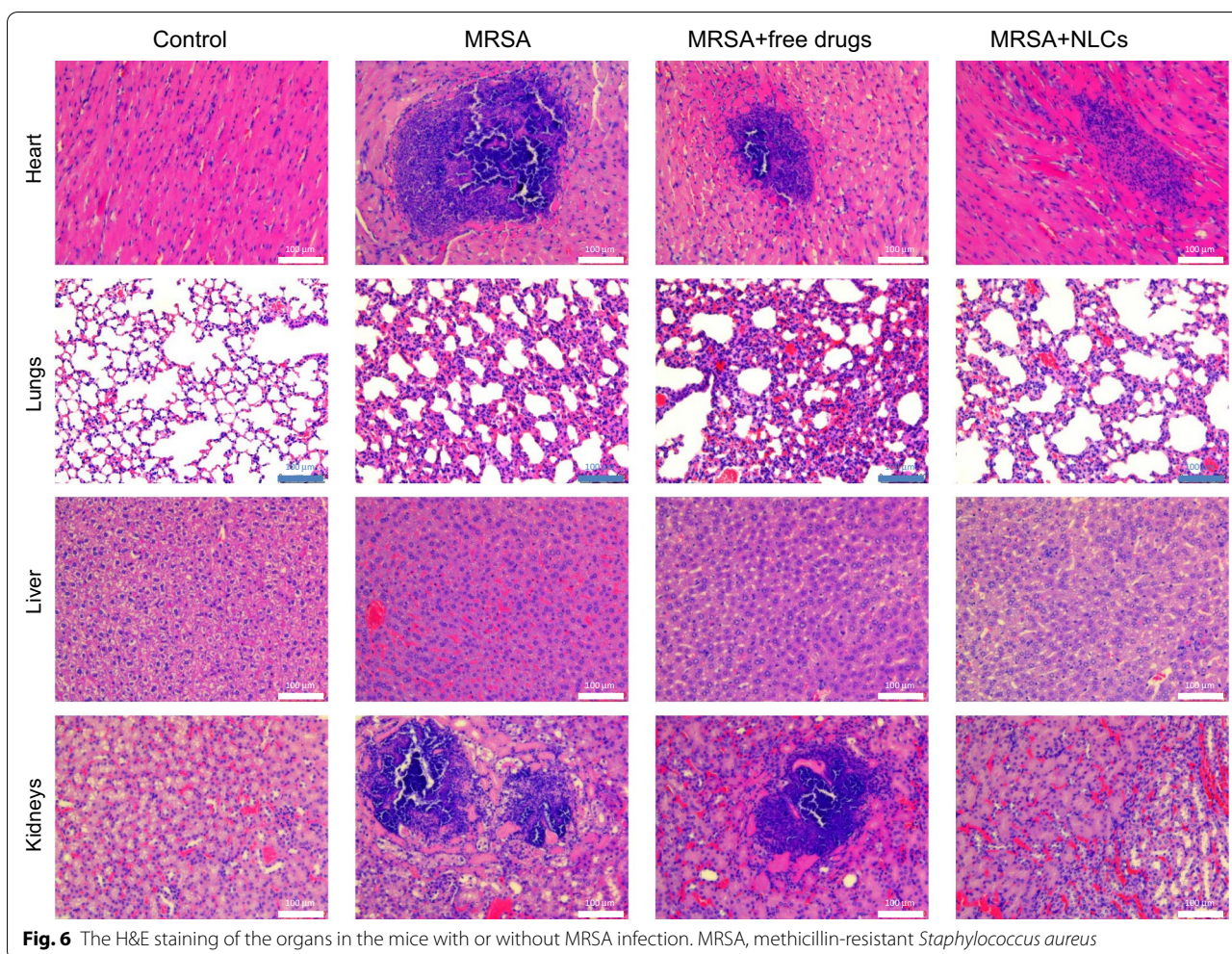


**Fig. 6** The H&E staining of the organs in the mice with or without MRSA infection. MRSA, methicillin-resistant *Staphylococcus aureus*

to obtain a negative charge of  $-39$  mV. This value was advantageous in showing sufficient storage stability because a zeta potential of  $>30$  or  $<-30$  mV indicates good electrostatic stabilization [37]. The high rate of rolipram encapsulation in the NLCs was attributed to the high lipophilicity of this compound, which allowed it to be retained in the lipid cores of the NLCs. Although ciprofloxacin is less lipophilic than rolipram, the encapsulation percentage of this drug reached nearly 90%. The mixture of lipids in solid and liquid forms in the cores of NLCs leads to imperfection in the matrix, which allows greater space for loading both lipophilic and hydrophilic chemicals [38].

Ciprofloxacin, but not rolipram, demonstrated anti-MRSA activity. The degree of MRSA suppression by ciprofloxacin was significantly reduced after combined treatment with rolipram in either the free or nanoparticulate forms (Table 2). A previous study [39] verified the possibility that ciprofloxacin could exhibit reduced antibacterial activity in the presence of PDE4 inhibitors.

In addition to their anti-inflammatory properties, PDE inhibitors have other bioactivities, such as antioxidative activity and protective activity against oxidative stress. Given the antibacterial mechanisms of ciprofloxacin, namely, the induction of reactive oxygen species to kill microbes, PDE inhibitors may restrict the antibacterial potency of ciprofloxacin. A possible drug-drug interaction between PDE4 inhibitors and ciprofloxacin was also observed in a previous investigation [40]. The combined treatment also exhibited a similar trend in its anti-inflammatory activity against activated neutrophils (Fig. 2b). The production of oxidative stress by ciprofloxacin may be the reason for the reduced ability of rolipram to inhibit superoxide anion production. The inclusion of ciprofloxacin in the nanoparticles inhibited MRSA growth compared to the free drugs (Fig. 1). Sustained and slow release of the drug from nanocarriers maintains drug retention near bacteria over a long period [9]. The surface of NLCs containing phosphatidylcholine and poloxamer 188 can easily fuse with the



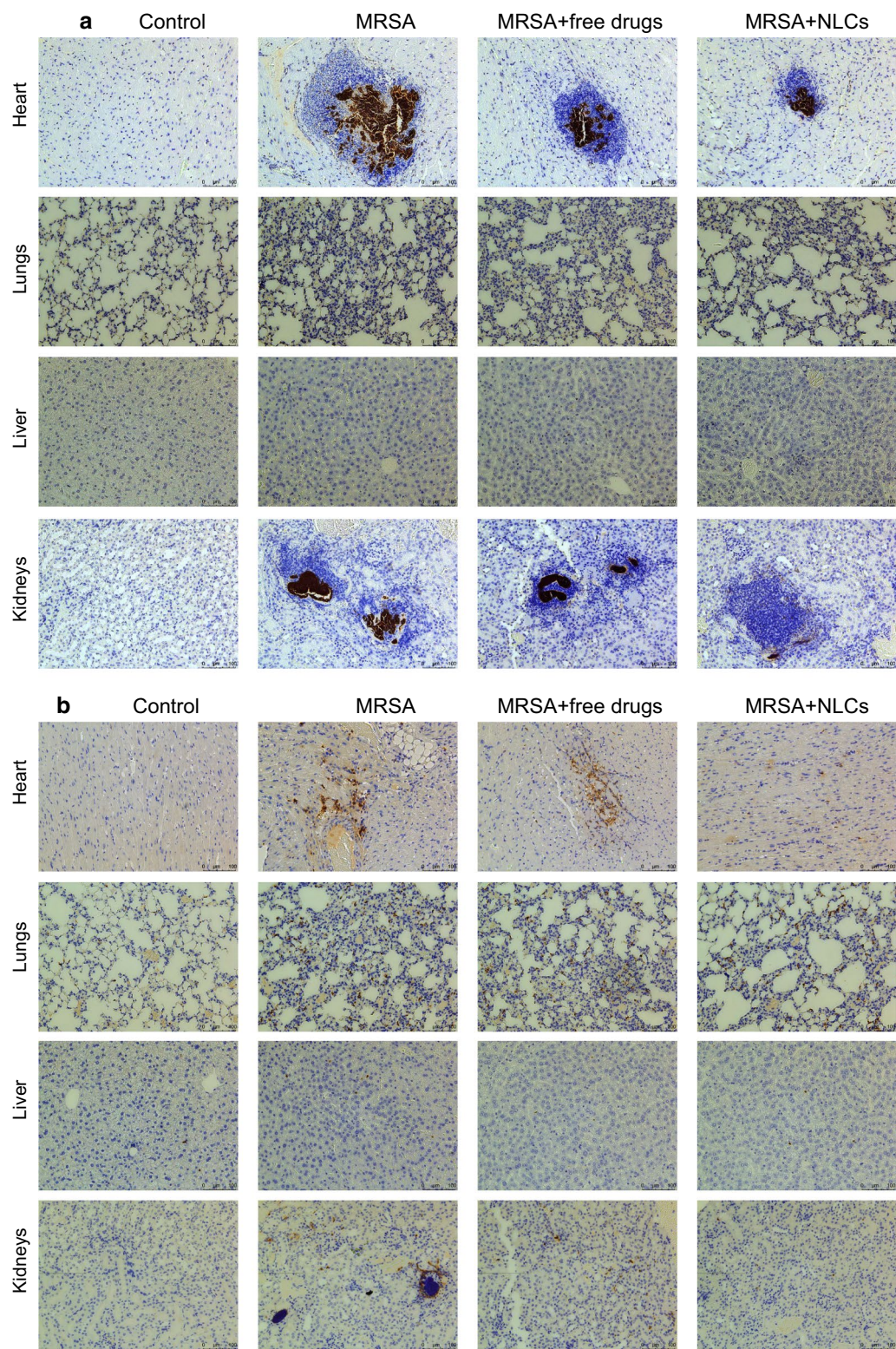


**Fig. 7** The histology of the organs in the mice with or without MRSA infection: **a** MRSA distribution determined by *S. aureus* Rosenbach antibody; and **b** neutrophil distribution determined by recombinant anti-Ly6G antibody. MRSA, methicillin-resistant *Staphylococcus aureus*

bacterial cell wall [41], resulting in the accumulation of antibacterial agents in large amounts in microbes.

Neutrophils are the major phagocytic cells that act as first-line responders in the fight against pathogenic microbes. Once uncontrolled activation of neutrophils occurs at the infected site, organs are possibly damaged. Neutrophils are recognized as essential players in acute inflammation, such as the inflammation elicited by bacteremia, sepsis, and traumatic hemorrhage [42]. Neutrophil stimulation is affected by the intracellular cAMP level, which can be regulated by PDE4 inhibition. Rolipram is a selective PDE4 inhibitor that reduces the number and activation of infiltrating neutrophils in inflammatory regions [43]. For intracellular drug delivery to inhibit neutrophil activation, nanocarriers must be internalized by neutrophils, and then, the drug is released. Our results demonstrated the easy ingestion of NLCs by neutrophils (Fig. 2c). A high zeta potential level, either positive or negative, has been established as a vital factor for assisting phagocytosis by neutrophils [44]. Soft nanoparticles can be deformed by cells during phagocytosis. This uptake is energetically less favorable [45]. Lipid-based nanoparticles can be classified as soft but not rigid structures that facilitate easy internalization by cells [46]. Neutrophil influx into peripheral organs mediates sepsis through superoxide generation. This oxidative stress induced by stimulated neutrophils is inactivated by the internalization of rolipram-loaded NLCs by neutrophils, which results in greater superoxide inhibition than drugs in free form (Fig. 2b).

An important feature for the treatment of bacteremia and sepsis is the appropriate penetration of drugs into tissues to limit organ damage. The therapeutic outcome can be improved when the drugs are delivered to the target organs. The biodistribution of intravenously injected NLCs showed the easy delivery of the nanoparticles to the kidneys (Fig. 3). An earlier study [12] also suggested higher deposition of NLCs in the kidneys than in other organs. Our NLCs possessed a size (150–180 nm) similar to that of the NLCs that were previously developed. The biodistribution results revealed a higher accumulation of NLCs with a higher concentration of retinol in the kidneys (Fig. 3). In the bloodstream, retinol is bound to specific retinol-binding proteins (RBPs), especially RBP4. RBPs play a principal role in promoting retinol transport in the body [47]. RBP4 is a plasma protein mainly secreted from the liver to transport retinol to peripheral organs via the bloodstream. The kidneys possess abundant RBP receptors with high retinol-binding activity [48]. In rats, approximately 50% of plasma retinol turnover is associated with the kidneys [49]. This may be the reason for the increased kidney deposition of the NLCs with high levels of incorporated retinol. The level of

RBP4 also increases during renal dysfunction but not during hepatic dysfunction [50]. Although the liver is also a main target of retinol transport, we observed minimal NLC deposition in this organ (Fig. 3). This result is quite different from the lipid-based nanoparticles prepared in our previous study [51], which demonstrated a large accumulation of retinol-loaded nanoparticles in the liver. The encapsulation percentage of retinol in the nanoparticles in the previous study was 0.02%, which was much lower than that in the present study (0.25%). It is difficult to compare the different nanocarriers since each nanosystem has its own intrinsic nature. In addition to the incorporation of materials, other factors, such as size, surface charge, and loaded drugs, also influence nanoparticle biodistribution. The biodistribution is nanocarrier-dependent and cannot be applied universally to all nanoformulations.

Once nanoparticles are administered into the blood, plasma proteins adsorb onto the particulate surface for opsonization. Opsonized nanoparticles are recognized by the mononuclear phagocyte system to be removed from circulation into the liver and spleen [52]. Nanoparticles with larger lipophilic surfaces tend to adsorb more proteins in circulation. The enhanced hydrophilic nature of the NLC surface can prevent uptake by the liver and spleen and thus prolong the circulation time [53]. The attachment of hydrophilic polymers, including polyethylene glycol, poloxamer, and chitosan, is effective for avoiding hepatic clearance [54]. Cationic nanoparticles show a high affinity for plasma proteins and parenchymal cells, leading to a broad distribution in the liver [55]. In our NLCs, the presence of poloxamers and a negative charge on their surfaces contributed to their low accumulation in the liver and spleen (Fig. 3). The nanoparticle diameter is a key parameter for controlling their biodistribution. Nanocarriers larger than 200 nm are rapidly delivered to the liver and spleen because of complement activation [56, 57]. A previous study [58] also suggested that nanoparticles with sizes of 50–100 nm and < 50 nm are largely distributed in the hepatic parenchyma and spleen, respectively. According to this evidence, the size of our NLCs might have enabled their escape to enter the liver and spleen. The kidneys have fenestrated capillaries that facilitate the entrance of nanoparticles [55]; however, nanoparticles with a size > 6 nm cannot be removed from the kidneys [54]. Dual drug-loaded NLCs could penetrate but could not flow out of the kidneys, causing their accumulation in renal tissues. The uptake of NLCs by the brain is negligible, which could be due to the incorporation of poloxamer 188 to generate hydrophilic and steric surfaces. These surfaces are not conducive to delivery to the brain [12]. Limited brain targeting is favorable for rolipram delivery because this compound causes



neurological disorders as side effects when it enters the brain.

In severe sepsis, the development of acute cardiac and renal dysfunction is commonly observed. *S. aureus* bacteremia has emerged as the most common cause of infective endocarditis [59]. Our results indicated decreased MRSA burden and elastase distribution in the heart after treatment with the combination of ciprofloxacin and rolipram (Fig. 5a and b). Moreover, NLCs exerted superior effects compared with free drugs. A previous study [60] demonstrated that ciprofloxacin is largely distributed in the cardiac cavity after injection. This observation explains the effectiveness of free ciprofloxacin in eradicating MRSA in the heart. Acute kidney injury is a major complication that arises due to sepsis. NLCs were helpful in inhibiting MRSA growth and elastase upregulation in the kidneys (Fig. 5a and b). This effect was not observed in the group treated with the free drugs, although PDE4 inhibition has been proven to attenuate acute renal failure in sepsis and endotoxemia [24, 61].

NLCs showed high efficiency for encapsulating ciprofloxacin and rolipram. Drugs encapsulated in nanoparticles can be protected from enzymatic attack to facilitate delivery to renal tissue. Ex vivo bioimaging in this study confirmed the large distribution of NLCs in the kidneys (Fig. 3). NLCs noticeably decreased the bacterial load and neutrophil recruitment in organs other than the kidneys, although the nanoparticle biodistribution in these organs was low. A large number of bacteria and neutrophils are present in bacteremic blood. It is suggested that NLCs inhibit MRSA growth and inflammation in circulation in the early stage of infection, followed by limited bacterial and neutrophil transport to peripheral organs. Ciprofloxacin molecules are rapidly cleared from circulation with 20%–40% protein binding [61, 62]. The adsorption of plasma proteins to the nanoparticulate surface is generally low to evade degradation. NLCs with a size of <200 nm, a poloxamer 188-incorporated surface and negative zeta potential can be retained in the bloodstream for an extended period of time [63]. Poloxamer 188 increases the hydrophilicity of nanoparticulate surfaces, resulting in diminished macrophage recognition and phagocytosis. The crystalline solid lipids present in NLCs cause slower degradation of the lipid matrix to produce long-term circulation formulations [12]. Nanoparticle uptake by neutrophils might occur in circulation to arrest neutrophil activation and subsequent migration to organs.

The mortality associated with sepsis depends on the dysregulated host cytokine storm. Cytokines are inflammatory mediators that trigger inflammatory pathology and subsequent organ damage. The cytokines IL-1 $\beta$ , IL-6, and TNF- $\alpha$  mediate the immunopathological features of sepsis and are released by neutrophils to exacerbate acute

inflammation [64]. IL-6 is an early biomarker in bacteremia that is used to evaluate the inflammatory response [6, 65]. TNF- $\alpha$  is produced in response to acute sepsis. IL-1 $\beta$  and IL-6 enhance TNF- $\alpha$  expression to stimulate neutrophil recruitment. Activated neutrophils are the major inflammatory cells that express IL-17A, which can be used as a predictor of *S. aureus* bacteremia [66]. The organs of MRSA-infected rats showed increased levels of these cytokines (Fig. 5c to g). Our nanocarriers inhibited cytokine expression, suggesting their capacity to inhibit inflammation. The NLCs containing antibiotics and PDE4 inhibitors could inhibit MRSA growth and neutrophil activation to limit the cytokine storm caused by the bacteremia-induced inflammatory response. The acute inflammation induced by dysregulated cytokines during sepsis leads to vasodilation and apoptosis in different tissues [23]. After MRSA challenge, we observed congestion and necrosis in the heart, lungs, and kidneys (Fig. 6). The increased permeability of blood vessels allowed neutrophils to migrate from the blood to peripheral organs. Histological analysis of Ly6G showed neutrophil accumulation in the organs (Fig. 7b), while NLCs inhibited the entrance of neutrophils into organs and thus prevented organ disruption. The organ failure caused by the host response to infection is a predominant mechanism of sepsis-related death. The mortality associated with bacteremia is dependent on cytokine overexpression, and attenuated cytokine release is a prerequisite for reducing mortality [61]. In this study, the mortality rate notably increased in the MRSA-infected mice (Fig. 4a), suggesting successful creation of the bacteremia model. Rolipram was found to be useful in improving cardiac and renal function during sepsis, thus promoting the survival of the animals [24]. Our data confirmed the role of rolipram in improving survival. This amelioration was further enhanced by the encapsulation of rolipram in lipid-based nanocarriers. The NLCs suppressed the release of proinflammatory cytokines in bacteremic mice, decreased the MRSA load, and increased survival.

There were some limitations in our study. The bacteremia model established in this study and its clinical relevance are still unclear. Treatment with drugs prior to the induction of bacteremia led to an effective and stable plasma drug concentration. However, in clinical practice, it is difficult to administer drugs before bacteremia onset; thus, our method of using NLCs to treat bacteremia could be used for prevention but not for therapy with rigorous definitions. The experimental periods for the in vivo study (40 h and 4 days) were too short to offer more information regarding the long-term outcome and augment the importance of our work. Additional basic studies are required to verify any potential effect of NLCs on bacteremia. The combination of free ciprofloxacin

and rolipram might cause interactions that would lower their antimicrobial and anti-inflammatory activities, but the detailed mechanisms are not completely understood. Further investigation is required to explore the inherent mechanisms.

## Conclusions

The present work demonstrated the successful preparation of dual drug-loaded NLCs to enhance the efficiency of bacteremia treatment. The encapsulation of ciprofloxacin and rolipram into lipid-based nanoparticles was nearly complete. In vitro evaluation revealed superior antibacterial and anti-inflammatory potencies of the NLCs compared to the combination of free drugs using MRSA and neutrophils as models, respectively. Intravenously injected NLCs were deposited primarily in the kidneys due to the incorporation of retinol in the nanoparticles. Treatment with NLCs encapsulating both ciprofloxacin and rolipram improved bacterial clearance, inhibited elastase expression, and prevented organ damage in rats infected with MRSA. The nanocarriers were found to suppress the cytokine overexpression in peripheral organs and improve the survival rate of rats with bacteremia-induced sepsis. The intravenous nanocarriers possibly mitigated MRSA growth and suppressed neutrophil activation in circulation, followed by minimizing MRSA and neutrophil transport to organs. The combination of anti-MRSA and anti-inflammatory nanocarriers relieved the acute inflammation caused by MRSA infection and thus showed potential application for bacteremia treatment.

## Methods

### Preparation of NLCs

The NLCs were fabricated by the homogenization-sonication method [41]. The aqueous and lipid phases were prepared separately. Three hundred fifty milligrams of Poloxamer 188 and 100 mg of deoxycholic acid were dissolved in water (8.89 ml). The lipid phase consisted of squalene (400 mg), hexadecyl palmitate (100 mg), soybean phosphatidylcholine (Phospholipon 80 H, 150 mg), retinol (25 mg), ciprofloxacin (5 mg), and rolipram (2 mg). Both phases were heated at 85°C for 15 min. Then, the aqueous phase was dispersed into the lipid phase with high-shear homogenization at 12,000 rpm for 20 min. The mixture was further sonicated using a probe-type sonicator at 35 W for 15 min. The final weight of the NLCs was 10 g.

### Estimation of the particle diameter and zeta potential

The average diameter and zeta potential of the NLCs were evaluated by a Nano ZS90 analyzer (Malvern). All

the samples were diluted 100-fold with water. Each sample was analyzed in triplicate.

### The encapsulation efficiency of the drugs

The encapsulation percentage of ciprofloxacin and rolipram was calculated by using the ultracentrifugation method to separate the encapsulated drugs from the free forms. The NLCs were centrifuged at 48,000x *g* and 4°C for 40 min. The free drugs in the supernatant and encapsulated drugs in the precipitate were analyzed by high-performance liquid chromatography (HPLC), whose setups for ciprofloxacin and rolipram have been previously described [67, 68].

### Drug release from the nanoparticles

The drug release of the ciprofloxacin- and rolipram-loaded NLCs was studied by the dialysis bag diffusion method. The drug-loaded control vehicle or NLCs (5 ml) were dispersed in a dialysis bag, and the dialysis bag (Cellu-Sep T2 with an MW cutoff of 6000–8000 Da) was then incubated in a beaker containing 100 ml of pH 7.4 phosphate buffer. The free control was drugs dissolved in 35% ethanol/pH 7.4 buffer. The beaker was placed on a magnetic stirrer with a stirring rate of 100 rpm, and the temperature of the assembly was maintained at 37°C. Samples (1 ml) were collected at definite time intervals and replaced with equal amounts of fresh buffer. After suitable dilutions, the samples were analyzed using HPLC.

### Minimum bactericidal concentration (MBC)

MRSA (ATCC33591) was purchased from the American Type Culture Collection. The MRSA suspension was diluted in tryptone soy broth to obtain a concentration of  $OD_{600} = 0.01$ . The TSB plate was incubated with different concentrations (0–31.25 µg/ml) of ciprofloxacin with or without rolipram either in their free or nanoparticulate forms at 37°C for 20 h. The CFU was then counted. The MBC was defined as the lowest ciprofloxacin concentration required to kill  $\geq 99.9\%$  of MRSA (ATCC33591).

### Time-response MRSA growth inhibition

The inhibition of MRSA growth by the drugs in their free or nanoparticulate form within 24 h was measured in 96-well plates. Ciprofloxacin (0.5 or 1 µg/ml), rolipram (0.2 or 0.4 µg/ml), or their combination was incubated with MRSA ( $OD_{600} = 0.01$ ) at 35°C for 24 h. The absorbance of each well was measured at 600 nm to detect MRSA growth in real-time.

### Isolation of human neutrophils

Neutrophils from healthy donors between the ages of 20–30 years old were isolated by using a protocol

approved by the Institutional Review Board at Chang Gung Memorial Hospital. Written informed consent was obtained from every subject. The neutrophils were purified by sedimentation prior to centrifugation in a Ficoll Hypaque gradient and the hypotonic lysis of erythrocytes [69].

#### Neutrophil viability

Lactate dehydrogenase (LDH) is an indicator of cellular membrane leakage and cell viability. The commercial kit CytoTox 96 (Promega) was used to estimate the LDH levels. The detailed protocol was previously described [70].

#### Superoxide anion production by neutrophils

Superoxide anion release from primary neutrophils was assessed using Ferricytochrome *c* [71]. Briefly, neutrophils ( $6 \times 10^5$  cells/ml) were incubated with ferricytochrome *c* (0.5 mg/ml) and  $\text{CaCl}_2$  (1 mM) at  $37^\circ\text{C}$ . Neutrophils were treated with ciprofloxacin (0.75–75 nM), rolipram (0.3–30 nM), or their combination in free or nanoparticulate form for 10 min. Then, the neutrophils were activated by formyl-methionyl-leucyl phenylalanine (fMLF, 0.1  $\mu\text{M}$ ) and cytochalasin B (1  $\mu\text{g}/\text{ml}$ ). Ferricytochrome *c* reduction was monitored by measuring the absorbance at 550 nm.

#### Nanoparticle uptake by neutrophils

NLCs were labeled with 0.1 mg/ml rhodamine 800 dye to observe their ingestion by neutrophils. Neutrophils ( $1 \times 10^7$  cells/ml) were incubated with NLCs (5 or 10  $\mu\text{l}$ ) at  $37^\circ\text{C}$  for 5 min, and the reaction was stopped by adding Hank's balanced salt solution at  $4^\circ\text{C}$ . The neutrophils were imaged using confocal microscopy. The fluorescence intensity of the rhodamine-labeled NLCs was also quantified by flow cytometry.

#### Animals

Male Sprague-Dawley rats (200–300 g) and Balb/c mice (20–25 g) were purchased from Lasco Biotechnology (Taipei, Taiwan). All the animals were treated in accordance with protocols approved by the Institute of Animal Care and the Use Committee of Chang Gung University.

#### Biodistribution of NLCs in rats

Near-infrared (NIR) dye (iFluor 790; 0.08%) was incorporated into the NLCs to monitor the biodistribution of intravenously injected NLCs. The rats were anesthetized with Zoletil 50 (30 mg/kg) and xylazine (6 mg/kg). The NLCs (0.8 ml/kg) were administered via the tail vein.

The rats were sacrificed after 2 h. The organs were harvested to detect the NIR signals with an *in vivo* imaging system (IVIS, Pearl Impulse Imaging System, Li-Cor). The NIR signal intensity was quantified by Pearl Impulse software.

#### Bacteremia model induced by MRSA in mice

A mouse model of bacteremia was induced according to a previous study with some modifications [72]. The mice were randomly assigned into four groups: (i) uninfected control receiving PBS, (ii) MRSA infection, (iii) MRSA infection with intravenous injection of two drugs in 10% ethanol, and (iv) MRSA infection with intravenous injection of dual drug-loaded NLCs. Bacteremia was induced by intravenous injection of MRSA ( $1 \times 10^7$  CFU). The mice were administered NLCs or 10% ethanol containing ciprofloxacin (2.5 mg/kg) and rolipram (1 mg/kg) 24 h before injection with MRSA. Mortality was monitored and recorded over four days with a camera. The mice were sacrificed at 40 h and 4 d postinfection to estimate the MRSA CFU counts in the blood and peripheral organs.

#### Elastase in organs

The neutrophil elastase 680 FAST imaging agent (PerkinElmer) was used to observe the levels of neutrophil elastase *in vivo*. Four hours after the intravenous injection of the imaging agent (100  $\mu\text{l}$ ), the animals were sacrificed to harvest the organs. The harvested organs were observed and photographed using a fluorescence IVIS system (Lumina LT Series III, PerkinElmer).

#### Cytokine expression in organs

Samples from the organs of mice were used to measure the levels of cytokines, including IFN- $\gamma$ , IL-1 $\beta$ , IL-6, IL-17A, and TNF- $\alpha$ , using commercial kits (BioLegend), following the manufacturer's instructions.

#### Histological observation

Specimens from different organs were immersed in 10% formaldehyde, embedded in paraffin, and then sliced into 5- $\mu\text{m}$ -thick sections for H&E staining. We also examined MRSA and Ly6G in the organs by immunohistochemistry. The organ sections were incubated with the relevant antibodies (*S. aureus* Rosenbach antibody for MRSA and recombinant anti-Ly6G antibody for neutrophils) for 1 h and then incubated with biotinylated donkey anti-rabbit IgG for 20 min. The sections were observed by optical microscopy.

## Statistical analysis

The data shown in this work are presented the mean and the standard error of the mean. Significant differences between different groups were examined by the Kruskal-Wallis method. Individual differences were evaluated post hoc by Dunn's test. Significance was demonstrated by  $p < 0.05$ .

## Supplementary Information

The online version contains supplementary material available at <https://doi.org/10.1186/s12951-021-00789-5>.

**Additional file 1: Figure S1.** The release kinetics of ciprofloxacin androlipram from free control and NLCs.

## Acknowledgements

The authors are grateful for the financial support from Ministry of Science and Technology of Taiwan (MOST-107-2320-B-182-016-MY3) Chang Gung Memorial Hospital (CMRPG3H0671-3).

## Authors' contributions

CCL, FCL, and JYF designed the research. CCL, HPY, SCY and YSD performed the experiments and collected and analyzed the data. CCL, HPY, and AA validated the results. HPY, SCY, and AA wrote the manuscript text and prepared the figures. FCL and JYF have read critically and edited the manuscript. CCL and JYF acquired the funding. All authors reviewed the manuscript. All authors read and approved the final manuscript.

## Availability of data and materials

The datasets used and/or analysed during the current study are available from the corresponding author on reasonable request.

## Ethics approval and consent to participate

Not applicable.

## Consent for publication

Not applicable.

## Competing interests

The authors declare that they have no competing interests.

## Author details

<sup>1</sup> Department of Anesthesiology, Chang Gung Memorial Hospital, 5 Fuxing Street, Kweishan, Taoyuan 333, Taiwan. <sup>2</sup> School of Medicine, College of Medicine, Chang Gung University, Kweishan, Taoyuan, Taiwan. <sup>3</sup> Department of Cosmetic Science, Providence University, Taichung, Taiwan. <sup>4</sup> Department of Pharmaceutics, College of Pharmacy, Prince Sattam Bin Abdulaziz University, Al Kharj, Saudi Arabia. <sup>5</sup> Pharmaceutics Laboratory, Graduate Institute of Natural Products, Chang Gung University, 259 Wen-Hwa 1st Road, Kweishan, Taoyuan 333, Taiwan. <sup>6</sup> Research Center for Food and Cosmetic Safety and Research Center for Chinese Herbal Medicine, Chang Gung University of Science and Technology, Kweishan, Taoyuan, Taiwan.

Received: 6 November 2020 Accepted: 2 February 2021  
Published online: 15 February 2021

## References

- Bergin SP, Holland TL, Fowler VG Jr, Tong SYC. Bacteremia, sepsis, and infective endocarditis associated with *Staphylococcus aureus*. *Curr Top Microbiol Immunol*. 2017;409:263–96.
- Holland TL, Arnold C, Fowler Jr VG. Clinical management of *Staphylococcus aureus* bacteremia. A review. *JAMA*. 2014;312:1330–41.
- Corl KA, Zeba F, Caffrey AR, Hermenau M, Lopes V, Phillips G, Merchant RC, Levy MM, LaPlante KL. Delay in antibiotic administration is associated with mortality among septic shock patients with *Staphylococcus aureus* bacteremia. *Crit Care Med*. 2020;48:525–32.
- Minejima E, Bensman J, She RC, Mack WJ, Tuan Tran M, Ny P, Lou M, Yamaki J, Nieberg P, Ho J, Wong-Beringer A. A dysregulated balance of proinflammatory and anti-inflammatory host cytokine response early during therapy predicts persistence and mortality in *Staphylococcus aureus* bacteremia. *Crit Care Med*. 2016;44:671–9.
- Anname D, Aegerter P, Jars-Guincestre MC, Guidet B. Current epidemiology of septic shock: the CUB-Rea network. *Am J Respir Crit Care Med*. 2003;168:165–72.
- Salas DE, Minejima E, Wu J, Fang C, Wang J, She R, Nieberg P, Wong-Beringer A. *Staphylococcus aureus* bacteremia in patients not meeting sepsis criteria: clinical features, host immune response and outcomes. *J Clin Med Ther*. 2017;2:27.
- Rello J, Valenzuela-Sánchez F, Ruis-Rodríguez M, Moyano S. Sepsis: a review of advances in management. *Adv Ther*. 2017;34:2393–411.
- Hassoun A, Linder PK, Friedman B. Incidence, prevalence, and management of MRSA bacteremia across patient populations—a review of recent developments in MRSA management and treatment. *Crit Care*. 2017;21:211.
- Aljuffali IA, Huang CH, Fang JY. Nanomedical strategies for targeting skin microbiomes. *Curr Drug Metab*. 2015;16:255–71.
- Ikoba U, Peng H, Li H, Miller C, Yu C, Wang Q. Nanocarriers in therapy of infections and inflammatory diseases. *Nanoscale*. 2015;7:4291.
- Yeh YC, Huang TH, Yang SC, Chen CC, Fang JY. Nano-based drug delivery or targeting to eradicate bacteria for infection mitigation: a review of recent advances. *Front Chem*. 2020;8:286.
- Beloque A, Solinis MA, Delgado A, Évora C, del Pozo-Rodríguez A, Rodríguez-Gascón A. Biodistribution of nanostructured lipid carriers (NLCs) after intravenous administration to rats: influence of technological factors. *Eur J Pharm Biopharm*. 2013;84:309–14.
- Hattori Y, Hattori K, Suzuki T, Matsuda N. Recent advances in the pathophysiology and molecular basis of sepsis-associated organ dysfunction: novel therapeutic implications and challenges. *Pharmacol Ther*. 2017;177:56–66.
- Liapis AP, Kan VL, Rochester CG, Simon GL. The effect of statins on mortality in patients with bacteremia. *Clin Infect Dis*. 2001;33:1352–7.
- Sung PH, Chiang HJ, Chen CH, Chen YL, Huang TH, Zhen YY, Chang MW, Liu CF, Chung SY, Chen YL, Chai HT, Sun CK, Yip HK. Combined therapy with adipose-derived mesenchymal stem cells and ciprofloxacin against acute urogenital organ damage in rat sepsis syndrome induced by intrapelvic injection of cecal bacteria. *Stem Cells Transl Med*. 2016;5:782–92.
- Choo EJ, Chambers HF. Treatment of methicillin-resistant *Staphylococcus aureus* bacteremia. *Infect Chemother*. 2016;48:267–73.
- Amodio-Groton M, Madu A, Madu CN, Briceland LL, Seligman M, McMaster P, Miller MH. Sequential parenteral and oral ciprofloxacin regimen versus parenteral therapy for bacteremia: a pharmacoeconomic analysis. *Ann Pharmacother*. 1996;30:596–602.
- Hur J, Lee A, Hong J, Jo WY, Cho OH, Kim S, Bae IG. *Staphylococcus aureus* bacteremia originating from urinary tract infections: a case report and literature review. *Infect Chemother*. 2016;48:136–9.
- Lo CL, Lee CC, Li CW, Lin MC, Hsueh PR, Lee NY, Ko WC. Fluoroquinolone therapy for bloodstream infections caused by extended-spectrum beta-lactamase-producing *Escherichia coli* and *Klebsiella pneumoniae*. *J Microb Immunol Infect*. 2017;50:355–61.
- Li H, Zuo J, Tang W. Phosphodiesterase-4 inhibitors for the treatment of inflammatory diseases. *Front Pharmacol*. 2018;9:1048.
- Chang X, Hu LF, Ma XJ, Yin J, Liu XY, Li JB. Influence of roflumilast on sepsis mice through the JAK/STAT signaling pathway. *Eur Rev Med Pharmacol Sci*. 2019;23:1335–41.
- Dalamaga M, Karampela I, Mantzoros CS. Commentary: phosphodiesterase 4 inhibitors as potential adjunct treatment targeting the cytokine storm in COVID-19. *Metab Clin Exp*. 2020;109:154282.
- Xu X, Liao L, Hu B, Jiang H, Tan M. Roflumilast, a phosphodiesterase-4 (PDE4) inhibitor, alleviates sepsis-induced acute kidney injury. *Med Sci Monit*. 2020;26:e921319.
- Sims CR, Singh SP, Mu S, Gokden N, Zakaria D, Nguyen TC, Mayeux PR. Rolipram improves outcome in a rat model of infant sepsis-induced cardiorenal syndrome. *Front Pharmacol*. 2017;8:237.

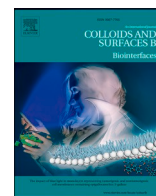


25. Lu X, Wang J, Chen X, Jiang Y, Pan ZK. Rolipram protects mice from Gram-negative bacterium *Escherichia coli*-induced inflammation and septic shock. *Sci Rep*. 2020;10:175.
26. Christaki E, Giamarellos-Bourboulis EJ. The complex pathogenesis of bacteremia. From antimicrobial clearance mechanisms to the genetic background of the host. *Virulence*. 2014;5:57–65.
27. Hindi KM, Ditto AJ, Panzner MJ, Medvetz DA, Han DS, Hovis CE, Hilliard JK, Taylor JB, Yun YH, Cannon CL, Youngs WJ. The antimicrobial efficacy of sustained release silver-carbene complex-loaded L-tyrosine polyphosphate nanoparticles: characterization, in vitro and in vivo studies. *Biomaterials*. 2009;30:3771–9.
28. Ansari MA, Khan HM, Khan AA, Pal R, Cameotra SS. Antibacterial potential of Al<sub>2</sub>O<sub>3</sub> nanoparticles against multidrug resistance strains of *Staphylococcus aureus* isolated from skin exudates. *J Nanopart Res*. 2013;15:1970.
29. Sun D, Zhang W, Li N, Zhao Z, Mou Z, Yang E, Wang W. Silver nanoparticles-quercetin conjugation to siRNA against drug-resistant *Bacillus subtilis* for effective gene silencing: in vitro and in vivo. *Mater Sci Eng C*. 2016;63:522–34.
30. Gao F, Xu L, Yang B, Fan F, Yang L. Kill the real with the fake: eliminate intracellular *Staphylococcus aureus* using nanoparticle coated with its extracellular vesicle membrane as active-targeting drug carrier. *ACS Infect Dis*. 2019;5:218–27.
31. Zhang C, Zhao W, Bian C, Hou X, Deng B, McComb DW, Chen X, Dong Y. Antibiotic-derived lipid nanoparticles to treat intracellular *Staphylococcus aureus*. *ACS Appl Bio Mater*. 2019;2:1270–7.
32. Vanamala K, Tatiparti K, Bhise K, Sau S, Scheetz MH, Rybak MJ, Andes D, Iyer AK. Novel approaches for the treatment of methicillin-resistant *Staphylococcus aureus*: using nanoparticles to overcome multidrug resistance. *Drug Discov Today*. 2020. <https://doi.org/10.1016/j.drudis.2020.10.011>.
33. Hickey JW, Santos JL, Williford JM, Mao HQ. Control of polymeric nanoparticle size to improve therapeutic delivery. *J Control Release*. 2015;219:536–47.
34. Zhang J, Froelich A, Michniak-Kohn B. Topical delivery of meloxicam using liposome and microemulsion formulation approaches. *Pharmaceutics*. 2020;12:282.
35. Bhattacharjee S. DLS and zeta potential—what they are and what they are not? *J Control Release*. 2016;235:337–51.
36. Dobrovol'skaia MA, Aggarwal P, Hall JB, McNeil SE. Preclinical studies to understand nanoparticle interaction with the immune system and its potential effects on nanoparticle biodistribution. *Mol Pharm*. 2008;5:487–95.
37. Alcantara KP, Zulfakar MH, Castillo AL. Development, characterization and pharmacokinetics of mupirocin-loaded nanostructured lipid carriers (NLCs) for intravascular administration. *Int J Pharm*. 2019;571:118705.
38. Zhang K, Lv S, Li X, Feng Y, Li X, Liu L, Li S, Li Y. Preparation, characterization, and in vivo pharmacokinetics of nanostructured lipid carriers loaded with oleanolic acid and gentiopiricin. *Int J Nanomed*. 2013;8:3227–39.
39. Masadeh MM, Alzoubi KH, Khabour OF, Al-Azzam SI. Ciprofloxacin-induced antibacterial activity is attenuated by phosphodiesterase inhibitors. *Curr Ther Res*. 2014;77:14–7.
40. Vignola AM. PDE4 inhibitors in COPD—a more selective approach to treatment. *Respir Med*. 2004;98:495–503.
41. Alalawi A, Wang PW, Lu PL, Chen YP, Fang JY, Yang SC. Synergistic anti-MRSA activity of cationic nanostructured lipid carriers in combination with oxacillin for cutaneous application. *Front Microbiol*. 2018;9:1493.
42. Lin MH, Lin CF, Yang SC, Hung CF, Fang JY. The interplay between nanoparticles and neutrophils. *J Biomed Nanotechnol*. 2018;14:66–85.
43. Tavares LP, Garcia CC, Vago JP, Queiroz-Junior CM, Galvão I, David BA, Rachid MA, Silva PMR, Russo RC, Teixeira MM, Sousa LP. Inhibition of phosphodiesterase-4 during pneumococcal pneumonia reduces inflammation and lung injury in mice. *Am J Respir Cell Mol Biol*. 2016;55:24–34.
44. Kelley WJ, Fromen CA, Lopez-Cazares G, Eniola-Adefeso O. PEGylation of model drug carriers enhances phagocytosis by primary human neutrophils. *Acta Biomater*. 2018;79:283–93.
45. Boraschi D, Italiani P, Palomba R, Decuzzi P, Duschl A, Fadeel B, Moghimi SM. Nanoparticles and innate immunity: new perspectives on host defense. *Semin Immunol*. 2017;34:33–51.
46. Yu HP, Liu FC, Umoro A, Lin ZC, Elzoghby AO, Hwang TL, Fang JY. Oleic acid-based nanosystems for mitigating acute respiratory distress syndrome in mice through neutrophil suppression: how the particulate size affects therapeutic efficiency. *J Nanobiotechnol*. 2020;18:25.
47. O'Byrne SM, Blaner WS. Retinol and retinyl esters: biochemistry and physiology. *J Lipid Res*. 2013;54:1731–43.
48. Smeland S, Bjerknes T, Malaba L, Eskild W, Norum KR, Blomhoff R. Tissue distribution of the receptor for plasma retinol-binding protein. *Biochem J*. 1995;305:419–24.
49. Raila J, Willnow TE, Schweigert FJ. Megalin-mediated reuptake of retinol in the kidneys of mice is essential for vitamin A homeostasis. *J Nutr*. 2005;135:2512–6.
50. Frey SK, Nagl B, Henze A, Raila J, Schlosser B, Berg T, Tepel M, Zidek W, Weickert MO, Pfeiffer AFH, Schweigert FJ. Isoforms of retinol binding protein (RBP4) are increased in chronic diseases of the kidney but not of the liver. *Lipids Health Dis*. 2008;7:29.
51. Pan TL, Wang PW, Hung CF, Aljuffali IA, Dai YS, Fang JY. The impact of retinol loading and surface charge on the hepatic delivery of lipid nanoparticles. *Colloids Surf B Biointerf*. 2016;141:584–94.
52. Shah NB, Vercellotti GM, White JG, Fegan A, Wagner CR, Bischof JC. Blood-nanoparticle interactions and in vivo biodistribution: impact of surface PEG and ligand properties. *Mol Pharm*. 2012;9:2146–55.
53. Su Z, Niu J, Xiao Y, Ping Q, Sun M, Huang A, You W, Sang X, Yuan D. Effect of octreotide-polyethylene glycol(100) monostearate modification on the pharmacokinetics and cellular uptake of nanostructured lipid carrier loaded with hydroxycamptothecin. *Mol Pharm*. 2011;8:1641–51.
54. Zhao Z, Ukidve A, Krishnan V, Mitragotri S. Effect of physicochemical and surface properties on in vivo fate of drug nanocarriers. *Adv Drug Deliv Rev*. 2019;143:3–21.
55. Javidi J, Haeri A, Nowroozi F, Dadashzadeh S. Pharmacokinetics, tissue distribution and excretion of Ag<sub>2</sub>S quantum dots in mice and rats: the effects of injection dose, particle size and surface charge. *Pharm Res*. 2019;36:46.
56. Almeida JPM, Chen AL, Foster A, Drezek R. In vivo biodistribution of nanoparticles. *Nanomedicine*. 2011;6:815–35.
57. Hoshyar N, Gray S, Han H, Bao G. The effect of nanoparticle size on in vivo pharmacokinetics and cellular interaction. *Nanomedicine*. 2016;11:673–92.
58. Xue W, Liu Y, Zhang N, Yao Y, Ma P, Wen H, Huang S, Luo Y, Fan H. Effects of core size and PEG coating layer of iron oxide nanoparticles on the distribution and metabolism in mice. *Int J Nanomed*. 2018;13:5719–31.
59. Dayan GH, Mohamed N, Scully IL, Cooper D, Begier E, Eiden J, Jansen KU, Gurtman A, Anderson AS. *Staphylococcus aureus*: the current state of disease, pathophysiology and strategies for prevention. *Expert Rev Vaccines*. 2016;15:1373–92.
60. De Winter F, Van de Wiele C, Dumont F, Van Durme J, Solanki K, Britton K, Slegers G, Dierckx RA, Thierens H. Biodistribution and dosimetry of <sup>99m</sup>Tc-ciprofloxacin, a promising agent for the diagnosis of bacterial infection. *Eur J Nucl Med*. 2001;28:570–4.
61. Tofovic SP, Zacharia LC, Carcillo JA, Jackson EK. Inhibition of cytokine release by and cardiac effects of type IV phosphodiesterase inhibition in early, profound endotoxaemia in vivo. *Clin Exp Pharmacol Physiol*. 2000;27:787–92.
62. Wise R, Lockley RM, Webberly M, Dent J. Pharmacokinetics of intravenously administered ciprofloxacin. *Antimicrob Agents Chemother*. 1984;26:208–10.
63. Luan J, Zhang D, Hao L, Qi L, Liu X, Guo H, Li C, Guo Y, Li T, Zhang Q, Zhai G. Preparation, characterization and pharmacokinetics of amoitone B-loaded long circulating nanostructured lipid carriers. *Colloids Surf B Biointerf*. 2014;114:255–60.
64. Qin M, Qiu Z. Changes in TNF- $\alpha$ , IL-6, IL-10 and VEGF in rats with ARDS and the effects of dexamethasone. *Exp Ther Med*. 2019;17:383–7.
65. Abe R, Oda S, Sadahiro T, Nakamura M, Hirayama Y, Tateishi Y, Shinozaki K, Hirasawa H. Gram-negative bacteremia induces greater magnitude of inflammatory response than Gram-positive bacteremia. *Crit Care*. 2010;14:27.
66. Cao Y, Guimaraes AO, Peck MC, Mayba O, Ruffin F, Hong K, Carrasco-Triguero M, Fowler VG Jr, Maskarinec SA, Rosenberger CM. Risk stratification biomarkers for *Staphylococcus aureus* bacteremia. *Clin Transl Immunol*. 2020;9:e1110.
67. Fang CL, Wen CJ, Aljuffali IA, Sung CT, Huang CL, Fang JY. Passive targeting of phosphatidylserine increases rolipram delivery to the lungs for treatment of acute lung injury: an animal study. *J Control Release*. 2015;213:69–78.

68. Hsu CY, Sung CT, Aljuffali IA, Chen CH, Hu KY, Fang JY. Intravenous anti-MRSA phosphatiosomes mediate enhanced affinity to pulmonary surfactants for effective treatment of infectious pneumonia. *Nanomed-Nanotechnol Biol Med*. 2018;14:215–25.
69. Yu HP, Hsieh PW, Chang YJ, Chung PJ, Kuo LM, Hwang TL. 2-(2-Fluoroben-zamido)benzoate ethyl ester (EFB-1) inhibits superoxide production by human neutrophils and attenuates hemorrhagic shock-induced organ dysfunction in rats. *Free Radic Biol Med*. 2011;50:1737–48.
70. Liu FC, Yu HP, Lin CY, Elzoghby AO, Hwang TL, Fang JY. Use of cilomilast-loaded phosphatiosomes to suppress neutrophilic inflammation for attenuating acute lung injury: the effect of nanovesicular surface charge. *J Nanobiotechnol*. 2018;16:35.
71. Yang SC, Chung PJ, Ho CM, Kuo CY, Hung MF, Huang YT, Chang WY, Chang YW, Chan KH, Hwang TL. Propofol inhibits superoxide production, elastase release, and chemotaxis in formyl peptide-activated human neutrophils by blocking formyl peptide receptor 1. *J Immunol*. 2013;190:6511–9.
72. Veloso TR, Chaouch A, Roger T, Giddey M, Vouillamoz J, Majcherczyk P, Que YA, Rousson V, Moreillon P, Entenza JM. Use of a human-like low-grade bacteremia model of experimental endocarditis to study the role of *Staphylococcus aureus* adhesions and platelet aggregation in early endocarditis. *Infect Immun*. 2013;81:697–703.

# Publisher's note

Springer Nature remains neutral with regard to jurisdictional claims in published maps and institutional affiliations.



# Multifunctional TiO<sub>2</sub>/SBA-15 mesoporous silica hybrids loaded with organic sunscreens for skin application: The role in photoprotection and pollutant adsorption with reduced sunscreen permeation

Yu-Chih Lin<sup>a</sup>, Yi-Ping Fang<sup>b,c,d</sup>, Chi-Feng Hung<sup>e,f,g</sup>, Huang-Ping Yu<sup>h,i</sup>, Ahmed Alalaiwe<sup>j</sup>, Zhi-Yuan Wu<sup>k</sup>, Jia-You Fang<sup>h,k,l,\*</sup>

<sup>a</sup> Department of Environmental Engineering and Health, Yuanpei University, Hsinchu, Taiwan

<sup>b</sup> School of Pharmacy, College of Pharmacy, Kaohsiung Medical University, Kaohsiung, Taiwan

<sup>c</sup> Department of Medical Research, Kaohsiung Medical University Hospital, Kaohsiung, Taiwan

<sup>d</sup> Regenerative Medical and Cell Therapy Center, Kaohsiung Medical University, Kaohsiung, Taiwan

<sup>e</sup> School of Medicine, Fu Jen Catholic University, New Taipei City, Taiwan

<sup>f</sup> Master Program in Transdisciplinary Long Term Care, Fu Jen Catholic University, New Taipei City, Taiwan

<sup>g</sup> Ph.D. Program in Pharmaceutical Biotechnology, Fu Jen Catholic University, New Taipei City, Taiwan

<sup>h</sup> Department of Anesthesiology, Chang Gung Memorial Hospital at Linkou, Taoyuan, Taiwan

<sup>i</sup> School of Medicine, College of Medicine, Chang Gung University, Taoyuan, Taiwan

<sup>j</sup> Department of Pharmaceutics, College of Pharmacy, Prince Sattam Bin Abdulaziz University, Al Kharj, Saudi Arabia

<sup>k</sup> Pharmaceutics Laboratory, Graduate Institute of Natural Products, Chang Gung University, Taoyuan, Taiwan

<sup>l</sup> Research Center for Industry of Human Ecology and Research Center for Chinese Herbal Medicine, Chang Gung University of Science and Technology, Taoyuan, Taiwan

## ARTICLE INFO

### Keywords:

Mesoporous silica  
SBA-15  
Titanium dioxide  
Avobenzone  
Photoprotection  
Adsorption

## ABSTRACT

TiO<sub>2</sub> acts as an inorganic sunscreen and photocatalyst to protect humans from environmental pollutants. We incorporated TiO<sub>2</sub> into mesoporous silica (SBA-15) for skin application to prevent environmental stresses including UVA irradiation and pollutant invasion. Organic ultraviolet (UV)A filters such as avobenzone and oxybenzone were then loaded into mesoporous support for synergistic sunscreen efficiency. The as-prepared formulations with different TiO<sub>2</sub> amounts (10 %–50 %) were fabricated. The pore size decreased from 4.72 to 4.00 nm following the increase in TiO<sub>2</sub> percentage. TiO<sub>2</sub>/SBA-15 captured about 60 % fluoranthene and 80 % furfural within 3 h with no significant difference due to different TiO<sub>2</sub> content. The in vitro photoprotection assessed by UVA/UVB ratio exhibited the increase in Boots star rating from 2 to 3 to 5 by entrapment of avobenzone into TiO<sub>2</sub>/SBA-15. Thirty-percent TiO<sub>2</sub>/SBA-15 in hydrogel decreased avobenzone and oxybenzone deposition by 70 % and 80 % compared to free form, respectively. Avobenzone and TiO<sub>2</sub> supplementation to SBA-15 significantly alleviated skin cell death and neutrophil recruitment in the photoaged mouse skin compared to the SBA-15 application alone. Compared to the UVA-irradiated skin, 30 % TiO<sub>2</sub>/SBA-15 showed a 2.5- and 3.1-fold decline in IL-1 $\beta$  and IL-6 levels, respectively. The TiO<sub>2</sub>/SBA-15 hybrid was considered non-irritant based on results of cytotoxicity assay, skin histology, and cutaneous barrier function. Our data indicate that the versatile mesoporous silica is an effective system for topical use in sunscreen and skin protection.

## 1. Introduction

The continuous rise in air pollution as a result of industrial production has led to global warming and ozone depletion. The ozone hole has caused an increase in the ultraviolet (UV)A and UVB irradiation to the earth's surface. Skin is the primary organ exposed to environmental

stress [1]. The photoaged skin reveals increased dyspigmentation and wrinkling due to the accumulation of oxidative stress and antioxidant defense impairment, which may further extend to induce cutaneous inflammation and cancer [2]. Sunscreen is an efficient approach to prevent the harmful impact of UV exposure. Because of the stability, non-toxicity, and low cost, TiO<sub>2</sub> is popularly used as UV filter sunscreen

\* Corresponding author at: Pharmaceutics Laboratory, Graduate Institute of Natural Products, Chang Gung University, 259 Wen-Hwa 1<sup>st</sup> Road, Kweishan, Taoyuan 333, Taiwan.

E-mail address: [fajy@mail.cgu.edu.tw](mailto:fajy@mail.cgu.edu.tw) (J.-Y. Fang).

<https://doi.org/10.1016/j.colsurfb.2021.111658>

Received 21 December 2020; Received in revised form 5 February 2021; Accepted 24 February 2021

Available online 27 February 2021

0927-7765/© 2021 Elsevier B.V. All rights reserved.

[3]. TiO<sub>2</sub> has another role in environmental protection because it can absorb light to perform photocatalytic reaction for destroying hazardous materials in air or water [4]. This procedure is non-energy intensive and mineralizes the pollutants using only atmospheric oxygen as the additional species [5]. Nevertheless, TiO<sub>2</sub> has limited applicability because of the recombination of charge carriers and aggregation tendency [6]. A suitable support substrate may be useful in resolving these drawbacks.

Mesoporous silica is ideal support for confining TiO<sub>2</sub> and displaying outstanding photocatalysis. Mesoporous silica has been studied as the catalysis support, drug carrier, and sensor because of its features of high surface area, tunable pore size, biocompatibility, facile synthesis process, and probable surface functionalization [7]. Mesoporous silica adsorbs pollutants efficiently and can be employed for decontamination [8]. Mesoporous silica can be potentially used for dermatological applications, as a drug delivery system, and cosmetic sunscreen [9]. The pores on the surface and the large surface area of mesoporous silica provide the sites for light scattering, which is one of the mechanisms for photoprotection [10]. It is desirable to develop novel technology for efficient UV protection and capturing pollutants to minimize aging and damage of the skin by environmental stress. SBA-15 is a type of mesoporous silica with high thermal stability, thick framework wall, and complementary textural porosity [11]. We aimed to develop TiO<sub>2</sub>-embedded SBA-15 as a multifunctional material for topical application to adsorb contaminants and protect the skin from photoaging.

UVB contributes to 5% and UVA contributes to 95 % of UV radiation reaching the earth's surface [12]. UVA radiation remains constant throughout the whole year, whereas UVB radiation is encountered more in the summer [13]. Avobenzone and oxybenzone are the UVA organic filters commonly used to avoid photoaging. The combination of organic and inorganic UV filters can improve the photoprotective capability. Incompatibility between UV filters may complicate the optimization of the formulation. Another purpose of the present study was to evaluate the sunscreen ability of TiO<sub>2</sub>/SBA-15 hybrid associated with avobenzone or oxybenzone. It is favorable that the UV filters locate onto the skin surface to exert light absorption or reflection. Avobenzone and oxybenzone easily permeate into/across the skin to elicit allergic dermatitis and phototoxic skin response [14,15]. Topical avobenzone/oxybenzone is also detected in plasma or urine and promotes the risk of endocrine interference [16,17]. We hypothesized that the storage of organic UV filters inside the pores of mesoporous silica may reduce the possible delivery into the skin. For commercial or clinical use, the UV filters should be incorporated into the acceptable dosage form. According to a previous study [18], hydrogel demonstrates a lower oxybenzone permeation than that from lotion and cream. We utilized Carbopol hydrogel as the vehicle for the mesoporous silica in this study. The TiO<sub>2</sub>/SBA-15 composite was applied on mouse skin with or without UVA exposure to evaluate the photoprotection and safety of the developed hybrid.

## 2. Experimental

### 2.1. Preparation of SBA-15

We employed the hydrothermal method to synthesize SBA-15. Pluronic P123 (4 g) was dissolved in 2 M HCl (160 mL) at 30 °C for 1 h. Then 9.1 mL of tetraethyl orthosilicate (TEOS) was added to the mixture and stirred for 24 h. The mixture was heated at 90 °C for 24 h. The resulting precursor was filtered, washed with water, and dried at 100 °C for 5 h. The resultant solid underwent calcination at 550 °C with a heating rate of 1 °C/min for 5 h to remove the Pluronic template.

### 2.2. Preparation of TiO<sub>2</sub>/SBA-15 hybrid

The support material (1.5 g) and titanium(IV) isopropoxide were incorporated in different amounts into butanol and stirred at 45 °C for 1 h, after which, the butanol was evaporated at 160 °C for 2 h. The sample

was heated at 450 °C (heating rate: 1 °C/min) for 4 h. The loading of TiO<sub>2</sub> in the mesoporous silica was 10 %, 20 %, 30 %, 40 %, or 50 %.

### 2.3. Analysis of physical adsorption

The pore diameter, pore-volume, and surface area of mesoporous silica were achieved based on the BET method. It was an estimation from the N<sub>2</sub> adsorption-desorption isotherm (ASAP2000, Micromeritics). The pore size and volume were measured on the adsorption branch of isotherm according to the Barrett-Joyner-Halenda (BJH) method.

### 2.4. Organic UVA filter loading in mesoporous silica

Ethanol (30 mL) was used to disperse avobenzone or oxybenzone (20 mg) and mesoporous silica (200 mg). The mixture was stirred at room temperature for 24 h, followed by removal of ethanol at 90 °C for 9 h. The sunscreen-loaded mesoporous silica was further vacuum-dried. The entrapment percentage of the organic sunscreen in mesoporous silica was determined by the ultracentrifugation technique as described previously [10].

### 2.5. Characterization of sunscreen-loaded mesoporous silica

Electron microscopy was carried out with the following tools: a high-resolution scanning electron microscope (SEM, SU7000, Hitachi), and scanning transmission electron microscope (STEM, JEM2100, Jeol). The element mapping was visualized by STEM under the mode of EDS. The XRD was performed by a diffractometer (Kappa Apex II, Bruker) with Cu-K $\alpha$  radiation at a scanning speed of 0.5°/min. For the preparation of the samples for SEM and STEM imaging, 5 mg of the mesoporous silica was suspended in acetone (100  $\mu$ L) and then placed on a aluminum stub. After solvent evaporation, the images were taken at an electron beam energy of 200 kV.

### 2.6. Adsorption of PAHs or furans in mesoporous silica

Fluoranthene or furfural at 20  $\mu$ M was dissolved in 30 % propylene glycol (PG)/water. The mesoporous silica (10 mg) was added into the solution (15 mL) for vigorous stirring in the dark for 3 h. Aliquots of 0.3 mL were withdrawn from the solution at 0.5, 1.5, and 3 h. After filtering to remove mesoporous silica, the filtrate containing free fluoranthene or furfural was detected by HPLC. To test the photocatalytic effect of mesoporous silica, a 20 W UVA or UVB lamp was used as the source of light. The distance between the lamp and the solution level was 30 cm. The irradiation was continuous throughout the experiment (3 h).

### 2.7. UVA protection test

The ratio of UVA to UVB absorbance was used to determine UVA protection capability by the Optometrics SPF 290S analyzer. Before the determination, mesoporous silica was dispersed into Carbopol 940 hydrogel. The formulation of the gel was mesoporous silica (13 %), Carbopol 940 (0.6 %), and triethanolamine (2%) in water. The gel was spread on a polymethylmethacrylate plate (2 mg/cm<sup>2</sup>), and then UV irradiated at a dose of 17.5 J/cm<sup>2</sup>. The absorbance in the UVA (320–400 nm) and UVB (290–320 nm) range was detected for calculating the UVA/UVB ratio. This ratio was employed to decide the Boots rating. The detailed process for UVA protection evaluation is described in the previous study [19].

### 2.8. Permeation of organic UVA filters through the skin

The dorsal skin of one-week-old pigswas used as the permeation barrier in this experiment. The skin was mounted between donor and receptor of Franz cell assembly with stratum corneum facing the donor. The receptor medium was 30 % ethanol/pH 7.4 buffer (5 mL) kept at 37



°C. The donor was loaded with the hydrogel containing avobenzone- or oxybenzone-loaded mesoporous silica at 0.5 mL volume. For each receptor, aliquots of 0.3 mL were withdrawn at the determined times, followed by replacement with a fresh medium. The avobenzone or oxybenzone amount in the receptor was detected by HPLC as described earlier [20]. The skin specimen was removed after a 24 h treatment of mesoporous silica to estimate skin deposition. The skin sample was weighed, cut, and homogenized by MagNA Lyser (Roche). The homogenate was centrifuged at 10,000 × g for 10 min to collect the supernatant for the HPLC assay.

## 2.9. In vitro keratinocyte assay

The mesoporous silica at the concentrations of 1–500 µg/mL was incubated with keratinocyte cells (HaCaT,  $1 \times 10^5$  cells/mL) for 24 h. The cytotoxicity was assessed by adding 3-(4,5-dimethylthiazol-yl)-2,5-diphenyltetrazolium bromide (MTT) at 5 mg/mL into the cell medium at 37 °C for 4 h. The viable cells were estimated by the photometric absorbance at 550 nm in a microplate reader. IL-6 and CXCL1 released from HaCaT were analyzed by ELISA kits (BioLegend).

## 2.10. In vivo skin tolerance

The eight-week-old male nude mice were categorized into four groups: the non-treated control, the Carbopol 940 hydrogel treatment, the SBA-15-loaded hydrogel treatment, and 30 % TiO<sub>2</sub>/SBA-15-loaded hydrogel treatment groups. There were six animals in each group. The hydrogel (0.4 g) was topically administered on the mouse back each day for 5 days. After a 5-day intervention, the skin was examined for its gross and microscopic appearances and hematoxylin and eosin (H&E)-stained histology. The erythema (a\*), transepidermal water loss (TEWL), and skin pH value of the treated skin were determined by Cutometer MPA580 (Courage and Khazaka).

## 2.11. In vivo photoprotection of mesoporous silica

The mice were divided into five groups: the normal mice without any treatment, the mice exposed to UVA, the UVA-exposed mice treated with hydrogel, SBA-15-loaded hydrogel, and 30 % TiO<sub>2</sub>/SBA-15-loaded hydrogel with six animals in each group. The hydrogel (0.4 g) was spread onto an area of  $2 \times 2$  cm<sup>2</sup> on the back skin of mice. The mouse back was then exposed under UVA (10 J/cm<sup>2</sup>) at 365 nm. The distance between the mouse back and UVA light source was 10 cm. The mouse was irradiated by UVA each day for five days. The animal was sacrificed on Day 6 and the microscopic appearance of dorsal skin was visualized by Mini Scope-V (M&T Optics). Analysis of H&E-stained histology and immunohistochemistry (IHC) were performed. IL-1β and IL-6 in the skin were determined by ELISA according to the manufacturer's instruction (BioLegend).

## 2.12. Immunohistochemistry (IHC)

The treated skin was fixed overnight in 10 % neutral buffered formalin, embedded in paraffin, and sectioned. The skin slices were immunostained with the rabbit polyclonal TUNEL antibody, Ki67 antibody, or Ly6 G antibody for 1 h, followed by treatment with biotinylated donkey anti-rabbit IgG for 20 min. The IHC image was obtained using the Leica DMI8 microscopy system.

## 2.13. Statistical analysis

Data were displayed as the mean and standard error of the mean (SEM). The result was analyzed by one-way ANOVA followed by Dunn's posthoc test. The 0.05 (\*), 0.01 (\*\*), and 0.001 (\*\*\*) levels of probability were considered statistically significant.

## 3. Results

### 3.1. Textural characterization of mesoporous silica

Six SBA-15 formulations with TiO<sub>2</sub> concentrations in the range from 0% to 50 % were selected for examination. The pore size, pore-volume, and Brunauer-Emmett-Teller (BET) specific surface area derived from N<sub>2</sub> adsorption-desorption are mentioned in Table 1. The type IV isotherm was identified according to IUPAC classification after detecting the mesoporous material with cylindrical mesostructure (Suppl. Fig. 1). The incorporation of 50 % TiO<sub>2</sub> still maintained the mesoporous adsorption-desorption behavior. The average pore diameter of SBA-15 was found to be 4.51 nm and the incorporation of 10 % TiO<sub>2</sub> increased the pore diameter to 4.72 nm. The pore diameter decreased gradually from 4.72 to 4.00 nm as the TiO<sub>2</sub> amount increased from 10 % to 50 %. The pore volume of TiO<sub>2</sub>/SBA-15 appeared lower than that of pure SBA-15 and more TiO<sub>2</sub> in mesoporous silica yielded smaller pore volume. The BET surface area of SBA-15 was 1112 m<sup>2</sup>/g and exhibited a shift towards a lower level with the increase in TiO<sub>2</sub> percentage. The surface area of 50 % TiO<sub>2</sub>/SBA-15 was reduced by 30 % compared to that of SBA-15, demonstrating the pore occupancy by TiO<sub>2</sub>.

The size and morphology of mesoporous silica were visualized by SEM (Fig. 1A). The particle morphology showed the worm-like shapes with some interconnections. The images revealed that the mesoporous silica had the particle size of about 2–5 µm. The morphology and shape of the mesoporous silica were similar among the six formulations, and their structure was characterized by a STEM (Fig. 1B). The pore distribution of SBA-15 did not change after TiO<sub>2</sub> incorporation. The surface elemental composition of TiO<sub>2</sub>/SBA-15 was analyzed by the elemental assay. Fig. 1C summarizes the levels of three elements: Ti, Si, and O in the samples. The mapping profile indicates the uniform distribution of the three elements on the surface. A close interaction was observed between these elements for all TiO<sub>2</sub>/SBA-15 hybrids. The atomic ratios from energy-dispersive X-ray spectroscopy (EDS) spectra are mentioned in Table 2. The increase in the TiO<sub>2</sub> amount led to an increase in the Ti ratio from 5.92 (10 % TiO<sub>2</sub>) to 13.30 (50 % TiO<sub>2</sub>). It can thus be confirmed that TiO<sub>2</sub> was embedded into SBA-15 material.

X-ray diffraction (XRD) study was performed to verify the crystalline state of TiO<sub>2</sub> in mesoporous silica (Fig. 1D). Pure TiO<sub>2</sub> showed intense diffraction peaks at 25°, 38°, 48°, 53°, 55°, and 63°. These peaks were ascribed to the anatase phase of TiO<sub>2</sub> [21]. There was no peak between 20° and 70° for pristine SBA-15. The peak intensity was larger for mesoporous silica with greater TiO<sub>2</sub>. Some weak peaks were still detectable for the samples with less TiO<sub>2</sub>, indicating the presence of traces of crystalline TiO<sub>2</sub>.

### 3.2. TiO<sub>2</sub>/SBA-15 efficiently adsorbs fluoranthene and furfural in the presence or absence of UV

The capacity of mesoporous silica to adsorb the hazards was

**Table 1**  
Structural parameters of mesoporous silica.

| Formulation                   | Pore diameter (nm) | Volume (cm <sup>3</sup> /g) | BET surface area (m <sup>2</sup> /g) |
|-------------------------------|--------------------|-----------------------------|--------------------------------------|
| SBA-15                        | 4.51               | 0.80                        | 1111.82                              |
| 10 % TiO <sub>2</sub> /SBA-15 | 4.72               | 0.76                        | 1030.87                              |
| 20 % TiO <sub>2</sub> /SBA-15 | 4.45               | 0.72                        | 979.81                               |
| 30 % TiO <sub>2</sub> /SBA-15 | 4.03               | 0.62                        | 876.71                               |
| 40 % TiO <sub>2</sub> /SBA-15 | 3.99               | 0.56                        | 872.48                               |
| 50 % TiO <sub>2</sub> /SBA-15 | 4.00               | 0.54                        | 772.91                               |

BET, specific surface area measured by Brunauer-Emmett-Teller method.

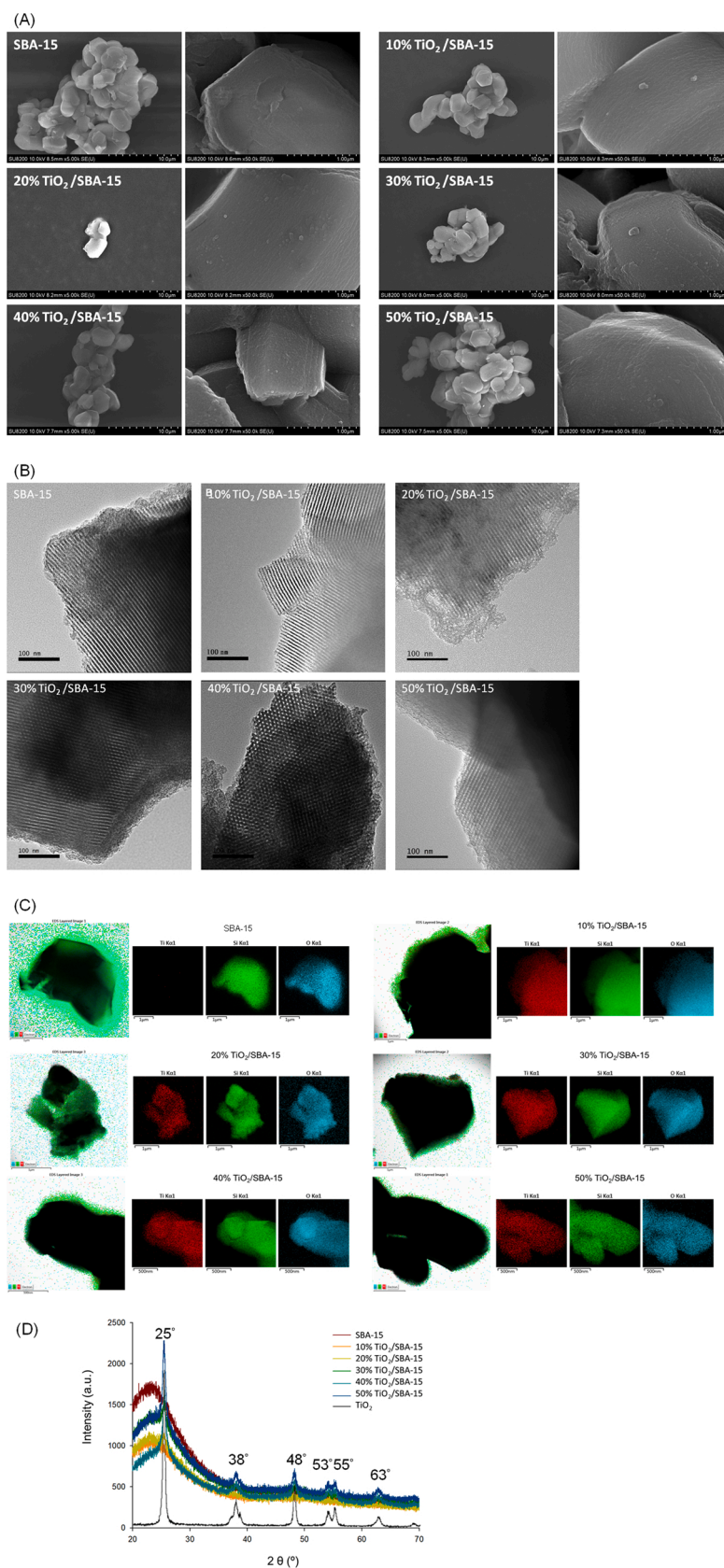


**Fig. 1.** The morphology of mesoporous silica formulations visualized by electron microscopy: (A) the SEM images with a lower magnification, (B) the STEM images with a higher magnification, (C) the element mapping visualized by STEM under the mode of EDS, and (D) XRD patterns.

**Table 2**

Ti, Si, and O element analysis by EDS.

| Formulation                   | Ti    | Si    | O     |
|-------------------------------|-------|-------|-------|
| SBA-15                        | 0     | 61.47 | 38.53 |
| 10 % TiO <sub>2</sub> /SBA-15 | 5.92  | 65.64 | 28.43 |
| 20 % TiO <sub>2</sub> /SBA-15 | 6.28  | 54.00 | 39.72 |
| 30 % TiO <sub>2</sub> /SBA-15 | 11.82 | 49.53 | 38.65 |
| 40 % TiO <sub>2</sub> /SBA-15 | 12.48 | 49.31 | 38.20 |
| 50 % TiO <sub>2</sub> /SBA-15 | 13.30 | 47.43 | 39.27 |

EDS, energy dispersive spectroscopy.

evaluated as an additional benefit in the use of mesoporous material for skin application. The supported SBA-15 could effectively adsorb fluoranthene by about 60 % under dark conditions (Fig. 2A). The adsorption percentage of fluoranthene did not increase as the time increased, indicating a saturation in adsorption by SBA-15 in a short time. Furthermore, UVA or UVB did not increase fluoranthene adsorption in SBA-15. The SBA-15 containing 10–40 % TiO<sub>2</sub> displayed a lower or comparative affinity for fluoranthene adsorption compared with that of SBA-15 alone. Fifty-percent TiO<sub>2</sub>/SBA-15 achieved 70 % fluoranthene adsorption at different periods. UVA or UVB irradiation generally

exhibit enhanced adsorption in the cases of most TiO<sub>2</sub>/SBA-15 hybrid formulations. The more binding sites in mesopores after TiO<sub>2</sub> incorporation might be the reason of the increased adsorption. Moreover, TiO<sub>2</sub>/SBA-15 could adsorb more fluoranthene under UVA than UVB. The efficiency of fluoranthene adsorption by 50 % TiO<sub>2</sub>/SBA-15 reached 81 % after UVA exposure for 1.5 h.

A parallel experiment was carried out for furfural adsorption. The extent of adsorption by SBA-15 gradually increased with time (Fig. 2B). The adsorption efficiency by SBA-15 in the dark was 69 % after 3 h. There was no significant difference in the adsorption percentage of furfural by SBA-15 with or without UV. The furfural sequestration by TiO<sub>2</sub>/SBA-15 also increased further with time. The mesoporous silicas with 40 % and 50 % TiO<sub>2</sub> exhibited better furfural adsorption, up to about 80 % after a 3 h incubation in the dark. The photocatalytic effect of TiO<sub>2</sub>/SBA-15 basically increased the affinity to capture furfural under UV. The mesoporous occupancy for furfural by TiO<sub>2</sub>/SBA-15 hybrids was comparable after UVA and UVB irradiation.

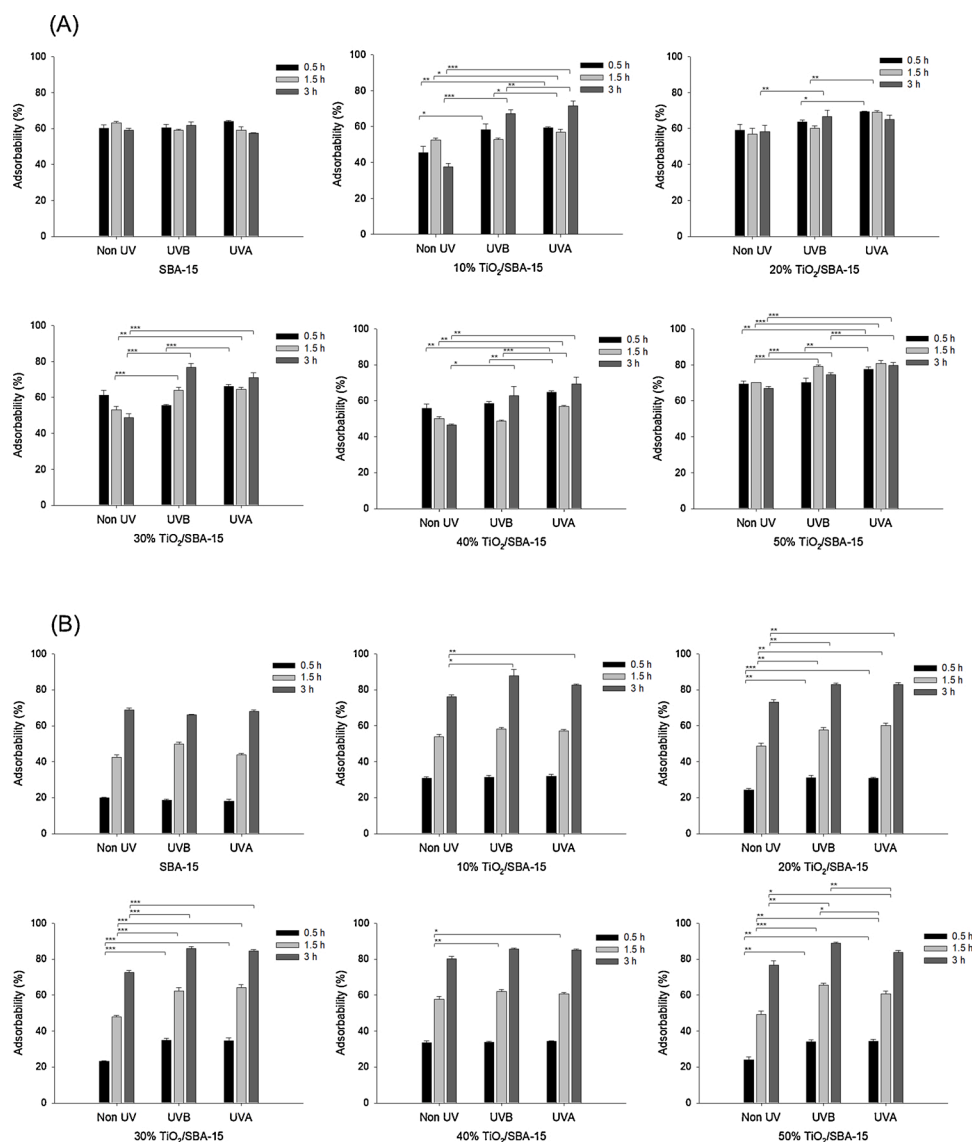


**Fig. 2.** The pollutant adsorbability percentage-time profiles of mesoporous silica formulations with various TiO<sub>2</sub> % in SBA-15: (A) the adsorption to fluoranthene and (B) the adsorption to furfural. Each value represents the mean  $\pm$  SEM ( $n = 4$ ).

### 3.3. Organic sunscreen loading increases in vitro UVA protection by TiO<sub>2</sub>/SBA-15

Avobenzone or oxybenzone was mixed with mesoporous silica to improve the UVA-protective capability. The encapsulation percentage of the organic sunscreens in all TiO<sub>2</sub>/SBA-15 was > 99 %, indicating successful adsorption in the mesoporous silica network. The 13 % TiO<sub>2</sub> in gel shows a UVA/UVB ratio of 0.9 (Suppl. Table 1). TiO<sub>2</sub>/SBA-15 without organic sunscreen had a lower UVA/UVB ratio than that by TiO<sub>2</sub> because of the lower TiO<sub>2</sub> amount (1.3%–6.5%) in mesoporous silica as compared to 13 % raw TiO<sub>2</sub>. The maximum UVA protection for TiO<sub>2</sub>/SBA-15 was found for the 50 % TiO<sub>2</sub> formulation. Nevertheless, the discrepancy of UVA protection with TiO<sub>2</sub> at different percentages was not large. The raw TiO<sub>2</sub> in the gel was characterized as maximum UVA protection according to Boots star rating (\*\*\*\*). The UVA protection by TiO<sub>2</sub>/SBA-15 was considered as moderate (\*\*) to good (\*\*\*). SBA-15 showed a low UVA/UVB ratio of 0.08. Free avobenzone and oxybenzone showed the Boots star ratings of \*\* and \*, respectively. Avobenzone and oxybenzone loading into SBA-15 exhibited increased UVA protection in comparison with organic sunscreen alone. A further increase in UVA protection was found by using TiO<sub>2</sub>/SBA-15 instead of SBA-15 alone. In the case of oxybenzone loading, 50 % TiO<sub>2</sub>/SBA-15 achieved a maximum UVA/UVB ratio of 1.27 (\*\*\*\*). The UVA/UVB ratio of oxybenzone-loaded 10 %–40 % TiO<sub>2</sub>/SBA-15 ranged between 0.54 and 0.89 with no statistical difference. All avobenzone-loaded TiO<sub>2</sub>/SBA-15 accomplished UVA ultra-protection according to Boots star rating (\*\*\*\*). The UVA/UVB ratio of avobenzone-loaded TiO<sub>2</sub>/SBA-15 was nearly 3 times that of avobenzone alone.

### 3.4. TiO<sub>2</sub>/SBA-15 inhibits the permeation of organic sunscreens through the skin

The possible delivery of avobenzone or oxybenzone from mesoporous silica into/across pig skin was examined. The mesoporous silica was incorporated into the hydrogel as the vehicle and both skin deposition and cumulative amount in receptor compartment were determined as the predictor of the uptake by the skin and possible transport into the systemic circulation, respectively. The avobenzone deposition in the skin from different formulations is shown in Fig. 3A. The free avobenzone in Carbopol gel delivered 158 nmol/mg into skin. The avobenzone entrapment into SBA-15 did not result in the change in deposition on the skin, whereas the addition of TiO<sub>2</sub> in SBA-15 lowered the uptake of avobenzone by the skin. The tendency of avobenzone deposition following the increase in TiO<sub>2</sub> concentration generally represented a parabolic pattern, with 30 % TiO<sub>2</sub>/SBA-15 displaying the least uptake. Thirty-percent TiO<sub>2</sub>/SBA-15 delivered about one-third of avobenzone molecules into the skin compared with free form. No avobenzone was detected in the receptor after a 24-h delivery, suggesting that avobenzone mainly stayed on the skin.

Fig. 3B shows oxybenzone deposition on the pig skin. The inclusion of SBA-15 reduced oxybenzone deposition by 56 %. There was no significant difference between oxybenzone deposition from the free form and encapsulated form in the presence of 10 % TiO<sub>2</sub>/SBA-15. A parabolic mode was observed for oxybenzone delivery from TiO<sub>2</sub>/SBA-15. Oxybenzone deposition from 30 % TiO<sub>2</sub>/SBA-15 was 8.4-fold lower than that from the free form in the gel. Oxybenzone was found to penetrate across skin to the receptor compartment (Fig. 3C). The trend of oxybenzone penetration into the receptor was similar to that of skin

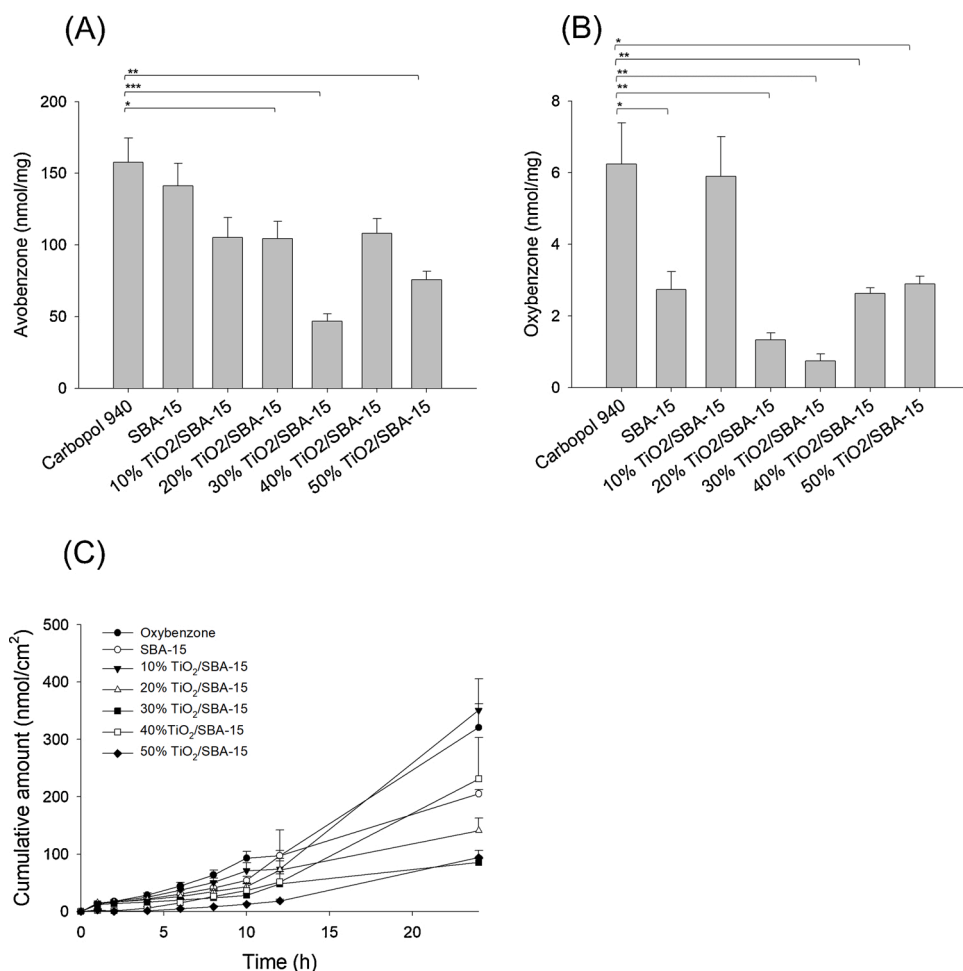


**Fig. 3.** Skin deposition and cumulative amount in receptor compartment after in vitro topical application of avobenzone or oxybenzone on pig skin from hydrogels: (A) pig skin deposition of avobenzone from various TiO<sub>2</sub>% in SBA-15, (B) pig skin deposition of oxybenzone from mesoporous silica formulations with various TiO<sub>2</sub>% in SBA-15, and (C) cumulative amount-time curves of oxybenzone from mesoporous silica formulations with various TiO<sub>2</sub>% in SBA-15. Each value represents the mean  $\pm$  SEM ( $n = 4$ ).



deposition. The time course of the penetrated oxybenzone amount from the free form and 10 % TiO<sub>2</sub>/SBA-15 was higher than that from other formulations. Both 30 % and 50 % TiO<sub>2</sub>/SBA-15 hybrids showed the least capacity to deliver oxybenzone into the receptor.

### 3.5. TiO<sub>2</sub>/SBA-15 causes limited skin toxicity in cell- and animal-based studies

The cell viability assay was employed to explore the cytotoxicity of mesoporous silica against keratinocytes (Fig. 4A). There was no cytotoxicity after a 24 h exposure of SBA-15 at 1–500 µg/mL. TiO<sub>2</sub> incorporation dose-dependently increased the cytotoxicity. The keratinocyte viability still maintained to > 80 % even at a very high concentration of TiO<sub>2</sub>/SBA-15. No relationship was observed between the cytotoxicity and TiO<sub>2</sub> dose. Cytokine (IL-6) and chemokine (CXCL1) were analyzed in keratinocytes treated with TiO<sub>2</sub>/SBA-15 at 50 µg/mL (Fig. 4B and C). TNF-α was used as a positive control. All mesoporous silicas induced no significant increase in IL-6, while CXCL1 expression increased as the TiO<sub>2</sub> percentage increased. The matrix containing 30 %, 40 %, and 50 % TiO<sub>2</sub> increased CXCL1 levels by 3.8-, 9.6-, and 8.7-fold, respectively.

We also examined in vivo safety of avobenzone-loaded mesoporous silica on mouse skin after a 5-day treatment. Thirty-percent TiO<sub>2</sub>/SBA-15 was selected as the representative TiO<sub>2</sub>-containing mesoporous silica. The phenotypic and microscopic appearance of the skin surface after the treatment is illustrated in Fig. 5A and B, respectively. No significant change was detected after the topical treatment of the hydrogels with or without mesoporous silica. The histological image of mouse skin also confirmed this result (Fig. 5C). The epidermis with TiO<sub>2</sub>/SBA-15 treatment showed an unperturbed appearance with normal thickness. We found no inflammatory infiltrate in the dermis after mesoporous silica

intervention. Skin erythema, TEWL, and skin pH value were assessed as shown in Fig. 5D, E, and F, respectively. The results indicated that TiO<sub>2</sub>/SBA-15 did not interfere with these physiological parameters.

### 3.6. TiO<sub>2</sub>/SBA-15 shows photoprotection to UVA-exposed skin

The photoprotective activity of avobenzone-loaded mesoporous silica in the hydrogel was appraised in a murine model of photoaging. The microscopic appearance of skin surface treated by UVA showed slight peeling, scaling, and some furrows (arrows in Fig. 6A). The furrows and erythema were still observed after topical administration of the hydrogel without mesoporous silica. Skin treated with SBA-15 or TiO<sub>2</sub>/SBA-15 exhibited no visible wrinkle and redness after UVA exposure. The UVA irradiation resulted in pronounced cell death in epidermis and dermis according to H&E-stained histology (Fig. 6B). The large loss of cellular nuclei in the UVA-treated skin indicated cell death. This death was partly inhibited after adding SBA-15 or 30 % TiO<sub>2</sub>/SBA-15 in the hydrogel. A remarkable increase in epidermal thickness accompanied by hyperkeratosis was observed after SBA-15 treatment on photoaged skin. In contrast, the hyperplasia and hyperkeratosis were negligible after TiO<sub>2</sub>/SBA-15 treatment.

The TUNEL staining in UVA-exposed skin was not significant because of nuclear-loss in most of the cells (Fig. 6C), suggesting severe damage to UVA-treated skin. SBA-15 intervention compared to blank hydrogel prior to UVA exposure partially suppressed apoptotic DNA damage in the epidermis. A substantial decline in the apoptotic rate was observed after TiO<sub>2</sub>/SBA-15 treatment. Some Ki67-positive cells were detected in the non-treatment control (Fig. 6D). A sharp decrease in the number of Ki67-expressed cells was observed after UVA irradiation. Keratinocyte hyperproliferation was observed in the UVA-treated skin with

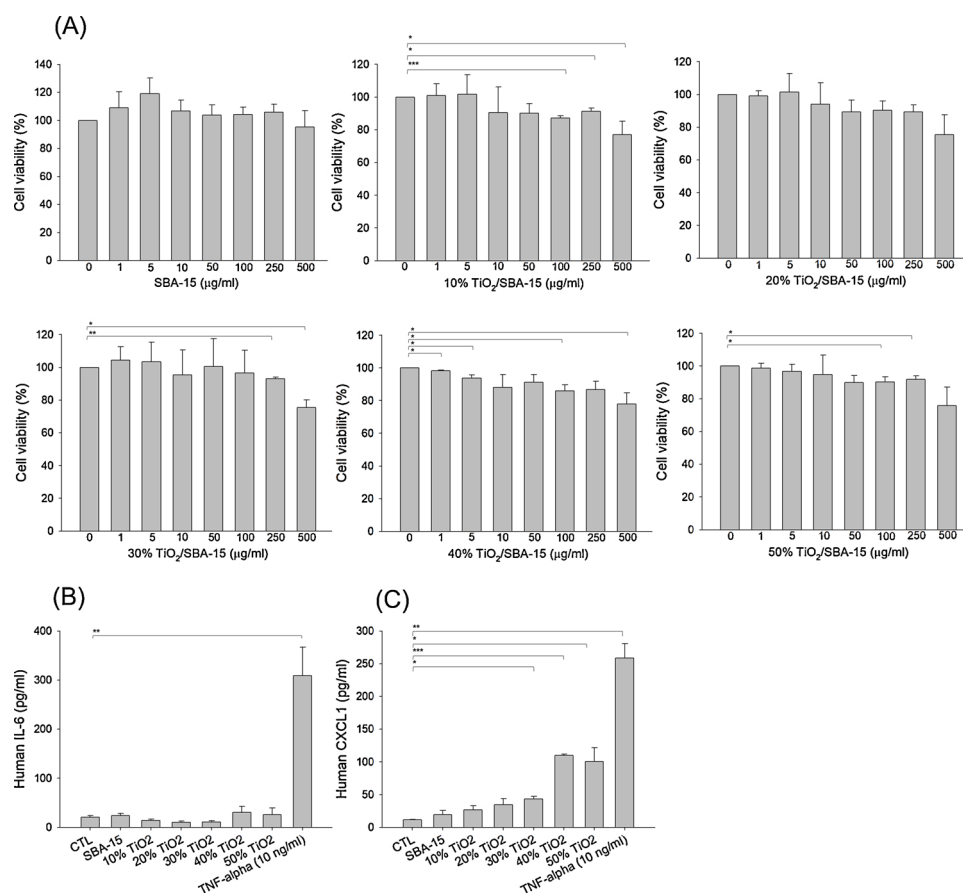


**Fig. 4.** The in vitro safety of mesoporous silica formulations with various TiO<sub>2</sub>% in SBA-15 on keratinocytes (HaCaT): (A) the cell viability examined by MTT, (B) IL-6 expression, and (C) CXCL1 expression. Each value represents the mean ± SEM (*n* = 3).

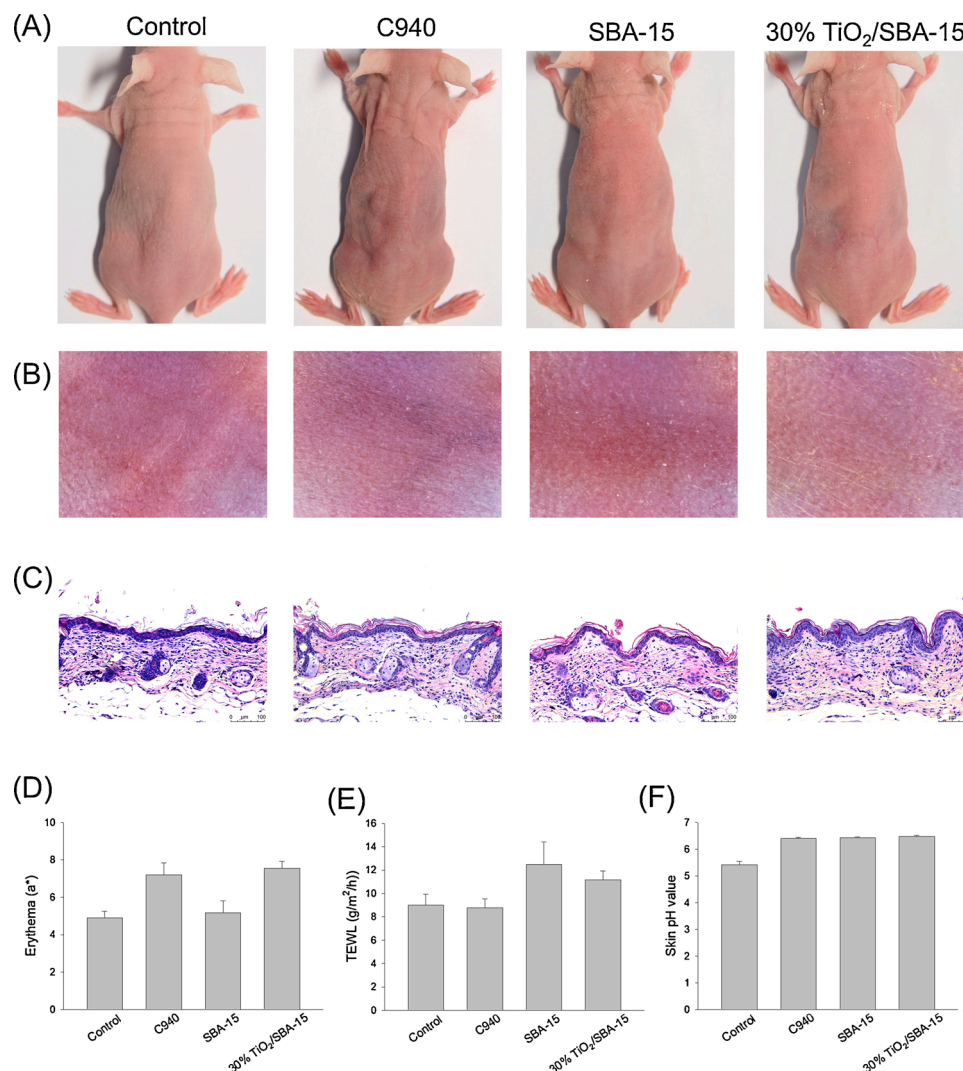


**Fig. 5.** The in vivo safety of hydrogels containing SBA-15 or 30 % TiO<sub>2</sub>/SBA-15 on nude mouse back skin: (A) macroscopic view of treated skin area, (B) microscopic view of treated skin area, (C) H&E-stained histology, (D) erythema (a\*) quantification, (E) TEWL measurement, and (F) skin pH value. Each value represents the mean  $\pm$  SEM ( $n = 6$ ).

mesoporous silica application with TiO<sub>2</sub>/SBA-15, which exhibited less Ki67 staining in the basal layer. Neutrophils are vital in regulating the inflammatory reaction of photoaging. Ly6 G-positive cells were absent in the control skin (Fig. 6E). The number of dermal neutrophils after UVA exposure increased significantly compared to those in the control. This elevation was not inhibited by the blank hydrogel. The neutrophils were scarcely found in SBA-15- or TiO<sub>2</sub>/SBA-15-treated dermis, demonstrating the photoprotective potential.

We also determined IL-1 $\beta$  and IL-6 in skin because of their important role in photoaging (Fig. 6F and G). The UVA-treated skin exhibited a 3.4-fold increase in IL-1 $\beta$  level than the healthy skin. The hydrogels with or without mesoporous silica could suppress IL-1 $\beta$  overexpression. Only TiO<sub>2</sub>/SBA-15 showed a statistically significant IL-1 $\beta$  inhibition than UVA alone. The overexpressed IL-6 by UVA could be reduced by SBA-15 and 30 % TiO<sub>2</sub>/SBA-15. Topical TiO<sub>2</sub>/SBA-15 was capable of restricting IL-6 to baseline control.

#### 4. Discussion

The mesoporous silica developed by us had a typical mesoporous structure as observed by STEM. The mesoporous silica with a hexagonal structure with the pore size of 5–15 nm and surface area of around 800 m<sup>2</sup>/g can be categorized as SBA-15 [22]. We confirmed that the

mesoporous silica prepared in this study belonged to the SBA-15 category. A decrease of the BET surface area was noticed by adding TiO<sub>2</sub> into SBA-15, indicating that the TiO<sub>2</sub> incorporation tended to store in some pore channels. The mesoporous silica particles with high surface volume (0.5–1 cm<sup>3</sup>/g) and surface area (> 1000 m<sup>2</sup>/g) facilitate the efficient loading of drugs [23]. Our mesoporous silica generally fitted this criterion, causing complete organic sunscreen impregnation. Considering the solvent evaporation method, the inclusion of loaded compound would be continuous along with the evaporation to load the compound on the mesoporous silica surface [24]. The XRD showed an anatase phase of TiO<sub>2</sub> in SBA-15, which is regarded as thermally stable [25].

Photocatalytic reaction under light has gained attention due to the ability to degrade pollutants and protect the environment. Semiconductor TiO<sub>2</sub>-mediated photocatalysis has been widely investigated to degrade organic contaminants [26]. TiO<sub>2</sub> simultaneously adsorb the hazards and photons for photolytic oxidation and generates  $\cdot\text{O}_2^-$ , OH, OH $^{\cdot-}$ , and H<sub>2</sub>O<sub>2</sub> under photoexcitation. These reactive oxygen species (ROS) can contribute to the oxidative degradation of the contaminants [27]. Mesoporous silica can be considered as a support to improve the adsorption capability and photocatalysis of TiO<sub>2</sub> because of the high surface area, tunable pore size, and alignment, [28]. SBA-15 developed in this study could efficiently capture fluoranthene and furfural by mesopores, whereas it was an inert support material without catalytic

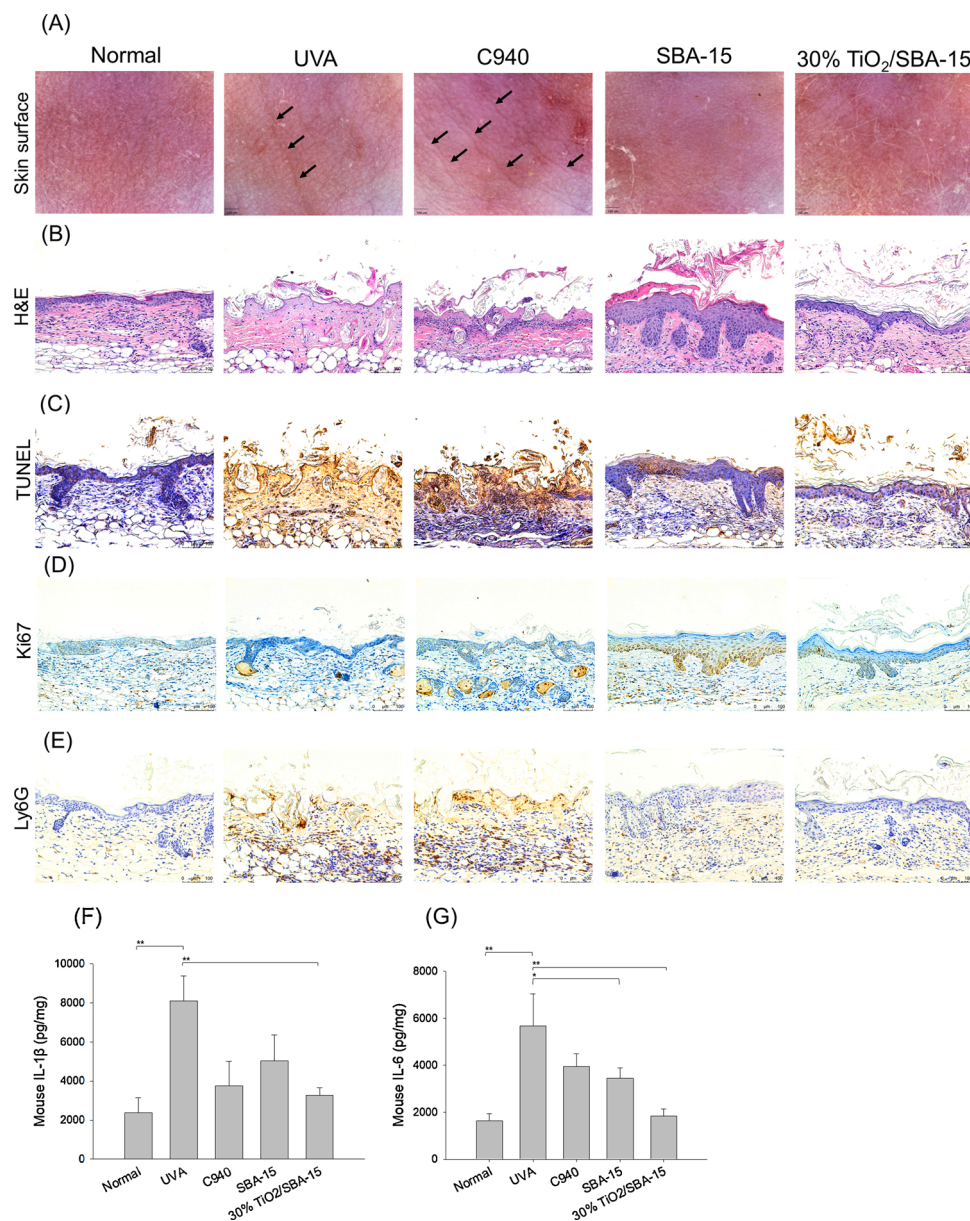


**Fig. 6.** In vivo examination of UVA protection capability of hydrogels containing SBA-15 or 30 % TiO<sub>2</sub>/SBA-15 on nude mouse back skin: (A) microscopic view of dorsal skin, (B) H&E-stained histology, (C) TUNEL-stained IHC, (D) Ki67-stained IHC, (E) Ly6 G-stained IHC, (F) IL-1 $\beta$  expression, and (G) IL-6 expression. Each value represents the mean  $\pm$  SEM ( $n = 6$ ).

performance because UV irradiation did not promote further adsorption. Mesoporous silica feasibly incorporate TiO<sub>2</sub> for developing photocatalyst material in a restricted and confined framework. TiO<sub>2</sub> inside the pores and on the surface of SBA-15 leads to a close interaction between the adsorption sites and the sites of ROS production [8]. Our TiO<sub>2</sub>/SBA-15 hybrid presented higher adsorption after UVA or UVB exposure, implying the occurrence of photocatalysis. Theoretically the adsorption and degradation ability should increase following the increase of TiO<sub>2</sub> content. It was not the case in our study because the mesoporous silica with greater TiO<sub>2</sub> amount only showed a minimal increase in adsorption compared to that with less TiO<sub>2</sub>. Too many catalysts can diminish light penetration into the pores and increase the intermolecular collision to reduce the photodegradation [29]. Another possibility involved the blocking of mesopores by excess TiO<sub>2</sub> to decrease adsorption capability. This inference could be validated by the lower pore volume of SBA-15 containing a higher amount of TiO<sub>2</sub>. These drawbacks offset the stronger photocatalysis by more TiO<sub>2</sub>.

Furfural is a toxic furan used for solvent extraction in the petroleum refining industry. It is also used as a weed killer, fungicide, and a flavoring agent [30]. Furfural is proved to cause skin toxicity, including contact dermatitis, eczema, and even skin cancer [31,32]. Furfural could be easily adsorbed by TiO<sub>2</sub>/SBA-15 hybrids according to our data. This adsorption increased significantly following the increase in treatment duration. Furfural degraded by photocatalytic processes inside the mesopores and liberated some spaces in the pores for accommodating more furfural molecules to be entrapped. Particle matter (PM) is one of the most harmful pollutants to human health. The skin can directly contact with PM to induce or exacerbate dermatitis, psoriasis, and premature aging [33]. The predominant ingredients in PM are PAHs. The environmental and occupational exposure of PAHs compromises dermal health to induce inflammation, phototoxicity, and skin tumor [34,35]. Fluoranthene is the most abundant compound detected in the environment among PAHs [36]. Our previous study also illustrated a facile absorption of fluoranthene into the skin [37]. Photocatalysis elicited by



TiO<sub>2</sub> can sensitively oxidize aromatic systems [27]. The TiO<sub>2</sub>/SBA-15 prepared in this study could effectively adsorb fluoranthene within 0.5 h. It is contrary to furfural that the percentage of fluoranthene adsorption did not increase with the increase in time. The adsorption was even reduced with the increase in time in some formulations with or without UV exposure. The compound could possibly be easily desorbed from mesoporous silica support after adsorption [4,38,39]. Another eventuality is that the mesopores offer limited space for accumulating fluoranthene. Further investigation is necessary to explore the mechanisms involving saturation and leakage of fluoranthene in TiO<sub>2</sub>/SBA-15.

UV filters alone cannot fully protect human skin against solar radiation-induced damage [40]. The combination of UV filters is beneficial in achieving a synergistic effect for the protection of the skin from UV exposure. We formulated an organic sunscreen-loaded TiO<sub>2</sub>-containing mesoporous silica in the hydrogel for testing photoprotection because of the semisolid and viscous properties of the carrier for improved adherence to the skin surface. The combination of avobenzone/oxybenzone, TiO<sub>2</sub>, and SBA-15 indicated a synergistic enhancement in the *in vitro* UVA protection. The uniform distribution of TiO<sub>2</sub> over mesoporous silica support prevents the aggregation of TiO<sub>2</sub> [41]. Maximum UVA protection could be achieved by using SBA-15 containing the greatest TiO<sub>2</sub> percentage (50 %) although the UVA protection by the formulations with 10 %–40 % TiO<sub>2</sub> was comparable. This can be attributed to the possibility that the lower content of inorganic filter may cause better dispersion on the SBA-15 matrix [22]. The physical scattering effect is verified as a mode of action of sunscreens. Mesoporous silica exhibits light scattering property [38,42]. Although SBA-15 alone showed a limited UVA/UVB ratio, the incorporation of organic and inorganic UV filters synergized the photoprotection. This may be because the light scattering of mesopores increases the opportunity for light absorption by the UV filters in the pores [43].

An ideal UVA filter should be formulated in a cosmetically acceptable vehicle and applied on the skin surface to block the UVA ray [13]. Unfortunately avobenzone and oxybenzone are UVA filters that can potentially permeate the skin. Both UVA filters can be found in skin, plasma, and urine after percutaneous absorption [16,17,44]. This skin absorption induces cutaneous allergy and systemic toxicity. For instance, oxybenzone is proved to affect endocrine activity [45,46]. Unlike organic UVA filters, the inorganic sunscreens such as TiO<sub>2</sub> and ZnO basically do not diffuse into the skin and cause toxicity [47,48]. We had evaluated avobenzone/oxybenzone absorption from mesoporous silica in hydrogel into and across pig skin. Pig skin is a suitable model to determine the penetration of UV filters for its histological and permeabilization properties mimicking human skin [49]. Our results demonstrated a significant skin permeation of avobenzone and oxybenzone in the hydrogel. The small-molecule permeants with less than 400 g/mol molecular weight can readily permeate into/through the skin [50]. It was applicable to both avobenzone (310 g/mol) and oxybenzone (228 g/mol). Most of the permeated oxybenzone transported across the skin to the receptor with a limited amount deposited in the skin reservoir. Skin deposition of oxybenzone was much lower than that of avobenzone. This result corroborated the large accumulation of topical oxybenzone in systemic circulation and urine as described previously [16,17,44]. The lower molecular size and lipophilicity of oxybenzone relative to that of avobenzone contribute to the preferred oxybenzone partitioning to viable skin and the subsequent delivery to circulation [47].

Loading in TiO<sub>2</sub>/SBA-15 could lower UVA filter absorption into/through the skin. The silane and hydroxyl moieties of mesoporous silica possibly interact with ketone groups in avobenzone/oxybenzone via hydrogen bonding and electrostatic interaction [51]. The affinity between mesoporous silica and UVA filters prevented the escape from the matrix, leading to reduced skin absorption. The particles with a nano-size can accumulate in hair follicles to be delivered deep into dermis or circulation to produce adverse effects [52]. The micron-sized TiO<sub>2</sub>/SBA-15 hybrids had a size of 2–5 µm to hinder the skin

penetration. The mesoporous silica was believed to be dispersed in hydrogel but not solubilized. The absence of transport of insoluble particles into and across the skin is reasonable [53]. The restrained UVA filter absorption by TiO<sub>2</sub>/SBA-15 maintained the filters on the skin surface for efficient photoprotection. The absorption of avobenzone/oxybenzone decreased following the increase in TiO<sub>2</sub> concentration. However, this strong reduction could not be maintained in the mesoporous silica with the highest TiO<sub>2</sub> percentage (40 % and 50 %). It could be due to the particle blocking of the mesopores by the excess TiO<sub>2</sub> to reduce the interaction and facilitate the release of organic sunscreen. The results suggest the need for optimizing TiO<sub>2</sub> loading to achieve the maximal effect.

The safety of daily care sunscreen on the skin is an important issue. Keratinocytes were the cell models used to test *in vitro* cytotoxicity of TiO<sub>2</sub>/SBA-15. Epidermal keratinocytes make up > 90 % of the cells in the epidermis [54]. Keratinocyte is an essential target in contact with sunscreen. TiO<sub>2</sub>/SBA-15 treatment (1–500 µg/mL) revealed an acceptable keratinocyte viability of > 80 %. The expression of CXCL1 increased by TiO<sub>2</sub>/SBA-15, suggesting an initiation of pro-inflammatory response. This reaction was not observed in the *in vivo* skin tolerance study. The application of TiO<sub>2</sub>/SBA-15 did not produce any measurable change in skin histology and physiology, implying that the hybrid did not cause skin toxicity. SBA-15 is previously proved to be non-toxic and biocompatible to skin [55]. TiO<sub>2</sub> is found to be generally recognized as safe (GRAS) in the USFDA proposed rule for the over-the-counter human use [56]. Nanoparticulate inorganic sunscreens should still be cautiously used because the nanoparticles accumulate in skin furrows and hair follicles for a duration long enough to provoke toxicity concern [57]. This effect was absent in our micron-sized TiO<sub>2</sub>/SBA-15. Additionally, the ability of TiO<sub>2</sub>/SBA-15 to suppress the permeation of UVA filters in the skin also diminished possible irritation.

We selected 30 % TiO<sub>2</sub>/SBA-15 hybrid with avobenzone for the *in vivo* photoprotection test because of the superior effect of UVA filter minimal absorption, low cytotoxicity, and adsorption of pollutants. Although the UVA/UVB ratio of 30 % TiO<sub>2</sub>/SBA-15 was inferior to that of 50 % TiO<sub>2</sub>/SBA-15, the Boots star rating was five stars for both formulations. Our photoaging mouse model showed wrinkling and laxity on the skin surface, consistent with the clinical signs in humans [58]. Both SBA-15 and 30 % TiO<sub>2</sub>/SBA-15 could ameliorate the furrow formation in UVA-irradiated skin. UVA at 10 J/cm<sup>2</sup> caused severe damage to the skin, leading to cell death in viable skin due to the nuclear loss. This damage was believed to be irreversible. UVA exposure promotes oxidative stress on the skin by the photosensitization process. The increased oxidative stress eventually results in structural disruption of cellular DNA, proteins, and lipids [59]. The keratinocytes in epidermis could survive with intact nuclei by SBA-15 and TiO<sub>2</sub>/SBA-15. Hyperplasia was observed in the photoaged skin treated with mesoporous silica. The Ki67 staining proved greater hyperproliferation of SBA-15 than of TiO<sub>2</sub>/SBA-15. The proliferating keratinocytes forecast the subsequent skin recovery from photoaging [60]. This indicates that the avobenzone-loaded mesoporous silica improved skin photoaging and created an opportunity for cutaneous recovery. TiO<sub>2</sub>/SBA-15 group could almost achieve a similar skin condition as that of the non-treated control, suggesting the strong protection against UVA. The TUNEL assay also indicated superior protection by TiO<sub>2</sub>/SBA-15 than SBA-15.

UVA radiation can reach deep layers of the skin. Exposure of UVA leads to an inflammatory response in the dermis. Neutrophils are among the first immune cells to infiltrate the UVA-irradiated skin [61]. The Ly6G staining displayed neutrophil accumulation in the dermis after UVA treatment. Neutrophil infiltration in dermis releases elastase and matrix metalloproteinases to break down elastin and collagen, resulting in wrinkling of the skin [62]. Our data showed evidence of wrinkling in the UVA-treated skin. Topical application of mesoporous silica retarded neutrophil recruitment in the dermis. The infiltrated immune cells and activated keratinocytes induce cytokine production. IL-1β and IL-6 are a part of the UVA-activated inflammatory reaction and contribute to the



generation of matrix metalloproteinases [63]. We found an inhibition of IL-1 $\beta$  and IL-6 in UVA-irradiated skin to approximate the baseline control after 30 % TiO<sub>2</sub>/SBA-15 treatment.

Our avobenzone-loaded TiO<sub>2</sub>/SBA-15 hybrid in hydrogel can act as a barrier formulation because of its ability to adsorb PAHs or furans. Combined TiO<sub>2</sub>, avobenzone, and mesopores demonstrated excellent skin protection under UVA exposure. The strong interaction and slow release of organic UVA filters in TiO<sub>2</sub>/SBA-15 prevented percutaneous absorption reduced the risk of toxicity and maintained UVA protection. The application of developed avobenzone-loaded mesoporous silica system exerts multifunctional effects on the skin (Suppl. Fig. 2). We expect the use of TiO<sub>2</sub>/SBA-15 hydrogel by outdoor swimmers who can apply this formulation topically to keep from sunlight. The pollutants in air and water would not contact with skin because of adsorption and photocatalysis by TiO<sub>2</sub>/SBA-15. The swimmers have a large area of the exposed body and always need to apply the sunscreens. The use of TiO<sub>2</sub>/SBA-15 may lessen the risk of sunscreen absorption.

## 5. Conclusion

The present work demonstrated a successful preparation of avobenzone-loaded TiO<sub>2</sub>/SBA-15 hybrids to enhance the efficacy of sunscreen and adsorption of hazardous pollutants. TiO<sub>2</sub> was uniformly incorporated into the mesoporous framework with a negligible influence on mesostructural ordering. In vitro evaluation revealed remarkable adsorption of pollutants by TiO<sub>2</sub>/SBA-15 and prevention of toxicant contact with skin. The permeation of avobenzone/oxybenzone into the skin could be prevented, preserving UVA filter efficiency and restricting the possible risk of toxicity. We observed that topical 30 % TiO<sub>2</sub>/SBA-15 application could significantly protect against UVA exposure in mouse, suppress cell death, neutrophil infiltration, and cytokine overexpression. This study offers insight into developing multifunctional mesoporous silica for skin protection against environmental stress.

## CRedit authorship contribution statement

**Yu-Chih Lin:** Conceptualization, Writing - review & editing. **Yi-Ping Fang:** Methodology, Validation. **Chi-Feng Hung:** Software, Validation. **Huang-Ping Yu:** Investigation, Data curation. **Ahmed Alalawi:** Investigation, Data curation. **Zhi-Yuan Wu:** Investigation. **Jia-You Fang:** Supervision, Writing - original draft.

## Declaration of Competing Interest

The authors report no declarations of interest.

## Acknowledgements

The authors are grateful for the financial support from Ministry of Science and Technology of Taiwan (MOST-107-2320-B-182-016-MY3) and Chang Gung Memorial Hospital (CMRPD1F0331-3).

## Appendix A. Supplementary data

Supplementary material related to this article can be found, in the online version, at doi:<https://doi.org/10.1016/j.colsurfb.2021.111658>.

## References

- [1] D. McDaniel, P. Farris, G. Valacchi, Atmospheric skin aging—Contributors and inhibitors, *J. Cosmet. Dermatol.* 17 (2018) 124–137.
- [2] C. Parrado, S. Mercado-Saenz, A. Perez-Davo, Y. Gilaberte, S. Gonzalez, A. Juarranz, Environmental stressors on skin aging. Mechanistic insights, *Front. Pharmacol.* 10 (2019) 759.
- [3] S.L. Schneider, H.W. Lim, A review of inorganic UV filters zinc oxide and titanium dioxide, *Photodermatol. Photoimmunol. Photomed.* 35 (2019) 442–446.
- [4] L. Yu, X. Yang, D. Wang, TiO<sub>2</sub> incorporated in magnetic mesoporous SBA-15 by a facile inner-pore hydrolysis process toward enhanced adsorption-photocatalysis performances for As(III), *J. Colloid Interface Sci.* 448 (2015) 525–532.
- [5] Z. Cinar, The role of molecular modeling in TiO<sub>2</sub> photocatalysis, *Molecules* 22 (2017) 556.
- [6] N.R. Srinivasan, R. Bandyopadhyaya, Sn<sub>x</sub>Ti<sub>1-x</sub>O<sub>2</sub> solid-solution-nanoparticle embedded mesoporous silica (SBA-15) hybrid as an engineered photocatalyst with enhanced activity, *Faraday Discuss.* 186 (2016) 353.
- [7] P. Verma, Y. Kuwahara, K. Mori, R. Raja, H. Yamashita, Functionalized mesoporous SBA-15 silica: recent trends and catalytic applications, *Nanoscale* 12 (2020) 11333–11363.
- [8] I. Barroso-Martín, E. Moretti, A. Talon, L. Storaro, E. Rodríguez-Castellón, A. Infantes-Molina, Au and AuCu nanoparticles supported on SBA-15 ordered mesoporous titania-silica as catalysts for methylene blue photodegradation, *Materials* 11 (2018) 890.
- [9] A. Nigro, M. Pellegrino, M. Greco, A. Comandè, D. Sisci, L. Pasqua, A. Leggio, C. Morelli, Dealing with skin and blood-brain barriers: the unconventional challenges of mesoporous silica nanoparticles, *Pharmaceutics* 10 (2018) 250.
- [10] Y.C. Lin, C.F. Lin, A. Alalawi, P.W. Wang, Y.P. Fang, J.Y. Fang, UV filter entrapment in mesoporous silica hydrogel for skin protection against UVA with minimization of percutaneous absorption, *Eur. J. Pharm. Sci.* 122 (2018) 185–194.
- [11] R. Huirache-Acuña, R. Nava, C.L. Peza-Ledesma, J. Lara-Romero, G. Alonso-Núñez, B. Pawelec, E.M. Rivera-Muñoz, SBA-15 mesoporous silica as catalytic support for hydrodesulfurization catalysts—review, *Materials* 6 (2013) 4139–4167.
- [12] R. Brem, M. Guven, P. Karan, Oxidatively-generated damage to DNA and proteins mediated by photosensitized UVA, *Free Radic. Biol. Med.* 107 (2017) 101–109.
- [13] M.S. Latha, J. Martis, V. Shobha, R.S. Shinde, S. Bangera, B. Krishnakutty, S. Bellary, S. Varughese, P. Rao, N. Kumar, Sunscreen agents. A review, *J. Clin. Aesthet. Dermatol.* 6 (2013) 16–26.
- [14] H.K. Jeon, S.N. Sarma, Y.J. Kim, J.C. Ryu, Toxicokinetics and metabolism of benzophenone-type UV-filters in rats, *Toxicology* 248 (2008) 89–95.
- [15] D.P. Uco, V.R. Leite-Silva, H.D.T. Silva, M.D. Duque, J. Grice, M.B. Mathor, N. Andréo-Filho, P.S. Lopes, UVA and UVB formulation phototoxicity in a three-dimensional human skin model: photodegradation effect, *Toxicol. In Vitro* 53 (2018) 37–44.
- [16] N.R. Janjua, B. Kongshoj, A.M. Andersson, H.C. Wulf, Sunscreens in human plasma and urine after repeated whole-body topical application, *J. Eur. Acad. Dermatol. Venereol.* 22 (2008) 456–461.
- [17] M.K. Matta, R. Zusterzeel, N.R. Pilli, V. Patel, D.A. Volpe, J. Florian, L. Oh, E. Bashaw, I. Zineh, C. Sanabria, S. Kemp, A. Godfrey, S. Adah, S. Coelho, J. Wang, L.A. Furlong, C. Ganley, T. Michele, D.G. Strauss, Effect of sunscreen application under maximal use conditions on plasma concentrations of sunscreen active ingredients. A randomized clinical trial, *JAMA* 321 (2019) 2082–2091.
- [18] A.P. Pawar, A.P. Gholap, A.B. Kuchekar, C. Bothiraja, A.J. Mali, Formulation and evaluation of optimized oxybenzone microsphere gel for topical delivery, *J. Drug Deliv.* 2015 (2015), 261068.
- [19] S.Q. Wang, J.W. Stanfield, U. Osterwalder, In vitro assessments of UVA protection by popular sunscreens available in the United States, *J. Am. Acad. Dermatol.* 59 (2008) 934–942.
- [20] W.Y. Chen, C.L. Fang, S.A. Al-Suwayeh, H.H. Yang, Y.C. Li, J.Y. Fang, Risk assessment of excess drug and sunscreen absorption via skin with ablative fractional laser resurfacing: optimization of the applied dose for postoperative care, *Lasers Med. Sci.* 28 (2013) 1363–1374.
- [21] H. Ijadanah-Saravy, M. Safari, A. Khodadadi-Darban, A. Rezaei, Synthesis of titanium dioxide nanoparticles for photocatalytic degradation of cyanide in wastewater, *Anal. Lett.* 47 (2014) 1772–1782.
- [22] C.O. Vieira, J.E. Grice, M.S. Roberts, I.N. Haridass, M.D. Duque, P.S. Lopes, V. R. Leite-Silva, T.S. Martins, ZnO:SBA-15 nanocomposites for potential use in sunscreen: preparation, properties, human skin penetration and toxicity, *Skin Pharmacol. Physiol.* 32 (2019) 32–42.
- [23] M. Eltohamy, J.W. Seo, J.Y. Hwang, W.C. Jang, H.W. Kim, U.S. Shin, Ionic and thermo-switchable polymer-masked mesoporous silica drug-nanocarrier: high drug loading capacity at 10 °C and fast drug release completion at 40 °C, *Colloids Surf. B Biointerface* 144 (2016) 229–237.
- [24] H. Geng, Y. Zhao, J. Liu, Y. Cui, Y. Wang, Q. Zhao, S. Wang, Hollow mesoporous silica as a high drug loading carrier for regulation insoluble drug release, *Int. J. Pharm.* 510 (2016) 184–194.
- [25] T.Z. Liou, L.W. Hung, H.S. Syu, L. Chu, Synthesis of TiO<sub>2</sub> nanoparticles and good dispersion on SBA-15 mesoporous materials for high photocatalytic activity, *J. Nanosci. Nanotechnol.* 18 (2018) 20–29.
- [26] Q. Guo, C. Zhou, Z. Ma, X. Yang, Fundamentals of TiO<sub>2</sub> photocatalysis: concepts, mechanisms, and challenges, *Adv. Mater.* 31 (2019), 1901997.
- [27] M. Tomás-Gamasa, J.L. Mascareñas, TiO<sub>2</sub>-based photocatalysis at the interface with biology and biomedicine, *ChemBioChem* 21 (2020) 294–309.
- [28] L. Bai, S. Wang, Z. Wang, E. Hong, Y. Wang, C. Xia, B. Wang, Kinetics and mechanism of photocatalytic degradation of methyl orange in water by mesoporous Nd-TiO<sub>2</sub>-SBA-15 nanocatalyst, *Environ. Pollut.* 248 (2019) 516–525.
- [29] J. Wang, X. Shao, J. Liu, X. Ji, J. Ma, G. Tian, Fabrication of Cds-SBA-15 nanomaterials and their photocatalytic activity for degradation of salicylic acid under visible light, *Ecotoxicol. Environ. Saf.* 190 (2020), 110139.
- [30] J.H.E. Arts, H. Muijsers, M.J. Appel, C.F. Kuper, J.G.M. Bessems, R.A. Woutersen, Subacute (28-day) toxicity of furfural in Fischer 344 rats: a comparison of the oral and inhalation route, *Food Chem. Toxicol.* 42 (2004) 1389–1399.
- [31] Y. Miyakawa, Y. Nishi, K. Kato, H. Sato, M. Takahashi, Y. Hayashi, Initiating activity of eight pyrolysates of carbohydrates in a two-stage mouse skin tumorigenesis model, *Carcinogenesis* 12 (1991) 1169–1173.

- [32] H.R. Moghimi, R. Varshochian, F. Kobarfard, M. Erfan, Reduction of percutaneous absorption of toxic chemicals by dendrimers, *Cutan. Ocul. Toxicol.* 29 (2010) 34–40.
- [33] A. Verdin, F. Cazier, R. Fitoussi, N. Blanchet, K. Vié, D. Courcot, I. Monas, N. Seta, S. Achard, An in vitro model to evaluate the impact of environmental fine particles (PM0.3-2.5) on skin damage, *Toxicol. Lett.* 305 (2019) 94–102.
- [34] L.K. Siddens, A. Larkin, S.K. Krueger, C.A. Bradfield, K.M. Waters, S.C. Tilton, C. B. Pereira, C.V. Löhr, V.M. Arlt, D.H. Phillips, D.E. Williams, W.M. Baird, Polycyclic aromatic hydrocarbons as skin carcinogens: comparison of benzo[*a*]pyrene, dibenzo[*def,p*]chrysene and three environmental mixtures in the FVB/N mouse, *Toxicol. Appl. Pharmacol.* 264 (2012) 377–386.
- [35] A. von Koschimbahr, A. Youssef, D. Béal, E. Bourgart, A. Rivier, M. Marques, M. T. Leccia, J.P. Ciot, A. Maitre, T. Douki, Metabolism and genotoxicity of polycyclic aromatic hydrocarbons in human skin explants: mixture effects and modulation by sunlight, *Arch. Toxicol.* 94 (2020) 495–507.
- [36] E.J. La Voie, Z.W. Cai, C.L. Meschter, E.H. Weyand, Tumorigenic activity of fluoranthene, 2-methylfluoranthene and 3-methylfluoranthene in newborn CD-1 mice, *Carcinogenesis* 15 (1994) 2131–2135.
- [37] A. Alalaiwe, Y.K. Lin, C.H. Lin, P.W. Wang, J.Y. Lin, J.Y. Fang, The absorption of polycyclic aromatic hydrocarbons into the skin to elicit cutaneous inflammation: the establishment of structure–permeation and in silico–in vitro–in vivo relationships, *Chemosphere* 255 (2020), 126955.
- [38] N.O. Ramoraswi, P.G. Ndungu, Photo-catalytic properties of TiO<sub>2</sub> supported on MWCNTs, SBA-15 and silica-coated MWCNTs nanocomposites, *Nanoscale Res. Lett.* 10 (2015) 427.
- [39] L. Wang, M. Yao, X. Hu, G. Hu, J. Lu, M. Luo, M. Fan, Amine-modified ordered mesoporous silica: the effect of pore size on CO<sub>2</sub> capture performance, *Appl. Surf. Sci.* 324 (2015) 286–292.
- [40] C. Souza, P.M.B.G. Maia Campos, Development and photoprotective effect of a sunscreen containing the antioxidants *Spirulina* and dimethylmethoxy chromanol on sun-induced skin damage, *Eur. J. Pharm. Sci.* 104 (2017) 52–64.
- [41] M.V.P. Sharma, V.D. Kumari, M. Subrahmanyam, TiO<sub>2</sub> supported over SBA-15: an efficient photocatalyst for the pesticide degradation using solar light, *Chemosphere* 73 (2008) 1562–1569.
- [42] N.Ž. Knežević, N. Ilić, V. Đokić, R. Petrović, D. Janačkvić, Mesoporous silica and organosilica nanomaterials as UV-blocking agents, *ACS Appl. Mater. Interfaces* 10 (2018) 20231–20236.
- [43] C.C. Li, Y.T. Chen, Y.T. Lin, S.F. Sie, Y.W. Chen-Yang, Mesoporous silica aerogel as a drug carrier for the enhancement of the sunscreen ability of benzophenone-3, *Colloids Surf. B Interfaces* 115 (2014) 191–196.
- [44] S. Kasichayanula, J.D. House, T. Wang, X.C. Gu, Percutaneous characterization of the insect repellent DEET and the sunscreen oxybenzone from topical skin application, *Toxicol. Appl. Pharmacol.* 223 (2007) 187–194.
- [45] M. Krause, A. Klit, M.B. Jensen, T. Søborg, H. Frederiksen, M. Schlumpf, W. Lichtensteiger, N.E. Skakkebaek, K.T. Drzewiecki, Sunscreens: are they beneficial for health? An overview of endocrine disrupting properties of UV-filters, *Int. J. Androl.* 35 (2012) 424–436.
- [46] A.N. Barone, C.E. Hayes, J.J. Kerr, R.C. Lee, D.B. Flaherty, Acute toxicity testing of TiO<sub>2</sub>-based vs. oxybenzone-based sunscreens on clownfish (*Amphiprion ocellaris*), *Environ. Sci. Pollut. Res.* 26 (2019) 14513–14520.
- [47] C.F. Hung, W.Y. Chen, I.A. Aljuffali, H.C. Shih, J.Y. Fang, The risk of hydroquinone and sunscreen over-absorption via photodamaged skin is not greater in senescent skin as compared to young skin: nude mouse as an animal model, *Int. J. Pharm.* 471 (2014) 135–145.
- [48] V.R. Leite-Silva, D.C. Liu, W.Y. Sanchez, H. Studier, Y.H. Mohammed, A. Holmes, W. Becker, J.E. Grice, H.A. Benson, M.S. Roberts, Effect of flexing and massage on in vivo human skin penetration and toxicity of zinc oxide nanoparticles, *Nanomedicine* 11 (2016) 1193–1205.
- [49] A.C. Cozzi, P. Perugini, S. Gourion-Arsigaud, Comparative behavior between sunscreens based on free or encapsulated UV filters in term of skin penetration, retention and photo-stability, *Eur. J. Pharm. Sci.* 121 (2018) 309–318.
- [50] G. Xu, J.M. Hughes-Oliver, J.D. Brooks, J.L. Yeatts, R.E. Baynes, Selection of appropriate training and validation set chemicals for modelling dermal permeability by U-optimal design, *SAR QSAR Environ. Res.* 24 (2013) 135.
- [51] A.L. Daneluti, F.M. Neto, N. Ruscinc, I. Lopes, M.V.R. Velasco, J.D.R. Matos, A. R. Baby, Y.N. Kalia, Using ordered mesoporous silica SBA-15 to limit cutaneous penetration and transdermal permeation of organic UV filters, *Int. J. Pharm.* 570 (2019), 118633.
- [52] Y. Deng, A. Ediriwickrema, F. Yang, J. Lewis, M. Girardi, W.M. Saltzman, A sunblock based on bioadhesive nanoparticles, *Nat. Mater.* 14 (2015) 1278–1285.
- [53] G.J. Nohynek, E.K. Dufour, Nano-sized cosmetic formulations or solid nanoparticles in sunscreens: a risk to human health? *Arch. Toxicol.* 86 (2012) 1063–1075.
- [54] J.R. Weng, T.H. Huang, Z.C. Lin, A. Alalaiwe, J.Y. Fang, Cutaneous delivery of [1-(4-chloro-3-nitrobenzenesulfonyl)-1*H*-indol-3-yl]-methanol, an indole-3-carbinol derivative, mitigates psoriasiform lesion by blocking MAPK/NF- $\kappa$ B/AP-1 activation, *Biomed. Pharmacother.* 119 (2019), 109398.
- [55] V.F. Vavari, G.M. Ziarani, A. Badiel, The role of SBA-15 in drug delivery, *RSC Adv.* 5 (2015) 91686.
- [56] US Food and Drug Administration, Sunscreen drug products for over-the-counter human use: proposed rule, *Fed. Regist.* 84 (2019) 6204–6275.
- [57] M.J. Osmond-McLeod, Y. Oytam, J.K. Kirby, L. Gomez-Fernandez, B. Baxter, M. J. McCall, Dermal absorption and short-term biological impact in hairless mice from sunscreens containing zinc oxide nano- or layer particles, *Nanotoxicology* 8 (2014) 72–84.
- [58] C. Battie, S. Jitsukawa, F. Bernerd, S. Del Bino, C. Marionnet, M. Verschoore, New insights in photoaging, UVA induced damage and skin types, *Exp. Dermatol.* 23 (Suppl. 1) (2014) 7–12.
- [59] A.P. Schuch, N.C. Moreno, N.J. Schuch, C.F.M. Menck, C.C.M. Garcia, Sunlight damage to cellular DNA: focus on oxidatively generated lesions, *Free Radic. Biol. Med.* 107 (2017) 110–124.
- [60] A.J. Armento, J. Oldach, G. Stolper, M. Li, M.A. Bachelor, P.J. Hayden, Evaluation of cutaneous damage and repair following acute solar ultraviolet radiation exposure: experiments with an in vitro reconstructed human skin model and excised human skin, *Appl. In Vitro Toxicol.* 1 (2015) 109–117.
- [61] C. Li, X. Shi, M. Chen, G. Xu, X. Su, P. Jiang, L. Pan, Ultraviolet light A irradiation induces immunosuppression associated with the generation of reactive oxygen species in human neutrophils, *J. Innov. Opt. Health Sci.* 9 (2016), 1650001.
- [62] F. Rijken, R.C.M. Kiekens, E. van den Worm, P.L. Lee, H. van Weelden, P.L. B. Bruijnzel, Pathophysiology of photoaging of human skin: focus on neutrophils, *Photochem. Photobiol. Sci.* 5 (2006) 184–189.
- [63] J.H. Oh, Y.H. Joo, F. Karadeniz, J. Ko, C.S. Kong, Syringaresinol inhibits UVA-induced MMP-1 expression by suppression of MAPK/AP-1 signaling in HaCaT keratinocytes and human dermal fibroblasts, *Int. J. Mol. Sci.* 21 (2020) 3981.

## Review

## Enterovirus A71 Vaccines

Mei-Ling Li <sup>1,\*</sup> , Shin-Ru Shih <sup>2,3,4,5</sup>, Blanton S. Tolbert <sup>6</sup> and Gary Brewer <sup>1</sup> 

- <sup>1</sup> Department of Biochemistry and Molecular Biology, Rutgers Robert Wood Johnson Medical School, Piscataway, NJ 08854, USA; brewerga@rwjms.rutgers.edu
- <sup>2</sup> Research Center for Emerging Viral Infections, College of Medicine, Chang Gung University, Taoyuan 333, Taiwan; srshih@mail.cgu.edu.tw
- <sup>3</sup> Department of Laboratory Medicine, Linkou Chang Gung Memorial Hospital, Taoyuan 333, Taiwan
- <sup>4</sup> Department of Medical Biotechnology and Laboratory Science, College of Medicine, Chang Gung University, Taoyuan 333, Taiwan
- <sup>5</sup> Research Center for Chinese Herbal Medicine, Research Center for Food and Cosmetic Safety, and Graduate Institute of Health Industry Technology, College of Human Ecology, Chang Gung University of Science and Technology, Taoyuan 333, Taiwan
- <sup>6</sup> Department of Chemistry, Case Western Reserve University, Cleveland, OH 44106, USA; bst18@case.edu
- \* Correspondence: lime@rwjms.rutgers.edu

**Abstract:** Enterovirus A71 (EV-A71) is a major causative agent of hand, foot, and mouth disease (HFMD) and herpangina. Moreover, EV-A71 infection can lead to neurological complications and death. Vaccination is the most efficient way to control virus infection. There are currently three inactivated, whole EV-A71 vaccines licensed by the China NMPA (National Medical Products Administration). Several other types of vaccines, such as virus-like particles and recombinant VP1 (capsid protein), are also under development. In this review, we discuss recent advances in the development of EV-A71 vaccines.



**Citation:** Li, M.-L.; Shih, S.-R.; Tolbert, B.S.; Brewer, G. Enterovirus A71 Vaccines. *Vaccines* **2021**, *9*, 199. <https://doi.org/10.3390/vaccines9030199>

Academic Editor: Francisco Sobrino

Received: 1 February 2021  
Accepted: 22 February 2021  
Published: 27 February 2021

**Publisher's Note:** MDPI stays neutral with regard to jurisdictional claims in published maps and institutional affiliations.



**Copyright:** © 2021 by the authors. Licensee MDPI, Basel, Switzerland. This article is an open access article distributed under the terms and conditions of the Creative Commons Attribution (CC BY) license (<https://creativecommons.org/licenses/by/4.0/>).

**Keywords:** Enterovirus A71; hand; foot and mouth disease (HFMD); vaccine; Sinovac

## 1. Introduction

Enterovirus A71 (EV-A71) is one of the most important neurotropic viruses and poses a serious threat to public health worldwide. EV-A71 is a major causative agent of hand, foot, and mouth disease (HFMD) which is highly contagious. EV-A71 infection in young children can also lead to neurological complications, rapid fatal pulmonary edema, myocarditis, hemorrhage, and death [1–5]. The absence of broadly protective vaccines and effective antivirals makes EV-A71 an important pathogen of public health concern. EV-A71 is a member of the genus Enterovirus within the family *Picornaviridae*. EV-A71 consists of three distinct genotypes (A, B, and C). Genotype B is divided into subgenotypes B1 to B5. Genotype C is divided into subgenotypes C1 to C5, and C4 is further divided into C4 a and C4 b. Subgenotypes B3, B4, C1, and C2 co-circulated in the Asia–Pacific region from 1999 to 2016. C4 is the most prevalent genotype circulating in China; C1 and C2 are most prevalent in Europe while B4 and B5 are most prevalent in other regions [6–8].

EV-A71 is a non-enveloped virus containing a positive-stranded RNA genome ~7400 nucleotides in length. The viral genome within its icosahedral capsid is flanked by highly structured 5' and 3' untranslated regions (UTR) and is polyadenylated at its 3' end. The large single polyprotein encoded by the viral genome is subsequently processed by viral proteases 2 A and 3 C into P1, P2, and P3.

P1 is further processed to produce four capsid proteins—VP1 to 4. P2 and P3 are processed into seven nonstructural proteins—2 A–2 C and 3 A–3 D—for viral replication (Figure 1). The VP1 protein contains the major neutralization epitopes that are used in viral serotype identification and phylogenetic studies [9,10].

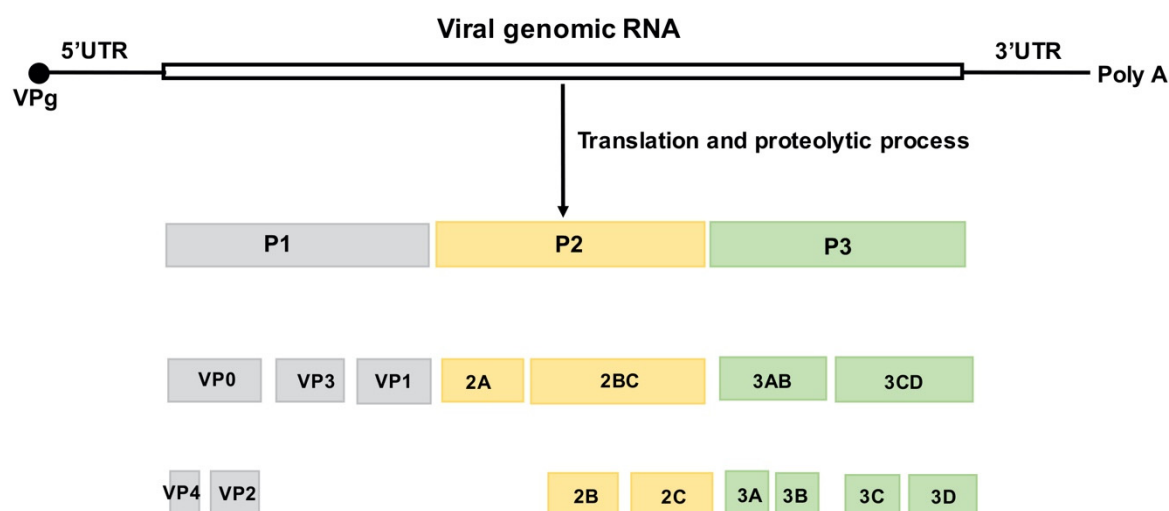


**Figure 1.** Structure of the EV-A71 genome and the encoded viral proteins. The single open reading frame (ORF) is flanked by a highly structured 5'UTR and 3'UTR followed by a poly (A) tail. The 5' end of the viral genome is covalently bound to the viral VPg protein. The ORF is divided into three regions. P1 encodes four structural (capsid) proteins, VP1–4. P2 and P3 encode seven nonstructural proteins, 2 A to 2 C and 3 A to 3 D, respectively [11].

Currently, there is no US FDA-approved antiviral agent or vaccine against EV-A71. However, there are three inactivated, EV-A71 whole-virus vaccines approved by the China National Medical Products Administration (NMPA) and are commercially available in China. Large-scale clinical trials showed that vaccine efficacy against EV-A71-associated Hand, foot, and mouth disease (HFMD) was at least 90%. Vaccine effectiveness in HFMD patients under five years old was 100% for severe cases and ~80% for mild cases, suggesting that the vaccine performs well in practice [8,12]. Vaccination is the most effective countermeasure against EV-A71 infection and epidemic. In this review, we summarize the recent progress in the development of vaccines against EV-A71 and discuss the prospects and challenges in this field.

## 2. Whole EV-A71 Vaccines

### 2.1. Inactivated Whole EV-A71 Vaccines

Inactivation of whole virus is the conventional and safest way to produce viral vaccine [13]. There are three inactivated whole virus EV-A71 vaccines that completed clinical trials and were licensed in China in 2015 [14,15]. However, the US FDA did not approve the vaccines due to concerns about the effectiveness against different pandemic strains, safety, and quality control of vaccine production. The three formalin-inactivated EV-A71 vaccines were developed by three different institutions: Sinovac Biotech, Beijing Vigoo, and Chinese Academy of Medical Science (CAMS). The three companies established their own seed lot system and cell banks. CAMS used diploid cells KMB–17 derived from human fetal lung, as a cell bank and the cells were grown in a cell factory, whereas Vigoo and Sinovac used Vero cells in a microcarrier bioreactor and cell factory, respectively. The screening and evaluation of virus strains used for vaccine production were carefully performed to select strains that could induce cross-protecting antibodies. Two animal models have been developed to study EV-A71 vaccines. One is the suckling monkey (rhesus) model which is used to study EV-A71 infection and pathogenicity, and the other is the suckling mouse model which is used to evaluate vaccine immunogenicity. The protective efficacy of EV-A71 vaccines was demonstrated using both animal models. The results of the animal model studies provided the rationale for proceeding with clinical trials [16,17]. The EV-A71 C4 subgenotype was chosen as the virus seed because it is the most prevalent genotype circulating in China [10,18].



The safety and efficacy of inactivated EV-A71 vaccines had been confirmed in large phase III clinical trials (Table 1). Vaccine efficacy was at least 90% against EV-A71-associated HFMD and 100% against EV-A71-associated HFMD with neurologic complications [19].

**Table 1.** China-licensed inactivated whole EV-A71 vaccines.

| Org.    | Cells  | Dosage | Phase III                | Age     | Efficacy | Approval Date |
|---------|--------|--------|--------------------------|---------|----------|---------------|
| CAMS    | KMB-17 | 100 U  | March 2012–February 2013 | 6–71 mo | 97.4%    | December 2015 |
| Vigoo   | Vero   | 320 U  | January 2012–March 2013  | 6–35 mo | 90%      | December 2016 |
| Sinovac | Vero   | 400 U  | January 2012–March 2013  | 6–35 mo | 94.8%    | December 2015 |

CAMS, Vigoo, and Sinovac (Beijing, China) initiated the phase I trials between December 2010 and February 2011. The phase III trials were completed in 2013. CAMS recruited 12,000 infants and children of 6 to 71 months of age for phase III clinical trials (ClinicalTrials.gov number: NCT01569581). Children randomly received two doses of 100 U (EV-A71 antigen unit) CAMS vaccine or placebo four weeks apart and were followed for two years. The EV-A71 antigen contents were measured by a quantitative ELISA. Based on the EV-A71 antigen reference standard (1600 U/mL) established by the China NMPA, the specific activity of EV-A71 antigen is 421.1 U/μg [20]. Vaccine efficacy against EV-A71-associated HFMD was 97.4% [21]. The Vigoo phase III clinical trial (ClinicalTrials.gov number: NCT01508247) has recruited 10,245 infants and children between 6 and 35 months of age. The participants were randomly given 320 U vaccine or placebo on days 1 and 28. The participants were followed for two years [22,23]. The efficacy of the vaccine against EV-A71 induced HFMD was 90% at the first year and reached 100 % at the second year. The efficacy of the vaccine against other illness associated with EV-A71 infection was 80.4% at the first year. The vaccine did not cause any serious adverse effects.

In the Sinovac (Beijing, China) phase III trial (NCT01507857), 10,077 children aged 6 to 35 months were given 400 U of Sinovac vaccine or placebo at days 1 and 28 and were followed for two years. At the end of the first year, the vaccine efficacy against EV-A71-induced HFMD and herpangina was 94.8%. The efficacy against EV-A71-associated HFMD that manifested to neurological complications was 100%. At the end of the second year, the vaccine efficacy against EV-A71-associated HFMD was 95.1% [19]. Sinovac then conducted a five-year follow-up survey to study the long-term immunogenicity. The study results showed that the Sinovac vaccine demonstrated the long-term persistence of immunogenicity within five years [24]. During this time, the Sinovac EV-A71 vaccine production capacity had reached more than 20 million doses/year. WHO organized a working group meeting in 2019 to develop WHO recommendations to assure the efficacy, safety and quality of EV-A71 vaccines. In view of its cross-reactivity with different genotypes of EV-A71, WHO recommendations suggested that the EV-A71-C4 a vaccine could be used worldwide [25].

The National Health Research Institutes (NHRI) (Hsinchu, Taiwan) in Taiwan used a subgenotype B4 strain to produce the inactivated whole virus EV-A71 vaccine [26,27]. For the vaccine safety and immunogenicity study in the phase I clinical trial (ClinicalTrials.gov number: NCT01268787) sixty healthy participants aged 20 to 60 years were recruited and randomly given 5 μg or 10 μg of EV-A71 antigen on days 1 and 21. The study showed that the NHRI EV-A71 vaccine elicited antibodies against EV-A71 without adverse effects [28]. The antibodies produced in most of the participants showed cross-neutralization against subgenotypes B1, B5, and C4 [29,30]. In phase II trials (ClinicalTrials.gov numbers: NCT02777411, NCT03268083 and NCT02200237) Enimmune Corp. and Medigen Vaccinology Corp. in Taiwan have continued the safety and immunogenicity evaluation of the inactivated EV-A71 vaccine with low, medium, and high doses. Medigen recruited 365 participants from 2 months to 11 years old and participants were randomly given different doses of vaccine or placebo. The EV-A71 vaccine elicited an immune response against subgenotypes B4, B5, C4 a, C4 b, and C5 without vaccine-related serious adverse events. Vaccine immunity persisted for two years [31]. Based upon the promising results

from phase II trials, the companies initiated phase III trials (ClinicalTrials.gov number: NCT03865238) in 2019 which should be completed in 2022.

The Korea National Research Institute of Health (Chungcheongbuk-do, Korea) developed an inactivated whole virus vaccine against EV-A71 using an EV-A71 strain (genotype C4 a) isolated from a Korean patient. [32]. The vaccine was able to induce a strong immunogenic response in mice. The vaccine is currently being evaluated in a blinded, randomized, placebo-controlled phase I study in healthy humans in Korea.

In Thailand, there was an early development of an inactivated EV-A71 vaccine. A genotype C4 EV71-A71 strain was grown in Vero cells in roller bottles. The purified, inactivated virus was able to induce neutralizing antibodies against EV-A71 in BALB/C mice. This prototype product will be further developed into an EV-A71 vaccine candidate [25].

## 2.2. Live-Attenuated Vaccines

Live-attenuated vaccines have the advantages of long-lasting immunity and cost-effective production; however, the molecular pathogenic mechanism of EV-A71 is not fully understood. The EV-A71 virulence determinants have not been completely elucidated. However, several EV-A71 virulence determinants have been identified in the 5'UTR, VP1, VP2, 2 A, 3 C, and 3 D [33]. One of the key virulence determinants is the amino acid at position 145 of VP1. Changing glutamine to glutamic acid at this position increased the virulence in monkeys [34,35]. The highly structured 5'UTR plays an important role in viral translation and virulence. Changing cytosine to uridine at position 158 in stem-loop II of the 5'UTR reduced EV-A71 viral translation and virulence in a mouse model [36]. Chang et al. [37] grew EV-A71 in Vero cells and then passaged it in RD cells to select mutant virus adapted to RD cells. There were three amino acid changes, E145 G, V146 I, and S241 L, in VP1 and a single nucleotide mutation at nt 494 of the 5'UTR of the selected mutant virus. These mutations contributed to the virulence attenuation of the mutant virus in mice.

The vaccine candidate EV7-A71 (S1–3'), a temperature-sensitive mutant of the prototype BrCr, demonstrated induction of an efficient immune response to a lethal dose of EV-A71 (BrCr-TR) (a temperature-resistant mutant of BrCr) in cynomolgus monkeys. However, inoculation of EV-A71 (S1–3') caused neurological symptoms in monkeys. Four and 10 days after inoculation, infectious virus was isolated from the monkeys' lumbar spinal cords. This raised serious safety concerns about this vaccine candidate [38].

Increasing the fidelity of the 3 D RNA-dependent RNA polymerase enhances the safety and stability of live-attenuated vaccines. G64 R, G64 T, and S264 L mutations in 3 D enhanced the polymerase fidelity. G64 R and L123 F mutations in 3 D polymerase attenuated EV-A71 virulence in mice [39,40]. Based upon the study, Tsai et al. constructed a mutant virus with codon deoptimized VP1 and with G64 R and L123 F mutations in the 3 D polymerase to increase the fidelity. This virus was less virulent in a mouse model [41]. Yee et al. [42] constructed a miRNA-based EV-A71 vaccine strain (pIY) carrying let-7 a and miR-124 a target genes in the EV-A71 genome, which has an 11-nucleotide deletion in the 5'UTR and a G64 R mutation in the 3 D RNA-dependent RNA polymerase. The pIY strain's viral RNA copy number and viral titers were much lower than that of the EV-A71 wild-type B4 strain in SHSY-5 Y cells, which express both let-7 a and miR-124 a. The pIY strain protected mice against a lethal dose of EV-A71.

## 3. VLP (Virus Like Particle)-Based Vaccines

VLP (virus-like particle) is a promising vaccine candidate because it resembles the authentic virus in appearance and antigenicity. VLP can elicit innate and adaptive immunity and is safer because the lack of a viral genome makes them incapable of replicating in the host. Several VLP-based vaccines, such as Recombivax HB and Engerix-B for hepatitis B virus, and Gardasil, Cervarix, and Gardasil-9 for human papillomavirus, have been licensed [43,44].

Several strategies have been employed to produce EV-A71 VLPs. The baculovirus expression system is widely used for the production of VLPs. To produce EV-A71 VLPs, in-

sect cells were infected with a recombinant baculovirus co-expressing the EV-A71 P1 region and the viral protease 3 CD from various promoters [45,46]. The P1 region is cleaved by the 3 CD protease to produce the viral capsids VP1–4. Baculovirus-produced EV-A71 VLPs protected monkeys from EV-A71 infection, suggesting that the VLP is a promising vaccine candidate [47]. However, the yield of EV-A71 VLPs was low due to their degradation. To increase the yield and purity, Zhao et al. [43] purified the baculovirus-expressed EV-A71 VLPs using Capto Core 700, Capto Adhere resin, and Capto Butyl columns (GE Healthcare). The multistep chromatography process resulted in EV-A71 VLPs with ~31.52% yield and >95% purity. An occupied N-glycosylation site was detected in VP1 using MALDI-TOF/TOF. Glycosylation is the most important post-translational modification of proteins and plays a critical role in antigen immunogenicity [48]. Hepatitis B virus (HBV) VLPs with additional N-glycosylation sites, induced enhanced immunogenicity [49]. Therefore, further study is needed to verify whether the identified N-glycosylation site on VP1 residue N176 is essential for an immune response. Nevertheless, EV-A71 VLPs could induce a high titer of neutralizing antibodies that protected newborn mice from a lethal challenge of the EV-A71 C4 strain.

Zhang et al. [50] improved the yield by expressing EV-A71 VLPs in the yeast *Pichia pastoris*. The EV-A71 VLP yield was high and potently induced neutralizing antibodies against various strains of EV-A71 in a mouse model [51]. More importantly, maternal immunization with VLPs protected neonatal mice against a lethal EV-A71 challenge [50,51].

Tsou et al. and Yan et al. used Adenovirus and Vesicular stomatitis virus-based vaccines on expressed EV-A71 VLPs in mammalian cells. Both VLPs elicited antibodies against EV-A71 infection in mice [52,53].

Hand, foot, and mouth disease (HFMD) is highly contagious and has led to significant morbidity and mortality worldwide [54]. EV-A71, CVA6 (coxsackievirus A6), CVA10, and CVA16 are major causative agents of HFMD. However, the inactivated EV-A71 whole virus vaccine failed to cross-protect against infections by other HFMD-causing enteroviruses. To develop a multivalent HFMD vaccine, Zhang et al. [55] used a baculovirus expression system to generate recombinant VLPs of EV-A71, CVA6, CVA10, and CVA16 and then combined EV-A71-VLP, CVA6-VLP, CVA10-VLP, and CVA16-VLP to formulate a tetravalent VLP vaccine. The antisera resulting from immunization with the tetravalent VLP vaccine protected mice from single or co-infection of EV-A71, CVA6, CVA10, and CVA16, suggesting that it is a promising HFMD vaccine candidate.

#### 4. Recombinant VP1 and P1 Vaccines

The EV-A71 VP1 capsid protein contains neutralization epitopes. Several expression strategies, such as *Escherichia coli* (*E. coli*), baculovirus, and HIV gag-based VLP carrier were used to express recombinant VP1 protein. The purified recombinant VP1 protein protected mice from EV-A71 infection; however, the protection was lower than that of inactivated EV-A71 vaccine [56–59].

Han et al. [60] expressed the modified EV-A71 polyprotein P1 in *Pichia pastoris* as a vaccine candidate. P1 protein induced persistent, high cross-neutralization antibodies for different EV-A71 subtypes in rabbits. Vaccination of pregnant mice cross-protected neonatal mice against different subtypes of EV-A71. EV-A71 antibody production elicited by P1 was one week later than that of inactivated EV-A71 virus. However, the level and duration of EV-A71 antibody production was stronger than that of inactivated EV-A71 virus. This could be related to antigen glycosylation [48] as studies showed that modification of the glycosylation sites of HCV E1 protein and HIV gp120 enhanced the immune response [61,62]. With strong immunogenicity and cross-protection against different EV-A71 subtypes, the *P. pastoris*-expressed P1 protein is a promising EV-A71 vaccine candidate.

## 5. Synthetic Peptide Vaccines

Synthetic peptides are safe and efficacious for multivalent vaccine development. Several groups have focused on mapping the antigen epitopes in EV-A71 capsid proteins (VP1–4).

Foo et al. [63] used synthetic, overlapping peptides spanning VP1 to map antigen epitopes. The study identified two epitopes—SP55 and SP70 (amino acids 163–177 and 208–222 in VP1, respectively). Both peptides elicited antibodies that protected mice from EV-A71 infection. Anti-SP70 antisera passively protected suckling mice against various EV-A71 strains [64].

Liu et al. [65] selected six peptides (P70–159 in VP2, P140–249 in VP2, P324–443 in VP3, P444–565 in VP3, P566–665 in VP1, and P746–876 in VP1) that individually protected from EV-A71 infection. They combined these into three vaccine candidates for further evaluation in neonatal mice. The studies showed that a combination of four synthetic peptides (P70–159 in VP2, P140–249 in VP2, P324–443 in VP3, and P746–876 in VP1) of the structural proteins provided effective protection of newborn mice against EV-A71 infection.

Aw-Yong et al. [66] synthesized 63 peptides spanning the four structural and seven non-structural proteins of EV-A71 to map the potential epitopes. The study showed that amino acids 41–55 in VP1 was an EV-A71 IgG-specific epitope amino acids 142–156 in VP1 was recognized as the EV-A71 IgM-specific immunodominant epitope.

Several groups used a fusion protein strategy to express EV-A71 epitopes. Xu et al. [67] fused EV-A71 VP2 (amino acids 141–155) epitope with hepatitis B virus core protein to generate HBc-VP2 (amino acids 141–155). This fusion protein induced cross-neutralizing antibodies against EV-A71 and protected newborn mice from EV-A71 infection. Huo et al. [68] fused EV-A71 VP1 epitope (amino acids 208–222) and CV-A16 VP1 epitope (amino acids 271–285) with hepatitis B virus core protein. The expressed epitopes induced an immune response and protected suckling mice against EV-A71 and CV-A16 infection. Jiang et al. [69] fused EV-A71 VP3 epitope (amino acids 176–190) with the P domain of norovirus capsid protein. The fusion protein elicited an immune response and protected suckling mice from a lethal dose of EV-A71 infection. Recently, Mustafa et al. [70] fused truncated EV-A71 VP1 (amino acids 198–297) with Newcastle disease virus capsid protein and expressed it in *E. coli*. The recombinant protein elicited neutralizing antibodies against EV-A71 in a mouse model.

## 6. Conclusions and Prospective

EV-A71 is a major causative agent of HFMD, and EV-A71 infection has also led to neurological complications and death in young children worldwide. Vaccines are the most effective way to prevent EV-A71 infection.

The primary strategy to develop EV-A71 vaccines is to use viral structural proteins as immunogens. The inactivated whole-virus vaccine, live-attenuated virus vaccine, VLP vaccine, recombinant VP1 vaccine, and synthetic peptide vaccine all deliver wholly or partially expressed viral proteins to the host to elicit host immunogenicity and produce neutralizing antibodies. The inactivated, whole-virus vaccines yield high immunogenicity levels with high neutralization titers and induce cross-genotype neutralizing antibody responses more effectively. Currently, there are three inactivated, whole-virus vaccines against EV-A71 approved by the China NMPA, and WHO recommendations believe the Sinovac vaccine could be used worldwide [25]. However, the inactivated EV-A71 vaccine still faces two major challenges—cross-genotype and long-term protection. Although the Vigoo, Sinovac, and CAMS vaccines (using the C4 genotype) and the NHRI vaccine (using the B4 genotype) showed cross-protection against current circulating EV-A71 strains, the B4-based vaccine poorly neutralized a C2 isolate. Although the study by Hu et al. observed that the neutralizing antibodies elicited by inactivated EV-A71 vaccine persisted for five years, immunity decreased after six months [8,24].

The advantages of recombinant VP1 and synthetic peptide vaccines are that they are safer and more cost-effective. These vaccines reduce the risk of unwanted immune



responses such as antibody-dependent enhancement (ADE). ADE is a general concern for vaccine design because the mechanisms underlying antibody protection against any pathogen infection have a theoretical potential to amplify the infection or trigger harmful immune responses [71]. However, the recombinant VP1, synthetic peptide, and VLP vaccines elicit low levels of virus-neutralizing antibody responses and require strong adjuvants [29]. If these vaccine candidates can be refined to boost immunogenicity levels, they could become powerful therapeutic options. For example, with the availability of the X-ray crystallographic structure of VP1 [72], bioinformatics, proteomics, and immunology can be applied to develop peptide-based, synthetic vaccines. These techniques can facilitate the design of potent peptides that contain virus-neutralization epitopes and efficiently induce high levels of virus-neutralizing antibody responses.

mRNA vaccines represent a promising alternative vaccine platform technology because of their high potency, rapid development, completely synthetic nature, low-cost manufacturing process, and safe administration. Nine months after the COVID-19 pandemic began, the US government granted emergency-use authorization to two COVID-19 mRNA vaccines—Pfizer-BioNTech [73] and Moderna mRNA-1273 [74,75]. It is also worth the effort to develop mRNA vaccines against EV-A71 in the future.

**Author Contributions:** Conceptualization, M.-L.L.; writing—original draft preparation, M.-L.L. and G.B.; writing—review and editing, M.-L.L., S.-R.S., G.B. and B.S.T.; funding acquisition, G.B., B.S.T. and S.-R.S. All authors have read and agreed to the published version of the manuscript.

**Funding:** This work was funded by National Institutes of Health R01 GM126833 to B.S.T. and G.B., and by the Research Center for Emerging Viral Infections from The Featured Areas Research Center Program within the framework of the Higher Education Sprout Project by the Ministry of Education in Taiwan and the Ministry of Science and Technology, Taiwan (MOST 108-3017-F-182-001) to S.R.S.

**Institutional Review Board Statement:** Not applicable.

**Informed Consent Statement:** Not applicable.

**Conflicts of Interest:** The authors declare no conflict of interest.

## References

- Alexander, J.P., Jr.; Baden, L.; Pallansch, M.A.; Anderson, L.J. Enterovirus 71 infections and neurologic disease—United States, 1977–1991. *J. Infect. Dis.* **1994**, *169*, 905–908. [\[CrossRef\]](#) [\[PubMed\]](#)
- Ooi, M.H.; Wong, S.C.; Lewthwaite, P.; Cardosa, M.J.; Solomon, T. Clinical features, diagnosis, and management of enterovirus 71. *Lancet Neurol.* **2010**, *9*, 1097–1105. [\[CrossRef\]](#)
- Lee, K.Y. Enterovirus 71 infection and neurological complications. *Korean J. Pediatr.* **2016**, *59*, 395–401. [\[CrossRef\]](#) [\[PubMed\]](#)
- Chang, L.Y.; Lin, H.Y.; Gau, S.S.; Lu, C.Y.; Hsia, S.H.; Huang, Y.C.; Huang, L.M.; Lin, T.Y. Enterovirus A71 neurologic complications and long-term sequelae. *J. Biomed. Sci.* **2019**, *26*, 57. [\[CrossRef\]](#)
- Puenpa, J.; Wanlapakorn, N.; Vongpunsawad, S.; Poovorawan, Y. The History of Enterovirus A71 Outbreaks and Molecular Epidemiology in the Asia-Pacific Region. *J. Biomed. Sci.* **2019**, *26*, 75. [\[CrossRef\]](#) [\[PubMed\]](#)
- Nikonov, O.S.; Chernykh, E.S.; Garber, M.B.; Nikonova, E.Y. Enteroviruses: Classification, Diseases They Cause, and Approaches to Development of Antiviral Drugs. *Biochemistry.* **2017**, *82*, 1615–1631. [\[CrossRef\]](#)
- Kung, Y.A.; Hung, C.T.; Liu, Y.C.; Shih, S.R. Update on the development of enterovirus 71 vaccines. *Expert Opin. Biol. Ther.* **2014**, *14*, 1455–1464. [\[CrossRef\]](#)
- Chang, Y.K.; Chen, K.H.; Chen, K.T. Hand, foot and mouth disease and herpangina caused by enterovirus A71 infections: A review of enterovirus A71 molecular epidemiology, pathogenesis, and current vaccine development. *Rev. Inst. Med. Trop. Sao Paulo* **2018**, *60*, e70. [\[CrossRef\]](#)
- Chen, B.S.; Lee, H.C.; Lee, K.M.; Gong, Y.N.; Shih, S.R. Enterovirus and Encephalitis. *Front. Microbiol.* **2020**, *11*, 261. [\[CrossRef\]](#) [\[PubMed\]](#)
- Lin, J.Y.; Kung, Y.A.; Shih, S.R. Antivirals and vaccines for Enterovirus A71. *J. Biomed. Sci.* **2019**, *26*, 65. [\[CrossRef\]](#)
- Shih, S.R.; Stollar, V.; Li, M.L. Host factors in enterovirus 71 replication. *J. Virol.* **2011**, *85*, 9658–9666. [\[CrossRef\]](#)
- Wang, X.; An, Z.; Huo, D.; Jia, L.; Li, J.; Yang, Y.; Liang, Z.; Wang, Q.; Wang, H. Enterovirus A71 vaccine effectiveness in preventing enterovirus A71 infection among medically-attended hand, foot, and mouth disease cases, Beijing, China. *Hum. Vaccin. Immunother.* **2019**, *15*, 1183–1190. [\[CrossRef\]](#)
- Minor, P.D. Polio eradication, cessation of vaccination and re-emergence of disease. *Nat. Rev. Microbiol.* **2004**, *2*, 473–482. [\[CrossRef\]](#) [\[PubMed\]](#)

14. Zhou, Y.; Li, J.X.; Jin, P.F.; Wang, Y.X.; Zhu, F.C. Enterovirus 71: A whole virion inactivated enterovirus 71 vaccine. *Expert Rev. Vaccin.* **2016**, *15*, 803–813. [[CrossRef](#)] [[PubMed](#)]
15. Mao, Q.Y.; Wang, Y.; Bian, L.; Xu, M.; Liang, Z. EV71 vaccine, a new tool to control outbreaks of hand, foot and mouth disease (HFMD). *Expert Rev. Vaccin.* **2016**, *15*, 599–606. [[CrossRef](#)] [[PubMed](#)]
16. Bek, E.J.; Hussain, K.M.; Phuektes, P.; Kok, C.C.; Gao, Q.; Cai, F.; Gao, Z.; McMinn, P.C. Formalin-inactivated vaccine provokes cross-protective immunity in a mouse model of human enterovirus 71 infection. *Vaccine* **2011**, *29*, 4829–4838. [[CrossRef](#)] [[PubMed](#)]
17. Dong, C.; Liu, L.; Zhao, H.; Wang, J.; Liao, Y.; Zhang, X.; Na, R.; Liang, Y.; Wang, L.; Li, Q. Immunoprotection elicited by an enterovirus type 71 experimental inactivated vaccine in mice and rhesus monkeys. *Vaccine* **2011**, *29*, 6269–6275. [[CrossRef](#)]
18. Chong, P.; Liu, C.C.; Chow, Y.H.; Chou, A.H.; Klein, M. Review of enterovirus 71 vaccines. *Clin. Infect. Dis. Off. Publ. Infect. Dis. Soc. Am.* **2015**, *60*, 797–803. [[CrossRef](#)]
19. Zhu, F.; Xu, W.; Xia, J.; Liang, Z.; Liu, Y.; Zhang, X.; Tan, X.; Wang, L.; Mao, Q.; Wu, J.; et al. Efficacy, safety, and immunogenicity of an enterovirus 71 vaccine in China. *N. Engl. J. Med.* **2014**, *370*, 818–828. [[CrossRef](#)] [[PubMed](#)]
20. Liang, Z.; Mao, Q.; Gao, Q.; Li, X.; Dong, C.; Yu, X.; Yao, X.; Li, F.; Yin, W.; Li, Q.; et al. Establishing China's national standards of antigen content and neutralizing antibody responses for evaluation of enterovirus 71 (EV71) vaccines. *Vaccine* **2011**, *29*, 9668–9674. [[CrossRef](#)] [[PubMed](#)]
21. Li, R.; Liu, L.; Mo, Z.; Wang, X.; Xia, J.; Liang, Z.; Zhang, Y.; Li, Y.; Mao, Q.; Wang, J.; et al. An inactivated enterovirus 71 vaccine in healthy children. *N. Engl. J. Med.* **2014**, *370*, 829–837. [[CrossRef](#)]
22. Zhu, F.C.; Meng, F.Y.; Li, J.X.; Li, X.L.; Mao, Q.Y.; Tao, H.; Zhang, Y.T.; Yao, X.; Chu, K.; Chen, Q.H.; et al. Efficacy, safety, and immunology of an inactivated alum-adjuvant enterovirus 71 vaccine in children in China: A multicentre, randomised, double-blind, placebo-controlled, phase 3 trial. *Lancet* **2013**, *381*, 2024–2032. [[CrossRef](#)]
23. Wei, M.; Meng, F.; Wang, S.; Li, J.; Zhang, Y.; Mao, Q.; Hu, Y.; Liu, P.; Shi, N.; Tao, H.; et al. 2-Year Efficacy, Immunogenicity, and Safety of Vigoo Enterovirus 71 Vaccine in Healthy Chinese Children: A Randomized Open-Label Study. *J. Infect. Dis.* **2017**, *215*, 56–63. [[CrossRef](#)]
24. Hu, Y.; Zeng, G.; Chu, K.; Zhang, J.; Han, W.; Zhang, Y.; Li, J.; Zhu, F. Five-year immunity persistence following immunization with inactivated enterovirus 71 type (EV71) vaccine in healthy children: A further observation. *Hum. Vaccin. Immunother.* **2018**, *14*, 1517–1523. [[CrossRef](#)] [[PubMed](#)]
25. Lei, D.; Griffiths, E.; Martin, J. WHO working group meeting to develop WHO Recommendations to assure the quality, safety and efficacy of enterovirus 71 vaccines. *Vaccine* **2020**, *38*, 4917–4923. [[CrossRef](#)]
26. Chang, J.Y.; Chang, C.P.; Tsai, H.H.; Lee, C.D.; Lian, W.C.; Ih Jen, S.; Sai, I.H.; Liu, C.C.; Chou, A.H.; Lu, Y.J.; et al. Selection and characterization of vaccine strain for Enterovirus 71 vaccine development. *Vaccine* **2012**, *30*, 703–711. [[CrossRef](#)]
27. Chong, P.; Hsieh, S.Y.; Liu, C.C.; Chou, A.H.; Chang, J.Y.; Wu, S.C.; Liu, S.J.; Chow, Y.H.; Su, I.J.; Klein, M. Production of EV71 vaccine candidates. *Hum. Vaccin. Immunother.* **2012**, *8*, 1775–1783. [[CrossRef](#)] [[PubMed](#)]
28. Cheng, A.; Fung, C.P.; Liu, C.C.; Lin, Y.T.; Tsai, H.Y.; Chang, S.C.; Chou, A.H.; Chang, J.Y.; Jiang, R.H.; Hsieh, Y.C.; et al. A Phase I, randomized, open-label study to evaluate the safety and immunogenicity of an enterovirus 71 vaccine. *Vaccine* **2013**, *31*, 2471–2476. [[CrossRef](#)] [[PubMed](#)]
29. Chou, A.H.; Liu, C.C.; Chang, C.P.; Guo, M.S.; Hsieh, S.Y.; Yang, W.H.; Chao, H.J.; Wu, C.L.; Huang, J.L.; Lee, M.S.; et al. Pilot scale production of highly efficacious and stable enterovirus 71 vaccine candidates. *PLoS ONE* **2012**, *7*, e34834. [[CrossRef](#)]
30. Chou, A.H.; Liu, C.C.; Chang, J.Y.; Jiang, R.; Hsieh, Y.C.; Tsao, A.; Wu, C.L.; Huang, J.L.; Fung, C.P.; Hsieh, S.M.; et al. Formalin-inactivated EV71 vaccine candidate induced cross-neutralizing antibody against subgenotypes B1, B4, B5 and C4A in adult volunteers. *PLoS ONE* **2013**, *8*, e79783. [[CrossRef](#)] [[PubMed](#)]
31. Huang, L.M.; Chiu, C.H.; Chiu, N.C.; Lin, C.Y.; Li, M.T.; Kuo, T.Y.; Weng, Y.J.; Hsieh, E.F.; Tai, I.C. Immunogenicity, safety, cross-reaction, and immune persistence of an inactivated enterovirus A71 vaccine in children aged from two months to 11 years in Taiwan. *Vaccine* **2019**, *37*, 1827–1835. [[CrossRef](#)]
32. In, H.J.; Lim, H.; Lee, J.A.; Kim, H.J.; Kim, J.W.; Hyeon, J.Y.; Yeo, S.G.; Lee, J.W.; Yoo, J.S.; Choi, Y.K.; et al. An inactivated hand-foot-and-mouth disease vaccine using the enterovirus 71 (C4a) strain isolated from a Korean patient induces a strong immunogenic response in mice. *PLoS ONE* **2017**, *12*, e0178259. [[CrossRef](#)] [[PubMed](#)]
33. Huang, S.W.; Cheng, D.; Wang, J.R. Enterovirus A71: Virulence, antigenicity, and genetic evolution over the years. *J. Biomed. Sci.* **2019**, *26*, 81. [[CrossRef](#)]
34. Fujii, K.; Sudaka, Y.; Takashino, A.; Kobayashi, K.; Kataoka, C.; Suzuki, T.; Iwata-Yoshikawa, N.; Kotani, O.; Ami, Y.; Shimizu, H.; et al. VP1 Amino Acid Residue 145 of Enterovirus 71 Is a Key Residue for Its Receptor Attachment and Resistance to Neutralizing Antibody during Cynomolgus Monkey Infection. *J. Virol.* **2018**, *92*. [[CrossRef](#)] [[PubMed](#)]
35. Nishimura, Y.; Lee, H.; Hafenstein, S.; Kataoka, C.; Wakita, T.; Bergelson, J.M.; Shimizu, H. Enterovirus 71 binding to PSGL-1 on leukocytes: VP1-145 acts as a molecular switch to control receptor interaction. *PLoS Pathog.* **2013**, *9*, e1003511. [[CrossRef](#)] [[PubMed](#)]
36. Yeh, M.T.; Wang, S.W.; Yu, C.K.; Lin, K.H.; Lei, H.Y.; Su, I.J.; Wang, J.R. A single nucleotide in stem loop II of 5'-untranslated region contributes to virulence of enterovirus 71 in mice. *PLoS ONE* **2011**, *6*, e27082. [[CrossRef](#)]
37. Chang, C.K.; Wu, S.R.; Chen, Y.C.; Lee, K.J.; Chung, N.H.; Lu, Y.J.; Yu, S.L.; Liu, C.C.; Chow, Y.H. Mutations in VP1 and 5'-UTR affect enterovirus 71 virulence. *Sci. Rep.* **2018**, *8*, 6688. [[CrossRef](#)]

38. Arita, M.; Nagata, N.; Iwata, N.; Ami, Y.; Suzaki, Y.; Mizuta, K.; Iwasaki, T.; Sata, T.; Wakita, T.; Shimizu, H. An attenuated strain of enterovirus 71 belonging to genotype A showed a broad spectrum of antigenicity with attenuated neurovirulence in cynomolgus monkeys. *J. Virol.* **2007**, *81*, 9386–9395. [\[CrossRef\]](#) [\[PubMed\]](#)
39. Sadeghipour, S.; Bek, E.J.; McMinn, P.C. Ribavirin-resistant mutants of human enterovirus 71 express a high replication fidelity phenotype during growth in cell culture. *J. Virol.* **2013**, *87*, 1759–1769. [\[CrossRef\]](#) [\[PubMed\]](#)
40. Meng, T.; Kwang, J. Attenuation of human enterovirus 71 high-replication-fidelity variants in AG129 mice. *J. Virol.* **2014**, *88*, 5803–5815. [\[CrossRef\]](#)
41. Tsai, Y.H.; Huang, S.W.; Hsieh, W.S.; Cheng, C.K.; Chang, C.F.; Wang, Y.F.; Wang, J.R. Enterovirus A71 Containing Codon-Deoptimized VP1 and High-Fidelity Polymerase as Next-Generation Vaccine Candidate. *J. Virol.* **2019**, *93*, e02308-18. [\[CrossRef\]](#) [\[PubMed\]](#)
42. Yee, P.T.I.; Tan, S.H.; Ong, K.C.; Tan, K.O.; Wong, K.T.; Hassan, S.S.; Poh, C.L. Development of live attenuated Enterovirus 71 vaccine strains that confer protection against lethal challenge in mice. *Sci. Rep.* **2019**, *9*, 4805. [\[CrossRef\]](#)
43. Zhao, D.; Sun, B.; Sun, S.; Fu, B.; Liu, C.; Liu, D.; Chu, Y.; Ma, Y.; Bai, L.; Wu, Y.; et al. Characterization of human enterovirus 71 virus-like particles used for vaccine antigens. *PLoS ONE* **2017**, *12*, e0181182. [\[CrossRef\]](#)
44. Qian, C.; Liu, X.; Xu, Q.; Wang, Z.; Chen, J.; Li, T.; Zheng, Q.; Yu, H.; Gu, Y.; Li, S.; et al. Recent Progress on the Versatility of Virus-Like Particles. *Vaccines (Basel)* **2020**, *8*, 139. [\[CrossRef\]](#) [\[PubMed\]](#)
45. Chung, Y.C.; Huang, J.H.; Lai, C.W.; Sheng, H.C.; Shih, S.R.; Ho, M.S.; Hu, Y.C. Expression, purification and characterization of enterovirus-71 virus-like particles. *World J. Gastroenterol.* **2006**, *12*, 921–927. [\[CrossRef\]](#)
46. Hu, Y.C.; Hsu, J.T.; Huang, J.H.; Ho, M.S.; Ho, Y.C. Formation of enterovirus-like particle aggregates by recombinant baculoviruses co-expressing P1 and 3CD in insect cells. *Biotechnol. Lett.* **2003**, *25*, 919–925. [\[CrossRef\]](#) [\[PubMed\]](#)
47. Lin, Y.L.; Yu, C.I.; Hu, Y.C.; Tsai, T.J.; Kuo, Y.C.; Chi, W.K.; Lin, A.N.; Chiang, B.L. Enterovirus type 71 neutralizing antibodies in the serum of macaque monkeys immunized with EV71 virus-like particles. *Vaccine* **2012**, *30*, 1305–1312. [\[CrossRef\]](#)
48. Rudd, P.M.; Elliott, T.; Cresswell, P.; Wilson, I.A.; Dwek, R.A. Glycosylation and the immune system. *Science* **2001**, *291*, 2370–2376. [\[CrossRef\]](#)
49. Hyakumura, M.; Walsh, R.; Thaysen-Andersen, M.; Kingston, N.J.; La, M.; Lu, L.; Lovrecz, G.; Packer, N.H.; Locarnini, S.; Netter, H.J. Modification of Asparagine-Linked Glycan Density for the Design of Hepatitis B Virus Virus-Like Particles with Enhanced Immunogenicity. *J. Virol.* **2015**, *89*, 11312–11322. [\[CrossRef\]](#)
50. Zhang, C.; Ku, Z.; Liu, Q.; Wang, X.; Chen, T.; Ye, X.; Li, D.; Jin, X.; Huang, Z. High-yield production of recombinant virus-like particles of enterovirus 71 in *Pichia pastoris* and their protective efficacy against oral viral challenge in mice. *Vaccine* **2015**, *33*, 2335–2341. [\[CrossRef\]](#)
51. Li, H.Y.; Han, J.F.; Qin, C.F.; Chen, R. Virus-like particles for enterovirus 71 produced from *Saccharomyces cerevisiae* potently elicits protective immune responses in mice. *Vaccine* **2013**, *31*, 3281–3287. [\[CrossRef\]](#) [\[PubMed\]](#)
52. Tsou, Y.L.; Lin, Y.W.; Shao, H.Y.; Yu, S.L.; Wu, S.R.; Lin, H.Y.; Liu, C.C.; Huang, C.; Chong, P.; Chow, Y.H. Recombinant adenovaccine expressing enterovirus 71-like particles against hand, foot, and mouth disease. *PLoS Negl. Trop. Dis.* **2015**, *9*, e0003692. [\[CrossRef\]](#)
53. Yan, Q.; Wu, L.; Chen, L.; Qin, Y.; Pan, Z.; Chen, M. Vesicular stomatitis virus-based vaccines expressing EV71 virus-like particles elicit strong immune responses and protect newborn mice from lethal challenges. *Vaccine* **2016**, *34*, 4196–4204. [\[CrossRef\]](#) [\[PubMed\]](#)
54. Ventarola, D.; Bordone, L.; Silverberg, N. Update on hand-foot-and-mouth disease. *Clin. Dermatol.* **2015**, *33*, 340–346. [\[CrossRef\]](#) [\[PubMed\]](#)
55. Zhang, W.; Dai, W.; Zhang, C.; Zhou, Y.; Xiong, P.; Wang, S.; Ye, X.; Liu, Q.; Zhou, D.; Huang, Z. A virus-like particle-based tetravalent vaccine for hand, foot, and mouth disease elicits broad and balanced protective immunity. *Emerg. Microbes Infect.* **2018**, *7*, 94. [\[CrossRef\]](#)
56. Wu, C.N.; Lin, Y.C.; Fann, C.; Liao, N.S.; Shih, S.R.; Ho, M.S. Protection against lethal enterovirus 71 infection in newborn mice by passive immunization with subunit VP1 vaccines and inactivated virus. *Vaccine* **2001**, *20*, 895–904. [\[CrossRef\]](#)
57. Zhou, S.L.; Ying, X.L.; Han, X.; Sun, X.X.; Jin, Q.; Yang, F. Characterization of the enterovirus 71 VP1 protein as a vaccine candidate. *J. Med. Virol.* **2015**, *87*, 256–262. [\[CrossRef\]](#) [\[PubMed\]](#)
58. Meng, T.; Kolpe, A.B.; Kiener, T.K.; Chow, V.T.; Kwang, J. Display of VP1 on the surface of baculovirus and its immunogenicity against heterologous human enterovirus 71 strains in mice. *PLoS ONE* **2011**, *6*, e21757. [\[CrossRef\]](#) [\[PubMed\]](#)
59. Wang, X.; Dong, K.; Long, M.; Lin, F.; Gao, Z.; Wang, L.; Zhang, Z.; Chen, X.; Dai, Y.; Wang, H.; et al. Induction of a high-titered antibody response using HIV gag-EV71 VP1-based virus-like particles with the capacity to protect newborn mice challenged with a lethal dose of enterovirus 71. *Arch. Virol.* **2018**, *163*, 1851–1861. [\[CrossRef\]](#) [\[PubMed\]](#)
60. Han, X.; Ying, X.L.; Zhou, S.L.; Han, T.; Huang, H.; Jin, Q.; Yang, F.; Sun, Q.Y.; Sun, X.X. Characterization of the enterovirus 71 P1 polyprotein expressed in *Pichia pastoris* as a candidate vaccine. *Hum. Vaccin. Immunother* **2014**, *10*, 2220–2226. [\[CrossRef\]](#)
61. Fournillier, A.; Wychowski, C.; Boucreux, D.; Baumert, T.F.; Meunier, J.C.; Jacobs, D.; Muguet, S.; Depla, E.; Inchauspe, G. Induction of hepatitis C virus E1 envelope protein-specific immune response can be enhanced by mutation of N-glycosylation sites. *J. Virol.* **2001**, *75*, 12088–12097. [\[CrossRef\]](#) [\[PubMed\]](#)

62. Chakrabarti, B.K.; Kong, W.P.; Wu, B.Y.; Yang, Z.Y.; Friborg, J.; Ling, X.; King, S.R.; Montefiori, D.C.; Nabel, G.J. Modifications of the human immunodeficiency virus envelope glycoprotein enhance immunogenicity for genetic immunization. *J. Virol.* **2002**, *76*, 5357–5368. [[CrossRef](#)] [[PubMed](#)]
63. Foo, D.G.; Alonso, S.; Phoon, M.C.; Ramachandran, N.P.; Chow, V.T.; Poh, C.L. Identification of neutralizing linear epitopes from the VP1 capsid protein of Enterovirus 71 using synthetic peptides. *Virus Res.* **2007**, *125*, 61–68. [[CrossRef](#)]
64. Foo, D.G.; Alonso, S.; Chow, V.T.; Poh, C.L. Passive protection against lethal enterovirus 71 infection in newborn mice by neutralizing antibodies elicited by a synthetic peptide. *Microbes. Infect.* **2007**, *9*, 1299–1306. [[CrossRef](#)] [[PubMed](#)]
65. Liu, J.N.; Wang, W.; Duo, J.Y.; Hao, Y.; Ma, C.M.; Li, W.B.; Lin, S.Z.; Gao, X.Z.; Liu, X.L.; Xu, Y.F.; et al. Combined peptides of human enterovirus 71 protect against virus infection in mice. *Vaccine* **2010**, *28*, 7444–7451. [[CrossRef](#)]
66. Aw-Yong, K.L.; Sam, I.C.; Koh, M.T.; Chan, Y.F. Immunodominant IgM and IgG Epitopes Recognized by Antibodies Induced in Enterovirus A71-Associated Hand, Foot and Mouth Disease Patients. *PLoS ONE* **2016**, *11*, e0165659. [[CrossRef](#)]
67. Xu, L.; He, D.; Li, Z.; Zheng, J.; Yang, L.; Yu, M.; Yu, H.; Chen, Y.; Que, Y.; Shih, J.W.; et al. Protection against lethal enterovirus 71 challenge in mice by a recombinant vaccine candidate containing a broadly cross-neutralizing epitope within the VP2 EF loop. *Theranostics* **2014**, *4*, 498–513. [[CrossRef](#)] [[PubMed](#)]
68. Huo, C.; Yang, J.; Lei, L.; Qiao, L.; Xin, J.; Pan, Z. Hepatitis B virus core particles containing multiple epitopes confer protection against enterovirus 71 and coxsackievirus A16 infection in mice. *Vaccine* **2017**, *35*, 7322–7330. [[CrossRef](#)]
69. Jiang, L.; Fan, R.; Sun, S.; Fan, P.; Su, W.; Zhou, Y.; Gao, F.; Xu, F.; Kong, W.; Jiang, C. A new EV71 VP3 epitope in norovirus P particle vector displays neutralizing activity and protection in vivo in mice. *Vaccine* **2015**, *33*, 6596–6603. [[CrossRef](#)]
70. Mustafa, S.; Abd-Aziz, N.; Saw, W.T.; Liew, S.Y.; Yusoff, K.; Shafee, N. Recombinant Enterovirus 71 Viral Protein 1 Fused to a Truncated Newcastle Disease Virus NP (NPt) Carrier Protein. *Vaccines (Basel)* **2020**, *8*, 742. [[CrossRef](#)] [[PubMed](#)]
71. Han, J.F.; Cao, R.Y.; Deng, Y.Q.; Tian, X.; Jiang, T.; Qin, E.D.; Qin, C.F. Antibody dependent enhancement infection of enterovirus 71 in vitro and in vivo. *Virol. J.* **2011**, *8*, 106. [[CrossRef](#)] [[PubMed](#)]
72. Wang, X.; Peng, W.; Ren, J.; Hu, Z.; Xu, J.; Lou, Z.; Li, X.; Yin, W.; Shen, X.; Porta, C.; et al. A sensor-adaptor mechanism for enterovirus uncoating from structures of EV71. *Nat. Struct. Mol. Biol.* **2012**, *19*, 424–429. [[CrossRef](#)]
73. Pardi, N.; Hogan, M.J.; Porter, F.W.; Weissman, D. mRNA vaccines—A new era in vaccinology. *Nat. Rev. Drug Discov.* **2018**, *17*, 261–279. [[CrossRef](#)] [[PubMed](#)]
74. Anderson, E.J.; Roupael, N.G.; Widge, A.T.; Jackson, L.A.; Roberts, P.C.; Makhene, M.; Chappell, J.D.; Denison, M.R.; Stevens, L.J.; Pruijssers, A.J.; et al. Safety and Immunogenicity of SARS-CoV-2 mRNA-1273 Vaccine in Older Adults. *N. Engl. J. Med.* **2020**, *383*, 2427–2438. [[CrossRef](#)]
75. Widge, A.T.; Roupael, N.G.; Jackson, L.A.; Anderson, E.J.; Roberts, P.C.; Makhene, M.; Chappell, J.D.; Denison, M.R.; Stevens, L.J.; Pruijssers, A.J.; et al. Durability of Responses after SARS-CoV-2 mRNA-1273 Vaccination. *N. Engl. J. Med.* **2020**. [[CrossRef](#)]





# Timing of the Diagnoses of Attention Deficit Hyperactivity Disorder and Autism Spectrum Disorder in Taiwan

Han-Ting Wei<sup>2,8</sup> · Ju-Wei Hsu<sup>1,2</sup> · Kai-Lin Huang<sup>1,2</sup> · Ya-Mei Bai<sup>1,2</sup> · Tung-Ping Su<sup>1,2,9</sup> · Cheng-Ta Li<sup>1,2</sup> · Wei-Chen Lin<sup>1,2</sup> · Shih-Jen Tsai<sup>1,2</sup> · Tai-Long Pan<sup>5,6,7</sup> · Tzeng-Ji Chen<sup>3,4</sup> · Mu-Hong Chen<sup>1,2</sup>

Published online: 7 July 2018

© Springer Science+Business Media, LLC, part of Springer Nature 2018

## Abstract

ADHD comorbidity has been associated with delayed diagnosis of ASD, but no study has investigated this association in an Asian country. Children with ASD were included and divided into three groups: ADHD before ASD, ADHD same/after ASD, and ASD only. Timing of ASD and ADHD diagnoses were assessed. The logistic regression model was performed to investigate the likelihood of being diagnosed with ASD after 6 years of age between three groups. ADHD before ASD (OR 10.93) group was more likely to being diagnosed with ASD after 6 years of age compared with ADHD same/after ASD (OR: 1.37) and ASD only groups. ADHD comorbidity would delay the diagnosis of ASD in the general clinical settings in Taiwan.

**Keywords** ASD · ADHD · Timing of the diagnosis · Delayed diagnosis

✉ Ju-Wei Hsu  
jwhsu@vghtpe.gov.tw

✉ Mu-Hong Chen  
kremer7119@gmail.com

Han-Ting Wei  
proudppwei@yahoo.com.tw

Kai-Lin Huang  
klhuang2@vghtpe.gov.tw

Ya-Mei Bai  
ymbi@mail2000.com.tw

Tung-Ping Su  
tpsu@vghtpe.gov.tw

Cheng-Ta Li  
on5083@msn.com

Wei-Chen Lin  
plin33@gmail.com

Shih-Jen Tsai  
tsai610913@gmail.com

Tai-Long Pan  
pan@mail.cgu.edu.tw

Tzeng-Ji Chen  
tjchen@vghtpe.gov.tw

<sup>1</sup> Department of Psychiatry, Taipei Veterans General Hospital, No. 201, Shih-Pai Road, Sec. 2, 11217 Taipei, Taiwan

<sup>2</sup> Department of Psychiatry, College of Medicine, National Yang-Ming University, Taipei, Taiwan

<sup>3</sup> Department of Family Medicine, Taipei Veterans General Hospital, Taipei, Taiwan

<sup>4</sup> Institute of Hospital and Health Care Administration, National Yang-Ming University, Taipei, Taiwan

<sup>5</sup> School of Traditional Chinese Medicine, Chang Gung University, Taoyuan, Taiwan

<sup>6</sup> Research Center for Industry of Human Ecology, Chang Gung University of Science and Technology, Taoyuan, Taiwan

<sup>7</sup> Liver Research Center, Division of Hepatology, Department of Gastroenterology and Hepatology, Chang Gung Memorial Hospital, Taoyuan, Taiwan

<sup>8</sup> Branch of Linsen, Chinese Medicine, and Kunming, Taipei City Hospital, Taipei, Taiwan

<sup>9</sup> Department of Psychiatry, General Cheng Hsin Hospital, Taipei, Taiwan

## Introduction

Both autism spectrum disorder (ASD) and attention-deficit hyperactivity disorder (ADHD) are neurodevelopmental disorders that begin in childhood and usually persist throughout life. They frequently co-occur in the same individual; they have distinct and overlapping clinical symptoms. ASD exhibits persistent deficits in social communication and social interaction and is accompanied by restricted and repetitive patterns of behaviors, interests, or activities. By contrast, ADHD manifests as the inability to marshal and sustain attention and modulate activity level (Rappley 2005; Baker 2013; Lai et al. 2013; Volkow and Swanson 2013). Studies have reported that up to 50% of ASD patients also meet the criteria for ADHD diagnosis, and this comorbidity interferes with their psychopathology, cognitive function, and interpersonal relationships, as well as school and family lives (Lee and Ousley 2006; Rommelse et al. 2010). Several recent large-scale genome-wide studies have suggested that ASD and ADHD share some genetic markers; this may explain the frequent co-occurrence of these two conditions (Ronald et al. 2008; Nijmeijer et al. 2010; Rommelse et al. 2010).

ASD can be accurately diagnosed in children as young as 2 years old; however, the median age at earliest ASD diagnosis is 52 months (Baio et al. 2018). A comparative study reported that one-third of the children with ADHD were diagnosed before the age of 6 years; however, the median age for ADHD diagnosis in children was 7 years (Visser et al. 2015). Increasing evidence indicates that certain family and childhood factors, such as belonging to an ethnic minority group, lower level of parents' education, disadvantaged socioeconomic circumstances, and the presence of co-occurring developmental and psychiatric conditions are related to a later diagnosis of ASD (Miodovnik et al. 2015). Davidovitch et al. examined a cohort of children diagnosed with ASD after age 6 years despite having undergone a comprehensive, multidisciplinary assessment before 6 years of age; they found that approximately 50% of the subjects had attention problems at the initial assessment (Davidovitch et al. 2015). Miodovnik et al. found that children diagnosed with ADHD before ASD were diagnosed with ASD approximately 3 years after those in whom ADHD was diagnosed with or after ASD (Miodovnik et al. 2015). They further reported that the children in whom ADHD was diagnosed first were nearly 30 times more likely to be diagnosed with ASD after 6 years of age [95% confidence interval (CI) 11.2–77.8] (Miodovnik et al. 2015).

The earliest symptoms of ASD, such as the delayed attainment of social skill milestones, were identified by parents or nonpsychiatrists, such as pediatricians and

general physicians, in Western countries (Oslejskova et al. 2007; Carbone et al. 2010; Kairys and Petrova 2016). Oslejsková et al. reported that the average duration between the recognition of the first ASD symptom by parents and the establishment of a correct ASD diagnosis was approximately 4 years (Oslejskova et al. 2007). Previous studies also suggested that symptoms of ADHD may overshadow or mask the symptoms of ASD, which could delay ASD diagnosis (Miodovnik et al. 2015; Yee and Millichap 2015). In addition, in the general clinical setting, it may be that a lack of experience in evaluating ASD resulted in missed diagnosis or misdiagnosis, which would delay referral for ASD assessment and delay ASD diagnosis.

To our knowledge, no study has been conducted in Asian countries to examine the relationship between the ages at ASD and ADHD diagnoses. In the current study, we investigated the timing of ASD and ADHD diagnoses in the general clinical practice in Taiwan. We also hypothesized that a diagnosis of ADHD before ASD would delay the diagnosis of ASD in these children compared to children diagnosed with ADHD at the same time or after ASD or to children with ASD only.

## Methods

### Data Source

Taiwan's National Health Insurance (NHI), a mandatory universal health insurance program, was implemented in 1995 and covers up to 99% of the country's 23 million residents. The National Health Research Institute (NHRI) is in charge of the entire insurance claims database, namely the National Health Insurance Research Database (NHIRD), and audits and releases the NHIRD for scientific and study purposes. Individual medical records included in the NHIRD are anonymous to protect personal privacy. Comprehensive information on insured individuals is included in the database, including demographic data, dates of clinical visits, and disease diagnoses. The diagnostic codes used were based on the International Classification of Diseases, 9th Revision, Clinical Modification (ICD-9-CM). The NHIRD has been used extensively in many epidemiologic studies in Taiwan (Li et al. 2012; Shen et al. 2013; Chen et al. 2015, 2016).

### Inclusion Criteria for Children and Adolescents with ASD

Children aged  $\leq 12$  years and adolescents aged between 13 and 17 years with a diagnosis of ASD (ICD-9-CM code: 299) given by board-certified psychiatrists on the basis of clinical judgment and psychiatric diagnostic interview between January 1, 2001 and December 31, 2011 were

included. The time of ASD and ADHD diagnoses were identified, separately. Based on the time of ASD and ADHD diagnoses, children and adolescents with ASD were divided to three subgroups: ASD only, ADHD same/after ASD, and ADHD before ASD. Co-occurring conditions, including developmental delay and intellectual disability, were also assessed. In Taiwan, the diagnosis of developmental delay was given based on a comprehensive and multidisciplinary assessment (motor, language, social, cognitive, and emotional functions) before 7 years of age; the diagnosis of intellectual disability was given based on the clinical judgment and intelligence quotient (IQ) test (Wechsler Intelligence Scale) when patients were able to complete the IQ test. However, the Intellectual disability would be diagnosed based on the clinical judgment for patients with severe Intellectual disability who were not able to complete the IQ test. The diagnoses of ASD, ADHD, and co-occurring conditions were given by board-certificated specialists at least twice, yielding the improved diagnostic validity. The level of urbanization (level 1 to level 5; level 1: most urbanized; level 5: least urbanized) was also assessed (Liu et al. 2006). Taipei Veterans General Hospital Institutional Review Board permitted this study.

## Statistical Analysis

For between-group comparisons, the F test was used for continuous variables and Pearson's  $\chi^2$  test was used for nominal variables, where appropriate. The logistic regression model was used to investigate the odds ratio (OR) with 95% CI of ASD diagnosis > 6 years of age between three subgroups after adjusting demographic data (age, sex, level of urbanization) and co-occurring conditions (developmental delay, intellectual disability). The age of ASD diagnosis was examined stratified by age of ADHD diagnosis between ADHD same/after ASD, and ADHD before ASD subgroups. The age of ASD diagnosis was also assessed stratified by presence and absence of co-occurring conditions (developmental delay, intellectual disability) between three subgroups. All data processing and statistical analyses were performed using the Statistical Package for Social Science (SPSS) Version 17 software (SPSS Inc.) and Statistical Analysis Software (SAS) Version 9.1 (SAS Institute, Cary, NC).

## Results

In all, 19,794 children and adolescents with ASD were enrolled in the study, with a mean/median age of  $5.94/5.20 \pm 3.33$  years and with a male predominance (84.8% vs. 15.2%). For 9539 (48.2%) of these children and adolescents, they had also received a diagnosis of ADHD. Of the children and adolescents with co-occurring ASD and

ADHD, 4369 (45.8%) comprised the ADHD before ASD group and 5170 (54.2%) comprised the ADHD same/after ASD group (Table 1). Overall, those with ADHD before ASD were approximately 3 years older ( $8.45 \pm 3.11$  vs.  $5.52 \pm 2.85$  vs.  $5.07 \pm 3.10$  years,  $p < 0.001$ ) when they received the ASD diagnosis and 77.9% (vs. 36.1% vs. 27.2%,  $p < 0.001$ ) were diagnosed after age 6 compared with ADHD same/after ASD and ASD only groups (Table 1). ADHD before ASD group had a lower prevalence of developmental delay (61.5% vs. 74.6% vs. 77.4%,  $p < 0.001$ ) and intellectual disability (21.7% vs. 27.6% vs. 25.1%,  $p < 0.001$ ) than did ADHD same/after ASD and ASD only groups (Table 1). In our study, 29.5% of patients with developmental delay had the diagnosis of Intellectual disability; 86.4% of patients with Intellectual disability had the diagnosis of developmental delay. The average ages of developmental delay and intellectual disability diagnoses were  $3.76 \pm 2.12$  and  $6.15 \pm 2.94$  years of age, respectively (Table 1).

The logistic regression model with an adjustment of demographic data and co-occurring conditions showed that both ADHD before ASD (OR 10.93, 95% CI 9.87–12.10) and ADHD same/after ASD (OR 1.37, 95% CI 1.25–1.49) groups were more likely to being diagnosed with ASD after 6 years of age compared with ASD only group (Table 2). In addition, in order control for differences in secular trends of ASD diagnosis over time, the year in which the child was diagnosed with ASD was included as a variable in the regression model. We found a consistent finding (ADHD before ASD: OR 1.89, 95% CI 1.46–2.45; ADHD same/after ASD: OR 1.40, 95% CI 1.77). Developmental delay (OR 0.1, 95% CI 0.18–0.21) was related to a reduced likelihood of being diagnosed with ASD after 6 years of age, but intellectual disability (OR 1.16, 95% CI 1.06–1.27) was associated with an elevated risk of being diagnosed with ASD after 6 years of age (Table 2). Figure 1 revealed how the gap in age at ASD diagnosis between ADHD before ASD and ADHD same/after ASD groups remained fairly constant across early childhood and into adolescence. Figure 2 illustrated the age of ASD diagnosis in three different groups based on the presence or absence of co-occurring conditions, namely developmental delay and intellectual disability.

## Discussion

Our results supported the study hypothesis that children and adolescents diagnosed with ADHD before ASD had a delayed diagnosis of ASD compared with those diagnosed with ADHD same/after ASD and those with ASD only. The presence of ADHD delayed the identification and diagnosis of ASD in children and adolescents with co-occurring ASD and ADHD.

**Table 1** Demographic and clinical characteristics of children stratified by study group

|                                   | Total (n = 19,794) | ADHD before ASD (n = 4369) | ADHD same/after ASD (n = 5170) | ASD only (n = 10,255) | P value |
|-----------------------------------|--------------------|----------------------------|--------------------------------|-----------------------|---------|
| Age <sup>a</sup> (years, SD)      | 11.25 (3.81)       | 12.33 (3.17)               | 11.65 (3.37)                   | 10.59 (4.12)          | <0.001  |
| Sex (n, %)                        |                    |                            |                                |                       | <0.001  |
| Male                              | 16,792 (84.8)      | 3852 (88.2)                | 4524 (87.5)                    | 8416 (82.1)           |         |
| Female                            | 3002 (15.2)        | 517 (11.8)                 | 646 (12.5)                     | 1839 (17.9)           |         |
| Age at ASD diagnosis (years, SD)  | 5.94 (3.33)        | 8.45 (3.11)                | 5.52 (2.85)                    | 5.07 (3.10)           | <0.001  |
| Age at ADHD diagnosis (years, SD) | 6.72 (2.76)        | 6.35 (2.48)                | 7.03 (2.94)                    | –                     | <0.001  |
| ASD diagnosed > 6 year-old (n, %) | 8060 (40.7)        | 3402 (77.9)                | 1867 (36.1)                    | 2791 (27.2)           | <0.001  |
| Co-occurring conditions (n, %)    |                    |                            |                                |                       |         |
| Developmental delay               | 14,489 (73.2)      | 2688 (61.5)                | 3859 (74.6)                    | 7942 (77.4)           | <0.001  |
| Age at diagnosis (years, SD)      | 3.76 (2.12)        | 4.85 (2.33)                | 3.90 (2.08)                    | 3.33 (1.91)           | <0.001  |
| Intellectual disability           | 4952 (25.0)        | 948 (21.7)                 | 1426 (27.6)                    | 2578 (25.1)           | <0.001  |
| Age at diagnosis (years, SD)      | 6.15 (2.94)        | 6.88 (2.93)                | 6.19 (2.79)                    | 5.86 (2.99)           | <0.001  |
| Level of urbanization (n, %)      |                    |                            |                                |                       | 0.001   |
| 1                                 | 3718 (18.8)        | 754 (17.3)                 | 927 (17.9)                     | 2037 (19.9)           |         |
| 2                                 | 6142 (31.0)        | 1381 (31.6)                | 1577 (30.5)                    | 3184 (31.0)           |         |
| 3                                 | 1436 (7.3)         | 304 (7.0)                  | 388 (7.5)                      | 744 (7.3)             |         |
| 4                                 | 1287 (6.5)         | 273 (6.2)                  | 335 (6.5)                      | 679 (6.6)             |         |
| 5                                 | 7211 (36.4)        | 1657 (37.9)                | 1943 (37.6)                    | 3611 (35.2)           |         |

ASD autism spectrum disorder, ADHD attention-deficit hyperactivity disorder, SD standard deviation

<sup>a</sup>Age at the end of inclusion period, 2011

**Table 2** Associations for ASD diagnosis > 6 years of age

|                         | OR           | 95% CI            |
|-------------------------|--------------|-------------------|
| Sex                     |              |                   |
| Male                    | 1.04         | 0.93–1.15         |
| Female                  | Ref.         | –                 |
| ASD subgroup            |              |                   |
| ADHD before ASD         | <b>10.93</b> | <b>9.87–12.10</b> |
| ADHD same/after ASD     | <b>1.37</b>  | <b>1.25–1.49</b>  |
| ASD only                | Ref.         | –                 |
| Co-occurring conditions |              |                   |
| Developmental delay     | <b>0.19</b>  | <b>0.18–0.21</b>  |
| Intellectual disability | <b>1.16</b>  | <b>1.06–1.27</b>  |
| Level of urbanization   |              |                   |
| 1                       | Ref.         |                   |
| 2                       | 1.09         | 0.97–1.22         |
| 3                       | <b>1.41</b>  | <b>1.20–1.67</b>  |
| 4                       | 1.16         | 0.98–1.38         |
| 5                       | 1.01         | 0.91–1.23         |

ASD autism spectrum disorder, ADHD attention-deficit hyperactivity disorder, OR odds ratio, CI, confidence interval

Bold indicates statistical significance

The universal screening for ASD at 18 and 24 months of age was suggested by the American Academy of Pediatrics guidelines (Johnson and Myers 2007). However, large-scale

surveillance studies have demonstrated that up to 40% children with ASD were not diagnosed with ASD until they were 6 years old in the real-world clinical practice (Johnson and Myers 2007, Developmental Disabilities Monitoring Network Surveillance Year Principal, Centers for Disease et al. 2014). In our study, 40.7% of the children and adolescents with ASD were diagnosed with ASD after 6 years of age in Taiwan. In particular, approximately 80% of the children and adolescents who were diagnosed with ADHD before ASD were diagnosed with ASD after 6 years of age. Johnson et al. reported that 74% of children, at an average age of 11.3 years with pervasive developmental disorder, not otherwise specified, had previously been diagnosed with ADHD and had been prescribed a psychostimulant for their symptoms (Jensen et al. 1997). Mandell et al. investigated the mental health of subjects before ASD diagnosis and found that only 43.8% of children at a mean age of 6.7 years with ASD were correctly diagnosed with ASD at the first clinical visit, whereas up to 25% were diagnosed with ADHD first (Mandell et al. 2007). Miodovnik et al. surveyed 1496 children and adolescents with a current diagnosis of ASD and reported that 39.5% were not diagnosed with ASD until they were ≥ 6 years old, and approximately 20% of these children had initially been diagnosed with ADHD (Miodovnik et al. 2015).

Most evidence required for establishing an accurate diagnosis of ASD in young children is based on the results



**Fig. 1** Age at ASD diagnosis by age at ADHD diagnosis for ADHD before ASD (black line) and ADHD same/after ASD (light gray line). *ASD* autism spectrum disorder, *ADHD* attention-deficit hyperactivity disorder

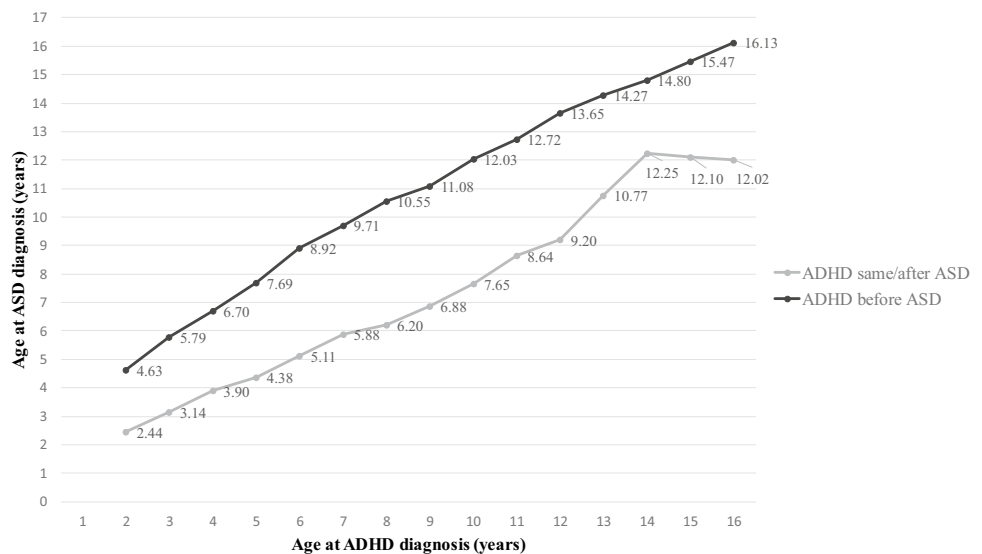
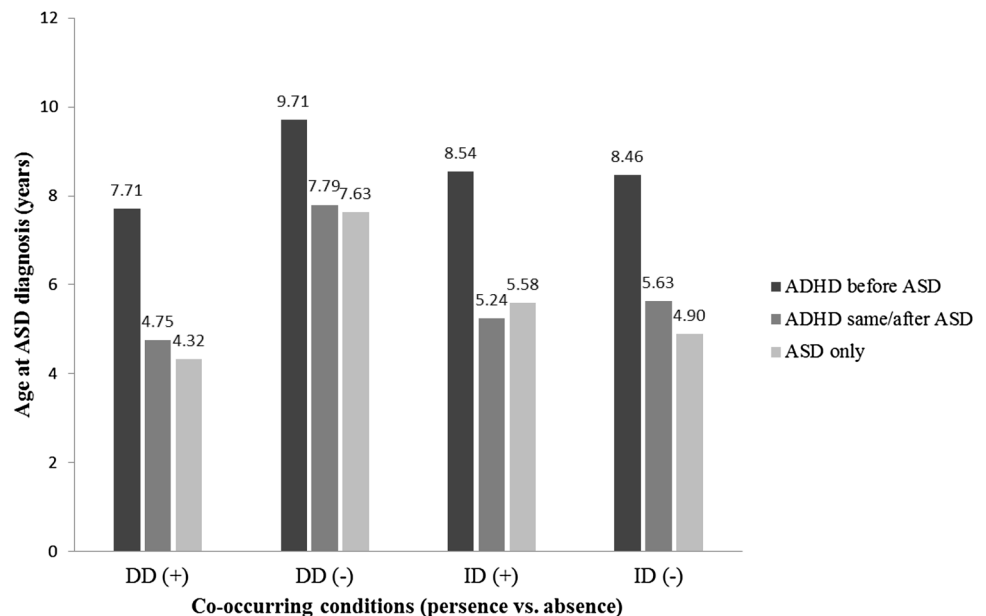


**Fig. 2** Mean age at ASD diagnosis stratified by co-occurring conditions. *ASD* autism spectrum disorder, *ADHD* attention-deficit hyperactivity disorder, *DD* developmental delay, *ID* Intellectual disability



of studies conducted with experienced and highly trained staff in research settings (Miodovnik et al. 2015). Mental comorbidities and co-occurring developmental conditions with ASD would increase the complexity of the psychopathology of ASD; this may interfere with the establishment of an accurate diagnosis of ASD at the initial assessment. Gadow et al. surveyed the ADHD symptoms among children aged 3–12 years with ASD and found that 41.4% of the children had ADHD symptoms that were identified by their parents and/or teachers (Gadow et al. 2006). A study involving a cohort of children diagnosed with ASD after the age of 6 years, who were not diagnosed with ASD during a comprehensive assessment before 6 years of age, indicated that approximately 46% of these children had ADHD symptoms (Davidovitch et al. 2015). Law et al. followed

120 children aged 3–6 years who had been diagnosed with ADHD after undergoing a multidisciplinary consultation and reported that 7 years after the initial evaluation, 11.4% of the children reported having a current ASD diagnosis (Law et al. 2014). ADHD symptoms, especially hyperactivity and impulsivity, were more likely to be observed and identified by parents, teachers, or clinicians than ASD symptoms, particularly when the social cognitive impairment was mild. In addition, because the prototypical behaviors and social deficits that characterize ASD may not be manifested during the relatively short duration of a consultation in a general clinical setting, clinicians may be inclined to attribute maladaptive behaviors to ADHD, the most common neurobehavioral disorder in children (Gabrielsen et al. 2015; Miodovnik et al. 2015). In our study, we also found that

the children diagnosed with ADHD before ASD were more likely to have a delayed diagnosis of ASD compared with the children in the other two groups. Furthermore, Miodovnik et al. reported that ADHD same/after ASD group had a similar age of ASD diagnosis with ASD only group. However, our findings suggested that ADHD same/after ASD group also had a slightly increased likelihood of being diagnosed with ASD after the age of 6 years than those with ASD only. These findings indicate that the diagnosis of ADHD before or after ASD diagnosis can delay the accurate diagnosis of ASD in Taiwan.

Consistent with the findings of a previous study that reported that developmental delay was related to an early diagnosis of ASD and intellectual disability was associated with the late diagnosis of ASD, we found that developmental delay was a protective factor for the diagnosis of ASD after 6 years of age, and intellectual disability was related to the increased likelihood of being diagnosed with ASD after the age of 6 years (Miodovnik et al. 2015). Developmental delay, especially speech delay, is one of the core symptoms of ASD that prompted the clinicians to comprehensively evaluate the social cognitive development in these at-risk children (Johnson and Myers 2007; Gabrielsen et al. 2015). By contrast, intellectual disability may interfere with the comprehensive evaluation of social cognition and communication, potentially delaying an accurate ASD diagnosis (Johnson and Myers 2007; Gabrielsen et al. 2015; Miodovnik et al. 2015).

Finally, as mentioned in the introduction, Oslejskova et al. suggested that a possible reason of the late diagnosis of ASD may be partly explained by the complicated and prolonged referral system in the Western countries (Oslejskova et al. 2007). However, contact and consultation with professional psychiatrists is easily accessible in Taiwan because of their highly convenient national health insurance system. If parents are concerned about any child's developmental or mental problems, they can take the child directly to a pediatric or psychiatric clinic for further evaluation. Excluding the factor that complicated referral system may delay the ASD diagnosis in Taiwan, our findings may more suggest that ADHD symptoms may overshadow or mask the ASD symptoms, which could delay ASD diagnosis (Miodovnik et al. 2015; Yee and Millichap 2015).

Some study limitations should be addressed here. First, the prevalence of ASD and ADHD may have been underestimated in the register-based study because only those who sought medical help and consultation could be identified. However, the diagnoses of ASD and ADHD were established by board-certificated psychiatrists, yielding an improved diagnostic validity. Second, the cross-sectional study design precluded us from making statements about the causality of our associations. Although the timing of ASD and ADHD diagnoses reported by the psychiatrist allowed us to examine the temporal order of events, we

could not prospectively control or account for other interfering factors. Third, in our study, the lower proportions of developmental delay and intellectual disability in the ADHD before ASD population may suggest that these children had a milder phenotype of ASD. However, ASD severity was not available in the database. Further clinical study would be necessary to clarify this issue. Fourth, suburban region may be related to an increased risk of being diagnosed with ASD older than six in our study. Further study may be required to elucidate whether the level of urbanization had an impact on age at ASD diagnosis. Fifth, children who had some ASD or ADHD symptoms may be assessed through the school system or by psychologists or other mental health providers in private practice. Because the diagnosis of ASD or ADHD were only given by board-certificated physicians in Taiwan, those children must be referred to medical system for a comprehensive psychiatric evaluation. In our study, the age of ASD or ADHD diagnosis was defined as the time of being diagnosed by board-certificated psychiatrists, but not the time of being assessed through the school system or by psychologists or other mental health providers. Sixth, an additional possible reason for the late diagnosis of ASD was that the diagnosis of ASD was not delayed in the group of children initially diagnosed with ADHD, but rather the children truly did not meet criteria for ASD earlier. Previous studies reported that between 12 and 20% of the high-risk infant siblings who did not meet criteria for ASD at 36 months of age went on to meet criteria for ASD by middle childhood (Brian et al. 2016; Shephard et al. 2017). The result may imply that there may be a subset of children, such as ADHD before ASD group, who do not manifest the full syndrome earlier in life but who eventually do meet criteria. Further clinical studies would be required to clarify this important topic whether it is possible that early ADHD may evolve into a phenotype more consistent with ASD over time in some cases. Seventh, some information, such as that pertaining to parental education, family history, ASD severity, intelligence quotient, personal life style factors, and environmental factors, were unavailable in the NHIRD. Therefore, we were unable to study their effects.

In conclusion, subjects in whom ADHD was diagnosed before ASD were more likely to be diagnosed with ASD after the age of 6 years, after adjusting for demographic characteristics and co-occurring conditions, compared with those for whom ADHD was diagnosed simultaneously with or after ASD and those with ASD only. ADHD comorbidity could delay the accurate diagnosis of ASD in the general clinical settings in Taiwan. Early diagnosis of ASD would enable early therapeutic intervention, potentially reducing the social adversity and issues associated with ASD in young patients. Our findings should prompt clinicians to perform

comprehensive evaluations of social communication skills and autistic symptoms in young children presenting with ADHD symptoms.

**Acknowledgments** We thank Mr I-Fan Hu for his friendship and support.

**Author Contributions** HTW, JWH, and MHC designed the study, performed the analysis, wrote the protocol and manuscripts; KLH, YMB, TPS, CTL, WCL, SJT, and TLP assisted with the preparation and proof-reading of the manuscript; YMB, TJC, and MHC provided the advices on statistical analysis.

**Funding** The study was supported by Grant from Taipei Veterans General Hospital (V103E10-001, V104E10-002, V105E10-001-MY2-1, V105A-049, V106B-020, V107B-010, V107C-181). The funding source had no role in any process of our study.

## Compliance with Ethical Standards

**Conflict of interest** All authors have no financial relationships and conflict of interest relevant to this article to disclose.

**Ethical Approval** This study was based on Taiwan National Health Insurance Research Database. Individual medical records included in the NHIRD are anonymous to protect personal privacy. Taipei Veterans General Hospital Institutional Review Board permitted this study.

## References

- Baio, J., Wiggins, L., Christensen, D. L., Maenner, M. J., Daniels, J., Warren, Z., Kurzius-Spencer, M., Zahorodny, W., Robinson Rosenberg, C., White, T., Durkin, M. S., Imm, P., Nikolaou, L., Yeargin-Allsopp, M., Lee, L. C., Harrington, R., Lopez, M., Fitzgerald, R. T., Hewitt, A., Pettygrove, S., Constantino, J. N., Vehorn, A., Shenouda, J., Hall-Lande, J., Van Naarden Braun K., & Dowling, N. F. (2018). Prevalence of autism spectrum disorder among children aged 8 years—Autism and Developmental Disabilities Monitoring Network, 11 Sites, United States, 2014. *MMWR Surveillance Summaries* 67(6):1–23.
- Baker, J. P. (2013). Autism at 70—redrawing the boundaries. *The New England Journal of Medicine*, 369(12), 1089–1091.
- Brian, J., Bryson, S. E., Smith, I. M., Roberts, W., Roncadin, C., Szatmari, P., & Zwaigenbaum, L. (2016). Stability and change in autism spectrum disorder diagnosis from age 3 to middle childhood in a high-risk sibling cohort. *Autism*, 20(7), 888–892.
- Carbone, P. S., Farley, M., & Davis, T. (2010). Primary care for children with autism. *American Family Physician*, 81(4), 453–460.
- Chen, M.-H., Lan, W.-H., Hsu, J.-W., Huang, K.-L., Su, T.-P., Li, C.-T., Lin, W.-C., Tsai, C.-F., Tsai, S.-J., & Lee, Y.-C. (2016). Risk of developing type 2 diabetes in adolescents and young adults with autism spectrum disorder: A nationwide longitudinal study. *Diabetes Care*, 39(5), 788–793.
- Chen, M.-H., Pan, T.-L., Li, C.-T., Lin, W.-C., Chen, Y.-S., Lee, Y.-C., Tsai, S.-J., Hsu, J.-W., Huang, K.-L., & Tsai, C.-F. (2015). Risk of stroke among patients with post-traumatic stress disorder: Nationwide longitudinal study. *The British Journal of Psychiatry*, 206(4), 302–307.
- Davidovitch, M., Levit-Binnun, N., Golan, D., & Manning-Courtney, P. (2015). Late diagnosis of autism spectrum disorder after initial negative assessment by a multidisciplinary team. *Journal of Developmental and Behavioral Pediatrics*, 36(4), 227–234.
- Developmental Disabilities Monitoring Network Surveillance Year 2010 Principal Investigators; Centers for Disease Control and Prevention (CDC). (2014). Prevalence of autism spectrum disorder among children aged 8 years—autism and developmental disabilities monitoring network, 11 sites, United States, 2010. *MMWR Surveillance Summaries* 63(2): 1–21.
- Gabrielsen, T. P., Farley, M., Speer, L., Villalobos, M., Baker, C. N., & Miller, J. (2015). Identifying autism in a brief observation. *Pediatrics*, 135(2), e330–338.
- Gadow, K. D., DeVincent, C. J., & Pomeroy, J. (2006). ADHD symptom subtypes in children with pervasive developmental disorder. *Journal of Autism and Developmental Disorders*, 36(2), 271–283.
- Jensen, V. K., Larrieu, J. A., & Mack, K. K. (1997). Differential diagnosis between attention-deficit/hyperactivity disorder and pervasive developmental disorder-not otherwise specified. *Clinical Pediatrics (Phila)*, 36(10), 555–561.
- Johnson, C. P., & Myers, S. M. & D. American Academy of Pediatrics Council on Children With (2007). Identification and evaluation of children with autism spectrum disorders. *Pediatrics* 120(5): 1183–1215.
- Kairys, S. W., & Petrova, A. (2016). Role of participation of pediatricians in the “Activated Autism Practice” program in practicing children with autism spectrum disorders at the primary care setting. *Global Pediatric Health* 3:2333794x16663544.
- Lai, M. C., Lombardo, M. V., & Baron-Cohen, S. (2013). Autism. *Lancet*, 383, 896–910.
- Law, E. C., Sideridis, G. D., Prock, L. A., & Sheridan, M. A. (2014). Attention-deficit/hyperactivity disorder in young children: predictors of diagnostic stability. *Pediatrics*, 133(4), 659–667.
- Lee, D. O., & Ousley, O. Y. (2006). Attention-deficit hyperactivity disorder symptoms in a clinic sample of children and adolescents with pervasive developmental disorders. *Journal of Child and Adolescent Psychopharmacology*, 16(6), 737–746.
- Li, C.-T., Bai, Y.-M., Huang, Y.-L., Chen, Y.-S., Chen, T.-J., Cheng, J.-Y., & Su, T.-P. (2012). Association between antidepressant resistance in unipolar depression and subsequent bipolar disorder: Cohort study. *The British Journal of Psychiatry*, 200(1), 45–51.
- Liu, C.-Y., Hung, Y., Chuang, Y., Chen, Y., Weng, W., Liu, J., & Liang, K. (2006). Incorporating development stratification of Taiwan townships into sampling design of large scale health interview survey. *Journal of Health Management*, 4(1), 1–22.
- Mandell, D. S., Ittenbach, R. F., Levy, S. E., & Pinto-Martin, J. A. (2007). Disparities in diagnoses received prior to a diagnosis of autism spectrum disorder. *Journal of Autism and Developmental Disorders*, 37(9), 1795–1802.
- Miodovnik, A., Harstad, E., Sideridis, G., & Huntington, N. (2015). Timing of the diagnosis of attention-deficit/hyperactivity disorder and autism spectrum disorder. *Pediatrics*, 136(4), e830–837.
- Nijmeijer, J. S., Arias-Vasquez, A., Rommelse, N. N., Altmink, M. E., Anney, R. J., Asherson, P., Banaschewski, T., Buschgens, C. J., Fliers, E. A., Gill, M., Minderaa, R. B., Poustka, L., Sergeant, J. A., Buitelaar, J. K., Franke, B., Ebstein, R. P., Miranda, A., Mulas, F., Oades, R. D., Roeyers, H., Rothenberger, A., Sonuga-Barke, E. J., Steinhausen, H. C., Faraone, S. V., Hartman, C. A., & Hoekstra, P. J. (2010). Identifying loci for the overlap between attention-deficit/hyperactivity disorder and autism spectrum disorder using a genome-wide QTL linkage approach. *Journal of the American Academy of Child and Adolescent Psychiatry*, 49(7), 675–685.
- Oslejskova, H., Kontrova, I., Foralova, R., Dusek, L., & Nemethova, D. (2007). The course of diagnosis in autistic patients: the delay between recognition of the first symptoms by parents and correct diagnosis. *Neuro Endocrinology Letters*, 28(6), 895–900.

- Rappley, M. D. (2005). Clinical practice. Attention deficit-hyperactivity disorder. *The New England Journal of Medicine*, 352(2), 165–173.
- Rommelse, N. N., Franke, B., Geurts, H. M., Hartman, C. A., & Buitelaar, J. K. (2010). “Shared heritability of attention-deficit/hyperactivity disorder and autism spectrum disorder. *European Child & Adolescent Psychiatry*, 19(3), 281–295.
- Ronald, A., Simonoff, E., Kuntsi, J., Asherson, P., & Plomin, R. (2008). Evidence for overlapping genetic influences on autistic and ADHD behaviours in a community twin sample. *Journal of Child Psychology and Psychiatry*, 49(5), 535–542.
- Shen, C.-C., Tsai, S.-J., Perng, C.-L., Kuo, B. I.-T., & Yang, A. C. (2013). Risk of Parkinson disease after depression A nationwide population-based study. *Neurology*, 81(17), 1538–1544.
- Shephard, E., Milosavljevic, B., Pasco, G., Jones, E. J., Gliga, T., Happe, F., Johnson, M. H., Charman, T., & Team, B. (2017). Mid-childhood outcomes of infant siblings at familial high-risk of autism spectrum disorder. *Autism Research*, 10(3), 546–557.
- Visser, S. N., Zablotsky, B., Holbrook, J. R., Danielson, M. L., & Bitsko, R. H. (2015). Diagnostic experiences of children with attention-deficit/hyperactivity disorder. *National Health Statistics Reports* 81, 1–7.
- Volkow, N. D., & Swanson, J. M. (2013). Clinical practice: Adult attention deficit-hyperactivity disorder. *The New England Journal of Medicine*, 369(20), 1935–1944.
- Yee, M. M., & Millichap, J. G. (2015). Relationship between age at diagnosis of ADHD and ASD. *Pediatric Neurology Briefs*, 29(10), 78.



## PAPER

[View Article Online](#)  
[View Journal](#) | [View Issue](#)
Cite this: *Food Funct.*, 2021, **12**, 3455

# Apoptotic mechanisms of gastric cancer cells induced by isolated erinacine S through epigenetic histone H3 methylation of FasL and TRAIL†

Shui-Yi Tung,<sup>a,b</sup> Ko-Chao Lee,<sup>c,d</sup> Kam-Fai Lee,<sup>e</sup> Ya-Ling Yang,<sup>f</sup> Wen-Shih Huang,<sup>b,g</sup> Li-Ya Lee,<sup>h</sup> Wan-Ping Chen,<sup>h</sup> Chin-Chu Chen,<sup>i</sup> Chih-Chuan Teng,<sup>i,j</sup> Chien-Heng Shen,<sup>a</sup> Meng-Chiao Hsieh,<sup>g,k</sup> Cheng-Yi Huang,<sup>g</sup> Jiunn-Ming Sheen<sup>l</sup> and Hsing-Chun Kuo<sup>i,m,n</sup>

Erinacine S, the new bioactive diterpenoid compound isolated from the ethanol extract of the mycelia of *Hericium erinaceus*, displays great health-promoting properties. However, the effects of erinacine S on inductive apoptosis in cancer cells such as gastric cancer and its molecular mechanisms remain unclear. Our results demonstrated that erinacine S treatment significantly induces cell apoptosis with increased ROS production in gastric cancer cells, but not in normal cells. Significantly, erinacine S also showed its inhibitory effects on tumor growth in an *in vivo* xenograft mouse model. Furthermore, immunohistochemical analyses revealed that erinacine S treatment significantly increases the FasL and TRAIL protein, whereas it decreases the levels of PCNA and cyclin D1 in the gastric cancer xenograft mice. Consistently, in AGS cells, erinacine S treatment not only triggers the activation of extrinsic apoptosis pathways (TRAIL, Fas-L and caspase-8, -9, -3), but it also suppresses the expression of the anti-apoptotic molecules Bcl-2 and Bcl-XL in a time-dependent manner. In addition, erinacine S also causes cell cycle G1 arrest by the inactivation of CDKs/cyclins. Moreover, our data revealed that activation of the ROS-derived and AKT/FAK/PAK1 pathways is involved in the erinacine S-mediated transcriptional activation of Fas-L and TRAIL through H3K4 trimethylation on their promoters. Together, this study sheds light on the anticancer effects of erinacine S on gastric cancer and its molecular mechanism *in vitro* and *in vivo*.

Received 28th November 2020,

Accepted 22nd February 2021

DOI: 10.1039/d0fo03089a

[rsc.li/food-function](http://rsc.li/food-function)

## 1. Introduction

Stomach cancer, also known as gastric cancer, is the fifth leading type of cancer and the third leading cause of death from cancer.<sup>1</sup> This type of cancer originally develops from the stomach lining and may spread from the stomach to other

parts of the body, particularly the liver, lungs, bones, lining of the abdomen and the lymph nodes.<sup>2</sup> Infection, smoking, dietary aspects and obesity are the risk factors for the development of gastric cancer.<sup>3</sup> Surgery, chemotherapy, and/or radiation therapy are mainly considered for the treatment of gastric cancer.<sup>4</sup> Although death rates for gastric cancer have

<sup>a</sup>Department of Hepato-Gastroenterology, Chang Gung Memorial Hospital, Chiayi, Taiwan. E-mail: ma1898@yahoo.com, gi2216@adm.cgmh.org.tw

<sup>b</sup>Chang Gung University College of Medicine, Taoyuan, Taiwan. E-mail: wshuang77@gmail.com

<sup>c</sup>Division of Colorectal Surgery, Department of Surgery, Chang Gung Memorial Hospital, Kaohsiung Medical Center, Chang Gung University College of Medicine, Kaohsiung, Taiwan. E-mail: kmch4329@gmail.com

<sup>d</sup>Department of Information Management & College of Liberal Education, Shu-Ten University, Kaohsiung, Taiwan

<sup>e</sup>Department of Pathology, Chang Gung Memorial Hospital, Chiayi, Taiwan. E-mail: lkf2002@cgmh.org.tw

<sup>f</sup>Department of Anesthesiology, Kaohsiung Chang Gung Memorial Hospital and Chang Gung University College of Medicine, Kaohsiung, Taiwan. E-mail: yaling453@yahoo.com.tw

<sup>g</sup>Division of Colon and Rectal Surgery, Department of Surgery, Chang Gung Memorial Hospital, Chiayi, Taiwan. E-mail: mr8872@gmail.com

<sup>h</sup>Grape King Biotechnology Inc. (Grape King Bio Ltd), Zhong-Li, Taiwan.

E-mail: ly.lee@grapeking.com.tw, wp.chen@grapeking.com.tw, gkbioeng@grapeking.com.tw

<sup>i</sup>Department of Nursing, Division of Basic Medical Sciences, Chang Gung University of Science and Technology, Chiayi, Taiwan. E-mail: guscsi@gmail.com; Fax: +886-5-3628866; Tel: +886-5-3628800

<sup>j</sup>Research Fellow, Chang Gung Memorial Hospital, Chiayi, Taiwan. E-mail: ccteng@gw.cgust.edu.tw

<sup>k</sup>Graduate Institute of Clinical Medical Sciences, College of Medicine, Chang Gung University, Taiwan

<sup>l</sup>Department of Pediatrics, Chiayi Chang Gung Memorial Hospital and Chang Gung University College of Medicine, Chiayi, Taiwan. E-mail: ray.sheen@gmail.com

<sup>m</sup>Research Center for Food and Cosmetic Safety, College of Human Ecology, Chang Gung University of Science and Technology, Taoyuan, Taiwan. E-mail: guscsi@gmail.com

<sup>n</sup>Chronic Diseases and Health Promotion Research Center, Chang Gung University of Science and Technology, Chiayi, Taiwan

† Electronic supplementary information (ESI) available. See DOI: 10.1039/d0fo03089a

been decreasing in many areas of the world since 1930,<sup>5</sup> the disease newly occurs in 1.03 million people annually and caused 783 000 deaths in 2018. Interestingly, a meta-analysis study demonstrated that a diet high in fruits, mushrooms, garlic, soybeans, and green onions was associated with a lower risk of stomach cancer.<sup>6</sup> In addition, some studies have indicated that chemopreventive compounds in dietary foods decrease the risk of stomach cancer.<sup>7</sup> Thus, to deal with this situation, finding novel diet compounds for the prevention or treatment of gastric cancer is a promising therapeutic strategy.

*Hericium erinaceus* (Lion's mane or Yamabushitake), an edible mushroom with medicinal properties, contains a variety of structurally different components with valuable biological properties<sup>8</sup> and is used in traditional folk medicine, medicinal cuisine and as a health-promoting compound in Japan and China without harmful effects.<sup>9</sup> Erinacines A–I and hericenone C–H components are identified as a series of diterpenoid derivatives in the extracts of mycelium and the fruit bodies of *H. erinaceus*.<sup>10</sup> The biological properties of *H. erinaceus* include antioxidant activity,<sup>11</sup> hypolipidemic activity,<sup>12</sup> hemagglutinating activity,<sup>13</sup> antimicrobial activity,<sup>14</sup> antiaging activity,<sup>15</sup> and immune modulation and anticancer activities.<sup>16–18</sup> Functional studies of erinacine S component (Fig. 1), which previously has been lately collected and purified by ethanol extraction and HPLC analysis techniques from *H. erinaceus* (Fig. 1) mainly focus on its neuroprotective effects in the animal model of Alzheimer's disease.<sup>19</sup> In this study, we aim to elucidate the inhibitory role of erinacine S in gastric cancer cell growth and its mechanism.

Cell apoptosis is an important physiological process of cell death without an inflammatory response.<sup>20</sup> The dysregulation

of cell apoptosis further causes the initiation, proliferation (uncontrolled cell division), growth and aggressiveness of cancer.<sup>21,22</sup> Therefore, inductive apoptosis of cancer cells is considered as an effective way to kill cancer cells. Classically, the intrinsic and extrinsic signaling pathways both contribute to the process of cell apoptosis. Under intrinsic apoptotic stimuli, the release of cytochrome c from the mitochondria further sequentially increases the activity of caspase-9 and caspase-3, causing cell apoptosis.<sup>23</sup> However, the binding of the ligands Fas, Fas-L, and TNFR1 to their corresponding receptors also activates caspase-8 and caspase-3, the extrinsic pathway for apoptosis.<sup>24</sup> Numerous studies have demonstrated that intracellular reactive oxygen species (ROS), the second messengers sensitive to oxidative damage, induce cell apoptosis *via* intrinsic or extrinsic apoptotic stimuli.<sup>25</sup> Most recently, epigenetic modification of histone H3 such as methylation with ROS or protein kinase has been shown to be a critical event for cell apoptosis *via* the upregulation of death-receptor-related protein.<sup>26</sup> Our data demonstrated that a novel biological property of erinacine S induces cell apoptosis of gastric cancer *via* the ROS and AKT/FAK/PAK1 pathway-mediated epigenetic histone H3 methylation of FasL and TRAIL.

## 2. Materials and methods

### 2.1. *Hericium erinaceus* extracts and the analysis of erinacine S

*H. erinaceus* (BCRC 35669) was purchased from the Bioresources Collection and Research Center (BCRC) of the Food Industry Research and Development Institute (Hsinchu, Taiwan). *H. erinaceus* was transferred from an agar slant into a potato dextrose agar plate, and was then maintained at 26 °C

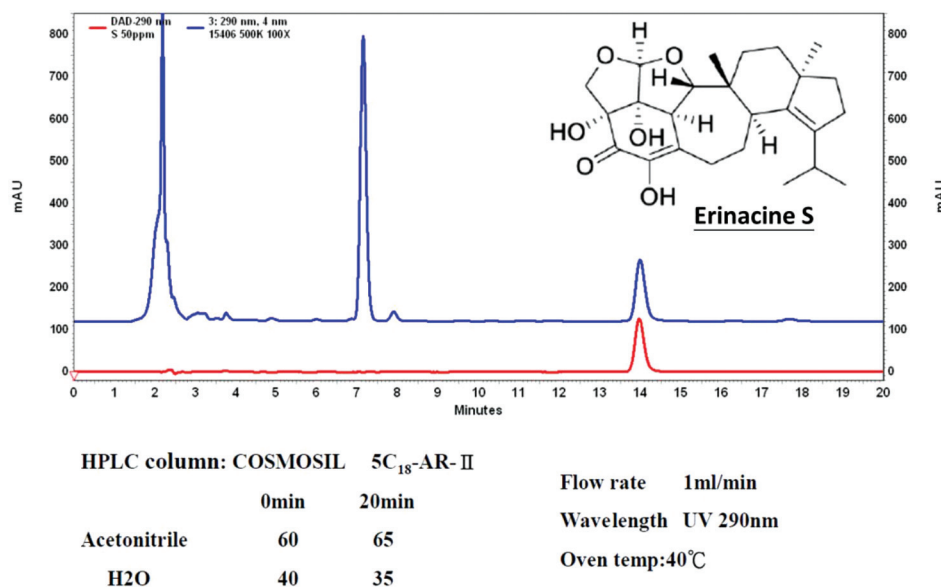


**Fig. 1** HPLC analysis of the ethanol *H. erinaceus* mycelium extract. For the conditions, see the Materials and methods section. The retention time peak at 14 min was demonstrated by a bioreactor (UV detection at 290 nm).

for 15 d, as previously described.<sup>19</sup> Following the fresh mycelium extraction of *H. erinaceus* by ethanol, the fermentation process of the *H. erinaceus* mycelia was performed. Then, these mycelia were cultivated, harvested, lyophilized, ground to powder, and kept in a desiccator at room temperature. The mycelia extract was further concentrated and fractionated by a solvent partition between ethyl acetate and water. Ethanol extract of erinacine S from *H. erinaceus* mycelia was prepared according to a published paper.<sup>19</sup> Following proximate composition analysis with silica gel column chromatography, HPLC analysis of erinacine S was executed according to a previous study with minor modifications. Using an analytical COSMOSIL 5C18-AR-II column (250 × 4.6 mm; particle size 5 µm; Nacalai USA, Inc., Kyoto, Japan), the retention time of erinacine S was approximately 14.1 min at a flow rate of 1.0 mL min<sup>-1</sup> with a scanning UV wavelength at 290 nm. The ~1 g kg<sup>-1</sup> yield rate of erinacine S in *H. erinaceus* with ethanol extraction was confirmed and quantified using HPLC. Fig. 1 shows the chemical compound of erinacine S (PubChem CID: 127047879).

## 2.2. Cell culture

All culture materials were purchased from Gibco (Grand Island, NY, USA). The human gastric cancer cell line AGS (CRL-1739) was purchased from the American Type Culture Collection (ATCC). The gastric carcinoma cell line TSGH 9201 cells was purchased from the Bioresources Collection and Research Center (BCRC) of the Food Industry Research and Development Institute (Hsinchu, Taiwan). The cells were cultured in Dulbecco's modified Eagle's medium (DMEM) supplemented with 10% fetal calf serum (Gibco), non-essential amino acids, 1 mM sodium pyruvate and 1% antibiotics (100 units per mL penicillin and 100 µg mL<sup>-1</sup> streptomycin). All experiments were performed in plastic tissue culture flasks, dishes or in microplates (Nunc, Naperville, Denmark). Incubation was carried out at 37 °C under a humidified atmosphere of 5% CO<sub>2</sub> and 95% oxygen. Passage number 1 of normal human colonic epithelial cells (HCoEpiC) was purchased from ScienCell Research Laboratories (Carlsbad, CA) and the cells were grown. Both cell types were maintained at 37 °C in a humidified 5% CO<sub>2</sub> incubator.<sup>27</sup>

## 2.3. Cell growth and cell cycle distribution analysis

The MTT quantitative colorimetric assay is a method for cell viability determination, as previously described. The cells were incubated with MTT (0.5 mg mL<sup>-1</sup>) for 4 h. After solubilization of the MTT-treated cells with isopropanol, the production of formazan was spectrophotometrically measured at 563 nm, which was directly proportional to the viable cells.<sup>28</sup>

Changes in cell morphology characteristic of apoptosis were examined with fluorescence microscopy of DAPI-stained cells. The monolayer of cells was washed in PBS and fixed with 4% paraformaldehyde for 30 min at room temperature. The fixed cells were incubated with 4,6-diamidino-2-phenylindole (DAPI) for 30 min, and, then, washed with PBS three times. The apoptotic nuclei (intensely stained, fragmented nuclei and

condensed chromatin) were examined and counted from 10 fields (200× magnification) of each sample. The results from the statistical analysis are the means of cells and were calculated per microscope field per group. Data are expressed as the mean ± SD of independent experiments.

The AGS cells were treated with either 0.1% DMSO (as control) or erinacine S for 24 h and collected, and only the proportion of surviving cells was measured by the cell cycle distribution analysis. Cell-cycle distribution was analyzed using flow cytometry. The cells stained with propidium iodide were analyzed with FACScalibur™ (Becton Dickinson), and the data were analyzed using a ModFit cell cycle analysis program.

## 2.4. Measurement of the apoptosis assay and reactive oxygen species

The morphological characteristics of the cells stained with 4',6-diamidino-2-phenylindole (DAPI) were observed under a fluorescence microscope. First, the cells were fixed with 4% paraformaldehyde for 30 min at room temperature and were then permeabilized in 0.2% Triton X-100 in phosphate-buffered saline 3 times for 15 min. After PBS washing, the cells were incubated with 1 µg mL<sup>-1</sup> of DAPI for 30 min. Under 200× magnification using a fluorescent microscope with a 340/380 nm excitation filter, the percentage of the apoptotic nuclei in the field of 200–300 cells was observed and scored according to a previous report.<sup>29</sup>

Co-staining with annexin V-FITC and propidium iodide (Biosource International, USA) was used to measure cell apoptosis, as previously described.<sup>16,17</sup> After staining, the cells were subjected to FACS analysis (Attune NxT Flow Cytometer, Thermo Fisher Scientific Inc.), and the number of apoptotic cells (V+/PI-) was quantified and analyzed using software. The data of fluorescence intensity are represented as a percentage of the untreated control group with three independent experiments.

The intracellular accumulation of ROS (O<sub>2</sub><sup>-</sup>) was determined using the fluorescent probes of H<sub>2</sub>DCFDA (2,7-dichlorodihydrofluorescein diacetate) and the cells were washed prior to FACS analysis and Cell Quest software was used (Becton Dickinson, Franklin Lakes, NJ, USA). The results are presented as a percentage of fluorescence intensity compared with the control sample. Data were analysed with CellQuest and WinMDI software. The apoptotic cells (V+/PI-) were measured by the fluorescence-activated cell sorter analysis in a FACS analyser (Becton Dickinson). The data represented three independent experiments.

## 2.5. Protein extraction and immunoblot analyses

The cells were lysed with a buffer comprising 1% NP-40, 0.5% sodium deoxycholate, 0.1% sodium dodecyl sulfate (SDS), and a protease-inhibitor mixture (phenylmethylsulfonyl fluoride, aprotinin, and sodium orthovanadate); the protein lysates were obtained, as previously described.<sup>30</sup> Following SDS-polyacrylamide gel electrophoresis (PAGE) (12% running, 4% stacking) and it was transferred to the PVDF member, protein expression was detected by using specific antibodies in the Western-

light chemiluminescent detection system (Bio-Rad, Hercules, CA, USA).

## 2.6. Animal study

The animal care and general protocols for animal experiments used in this study were approved by the Institutional Animal Care and Use Committee of Chang Gung Memorial Hospital, Chiayi, Animal Ethics Research Board (IACUC approval: 2017121409). Male BALB/c-nu nude mice, 4–6 weeks old (18–20 g), were purchased from the National Laboratory Animal Center in Taiwan and maintained under specific pathogen-free (SPF) conditions with sterilized food and water. The AGS cells ( $10^6$  cells per 0.2 ml) were injected subcutaneously into the flanks of 4–6-week-old male athymic BALB/c-nu mice. After tumor inoculation, the mice were randomly divided into four groups ( $n = 8$  per group). The control group animals were treated daily with 0.1 mL DMSO (0.25%; i.p.); the test animals were treated with erinacine S at different concentrations of 1 and 5 mg per day, i.p. for 5 d. Tumor volumes were monitored and measured every 4 d using calipers. The calculation of tumor volumes was based on the following formula:  $\text{length} \times \text{width}^2 \times \pi/6$ . The body weights of the mice were measured every week to monitor drug toxicity. After 18 d of drug treatment, the mice were euthanized, and their tumors and organs, including the liver, lungs, and kidneys, were collected for further analysis.<sup>16</sup>

## 2.7. Immunoprecipitation assay

The effect of erinacine S on the interaction of CDK2/cyclin E and CDK4/cyclin D1 was analyzed with the immunoprecipitation assay. Briefly, the AGS cells were exposed and then lysed with lysis buffer. The lysates were immunoprecipitated using monoclonal anti-CDK2 or anti-CDK4 and protein A/G-agarose. The eluates from the beads were analyzed with immunoblotting using specific antibodies against cyclin E or cyclin D1 or the control antibody (normal rabbit IgG), as a negative control. Heavy chain IgG bands show that an equivalent amount of each antibody was used.

## 2.8. Histochemistry and immunohistochemistry analysis

The tumor tissue sections were fixed in 4% formaldehyde and were then embedded in paraffin blocks. After staining with hematoxylin and eosin, these tissue slides were mounted for microscopic examination. For the immunohistochemical analysis, 5- $\mu\text{m}$ -thick sections of each subcutaneous tumor specimen were incubated with monoclonal anti-p21 and p70S6K antibodies (Santa Cruz, CA, USA) overnight at 4 °C after blocking, and were then incubated with 1:100 diluted biotinylated horse anti-mouse IgG for 1 h. After PBS washing, the tissue sections were reacted with a 1:100 diluted avidin–biotin peroxidase mixture (Vectastain Universal Elite ABC Kit) for 30 min. Following a thorough PBS wash, these slides were counterstained with hematoxylin, dehydrated, and mounted for microscopic examination. The digital images were captured using a digital camera (Canon A640), and the positive area and optical density (OD) of the immunoreactive cells

(brown) were analyzed in three randomly selected microscopic fields (400 $\times$  magnification) for each slide. In accordance with the previous reports, the IHC index was defined as having an average integral optical density (AIOD; positive area  $\times$  OD/total area).<sup>31</sup>

## 2.9. Chromatin immunoprecipitation (ChIP) analysis

The AGS cells were incubated with 1% formaldehyde at room temperature to generate a DNA–protein cross-link, and then, 10 min later, 125 mM glycine was added to the cells for 5 min. The cells were scraped into a sodium dodecyl sulfate (SDS) lysis buffer (50 mM Tris-HCl [pH 8.1], 1% SDS, and 10 mM EDTA), and rotated with specific antibodies against the histone H3K4me3 and 2  $\mu\text{l}$  of non-immunized rabbit IgG, as a ‘no antibody’ negative control, overnight at 4 °C in the presence of protease inhibitors (1  $\mu\text{g ml}^{-1}$  leupeptin, aprotinin and pepstatin A and 1 mM phenylmethylsulfonyl fluoride [PMSF]). After elution with an elution buffer (50 mM Tris-Cl [pH 7.5], 1 mM EDTA, 1% SDS), the cross-linking immunoprecipitated complexes were reversed at the temperature of 65 °C incubation for at least 2 h. DNA fragments were purified using a ChIP DNA Clean & Concentrator Kit (Zymo), and a quantitative PCR analysis was then performed to amplify the promoter region of the TNFR1 and TRAIL genes, by using specific primers (Table 1) under the following conditions: 40 cycles of denaturation at 94 °C, primer annealing at 60 °C, and extension at 72 °C. Disassociation curves were generated after each PCR to ensure that a single PCR product of the amplified appropriate length ran in electrophoresis. The test samples may also be expressed as a percentage of a reference gene that is calculated as the percentage of input for each ChIP: % Input =  $2(-\Delta\text{Ct} [\text{normalized ChIP}])$ . Normalize the positive locus  $\Delta\text{Ct}$  values to negative locus ( $\Delta\Delta\text{Ct}$ ) by subtracting the  $\Delta\text{Ct}$  value obtained for the positive locus from the  $\Delta\text{Ct}$  value for negative locus: ( $\Delta\Delta\text{Ct} = \Delta\text{Ct}_{\text{positive}} - \Delta\text{Ct}_{\text{negative}}$ ). Calculate the fold enrichment of the positive locus sequence in ChIP DNA over the negative locus: Fold enrichment =  $2\Delta\Delta\text{Ct}$ . In addition, the mean CT  $\pm$  SE was calculated from the individual CT values, which were obtained from triplicate determinations at each stage. The normalized mean CT was estimated as  $\Delta\text{CT}$  by subtracting the mean CT of the input from that of the individual region among the untreated control group and the drug treatment groups. Specific genes was calculated by the  $\Delta\Delta\text{Ct}$  method:  $2^{(-\Delta\Delta\text{Ct}[\text{treatment/control}])}$ , where  $\Delta\Delta\text{Ct}[\text{treatment/control}] = (\Delta\text{Ct}[\text{treatment}]) - (\Delta\text{Ct}[\text{control}])$ . The results were statistically analyzed using Student's paired  $t$  test. A  $P$  value of  $<0.05$  was considered to be statistically significant.<sup>18,32</sup>

**Table 1** The specific primers

|       |  |
|-------|--|
| FasL  | 5'-GGGGGCGAGTGTTCATCTTA-3'<br>5'-TGGAAAGAATCCCAAGTGC-3'        |
| TRAIL | 5'-TGCATGGATCCTGA GGGCAAGG-3'<br>5'-TTGAACCTGCAACTGTCCCTCCC-3' |



### 2.10. Statistical analysis

All data, expressed as the mean  $\pm$  standard deviation, were compared between the groups, using Student's *t*-test, or one-way Analysis of Variance (ANOVA), with Tukey's multiple comparison test. The statistically significant difference between the values was set at  $P < 0.05$ .

## 3. Results

### 3.1. Erinacine S induces cell apoptosis of human gastric cancer cells

The method for extraction and purification of erinacine S from the fresh mycelium of *H. erinaceus* by respective ethanol extraction and HPLC quantification was the same as that used in our previous study but with minor modifications.<sup>19</sup> Erinacine S was separated by an approximate 14.1 retention time, a flow rate of 1.0 mL min<sup>-1</sup> and a scanning UV wavelength (Fig. 1). We wanted to determine whether erinacine S treatment had cytotoxic effects on gastric cancer cells. MTT assays revealed that erinacine S treatment at 5 and 10  $\mu$ M concentrations for 24 h significantly and dose-dependently decreased the cell viability of AGS and TSGH-9201 cells compared to the untreated cells (Fig. 2A). In contrast, erinacine S had no effect on the viability of normal epithelial HCoEpiC cells (Fig. 2A). Furthermore, the erinacine S treatment at concentrations of 1 and 10 mM induced the early apoptotic chromatin condensation that was shown by DAPI staining in AGS (Fig. 2B) and TSGH-9201 cells (Fig. 2C).

Moreover, flow cytometry analysis for annexin-V and PI also revealed that erinacine S treatment increased the percentage of annexin V-positive cells, a characteristic feature of cell apoptosis, in all AGS cells in a dose-dependent manner (Fig. 3A). However, AGS cells treated with erinacine S dose-dependently had a higher portion of G1 stage in the cell cycle (G1 arrest) (Fig. 3B) and increased intracellular ROS (Fig. 3C) compared to the cells without erinacine S treatment. Together, our data showed a novel anticancer effect of erinacine S on human gastric cancer cells *via* the intracellular ROS-mediated G1 arrest and cell apoptosis.

### 3.2. *In vivo* growth inhibition of gastric cancer cell xenograft with erinacine S

To further confirm the *in vitro* findings on the anticancer effect of erinacine S, an *in vivo* nude mouse model of a gastric cancer cell xenograft was used. Time-course studies showed that erinacine S treatment significantly decreased the tumor volume (tumor size and weight) of the AGS xenograft in nude mice in a dose-dependent manner at 18 d (Fig. 4A), suggesting an inhibitory effect of erinacine S on gastric cancer cell growth. Furthermore, we measured the protein level of PCNA (a marker for cell proliferation), cyclin D1 (a key regulator for the cell cycle), FasL (a marker for extrinsic cell apoptosis) and TRAIL (a marker for extrinsic cell apoptosis) in these animals. Our results showed that erinacine S treatment reduced the expression of PCNA and cyclin D1, whereas it increased the

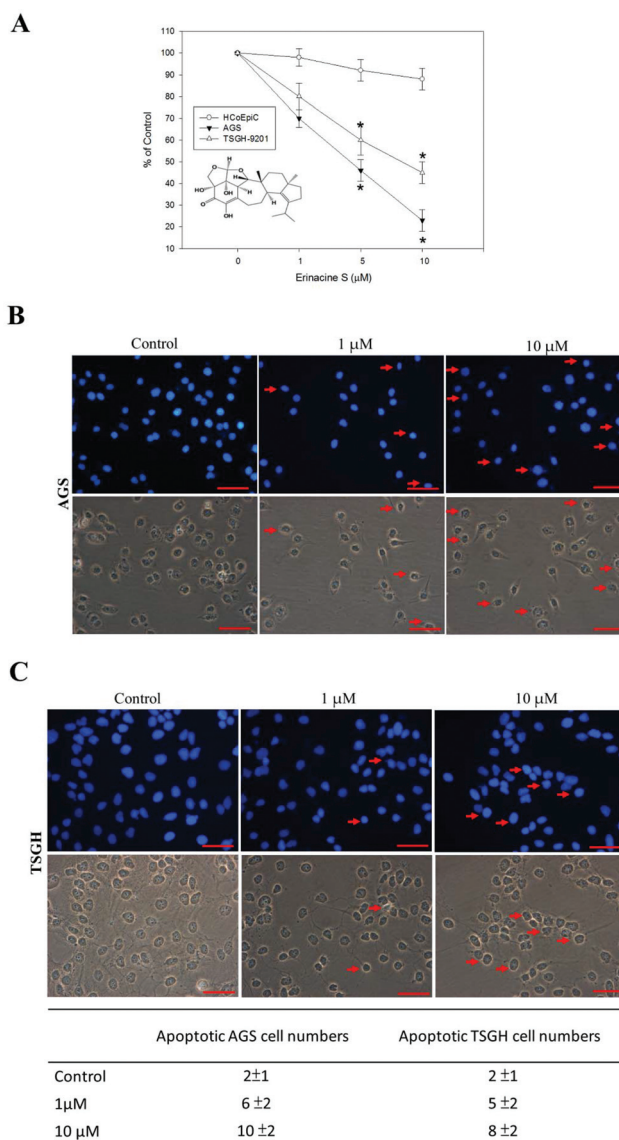
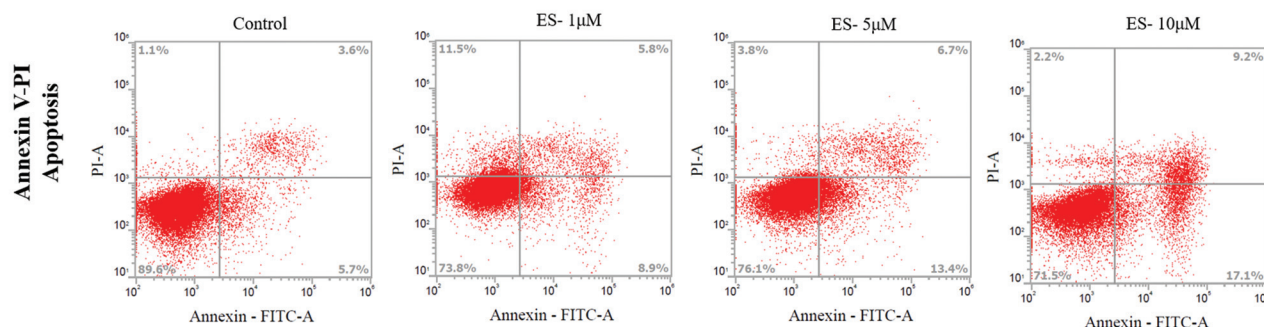
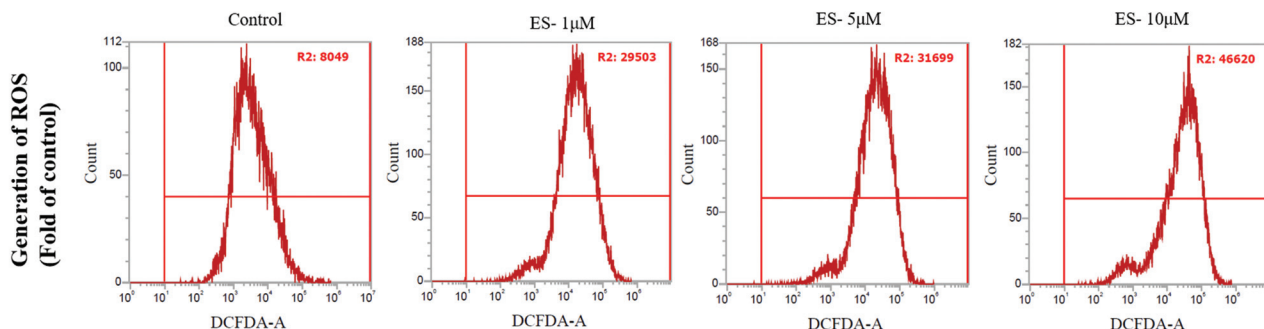


**Fig. 2** Effects of erinacine S on cell viability and morphological characteristics of cell death in human gastric cancer. (A) Human HCoEpiC, AGS, and TSGH-9201 cells were treated with either 0.1% DMSO (as the control) or erinacine S (1–10  $\mu$ M) for 24 h and the proportion of surviving cells in these treated cells was measured with an MTT assay. The data are presented as the mean  $\pm$  SD of three independent experiments. & indicates the means that are significantly different when compared to the control group (0.2% DMSO) of HCoEpiC with  $P < 0.05$ . \* indicates the means that are significantly different when compared to the control group (0.2% DMSO) of AGS with  $P < 0.05$ . # indicates the means that are significantly different when compared to the control group (0.2% DMSO) of TSGH-9201 with  $P < 0.05$ . (B and C) The morphological alteration of the nuclei of cell death was measured with DAPI staining. Representative DAPI immunofluorescence (IF) images of the AGS and TSGH-9201 cells were treated with vehicle or erinacine S for 24 h. Quantitation of apoptotic cells was done using DAPI staining. The cells were counted from 10 fields of each sample. The results from statistical analysis are the means of cells and were calculated per microscope field per group. The red arrow indicates apoptotic cells. The data are presented as the mean of three repeats from one independent experiment. The quantitative data are presented as the mean  $\pm$  SD of three independent experiments in triplicate technical repeats. # $P < 0.05$ , as compared to the control group.

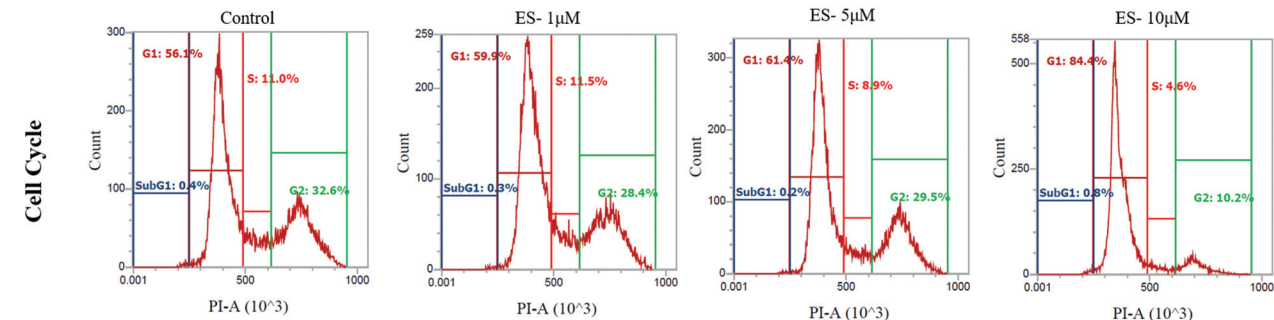
A



B



C



|          | Annexin V-PI<br>Apoptosis (%) | ROS<br>(Fold of control) | G (%)  | S (%)  | G2 (%) |
|----------|-------------------------------|--------------------------|--------|--------|--------|
| Control  | 8 ± 2                         | 1                        | 56 ± 2 | 11 ± 2 | 33 ± 2 |
| ES- 1µM  | 13 ± 2                        | 3 ± 1                    | 60 ± 3 | 12 ± 3 | 28 ± 3 |
| ES- 5µM  | 19 ± 2                        | 4 ± 1                    | 63 ± 2 | 8 ± 1  | 29 ± 2 |
| ES- 10µM | 26 ± 2                        | 6 ± 1                    | 85 ± 1 | 5 ± 1  | 10 ± 2 |

**Fig. 3** Effects of erinacine S on inductive apoptosis, cell cycle arrest and ROS production in AGS cells. (A) After 24 h of erinacine S treatment (1, 5 and 10 µM), the AGS cells were co-stained with FITC-conjugated annexin-V and PI and then subjected to flow cytometry analysis as described in the "Materials and methods" section. The percentages presented in the left quadrant (annexin-positive) of each frame depicted the population of apoptotic cells. \* $P < 0.01$ , compared with the control group (0.2% DMSO). (B) Treated AGS cells with or without erinacine S (1, 5 and 10 µM) for 24 h were fixed and stained with propidium iodide, and the DNA content (G1, S, G2/M) in these cells was analyzed with flow cytometry (FACS). The percentage of the cells in each phase (G1, S, and G2/M) of the cell cycle was calculated and shown. Data are presented based on three independent experiments. (C) AGS cells were treated with erinacine S for 24 h, and FACS analysis with H<sub>2</sub>DCFDA staining was used to measure the intracellular ROS in these cells as described in the "Materials and methods" section. Representative histograms showed typical H<sub>2</sub>DCFDA profiles of ROS production. Data are expressed as the fold of the control group.

levels of TRAIL and FasL (Fig. 4B and C). In addition, a TUNEL assay also exhibited that erinacine S treatment increased the cell apoptosis of the AGS xenograft in nude mice (Fig. 4B and C). Consistent with the *in vitro* data, erinacine S treatment displayed growth inhibition of the gastric cancer cell xenograft.

### 3.3. Activation of the extrinsic cell apoptosis pathway in AGS cells with erinacine S

To further determine the apoptotic mechanism of gastric cancer cells by erinacine S, the cell-death-related proteins including Bcl-2, Bcl-XL, cleaved caspase 8, cleaved caspase 9, cleaved caspase 3, PARP, TRAIL and FasL were measured in

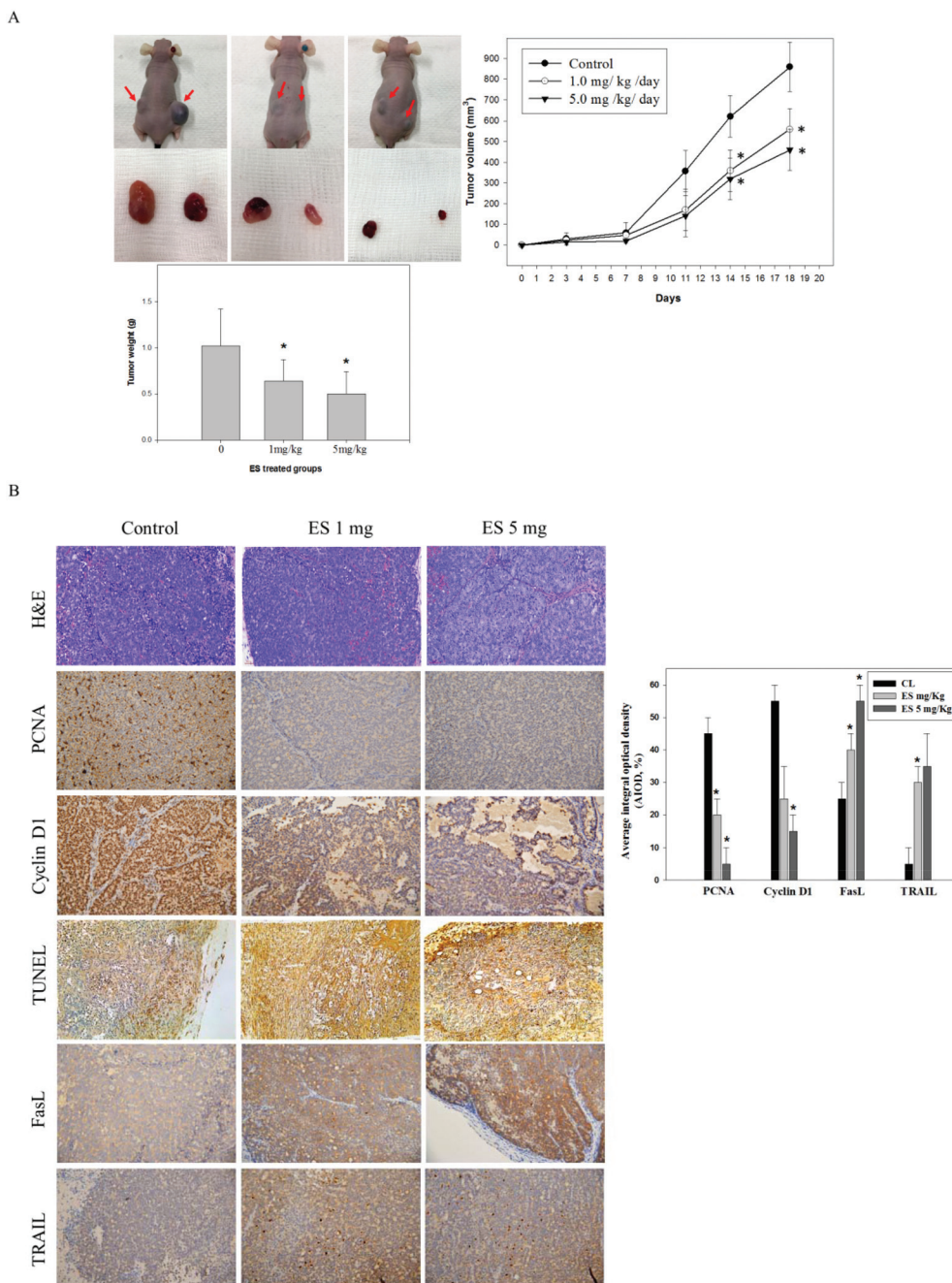


**Fig. 4** Growth inhibition of the gastric cancer cell xenograft by erinacine S. (A) Nude mice were implanted subcutaneously with AGS cells into their flanks on day 0, and were then treated with or without (as a control) erinacine S as described in the "Materials and methods" section. The time-course effect of erinacine S on the growth of the AGS xenograft was evaluated by weighing the tumor volume every 4 d. The data pertaining to the isolated tumors are presented as tumor sizes and tumor weights. (B) Immunohistochemical analysis of these tumors from each treatment group was conducted and evaluated in multiple tumor fields. Representative IHC (for PCNA, cyclin D1, FasL and TRAIL proteins) and H&E staining images in each treatment group are presented. Quantitative immunohistochemical proteins PCNA, cyclin D1, FasL and TRAIL were evaluated with average integrated optical density (AIOD). The positive stained area was evaluated from three randomly selected observation fields of each tissue section. Data are expressed as mean  $\pm$  S.D. ( $n = 6$  per group). \* $P < 0.05$ , compared with the control group, magnification  $\times 400$ .

erinacine S-treated AGS cells by western blotting. Our results showed that erinacine S treatment increased the active form of caspase-3, -9, and -8 as well as the upstream proteins TRAIL and FasL (Fig. 5A). These proteins have been classically considered as hallmarks of apoptotic cell death.<sup>20,22</sup> In contrast,

the anti-apoptotic proteins Bcl-2 and Bcl-XL and the DNA repair protein PARP1 were decreased in the AGS cells with erinacine S treatment (Fig. 5A). In contrast, erinacine S treatment affected the protein level of cell-cycle-related protein, including increased p16, and decreased the interaction of cyclin E and



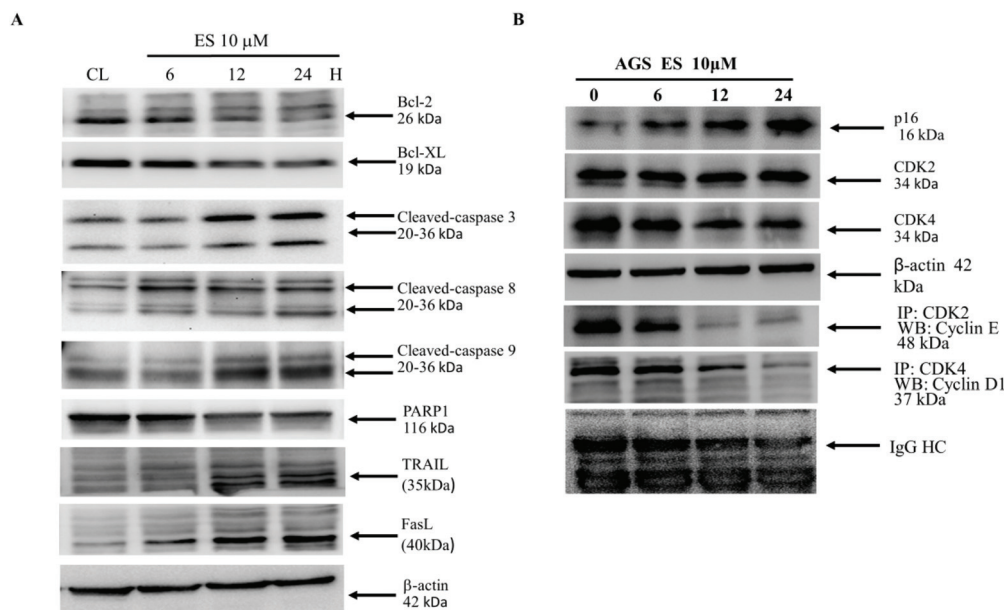


**Fig. 5** Regulation of the cell-death-related protein expression by erinacines. (A) After treatment of the AGS cells with erinacine S at 6, 12 and 24 h, their protein lysates were collected and subjected to immunoblotting with antibodies against Bcl-2, Bcl-XL, cleaved caspase 3, PARP, TRAIL and FasL, or β-actin, which served as the internal control. Equal amounts of the protein from the total fraction of AGS cells, which had been treated with 10 μM erinacine S. (B) The protein levels of p16, CDK2 and CDK4 in these treated cells were measured with immunoblotting. The CDK2-cyclin binding and the CDK4-cyclin D1 binding were determined, respectively, by immunoprecipitation as indicated. β-actin served as the internal control.

CDK2/4 (Fig. 5B). Accordingly, our data showed that erinacine S had a novel biological property for inductive cell apoptosis and cell cycle arrest of gastric cancer cells through regulating the multiple-protein network involved in extrinsic cell apoptosis and cell cycle pathways. Moreover, phosphorylation of AKT Ser<sup>473</sup> at 1 h, 2 h, 3 h and 6 h increased in the erinacine S-treated AGS cells in a time-dependent manner. Activation of FAK Tyr<sup>579/577</sup> with erinacine S was also observed at an early time point and markedly sustained for at least 6 h (Fig. 6). Similarly, the phosphorylation of PAK1 Thr<sup>423</sup> was constitutively activated for a certain time period after erinacine S treatment (Fig. 6). Indeed, treatment with erinacine S increased the levels of p-AKT, p-FAK and p-PAK1. The effects of these kinase inhibitors in blocking erinacine S-induced cell death were assessed, and the apoptotic (%) was determined using the flow cytometry analysis for annexin-V and PI. As shown in Table 2, AKT/PAK1/FAK siRNA almost blocked erinacine S-induced cell death by 18%, 15% and 7%, respectively. Using caspase-3 inhibitors Z-DEVD-FMK and caspase-8 inhibitors Z-IETD-FMK, the effects of these inhibitors in blocking erinacine S-induced cell death were assessed, and the apoptotic (%) was determined. Caspase-3 and caspase-8 inhibitors almost blocked erinacine S-induced cell death by 16% and 24%, respectively.

### 3.4. Erinacine S increases the expression of FasL and TRAIL via ROS-, Akt-, FAK- and PAK1-mediated epigenetic histone methylation

Accumulating evidence demonstrates that multiple signaling molecules are involved in the upregulation of FasL and TRAIL

in the apoptotic cells through the trimethylation of histone H3.<sup>26,33,34</sup> Thus, we wanted to determine whether erinacine S treatment can increase the trimethylation of histone H3 on the promoter regions of FasL and the TRAIL genes and which signaling molecules may be involved in this epigenetic modification.<sup>35</sup> The ChIP assay results showed that erinacine S treatment increased the trimethylation of histone H3 binding on the promoter regions of both FasL and TRAIL genes, and these modifications were reversed by the inhibition of ROS and multiple protein kinases such as Akt, FAK and PAK1 (Fig. 7). Taken together, these results suggest the presence of a novel biological property of erinacine S for growth inhibition and apoptosis in gastric cancer by epigenetic histone H3 methylation of FasL and TRAIL.

## 4. Discussion

Gastric cancer is one of the most common causes of cancer-related death worldwide, especially in East Asian countries such as China and Japan.<sup>1,2</sup> Many drugs have been tested through animal experiments and clinical trials for the treatment of gastric cancer.<sup>36</sup> Some dietary foods, which are considered as the potential source of bioactive safe compounds, display a chemopreventive property for cancer formation.<sup>37</sup> ROS-mediated damage to DNA and apoptotic signals play an important role in the inhibition of cancer formation by dietary-food-derived bioactive compounds.<sup>38</sup> Indeed, ROS functions as a class of oxygen-containing and active species to



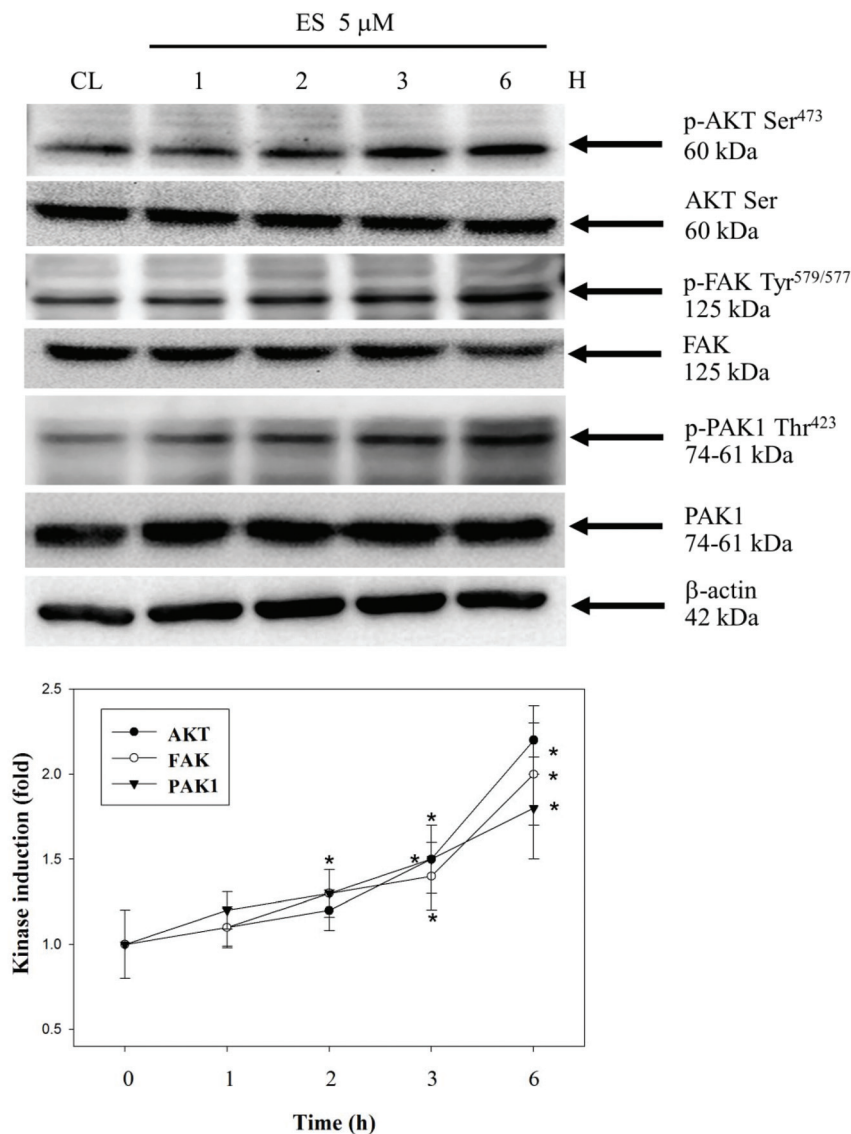


**Fig. 6** Activation of the AKT/FAK and PAK1 pathways by erinacine S. The protein levels of phosphorylated AKT, FAK, PAK1 and b-actin were detected in the AGS cells treated with or without erinacine S at the indicated time by western blotting. The protein levels were quantified with densitometric analysis with the ratio of the untreated control set as 1-fold. The quantitative data are presented as the mean of three repeats from three independent experiments. \* $P < 0.05$ , compared with the control group.

**Table 2** The effects of kinase inhibitors in blocking erinacine S-induced cell death

|                 | Apoptosis (%) |
|-----------------|---------------|
| Control         | 10 ± 2        |
| ES              | 50 ± 1        |
| ES + AKTsiRNA   | 18 ± 3        |
| ES + PAKsiRNA   | 15 ± 3        |
| ES + FAKsiRNA   | 7 ± 2         |
| ES + Z-DEVD-FMK | 16 ± 2        |
| ES + Z-IETD-FMK | 24 ± 1        |

facilitate the activation of many tyrosine kinases and tyrosine phosphatases that are involved in cellular apoptosis.<sup>39</sup> Through targeting on the mechanism of phytochemicals' anti-

oxidant, those signal molecules including Akt, FAK and PAK1 and MAPK further induce the toxicity of cancer cells.<sup>40</sup> In this study, we demonstrated for the first time a novel role of erinacine S, isolated from the *H. erinaceus* mycelium, to inhibit gastric cancer cells' viability *in vitro* in the AGS and TSGH 9201 cells and *in vivo* in the xenograft mouse model (Fig. 2, 3 and 4). Our results also indicated that increased ROS and cell cycle arrest at the G1 stage occurred in the gastric cancer cells after treatment with erinacine S (Fig. 3 and 4). In addition to the time-dependent induction of apoptosis in the AGS and TSGH 9201 cells, the same phenomena can be observed in the MKN28 cells with erinacine S treatment (unpublished data). Meanwhile, intraperitoneal injections with erinacine S (1 or 5 mg kg<sup>-1</sup> per day) significantly reduced the tumor volume

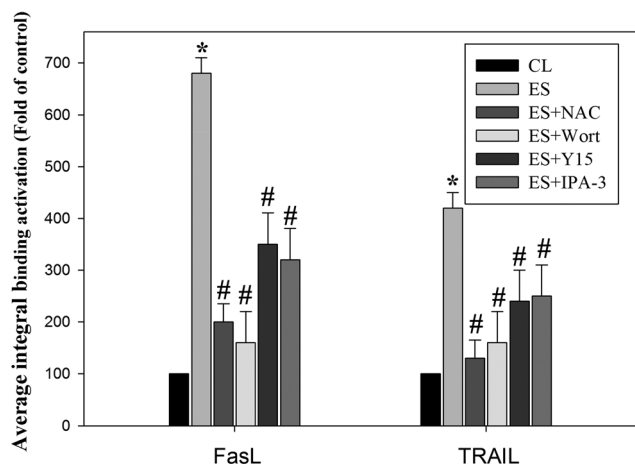


**Fig. 7** Involvement of the ROS-derived and AKT/FAK/PAK1 signals in erinacine S-mediated epigenetic methylation of FasL and TRAIL promoter. AGS cells were treated with or without the specific ROS scavenger NAC, AKT inhibitor wortmannin, FAK inhibitor Y15, or the PAK1 inhibitor IPA-3 in the presence or absence of erinacine S for 24 h. These treated cells were then subjected to chromatin immunoprecipitation (ChIP) assays by using antibodies against Histone H3 trimethylation at lysine 4 (H3K4me3). The precipitated DNA was amplified by quantitative real-time polymerase chain reaction (qRT-PCR) using primer sets specific to the target sites of FasL and TRAIL promoters. The anti-IgG antibody served to identify the background amplification. Input DNA was amplified as a loading control. The amount of immunoprecipitated DNA in each sample is represented as normalized signal to the negative control ChIP. The normalized mean CT was estimated as  $\Delta\text{CT}$  by subtracting the mean CT of the input from that of the individual region among the untreated control group. Effect of erinacine S treatment on specific genes were calculated by the  $\Delta\Delta\text{CT}$  method. The quantitative data were presented as the mean  $\pm$  SD of three independent experiments in triplicate technical repeats. # $P < 0.05$ , as compared to the control group; \* $P < 0.05$ , as compared to the erinacine S-treated group.

(tumor size and weight) of the AGS xenograft in nude mice (Fig. 4A). Furthermore, the levels of PCNA and cyclin D1 decreased in the tumor region of the AGS xenograft in nude mice, whereas the FasL and TRAIL expression increased (Fig. 4B). Our results showed that both death-receptor-mediated extrinsic apoptosis (caspase 8, caspase 9, caspase 3, FasL and TRAIL) and the mitochondria-mediated apoptotic pathway (Bcl-2 and Bcl-XL) were involved in the induction of gastric cancer cells by erinacine S (Fig. 5A). In addition, the assembly of cell-cycle-related protein (increased p16 and decreased cyclin E-CDK2/4 interaction) was altered by erinacine S treatment (Fig. 5B).

Similarly, dietary phytochemicals that widely exist in food and nutraceuticals also activate the MAPK pathway and ROS-derived AKT/FAK/PAK1 pathways in order to regulate cell motility and adhesion, prevent cancer growth and induce tumor apoptosis.<sup>40–42</sup> Accordingly, these signaling pathways are promising targets for anticancer effects.<sup>43,44</sup> Several studies' mechanisms have been described to explain G1 cell cycle arrest in response to nature phytochemicals.<sup>45</sup> One of them is the increase in the levels of FasL and TRAIL, induced apoptosis to inhibits their growth. Another is a decrease in the levels

of these proteins results in inhibition of the CDKs/cyclins due to a cell cycle arrest in G1 arrest.<sup>46</sup> Consistent with our previous data, treatment with erinacine A, which was also extracted from the mycelia of *H. erinaceus*, shows dramatic anticancer effects on human colorectal cancer cells through the ROS-mediated p70S6K/NF- $\kappa$ B pathways and p21 expression.<sup>16,17</sup> Furthermore, both PI3K/mTOR/p70S6K and ROCK1/LIMK2/cofilin pathways are considered as the upstream signals of the ROS accumulation initiated by erinacine A.<sup>16,18,47</sup> Additionally, other studies indicate that erinacine A modulates the reorganization of the actin cytoskeleton through the FAK/AKT/p70S6K/PAK1 signaling pathway and the upregulation of 1433S and MTUS2 expression.<sup>40</sup> However, whether different bioactive erinacine molecules isolated from the cultured mycelia of *H. erinaceus* have the same property of anticancer growth and signaling activation remains unclear. It is also interesting to determine the effective application of these erinacine-related molecules in treating different types of cancers. Precisely, the activation of the ROS-derived and AKT/FAK/PAK1 pathways is required for erinacine S-induced apoptosis and cell cycle arrest in gastric cancer (Fig. 6). The PI3K/Akt/FAK pathway is directly involved in inducing oxidative stress with phytochemicals for several hours (Fig. 6), showing redox-sensitive activity-induced cell apoptosis.<sup>48</sup>

The epigenome is defined by the associated post-translational modifications of histone and the effective status of H3 and H4 currently under development in anticancer agents, which potentiated inhibiting tumor-to-tumor necrosis factor-related apoptosis-inducing ligand (TRAIL)-induced apoptosis.<sup>26</sup> Several recent studies have demonstrated that many natural phytochemicals derived from various vegetables, fruits, spices, and herbal medicines not only restore aberrant epigenetic alterations, but also trigger sustained DNA damage and cell apoptosis *in vitro* and *in vivo*.<sup>47</sup> For instance, all polyphenols, isothiocyanates, epigallocatechin-3-gallate (EGCG), curcumin, resveratrol, sulforaphane, isoflavones, quercetin, genistein, caffeine and anacardic acid show a capability of epigenetic modification.<sup>49,50</sup> However, the linkage between their epigenetic modification and the anticancer effects of erinacine S, extracted from the mycelia of *H. erinaceus*, is still unclear. Interestingly, methylation of histone 3 lysine 4 (H3K4), a critical feature of the active promoter state, occurs in human cancer cells. The induction of FasL and TRAIL genes is associated with histone H3 methylation that is regulated by the protein kinases such as Akt, FAK and PAK1.<sup>51–54</sup> Consistently, for the first time, our *in vitro* study demonstrated that erinacine S treatment significantly increased the activation of Akt, FAK and PAK1 signaling molecules in the AGS cells as well as the transcriptional activation of histone H3 methylation (H3K4me3) of the FasL and TRAIL promoters (Fig. 7). Thus, erinacine S, as an individual natural phytochemical, may be seen as a novel regulator of the chemotherapeutic agent for histone H3 methylation in the treatment of gastric cancer. Several studies have demonstrated that the signaling kinases including AKT, FAK and PAK1 in cancer cells are manifested by the downstream effectors of cytoplasmic signaling cascades

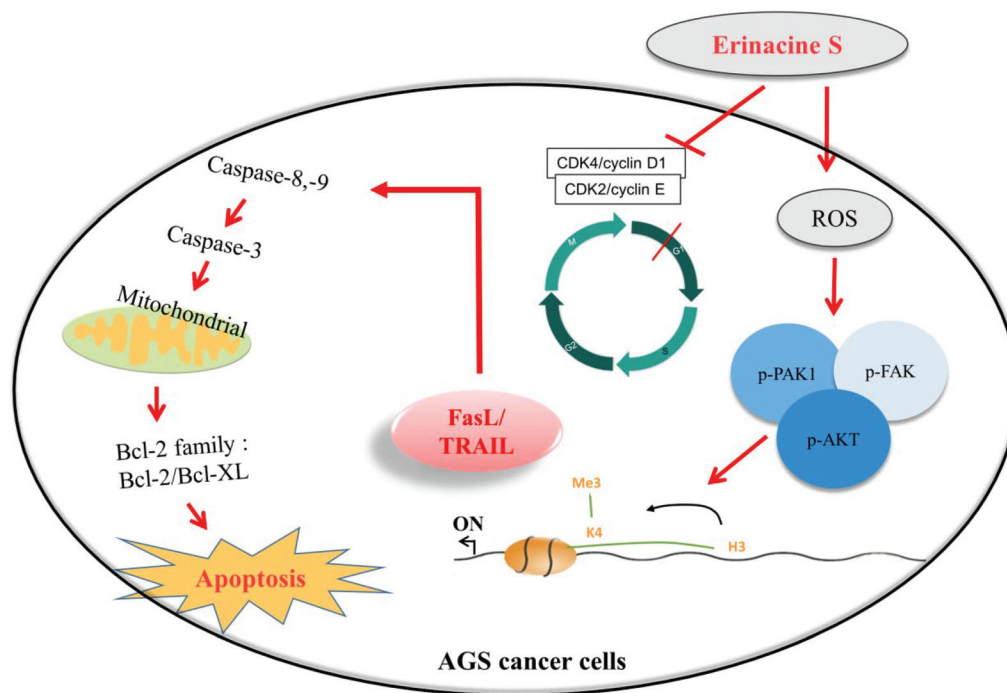


**Fig. 8** Schematic presentation of the molecular mechanism underlying erinacine S that induces cell apoptosis of AGS gastric cancer cells. Erinacine S treatment increases the expression levels of the death receptors FasL and TRAIL through the ROS-derived and the AKT/FAK/PAK1 signaling-pathway-mediated histone H3 trimethylation in AGS cells. Activation of FasL and TRAIL by erinacine S triggers cell apoptosis through the inhibition of Bcl-2 and Bcl-XL and the activation of Bax, caspase-8, 3, and 9. However, erinacine S treatment also causes cell cycle G1 arrest through the downregulation of cyclin D1 in AGS cells.

to the nucleus leading to phosphorylation of histones, methylases (HMTs), histone acetyltransferases (HATs), histone deacetylases (HDACs), DNA-binding factors and coregulators, serving as a regulatory switch for post-translational modification (PTM) of histone remodeling complexes into gene transcription and gene activity.<sup>55</sup> For instance, PI3K/AKT signaling regulates the cancer epigenome through controlling H3K4 methylation, involved in KDM5A (histone demethylase) subcellular localization to the cytoplasm increasing promoter-associated H3K4me3 and gene expression patterns in cancer cells.<sup>54</sup> PAK1 signaling mediated gene expression *via* phosphorylation of histones and coregulators. Signaling of FAK in regulating heterochromatin remodeling by its interaction with MBD2 (Methyl CpG binding domain protein 2) demonstrates a potential link between cell adhesion and cell differentiation.<sup>56</sup> Additional studies are still needed to elucidate the action mechanisms of erinacine S in these epigenetic modifications through modulating histone methyltransferases (HMTs) or demethylases (HDMs) *in vitro* and *in vivo*.

In conclusion, this study demonstrates the novel roles of the *H. erinaceus* mycelium component erinacine S that not only causes cell cycle G1 arrest by the inactivation of CDK4/cyclin D1 and CDK2/cyclin E but also the novel mechanism of erinacine S which plays a significant role in stimulating the histone H3K4me3 binding of the FasL and TRAIL promoters *via* the ROS-derived and AKT/FAK/PAK1 pathways involved in gastric cancer AGS cell apoptosis. Our data have shown that

the activation of the ROS-derived and AKT/FAK/PAK1 pathways by erinacine S is a key event that triggers both death-receptor-mediated extrinsic apoptosis and the mitochondria-mediated apoptotic pathway involved in the induction of gastric cancer cells (Fig. 8).

## Abbreviations

|         |   |
|---------|---|
| FasL    | Fas ligand                                |
| TRAIL   | TNF-related apoptosis-inducing ligand     |
| FAK     | Focal adhesion kinase                     |
| PAK1    | P21 (RAC1) activated kinase 1             |
| ROS     | Reactive oxygen species                   |
| H3K4me3 | Tri-methylation of lysine 4 on histone H3 |
| HDACs   | Histone deacetylase inhibitors            |
| HMTs    | Histone methyltransferases                |
| ChIP    | Chromatin immunoprecipitation assays      |

## Author contributions

SYT: provision of study material, collection and assembly of data and histopathological evaluation and manuscript writing; KCL: design, collection, assembly of data; KFL and YLY: conception, collection, and assembly of data; WSH: provision of study material or animals; CCT: provision of study material or

animals; CHS: provision of study material or animals; MCH: provision of study material, collection, and assembly of data; JMS: administrative support, collection, and assembly of data (flow cytometry); LYL, CCC and WPC: provision of study material or animals; and CYH and HCK: conception and design, financial support, administrative support, manuscript writing and final approval of manuscript. All authors read and approved the final manuscript.

## Availability of data and materials

All relevant data are within the paper. The raw data supporting the conclusions of this manuscript will be made available by the authors, without undue reservation, to any qualified researcher.

## Ethics approval and consent to participate

Animal care and the general protocols for animal use were approved by the Institutional Animal Care and Use Committee of Chang Gung Memorial Hospital, Chiayi, Animal Ethics Research Board (IACUC approval: 2017121409). All procedures and the reporting thereof comply with the Institutional Animal Care and Use Committee (IACUC) guidelines.

## Funding

The Ministry of Science and Technology, Taiwan (MOST 107-2320-B-255-001-MY3 and MOST 108-2622-B-255-001-CC3).

## Conflicts of interest

The authors declare that no competing interests exist. Authors L.-Y. L., W.-P. C., and C.-C. C. were employed by company Grape King Biotechnology Inc. (Grape King Bio, Ltd.). All other authors declare no competing interests.

## Acknowledgements

The funding for this study was provided in part by research grants from the Chang Gung Memorial Hospital, Chiayi, Taiwan. This study was supported by grants BMRPD42, CLRPG8G0591, CMRPG6H0261, CMRPG6H0262, CMRPG6H0263, CMRPF6G0011, CMRPF6G0012, CMRPF6G0013, CMRPF6I0021, CMRPF6J0081 and CMRPF6K0071 from the Chang Gung Memorial Hospital, Chiayi, Taiwan, and the Chang Gung University of Science and Technology, Chia-Yi Campus, Taiwan. The authors thank Dr Chun-Hsien Chu (Institute of Molecular Medicine, College of Medicine, National Cheng Kung University) for the assistance with scientific consulting and manuscript editing. We

thank the “Tissue Bank, Chang Gung Memorial Hospital, Chiayi and Laboratory Animal Center, Chang Gung Memorial Hospital, Chiayi and Proteomics Core Laboratory, Chang Gung Memorial Hospital, Linkou, Taiwan” for their technical services.

## References

- 1 A. Jemal, F. Bray, M. M. Center, J. Ferlay, E. Ward and D. Forman, Global cancer statistics, *CA Cancer J. Clin.*, 2011, **61**, 69–90.
- 2 L. Herszenyi and Z. Tulassay, Epidemiology of gastrointestinal and liver tumors, *Eur. Rev. Med. Pharmacol. Sci.*, 2010, **14**, 249–258.
- 3 A. D. Wagner, S. Unverzagt, W. Grothe, G. Kleber, A. Grothey, J. Haerting and W. E. Fleig, Chemotherapy for advanced gastric cancer, *Cochrane Database Syst. Rev.*, 2010, CD004064.
- 4 I. Ogino, S. Watanabe, T. Misumi, M. Hata and C. Kunisaki, Lymph Node Metastases Diagnosed by (18) F-FDG-PET/CT in Esophageal Squamous Cell Cancer Treated With Concurrent Chemoradiotherapy, *Anticancer Res.*, 2019, **39**, 4977–4985.
- 5 M. Balakrishnan, R. George, A. Sharma and D. Y. Graham, Changing Trends in Stomach Cancer Throughout the World, *Curr. Gastroenterol. Rep.*, 2017, **19**, 36.
- 6 H. D. Woo, S. Park, K. Oh, H. J. Kim, H. R. Shin, H. K. Moon and J. Kim, Diet and cancer risk in the Korean population: a meta-analysis, *Asian Pac. J. Cancer Prev.*, 2014, **15**, 8509–8519.
- 7 A. Ranjan, S. Ramachandran, N. Gupta, I. Kaushik, S. Wright, S. Srivastava, H. Das, S. Srivastava, S. Prasad and S. K. Srivastava, Role of Phytochemicals in Cancer Prevention, *Int. J. Mol. Sci.*, 2019, **20**, 4981.
- 8 M. Friedman, Chemistry, Nutrition, and Health-Promoting Properties of *Herichium erinaceus* (Lion's Mane) Mushroom Fruiting Bodies and Mycelia and Their Bioactive Compounds, *J. Agric. Food Chem.*, 2015, **63**, 7108–7123.
- 9 M. Wang, Y. Gao, D. Xu, T. Konishi and Q. Gao, *Herichium erinaceus* (Yamabushitake): a unique resource for developing functional foods and medicines, *Food Funct.*, 2014, **5**(12), 3055–3064.
- 10 K. F. Lee, S. Y. Tung, C. C. Teng, C. H. Shen, M. C. Hsieh, C. Y. Huang, K. C. Lee, L. Y. Lee, W. P. Chen, C. C. Chen, W. S. Huang and H. C. Kuo, Post-Treatment with Erinacine A, a Derived Diterpenoid of *H. erinaceus*, Attenuates Neurotoxicity in MPTP Model of Parkinson's Disease, *Antioxidants*, 2020, **9**, 137.
- 11 E. Malinowska, W. Krzycki, F. Herold, G. Lapienis, J. Slusarczyk, P. Suchocki, M. Kuras and J. Turlo, Biosynthesis of selenium-containing polysaccharides with antioxidant activity in liquid culture of *Herichium erinaceum*, *Enzyme Microb. Technol.*, 2009, **44**, 334–343.



- 12 B. K. Yang, J. B. Park and C. H. Song, Hypolipidemic effect of an Exo-biopolymer produced from a submerged mycelial culture of *Herichium erinaceus*, *Biosci. Biotechnol. Biochem.*, 2003, **67**, 1292–1298.
- 13 M. Gong, J. An, H. Z. Lu, C. F. Wu, Y. J. Li, J. Q. Cheng and J. K. Bao, Effects of denaturation and amino acid modification on fluorescence spectrum and hemagglutinating activity of *Herichium erinaceum* Lectin, *Acta Biochim. Biophys. Sin.*, 2004, **36**, 343–350.
- 14 M. H. Yim, J. W. Shin, J. Y. Son, S. M. Oh, S. H. Han, J. H. Cho, C. K. Cho, H. S. Yoo, Y. W. Lee and C. G. Son, Soluble components of *Herichium erinaceum* induce NK cell activation via production of interleukin-12 in mice splenocytes, *Acta Pharmacol. Sin.*, 2007, **28**, 901–907.
- 15 M. Shimbo, H. Kawagishi and H. Yokogoshi, Erinacine A increases catecholamine and nerve growth factor content in the central nervous system of rats, *Nutr. Res.*, 2005, **25**, 617–623.
- 16 C. C. Lu, W. S. Huang, K. F. Lee, K. C. Lee, M. C. Hsieh, C. Y. Huang, L. Y. Lee, B. O. Lee, C. C. Teng, C. H. Shen, S. Y. Tung and H. C. Kuo, Inhibitory effect of Erinacines A on the growth of DLD-1 colorectal cancer cells is induced by generation of reactive oxygen species and activation of p70S6K and p21, *J. Funct. Foods*, 2016, **21**, 474–484.
- 17 K. C. Lee, H. C. Kuo, C. H. Shen, C. C. Lu, W. S. Huang, M. C. Hsieh, C. Y. Huang, Y. H. Kuo, Y. Y. Hsieh, C. C. Teng, L. Y. Lee and S. Y. Tung, A proteomics approach to identifying novel protein targets involved in erinacine A-mediated inhibition of colorectal cancer cells' aggressiveness, *J. Cell. Mol. Med.*, 2017, **21**, 588–599.
- 18 K. C. Lee, K. F. Lee, S. Y. Tung, W. S. Huang, L. Y. Lee, W. P. Chen, C. C. Chen, C. C. Teng, C. H. Shen, M. C. Hsieh and H. C. Kuo, Induction Apoptosis of Erinacine A in Human Colorectal Cancer Cells Involving the Expression of TNFR, Fas, and Fas Ligand via the JNK/p300/p50 Signaling Pathway With Histone Acetylation, *Front. Pharmacol.*, 2019, **10**, 1174.
- 19 C. C. Chen, T. T. Tzeng, C. C. Chen, C. L. Ni, L. Y. Lee, W. P. Chen, Y. J. Shiao and C. C. Shen, Erinacine S, a Rare Sesterterpene from the Mycelia of *Herichium erinaceus*, *J. Nat. Prod.*, 2016, **79**, 438–441.
- 20 D. Hanahan and R. A. Weinberg, The hallmarks of cancer, *Cell*, 2000, **100**, 57–70.
- 21 H. Brenner, M. Kloor and C. P. Pox, Colorectal cancer, *Lancet*, 2014, **383**, 1490–1502.
- 22 M. A. Feitelson, A. Arzumanyan, R. J. Kulathinal, S. W. Blain, R. F. Holcombe, J. Mahajna, M. Marino, M. L. Martinez-Chantar, R. Nawroth, I. Sanchez-Garcia, D. Sharma, N. K. Saxena, N. Singh, P. J. Vlachostergios, S. Guo, K. Honoki, H. Fujii, A. G. Georgakilas, A. Bilsland, A. Amedei, E. Niccolai, A. Amin, S. S. Ashraf, C. S. Boosani, G. Guha, M. R. Ciriolo, K. Aquilano, S. Chen, S. I. Mohammed, A. S. Azmi, D. Bhakta, D. Halicka, W. N. Keith and S. Nowsheen, Sustained proliferation in cancer: Mechanisms and novel therapeutic targets, *Semin. Cancer Biol.*, 2015, **35**(Suppl), S25–S54.
- 23 F. P. Chen and M. H. Chien, Phytoestrogens induce apoptosis through a mitochondria/caspase pathway in human breast cancer cells, *Climacteric*, 2014, **17**, 385–392.
- 24 J. C. Reed, Mechanisms of apoptosis, *Am. J. Pathol.*, 2000, **157**, 1415–1430.
- 25 M. Li-Weber, Targeting apoptosis pathways in cancer by Chinese medicine, *Cancer Lett.*, 2013, **332**, 304–312.
- 26 S. K. Patra and M. Szyf, DNA methylation-mediated nucleosome dynamics and oncogenic Ras signaling: insights from FAS, FAS ligand and RASSF1A, *FEBS J.*, 2008, **275**, 5217–5235.
- 27 T. H. Tseng, C. H. Shen, W. S. Huang, C. N. Chen, W. H. Liang, T. H. Lin and H. C. Kuo, Activation of neutral-sphingomyelinase, MAPKs, and p75 NTR-mediated caffeic acid phenethyl ester-induced apoptosis in C6 glioma cells, *J. Biomed. Sci.*, 2014, **21**, 61.
- 28 W. S. Huang, M. C. Hsieh, C. Y. Huang, Y. H. Kuo, S. Y. Tung, C. H. Shen, Y. Y. Hsieh, C. C. Teng, K. F. Lee, T. C. Chen, K. C. Lee and H. C. Kuo, The Association of CXC Receptor 4 Mediated Signaling Pathway with Oxaliplatin-Resistant Human Colorectal Cancer Cells, *PLoS One*, 2016, **11**, e0159927.
- 29 W. S. Huang, Y. H. Kuo, H. C. Kuo, M. C. Hsieh, C. Y. Huang, K. C. Lee, K. F. Lee, C. H. Shen, S. Y. Tung and C. C. Teng, CIL-102-Induced Cell Cycle Arrest and Apoptosis in Colorectal Cancer Cells via Upregulation of p21 and GADD45, *PLoS One*, 2017, **12**, e0168989.
- 30 Y. Y. Hsieh, C. H. Shen, W. S. Huang, C. C. Chin, Y. H. Kuo, M. C. Hsieh, H. R. Yu, T. S. Chang, T. H. Lin, Y. W. Chiu, C. N. Chen, H. C. Kuo and S. Y. Tung, Resistin-induced stromal cell-derived factor-1 expression through Toll-like receptor 4 and activation of p38 MAPK/NFκB signaling pathway in gastric cancer cells, *J. Biomed. Sci.*, 2014, **21**, 59.
- 31 J. J. Tsai, H. C. Kuo, K. F. Lee and T. H. Tsai, Proteomic analysis of plasma from rats following total parenteral nutrition-induced liver injury, *Proteomics*, 2015, **15**, 3865–3874.
- 32 W. S. Huang, C. Y. Huang, M. C. Hsieh, Y. H. Kuo, S. Y. Tung, C. H. Shen, Y. Y. Hsieh, C. C. Teng, K. C. Lee, K. F. Lee and H. C. Kuo, Expression of PRDX6 Correlates with Migration and Invasiveness of Colorectal Cancer Cells, *Cell. Physiol. Biochem.*, 2018, **51**, 2616–2630.
- 33 M. J. Knight, C. D. Riffkin, A. M. Muscat, D. M. Ashley and C. J. Hawkins, Analysis of FasL and TRAIL induced apoptosis pathways in glioma cells, *Oncogene*, 2001, **20**, 5789–5798.
- 34 S. S. Ghare, S. Joshi-Barve, A. Moghe, M. Patil, D. F. Barker, L. Gobejishvili, G. N. Brock, M. Cave, C. J. McClain and S. S. Barve, Coordinated histone H3 methylation and acetylation regulate physiologic and pathologic fas ligand gene expression in human CD4+T cells, *J. Immunol.*, 2014, **193**, 412–421.
- 35 A. Shilatifard, Molecular implementation and physiological roles for histone H3 lysine 4 (H3K4) methylation, *Curr. Opin. Cell Biol.*, 2008, **20**, 341–348.

- 36 L. Zheng, L. Wang, J. Ajani and K. Xie, Molecular basis of gastric cancer development and progression, *Gastric Cancer*, 2004, **7**, 61–77.
- 37 A. Link, F. Balaguer and A. Goel, Cancer chemoprevention by dietary polyphenols: promising role for epigenetics, *Biochem. Pharmacol.*, 2010, **80**, 1771–1792.
- 38 C. C. Teng, H. C. Kuo, H. C. Cheng, T. C. Wang and C. I. Sze, The inhibitory effect of CIL-102 on the growth of human astrocytoma cells is mediated by the generation of reactive oxygen species and induction of ERK1/2 MAPK, *Toxicol. Appl. Pharmacol.*, 2012, **263**, 73–80.
- 39 G. Loo, Redox-sensitive mechanisms of phytochemical-mediated inhibition of cancer cell proliferation (review), *J. Nutr. Biochem.*, 2003, **14**, 64–73.
- 40 H. C. Kuo, Y. R. Kuo, K. F. Lee, M. C. Hsieh, C. Y. Huang, Y. Y. Hsieh, K. C. Lee, H. L. Kuo, L. Y. Lee, W. P. Chen, C. C. Chen and S. Y. Tung, A Comparative Proteomic Analysis of Erinacine A's Inhibition of Gastric Cancer Cell Viability and Invasiveness, *Cell. Physiol. Biochem.*, 2017, **43**, 195–208.
- 41 J. Y. Zhu, I. N. Lavrik, U. Mahlknecht, M. Giaisi, P. Proksch, P. H. Krammer and M. Li-Weber, The traditional Chinese herbal compound rocaglamide preferentially induces apoptosis in leukemia cells by modulation of mitogen-activated protein kinase activities, *Int. J. Cancer*, 2007, **121**, 1839–1846.
- 42 B. Sung, B. Park, V. R. Yadav and B. B. Aggarwal, Celastrol, a Triterpene, Enhances TRAIL-induced Apoptosis through the Down-regulation of Cell Survival Proteins and Up-regulation of Death Receptors (Retracted article. See vol. 291, pg. 16920, 2016), *J. Biol. Chem.*, 2010, **285**, 11498–11507.
- 43 M. Raman, W. Chen and M. H. Cobb, Differential regulation and properties of MAPKs, *Oncogene*, 2007, **26**, 3100–3112.
- 44 M. Li-Weber, New therapeutic aspects of flavones: the anti-cancer properties of Scutellaria and its main active constituents Wogonin, Baicalein and Baicalin, *Cancer Treat. Rev.*, 2009, **35**, 57–68.
- 45 M. R. Bhonde, M. L. Hanski, M. Notter, B. F. Gillissen, P. T. Daniel, M. Zeitz and C. Hanski, Equivalent effect of DNA damage-induced apoptotic cell death or long-term cell cycle arrest on colon carcinoma cell proliferation and tumour growth, *Oncogene*, 2006, **25**, 165–175.
- 46 K. Ahmed, S. F. Zaidi, Z. G. Cui, D. Zhou, S. A. Saeed and H. Inadera, Potential proapoptotic phytochemical agents for the treatment and prevention of colorectal cancer, *Oncol. Lett.*, 2019, **18**, 487–498.
- 47 P. Rajendran, E. Ho, D. E. Williams and R. H. Dashwood, Dietary phytochemicals, HDAC inhibition, and DNA damage/repair defects in cancer cells, *Clin. Epigenet.*, 2011, **3**, 4.
- 48 C. C. Teng, H. C. Kuo and C. I. Sze, Quantitative proteomic analysis of the inhibitory effects of CIL-102 on viability and invasiveness in human glioma cells, *Toxicol. Appl. Pharmacol.*, 2013, **272**, 579–590.
- 49 E. Kim, W. H. Bisson, C. V. Lohr, D. E. Williams, E. Ho, R. H. Dashwood and P. Rajendran, Histone and Non-Histone Targets of Dietary Deacetylase Inhibitors, *Curr. Top. Med. Chem.*, 2016, **16**, 714–731.
- 50 J. H. Lee, T. O. Khor, L. Shu, Z. Y. Su, F. Fuentes and A. N. Kong, Dietary phytochemicals and cancer prevention: Nrf2 signaling, epigenetics, and cell death mechanisms in blocking cancer initiation and progression, *Pharmacol. Ther.*, 2013, **137**, 153–171.
- 51 R. R. Rosato, J. A. Almenara, Y. Dai and S. Grant, Simultaneous activation of the intrinsic and extrinsic pathways by histone deacetylase (HDAC) inhibitors and tumor necrosis factor-related apoptosis-inducing ligand (TRAIL) synergistically induces mitochondrial damage and apoptosis in human leukemia cells, *Mol. Cancer Ther.*, 2003, **2**, 1273–1284.
- 52 X. D. Zhang, S. K. Gillespie, J. M. Borrow and P. Hersey, The histone deacetylase inhibitor suberic bishydroxamate: a potential sensitizer of melanoma to TNF-related apoptosis-inducing ligand (TRAIL) induced apoptosis, *Biochem. Pharmacol.*, 2003, **66**, 1537–1545.
- 53 H. Alam, B. Gu and M. G. Lee, Histone methylation modifiers in cellular signaling pathways, *Cell. Mol. Life Sci.*, 2015, **72**, 4577–4592.
- 54 J. M. Spangle, K. M. Dreijerink, A. C. Groner, H. Cheng, C. E. Ohlson, J. Reyes, C. Y. Lin, J. Bradner, J. J. Zhao, T. M. Roberts and M. Brown, PI3 K/AKT Signaling Regulates H3K4 Methylation in Breast Cancer, *Cell Rep.*, 2016, **15**, 2692–2704.
- 55 R. Kumar, S. Deivendran, T. R. Santhoshkumar and M. R. Pillai, Signaling coupled epigenomic regulation of gene expression, *Oncogene*, 2017, **36**, 5917–5926.
- 56 L. Mei and W. C. Xiong, FAK interaction with MBD2: A link from cell adhesion to nuclear chromatin remodeling?, *Cell Adhes. Migr.*, 2010, **4**, 77–80.

## Research Paper

# Monovalent antibody-conjugated lipid-polymer nanohybrids for active targeting to desmoglein 3 of keratinocytes to attenuate psoriasiform inflammation

Zih-Chan Lin<sup>1</sup>, Tsong-Long Hwang<sup>2,3,4,5,6</sup>, Tse-Hung Huang<sup>4,7,8,9</sup>, Kohei Tahara<sup>10</sup>, Jiří Trousil<sup>11</sup>, Jia-You Fang<sup>2,3,4,6</sup>✉

1. Graduate Institute of Biomedical Sciences, Chang Gung University, Kweishan, Taoyuan, Taiwan.
2. Graduate Institute of Natural Products, Chang Gung University, Kweishan, Taoyuan, Taiwan.
3. Chinese Herbal Medicine Research Team, Healthy Aging Research Center, Chang Gung University, Kweishan, Taoyuan, Taiwan.
4. Research Center for Food and Cosmetic Safety and Research Center for Chinese Herbal Medicine, Chang Gung University of Science and Technology, Kweishan, Taoyuan, Taiwan.
5. Department of Chemical Engineering, Ming Chi University of Technology, New Taipei City, Taiwan.
6. Department of Anesthesiology, Chang Gung Memorial Hospital, Kweishan, Taoyuan, Taiwan.
7. Department of Traditional Chinese Medicine, Chang Gung Memorial Hospital, Keelung, Taiwan.
8. School of Traditional Chinese Medicine, Chang Gung University, Kweishan, Taoyuan, Taiwan.
9. School of Nursing, National Taipei University of Nursing and Health Sciences, Taipei, Taiwan.
10. Laboratory of Pharmaceutical Engineering, Gifu Pharmaceutical University, Gifu, Japan.
11. Institute of Macromolecular Chemistry, Czech Academy of Sciences, Prague, Czech Republic.

✉ Corresponding author: Jia-You Fang, Pharmaceutics Laboratory, Graduate Institute of Natural Products, Chang Gung University, 259 Wen-Hwa 1st Road, Kweishan, Taoyuan 333, Taiwan, Tel: +886-3-2118800, Fax: +886-3-2118236 E-mail: fajy@mail.cgu.edu.tw.

© The author(s). This is an open access article distributed under the terms of the Creative Commons Attribution License (<https://creativecommons.org/licenses/by/4.0/>). See <http://ivyspring.com/terms> for full terms and conditions.

Received: 2020.12.10; Accepted: 2021.02.17; Published: 2021.03.04

## Abstract

To improve the treatment of psoriasiform inflammation, we developed actively targeted nanocarriers loaded with the phosphodiesterase 4 inhibitor AN2728.

**Methods:** Phospholipid-poly(lactic-co-glycolic acid) nanohybrids were prepared and conjugated with monovalent anti-desmoglein 3 antibody to bind keratinocytes.

**Results:** The actively targeted nanohybrids were 229 nm in mean size with a nearly neutral surface charge. Flow cytometry and confocal microscopy showed a 9-fold increase in keratinocyte uptake of targeted nanohybrids relative to non-targeted nanoparticles. The nanoparticles localized mainly in lysosomes after internalization. AN2728-loaded antibody-conjugated nanocarriers inhibited cytokine/chemokine overexpression in activated keratinocytes without affecting cell viability. The targeted nanohybrids also suppressed neutrophil migration by reducing CXCL1 and CXCL2 release from keratinocytes. Following subcutaneous administration in mice, the nanohybrids distributed to the epidermis and hair follicles. In a psoriasis-like skin mouse model, the actively targeted nanoparticles were superior to free drug and non-targeted nanoparticles in mitigating skin inflammation. Intervention with the targeted nanosystem reduced the epidermal thickness of the psoriasiform lesion from 191 to 42  $\mu$ m, decreased the Psoriasis Area Severity Index by 74%, restored barrier function, and returned chemokine levels to baseline.

**Conclusions:** Our developed nanosystem was safe and demonstrated efficient targeting properties for the treatment of cutaneous inflammation.

Key words: desmoglein 3; keratinocyte; psoriasis; lipid-polymer nanohybrid; active targeting; monovalent antibody

## Introduction

Psoriasis is an autoimmune skin inflammation involving interactions between keratinocytes and immune cells. Psoriasis is characterized by keratinocyte proliferation and immune cell

accumulation in epidermis/dermis [1]. The clinical observation includes erythematous papules with white multilayered scales and thickened acanthotic epidermis. While the global prevalence of psoriasis is about 2-3%, its incidence seems to be increasing [2]. Keratinocytes demonstrate a critical capacity to initiate psoriatic inflammation by activating the onset of the pathogenic event and sustaining the prolonged phase [3]. Long-term therapies incompletely resolve psoriasis because of their inefficiency after prolonged application and side effects [4]. Therefore, new treatment strategies are needed to improve therapy.

Loading antipsoriatic drugs into nanocarriers is one approach to improve their therapeutic efficiency. The nanoparticles protect the drugs from degradation and provide controlled and targeted delivery, leading to improved therapy, reduced dose, and minimized adverse effects [5]. Active targeting of nanoparticles to target cells is possible by furnishing the nanoparticle surface with specific ligands for receptors on the cell membrane. Antibody-based targeting is promising for active targeting due to its high specificity [6]. Increasing applications of monoclonal antibodies in the targeted treatment of psoriasis also encourages the potential of antibody-conjugated nanocarriers. Desmoglein 3 (Dsg3) is a desmosomal glycoprotein that provides calcium-dependent adhesive integrity among keratinocytes [7]. Anti-Dsg monoclonal antibody has been proven to specifically target keratinocytes [8, 9]. Since Dsg3 is overexpressed in keratinocytes, it is an appropriate target for mitigating psoriatic inflammation with minimum effects on normal tissue.

There are very few actively targeted antibody-conjugated nanosystems for treating cutaneous inflammation. To improve psoriasis management, we developed Dsg3 antibody-conjugated lipid-polymer hybrid nanoparticles encapsulating AN2728. The model drug AN2728 (crisaborole) is a phosphodiesterase 4 (PDE4) inhibitor approved by the USFDA for atopic dermatitis treatment [10] and is also successful in relieving psoriasis [11]. PDE4 inhibitors limit the breakdown of cyclic adenosine monophosphate (cAMP) to decrease the levels of proinflammatory cytokines and chemokines [12]. Apremilast is an oral PDE4 inhibitor that was approved for psoriasis treatment in 2014 [13]. PDE4 inhibitors attenuate inflammation by directly modulating the function of keratinocytes [14]. Lipid-polymer nanohybrids were selected as the AN2728 nanocarrier because these hybrid materials combine the advantages of lipid-based and polymer-based nanosystems, including excellent storage stability, easy fabrication, high biocompatibility, facile cell uptake, and high loading capacity of lipophilic drugs

[15]. Polyethylene glycol (PEG)ylated phospholipid and poly(lactic-co-glycolic acid) (PLGA) were used to fabricate the nanocarriers because of their biodegradability and approval by the USFDA [15]. To effectively target the nanoparticles to keratinocytes, we used a monovalent anti-Dsg3 antibody fragment with free thiol moieties. Full antibody ligands have a number of disadvantages for nanoparticle conjugation that lead to off-target effects [16]. Foremost, the orientation of the antibody on the nanoparticle surface is usually random, which reduces its selective binding ability [17]. Further, the large size of whole antibodies causes steric hindrance during receptor targeting. Full antibody ligands are also immunogenic and have poor stability. In comparison, antibody fragments, including fragment antigen-binding (Fab) region, single-chain variable fragment (scFv), and monovalent fragment, retain specific antigen binding and specificity during nanoparticle conjugation [18]. Of these fragment types, monovalent fragments involve less complicated preparations. The monovalent antibody used in this study is a half-antibody fragment that has better stability than the full-length antibody [19]. We evaluated the effects of our nanosystem on psoriasis mitigation in imiquimod (IMQ)-stimulated keratinocytes and an IMQ-induced psoriasisform lesion mouse model.

## Methods

### Preparation of Dsg3 antibody-conjugated nanoparticles

PLGA (50 mg) and AN2728 (2 mg) or rhodamine 800 (0.2 mg) in dichloromethane were injected into 1,2-distearoyl-*sn*-glycero-3-phosphoethanolamine-*N*-[maleimide(polyethylene glycol)-2000] (DSPE-PEG-maleimide, 1 mg), soybean phosphatidylcholine (SPC, 1 mg), and polyvinyl alcohol emulsifier then immediately rigorously emulsified using a high-power sonicator. This resulted in the formation of PLGA nanoparticles encapsulating AN2728 or rhodamine 800. Dsg3 antibody (50  $\mu$ L, 1 mg/mL, Invitrogen) was reduced to a monovalent fragment by incubating the antibody in 7.5 mM 2-mercaptoethylamine (2ME) in HEPES buffer at 37  $^{\circ}$ C for 1 h [20]. The nanoparticles were incubated with the monovalent antibody for 4 h at room temperature to fabricate Dsg3 antibody-conjugated nanoparticles (DPNPs). Four types of nanoparticles were fabricated with the following compositions from core to outer surface: (i) PLGA matrix, (ii) SPC-decorated surface, (iii) DSPE-PEG-maleimide cross-linker intercalated in the SPC surface, and (iv) anti-Dsg3 antibody conjugated to DSPE-PEG-maleimide (DPNPs). The proposed structure of DPNPs loaded with AN2728 is



illustrated in Figure 1A. The nanoparticles (iii) without antibody conjugation were named PNPs. We removed the solvent by evaporation on a magnetic stirrer for 24 h and purified AN2728- or rhodamine 800-loaded nanoparticles by ultracentrifugation (12,000  $\times g$ ) for 30 min followed by washing thrice and resuspending in phosphate-buffered saline (PBS). The nanodispersions were centrifuged at 48,000  $\times g$  and 4  $^{\circ}C$  for 30 min to withdraw unencapsulated AN2728 in the supernatant. The nanoparticle pellet was reconstituted in water to achieve the desired concentration of AN2728. This procedure ensured complete entrapment of AN2728 or rhodamine 800 in the nanohybrids for further experiments.

### Nanoparticle size measurement

Dynamic light scattering (DLS, Malvern Nano ZS90) was used to measure the particle size distribution, polydispersity index (PDI), and zeta potential of the various nanoparticles. The z-average was calculated as the intensity-based average size from a specific fit to the light scattering correlation function data. The mean of the particle distribution is the z-average and the width determines the PDI.

### Nanoparticle morphology assessment

The morphology of the nanoparticles was visualized by transmission electron microscopy (TEM). A drop of the nanodispersion was deposited onto a grid to form a thin-film without staining. Images were obtained at 200 kV on an ultra-high-resolution TEM (Hitachi HT7800).

### Surface functional group assessment

Fourier transform infrared spectroscopy (FTIR, RX1, Perkin-Elmer) was applied to confirm antibody conjugation on DPNNs and the absence of surface functional groups on PNPs. All experiments were performed at room temperature. The spectral region between 4000 and 400  $cm^{-1}$  was scanned and the spectra were recorded using the KBr disc method.

### Thermogravimetric analysis

Thermal stability of the nanoparticles was determined by thermogravimetric analysis (TGA) using a TA Instrument TGA 2050 thermogravimetric analyzer under nitrogen atmosphere from 25 to 700  $^{\circ}C$ .

### Antibody conjugation efficacy

PNPs and DPNNs were resuspended in equal amounts of ddH<sub>2</sub>O and then protein content was quantified using a Bradford assay. The samples were incubated at room temperature for 10 min, and then absorbance was measured at 590 nm in an enzyme-linked immunosorbent assay (ELISA). To

determine the extent of anti-Dsg3 antibody immobilization, DPNNs were incubated with Alexa Fluor 488-conjugated goat anti-rabbit IgG secondary antibody (Invitrogen) for 1 h at room temperature. After centrifugation, unbound secondary antibody was removed, and the fluorescence of the conjugated secondary antibody was measured using a fluorescence spectrophotometer (Hitachi F2500) and flow cytometer (BD Biosciences FACSCalibur).

### Drug encapsulation efficiency

Nanoparticle precipitate was obtained by ultracentrifugation at 12,000  $\times g$  for 30 min at 4  $^{\circ}C$ . The nanoparticle precipitate was dissolved directly in acetonitrile and the amount of AN2728 in the solution was measured by HPLC. A stainless steel C18 column (25 cm long, 4 mm inner diameter, Merck LiChrospher) was used as the stationary phase. The mobile phase consisted of acetonitrile and ammonium dihydrogen phosphate buffer (65:35). The encapsulated drug was detected by absorption at 282 nm to measure the entrapment efficiency.

### Cell culture

Immortalized human keratinocytes (HaCaT) were obtained from AddexBio and human foreskin fibroblast Hs68 cells were obtained from Bioresource Collection and Research Center. The cells were routinely cultured in Dulbecco's modified eagle medium (DMEM) supplemented with 10% fetal bovine serum and 1% antibiotic-antimycotic in an atmosphere of 5% CO<sub>2</sub> at 37  $^{\circ}C$ . Cells from passages 5-10 were used for the experiments. To activate an inflammatory condition, the cells were stimulated with IMQ (5  $\mu g/mL$ ) for 24 h.

### Cellular uptake efficiency

The fluorescence of the cells was analyzed by flow cytometry after treating with PNPs and DPNNs containing 1  $\mu M$  AN2728 for 8 h. The isotype control of DPNNs was nanocarriers decorated with lymphocyte antigen 6 complex locus G6D (Ly6G) antibody. The conjugation method for anti-Ly6G antibody was the same as that described above for anti-Dsg3 antibody. Fluorescence from a gated population of HaCaT cells labeled with rhodamine 800 was acquired on channel FL3 (> 650 nm) with excitation by a 488 nm solid-state laser. Data were collected from at least 10,000 cells at a flow rate of 35  $\mu L/min$ . A logarithmic scale was used to measure both background and cell fluorescence. Cell internalization of rhodamine 800-labeled nanohybrids was also assessed by confocal fluorescence microscopy (Leica TCS SP8 X AOBs). Cells were labelled with 4',6-diamidino-2-phenylindole (DAPI) and LysoTracker Green DND-26 according to the

manufacturer's instructions (Invitrogen). Images were pseudocolored blue for DAPI, green for LysoTracker, and red for rhodamine 800. The fluorescence intensity of rhodamine 800 was quantified from the captured images using ImageJ software.

### Cytotoxicity assay

HaCaT cells ( $10^5$  cells/well) were seeded in 96-well plates overnight. The cells were incubated with free AN2728 or AN2728-loaded nanoparticles at various concentrations for 24 h. Then, 3-(4,5-dimethylthiazol-2-yl)-2,5-diphenyltetrazolium bromide (MTT) was added to a final concentration of 0.5 mg/mL, and the plates were incubated for 4 h at 37 °C in a 5% CO<sub>2</sub> incubator. The cellular MTT was resolved with DMSO. Absorbance at 550 nm was measured using a spectrophotometer.

### Enzyme-linked immunosorbent assay (ELISA)

The protein expressions of various cytokines and chemokines were measured in HaCaT-conditioned medium following incubation with nanohybrids encapsulating AN2728 (1 µM) for 24 h. Samples were also collected from the back skin tissue of mice exposed to nanohybrids following the methods described below. The levels of cytokines (IL-1β, IL-6, IL-17A, IL-17E, IL-22, IL-23, IFN-γ, TNF-α), and chemokines (IL-8, CXCL1, CXCL2) were measured using commercial kits (BioLegend) following the manufacturer's instructions.

### Chemotaxis assay

A chemotaxis assay was carried out in 24-chamber Transwell plates with a pore size of 3 µm. Neutrophils ( $2.5 \times 10^6$  cells/well) were separated from blood samples of healthy volunteers using a protocol approved by the Institutional Review Board at Chang Gung Memorial Hospital, Taiwan (approval number: 201701925B0). The volunteers provided written informed consent to participate. The procedure for neutrophil purification was previously reported [21]. Neutrophils were added to the upper wells and conditioned medium harvested from IMQ-stimulated HaCaT cells (DMEM supplemented with 0.25% bovine serum albumin (BSA)) pretreated with free AN2728 (1 µM) or AN2728-loaded nanocarriers was added to the lower wells. The plates were stored at 37 °C for 1.5 h and then placed on ice. Then, 0.5 M EDTA (100 µL) was pipetted into each well and incubated for 10 min. The well insert was removed, and the cell suspension was collected for washing. The cells were counted using an automated cell counter kit (Moxi Z, Orflo).

### Immunoblotting

HaCaT cells ( $1 \times 10^5$  cells/well) were seeded onto

12-well plates and serum starved for 24 h. Then, the cells were incubated with IMQ (5 mg/mL) in the presence or absence of free AN2728 (1 µM) or AN2728-loaded nanoparticles. The cells were collected and centrifuged at 400 ×g for 5 min at 4 °C. After probe sonication, the nuclear proteins were obtained by centrifugation at 8000 ×g and 4 °C for 10 min. The final supernatant represented the nuclear protein fraction. The protein concentration was estimated using Protein Assay Dye Reagent (Bio-Rad). The proteins were analyzed by SDS-PAGE and transferred onto polyvinylidene difluoride membranes. The membranes were incubated with phospho (p)-NF-κB or anti-lamin B1 antibody (1:1000, Abcam) overnight at 4 °C. Then, secondary anti-rabbit or anti-mouse horseradish peroxidase antibody (1:2000, Abcam) was added and incubated for 1 h at room temperature, and the bands were visualized using enhanced chemiluminescence reagent.

### Immunocytochemistry

HaCaT cells were grown on coverslips at a density of  $1 \times 10^5$  cells/mL, treated with the indicated treatments, then fixed in 4% paraformaldehyde for 30 min. Cells were permeabilized for 15 min at room temperature with PBS containing 0.2% Triton X-100 and then blocked with 2% BSA for 1 h. The coverslips were then incubated overnight with NF-κB p65 primary antibody (1:200 dilution, GeneTex) at 4 °C, then treated with goat anti-rabbit IgG secondary antibody conjugated with Alexa Fluor 488 (1:1000 dilution, Invitrogen) for 1 h. The coverslips were mounted onto glass slides using Slowfade® Gold Antifade Mountant with DAPI and examined by confocal laser scanning microscopy (Leica TCS SP8 X AOBIS).

### In vivo toxicity assay

Male BALB/c mice (8 weeks old) were used to assay the possible *in vivo* toxicity of the nanohybrids. Free AN2728, AN2728-loaded PNPs and DPNNs, and monovalent Dsg3 antibody (2.5 µg) in 100 µL PBS was subcutaneously injected into the backs of mice (n = 6) every other day for 5 days (3 treatments). The concentration of AN2728 was 5 mg/mL for free form, PNPs, and DPNNs. The control group received PBS only (100 µL). The skin was examined for its gross and microscopic appearances, transepidermal water loss (TEWL), skin surface pH, erythema quantification (a\*), and hematoxylin and eosin (H&E) histology. TEWL, pH, and a\* were determined using a skin physiological evaluation system (MPA580, Courage and Khazaka) with probes positioned onto the treated skin region. The animals were sacrificed by overdose of isoflurane on day 6 for histology. Skin specimens

were fixed in 10% neutral buffered formalin for 24 h, then embedded in paraffin wax, sliced (5  $\mu$ m thickness), and stained with H&E. Hepatic and renal functions were tested to evaluate any possible toxicity of the injected nanoparticles. Plasma was collected from the tail vein before sacrifice. Glutamic oxaloacetic transaminase (GOT), glutamic pyruvic transaminase (GPT), creatinine (CRE) activity, and blood urea nitrogen (BUN) in the plasma were measured using an automated clinical chemistry analyzer (Fuji Dry-Chem 4000i) following the manufacturer's instructions.

### IMQ-induced psoriasis-like skin inflammation model

Psoriasiform skin was induced in the backs of male BALB/c mice (8 weeks old) according to a protocol modified from van der Fits et al. [22]. The animals were categorized into five groups (non-treatment control, IMQ stimulation, free AN2728/IMQ, PNPs/IMQ, and DPNNs/IMQ) with six mice in each group. The dorsal skin of all mice including the control group was shaved. The mice received a daily topical dose of 62.5 mg 5% IMQ cream (Aldara®, 3 M Health Care) on their shaved backs for five consecutive days (days 1-5). Mice in the treatment groups were subcutaneously injected in the back with 100  $\mu$ L free AN2728, PNPs, or DPNNs encapsulated with 5 mg/mL AN2728 on days 1, 3, and 5. Mice in the control group were injected with 100  $\mu$ L double-distilled water. The mice were sacrificed on day 6 by isoflurane overdose. Psoriasis Area and Severity Index (PASI) was objectively scored as described previously [23]. Erythema, scaling, and thickness were recorded independently as a score from 0 to 4. Samples of the dorsal skin were taken for protein extraction and histological visualization. Skin was extracted following a previously described method [24]. For Western blotting of Dsg3 and p-NF- $\kappa$ B, the skin extract was transferred to a nitrocellulose membrane and probed with primary antibodies against Dsg3, NF- $\kappa$ B, and GAPDH overnight at 4 °C. The membrane was washed three times and then incubated with anti-mouse horseradish peroxidase antibody (Abcam) for 1 h. The bound antibody was observed by enhanced chemiluminescence reagent.

### Immunohistochemistry (IHC)

Dorsal skin samples were fixed overnight in 10% neutral buffered formalin, embedded in paraffin, and sectioned. After dewaxing and rehydration, the paraffin-embedded sections were subjected to heat-induced epitope retrieval using Bond Epitope Retrieval Solution 2 (Leica Biosystems), according to

the manufacturer's instructions, then blocked with diluted normal serum. The sections were incubated with rabbit polyclonal anti-mouse IL-17 (MyBioSource MBS2026152), CXCL1 (Invitrogen PA5-86508), CXCL2 (Invitrogen 701126), Ki67 (Abcam ab15580), Ly6G (Abcam ab238132), or myeloperoxidase (MPO, Abcam ab139748) antibody for 1 h at room temperature (1:1000 dilution), washed with saline containing 0.5% Tween 20, and subsequently incubated at ambient temperature with biotinylated donkey anti-rabbit IgG (Jackson ImmunoResearch Laboratories) for 20 min. Color reaction was visualized using an avidin-biotin complex kit (Vectastain Elite, Vector Laboratories). Photomicrographs were obtained using a digital color camera for microscopy (Olympus DP72). To calculate the neutrophil microabscess number in the epidermis, five areas in three independent experimental tissue sections were analyzed with cellSens software (Olympus Life Science).

### Statistical analysis

All data were analyzed using GraphPad Prism 5 software. Data are expressed as mean  $\pm$  SEM. Dual comparisons were made with an unpaired Student's *t*-test. Groups were analyzed by ANOVA with Tukey or Dunnett posttests.

### Ethics

All animal experiments were conducted in strict accordance with the Guidelines for the Institutional Animal Care and Use Committee of Chang Gung University (approval number: CGU107-211) and complied with Directive 86/109/EEC from the European Commission.

## Results

### Nanocarrier fabrication and antibody conjugation

A PLGA core was prepared by emulsion-solvent evaporation and then coated with SPC and DSPE-PEG-maleimide to form lipid-polymer nanohybrids. Full-length anti-Dsg3 antibody was divided into two monovalent fragments using 2ME. The SDS-PAGE profile showed a band for the full-length antibody with a molecular weight of ~150 kDa (Figure S1). The band representing half-fragment monovalent antibody was more mobile in the electric field than the full-length antibody, indicating a successful fragmentation. Monovalent anti-Dsg3 antibody was immobilized to PEG crosslinker on the nanohybrid surface by maleimide-thiol conjugation to generate DPNNs.

The size and morphology of the nanosystems were characterized by DLS and TEM. Bare PLGA



nanoparticles were determined to have an average size of 220 nm by DLS (Table 1), which reduced to 163 nm after SPC decoration because of the emulsifying capability of the phospholipids. SPC-coated nanoparticles with DSPE-PEG-maleimide crosslinker but without antibody conjugation had an average size of 191 nm. This diameter increased to 229 nm upon antibody immobilization (DPNPs). Both PNPs and DPNPs showed a monomodal distribution (Figure 1B). All nanosystems had a PDI of <0.3, suggesting a narrow particle distribution. The TEM micrographs in Fig. 1b show that the nanoparticles are discrete, spherical structures. The zeta potentials of all nanoformulations were negative, with bare PLGA nanoparticles having the largest negative charge

(Table 1). Antibody conjugation significantly shielded the negative charge to near zero (Figure 1C).

**Table 1.** The size, polydispersity index (PDI) and zeta potential of the nanoparticles

| Formulation | Size (nm)   | Polydispersity Index (PDI) | Zeta potential (mV) |
|-------------|-------------|----------------------------|---------------------|
| PLGA        | 220.07±6.61 | 0.05±0.01                  | -26.51±5.65         |
| PLGA+SPC    | 162.50±1.31 | 0.11±0.03                  | -12.12±1.20         |
| PNPs        | 190.50±2.76 | 0.12±0.02                  | -13.25±0.15         |
| DPNPs       | 229.11±3.81 | 0.22±0.01                  | -2.10±0.19          |

DPNPs, the nanoparticles with antibody conjugation; PLGA, poly(lactic-co-glycolic acid); PNPs, the nanoparticles without antibody conjugation; SPC, soybean phosphatidylcholine.

Each value represents mean and SEM ( $n=3$ ).

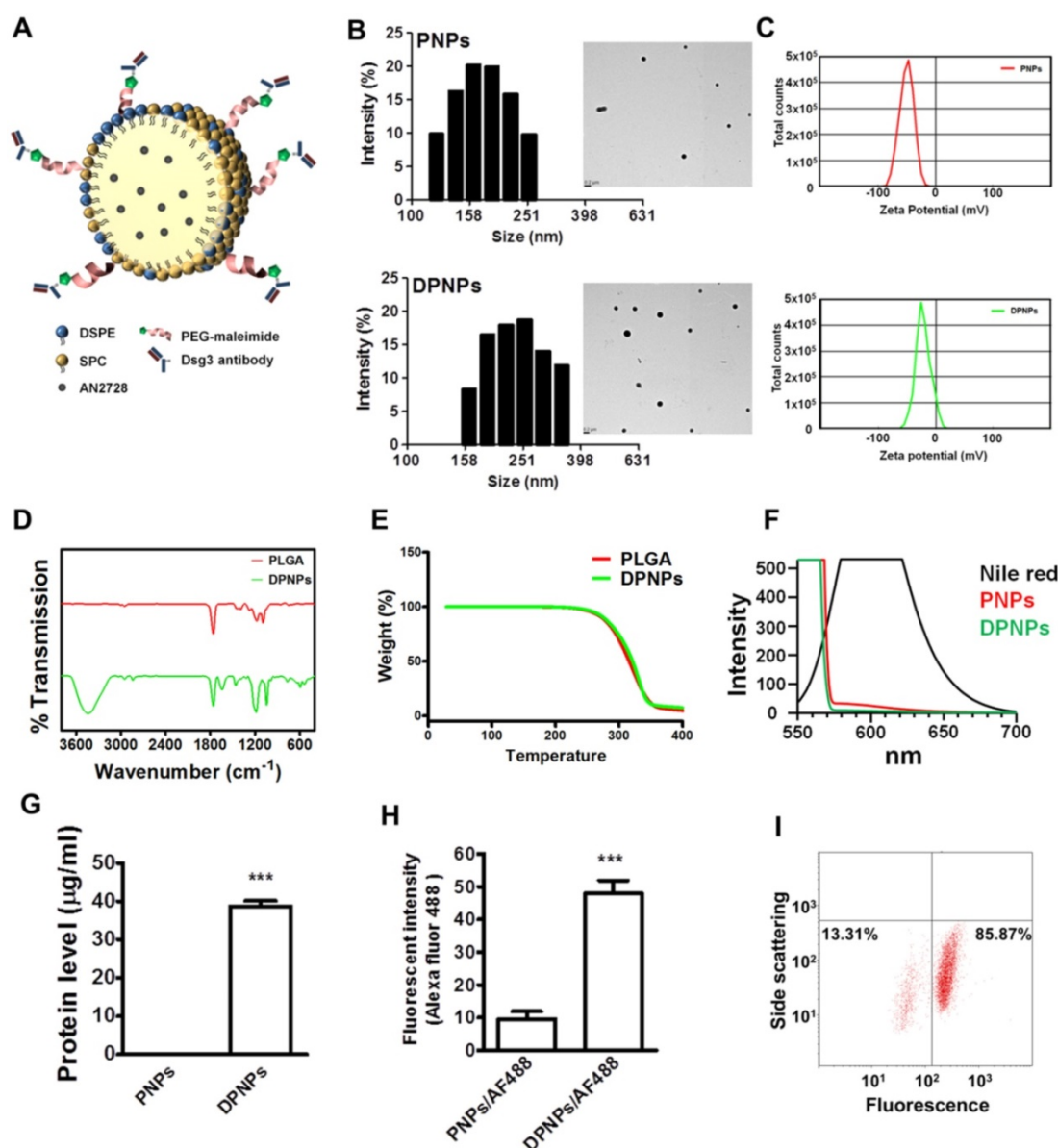


**Figure 1.** Preparation and characterization of lipid-polymer nanohybrids. (A) Schematic diagram of keratinocyte-targeted hybrid nanoparticles. (B) Dynamic laser scattering and transmission electron microscopy verifying the size and shape (spherical) of the nanoparticles. (C) Zeta potential of PNPs and DPNPs. (D) FTIR spectra recorded in the spectral range of 400–4000  $\text{cm}^{-1}$ . (E) TGA data for checking thermal stability. (F) Fluorescence emission profiles of Nile red in hybrid nanoparticles. (G) The standard Bradford protein assay demonstrating the efficacy of antibody conjugation on nanoparticles. (H) Antibody immobilization on the hybrid nanoparticle surface. (I) Flow cytometry detection of the binding efficiency of hybrid nanoparticles. Data are expressed as mean  $\pm$  SEM ( $n=3$ ), \*\*\* $P < 0.001$ .



The impact of antibody conjugation on the properties of the nanoparticles was further assessed by FTIR, TGA, and polarity measurements. The FTIR spectrum for bare PLGA nanoparticles is shown in Figure 1D and is similar to results from previous studies [25, 26]. After antibody conjugation, a peak appeared at  $1600\text{ cm}^{-1}$  to  $1730\text{ cm}^{-1}$  from the carbonyl groups of DSPE-PEG-maleimide and C-S bonding was observed at  $500\text{ cm}^{-1}$  to  $600\text{ cm}^{-1}$ . Also, a strong and wide peak was observed at  $3467\text{ cm}^{-1}$ , which is correlated to the amine and amide groups of the antibody [27, 28]. We then examined the thermal stability of the hybrid nanocarriers by TGA. There was no significant change in thermal stability after antibody conjugation (Figure 1E). Antibody conjugation was further assessed by a polarity assay. The emission spectra of Nile red in acetone, PNPs, and DPNNs are presented in Figure 1F. Nile red fluorescence is quenched in environments with low lipophilicity. The nanoparticles provided a more hydrophilic environment for Nile red than acetone. Nile red emission in DPNNs was weaker than in PNPs, indicating an increase in hydrophilicity after antibody conjugation.

Successful conjugation of the monovalent antibody to the nanohybrids was demonstrated by protein quantification (Figure 1G). To further verify the conjugation, the antibody fragment was labeled with an Alexa Fluor 488-labelled secondary antibody and the fluorescence intensity was measured (Figure 1H). Immobilization of the monovalent antibodies on DPNNs led to a 5-fold increase in Alexa Fluor 488 emission compared to PNPs. Nearly 86% of DPNNs were successfully conjugated with anti-Dsg3 antibody, as measured by flow cytometry (Figure 1I).

### Anti-Dsg3 antibody conjugation enhances keratinocyte uptake of the nanohybrids

To confirm the presence of Dsg3 on keratinocyte membrane, keratinocytes were treated with full-length anti-Dsg3 antibody conjugated with Alexa Fluor 488. Confocal imaging results reveal abundant Dsg3 on the cell membrane of non-treated and IMQ-treated keratinocytes (Figure S2). Next, a cell dissociation assay was conducted to examine if the anti-Dsg3 antibody affects cell-cell adhesion. Both full-length and monovalent antibody treatments maintained keratinocyte aggregation (Figure S3). Therefore, the antibody is not bioactive and is not involved in signal transduction. Keratinocyte uptake of rhodamine 800-loaded PNPs and DPNNs was assessed for 8 h by flow cytometry and confocal microscopy. The flow cytometry results show a dramatic signal shift for DPNNs compared to PNPs (Figure 2A), indicating the specificity of the

monovalent antibody to Dsg3. The isotype control nanoparticles showed no signal shift when compared to PNPs, suggesting that only the Dsg3 antibody was capable of binding the keratinocyte membrane. The fluorescence histogram of Dsg3-negative skin fibroblasts incubated with DPNNs was similar to that of fibroblasts incubated with PNPs. Further, the fluorescence intensity measured by flow cytometry was 6-fold higher in keratinocytes treated with DPNNs than PNPs (Figure 2B). The uptake of nanohybrids in keratinocytes was also parallelly analyzed by confocal image (Figure 2C). Intense fluorescence from Alexa Fluor 488 (pseudocolored red) was detected in the cytoplasm of keratinocytes treated with DPNNs but not PNPs. The morphology of the nuclei (blue) remained intact after treatment. Punctate DPNNs signal was colocalized with lysosomes (green). No red fluorescence was observed in the skin fibroblasts incubated with DPNNs (Figure 2D), suggesting the selective targeting of DPNNs to keratinocytes but not fibroblasts. The fluorescent intensity estimated from the confocal image shows 9-fold stronger uptake of DPNNs in HaCaT cells than of PNPs (Figure 2E). Therefore, the anti-Dsg3 antibody fragment exhibits the potential as a ligand to enhance internalization of the nanohybrids in keratinocytes.

### Actively targeted nanohybrids effectively suppress keratinocyte stimulation

To test whether PDE4 inhibitor-loaded DPNNs could suppress inflammation in IMQ-stimulated keratinocytes by binding to Dsg3, we first evaluated the AN2728 encapsulation efficiency. The entrapment percentages for PNPs and DPNNs were 83% and 50%, respectively (Figure 3A). The nanosystems were centrifuged to remove non-encapsulated AN2728 in the supernatant, and then the nanocarriers were reconstituted in water to achieve the desired concentrations. Thus, all the drug molecules were loaded in the nanohybrids. Treatment with free drug and drug-loaded nanohybrids exerted a dose-dependent decline in IMQ-stimulated keratinocyte viability within the concentration range of 1-100  $\mu\text{M}$  (Figure 3B). This cytotoxic effect was modest, as >80% viability was maintained with 100  $\mu\text{M}$  AN2728. We observed no significant difference in viability between free drug and nanocarriers treatments. Thus, the non-toxic dose of 1  $\mu\text{M}$  was chosen to explore cell uptake and anti-inflammatory activity. We detected marked increases in the levels of the proinflammatory mediators IL-1 $\beta$ , IL-6, IL-8, CXCL1, and CXCL2 in IMQ-stimulated keratinocytes (Figure 3C-G). All AN2728 formulations inhibited the overexpression of these mediators at the protein level. There was no

statistically significant difference in the reductions of IL-1 $\beta$  and IL-8 by free drug and nanocarriers, indicating that not all cytokines could be regulated by AN2728. The general trend in reduction of cytokines/chemokines levels was DPNPs > free

AN2728 > PNPs. Further, compared to the other mediator markers, a greater reduction in IL-6 (55%) and CXCL1 (50%) levels was observed in cells treated with DPNPs.

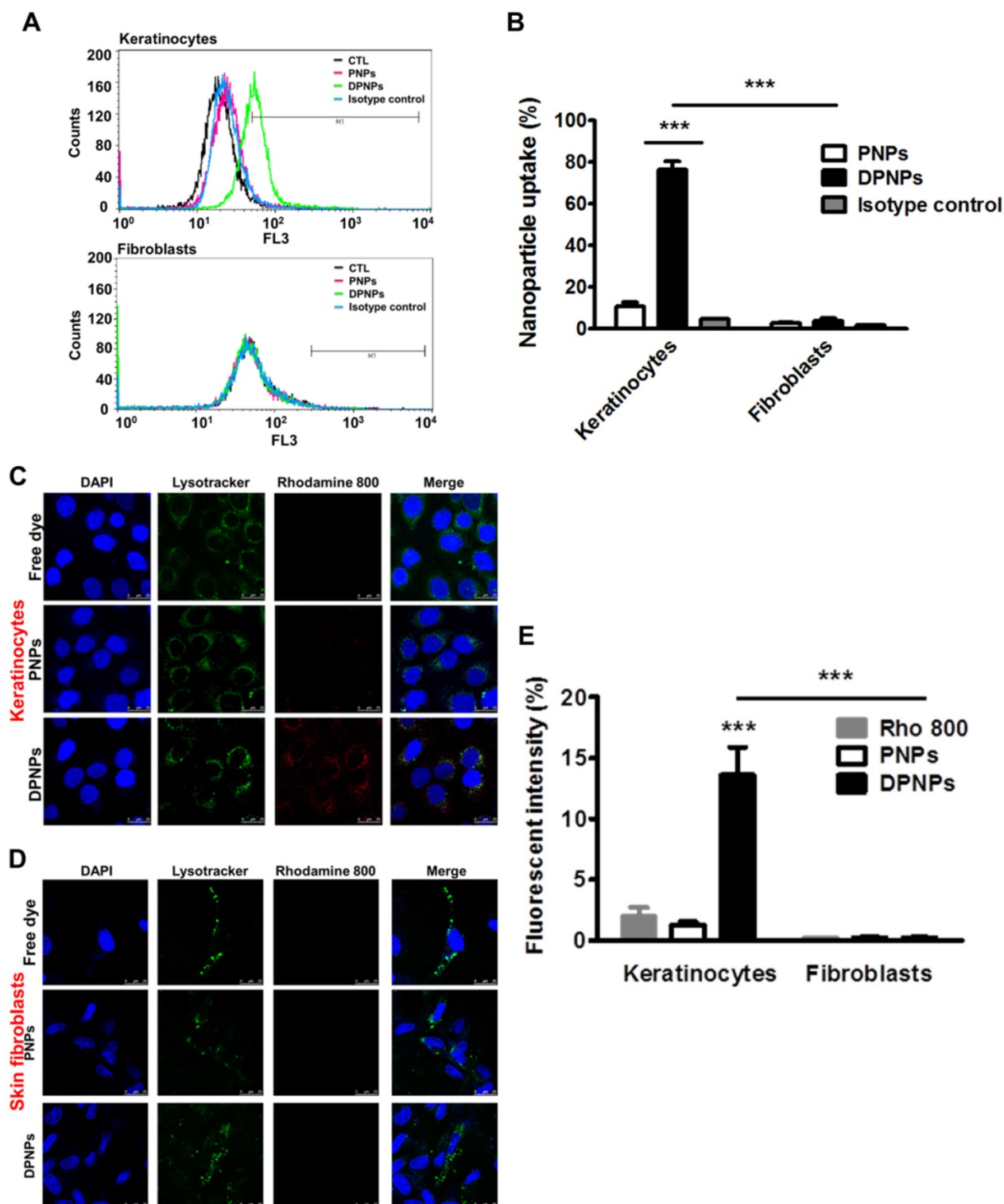


**Figure 2.** *In vitro* targeting efficiency of lipid-polymer nanohybrids. (A) Representative flow cytometry histogram of rhodamine 800-labeled hybrid nanoparticles uptake in human keratinocytes and fibroblasts over a period of 8 h. (B) Percentage of the cell population for human keratinocytes and fibroblasts that has internalized rhodamine 800-labeled hybrid nanoparticles. (C, D) Overlay of DAPI (blue), lysotracker (green), and rhodamine 800 (red) in fluorescence microscopic images showing uptake of rhodamine 800-labeled DPNPs in keratinocytes (HaCaT) and fibroblasts (Hs68) over a period of 8 h. Free rhodamine 800 solution was served as a control. Scale bars, 25  $\mu$ m. (E) The fluorescence intensity was plotted graphically. Data are expressed as mean  $\pm$  SEM (n=4). \*\*\*P < 0.001, compared to control or free dye. The control is the HaCaT cells treated by PBS only.

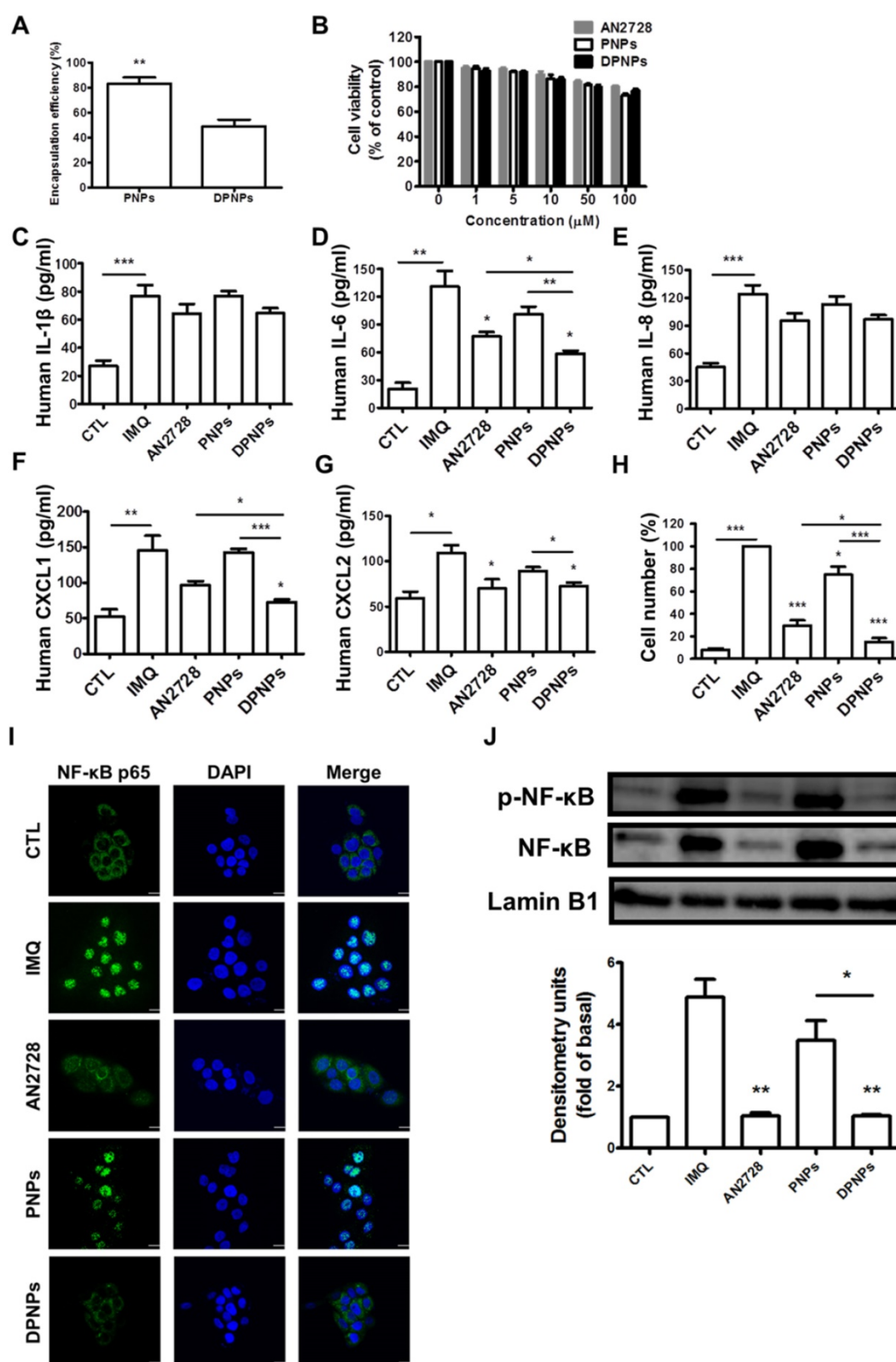


**Figure 3.** The effect of the AN2728-loaded lipid-polymer nanohybrids on cytokine and chemokine expression in IMQ-induced HaCaT keratinocytes. (A) The encapsulation efficiency of nanoparticles. (B) HaCaT keratinocytes were treated with various concentrations of different AN2728-loaded nanoparticles for 24 h. The cell viability of the cells was determined by MTT assay. (C–G) HaCaT keratinocytes were pretreated with free AN2728, PNPs, or DPNPs for 4 h before the addition of IMQ for 24 h, after which, cytokines (C) IL-1β, (D) IL-6 and chemokine (E) IL-8, (F) CXCL1, (G) CXCL2 protein expression was examined using ELISA. (H) Chemotaxis assay of neutrophils from IMQ-induced HaCaT keratinocyte condition medium pretreated with free AN2728, PNPs, or DPNPs before stimulation with IMQ. Scale bars, 25 μm. (I) Representative immunofluorescence of p-NF-κB in HaCaT cells. The cells were pretreated with different condition for 4 h and then stimulated with IMQ. Scale bars, 25 μm. (J) Representative immunoblot analysis using antibodies against p-NF-κB, and lamin B1. Data are expressed as mean ± SEM (n=4). \*  $P < 0.05$ , \*\*  $P < 0.01$ , \*\*\*  $P < 0.001$ , compared with the group of IMQ treatment alone. The statistical difference was also detected between the different treatment groups. The control is the HaCaT cells without IMQ activation.



The chemokines released by keratinocytes are vital for prompting neutrophil infiltration and activation. A chemotaxis assay of human neutrophils

was carried out to examine their migration toward medium conditioned by IMQ-stimulated keratinocytes treated with free drug or nanocarriers.

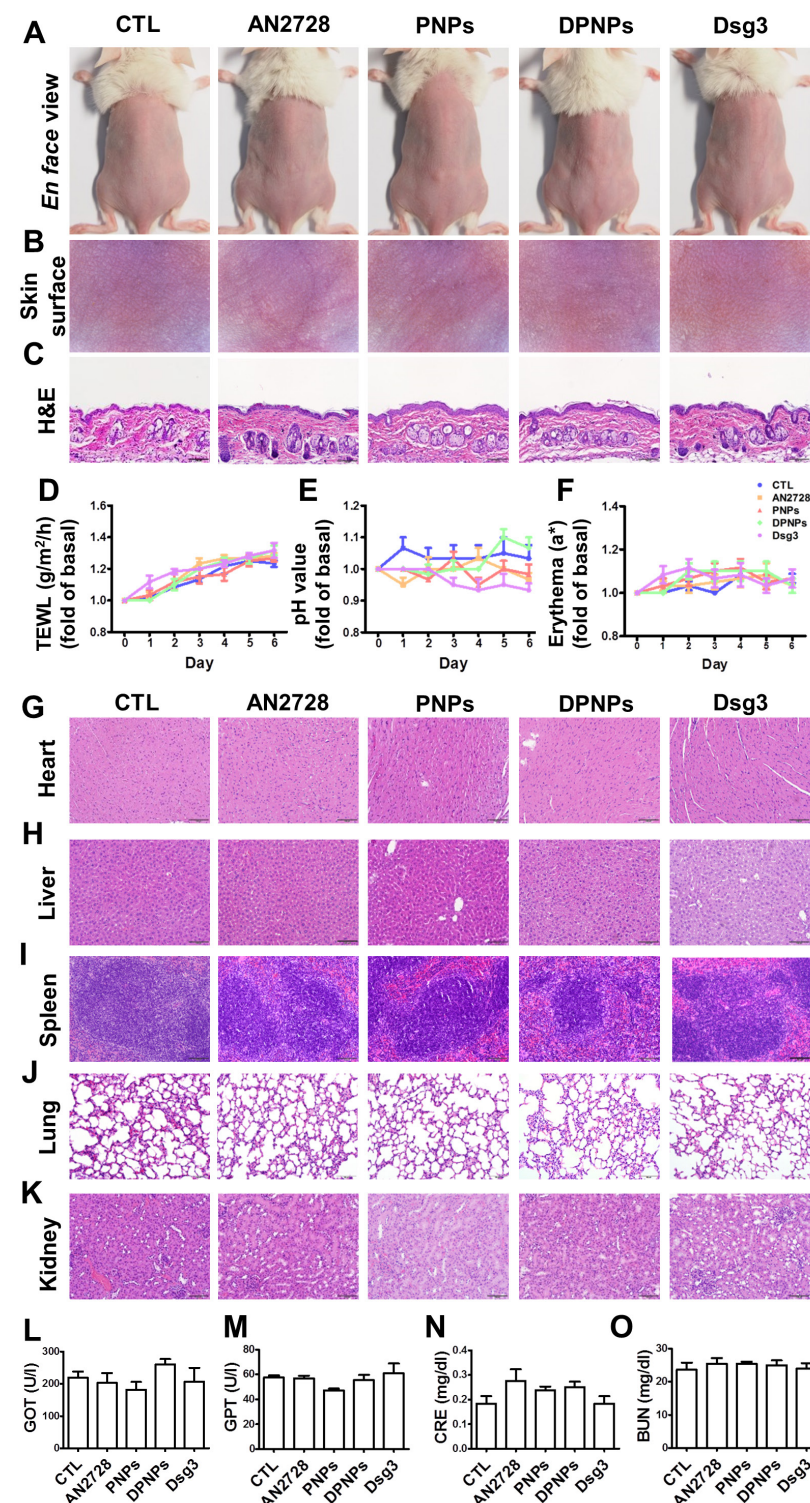


**Figure 4.** Physiological and histological observations for mice received different administration of AN2728, PNPs, DPNPs, or Dsg3 antibody. Mice were intradermally injected with 100  $\mu$ l of 1 mg/ml free AN2728 or different nanoparticles or 2.5  $\mu$ g Dsg3 antibody in PBS on Day 1, 3, and 5. Tissue samples of heart, liver, spleen, lung, kidney, skin, and blood were collected on Day 6: (A) The gross images of mouse back skin were represented on Day 6 by digital camera. (B) The close-up images by hand-held digital microscopy. (C) Skin sections represented by H&E staining. (D) TEWL. (E) skin surface pH value. (F) erythema quantification. H&E staining of (G) heart, (H) liver, (I) spleen, (J) lung, and (K) kidney. Scale bars, 100  $\mu$ m. Blood biochemical parameters of (L) GOT, (M) GPT, (N) CRE, and (O) BUN. Scale bars, 100  $\mu$ m. Data are expressed as mean  $\pm$  SEM (n=6).

The greatest inhibition in neutrophil migration number was observed for DPNPs, followed by free drug and PNPs (Figure 3H). The antibody-conjugated nanocarriers completely restrained neutrophil migration to baseline. PDE4 inhibitor participates crucially in the NF- $\kappa$ B signaling pathway. To further elucidate the role of NF- $\kappa$ B in nanohybrid inhibition of activated keratinocytes, we assessed the IMQ-induced nuclear translocation of p-NF- $\kappa$ B and total NF- $\kappa$ B by confocal microscopy (Figure 3I). This translocation was prevented by AN2728 in keratinocytes. DPNPs dramatically retarded the nuclear expression of p-NF- $\kappa$ B, and this effect was superior to that of PNPs. Western blot demonstrated that both free AN2728 and DPNPs almost completely suppressed p-NF- $\kappa$ B and total NF- $\kappa$ B expressions in the nuclei, while this was not the case for PNPs (Figure 3J). These results, therefore, suggest that the anti-Dsg3 antibody promoted the ability of the drug-loaded nanoparticles to reduce keratinocyte activation by enhancing binding to the cells.

### The nanohybrids demonstrate negligible acute toxicity in the skin and other organs

Administration of nanoparticles or antibodies via a subcutaneous route may evoke skin and systemic side effects. Free drug, PNPs, DPNPs, or free antibody were subcutaneously delivered to healthy mouse skin every two days for five days. The gross and en face appearances of the skin surface did not change after treatment (Figure 4A-B). Histological examination further revealed that the skin morphology remained intact without any significant changes (Figure 4C). During the five days, there was no increase in TEWL, skin pH, or erythema for all the formulations compared with the control (Figure



4D-F). The gradual elevation of TEWL in the control and treated samples over six days could be due to the hydration of epidermis by injection vehicle (water). These results demonstrate that the nanohybrids and antibody were well-tolerated for skin application.

When subcutaneously administered nanoparticles enter the blood or lymphatic vessels, they distribute to the peripheral organs. Histopathological analysis of the major organs including heart, liver, spleen, lung, and kidney reveal no abnormality for all formulations tested (Figure 4G-K). Therefore, these formulations were relatively non-toxic even if they spread to other organs. We also performed blood tests to measure liver and kidney functions (Figure 4L-O). Blood biochemical markers were within normal ranges after treatment. Thus, free AN2728, the nanocarriers, and the monovalent antibody did not inflict any adverse effect over the 5-day treatment.

### Actively targeted nanohybrids effectively mitigate psoriasiform lesions

As a proof of concept, a psoriasis-like animal model was established by topical IMQ intervention, and the *in vivo* anti-inflammatory activity of the nanohybrids was examined and compared to that of free AN2728. Phenotypic and microscopic images of the IMQ-treated skin surface exhibit white scaling,

erythema, and thickening (Figure 5A-B). Subcutaneous injection of free drug partly ameliorated psoriasis-like symptoms. A further improvement was seen in the DPNNPs treatment group. H&E-stained skin sections indicate that IMQ induced epidermal hyperplasia with hyperkeratosis, rete ridge elongation, and dermal immune cell infiltration (Figure 5C). Munro's microabscesses in the stratum corneum were also detected after IMQ treatment. DPNNPs manifested the most significant attenuation of histological pathology, followed by free drug and PNPs. However, there was still some epidermal thickening and immune cell infiltration in DPNNPs-treated psoriasiform skin. Epidermal thickness, desquamation, and erythema were rated and summarized as a PASI score (Figure 5D). The highest total PASI score was obtained for the IMQ treatment. Intervention with DPNNPs decreased the PASI score by 74% compared to IMQ only. The PASI scores for the free drug and PNPs groups fell between those of the DPNNPs and IMQ only groups, presenting limited therapy of the psoriasiform lesion. Free AN2728 and DPNNPs significantly reduced the epidermal thickness from 191 to 103 and 42  $\mu\text{m}$ , respectively (Figure 5E), whereas PNPs did not decrease the IMQ-treated epidermal thickness. IMQ

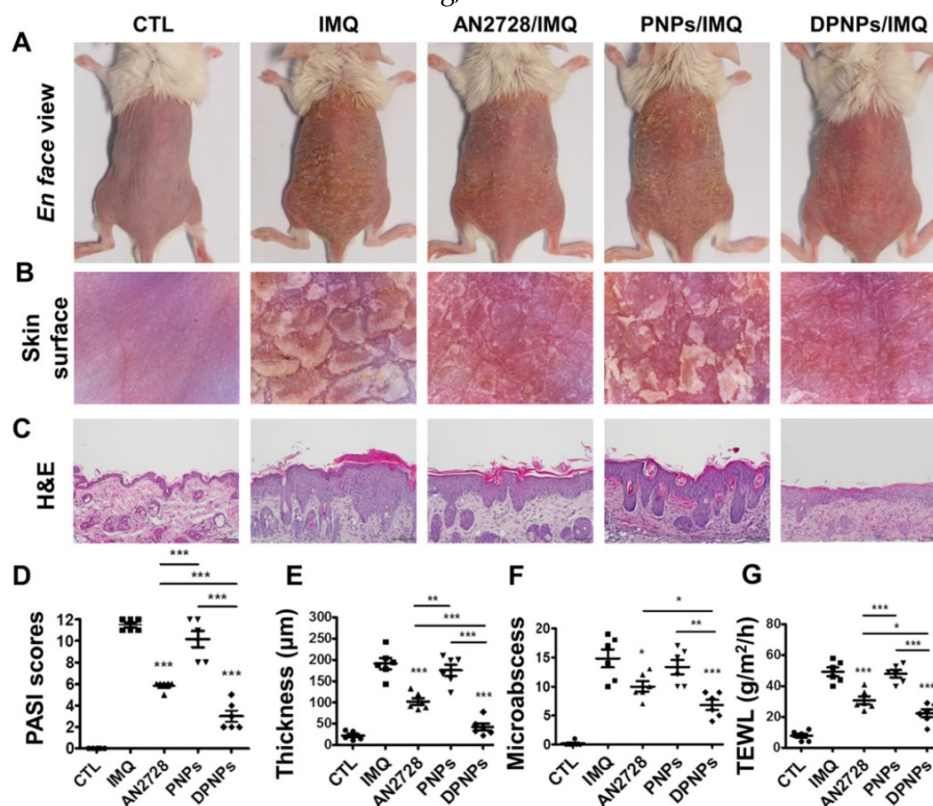


**Figure 5.** The keratinocyte-targeted lipid-polymer nanohybrids attenuate IMQ-induced mouse psoriatic skin inflammation. The mice were subcutaneously application with different nanoparticles for three times on Day 1, 3, and 5, then the psoriasis-like skin were induced by IMQ cream from Day 1 to Day 5. Mouse back skin was collected on Day 6. (A) The gross images of mouse back skin were represented on Day 6 by digital camera. (B) The close-up images by hand-held digital microscopy. (C) Skin sections were represented by H&E staining. Scale bars, 100  $\mu\text{m}$ . (D) Quantification of mouse skin histology using the PASI score. (E) Epidermal thickness quantified by H&E staining. (F) Total counts of abscesses by Ly6G and MPO IHC staining. (G) TEWL measurement. Data are expressed as mean  $\pm$  SEM ( $n=6$ ). \*  $P < 0.05$ , \*\*  $P < 0.01$ , \*\*\*  $P < 0.001$ .

application also led to a marked increase in microabscesses and damaged the barrier function of the skin, as determined by TEWL. Both microabscess number and TEWL were improved by the interventions in the order DPNPs > AN2728 > PNPs (Figure 5F-G).

Inflammation mitigation by the nanoformulations was further evaluated by IHC. Overexpression of IL-17 in psoriasiform plaques, detected with a pan-IL-17 antibody, was reduced by AN2728 and the nanocarriers (Figure 6A). Similar results were observed for the expressions of chemokines CXCL1 and CXCL2 (Figure 6B-C). Compared to free drug and PNPs, DPNPs further suppressed the level of CXCL2. IHC revealed a much higher Ki67<sup>+</sup> cell number in the epidermis of IMQ-treated skin than normal control, suggesting there was significant cell proliferation in the plaque (Figure 6D). Keratinocyte proliferation was arrested by DPNPs but not free drug or PNPs. Neutrophil recruitment in the upper epidermis is the primary contribution of Munro's microabscesses. The location of neutrophils in the skin was visualized by Ly6G and MPO (Figure 6E-F). A cluster of neutrophils was found in the upper epidermis. Neutrophil infiltration was also observed in the dermis. Neutrophil accumulation was attenuated in all treated groups,

especially by DPNPs.

Certain cytokines play essential roles in the development of psoriasis. We detected a series of cytokines in mouse skin (Figure 7A-H). Compared to normal control, the protein levels of cytokines dramatically increased in the skin due to IMQ activation. The mice dosed with free AN2728 had significantly decreased levels of IL-6, IL-17A, IL-22, IL-23, and TNF- $\alpha$  but did not achieve complete attenuation compared to the control. Free AN2728 did not suppress IFN- $\gamma$ , IL-1 $\beta$ , or IL-17E. A similar result was found for the PNPs-treated group. In comparison, DPNPs inhibited the expressions of IFN- $\gamma$ , IL-6, IL-17A, IL-17E, and IL-23 to a greater extent and completely inhibited IL-17A and IL-17E expressions to baseline. DPNPs also thoroughly inhibited the chemokines CXCL1 and CXCL2 (Figure 7I-J). NF- $\kappa$ B is an upstream modulator of immune response. Phosphorylation of NF- $\kappa$ B induces cytokines/chemokines to activate psoriatic inflammation. IMQ application on mouse skin significantly increased the p-NF- $\kappa$ B level in the epidermis (Figure 7K), and this overexpression was prevented by DPNPs. This result was further supported by a western blot assay (Figure 7L). p-NF- $\kappa$ B was downregulated 62% by DPNPs compared to IMQ treatment only.

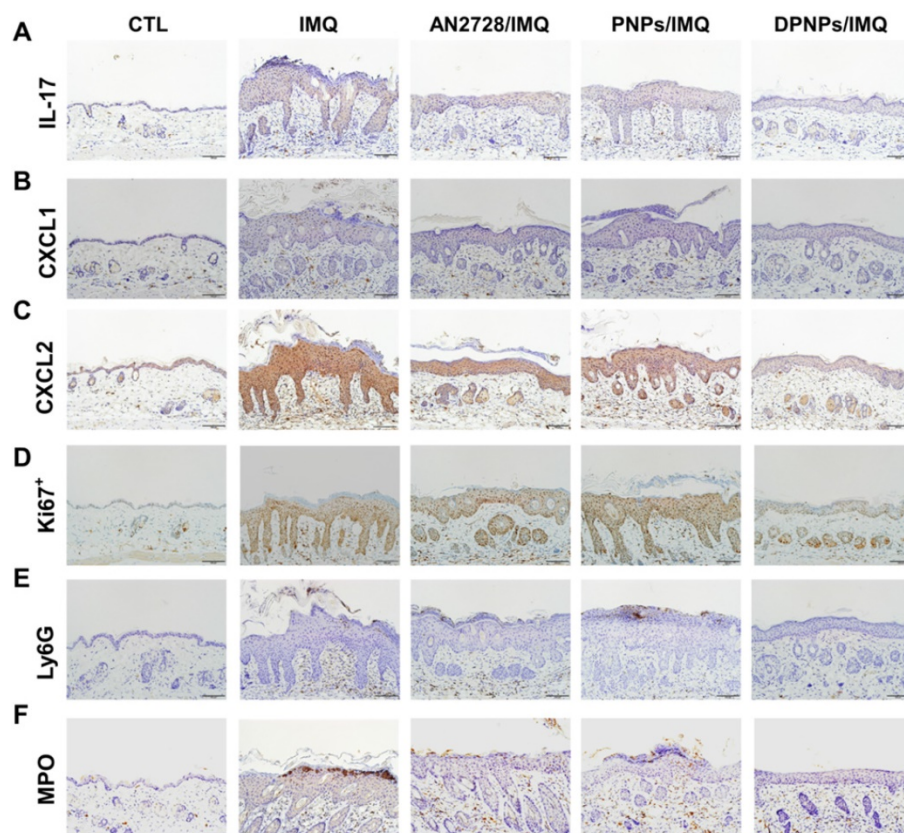


**Figure 6.** The keratinocyte-target lipid-polymer nanohybrids suppress IMQ-induced cytokine and chemokine expression, as well as neutrophil infiltration in psoriasis-like skin. IHC analysis represents (A) IL-17, (B) CXCL1, (C) CXCL2, (D) Ki67<sup>+</sup>, (E) Ly6G, and (F) MPO in psoriasis-like skin. Scale bars, 100  $\mu$ m.

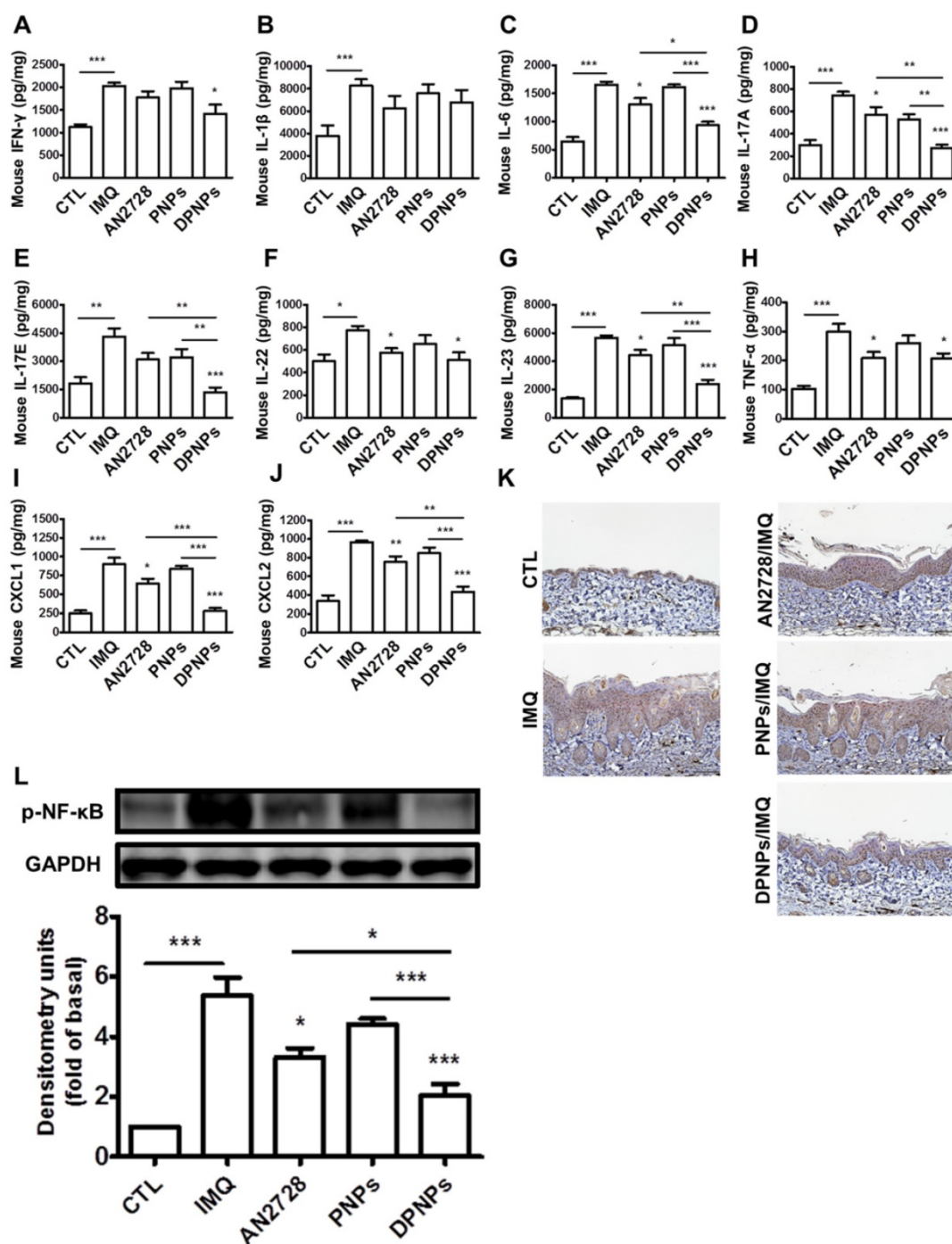


**Figure 7.** The keratinocyte-targeted lipid-polymer nanohybrids downregulate IMQ-induced NF-κB activation leading to the decrease of cytokine and chemokine expression of psoriasis-like skin. The protein expression of (A) IFN-γ, (B) IL-1β, (C) IL-6, (D) IL-17A, (E) IL-17E, (F) IL-22, (G) IL-23, (H) TNF-α, (I) CXCL1, and (J) CXCL2 in IMQ-induced psoriatic skin. (K) Representative IHC staining for p-NF-κB. Scale bars, 100 μm. (L) Immunoblotting analysis with p-NF-κB. DSC, desmocollin; DP, desmoplakin; PG, plakoglobin; PP, plakophilin. Data are expressed as mean ± SEM (n=4). \*P < 0.05, \*\*P < 0.01, \*\*\*P < 0.001, compared with control group.

### Actively targeted nanohybrids broadly accumulate in epidermis after subcutaneous administration

To investigate if the nanocarriers could transit from the dermis to the epidermis and bind to keratinocytes after subcutaneous injection, the distribution of rhodamine 800-loaded nanohybrids in the skin area of the injection site was imaged by

confocal microscopy. First, we examined the distribution of Dsg3 in skin. Both healthy and psoriasiform mouse skin showed Dsg3 expression in the epidermis, as observed by confocal microscopy (Figure S4A). Western blotting also revealed higher Dsg3 expression in psoriasiform skin than in normal skin (Figure S4B). No fluorescence signal from rhodamine 800 was observed in normal mouse skin treated with free dye or PNPs (Figure 8A).



Cumulative fluorescence was observed in the epidermis and hair follicles of healthy mice treated with rhodamine-loaded DPNPs (Figure 8B). Epidermis thickening was observed in IMQ-treated skin (Figure 8C). While no fluorescence attributed to free dye was observed in psoriasis-like skin, faint fluorescence from PNPs was detected in psoriasiform skin. In comparison, antibody incorporation increased nanoparticle transit through the dermis into the epidermis. DPNPs were specifically and evenly distributed throughout the epidermis and hair follicles. The fluorescence intensity in psoriasis-like skin treated with DPNPs was much higher than that treated with free dye or PNPs (Figure 8D). Cumulatively, these results confirm the efficient targeting of the antibody-conjugated nanohybrids to inflamed tissue. The DPNPs could diffuse to the epidermis from the subcutaneous injection site.

## Discussion

Dsg3 is overexpressed during keratinocyte proliferation [29, 30]. We anticipated that decoration of nanocarriers with anti-Dsg3 antibody could enable them to bind to keratinocytes. Therefore, we designed

AN2728-loaded phospholipid-PLGA nanohybrids conjugated with a monovalent anti-Dsg3 antibody. This nanosystem effectively suppressed psoriatic inflammation in cell and animal models. Our data demonstrate that this nanosystem prevented keratinocyte activation and psoriasiform deterioration. The nanoparticles were broadly distributed in the epidermis, where they exerted bioactivity. To our knowledge, this study is the first report investigating antibody-conjugated nanohybrids targeting active keratinocytes to treat cutaneous inflammation. PLGA was used as the nanoparticle matrix because it effectively intercalates the cross-linker and antibody. The SPC coating maintained the lipophilicity of the nanoparticle surface for facile uptake and interaction with cells. We utilized DSPE-PEG-maleimide as the conjugation linker to connect the antibody and nanoparticles. PEGylation also improves resistance to enzymatic degradation and protein binding for prolonged residence in the target site [31]. DPNPs had an average diameter of 229 nm (Table 1), which is around the ideal size ( $\leq 200$  nm) for polymeric nanoparticles to avoid premature clearance by macrophages [32].

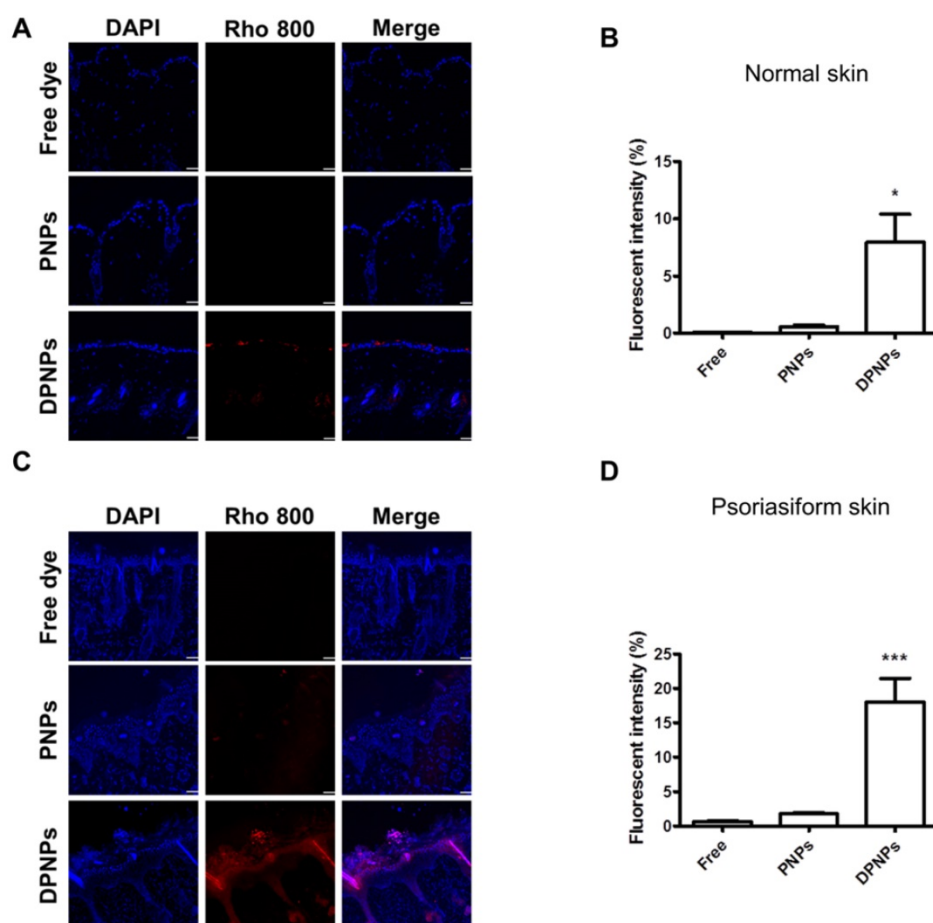


**Figure 8.** Fluorescent distribution of dye-loaded lipid-polymer nanohybrids in frozen skin section after intradermal injection with free dye, PNPs, or DPNPs into (A) normal mice skin and (C) IMQ-induced psoriasis-like mouse skin by confocal microscopy. Scale bars, 10  $\mu$ m. (B, D) Quantification of the mean fluorescence intensity of rhodamine 800 by Leica Application Suite X imaging software. Data are expressed as mean  $\pm$  SEM ( $n=6$ ).



The targeted nanocarriers showed significant internalization by keratinocytes (Figure 2A–B). This result confirmed the conservation of Dsg3 binding activity after reduction of the full antibody to a monovalent antibody fragment. It has been recognized that the cellular uptake efficiency of targeted nanoparticles can be limited in serum because the protein corona masks the targeting ligands [33]. In this study, DPNNs were internalized by keratinocytes within 8 h in culture medium containing serum. The cytosolic distribution of the DPNNs indicated that the nanoparticles penetrated across the cell membrane after initially binding to Dsg3. Lysosomal leakage is generally a critical stage in nanoparticle degradation to release encapsulated drug into the cytoplasm [34]. Based on confocal imaging of LysoTracker-stained keratinocytes (Figure 2C), we propose that once internalized by keratinocytes, the targeted nanohybrids localized to lysosomes, where they were degraded and their drug cargo was liberated.

Keratinocytes are regarded as the first-line cells of the skin-resident immune system to release proinflammatory mediators for immune cell infiltration in psoriasis [35]. A cytotoxicity assay demonstrated that the free drug and drug-loaded nanoformulations did not significantly affect keratinocyte viability (Figure 3B). The nanohybrids also did not cause anti-inflammatory effects on activated keratinocytes. Suppression of keratinocyte activation depends on the intracellular drug dose. Compared with free drug and PNNs, DPNNs better inhibited cytokines/chemokines in keratinocytes (Figure 3C–G) due to their extensive cell uptake via active Dsg3 targeting (Figure 2). Additionally, free AN2728 inhibited cytokines/chemokines more than PNNs. Lipophilic small molecules such as AN2728 can enter cells by passive diffusion when they accumulate outside the cells [36]. In comparison, PEGylated PNNs are sterically hindered from entering cells. Stimulated keratinocytes release chemokines during the early phase of psoriasis to recruit neutrophils and dendritic cells in psoriatic plaque [37]. PDE4 inhibitors effectively suppress chemokine secretion in keratinocytes in a dose-dependent manner [38]. DPNNs better inhibited chemokines than free drug and PNNs (Figure 3F–G), implying that DPNN treatment can best reduce immune cell infiltration. Through chemotaxis analysis, we confirmed significant inhibition of neutrophil migration by DPNNs to nearly baseline (Figure 3H).

Subcutaneous administration of DPNNs dramatically relieved psoriasiform symptoms compared to free drug and PNNs (Figure 5). DPNNs inhibited proinflammatory mediators more than free

AN2728, and this difference was more significant in the animal model than the cell-based assay. This result could be due to the reported poor stability and extensive hydrolysis of free AN2728 to produce inactive metabolites [39]. Loading active agents into a nanoparticle matrix has been shown to prevent drug leaching and protein or enzymatic attack [40]. Although PNNs may also protect loaded AN2728 from degradation, their non-targeted nature led to inefficient delivery and therapy. Additionally, PNNs have a higher surface charge than DPNNs, which may increase clearance by non-targeted immune cells [33]. Nanoparticle size is another factor governing immune cell uptake [41]. A particle diameter of <300 nm is needed to escape uptake by immune cells [42], and DPNNs fit this criterion.

Dsg3 expression predominantly occurs in the squamous epithelium and hair follicles [43, 44]. Subcutaneous nanoparticles must diffuse across the dermis and penetrate tight junctions to reach target keratinocytes. An earlier study demonstrated that 250 nm lipid-based nanoparticles could transport across the keratinocyte monolayer without disturbing the tight junction [45]. DPNNs may reach keratinocytes in this way as they are ~250 nm in size. PEG decoration can also improve nanoparticle permeation across the skin by reducing interactions with cellular barriers, biological fluids, and extracellular matrix [46]. Although PNNs also possess a PEG coating, their high surface charge and steric hindrance to cellular internalization reduce keratinocyte interactions. We also found accumulation of DPNNs in hair follicles where Dsg3 largely distributes. Keratinocytes are the major cells contributing to the follicular epithelium. The follicular epithelium is an insufficient barrier, so nanoparticles readily diffuse from the dermis to the follicular canal [47].

Psoriasis involves interplay between keratinocytes and immune cells. The cytokine production in psoriasis relates to the overstimulation of keratinocytes, dendritic cells, neutrophils, T cells, and macrophages [48]. *In vivo* treatment with free AN2728 had limited impact on cytokine inhibition. In contrast, targeted delivery of the drug in DPNNs significantly increased inhibition (Figure 7A–H). IMQ-induced inflammation development depends critically on IL-17 and IL-23 [49]. IL-23 can be released by dendritic cells, T lymphocytes, and macrophages to activate IL-17A-producing T cells, neutrophils, and mast cells [50]. Keratinocytes respond to cytokines such as IL-17A by upregulating a range of inflammatory products, including IL-1 $\beta$ , IL-6, IL-17E, and chemokines. IL-17E secreted by keratinocytes destabilizes the epidermal barrier by filaggrin inhibition [51]. DPNNs were shown to restrain IL-17E

upregulation and restore skin barrier function, as determined by a reduction in TEWL (Figure 5G). The cytokines/chemokines produced by activated keratinocytes stimulate immune cells to expand the inflammatory response. This becomes a vicious circle prompting keratinocyte proliferation in the lesion area [52]. For instance, keratinocytes are an important IL-22 target in the skin. IL-22 regulates keratinocyte proliferation to induce epidermal hyperplasia in IMQ-induced inflammation [53]. Our data revealed superior suppression of Ki67 expression by DPNPs than other formulations.

Keratinocyte-neutrophil interaction characterizes the early pathogenesis of psoriasis [54]. Stimulated keratinocytes generate neutrophil-tropic chemokines IL-8, CXCL1, and CXCL2 [55]. IL-17E from keratinocytes also recruits neutrophils in psoriasis [56]. The infiltrated neutrophils produce IL-6, IL-17A, and TNF- $\alpha$  to stimulate keratinocytes, resulting in positive feedback to deteriorate psoriasis. DPNPs inhibited the expressions of IL-17E, CXCL1, and CXCL2 to baseline (Figure 7E, I–J). Thus, the neutrophil infiltration was blocked, stalling the vicious loop. IMQ is known to decrease cAMP and then induce NF- $\kappa$ B phosphorylation [24]. This activation enhances expression of IL-1 $\beta$ , IL-6, TNF- $\alpha$ , and chemokines in keratinocytes [57]. PDE4 inhibitors

elevate cellular cAMP by suppressing NF- $\kappa$ B phosphorylation. It is hypothesized that arresting p-NF- $\kappa$ B would be effective in preventing inflammation. Our results suggest that AN2728-loaded nanohybrids inhibit p-NF- $\kappa$ B translocation from cytoplasm to the nucleus (Figure 3J). DPNPs also significantly reduced the distribution of p-NF- $\kappa$ B in the psoriasis-like lesion (Figure 7L). Therefore, this actively targeted nanosystem potentially inhibited overexpressed cytokines/chemokines via the NF- $\kappa$ B pathway, leading to attenuation of keratinocyte activation and neutrophil recruitment (Figure 9). NF- $\kappa$ B is fundamental for cell viability in multiple organs [58]. Its systemic blockade can cause adverse reactions. Our data show that the nanohybrids were well-tolerated in mice with no significant changes in organ histology or biochemical markers following subcutaneous administration. Most studies consider that a PASI reduction of 75% is successful for psoriasis treatment [14]. Our DPNPs fulfilled this aim in decreasing the PASI score by 74%. A limitation of this study is the use of a subcutaneous route for delivering the nanohybrids. We used injection to confirm the contact of intact nanocarriers with keratinocytes. In clinical conditions, topical application may be a feasible choice for convenient and noninvasive administration. The nanohybrids still have the

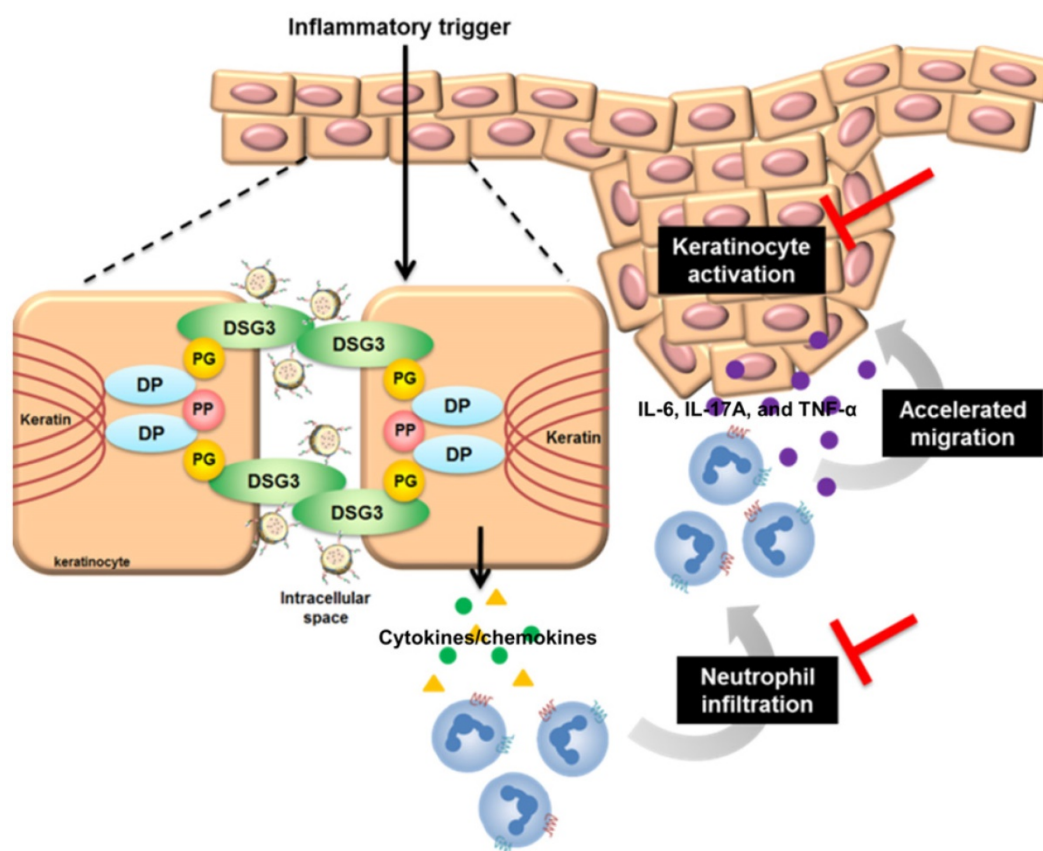


**Figure 9.** The possible anti-inflammatory mechanisms of DPNPs after internalization into activated keratinocytes.

opportunity to facilely permeate into the psoriatic skin because of its dysfunctional barrier. Whether topical delivery is beneficial for treating psoriasis remains to be explored. We expected that the subcutaneous DPNNs diffused to epidermis for exerting anti-inflammatory activity. However, we cannot exclude the possibility that DPNNs diffused to circulation or the skin region not in close contact to the injection site for achieving psoriatic lesion targeting. Further pharmacokinetic study is also needed in the future.

## Conclusions

Anti-Dsg3 antibody-conjugated lipid-polymer nanohybrids were successfully fabricated and loaded with a PDE4 inhibitor to improve the therapeutic efficiency of psoriatic inflammation. Uniquely, this nanosystem uses a monovalent antibody with a small size and less complicated preparation than other antibody fragments. The actively targeted nanocarriers had an average size of 229 nm with a neutral surface charge, implying low protein adsorption and minimized immune cell clearance. DPNNs exhibited Dsg3-mediated cell uptake, which contributed to specific targeting to keratinocytes. DPNNs inhibited cytokine/chemokine overexpression in activated keratinocytes more significantly than free AN2728 and non-targeted nanoparticles. DPNNs also suppressed neutrophil migration by inhibiting keratinocyte-released chemokines. Cytokines/chemokines suppression was involved in the translocation of inhibited p-NF- $\kappa$ B through PDE4 suppression. The actively targeted nanocarriers mitigated psoriasiform symptoms in an IMQ-treated mouse model. DPNNs arrested keratinocyte proliferation and recovered skin barrier function by restraining the production of cytokines/chemokines.

## Supplementary Material

Supplementary figures.

<http://www.thno.org/v11p4567s1.pdf>

## Acknowledgements

The authors are grateful for the financial support from Ministry of Science and Technology of Taiwan (MOST-107-2320-B-182-016-MY3) and Chang Gung Memorial Hospital (CMRPD1J0061-3, CMRPG2H 0361-2, and CMRPG2K0031).

## Competing Interests

The authors have declared that no competing interest exists.

## References

- Huang TH, Lin CF, Alalaiwe A, Yang SC, Fang JY. Apoptotic or antiproliferative activity of natural products against keratinocytes for the treatment of psoriasis. *Int J Mol Sci*. 2019; 20: 2558.
- Greb JE, Goldminz AM, Elder JT, Lebwohl MG, Gladman DD, Wu JJ, et al. Psoriasis. *Nat Rev Dis Primers*. 2016; 2: 1-17.
- Shao S, Gudjonsson JE. Epigenetics of psoriasis. *Adv Exp Med Biol*. 2020; 1253: 209-21.
- Boehncke WH, Schön MP. Psoriasis. *Lancet*. 2015; 386: 983-94.
- Damiani G, Pacifico A, Linder DM, Pigatto PDM, Conic R, Grada A, et al. Nanodermatology-based solutions for psoriasis: state-of-the-art and future prospects. *Dermatol Ther*. 2019; 32: e13113.
- Richards DA, Maruani A, Chudasama V. Antibody fragments as nanoparticle targeting ligands: a step in the right direction. *Chem Sci*. 2017; 8: 63-77.
- Yamamoto Y, Aoyama Y, Shu E, Tsunoda K, Amagai M, Kitajima Y. No activation of urokinase plasminogen activator by anti-desmoglein 3 monoclonal IgG antibodies in cultured human keratinocytes. *J Dermatol Sci*. 2007; 47: 119-25.
- Kouno M, Lin C, Schechter NM, Siegel D, Yang X, Seykora JT, Stanley JR. Targeted delivery of tumor necrosis factor-related apoptosis-inducing ligand to keratinocytes with apemphigus mAb. *J Invest Dermatol*. 2013; 133: 2212-20.
- Ross K. Towards topical microRNA-directed therapy for epidermal disorders. *J Control Release*. 2018; 269: 136-47.
- Simpson E.L., Paller A.S., Boguniewicz M., Eichenfield L.F., Feldman S.R., Silverberg J.L., et al. Crisaborole ointment improves quality of life of patients with mild to moderate atopic dermatitis and their families. *Dermatol Ther*. (Heidelberg) 2018; 8: 605-19.
- Akama T, Baker SJ, Zhang YK, Hernandez V, Zhou H, Sanders V, et al. Discovery and structure-activity study of a novel benzoxaborole anti-inflammatory agent (AN2728) for the potential topical treatment of psoriasis and atopic dermatitis. *Bioorg Med Chem Lett*. 2009; 19: 2129-32.
- Pomadakis CE, Han G. New and emerging topical therapies for psoriasis and atopic dermatitis. *J Clin Aesthet Dermatol*. 2019; 12: 28-34.
- Wcisło-Dziadecka D, Zbiciak-Nylec M, Brzezińska-Wcisło L, Bebenek K, Kaźmierczak A. Newer treatments of psoriasis regarding IL-23 inhibitors, phosphodiesterase 4 inhibitors, and Janus kinase inhibitors. *Dermatol Ther*. 2017; 30: e12555.
- Palfreeman AC, McNamee KE, McCann FE. New developments in the management of psoriasis and psoriatic arthritis: a focus on apremilast. *Drug Des Develop Ther*. 2013; 7: 201-10.
- Date T, Nimbalkar V, Kamat J, Mittal A, Mahato RI, Chitkara D. Lipid-polymer hybrid nanocarriers for delivering cancer therapeutics. *J Control Release*. 2018; 271: 60-73.
- Xu C, Chen X, Yang M, Yuan X, Zhao A, Bao H. Simple strategy for single-chain fragment antibody-conjugated probe construction. *Life Sci*. 2019; 239: 117052.
- Jeong S, Park J.Y., Cha M.G., Chang H., Kim Y.I., Kim H.M., et al. Highly robust and optimized conjugation of antibodies to nanoparticles using quantitatively validated protocols. *Nanoscale*. 2017; 9: 2548.
- Sharma H, Mutharasan R. Half antibody fragments improve biosensor sensitivity without loss of selectivity. *Anal Chem*. 2013; 85: 2472-7.
- Makaraviciute A, Jackson CD, Millner PA, Ramanaviciene A. Considerations in producing preferentially reduced half-antibody fragments. *J Immunol Methods*. 2016; 429: 50-6.
- Vij N, Min T, Bodas M, Gorde A, Roy I. Neutrophil targeted nano-drug delivery system for chronic obstructive lung diseases. *Nanomed Nanotechnol Biol Med*. 2016; 12: 2415-27.
- Yu HP, Hsieh PW, Chang YJ, Chung PJ, Kuo LM, Hwang TL. 2-(2-Fluorobenzoamido)benzoate ethyl ester (EFB-1) inhibits superoxide production by human neutrophils and attenuates hemorrhagic shock-induced organ dysfunction in rats. *Free Radic Biol Med*. 2011; 50: 1737-48.
- van der Fits L, Mourits S, Voerman JS, Kant M, Boon L, Laman JD, et al. Imiquimod-induced psoriasis-like skin inflammation in mice is mediated via the IL-23/IL-17 axis. *J Immunol*. 2009; 182: 5836-45.
- Sumida H, Yanagida K, Kita Y, Abe J, Matsushima K, Nakamura M, et al. Interplay between CXCR2 and BLT1 facilitates neutrophil infiltration and resultant keratinocyte activation in a murine model of imiquimod-induced psoriasis. *J Immunol*. 2014; 192: 4361-9.
- Lin ZC, Hsieh PW, Hwang TL, Chen CY, Sung CT, Fang JY. Topical application of anthranilate derivatives ameliorates psoriatic inflammation in a mouse model by inhibiting keratinocyte-derived chemokine expression and neutrophil infiltration. *FASEB J*. 2018; 32: 6783-95.
- Marques DR, Dos Santos L, O'Brien MA, Cartmell SH, Gough JE. *In vitro* evaluation of poly (lactic-co-glycolic acid)/polyisoprene fibers for soft tissue engineering. *J Biomed Mater Res B Appl Biomater*. 2017; 105: 2581-91.
- Lu B, Lv X, Le Y. Chitosan-modified PLGA nanoparticles for control-released drug delivery. *Polymers*. 2019; 11: 304.
- Esfandiyari-Manesh M, Abdi M, Talasaz AH, Ebrahimi SM, Atyabi F, Dinarvand R. S2P peptide-conjugated PLGA-Maleimide-PEG nanoparticles containing Imatinib for targeting drug delivery to atherosclerotic plaques. *Daru J Pharm Sci*. 2020; 28: 131-8.
- Saei A, Asfia S, Kouchakzadeh H, Rahmandoust M. Antibody-modified magnetic nanoparticles as specific high-efficient cell-separation agents. *J Biomed Mater Res B Appl Biomater*. 2020; 108: 2633-42.



29. Hartlieb E, Kempf B, Partilla M, Vigh B, Spindler V, Waschke J. Desmoglein 2 is less important than desmoglein 3 for keratinocyte cohesion. *PLoS ONE*. 2013; 8: e53739.
30. Uttagomol J, Ahmed US, Rehman A, Huang Y, Laly AC, Kang A, et al. Evidence for the desmosomal cadherin desmoglein-3 in regulating YAP and phosphor-YAP in keratinocyte responses to mechanical forces. *Int J Mol Sci*. 2019; 20: 6221.
31. Marques AC, Costa PJ, Velho S, Amaral MH. Functionalizing nanoparticles with cancer-targeting antibodies: a comparison of strategies. *J Control Release*. 2020; 320: 180-200.
32. Zhao P, Wang H, Yu M, Cao S, Zhang F, Chang J, et al. Paclitaxel-loaded, folic-acid-targeted and TAT-peptide-conjugated polymeric liposomes: *in vitro* and *in vivo* evaluation. *Pharm Res*. 2010; 27: 1914-26.
33. Li J, Ghatak S, El Masry MS, Das A, Liu Y, Roy S, et al. Topical lyophilized targeted lipid nanoparticles in the restoration of skin barrier function following burn wound. *Mol Ther*. 2018; 26: 2178-88.
34. Yu HP, Liu FC, Umoro A, Lin ZC, Elzoghby AO, Hwang TL, et al. Oleic acid-based nanosystems for mitigating acute respiratory distress syndrome in mice through neutrophil suppression: how the particulate size affects therapeutic efficiency. *J Nanobiotechnol*. 2020; 18: 25.
35. Monteleone G, Pallone F, MacDonald TT, Chimenti S, Costanzo A. Psoriasis: from pathogenesis to novel therapeutic approaches. *Clin Sci*. 2011; 120: 1-11.
36. Yang YS, Moynihan KD, Bekdemir A, Dichwalkar TM, Noh MM, Watson N, et al. Targeting small molecule drugs to T cells with antibody-directed cell-penetrating gold nanoparticles. *Biomater Sci*. 2019; 7: 113.
37. Albanesi C, Madonna S, Gisondi P, Girolomoni G. The interplay between keratinocytes and immune cells in the pathogenesis of psoriasis. *Front Immunol*. 2018; 9: 1549.
38. Bäumer W, Kietzmann M. Effect of cyclosporin A and cilomilast on activated canine, murine and human keratinocytes. *Vet Dermatol*. 2007; 18: 107-14.
39. Jarnagin K, Chanda S, Coronado D, Ciaravino V, Zane LT, Guttman-Yassky E, et al. Crisaborole topical ointment, 2%: a nonsteroidal, topical, anti-inflammatory phosphodiesterase 4 inhibitor in clinical development for the treatment of atopic dermatitis. *J Drugs Dermatol*. 2016; 15: 390-6.
40. Lin CY, Hsu CY, Elzoghby AO, Alalaiwe A, Hwang TL, Fang JY. Oleic acid as the active agent and lipid matrix in cilomilast-loaded nanocarriers to assist PDE4 inhibition of activated neutrophils for mitigating psoriasis-like lesions. *Acta Biomater*. 2019; 90: 350-61.
41. Hoshyar N, Gray S, Han H, Bao G. The effect of nanoparticle size on *in vivo* pharmacokinetics and cellular interaction. *Nanomedicine*. 2016; 11: 673-92.
42. Boraschi D, Italiani P, Palomba R, Decuzzi P, Duschl A, Fadeel B, et al. Nanoparticles and innate immunity: new perspectives on host defense. *Semin Immunol*. 2017; 34: 33-51.
43. Mao X, Cho MJT, Ellebrecht CT, Mukherjee EM, Payne AS. Stat3 regulates desmoglein 3 transcription in epithelial keratinocytes. *JCI Insight*. 2017; 2: e92253.
44. Wu H, Stanley JR, Cotsarelis G. Desmoglein isotype expression in the hair follicle and its cysts correlates with type of keratinization and degree of differentiation. *J Invest Dermatol*. 2003; 120: 1052-7.
45. Silva E, Barreiros L, Segundo MA, Costa Lima SA, Reis S. Cellular interactions of a lipid-based nanocarrier model with human keratinocytes: unraveling transport mechanisms. *Acta Biomater*. 2017; 53: 439-49.
46. Frombach J, Unbehauen M, Kurniasih IN, Schumacher F, Volz P, Hadam S, et al. Core-multishell nanocarriers enhance drug penetration and reach keratinocytes and antigen-presenting cells in intact human skin. *J Control Release*. 2019; 299: 138-48.
47. Hsu CY, Yang SC, Sung CT, Weng YH, Fang JY. Anti-MRSA malleable liposomes carrying chloramphenicol for ameliorating hair follicle targeting. *Int J Nanomed*. 2017; 12: 8227-38.
48. Kim J, Krueger JG. The immunopathogenesis of psoriasis. *Dermatol Clin*. 2015; 33: 13-23.
49. Yoshiki R, Kabashima K, Honda T, Nakamizo S, Sawada Y, Sugita K, et al. IL-23 from Langerhans cells is required for the development of imiquimod-induced psoriasis-like dermatitis by induction of IL-17A-producing  $\gamma\delta$  T cells. *J Invest Dermatol*. 2014; 134: 1912-21.
50. Leys J, Wang Y, Paulsboe S, Edelmayer R, Salte K, Wetter J, et al. Characterization of psoriasiform dermatitis induced by systemic injection of interleukin-23 minicircles in mice. *J Dermatol*. 2019; 46: 482-97.
51. Boehncke WH, Brembilla NC. Unmet needs in the field of psoriasis: pathogenesis and treatment. *Clin Rev Allergy Immunol*. 2018; 55: 295-311.
52. Lowes MA, Suárez-Fariñas M, Krueger JG. Immunology of psoriasis. *Ann Rev Immunol*. 2014; 32: 227-55.
53. Van Belle AB, de Heusch M, Lemaire MM, Hendrickx E, Warnier G, Dunussi-Joannopoulos K, et al. IL-22 is required for imiquimod-induced psoriasiform skin inflammation in mice. *J Immunol*. 2012; 188: 462-9.
54. Jiang M, Fang H, Shao S, Dang E, Zhang J, Qiao P, et al. Keratinocyte exosomes activate neutrophils and enhance skin inflammation in psoriasis. *FASEB J*. 2019; 33: 13241-53.
55. Chiang CC, Cheng WJ, Korinek M, Lin CY, Hwang TL. Neutrophils in psoriasis. *Front Immunol*. 2019; 10: 2376.
56. Senra L, Mylonas A, Kavanagh R, Fallon PG, Conrad C, Borowczyk-Michalowska J, et al. IL-17E (IL-25) enhances innate immune responses during skin inflammation. *J Invest Dermatol*. 2019; 139: 1732-42.
57. Li L, Cataisson C, Flowers B, Fraser E, Sanchez V, Day CP, et al. Topical application of a dual ABC transporter substrate and NF- $\kappa$ B inhibitor blocks multiple sources of cutaneous inflammation in mouse skin. *J Invest Dermatol*. 2019; 139: 1506-15.
58. Zhang Q, Lenardo MJ, Baltimore D. 30 years of NF- $\kappa$ B: a blossoming of relevance to human pathobiology. *Cell*. 2017; 168: 37-57.





# Analysis and formation of polycyclic aromatic hydrocarbons and cholesterol oxidation products in thin slices of dried pork during processing

Yu-Ting Hung<sup>a</sup>, Yu-Tsung Lee<sup>b</sup>, Baskaran Stephen Inbaraj<sup>a</sup>, Kandi Sridhar<sup>a</sup>, Bing-Huei Chen<sup>a,c,\*</sup>

<sup>a</sup> Department of Food Science, Fu Jen Catholic University, New Taipei City 242, Taiwan

<sup>b</sup> Research Center for Chinese Herbal Medicine and Research Center for Food and Cosmetic Safety, Chang Gung University of Science and Technology, Taoyuan City 333, Taiwan

<sup>c</sup> Department of Nutrition, China Medical University, Taichung 404, Taiwan

## ARTICLE INFO

### Keywords:

Polycyclic aromatic hydrocarbons (PAHs)  
Cholesterol oxidation products (COPs)  
Thin slices of dried pork  
QuEChERS  
GC-MS  
GC-MS/MS

## ABSTRACT

This study aims to determine toxic compounds polycyclic aromatic hydrocarbons (PAHs) and cholesterol oxidation products (COPs) in thin slices of dried pork as affected by different flavorings and roasting temperature treatments through employing a QuEChERS method coupled with gas chromatograph–tandem mass spectrometer (GC-MS/MS) and gas chromatograph–mass spectrometer (GC-MS), respectively. By employing this method, high accuracy and precision was attained for freeze-dried pork hind leg sample. Following addition of 8 different flavorings with roasting temperature at 120, 160, and 200 °C, the levels of total COPs and PAHs in thin slices of dried pork followed a temperature-dependent increase during roasting, which was further confirmed by principle component analysis. High level of soy sauce or sugar inhibited COP formation, while the low-level minimized PAH formation in thin slices of dried pork during roasting. Sugar was more effective in inhibiting COP formation while soy sauce was more efficient in reducing PAH formation.

## 1. Introduction

Polycyclic aromatic hydrocarbons (PAHs), composed of only carbon and hydrogen atoms with two or more aromatic rings, can be formed through incomplete combustion or pyrolysis of coal, oil, gas and wood. According to a report issued by European Food Safety Authority (2008) and European Commission (2011), a total of 24 PAHs have been listed as the most frequently occurring PAHs in food and environment. Of the various PAHs, benzo[a]pyrene (BaP) was classified into Group 1 carcinogens (carcinogenic to humans), cyclopenta[c,d]pyrene (CPP), dibenzo[a,h]anthracene (DBaA) and dibenzo[a,i]pyrene (DBaIP) classified into Group 2A carcinogens (probable human carcinogen), naphthalene (NaP), benzo[a]anthracene (BaA), chrysene (CHR), 5-methylchrysene (MCH), benzo[b]fluoranthene (BbFA), benzo[j]fluoranthene (BjFA), indeno[1,2,3-c,d]pyrene (IP), dibenzo[a,i]pyrene (DBaIP), and dibenzo[a,h]pyrene (DBaHP) classified into Group 2B carcinogens (possible human carcinogen), acenaphthene (AcP), fluorene (Flu), phenanthrene (Phe), anthracene (Ant), pyrene (Pyr), benzo[c]fluorene (BcF), dibenzo[a,e]pyrene (DBaEP) and benzo[ghi]perylene

(BghiP) classified into Group 3 (not carcinogenic to human) based on a report issued by the International Agency for Research on Cancer (IARC, 2012).

Human exposure to PAHs has been reported to be mainly from air pollution and processed foods, especially edible oil and meat products (Alomirah et al., 2011). In a study dealing with vegetable oils in canned foods, a BaP level of > 0.0020 and 0.0019 mg/L were reported in sunflower oil of 15% canned vegetable samples and olive oil from canned tuna fish, while the highest level of 0.0113 mg/L was shown in oil from canned mushroom (Moret, Purcaro, & Conte, 2005). In a later study, Chen, Kao, Chen, Huang, and Chen (2013) demonstrated that the longer the sugar smoking time, the more the formation of PAHs in meat. Following sugar smoking for 6 min, red meat could produce the highest level of total PAHs (0.0339–0.1255 mg/L), followed by poultry meat (0.0191–0.0282 mg/L) and fish meat (0.0091–0.0318 mg/L) with the highly toxic BaP being undetected.

Cholesterol oxidation products (COPs), formed from cholesterol in the presence of heat, light, free radical, enzyme or metal ion, can be generated in high level in cholesterol-rich foods such as eggs and animal

\* Corresponding author.

E-mail address: [002622@mail.fju.edu.tw](mailto:002622@mail.fju.edu.tw) (B.-H. Chen).

<https://doi.org/10.1016/j.foodchem.2021.129474>

Received 14 November 2020; Received in revised form 8 February 2021; Accepted 22 February 2021

Available online 7 March 2021

0308-8146/© 2021 Elsevier Ltd. All rights reserved.

meats (Lee, Chien, & Chen, 2008). The mechanism of cholesterol oxidation is similar to lipid oxidation, with autoxidation, enzymatic oxidation and photooxidation dominating based on the formation route of various types of COPs reported elsewhere (Chen, Lu, Chien, & Chen, 2010). Of the various COPs, the epoxy-containing COPs (5,6 $\alpha$ -epoxycholesterol, 5,6 $\alpha$ -EP or 5,6 $\beta$ -epoxycholesterol, 5,6 $\beta$ -EP) were reported to possess high mutagenicity (Sevanian & Peterson, 1986), while triol was shown to induce carcinogenicity through over expression of COX-2 and subsequent increased production of PGE2 (Lo, 2005). It has been well documented that many factors such as heating condition, cooking method, light and the presence of oxygen or oxidizing agent can alter both variety and amount of COPs formed in foods (Hsu & Chen, 2020; Hsu, Inbaraj, & Chen, 2020). For instance, Derewiaka and Molińska (2015) studied the effect of temperature (120–220 °C) and time length (30–180 min) on COP formation and reported that the highest level of total COPs was generated at 150 °C for 120 min with 7-keto dominating, while the cholesterol degradation occurred with temperature  $\geq$  180 °C.

The analysis of PAHs or COPs in meat and meat products has been difficult due to presence of trace amount (ppb for PAHs and ppm for COPs) and complex matrix in meat. Many methods have been developed to determine PAHs or COPs in meat products, including extraction by solvent, purification by solid-phase extraction, and identification and quantitation by GC-MS or HPLC-MS (Gosetti et al., 2011; Lee, Chien, & Chen, 2008). However, most extraction and purification methods are time consuming. Recently, the QuEChERS method has been developed to extract and purify COPs or PAHs in various meat products (Chiu, Kao, & Chen, 2018; Kao, Chen, Chen, Huang, & Chen, 2012). Its application in the determination of pesticides, animal drugs, mycotoxins, acrylamides, environmental hormones and bisphenols in various kinds of food products have been well documented (Rejczak & Tuzimski, 2015). The major advantages of QuEChERS method include simplicity, fastness and cost-effectiveness involving minimum pretreatment steps (minimizes both time and experimental error), less solvent consumption and attainment of excellent recoveries (Musarurwa, Chimuka, Pakade, & Tavengwa, 2019). However, the application of QuEChERS method coupled with GC-MS/MS and GC-MS for determination of PAHs and COPs in thin slices of dried pork remains unexplored. Also, there is a paucity of data regarding their formation as affected by flavorings containing sugar and soy sauce as well as the other ingredients at different roasting temperatures. Thus, in this study we intend to evaluate current QuEChERS methods coupled with GC-MS/MS and GC-MS for determination of PAHs and COPs, respectively, in thin slices of dried pork, a popular meat commodity in Asian countries especially Taiwan and China, as affected by 8 flavorings containing different levels of sugar

(0, 4, 8, 16%) and soy sauce (0, 4 and 8%) and 3 roasting temperatures (120, 160 and 200 °C).

## 2. Materials and methods

### 2.1. Preparation of thin slices of dried pork

Pork hind leg samples were purchased from 10 different commercial vendors in a local market of New Taipei City, Taiwan. After removal of fascia and fur, the pork hind leg samples were homogenized into minced meat, divided into several portions of about 100 g each, vacuum packed and stored in a refrigerator at 4 °C for further use. Then each portion was seasoned with different flavorings including salt (1.5 g/100 g; 1.5%), soybean oil (5 g/100 g; 5%), black pepper (1 g/100 g; 1%), almond slices (1 g/100 g; 1%) as well as various proportions of sugar (0, 4, 8 or 16 g/100 g; 0, 4, 8 or 16%) and soy sauce (0, 4 or 8 g/100 g; 0, 4 or 8%). In the subsequent sections the proportion of all the flavorings will be expressed as percentage. Fig. 1 illustrates 8 different flavoring treatments along with their composition used in this study. The proportions of salt, soybean oil, black pepper and almond slices as shown above was fixed, while both sugar and soy sauce were added in 8 different proportions: 8% sugar plus 8% soy sauce and the other ingredients (standard flavoring, STF), 8% sugar plus 4% soy sauce and the other ingredients (F1), 4% sugar plus 8% soy sauce and the other ingredients (F2), 16% sugar plus 4% soy sauce and the other ingredients (F3), 4% sugar plus 4% soy sauce and the other ingredients (F4), 16% sugar plus 8% soy sauce and the other ingredients (F5), the STF without soy sauce (F6), and the STF without sugar (F7). The STF, composed of 8% sugar, 8% soy sauce, 1.5% salt, 5% soybean oil, 1% black pepper, and 1% almond slices, was selected as it is often used in many factories for processing thin slices of dried pork with a roasting temperature 160 °C in Taiwan. As a decrease in COP formation in thin pork slices was observed following a rise in both sugar and soy sauce levels (sugar more effective than soy sauce) in our study, the flavorings F3 and F5 containing one higher level of sugar at 16% was also included in addition to 4% and 8% sugar. After mixing thoroughly, the flavored minced meat was flattened into thin slices (1 mm thin slices) by a KW-RP01 model rolling pin from Holar Industrial Inc. (Taipei, Taiwan), followed by drying in a cold air dryer (RO-340 model, Firstek Scientific Co. (New Taipei City, Taiwan) at 50 °C for 2 h one side and then turning over for the other side (2 h) for a total of 4 h (0.1 mm thin slices after drying). Then the air-dried pork slices were further heated in an oven (SM-803 T+3S+3B model, Sinmag Equipment Corp., Taipei, Taiwan) with temperature at 120, 160 or 200 °C for 2 min one side and then turned over for the other side (2 min)

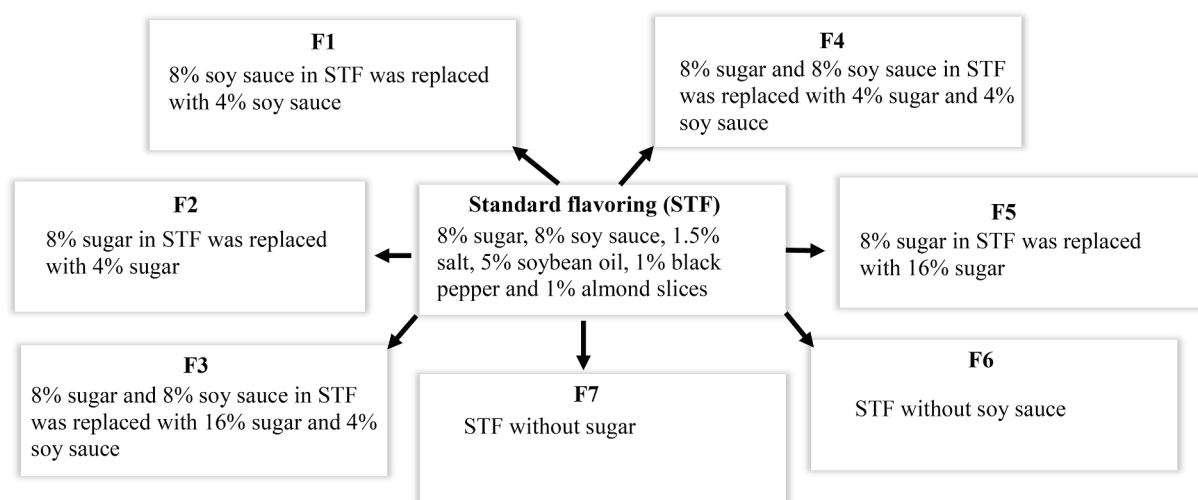


Fig. 1. Different flavouring treatments along with their composition used in this study.

for a total of 4 min to obtain the final product of thin slices of dried pork. The entire processing steps involved in the preparation of thin slices of dried pork from pork hind leg and their products with different flavorings and roasting temperatures are shown in Fig. S1 (supplementary information).

## 2.2. Chemical reagents

A total of 23 PAH standards, including NaP, acenaphthylene (AcPy), AcP, Flu, Phe, Ant, fluoranthene (FL), Pyr, BcF, BaA, CPP, CHR, MCH, BbFA, BbFA, BaP, IP, DBaH, BghiP, DBaP, DBaP, DBaP and DBaP were obtained from Sigma Co. (St. Louis, MO, USA). Cholesterol and 5 COP standards including 7-ketocholesterol (7-keto), 5,6 $\alpha$ -EP, 5,6 $\beta$ -EP, 25-hydroxycholesterol (25-OH) and triol, as well as internal standard 5 $\alpha$ -cholestane were also procured from Sigma Co., while both 7 $\alpha$ -hydroxycholesterol (7 $\alpha$ -OH) and 7 $\beta$ -hydroxycholesterol (7 $\beta$ -OH) standards were obtained from Steraloids Co (Wilton, NH, USA).

The HPLC-grade acetonitrile and analytical grade acetone were from Merck Co. (Darmstadt, Germany), pyridine from J.T. Baker Co (Phillipsburg, NJ, USA) and both toluene and hexane from Sigma Co. Deionized water was made using a Milli-Q water purification system (Millipore Co, Bedford, MA, USA). The COP derivatization agent Tri-Sil TBT, composed of *N*-trimethylsilylimidazole (TMSI), *N*,*O*-bis trimethylsilyl acetamide (BSA) and trimethylchlorosilane (TMCS) at a ratio of 3:3:2, was from Thermo Fisher Scientific Co (San Jose, CA, USA). The QuEChERS extraction kit containing extraction and purification powders was from Yo-Ho Co (New Taipei City, Taiwan). Two DB-5MS capillary columns with film thickness 0.25  $\mu$ m used for separation of COPs (30 m  $\times$  0.25 mm ID) and PAHs (15 m  $\times$  0.25 mm ID) were from Agilent Technologies Co. (Palo Alto, CA, USA).

## 2.3. Extraction and purification of PAHs and COPs in freeze-dried pork and thin slices of dried pork

A QuEChERS method based on Kao, Chen, Chen, Huang, and Chen (2012) was used to extract and purify PAHs from freeze-dried pork and thin slices of dried pork. Although this study mainly focusses on determining PAH or COP contents in thin pork slices as affected by different flavoring and roasting temperature, their levels in freeze-dried pork were also determined as it was used as a blank sample matrix for matrix effect determination and method validation. Accordingly, from the analytical point of view, it is important to evaluate the reported QuEChERS method coupled with GC-MS/MS and GC-MS for determination of PAHs and COPs in thin pork slices, respectively. Initially, a 5-g homogenized sample was mixed with a ceramic homogenizer in a 50-mL centrifuge tube, followed by adding 10 mL of deionized water and shaking for one min. Then, 10 mL of acetonitrile was added, shaken for one min, the extraction powder (1 g MgSO<sub>4</sub>; 1 g CH<sub>3</sub>COONa, 1 g) added, shaken again for one min and centrifuged at 4000 g for 5 min (15 °C). The supernatant (6 mL) was then collected and poured into a 15-mL centrifuge tube containing the purification powder (300 mg PSA; 900 mg MgSO<sub>4</sub>; 300 mg C18EC), followed by shaking for one min, centrifuging at 4000 g for 5 min (15 °C), collecting the supernatant (1 mL) and evaporating to dryness under nitrogen. Finally, the residue was dissolved in one mL hexane, filtered through a 0.22- $\mu$ m Nylon membrane filter and injected for GC-MS/MS analysis. For extraction and purification of COPs, the same QuEChERS method as used above for PAHs was adopted with the exception that acetonitrile solvent was replaced with acetone and 1 g MgSO<sub>4</sub> in extraction powder with 4 g MgSO<sub>4</sub> as well as the final residue dissolved in pyridine instead of hexane for GC-MS analysis (Chiu, Kao, & Chen, 2018).

## 2.4. Evaluation of matrix effect

The evaluation of matrix effect for PAHs and COPs was based on a method described by Chang, Zhang, Wang, and Chen (2019). Initially, a

standard calibration curve was developed by preparing five concentrations of each PAH standard (10, 30, 50, 70 and 100 ng/mL) in hexane or six concentrations (0.625, 1.25, 2.5, 5, 10 and 20  $\mu$ g/mL) of each COP in pyridine and injecting into GC-MS/MS or GC-MS. Likewise, the same number of concentrations of each PAH or COP standard were prepared and added to freeze-dried pork hind leg extract (blank sample matrix) for GC-MS/MS or GC-MS analysis to prepare matrix-matched calibration curves. Then the matrix effect of PAHs and COPs was determined by using the formula as shown below (Chang, Zhang, Wang, & Chen, 2019):

$$\text{Matrix effect (\%)} = \frac{A_{\text{matrix}}}{A_{\text{solvent}}} \times 100$$

where,  $A_{\text{matrix}}$  and  $A_{\text{solvent}}$  are the peak areas of each PAH or COP in freeze-dried pork hind leg extract and standard solution, respectively.

## 2.5. Method validation of PAHs and COPs

Both limit of detection (LOD) and limit of quantitation (LOQ) for 23 PAHs were determined by preparing a series of 16 concentrations (0.03, 0.05, 0.1, 0.3, 0.5, 0.7, 0.9, 1.0, 3.0, 5.0, 7.0, 9.0, 10, 30, 50 and 70 ng/mL) for each PAH and adding to blank sample matrix for extraction, purification and GC-MS/MS analysis. Similarly, both LOD and LOQ for COPs was determined by preparing a series of 14 concentrations (2.5, 5, 10, 20, 30, 40, 50, 100, 150, 200, 300, 400, 500 and 600  $\mu$ g/mL) for each COP and adding to blank sample matrix for extraction, purification and GC-MS analysis. The LOD of PAHs or COPs was then determined based on the signal/noise ratio (S/N)  $\geq$  3, while the LOQ was based on S/N  $\geq$  10.

The recovery of PAHs or COPs was determined by adding separately two standard solutions of PAHs (10 and 50 ng/g) or COPs (1 and 5  $\mu$ g/g) to blank sample matrix, followed by extraction, purification, and GC-MS/MS or GC-MS analysis for obtaining the amount of various PAHs or COPs in meat samples. Then the recovery of PAHs or COPs was obtained by using the formula as shown below:

$$\text{Recovery (\%)} = \frac{\text{PAH/COP}_{\text{found}} - \text{PAH/COP}_{\text{original}}}{\text{PAH/COP}_{\text{amount added}}}$$

where, PAH/COP<sub>found</sub> and PAH/COP<sub>original</sub> are the amounts of PAH/COP determined after adding the respective standards and that originally present in the sample respectively, while PAH/COP<sub>amount added</sub> is the amount of standard added to the sample matrix.

For the precision study, the intra-day variability was determined by adding 10 ng/g of PAH or 1  $\mu$ g/g of COP standard to blank sample matrix, followed by extraction, purification and GC-MS/MS or GC-MS analysis for obtaining the amount of various PAHs or COPs in meat samples. The intra-day variability was based on triplicate analyses in morning, afternoon and evening on the same day for a total of 9 analyses. Likewise, the inter-day variability was determined in the same way with the exception that triplicate analyses was performed one day for three consecutive days for a total of 9 analyses. Then, the coefficient of variation (CV) was determined by calculating the standard deviation and substituting in the formula, CV = (standard deviation/average)  $\times$  100.

## 2.6. Separation, identification and quantification of PAHs or COPs

A DB-5MS capillary column (15 m  $\times$  0.25 mm ID, film thickness 0.25  $\mu$ m) was used to separate 23 PAHs within 78 min in the splitless mode with helium carrier gas at 1.25 mL/min, MS-interface temperature at 280 °C and injector temperature at 320 °C. The following temperature programming condition was used: initial temperature at 80 °C, maintained for one min, raised to 200 °C at 5 °C/min, maintained for 10 min, raised to 220 °C at 5 °C/min, maintained for 5 min, raised to 230 °C at 1 °C/min, maintained for 10 min, and raised to 320 °C at 10 °C/min, maintained for 10 min. A triple quadrupole tandem mass spectrometer

(QqQ) (model 7890 B and 7000 C) from Agilent was used with electrospray ionization and the operation parameters of 23 PAH standards detected by multiple reaction monitoring (MRM) mode are shown in Table S1.

For COP separation and identification, a DB-5MS capillary column (30 m × 0.25 mm ID, film thickness 0.25 μm) was used in the splitless mode to separate 7 COPs and internal standard (5α-cholestane) within 14 min with helium carrier gas at 1 mL/min, injector temperature at 280 °C, MS-interface temperature at 300 °C and the temperature programming as shown below: initial temperature at 250 °C, raised to 290 °C at 10 °C/min, maintained for 5 min, raised to 291 °C at 0.1 °C/min, and maintained for one min. A GC-MS instrument (Model 7890 and 5975) from Agilent was used. After calibrating with perfluorotributylamine (PFTBA) standard with mass-to-charge (*m/z*) ratio at 69, 219, and 50, the various COPs in samples were detected by selected ion monitoring (SIM) mode based on the elution order and the characteristic *m/z* ratio (Table S2, supplementary information).

For PAH quantitation, 5 concentrations (10, 30, 50, 70 and 100 ng/mL) of 21 PAH standards were prepared in hexane separately, added to blank sample matrix for GC-MS/MS analysis and the matrix-matched calibration curves developed by plotting concentration against peak area of quantitative ion and the linear regression equations along with coefficient of determination (*R*<sup>2</sup>) were calculated. It is worth pointing out that PAHs were quantified using the matrix-matched calibration curves instead of standard calibration curves mainly because the latter could result in quantitation of 4 priority PAHs (BaP, CHR, BaA and BbFA) exceeding the maximum safety limit (0.01 mg/L for 4 PAHs) regulated by European Commission (2011).

For COP quantitation, 6 concentrations (0.625, 1.25, 2.5, 5, 10 and 20 μg/mL) of 7 COP standards dissolved in pyridine were prepared separately. Then 40-μL of each standard solution was collected into a 2-mL vial containing 250-μL inner tube, followed by adding 20 μL 5α-cholestane (2 μg/mL) and 40 μL derivatization agent (Tri-Sil TBT) for reaction at room temperature in the dark for 1 h and subsequent injection into GC-MS for analysis. The standard calibration curve of each COP was prepared by plotting concentration ratio (COP standard *versus* internal standard) against area ratio (COP standard *versus* internal standard) and both linear regression equations and *R*<sup>2</sup> were determined. The contents of PAHs or COPs in meat samples were calculated using a formula as described in our previous studies (Hsu & Chen, 2020; Hsu, Inbaraj, & Chen, 2020).

$$\text{Amount of PAH (ng/g)} = (A_s - b) \times \left(\frac{1}{a}\right) \times \text{EV} \times \text{DF} \times \left(\frac{1}{\text{recovery}}\right) \times \left(\frac{1}{\text{sample weight}}\right)$$

$$\text{Amount of COP (μg/g)} = \left(\frac{A_s}{A_i} - b\right) \times \left(\frac{1}{a}\right) \times C_i \times \text{EV} \times \text{DF} \times \left(\frac{1}{\text{recovery}}\right) \times \left(\frac{1}{\text{sample weight}}\right)$$

where, *A<sub>i</sub>* and *C<sub>i</sub>* are the peak area and concentration of COP internal standard (5α-cholestane) respectively, while *a* and *b* are the slope and intercept of standard curve. EV is the extraction volume, DF is the dilution factor and *A<sub>s</sub>* is the peak area of PAH or COP in sample.

## 2.7. Statistical analysis

All the data were obtained in triplicate and analyzed by using the statistical analysis system (SAS, 2014) with MANOVA (multivariate analysis of variance) and Duncan's multiple range test for elucidating statistical significance in comparison (*p* < 0.05). Principal component analysis (PCA) was performed to analyze the relative contribution of flavorings and temperature on generation of PAHs and COPs by using Origin® 2019b version 9.65 (OriginLab Corporation, Northampton, MA,

USA).

## 3. Results and discussion

### 3.1. Evaluation of PAH analysis by QuEChERS and GC-MS

In many published reports the solid-phase extraction method was frequently used for extraction and purification of PAHs in meat products, while the QuEChERS method was less often used. Forsberg, Wilson, and Anderson (2011) compared the effect of 5 QuEChERS extraction powders on the recovery of 15 PAHs in fish meat and reported that a high recovery (90%) was attained by using the extraction powder containing MgSO<sub>4</sub> (6 g) and NaC<sub>2</sub>H<sub>3</sub>O<sub>2</sub> (1.5 g). Recently Taiwan Food and Drug Administration (TFDA, 2018) demonstrated that with the extraction powder containing 4 g MgSO<sub>4</sub> and 1 g NaC<sub>2</sub>H<sub>3</sub>O<sub>2</sub> and the purification powder containing PSA-C18 EC-MgSO<sub>4</sub> (1:1:3), the highest accuracy and precision of PAHs in meat products was obtained by GC-MS/MS. Thus, in this study we used extraction powder (4 g MgSO<sub>4</sub> and 1 g NaC<sub>2</sub>H<sub>3</sub>O<sub>2</sub>) and purification powder containing PSA-C18 EC-MgSO<sub>4</sub> (1:1:3) for PAH determination in thin slices of dried pork by GC-MS/MS.

It has been well established that GC-MS/MS is superior to GC-MS in terms of sensitivity and selectivity (Varlet, Serot, Monteau, Le Bizec, & Prost, 2007). Fig. 2A shows the GC-MS/MS chromatogram of PAHs detected by MRM mode. A total of 23 PAH standards was adequately separated within 77 min (Fig. 2A and B). Table S3 shows the matrix effect of 21 PAHs in freeze-dried pork hind leg by GC-MS/MS to be from 1.18 to 1.80, implying a signal enhancement occurred for all the 21 PAHs. However, the matrix effect of NaP and Pyr was not determined as the former was detected in hexane and the latter in blank samples (freeze-dried pork hind leg). Thus, in this study NaP was not quantified in meat sample while Pyr was quantified based on the standard curve instead of matrix-matched calibration curve. In many studies the signal enhancement was observed with GC-MS/MS analysis (Liu, 2015). However, with LC-MS/MS analysis, the signal can be enhanced or suppressed depending on ion source. For instance, with electrospray ionization the signal can be suppressed, while with atmospheric pressure chemical ionization the signal can be enhanced (Chang, Zhang, Wang, & Chen, 2019).

Of the various PAHs, the LOD of AcPy, Flu, AcP, Phe, Pyr, BcF, BaA, CPP, CHR, DBaP and DBaI were 0.1 ng/mL, while that of BbFA, BbFA, BaP, IP, DBaA, benzo[*g,h,i*]pyrene and DBaP was 0.3 ng/mL. For the other two PAHs, the LOD of MCH and DBaP was 1 and 0.03 ng/mL, respectively. Compared to LOD, the LOQ of all the 22 PAHs were three times higher with the exception of DBaP at 0.1 ng/mL. Similar LOD and LOQ of PAHs in meat products as determined by GC-MS/MS was reported (Veyrand et al., 2007).

Table S4 shows the recovery data of 22 PAH standards and standards added to freeze-dried pork hind leg by GC-MS/MS. The average recovery of 22 PAH standards ranged from 81.2 to 98.3 % and from 76.5 to 90.7 % in freeze-dried pork hind leg. This result conforms to a regulation set up by Taiwan Food and Drug Administration (TFDA, 2013), stipulating that with the added standard concentrations at 0.01 and 0.05 mg/L, the recovery should be from 60 to 125 % and from 70 to 120 %, respectively. This outcome also revealed that a high accuracy method was attained in our study. In a previous study, Kao, Chen, Chen, Huang, and Chen (2012) also used QuEChERS and GC-MS to determine 16 PAHs in poultry meat and the recovery was from 71.7 to 107 %.

Table S5 shows the precision data of 22 PAH standards analyzed by GC-MS/MS. The CV of repeatability was from 5.35 to 11.81 %, while that of intermediate precision was from 6.47 to 13.39 %. Similarly, the CV of repeatability of 22 PAH standards added to freeze-dried pork hind leg was from 3.70 to 12.63 %, while that of intermediate precision was from 7.47 to 14.08 % (Table S6). All the repeatability and intermediate precision data meets the regulation of TFDA (2013), stating that the CV of the former should be < 30% for the analyte concentration ≥



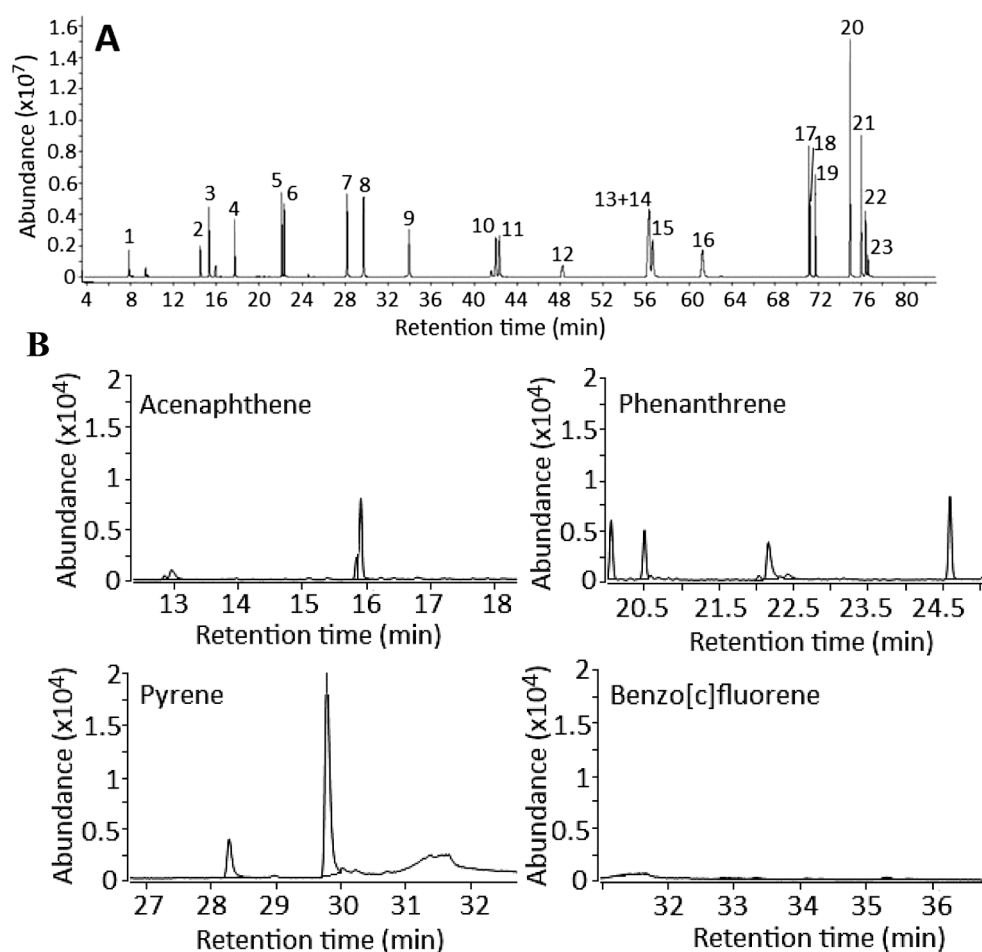


**Fig. 2.** GC-MS/MS chromatogram of PAHs detected by multiple reaction monitoring (MRM) mode in 23 PAH standard mixtures (A) and selected PAHs in roasted thin slices of dried pork at 160 °C with standard flavoring (STF) (B). Peaks: 1, naphthalene; 2, acenaphthylene; 3, acenaphthene; 4, fluorene; 5, phenanthrene; 6, anthracene; 7, fluoranthene; 8, pyrene; 9, benzo[*c*]fluorene; 10, benzo[*a*]anthracene; 11, chrysene; 12, methyl chrysene; 13, benzo[*b*]fluoranthene; 14, benzo[*j*]fluoranthene; 15, cyclopenta[*c*, *d*]pyrene; 16, benzo[*a*]pyrene; 17, indeno[1,2,3-*cd*]pyrene; 18, dibenzo[*a,h*]anthracene; 19, benzo[*g,h,i*]perylene; 20, dibenzo[*a,l*]pyrene; 21, dibenzo[*a,e*]pyrene; 22, dibenzo[*a,i*]pyrene; 23, dibenzo[*a,h*]pyrene. STF: 8% sugar, 8% soy sauce, 1.5% salt, 5% oil, 1% black pepper and 1% almond slices. PAHs = polycyclic aromatic hydrocarbons and GC-MS/MS = gas chromatograph–tandem mass spectrometer.

0.001–0.01 mg/L, while the CV of the latter should be < 32% for the same analyte concentration. This outcome also implied that a high precision was attained for the method employed in our study.

### 3.2. PAH contents in thin slices of dried pork

Table 1 shows PAH contents (ng/g) in raw pork and thin slices of dried pork added with the STF and flavoring without soy sauce or sugar. Only three PAHs including AcP (0.450 ng/g), Ant (0.332 ng/g) and Pyr (1.513 ng/g) were detected in raw pork. However, following the STF treatment and heating at 120, 160 and 200 °C for 4 min, some more PAHs such as BcF, AcPy or IP were generated. A temperature-dependent increase was also observed for the variety and total PAH contents in thin slices of dried pork, with the highest level shown at 200 °C (6.504 ng/g), followed by 160 °C (5.213 ng/g) and 120 °C (4.447 ng/g). A similar trend was also shown for the treatment of flavoring without soy sauce or sugar. By comparison, at the same roasting temperature, STF treatment resulted in the highest level of total PAHs, followed by the flavoring treatment without soy sauce or sugar. This result indicated that the addition of both soy sauce (8%) and sugar (8%) to the flavoring may promote PAH formation in thin slices of dried pork during roasting, while the absence of soy sauce or sugar in the flavoring may reduce the formation of total PAHs. Compared to STF, this outcome also implied that the addition of soy sauce (8%) or sugar (8%) may minimize PAH formation.

The formation of PAHs in thin slices of dried pork is probably due to formation of lipid degradation products during roasting. In a previous report [Chen and Chen \(2001\)](#) studied the formation mechanism of PAHs in model lipids and food lipids and postulated that the lipid degradation

products containing conjugated double bonds may react with dienophile compounds to form PAHs through Diels-Alder reaction. In another study [Shukla and Koshi \(2011\)](#) illustrated that PAHs can be formed through hydrogen abstraction/acetylene addition, phenyl addition/cyclization and methyl addition/cyclization. In addition, the benzene ring-containing compounds from lipid degradation may further react with C1-C4 compounds from hydrogen abstraction/acetylene addition through Diels-Alder reaction for PAH formation ([Chen & Chen, 2001](#)). It is worth pointing out that the highly toxic BaP remained undetected in thin slices of dried pork probably because of short roasting time. In a similar study [Chung, Yettella, Kim, Kwon, Kim, and Min \(2011\)](#) studied the effect of grilling and roasting on the levels of PAHs in beef and pork and reported that following grilling at 200 °C, both pork loin and pork chop with sauce generated a higher level of total PAHs than beef loin and steak with sauce, respectively. Based on a report by [Shukla and Koshi \(2012\)](#), indene and benzene ring may undergo hydrogen abstraction/acetylene addition to generate BcF and NaP, respectively, followed by formation of AcP and Phe, and leading to Pyr formation. Alternatively, AcP may also undergo hydrogen abstraction to produce AcPy during roasting at 200 °C, while Pyr may be oxidized to generate IP, a PAH composed of 6 rings. [Kaneko, Kumazawa, and Nishimura \(2013\)](#) further pointed out that the benzene-containing compounds in soy sauce may increase from 3.37 mg/L to 40.4 mg/L after heating. As the benzene-containing compounds can be a precursor for PAH formation ([Chen & Chen, 2001](#)), the addition of high level of soy sauce (8%) as flavoring may accelerate PAH formation in thin slices of dried pork during heating. Furthermore, the formation of 5-hydroxymethylfurfural (5-HMF) from sucrose degradation during heating may result in PAH formation through Diels-Alder reaction ([Settle et al., 2017](#)). This may

**Table 1**PAH contents (ng/g) in raw pork and thin slices of dried pork with standard flavoring and flavoring without soy sauce or sugar.<sup>1</sup>

| PAHs <sup>2</sup>       | Raw pork                   | STF <sup>3</sup>           |                            |                            | F6 <sup>3</sup>            |                            |                            | F7 <sup>3</sup>            |                            |                            |
|-------------------------|----------------------------|----------------------------|----------------------------|----------------------------|----------------------------|----------------------------|----------------------------|----------------------------|----------------------------|----------------------------|
|                         |                            | 120 °C                     | 160 °C                     | 200 °C                     | 120 °C                     | 160 °C                     | 200 °C                     | 120 °C                     | 160 °C                     | 200 °C                     |
| Acenaphthylene          | trace <sup>4</sup>         | trace                      | trace                      | 0.335 ± 0.015 <sup>A</sup> | trace                      | trace                      | trace                      | trace                      | trace                      | trace                      |
| Acenaphthene            | 0.450 ± 0.080 <sup>E</sup> | 0.548 ± 0.090 <sup>E</sup> | 0.706 ± 0.015 <sup>B</sup> | 0.721 ± 0.050 <sup>B</sup> | 0.560 ± 0.090 <sup>D</sup> | 0.581 ± 0.080 <sup>D</sup> | 0.801 ± 0.080 <sup>A</sup> | 0.567 ± 0.100 <sup>D</sup> | 0.566 ± 0.050 <sup>D</sup> | 0.678 ± 0.090 <sup>C</sup> |
| Fluorene                | nd <sup>5</sup>            | trace                      | trace                      | trace                      | nd                         | trace                      | trace                      | trace                      | trace                      | trace                      |
| Phenanthrene            | nd                         | 0.350 ± 0.060 <sup>B</sup> | 0.427 ± 0.025 <sup>A</sup> | 0.430 ± 0.070 <sup>A</sup> | trace                      | trace                      | 0.470 ± 0.030 <sup>A</sup> | trace                      | trace                      | 0.395 ± 0.080 <sup>B</sup> |
| Anthracene              | 0.332 ± 0.030 <sup>A</sup> | trace                      | trace                      | trace                      | trace                      | trace                      | trace                      | trace                      | trace                      | trace                      |
| Fluoranthene            | nd                         | trace                      | trace                      | trace                      | trace                      | trace                      | trace                      | trace                      | trace                      | trace                      |
| Pyrene                  | 1.513 ± 0.060 <sup>D</sup> | 3.243 ± 0.300 <sup>B</sup> | 3.770 ± 0.270 <sup>A</sup> | 4.356 ± 0.350 <sup>A</sup> | 2.035 ± 0.450 <sup>D</sup> | 3.317 ± 0.050 <sup>B</sup> | 3.769 ± 0.040 <sup>B</sup> | 1.911 ± 0.210 <sup>D</sup> | 3.084 ± 0.200 <sup>C</sup> | 3.385 ± 0.160 <sup>B</sup> |
| Benzo[c]fluorene        | trace                      | 0.306 ± 0.003 <sup>A</sup> | 0.310 ± 0.003 <sup>A</sup> | 0.328 ± 0.040 <sup>A</sup> | trace                      | trace                      | trace                      | trace                      | trace                      | trace                      |
| Benzo[a]anthracene      | nd                         | nd                         | nd                         | nd                         | nd                         | nd                         | nd                         | nd                         | nd                         | nd                         |
| Cyclopenta[c,d]pyrene   | trace                      | trace                      | trace                      | trace                      | trace                      | trace                      | trace                      | trace                      | trace                      | trace                      |
| Chrysene                | trace                      | trace                      | trace                      | trace                      | trace                      | trace                      | trace                      | trace                      | trace                      | trace                      |
| Benzo[a]pyrene          | trace                      | nd                         | nd                         | nd                         | nd                         | nd                         | nd                         | nd                         | nd                         | nd                         |
| Indeno[1,2,3-c,d]pyrene | trace                      | trace                      | trace                      | 0.314 ± 0.030 <sup>A</sup> | trace                      | trace                      | trace                      | trace                      | trace                      | trace                      |
| Total                   | 2.295 <sup>H</sup>         | 4.447 <sup>D</sup>         | 5.213 <sup>B</sup>         | 6.504 <sup>A</sup>         | 2.595 <sup>G</sup>         | 3.898 <sup>E</sup>         | 5.040 <sup>C</sup>         | 2.478 <sup>G</sup>         | 3.650 <sup>F</sup>         | 4.458 <sup>D</sup>         |

<sup>1</sup> Mean of triplicate analyses ± standard error. <sup>2</sup>Polycyclic aromatic hydrocarbons (PAHs) such as 5-methylchrysene, benzo[b]fluoranthene and benzo[j]fluoranthene found in traces as well as undetected PAHs such as dibenzo[a,h]anthracene, benzo[g,h,i]perylene, dibenzo[a,l]pyrene, dibenzo[a,e]pyrene, dibenzo[a,i]pyrene and dibenzo[a,h]pyrene are not shown in this table. <sup>3</sup>Flavorings: standard flavoring (STF) = 8% sugar, 8% soy sauce, 1.5% salt, 5% oil, 1% black pepper and 1% almond slices; F6 = 8% sugar, 1.5% salt, 5% oil, 1% black pepper and 1% almond slices; F7 = 8% soy sauce, 1.5% salt, 5% oil, 1% black pepper and 1% almond slices. <sup>4</sup>trace = PAHs levels are higher than or equal to limit of detection (LOD), but below limit of quantitation (LOQ), or the negative data obtained due to PAH levels being lower than the background values of calibration curves; <sup>5</sup>nd = not detected (below LOD). Mean values bearing different capital letters (A-H) in the same row are significantly different ( $p < 0.05$ ; Duncan's multiple range test) at different temperatures compared to that in raw pork.

explain why the level of total PAHs was higher for STF (8% soy sauce and 8% sugar) and F5 (8% soy sauce and 16% sugar) treatments. Also, the level of total PAHs was lower for the F7 treatment (without sugar) than that for F6 (without soy sauce), indicating that soy sauce (8%) should be more effective in inhibiting PAH formation than sugar (8%), which may be attributed to the presence of isoflavone in soy sauce (Hsu & Chen, 2020). This phenomenon may also explain why two more PAHs, BcF and IP, were generated in thin slices of dried pork with the STF when compared to the flavoring without soy sauce or sugar at 200 °C (Table 1).

### 3.3. PAH contents (ng/g) in thin slices of dried pork as affected by different flavorings and processing conditions

The effect of different flavorings and processing condition on PAH levels in thin slices of dried pork is shown in Table 2. Following heating at 120 °C, a total of 4 PAHs including AcP, Phe, Pyr and BcF were formed for all the 6 flavoring treatments. More specifically, with F5, the highest level of total PAHs (5.520 ng/g) was shown with Pyr present in the largest amount (3.957 ng/g), followed by AcP (0.662 ng/g), Phe (0.539 ng/g) and BcF (0.362 ng/g). Conversely, the lowest level of total PAHs (2.482 ng/g) was observed for the flavoring treatment (F4), with Pyr present in the highest content (1.505 ng/g), followed by AcP (0.381 ng/g), Phe (0.300 ng/g) and BcF (0.296 ng/g). A similar trend was observed for the other 4 flavoring treatments: STF, F1, F2, as well as F3. By comparison at the same level of sugar, a low level of soy sauce (4%) could generate a low amount of total PAHs. Likewise, at the same level of soy sauce, a low level (4%) of sugar could produce a small amount of total PAHs. This outcome revealed that the addition of low level of sugar (4%) or soy sauce (4%) may prevent PAH formation, with the latter being more effective than the former, probably because of presence of isoflavone in the latter. Collectively, the lower the level of sugar or soy sauce, the less the formation of PAHs in thin slices of dried pork during roasting.

Like 120 °C, a similar tendency was observed at 160 °C and 200 °C

with the flavoring (F5) generating the highest level of total PAHs, followed by F3, STF, F2, F1, and F4. However, compared to the treatment at 120 °C and 160 °C, some more PAHs including AcPy and IP were produced at 200 °C for the 3 flavoring treatments including STF, F3 as well as F5. This phenomenon further demonstrated that the addition of high level of sugar (8% or 16%) or soy sauce (8%) to the flavoring could promote formation of PAHs with 6 rings such as IP. Also, the formation of AcPy is probably due to oxidation of AcP. Nevertheless, the highly toxic BaP remained undetected in thin slices of dried pork treated with 6 different flavorings, probably because of short roasting time. As mentioned above, with heating temperature > 170 °C, sugar can be dehydrated to form 5-HMF for subsequent indene formation through Diels-Alder reaction, leading to FL formation through hydrogen abstraction/acetylene addition. In several previous studies Duedahl-Olesen, Navaratnam, Jewula, and Jensen (2015) reported that both BaA and CHR were present at a much higher level in heavy roast coffee than in medium roast coffee due to caramelization occurred during roasting. In another study Chen, Kao, Chen, Huang, and Chen (2013) studied the PAH formation in sugar-smoked meat and reported that the longer the smoking time, the more the formation of PAHs. Also, the level of total PAHs was higher in red meat than in poultry meat. However, the highly toxic BaP remained undetected in sugar-smoked meat, revealing that sugar-smoking is safer than the other traditional smoking methods such as wood-smoking. Similarly, Kao, Chen, Chen, Huang, and Chen (2012) studied the effect of marinating and frying on PAH formation in poultry meat and reported that PAHs with 2–4 rings were more rapidly formed, in which NaP dominated. However, a large amount of total PAHs (79.7 ng/g) in duck meat was produced after 15-min frying. Apparently, the variety and amount of PAHs formed in meat products can be dependent upon meat variety, cooking method, heating temperature and time.

### 3.4. Evaluation of COPs analysis by QuEChERS and GC-MS

A method based on Chiu, Kao, & Chen, 2018 was used to extract and purify COPs in thin slices of dried pork by QuEChERS for subsequent

**Table 2**PAH contents (ng/g) in thin slices of dried pork as affected by different flavorings and processing conditions.<sup>1</sup>

| PAHs <sup>2</sup>       | Flavoring <sup>3</sup> |                    |                    |                    |                    |                    |
|-------------------------|------------------------|--------------------|--------------------|--------------------|--------------------|--------------------|
|                         | STF                    | F1                 | F2                 | F3                 | F4                 | F5                 |
| 120 °C                  |                        |                    |                    |                    |                    |                    |
| Acenaphthylene          | trace <sup>4</sup>     | trace              | trace              | trace              | trace              | trace              |
| Acenaphthene            | 0.548                  | 0.459              | 0.531              | 0.572              | 0.381              | 0.662              |
|                         | ±                      | ±                  | ±                  | ±                  | ±                  | ±                  |
|                         | 0.090 <sup>B</sup>     | 0.036 <sup>C</sup> | 0.070 <sup>B</sup> | 0.068 <sup>B</sup> | 0.040 <sup>D</sup> | 0.040 <sup>A</sup> |
| Fluorene                | trace                  | trace              | trace              | trace              | trace              | trace              |
| Phenanthrene            | 0.350                  | 0.335              | 0.349              | 0.363              | 0.300              | 0.539              |
|                         | ±                      | ±                  | ±                  | ±                  | ±                  | ±                  |
|                         | 0.060 <sup>B</sup>     | 0.024 <sup>C</sup> | 0.060 <sup>B</sup> | 0.055 <sup>B</sup> | 0.020 <sup>C</sup> | 0.020 <sup>A</sup> |
| Anthracene              | trace                  | trace              | trace              | trace              | trace              | trace              |
| Fluoranthene            | trace                  | trace              | trace              | trace              | trace              | trace              |
| Pyrene                  | 3.243                  | 2.583              | 3.031              | 3.490              | 1.505              | 3.957              |
|                         | ±                      | ±                  | ±                  | ±                  | ±                  | ±                  |
|                         | 0.300 <sup>B</sup>     | 0.181 <sup>C</sup> | 0.420 <sup>B</sup> | 0.557 <sup>B</sup> | 0.210 <sup>D</sup> | 0.410 <sup>A</sup> |
| Benzo[c]fluorene        | 0.306                  | 0.302              | 0.306              | 0.314              | 0.296              | 0.362              |
|                         | ±                      | ±                  | ±                  | ±                  | ±                  | ±                  |
|                         | 0.003 <sup>A</sup>     | 0.030 <sup>A</sup> | 0.021 <sup>A</sup> | 0.064 <sup>A</sup> | 0.002 <sup>A</sup> | 0.014 <sup>A</sup> |
| Benzo[a]anthracene      | nd <sup>5</sup>        | nd                 | nd                 | nd                 | nd                 | nd                 |
| Cyclopenta[c,d]pyrene   | trace                  | trace              | trace              | trace              | trace              | trace              |
| Chrysene                | trace                  | trace              | trace              | trace              | trace              | trace              |
| Benzo[a]pyrene          | nd                     | nd                 | nd                 | nd                 | nd                 | nd                 |
| Indeno[1,2,3-c,d]pyrene | trace                  | trace              | trace              | trace              | trace              | trace              |
| Total PAHs              | 4.447 <sup>C</sup>     | 3.679 <sup>E</sup> | 4.217 <sup>D</sup> | 4.739 <sup>B</sup> | 2.482 <sup>F</sup> | 5.520 <sup>A</sup> |
| 160 °C                  |                        |                    |                    |                    |                    |                    |
| Acenaphthylene          | trace                  | trace              | trace              | trace              | trace              | trace              |
| Acenaphthene            | 0.706                  | 0.616              | 0.690              | 0.747              | 0.605              | 0.876              |
|                         | ±                      | ±                  | ±                  | ±                  | ±                  | ±                  |
|                         | 0.015 <sup>C</sup>     | 0.070 <sup>D</sup> | 0.170 <sup>C</sup> | 0.079 <sup>B</sup> | 0.102 <sup>D</sup> | 0.059 <sup>A</sup> |
| Fluorene                | trace                  | trace              | trace              | trace              | trace              | trace              |
| Phenanthrene            | 0.427                  | 0.352              | 0.358              | 0.436              | 0.336              | 0.542              |
|                         | ±                      | ±                  | ±                  | ±                  | ±                  | ±                  |
|                         | 0.025 <sup>B</sup>     | 0.014 <sup>C</sup> | 0.040 <sup>C</sup> | 0.062 <sup>B</sup> | 0.058 <sup>C</sup> | 0.041 <sup>A</sup> |
| Anthracene              | trace                  | trace              | trace              | trace              | trace              | trace              |
| Fluoranthene            | trace                  | trace              | trace              | trace              | trace              | trace              |
| Pyrene                  | 3.770                  | 3.224              | 3.280              | 3.908              | 2.774              | 3.970              |
|                         | ±                      | ±                  | ±                  | ±                  | ±                  | ±                  |
|                         | 0.270 <sup>A</sup>     | 0.160 <sup>B</sup> | 0.334 <sup>B</sup> | 0.151 <sup>A</sup> | 0.067 <sup>C</sup> | 0.474 <sup>A</sup> |
| Benzo[c]fluorene        | 0.310                  | 0.307              | 0.309              | 0.324              | 0.316              | 0.383              |
|                         | ±                      | ±                  | ±                  | ±                  | ±                  | ±                  |
|                         | 0.003 <sup>A</sup>     | 0.013 <sup>A</sup> | 0.026 <sup>A</sup> | 0.024 <sup>A</sup> | 0.065 <sup>A</sup> | 0.040 <sup>A</sup> |
| Benzo[a]anthracene      | nd                     | nd                 | nd                 | nd                 | nd                 | nd                 |
| Cyclopenta[c,d]pyrene   | trace                  | trace              | trace              | trace              | trace              | trace              |
| Chrysene                | trace                  | trace              | trace              | trace              | trace              | trace              |
| Benzo[a]pyrene          | nd                     | nd                 | nd                 | nd                 | nd                 | nd                 |
| Indeno[1,2,3-c,d]pyrene | trace                  | trace              | trace              | trace              | trace              | trace              |
| Total PAHs              | 5.213 <sup>C</sup>     | 4.499 <sup>E</sup> | 4.637 <sup>D</sup> | 5.415 <sup>B</sup> | 4.031 <sup>F</sup> | 5.771 <sup>A</sup> |
| 200 °C                  |                        |                    |                    |                    |                    |                    |
| Acenaphthylene          | 0.335                  | trace              | trace              | 0.341              | trace              | 0.357              |
|                         | ±                      |                    |                    | ±                  |                    | ±                  |
|                         | 0.020 <sup>A</sup>     |                    |                    | 0.005 <sup>A</sup> |                    | 0.012 <sup>A</sup> |
| Acenaphthene            | 0.721                  | 0.629              | 0.632              | 0.788              | 0.674              | 0.893              |
|                         | ±                      | ±                  | ±                  | ±                  | ±                  | ±                  |
|                         | 0.050 <sup>C</sup>     | 0.090 <sup>D</sup> | 0.020 <sup>D</sup> | 0.020 <sup>B</sup> | 0.120 <sup>D</sup> | 0.050 <sup>A</sup> |
| Fluorene                | trace                  | trace              | trace              | trace              | trace              | trace              |
| Phenanthrene            | 0.430                  | 0.332              | 0.345              | 0.438              | 0.311              | 0.586              |
|                         | ±                      | ±                  | ±                  | ±                  | ±                  | ±                  |
|                         | 0.070 <sup>B</sup>     | 0.030 <sup>C</sup> | 0.030 <sup>C</sup> | 0.060 <sup>B</sup> | 0.030 <sup>D</sup> | 0.035 <sup>A</sup> |
| Anthracene              | trace                  | trace              | trace              | trace              | trace              | trace              |
| Fluoranthene            | trace                  | trace              | trace              | 0.309              | trace              | 0.314              |
|                         |                        |                    |                    | ±                  |                    | ±                  |
|                         |                        |                    |                    | 0.025 <sup>A</sup> |                    | 0.009 <sup>A</sup> |
| Pyrene                  | 4.356                  | 3.385              | 3.880              | 4.679              | 3.351              | 5.101              |
|                         | ±                      | ±                  | ±                  | ±                  | ±                  | ±                  |
|                         | 0.350 <sup>C</sup>     | 0.159 <sup>E</sup> | 0.480 <sup>D</sup> | 0.410 <sup>B</sup> | 0.340 <sup>E</sup> | 0.170 <sup>A</sup> |
| Benzo[c]fluorene        |                        |                    |                    |                    |                    |                    |

**Table 2 (continued)**

| PAHs <sup>2</sup>       | Flavoring <sup>3</sup> |                    |                    |                    |                    |                    |
|-------------------------|------------------------|--------------------|--------------------|--------------------|--------------------|--------------------|
|                         | STF                    | F1                 | F2                 | F3                 | F4                 | F5                 |
|                         | 0.328                  | 0.311              | 0.313              | 0.361              | 0.309              | 0.390              |
|                         | ±                      | ±                  | ±                  | ±                  | ±                  | ±                  |
|                         | 0.040 <sup>A</sup>     | 0.050 <sup>A</sup> | 0.002 <sup>A</sup> | 0.004 <sup>A</sup> | 0.030 <sup>A</sup> | 0.003 <sup>A</sup> |
| Benzo[a]anthracene      | nd                     | nd                 | nd                 | nd                 | nd                 | nd                 |
| Cyclopenta[c,d]pyrene   | trace                  | trace              | trace              | trace              | trace              | trace              |
| Chrysene                | trace                  | trace              | trace              | trace              | trace              | trace              |
| Benzo[a]pyrene          | nd                     | nd                 | nd                 | nd                 | nd                 | nd                 |
| Indeno[1,2,3-c,d]pyrene | 0.314                  | 0.305              | 0.311              | 0.319              | 0.302              | 0.320              |
|                         | ±                      | ±                  | ±                  | ±                  | ±                  | ±                  |
|                         | 0.030 <sup>A</sup>     | 0.030 <sup>A</sup> | 0.030 <sup>A</sup> | 0.030 <sup>A</sup> | 0.030 <sup>A</sup> | 0.033 <sup>A</sup> |
| Total PAHs              | 6.504 <sup>C</sup>     | 4.962 <sup>E</sup> | 5.481 <sup>D</sup> | 7.235 <sup>B</sup> | 4.947 <sup>E</sup> | 7.961 <sup>A</sup> |

<sup>1</sup> Mean of triplicate analyses ± standard error. <sup>2</sup>Polycyclic aromatic hydrocarbons (PAHs) such as 5-methylchrysene, benzo[b]fluoranthene and benzo[j]fluoranthene found in traces as well as undetected PAHs such as dibenzo[a,h]anthracene, benzo[g,h,i]perylene, dibenzo[a,l]pyrene, dibenzo[a,e]pyrene, dibenzo[a,i]pyrene and dibenzo[a,h]pyrene are not shown in this table. <sup>3</sup>Flavorings: standard flavoring (STF) = 8% sugar, 8% soy sauce, 1.5% salt, 5% oil, 1% black pepper and 1% almond slices; F1 = 8% soy sauce in STF was replaced with 4% soy sauce; F2 = 8% sugar in STF was replaced with 4% sugar; F3 = 8% sugar and 8% soy sauce in STF was replaced with 16% sugar and 4% soy sauce; F4 = 8% sugar and 8% soy sauce in STF was replaced with 4% sugar and 4% soy sauce; F5 = 8% sugar in STF was replaced with 16% sugar. <sup>4</sup>trace = PAHs levels are higher than or equal to limit of detection (LOD), but below limit of quantitation (LOQ), or the negative data obtained due to PAH levels being lower than the background values of calibration curves; <sup>5</sup>nd = not detected (below LOD). Mean values bearing different capital letters (A-F) in the same row are significantly different ( $p < 0.05$ ; Duncan's multiple range test) at different temperatures compared to that in raw pork.

separation, identification and quantification by GC-MS. Fig. 3A shows GC-MS chromatogram of cholesterol, internal standard (5 $\alpha$ -cholestene) and 7 COP standards with good separation efficiency within 14 min. The various COPs in thin slices of dried pork were thus identified by employing SIM detection mode as described in the method section. The matrix effect of COPs in freeze-dried pork hind leg by GC-MS is shown in Table S7, with the average value being from 1.37 to 1.76, implying that all the 7 COPs possessed a signal enhancement effect. This outcome is similar to a study by Georgiou, Constantinou, Andreou, Hapeshi, Fattakassinou, and Kapnissi-Christodoulou (2016), reporting the matrix effect of 7 COPs in freeze-dried pork hind leg to be from 0.95 to 1.23 by UPLC-MS/MS analysis. The LOD of 7 $\alpha$ -OH, 7 $\beta$ -OH, 5,6 $\beta$ -EP, 5,6 $\alpha$ -EP, triol, 25-OH and 7-keto were 2.5, 5, 200, 200, 20, 50 and 200  $\mu$ g/g respectively, while the LOQ were 10, 15, 600, 600, 100, 150 and 600  $\mu$ g/g. The recovery of 7 COP standards and standards added to blank sample is shown in Table S8, with the former ranging from 83.09 to 99.86 % and CV from 1.74 to 6.77 %, and the latter from 83.81 to 99.71 % and CV from 2.62 to 4.72 %. This result is similar to a report by Chen, Chien, Inbaraj, and Chen (2012), showing the recovery of COPs in marinated pig feet to be from 86.5 to 102.5 %. Also, the recovery data of COPs obtained in our study meets the regulation issued by TFDA (2013), stating the recovery should be from 70 to 120 % and from 75 to 120 % for the analyte concentration 1 mg/L and 5 mg/L, respectively. Table S9 shows precision data of 7 COP standards and standards added to blank samples, with the CV of repeatability and intermediate precision being 2.13–6.20% and 2.88–8.32% respectively for the former, as well as 2.69–8.63% and 3.11–11.26% for the latter. Like recovery data, the precision data obtained in our study also meets the regulation issued by TFDA (2013), stating that the CV should be < 14% for the analyte concentration  $\geq 1$  mg/L. Collectively, all the method validation data shown in this study demonstrated that a high accuracy and precision was attained for COP analysis in freeze-dried pork hind leg by QuEChERS coupled with GC-MS.

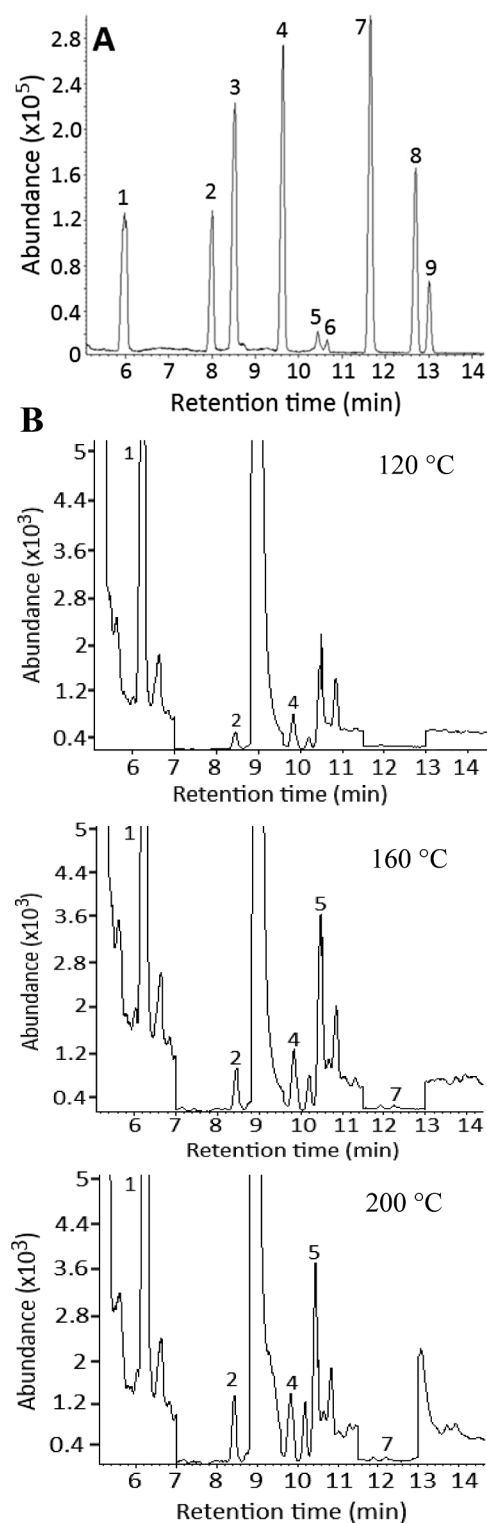


**Fig. 3.** GC-MS-TIC chromatogram of COP and cholesterol standards (A) as well as GC-MS-SIM chromatograms of COPs in thin slices of dried pork as affected by different roasting temperatures with standard flavoring (B). Standard flavoring (STF): 8% sugar, 8% soy sauce, 1.5% salt, 5% oil, 1% black pepper and 1% almond slices. Peaks: 1, 5 $\alpha$ -cholestane (internal standard); 2, 7 $\alpha$ -hydroxycholesterol; 3, cholesterol; 4, 7 $\beta$ -hydroxycholesterol; 5, 5,6 $\beta$ -epoxycholesterol; 6, 5,6 $\alpha$ -epoxycholesterol; 7, triol; 8, 25-hydroxycholesterol; 9, 7-ketocholesterol. COPs = cholesterol oxidation products, GC-MS-TIC = gas chromatograph-mass spectrometer-total-ion-chromatogram and GC-MS-SIM = gas chromatograph-mass spectrometer-selected ion monitoring chromatogram.

### 3.5. COP contents in raw pork and thin slices of dried pork with STF and flavoring without soy sauce or sugar

Table 3 shows COP contents ( $\mu\text{g/g}$ ) in raw pork and thin slices of dried pork with STF and flavoring without soy sauce or sugar (flavorings F6 and F7). Only 7 $\alpha$ -OH (0.077  $\mu\text{g/g}$ ) and 7 $\beta$ -OH (0.090  $\mu\text{g/g}$ ) were determined in raw pork, probably caused by increased surface exposure of cholesterol to air during pork homogenization. The formation of 7 $\alpha$ -OH and 7 $\beta$ -OH is probably due to reduction of 7 $\alpha$ -hydroperoxycholesterol (7 $\alpha$ -OOH) and 7 $\beta$ -hydroperoxycholesterol (7 $\beta$ -OOH), the initial cholesterol oxidation products, respectively (Chen, Lu, Chien, & Chen, 2010). Also, 7 $\beta$ -OH was formed at a higher level than 7 $\alpha$ -OH, probably due to a smaller steric hindrance effect of the former (Chen, Lu, Chien, & Chen, 2010). However, with STF and roasting at 120 °C for 4 min, both 7 $\alpha$ -OH and 7 $\beta$ -OH in thin slices of dried pork decreased to 0.011 and 0.016  $\mu\text{g/g}$ , respectively, probably due to degradation. In contrast, with STF, two more COPs, 5,6 $\beta$ -EP and triol were generated when roasted at 160 and 200 °C for 4 min respectively, probably due to the accelerated cholesterol oxidation and degradation as the cholesterol melting point is 147–148.5 °C. Also, the total COP contents followed a temperature-dependent increase, which equaled 0.027, 1.217 and 1.269  $\mu\text{g/g}$  at 120, 160 and 200 °C, respectively. The formation of 5,6 $\beta$ -EP is probably due to cholesterol oxidation in the presence of 7 $\beta$ -OOH, while the triol formation is due to hydration of 5,6 $\beta$ -EP under acidic condition caused by hydrolysis of triglyceride during roasting of air-dried pork (Hsu & Chen, 2020). Similarly, a temperature-dependent rise of total COPs was shown for the treatment of flavoring without soy sauce (F6). However, at 160 or 200 °C, only three COPs (7 $\alpha$ -OH, 7 $\beta$ -OH and 5,6 $\beta$ -EP) were formed for the flavoring treatment without soy sauce or sugar, while five COPs (7 $\alpha$ -OH, 7 $\beta$ -OH, 5,6 $\beta$ -EP, 5,6 $\alpha$ -EP and triol) were generated for the flavoring treatment without sugar (F7). This outcome implied that sugar may be more effective than soy sauce in inhibiting cholesterol oxidation. By comparison at the same temperature (120 or 200 °C), the flavoring treatment without sugar generated the highest level of total COPs, followed by that without soy sauce and STF. Interestingly, with the flavoring treatment at 160 °C, the treatment without soy sauce produced the lowest level of total COPs (0.98  $\mu\text{g/g}$ ). It may be postulated that the addition of sugar may minimize COP formation, probably due to formation of diketo compound from sugar degradation for subsequent chelation of prooxidants such as Fe<sup>+2</sup> or Cu<sup>+2</sup> (Hsu & Chen, 2020). Nevertheless, the addition of soy sauce (8%) and sugar (8%) in the STF may also minimize formation of total COPs. As mentioned above, the presence of small amount of isoflavone in soy sauce may also be effective in inhibiting cholesterol oxidation. Comparatively, sugar may be more effective than soy sauce in retarding cholesterol oxidation. Similar outcome was reported by Lee, Chien, and Chen (2008), demonstrating that sugar was more effective than soy sauce in inhibiting COP formation in marinated pork during heating.

### 3.6. COP contents in thin slices of dried pork as affected by different flavorings and roasting temperature

The COP contents in thin slices of dried pork as affected by different flavorings and roasting temperature is also shown in Table 3. Fig. 3B shows GC-MS-SIM chromatograms of COPs in thin slices of dried pork as affected by different roasting temperature at 120 °C, 160 °C and 200 °C with STF. Only two COPs, 7 $\alpha$ -OH and 7 $\beta$ -OH, were detected in thin slices of dried pork for all the 6 flavoring treatments (STF and F1-F5), while only minor difference in the level of total COPs was shown among the various treatments. However, after roasting at 160 °C, two more COPs, 5,6 $\beta$ -EP and triol, were generated, with the flavoring containing F7 produced the highest level of total COPs (1.927  $\mu\text{g/g}$ ), followed by F4 (1.47  $\mu\text{g/g}$ ), F2 (1.385  $\mu\text{g/g}$ ), F1 (1.313  $\mu\text{g/g}$ ), F3 (1.288  $\mu\text{g/g}$ ), STF (1.217  $\mu\text{g/g}$ ), F5 (1.105  $\mu\text{g/g}$ ) and F6 (0.980  $\mu\text{g/g}$ ). As mentioned before, the formation of 5,6 $\beta$ -EP is probably due to cholesterol oxidation in the presence of the initial oxidation product 7 $\beta$ -OOH, while the triol



**Table 3**COP contents ( $\mu\text{g/g}$ ) in raw pork and thin slices of dried pork as affected by different flavorings and roasting temperatures.<sup>1</sup>

| Flavoring <sup>2</sup> | COP contents                   |                                |                                 |                                |                                |       |        |                    |
|------------------------|--------------------------------|--------------------------------|---------------------------------|--------------------------------|--------------------------------|-------|--------|--------------------|
|                        | 7 $\alpha$ -OH                 | 7 $\beta$ -OH                  | 5,6 $\beta$ -EP                 | 5,6 $\alpha$ -EP               | triol                          | 25-OH | 7-keto | total              |
| Raw pork               | 0.077 $\pm$ 0.003              | 0.090 $\pm$ 0.001              | nd <sup>3</sup>                 | nd                             | nd                             | nd    | nd     | 0.167 <sup>F</sup> |
| 120 °C                 |                                |                                |                                 |                                |                                |       |        |                    |
| STF                    | 0.011 $\pm$ 0.000 <sup>E</sup> | 0.016 $\pm$ 0.001 <sup>E</sup> | nd                              | nd                             | nd                             | nd    | nd     | 0.027 <sup>G</sup> |
| F1                     | 0.011 $\pm$ 0.000 <sup>E</sup> | 0.016 $\pm$ 0.001 <sup>E</sup> | nd                              | nd                             | nd                             | nd    | nd     | 0.027 <sup>G</sup> |
| F2                     | 0.011 $\pm$ 0.000 <sup>E</sup> | 0.016 $\pm$ 0.001 <sup>E</sup> | nd                              | nd                             | nd                             | nd    | nd     | 0.027 <sup>G</sup> |
| F3                     | 0.011 $\pm$ 0.000 <sup>E</sup> | 0.016 $\pm$ 0.001 <sup>E</sup> | nd                              | nd                             | nd                             | nd    | nd     | 0.027 <sup>G</sup> |
| F4                     | 0.012 $\pm$ 0.001 <sup>E</sup> | 0.020 $\pm$ 0.001 <sup>E</sup> | nd                              | nd                             | nd                             | nd    | nd     | 0.032 <sup>G</sup> |
| F5                     | 0.011 $\pm$ 0.000 <sup>E</sup> | 0.016 $\pm$ 0.001 <sup>E</sup> | nd                              | nd                             | nd                             | nd    | nd     | 0.027 <sup>G</sup> |
| F6                     | 0.014 $\pm$ 0.001 <sup>E</sup> | 0.019 $\pm$ 0.001 <sup>E</sup> | trace                           | nd                             | trace                          | nd    | nd     | 0.033 <sup>G</sup> |
| F7                     | 0.013 $\pm$ 0.001 <sup>E</sup> | 0.018 $\pm$ 0.001 <sup>E</sup> | 0.275 $\pm$ 0.009 <sup>E</sup>  | nd                             | trace                          | nd    | nd     | 0.306 <sup>F</sup> |
| 160 °C                 |                                |                                |                                 |                                |                                |       |        |                    |
| STF                    | 0.054 $\pm$ 0.001 <sup>D</sup> | 0.074 $\pm$ 0.001 <sup>D</sup> | 0.976 $\pm$ 0.050 <sup>C</sup>  | trace <sup>4</sup>             | 0.113 $\pm$ 0.000 <sup>B</sup> | trace | nd     | 1.217 <sup>D</sup> |
| F1                     | 0.052 $\pm$ 0.001 <sup>D</sup> | 0.071 $\pm$ 0.001 <sup>D</sup> | 1.076 $\pm$ 0.013 <sup>B</sup>  | trace                          | 0.114 $\pm$ 0.001 <sup>B</sup> | trace | nd     | 1.313 <sup>C</sup> |
| F2                     | 0.055 $\pm$ 0.000 <sup>D</sup> | 0.076 $\pm$ 0.001 <sup>D</sup> | 1.139 $\pm$ 0.030 <sup>AB</sup> | trace                          | 0.115 $\pm$ 0.001 <sup>B</sup> | trace | nd     | 1.385 <sup>C</sup> |
| F3                     | 0.052 $\pm$ 0.001 <sup>D</sup> | 0.070 $\pm$ 0.001 <sup>D</sup> | 1.051 $\pm$ 0.030 <sup>B</sup>  | trace                          | 0.113 $\pm$ 0.000 <sup>B</sup> | trace | nd     | 1.288 <sup>D</sup> |
| F4                     | 0.053 $\pm$ 0.001 <sup>D</sup> | 0.074 $\pm$ 0.001 <sup>D</sup> | 1.230 $\pm$ 0.040 <sup>A</sup>  | trace                          | 0.113 $\pm$ 0.000 <sup>B</sup> | trace | nd     | 1.470 <sup>B</sup> |
| F5                     | 0.052 $\pm$ 0.001 <sup>D</sup> | 0.070 $\pm$ 0.001 <sup>D</sup> | 0.870 $\pm$ 0.050 <sup>D</sup>  | trace                          | 0.113 $\pm$ 0.001 <sup>B</sup> | trace | nd     | 1.105 <sup>E</sup> |
| F6                     | 0.068 $\pm$ 0.008 <sup>C</sup> | 0.099 $\pm$ 0.013 <sup>C</sup> | 0.813 $\pm$ 0.042 <sup>D</sup>  | trace                          | trace                          | trace | trace  | 0.980 <sup>E</sup> |
| F7                     | 0.062 $\pm$ 0.001 <sup>C</sup> | 0.094 $\pm$ 0.002 <sup>C</sup> | 1.012 $\pm$ 0.024 <sup>B</sup>  | 0.645 $\pm$ 0.033 <sup>A</sup> | 0.114 $\pm$ 0.001 <sup>B</sup> | trace | trace  | 1.927 <sup>A</sup> |
| 200 °C                 |                                |                                |                                 |                                |                                |       |        |                    |
| STF                    | 0.054 $\pm$ 0.000 <sup>D</sup> | 0.075 $\pm$ 0.001 <sup>D</sup> | 1.021 $\pm$ 0.030 <sup>B</sup>  | trace                          | 0.119 $\pm$ 0.001 <sup>A</sup> | trace | nd     | 1.269 <sup>D</sup> |
| F1                     | 0.054 $\pm$ 0.000 <sup>D</sup> | 0.077 $\pm$ 0.001 <sup>D</sup> | 1.085 $\pm$ 0.030 <sup>B</sup>  | trace                          | 0.119 $\pm$ 0.001 <sup>A</sup> | trace | nd     | 1.335 <sup>C</sup> |
| F2                     | 0.054 $\pm$ 0.000 <sup>D</sup> | 0.075 $\pm$ 0.001 <sup>D</sup> | 1.211 $\pm$ 0.025 <sup>A</sup>  | trace                          | 0.118 $\pm$ 0.001 <sup>A</sup> | trace | nd     | 1.458 <sup>B</sup> |
| F3                     | 0.055 $\pm$ 0.000 <sup>D</sup> | 0.078 $\pm$ 0.001 <sup>D</sup> | 1.062 $\pm$ 0.023 <sup>B</sup>  | trace                          | 0.120 $\pm$ 0.000 <sup>A</sup> | trace | nd     | 1.315 <sup>C</sup> |
| F4                     | 0.053 $\pm$ 0.001 <sup>D</sup> | 0.072 $\pm$ 0.001 <sup>D</sup> | 1.268 $\pm$ 0.045 <sup>A</sup>  | trace                          | 0.120 $\pm$ 0.001 <sup>A</sup> | trace | nd     | 1.513 <sup>B</sup> |
| F5                     | 0.053 $\pm$ 0.000 <sup>D</sup> | 0.074 $\pm$ 0.001 <sup>D</sup> | 0.912 $\pm$ 0.014 <sup>C</sup>  | trace                          | 0.119 $\pm$ 0.001 <sup>A</sup> | trace | nd     | 1.158 <sup>E</sup> |
| F6                     | 0.117 $\pm$ 0.002 <sup>A</sup> | 0.174 $\pm$ 0.003 <sup>A</sup> | 1.004 $\pm$ 0.012 <sup>B</sup>  | trace                          | trace                          | trace | trace  | 1.295 <sup>D</sup> |
| F7                     | 0.076 $\pm$ 0.005 <sup>B</sup> | 0.106 $\pm$ 0.001 <sup>B</sup> | 1.063 $\pm$ 0.023 <sup>B</sup>  | 0.665 $\pm$ 0.014 <sup>A</sup> | 0.120 $\pm$ 0.001 <sup>A</sup> | trace | trace  | 2.030 <sup>A</sup> |

<sup>1</sup> Mean of triplicate analyses  $\pm$  standard error. <sup>2</sup>Flavorings: standard flavoring (STF) = 8% sugar, 8% soy sauce, 1.5% salt, 5% oil, 1% black pepper and 1% almond slices; F1 = 8% soy sauce in STF was replaced with 4% soy sauce; F2 = 8% sugar in STF was replaced with 4% sugar; F3 = 8% sugar and 8% soy sauce in STF was replaced with 16% sugar and 4% soy sauce; F4 = 8% sugar and 8% soy sauce in STF was replaced with 4% sugar and 4% soy sauce; F5 = 8% sugar in STF was replaced with 16% sugar; F6 = 8% sugar, 1.5% salt, 5% oil, 1% black pepper and 1% almond slices; F7 = 8% soy sauce, 1.5% salt, 5% oil, 1% black pepper and 1% almond slices. <sup>3</sup>nd = not detected (below LOD). <sup>4</sup>trace = COP levels are higher than or equal to limit of detection (LOD), but below limit of quantitation (LOQ), or the negative data obtained due to PAH levels being lower than the background values of calibration curves. Mean values with different capital letters (A-G) in the same column are significantly different ( $p < 0.05$ ; Duncan's multiple range test) with different flavorings.

formation is probably caused by hydration of 5,6 $\beta$ -EP under acidic condition. By comparison, the addition of high level of sugar (8%) without soy sauce to the flavoring possessed the most pronounced effect in inhibiting cholesterol oxidation, while the addition of 8% soy sauce without sugar (F7) was the least effective in minimizing cholesterol oxidation. Like 160 °C, the same trend was observed for the roasting temperature at 200 °C, with F7 in the flavoring generated the highest level of total COPs (2.030  $\mu\text{g/g}$ ), while 16% sugar and 8% soy sauce produced the lowest level of COPs (1.158  $\mu\text{g/g}$ ). Of the various COPs, 5,6 $\beta$ -EP was formed in the highest amount, followed by triol, 7 $\beta$ -OH and 7 $\alpha$ -OH. As explained above, compared to 7 $\alpha$ -OH, 7 $\beta$ -OH was more susceptible to formation probably due to a smaller steric hindrance effect. Also, 5,6 $\beta$ -EP was formed at a higher level than 5,6 $\alpha$ -EP, which can be due to a higher stability of the former (Lee, Chien, & Chen, 2008). In a previous study Conchillo, Ansorena, and Astiasarán (2005) pointed out that the amount of total COPs was very low in raw chicken (2.88  $\mu\text{g/g}$ ). However, the level of total COPs increased by 4–7 folds with 5,6 $\beta$ -EP, 7 $\beta$ -OH and 7-keto dominating. Eder, Grünthal, Kluge, Hirsche, Spilke, and Brandsch (2005) also reported that the major COPs in heat-processed broiler chickens included 7 $\alpha$ -OH, 7 $\beta$ -OH, 5,6 $\beta$ -EP and 7-keto. Comparatively, 7-keto and 25-OH remained undetected in thin slices of dried pork during roasting in our study, probably due to short roasting time (4 min), as both can only be formed under drastic condition.

### 3.7. Principal component analysis

As shown in Fig. S2, a total of two components including PC 1 with 42.98% and PC 2 with 20.59% illustrated a total of 63.57% variation in PAH and COP formation as affected by different flavorings (STF and F1–F7) and roasting temperatures (T-120, T-160 and T-200). Evidently,

with the exception of F6 for COP formation as well as F6 and F7 for PAH formation (group 5), PAHs (group 1) were well-separated from those of COPs (group 3) in the score plot with PAHs formation being higher than COPs for all the 8 flavorings (Fig. S2A). For roasting temperature, both PAHs and COPs formation appeared in two groups with their levels at 200 °C corresponded to group 2 while that at both 120 and 160 °C to group 4, suggesting that a temperature-dependent increase in PAH or COP formation during roasting (Fig. S2A). In addition, the relationship between PCs and original variables of different flavoring and roasting temperature treatments is shown as loading plots in Fig. S2B. Most of the PAH and COP variables for different flavoring treatments were shown to point towards the same direction of PC1, while for roasting temperatures, they were spread in the directions of both PC1 and PC2, implying that both PC1 and PC2 were strongly influenced by different flavorings and roasting temperatures. Also, the smaller the degree of angle between the treatments, the higher the correlation in the formation of COPs or PAHs. Accordingly, from Fig. S2B, the projected lines corresponding to flavorings F1–F5 (set 1 containing both sugar and soy sauce) as well as F6 and F7 (set 2 containing only sugar or soy sauce) showed a small degree of angle between them for the formation of PAHs, with the angle between two sets diverging to a larger extent. Likewise, the projected lines of flavorings F1–F5 for COPs formation converged by a small angle revealing a higher correlation between these flavorings. However, the projected lines of F6 and F7 deviated largely from F1–F5. On the other hand, among different roasting temperatures, the projected lines of T120 and T160 for PAH formation as well as T160 and T200 for COP formation deviated only by a small angle. However, they diverged respectively to a larger extent with T200 and T120, in accordance with the results observed in the score plot discussed above. Both the score plot and loading plot were merged to obtain a biplot as shown in

Fig. S2C, illustrating an overall grouping and correlation for PAH or COP formation as affected by different flavorings and roasting temperature. All the PCA data were in agreement with the results discussed in sections 3.3 and 3.6 for PAH and COP formation as affected by different flavorings and roasting temperature. Similar finding was reported by Kao, Chen, Chen, Huang, and Chen (2012) for studying formation of PAHs in meat products as affected by roasting. Overall, the PCA analysis revealed that regardless of flavoring type, PAHs were formed at a higher level than COPs, with roasting at 120 and 160 °C generating a lower PAH/COP content than that at 200 °C.

#### 4. Conclusion

In conclusion, a high accuracy and precision method was attained for analysis of COPs and PAHs in thin slices of dried pork by QuEChERS coupled with GC-MS and GC-MS/MS, respectively. A temperature-dependent increase was shown for the total amount of both COPs and PAHs in thin slices of dried pork during roasting at 120, 160, and 200 °C. The addition of high level of sugar (8 or 16%) and soy sauce (8%) to the flavoring may reduce COP formation, while the low level (4% sugar and 4% soy sauce) may minimize PAH formation. Sugar was more effective in inhibiting COP formation, while soy sauce was more efficient in retarding PAH formation. Nevertheless, the highly toxic BaP remained undetected in thin slices of dried pork, while the various COPs were only present in small amounts. The PCA showed that regardless of flavoring type, PAHs were formed at a higher level than COPs, while roasting at 120 and 160 °C, a lower PAH/COP content was generated than at 200 °C. Taken together, based on the experimental data obtained, the consumption of thin slice of dried pork may pose no risk to human health.

#### CRediT authorship contribution statement

**Yu-Ting Hung:** Methodology, Investigation, Formal analysis. **Yu-Tsung Lee:** Methodology, Investigation, Data curation. **Baskaran Stephen Inbaraj:** Data curation, Validation, Writing - original draft, Writing - review & editing. **Kandi Sridhar:** Formal analysis, Software, Writing - original draft, Writing - review & editing. **Bing-Huei Chen:** Conceptualization, Supervision, Resources, Funding acquisition, Project administration, Writing - original draft, Writing - review & editing.

#### Declaration of Competing Interest

The authors declare that they have no known competing financial interests or personal relationships that could have appeared to influence the work reported in this paper.

#### Acknowledgements

This research was funded by a grant (MOST-110-2327-B-030-001) from Ministry of Science and Technology, Taiwan.

#### Appendix A. Supplementary data

Supplementary data to this article can be found online at <https://doi.org/10.1016/j.foodchem.2021.129474>.

#### References

- Alomirah, H., Al-Zenki, S., Al-Hooti, S., Zaghoul, S., Sawaya, W., Ahmed, N., & Kannan, K. (2011). Concentrations and dietary exposure to polycyclic aromatic hydrocarbons (PAHs) from grilled and smoked foods. *Food Control*, 22, 2028–2035. <https://doi.org/10.1016/j.foodcont.2011.05.024>.
- Chang, C.-C., Zhang, D., Wang, Z., & Chen, B.-H. (2019). Simultaneous determination of twenty heterocyclic amines in cooking oil using dispersive solid phase extraction (QuEChERS) and high performance liquid chromatography-electrospray-tandem mass spectrometry. *Journal of Chromatography A*, 1585, 82–91. <https://doi.org/10.1016/j.chroma.2018.11.050>.
- Chen, B. H., & Chen, Y. C. (2001). Formation of polycyclic aromatic hydrocarbons in the smoke from heated model lipids and food lipids. *Journal of Agricultural and Food Chemistry*, 49, 5238–5243. <https://doi.org/10.1021/jf0106906>.
- Chen, L. J., Lu, Y. F., Chien, J. T., & Chen, B. H. (2010). Formation and inhibition of cholesterol oxidation products in tea-leaf eggs during marinating. *Journal of Agricultural and Food Chemistry*, 58, 10467–10474. <https://doi.org/10.1021/jf102487j>.
- Chen, S., Kao, T. H., Chen, C. J., Huang, C. W., & Chen, B. H. (2013). Reduction of carcinogenic polycyclic aromatic hydrocarbons in meat by sugar-smoking and dietary exposure assessment in Taiwan. *Journal of Agricultural and Food Chemistry*, 61, 7645–7653. <https://doi.org/10.1021/jf402057s>.
- Chen, Y. C., Chien, J. T., Inbaraj, B. S., & Chen, B. H. (2012). Formation and inhibition of cholesterol oxidation products during marinating of pig feet. *Journal of Agricultural and Food Chemistry*, 60, 173–179. <https://doi.org/10.1021/jf204158a>.
- Chiu, C.-W., Kao, T.-H., & Chen, B.-H. (2018). Improved analytical method for determination of cholesterol-oxidation products in meat and animal fat by QuEChERS coupled with gas chromatography-mass spectrometry. *Journal of Agricultural and Food Chemistry*, 66, 3561–3571. <https://doi.org/10.1021/acs.jafc.8b00250>.
- Chung, S. Y., Yettella, R. R., Kim, J. S., Kwon, K., Kim, M. C., & Min, D. B. (2011). Effects of grilling and roasting on the levels of polycyclic aromatic hydrocarbons in beef and pork. *Food Chemistry*, 129, 1420–1426. <https://doi.org/10.1016/j.foodchem.2011.05.092>.
- Conchillo, A., Ansorena, D., & Astiasarán, I. (2005). Intensity of lipid oxidation and formation of cholesterol oxidation products during frozen storage of raw and cooked chicken. *Journal of the Science of Food and Agriculture*, 85, 141–146. <https://doi.org/10.1002/jsfa.1969>.
- Dereviak, D., & Molinska, E. (2015). Cholesterol transformations during heat treatment. *Food Chemistry*, 171, 233–240. <https://doi.org/10.1016/j.foodchem.2014.08.117>.
- Duedahl-Olesen, L., Navaratnam, M. A., Jewula, J., & Jensen, A. H. (2015). PAH in some brands of tea and coffee. *Polycyclic Aromatic Compounds*, 35, 74–90. <https://doi.org/10.1080/10406638.2014.918554>.
- Eder, K., Grünthal, G., Kluge, H., Hirsche, F., Spilke, J., & Brandsch, C. (2005). Concentrations of cholesterol oxidation products in raw, heat-processed and frozen-stored meat of broiler chickens fed diets differing in the type of fat and vitamin E concentrations. *British Journal of Nutrition*, 93, 633–643. <https://doi.org/10.1079/bjn20051411>.
- European Commission. (2011). Commission Regulation (EU) No 835/2011 of 19 August 2011 amending Regulation (EC) No 1881/2006 as regards maximum levels for polycyclic aromatic hydrocarbons in foodstuffs. Official Journal of the European Union, 215, 1–5. Retrieved from <https://eur-lex.europa.eu/> [Last accessed 20 February, 2020].
- European Food Safety Authority. (2008). Polycyclic aromatic hydrocarbons in food—scientific opinion of the panel on contaminants in the food chain. *The EFSA Journal*, 724, 1–114. <https://doi.org/10.2903/j.efsa.2008.724>.
- Forsberg, N. D., Wilson, G. R., & Anderson, K. A. (2011). Determination of parent and substituted polycyclic aromatic hydrocarbons in high-fat salmon using a modified QuEChERS extraction, dispersive SPE and GC-MS. *Journal of Agricultural and Food Chemistry*, 59, 8108–8116. <https://doi.org/10.1021/jf201745a>.
- Georgiou, C. A., Constantinou, M. S., Andreou, R., Hapeshi, E., Fatta-Kassinos, D., & Kapnissi-Christodoulou, C. P. (2016). Novel approach to fast determination of cholesterol oxidation products in Cypriot foodstuffs using ultra-performance liquid chromatography-tandem mass spectrometry. *Electrophoresis*, 37, 1101–1108. <https://doi.org/10.1002/elps.201500196>.
- Gosetti, F., Chiuminatto, U., Mazzucco, E., Robotti, E., Calabrese, G., Gennaro, M. C., & Marengo, E. (2011). Simultaneous determination of thirteen polycyclic aromatic hydrocarbons and twelve aldehydes in cooked food by an automated on-line solid phase extraction ultra high performance liquid chromatography tandem mass spectrometry. *Journal of Chromatography A*, 1218, 6308–6318. <https://doi.org/10.1016/j.chroma.2011.06.085>.
- Hsu, K.-Y., & Chen, B.-H. (2020). Analysis and reduction of heterocyclic amines and cholesterol oxidation products in chicken by controlling flavorings and roasting condition. *Food Research International*, 131, 109004. <https://doi.org/10.1016/j.foodres.2020.109004>.
- Hsu, K.-Y., Inbaraj, B. S., & Chen, B.-H. (2020). Evaluation of analysis of cholesterol oxidation products and heterocyclic amines in duck and their formation as affected by roasting methods. *Journal of Food and Drug Analysis*, 28, 323–336. <https://doi.org/10.38212/2224-6614.1066>.
- IARC. (2012). International Agency for Research on Cancer. Agents classified by the IARC monographs. Retrieved from <https://monographs.iarc.fr/> [Last accessed 11 February, 2020].
- Kaneko, S., Kumazawa, K., & Nishimura, O. (2013). Studies on the key aroma compounds in raw (unheated) and heated Japanese soy sauce. *Journal of Agricultural and Food Chemistry*, 61, 3396–3402. <https://doi.org/10.1021/jf400353h>.
- Kao, T. H., Chen, S., Chen, C. J., Huang, C. W., & Chen, B. H. (2012). Evaluation of analysis of polycyclic aromatic hydrocarbons by the QuEChERS method and gas chromatography-mass spectrometry and their formation in poultry meat as affected by marinating and frying. *Journal of Agricultural and Food Chemistry*, 60, 1380–1389. <https://doi.org/10.1021/jf204650u>.
- Lee, H. W., Chien, J. T., & Chen, B. H. (2008). Inhibition of cholesterol oxidation in marinated foods as affected by antioxidants during heating. *Food Chemistry*, 108, 234–244. <https://doi.org/10.1016/j.foodchem.2007.10.072>.
- Liu, J. H. (2015). Test of residual pesticides in fruits and vegetables (in Chinese). In Taiwan Health Bureau of New Taipei City (Ed.), Taiwan. Retrieved from <https://english.doh.gov.taipei/> [Last accessed 21 February, 2020].

- Lo, Y. L. (2005). Cholesterol-3 $\beta$ -5 $\alpha$ -6 $\beta$ -triol induced cyclooxygenase-2 expression in endothelial cells: Implementation for carcinogenesis. Taipei Medical University, Taipei City, Taiwan. Retrived from <http://eng.tmu.edu.tw/> [Last accessed 19 February, 2020].
- Moret, S., Purcaro, G., & Conte, L. S. (2005). Polycyclic aromatic hydrocarbons in vegetable oils from canned foods. *European Journal of Lipid Science and Technology*, 107, 488–496. <https://doi.org/10.1002/ejlt.200501060>.
- Musarurwa, H., Chimuka, L., Pakade, V. E., & Tavengwa, N. T. (2019). Recent developments and applications of QuEChERS based techniques on food samples during pesticide analysis. *Journal of Food Composition and Analysis*, 84, 103314. <https://doi.org/10.1016/j.jfca.2019.103314>.
- Rejczak, T., & Tuzimski, T. J. O. C. (2015). A review of recent developments and trends in the QuEChERS sample preparation approach. *Open Chemistry*, 1, 980–1010. <https://doi.org/10.1515/chem-2015-0109>.
- SAS. (2014). *SAS procedures and SAS/graph user's guide, version 6*. Gary, NC: SAS Institute Inc.
- Settle, A. E., Berstis, L., Rorrer, N. A., Roman-Leshkóv, Y., Beckham, G. T., Richards, R. M., & Vardon, D. R. (2017). Heterogeneous Diels-Alder catalysis for biomass-derived aromatic compounds. *Green Chemistry*, 19, 3468–3492. <https://doi.org/10.1039/C7GC00992E>.
- Sevanian, A., & Peterson, A. R. (1986). The cytotoxic and mutagenic properties of cholesterol oxidation products. *Food and Chemical Toxicology*, 24, 1103–1110. [https://doi.org/10.1016/0278-6915\(86\)90295-4](https://doi.org/10.1016/0278-6915(86)90295-4).
- Shukla, B., & Koshi, M. (2011). Comparative study on the growth mechanisms of PAHs. *Combustion and Flame*, 158, 369–375. <https://doi.org/10.1016/j.combustflame.2010.09.012>.
- Shukla, B., & Koshi, M. (2012). A novel route for PAH growth in HACA based mechanisms. *Combustion and Flame*, 159, 3589–3596. <https://doi.org/10.1016/j.combustflame.2012.08.007>.
- TFDA Method validation of food analysis (In Chinese). Available from: <https://www.fda.gov.tw> 2013 Last accessed 21 February, 2020.
- TFDA. (2018). Method development of polycyclic aromatic hydrocarbons in foods (In Chinese). Available from <https://consumer.fda.gov.tw/Food/TestingDetail.aspx?nodeID=1037&id=8131> [Last accessed 21 February, 2020].
- Varlet, V., Serot, T., Monteau, F., Le Bizec, B., & Prost, C. (2007). Determination of PAH profiles by GC-MS/MS in salmon processed by four cold-smoking techniques. *Food Additives Contaminants*, 24, 744–757. <https://doi.org/10.1080/02652030601139946>.
- Veyrand, B., Brosseaud, A., Sarcher, L., Varlet, V., Monteau, F., Marchand, P., ... Le Bizec, B. (2007). Innovative method for determination of 19 polycyclic aromatic hydrocarbons in food and oil samples using gas chromatography coupled to tandem mass spectrometry based on an isotope dilution approach. *Journal of Chromatography A*, 1149, 333–344. <https://doi.org/10.1016/j.chroma.2007.03.043>.

## Original research

# Gut microbiota modulates COPD pathogenesis: role of anti-inflammatory *Parabacteroides goldsteinii* lipopolysaccharide

Hsin-Chih Lai,<sup>1,2,3,4,5</sup> Tzu-Lung Lin,<sup>1</sup> Ting-Wen Chen,<sup>6,7,8</sup> Yu-Lun Kuo,<sup>9</sup> Chih-Jung Chang,<sup>3</sup> Tsung-Ru Wu,<sup>10</sup> Ching-Chung Shu,<sup>11</sup> Ying-Huang Tsai,<sup>3</sup> Simon Swift,<sup>12</sup> Chia-Chen Lu<sup>13,14</sup> 

► Additional material is published online only. To view please visit the journal online (<http://dx.doi.org/10.1136/gutjnl-2020-322599>).

For numbered affiliations see end of article.

## Correspondence to

Dr Chia-Chen Lu, Department of Respiratory Therapy, Fu Jen Catholic University, New Taipei City, Taiwan; [chiachen.lulu@gmail.com](mailto:chiachen.lulu@gmail.com)

H-CL and T-LL contributed equally.

Received 23 July 2020  
Revised 11 February 2021  
Accepted 27 February 2021

## ABSTRACT

**Objective** Chronic obstructive pulmonary disease (COPD) is a global disease characterised by chronic obstruction of lung airflow interfering with normal breathing. Although the microbiota of respiratory tract is established to be associated with COPD, the causality of gut microbiota in COPD development is not yet established. We aimed to address the connection between gut microbiota composition and lung COPD development, and characterise bacteria and their derived active components for COPD amelioration.

**Design** A murine cigarette smoking (CS)-based model of COPD and strategies evaluating causal effects of microbiota were performed. Gut microbiota structure was analysed, followed by isolation of target bacterium. Single cell RNA sequencing, together with sera metabolomics analyses were performed to identify host responsive molecules. Bacteria derived active component was isolated, followed by functional assays.

**Results** Gut microbiota composition significantly affects CS-induced COPD development, and faecal microbiota transplantation restores COPD pathogenesis. A commensal bacterium *Parabacteroides goldsteinii* was isolated and shown to ameliorate COPD. Reduction of intestinal inflammation and enhancement of cellular mitochondrial and ribosomal activities in colon, systematic restoration of aberrant host amino acids metabolism in sera, and inhibition of lung inflammations act as the important COPD ameliorative mechanisms. Besides, the lipopolysaccharide derived from *P. goldsteinii* is anti-inflammatory, and significantly ameliorates COPD by acting as an antagonist of toll-like receptor 4 signalling pathway.

**Conclusion** The gut microbiota–lung COPD axis was connected. A potentially beneficial bacterial strain and its functional component may be developed and used as alternative agents for COPD prevention or treatment.

## INTRODUCTION

Chronic obstructive pulmonary disease (COPD) is a multidimensional progressive lung inflammatory disease, with pathological changes in the large and small airways.<sup>1,2</sup> COPD has a huge global prevalence (251 million cases in 2016) and causes high mortality (3.17 million deaths in 2015), with a prediction of being the third leading cause of

## Significance of this study

### What is already known on this subject?

- Although there were many previous studies, ways of management of chronic obstructive pulmonary disease (COPD) were still encountered with difficulty.
- The microbiota composition in the respiratory tract was shown to closely related to COPD severity and development. However, whether the gut microbiota–lung COPD axis also existed was not established.
- Furthermore, there were no microbiota derived agent(s) identified to effectively ameliorate COPD.

### What are the new findings?

- The gut microbiota–lung COPD axis was established in this study.
- A bacterial strain that showed COPD amelioration effect was isolated.
- An anti-inflammatory lipopolysaccharide (LPS) molecule purified from this bacterium can ameliorate COPD.

### How might it impact on clinical practice in the foreseeable future?

- The beneficial bacterial strain (*Parabacteroides goldsteinii* MTS01), together with its derived LPS (*P. goldsteinii*-LPS) may be developed as an agent for clinical practice in COPD.

mortality in 2020.<sup>3–5</sup> There are many measures for COPD management; however, persistent and progressive pulmonary inflammation is still common among patients.<sup>6,7</sup>

The roles of microbiota in development of host health are emphasised,<sup>8–10</sup> some supporting the role of respiratory tract microbes towards the onset, progression, promotion and severity of COPD chronicity.<sup>11</sup> Emerging evidences indicate close interactions between gut microbiota composition and lung immunity.<sup>12</sup> However, the relationship between gut microbiota composition and COPD development is still to be well characterised.

We established the gut microbiota–lung COPD axis using a mouse cigarette smoking (CS) model,



© Author(s) (or their employer(s)) 2021. No commercial re-use. See rights and permissions. Published by BMJ.

**To cite:** Lai H-C, Lin T-L, Chen T-W, et al. Gut Epub ahead of print: [please include Day Month Year]. doi:10.1136/gutjnl-2020-322599



and strategy of faecal microbiota transplantation (FMT) and antibiotics (ABX) treatment. An intestinal commensal *Parabacteroides goldsteinii* (Pg) was highlighted to be significantly negatively associated with severity of COPD. Oral administration of isolated Pg MTS01 on its own significantly ameliorated CS-induced COPD syndromes, characterised by reducing inflammation and improving cellular ribosomal biogenesis activity and mitochondrial functions in intestine, systematically restoring aberrant amino acids metabolism in sera, and reducing lung tissue inflammations. The lipopolysaccharide (LPS) derived from Pg-LPS was subsequently characterised to act as a toll-like receptor 4 (TLR-4) receptor antagonist and worked as an active component that ameliorated CS-induced COPD. Our study highlighted the important causality role of gut microbiota in COPD pathogenesis and established the gut-lung COPD axis. Furthermore, a potential probiotic bacterium whose LPS might work as a COPD ameliorating agent was reported.

## METHODS

### Model of CS-induced COPD

C57BL/6 mice (8–10 weeks old) were purchased from the National Laboratory Animal Center (Taipei, Taiwan) and kept under sterile conditions (following a 12 hours light/dark cycle), with 1-week acclimatisation period. Mice were fed with normal chow diet (Laboratory Autoclavable Rodent Diet 5010; LabDiet, USA) during the entire experiment.

The CS-induced COPD model used was modified from He *et al.*<sup>13</sup> Briefly, mice were exposed to CS from 12 3R4F cigarettes (Kentucky University) twice a day (twenty-four cigarettes per day), 5 day-week for 12 weeks, with body weights being monitored weekly. Pulmonary function was assessed by forced pulmonary manoeuvre system (Buxco Research Systems, Wilmington, USA), and bronchoalveolar lavage fluid (BALF) and paraffin sections of the lungs were obtained in every mouse to confirm the COPD phenotypes. Detailed methods of animal experiments and measurements can be found in online supplemental methods.

### Analysis of gut microbiota structure

We followed the protocol per our previous studies<sup>14–16</sup> and detailed methods and workflow can be found in online supplemental methods and online supplemental figure S1. In brief, partial least squares discriminant analysis (PLS-DA) analysis was used to evaluate sample-species complexity (Beta diversity analysis). The statistically significant biomarkers (LDA score (log10) >4.0 with  $p < 0.05$ ) in CS mice were identified using the LEfSe analysis and also confirmed by using metagenomeSeq ( $q < 0.05$ ). Furthermore, bacterial species significantly altered by ABX treatment ( $q < 0.05$ ) or FMT ( $p < 0.05$ ) were identified by using metagenomeSeq.

### Pg cultivation and genome sequencing

Pg MTS01 was isolated from faeces of mice in ABX experiments and grown at 37°C in anaerobic condition. Illumina and Pacbio platforms were used for Pg MTS01's full-genome sequencing. Detailed methods of experiments can be found in online supplemental methods.

### ScRNAseq analysis of colon and lung tissues and sera metabolomics analysis

The colon and lung tissues of CTL, CS and CS administered with Pg mice groups were collected after 12 weeks and subjected for 10x Genomics Single Cell 3' Gene Expression analysis. The sera metabolites were analysed by GC-MS and LC-MS. Detailed

methods of experiments and analysis can be found in online supplemental methods.

### Pg-LPS purification and its antagonistic effects

Pg-LPS were isolated by using the hot phenol-water extraction. The antagonistic effect was analysed on HEK-Blue-mTLR4 cells, mouse CD11c+ dendritic cells (DC) cells, human PBMC cells and mouse B cells treated with *Escherichia coli* O111:B4 LPS. Detailed methods of experiments can be found in online supplemental methods.

### Statistical analysis

Data are shown as means  $\pm$  SD and medians  $\pm$  IQR for parametric and non-parametric analysis, respectively. Differences between two groups are assessed using unpaired two-tailed Student's t-test. Data sets involving more than two groups are assessed by one-way analysis of variance, followed by non-parametric Kruskal-Wallis test with Newman-Keuls multiple comparison (see figure legends).

## RESULTS

### Evidence of gut microbiota involvement in COPD development

To see whether gut microbiota may contribute to CS induced COPD development, we used a murine CS model of chronic pulmonary inflammation (online supplemental figure S2). CS mice smoking for 12 weeks significantly lost body weight (online supplemental figure S2a, b), and increased infiltration of immune cells in BALF (online supplemental figure S2c). By contrast, weight gain and decreased infiltrated immune cells were observed in CS mice cohoused with control (CO-CTL) group (online supplemental figure S2a–c). Comparatively, control group cohoused with CS (CO-CS) group developed aberrant phenotypes (online supplemental figure S2a–c).

Concordantly, histological analysis of lung tissue sections revealed CS-exposed mice show peripheral emphysematous changes characterised by alveolar wall destruction and enlargement of airspace compared with CTL mice. By contrast, CO-CTL group restored the pathology, while CO-CS group exacerbated (online supplemental figure S2d, e). Concordantly, similar phenomena on production of interleukin (IL)-1 $\beta$  and tumour necrosis factor (TNF)- $\alpha$  in CD11c+ DCs, and F4/80+CD11b+ macrophage cells (online supplemental figure S2f, g), IL-17A production in CD4+NKP46+Th17 cells, and IL-10 production in CD4+FoxP3+Treg cells were also observed (online supplemental figure S2h). Furthermore, assessment of pulmonary function also showed consistent results (online supplemental figure S2i–l). Although the gut microbiota was not determined, cohousing results speculated that beneficial and adverse gut bacteria may respectively exist in CTL and CS mice.

### ABX treatment reduces CS-induced COPD pathogenesis

To determine the importance of gut microbiota composition in COPD development, individual (vancomycin (VAN), neomycin (NEO), metronidazole (MET) and ampicillin (AMP)) and combination ABX<sup>17</sup> were orally administrated to mice 2 weeks before CS. Aberrant phenotypes observed in CS mice (figure 1A–K) were significantly ameliorated in the ABX, AMP and VAN-treated groups. In contrast, oral NEO or MET treatment did not significantly affect COPD pathogenesis (figure 1A–K). Thus, commensal microbiota composition affect the inflammations and pathogenesis of CS-induced COPD and treatment with

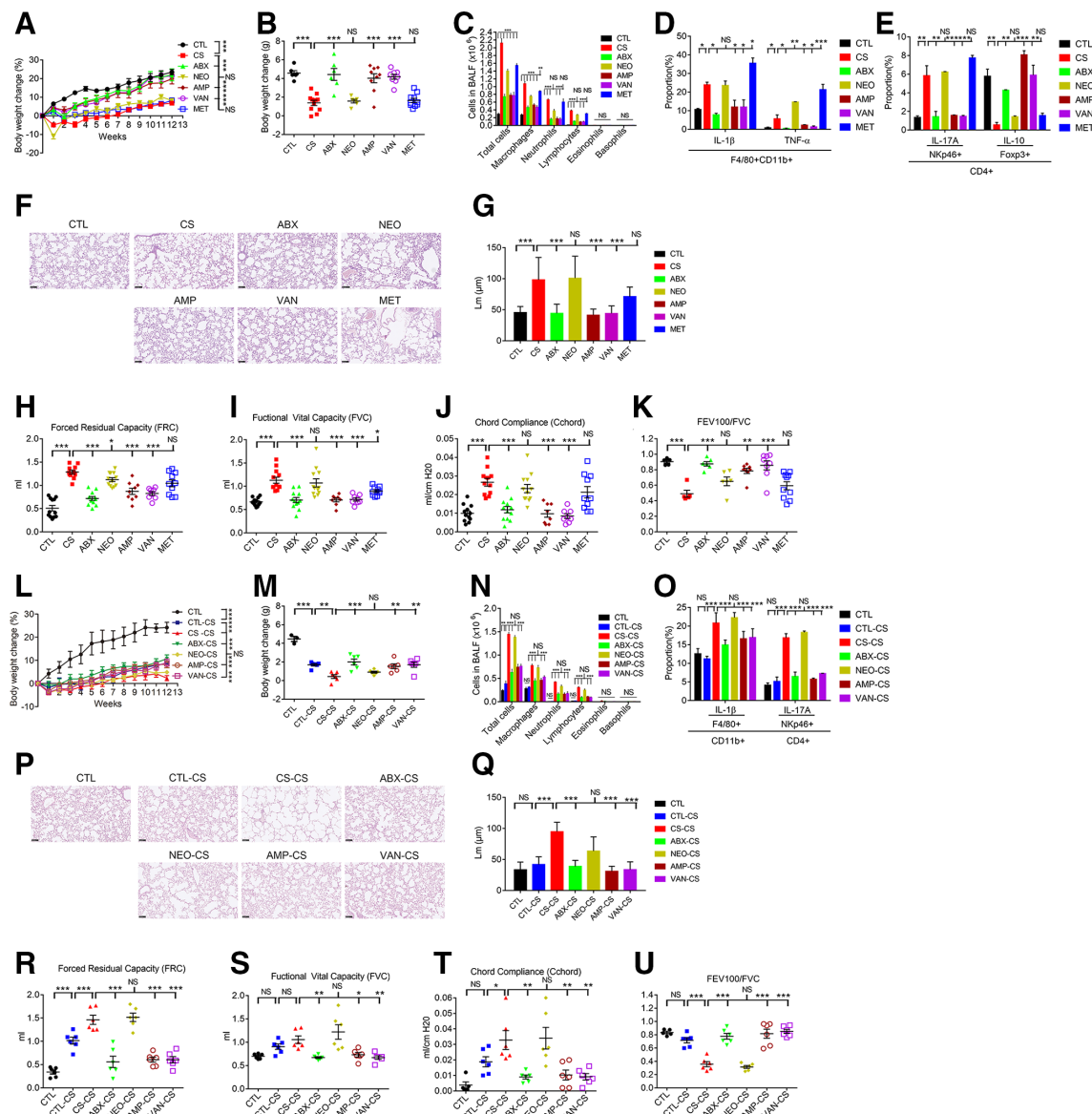


**Figure 1** Establishment of the gut microbiota-COPD development relationship. Mice were orally administered with antibiotics (NEO, AMP, VAN, MET and ABX) to evaluate the effect of antibiotics treatment on COPD development in CS mice. Percentage of body weight change was measured throughout the 12-week period (A). Body weight change (B), BALF cellular composition (C), flow cytometry analysis on production of IL-1 $\beta$  and TNF- $\alpha$  in F4/80+CD11b+ macrophages (D), IL-17A in CD4+NKp46+Th17 cells and IL-10 in CD4+FoxP3+Treg cells (E), histopathology in lung (F) and the mean linear intercept of lung tissue (G) and lung functions analyses including FRC (H), FVC (I), Chord (J) and FEV100/FVC (K) were measured after 12 weeks. Through use of the faeces microbiota of antibiotics-treated mice as the donor, FMT was performed to see their effects on COPD development in CS recipient mice. Percentage of body weight change was measured throughout the 12-week period (L). Body weight change (M), BALF cellular composition (N), flow cytometry analysis on production of IL-1 $\beta$  in F4/80+CD11b+ macrophages and IL-17A in CD4+NKp46+Th17 cells (O), lung histopathology (P) and the mean linear intercept of lung tissue (Q), and lung functions analyses including FRC (R), FVC (S), Chord (T), and FEV100/FVC (U) were measured after 12 weeks. For FMT, faeces microbiota of control (CTL), CS, ABX, NEO, AMP and VAN were collected, followed by oral administration to recipient CS mice. Except panels F and P, the data representing means $\pm$ SD or medians $\pm$ IQR were analysed using the Newman-Keuls multiple comparison post hoc one-way ANOVA analysis (n=6–12 for panel a-j and n=5–6 for panel k-s). \*p<0.05; \*\*p<0.01; \*\*\*p<0.001. ANOVA, analysis of variance; ABX, antibiotics; AMP, ampicillin; BALF, bronchoalveolar lavage fluid; CS, cigarette smoking; COPD, chronic obstructive pulmonary disease; FMT, faecal microbiota transplantation; IL-1 $\beta$ , interleukin 1 $\beta$ ; MET, metronidazole; NS, not significant; TNF- $\alpha$ , tumour necrosis factor  $\alpha$ ; VAN, vancomycin.

optimal ABX predisposes the mice to reduced pathogenesis in the lung of COPD.

### Gut microbiota composition plays a causal effect on COPD development

The beneficial effects of ABX treatment may be mediated through the changed gut microbiota composition. To see

whether the changed gut microbiota structure may play a causal effect on COPD development, FMT experiment was performed. Donor faecal microbiota from CTL or CS mice treated by either ABX, NEO, AMP or VAN were transferred to CS-recipient mice. Faecal microbiota from CTL, ABX-treated, AMP-treated or VAN-treated mice significantly ameliorated COPD syndromes (figure 1L–U). In contrast, microbiota derived from



**Figure 2** Negative association of *Parabacteroides goldsteinii* with COPD severity in different mice groups. The top 10 most abundant faecal microbiota bacterial families of CTL, CS, ABX, NEO, AMP and VAN treated mice groups were shown in (A). Bacterial species significantly altered by antibiotics (ABX, NEO, AMP and VAN) in comparison with the CS group ( $p < 0.05$ ) were shown in the heatmap (B). Spearman's correlation analysis between the 17 identified bacterial species and COPD traits (C). The p values were corrected for multiple comparisons by using Benjamini and Hochberg (BH) method. (+ $p < 0.05$ ; ++ $p < 0.01$ ; #adjusted  $p < 0.05$ ; ##adjusted  $p < 0.01$ ). bacterial species significantly altered by FMT (CTL-CS, CS-CS, ABX-CS, NEO-CS, AMP-CS and VAN-CS) between any two groups ( $p < 0.05$ ) were shown in the heatmap (D). The values of the heatmap (B, D) are based on the row scaling (z-scores) of the relative abundance. ABX, antibiotics; AMP, ampicillin; CS, cigarette smoking; COPD, chronic obstructive pulmonary disease; CTL, control; FEV, forced expiratory volume; FMT, faecal microbiota transplantation; FVC, forced vital capacity; NEO, neomycin; VAN, vancomycin.

CS or NEO-treated mice failed to reverse COPD traits of CS recipients (figure 1L–U). Briefly, the COPD ameliorative effects produced by treatment of CS mice with ABX, AMP or VAN are transferrable through gut microbiota transplantation. Therefore, the changed gut microbiota structure may play a causal effect on COPD pathogenesis.

The gut microbiota compositions in each mice group were determined using 16S microbiota ribosomal DNA sequencing (figure 2A). Relative abundance of Erysipelotrichaceae, Bacteroidales and Ruminococcaceae were significantly reduced, while those of Lachnospiraceae were increased in the faeces of CS mice in contrast to the CTL mice (online supplemental figure S3a–c). ABX treatment and FMT both affects the composition of gut microbiota in CS mice (figure 2a and online supplemental figure S3d, e). Seventeen bacterial species significantly altered by antibiotics (ABX, NEO, AMP and VAN) in comparison with the CS group were identified by using metagenomeSeq (figure 2B)

and the correlation between the 17 identified bacterial species and COPD traits was further analysed (figure 2C). *P. goldsteinii* and *E. coli* were significantly negatively correlated with the COPD severity (figure 2C), and the relative abundance of Pg and *E. coli* in 16S sequencing data was mostly consistent with those validated by qPCR, except that the relative abundance of Pg in the AMP group was not significantly altered in qPCR data (online supplemental figure S3f–i). Furthermore, bacterial species significantly altered by FMT between any two groups indicated only Pg was increased by trend in ABX, VAN and AMP treated mice groups (figure 2D and online supplemental figure S3j). Additionally, a positive correlation between COPD severity and Lachnospiraceae which was significantly increased in CS mice was observed (figure 2C and online supplemental figure S3k). Therefore, together with all the data obtained, Pg was selected for subsequent studies.



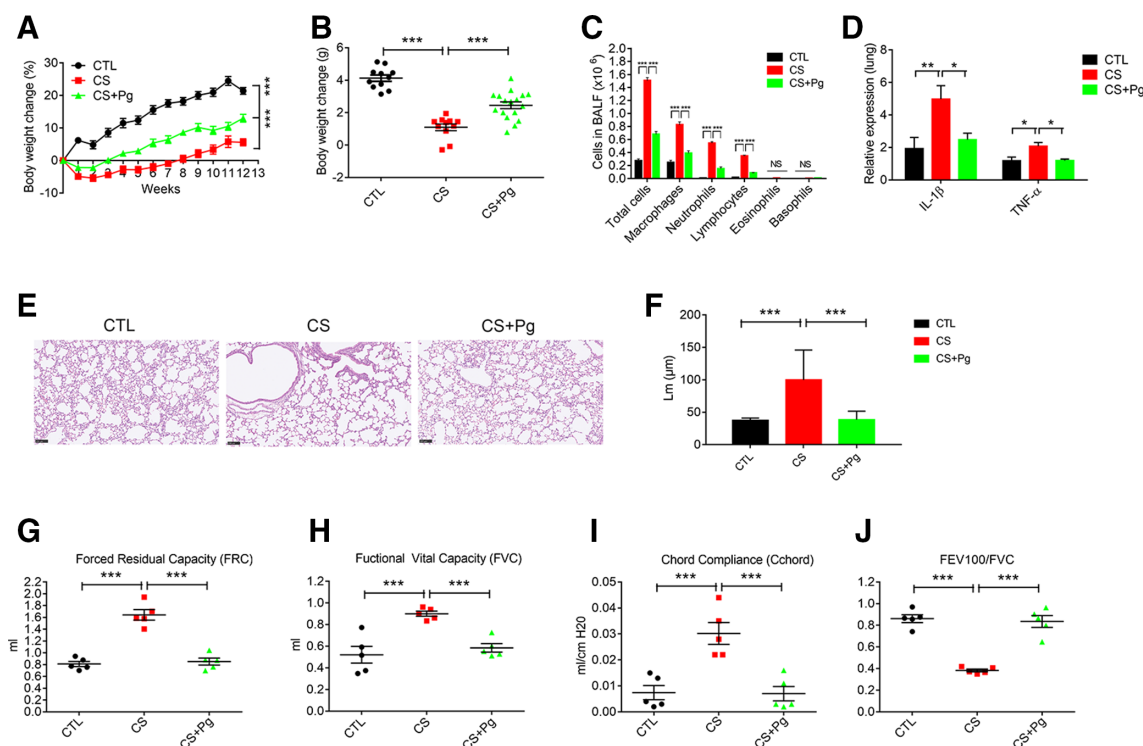


**Figure 3** *Parabacteroides goldsteinii* MTS01 ameliorates COPD. Live *P. goldsteinii* (Pg) MTS01 at the colony-forming units of  $2 \times 10^8$  were orally administered to CS mice to evaluate their effects on COPD development. Percentage of body weight change was measured throughout the 12-week period (A). Body weight change (B), BALF cellular composition (C), RNA expression of IL-1 $\beta$  and TNF- $\alpha$  in lung (D), histopathology in lung (E) and the mean linear intercept of lung tissue (F), and lung functions analyses including FRC (G), FVC (H), Cchord (I) and FEV100/FVC (J) were measured after 12 weeks. Except panel E, the data representing means $\pm$ SD or medians $\pm$ IQR ( $n=5-17$ ) were analysed using the Newman-Keuls multiple comparison post hoc one-way ANOVA analysis. \* $p<0.05$ ; \*\* $p<0.01$ ; \*\*\* $p<0.001$ . ANOVA, analysis of variance; BALF, bronchoalveolar lavage fluid; COPD, chronic obstructive pulmonary disease; CS, cigarette smoking; CTL, control; IL-1 $\beta$ , interleukin 1 $\beta$ ; NS, not significant; TNF- $\alpha$ , tumour necrosis factor  $\alpha$ .

### Pg MTS01 ameliorates COPD

A Pg bacterial strain MTS01 (online supplemental figure S4a) was subsequently isolated from ABX-treated faecal microbiota samples. Full-length sequencing of 16S rRNA gene of Pg MTS01 showed 99.9% identity to that of Pg JCM13446.<sup>14</sup> Oral treatment of Pg MTS01 ( $2 \times 10^8$  colony-forming units per day per mouse) significantly increased body weight gain (by 7.4%) and ameliorated COPD phenotypes (figure 3A–J). In parallel, the expression of lung ZO-1 and Occludin mRNA-linked with the respiratory tract integrity was also increased (online supplemental figure S4b, c).

CS has been shown as a risk factor of intestinal mucosal damages.<sup>18</sup> In colon, Pg MTS01 treatment reduced expression of proinflammatory cytokines such as IL-1 $\beta$  and TNF- $\alpha$  (online supplemental figure S4d), and increased expression of ZO-1 and Occludin (online supplemental figure S4e, f) in CS mice. Pg MTS01 further restored TNF- $\alpha$ -induced increase of cell layer TEER permeability in a Caco-2-cells in vitro model (online supplemental figure S4g). Effects of Pg MTS01 on body weight change, histopathology in lung and liver, serum GPT and BUN levels revealed that Pg MTS01 has no adverse effect on healthy mice (online supplemental figure S4h–l).

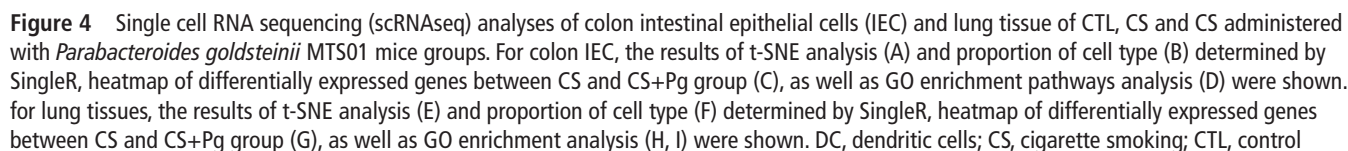
### Pg MTS01 reduces intestinal inflammation and enhances cellular ribosomal and mitochondrial activity in CS mice

Pg MTS01 administration reduced pro-inflammatory cytokines production and increased intestinal integrity in colon (online supplemental figure S4d–g). To further characterise the effects of Pg MTS01 administration on physiology of colon cells,

single-cell RNA sequencing (scRNAseq) and analyses of colon tissue-derived cells of CS mice with/without Pg MTS01 treatment were conducted (figure 4A,B). Specifically, in CS compared with CTL mice, an increased expression of genes involved in fatty acid/eicosanoids metabolism, membrane microvillus formation and endopeptidase activity, while reduced expression of genes involving ribosomal biogenesis and mitochondrial activity were observed (online supplemental dataset 1 and figure S5a, b). By contrast, Pg MTS01 administration significantly upregulated genes of cellular antioxidants, redox processes, antibacterials, mitochondrial depolarisation, ribosomal activity and mucin production in CS mice (figure 4C,D and online supplemental dataset 2). Expression levels of Mptx1 (mucosal pentraxin 1), Ang4 (angiogenin, ribonuclease A family, member 4) and Muc2 (mucin 2) (online supplemental figure S5c–e), RNR1 (mitochondria encoded 12S rRNA), RNR2 (mitochondria encoded 16S rRNA), Cytb (mitochondria encoded cytochrome B), PGC-1 $\alpha$  (peroxisome proliferator-activated receptor  $\gamma$  coactivator 1 $\alpha$ ), ND-5 (mitochondria encoded NADH-ubiquinone oxidoreductase chain 5 protein) and mitochondria encoded Transcription Factor A genes related to oxidative stresses and ribosomal/mitochondrial activities, were further validated by qPCR (online supplementary table S1 and figure S5f–k). By contrast, Pg MTS01 did not significantly downregulate any GO pathway in CS mice.

In COPD, reduced ribosomal biogenesis activity is linked to mitochondria dysfunction.<sup>19</sup> The oxygen consumption rate (OCR) and extracellular acidification rate (ECAR) linked to oxidative phosphorylation and non-mitochondria glycolysis





function, respectively, were measured. Pg MTS01 increased the aberrant OCR activity, and reduced ECAR in CS mice (online supplemental figure S5I, m). Pg MTS01 may therefore reduce inflammations and restore the abrogated cellular ribosomal and mitochondrial activity in colon of CS mice.

### Pg MTS01 systematically restores aberrant amino acid-metabolism in Cs mice

The phenomenon that oral administration of Pg MTS01 ameliorated COPD lung pathogenesis might be related to restoration of systematic aberrant metabolism in blood. To further characterise whether any metabolomics in mice sera were affected by Pg MTS01 treatment, non-targeted positively and negatively charged metabolite-analyses were analysed. Ingenuity canonical pathways analyses on sera metabolites indicated that Pg MTS01 administration most significantly improved aberrant amino acid-related metabolism and tRNA-amino acid charging activities in CS mice, including increased biosynthesis of citrulline and proline, degradation of phenylalanine and glycine, and turnover of arginine (online supplemental figure S6a–d). Pg MTS01 may therefore enhance amino acids metabolism related to cellular ribosomal and mitochondrial activities and urea cycle turnover (online supplemental figure S6c).

### Pg MTS01 reduces lung inflammations in Cs mice

Administration of Pg MTS01 enhanced lung integrity (online supplemental figure S4b, c) and reduced inflammations in COPD lung (figure 3D). Further lung tissue single-cell RNA sequencing analyses indicated that CS also increased viable counts of B cells, macrophages as well as reduced T cells and neutrophils counts, which were reversed by Pg MTS01 administration (figure 4E,F). Furthermore, Pg MTS01 significantly restored the aberrant gene expression patterns identified in CS mice. Especially, genes involved in antigen processing and presentation via MHCII, and B cell receptor signalling pathway in B cells were reduced (figure 4G–I, online supplemental dataset 3, 4 and figure S7a, b). By contrast, genes involving antioxidant activity, eicosanoid-binding activities, fatty acids synthesis and immune responses were upregulated (figure 4G–I, online supplemental dataset 3–4 and figure S7a, b). Among these, expression of *Scgb1a1* that played important functions in anti-inflammatory properties was most significantly upregulated by Pg MTS01<sup>20 21</sup> (online supplemental figure S7c). However, Pg MTS01 did not significantly reduce sera IgG level in CS mice (online supplemental figure S7d). Briefly, Pg MTS01 reduced overinflammatory immune responses, including those related to B cells receptor signalling in lung tissues.

### Pg MTS01 LPS (Pg-LPS) antagonises *E. coli* LPS-induced inflammations

The proinflammatory LPS has been associated with increased oxidative stress, production of proinflammatory cytokines and COPD pathogenesis.<sup>22</sup> As shown in figure 5A,B, LPS activities measured in the sera and lung BALF were all significantly increased in CS mice compared with CTL mice. By contrast, Pg MTS01 administration significantly reduced these LPS activities detected.

A BLAST analysis of whole genome sequence of Pg MTS01 (figure 5C) highlighted genes involved in lipid A synthesis resembled those identified in *Bacteroides dorei* (figure 5D,E) and *Bacteroides thetaiotaomicron*.<sup>23</sup> *Bacteroides* species-derived LPS subtypes exhibited significantly lower endotoxicity and immunostimulatory responses relative to enteric bacteria-isolated

proinflammatory LPS.<sup>24 25</sup> *E. coli* normally produced a lipid A molecule with six acyl chains.<sup>26</sup> By contrast, Pg MTS01 lacked *LpxM*, one ortholog of the acyltransferases genes, and was expected to produce lipid A with five acyl chains (figure 5D,E).

To see whether Pg MTS01 and *E. coli* exhibited subtype-specific LPS immunogenicity differences, their effects on cellular activation were measured. The NF- $\kappa$ B activations in HEK-Blue-mTLR4 reporter cells that specifically measured the proinflammatory LPS activity were used. While LPS derived from *E. coli* O111:B4 (EC-LPS) started to activate NF- $\kappa$ B activity at the concentration of 1 ng/mL, Pg-LPS at the concentration of 1000 ng/mL still failed in activation (figure 5F). Pg-LPS further showed antagonistic effects on EC-LPS activity. Under the concentration ratio of 1:1, the NF- $\kappa$ B activity activated by EC-LPS was reduced up to 80% by addition of Pg-LPS (figure 5G). Further studies indicated that Pg-LPS competed with EC-LPS for TLR4 receptor binding in a dose-dependent manner (figure 5H).

Whether the phenomenon of EC-LPS and Pg-LPS interaction also occurs in other immune cells was next addressed. Expression of CD86 and proliferation of CD19<sup>+</sup> B cells by EC-LPS were antagonised by Pg-LPS (figure 5I,J). Concordantly, overproduction of TNF- $\alpha$  in CD11c<sup>+</sup> bone marrow derived DCs (figure 5K), and IL-1 $\beta$  in human peripheral mononuclear cells (figure 5L) by EC-LPS treatment was also dose-dependently reduced by Pg-LPS administration, respectively. No cytotoxicity revealed in cell treated with Pg-LPS (online supplemental figure S8a). Briefly, Pg-LPS competes with EC-LPS and antagonises its proinflammatory activity.

### Pg-LPS ameliorates CS-induced COPD syndromes

Pg-LPS was subsequently investigated to see its potentiality in ameliorating CS-induced COPD pathogenesis. As intraperitoneal (i.p.) administration of proinflammatory LPS enhanced emphysema development in COPD,<sup>27</sup> we tested the effect of i.p. treatment of Pg-LPS in CS mice. CS mice with or without i.p. treatment of Pg-LPS (0.2 or 2  $\mu$ g in 100  $\mu$ L saline for each mice) twice per week were phenotyped for COPD. Contrary to the CS mice, Pg-LPS treatment significantly increased body weight gain by 18% and 13.9% in low and high doses, respectively (figure 6A,B), reduced BALF cellular-infiltration (figure 6C), and normalised lung pathology and functions (figure 6D–I). Furthermore, Pg-LPS reduced over-expression of proinflammatory cytokines such as IL-1 $\beta$  and TNF- $\alpha$  in lung tissues (figure 6J,K) and colon (figure 6L,M) in COPD mice. Concordantly, increased LPS concentration and activity in the BALF (figure 6N) and sera (figure 6O) of COPD mice were all significantly reduced by Pg-LPS. Further study indicated that control mice treated with Pg-LPS had normal liver and kidney functions (online supplemental figure S8b, c). Therefore, LPS of Pg MTS01 origin ameliorated CS-induced COPD in mice.

### DISCUSSION

This study highlighted that gut microbiota dysbiosis plays a causal effect influencing the severity of CS-induced COPD pathogenesis. Therefore, the potential axis between gut microbiota composition and lung COPD can be established. A recent human study also found bacterial species differ between the faecal microbiome of COPD patients and healthy controls.<sup>28</sup> Current evidences strongly indicated that not only respiratory tract, but also gut microbiota structure may both be involved in controlling COPD development. The composition of microbiota in BALF of CTL, CS and ABX mice groups was determined using 16S microbiota ribosomal DNA sequencing (online

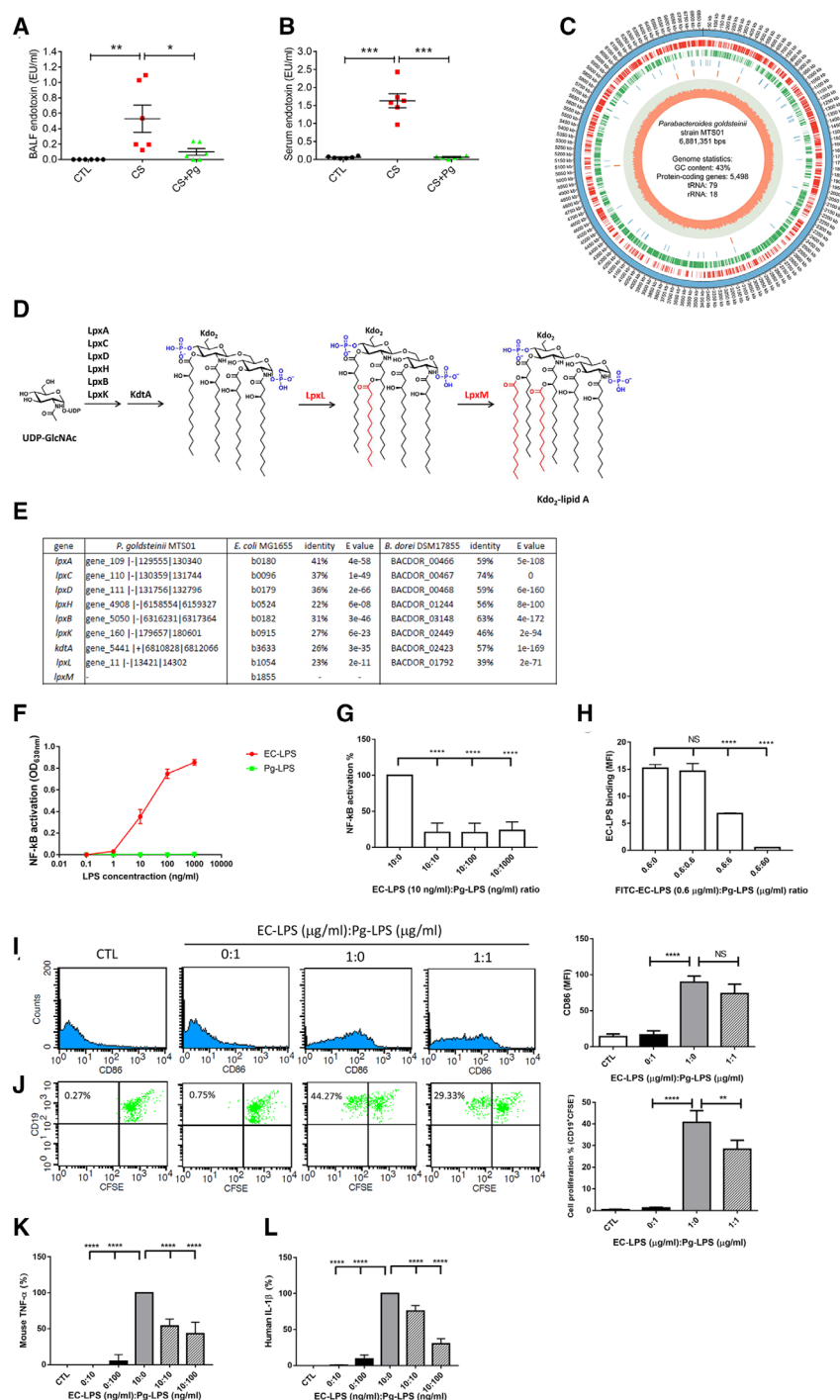


**Figure 5** LPS purified from *Parabacteroides goldsteinii* (Pg) MTS01 (Pg-LPS) antagonises the inflammation elicited by *Escherichia coli* O111:B4 LPS (EC-LPS). The proinflammatory LPS activities in BALF (A) and sera (B) among CTL, CS and CS+Pg groups detected by HEK-Blue-mTLR4 reporter cells were shown. The circular genome map of Pg MTS01 was shown in (C). The biosynthesis pathway of kdo2-lipid A in EC was shown in (D), indicating LpxL and LpxM are responsible for adding the fifth and sixth acyl chains to EC lipid A. The putative genes for Kdo2-lipid A synthesis of Pg MTS01 were identified by blast searches using the EC MG1655 lipid A biosynthesis genes as queries. The gene ID and locations as well as identities in comparison with those in EC MG1655 and *Bacteroides dorei* DSM17855 were indicated (E). Effects of different doses of LPS derived from EC O111:B4 (EC-LPS) or Pg MTS01 (Pg-LPS) on NF-κB activations in HEK-Blue-mTLR4 reporter cells were shown in (F). The antagonistic results of Pg-LPS on EC-LPS induced NF-κB activations in HEK-Blue-mTLR4 cells were shown in (G). The competition of Pg-LPS on FITC-EC-LPS binding on HEK-Blue-mTLR4 cells were shown in (H). Effects of EC-LPS or Pg-LPS in single or in combination administration on expression of CD86 and proliferation of B cells were analysed by flow cytometry and shown in (I) and (J), respectively. The antagonistic results of Pg-LPS on EC-LPS induced TNF-α in CD11c+ bone marrow derived dendritic cells and IL-1β in human peripheral mononuclear cells were shown in (K) and (L), respectively. Cytokine levels were expressed as relative percentage in comparison with the level induced by EC-LPS (grey bar). The data represent means±SD analysed using the Newman-Keuls multiple comparison post hoc one-way ANOVA analysis. \**p*<0.05; \*\**p*<0.01; \*\*\**p*<0.001; \*\*\*\**p*<0.0001. B cell proliferation indicated by halving of CFSE, a green fluorescence dye, which is partitioned approximately equally between the progeny on division. ANOVA, analysis of variance; BALF, bronchoalveolar lavage fluid; CS, cigarette smoking; CTL, control; IL-1β, interleukin 1β; LPS, lipopolysaccharide; NS, not significant.

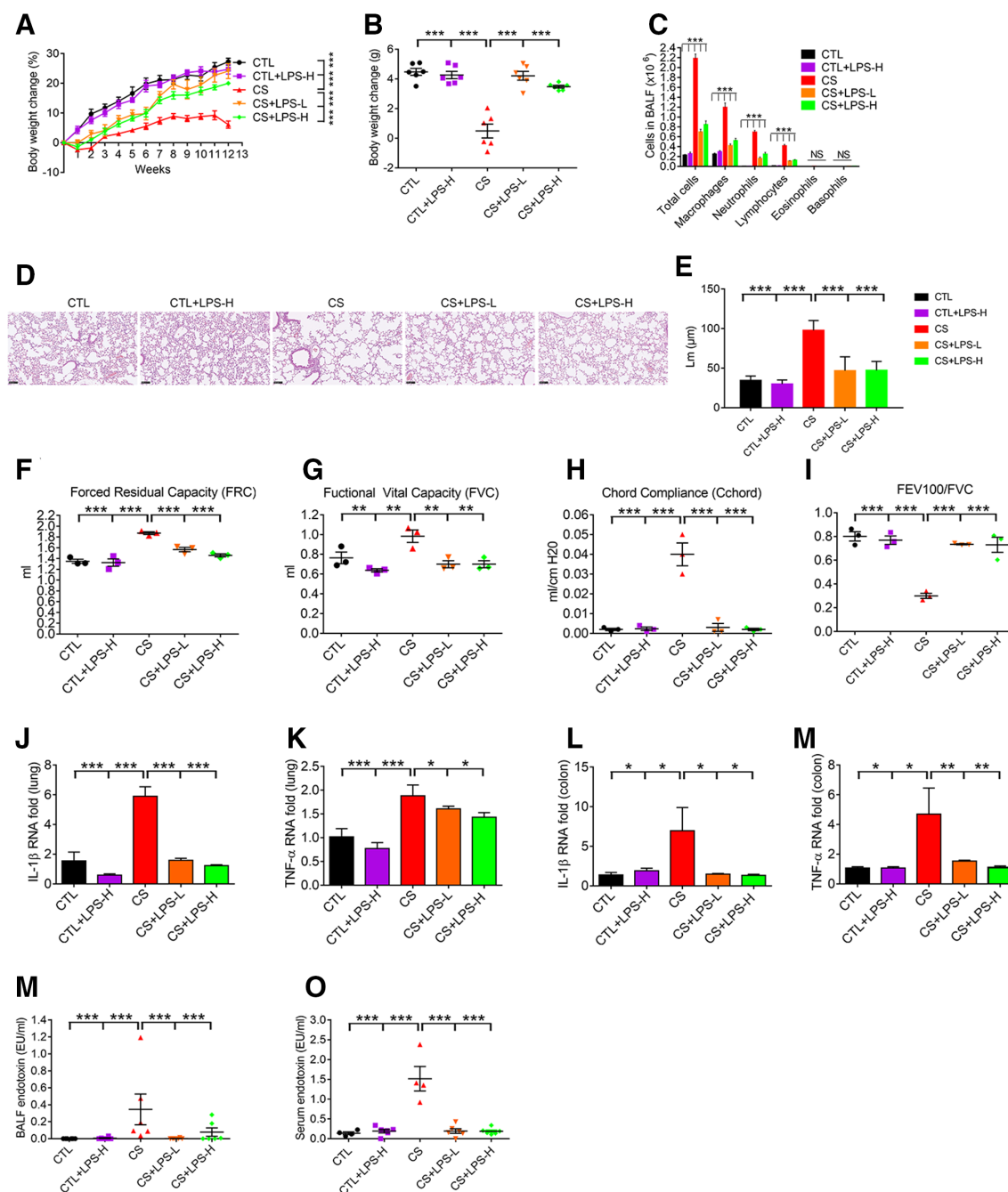


**Figure 6** Pg-LPS ameliorates COPD development in CS mice. After i.p. treatment of Pg-LPS, the body weight change (A, B), BALF cellular composition (C), lung histopathology (D), the mean linear intercept of lung tissue (E), lung functions analyses including FRC (F), FVC (G), Cchord (H) and FEV100/FVC (I), mRNA expression level analysis of IL-1 $\beta$  and TNF- $\alpha$  in lung tissue (J, K) and colon (L, M), respectively, and endotoxin activity in BALF (N), and sera (O) were shown. LPS-L, and H: Pg-LPS administered at 0.2 and 2  $\mu$ g/twice per week, for 3 months. Except panel D, statistical analysis was performed using the Newman-Keuls multiple comparison post hoc one-way ANOVA analysis (n=3–6). \*p<0.05; \*\*p<0.01; \*\*\*p<0.001. ANOVA, analysis of variance; BALF, bronchoalveolar lavage fluid; CS, cigarette smoking; COPD, chronic obstructive pulmonary disease; CTL, control; FEV, forced expiratory volume; FVC, forced vital capacity; IL-1 $\beta$ , interleukin 1 $\beta$ ; i.p., intraperitoneal; LPS, lipopolysaccharide; TNF- $\alpha$ , tumour necrosis factor  $\alpha$ .

supplemental figure S9), indicating that CS or ABX treatment affect the composition of BALF microbiota. The ameliorative effect of ABX treatment in CS mice may also be partly due to changes of the lung microbiota composition. Based on these results, to maintain microbiota homeostasis in both colon and the respiratory tract has to be taken into consideration in designing an effective strategy for prevention/treatment of COPD.

During the process of 12 weeks' smoke exposure and co-housing experiment, control group cohoused with CS

(CO-CS) group developed aberrant phenotypes, as shown in online supplemental figure S2. Even so, we could not come to solid conclusion that CS-induced abnormal gut microbiota composition plays a causing effect on aberrant COPD-related phenotypes in control mice. Part of the reasons is that not only uptake each other's faeces bacteria, cohoused mice may also lick each other's skin fur and expose to cigarette-derived substances that could be adhered to the bedding and walls of the cage due to smoke exposure. Therefore, the aberrant COPD-related



phenotypes observed in the control mice might only partially be due to transfer of abnormal gut microbiota bacteria from the smoke-exposed mice. Besides faeces microbiota, other factors may also participate in affecting COPD-related phenotypes. We, therefore, did not determine gut microbiota composition in this scenario. To confirm the possibility of gut microbiota-COPD axis, FMT was subsequently performed to establish the relationship.

Among the gut microbiota bacteria affected, increased abundance in Lachnospiraceae (online supplemental figure S3a–c, k) might be one of the contributing factors leading to aberrant inflammations and reduction of cellular physiological activities in colon. Consistently, increased abundance of Lachnospiraceae was also reported in many other chronic inflammations related diseases such as inflammatory bowel disease, irritable bowel syndrome with diarrhoea, obesity and after stress.<sup>29</sup> A recent human study also reported multiple members of the family Lachnospiraceae correlate with reduced lung function.<sup>28</sup> On the other hand, FMT from ABX-treated mice reduced intestinal inflammation, promoted intestinal integrity, and ameliorated lung COPD pathogenesis, which was positively correlated with Pg abundance (figure 2B–D and online supplemental figure S3f, h, j). An assumption was developed that optimal depletion of potentially harmful bacteria and/or enrichment of beneficial bacteria in gut may be considered as an alternative strategy for amelioration of COPD. Subsequent studies using the isolated Pg MTS01 as the sole bacterium for oral administration validated its effect on COPD amelioration, thus attracting the investigation of the underlying mechanism by which orally-administered Pg MTS01 ameliorated COPD.

A recent study found that Pg was significantly decreased in patients of chronic kidney disease which was also a chronic inflammatory disease.<sup>30</sup> There seemed to be not many reports related to Pg abundance. One of the reasons may be that growth of Pg was heavily and selectively affected by some sugars and polysaccharides. For example, those derived from traditional Chinese medicinal (TCM) fungi, such as *Ganoderma lucidum* and *Hirsutella sinensis* stimulated the growth (Lai *et al*, unpublished). Larger scale human investigation, especially those related to TCM polysaccharides administration, will be necessary to provide more in-depth information.

Previous can lead to intestinal inflammations and severe colitis,<sup>31</sup> closely connected to impaired intestinal ribosomal biogenesis.<sup>32</sup> Furthermore, CS-related deregulated ribosomal biogenesis has also been linked to cellular senescence phenotypes<sup>33</sup> and ageing, such as progeria and the Hutchinson-Gilford progeria syndrome.<sup>34</sup> On the other hand, inhibition of mitochondrial respiratory activity was associated with pathogenesis of COPD,<sup>19 34</sup> and might be the key mechanism of lung CS toxicity. Specifically, the mitochondrial dysfunction is linked to loss of RNA Pol I transcription, thus, compromising translational fidelity, and causing endoplasmic reticulum stress and apoptosis.<sup>34</sup> Additionally, CS has been linked to subcutaneous fat losses that might lead to weight loss in CS mice<sup>35</sup> (figure 1A,B), cachexia,<sup>36</sup> atherosclerosis, alopecia, osteoporosis, and cataracts.<sup>37</sup> Therefore, Pg MTS01 perturbation or restoration of aberrant colon ribosomal biogenesis and mitochondrial activity by CS-induced chronic inflammations may be more detrimental.

CS also systematically manifested aberrant amino acid-metabolism, including decreased protein anabolism and increased protein catabolism<sup>38</sup> (online supplemental figure S6). Notably, Pg MTS01 systematically promoted amino acids turnovers, especially those involved in upregulated urea cycle, nitric oxide-biosynthesis and TCA cycle activities (online supplemental figure

S6). The decreased metabolic turnovers of L-arginine and L-citrulline involved in mitochondrial TCA, argino-succinate shunt and urea cycle, and nitric oxide-biosynthesis activities (online supplemental figure S6) were restored by Pg MTS01 administration. While the Pg MTS01 effects on restoration of amino acids metabolism might be related to the enhanced cellular ribosomal and mitochondrial activities, more detailed molecular mechanistic studies are warranted.

Previous studies also have shown that the amount of IgG<sub>1</sub> isotypes antibodies positively correlated with COPD pathogenesis and severity.<sup>39</sup> Pg MTS01 administration did not significantly reduce the total IgG level in sera of COPD mice, although a weak trend was observed (online supplemental figure S7d). Effect of Pg MTS01 on other isotypes needs further investigations. At the same time, Pg MTS01 significantly reduced the expression level of scgb1a1 (online supplemental figure S7c) where bronchiolar cells derived from Scgb1a1-expressing progenitors function as major sentinel cells of the airway, responsible for controlling immune responses. Besides, concerning COPD-pathogenesis, particularly emphysema that was developed as the later stage of COPD, the role of B cells and B cell-rich lymphoid follicles have been highlighted.<sup>40</sup> Specifically, increased IgA1-production B-cell counts were observed in lung lymphoid-follicles within distal lung parenchyma of COPD subjects.<sup>41</sup> Apart from DCs and macrophages, B cells can internalise, process and present the antigen to responding T cells.<sup>40</sup> Results shown in this study indicated that the over-activated B cells signalling pathways observed in lung of CS mice were significantly reduced by Pg MTS01 (figure 4G–I). Besides, expression levels of CD86 and proliferation in the B cells induced by EC-LPS were also antagonised by Pg-LPS (figure 5I,J). These results indicated the restoring effects of Pg MTS01 might be, at least in part, through modulation of B cells activities, and Pg-LPS may play some direct regulatory role on B cells. Whether the ameliorative mechanism of Pg MTS01/Pg-LPS in COPD lung may be dependent on interactions between B and T cells, and even other immune cells remains to be further determined.

Unexpectedly, scRNAseq analysis of lung of COPD animals revealed reductions in number of neutrophils and T cells relative to the control group (figure 4F), different from those obtained from cellular analysis (figure 1C). Neutrophils are central in COPD pathogenesis, with NETosis enriched in neutrophil-dominant refractory lung diseases as a cell death indicator.<sup>42</sup> On the other hand, T cells also play important role in COPD inflammations,<sup>43</sup> and a mean 103% increase in apoptosis in T-lymphocyte was found in COPD patients in contrast to normal population.<sup>43</sup> Since scRNAseq mainly analysed live and intact cells, our observed phenomena might suggest that CS induced NETosis<sup>42</sup> and apoptosis of T cells,<sup>44</sup> leading to subsequent inflammations development. Treatment with Pg MTS01 increased the number of viable neutrophils and T cells, which may be closely related to its ameliorative effects.

The proinflammatory LPS mainly produced from Gram-negative Proteobacteria has been closely implicated in COPD development.<sup>45</sup> Furthermore, cigarettes often contain proinflammatory LPS contaminants.<sup>46</sup> The increased release of proinflammatory LPS in sera and BALF of CS mice may initiate and proceed with COPD development (figure 5A,B), and suggested the level of proinflammatory LPS activity is closely correlated with the inflammation severity. Pg-LPS reduced LPS activities in sera and BALF and downregulated genes involving CS-induced, and LPS-related inflammations, leading to alleviation of COPD-pathogenesis (figure 6J–O). Subsequent studies indicated that Pg-LPS did not significantly enhance cellular activation activity,

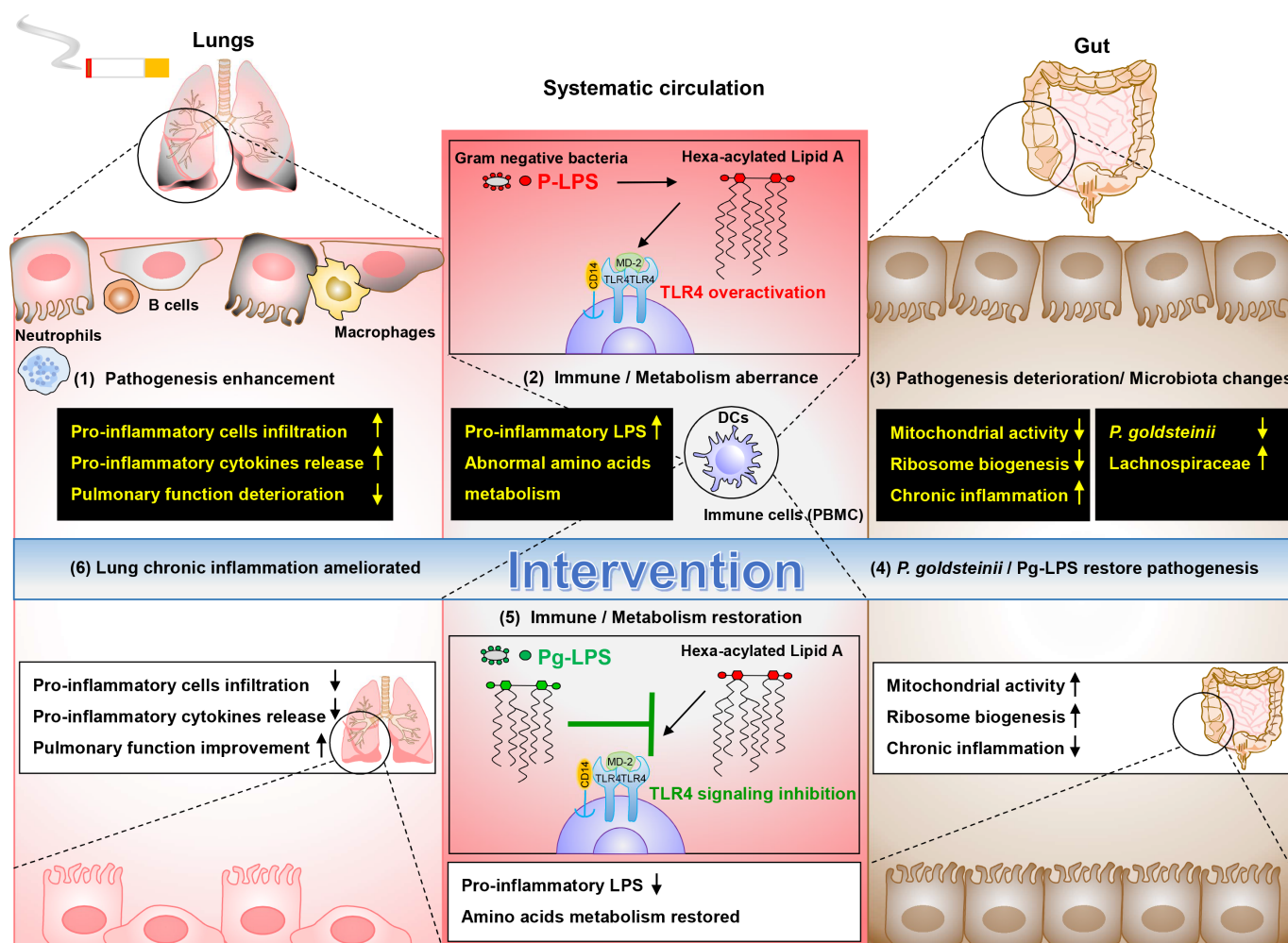


**Figure 7** Hypothetic working model of the ameliorative effects *Parabacteroides goldsteinii* (Pg) MTS01 and Pg-LPS on CS-induced COPD. In CS-induced COPD model, pathogenesis enhancement in lung such as increased infiltration of proinflammatory cells, increased release of proinflammatory cytokines and pulmonary function deterioration was observed (1). Increased pro-inflammatory LPS in systematic circulation was evident (2). These were closely related to aberrant systematic immune (TLR4 overactivation) and metabolic (amino acids metabolism disturbance) activities in the host. Besides, CS also resulted in pathogenesis deterioration in colon, including reduced ribosome biogenesis, mitochondrial activities, and reduced ZO-1 and occludin production (3). Furthermore, microbiota changes were correlated with pathogenesis of COPD (abundance of Lachnospiraceae was positively correlated with disease severity, while abundance of Pg was negative correlated) (3). Interventions by administration of Pg MTS01 or its derived LPS (Pg-LPS) restored the pathogenesis in colon (4). Pg MTS01 might, at least in part, use its LPS by acting as an antagonist of TLR4 signalling pathway to restore the aberrant inflammatory and metabolic phenotypes (5). Consequently, amelioration of lung chronic inflammation, leading to reduced COPD pathogenesis was achieved (6). P-LPS, pro-inflammatory LPS. COPD, chronic obstructive pulmonary disease; CS, cigarette smoking; LPS, lipopolysaccharide; TLR4, toll-like receptor 4.

and even antagonised the *E. coli* LPS induced activation activities (figure 5F–L). These results indicated the development of a potential new strategy on COPD treatment by using the anti-inflammatory LPS as therapeutic agents.<sup>25</sup> The ameliorative effect of Pg-LPS was also examined in another CS COPD model of BALB/c mice which have been reported to have a very different composition of gut microbiome compared with C57BL/6 mice.<sup>47</sup> The result revealed that Pg-LPS also ameliorates COPD development in CS BALB/c mice (online supplemental figure S10). Therefore, effects of Pg-LPS are not specific to C57BL/6 mice. While the underlying ameliorative mechanism of Pg-LPS might be through competing with EC-LPS for TLR4 receptor, further studies on modification of Pg-LPS to improve its anti-inflammatory efficacy are essential.

The general effects of hypoacylated lipid A on inhibition of immune activity have been reported before.<sup>25</sup> Through genome comparison, the *lpxM* that might encode an acyltransferase

during the processes of lipid A synthesis was found to be absent in Pg MTS01 genome (figure 5D,E). Therefore it was predicted that the structure of lipid A in Pg MTS01 was similar to those identified in *Bacteroides spp* such as *Bacteroides thetaiotaomicron*, *Bacteroides dorei*, *Bacteroides fragilis*, *Bacteroides ovatus*, *Rhodobacter capsulatus* and *Rhodobacter sphaeroides*, which is penta-acylated rather than hexa-acylated<sup>25 48</sup> (figure 5E). These anti-inflammatory LPSs are generally characterised by showing no potent agonist activity, and even presenting antagonistic effects to *E. coli* derived proinflammatory LPS.<sup>23–25</sup> For example, LPS derived from *Rhodobacter* demonstrated potent antagonism of proinflammatory LPS-mediated cellular activation and protected mice from proinflammatory LPS-induced death.<sup>49 50</sup> Among these, E5564 developed form *Rhodobacter sphaeroides* was shown to prevent chronic airway hyperreactivity and inflammation caused by inhaled LPS. In addition, *B. fragilis* and *B. ovatus* also alleviated LPS-induced inflammation in mice,<sup>51</sup> while *B.*

*vulgatus* and *B. dorei* ameliorated endotoxaemia, decreased gut microbial LPS production, and suppressed proinflammatory immune responses.<sup>52</sup> Recently, anti-inflammatory properties of weak agonistic LPS derived from *Bacteroides spp* were attributed to endotoxin tolerance induction via the MD-2/TLR4 receptor complex axis in intestinal lamina propria CD11c<sup>+</sup> cells.<sup>53</sup> Pg-LPS may, therefore, belong to a family of hypoacylated LPS that generally show anti-inflammatory functions.

In conclusion, Pg MTS01 and Pg-LPS are potential therapeutic agents that may be developed into functional probiotics<sup>10 25 54 55</sup> and postbiotics,<sup>25</sup> respectively, to ameliorate COPD (figure 7).

#### Author affiliations

<sup>1</sup>Department of Medical Biotechnology and Laboratory Science, College of Medicine, Chang Gung University, Taoyuan, Taiwan

<sup>2</sup>Microbiota Research Center and Emerging Viral Infections Research Center, Chang Gung University, Taoyuan, Taiwan

<sup>3</sup>Central Research Laboratory, Xiamen Chang Gung Hospital, Xiamen, China

<sup>4</sup>Department of Laboratory Medicine, Linkou Chang Gung Memorial Hospital, Taoyuan, Taiwan

<sup>5</sup>Research Center for Chinese Herbal Medicine and Research Center for Food and Cosmetic Safety, College of Human Ecology, Chang Gung University of Science and Technology, Taoyuan, Taiwan

<sup>6</sup>Institute of Bioinformatics and Systems Biology, National Chiao Tung University, Hsinchu, Taiwan

<sup>7</sup>Department of Biological Science and Technology, National Chiao Tung University, Hsinchu, Taiwan

<sup>8</sup>Center For Intelligent Drug Systems and Smart Bio-devices (IDS2B), National Chiao Tung University, Hsinchu, Taiwan

<sup>9</sup>Bioteools, Co, Ltd, New Taipei City, Taiwan

<sup>10</sup>Institute of Biomedical Science, Academia Sinica, Taipei, Taiwan

<sup>11</sup>Department of Internal Medicine, National Taiwan University Hospital, Taipei, Taiwan

<sup>12</sup>Department of Molecular Medicine and Pathology, University of Auckland, Auckland, New Zealand

<sup>13</sup>Department of Respiratory Therapy, Fu Jen Catholic University, New Taipei City, Taiwan

<sup>14</sup>Department of Chest Medicine, Internal Medicine, Fu Jen Catholic University Hospital, New Taipei City, Taiwan

**Contributors** T-LL conceived the project, contributed to experimental design, performed experiments, interpreted the results, prepared the figures and wrote the manuscript; T-WC performed the scRNAseq analysis; Y-LK performed the microbiota analysis; C-JC and T-RW contributed to experimental design and performed experiments; C-CS, Y-HT and SS reviewed and edited the manuscript; H-CL and C-CL conceived and supervised the project, interpreted the results and wrote the manuscript; all authors discussed the results and approved the manuscript.

**Funding** This study was funded by CORPD1F0013 and CORPD1J0052 from Chang Gung Memorial Hospital, 108–2321-B-182–002, 109–2320-B-030–010, 109–2327-B-182–001 from Ministry of Science and Technology (MOST), Microbiota Research Center/Centre from Chang Gung University, and the Research Center/Centre for Emerging Viral Infections from The Featured Areas Research Center/Centre Programme within the framework of the Higher Education Sprout Project by the Ministry of Education (MOE) in Taiwan and MOST, Taiwan (MOST109-3017-F-182–001).

**Competing interests** None declared.

**Patient consent for publication** Not required.

**Ethics approval** Animal experiments were approved by the Institutional Animal Care and Use Protocol of Fu Jen Catholic University and were performed according to their guidelines (animal ethics approval numbers A10558 and A10849).

**Provenance and peer review** Not commissioned; externally peer reviewed.

**Data availability statement** Data are available on reasonable request. All data relevant to the study are included in the article or uploaded as online supplemental information. The data that support the findings of this study are available from the corresponding author, on reasonable request.

**Supplemental material** This content has been supplied by the author(s). It has not been vetted by BMJ Publishing Group Limited (BMJ) and may not have been peer-reviewed. Any opinions or recommendations discussed are solely those of the author(s) and are not endorsed by BMJ. BMJ disclaims all liability and responsibility arising from any reliance placed on the content. Where the content includes any translated material, BMJ does not warrant the accuracy and reliability of the translations (including but not limited to local regulations, clinical guidelines,

terminology, drug names and drug dosages), and is not responsible for any error and/or omissions arising from translation and adaptation or otherwise.

#### ORCID iD

Chia-Chen Lu <http://orcid.org/0000-0002-0443-7248>

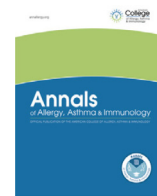
#### REFERENCES

- Hogg JC, Chu F, Utokaparch S, et al. The nature of small-airway obstruction in chronic obstructive pulmonary disease. *N Engl J Med* 2004;350:2645–53.
- Holtzman MJ, Byers DE, Alexander-Brett J, et al. The role of airway epithelial cells and innate immune cells in chronic respiratory disease. *Nat Rev Immunol* 2014;14:686–98.
- Rabe KF, Watz H. Chronic obstructive pulmonary disease. *Lancet* 2017;389:1931–40.
- GBD 2015 Chronic Respiratory Disease Collaborators. Global, regional, and national deaths, prevalence, disability-adjusted life years, and years lived with disability for chronic obstructive pulmonary disease and asthma, 1990–2015: a systematic analysis for the global burden of disease study 2015. *Lancet Respir Med* 2017;5:691–706.
- Sin DD, Anthonisen NR, Soriano JB, et al. Mortality in COPD: role of comorbidities. *Eur Respir J* 2006;28:1245–57.
- Barnes PJ. New anti-inflammatory targets for chronic obstructive pulmonary disease. *Nat Rev Drug Discov* 2013;12:543–59.
- Riley CM, Sciruba FC. Diagnosis and outpatient management of chronic obstructive pulmonary disease: a review. *JAMA* 2019;321:786–97.
- Maynard CL, Elson CO, Hatton RD, et al. Reciprocal interactions of the intestinal microbiota and immune system. *Nature* 2012;489:231–41.
- Blander JM, Longman RS, Iliev ID, et al. Regulation of inflammation by microbiota interactions with the host. *Nat Immunol* 2017;18:851–60.
- Chang C-J, Lin T-L, Tsai Y-L, et al. Next generation probiotics in disease amelioration. *J Food Drug Anal* 2019;27:615–22.
- Faner R, Sibila O, Agustí A, et al. The microbiome in respiratory medicine: current challenges and future perspectives. *Eur Respir J* 2017;49:1602086.
- Yadava K, Pattaroni C, Sichelstiel AK, et al. Microbiota promotes chronic pulmonary inflammation by enhancing IL-17A and autoantibodies. *Am J Respir Crit Care Med* 2016;193:975–87.
- He Z-H, Chen P, Chen Y, et al. Comparison between cigarette smoke-induced emphysema and cigarette smoke extract-induced emphysema. *Tob Induc Dis* 2015;13:6.
- Wu T-R, Lin C-S, Chang C-J, et al. Gut commensal *Parabacteroides goldsteinii* plays a predominant role in the anti-obesity effects of polysaccharides isolated from *Hirsutiella sinensis*. *Gut* 2019;68:248–62.
- Chang C-J, Lin C-S, Lu C-C, et al. Ganoderma lucidum reduces obesity in mice by modulating the composition of the gut microbiota. *Nat Commun* 2015;6:7489.
- Chang C-J, Lu C-C, Lin C-S, et al. *Antrodia cinnamomea* reduces obesity and modulates the gut microbiota in high-fat diet-fed mice. *Int J Obes* 2018;42:231–43.
- Ichinohe T, Pang IK, Kumamoto Y, et al. Microbiota regulates immune defense against respiratory tract influenza A virus infection. *Proc Natl Acad Sci U S A* 2011;108:5354–9.
- Berkowitz L, Schultz BM, Salazar GA, et al. Impact of cigarette smoking on the gastrointestinal tract inflammation: opposing effects in Crohn's disease and ulcerative colitis. *Front Immunol* 2018;9:74.
- Dela Cruz CS, Kang M-J. Mitochondrial dysfunction and damage associated molecular patterns (DAMPs) in chronic inflammatory diseases. *Mitochondrion* 2018;41:37–44.
- Mukherjee AB, Zhang Z, Chilton BS. Uteroglobin: a steroid-inducible immunomodulatory protein that founded the secretoglobulin superfamily. *Endocr Rev* 2007;28:707–25.
- McCauley KB, Alysandratos K-D, Jacob A, et al. Single-Cell transcriptomic profiling of pluripotent stem cell-derived SCGB3A2+ airway epithelium. *Stem Cell Reports* 2018;10:1579–95.
- McGuinness AJA, Sapely E. Oxidative stress in COPD: sources, markers, and potential mechanisms. *J Clin Med* 2017;6:21.
- Jacobson AN, Choudhury BP, Fischbach MA. The Biosynthesis of Lipooligosaccharide from *Bacteroides thetaiotaomicron*. *mBio* 2018;9:e02289–17. doi:10.1128/mBio.02289-17
- Poxton IR, Edmond DM. Biological activity of *Bacteroides* lipopolysaccharide--reappraisal. *Clin Infect Dis* 1995;20 Suppl 2:S149–53.
- Lin T-L, Shu C-C, Chen Y-M, et al. Like cures like: pharmacological activity of anti-inflammatory lipopolysaccharides from gut microbiome. *Front Pharmacol* 2020;11:554.
- Raetz CRH, Reynolds CM, Trent MS, et al. Lipid A modification systems in gram-negative bacteria. *Annu Rev Biochem* 2007;76:295–329.
- da Fonseca LMC, Reboredo MM, Lucinda LMF, et al. Emphysema induced by elastase enhances acute inflammatory pulmonary response to intraperitoneal LPS in rats. *Int J Exp Pathol* 2016;97:430–7.
- Bowerman KL, Rehman SF, Vaughan A, et al. Disease-associated gut microbiome and metabolome changes in patients with chronic obstructive pulmonary disease. *Nat Commun* 2020;11:5886.



- 29 Pensec C, Gillaizeau F, Guenot D, *et al.* Impact of pemetrexed chemotherapy on the gut microbiota and intestinal inflammation of patient-lung-derived tumor xenograft (PDX) mouse models. *Sci Rep* 2020;10:9094.
- 30 Wu I-W, Lin C-Y, Chang L-C. Gut microbiota as diagnostic tools for Mirroring disease progression and circulating nephrotoxin levels in chronic kidney disease: discovery and validation study. *Int J Biol Sci* 2020;16:420–34.
- 31 Allais L, Kerckhof F-M, Verschuere S, *et al.* Chronic cigarette smoke exposure induces microbial and inflammatory shifts and mucin changes in the murine gut. *Environ Microbiol* 2016;18:1352–63.
- 32 Figueiredo VC, Markworth JF, Durainayagam BR, *et al.* Impaired ribosome biogenesis and skeletal muscle growth in a murine model of inflammatory bowel disease. *Inflamm Bowel Dis* 2016;22:268–78.
- 33 Zhang X, Azhar G, Rogers SC, *et al.* Overexpression of p49/STRAP alters cellular cytoskeletal structure and gross anatomy in mice. *BMC Cell Biol* 2014;15:32.
- 34 Phan T, Khalid F, Iben S. Nucleolar and ribosomal Dysfunction-A common pathomechanism in childhood progerias? *Cells* 2019;8:534. doi:10.3390/cells8060534
- 35 Chen H, Hansen MJ, Jones JE, *et al.* Cigarette smoke exposure reprograms the hypothalamic neuropeptide Y axis to promote weight loss. *Am J Respir Crit Care Med* 2006;173:1248–54.
- 36 Sanders KJC, Kneppers AEM, van de Boel C, *et al.* Cachexia in chronic obstructive pulmonary disease: new insights and therapeutic perspective. *J Cachexia Sarcopenia Muscle* 2016;7:5–22.
- 37 Nicita-Mauro V, Basile G, Maltese G, *et al.* Smoking, health and ageing. *Immun Ageing* 2008;5:10. doi:10.1186/1742-4933-5-10
- 38 Zhang W-Z, Venardos K, Chin-Dusting J, *et al.* Adverse effects of cigarette smoke on NO bioavailability: role of arginine metabolism and oxidative stress. *Hypertension* 2006;48:278–85.
- 39 Feghali-Bostwick CA, Gadgil AS, Otterbein LE, *et al.* Autoantibodies in patients with chronic obstructive pulmonary disease. *Am J Respir Crit Care Med* 2008;177:156–63.
- 40 Polverino F, Seys LJM, Bracke KR, *et al.* B cells in chronic obstructive pulmonary disease: moving to center stage. *Am J Physiol Lung Cell Mol Physiol* 2016;311:L687–95.
- 41 Curtis JL. B cells caught in the act: class switching to IgA in lung lymphoid follicles in chronic obstructive pulmonary disease. *Am J Respir Crit Care Med* 2019;199:548–50.
- 42 Uddin M, Watz H, Malmgren A, *et al.* NETopathic inflammation in chronic obstructive pulmonary disease and severe asthma. *Front Immunol* 2019;10:47.
- 43 Hodge S, Hodge G, Holmes M, *et al.* Increased airway epithelial and T-cell apoptosis in COPD remains despite smoking cessation. *Eur Respir J* 2005;25:447–54.
- 44 Hodge SJ, Hodge GL, Reynolds PN, *et al.* Increased production of TGF-beta and apoptosis of T lymphocytes isolated from peripheral blood in COPD. *Am J Physiol Lung Cell Mol Physiol* 2003;285:L492–9.
- 45 Gupta V, Banyard A, Mullan A, *et al.* Characterization of the inflammatory response to inhaled lipopolysaccharide in mild to moderate chronic obstructive pulmonary disease. *Br J Clin Pharmacol* 2015;79:767–76.
- 46 Hasday JD, Bascom R, Costa JJ, *et al.* Bacterial endotoxin is an active component of cigarette smoke. *Chest* 1999;115:829–35.
- 47 Fransen F, Zagato E, Mazzini E, *et al.* Balb/C and C57BL/6 mice differ in polyreactive IgA abundance, which impacts the generation of antigen-specific IgA and microbiota diversity. *Immunity* 2015;43:527–40.
- 48 Vatanen T, Kostic AD, d'Hennezel E, *et al.* Variation in microbiome LPS immunogenicity contributes to autoimmunity in humans. *Cell* 2016;165:842–53.
- 49 Christ WJ, Asano O, Robidoux AL, *et al.* E5531, a pure endotoxin antagonist of high potency. *Science* 1995;268:80–3.
- 50 Barochia A, Solomon S, Cui X, *et al.* Eritoran tetrasodium (E5564) treatment for sepsis: review of preclinical and clinical studies. *Expert Opin Drug Metab Toxicol* 2011;7:479–94.
- 51 Tan H, Zhao J, Zhang H, *et al.* Novel strains of *Bacteroides fragilis* and *Bacteroides ovatus* alleviate the LPS-induced inflammation in mice. *Appl Microbiol Biotechnol* 2019;103:2353–65.
- 52 Yoshida N, Emoto T, Yamashita T, *et al.* *Bacteroides vulgatus* and *Bacteroides dorei* reduce gut microbial lipopolysaccharide production and inhibit atherosclerosis. *Circulation* 2018;138:2486–98.
- 53 Steimle A, Michaelis L, Di Lorenzo F, *et al.* Weak agonistic LPS restores intestinal immune homeostasis. *Mol Ther* 2019;27:1974–91.
- 54 Tsai Y-L, Lin T-L, Chang C-J, *et al.* Probiotics, prebiotics and amelioration of diseases. *J Biomed Sci* 2019;26:3.
- 55 Lin T-L, Shu C-C, Lai W-F, *et al.* Investiture of next generation probiotics on amelioration of diseases – strains do matter. *Medicine in Microecology* 2019;1-2:100002.





# Atopic dermatitis and dementia risk

## A nationwide longitudinal study

Tai-Long Pan, PhD<sup>\*,†,‡</sup>; Ya-Mei Bai, MD, PhD<sup>§,||</sup>; Chih-Ming Cheng, MD<sup>§,||</sup>; Shih-Jen Tsai, MD<sup>§,||</sup>; Chia-Fen Tsai, MD<sup>§,||</sup>; Tung-Ping Su, MD<sup>§,||,¶</sup>; Cheng-Ta Li, MD, PhD<sup>§,||</sup>; Wei-Chen Lin, MD<sup>§,||</sup>; Tzeng-Ji Chen, MD, PhD<sup>#,\*\*</sup>; Chih-Sung Liang, MD<sup>††,‡‡</sup>; Mu-Hong Chen, MD, PhD<sup>§,||</sup>

<sup>\*</sup> School of Traditional Chinese Medicine, Chang Gung University, Taoyuan, Taiwan

<sup>†</sup> Research Center for Chinese Herbal Medicine and Research Center for Food and Cosmetic Safety, College of Human Ecology, Chang Gung University of Science and Technology, Taoyuan, Taiwan

<sup>‡</sup> Liver Research Center, Chang Gung Memorial Hospital, Taoyuan, Taiwan

<sup>§</sup> Department of Psychiatry, Taipei Veterans General Hospital, Taipei, Taiwan

<sup>||</sup> Department of Psychiatry, College of Medicine, National Yang Ming Chiao Tung University, Taipei, Taiwan

<sup>¶</sup> Department of Psychiatry, Cheng Hsin General Hospital, Taipei, Taiwan

<sup>#</sup> Department of Family Medicine, Taipei Veterans General Hospital, Taipei Taiwan

<sup>\*\*</sup> Institute of Hospital and Health Care Administration, National Yang Ming Chiao Tung University, Taipei, Taiwan

<sup>††</sup> Department of Psychiatry, Beitou Branch, Tri-Service General Hospital, National Defense Medical Center, Taipei, Taiwan

<sup>‡‡</sup> Graduate Institute of Medical Sciences, National Defense Medical Center, Taipei, Taiwan

### ARTICLE INFO

#### Article history:

Received for publication January 1, 2021.

Received in revised form February 24, 2021.

Accepted for publication March 5, 2021.

### ABSTRACT

**Background:** Retrospective studies have suggested that patients with dementia have higher prevalence of atopic dermatitis (AD) than those without dementia. However, the temporal association of AD with subsequent dementia remains unknown.

**Objective:** To assess the temporal association of AD with subsequent dementia.

**Methods:** We included data of patients with AD aged 45 years and older (n = 1059) and 1:10 age, sex, residence, income, and dementia-related comorbidity-matched controls (n = 10,590) from the Taiwan National Health Insurance Research Database and reviewed their subsequent dementia development from the enrollment date to the end of 2013.

**Results:** After adjustments for dementia-related comorbidities, patients with AD were found to be more likely to develop any dementia (hazard ratio [HR], 2.02; 95% confidence interval [CI], 1.24–3.29), particularly Alzheimer's disease (HR, 3.74; 95% CI, 1.17–11.97), during the follow-up period than those in the control group. Moderate-to-severe AD was associated with a high subsequent dementia risk (HR, 4.64; 95% CI, 2.58–8.33). Sensitivity analyses with the exclusion of the first 3 (HR, 2.20; 95% CI, 1.28–3.80) or 5 (HR, 2.05; 95% CI, 1.08–3.89) years of observation revealed consistent findings.

**Conclusion:** AD may be an independent risk factor for new-onset dementia. Clinicians may monitor the trajectory of neurocognitive function among elderly patients with AD. Additional studies elucidating the pathomechanisms between AD and subsequent dementia are warranted.

© 2021 American College of Allergy, Asthma & Immunology. Published by Elsevier Inc. All rights reserved.

**Reprints:** Mu-Hong Chen, MD, PhD, Department of Psychiatry, Taipei Veterans General Hospital, No. 201, Shih-Pai Road, Sec. 2, Taipei 11217, Taiwan

**Reprints:** Chih-Sung Liang, MD, Department of Psychiatry, Beitou Branch, Tri-Service General Hospital, No. 60, Xinmin Road, Taipei 11243, Taiwan. E-mail: lcsyfw@gmail.com. kremer7119@gmail.com.

**Disclosures:** The authors have no conflicts of interest to report.

**Funding:** The study was supported by grants from Taipei Veterans General Hospital (V106B-020, V107B-010, V107C-181, and V108B-012), Yen Tjing Ling Medical Foundation (CI-109-21, CI-109-22, CI-110-30), and the Ministry of Science and Technology, Taiwan, Republic of China (107-2314-B-075-063-MY3 and 108-2314-B-075-037). The funding sources had no role in any process of our study.

<https://doi.org/10.1016/j.anai.2021.03.001>

1081-1206/© 2021 American College of Allergy, Asthma & Immunology. Published by Elsevier Inc. All rights reserved.

### Introduction

According to World Health Organization, atopic dermatitis (AD) ranks 15th among all nonfatal diseases and exhibits the largest disease burden among skin diseases, as measured using disability-adjusted life years.<sup>1,2</sup> The distribution of AD based on age group reveals a bimodal curve, with the highest peak in early childhood, reduced prevalence among young adults, and the second peak in middle-aged and older populations.<sup>1–3</sup> The worldwide prevalence of AD has increased 2-fold to 3-fold over the past decades.<sup>2</sup> The prevalence of AD in the older populations of industrialized countries is currently estimated to be 3% to 4%, and it continues to increase.<sup>4</sup>

Studies have suggested an association between AD and dementia-related risk factors, such as diabetes mellitus, hypertension, and

cerebrovascular diseases.<sup>5–7</sup> A cross-sectional study of 116,816 patients with AD and 116,812 comparison enrollees found that moderate and severe AD were associated with high prevalence rates of obesity (22.2% vs 18.6%), diabetes mellitus (15.9% vs 9.2%), hypertension (27.9% vs 15.3%), and dyslipidemia (47.1% vs 28.5%; all  $P < .001$ ).<sup>6</sup> A Swedish nationwide study including 104,832 patients with AD and 1,022,435 controls found that diabetes mellitus, hyperlipidemia, and hypertension were more prevalent in patients with severe AD than in controls and indicated that severe AD was associated with ischemic stroke.<sup>5</sup> Silverberg et al<sup>8</sup> assessed cognitive functions by using the Patient-Reported Outcomes Measurement Information System (PROMIS) Cognitive Function 8-Item Short-Form in 386 adults with AD and found that approximately 60% of the patients reported at least 1 symptom of cognitive dysfunction in the past 4 weeks, with 29 (14.3%) having mild, 11 (5.4%) moderate, and 4 (2.0%) severe PROMIS Cognitive Function T-scores. Furthermore, they reported an inverse association between PROMIS Cognitive Function T-scores and patient-reported global AD severity and suggested that clinicians should regularly monitor the cognitive functions of patients with AD.<sup>8</sup> However, the association between AD and subsequent neurodegenerative disorders, particularly dementia, remains unknown and has not been explored, even though previous studies have suggested a relationship of other atopic diseases, particularly asthma, with an increased risk of subsequent dementia.<sup>9,10</sup>

In this study, we used the Taiwan National Health Insurance Research Database (NHIRD) with a large sample size and a longitudinal follow-up study design to investigate the temporal association between AD and dementia, including Alzheimer's disease and vascular dementia. We hypothesize that patients with AD are more likely to develop new-onset dementia later in life than those without AD and that the AD severity–dementia risk relationship is positive.

## Methods

### Data Source

The Taiwan National Health Insurance Research Database (NHIRD) was established for research purposes and audited by the Department of Health and the Bureau of the National Health Insurance (NHI) program and contains comprehensive information the insured patients, such as demographics (birthdate, sex, residential location, income status), clinical visits (dates and diagnoses) and prescription. The database that was used in current study includes comprehensive information between 1996 and 2013. To protect privacy, each patient is assigned a unique and anonymous identifier enrollment by the NHI, which allows researchers to follow their diseases and outcomes. Diagnoses were captured using the International Classification of Diseases, Ninth Revision, Clinical Modification (ICD-9-CM). The NHIRD has been used extensively for epidemiologic studies.<sup>11–14</sup> This study was approved by the Taipei Veterans General Hospital institutional review board.

### Inclusion Criteria for Patients with Atopic Dermatitis and Matched Controls

Adults aged 45 years and older who were diagnosed as having AD (ICD-9-CM code: 691.8) by board-certified dermatologists based on skin allergy test between January 1, 1997, and December 31, 2013, and who had no history of dementia before their AD diagnoses were included in the AD cohort. The time of enrollment was defined as the time of AD diagnosis. The AD diagnosis on the basis of the results of skin allergy test is to ensure diagnostic validity. The age-, sex-, residence-, income- and comorbidities-matched (1:10) control cohort was randomly identified after eliminating study participants who had been received a diagnosis of AD at any time in the database, or who had any dementia before enrollment. Dementia-related

comorbidities included a history of cerebrovascular diseases, traumatic brain injury, hypertension, dyslipidemia, diabetes mellitus, and smoking. Other allergic diseases, including asthma, allergic rhinitis, and allergic conjunctivitis, were also matched between the groups. In addition, Charlson Comorbidity Index (CCI) and all-cause clinical visits were provided for the AD and the matched-control cohorts. CCI consisting of 22 physical conditions was also assessed to determine the systemic health conditions of all enrolled patients.<sup>15</sup> All-cause clinical visits (the numbers of clinical visits per year) for the AD cohort and the matched-controls cohort were included as a variable to account for potential detection bias. Income level (levels 1–3:  $\leq$ NT \$15,840 or \$528, NT\$15,841– NT\$25,000 or \$528–\$833, and NT  $\geq$ \$25,000 or  $\geq$ \$833 per month, respectively) and urbanization level of residence (levels 1 being the most urbanized and 5 the least urbanized) were regarded as the proxies for health care availability in Taiwan.<sup>16</sup> Finally, patients with a history of systemic corticosteroid use prescribed by dermatologists corresponding to the AD diagnosis were deemed to have moderate-to-severe disease.

### Outcome Assessment

The diagnosis of dementia (ICD-9-CM codes: 290.0, 290.1, 290.2, 290.3, 290.4, 294.1, 294.2, 331.0, 331.1, 331.2, or 331.82) was documented at least twice by board-certified psychiatrists or neurologists during the follow-up period (from enrollment to December 31, 2013 or death). Alzheimer's disease was defined either by the specific ICD-9-CM code of 331.0 or identified by ICD-9-CM codes of dementia (ICD-9-CM codes: 290.0, 290.1, 290.2, 290.3, 290.4, 294.1, or 294.2) while also receiving medications for dementia. Based on the NHI regulations, reimbursable therapies for dementia (ie, cholinesterase inhibitors) were only approved after comprehensive laboratory and imaging examinations excluded cognitive decline attributed to other causes including thyroid dysfunction, vitamin B12 deficiency, or cerebrovascular events; medications were not approved for Alzheimer's disease with any evidence of cerebrovascular lesions. Furthermore, vascular dementia is defined by the specific ICD-9-CM code of 290.4. Other types of dementia, especially the diagnosis of Alzheimer's disease with evidence of any cerebrovascular lesion, were defined as unspecified dementia in our study because the definite pathology of dementia cannot be clearly defined on the basis of the ICD-9-CM codes of 290.0, 290.1, 290.2, 290.3, 290.4, 294.1, or 294.2 alone without concurrent medication prescription for Alzheimer's disease reflecting the clinical practice in Taiwan. For this reason, Alzheimer's disease with cerebrovascular lesions was defined as unspecified dementia, and the diagnostic validity of Alzheimer's disease as the sole reason for neurocognitive degeneration is high.

### Statistical Analysis

For between-group comparisons, the F-test was used for continuous variables and Pearson's  $\chi^2$  test for nominal variables. Cox regression analysis with adjustment for demographic data (age, sex, income, and residence), medical comorbidities (cerebrovascular diseases, traumatic brain injury, hypertension, dyslipidemia, diabetes mellitus, smoking, asthma, allergic rhinitis, and allergic conjunctivitis), CCI score, and all-cause clinical visits was applied to investigate the dementia risk between the AD and the control groups. Furthermore, Cox regression model was also obtained to investigate the disease severity (mild vs moderate-to-severe) of AD with subsequent dementia risk. Given the insidious onset of dementia, 2 types of sensitivity analyses were performed to validate the results by minimizing the underdiagnosis of occult dementia at the time of AD diagnosis. In the “exclusion of observation period” model, the first 3 or 5 years of observation after the AD diagnosis were excluded, eliminating all cases of dementia diagnosed within these first years after

AD diagnosis. In the exclusion of enrollment period model, only patients diagnosed as having AD before the dates January 1, 2008, or January 1, 2010, were included in the analysis; patients with AD diagnosed after these time points were selectively excluded. Statistical significance was set at 2-tailed *P* less than or equal to .05. Data processing and statistical analyses were performed using the Statistical Analysis System (version 9.1, SAS Institute, Cary, North Carolina).

#### Data Availability Statement

The NHIRD was released and audited by the Department of Health and Bureau of the NHI Program for the purpose of scientific research (<https://nhird.nhri.org.tw/>). NHIRD can be obtained through the formal application that is regulated by the Department of Health and Bureau of the NHI Program.

#### Results

Overall, 1059 patients with AD (726 with mild disease and 333 with moderate-to-severe disease) aged 58.09 ( $\pm 10.18$ ) years and 10,590 matched comparison controls were included in current study. Patients with AD had a higher incidence of new-onset dementia (2.5% vs 0.7%; *P* < .001), including Alzheimer's disease (0.6% vs 0.1%; *P* = .001), vascular dementia (0.5% vs 0.1%; *P* = .03), and unspecified dementia (1.4% vs 0.5%; *P* = .002), and had an earlier age of being diagnosed as having dementia ( $74.98 \pm 9.46$  vs  $80.09 \pm 6.62$  years; *P* = .003) than the controls did (Table 1). In addition, patients with AD had greater CCI scores (*P* < .001) and higher all-cause clinical visits per year (*P* < .001) than the comparison controls (Table 1).

The Kaplan-Meier survival analyses with the log-rank test (*P* < .001) revealed that patients with AD were more likely to develop any dementia than the control group (Figure 1). The Cox regression analyses with the adjustment of demographic data, comorbidities, CCI scores, and all-cause clinical visits found that AD in the middle adulthood and elderhood was associated with an increased risk of developing any dementia (hazard ratio [HR], 2.02; 95% confidence interval [CI], 1.24–3.29), especially Alzheimer's disease (HR, 3.74; 95% CI, 1.17–11.97), later in life compared with the matched controls (Table 2). Patients with moderate-to-severe AD had the greatest likelihood of developing dementia (HR, 4.64; 95% CI, 2.58–8.33) compared with those with mild AD (HR, 2.57; 95% CI, 1.43–4.62) and the controls (Table 3). However, the statistical significance of moderate-to-severe AD with greater dementia risk disappeared after adjusting for demographic data, comorbidities, CCI scores, and all-cause clinical visits (Table 3).

Given the insidious onset of dementia, we performed 2 types of sensitivity analyses. In the exclusion of observation period sensitivity analysis, selective exclusion of patients with AD and matched controls who were enrolled in our study and subsequently developed dementia within 3 (HR, 2.20; 95% CI, 1.28–3.80) or 5 years (HR, 2.05; 95% CI, 1.08–3.89) after the diagnosis of AD yielded consistent findings that the lifetime dementia risk was significantly higher among patients with AD than controls (Table 4). The results were confirmed through the exclusion of enrollment period sensitivity analysis, in which patients and controls enrolled after the years 2010 (HR, 2.47; 95% CI, 1.51–4.03) or 2008 (HR, 3.11; 95% CI, 1.85–5.23) were selectively excluded (Table 4).

**Table 1**  
Demographic Data and Incidence of Dementia Among Patients With Atopic Dermatitis and Control Group

| Demographic data                                 | Patients with atopic dermatitis (n = 1059) | Controls (n = 10,590) | <i>P</i> value |
|--|--|-----------------------|----------------|
| Age at enrollment, y (SD)                        | 58.09 (10.18)                              | 57.87 (10.34)         | .50            |
| Sex, n (%)                                       |  |                       | >.99           |
| Male   | 518 (48.9)                                 | 5180 (48.9)           |                |
| Female   | 541 (51.1)                                 | 5410 (51.1)           |                |
| Disease severity, n (%)                          |  |                       |                |
| Mild   | 726 (68.6)                                 |                       |                |
| Moderate-to-severe                               | 333 (31.4)                                 |                       |                |
| Other atopic diseases                            |  |                       |                |
| Asthma   | 168 (15.9)                                 | 1680 (15.9)           | .99            |
| Allergic rhinitis                                | 389 (36.7)                                 | 3890 (36.7)           | .99            |
| Allergic conjunctivitis                          | 228 (21.5)                                 | 2280 (21.5)           | .99            |
| Dementia-related comorbidities, n (%)            |  |                       |                |
| Cerebrovascular diseases                         | 119 (11.2)                                 | 1190 (11.2)           | .99            |
| Traumatic brain injury                           | 12 (1.1)                                   | 120 (1.1)             | >.99           |
| Hypertension                                     | 454 (42.9)                                 | 4540 (42.9)           | .99            |
| Dyslipidemia                                     | 309 (29.2)                                 | 3090 (29.2)           | .99            |
| Diabetes mellitus                                | 194 (18.3)                                 | 1940 (18.3)           | .99            |
| Smoking  | 27 (2.5)                                   | 270 (2.5)             | .99            |
| CCI score (SD)                                   | 2.75 (2.17)                                | 2.30 (2.19)           | <.001          |
| Level of urbanization, n (%)                     |  |                       | >.99           |
| 1 (most urbanized)                               | 141 (13.3)                                 | 1410 (13.3)           |                |
| 2  | 206 (19.5)                                 | 2060 (19.5)           |                |
| 3  | 55 (5.2)                                   | 550 (5.2)             |                |
| 4  | 97 (9.2)                                   | 970 (9.2)             |                |
| 5 (most rural)                                   | 560 (52.9)                                 | 5600 (52.9)           |                |
| Income-related insured amount                    |  |                       | >.99           |
| ≤NT\$15,840 per month                            | 383 (36.2)                                 | 3830 (36.2)           |                |
| NT\$15,841–NT\$25,000 per month                  | 371 (35.0)                                 | 3710 (35.0)           |                |
| ≥NT\$25,001 per month                            | 305 (28.8)                                 | 3050 (28.8)           |                |
| Incidence of any dementia, n (%)                 | 26 (2.5)                                   | 80 (0.7)              | <.001          |
| Age at diagnosis of any dementia (y, SD)         | 74.98 (9.46)                               | 80.09 (6.62)          | .003           |
| Duration between enrollment and dementia, y (SD) | 4.81 (2.96)                                | 6.00 (3.14)           | .09            |
| Dementia type, n (%)                             |  |                       |                |
| Alzheimer's disease                              | 6 (0.6)                                    | 9 (0.1)               | .001           |
| Vascular dementia                                | 5 (0.5)                                    | 15 (0.1)              | .03            |
| Unspecified                                      | 15 (1.4)                                   | 56 (0.5)              | .002           |
| All-cause clinical visits, times per year (SD)   | 20.54 (19.68)                              | 14.70 (14.00)         | <.001          |

Abbreviation: CCI, Charlson Comorbidity Index.

**Table 2**  
Risk of Developing Dementia Among Patients With Atopic Dermatitis and Controls

| Incidence of dementia | Cox regression model (HR, 95% CI) <sup>a</sup> |                   |                      |                         |
|-----------------------|--|-------------------|----------------------|-------------------------|
|                       | Alzheimer's disease                            | Vascular dementia | Unspecified dementia | Total                   |
| Atopic dermatitis     |  |                   |                      |                         |
| Absent                | 1 (ref)  | 1 (ref)           | 1 (ref)              | 1 (ref)                 |
| Present               | <b>3.74 (1.17–11.97)</b>                       | 2.04 (0.67–6.17)  | 1.69 (0.91–3.15)     | <b>2.02 (1.24–3.29)</b> |

Abbreviations: CCI, Charlson Comorbidity Index; CI, confidence interval; HR, hazard ratio; ref, reference.

NOTE: Boldface emphasis indicates statistical significance.

<sup>a</sup>Adjusted by demographic data, medical comorbidities, CCI score, and all-cause clinical visits.

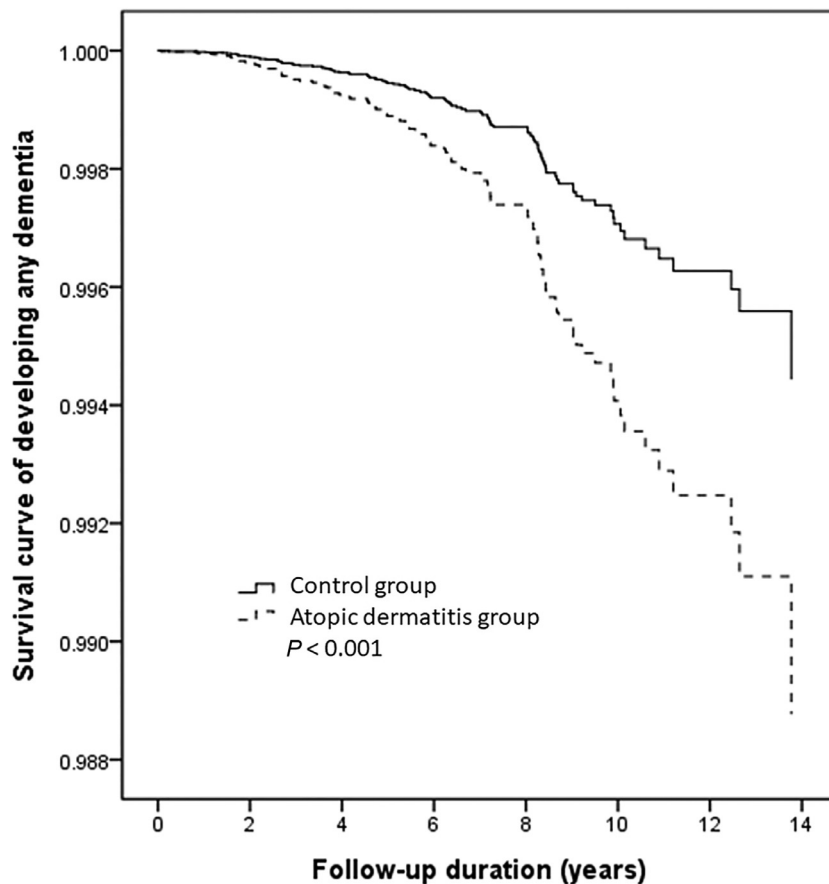


**Figure 1.** Survival curve of developing any dementia among patients with atopic dermatitis and control group.

## Discussion

After adjustments for dementia-related confounders, the current findings support our study hypothesis that patients with AD are more likely to develop any dementia, particularly Alzheimer's disease,

**Table 3**  
Risk of Developing Dementia Among Patients With Atopic Dermatitis and Controls Based on the Proxy of Disease Severity

| Incidence of dementia        | Dementia n, % | Crude HR 95% CI         | Adjusted HR <sup>a</sup> 95% CI |
|------------------------------|---------------|-------------------------|---------------------------------|
| Control group (n = 10,590)   | 80 (0.8)      | 1 (ref)                 | 1 (ref)                         |
| Atopic dermatitis group      |               |                         |                                 |
| Mild (n = 726)               | 13 (1.8)      | <b>2.57 (1.43–4.62)</b> | <b>2.32 (1.28–4.23)</b>         |
| Moderate-to-severe (n = 333) | 13 (3.9)      | <b>4.64 (2.58–8.33)</b> | 1.69 (0.83–3.44)                |

Abbreviations: CCI, Charlson Comorbidity Index; CI, confidence interval; HR, hazard ratio; ref, reference.

NOTE: Boldface emphasis indicates statistical significance.

<sup>a</sup>Adjusted by demographic data, medical comorbidities, CCI score, and all-cause clinical visits.

during the follow-up period than the matched controls, and that AD severity is associated with dementia risk, with moderate-to-severe AD increasing the likelihood of new-onset dementia development.

Accumulating evidence is suggesting that AD is a systemic inflammatory disease, which was further related to the increased risk of various dementia-related risk factors, such as diabetes and cerebrovascular diseases.<sup>5–7</sup> Ivert et al<sup>5</sup> reported that patients with AD exhibited a high prevalence of hypertension, dyslipidemia, diabetes mellitus, and smoking compared with patients without AD. They further revealed that severe AD was associated with ischemic stroke (odds ratio [OR], 1.19; 95% CI, 1.07–1.33).<sup>5</sup> Furthermore, a relationship of AD with increased risk of metabolic disorders was observed in the Asian population.<sup>17</sup> A cross-sectional Korean study of 5007 adult patients reported that obesity (OR, 1.73; 95% CI, 1.09–2.75) and dyslipidemia (OR, 2.20; 95% CI, 1.19–4.05) were positively correlated with AD.<sup>17</sup> However, the association between AD and subsequent dementia remained unknown despite evidence suggesting that AD is a detrimental factor in the overall cognitive function in adult patients.<sup>8</sup> Our findings proposed a definite association between AD and subsequent



**Table 4**

Sensitivity Analyses of Developing Any Dementia Among Patients With Atopic Dermatitis and Controls

| Incidence of dementia | Total                   | Cox regression model (HR, 95% CI) <sup>a</sup> |                         |                                |                         |
|-----------------------|-------------------------|--|-------------------------|--------------------------------|-------------------------|
|                       |                         | Exclusion of observation period                |                         | Exclusion of enrollment period |                         |
|                       |                         | >3 y   | >5 y                    | Enrollment year <2010          | Enrollment year <2008   |
| Atopic dermatitis     |                         |  |                         |                                |                         |
| Present               | <b>2.02 (1.24–3.29)</b> | <b>2.20 (1.28–3.80)</b>                        | <b>2.05 (1.08–3.89)</b> | <b>2.47 (1.51–4.03)</b>        | <b>3.11 (1.85–5.23)</b> |
| Absent                | 1 (ref)                 | 1 (ref)  | 1 (ref)                 | 1 (ref)                        | 1 (ref)                 |

Abbreviations: CCI, Charlson Comorbidity Index; CI, confidence interval; HR, hazard ratio; ref, reference.

NOTE: Boldface emphasis indicates statistical significance.

<sup>a</sup>Adjusted by demographic data, medical comorbidities, CCI score, and all-cause clinical visits.

dementia, particularly Alzheimer's disease, because the diagnostic validities of AD and Alzheimer's disease were confirmed on the basis of skin tests and antidementia medications, respectively, and dementia-related risk factors, such as diabetes and cerebrovascular diseases, were well matched and adjusted for. Compatible with the previous findings of a positive relationship between AD severity and metabolic disorder risks, we found that moderate-to-severe AD was associated with the highest likelihood of developing any dementia, although the statistical significance disappeared after adjustments for various confounders, particularly all-cause clinical visits (HR, 3.85; 95% CI, 2.13–6.96 vs adjusted HR, 1.69; 95% CI, 0.83–3.44).

From the neurobiological perspective, AD-related immunologic dysregulation and disturbance may explain the temporal association between AD and dementia, particularly Alzheimer's disease.<sup>7,18–20</sup> Increasing evidence reported that T-helper type 2 (T<sub>H</sub>2) inflammation and proinflammatory cytokines released during the allergic responses of AD may play a crucial role in the pathophysiology of dementia and Alzheimer's disease, and further indicated that the altered and dysregulated inflammatory pathway may affect the central nervous system and may be involved in dementia pathomechanisms.<sup>21–25</sup> Ringheim et al<sup>26</sup> reported that interleukin (IL)-6 promotes the expression of the amyloid-β precursor protein, and Quintanilla et al<sup>27</sup> suggested that IL-6 further contributes to neurofibrillary tangle formation by inducing Tau phosphorylation. Griffin et al<sup>28,29</sup> proposed an increase in IL-1 and astrocyte-derived neurotogenic cytokine S100B expression before detecting either β-amyloid plaques or neurofibrillary tangles and indicated that dysregulated neuroinflammation may precede dementia and Alzheimer's disease. Interleukin-33, a member of the IL-1 family and a potent inducer for the T<sub>H</sub>2 immune response, is constitutively expressed in the central nervous system and thought to be an important mediator of glial cell response to neuropathological lesions.<sup>24,25</sup> Xiong et al<sup>24</sup> found that IL-33/ST2-positive cells were also significantly increased in AD brains when compared with non-AD brains. Evidence indicated that dysregulated proinflammatory cytokines penetrate the blood-brain barrier during an allergic response and activate abnormal neuroimmune mechanisms involving some specific neural circuits related to cognitive modulation.<sup>30,31</sup> AD-related neuroimmune changes, as in a vicious cycle, take time to impair the specific brain function and neural circuitry involved in memory and cognition, which may explain the sequential phenomenon of AD followed by dementia. Additional studies on investigating the definite underlying pathomechanisms between AD and dementia and Alzheimer's disease are necessary.

The limitations of this study are similar to those of other registry-based analyses. First, an inevitable potential underestimation of dementia incidence existed. Our study design maximized diagnostic validity by considering only the diagnoses made by board-certified psychiatrists and neurologists. Diagnoses and coding are highly reliable as this is mandated by the Taiwanese government for medical reimbursement.<sup>32</sup> Second, despite emphasizing the unidirectional association between AD and subsequent dementia, a causal relationship could not be inferred. Third, childhood AD that occurred before

1996 cannot be identified in the database. Therefore, those who had a diagnosis of childhood AD but remitted in adulthood may be misclassified as the controls in our study. In addition, whether those who had a childhood AD but remitted in adulthood were also more likely to develop any dementia later in life would need further investigation. Fourth, antihistamine agents are typically used for not only AD but also other atopic diseases and related symptoms (ie, running nose and itching). Antihistamine agents were not investigated in our study because the prescribed medications were very complicated and difficult to adjust for in the regression models. Several studies suggested a possible association between anticholinergic agents and incident dementia and further indicated that one of the most common anticholinergic classes used is the first-generation antihistamines.<sup>33,34</sup> However, Andre et al<sup>35</sup> found no association between anticholinergic exposure and cognitive decline in older adults. The exact association between antihistamine agents and dementia risk would need further investigation. Finally, information on family history, environmental factors, lifestyle, and other factors is unavailable in the NHIRD.

In conclusion, we found an increased risk of dementia after AD diagnosis, with the average age of onset being 5 years less than in matched controls. Regarding the early detection and timely medical care through a multidisciplinary approach, regular assessment for memory and cognitive function may be necessary for elderly patients with AD. Future studies on the pathomechanisms and molecular underpinning between the 2 disease conditions may lead to further development of novel therapeutics.

## Acknowledgment

The authors thank Mr I-Fan Hu for his assistance in English editing.

## References

- Laughter MR, Maymone MBC, Mashayekhi S, et al. The global burden of atopic dermatitis: lessons from the Global Burden of Disease Study 1990–2017. *Br J Dermatol*. 2021;184(2):304–309.
- Katsarou A, Armenaka M. Atopic dermatitis in older patients: particular points. *J Eur Acad Dermatol Venereol*. 2011;25(1):12–18.
- Chello C, Carnicelli G, Sernicola A, et al. Atopic dermatitis in the elderly Caucasian population: diagnostic clinical criteria and review of the literature. *Int J Dermatol*. 2020;59(6):716–721.
- Howell AN, Ghamrawi RI, Strowd LC, Feldman SR. Pharmacological management of atopic dermatitis in the elderly. *Expert Opin Pharmacother*. 2020;21(7):761–771.
- Ivert LU, Johansson EK, Dal H, Lindelof B, Wahlgren CF, Bradley M. Association between atopic dermatitis and cardiovascular disease: a Nationwide Register-based Case-control Study from Sweden. *Acta Derm Venereol*. 2019;99(10):865–870.
- Shalom G, Dreier J, Kridin K, et al. Atopic dermatitis and the metabolic syndrome: a cross-sectional study of 116 816 patients. *J Eur Acad Dermatol Venereol*. 2019;33(9):1762–1767.
- Darlenski R, Kazandjieva J, Hristakieva E, Fluhr JW. Atopic dermatitis as a systemic disease. *Clin Dermatol*. 2014;32(3):409–413.
- Silverberg JI, Lei D, Yousaf M, et al. Association of atopic dermatitis severity with cognitive function in adults. *J Am Acad Dermatol*. 2020;83(5):1349–1359.

9. Chen MH, Li CT, Tsai CF, et al. Risk of dementia among patients with asthma: a nationwide longitudinal study. *J Am Med Dir Assoc*. 2014;15(10):763–767.
10. Rusanen M, Ngandu T, Laatikainen T, Tuomilehto J, Soininen H, Kivipelto M. Chronic obstructive pulmonary disease and asthma and the risk of mild cognitive impairment and dementia: a population based CAIDE study. *Curr Alzheimer Res*. 2013;10(5):549–555.
11. Cheng CM, Chang WH, Chen MH, et al. Co-aggregation of major psychiatric disorders in individuals with first-degree relatives with schizophrenia: a nationwide population-based study. *Mol Psychiatry*. 2018;23(8):1756–1763.
12. Chen MH, Lan WH, Hsu JW, et al. Risk of developing Type 2 diabetes in adolescents and young adults with autism spectrum disorder: a nationwide longitudinal study. *Diabetes Care*. 2016;39(5):788–793.
13. Chen MH, Pan TL, Li CT, et al. Risk of stroke among patients with post-traumatic stress disorder: nationwide longitudinal study. *Br J Psychiatry*. 2015;206(4):302–307.
14. Chen MH, Hsu JW, Huang KL, et al. Sexually transmitted infection among adolescents and young adults with attention-deficit/hyperactivity disorder: a nationwide longitudinal study. *J Am Acad Child Adolesc Psychiatry*. 2018;57(1):48–53.
15. Charlson ME, Pompei P, Ales KL, MacKenzie CR. A new method of classifying prognostic comorbidity in longitudinal studies: development and validation. *J Chronic Dis*. 1987;40(5):373–383.
16. Liu CY, Hung YT, Chuang YL, Chen YJ, Weng WS, Liu JS. Incorporating development stratification of Taiwan townships into sampling design of large scale health interview survey. *J Health Manag*. 2006;4(1):1–22.
17. Lee JH, Jung HM, Han KD, et al. Association between metabolic syndrome and atopic dermatitis in Korean adults. *Acta Derm Venereol*. 2017;97(1):77–80.
18. Cosmi L, Maggi L, Mazzoni A, Liotta F, Annunziato F. BioLogicals targeting type 2 immunity: lessons learned from asthma, chronic urticaria and atopic dermatitis. *Eur J Immunol*. 2019;49(9):1334–1343.
19. Langan SM, Irvine AD, Weidinger S. Atopic dermatitis. *Lancet*. 2020;396(10247):345–360.
20. Roesner LM, Werfel T. Autoimmunity (or Not) in Atopic Dermatitis. *Front Immunol*. 2019;10:2128.
21. Griffin WS. Neuroinflammatory cytokine signaling and Alzheimer's disease. *N Engl J Med*. 2013;368(8):770–771.
22. Meraz-Rios MA, Toral-Rios D, Franco-Bocanegra D, Villeda-Hernandez J, Campos-Pena V. Inflammatory process in Alzheimer's disease. *Front Integr Neurosci*. 2013;7:59.
23. Ferretti MT, Cuello AC. Does a pro-inflammatory process precede Alzheimer's disease and mild cognitive impairment? *Curr Alzheimer Res*. 2011;8(2):164–174.
24. Xiong Z, Thangavel R, Kempuraj D, Yang E, Zaheer S, Zaheer A. Alzheimer's disease: evidence for the expression of interleukin-33 and its receptor ST2 in the brain. *J Alzheimers Dis*. 2014;40(2):297–308.
25. Abd Rachman Isnadi MF, Chin VK, Abd Majid R, et al. Critical roles of IL-33/ST2 pathway in neurological disorders. *Mediators Inflamm*. 2018;2018: 5346413.
26. Ringheim GE, Szczepanik AM, Petko W, Burgher KL, Zhu SZ, Chao CC. Enhancement of beta-amyloid precursor protein transcription and expression by the soluble interleukin-6 receptor/interleukin-6 complex. *Brain Res Mol Brain Res*. 1998;55(1):35–44.
27. Quintanilla RA, Orellana DI, Gonzalez-Billault C, Maccioni RB. Interleukin-6 induces Alzheimer-type phosphorylation of Tau protein by deregulating the cdk5/p35 pathway. *Exp Cell Res*. 2004;295(1):245–257.
28. Griffin WS, Barger SW. Neuroinflammatory cytokines-The Common thread in Alzheimer's pathogenesis. *US Neurol*. 2010;6(2):19–27.
29. Griffin WS, Stanley LC, Ling C, et al. Brain interleukin 1 and S-100 immunoreactivity are elevated in Down syndrome and Alzheimer disease. *Proc Natl Acad Sci U S A*. 1989;86(19):7611–7615.
30. Pfab F, Valet M, Napadow V, et al. Itch and the brain. *Chem Immunol Allergy*. 2012;98:253–265.
31. Schut C, Mochizuki H, Grossman SK, et al. Brain processing of contagious itch in patients with atopic dermatitis. *Front Psychol*. 2017;8:1267.
32. Lin JC, Lin CS, Hsu CW, Lin CL, Kao CH. Association between Parkinson's disease and inflammatory bowel disease: a nationwide Taiwanese retrospective cohort study. *Inflamm Bowel Dis*. 2016;22(5):1049–1055.
33. Gray SL, Anderson ML, Dublin S, et al. Cumulative use of strong anticholinergics and incident dementia: a prospective cohort study. *JAMA Intern Med*. 2015;175(3):401–407.
34. Joung KI, Kim S, Cho YH, Cho SI. Association of anticholinergic use with incidence of Alzheimer's disease: population-based cohort study. *Sci Rep*. 2019;9(1):6802.
35. Andre L, Gallini A, Montastruc F, et al. Anticholinergic exposure and cognitive decline in older adults: effect of anticholinergic exposure definitions in a 3-year analysis of the multidomain Alzheimer preventive trial (MAPT) study. *Br J Clin Pharmacol*. 2019;85(1):71–99.



## Research Article

## Ginsenoside Rg3 ameliorates allergic airway inflammation and oxidative stress in mice

Wen-Chung Huang<sup>a, b, c, 1</sup>, Tse-Hung Huang<sup>a, d, e, f, 1</sup>, Kuo-Wei Yeh<sup>c</sup>, Ya-Ling Chen<sup>g</sup>, Szu-Chuan Shen<sup>h</sup>, Chian-Jiun Liou<sup>b, c, \*</sup><sup>a</sup> Graduate Institute of Health Industry Technology, Research Center for Food and Cosmetic Safety, Chang Gung University of Science and Technology, Taoyuan City, Taiwan<sup>b</sup> Department of Nursing, Division of Basic Medical Sciences, Research Center for Chinese Herbal Medicine, Chang Gung University of Science and Technology, Taoyuan City, Taiwan<sup>c</sup> Division of Allergy, Asthma, and Rheumatology, Department of Pediatrics, Chang Gung Memorial Hospital, Linkou, Taoyuan City, Taiwan<sup>d</sup> Department of Traditional Chinese Medicine, Chang Gung Memorial Hospital, Keelung, Taiwan<sup>e</sup> School of Traditional Chinese Medicine, Chang Gung University, Taoyuan City, Taiwan<sup>f</sup> School of Nursing, National Taipei University of Nursing and Health Sciences, Taipei City, Taiwan<sup>g</sup> School of Nutrition and Health Sciences, Taipei Medical University, Taipei City, Taiwan<sup>h</sup> Graduate Program of Nutrition Science, National Taiwan Normal University, Taipei City, Taiwan

## ARTICLE INFO

## Article history:

Received 29 February 2020

Received in revised form

8 January 2021

Accepted 6 March 2021

Available online 13 March 2021

## Keywords:

Airway hyperresponsiveness

Asthma

Eosinophil

Ginsenoside Rg3

Oxidative stress

## ABSTRACT

**Background:** Ginsenoside Rg3, isolated from *Panax ginseng*, has anti-inflammatory and anti-tumor activities. It is known to reduce inflammation in acute lung injury in mice, and to reduce the expression of inflammatory cytokines and COX-2 in human asthmatic airway epithelium. In this study, we attempted to determine whether ginsenoside Rg3 inhibits airway inflammation, oxidative stress, and airway hyperresponsiveness (AHR) in the lungs of asthmatic mice. We also investigated its effects on oxidative stress and the inflammatory response in tracheal epithelial cells.

**Methods:** Asthma symptoms were induced in female BALB/c mice sensitized with ovalbumin (OVA). Mice were divided into five groups: normal controls, OVA-induced asthmatic controls, and asthmatic mice treated with ginsenoside Rg3 or prednisolone by intraperitoneal injection. Inflammatory BEAS-2B cells (human tracheal epithelial cells) treated with ginsenoside Rg3 to investigate its effects on inflammatory cytokines and oxidative responses.

**Results:** Ginsenoside Rg3 treatment significantly reduced eosinophil infiltration, oxidative responses, airway inflammation, and AHR in the lungs of asthmatic mice. Ginsenoside Rg3 reduced Th2 cytokine and chemokine levels in bronchoalveolar lavage fluids and lung. Inflammatory BEAS-2B cells treated with ginsenoside Rg3 reduced the eotaxin and pro-inflammatory cytokine expressions, and monocyte adherence to BEAS-2B cells was significantly reduced as a result of decreased ICAM-1 expression. Furthermore, ginsenoside Rg3 reduced the expression of reactive oxygen species in inflammatory BEAS-2B cells.

**Conclusion:** Ginsenoside Rg3 is a potential immunomodulator that can ameliorate pathological features of asthma by decreasing oxidative stress and inflammation

© 2021 The Korean Society of Ginseng. Publishing services by Elsevier B.V. This is an open access article under the CC BY-NC-ND license (<http://creativecommons.org/licenses/by-nc-nd/4.0/>).

\* Corresponding author. Department of Nursing, Division of Basic Medical Sciences, Research Center for Chinese Herbal Medicine, Chang Gung University of Science and Technology, Taoyuan City, Taiwan.

E-mail address: [ccliu@mail.cgu.edu.tw](mailto:ccliu@mail.cgu.edu.tw) (C.-J. Liou).

<sup>1</sup> Wen-Chung Huang and Tse-Hung Huang are equal contributors to this paper.

## 1. Introduction

Asthma is a chronic allergic and inflammatory disease of the airways. Exposure to allergens or microbes can induce asthma attacks [1]. The clinical symptoms of asthma are complex, with chest tightness, cough, shortness of breath, and dyspnea being the main symptoms during an acute asthma attack [2]. Allergens stimulate the immune system to exacerbate airway narrowing by smooth

muscle contraction during asthma attacks, and airway epithelial cells also secrete more mucus, which obstructs the airways [3]. Lung infiltration by a large number of inflammatory immune cells (especially eosinophils) causes more severe respiratory inflammation and allergic symptoms, and also increases airway hyper-responsiveness (AHR), causing shortness of breath and dyspnea [2]. These pathological symptoms of asthma are related to Th2 cell activation, which releases massive amounts of IL-4, IL-13, and IL-5 [4]. These cytokines induce excessive secretion of IgE and trigger the activation of immune cells. They also contribute to excessive secretion of mucus, AHR, and airway remodeling [5].

Airway epithelial cells secrete mucus that traps inhaled microorganisms and allergens, and these cells also regulate the allergic and inflammatory reactions caused by exposure to these environmental substances [6]. These cells release more inflammatory cytokines, which exacerbate respiratory system inflammation, and chemokines, which attract immune cells to infiltrate the lungs [7]. Inflamed tracheal epithelial cells can activate oxidase expression to induce reactive oxygen species (ROS) and free radical production, causing oxidative stress and consequent lung damage [7].

*Panax ginseng* is distributed throughout China and Korea, and its root is one of the most widely used herbs for Qi-invigorating therapy [8]. Both Korean Red Ginseng and white ginseng have been demonstrated to improve asthma in mice, and Korean Red Ginseng improves asthma better than Korean white ginseng [9]. Ginsenosides are the main biologically active compounds of ginseng. Known ginsenosides include Rb1, Rb3, Rg1, Rc, Rh2, Rg2, and Rg3 [10,11]. Ginsenoside Rg3 could reduce acute lung injury by activating PI3K/AKT/mTOR and suppressing NF- $\kappa$ B signaling pathways [12,13]. Ginsenoside Rg3 also reduced inflammatory mediators in IL-1 $\beta$ -activated A549 lung epithelial cells by blocking NF- $\kappa$ B signaling pathways [14]. Furthermore, Rb1 and Rh2 improved AHR and airway inflammation in asthmatic mice by modulating Th2-cell activity and NF- $\kappa$ B signaling [15,16]. However, the effects of ginsenoside Rg3 on AHR, inflammation, and oxidative stress are unclear. In the current study, we would evaluate the ability of ginsenoside Rg3 to ameliorate asthma symptoms, and investigated the effects of ginsenoside Rg3 on immune function, oxidative stress, and inflammation in asthmatic mice.

## 2. Material and methods

### 2.1. Animals

Female BALB/c mice (20–25 g of body weight), 6 weeks of age, were purchased from the National Laboratory Animal Center (Taiwan). Mice were kept in an air-conditioned animal room with a 12-hour light/dark cycle and allowed to consume water and standard chow diet *ad libitum*. Animal experiments were conducted in accordance with the Animal Care and Protection Committee of Chang Gung University of Science and Technology (Approval number: 2014-007).

### 2.2. Drug treatment and sensitization

20(S)-ginsenoside Rg3 ( $\geq 98\%$  purity) was purchased from Sigma-Aldrich Co. (St. Louis, MO, USA), and was dissolved in DMSO solution. The experimental protocol for sensitized asthma mouse model is shown in Fig. 1A. Recent studies have demonstrated that 10mg/kg ginsenoside Rg3 could attenuates LPS-induced acute lung injury in mice [17]. Hence, subsequent experiments used ginsenoside Rg3 at 5 and 10mg/kg for all animal experiments. Briefly, the mice were sensitized using ovalbumin (OVA; Sigma) sensitizing solution (50  $\mu$ g OVA in 200  $\mu$ L normal saline containing 0.8 mg (AlOH<sub>3</sub>) adjuvant), administered by intraperitoneal injection on

days 1–3 and day 14. Next, mice inhaled 2% atomized OVA to challenge lung allergy on days 14, 17, 20, 23, and day 27. Mice gave with prednisolone, ginsenoside Rg3, or DMSO by intraperitoneal injection 1 h before methacholine inhalation or OVA challenge. Experimental mice were tested for AHR by methacholine inhalation on day 28. On day 29, mice were sacrificed to investigate oxidative response, inflammatory, immunomodulatory, and asthma pathology symptoms. The mice divided into five groups ( $n = 10$  in each group): (A) normal control (N group), mice treated with 50  $\mu$ L DMSO by intraperitoneal injection; (B) OVA-sensitized control (OVA group), mice sensitized with OVA and treated with 50  $\mu$ L DMSO by intraperitoneal injection; (C) the prednisolone control (P group), OVA-sensitized mice treated with 5 mg/kg prednisolone (dissolved in DMSO) by intraperitoneal injection; and (D) the OVA-sensitized mice treated with 5 mg/kg or 10 mg/kg ginsenoside Rg3 (dissolved in DMSO) by intraperitoneal injection (Rg5 and Rg10 groups, respectively).

### 2.3. AHR assay

Mice tested for AHR evaluated using airway flow and function, as described previously [18]. Briefly, mice were exposed to inhale an increasing dose of aerosolized (0 to 40 mg/mL) methacholine for 3 min. Next, mice were placed in a closed chamber, where the enhanced pause (Penh) signal data were measured in order to determine AHR values, using the whole-body plethysmograph system (Buxco Electronics, Troy, NY, USA). Furthermore, the mice were anesthetized and intubated to evaluate their lung function by detecting respiratory resistance by use of a low-frequency forced oscillation technique (Buxco Electronics) [19].

### 2.4. Malondialdehyde (MDA)

MDA was detected using the lipid peroxidation assay kit (Sigma) as described previously [20]. Mice lungs were removed and homogenized (FastPrep-24, MP Biomedicals, Santa Ana, CA, USA). The tissue solution was treated with perchloric acid and centrifuged to collect the supernatant. Finally, the level of MDA was assayed by a multi-mode microplate reader (SpectraMax i3X, Molecular Devices, San Jose, CA, USA).

### 2.5. Glutathione (GSH) and superoxide dismutase (SOD) assay

The levels of glutathione in lung tissues were detected using a glutathione assay kit (Sigma), and SOD activity was assayed using a SOD determination kit (Sigma) according to the manufacturer's instructions as described previously [21]. The GSH and SOD levels were detected using a microplate reader (Multiskan FC, Thermo, Waltham, MA, USA).

### 2.6. Serum collection and splenocyte culture

Mice were anesthetized with 4% isoflurane, and blood was harvested from the orbital vascular plexus. The sample centrifuged to collect the serum in order to detect OVA-specific antibodies, as described previously [22]. The spleens were removed, and splenocytes ( $5 \times 10^6$  cells/mL) seeded on 24-well culture plates containing 100  $\mu$ g/mL OVA and grown for 5 days. The supernatant was assayed for cytokines as described previously [23].

### 2.7. Bronchoalveolar lavage fluid (BALF)

Mice were sacrificed, and BALF collected as described previously [24]. Briefly, using an indwelling needle intubating the trachea, lungs were washed with 1 mL sterile normal saline. The BALF



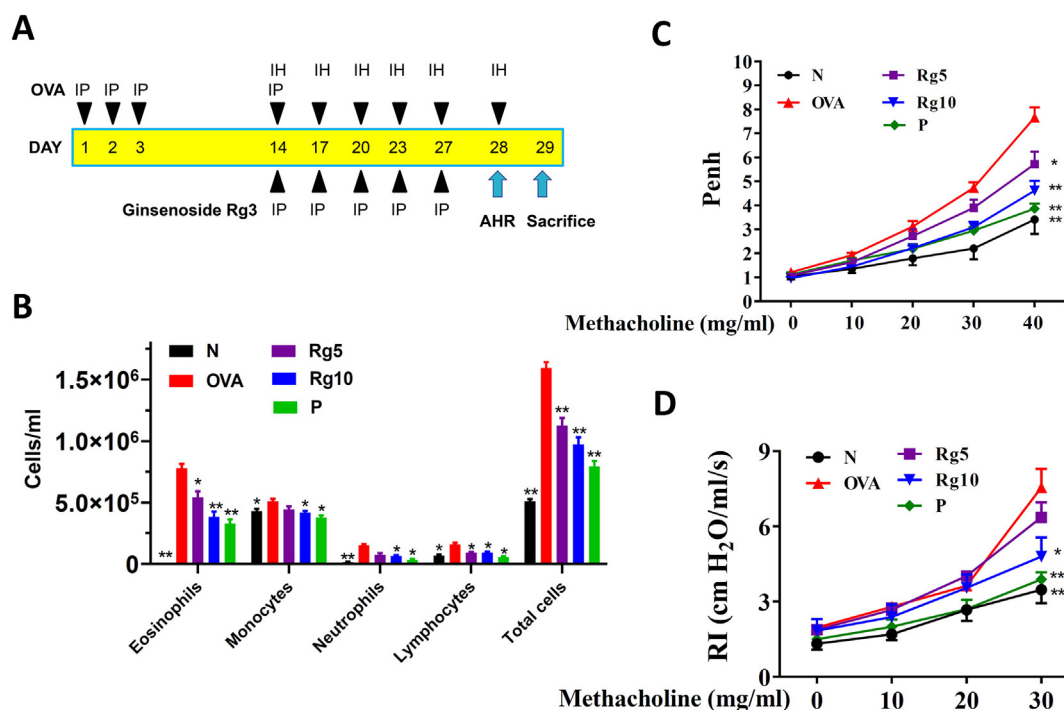


**Fig. 1.** Effect of ginsenoside Rg3 on AHR and cell counts in BALF from asthmatic mice. (A) Experimental procedures for asthmatic mouse studies. (B) Inflammatory cells in BALF were counted. (C) Mice inhaled increasing doses of methacholine, and AHR was assessed and is shown as Penh values. (D) AHR was measured as a percentage from the baseline level of lung resistance (RI). Three independent experiments were analyzed, and all data are presented as the mean  $\pm$  SEM. \* $p < 0.05$  and \*\* $p < 0.01$  compared with the OVA control group. Mice were divided into normal (N), OVA-sensitized mice (OVA), 5 mg/kg prednisolone control (P), 5 mg/kg ginsenoside Rg3 (Rg5) and 10 mg/kg ginsenoside Rg3 (Rg10) groups. IP, intraperitoneal injection; IH, inhalation.

collected and chemokines and cytokines were assayed by use of an ELISA. Next, BALF centrifuged using cytospin centrifugation (Cytospin 4, Thermo), and BALF cells stained with Giemsa stain (Sigma) for counting and to record cell morphology.

## 2.8. Histopathological assessment

Lung was fixed with formalin, and embedded in paraffin. Lung sections stained with periodic acid-Schiff solution (PAS; Sigma) to investigate tracheal goblet cell hyperplasia, as described previously [21]. The lung tissue sections stained with hematoxylin and eosin (HE) to observe eosinophil infiltration. The pathology scores of eosinophil infiltration were evaluated using a five-point grading system described previously [25]. Lung tissue stained with Masson's trichrome solution (Sigma) to observed collagen expression, as described previously [19].

## 2.9. Immunohistochemical staining

Lungs embedded in paraffin and sectioned, and the sections treated with COX-2 antibody (Abcam, Cambridge, UK) overnight. The slides were then treated with secondary antibodies and incubated with DAB substrate to detect COX-2 expression, as described previously [26].

## 2.10. ELISA assay

Serum OVA-specific antibodies were detected by use of an ELISA kit (BD Biosciences, Franklin Lakes, NJ, USA) [24]. Serum diluted 5-fold to evaluate OVA-IgE expressions as the OD<sub>450</sub> values. The units of OVA-IgG2a and OVA-IgG1 were defined using OD<sub>450</sub> values from standard curves of pooled serum from OVA-sensitized mice. The

levels of chemokines and cytokines in cell culture media and BALF were detected using the specific ELISA kit (R&D Systems, Minneapolis, MN, USA) [27].

## 2.11. Western blots

Lung proteins separated by SDS polyacrylamide gel electrophoresis. The proteins transferred to polyvinylidene fluoride membranes, which incubated with specific antibodies overnight. Next, the membranes treated with secondary antibodies, then incubated with luminol/enhancer solution (Merck Millipore, Burlington, MA, USA) to present protein signals by BioSpectrum AC Imaging System (UVP, Upland, CA, USA). Specific antibodies included ICAM-1 (Abcam); lamin B1, Nrf2, and HO-1 (Santa Cruz, CA, USA); and  $\beta$ -actin (Sigma).

## 2.12. Real-time PCR analysis

TRIzol reagent solution (Life Technologies, Carlsbad, CA, USA) was used to extract RNA, and cDNA synthesized by the cDNA synthesis kit (Bio-Rad, San Francisco, CA, USA) [18]. Gene-specific cDNAs were amplified using a SYBR green master mix kit and the spectrofluorometric thermal cycler (iCycler; Bio-Rad) as described previously [18].

## 2.13. BEAS-2B cell and ginsenoside Rg3 treatment

BEAS-2B, human bronchial epithelial cells, (American Type Culture Collection, Manassas, VA, USA) were cultured in DMEM/F12 medium. Ginsenoside Rg3 was dissolved in 100% DMSO at a concentration of 100 mM. The DMSO content was  $\leq 0.1\%$  in all experimental media. BEAS-2B cells seeded on a 24-well plate, and treated

with ginsenoside Rg3 (0–30  $\mu$ M) for 1 h. Subsequently, cells treated with 10 ng/mL IL-4/TNF- $\alpha$  for 24 h. The supernatants were collected and chemokines or cytokines measured using specific ELISA kits.

#### 2.14. ROS analysis

IL-4/TNF- $\alpha$ -induced BEAS-2B cells treated with ginsenoside Rg3 for 24 h. The cells incubated with 2',7'-dichlorofluorescein diacetate (DCFH-DA) and ROS levels were then detected by use of a Multi-Mode microplate reader (SpectraMax i3X, Molecular Devices), as described previously [18]. Additionally, intracellular ROS was detected using a fluorescence microscope (Olympus, Tokyo, Japan).

#### 2.15. Cell-cell adhesion analysis

BEAS-2B cells treated with or without ginsenoside Rg3 for 1 h, and then stimulated with 10 ng/mL IL-4/TNF- $\alpha$  for 24 h. THP-1 human monocytes were incubated with calcein-AM (Sigma) as described previously [18]. Subsequently, THP-1 cells co-cultured with BEAS-2B cells to observe THP-1 cell adhesion using a fluorescence microscope (Olympus).

#### 2.16. Statistical analysis

The values are each presented as the mean  $\pm$  SEM of at least three independent experiments. Statistical significance was determined using one-way analysis of variance followed by the Tukey-Kramer post hoc test. Data with values of  $p < 0.05$  were considered to be statistically significant.

### 3. Results

#### 3.1. Ginsenoside Rg3 suppressed eosinophil numbers in the BALF

Compared with the OVA-sensitized mice, asthmatic mice treated with prednisolone or ginsenoside Rg3 significantly decreased the numbers of eosinophils in BALF. We also found that ginsenoside Rg3 or prednisolone could significantly suppress the total number of cells in BALF when compared with the number in the OVA group mice (Fig. 1B).

#### 3.2. Ginsenoside Rg3 attenuated AHR in mice

In mice that inhaled 40 mg/mL methacholine, treatment with ginsenoside Rg3 and prednisolone significantly attenuated Penh values when compared with the OVA group mice (Fig. 1C). The airway resistance of mice was measured by the forced intubation technique. In mice that inhaled 30 mg/mL methacholine, 10 mg/kg ginsenoside Rg3 and prednisolone significantly reduced airway resistance, in comparison with OVA-sensitized mice (Fig. 1D).

#### 3.3. Ginsenoside Rg3 regulated chemokine and cytokine expressions in BALF and lung tissue

In BALF, ginsenoside Rg3 significantly decreased CCL11, CCL24, TNF- $\alpha$ , IL-5, IL-4, IL-13, and IL-6 levels in comparison with asthmatic mice (Fig. 2A–G). Treatment of asthmatic mice with ginsenoside Rg3 also significantly attenuated CCL11, CCL24, TNF- $\alpha$ , IL-4, IL-13, IL-5, and IL-6 gene expression in the lungs (Fig. 2I–O). Furthermore, in BALF and lung tissue, ginsenoside Rg3 significantly increased IFN- $\gamma$  production over that in untreated asthmatic mice (Fig. 2H and P).

#### 3.4. Ginsenoside Rg3 reduced OVA-induced goblet cell hyperplasia and eosinophil infiltration in lungs

Asthmatic mice treated with ginsenoside Rg3 had reduced eosinophil infiltration and decreased tracheal goblet cell hyperplasia of the lungs compared with that of the OVA-sensitized mice (Fig. 3A–D). We also found that ginsenoside Rg3 reduced collagen production in the lung of asthmatic mice (Fig. 3E–F). Furthermore, immunohistochemical staining of COX-2 in lung tissue showed that ginsenoside Rg3 treatment decreased COX-2 productions in comparison with the OVA group asthma mice (Fig. 3G–H). Moreover, ginsenoside Rg3 significantly decreased Muc5Ac and ICAM-1 gene expression, and reduced ICAM-1 protein expression in lung tissue, compared with their levels in untreated asthmatic mice (Fig. 4A–C).

#### 3.5. Ginsenoside Rg3 modulated MDA and GSH in the lungs

Compared with untreated OVA-sensitized mice, mice treated with ginsenoside Rg3 significantly increased GSH levels and SOD activity and lower MDA levels in their lung tissue (Fig. 4D–F). Ginsenoside Rg3-treatment of asthmatic mice promoted HO-1 expression and increased nuclear Nrf2 production in lung tissue (Fig. 4G).

#### 3.6. Ginsenoside Rg3 modulated OVA-specific antibodies in serum and cytokine expressions in splenocyte

Ginsenoside Rg3 significantly decreased serum OVA-IgG1 and OVA-IgE and increased OVA-IgG2a expression in asthmatic mice (Fig. 4H–J). Furthermore, the supernatant of splenocytes from asthmatic mice treated with ginsenoside Rg3 showed reduced the levels of IL-13, IL-5, and IL-4 and increased IFN- $\gamma$  expressions compared with the OVA group mice (Fig. 4K–N).

#### 3.7. Ginsenoside Rg3 reduced inflammatory response and cell adhesion in BEAS-2B cells

Ginsenoside Rg3-treated cells significantly decreased levels of CCL24, CCL11, CCL5, MCP-1, IL-8, and IL-6 compared with untreated activated BEAS-2B cells (Fig. 5). Ginsenoside Rg3-treated cells had decreased ICAM-1 levels (Fig. 6A), and were less adherent to THP-1 cells, compared with IL-4/TNF- $\alpha$ -activated BEAS-2B cells (Fig. 6B and C).

#### 3.8. Ginsenoside Rg3 suppressed ROS expression in BEAS-2B cells

Fluorescence microscopy revealed that ROS expression was lower in ginsenoside Rg3-treated, TNF- $\alpha$ /IL-4-activated BEAS-2B cells compared with untreated activated BEAS-2B cells (Fig. 6D and E). The DCFH-DA assay also showed that ginsenoside Rg3 treatment significantly attenuated ROS productions in IL-4/TNF- $\alpha$ -activated BEAS-2B cells (Fig. 6F).

### 4. Discussion

In Chinese and Korean traditional medicine, the root of *P. ginseng* is commonly used to treat cardiovascular diseases and diabetes, promote immune function, and improve central nervous system function [10,28]. Ginsenoside Rg3 also reduces endothelial dysfunction caused by oxidative stress, by upregulating the Nrf2/HO-1 signaling pathway [29]. Ginsenoside Rg3 also inhibits COX-2 expression in IL-1 $\beta$ -activated lung epithelial cells, and decreases the levels of eotaxin, IL-13, IL-9, IL-4, and IL-6 in human asthmatic airway epithelial tissue [14]. However, how ginsenoside Rg3

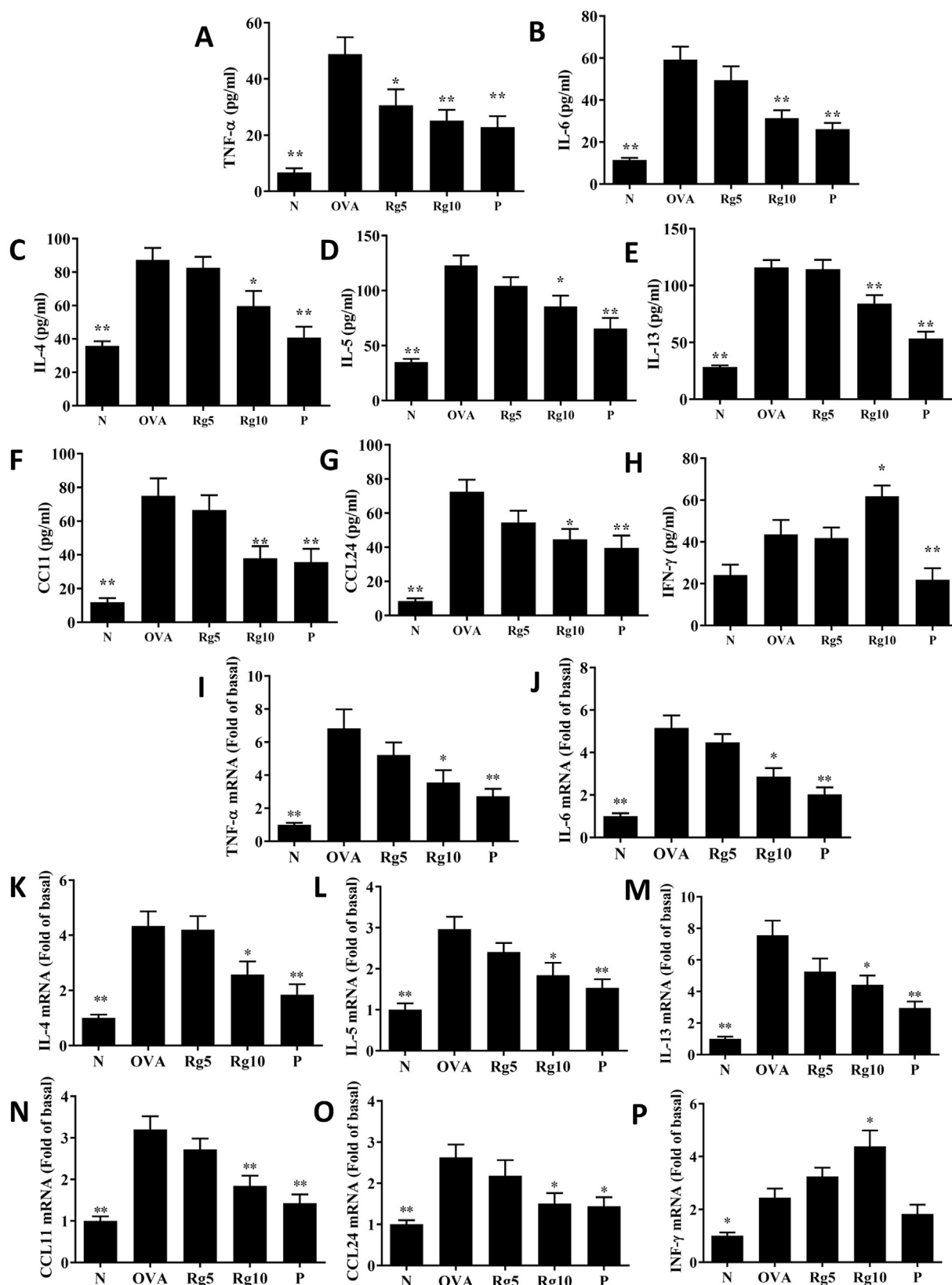


**Fig. 2.** (A–H) Effects of ginsenoside Rg3 on the levels of cytokines and chemokines in BALF. (I–P) Gene expression of the lungs was determined using real-time RT-PCR with lung tissue from normal (N) and OVA-stimulated (OVA) mice with or without ginsenoside Rg3 (Rg5, Rg10) or prednisolone (P) treatment. Fold changes in expression were measured relative to  $\beta$ -actin (internal control). The data are presented as the mean  $\pm$  SEM of three independent experiments ( $n = 10$ ). \* $p < 0.05$ , \*\* $p < 0.01$  compared to OVA control mice. 5 mg/kg and 10 mg/kg ginsenoside Rg3 were named as Rg5 and Rg10, respectively.

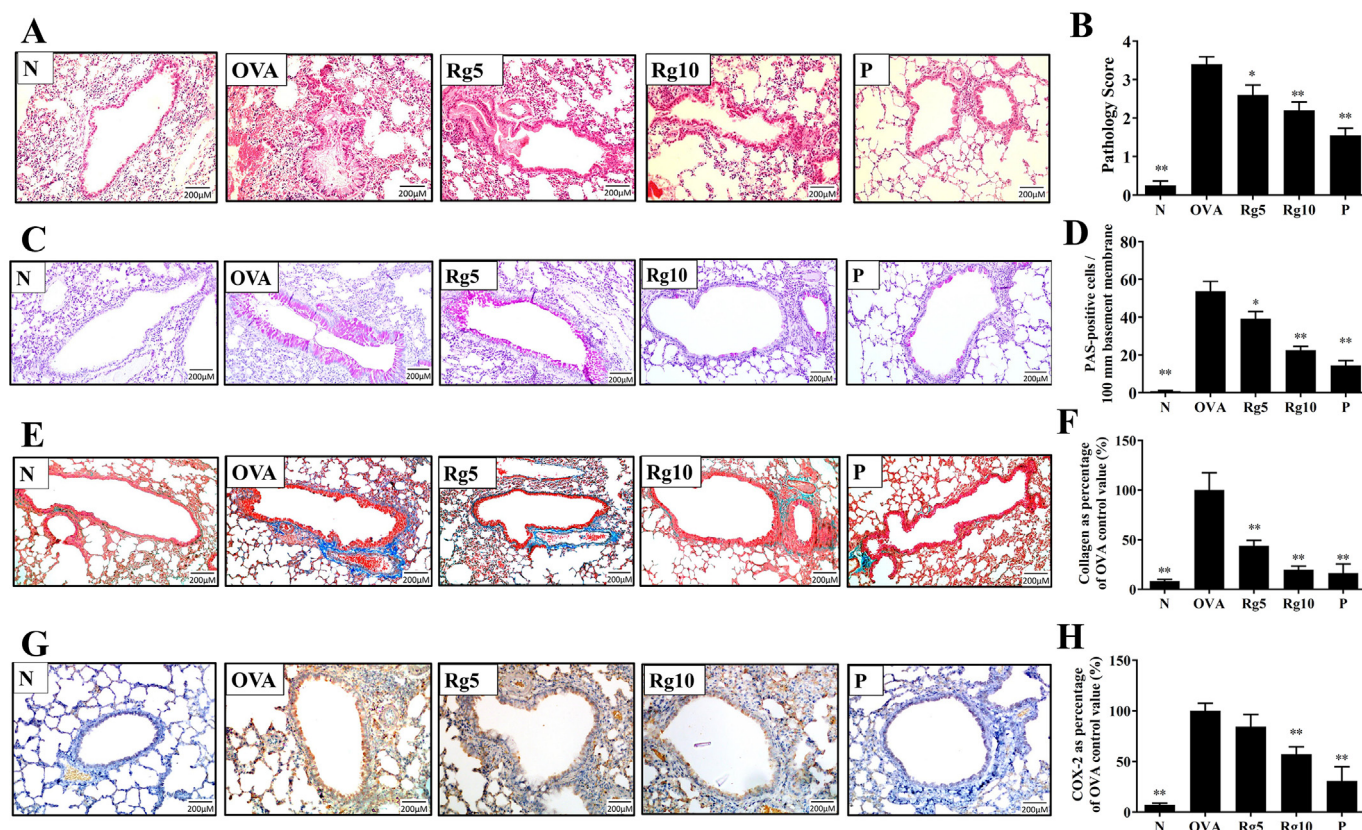


**Fig. 3.** Ginsenoside Rg3 effects on asthmatic lung tissue. Sections of lung tissue from normal (N) and OVA-stimulated (OVA) mice with or without ginsenoside Rg3 (Rg5, Rg10) or prednisolone (P) treatment. (A) Ginsenoside Rg3 reduced eosinophil infiltration (HE stain; 200 × magnification). (B) The pathological scores reflect the degree of eosinophil infiltration in lung tissue. (C) PAS-stained lung sections show goblet cell hyperplasia (200 × magnification). (D) The number of PAS-positive cells per 100 μm of basement membrane. (E) Lung sections were stained with Masson's trichrome stain to detect collagen expression (200 × magnification). (F) Quantitative analysis of collagen in lung sections. (G) Ginsenoside Rg3 decreased COX-2 expression in the lungs. COX-2 expression was analyzed by immunohistochemistry (brown color). (H) Quantitative analysis of COX-2 expression in lung sections. Three independent experiments were analyzed, and all data are presented as the mean ± SEM. \**p* < 0.05 and \*\*\**p* < 0.01 compared with the OVA control group. 5 mg/kg and 10 mg/kg ginsenoside Rg3 were named as Rg5 and Rg10, respectively.

ameliorates AHR, eosinophil infiltration, oxidative stress, and airway inflammation in the asthmatic lung was unclear. In the current study, ginsenoside Rg3 could suppress tracheal goblet cell hyperplasia, collagen expression, eosinophil infiltration, and AHR in the lungs of asthmatic mice. It also attenuated COX-2 expression and oxidative stress in the lung, and lowered Th2-associated cytokine and chemokine expressions in lung tissue and BALF. Furthermore, ginsenoside Rg3 inhibited ROS expression and decreased the secretion of chemokines and pro-inflammatory cytokines by inflammatory BEAS-2B cells.

AHR values can be used to detect airway flow and respiratory frequency, and to assess the patient's respiratory pathological changes and respiratory system function [30]. Especially in patients with chronic asthma, the connective tissues of the lungs and airways gradually thicken and become weaker, reducing airway contractility and lowering alveolar surface tension [3]. Therefore, the patient's intake of air during an emergency asthma attack is insufficient, resulting in an increased respiratory rate and shortness of breath. Our experiment found that ginsenoside Rg3 reduced both AHR and respiratory resistance in asthmatic mice. These results confirmed that ginsenoside Rg3 can improve respiratory function in asthmatic mice.

High levels of IL-13 can be detected in the lungs of asthmatic patients, and excess IL-13 secretion by Th2 cells worsens AHR [4]. Our experiments confirmed that asthmatic mice treated with ginsenoside Rg3 had decreased IL-13 levels in both lung and BALF, and

AHR was also found to be significantly lower in ginsenoside Rg3-treated asthmatic mice. These results suggest that ginsenoside Rg3 inhibited AHR in asthmatic mice mainly by blocking the expression of IL-13. The lungs of most asthma patients are infiltrated by large numbers of eosinophils, and activated Th2 cells secrete excess IL-5, inducing the differentiation of more mature eosinophils from bone marrow [31]. Tracheal epithelial cells release high amounts of eotaxin under the induction of IL-4 and TNF-α, and human lung epithelial cells also release CCL26 in response to IL-4 [18,32]. These eotaxins attract more eosinophils to the airways and lungs in asthmatic patients [4]. Activated eosinophils undergo degranulation and release cytotoxic molecules causing edema and inflammation of the airways and tracheal epithelial cells [33,34]. Previous studies demonstrated that ginsenoside Rg3 significantly inhibits mast cell histamine release and reduces allergic inflammation [35]. Our experiments showed that ginsenoside Rg3 treatment of asthmatic mice not only inhibited IL-4 and IL-5 expression in BALF, lung, and splenocytes stimulated by OVA, but also decreased serum OVA-IgG1 and OVA-IgE levels. In addition, ginsenoside Rg3 reduced the releases of eotaxin (CCL11 and CCL24) from tracheal epithelial cells and decreased the expression of ICAM-1, blocking immune cell adhesion to tracheal epithelial cells. In the lungs of patients with asthma, Th2 cells secrete excess IL-4, IL-5, and IL-13 to inhibit the expression of Th1 cells, which reduces IFN-γ production [5]. The IgG2a and IgG1 immunoglobulin were confirmed as markers for Th1 and Th2 cells, respectively [4].



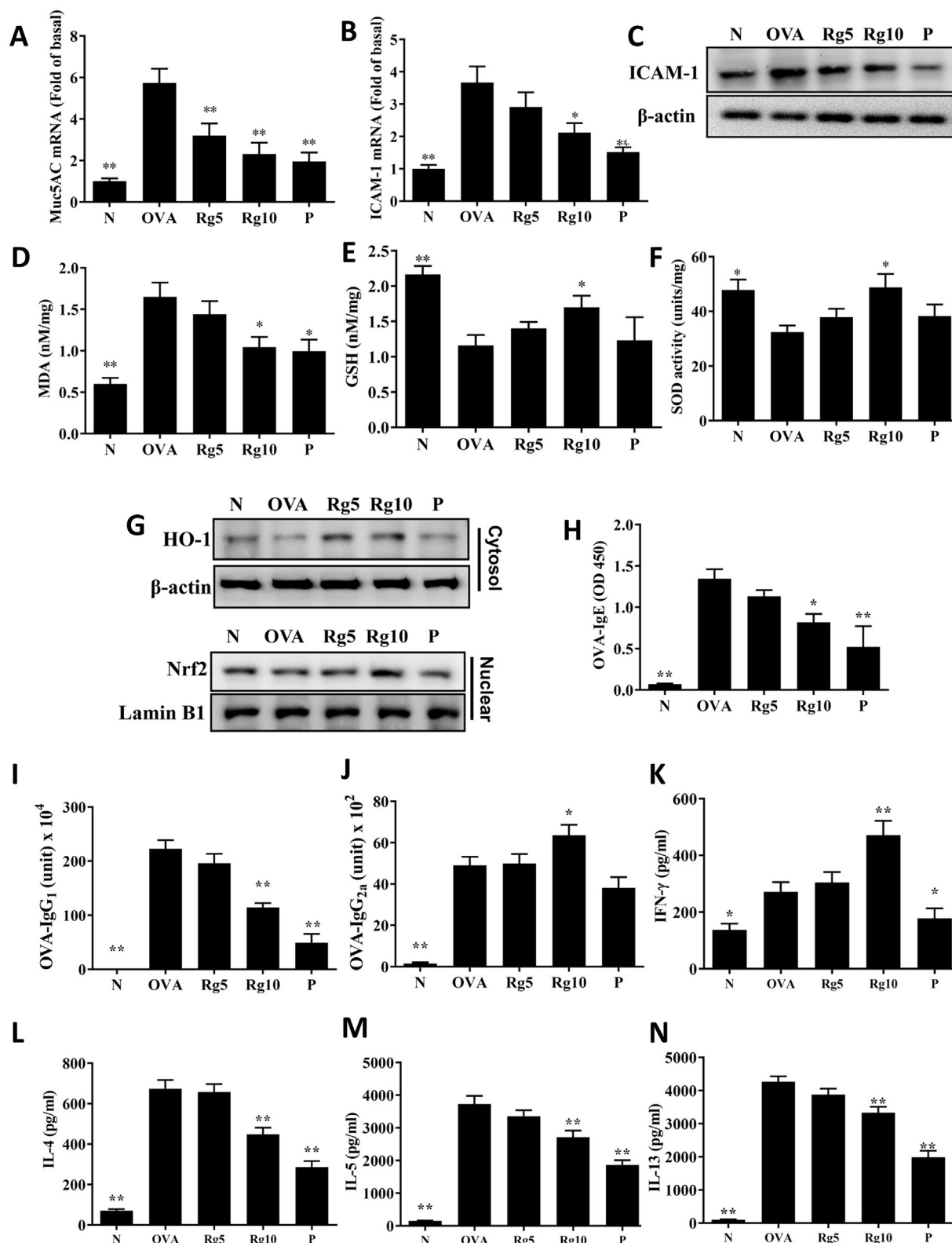


**Fig. 4.** Real-time RT-PCR results showing gene expression levels of (A) Muc5AC and (B) ICAM-1 in lung tissue from normal (N) and OVA-stimulated (OVA) mice with or without ginsenoside Rg3 (Rg5, Rg10) or prednisolone (P) treatment. Fold changes in expression levels were calculated relative to that of  $\beta$ -actin (internal control). (C) Western blot showing that ginsenoside Rg3 suppressed ICAM-1 expression in lung tissue. Effects of ginsenoside Rg3 on oxidative stress factors. (D) MDA activity, (E) GSH activity, and (F) SOD activity were measured in mouse lung tissue. (G) Western blots show ginsenoside Rg3 modulation of Nrf2 and HO-1 expression in lung tissue. Furthermore, serum levels of (H) OVA-IgE, (I) OVA-IgG1, and (J) OVA-IgG2a in mice. Ginsenoside Rg3 modulated the levels of (K) IFN- $\gamma$ , (L) IL-4, (M) IL-5, and (N) IL-13 produced by OVA-activated splenocytes. The data are presented as the mean  $\pm$  SEM of three independent experiments. \* $p < 0.05$ , \*\* $p < 0.01$  compared with the OVA control group. 5 mg/kg and 10 mg/kg ginsenoside Rg3 were named as Rg5 and Rg10, respectively.

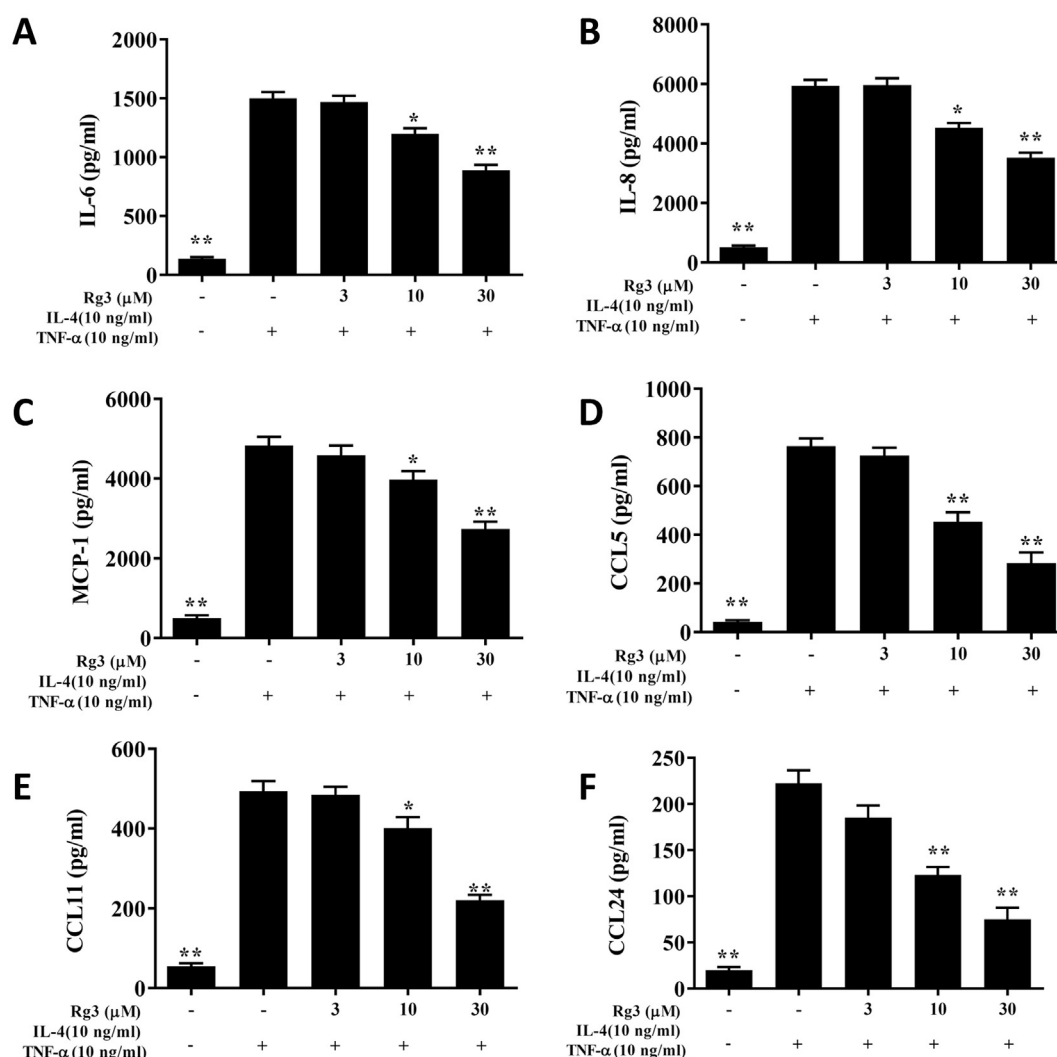


**Fig. 5.** Effects of ginsenoside Rg3 (Rg3) on cytokine and chemokine production in BEAS-2B cells. ELISA showing (A) IL-6, (B) IL-8, (C) MCP-1, (D) CCL5, (E) CCL11, and (F) CCL24 levels in BEAS-2B cells treated with ginsenoside Rg3. The data are presented as the mean  $\pm$  SEM of three independent experiments. \* $p < 0.05$ , \*\* $p < 0.01$  compared to BEAS-2B cells stimulated with TNF- $\alpha$  and IL-4.

We therefore detected the expression of IFN- $\gamma$ , a Th1-polarizing cytokine. Ginsenoside Rg3 could increase IFN- $\gamma$  levels in the BALF and spleen cell supernatants. We believe that ginsenoside Rg3 suppressed the development of asthma by suppressing Th2 cell activity and reducing eotaxin secretion in asthmatic mice, thereby inhibiting eosinophilic infiltration into the lung tissue.

Allergens stimulate the differentiation of airway epithelial cells to goblet cells, which then secrete excess mucus, and goblet cell proliferation is one of the characteristics of airway remodeling in asthmatic patients [2]. Muc5AC gene expression in the lung and goblet cell proliferation in the airways do not increase in response to an allergen in IL-13 or IL-4 knockout asthmatic mice [36]. *P. ginseng* extract can ameliorate Muc5AC gene expression in asthma mice [37]. In our experiments, ginsenoside Rg3 treatment reduced Muc5AC gene expression in the lungs of asthmatic mice and also attenuated airway goblet cell proliferation, both of which improve breathing. We believe ginsenoside Rg3 achieves these effects by reducing the expression of IL-4 and IL-13 in asthmatic mice.

Chronic inflammation of the lungs causes pulmonary fibrosis characterized by collagen deposition, persistent inflammation, and oxidative damage to lung epithelial cells [2]. Fibrotic alveolar walls harden and lose elasticity, reducing vital capacity and impeding

oxygen inhalation and carbon dioxide exhalation [2]. Inflammatory eosinophils release osteopontin to induce airway fibrosis through promoted Th2 cell activity [38]. Total ginsenoside suppressed pulmonary fibrosis in mice by regulating the matrix metalloproteinase system and TGF- $\beta$ 1/Smad signaling pathway [39]. Here, ginsenoside Rg3 treatment significantly reduced the expression of the proinflammatory cytokines IL-6 and TNF- $\alpha$  in the lung, thereby suppressing collagen deposition and reducing pulmonary fibrosis in asthmatic mice.

Allergens or microorganisms stimulate respiratory epithelial cells, which induce inflammation and activate epithelial cells to release inflammatory cytokines causing inflammation in the airways and lungs [6]. These inflammatory epithelial cells also release MCP-1, CCL5, and IL-8 to attract more macrophages and neutrophils to the lungs [40]. These activated immune cells release more inflammatory cytokines and inflammatory mediators, which exacerbate cell damage and fibrosis in the lungs [41]. Here, we found that ginsenoside Rg3 not only suppressed the release of CCL5, MCP-1, IL-8, and IL-6 by inflammatory BEAS-2B cells, but also decreased the inflammatory cytokine and chemokine expressions in BALF and the lung. Immunohistochemical staining showed that ginsenoside Rg3 reduced the expression of COX-2 in the lungs of asthmatic

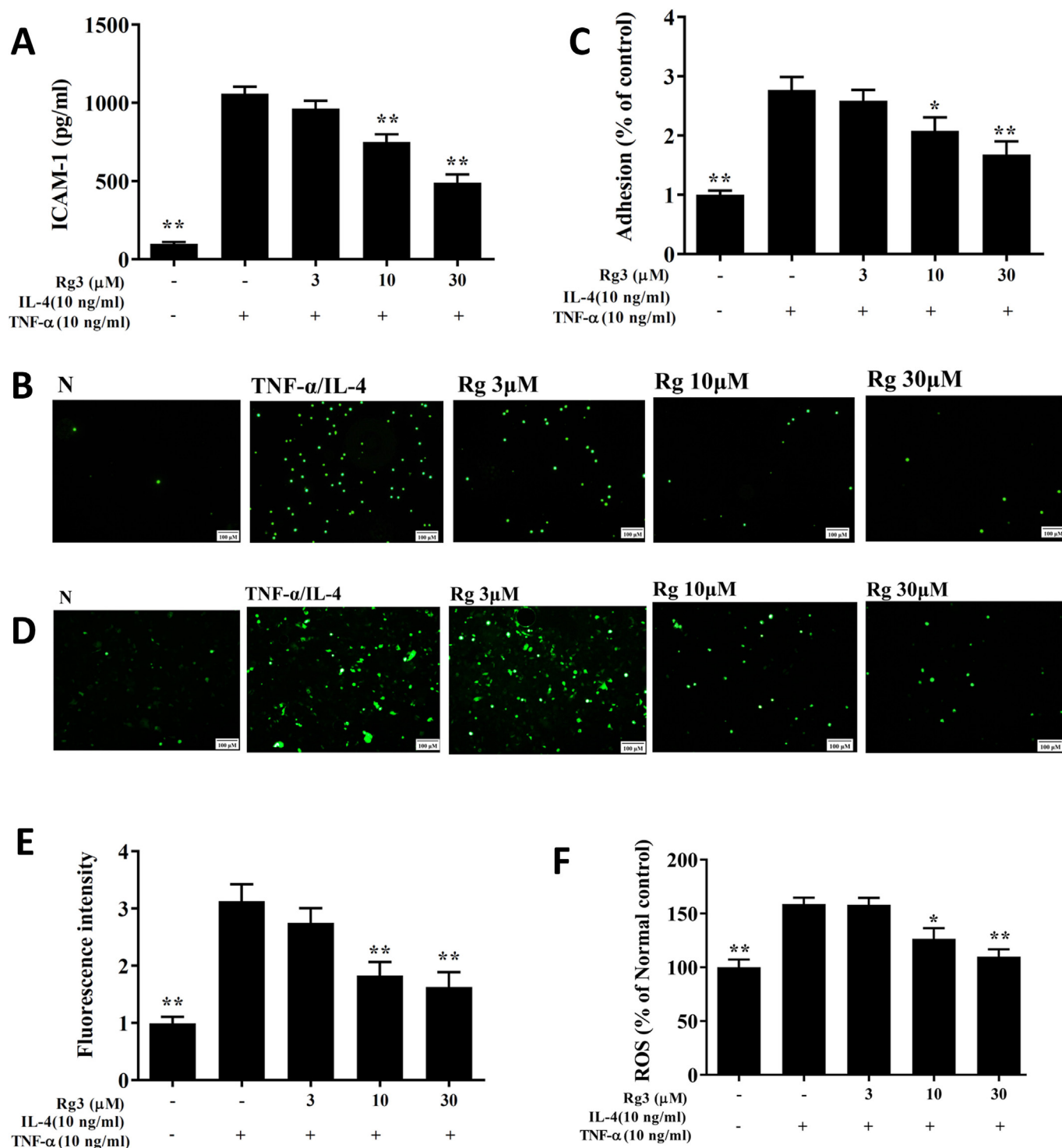


**Fig. 6.** Ginsenoside Rg3 (Rg3) inhibited THP-1 cell adhesion to activated BEAS-2B cells. (A) Ginsenoside Rg3 decreased the levels of ICAM-1 in BEAS-2B cells activated with TNF- $\alpha$ /IL-4. (B) Fluorescence microscope images of THP-1 cells labeled with calcein-AM and mixed with untreated cells (normal control, N) and TNF- $\alpha$ /IL-4-activated BEAS-2B cells in the absence or presence of ginsenoside Rg3. (C) Fluorescence intensity of monocytic cell adhesion to BEAS-2B cells. Ginsenoside Rg3 effects on ROS production in activated BEAS-2B cells. (D) Fluorescence microscopy images of intracellular ROS. (E) Fluorescence intensity of intracellular ROS. (F) Percentages of ROS detected in TNF- $\alpha$ /IL-4-activated BEAS-2B cells in the absence or presence of ginsenoside Rg3, compared with untreated cells (N). Three independent experiments were analyzed, and data represent the mean  $\pm$  SEM. \* $p$  < 0.05, \*\* $p$  < 0.01, compared with BEAS-2B cells stimulated with TNF- $\alpha$  and IL-4.

mice. Thus, ginsenoside Rg3 could significantly reduce lung inflammation and pulmonary cachexia by reducing alveolar cell damage in asthmatic mice.

Sudden or persistent oxidative stress in the lungs induces sputum production and damages alveolar cells or tracheal epithelial cells in patients with asthma [42]. Inflammatory immune cells infiltrating the lungs release more oxidative stress, and stimulate

respiratory epithelial cells to release more inflammatory cytokines and ROS [43]. Activated eosinophils release eosinophil peroxidase and cause oxidative damage in asthmatic patients [44]. Oxidative stress exacerbates bronchoconstriction, stimulates mucus secretion, increases AHR, and causes shortness of breath and difficulty breathing [42]. Ginsenoside Rg3 increases Nrf2/HO-1 expression and thereby attenuates oxidative stress in endothelial cells [29]. In our experiments, ginsenoside Rg3 significantly increased the expression of Nrf2, HO-1, SOD, and GSH, and reduced MDA levels in the lungs of asthmatic mice. Collectively, our experiments confirmed that ginsenoside Rg3 is an excellent stimulator of anti-oxidant activity and can attenuate allergen-induced lung cell damage in asthmatic mice.

In conclusion, ginsenoside Rg3 significantly suppressed oxidative stress and inflammation in the lungs of asthmatic mice. It also decreased AHR, eosinophil infiltration, and mucus hypersecretion by inhibiting Th2 cytokine and eotaxin expressions. We suggest that ginsenoside Rg3 has extremely good potential as a regulator in reducing anti-oxidative stress and inflammation in asthma.

### Author contributions

WCH, THH, KKY, YLC, and CJL performed and designed the experiments; KKY, YLC, and SCS interpreted and analyzed the experimental data; WCH, THH, and CJL drafted the manuscript.

### Declaration of competing interest

The authors declare that there are no conflicts of interest.

### Acknowledgments

This study supported by grants from Chang Gung Memorial Hospital in Taiwan (CMRPF1K0051, CMRPF1J0062, CMRPF1H0022, CMRPF1H0042, and CMRPF1J0021) and from the Ministry of Science and Technology in Taiwan (106-2320-B-255-008-MY3 and 106-2320-B-255-007-MY3).

### References

- [1] Chen X, Corry DB, Li E. Mechanisms of allergy and adult asthma. *Curr Opin Allergy Clin Immunol* 2020;20:36–42.
- [2] Kudo M, Ishigatsubo Y, Aoki I. Pathology of asthma. *Front Microbiol* 2013;4:263.
- [3] Ray A, Raundhal M, Oriss TB, Ray P, Wenzel SE. Current concepts of severe asthma. *J Clin Invest* 2016;126:2394–403.
- [4] Lambrecht BN, Hammad H, Fahy JV. The cytokines of asthma. *Immunity* 2019;50:975–91.
- [5] Caminati M, Pham DL, Bagnasco D, Canonica GW. Type 2 immunity in asthma. *World Allergy Organ J* 2018;11:13.
- [6] Roan F, Obata-Ninomiya K, Ziegler SF. Epithelial cell-derived cytokines: more than just signaling the alarm. *J Clin Invest* 2019;129:1441–51.
- [7] Goleva E, Berdyshev E, Leung DY. Epithelial barrier repair and prevention of allergy. *J Clin Invest* 2019;129:1463–74.
- [8] Choi MK, Song IS. Interactions of ginseng with therapeutic drugs. *Arch Pharm Res* 2019;42:862–78.
- [9] Lim CY, Moon JM, Kim BY, Lim SH, Lee GS, Yu HS, et al. Comparative study of Korean White Ginseng and Korean Red Ginseng on efficacies of OVA-induced asthma model in mice. *J Ginseng Res* 2015;39:38–45.
- [10] Kim JH. Pharmacological and medical applications of *Panax ginseng* and ginsenosides: a review for use in cardiovascular diseases. *J Ginseng Res* 2018;42:264–9.
- [11] Mohanan P, Subramaniam S, Mathiyalagan R, Yang DC. Molecular signaling of ginsenosides Rb1, Rg1, and Rg3 and their mode of actions. *J Ginseng Res* 2018;42:123–32.
- [12] Cheng Z, Li L. Ginsenoside Rg3 ameliorates lipopolysaccharide-induced acute lung injury in mice through inactivating the nuclear factor-kappaB (NF-kappaB) signaling pathway. *Int Immunopharmacol* 2016;34:53–9.
- [13] Yang J, Li S, Wang L, Du F, Zhou X, Song Q, et al. Ginsenoside Rg3 attenuates lipopolysaccharide-induced acute lung injury via MerTK-dependent activation of the PI3K/AKT/mTOR pathway. *Front Pharmacol* 2018;9:850.
- [14] Lee IS, Uh I, Kim KS, Kim KH, Park J, Kim Y, et al. Anti-inflammatory effects of ginsenoside Rg3 via NF-kappaB pathway in A549 cells and human asthmatic lung tissue. *J Immunol Res* 2016;2016:7521601.
- [15] Chen T, Xiao L, Zhu L, Ma S, Yan T, Ji H. Anti-asthmatic effects of Ginsenoside Rb1 in a mouse model of allergic asthma through relegating Th1/Th2. *Inflammation* 2015;38:1814–22.
- [16] Li LC, Piao HM, Zheng MY, Lin ZH, Choi YH, Yan GH. Ginsenoside Rh2 attenuates allergic airway inflammation by modulating nuclear factor-kappaB activation in a murine model of asthma. *Mol Med Rep* 2015;12:6946–54.
- [17] Cheng Z, Li L. Ginsenoside Rg3 ameliorates lipopolysaccharide-induced acute lung injury in mice through inactivating the nuclear factor-kappaB (NF-kappaB) signaling pathway. *Int Immunopharmacol* 2016;34:53–9.
- [18] Huang WC, Fang LW, Liou CJ. Phloretin attenuates allergic airway inflammation and oxidative stress in asthmatic mice. *Front Immunol* 2017;8:134.
- [19] Huang WC, Liu CY, Shen SC, Chen LC, Yeh KW, Liu SH, et al. Protective effects of licochalcone A improve airway hyper-responsiveness and oxidative stress in a mouse model of asthma. *Cells* 2019;8:617.
- [20] Liou CJ, Huan YL, Huang WC, Yeh KW, Huang TY, Lin CF. Water extract of *Helminthostachys zeylanica* attenuates LPS-induced acute lung injury in mice by modulating NF-kB and MAPK pathways. *J Ethnopharmacol* 2017;199:30–8.
- [21] Liou CJ, Chen YL, Yu MC, Yeh KW, Shen SC, Huang WC. Sesamol alleviates airway hyperresponsiveness and oxidative stress in asthmatic mice. *Antioxidants (Basel)* 2020;9.
- [22] Huang WC, Chan CC, Wu SJ, Chen LC, Shen JJ, Kuo ML, et al. Matrine attenuates allergic airway inflammation and eosinophil infiltration by suppressing eotaxin and Th2 cytokine production in asthmatic mice. *J Ethnopharmacol* 2014;151:470–7.
- [23] Liou CJ, Cheng CY, Yeh KW, Wu YH, Huang WC. Protective effects of casticin from *Vitex trifolia* alleviate eosinophilic airway inflammation and oxidative stress in a murine asthma model. *Front Pharmacol* 2018;9:635.
- [24] Liou CJ, Huang WC, Kuo ML, Yang RC, Shen JJ. Long-term oral administration of *Gynostemma pentaphyllum* extract attenuates airway inflammation and Th2 cell activities in ovalbumin-sensitized mice. *Food Chem Toxicol* 2010;48:2592–8.
- [25] Myou S, Leff AR, Myo S, Boetticher E, Tong J, Meliton AY, et al. Blockade of inflammation and airway hyperresponsiveness in immune-sensitized mice by dominant-negative phosphoinositide 3-kinase-TAT. *J Exp Med* 2003;198:1573–82.
- [26] Liou CJ, Huang WC. Dehydroepiandrosterone suppresses eosinophil infiltration and airway hyperresponsiveness via modulation of chemokines and Th2 cytokines in ovalbumin-sensitized mice. *J Clin Immunol* 2011;31:656–65.
- [27] Huang WC, Ting NC, Huang YL, Chen LC, Lin CF, Liou CJ. *Helminthostachys zeylanica* water extract ameliorates airway hyperresponsiveness and eosinophil infiltration by reducing oxidative stress and Th2 cytokine production in a mouse asthma model. *Mediators Inflamm* 2020;2020:1702935.
- [28] Chen W, Balan P, Popovich DG. Review of ginseng anti-diabetic studies. *Molecules* 2019;24.
- [29] Wang X, Chen L, Wang T, Jiang X, Zhang H, Li P, et al. Ginsenoside Rg3 antagonizes adriamycin-induced cardiotoxicity by improving endothelial dysfunction from oxidative stress via upregulating the Nrf2-ARE pathway through the activation of akt. *Phytomedicine* 2015;22:875–84.
- [30] Saeki M, Nishimura T, Kitamura N, Hiroi T, Mori A, Kaminuma O. Potential mechanisms of T cell-mediated and eosinophil-independent bronchial hyperresponsiveness. *Int J Mol Sci* 2019;20:2980.
- [31] Pelaia C, Paoletti G, Puggioni F, Racca F, Pelaia G, Canonica GW, et al. Interleukin-5 in the pathophysiology of severe asthma. *Front Physiol* 2019;10:1514.
- [32] Coleman SL, Kruger MC, Sawyer GM, Hurst RD. Procyanidin A2 modulates IL-4-induced CCL26 production in human alveolar epithelial cells. *Int J Mol Sci* 2016;17:1888.
- [33] Yancey SW, Keene ON, Albers FC, Ortega H, Bates S, Bleeker ER, et al. Biomarkers for severe eosinophilic asthma. *J Allergy Clin Immunol* 2017;140:1509–18.
- [34] Weissler JC. Eosinophilic lung disease. *Am J Med Sci* 2017;354:339–49.
- [35] Kee JY, Hong SH. Ginsenoside Rg3 suppresses mast cell-mediated allergic inflammation via mitogen-activated protein kinase signaling pathway. *J Ginseng Res* 2019;43:282–90.
- [36] Oeser K, Maxeiner J, Symowski C, Stassen M, Voehringer D. T cells are the critical source of IL-4/IL-13 in a mouse model of allergic asthma. *Allergy* 2015;70:1440–9.
- [37] Kim DY, Yang WM. *Panax ginseng* ameliorates airway inflammation in an ovalbumin-sensitized mouse allergic asthma model. *J Ethnopharmacol* 2011;136:230–5.
- [38] Hirahara K, Aoki A, Morimoto Y, Kiuchi M, Okano M, Nakayama T. The immunopathology of lung fibrosis: amphiregulin-producing pathogenic memory T helper-2 cells control the airway fibrotic responses by inducing eosinophils to secrete osteopontin. *Semin Immunopathol* 2019;41:339–48.
- [39] Yang L, Chen PP, Luo M, Shi WL, Hou DS, Gao Y, et al. Inhibitory effects of total ginsenoside on bleomycin-induced pulmonary fibrosis in mice. *Biomed Pharmacother* 2019;114:108851.
- [40] Liu C, Zhang X, Xiang Y, Qu X, Liu H, Tan M, et al. Role of epithelial chemokines in the pathogenesis of airway inflammation in asthma (Review). *Mol Med Rep* 2018;17:6935–41.
- [41] Bush A. Cytokines and chemokines as biomarkers of future asthma. *Front Pediatr* 2019;7:72.



- [42] Antus B. Oxidative stress markers in sputum. *Oxid Med Cell Longev* 2016;2016:2930434.
- [43] Menzel M, Ramu S, Calven J, Olejnicka B, Sverrild A, Porsbjerg C, et al. Oxidative stress attenuates TLR3 responsiveness and impairs anti-viral mechanisms in bronchial epithelial cells from COPD and asthma patients. *Front Immunol* 2019;10:2765.
- [44] Drake MG, Lebold KM, Roth-Carter QR, Pincus AB, Blum ED, Proskocil BJ, et al. Eosinophil and airway nerve interactions in asthma. *J Leukoc Biol* 2018;104: 61–7.



Review

# Functionalized Reduced Graphene Oxide as a Versatile Tool for Cancer Therapy

Banendu Sunder Dash <sup>1</sup>, Gils Jose <sup>1</sup> , Yu-Jen Lu <sup>2</sup> and Jyh-Ping Chen <sup>1,3,4,5,\*</sup>

- <sup>1</sup> Department of Chemical and Materials Engineering, Chang Gung University, Kwei-San, Taoyuan 33302, Taiwan; banendusunder@gmail.com (B.S.D.); gilsjose84@gmail.com (G.J.)  
<sup>2</sup> Department of Neurosurgery, Chang Gung Memorial Hospital, Linkou, Kwei-San, Taoyuan 33305, Taiwan; luyj@cgmh.org.tw  
<sup>3</sup> Department of Plastic and Reconstructive Surgery and Craniofacial Research Center, Chang Gung Memorial Hospital, Linkou, Kwei-San, Taoyuan 33305, Taiwan  
<sup>4</sup> Research Center for Food and Cosmetic Safety, Research Center for Chinese Herbal Medicine, College of Human Ecology, Chang Gung University of Science and Technology, Taoyuan 33305, Taiwan  
<sup>5</sup> Department of Materials Engineering, Ming Chi University of Technology, Tai-Shan, New Taipei City 24301, Taiwan  
\* Correspondence: jpchen@mail.cgu.edu.tw; Tel.: +886-3-2118800

**Abstract:** Cancer is one of the deadliest diseases in human history with extremely poor prognosis. Although many traditional therapeutic modalities—such as surgery, chemotherapy, and radiation therapy—have proved to be successful in inhibiting the growth of tumor cells, their side effects may vastly limited the actual benefits and patient acceptance. In this context, a nanomedicine approach for cancer therapy using functionalized nanomaterial has been gaining ground recently. Considering the ability to carry various anticancer drugs and to act as a photothermal agent, the use of carbon-based nanomaterials for cancer therapy has advanced rapidly. Within those nanomaterials, reduced graphene oxide (rGO), a graphene family 2D carbon nanomaterial, emerged as a good candidate for cancer photothermal therapy due to its excellent photothermal conversion in the near infrared range, large specific surface area for drug loading, as well as functional groups for functionalization with molecules such as photosensitizers, siRNA, ligands, etc. By unique design, multifunctional nanosystems could be designed based on rGO, which are endowed with promising temperature/pH-dependent drug/gene delivery abilities for multimodal cancer therapy. This could be further augmented by additional advantages offered by functionalized rGO, such as high biocompatibility, targeted delivery, and enhanced photothermal effects. Herewith, we first provide an overview of the most effective reducing agents for rGO synthesis via chemical reduction. This was followed by in-depth review of application of functionalized rGO in different cancer treatment modalities such as chemotherapy, photothermal therapy and/or photodynamic therapy, gene therapy, chemotherapy/phototherapy, and photothermal/immunotherapy.

**Keywords:** reduced graphene oxide; chemotherapy; photothermal therapy; photodynamic therapy; gene therapy; immunotherapy



**Citation:** Dash, B.S.; Jose, G.; Lu, Y.-J.; Chen, J.-P. Functionalized Reduced Graphene Oxide as a Versatile Tool for Cancer Therapy. *Int. J. Mol. Sci.* **2021**, *22*, 2989. <https://doi.org/10.3390/ijms22062989>

Academic Editor: Ana María Díez-Pascual

Received: 1 February 2021  
Accepted: 11 March 2021  
Published: 15 March 2021

**Publisher's Note:** MDPI stays neutral with regard to jurisdictional claims in published maps and institutional affiliations.



**Copyright:** © 2021 by the authors. Licensee MDPI, Basel, Switzerland. This article is an open access article distributed under the terms and conditions of the Creative Commons Attribution (CC BY) license (<https://creativecommons.org/licenses/by/4.0/>).

## 1. Introduction

Cancer, unrestrained cell growth in the human body, has severely threatened human health worldwide due to its incurability and high death rate [1]. Although reasons for this fatal disease are uncountable, the mechanism of cancer development is associated with the failure of a body's normal control mechanism, which results in the abnormal proliferation of new cells [2]. Owing to the severity of this disease, researchers and medical professionals have made huge contributions in advancing various treatment modalities—including surgery, chemotherapy, and radiation therapy—for saving human life [3,4]. Although conventional drug delivery systems and treatment approaches have provided some treatment

efficacy, its effectiveness is limited by various factors, including multi-drug resistance, rapid metabolism and elimination of drugs, non-specific cytotoxicity, etc. [5–7].

Considering the drawbacks of conventional therapies, introduction of nanomaterials in biomedical research has provided a revolutionary application of biomaterials in cancer therapy [8]. Indeed, due to their unique properties, nanomaterials have gained increasing attention for new and innovative use in biomedical research, particularly as nanocarriers for delivery of therapeutic drugs in cancer therapy [9]. To date, a wide variety of nanocarriers—including liposomes, micelles, peptides, and inorganic particles—are being explored as nanovehicles for delivery of cancer therapeutics [10–18]. Among these, carbon-based nanomaterials in the graphene family have gained particular attention due to their effectiveness and versatility for cancer treatment [19–22]. The carbon-based nanomaterials have essential structural and surface features for loading and pH-sensitive release of aromatic anticancer drugs [23]. Considering certain limitations associated with other materials, these nanomaterials attracted tremendous attention for delivery of cancer therapeutics not only due to their unique physico-chemical properties such as high surface area for drug loading [24], but also due to preferred biological properties such as endosomal escape after intracellular uptake for gene delivery and gene therapy [25,26].

The lateral dimensions and thickness of graphene family nanomaterials, such as graphene oxide (GO), reduced graphene oxide (rGO), graphene quantum dots, and graphene nanoribbons can be fine-tuned from original two-dimensional (2D) structure into zero-, one-, or three-dimensional assemblies [27], which provide improved accumulation as drug vehicles and contrast agents at specific target sites [28]. Such unique and tunable features have promised their new applications in drug delivery [29]. Nonetheless, the promise that these nanomaterials have shown in nanomedicine is not only limited to drug delivery, but also in highly sensitive biosensors and high throughput bioassays, as well as scaffolds for tissue engineering [30].

Similar to GO, rGO is a 2D nanomaterial in graphene family with a single-atom-thick layer of sp<sup>2</sup> hybridized carbon atoms arranged in a honeycomb lattice structure, which is obtained by reducing GO through chemical, thermal, or electrical methods to eliminate the oxygen-containing functional groups on the surface. Owing to the unique surface property and presence of functional groups, functionalized rGO can accommodate high loading of genes to increase the delivery efficacy of nucleic acid therapeutics in gene therapy. The high surface area also enables the loading of abundant hydrophobic aromatic anticancer drugs for chemotherapy or photosensitizers for photodynamic therapy (PDT) via  $\pi$ – $\pi$  interaction [31]. Besides being excellent photo-absorbers with high light absorption ability in the near infrared (NIR) range, rGO is associated with pronounced photothermal effect compared with GO, rendering potential applications in cancer photothermal therapy (PTT) [32]. Indeed, with its facile synthesis, high water dispersibility, easy surface functionalization, and good biocompatibility, rGO has emerged as an excellent multifunctional nanomaterial for PTT [33]. After combining this unique characteristic with the high loading capacity of anticancer drugs, rGO reveals itself as a promising nanomaterial for chemo-photothermal therapy [34]. Surface functionalization with multiple therapeutic moieties or conjugation with targeting ligands on rGO surface further permit its use in targeted synergistic cancer therapy such as chemo-phototherapy and photothermal/immunotherapy.

## 2. Preparation of Reduced Graphene Oxide (rGO) by Chemical Reduction

The typical methods for preparation of rGO involve reducing GO by thermal, chemical or electrical methods. Among them, the chemical reduction method that deoxygenates GO with a reducing agent prevails over other non-chemical routes for rGO synthesis, which can produce stable dispersions of rGO with improved quality. Herein, we review the most effective chemical reagents that can act as a direct or indirect reducing agent to convert oxygenated graphene (GO) into rGO (Figure 1). The characteristics of as-produced rGO and its applications are summarized in Table 1.

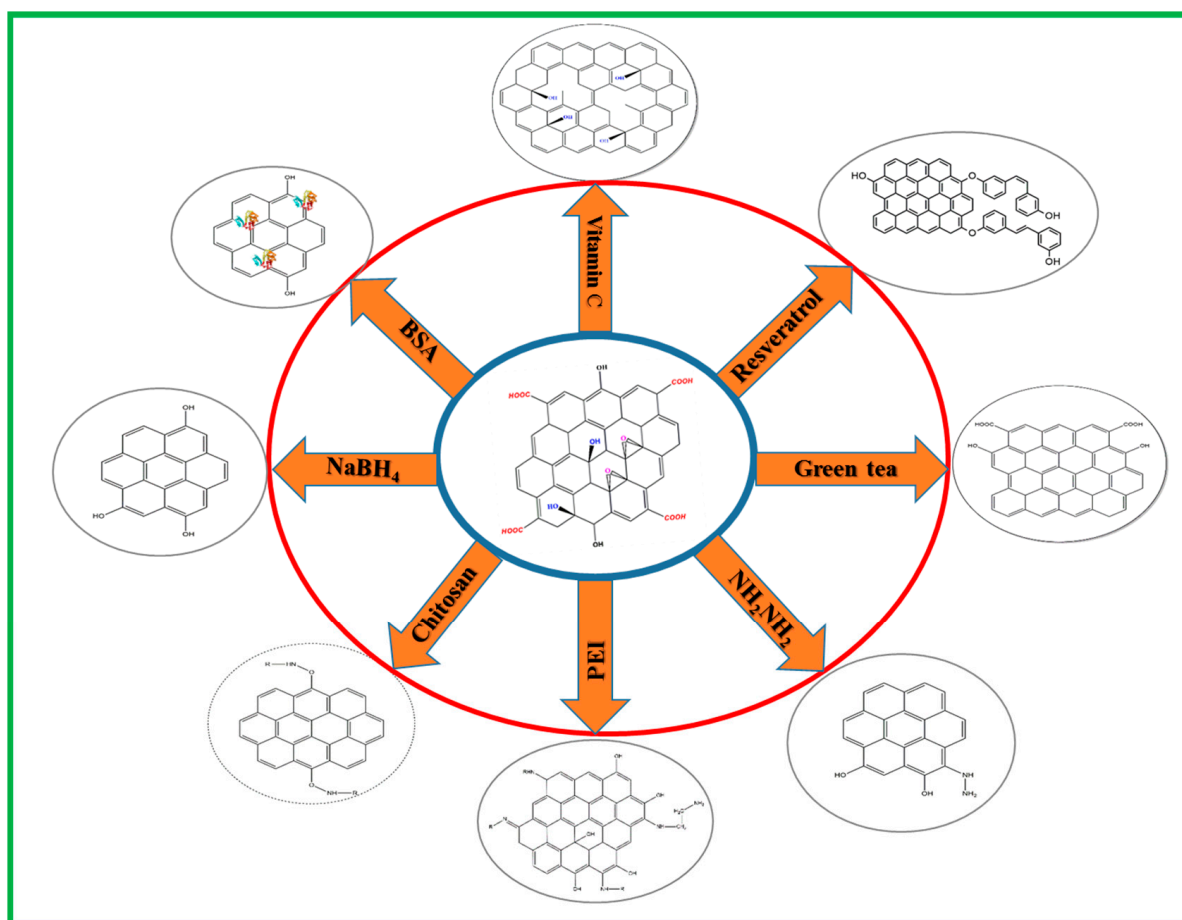


**Figure 1.** Schematic diagram illustrating the preparation of rGO from GO using different chemical reducing agents. BSA, bovine serum albumin; PEI, polyethyleneimine.

It should be noted that although different synthesis routes were reported for rGO synthesis, chemical reduction is widely accepted as the most promising method for large-scale production of rGO. However, considering the toxicity of many chemical reducing agents, biomedical application of rGO prefers non-toxic green chemicals for the reduction process, which could provide stability, non-toxicity, and functionality to resulting rGO products. However, as various kinds of rGO synthesized via different routes have been used successfully for cancer therapy, there is still no definite answer regarding which synthesis route could produce the most effective rGO product for application in cancer therapy.

### 2.1. Vitamin C

Vitamin C (L-hexuronic acid or L-ascorbic acid) is a mild reducing chemical widely used as a reducing agent for GO due to its non-toxicity. It is considered as one of the suitable choices for reducing GOs, not only because it produces highly reduced GO nanosheet suspended in water or in hydrogels at room temperature or mild temperatures, but also because it produces an environmentally friendly by-product, dehydroascorbic acid, after the reaction [35,36]. The chemical reduction of GO by vitamin C has been described in many reports and most of them describing simple mixing of GO with vitamin C using a magnetic stirrer at 60–70 °C and react for 30 min to 2 h. The reduction of GO to rGO is confirmed by color change from brown to black [37–39]. A stable suspension of highly reduced GO could be produced using vitamin C in aqueous solution as well as in organic solvent such as dimethylformamide and N-methyl-2-pyrrolidone. Moreover, as vitamin C is composed of carbon, oxygen, and hydrogen, the possibility of introducing heteroatoms to rGO could be avoided.



## 2.2. Hydrazine Hydrate

Hydrazine ( $\text{N}_2\text{H}_4$ ) or hydrazine hydrate ( $\text{N}_2\text{H}_4 \cdot \text{H}_2\text{O}$ ) is one of the most widely used reductants for rGO synthesis in large scale. Nonetheless, considering the explosive and toxic nature of hydrazine hydrate, the reduction of GO using this reducing agent should be performed with care [40]. Literature describes the reduction process by mixing dispersion of GO with hydrazine hydrate and ammonia solution with a weight ratio of hydrazine to GO at 7:10. After being vigorously shaken or stirred for a few minutes, the reaction was carried out in a water bath at  $96^\circ\text{C}$  for 1 h. Once the reduction is complete, excess hydrazine must be removed by dialysis against 0.5% ammonia solution [41]. In another study, GO was reduced by hydrazine hydrate in the presence of poly(sodium 4-styrenesulfonate) (PSS) to produce stable PSS-coated rGO nanosheet in aqueous dispersion [42]. Treatment of GO (5 mL, 0.5 mg/mL) with hydrazine (0.50 mL, 32.1 mM) at  $100^\circ\text{C}$  for 24 h is another way of reducing GO [43]. There are some other studies that used  $80^\circ\text{C}$  for reaction, where aqueous solution of GO was stirred and sonicated for at least 1 h before reacting with hydrazine hydrate (weight ratio of hydrazine hydrate to GO = 1:1) with continuous stirring and sonication [44]. All studies confirm that hydrazine is a good reducing agent for producing rGO.

## 2.3. Resveratrol

Resveratrol is polyphenol compound used both as a reducing agent and a stabilizer. Resveratrol-guided reduction of GO could provide better biocompatibility, solubility, and selectivity compared to many other reducing agents. The reduction process involves addition of 50  $\mu\text{M}$  resveratrol into GO (1 mg/mL), which was sonicated for 15 min beforehand, and reacted at  $40^\circ\text{C}$  for 1 h. This was continued by cooling and sonication for 15 min, followed by continuous stirring for 1 h at  $90^\circ\text{C}$ . After centrifugation and washing in distilled water, prepared rGO could be recovered from the solution [45].

## 2.4. Chitosan

Chitosan, a biocompatible and biodegradable polysaccharide derived from incomplete deacetylation of chitin, serves as a reducing agent in the synthesis of many nanoparticles [46,47]. Suspension of rGO in aqueous solution has been prepared by chemical reduction of GO at room temperature in the presence of chitosan. To perform the synthesis, a 1:1(w/w) mixture of GO and chitosan were heated at  $37^\circ\text{C}$  for 72 h under constant stirring. Followed by this, excess chitosan in the solution was removed by centrifugation at 8000 rpm for 1 h and subsequently washed with 2% acetic acid solution. The rGO was dispersed in distilled water by sonication [48,49]. Due to the higher biocompatibility, chitosan-based reduction can enhance the potential biological and medicinal applications of rGO.

## 2.5. Polyethyleneimine (PEI)

Polyethyleneimine (PEI) is a widely used reducing agent and surface modifier in the fabrication of rGO [50], which is a water soluble cationic polymer containing primary, secondary, and tertiary amino groups. To reduce GO, 60 mL of GO (0.1 mg/mL) dispersion and PEI solution was mixed under vigorous stirring at  $80^\circ\text{C}$  for 2 h. The transformation of yellowish-brown to black dispersion indicates the successful transformation of GO to rGO. The mixture was then centrifuged and washed with water for recovery of PEI-rGO [50–52]. The incorporation of PEI molecule into GO can act as a source of carbon and produce rGO in a one-step hydrothermal process.

## 2.6. Sodium Borohydride

Sodium borohydride ( $\text{NaBH}_4$ ) is considered as one of the efficient, nontoxic, noncorrosive, inexpensive reducing agents available for reduction of GO.  $\text{NaBH}_4$  has been frequently used as a reducing agent for aldehydes and ketones to produce alcohols. For synthesizing rGO from GO, a GO suspension (0.5 mg/mL) was mixed with  $\text{NaBH}_4$  as well as  $\text{CaCl}_2$  and

stirred for 12 h at room temperature [53]. In another study, the reduction of GO by NaBH<sub>4</sub> was carried out at different temperatures, showing the highest extent of reduction when the reaction was conducted at 80 °C [54].

## 2.7. Bovine Serum Albumin (BSA)

Bovine serum albumin (BSA) is an affordable protein with high biocompatibility, which can act as a reductant and a stabilizer of GO due to the presence of the amino acid tyrosine (Tyr) within it [55,56]. The reduction of GO was carried out by reacting 1 mg/mL GO solution with 50 mg/mL BSA at 70 °C. After the solution pH was brought up to 12 with 1 M NaOH, the mixture was stirred at 50 °C for 24 h to observe a transition of solution color from light brown (GO) to dark black (rGO) [57]. Excess BSA was removed by centrifugal filtration with a 150 kD molecular-weight-cut-off (MWCO) membrane to obtain purified rGO/BSA hybrids suspended in water and stored at 4 °C [57,58].

**Table 1.** Reducing agents for producing reduced graphene oxide (rGO) from graphene oxide (GO).

| Reducing Agent       | Characterisitics  | Applications   | Reference |
|----------------------|---|--|-----------|
| Vitamin C            | Natural compound; non-toxic; mild reaction temperature; environment friendly byproducts; avoid introducing heteroatoms; reaction in aqueous or organic solution | Embedded in chitosan hydrogel for bone tissue engineering; functionalized with antimicrobial peptide for antibacterial activity  | [37–39]   |
| Hydrazine hydrate    | Explosive; toxic; large scale production; low cost  | Improve electrical conductivity; embedded in polyacrylic acid nanofiber mats for controlled release of antibiotics   | [41–44]   |
| Resveratrol          | Natural phenolic compound; anti-oxidant; stabilizer; biocompatibility; solubility; green synthesis  | Produce marked changes in cellular morphology and reduce cell viability of cancer cells for cancer therapy   | [45]      |
| Chitosan             | Biocompatible; biodegradable; reduction at body temperature; biological and medicinal applications  | Reversible change of dispersion/aggregation state with pH; pH-sensitive release of drug; loading with drug and photosensitizer for cancer chemotherapy/phototherapy    | [48,49]   |
| Polyethylenimine     | Surface modifier; one-step hydrothermal reduction; high cargo loading; prevent agglomeration  | Improved gas barrier property in composite films; in hemin-bovine serum albumin composite as peroxidase mimetics; gene delivery; increase strength of nylon composites | [50–52]   |
| Sodium borohydride   | Efficient; ambient conditions; reaction in aqueous solution   | Decrease electrical resistance; enhance electrical conductivity  | [53,54]   |
| Bovine serum albumin | Biocompatible; stabilizer; binding by adhesion to surface; metal particle-binding platform; cell adhesive   | For cancer chemo-photothermal therapy; adsorption and assembly of metal particles; create protein–metal nanocluster for detecting trypsin                              | [57,58]   |
| Gree tea polyphenols | Biocompatible, biodegradable; green synthesis; good dispersion in both aqueous and organic solutions; non-toxic   | Enhance thermal conductivity in chitosan polymer composites; deposit onto electrode for detection of sunset yellow in foods; reduce cytotoxicity of GO                 | [59–61]   |

### 2.8. Green Tea Polyphenols

Considering the harmful and hazardous natures of many commercial chemical reducing agents, researchers have focused on green methods for the production of rGO by chemical reduction. As a result, green tea extract is considered as a good option considering its easy availability, eco-friendly characteristics, and cheap price. Green tea is rich in polyphenolic compounds, with epigallocatechin gallate (EGCG) making up about 50–60% of total tea polyphenols. To reduce GO, green tea powder (2 g) was added to 100 mL of deionized water and boiled at 100 °C for 20 min, and then filtered. The GO (50 mg) was added to the green tea solution and sonicated for 30 min, followed by reflux at 90 °C under nitrogen atmosphere. After that, the solution was washed with water to remove excess green tea powder [59]. Alternatively, 10 mL green tea extract was added dropwise to 20 mL of GO aqueous suspension (0.5 mg/mL) within 45 min and the mixture was refluxed at 60 °C for 6 h before precipitation of rGO out of the solution [60,61].

## 3. Application of Reduced Graphene Oxide (rGO) in Cancer Therapy

rGO-based nanocomposite has emerged as a promising nanomaterial in nanomedicine. Most recent cytotoxicity studies indicate that surface functionalization of rGO could lead to enhanced biocompatibility as well as increased stability in physiological buffers. Therefore, the use of rGO-based nanomaterials for targeted pH-responsive drug delivery may overcome current challenges and provide new treatment modality in cancer therapy. Nonetheless, other than cytotoxicity study, the distribution and excretion of rGO-based nanomaterials is of paramount importance before clinical translation. The first hurdle that rGO-based cancer therapeutics faces will be the reticuloendothelial system (RES) after intravenous delivery. Overall, nanoparticles with a particle size of ~100 nm are expected to have prolonged circulating half-lives, which should be the preferred size of rGO-based nanocomposites. After escaping the RES, circulating rGO can exit tumor blood vessels and accumulate in cancerous interstitium due to the leaky tumor blood vessels by the enhanced permeation and retention (EPR) effect. For rGO-based nanomaterials to extravasate the vasculature, they should preferably possess neutral or negative charge and be within 10–100 nm in size. Indeed, nanomaterials coated with biocompatible moieties with size smaller than 100 nm are believed to be cleared from the body without noticeable toxicity after systemic administration. Even though the EPR effect may increase accumulation at the tumor site, improving the active targeting ability of rGO-based nanocomposites or using administration route other than intravenous injection should be studied. A systematic study of the biological behavior of injected rGO in vivo—such as stability, biodistribution, secretion, etc.—should be attempted for better clinical use. Furthermore, the functionalization of rGO may be difficult in large scale, which might limit the application of functionalized rGO in cancer therapy from bench to bedside.

rGO is widely accepted for application in single mode cancer therapy such as chemotherapy, photothermal therapy (PTT), photodynamic therapy (PDT), and gene therapy as well as in dual mode cancer therapy including chemotherapy/phototherapy and photothermal therapy/immunotherapy. A schematic diagram illustrating the mechanisms involved is depicted in Figure 2. In this section, we categorize most up-to-date studies using functionalized rGO-based nanocarriers in cancer therapy into several sections based on the treatment modality involved. A summary of rGO-based nanocarriers, the agents used for functionalizing rGO, cancer cell lines used in the study and the type of study is provided in Table 2.

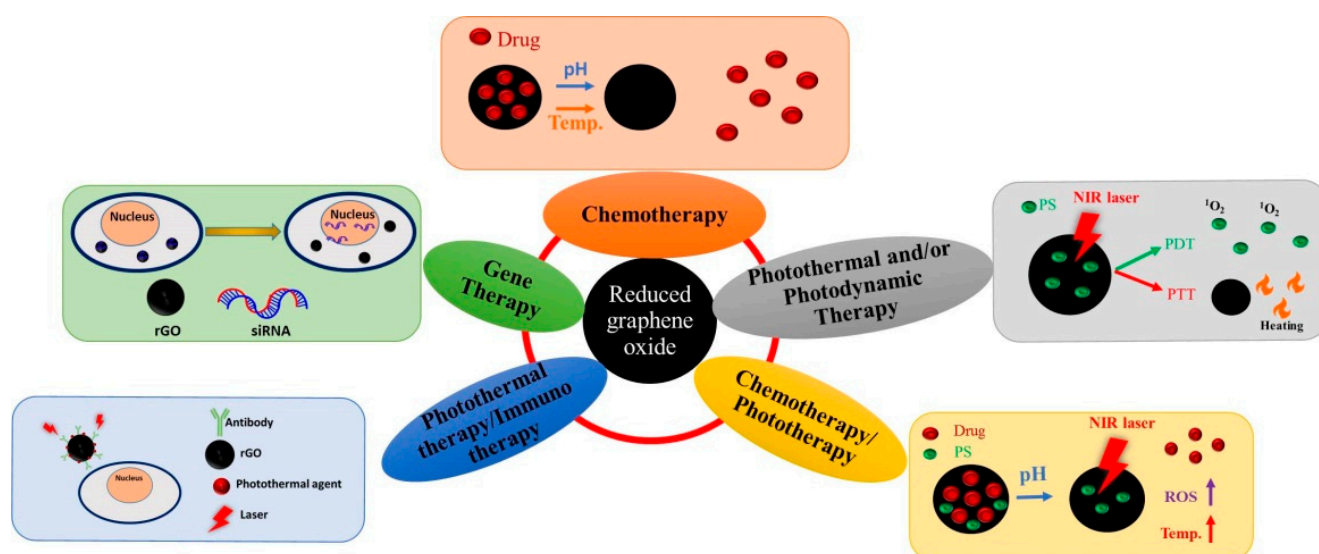


**Figure 2.** Applications of reduced graphene oxide (rGO) in cancer therapy.

### 3.1. Chemotherapy

The chemotherapy that cures malignancy by means of chemical drugs has gained worldwide acceptance due to its capability to block cell proliferation and to cause cell apoptosis [62]. The chemotherapeutic drugs like doxorubicin (DOX), cisplatin, paclitaxel (PTX), mitoxantrone (MTX), and 5-fluorouracil (5-FU) have been proved to inhibit growth rates of different cancer cells and to limit their metabolic functions. However, the associated unwanted complications with these drugs due to their cytotoxicity towards normal/healthy cells have limited the application of chemotherapy in cancer therapy. Hence, nanocarrier-based drug delivery system was introduced as an effective approach to alleviate this limitation, with the aim to deliver chemotherapeutic drugs with minimum side effects. Indeed, many nanomaterials—such as polymeric nanoparticles, liposomes, micelles, and metal nanoparticles—have been employed for this purpose to deliver different chemotherapeutic drugs due to their unique characteristics unattainable through free drug administration. Recently, researchers are turning to development of rGO-based drug delivery platforms for carrying large amount of chemotherapeutic drugs with large surface area, as well as the pH-responsive drug release behavior offered by rGO.

Ma and co-workers used a green approach to convert GO to rGO using riboflavin as a reducing agent and the resulting riboflavin-rGO nanocarrier was used for DOX loading through  $\pi$ - $\pi$  interaction [63]. The results suggested that rGO exhibits high DOX loading, good stability, and pH-sensitive sustained drug release, which is evident from the effective cytotoxicity against MCF-7 and A549 cancer cells in vitro [64]. In another study, Wei et al. used rGO-C<sub>6</sub>H<sub>4</sub>-COOH for DOX loading, followed by modifying with PEI to enhance water solubility and conjugating with folic acid (FA) for targeted drug delivery. Due to specific targeting of FA to CBRH7919 cancer cells as well as pH-responsive drug release after endocytosis, the conjugation of DOX with rGO-PEI-FA could arrest cancer cells in the G2 phase and lead to cell apoptosis. There are plenty of other examples for rGO-based targeted delivery of DOX. Daysi et al. also used FA-functionalized nanocomposite consisting of chemically-reduced rGO and manganese-doped zinc sulfide quantum dots (FA-rGO/ZnS:Mn) for targeted delivery of DOX [65]. The dispersion stability, DOX loading and release efficiency, internalization, and biocompatibility of FA-rGO/ZnS:Mn resulted in excellent anti-cancer efficiency against breast cancer cells. Moreover, FA functionalization improved the selectivity of this drug delivery platform for specific targeting of folate receptor molecules overexpressed on cancer cell surface. Taken together, the FA-rGO/ZnS:Mn was suggested to be an excellent theranostic nanocomposite for breast cancer treatment. Similarly, Miao et al. explained the application of DOX-loaded cholesteryl hyaluronic



acid (CHA)-coated rGO nanosheets (CHA-rGO) for the treatment of CD44-overexpressing tumors [66]. As a primary ligand of CD44, HA increases the stability and safety of rGO by enhancing the tumor-targeted distribution of DOX to CD44-overexpressing cancer cells, thereby providing better drug accumulation and substantial reduction of tumor volume from in vivo study in nude mice. He and co-workers used rGO capped by alkyl-grafted mesoporous silica (MSN-C<sub>18</sub>) as a carrier of DOX for chemotherapy [67]. The in vitro cell viability assay performed using SMMC-7721 cancer cells showed enhanced DOX release upon near NIR light exposure, which led to higher cytotoxicity toward cancer cells, indicating its potential use as a nanocarrier for controlled drug release.

The application of rGO in chemotherapy is not only limited to targeted delivery of DOX, as other drugs or natural compounds with anti-cancer activity were reported to be delivered through rGO. Chen et al. used methoxypolyethylene glycol amine (mPEG-NH<sub>2</sub>) for one-step green reduction and PEGylation of GO to synthesize rGO/PEG [68]. The rGO/PEG showed excellent water stability and two-fold increase of resveratrol loading over GO/PEG via hydrophobic interactions and  $\pi$ - $\pi$  stacking. From in vitro experiments, NIR laser irradiation (808 nm) could enhance resveratrol release from rGO/PEG to increase the cytotoxicity against 4T1 murine breast cancer cells by lowering cell viability and inducing cell apoptosis. In animal models with subcutaneously implanted cancer cells, resveratrol-loaded rGO/PEG injected intratumorally to tumor-bearing nude mice also significantly suppress tumor growth under photothermally controlled drug delivery. In another study, rGO synthesized through reduction by *Euphorbia milii* plant extract was used as a carrier of the chemotherapeutic drug paclitaxel for cancer treatment [69]. The drug-loaded rGO showed high cytotoxicity toward human lung cancer cell line (A549) for potential chemotherapy of lung carcinoma.

The chemotherapy using dual drugs may be a better approach to kill cancer cells in the metastatic stage as the synergistic effect offered by dual drugs may introduce more anti-proliferative effect to cause cancer cell death. Muthoosamy et al. developed amphiphilic polymer PF-127 functionalized rGO for co-loading of anti-cancer drugs paclitaxel and curcumin on the surface through  $\pi$ - $\pi$  interactions [70]. The drug-loaded composite showed synergistic anti-tumor efficacy towards both A549 lung cancer cells and MDA-MB-231 breast cancer cells. However, loading of an aromatic hydrophobic drug like paclitaxel on the surface of a hydrophobic carrier like rGO by  $\pi$ - $\pi$  stacking and hydrophobic-hydrophobic interactions is challenging as hydrophobic carriers are not stable in physiological solutions. To address this problem, Hashemi et al. introduced a rGO-based nanocarrier with high paclitaxel loading capacity through functionalization and stabilization with R9 peptides, where pristine rGO sheets were found to be unstable in aqueous solutions and aggregated to decrease the surface area available for drug loading [71]. In a different study, Dhanavel et al. developed dual drug-encapsulated chitosan/rGO nanocomposite by entrapping 5-fluorouracil (5-FU) and curcumin in chitosan/sodium tripolyphosphate gel in the presence of rGO nanosheet for dual drug delivery to HT-29 colon cancer cells [72]. The synergistic cytotoxicity was observed for dual drug-loaded nanocomposite to inhibit the growth of HT-29 colon cancer cells compared with single drug therapy.

Considering the biological aspects, researchers have developed composites of rGO with nanoparticles or polymers for cancer treatment. Among these, combination of rGO with gold (Au) nanoparticle has gained considerable attention. In one study, Sanad et al. prepared rGO-gold nanocomposites (rGO-Au) by incorporating Au nanoparticles inside the rGO matrix through in situ reduction with sodium borohydride, followed by loading 5-FU by pore capping [73]. The results obtained from cytotoxicity assay determined by the reduced half maximal inhibitory concentration (IC<sub>50</sub>) using MTT assay in addition to enhanced cell apoptosis from flow cytometry analysis suggested the nanocomposite can enhance targeted delivery of 5-FU as well as cytotoxicity to MCF-7 breast cancer cells. In a similar study, Jafarizad et al. prepared Au nanoparticle-loaded rGO as a covalent drug delivery system for pH-dependent release of mitoxantrone (MTX) [74]. For polymer coating, Ryu and co-workers prepared PEI-rGO nanocarrier for pH-responsive delivery of

DOX to HeLa and A549 cancer cell lines [75]. The drug-loaded nanocomposite was further coated with pH-responsive charge-conversional polymer polyethyleneimine-poly-L-lysine-poly-L-glutamic acid (PKE) to endow charge-conversional property and serum stability to PEI-rGO-based drug delivery system. They found that DOX-loaded PEI-rGO after PKE coating released more DOX under low pH lysosomal condition and showed enhanced anticancer activity in HeLa and A549 cancer cells. Considering the side effects associated with chemotherapy, SreeHarsha et al. prepared hybrid nanoparticle by coating rGO with chitosan and stabilized with tripolyphosphate to produce stabilized nanocomposite for delivery of DOX to PC-3 cancer cells [76]. The sustained DOX release observed under photothermal conditions endowed this nanocarrier with improved efficacy in treating prostate cancer.

### 3.2. Photothermal Therapy (PTT) and/or Photodynamic Therapy (PDT)

Photothermal therapy (PTT) involves local temperature rise after exposing a photothermal agent to electromagnetic radiation such as visible or NIR light, which up converting light energy into heat, can induce death of cancer cells [77]. Many nanomaterials are effective photothermal agents in causing cancer cell apoptosis/necrosis with local hyperthermia from NIR laser exposure [78]. Graphene-based materials are good photothermal agents used for PTT considering its multifunctionality [79]. Moreover, the combination of graphene-based materials with inorganic particles, like iron oxide and gold nanoparticles, can further enhance the photothermal effect and lead to higher cancer cell death rate during PTT [80–83]. On the other hand, photodynamic therapy (PDT) is another form of phototherapy involving light and a photosensitizer (PS), which when used together with oxygen, can produce molecular oxygen or reactive oxygen species to elicit cancer cell death [84,85]. In one study, GO was found to act both as a photothermal agent for PTT and a photosensitizer for PDT, making it an excellent candidate for synergistic phototherapy [86].

Robison et al. pioneered the use of rGO for PTT, who showed nano-sized rGO produced by chemical reduction of GO has six-fold higher NIR absorption rate than GO, endorsing its preferred use over GO as a photothermal agent [87]. The modification with targeting peptide bearing the Arg-Gly-Asp (RGD) motif further provided rGO with selective cellular uptake ability by U87MG glioma cancer cells, indicating rGO is a multi-functional photothermal agent. Their results also provided strong evidence that nano-sized rGO is highly effective as a photothermal agent when compared to other carbon-based nanomaterials as well as inorganic nanoparticles like gold or iron oxide. Similarly, Shim et al. modified rGO with clostridium perfringens enterotoxin peptide-linked chlorin e6 (Ce6) as a dual photodynamic and photothermal cancer therapeutic platform [88]. The intracellular uptake studies performed on U87 glioblastoma cells confirmed the ligand-mediated cellular uptake. The combined therapy using 660 nm light source for the PDT agent (Ce6) and 808 nm for rGO showed enhanced targeted dual phototherapy. In another study, He and co-workers synthesised palladium nanoflowers-decorated rGO (rGO/PdNFs) and explored its versatile applications in catalysts, sensor, and PTT [89]. The modification of rGO with PdNFs increased its photothermal conversion due to enhanced absorption in the NIR window. Both in vitro study using HeLa cells and in vivo animal experiments performed in tumor-bearing mice model indicates rGO/PdNFs could result in effective photothermal antitumor efficacy. The study using alanine-grafted rGO as a photothermal platform for cancer therapy confirmed that PTT using 808 nm laser irradiation produced 89% and 33% higher photothermal effect compared to GO and rGO, respectively. The conjugation of alanine to GO via  $\pi$ - $\pi$  interactions reduced GO to rGO, not only increased the 808 nm absorbance but also acted as a targeting ligand to kill U87MG cancer cells selectively [90].

The photothermal applications rGO were further explored in combination with other nanoparticles and photosensitizers in synergistic cancer therapy. Otari et al. performed one-step reduction of GO to rGO and decoration of rGO with Au nanoparticles and thermostable antimicrobial nisin peptides to synthesize NAu-rGO [91]. After treating MCF-7

breast cancer cells with the nanocomposite followed by 800-nm diode laser ( $0.5 \text{ W/cm}^2$ ) treatment for 5 min, 80% cell growth inhibition was found. Similarly, Zhang et al. attached polyethylene glycol (PEG) modified Ru (II) complex (Ru-PEG) to rGO surface by hydrophobic  $\pi$ - $\pi$  interaction, and applied the nanocomposite as a photothermal agent and a photosensitizer for PTT/PDT [92]. The A549 lung cancer cells treated with rGO-Ru-PEG and sequentially exposed to of 808 nm (for PTT) and 450 nm (for PDT) wavelength light source resulted in enhanced cytotoxicity due to combined phototherapeutic effects. The rapid reduction in relative tumor volume observed from animal experiments also confirmed the synergistic effect of dual phototherapy.

For localized combination cancer therapy, Chang and co-workers developed rGO/AE/AuNPs hydrogel containing rGO and Au nanoparticles, by using amaranth extract (AE) both as a reducing agent and a precursor, which crosslinked upon 660 nm laser exposure to form a composite hydrogel [93]. Both Au nanoparticles and rGO acted as photothermal agents while the chlorophyll derivatives in AE acted as a photosensitizer to accelerate the generation of cytotoxic singlet oxygen. Upon hydrogel formation on the surface of HeLa cancer cells in situ, the composite hydrogel was used as a combined PTT/PDT platform by repeated irradiation with 808 nm laser in multiple antitumor therapies. In another study, a PTT/PDT reagent was synthesized by conjugating tetrakis(4-carboxyphenyl) porphyrin (TCPP) to rGO-PEI, which was formed based on carboxylic acid functionalized rGO for combination PTT/PDT therapy [94]. The rGO-PEI-TCPP composite showed excellent stability in different biological solutions. The results obtained from studies with CBRH7919 cancer cells indicates induced cell apoptosis upon laser irradiation, due to the combined photothermal and photodynamic effects with the production of heat and singlet oxygen. The increase in temperature upon exposing a photothermal agent to laser light may cause side effects, and hence determining the optimum concentration of PTT agent or performing experiment at lower laser power is important in phototherapy. Jafarirad and team developed a non-invasive strategy for low-level laser induced cancer therapy. The hybrid nanocomposites (ZnO/rGO, Ag-ZnO/rGO, and Nd-ZnO/rGO) synthesized by green synthesis methods were further optimized for concentration in anti-tumor study in vitro using MCF-7 cancer cells [95]. The results confirmed a low concentration ( $12.5 \mu\text{g/mL}$ ) of hybrid together with low irradiation doses ( $8\text{--}32 \text{ J/cm}^2$ ) could lead to higher cell death.

In conventional PDT, the unfavourable bioavailability, low absorption band and limitations in tissue oxygenation are considered as possible limitations. To overcome these limitations, Kapri et al. fabricated a  $\sim 5 \text{ nm}$  thick  $\text{MoS}_2$  nanoplatelet and integrated them with n-type nitrogen doped rGO for PDT [96]. The p- $\text{MoS}_2$ /n-rGO- $\text{MnO}_2$ -PEG composite was prepared by modifying the nanosheet with poly(ethylene glycol) (PEG) to improve biocompatibility and colloidal stability in physiological solution, which was further surface decorated with  $\text{MnO}_2$  to overcome the hypoxic conditions prevalent in tumor microenvironment, by increasing intracellular  $\text{O}_2$  after reaction of  $\text{MnO}_2$  with endogenous  $\text{H}_2\text{O}_2$  in cancer cells. The nanosheet reveals increased apoptosis under NIR light irradiation by alleviating hypoxia and enhances the efficacy of PDT on HeLa cells in vitro. It is difficult to selectively kill cancer cells during PTT as normal cells are also simultaneously affected by the photothermal effect, which is the most common disadvantage associated with phototherapy. To solve this problem, an interesting design based on rGO was demonstrated by synthesizing water dispersible  $\text{Cu}_2\text{O}$  nanocrystal-rGO nanocomposites. In contrast to the highly efficient killing of both normal and cancer cells initiated by the photothermal effect under NIR irradiation, the photocatalytic effect of this nanomaterial results in selective killing of cancer cells in contrast to unselective cell-killing under NIR light [97]. This was demonstrated from the cytotoxicity assay performed on A549, HK-2 and MDA-MB-231 cancer cell lines in vitro.

The efficacy of rGO-based PDT/PTT could be upregulated by conjugating rGO with a ligand molecule to actively targeting cancer cells. Jiang et al. used hyaluronic acid (HA) as a targeting ligand to specifically deliver a photosensitizer Ce6 to CD44 over-expressing cancer cells for PDT with NIR irradiation [98]. The nanoplatform was prepared

by dopamine-reduced rGO sheet and coated with mesoporous silica to load Ce6 as well as HA. The combination of photothermal conversion and controllable Ce6 release after NIR irradiation confers the nanoplatform with enhanced singlet oxygen generation that could lead to more significant destruction of targeted cancer cells. Lima-Sousa and co-workers also functionalized rGO with HA-grafted poly-maleic anhydride-*alt*-1-octadecene (HA-g-PMAO) for targeted PTT [99]. In vitro studies confirmed internalization by CD44 overexpressing MCF-7 cells as an on-demand PTT platform to elicit cancer cell ablation for potential targeted cancer therapy. Taking advantage of the fact that polyphenol compounds in green tea (GT)-reduced rGO can act as targeting ligand, targeted delivery of the nanocomposite resulted in 20% higher photothermal destruction of the high metastatic SW48 cancer cells than that of the low metastatic HT29 cells [100]. Although the exact mechanism is still under investigation, the attachment of polyphenol-modified rGO to cancer cell surface could be confirmed from flow cytometry studies for photothermal destruction of colon cancer cell line at 0.3 mg/mL rGO and 0.25 W/cm<sup>2</sup> NIR laser power density. To use heparin sulphate proteoglycan-3 (GPC3) as a targeting ligand for hepatocellular carcinoma, Liu et al. conjugated biotinylated GPC3 antibody to rGO (rGO-GPC3) and bind avidinylated nanobubbles to rGO-GPC3 using the biotin-avidin bioaffinity system for PTT. Using ultrasound-targeted nanobubble destruction, the local concentration of rGO around HepG2 cell line could be increased for photothermal ablation and PTT of hepatocellular carcinoma under 808 nm NIR irradiation [101].

Indocyanine green (ICG), a NIR dye approved by the U.S. Food and Drug Administration (FDA), can combine with rGO to promote the NIR absorption ability of rGO and enhance the PTT efficacy. A novel nanoagent using ICG-loaded polydopamine (PDA)-reduced graphene oxide nanocomposites (PDA-rGO) was found to be loaded with a large amount of ICG molecules for exhibiting stronger photothermal effect and amplify the PTT efficacy for cancer theranostics [102]. After photoacoustic imaging-guided PTT treatments using 808 nm NIR laser at 0.6 W/cm<sup>2</sup> for 5 min, the tumors in orthotopic 4T1 breast cancer mice model were completely eradicated with no observable treatment toxicity. Also using ICG, Sharker et al. designed a pH-responsive, NIR-sensitive rGO-based nanocomposite (ICG-CPPDN/rGO), by ionic complexation of ICG with CPPDN/rGO, for local destruction of cancer cells with minimal invasiveness to surrounding normal cells [103]. The nanocomposites showed pH-dependent photothermal effect from pH 5.0 to 7.4 due to the pH response relief and quenching effects of ICG on rGO sheet, which leads to photo-thermolysis as the pH was changed from 5.0 to 7.4 in vitro. Due to acidic tumor microenvironment, the nanocomposite showed improved photothermal destruction of MDA-MB-231 cancer cells both in vitro and in vivo compared to free ICG upon local NIR laser treatment.

### 3.3. Gene Therapy

Inhibiting gene expression by promoting site specific cleavage of target messenger RNA, small interfering RNA (siRNA) regulates the expression of genes by RNA interference (RNAi) and represents one of the promising developments in cancer therapy [104]. Considering the limitations of delivery of naked siRNA, which include endosomal escape, rapid excretion, low stability in blood serum, non-specific accumulation in tissues, siRNAs were usually delivered by loading to nanoparticles [105]. The use nanoparticles as nano-vehicles for siRNA delivery also offers the possibility of targeted gene therapy for more effective cancer treatment outcomes [106]. Various nano-sized particulate systems, including silica and silicon-based nanoparticles, metal and metal oxide nanoparticles, carbon nanotube, graphene, dendrimer, polymers, cyclodextrin, liposome, and semiconductor nanocrystals have been developed for systematic delivery of siRNA [107]. The cationic PEI-rGO nanoparticles after reducing and modifying GO with PEI have gained particular attention in rGO-based cancer gene therapy, since PEI is widely used for non-viral transfection and offers advantages over other polycations with high endosomolytic activity and strong DNA compaction ability [108,109].



As low molecular weight PEI was proved to exhibit less cytotoxicity, Chau et al. studied the covalent functionalization of GO with triethyleneglycoldiamine or 800 Da molecular weight PEI via the epoxy ring opening reaction. The data obtained using gel electrophoresis confirmed that PEI-rGO was more efficient in complexing with siRNA to offer higher complexing capacity, making it an excellent candidate for gene silencing applications [110]. In a separate study, rGO was modified with low molecular weight branched polyethyleneimine (BPEI) via polyethylene glycol (PEG) spacer (PEG-BPEI-rGO) as a nano-vehicle for photothermally controlled gene delivery [111,112]. The nanocomposite formed stable nano-sized complex with plasmid DNA to offer high gene transfection efficiency for experiments performed with PC-3 and NIH/3T3 cell lines without significant cytotoxicity. Most importantly, PEG-BPEI-rGO demonstrated enhanced gene transfection efficiency upon NIR irradiation. After investigating with a proton sponge effect inhibitor Bafilomycin A1, the enhancement of gene transfer was found to be associated with accelerated endosomal escape of the nanocomposite, with the photothermal effect of rGO.

### 3.4. Chemotherapy/Phototherapy

As chemotherapy and phototherapy have produced promising outcomes in cancer therapy, researchers started combining these therapeutic modalities for synergistic cancer treatment [113]. Specifically, considering the high loading efficiency of chemotherapeutic drugs and the unique NIR laser-responsive characteristics for PTT/PDT, graphene-based nanomaterials have received attention for chemo-phototherapy [114]. By intravenous delivery of rGO-based nanocomposites, the combination of chemotherapy with phototherapy (PTT and/or PDT) also demonstrated promising anti-cancer efficacy with subcutaneously implanted cancer cells in vivo, as depicted schematically in Figure 3 [115,116].

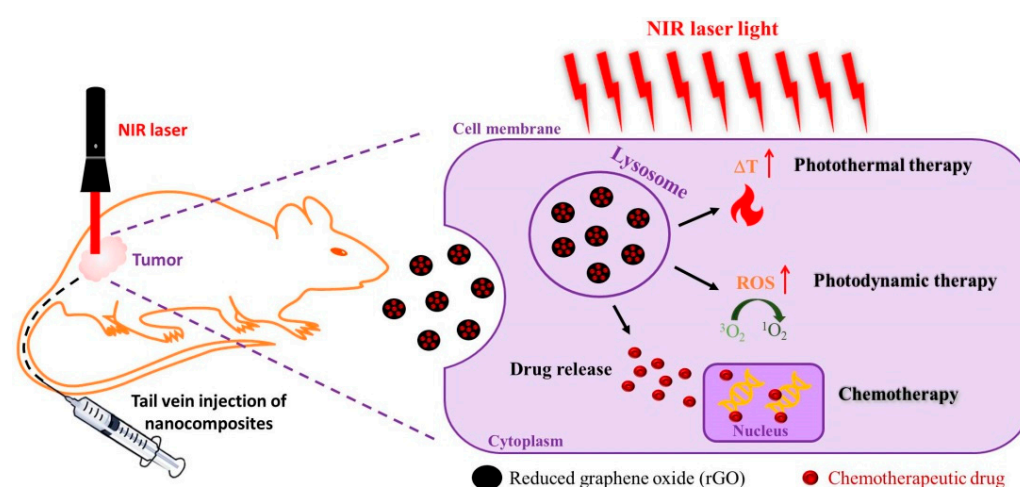


**Figure 3.** A schematic diagram showing the treatment of subcutaneously implanted cancer cells by combined chemotherapy/phototherapy using reduced graphene oxide (rGO).

Oz and co-workers functionalized rGO by surface anchoring maleimide-containing catechol (dopa-MAL) through noncovalent interaction. Using thiol-maleimide chemistry, they modify rGO with cyclic peptide c(RGDfC) as a targeting ligand for targeted delivery of DOX to cancer cells. The *in vitro* studies performed with MDA-MB-231 cell line indicated that DOX loaded rGO/dopa-MAL-c(RGDfC) was more effective than free DOX in killing the cancer cells after exposure to 980 nm laser irradiation ( $2 \text{ W/cm}^2$ ) for 10 min [117]. This was attributed to the enhancement of chemotherapy with PTT from the endocytosed nanocomposite upon NIR laser exposure for targeted synergistic cancer cell killing. Surface functionalization of rGO for enhancing the hydrophilicity is a strategy for effective drug delivery. Hu et al. used folic acid modified dextran-g-octadecanoic acid to decorate rGO surface with hydrophilic dextran moiety through octadecanoic acid hydrophobic anchoring and with folic acid for enhanced intracellular uptake by cancer cells. The nanocomposite

was loaded with anticancer drug DOX for chemotherapy/phototherapy where in vitro analysis performed with HeLa cells at endosomal acidic environment (pH 5.3) confirms increased DOX release upon weakening of noncovalent binding between DOX and rGO. Compared with single mode chemotherapy, the combination of local chemotherapy with external NIR-induced PTT demonstrated dual therapy and offered higher therapeutic efficacy [118]. The study confirmed that by eliciting higher cytotoxicity toward cancer cells through the photothermal response of rGO under NIR irradiation, the concentration of DOX needed for chemotherapy could be significantly reduced to minimize the potential side effect of chemo drugs. Similarly, Hu and co-workers also delivered DOX using dextran-reduced rGO through direct conjugation of dextran on rGO surface by hydrogen bonds. This was followed by self-assembly to form rGO/Dex nanoparticles. After conjugating with RGD peptide for recognition by  $\alpha_v\beta_3$  integrin on cancer cell surface to enhance intracellular uptake, the in vitro chemo-phototherapy performed with external NIR laser on B16F10 cell line resulted in higher anti-cancer efficacy [119].

Considered as one of the most widely used chemotherapeutic drugs, DOX has been loaded to rGO synthesized with various reducing agents. For this purpose, functionalized rGO with bovine serum albumin (BSA) as a reduced agent was used as a carrier of DOX [57]. Brain tumor cells (U87MG) treated with BSA-rGO revealed that combination of photo-chemo treatment enhanced the treatment efficacy as compared to single mode phototherapy using BSA-rGO or DOX (chemotherapy). Similarly, Zaharie-Butucel and team reduced GO using chitosan to combine PTT and PDT, followed by using chitosan-rGO as a carrier for DOX in synergetic therapy of colon cancer [49]. Targeted delivery of DOX using polydopamine-functionalized rGO (pRGO) is another example in this category [120]. pRGO modified with CD44 targeting ligand hyaluronic acid (HA) was used in combination with DOX-loaded mesoporous silica (MS) (pRGO@MS-HA) to generate both pH and NIR-triggered DOX release from the multifunctional nanosystems, showing excellent combined effect in multimodal cancer therapy. In another example, Hao et al. used tea polyphenol to produce rGO as a nanocarrier for delivery of DOX [121]. After exposure to 808 nm NIR laser irradiation at 3 W/cm<sup>2</sup> for 5 min, combined chemo-PTT can enhance cytotoxicity of DOX toward human tongue squamous cancer cells, CAL27.

To improve photothermal properties, Ma et al. added gold (Au) clusters to rGO surface by electrostatic interaction. Afterward, rGO was functionalized with 3-(3-phenylureido) propanoic acid–polyethylene glycol (PPEG) via  $\pi$ – $\pi$  bond interaction for improving the biocompatibility. Using DOX for chemotherapy, rGO/Au/PPEG elicited effective phototherapy/chemotherapy effect on HeLa cell line [122]. In a separate study, Yang et al. introduced Au nanorods as well as hydroxyapatite to rGO surface (RGO/AuNR/HA) for delivery of the anticancer drug 5-fluorouracil (5-FU). The nanocomposite was designed for synergistic dual therapy, in which hydroxyapatite was used to enhance 5-FU loading, while RGO and Au nanorods (AuNR) offer enhanced photothermal effect under NIR laser irradiation [123]. Due to sequential drug release with the pH-sensitive drug release behavior of hydroxyapatite in the first stage and photothermal conversion from RGO/AuNR after NIR laser irradiation in the second stage, the designed nanocomposite exhibits greater antitumor activity from the chemo-photo effect. A hybrid with ultra-small plasmonic gold nanorods vesicles (rGO-AuNRVe) loaded on the surface of rGO was shown to be endowed with amplified photothermal effect. This hybrid could provide a high loading capacity of DOX, provided by the cavity of the vesicle and the large surface area of rGO. Furthermore, the release of DOX was sequential with DOX release first from the vesicular cavity under NIR photothermal heating and followed by release from rGO surface induced by the intracellular acidic environment [124]. Intravenous injection of rGO-AuNRVe-DOX followed by low power 808 nm NIR laser irradiation (0.25 W/cm<sup>2</sup>) leads to effective inhibition of tumor growth of subcutaneously implanted U87MG human glioblastoma cells in nude mice from combinatory chemo- and photothermal therapies.

Of course, the application of rGO in chemo-phototherapy is not limited to DOX as there are reports employing different chemotherapeutic drugs in combination with

rGO to enhance the cytotoxicity of the chemo drug through combination with PTT. In one study, a nanocookie prepared by coating amorphous carbon on a mesoporous silica support (PSS) and self-assembled on rGO nanosheet, was used as a photo-responsive drug carrier for delivery of a hydrophobic anticancer drug camptothecin (CPT). Other than providing a large payload of CPT, this nanocomposite provided a burst-like drug release and intense photothermal effect upon NIR exposure [125]. The tumor volume change observed from MDA-MB231 tumor-bearing nude mice confirmed chemo-phototherapy due to synergistic photothermal and chemo therapeutic effects (nanocookie-CPT + NIR) was more effective than chemotherapy alone (nanocookie-CPT) or photothermal effect alone (nanocookie + NIR). In a separate study, Vinothini et al. developed magnetic iron oxide nanoparticles functionalized rGO for loading CPT. Furthermore, a photosensitizer 4-hydroxycoumarin (4-HC) was bound to rGO via allyl amine (AA) linker. The cytotoxicity study using MCF-7 human breast cancer cells upon 365 nm laser irradiation at 20 mW/cm<sup>2</sup> for 3 min indicated CPT-loaded MrGO-AA-g-4-HC could produce reactive oxygen species (ROS) for killing of MCF-7 cancer cells for PDT. Unfortunately, with the limited penetration depth of light source in the visible wavelength range (365 nm) for inducing PDT effect of 4-HC, the in vivo results only demonstrated significant tumor growth suppression for CPT-loaded MrGO-AA-g-4-HC without laser treatment [126].

### 3.5. Photothermal Therapy/Immunotherapy

Immunotherapy, which kills cancer cells by improving immunity, is a new approach for cancer therapy. The success of immunotherapy is determined by two main tools, checkpoint inhibitors (CPIs) and chimeric antigen receptor (CAR) T cells [127,128]. Although immunotherapies have achieved promising results against metastatic cancers, traditional immunotherapies are often expensive and can have toxic side effects. During the process of PTT, the heat generated by the photothermal agent not only ablates the tumor but also produces tumor-associated antigens by causing immunogenic cell death, which can lead to antitumor immunity in the body. Hence, the combination of PTT and immunotherapy (photo-immunotherapy) has shown great promise in cancer therapy recently [129,130]. Although many nanoparticles have been used for photo-immunotherapy, rGO stands out as one of the best choice among them [131]. Wang et al. prepared a nanocomposite consisting of PEGylated rGO hybridized with iron oxide nanoparticles through electrostatic interaction for photothermal-immunotherapy of metastatic cancer. This nanocomposite was an excellent photothermal agent for direct killing of cancer cells by PTT, which also stimulated immune responses by triggering the maturation of dendritic cells as well as the secretion of cytokines to cause immunogenic cell death of tumor cells [131]. In vivo antitumor studies revealed the nanocomposite to be an excellent photothermal agent for PTT when exposed to NIR laser to destroy primary tumor effectively. After NIR laser treatment of 4T1 orthotopic mouse breast tumor, the intratumorally injected nanocomposites could significantly increase the survival time of tumor-bearing mice by eliciting strong antitumor immunological response of the treated animal.

**Table 2.** Summary of functionalized rGO-based nanocomposites used for cancer therapy.

| Nanocarrier         | Functionalization Agent  | Cancer Cell Line | Type of Study     | Reference |
|---------------------|--|------------------|-------------------|-----------|
| <b>Chemotherapy</b> |  |                  |                   |           |
| Riboflavin-rGO      | DOX, riboflavin  | MCF-7, A549      | In vitro          | [63]      |
| rGO-PEI-FA          | DOX, folic acid (FA)   | CBRH7919         | In vitro          | [64]      |
| FA-rGO/ZnS:Mn       | DOX, folic acid (FA), Mn-doped ZnS quantum dots                  | MDA-MB-231       | In vitro          | [65]      |
| CHA-rGO             | DOX, cholesteryl hyaluronic acid (CHA)                           | KB               | In vitro, in vivo | [66]      |
| PEG-BPEI-rGO        | DOX, branched polyethylenimine (BPEI), polyethylene glycol (PEG) | PC-3             | In vitro          | [112]     |

Table 2. Cont.

| Nanocarrier                                     | Functionalization Agent   | Cancer Cell Line       | Type of Study     | Reference |
|---|---|------------------------|-------------------|-----------|
| NrGO/PEG  | Resveratrol, PEG  | 4T1                    | In vitro, in vivo | [68]      |
| MSN-C <sub>18</sub> -rGO                        | DOX, mesoporous silica grafted with alkyl chains (MSN-C <sub>18</sub> ) | SMMC-7721              | In vitro          | [67]      |
| GP  | PF-127 polymer, curcumin, paclitaxel                                    | A549, MDA-MB-231       | In vitro          | [70]      |
| CS/rGO  | Chitosan (CS), 5-FU, curcumin   | HT-29                  | In vitro          | [72]      |
| R9-rGO  | R9 peptide, paclitaxel  | HeLa, MCF-7            | In vitro          | [71]      |
| rGO-Au  | 5-FU, gold (Au)   | MCF-7                  | In vitro          | [73]      |
| MPA-AuNPs/rGO                                   | MTX, SMTX-gold nanoparticles (AuNPs)                                    | MCF-7                  | In vitro          | [74]      |
| PK <sub>5</sub> E <sub>7</sub> (PEI-rGO)        | DOX, PK <sub>5</sub> E <sub>7</sub> polymer, PEI                        | Hela, A549             | In vitro          | [75]      |
| rGOD-hNP  | DOX, chitosan   | PC-3                   | In vitro          | [76]      |
| RGO   | Leaf extract, paclitaxel  | A549                   | In vitro          | [69]      |
| <b>Photothermal and/or Photodynamic Therapy</b> |   |                        |                   |           |
| rGO-RGD   | RGD peptide   | U87MG                  | In vitro          | [87]      |
| CPC/rGO   | Chlorin (Ce6), claudin 4-binding peptide                                | U87, HeLa              | In vitro          | [88]      |
| rGO/PdNFs                                       | Palladium nanoflowers (PdNFs)   | HeLa                   | In vitro, in vivo | [89]      |
| Ag(Nd)-ZnO/rGO                                  | Ag(Nd)/ZnO  | MCF-7                  | In vitro          | [95]      |
| ARGO  | Alanine   | U87MG                  | In vitro          | [90]      |
| ICG-CPPDN/rGO                                   | Catechol, PPDN polymer, ICG   | MDA-MB-231             | In vitro, in vivo | [103]     |
| rGO/AE/AuNPs                                    | Amaranth extract (AE), gold nanoparticles (AuNPs)                       | HeLa                   | In vitro          | [93]      |
| rGO-Ru-PEG                                      | PEG, Ru(II)   | A549                   | In vitro, in vivo | [92]      |
| NAu-rGO   | Nisin peptides, gold nanoparticles (AuNPs)                              | MCF-7, HeLa            | In vitro          | [91]      |
| p-MoS <sub>2</sub> /n-rGO-MnO <sub>2</sub> -PEG | p-type molybdenum sulfide (p-MoS <sub>2</sub> ), MnO <sub>2</sub> , PEG | HeLa, HEK293           | In vitro          | [96]      |
| Cu <sub>2</sub> O-rGO                           | Cu <sub>2</sub> O   | HK-2, MDA-MB-231, A549 | In vitro          | [97]      |
| rGO-PEI-TCPP                                    | Polyethyleneimine (PEI), tetrakis(4-carboxyphenyl) porphyrin (TCPP)     | CBRH7919               | In vitro          | [94]      |
| rGO-PDA@MS/HA                                   | Mesoporous silica (MS), hyaluronic acid (HA), polydopamine (PDA), Ce6   | HT-29, HCT-116         | In vitro          | [98]      |
| rGO/HA-g-PMAO                                   | Hyaluronic acid (HA) grafted PMAO                                       | MCF-7, NHDF            | In vitro          | [99]      |
| GT-rGO  | Green tea   | SW48, HT29             | In vitro          | [100]     |
| NBs-GPC3-rGO                                    | GPC3 antibody, nanobubbles  | HepG2                  | In vitro          | [101]     |
| ICG-PDA-rGO                                     | ICG, polydopamine   | 4T1                    | In vitro, in vivo | [102]     |
| <b>Gene Therapy</b>                             |   |                        |                   |           |
| rGO-PEI   | PEI, siRNA  | None                   | None              | [110]     |
| PEG-BPEI-rGO                                    | Low molecular-weight branched polyethylenimine (BPEI)                   | PC-3                   | In vitro          | [111]     |
| <b>Chemotherapy/Phototherapy</b>                |   |                        |                   |           |
| rGO/dopa-MAL-c(RGDfC)                           | Catechol, DOX, c(RGDfC) peptide   | HeLa, MDA-MB-231       | In vitro          | [117]     |



Table 2. Cont.

| Nanocarrier                               | Functionalization Agent   | Cancer Cell Line | Type of Study     | Reference |
|---|---|------------------|-------------------|-----------|
| rGO/C18D                                  | DOX, octadecanic acid conjugated on dextran (C18D)                  | HeLa             | In vitro          | [118]     |
| rGO@PSS                                   | Camptothecin (CPT), mesoporous silica                               | MDA-MB-231       | In vitro, in vivo | [125]     |
| rGO/Dex                                   | DOX, dextran, RGD peptide   | B16F10           | In vitro          | [119]     |
| BSA-rGO                                   | DOX, bovine serum albumin (BSA)                                     | U87MG            | In vitro          | [57]      |
| rGO/Au/PPEG                               | DOX, 3-(3-phenylureido) propanoic acid (PPA)-PEG (PPEG), Au         | HeLa             | In vitro          | [122]     |
| Chit-rGO-IR-820                           | DOX, chitosan, IR-820   | C26              | In vitro          | [49]      |
| pRGO@MS-HA                                | DOX, hyaluronic acid (HA), mesoporous silica, polydopamine          | HeLa             | In vitro, in vivo | [120]     |
| TPDL1-rGO                                 | DOX, tea polyphenol, anti-PDL1 antibody                             | CAL-27, PDLcs    | In vitro          | [121]     |
| MrGO-AA-g-4-HC                            | CPT, 4-hydroxycoumarin (4-HC), magnetic nanoparticles, camptothecin | MCF-7            | In vitro, in vivo | [126]     |
| rGO/AuNR/HAP                              | 5-FU, gold nanorod (AuNR), hydroxyapatite                           | HeLa             | In vitro          | [123]     |
| rGO-AuNRVe                                | DOX, gold nanorod vesicle   | U87MG            | In vitro, in vivo | [124]     |
| <b>Photothermal Therapy/Immunotherapy</b> |   |                  |                   |           |
| FNPs/rGO-PEG                              | Fe <sub>3</sub> O <sub>4</sub> nanoparticles, PEG                   | 4T1              | In vitro, in vivo | [131]     |
| PEG-rGO-FA-IDOi                           | IDO inhibitor (IDOi), folic acid, PEG                               | CT26             | In vitro, in vivo | [132]     |

Yan et al. also combined immunotherapy with PTT with folic acid as a targeting ligand by conjugating indoleamine-2,3-dioxygenase (IDO) inhibitor to rGO to induce IDO inhibition and programmed cell death-ligand 1 (PD-L1) blockade for synergistic antitumor immunity. After laser irradiation, the nanocomposite can directly kill tumor cells due to PTT and trigger antitumor immune response synergistically by IDO inhibition as well as PD-L1 blockade in CT26 colon cancer cells. By combining PTT, IDO inhibition, and PD-L1 blockade, the growth of irradiated tumor in distant sites without PTT treatment can be effectively inhibited by targeting multiple antitumor immune pathways to induce synergistic antitumor immunity [132].

#### 4. Conclusions and Outlook

Due to improved photothermal response by absorbing light in the NIR range and the potential for high loading of chemotherapeutic drugs, photosensitizers and siRNA, rGO synthesized by means of various reducing agents is well suited for applications in single or multi-mode cancer therapy. Based on the reducing agent used for rGO synthesis, and the moieties conjugated with it, rGO-based nanocomposite is endowed with triggered drug release capability after intracellular uptake, by pH change or hyperthermia. This temperature-dependent and pH-responsive drug release, when combined with PTT and/or PDT, can lead to pronounced cytotoxicity from in vitro and in vivo studies performed with various cancer cells. rGO can also act as a good vehicle for gene delivery after modification/conjugation with cationic polymers, especially PEI, which can act alone for RNAi or combined with rGO-induced PTT for combination therapy involving immunotherapy. Overall, this review concludes that rGO is a promising and versatile tool after functionalization for cancer therapy, especially in combination cancer therapy such as PTT/PDT, chemotherapy/phototherapy and photothermal therapy/immunotherapy to elicit synergistic anti-tumor efficacy. Undoubtedly, despite remarkable therapeutic efficacy demonstrated from combination cancer therapy using rGO, rationally combining the therapeutic modalities into rGO-based platform for 'smart' drug delivery will be desirable. In addition, for

successful cancer therapy, the designed rGO-based nanocomposites should preferably be endowed with both therapeutic and diagnostic functions for precision nanomedicine. Additionally, the function of combined cancer therapeutics offered by rGO may be required to be programmed for realizing the synergistic effects. Moreover, it would be helpful to develop better PDT/PTT cancer therapeutics using rGO, which can alleviate the limit of penetration depth of NIR laser for effective eradication of tumors located deep in the body.

**Author Contributions:** Conceptualization, B.S.D., Y.-J.L., and J.-P.C.; Writing—original draft preparation, B.S.D.; Writing—review and editing, G.J. and J.-P.C.; Visualization, B.S.D.; Supervision, J.-P.C.; Funding acquisition, J.-P.C. All authors have read and agreed to the published version of the manuscript.

**Funding:** This research was funded by the Ministry of Science and Technology, Taiwan, ROC (MOST106-2221-E-182-056-MY3) and Chang Gung Memorial Hospital, Taiwan, ROC (BMRP249, CMRPD2I0041 and CMRPD2I0042). The APC was funded by Chang Gung University.

**Institutional Review Board Statement:** Not applicable.

**Informed Consent Statement:** Not applicable.

**Acknowledgments:** We acknowledge the technical support by the Microscope Core Laboratory, Chang Gung Memorial Hospital, Linkou and the Microscopy Center, Chang Gung University.

**Conflicts of Interest:** The authors declare no conflict of interest. The funders had no role in the design of the study; in the collection, analyses, or interpretation of data; in the writing of the manuscript, or in the decision to publish the results.

## References

1. Siegel, R.L.; Miller, K.D.; Jemal, A. Cancer statistics, 2020. *A Cancer J. Clin.* **2020**, *70*, 7–30. [\[CrossRef\]](#)
2. Soto, A.M.; Sonnenschein, C. Environmental causes of cancer: Endocrine disruptors as carcinogens. *Nat. Rev. Endocrinol.* **2010**, *6*, 363–370. [\[CrossRef\]](#)
3. Feng, S.-S.; Chien, S. Chemotherapeutic engineering: Application and further development of chemical engineering principles for chemotherapy of cancer and other diseases. *Chem. Eng. Sci.* **2003**, *58*, 4087–4114. [\[CrossRef\]](#)
4. Patel, S.C.; Lee, S.; Lalwani, G.; Suhrland, C.; Chowdhury, S.M.; Sitharaman, B. Graphene-based platforms for cancer therapeutics. *Ther. Deliv.* **2016**, *7*, 101–116. [\[CrossRef\]](#) [\[PubMed\]](#)
5. Skalickova, S.; Loffelmann, M.; Gargulak, M.; Kepinska, M.; Docekalova, M.; Uhlirova, D.; Stankova, M.; Fernandez, C.; Milnerowicz, H.; Ruttkay-Nedecky, B.; et al. Zinc-Modified Nanotransporter of Doxorubicin for Targeted Prostate Cancer Delivery. *Nanomaterials* **2017**, *7*, 435. [\[CrossRef\]](#) [\[PubMed\]](#)
6. Baskar, R.; Lee, K.A.; Yeo, R.; Yeoh, K.-W. Cancer and radiation therapy: Current advances and future directions. *Int. J. Med. Sci.* **2012**, *9*, 193–199. [\[CrossRef\]](#) [\[PubMed\]](#)
7. Arruebo, M.; Vilaboa, N.; Sáez-Gutierrez, B.; Lambea, J.; Tres, A.; Valladares, M.; González-Fernández, A. Assessment of the evolution of cancer treatment therapies. *Cancers* **2011**, *3*, 3279–3330. [\[CrossRef\]](#) [\[PubMed\]](#)
8. Mozafari, M.R.; Pardakhty, A.; Azarmi, S.; Jazayeri, J.A.; Nokhodchi, A.; Omri, A. Role of nanocarrier systems in cancer nanotherapy. *J. Liposome Res.* **2009**, *19*, 310–321. [\[CrossRef\]](#) [\[PubMed\]](#)
9. Li, Z.; Tan, S.; Li, S.; Shen, Q.; Wang, K. Cancer drug delivery in the nano era: An overview and perspectives (Review). *Oncol Rep.* **2017**, *38*, 611–624. [\[CrossRef\]](#)
10. Deshpande, P.P.; Biswas, S.; Torchilin, V.P. Current trends in the use of liposomes for tumor targeting. *Nanomed. Lond. Engl.* **2013**, *8*, 1509–1528. [\[CrossRef\]](#)
11. Gong, Z.; Chen, M.; Ren, Q.; Yue, X.; Dai, Z. Fibronectin-targeted dual-acting micelles for combination therapy of metastatic breast cancer. *Signal. Transduct. Target. Ther.* **2020**, *5*, 12. [\[CrossRef\]](#)
12. Thundimadathil, J. Cancer Treatment Using Peptides: Current Therapies and Future Prospects. *J. Amino Acids* **2012**, *2012*, 967347. [\[CrossRef\]](#)
13. Peng, X.-H.; Qian, X.; Mao, H.; Wang, A.Y.; Chen, Z.G.; Nie, S.; Shin, D.M. Targeted magnetic iron oxide nanoparticles for tumor imaging and therapy. *Int. J. Nanomed.* **2008**, *3*, 311–321. [\[CrossRef\]](#)
14. Jain, S.; Hirst, D.G.; O'Sullivan, J.M. Gold nanoparticles as novel agents for cancer therapy. *Br. J. Radiol.* **2012**, *85*, 101–113. [\[CrossRef\]](#)
15. Yuan, Y.-G.; Zhang, S.; Hwang, J.-Y.; Kong, I.-K. Silver Nanoparticles Potentiates Cytotoxicity and Apoptotic Potential of Camptothecin in Human Cervical Cancer Cells. *Oxidative Med. Cell. Longev.* **2018**, *2018*, 6121328. [\[CrossRef\]](#) [\[PubMed\]](#)
16. Huang, D.; He, B.; Mi, P. Calcium phosphate nanocarriers for drug delivery to tumors: Imaging, therapy and theranostics. *Biomater. Sci.* **2019**, *7*, 3942–3960. [\[CrossRef\]](#) [\[PubMed\]](#)

17. Yi, X.; Chen, L.; Chen, J.; Maiti, D.; Chai, Z.; Liu, Z.; Yang, K. Biomimetic Copper Sulfide for Chemo-Radiotherapy: Enhanced Uptake and Reduced Efflux of Nanoparticles for Tumor Cells under Ionizing Radiation. *Adv. Funct. Mater.* **2018**, *28*, 1705161. [\[CrossRef\]](#)
18. Tanaka, M.; Kataoka, H.; Yano, S.; Ohi, H.; Kawamoto, K.; Shibahara, T.; Mizoshita, T.; Mori, Y.; Tanida, S.; Kamiya, T.; et al. Anti-cancer effects of newly developed chemotherapeutic agent, glycoconjugated palladium (II) complex, against cisplatin-resistant gastric cancer cells. *BMC Cancer* **2013**, *13*, 1–9. [\[CrossRef\]](#) [\[PubMed\]](#)
19. Pei, X.; Zhu, Z.; Gan, Z.; Chen, J.; Zhang, X.; Cheng, X.; Wan, Q.; Wang, J. PEGylated nano-graphene oxide as a nanocarrier for delivering mixed anticancer drugs to improve anticancer activity. *Sci. Rep.* **2020**, *10*, 2717. [\[CrossRef\]](#)
20. Lu, Y.-J.; Lin, P.-Y.; Huang, P.-H.; Kuo, C.-Y.; Shalumon, K.T.; Chen, M.-Y.; Chen, J.-P. Magnetic Graphene Oxide for Dual Targeted Delivery of Doxorubicin and Photothermal Therapy. *Nanomaterials* **2018**, *8*, 193. [\[CrossRef\]](#)
21. Wang, Y.; Qiu, M.; Won, M.; Jung, E.; Fan, T.; Xie, N.; Chi, S.-G.; Zhang, H.; Kim, J.S. Emerging 2D material-based nanocarrier for cancer therapy beyond graphene. *Coord. Chem. Rev.* **2019**, *400*, 213041. [\[CrossRef\]](#)
22. Chen, Y.-W.; Su, Y.-L.; Hu, S.-H.; Chen, S.-Y. Functionalized graphene nanocomposites for enhancing photothermal therapy in tumor treatment. *Adv. Drug Deliv. Rev.* **2016**, *105*, 190–204. [\[CrossRef\]](#)
23. Patel, K.D.; Singh, R.K.; Kim, H.-W. Carbon-based nanomaterials as an emerging platform for theranostics. *Mater. Horiz.* **2019**, *6*, 434–469. [\[CrossRef\]](#)
24. Mousavi, S.M.; Low, F.W.; Hashemi, S.A.; Samsudin, N.A.; Shakeri, M.; Yusoff, Y.; Rahsepar, M.; Lai, C.W.; Babapoor, A.; Soroshnia, S.; et al. Development of hydrophobic reduced graphene oxide as a new efficient approach for photochemotherapy. *RSC Adv.* **2020**, *10*, 12851–12863. [\[CrossRef\]](#)
25. Degors, I.M.S.; Wang, C.; Rehman, Z.U.; Zuhorn, I.S. Carriers Break Barriers in Drug Delivery: Endocytosis and Endosomal Escape of Gene Delivery Vectors. *Acc. Chem. Res.* **2019**, *52*, 1750–1760. [\[CrossRef\]](#) [\[PubMed\]](#)
26. Fortuni, B.; Inose, T.; Ricci, M.; Fujita, Y.; Van Zundert, I.; Masuhara, A.; Fron, E.; Mizuno, H.; Latterini, L.; Rocha, S.; et al. Polymeric Engineering of Nanoparticles for Highly Efficient Multifunctional Drug Delivery Systems. *Sci. Rep.* **2019**, *9*, 2666. [\[CrossRef\]](#) [\[PubMed\]](#)
27. Kostarelos, K.; Novoselov, K.S. Exploring the Interface of Graphene and Biology. *Science* **2014**, *344*, 261–263. [\[CrossRef\]](#) [\[PubMed\]](#)
28. Kostarelos, K.; Novoselov, K.S. Graphene devices for life. *Nat. Nanotechnol.* **2014**, *9*, 744–745. [\[CrossRef\]](#) [\[PubMed\]](#)
29. Chau, N.D.Q.; Ménard-Moyon, C.; Kostarelos, K.; Bianco, A. Multifunctional carbon nanomaterial hybrids for magnetic manipulation and targeting. *Biochem. Biophys. Res. Commun.* **2015**, *468*, 454–462. [\[CrossRef\]](#)
30. Reina, G.; González-Domínguez, J.M.; Criado, A.; Vázquez, E.; Bianco, A.; Prato, M. Promises, facts and challenges for graphene in biomedical applications. *Chem. Soc. Rev.* **2017**, *46*, 4400–4416. [\[CrossRef\]](#)
31. Karki, N.; Tiwari, H.; Tewari, C.; Rana, A.; Pandey, N.; Basak, S.; Sahoo, N.G. Functionalized graphene oxide as a vehicle for targeted drug delivery and bioimaging applications. *J. Mater. Chem. B* **2020**, *8*, 8116–8148. [\[CrossRef\]](#) [\[PubMed\]](#)
32. Li, D.; Zhang, W.; Yu, X.; Wang, Z.; Su, Z.; Wei, G. When biomolecules meet graphene: From molecular level interactions to material design and applications. *Nanoscale* **2016**, *8*, 19491–19509. [\[CrossRef\]](#) [\[PubMed\]](#)
33. Mun, S.G.; Choi, H.W.; Lee, J.M.; Lim, J.H.; Ha, J.H.; Kang, M.-J.; Kim, E.-J.; Kang, L.; Chung, B.G. rGO nanomaterial-mediated cancer targeting and photothermal therapy in a microfluidic co-culture platform. *Nano Conver.* **2020**, *7*, 10. [\[CrossRef\]](#)
34. Bao, Z.; Liu, X.; Liu, Y.; Liu, H.; Zhao, K. Near-infrared light-responsive inorganic nanomaterials for photothermal therapy. *Asian J. Pharm. Sci.* **2016**, *11*, 349–364. [\[CrossRef\]](#)
35. Zhang, J.; Yang, H.; Shen, G.; Cheng, P.; Zhang, J.; Guo, S. Reduction of graphene oxide vial-ascorbic acid. *Chem. Commun.* **2010**, *46*, 1112–1114. [\[CrossRef\]](#) [\[PubMed\]](#)
36. Fernández-Merino, M.J.; Guardia, L.; Paredes, J.I.; Villar-Rodil, S.; Solís-Fernández, P.; Martínez-Alonso, A.; Tascón, J.M.D. Vitamin C Is an Ideal Substitute for Hydrazine in the Reduction of Graphene Oxide Suspensions. *J. Phys. Chem. C* **2010**, *114*, 6426–6432. [\[CrossRef\]](#)
37. Habte, A.T.; Ayele, D.W. Synthesis and Characterization of Reduced Graphene Oxide (rGO) Started from Graphene Oxide (GO) Using the Tour Method with Different Parameters. *Adv. Mater. Sci. Eng.* **2019**, *2019*, 5058163. [\[CrossRef\]](#)
38. Kosowska, K.; Domalik-Pyzik, P.; Krok-Borkowicz, M.; Chłopek, J. Synthesis and Characterization of Chitosan/Reduced Graphene Oxide Hybrid Composites. *Materials* **2019**, *12*, 2077. [\[CrossRef\]](#) [\[PubMed\]](#)
39. Joshi, S.; Siddiqui, R.; Sharma, P.; Kumar, R.; Verma, G.; Saini, A. Green synthesis of peptide functionalized reduced graphene oxide (rGO) nano bioconjugate with enhanced antibacterial activity. *Sci. Rep.* **2020**, *10*, 9441. [\[CrossRef\]](#)
40. Iskandar, F.; Hikmah, U.; Stavila, E.; Aimon, A.H. Microwave-assisted reduction method under nitrogen atmosphere for synthesis and electrical conductivity improvement of reduced graphene oxide (rGO). *RSC Adv.* **2017**, *7*, 52391–52397. [\[CrossRef\]](#)
41. Li, D.; Müller, M.B.; Gilje, S.; Kaner, R.B.; Wallace, G.G. Processable aqueous dispersions of graphene nanosheets. *Nat. Nanotechnol.* **2008**, *3*, 101–105. [\[CrossRef\]](#) [\[PubMed\]](#)
42. Cong, H.-P.; He, J.-J.; Lu, Y.; Yu, S.-H. Water-Soluble Magnetic-Functionalized Reduced Graphene Oxide Sheets: In situ Synthesis and Magnetic Resonance Imaging Applications. *Small* **2010**, *6*, 169–173. [\[CrossRef\]](#) [\[PubMed\]](#)
43. Altinbasak, I.; Jijie, R.; Barras, A.; Golba, B.; Sanyal, R.; Bouckaert, J.; Drider, D.; Bilyy, R.; Dumych, T.; Paryzhak, S.; et al. Reduced Graphene-Oxide-Embedded Polymeric Nanofiber Mats: An “On-Demand” Photothermally Triggered Antibiotic Release Platform. *ACS Appl. Mater. Interfaces* **2018**, *10*, 41098–41106. [\[CrossRef\]](#)

44. Ren, P.-G.; Yan, D.-X.; Ji, X.; Chen, T.; Li, Z.-M. Temperature dependence of graphene oxide reduced by hydrazine hydrate. *Nanotechnology* **2010**, *22*, 055705. [[CrossRef](#)] [[PubMed](#)]
45. Gurunathan, S.; Han, J.W.; Kim, E.S.; Park, J.H.; Kim, J.-H. Reduction of graphene oxide by resveratrol: A novel and simple biological method for the synthesis of an effective anticancer nanotherapeutic molecule. *Int. J. Nanomed.* **2015**, *10*, 2951–2969. [[CrossRef](#)]
46. Bhumkar, D.R.; Joshi, H.M.; Sastry, M.; Pokharkar, V.B. Chitosan Reduced Gold Nanoparticles as Novel Carriers for Transmucosal Delivery of Insulin. *Pharm. Res.* **2007**, *24*, 1415–1426. [[CrossRef](#)]
47. Fang, M.; Long, J.; Zhao, W.; Wang, L.; Chen, G. pH-Responsive Chitosan-Mediated Graphene Dispersions. *Langmuir* **2010**, *26*, 16771–16774. [[CrossRef](#)] [[PubMed](#)]
48. Justin, R.; Chen, B. Body temperature reduction of graphene oxide through chitosan functionalisation and its application in drug delivery. *Mater. Sci. Eng. C* **2014**, *34*, 50–53. [[CrossRef](#)]
49. Zaharie-Butucel, D.; Potara, M.; Suarasan, S.; Licarete, E.; Astilean, S. Efficient combined near-infrared-triggered therapy: Phototherapy over chemotherapy in chitosan-reduced graphene oxide-IR820 dye-doxorubicin nanoplateforms. *J. Colloid Interface Sci.* **2019**, *552*, 218–229. [[CrossRef](#)]
50. Liu, H.; Kuila, T.; Kim, N.H.; Ku, B.-C.; Lee, J.H. In situ synthesis of the reduced graphene oxide–polyethyleneimine composite and its gas barrier properties. *J. Mater. Chem. A* **2013**, *1*, 3739–3746. [[CrossRef](#)]
51. Zhang, X.; Yu, Y.; Shen, J.; Qi, W.; Wang, H. Fabrication of polyethyleneimine-functionalized reduced graphene oxide-hemin-bovine serum albumin (PEI-rGO-hemin-BSA) nanocomposites as peroxidase mimetics for the detection of multiple metabolites. *Anal. Chim. Acta* **2019**, *1070*, 80–87. [[CrossRef](#)]
52. Roy, S.; Tang, X.; Das, T.; Zhang, L.; Li, Y.; Ting, S.; Hu, X.; Yue, C.Y. Enhanced Molecular Level Dispersion and Interface Bonding at Low Loading of Modified Graphene Oxide To Fabricate Super Nylon 12 Composites. *ACS Appl. Mater. Interfaces* **2015**, *7*, 3142–3151. [[CrossRef](#)]
53. Yang, Z.-Z.; Zheng, Q.-B.; Qiu, H.-X.; Li, J.; Yang, J.-H. A simple method for the reduction of graphene oxide by sodium borohydride with CaCl<sub>2</sub> as a catalyst. *New Carbon Mater.* **2015**, *30*, 41–47. [[CrossRef](#)]
54. Guex, L.G.; Sacchi, B.; Peuvot, K.F.; Andersson, R.L.; Pourrahimi, A.M.; Ström, V.; Farris, S.; Olsson, R.T. Experimental review: Chemical reduction of graphene oxide (GO) to reduced graphene oxide (rGO) by aqueous chemistry. *Nanoscale* **2017**, *9*, 9562–9571. [[CrossRef](#)]
55. Liu, J.; Fu, S.; Yuan, B.; Li, Y.; Deng, Z. Toward a Universal “Adhesive Nanosheet” for the Assembly of Multiple Nanoparticles Based on a Protein-Induced Reduction/Decoration of Graphene Oxide. *J. Am. Chem. Soc.* **2010**, *132*, 7279–7281. [[CrossRef](#)]
56. Dasgupta, N.; Ranjan, S.; Patra, D.; Srivastava, P.; Kumar, A.; Ramalingam, C. Bovine serum albumin interacts with silver nanoparticles with a “side-on” or “end on” conformation. *Chem. Biol. Interact.* **2016**, *253*, 100–111. [[CrossRef](#)]
57. Cheon, Y.A.; Bae, J.H.; Chung, B.G. Reduced Graphene Oxide Nanosheet for Chemo-photothermal Therapy. *Langmuir* **2016**, *32*, 2731–2736. [[CrossRef](#)]
58. Griep, M.H.; Demaree, J.D.; Cole, D.P.; Henry, T.C.; Karna, S.P. Protein-Mediated Synthesis of Au Nanocluster Decorated Reduced Graphene Oxide: A Multifunctional Hybrid Nano-Bio Platform. *Plasmonics* **2020**, *15*, 897–903. [[CrossRef](#)]
59. Wang, Y.; Shi, Z.; Yin, J. Facile Synthesis of Soluble Graphene via a Green Reduction of Graphene Oxide in Tea Solution and Its Biocomposites. *ACS Appl. Mater. Interfaces* **2011**, *3*, 1127–1133. [[CrossRef](#)] [[PubMed](#)]
60. Vatandost, E.; Ghorbani-HasanSaraei, A.; Chekin, F.; Naghizadeh Raeisi, S.; Shahidi, S.-A. Green tea extract assisted green synthesis of reduced graphene oxide: Application for highly sensitive electrochemical detection of sunset yellow in food products. *Food Chem.* **2020**, *6*, 100085. [[CrossRef](#)] [[PubMed](#)]
61. Abdullah, M.F.; Zakaria, R.; Zein, S.H.S. Green tea polyphenol–reduced graphene oxide: Derivatisation, reduction efficiency, reduction mechanism and cytotoxicity. *RSC Adv.* **2014**, *4*, 34510–34518. [[CrossRef](#)]
62. Jose, G.; Lu, Y.-J.; Hung, J.-T.; Yu, A.L.; Chen, J.-P. Co-Delivery of CPT-11 and Panobinostat with Anti-GD2 Antibody Conjugated Immunoliposomes for Targeted Combination Chemotherapy. *Cancers* **2020**, *12*, 3211. [[CrossRef](#)]
63. Ma, N.; Zhang, B.; Liu, J.; Zhang, P.; Li, Z.; Luan, Y. Green fabricated reduced graphene oxide: Evaluation of its application as nano-carrier for pH-sensitive drug delivery. *Int. J. Pharm.* **2015**, *496*, 984–992. [[CrossRef](#)] [[PubMed](#)]
64. Wei, G.; Yan, M.; Dong, R.; Wang, D.; Zhou, X.; Chen, J.; Hao, J. Covalent Modification of Reduced Graphene Oxide by Means of Diazonium Chemistry and Use as a Drug-Delivery System. *Chem. A Eur. J.* **2012**, *18*, 14708–14716. [[CrossRef](#)] [[PubMed](#)]
65. Diaz-Diestra, D.; Thapa, B.; Badillo-Diaz, D.; Beltran-Huarac, J.; Morell, G.; Weiner, B.R. Graphene Oxide/ZnS:Mn Nanocomposite Functionalized with Folic Acid as a Nontoxic and Effective Theranostic Platform for Breast Cancer Treatment. *Nanomaterials* **2018**, *8*, 484. [[CrossRef](#)] [[PubMed](#)]
66. Miao, W.; Shim, G.; Kang, C.M.; Lee, S.; Choe, Y.S.; Choi, H.-G.; Oh, Y.-K. Cholesteryl hyaluronic acid-coated, reduced graphene oxide nanosheets for anti-cancer drug delivery. *Biomaterials* **2013**, *34*, 9638–9647. [[CrossRef](#)]
67. He, D.; Li, X.; He, X.; Wang, K.; Tang, J.; Yang, X.; He, X.; Yang, X.; Zou, Z. Noncovalent assembly of reduced graphene oxide and alkyl-grafted mesoporous silica: An effective drug carrier for near-infrared light-responsive controlled drug release. *J. Mater. Chem. B* **2015**, *3*, 5588–5594. [[CrossRef](#)]
68. Chen, J.; Liu, H.; Zhao, C.; Qin, G.; Xi, G.; Li, T.; Wang, X.; Chen, T. One-step reduction and PEGylation of graphene oxide for photothermally controlled drug delivery. *Biomaterials* **2014**, *35*, 4986–4995. [[CrossRef](#)]



69. Lin, S.; Ruan, J.; Wang, S. Biosynthesized of reduced graphene oxide nanosheets and its loading with paclitaxel for their anti cancer effect for treatment of lung cancer. *J. Photochem. Photobiol. B Biol.* **2019**, *191*, 13–17. [[CrossRef](#)] [[PubMed](#)]
70. Muthoosamy, K.; Abubakar, I.B.; Bai, R.G.; Loh, H.-S.; Manickam, S. Exceedingly Higher co-loading of Curcumin and Paclitaxel onto Polymer-functionalized Reduced Graphene Oxide for Highly Potent Synergistic Anticancer Treatment. *Sci. Rep.* **2016**, *6*, 32808. [[CrossRef](#)]
71. Hashemi, M.; Yadegari, A.; Yazdanpanah, G.; Jabbehdari, S.; Omid, M.; Tayebi, L. Functionalized R9–reduced graphene oxide as an efficient nano-carrier for hydrophobic drug delivery. *RSC Adv.* **2016**, *6*, 74072–74084. [[CrossRef](#)]
72. Dhanavel, S.; Revathy, T.A.; Sivarajani, T.; Sivakumar, K.; Palani, P.; Narayanan, V.; Stephen, A. 5-Fluorouracil and curcumin co-encapsulated chitosan/reduced graphene oxide nanocomposites against human colon cancer cell lines. *Polym. Bull.* **2020**, *77*, 213–233. [[CrossRef](#)]
73. Sanad, M.F.; Shalan, A.E.; Bazid, S.M.; Abu Serea, E.S.; Hashem, E.M.; Nabih, S.; Ahsan, M.A. A graphene gold nanocomposite-based 5-FU drug and the enhancement of the MCF-7 cell line treatment. *RSC Adv.* **2019**, *9*, 31021–31029. [[CrossRef](#)]
74. Jafarizad, A.; Aghanejad, A.; Sevim, M.; Metin, Ö.; Barar, J.; Omid, Y.; Ekin, D. Gold Nanoparticles and Reduced Graphene Oxide-Gold Nanoparticle Composite Materials as Covalent Drug Delivery Systems for Breast Cancer Treatment. *Chem. Sel.* **2017**, *2*, 6663–6672. [[CrossRef](#)]
75. Ryu, K.; Park, J.; Kim, T.-I. Effect of pH-Responsive Charge-Conversional Polymer Coating to Cationic Reduced Graphene Oxide Nanostructures for Tumor Microenvironment-Targeted Drug Delivery Systems. *Nanomaterials* **2019**, *9*, 1289. [[CrossRef](#)] [[PubMed](#)]
76. SreeHarsha, N.; Maheshwari, R.; Al-Dhubiab, B.E.; Tekade, M.; Sharma, M.C.; Venugopala, K.N.; Tekade, R.K.; Alzahrani, A.M. Graphene-based hybrid nanoparticle of doxorubicin for cancer chemotherapy. *Int. J. Nanomed.* **2019**, *14*, 7419–7429. [[CrossRef](#)] [[PubMed](#)]
77. Nomura, S.; Morimoto, Y.; Tsujimoto, H.; Arake, M.; Harada, M.; Saitoh, D.; Hara, I.; Ozeki, E.; Satoh, A.; Takayama, E.; et al. Highly reliable, targeted photothermal cancer therapy combined with thermal dosimetry using a near-infrared absorbent. *Sci. Rep.* **2020**, *10*, 9765. [[CrossRef](#)]
78. Doughty, A.C.V.; Hoover, A.R.; Layton, E.; Murray, C.K.; Howard, E.W.; Chen, W.R. Nanomaterial Applications in Photothermal Therapy for Cancer. *Materials* **2019**, *12*, 779. [[CrossRef](#)]
79. de Melo-Diogo, D.; Lima-Sousa, R.; Alves, C.G.; Correia, I.J. Graphene family nanomaterials for application in cancer combination photothermal therapy. *Biomater. Sci.* **2019**, *7*, 3534–3551. [[CrossRef](#)]
80. Alegret, N.; Criado, A.; Prato, M. Recent Advances of Graphene-based Hybrids with Magnetic Nanoparticles for Biomedical Applications. *Curr. Med. Chem.* **2017**, *24*, 529–536. [[CrossRef](#)]
81. Vines, J.B.; Yoon, J.-H.; Ryu, N.-E.; Lim, D.-J.; Park, H. Gold Nanoparticles for Photothermal Cancer Therapy. *Front. Chem.* **2019**, *7*, 167. [[CrossRef](#)]
82. Modugno, G.; Ménard-Moyon, C.; Prato, M.; Bianco, A. Carbon nanomaterials combined with metal nanoparticles for theranostic applications. *Br. J. Pharm.* **2015**, *172*, 975–991. [[CrossRef](#)]
83. Bai, L.-Z.; Zhao, D.-L.; Xu, Y.; Zhang, J.-M.; Gao, Y.-L.; Zhao, L.-Y.; Tang, J.-T. Inductive heating property of graphene oxide-Fe<sub>3</sub>O<sub>4</sub> nanoparticles hybrid in an AC magnetic field for localized hyperthermia. *Mater. Lett.* **2012**, *68*, 399–401. [[CrossRef](#)]
84. Gazzi, A.; Fusco, L.; Khan, A.; Bedognetti, D.; Zavan, B.; Vitale, F.; Yilmazer, A.; Delogu, L.G. Photodynamic Therapy Based on Graphene and MXene in Cancer Theranostics. *Front. Bioeng. Biotechnol.* **2019**, *7*, 295. [[CrossRef](#)]
85. Li, W.; Yang, J.; Luo, L.; Jiang, M.; Qin, B.; Yin, H.; Zhu, C.; Yuan, X.; Zhang, J.; Luo, Z.; et al. Targeting photodynamic and photothermal therapy to the endoplasmic reticulum enhances immunogenic cancer cell death. *Nat. Commun.* **2019**, *10*, 3349. [[CrossRef](#)] [[PubMed](#)]
86. Luo, S.; Yang, Z.; Tan, X.; Wang, Y.; Zeng, Y.; Wang, Y.; Li, C.; Li, R.; Shi, C. Multifunctional Photosensitizer Grafted on Polyethylene Glycol and Polyethylenimine Dual-Functionalized Nanographene Oxide for Cancer-Targeted Near-Infrared Imaging and Synergistic Phototherapy. *ACS Appl. Mater. Interfaces* **2016**, *8*, 17176–17186. [[CrossRef](#)] [[PubMed](#)]
87. Robinson, J.T.; Tabakman, S.M.; Liang, Y.; Wang, H.; Sanchez Casalongue, H.; Vinh, D.; Dai, H. Ultrasmall Reduced Graphene Oxide with High Near-Infrared Absorbance for Photothermal Therapy. *J. Am. Chem. Soc.* **2011**, *133*, 6825–6831. [[CrossRef](#)] [[PubMed](#)]
88. Shim, G.; Kim, M.-G.; Jin, H.; Kim, J.; Oh, Y.-K. Claudin 4-targeted nanographene phototherapy using a Clostridium perfringens enterotoxin peptide-photosensitizer conjugate. *Acta Pharmacol. Sin.* **2017**, *38*, 954–962. [[CrossRef](#)]
89. He, Y.; Cao, W.; Cong, C.; Zhang, X.; Luo, L.; Li, L.; Cui, H.; Gao, D. Rationally Designed Multifunctional Carbon–Palladium Nanohybrids for Wide Applications: From Electrochemical Catalysis/Nonenzymatic Sensor to Photothermal Tumor Therapy. *ACS Sustain. Chem. Eng.* **2019**, *7*, 3584–3592. [[CrossRef](#)]
90. Chen, X.; Li, C.; Wang, X.; Zhao, X. Infrared heating of reduced graphene oxide nanosheets as photothermal radiation therapeutic agents for tumor regressions. *Mater. Res. Express* **2019**, *6*, 085080. [[CrossRef](#)]
91. Otari, S.V.; Kumar, M.; Anwar, M.Z.; Thorat, N.D.; Patel, S.K.S.; Lee, D.; Lee, J.H.; Lee, J.-K.; Kang, Y.C.; Zhang, L. Rapid synthesis and decoration of reduced graphene oxide with gold nanoparticles by thermostable peptides for memory device and photothermal applications. *Sci. Rep.* **2017**, *7*, 10980. [[CrossRef](#)] [[PubMed](#)]
92. Zhang, D.-Y.; Zheng, Y.; Tan, C.-P.; Sun, J.-H.; Zhang, W.; Ji, L.-N.; Mao, Z.-W. Graphene Oxide Decorated with Ru(II)–Polyethylene Glycol Complex for Lysosome-Targeted Imaging and Photodynamic/Photothermal Therapy. *ACS Appl. Mater. Interfaces* **2017**, *9*, 6761–6771. [[CrossRef](#)] [[PubMed](#)]

93. Chang, G.; Wang, Y.; Gong, B.; Xiao, Y.; Chen, Y.; Wang, S.; Li, S.; Huang, F.; Shen, Y.; Xie, A. Reduced Graphene Oxide/Amaranth Extract/AuNPs Composite Hydrogel on Tumor Cells as Integrated Platform for Localized and Multiple Synergistic Therapy. *ACS Appl. Mater. Interfaces* **2015**, *7*, 11246–11256. [\[CrossRef\]](#) [\[PubMed\]](#)
94. Wei, G.; Yan, M.; Ma, L.; Wang, C. Photothermal and photodynamic therapy reagents based on rGO-C<sub>6</sub>H<sub>4</sub>-COOH. *RSC Adv.* **2016**, *6*, 3748–3755. [\[CrossRef\]](#)
95. Jafarirad, S.; Hammami Torghabe, E.; Rasta, S.H.; Salehi, R. A novel non-invasive strategy for low-level laser-induced cancer therapy by using new Ag/ZnO and Nd/ZnO functionalized reduced graphene oxide nanocomposites. *Artif. Cells Nanomed. Biotechnol.* **2018**, *46*, 800–816. [\[CrossRef\]](#)
96. Kapri, S.; Bhattacharyya, S. Molybdenum sulfide-reduced graphene oxide p–n heterojunction nanosheets with anchored oxygen generating manganese dioxide nanoparticles for enhanced photodynamic therapy. *Chem. Sci.* **2018**, *9*, 8982–8989. [\[CrossRef\]](#)
97. Hou, C.; Quan, H.; Duan, Y.; Zhang, Q.; Wang, H.; Li, Y. Facile synthesis of water-dispersible Cu<sub>2</sub>O nanocrystal-reduced graphene oxide hybrid as a promising cancer therapeutic agent. *Nanoscale* **2013**, *5*, 1227–1232. [\[CrossRef\]](#)
98. Jiang, W.; Mo, F.; Jin, X.; Chen, L.; Xu, L.J.; Guo, L.; Fu, F. Tumor-Targeting Photothermal Heating-Responsive Nanoplatfrom Based on Reduced Graphene Oxide/Mesoporous Silica/Hyaluronic Acid Nanocomposite for Enhanced Photodynamic Therapy. *Adv. Mater. Interfaces* **2017**, *4*, 1700425. [\[CrossRef\]](#)
99. Lima-Sousa, R.; de Melo-Diogo, D.; Alves, C.G.; Costa, E.C.; Ferreira, P.; Louro, R.O.; Correia, I.J. Hyaluronic acid functionalized green reduced graphene oxide for targeted cancer photothermal therapy. *Carbohydr. Polym.* **2018**, *200*, 93–99. [\[CrossRef\]](#)
100. Abdollahad, M.; Janmaleki, M.; Mohajerzadeh, S.; Akhavan, O.; Abbasi, S. Polyphenols attached graphene nanosheets for high efficiency NIR mediated photodestruction of cancer cells. *Mater. Sci. Eng. C* **2013**, *33*, 1498–1505. [\[CrossRef\]](#)
101. Liu, Z.; Zhang, J.; Tian, Y.; Zhang, L.; Han, X.; Wang, Q.; Cheng, W. Targeted delivery of reduced graphene oxide nanosheets using multifunctional ultrasound nanobubbles for visualization and enhanced photothermal therapy. *Int. J. Nanomed.* **2018**, *13*, 7859–7872. [\[CrossRef\]](#)
102. Hu, D.; Zhang, J.; Gao, G.; Sheng, Z.; Cui, H.; Cai, L. Indocyanine Green-Loaded Polydopamine-Reduced Graphene Oxide Nanocomposites with Amplifying Photoacoustic and Photothermal Effects for Cancer Theranostics. *Theranostics* **2016**, *6*, 1043–1052. [\[CrossRef\]](#)
103. Sharker, S.M.; Lee, J.E.; Kim, S.H.; Jeong, J.H.; In, I.; Lee, H.; Park, S.Y. pH triggered in vivo photothermal therapy and fluorescence nanoplatfrom of cancer based on responsive polymer-indocyanine green integrated reduced graphene oxide. *Biomaterials* **2015**, *61*, 229–238. [\[CrossRef\]](#) [\[PubMed\]](#)
104. Mahmoodi Chalbatani, G.; Dana, H.; Gharagouzloo, E.; Grijalvo, S.; Eritja, R.; Logsdon, C.D.; Memari, F.; Miri, S.R.; Rad, M.R.; Marmari, V. Small interfering RNAs (siRNAs) in cancer therapy: A nano-based approach. *Int. J. Nanomed.* **2019**, *14*, 3111–3128. [\[CrossRef\]](#) [\[PubMed\]](#)
105. Zhi, D.; Zhao, Y.; Cui, S.; Chen, H.; Zhang, S. Conjugates of small targeting molecules to non-viral vectors for the mediation of siRNA. *Acta Biomater.* **2016**, *36*, 21–41. [\[CrossRef\]](#)
106. Keles, E.; Song, Y.; Du, D.; Dong, W.-J.; Lin, Y. Recent progress in nanomaterials for gene delivery applications. *Biomater. Sci.* **2016**, *4*, 1291–1309. [\[CrossRef\]](#) [\[PubMed\]](#)
107. Draz, M.S.; Fang, B.A.; Zhang, P.; Hu, Z.; Gu, S.; Weng, K.C.; Gray, J.W.; Chen, F.F. Nanoparticle-mediated systemic delivery of siRNA for treatment of cancers and viral infections. *Theranostics* **2014**, *4*, 872–892. [\[CrossRef\]](#)
108. Zakeri, A.; Kouhbanani, M.A.J.; Beheshtkhoo, N.; Beigi, V.; Mousavi, S.M.; Hashemi, S.A.R.; Karimi Zade, A.; Amani, A.M.; Savardashtaki, A.; Mirzaei, E.; et al. Polyethylenimine-based nanocarriers in co-delivery of drug and gene: A developing horizon. *Nano Rev. Exp.* **2018**, *9*, 1488497. [\[CrossRef\]](#) [\[PubMed\]](#)
109. Feng, L.; Yang, X.; Shi, X.; Tan, X.; Peng, R.; Wang, J.; Liu, Z. Polyethylene glycol and polyethylenimine dual-functionalized nano-graphene oxide for photothermally enhanced gene delivery. *Small* **2013**, *9*, 1989–1997. [\[CrossRef\]](#) [\[PubMed\]](#)
110. Chau, N.D.Q.; Reina, G.; Raya, J.; Vacchi, I.A.; Ménard-Moyon, C.; Nishina, Y.; Bianco, A. Elucidation of siRNA complexation efficiency by graphene oxide and reduced graphene oxide. *Carbon* **2017**, *122*, 643–652. [\[CrossRef\]](#)
111. Kim, H.; Kim, W.J. Photothermally controlled gene delivery by reduced graphene oxide-polyethylenimine nanocomposite. *Small* **2014**, *10*, 117–126. [\[CrossRef\]](#)
112. Kim, H.; Lee, D.; Kim, J.; Kim, T.-i.; Kim, W.J. Photothermally Triggered Cytosolic Drug Delivery via Endosome Disruption Using a Functionalized Reduced Graphene Oxide. *ACS Nano* **2013**, *7*, 6735–6746. [\[CrossRef\]](#)
113. Cao, J.; Chen, Z.; Chi, J.; Sun, Y.; Sun, Y. Recent progress in synergistic chemotherapy and phototherapy by targeted drug delivery systems for cancer treatment. *Artif. Cells Nanomed. Biotechnol.* **2018**, *46*, 817–830. [\[CrossRef\]](#) [\[PubMed\]](#)
114. Biagiotti, G.; Fedeli, S.; Tuci, G.; Luconi, L.; Giambastiani, G.; Brandi, A.; Pisaneschi, F.; Cicchi, S.; Paoli, P. Combined therapies with nanostructured carbon materials: There is room still available at the bottom. *J. Mater. Chem. B* **2018**, *6*, 2022–2035. [\[CrossRef\]](#) [\[PubMed\]](#)
115. Shen, J.-M.; Gao, F.-Y.; Guan, L.-P.; Su, W.; Yang, Y.-J.; Li, Q.-R.; Jin, Z.-C. Graphene oxide-Fe<sub>3</sub>O<sub>4</sub> nanocomposite for combination of dual-drug chemotherapy with photothermal therapy. *RSC Adv.* **2014**, *4*, 18473–18484. [\[CrossRef\]](#)
116. Liu, Z.; Robinson, J.T.; Tabakman, S.M.; Yang, K.; Dai, H. Carbon materials for drug delivery & cancer therapy. *Mater. Today* **2011**, *14*, 316–323. [\[CrossRef\]](#)

117. Oz, Y.; Barras, A.; Sanyal, R.; Boukherroub, R.; Szunerits, S.; Sanyal, A. Functionalization of Reduced Graphene Oxide via Thiol–Maleimide “Click” Chemistry: Facile Fabrication of Targeted Drug Delivery Vehicles. *ACS Appl. Mater. Interfaces* **2017**, *9*, 34194–34203. [[CrossRef](#)] [[PubMed](#)]
118. Hu, Y.; Sun, D.; Ding, J.; Chen, L.; Chen, X. Decorated reduced graphene oxide for photo-chemotherapy. *J. Mater. Chem. B* **2016**, *4*, 929–937. [[CrossRef](#)]
119. Hu, Y.; He, L.; Ding, J.; Sun, D.; Chen, L.; Chen, X. One-pot synthesis of dextran decorated reduced graphene oxide nanoparticles for targeted photo-chemotherapy. *Carbohydr. Polym.* **2016**, *144*, 223–229. [[CrossRef](#)] [[PubMed](#)]
120. Shao, L.; Zhang, R.; Lu, J.; Zhao, C.; Deng, X.; Wu, Y. Mesoporous Silica Coated Polydopamine Functionalized Reduced Graphene Oxide for Synergistic Targeted Chemo-Photothermal Therapy. *ACS Appl. Mater. Interfaces* **2017**, *9*, 1226–1236. [[CrossRef](#)]
121. Hao, L.; Song, H.; Zhan, Z.; Lv, Y. Multifunctional Reduced Graphene Oxide-Based Nanoplatforam for Synergistic Targeted Chemo-Photothermal Therapy. *ACS Appl. Biol. Mater.* **2020**, *3*, 5213–5222. [[CrossRef](#)]
122. Ma, W.; Hu, Y.; Yang, H.; Zhang, Y.; Ding, J.; Chen, L. Au-aided reduced graphene oxide-based nanohybrids for photo-chemotherapy. *Mater. Sci. Eng. C* **2019**, *95*, 256–263. [[CrossRef](#)] [[PubMed](#)]
123. Yang, Y.; Wang, Y.; Zhu, M.; Chen, Y.; Xiao, Y.; Shen, Y.; Xie, A. RGO/AuNR/HA-5FU nanocomposite with multi-stage release behavior and efficient antitumor activity for synergistic therapy. *Biomater. Sci.* **2017**, *5*, 990–1000. [[CrossRef](#)]
124. Song, J.; Yang, X.; Jacobson, O.; Lin, L.; Huang, P.; Niu, G.; Ma, Q.; Chen, X. Sequential Drug Release and Enhanced Photothermal and Photoacoustic Effect of Hybrid Reduced Graphene Oxide-Loaded Ultrasmall Gold Nanorod Vesicles for Cancer Therapy. *ACS Nano* **2015**, *9*, 9199–9209. [[CrossRef](#)]
125. Chen, Y.-W.; Chen, P.-J.; Hu, S.-H.; Chen, I.-W.; Chen, S.-Y. NIR-Triggered Synergic Photo-chemothermal Therapy Delivered by Reduced Graphene Oxide/Carbon/Mesoporous Silica Nanocookies. *Adv. Funct. Mater.* **2014**, *24*, 451–459. [[CrossRef](#)]
126. Vinothini, K.; Rajendran, N.K.; Rajan, M.; Ramu, A.; Marraiki, N.; Elgorban, A.M. A magnetic nanoparticle functionalized reduced graphene oxide-based drug carrier system for a chemo-photodynamic cancer therapy. *New J. Chem.* **2020**, *44*, 5265–5277. [[CrossRef](#)]
127. Kruger, S.; Ilmer, M.; Kobold, S.; Cadilha, B.L.; Endres, S.; Ormanns, S.; Schuebbe, G.; Renz, B.W.; D’Haese, J.G.; Schloesser, H.; et al. Advances in cancer immunotherapy 2019–latest trends. *J. Exp. Clin. Cancer Res.* **2019**, *38*, 268. [[CrossRef](#)]
128. Liu, M.; Guo, F. Recent updates on cancer immunotherapy. *Precis Clin. Med.* **2018**, *1*, 65–74. [[CrossRef](#)]
129. Wieder, T.; Eigentler, T.; Brenner, E.; Röcken, M. Immune checkpoint blockade therapy. *J. Allergy Clin. Immunol.* **2018**, *142*, 1403–1414. [[CrossRef](#)]
130. Joshi, S.; Durden, D.L. Combinatorial Approach to Improve Cancer Immunotherapy: Rational Drug Design Strategy to Simultaneously Hit Multiple Targets to Kill Tumor Cells and to Activate the Immune System. *J. Oncol.* **2019**, *2019*, 5245034. [[CrossRef](#)] [[PubMed](#)]
131. Wang, L.; Wang, M.; Zhou, B.; Zhou, F.; Murray, C.; Towner, R.A.; Smith, N.; Saunders, D.; Xie, G.; Chen, W.R. PEGylated reduced-graphene oxide hybridized with Fe<sub>3</sub>O<sub>4</sub> nanoparticles for cancer photothermal-immunotherapy. *J. Mater. Chem. B* **2019**, *7*, 7406–7414. [[CrossRef](#)] [[PubMed](#)]
132. Yan, M.; Liu, Y.; Zhu, X.; Wang, X.; Liu, L.; Sun, H.; Wang, C.; Kong, D.; Ma, G. Nanoscale Reduced Graphene Oxide-Mediated Photothermal Therapy Together with IDO Inhibition and PD-L1 Blockade Synergistically Promote Antitumor Immunity. *ACS Appl. Mater. Interfaces* **2019**, *11*, 1876–1885. [[CrossRef](#)] [[PubMed](#)]

# The bioactivities of resveratrol and its naturally occurring derivatives on skin

Ming-Hsien Lin<sup>a,1</sup>, Chi-Feng Hung<sup>b,1</sup>, Hsin-Ching Sung<sup>c,d</sup>, Shih-Chun Yang<sup>e</sup>,  
Huang-Ping Yu<sup>f,g</sup>, Jia-You Fang<sup>f,h,i,\*</sup>

<sup>a</sup> Department of Dermatology, Chi Mei Medical Center, Tainan, Taiwan

<sup>b</sup> School of Medicine, Fu Jen Catholic University, Hsinchuang, New Taipei City, Taiwan

<sup>c</sup> Department of Anatomy, College of Medicine, Chang Gung University, Kweishan, Taoyuan, Taiwan

<sup>d</sup> Aesthetic Medical Center, Department of Dermatology, Chang Gung Memorial Hospital, Kweishan, Taoyuan, Taiwan

<sup>e</sup> Department of Cosmetic Science, Providence University, Taichung, Taiwan

<sup>f</sup> Department of Anesthesiology, Chang Gung Memorial Hospital, Kweishan, Taoyuan, Taiwan

<sup>g</sup> School of Medicine, College of Medicine, Chang Gung University, Kweishan, Taoyuan, Taiwan

<sup>h</sup> Pharmaceuticals Laboratory, Graduate Institute of Natural Products, Chang Gung University, Kweishan, Taoyuan, Taiwan

<sup>i</sup> Research Center for Food and Cosmetic Safety and Research Center for Chinese Herbal Medicine, Chang Gung University of Science and Technology, Kweishan, Taoyuan, Taiwan

## Abstract

Resveratrol has been extensively reported as a potential compound to treat some skin disorders, including skin cancer, photoaging, allergy, dermatitis, melanogenesis, and microbial infection. There has been an increasing interest in the discovery of cosmetic application using resveratrol as the active ingredient because of its anti-aging and skin lightening activities. The naturally occurring derivatives of resveratrol also exert a beneficial effect on the skin. There are four groups of resveratrol derivatives, including hydroxylated compounds, methoxylated compounds, glycosides, and oligomers. The major mechanism of resveratrol and its derivatives for attenuating cutaneous neoplasia, photoaging and inflammation, are related with its antioxidative activity to scavenge hydroxyl radical, nitric oxide and superoxide anion. A systematic review was conducted to describe the association between resveratrol-related compounds and their benefits on the skin. Firstly, the chemical classification of resveratrol and its derivatives was introduced. In this review the cases which were treated for different skin conditions by resveratrol and the derivatives were also described. The use of nanocarriers for efficient resveratrol skin delivery is also introduced here. This review summarizes the cutaneous application of resveratrol and the related compounds as observed in the cell-based, animal-based and clinical models. The research data in the present study relates to the management of resveratrol for treating skin disorders and suggesting a way forward to achieve advancement in using it for cosmetic and dermatological purpose.

**Keywords:** Antioxidant, Nanocarriers, Naturally occurring derivatives, Resveratrol, Skin

## 1. Introduction

**P**olyphenols are the phytochemicals containing many bioactive compounds, mostly found in vegetables, fruits and soy [1]. These molecules can be classified into 5 major categories, including hydrobenzoic acids, hydroxycinnamic acids, flavonoids, stilbenes, and lignans [2]. Among these, resveratrol (3,5,4'-trihydroxystilbene) from the

group stilbenes has gained lot of attention as it considered to be beneficial for human health. This compound was first isolated from the roots of *Veratrum grandiflorum* in 1940. It was initially characterized as a phytoalexin, providing defense against the attacks from insects and pathogens [3]. This natural phytoalexin is detected in more than 70 different plants such as grapes and berries, and is also found in human foods and in all kinds of

Received 29 May 2020; revised 19 August 2020; accepted 5 October 2020.  
Available online 15 March 2021.

\* Corresponding author: Pharmaceuticals Laboratory, Graduate Institute of Natural Products, Chang Gung University, 259 Wen-Hwa 1<sup>st</sup> Road, Kweishan, Taoyuan 333, Taiwan. Fax: +886 3 2118236.

E-mail address: fajy@mail.cgu.edu.tw (J.-Y. Fang).

<sup>1</sup> Equal contribution.

<https://doi.org/10.38212/2224-6614.1151>

2224-6614/© 2021 Taiwan Food and Drug Administration. This is an open access article under the CC-BY-NC-ND license (<http://creativecommons.org/licenses/by-nc-nd/4.0/>).



red wines. Resveratrol has attracted a lot of interest in 1992 because of a report demonstrating the cardioprotective activity discovered in red wine [4]. Resveratrol is a stilbenoid possessing two phenols linked by an ethylene bridge (Fig. 1). The chemical structure can be identified as two isomers: *trans*- and *cis*-resveratrol. The *trans* form is found in the plants, while the *cis* form is produced by isomerization of *trans* form and as a result of disintegration of resveratrol oligomers

during the fermentation of grape skin in the presence of ultraviolet (UV) irradiation [5]. The *trans* form generally shows greater bioactivities than the *cis* structure.

Resveratrol can act as an antioxidant to modulate cellular functions. It scavenges hydroxyl radical, nitric oxide and superoxide anion [6]. The prevention and treatment of oxidative stress-related pathological conditions by resveratrol are largely investigated. Polyphenol is reported to prevent or treat cardiovascular disorder, cancer, diabetes

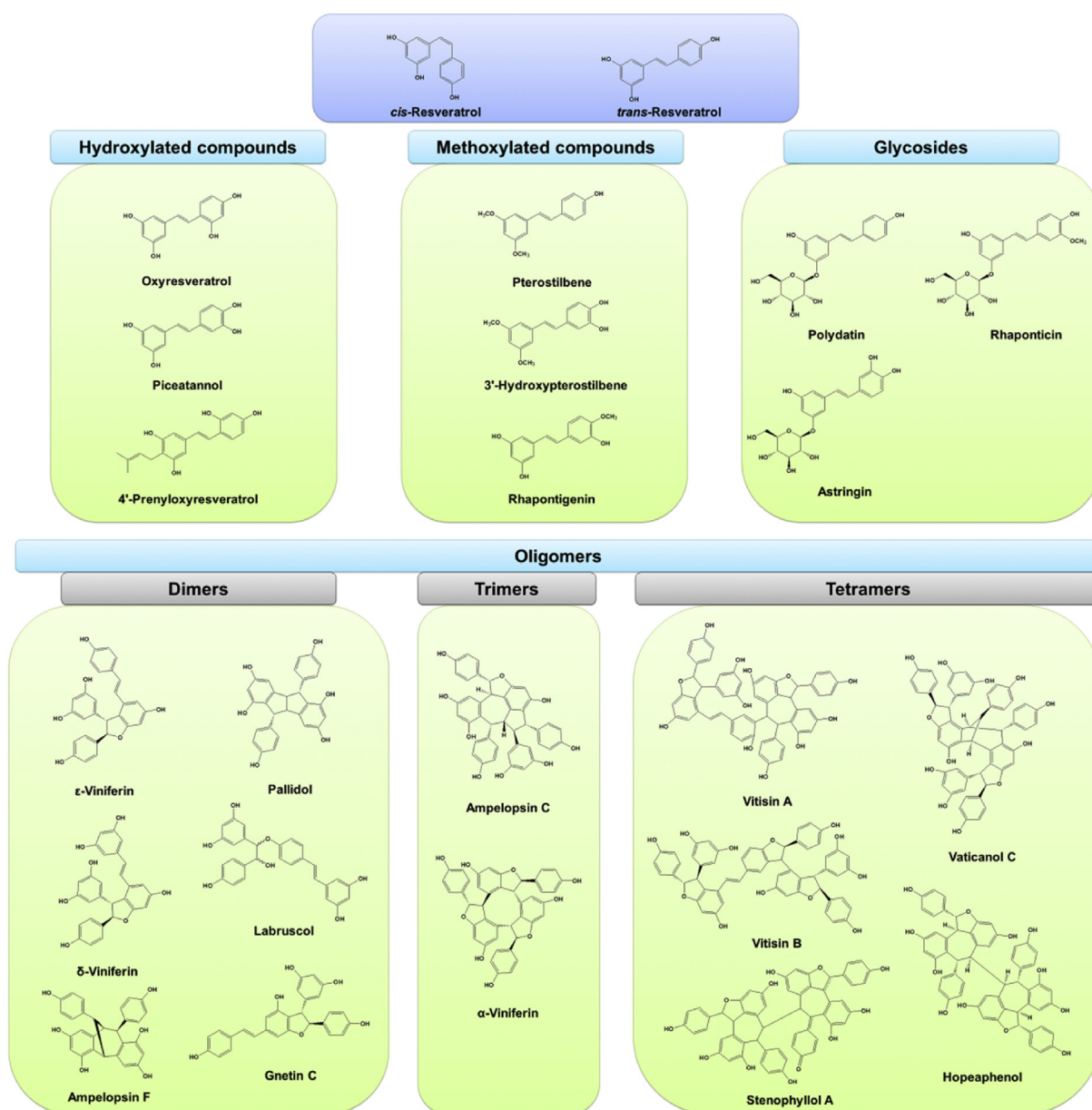


Fig. 1. The chemical structures of resveratrol and its naturally occurring derivatives discussed in this review. There are four groups of resveratrol derivatives, including hydroxylated compounds, methoxylated compounds, glycosides, and oligomers. The major oligomers with bioactivities on skin are dimmers, trimers, and tetramers.

mellitus, microbial infection, aging, and inflammation [7]. Many resveratrol derivatives have been found in natural resources. These derivatives exhibit stilbene skeleton with various substituting moieties. There are four groups of resveratrol derivatives, including hydroxylated compounds, methoxylated compounds, glycosides and oligomers. The resveratrol derivatives also demonstrate biological activities covering wide diversities, such as anticancer, anti-aging, anti-inflammatory and antibacterial effects [8,9]. The predominant problem of resveratrol and its analogs associated with its applicability on disease treatment is the low oral bioavailability, as it gets metabolized via phase II enzymes [10]. In addition to the low bioavailability, resveratrol has very short half-life (8–14 min) and undergoes extensive metabolism in the circulation [11]. Some strategies are employed to overcome the issues related with the low bioavailability. Among these strategies, skin delivery is a useful alternative of oral delivery for treating dermatological diseases. Resveratrol is reported to be readily absorbed through skin [12]. Additionally, the possible skin irritation caused by topical resveratrol is also reported to be low [13,14].

Another approach for increasing the applicability of resveratrol-based therapy is to implement the use of nanomedicine [15]. Because of the low aqueous solubility and instability of resveratrol and its derivatives, nanoencapsulation is verified to be an efficient way to increase its solubility, bioavailability and other biological functions. The incorporation of resveratrol in nanocarriers will help to achieve the aim of enhanced stability, controlled release and tissue or organ targeting and therefore causes less side effects [16]. To increase the skin absorption of resveratrol, some nanoformulations such as liposomes, niosomes, solid lipid nanoparticles (SLNs), nanostructured lipid carriers (NLCs), nanoemulsions, polymeric nanoparticles, and dendrimers are utilized to promote the possible application of topical resveratrol (Fig. 2). Liposomes and niosomes can be classified as the nanovesicles with bilayers and aqueous cores. SLNs, NLCs, and nanoemulsions are the lipid-based nanocarriers with lipids in the cores. Polymer-based nanocarriers include poly(lactic-co-glycolic acid) (PLGA), polylactic acid (PLA), and dendrimers, which are commonly used in biomedical investigation due to their safety and tunable size. In the past few decades a great advancement in the investigation of resveratrol and its derivatives has demonstrated that it holds significant promise for skin use. In this review, we highlight the cutaneous application of resveratrol and its naturally occurring derivatives

for treating skin disorders. We mainly focus on the reports of skin diseases treated by these stilbenoids using different evaluation platforms, including *in vitro*, *ex vivo* and *in vivo* examinations. The promising perspective associated with this emerging application is also discussed in the present study. The development of nanocarriers for improving the skin absorption capability and therapeutic efficacy of topical resveratrol is also introduced in this review article.

## 2. Chemical structure of resveratrol and its derivatives

The chemical structure of resveratrol consists of two phenolic rings which are bonded together by a double styrene bond. Resveratrol is equipped with different functional moieties including aromatic ring, hydroxyl group, and double bond. These groups offer a great potential to be conjugated with other moieties for structure modifications [17]. A large number of natural resveratrol derivatives are broadly investigated for their bioactivities. The structures of these compounds can be divided into hydroxylated derivatives, methoxylated derivatives, glycosides, and oligomers (Fig. 1). Some hydroxylated resveratrol derivatives are derived from natural products. These include oxyresveratrol, piceatannol, and prenyloxyresveratrol. The addition of hydroxyl group in resveratrol structure can increase the therapeutic versatility of the parent compound [18]. Oxyresveratrol can be derived from many plants, showing antioxidant and anti-inflammatory potential [19,20]. Oxyresveratrol has proved to reveal greater inhibition of tyrosine oxidation catalyzed by tyrosinase ( $IC_{50} = 53 \mu M$ ) than that observed in the parent compound ( $IC_{50} > 100 \mu M$ ) [21]. Another hydroxylated resveratrol derivative commonly studied is piceatannol, which possesses an additional hydroxyl group than resveratrol. Piceatannol is reported to have antioxidative, anticancer, immunomodulatory and anti-inflammatory effects [22].

The substitution of hydroxyl group by methoxyl group can increase the structural stability of resveratrol. The methoxyl resveratrol compounds demonstrate better bioavailability than the parent compound because of their higher lipophilicity [23]. The glucuronidation and sulfidation of methoxyl derivatives is less than the parent resveratrol during metabolism, confirming that methoxylation leads to stronger bioactivity response. Pterostilbene is a methoxylated resveratrol isolated from grapes, blueberries and some plant woods [24]. The anticancer, antilipidemic, and cardioprotective properties of pterostilbene are greater than that observed

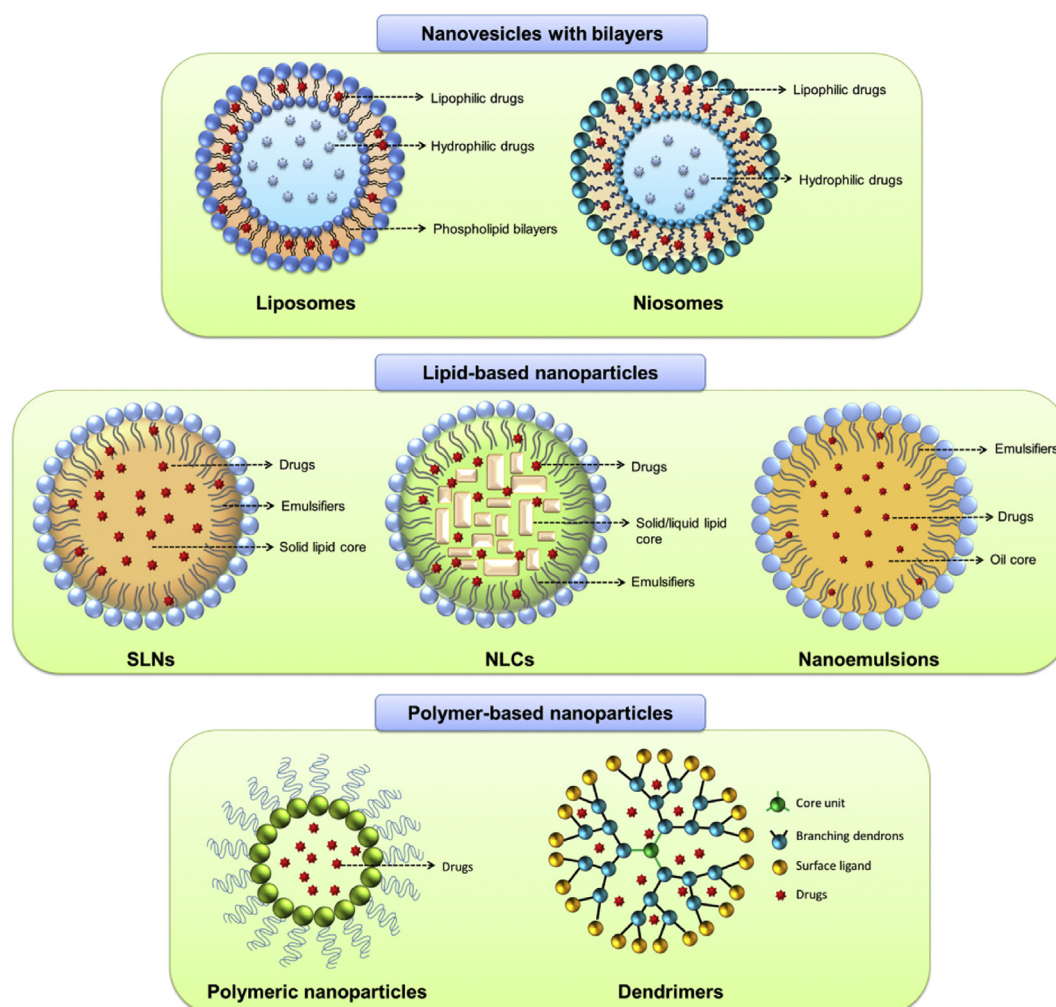


Fig. 2. The structures of nanocarriers used for cutaneous delivery of resveratrol and its naturally occurring derivatives. These nanosystems include liposomes, niosomes, solid lipid nanoparticles (SLNs), nanostructured lipid carriers (NLCs), nanoemulsions, polymeric nanoparticles, and dendrimers. The detailed description of the structures of these nanocarriers is shown in the text.

in resveratrol [25,26]. It is also reported that 3,4',5'-trimethoxystilbene has more potent antioxidant and proapoptotic activities than that seen in resveratrol [18]. Another way to increase resveratrol bioavailability is through glycosylation. Glycosylation enhances resveratrol solubility in aqueous environment, leading to an improvement in its bioavailability [27]. The glycosylation process also prevents enzymatic oxidation which in turn preserves the biological activities and increases the stability. Polydatin, also known as piceid or resveratrol 3-O- $\beta$ -D-glucopyranoside, is the most common resveratrol glycoside examined for bioactivities. This glycoside shows a structure in which a glucose is transferred to the C-3 hydroxyl moiety. Polydatin is abundant in red wine and grape juice. The concentration of polydatin in red wine is even higher than that of aglycone [28]. It is also

detected in hop cones, beer and chocolates. Polydatin appears to be more efficacious than resveratrol in terms of antioxidant capacity because of the reaction linked with its radical form [29].

Resveratrol oligomers are biosynthesized via regioselective oxidative coupling of 2 to 8 monomers [30]. The oligomers can be formed through several self-mergers done by numerous distinct C–C and C–O binding [31]. At least 92 new resveratrol oligomers have been identified in plants in the last decade [32]. These oligomers have been reported to exert anticancer, antidiabetic, antibacterial and cardiovascular-protective effects [33,34]. The biological activities of resveratrol oligomers depend upon their molecular size and stereochemistry. Some studies [35,36] have demonstrated that the addition of increasing number of resveratrol units increase the biological potency and specificity. It is documented

that the scavenging capacity and metal ion chelating ability of the oligomers are higher than that of the monomer by 20- and 1000-fold [33]. The structures of resveratrol derivatives described in this review are illustrated in Fig. 1. Table 1 summarizes the physicochemical properties of these compounds as predicted by silico molecular modeling. Molecular volume, estimated lipophilicity (Alog *P*), hydrogen bond (H-bond) number and total surface polarity were also determined using Discovery Studio 4.1 (Accelrys).

### 3. Skin disorders treated by resveratrol and its derivatives

Skin is the largest and outermost organ, it provides the most accessible way to administer drugs and active ingredients. It is also a semipermeable barrier that protects the body from the external environment and it also prevents water loss. The skin of an average adult human covers a surface region of approximately 2 m<sup>2</sup> and receives one-third of the blood circulation throughout the body. The largest organ of the human body, the skin, is composed of three histological layers: epidermis, dermis, and subcutaneous tissues. The skin delivery

of drugs or active agents is often challenging due to the outer barrier of the skin. This barrier includes the stratum corneum (SC) and tight junction (TJ) [37]. SC, in particular, presents rigid resistance to the topical delivery of drugs. Successful skin delivery of drugs necessitates distinct characteristics regarding molecular size and physicochemical properties. The ideal physicochemical characteristics for facile skin absorption of permeates include low molecular weight (<500 g/mol), moderate lipophilicity (partition coefficient log *P* = 1–3), adequate solubility in both water and oil, as well as have a low melting point [38]. Resveratrol and some of its derivatives fit in these criteria, resulting as the ideal candidate for topical administration to treat skin diseases and other abnormalities.

Skin disorder is a commonly found human illness, affecting about 70% of the population worldwide. It is the fourth leading cause of disability in the world [39]. For the management of skin diseases by drug therapy, topical administration renders an appealing approach as it provides various advantages including, direct nidus targeting, avoidance of systemic toxicity, and non-invasive application [40]. Recent application of resveratrol and its analogs in skin-related diseases includes therapies for skin

Table 1. Anti-skin cancer activity of resveratrol and its derivatives.

| Compound                               | Experimental model  | Cell or animal type        | Outcomes offered by the compound  | Reference |
|--|---|----------------------------|---|-----------|
| Resveratrol                            | <i>In vitro</i> SCC   | Colo-16 cells              | Cell growth inhibition via Wnt signaling  | [68]      |
| Resveratrol                            | <i>In vitro</i> SCC   | Ca3/7 cells                | Synergistic effect with ursolic acid  | [69]      |
| Resveratrol                            | <i>In vivo</i> phorbol ester induction                              | ICR mouse                  | Tumor suppression by COX-2 inhibition   | [71]      |
| Resveratrol                            | <i>In vivo</i> phorbol ester induction                              | ICR mouse                  | Tumor suppression via NF-κB and AP-1 pathways                                     | [72]      |
| Resveratrol                            | <i>In vivo</i> DMBA induction                                       | Albino mouse               | Tumor suppression via PI3K and protein kinase B regulation                        | [73]      |
| Resveratrol                            | <i>In vitro</i> melanoma  | B16–F10 and A375 cells     | Apoptosis via PI3K and protein kinase B regulation                                | [75]      |
| Resveratrol                            | <i>In vitro in vivo</i> melanoma                                    | DM738 and DM443 cells      | Synergistic effect with temozolomide  | [76]      |
| ε-Viniferin and pallidol               | <i>In vitro</i> melanoma  | HT-144 and SKMEL-28 cells  | ε-Viniferin displayed a greater melanoma inhibition than resveratrol and pallidol | [77]      |
| ε-Viniferin and labruscol              | <i>In vitro</i> melanoma  | HT-144 and SKMEL-28 cells  | Melanoma inhibition via cell cycle blocking in S phase                            | [78]      |
| Resveratrol in liposomes               | <i>In vitro</i> melanoma  | SKMEL-28 and Colo-38 cells | Ultradeformable liposomes enhanced cytotoxicity and percutaneous permeation       | [80]      |
| Resveratrol in polymeric nanoparticles | <i>In vitro</i> melanoma and <i>in vivo</i> phorbol ester induction | B16–F10 cells and mouse    | Nanoparticles enhanced cytotoxicity and <i>in vivo</i> tumor incidence            | [81]      |

AP-1; activator protein-1; COX-2, cyclooxygenase-2; DMBA, 7,12-dimethylbenz[a]anthracene; NF-κB, nuclear factor-κB; PI3K, phosphatidylinositol-3-kinase; SCC, squamous cell carcinoma.



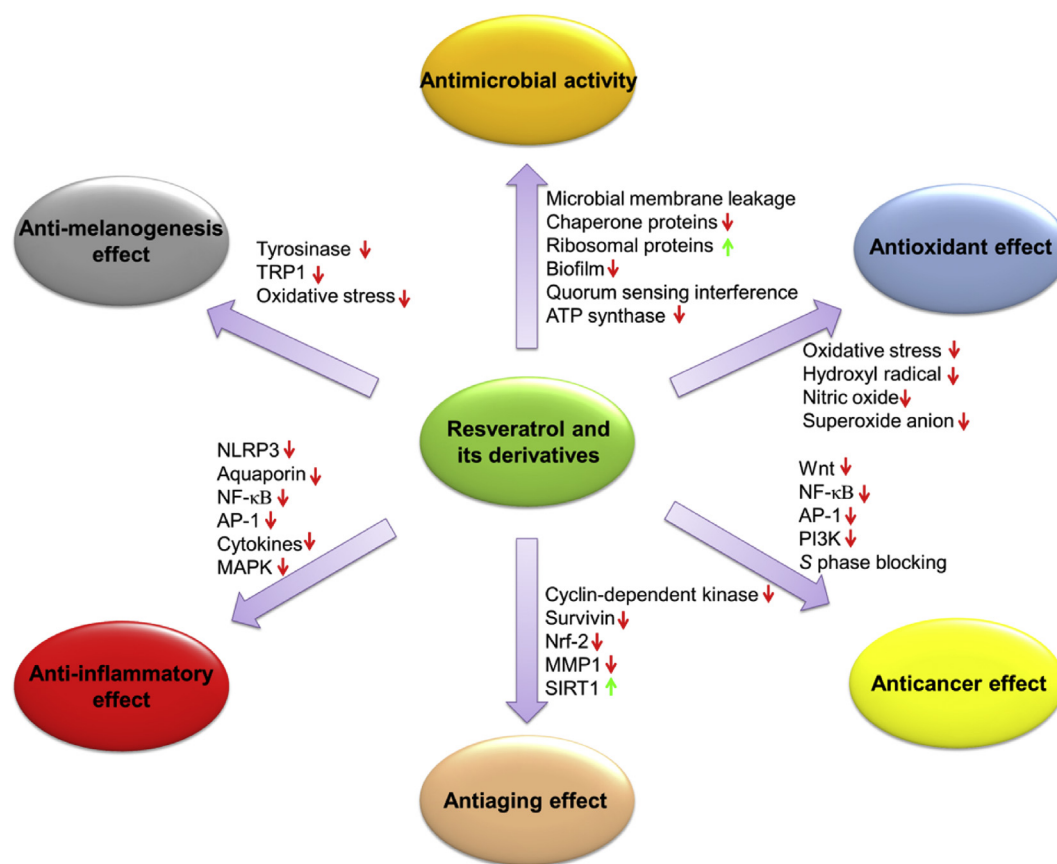


Fig. 3. The skin diseases that can be ameliorated by resveratrol and its naturally occurring derivatives in cell- or animal-based studies. The possible signaling pathways for the treatment of these skin disorders are summarized in this figure. Resveratrol and its analogs demonstrate antioxidant, anticancer, antiaging, anti-inflammatory, anti-melanogenesis, and antimicrobial impacts for skin application.

cancers, photoaging, intrinsic aging, cutaneous inflammation, melanogenesis, and microbial infection (Fig. 3). The possible mechanisms involving in the bioactivity of resveratrol and its analogs are also illustrated in this figure. The use of these active compounds can ameliorate the symptoms of the skin diseases. Some therapies based on resveratrol properties have been approved for clinical use or are under clinical trial for preventive or therapeutic use. In addition, some resveratrol or the derivatives are approved to manage various skin diseases in cell-based and animal studies. Some of these resveratrol-related compounds are included in topical formulations for cosmetic purposes [41].

Skin cancer is the most common form of cancer, globally accounting for at least 40% of cancer cases [42]. There are three major types of cutaneous tumors, including basal cell carcinoma (BCC), squamous cell carcinoma (SCC) and melanoma. The first two can be classified as non-melanoma skin cancers (NMSC). Mohs micrographic surgery (Mohs surgery) is a technique used to remove the cancer with the least amount of surrounding tissue and the edges are

checked immediately to see if any tumor is detected. For low-risk diseases, radiation therapy, topical chemotherapy and cryotherapy can provide adequate control of the disease [43]. The topical chemotherapy is also used for the prevention of tumor recurrence after surgical removal. Some polyphenolic compounds such as phenolic acids, flavonoids, stilbenes, and lignans have proved to be effective for mitigating the tumor growth of NMSC and melanoma [44]. These compounds act on several biomolecular pathways including, cell division cycle arrest, autophagy, and apoptosis. Cutaneous aging can be divided into photoaging and chronological aging. Photoaging is activated via the human skin damage attributable to repeated UV exposure from sunlight. Exposure to UV radiation from the sun is the main risk factor for causing skin cancer [45]. UV elicits both acute and chronic adverse effects on the skin. These include sunburn, photosensitivity, inflammation, immunosuppression, and photocarcinogenesis [46]. UV exposure of the skin creates reactive oxygen species (ROS), leading to the massive infiltration of immune cells such as neutrophils and macrophages

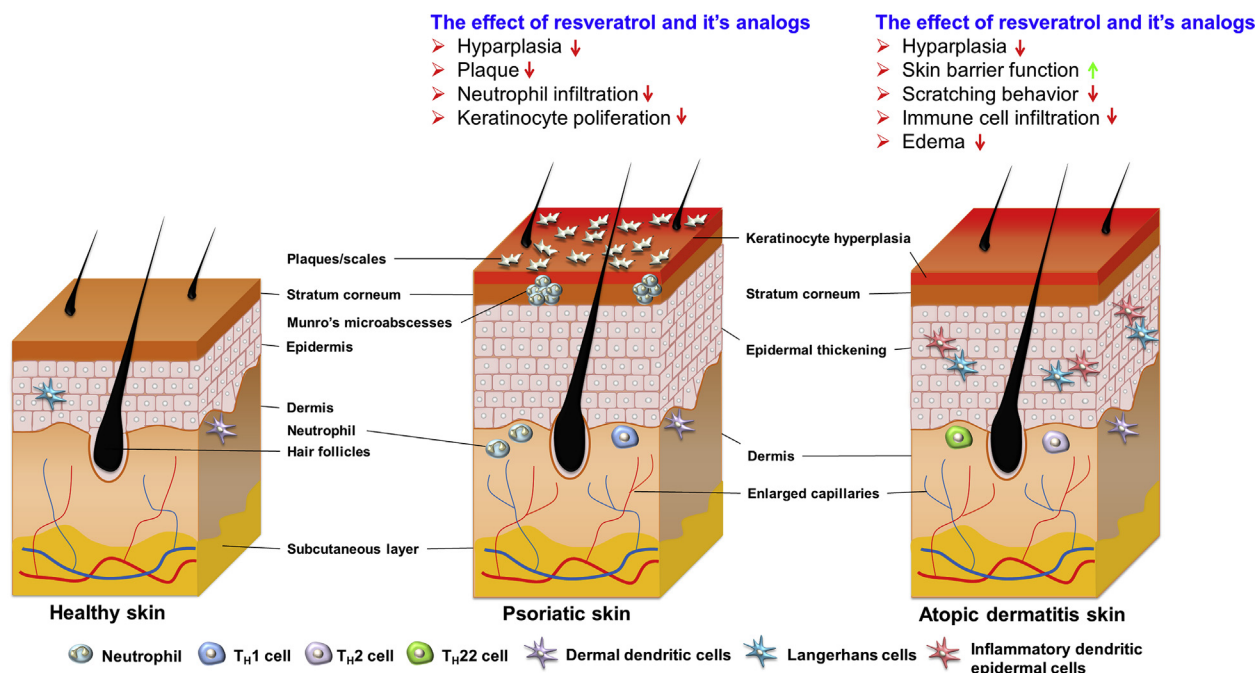


Fig. 4. The morphologies and features of psoriasis and atopic dermatitis skins. Typical histologic features of psoriasis includes epidermal hyperplasia with elongated rete ridges, a less discrete epidermal granular layer, parakeratosis, and leukocyte infiltration of the viable skin. Dermatitis is an inflammatory skin disease characterized by presence of erythema, edema, vesicles, and lichenification. The effects of resveratrol and its analogs on psoriasis and dermatitis for ameliorating the signs and symptoms are summarized in this figure.

in viable skin cells [47]. Due to its antioxidant property, resveratrol and its derivatives have the capability to ameliorate cutaneous photoaging.

Inflammatory skin diseases are the most common problem in dermatology. They can range from occasional rashes accompanied by skin itching and redness, to chronic conditions such as psoriasis, dermatitis, and rosacea. Both psoriasis and atopic dermatitis (AD) are autoimmune diseases affecting skin. Psoriasis, a chronic inflammatory disease of the skin, affects approximately 125 million people globally [48]. Clinically, psoriasis is characterized by red plaques with silver or white multilayered scales with a thickened acanthotic epidermis in patients who are markedly demarcated from adjacent non-lesional skin (Fig. 4) and its lesions often occur at sites of epidermal trauma, such as the elbows and knees, the back, and the trunk, but it can appear anywhere on the body, which severely impairs patients' quality of life [49]. Typical histologic features of psoriasis includes epidermal hyperplasia with elongated rete ridges, a less discrete epidermal granular layer, parakeratosis, and leukocyte infiltration of the viable skin. More than 80% of patients show a mild-to-moderate level of severity [50], which can be controlled by topical therapy. However, conventional topical-application treatment is usually time-consuming with incomplete lesion resolution and some adverse effects. The

development of new topically applied agents is definitely needed, especially the ones discovered from natural resources [51]. Some natural compounds are useful for treating psoriasis because of their antioxidant, anti-inflammatory and apoptotic activities [52].

AD is an inflammatory skin disease characterized by presence of erythema, edema, vesicles, and lichenification (Fig. 4). The pathogenesis of AD involves dysregulation in the inflammatory process and a change in response to antigens. The prevalence of AD has increased 3-fold over the past 30 years because of environmental risks [53]. It is a common skin disorder affecting 10–25% of children and 2–10% of adults [54]. The anti-AD drugs such as coal tar, doxepin, calcineurin inhibitors and steroids are reported to cause skin itching and stinging sensation [55]. The excessive use of topically applied calcineurin inhibitors may elicit systemic absorption, therefore, causing toxicity and increasing the malignancy risk. Corticosteroids are usually accompanied by side effects such as skin thinning, striae, corticophobia and also demonstrate insufficient clinical response [56]. The development of new agents for AD treatment is urgently needed to minimize these side effects and enhance the efficacy. Several investigations assessing anti-AD therapy based on natural sources have revealed some potential activities in this area [57]. There are

two important features associated with AD that make it difficult to treat. Firstly, it compromises the skin barrier and secondly, increases the risk of cutaneous infection. As the integrity of barrier is reduced this leads to *Staphylococcus aureus* invasion and exacerbates eczema [58]. More than 90% of AD patients are colonized with *S. aureus* [59]. The bacterial population increases in the skin involving lesions of AD and chronic wounds. Hence it plays a critical role in infection-induced inflammation and cutaneous disease progression [60]. Polyphenols including resveratrol-related compounds can be used to treat cutaneous and subcutaneous infections caused by bacteria and fungi [61,62].

Resveratrol and its derivatives are also investigated for skin hyperpigmentation treatment. These compounds can act as skin lightening agents to improve skin aesthetics. Hyperpigmentation occurs when the skin releases more melanin content. Melanin is the pigment which gives skin its color. This can make spots or patches of skin appear darker than surrounding areas. Hyperpigmentation can occur after an injury or due to skin inflammation caused during cuts, burns, acne, and lupus. Excessive sun exposure and melasma can also cause hyperpigmentation [63]. Tyrosinase is regarded as a key enzyme implicated in the metabolism of melanin in melanocytes and its inhibitors have become increasingly important in medicinal and cosmetic products in relation to hyperpigmentation. Resveratrol has been already proved as a tyrosinase inhibitor which can reduce the cutaneous pigmentation [64].

#### 4. Resveratrol and its derivatives as the active agents for skin-related disease therapy

The following review describes the different therapeutic and cosmetic approaches of resveratrol and its analogs on skin. These include the cell-based study, animal-based study and clinical human trial. The pharmacodynamics outcome of these compounds are the main evaluation platform used to define the preventive or therapeutic effects in our present description.

##### 4.1. Skin cancers

Chemotherapy or chemoprevention by natural compounds is appreciated as a new strategy in the management of carcinomas including skin cancers. The anticancer ability of resveratrol is verified by *in vitro* and *in vivo* evaluations. The tumor inhibition by resveratrol involves its antioxidant, anti-inflammatory, antiproliferative and pro-apoptotic activities

[65]. Resveratrol can suppress carcinogenesis at different stages, including initiation, promotion, and progression [66]. SCC is a common form of skin cancer which develops in the squamous cells that make up the middle and outer layers of the skin. It is usually found in areas of the skin damaged by excessive UV exposure from the sun. Surgery is the first choice for treating SCC, whereas the adjuvant therapy by chemotherapy can improve the survival rate and life's quality. Wnt/ $\beta$ -catenin signaling is activated in the process of development of SCC [67]. The effect of resveratrol on cell growth and how it impacts Wnt signaling of SCC Colo-16 cells was investigated by Liu et al. [68]. The concentration of resveratrol that inhibited 50% of SCC cell growth ( $IC_{50}$ ) was 114  $\mu$ M. It was reported that Wnt2 expression was downregulated accompanied by increased expression of Wnt inhibitor Axin2. It was suggested that the inactivation of Wnt pathway was the main target of resveratrol associated with restraining SCC growth. Resveratrol can also be used as an enhancer to synergize anti-SCC activity of ursolic acid [69]. Ursolic acid is approved as an efficient natural compound to induce death of skin cancer cell lines via AMP-activated protein kinase [70]. Resveratrol if used at a concentration of 25  $\mu$ M enhances antiproliferative effects of ursolic acid in the Ca3/7 cell lines in a dose-dependent fashion. The  $IC_{50}$  of ursolic acid could be reduced by 2.3-fold after the co-treatment with resveratrol at 100  $\mu$ M.

An earlier study [71] has investigated the impact of resveratrol on phorbol ester-induced skin cancer in mouse. Phorbol ester can be used as an activator to induce NMSC-like model. Aberrant cyclooxygenase (COX)-2 expression is an indicator of tumor promotion. It was seen that the topical delivery of resveratrol at 1  $\mu$ mol, 30 mins prior to phorbol ester treatment decreased COX-2 level in mouse skin. Phorbol ester intervention resulted in the induction of I $\kappa$ B kinase activity in skin, which could be abolished by topical application of resveratrol. Besides I $\kappa$ B kinase, the COX-2 upregulation in the skin cancer is activated via nuclear factor (NF)- $\kappa$ B that is regulated by mitogen-activated protein kinase (MAPK). Kundu et al. [72] found that topical resveratrol inhibited NF- $\kappa$ B and activator protein (AP)-1 activities in phorbol ester-induced skin tumor. Both signal pathways could be the prime targets of resveratrol to inhibit skin cancer. In a study, the chemopreventive effect of topical resveratrol was also examined in the 7,12-dimethylbenz[a]anthracene (DMBA)-induced mouse skin tumor [73]. Topical resveratrol treatment was given to mice 1 hour before initiating DMBA treatment for 28 weeks. The induction of first tumor was

detected after 52 days with regard to the vehicle control. The onset could be delayed by 73 to 79 days after receiving resveratrol at a dosage of 25 and 50  $\mu\text{M}$  respectively. Resveratrol administration at 25  $\mu\text{M}$  and 50  $\mu\text{M}$  led to a reduction in tumor volume by 51% and 65% respectively. This inhibition by resveratrol was confirmed due to the involvement of phosphatidylinositol-3-kinase (PI3K) and protein kinase B.

Melanoma is a type of skin cancer characterized by an aggressive pathogenesis and poor response to therapy. Cutaneous melanoma originates from genetically altered melanocytes in the epidermal basal layer. It is reported that some polyphenols such as curcumin, quercetin, coumarin and resveratrol display antioxidant, anti-inflammatory and antiproliferative efficacies to inhibit melanoma [74]. In a cell-based assay [75], murine melanoma (B16–F10) and human melanoma (A375) cell lines were used as the models to examine the effect of resveratrol on melanoma. Resveratrol at a dose of 100  $\mu\text{M}$  increases apoptosis of both cell lines by 4–6-fold as compared to that of the control. The autophagy-related proteins including Beclin 1 and microtubule-associated protein 1A/1B-light chain 3 (LC3)-II/I were upregulated after resveratrol treatment. Phosphorylated PI3K and protein kinase B were also reduced by this compound. Since autophagy is vital for the growth of malignancies, the results have led to the development of targeted melanoma treatment by resveratrol. Osmond et al. [76] conducted *in vitro* and *in vivo* cytotoxicity of resveratrol against melanoma cell lines, DM738 and DM443. Resveratrol treatment at doses of <50  $\mu\text{M}$  manifested a dose-dependent cytotoxicity, whereas the doses between 50  $\mu\text{M}$  and 100  $\mu\text{M}$  showed no additional effect. It is demonstrated that resveratrol also significantly enhances cytotoxicity of temozolomide, an anti-melanoma drug. The mouse with subcutaneous DM738 xenograft was treated with resveratrol (90 mg/kg) 2 days prior to initiating temozolomide treatment. The results showed that cyclin B and D1 were reduced by resveratrol after a 2-day treatment.

$\epsilon$ -Viniferin and pallidol are the dimers of resveratrol. Nivelle et al. [77] found that pallidol revealed a comparable inhibition of the growth of melanoma cell lines, namely HT-144 and SKMEL-28 which are similar to that observed with resveratrol treatment. The dehydrodimer  $\epsilon$ -viniferin showed considerably higher inhibition than resveratrol and pallidol. The  $\text{IC}_{50}$  of  $\epsilon$ -viniferin against HT-144 and SKMEL-28

was 18  $\mu\text{M}$  and 16  $\mu\text{M}$  respectively which was lower than that of resveratrol and pallidol (>100  $\mu\text{M}$ ). The mechanisms behind anti-melanoma activity of  $\epsilon$ -viniferin were further explored in the cell-based study [78]. Another dimer, labruscol, was also employed for comparison. The  $\text{IC}_{50}$  of  $\epsilon$ -viniferin and labruscol against HT-144 metastatic cells in the presence of fetal bovine serum was 65  $\mu\text{M}$  and 54  $\mu\text{M}$  respectively. Labruscol induced more necrosis (40%) in HT-144 metastatic cells as compared to  $\epsilon$ -viniferin (25%) and resveratrol (18%). All these compounds blocked cell cycle of melanoma during S phase by modulating cell cycle regulators such as cyclin A, E, and D1. It was reported that this effect demonstrated no cytotoxicity on normal dermal fibroblasts.

Nanocarriers are used to load resveratrol for enhanced skin delivery to treat skin cancers. Ultra-deformable liposomes are forms of nano-sized vesicles consisting of phospholipids and edge activator, capable of increasing the flexibility of liposomal bilayers to squeeze into SC [79]. Cosco et al. [80] prepared the ultradeformable liposomes with a mean diameter of <120 nm. The co-entrapment of resveratrol and 5-fluorouracil in ultradeformable liposomes increases the cytotoxicity more against SKMEL-28 and Colo-38 cells than that observed with free compounds and single compounds in liposomes. This nanoformulation arrested cell proliferation in G1/S phase. The skin permeation of resveratrol and 5-fluorouracil across human epidermis was increased by 8.3- and 6.2-fold respectively after liposomal encapsulation. Bano et al. [81] developed polymeric nanoparticles made with poly (N-isopropylacrylamide) (PNIPAAm)-polyethylene glycol (PEG) encapsulated with resveratrol for evaluating inhibitory efficacy on skin cancer. The nanoparticle size was around 100 nm with a high resveratrol encapsulation percentage of >80%. The loading of resveratrol into nanoparticles decreased B16–F10 cell viability from 60% to 40%. In the promotion phase of *in vivo* skin cancer induced by phorbol ester, a significant reduction was found in tumor incidence and tumor burden in mice which were pretreated with nanoparticles. The percentage of mice with tumors was 82% after intervention. This percentage was reduced to 19% and 6% by treatment with free resveratrol and resveratrol-loaded nanoparticles respectively. The nanocarriers upregulated Bax expression, leading to the apoptosis of the phorbol ester-induced tumor. The anti-skin cancer activity of resveratrol and its analogs is summarized in Table 1.



#### 4.2. Extrinsic aging and photoaging

Skin aging is divided into intrinsic and extrinsic modes. Extrinsic and intrinsic aging is caused by environmental and genetic factors respectively [82]. Extrinsic skin aging can be induced by UV exposure, smoking, air pollution and poor nutrition. Intrinsic aging, also named as chronological aging, is a slow biological process characterized by fine wrinkling, fragility, reduced elasticity, loss of skin tone and mottled pigmentation [83]. Polyphenols can be used as antioxidants to treat skin aging because of the capability to donate hydrogen atoms which helps to neutralize free radical species produced during oxidative stress [84]. The free radicals are formed under the influence of UV exposure, toxins, and smoking. Sirtuin is an enzyme that is associated with regeneration, vitality, and resistance of the mammalian cells. The activity of sirtuin decreases with the increase in age [85]. Resveratrol can slow the process of skin aging due its role as a sirtuin activator and free radical scavenger [86]. Topical delivery is beneficial to replenish resveratrol in skin, resulting in the efficient prevention of skin aging and damage by oxidative stress. Alonso et al. [87] compared the antioxidative effect of five polyphenols on skin after their topical application. The polyphenols included epicatechin, quercetin, rutin, trolox and resveratrol. Polyphenols were extracted from the pig skin treated by topically applied polyphenols using Franz cell assembly. 1,1-Diphenyl-2-picrylhydrazyl (DPPH) assay was used to determine antioxidant activity. Among the polyphenols, rutin and resveratrol were observed to be more favorable for inhibiting DPPH. Resveratrol deposition in epidermis was  $2.02 \text{ nmol/cm}^2$ , which was much higher than rutin ( $0.66 \text{ nmol/cm}^2$ ), indicating a satisfactory percutaneous absorption of resveratrol. The skin absorption of resveratrol was further investigated in the *in vivo* human model [88]. Six volunteers who participated in this study received topically applied resveratrol ( $500 \text{ } \mu\text{g/cm}^2$ ) on the forearm surface. The results showed that the major amount (77%) of permeated compound was located in the upper SC layer. The DPPH inhibition caused by resveratrol which was deposited in SC layer was 28%.

The UV radiation is the main etiological factor which elicits premature skin aging. It is also the major cause behind skin cancer [89]. To prove the photoprotective properties of resveratrol on skin, Park and Lee [90] treated UVB-irradiated HaCaT keratinocytes by resveratrol. It was observed that pretreatment by resveratrol at the doses of 5–100  $\mu\text{M}$  markedly increased keratinocyte survival in the

presence of UVB. The ROS production was also attenuated by resveratrol pretreatment. The activation of caspase-3 and -8 was inhibited in resveratrol-treated (100  $\mu\text{M}$ ) HaCaT keratinocytes by one and a half times. In an *in vivo* hairless mouse model, topical resveratrol (10  $\mu\text{mol}$  per mouse) was applied on the dorsal skin exposed to UVB at  $180 \text{ mJ/cm}^2$  [91]. The findings demonstrated that UVB increased skin thickness (2-fold), cyclin-dependent kinase-2 (cdk) (3-fold), cdk-4 (3 fold), cdk-6 (4-fold), cyclin D1 (2-fold), and cyclin D2 (2-fold) in epidermis. Resveratrol could downregulate these cell cycle regulatory proteins, suggesting the antiproliferative activity of resveratrol on photoaged skin. Aziz et al. [92] further verified the primary role of survivin, the inhibitor of apoptosis protein family, on resveratrol-mediated protection from UVB in hairless mouse model. It was seen that UVB light significantly upregulated survivin expression in skin. In the UVB-exposed mouse topical pretreatment of resveratrol, at a dose of 10  $\mu\text{mol}$ , resulted in the inhibition of survivin protein by two-third.

Pterostilbene is a methoxylated resveratrol with potent antioxidative activity. The inhibitory effect of pterostilbene on UVB-induced photodamage in keratinocytes was investigated in a study [93]. HaCaT keratinocytes were pretreated with pterostilbene at a dose of 5 or 10  $\mu\text{M}$  prior to UVB irradiation ( $300 \text{ mJ/cm}^2$ ). Pterostilbene attenuated UVB-evoked cell death and ROS generation. The nuclear translocation of nuclear factor erythroid 2-related factor 2 (Nrf2) and the Nrf2-dependent antioxidant enzymes were increased after pterostilbene intervention. Nrf2 pathway exerts a critical role in promoting defense against oxidative stress [94]. SKH-1 hairless mouse was used as the *in vivo* model to test whether pterostilbene was effective for treating UVB-induced skin disruption [95]. Topical application of pterostilbene demonstrated a dramatic decrease in UVB-evoked skin tumorigenesis (90% tumor-free animals) after 40 weeks, whereas resveratrol showed no such effect (0%). The results highlighted that pterostilbene could suppress oxidative damage caused by UVB but resveratrol is unable to do so. Pterostilbene maintained a high level (150  $\mu\text{mol/kg}$ ) in the skin after a 6-h topical administration at a dose of 1  $\mu\text{mol/cm}^2$ . Polydatin is a resveratrol glycoside displaying strong antioxidative activities. He et al. [96] demonstrated that polydatin protects the skin from UVB-induced damage as seen in both *in vitro* and *in vivo* experiments. There was no cytotoxicity noticed in HaCaT cells, treated with polydatin at a dose up to 100  $\mu\text{g/ml}$ . UVB exposure at  $30 \text{ mJ/cm}^2$  led to 43% HaCaT cell death compared to that of the control. Polydatin

reduced the cell death and ROS production elicited by UVB in a dose-dependent manner (0–80  $\mu\text{g/ml}$ ). The findings of the study confirmed that UVB irradiation (360  $\text{mJ/cm}^2$ ) on nude mouse skin resulted in desquamation and erythema and topical delivery of polydatin (10  $\text{mg/ml}$ ) could reverse these symptoms. The results showed that the epidermal thickness is increased by UVB (87  $\mu\text{m}$ ) and decreased by using polydatin (38  $\mu\text{m}$ ). In addition to the role of antioxidant, polydatin acted as a sunscreen to retard UVB-induced photoaging. Matrix metalloproteinase (MMP)-1 plays a major role and is involved at multiple stages of skin photoaging [97]. Some resveratrol oligomers derived from *Vatica albiramis* have proved to exert the ability to arrest MMP-1 in dermal fibroblasts [36]. IL-1 $\beta$  initiated MMP-1 production from human foreskin fibroblasts. Three oligomers including (–)-hopeaphenol, vaticanol C and stenophyllol C exhibited significant inhibition on MMP-1. These oligomers were tetramers. Resveratrol dimers had negligible or very less activity associated with the suppression of MMP-1 release.

Like the ultradeformable liposomes, transfersomes and ethosomes are elastic nanovesicles used for improving skin delivery of the bioactive agents [98]. Transfersomes consist of surfactants such as polysorbate 80, sodium cholate, and sodium deoxycholate which helps to increase the phospholipid bilayer flexibility. Nanovesicles are composed of phospholipids, water and ethanol, they form ethosomes which interacts with SC layer. Scognamiglio et al. [99] prepared transfersomes and ethosomes for loading resveratrol. The prepared nanovesicles showed mean diameters between 83 and 116 nm with a high resveratrol encapsulation of >70%.  $\text{H}_2\text{O}_2$  treatment on HaCaT cells increases ROS production. This elevation was inhibited by polysorbate 80-incorporated (62%), sodium cholate-incorporated (62%), and sodium deoxycholate-incorporated (48%) transfersomes loaded with 2  $\mu\text{g/ml}$  resveratrol. It was seen that the ROS reduction by ethosomes was only 23%. The *in vitro* study involving pig ear skin permeation demonstrated that only ethosomes could increase resveratrol delivery across the skin. Wu et al. [100] also prepared resveratrol-loaded transfersomes which were incorporated with polysorbate 20, polysorbate 80, or Plantacare 1200 UP. The vesicle size ranged between 43 and 81 nm. The antioxidant activity as determined by DPPH and 2,2'-azino-bis(3-ethylbenz thiazoline-6-sulphonic acid) (ABTS) assays revealed a comparable inhibition associated with free resveratrol. However, the *in vitro* permeation study showed that polysorbate 20-

incorporated transfersomes enhanced resveratrol delivery by 28%. Lipid nanocarriers, such as SLNs, NLCs, and nanoemulsions, appear to be suitable as drug-carrier systems due to their very low cytotoxicity as compared to polymeric nanoparticles [101]. The predominant difference among SLNs, NLCs and nanoemulsions is related to the composition of the inner core. SLNs are particles that are made from crystalline solid lipids, whereas NLCs are composed of a solid lipid matrix with a certain content of liquid lipid; they are a more advanced generation of SLNs. Nanoemulsions are nanocarriers with neat liquid oil in the inner phase. Gokce et al. [102] in a study entrapped resveratrol into SLNs and NLCs to examine its antioxidative effect and skin absorption capacity. The average size of SLNs and NLCs was 287 and 111 nm respectively. The smaller size of NLCs with a reduced negative surface charge favored endocytosis into dermal fibroblasts, resulting in less ROS production than that observed in SLNs. In the *in vitro* study, rat skin absorption indicated a higher resveratrol deposition in epidermis by application of NLCs (1.99  $\mu\text{g/cm}^2$ ) than that seen with SLNs (1.55  $\mu\text{g/cm}^2$ ).

#### 4.3. Intrinsic aging and cosmetic use

Intrinsic skin aging is caused by senescence and other intrinsic factors which leads to skin atrophy. Presence of wrinkles, collagen loss, decreased hydration and skin thinning are the symptoms commonly observed in the aged skin. Oxidative stress is strongly associated with skin aging because of the progressive accumulation of ROS in skin, as age increases [103]. Natural antioxidants are used in the production of pharmaceutical or cosmetic formulations with the aim of delaying the skin aging process and ameliorating skin aesthetics [104]. *Gnetum gnemon* (melinjo) is an arboreal dioecious plant extensively cultivated in South Asia. The seeds of this plant are abundant in resveratrol and its glycosides and dimers [105]. Watanabe et al. [106] evaluated the protective effects of melinjo seed extract on age-related skin pathology as demonstrated in mouse. Superoxide dismutase 1 (SOD1) is an enzyme that is essential for the maintenance of skin homeostasis. The seed extract or resveratrol was orally administered to *Sod*<sup>-/-</sup> mice daily for 12 weeks. The treatment that was conducted by using extract or resveratrol reversed skin thinning associated with increased oxidative damage in *Sod*<sup>-/-</sup> mice. The gene expression of *Sirt1* in skin was upregulated by the usage of extract and resveratrol. The *in vitro*

experiment also verified that resveratrol could elevate the viability of *Sod*<sup>-/-</sup> fibroblasts.

Resveratrol and its derivatives showed beneficial outcomes when added into the skincare products. Some clinical trials are being conducted to test the improvement associated with skin aging by resveratrol-related products. A clinical study was carried out in 20 subjects over a period of 6 weeks, receiving topically applied resveratrol (0.007%)-containing oil-in-water cold cream [107]. The skin hydration was assessed in both the groups (with or without resveratrol intervention). The results showed that the hydration level was increased up to 2-fold as compared to the vehicle control after resveratrol was applied for 4 weeks. Resveratrol permeated into the epidermis to supplement the lipids and protective layers, increasing the moisturizing and tightening characteristics. Another clinical study was performed among 50 volunteers who received dietary supplement of grape fruit extract, rich in resveratrol and procyanidins for estimating skin condition [108]. It is important to note that 133 mg of extract contains 8 mg of resveratrol and 14.63 mg of procyanidins. The study results showed that skin moisturization and elasticity had been improved by the dietary supplementation as measured by bioengineering techniques, while the skin roughness and wrinkling also reduced. The antioxidant capacity detected by oxyadsorbent assay showed a significant improvement in the treated group than that of the placebo group.

Pterostilbene (0.4%) loaded in cream was topically applied for 8 weeks on 38 volunteers in an open-label, single-arm study [109]. The skin hydration, brightness, elasticity were examined by bioengineering methods to achieve quantifiable results. The findings showed that pterostilbene cream successfully reduced wrinkles and fine lines. The skin moisturization and elasticity were also improved with no demonstration of adverse effects. A significant improvement in skin fairness was observed according to the subjective assessment conducted by dermatologists. Lipid-based nanoparticles such as SLNs, NLCs, and nanoemulsions have proved to exert occlusive effect, enhancing skin hydration [110]. Montenegro et al. [111] evaluated the capability of cutaneous hydration as increased by SLNs, NLCs and nanoemulsions, encapsulated with 1% resveratrol. The nanoparticle diameters of SLNs, NLCs and nanoemulsions were 46, 26, and 27 nm respectively. The prepared nanocarriers were incorporated in the hydrogels to be applied on the forearm of 12 healthy subjects for one week. An increase in skin hydration was detected for all nanocarriers with a tendency of SLNs > NLCs > nanoemulsions. This could be due to

the higher degree of crystallinity seen in SLNs than that observed in the other nanosystems which led to a better occlusion effect. The inhibitory effect of resveratrol and its natural derivatives on extrinsic and intrinsic aging is listed in Table 2.

#### 4.4. Skin inflammation and autoimmune diseases

Skin appears to act not only as the sensor during stressful conditions (toxin, pathogen, UV), but also plays a major role in conducting an orchestrated recruitment and promoting function of the immune cells which are involved in inflammation. Inflammation is central to the pathogenesis of some skin-related diseases such as eczema, psoriasis, dermatitis, vitiligo, and lupus erythematosus [112]. Resveratrol is a molecule that can mitigate skin inflammation, including autoimmune diseases [113]. Resveratrol targets some of the molecules such as COX-2, 5-lipoxygenase, and protein kinase B and is associated with the ability to suppress COX-1 or COX-2 activity [114]. Resveratrol was able to restrain keratinocyte proliferation through the inhibition of aquaporin 3, a vital cell survival regulator [115]. This inhibition occurred due to SIRT1 activation, resulting in the increased activation of aryl hydrocarbon receptor nuclear translocator (ARNT). This led to extracellular signal-regulated kinase (ERK) dephosphorylation, preventing aquaporin 3 activation. This inhibition process caused by resveratrol implicated that it can be used to treat hyperplastic skin disorders such as psoriasis.

Kjaer et al. [116] examined the impact of orally administered resveratrol on imiquimod-induced psoriasiform skin in mouse. Resveratrol was given at a dose of 400 mg/kg per day. Skinfold thickness increased from 0.55 to 0.82 mm after imiquimod intervention. This is a typical sign of psoriasis development. It was observed that oral resveratrol reduced the thickness to 0.71 mm. The results presented that the severity of scaling and erythema evoked by imiquimod could be alleviated by resveratrol. In addition, the gene expression of IL-17A, IL-19, and IL-23p19 in skin which was increased by imiquimod was downregulated after resveratrol treatment. Besides inducing skin cancer, 12-O-tetradecanoylphorbol-13-acetate (TPA) can act as a stimulator eliciting psoriasis-like lesion in mouse because of its capability to cause hyperplasia and evoke inflammatory cell infiltration [117]. Murakami et al. [118] used TPA to induce acute skin inflammation in the ear skin of the mouse for examining whether resveratrol could reduce the inflammatory response. The skin thickness which was increased by TPA (0.30 mm) could be

Table 2. Extrinsic and intrinsic aging treated by resveratrol and its derivatives.

| Compound                                     | Experimental model  | Cell or animal type             | Outcomes offered by the compound  | Reference |
|--|---|---------------------------------|---|-----------|
| Resveratrol                                  | <i>In vitro</i> skin absorption   | Pig                             | Resveratrol showed a satisfied skin absorption to exert antioxidative activity            | [87]      |
| Resveratrol                                  | <i>In vivo</i> skin absorption  | Human                           | Topically applied resveratrol mainly located in SC layer                                  | [88]      |
| Resveratrol                                  | <i>In vitro</i> photoaging  | HaCaT cells                     | Resveratrol increased cell survival and attenuated ROS in UVB-treated cells               | [90]      |
| Resveratrol                                  | <i>In vivo</i> photoaging   | Hairless mouse                  | Resveratrol downregulated cell cycle regulatory proteins                                  | [91]      |
| Resveratrol                                  | <i>In vivo</i> photoaging   | Hairless mouse                  | Resveratrol downregulated survivin  | [92]      |
| Pterostilbene                                | <i>In vitro</i> photoaging  | HaCaT cells                     | Resveratrol attenuated UVB-evoked cell death and ROS generation via Nrf2 signaling        | [93]      |
| Pterostilbene                                | <i>In vivo</i> photodamage  | Hairless mouse                  | Pterostilbene showed superior oxidative damage inhibition than resveratrol                | [95]      |
| Polydatin                                    | <i>In vitro</i> and <i>in vivo</i> photoaging                               | HaCaT cells and nude mouse      | Polydatin as the antioxidant and sunscreen to inhibit UVB-induced skin damage             | [96]      |
| Oligomers                                    | <i>In vitro</i> IL-1 $\beta$ -induced aging                                 | Dermal fibroblasts              | (–)-Hopeaphenol, vaticanol C, stenophyllol C exhibited significant inhibition on MMP-1    | [36]      |
| Resveratrol in transfersomes and ethosomes   | <i>In vitro</i> H <sub>2</sub> O <sub>2</sub> treatment                     | HaCaT cells                     | Ethosomes reduced ROS production and increased resveratrol absorption                     | [99]      |
| Resveratrol in transfersomes                 | <i>In vitro</i> skin permeation   | Strat-M membrane                | Transfersomes increased resveratrol delivery  | [100]     |
| Resveratrol in SLNs and NLCs                 | <i>In vitro</i> H <sub>2</sub> O <sub>2</sub> treatment and skin permeation | Dermal fibroblasts              | NLCs showed greater ROS reduction than SLNs   | [102]     |
| Resveratrol                                  | <i>In vivo</i> skin atrophy   | <i>Sod</i> <sup>–/–</sup> mouse | Resveratrol reversed skin thinning via <i>Sirt1</i> upregulation                          | [106]     |
| Resveratrol                                  | <i>In vivo</i> skin hydration   | Human                           | Resveratrol increased skin hydration by 2-fold  | [107]     |
| Resveratrol and procyanidins                 | <i>In vivo</i> skin hydration and elasticity                                | Human                           | Skin moisturization and elasticity were increased by dietary supplementation              | [108]     |
| Pterostilbene                                | <i>In vivo</i> skin hydration and brightness                                | Human                           | The skin moisturization and elasticity were improved with no adverse effects              | [109]     |
| Resveratrol in SLNs, NLCs, and nanoemulsions | <i>In vivo</i> skin hydration   | Human                           | An increase of skin hydration was detected with a tendency of SLNs > NLCs > nanoemulsions | [111]     |

IL, interleukin; MMP-1, matrix metalloproteinase-1; NLCs, nanostructured lipid carriers; Nrf2, nuclear factor erythroid 2-related factor 2; ROS, reactive oxygen species; SC, stratum corneum; SLNs, solid lipid nanoparticles; Sod: superoxide dismutase; UVB, ultraviolet B.

diminished to 0.21 mm by topical resveratrol delivery. This thickness approximated the healthy control (0.22 mm) group. It was reported that ear weight was significantly lesser in the topical resveratrol group (6.3 mg) as compared to the TPA treated group (9.4 mg).

Resveratrol-enriched rice is developed by genetic engineering to combine the properties of resveratrol and rice [119]. Kang et al. [120] used dinitrochlorobenzene (DNCB)-induced AD-like mouse model to evaluate the amount of inflammatory inhibition caused by resveratrol-enriched rice. The rice intake reduced scratching frequency, dermatitis severity, and transepidermal water loss (TEWL) in

the DNCB-treated mouse. Topical treatment with the rice remarkably decreased immunoglobulin E level by 80%. In the cell-based analysis, the rice and resveratrol inhibited IL-1 $\beta$  and IL-6 expression in HaCaT cells with a negligible cytotoxicity. Sozmen et al. [121] also assessed the effects of orally delivered resveratrol (30 mg/kg per day) on dinitrofluorobenzene (DNFB)-induced AD-like lesion. The results demonstrated that DNFB treatment elevated epidermal thickness of Balb/c mouse from 20 to 97  $\mu$ m. This thickness elevation was lowered to 41  $\mu$ m by resveratrol usage. IL-25, IL-33, and thymic stromal lymphopoietin (TSLP) are released from keratinocytes to activate Th2-type immune response.



According to immunohistochemical analysis, the number of these proteins in epidermis was lower in resveratrol-treated group than that where only DNFB treatment was conducted. Shen and Xu [122] also found that oral resveratrol (25 mg/kg) down-regulated Th2-type cytokines such as IL-4, IL-5, and IL-13; and Th1-type cytokines such as IL-12 and interferon- $\gamma$  in DNCB-induced mouse.

In addition to resveratrol, its methoxylated form pterostilbene has also shown anti-inflammatory potency for dermatitis treatment. Wang et al. [123] found that oral pterostilbene (500 mg/kg per day) attenuated erythema, immune cell infiltration and skin thickness in the chromium-induced allergic contact dermatitis as seen in the mouse. Pterostilbene suppressed IL-1 $\beta$  and tumor necrosis factor (TNF)- $\alpha$  expression in epidermis induced by chromium exposure. The cell-based study demonstrated that pterostilbene at 20  $\mu$ M protected HaCaT cells against chromium-induced apoptosis and cell death. Pterostilbene decreased ROS production and cytokine expression through activation of p38 MAPK signaling pathway. The molecular mechanism associated with inhibition of inflammation by polydatin was elucidated in primary human keratinocytes [124]. Polydatin significantly suppressed lipopolysaccharide- and TNF- $\alpha$ /interferon- $\gamma$ -induced ERK phosphorylation and NF- $\kappa$ B activation, whereas IL-8 was upregulated by this glycoside under the stimulation of transforming growth factor (TGF)- $\alpha$ . HaCaT cell lines were activated by TGF- $\alpha$ , promoting the anti-inflammatory mechanism of polydatin [125]. Polydatin at a dose between 10–50  $\mu$ M downregulated monocyte chemotactic protein (MCP)-1, TNF- $\alpha$ , and IL-6 through ERK pathway. The cytokines such as TNF- $\alpha$ , IL-6, and IL-8 which were elevated by heat-stressed HaCaT cells and reduced with polydatin (44  $\mu$ M) treatment [126]. All these data support the fact that polydatin can act as a potential anti-inflammatory agent.

The nanoformulation is a strategy to increase the anti-inflammatory activity of resveratrol. Caddeo et al. [127] developed the liposomes loaded with both resveratrol and quercetin for mitigating inflammatory and oxidative responses in skin. The liposomes exhibited a mean diameter of about 80 nm with the entrapment percentage of >70% in both the compounds. The intracellular concentration in dermal fibroblasts was increased by 4.4- and 4.7-fold after liposomal encapsulation of resveratrol and quercetin respectively. TPA treatment on CD-1 mouse skin caused dry and thickened lesion. TPA-induced edema was decreased by both compounds, especially the liposomes approaching 50% reduction. Myeloperoxidase activity was inhibited by 80% after

topical liposome application, indicating an inhibited neutrophil infiltration. Niosomes are nanovesicles mainly composed of non-ionic surfactants and cholesterol. These vesicles have a bilayer structure simulating liposomes. Niosomes can be an alternative of liposomes with the advantage of low cost and easy large-scale preparation [128]. Resveratrol-loaded niosomes were prepared by thin-film method to test anti-inflammatory action on skin [129]. The vesicle size ranged between 214 and 332 nm with an encapsulation efficiency of >45%. The skin deposition as determined by *in vitro* rat skin showed an outcome of 4.76 and 0.98  $\mu$ g/cm<sup>2</sup> for niosomes and aqueous suspension respectively. *In vivo* anti-inflammatory activity was assessed by carrageenan-induced paw edema. The percentage increase of paw volume for niosomal group was lower than that of saline control group. A prolonged therapeutic efficiency was also observed in the niosomes. Docosahexaenoic acid (DHA) derived from marine origin reveals anti-inflammatory activity which can be used to treat cardiovascular, neurodegenerative, and neoplastic disorders [130]. Serini et al [131] found that DHA loaded in resveratrol-containing SLNs could synergize the inhibition of keratinocyte activation. Free DHA at dose of 30  $\mu$ M suppressed sodium dodecyl sulfate (SDS)-induced IL-1 $\beta$  expression in HaCaT cells resulting in 63% inhibition. The inhibition was increased to 80% by encapsulating into resveratrol-loaded SLNs. A similar result was detected by using TNF- $\alpha$  as the stimulator. Resveratrol that was loaded into SLNs inhibited NOD-, LRR- and pyrin domain-containing protein 3 (NLRP3) inflammasome activation and enhancing the anti-inflammatory effect of DHA. In the *in vivo* contact dermatitis model, resveratrol loaded into SLNs was confirmed to possess the capacity of reducing inflammation [132]. SLNs improved resveratrol delivery into the skin by 3-fold as compared to that of free compound. The SLNs are effectively used in the marketed corticosteroid formulation to restrict edema development. The anti-inflammatory activity of resveratrol and its analogs on keratinocytes or skin is depicted in Table 3. The effects of resveratrol and its analogs on psoriasis and dermatitis for ameliorating the signs and symptoms are listed in Fig. 4.

#### 4.5. Hyperpigmentation

Melanin produced by melanocytes gets stored in melanosomes, after which it is deposited in epidermis as the determinant of skin color. Despite the protective effect against sun exposure, abnormal melanin accumulation leads to several disorders

Table 3. Anti-inflammatory activity of resveratrol and its derivatives.

| Compound                               | Experimental model  | Cell or animal type               | Outcomes offered by the compound  | Reference |
|--|---|-----------------------------------|---|-----------|
| Resveratrol                            | <i>In vitro</i> hyperproliferation                              | Human keratinocytes               | Resveratrol restrained keratinocyte proliferation via aquaporin 3 inhibition          | [115]     |
| Resveratrol                            | <i>In vivo</i> psoriasiform plaque                              | Balb/c mouse                      | Oral resveratrol alleviated the severity of scaling and skin redness                  | [116]     |
| Resveratrol                            | <i>In vivo</i> psoriasiform plaque                              | Balb/c mouse                      | Topical resveratrol reduced skin thickness and edema                                  | [118]     |
| Resveratrol-enriched rice              | <i>In vivo</i> AD-like lesion                                   | NC/Nga mouse                      | The rice reduced scratching frequency and dermatitis severity                         | [120]     |
| Resveratrol                            | <i>In vivo</i> AD-like lesion                                   | Balb/c mouse                      | Oral resveratrol reduced skin thickness and immune response                           | [121]     |
| Resveratrol                            | <i>In vivo</i> AD-like lesion                                   | Balb/c mouse                      | Oral resveratrol downregulated Th2-type cytokines                                     | [122]     |
| Pterostilbene                          | <i>In vivo</i> contact dermatitis-like skin                     | C57BL/6 mouse                     | Oral pterostilbene attenuated erythema and immune cell infiltration                   | [123]     |
| Polydatin                              | <i>In vitro</i> inflammation                                    | Human keratinocytes               | Polydatin inhibited ERK phosphorylation and NF- $\kappa$ B activation                 | [124]     |
| Polydatin                              | <i>In vitro</i> inflammation                                    | HaCaT cells                       | Polydatin inhibited MCP-1, TNF- $\alpha$ , and IL-6                                   | [125]     |
| Polydatin                              | <i>In vitro</i> inflammation                                    | HaCaT cells                       | Polydatin inhibited TNF- $\alpha$ , IL-6, and IL-8                                    | [126]     |
| Resveratrol and quercetin in liposomes | <i>In vitro</i> uptake and <i>in vivo</i> inflammation          | Dermal fibroblasts and CD-1 mouse | The liposomes increased cellular uptake and reduced edema and neutrophil infiltration | [127]     |
| Resveratrol in niosomes                | <i>In vitro</i> skin absorption and <i>in vivo</i> inflammation | Wistar rat                        | The enhanced resveratrol skin absorption with reduced edema                           | [129]     |
| Resveratrol and DHA in SLNs            | <i>In vitro</i> inflammation                                    | HaCaT cells                       | DHA could synergize with resveratrol in SLNs to inhibit cytokine expression           | [131]     |
| Resveratrol in SLNs                    | <i>In vivo</i> contact dermatitis-like skin                     | Mouse                             | SLNs inhibited skin edema   | [132]     |

AD, atopic dermatitis; DHA, docosahexaenoic acid; ERK, extracellular signal-regulated kinase; IL, interleukin; MCP-1, monocyte chemoattractant protein-1; NF- $\kappa$ B, nuclear factor- $\kappa$ B; SLNs, solid lipid nanoparticles; TNF- $\alpha$ , tumor necrosis factor- $\alpha$ .

related to hyperpigmentation, including melasma, freckle, age spot, and lentigo [133]. Tyrosinase is a principal enzyme involved in melanogenesis (Fig. 5). Most of the hypopigmenting or skin lightening agents, especially the natural compounds work on the mechanism of tyrosinase inhibition [134]. Resveratrol is a direct tyrosinase inhibitor. It also can inhibit melanogenic enzymes (Fig. 5). Moreover, it can affect keratinocytes that regulate the function of melanocytes. Being an antioxidant, resveratrol prevents keratinocyte-induced melanocyte activation [135]. Park and Boo [136] tested the tyrosinase inhibition caused by resveratrol. It is noticed that treatment of human epidermal melanocytes with tyrosine increased intracellular melanin production. The melanin synthesis was attenuated by resveratrol at a dose of 3–100  $\mu$ M. The HEK293 cells were transformed to express itself as human tyrosinase. It is verified that resveratrol is a strong inhibitor of human tyrosinase with  $IC_{50}$  of 0.39  $\mu$ g/ml, which is lower than p-coumaric acid (0.66  $\mu$ g/ml) and arbutin

(>100  $\mu$ g/ml). This skin whitening activity of resveratrol is certified in human [137]. In a study the skin tanning was induced by repetitive UV irradiation on the skin of 15 healthy subjects, followed by the topical administration of resveratrol. The lightness degree ( $L^*$ ) reduced from 64.2 to 59.3 when treated with resveratrol for 4 days post-irradiation as compared to UV irradiation alone, suggesting that it causes hypopigmentation. Histological assay supported the inhibition of sunburn cell formation when resveratrol intervention was implemented.

Some resveratrol analogs have demonstrated greater capability to inhibit tyrosinase than that seen with resveratrol. Oxyresveratrol has displayed inhibitory effects on mushroom tyrosinase with an  $IC_{50}$  of 1.2  $\mu$ M, which was 32-fold stronger than kojic acid [138]. The  $IC_{50}$  of oxyresveratrol for inhibiting murine tyrosinase activity was 52.7  $\mu$ M. Mulberry extract is found to strongly inhibit tyrosinase [139]. Two resveratrol derivatives, namely oxyresveratrol and 4'-prenyloxyresveratrol were isolated from the

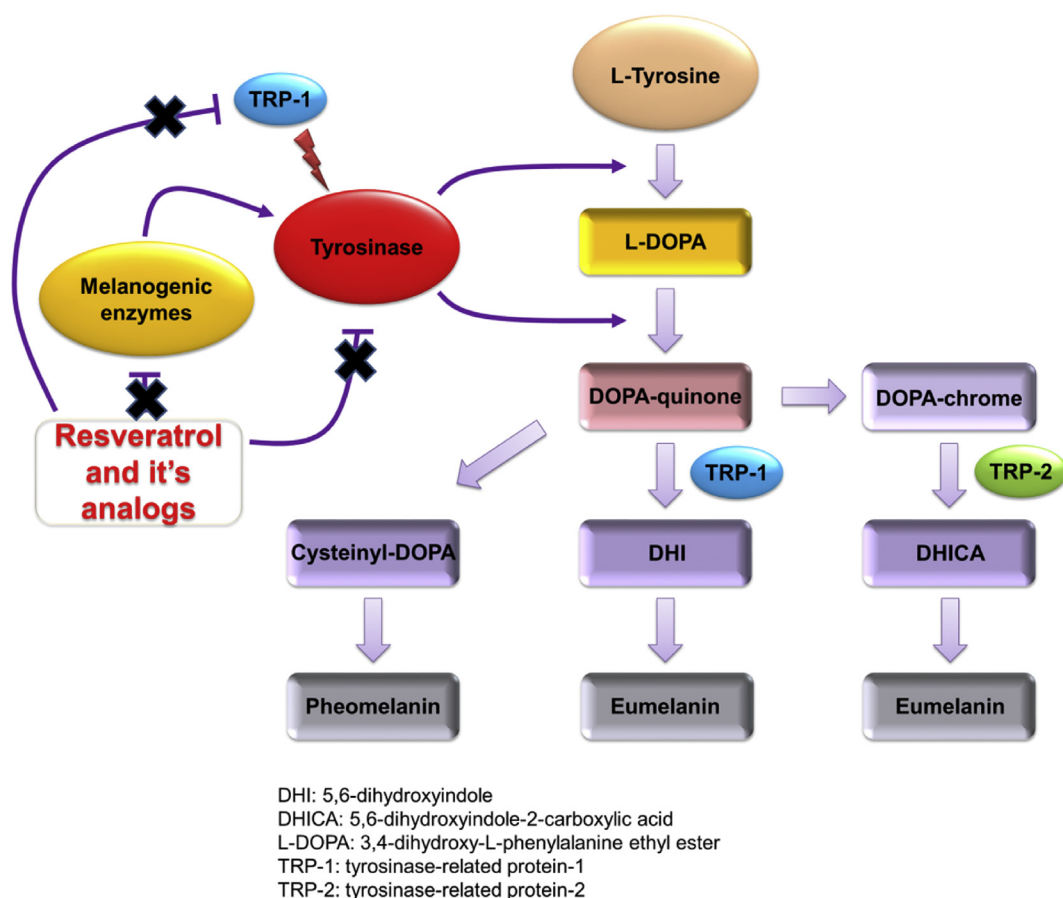


Fig. 5. The pathogenic mechanisms of skin hyperpigmentation. Melanin synthesis begins with catalysation of the substrates phenylalanine and tyrosine to produce L-DOPA via tyrosinase. The pathways are then divided into eumelanogenesis or pheomelanogenesis. The other melanogenic enzyme is TRP-1 for eumelanogenesis. Resveratrol is a direct tyrosinase inhibitor. It also can inhibit melanogenic enzymes.

methanol extract of mulberry leaves [140]. The  $IC_{50}$  of oxyresveratrol and 4'-prenyloxyresveratrol required to suppress mushroom tyrosinase was 0.57 and 0.90  $\mu M$  respectively. This inhibitory activity was stronger than that of arbutin ( $IC_{50} = 14.18 \mu M$ ). Park et al. [141] has evaluated the anti-melanogenic potency of oxyresveratrol by using a 3D reconstituted skin model (MelanoDerm®). The reconstituted skin was topically treated with the compounds at a dose of 125  $\mu mol$  per tissue. It was seen that resveratrol and oxyresveratrol lowered melanin amount to 41% and 65% respectively. However, the cell viability after undergoing treatment with resveratrol and oxyresveratrol was 20% and 95% respectively. This outcome suggested that resveratrol possess high cytotoxicity. In the tyrosinase-transformed HEK293 cell model, oxyresveratrol ( $IC_{50} = 0.09 \mu M$ ) inhibited human tyrosinase strongly as compared to resveratrol ( $IC_{50} = 1.8 \mu M$ ). Besides oxyresveratrol, another hydroxylated resveratrol derivative which causes melanogenesis inhibition is piceatannol. The mushroom

tyrosinase inhibition caused by piceatannol ( $IC_{50} = 1.53 \mu M$ ) was higher than that of resveratrol ( $IC_{50} = 63.2 \mu M$ ) and kojic acid ( $IC_{50} = 50.1 \mu M$ ) [142]. Piceatannol at a dose of 50  $\mu M$  decreased melanin concentration in B16 cells to 14.8%, which was lower than that of resveratrol (58.4%). Piceatannol also exhibited a greater inhibition of reactive oxygen species than that observed with resveratrol.

Jeong et al. [143] explored the inhibitory action of polydatin on melanogenesis. Polydatin at a dosage of 10, 20 and 50  $\mu g/ml$  decreased melanin level in melan-a melanocytes by about 20%, 60% and 70% respectively. The enzymes related with melanogenesis such as tyrosinase, tyrosinase-related protein (TRP)-1, and TRP-2 were downregulated by polydatin in a concentration-dependent fashion. The investigation conducted by Uesugi et al. [144] also demonstrated a higher degree of mushroom tyrosinase suppression caused by polydatin ( $IC_{50} = 14 \mu M$ ) as compared with resveratrol ( $IC_{50} = 565 \mu M$ ), implying that glycosylation has improved tyrosinase inhibitory effect. Gnetin C is a resveratrol dimer

Table 4. Hypopigmenting activity of resveratrol and its derivatives.

| Compound                                   | Experimental model  | Cell or animal type               | Outcomes offered by the compound  | Reference |
|--|---|-----------------------------------|---|-----------|
| Resveratrol                                | Cell-based tyrosinase inhibition                            | HEK293 cells                      | Resveratrol was effective to inhibit human tyrosinase                         | [136]     |
| Resveratrol                                | <i>In vivo</i> UV irradiation                               | Human                             | Resveratrol inhibited sunburn cell formation                                  | [137]     |
| Oxyresveratrol                             | Cell-based tyrosinase inhibition                            | B16 cells                         | Oxyresveratrol was effective to inhibit mushroom and murine tyrosinases       | [138]     |
| Oxyresveratrol and 4'-prenyloxyresveratrol | <i>In vitro</i> tyrosinase inhibition                       | Mushroom tyrosinase               | Oxyresveratrol and 4'-prenyloxyresveratrol from mulberry inhibited tyrosinase | [140]     |
| Resveratrol and oxyresveratrol             | Cell-based 3D reconstituted skin                            | MelanoDerm®                       | Oxyresveratrol showed higher melanin inhibition than resveratrol              | [141]     |
| Resveratrol and piceatannol                | <i>In vitro</i> tyrosinase inhibition                       | Mushroom tyrosinase and B16 cells | Piceatannol showed higher tyrosinase inhibition than resveratrol              | [142]     |
| Polydatin                                  | Cell-based tyrosinase inhibition                            | Melan-a cells                     | Polydatin inhibited melanin content and tyrosinase                            | [143]     |
| Polydatin                                  | <i>In vitro</i> tyrosinase inhibition                       | Mushroom tyrosinase               | Polydatin showed higher tyrosinase inhibition than resveratrol                | [144]     |
| Resveratrol and gnetin C                   | Cell-based tyrosinase inhibition                            | B16 cells                         | Resveratrol and gnetin showed a comparable tyrosinase inhibition              | [145]     |
| $\alpha$ -Viniferin                        | Cell-based tyrosinase inhibition and <i>in vivo</i> melasma | Melan-a cells and human           | $\alpha$ -Viniferin decreased melanin index in the patients with melasma      | [146]     |
| Resveratrol in nanoparticles               | <i>In vivo</i> UV irradiation                               | Guinea pig                        | The nanoparticles decreased melanin granules in skin                          | [147]     |
| Resveratrol in SLNs                        | <i>In vitro</i> tyrosinase inhibition                       | Mushroom tyrosinase               | Resveratrol loaded in SLNs promoted tyrosinase inhibition                     | [148]     |

SLNs, solid lipid nanoparticles; UV, ultraviolet.

which is purified from melinjo seeds. The inhibitory potency of gnetin C and resveratrol was shown to be equally effective against tyrosinase and melanin biosynthesis as observed in the murine B16 cells [145]. The IC<sub>50</sub> of gnetin C activity against tyrosinase and melanin biosynthesis was 7.0 and 7.6  $\mu$ M respectively, whereas resveratrol exerted IC<sub>50</sub> of 7.2 and 7.3  $\mu$ M respectively. The anti-melanogenesis response of resveratrol trimer,  $\alpha$ -viniferin which is present in melanocytes and human skin was evaluated in a study conducted by Yun et al. [146].

Treatment performed with  $\alpha$ -viniferin in a concentration-dependent manner reduced melanin production in melan-a cells, demonstrating a stronger activity (>5-fold) than that seen in arbutin. In the research twenty-three patients who had melasma and freckles were treated with topically applied *Caragana sinica* cream which is rich in  $\alpha$ -viniferin. After 6–8 weeks it was observed that after the treatment with *C. sinica* cream there was a decrease in melanin index and lightening index was increased as

Table 5. Antimicrobial activity of resveratrol and its derivatives.

| Compound                                 | Experimental model   | Microbial or animal type | Outcomes offered by the compound                                      | Reference |
|--|--|--------------------------|---|-----------|
| Resveratrol                              | <i>In vitro</i> susceptibility                                   | Dermatophytes            | Resveratrol effectively retarded dermatophyte growth                  | [152]     |
| Resveratrol                              | <i>In vivo</i> skin infection                                    | HSV                      | Resveratrol mitigated skin lesion caused by HSV                       | [155]     |
| Oxyresveratrol                           | <i>In vivo</i> skin infection                                    | HSV                      | Oxyresveratrol delayed the development of skin lesion caused by HSV   | [156]     |
| Pterostilbene                            | <i>In vitro</i> susceptibility and <i>in vivo</i> skin infection | MRSA                     | Pterostilbene showed superior MRSA growth inhibition than resveratrol | [157]     |
| Resveratrol and gallic acid in liposomes | <i>In vitro</i> skin absorption and microbial inhibition         | Skin pathogens           | Liposomes improved antimicrobial activity of resveratrol              | [158]     |

HSV, herpes simplex virus; MRSA, methicillin-resistant *Staphylococcus aureus*.



recorded by chromameter. The response was much better than the vehicle control group.

The resveratrol-enriched rice was grounded to nano-sized particles by applying high pressure homogenization [147]. The average particle size of the products was approximately 500 nm. The nanoparticles were topically applied on UVB-exposed guinea pig skin for 15 days. The results showed that the color index of UVB-treated skin was 72.2 which decreased to 55.1 due to the presence of nanoparticles for 15 days. The amount of melanin granules in skin increased by 2.6-fold after UVB irradiation. This increase was attenuated by 1.6-fold due to the presence of nanoparticles. The deposition of resveratrol in skin was dramatically enhanced by this high pressure homogenization technique. Resveratrol-loaded SLNs were developed to examine skin delivery and tyrosinase inhibition [148]. The prepared nanoformulations had a mean diameter of <200 nm. It is noticed that up to 45% of resveratrol could permeate through pig skin from SLNs. The tyrosinase inhibitory percentage was increased from 63% to 90% after resveratrol entrapment into SLNs. An additional advantage of using the SLNs is that the nanocarriers are non-toxic towards keratinocytes. It is difficult to compare the IC<sub>50</sub> of resveratrol and its derivatives since the methodology and experimental setup of different investigations varies. Table 4 summarizes the tyrosinase inhibitory or anti-melanogenesis activity of resveratrol and its derivatives.

#### 4.6. Microbial infection

Microorganisms including viruses, bacteria, fungi and parasites can cause infectious diseases. Infection-related illness is a leading cause of death globally [149]. Microbial infection is usually associated with an inflammatory response because it activates immune cell defense against the pathogens. The treatment done with active agents which possess anti-inflammatory and antimicrobial effects will lead to favorable outcomes and will help in alleviating many cutaneous conditions. For instance, more than 90% of AD patients are colonized with *Staphylococcus aureus* [150]. The occurrence of *S. aureus* has emerged as a predominant threat for AD treatment. Efficient AD management requires involvement of multiple drug treatments, including the immunomodulatory agents or steroids for anti-inflammation and antibiotics for reducing infection [151]. Resveratrol is a phytoalexin that helps to retard the growth of pathogens such as bacteria, fungi, and viruses [114]. Resveratrol could inhibit the growth of some dermatophytes, including

*Trichophyton mentagrophytes*, *T. tonsurans*, *T. rubrum*, *Epidermophyton floccosum*, and *Microsporum gypseum* [152]. The effective resveratrol concentration to inhibit growth of these dermatophytes is 110–220  $\mu$ M. Resveratrol is reported to bind ATP synthase, suppressing ATP hydrolysis and synthesis function to inhibit microbial growth [62]. Resveratrol also shows antivirulence nature via biofilm reduction, bacterial motility inhibition, and quorum sensing interference [153]. At this dose range resveratrol is expected to not induce cytotoxicity against human fibroblasts. Along with the antifungal activity, resveratrol effectively displays anti-herpes simplex virus (HSV) potency in skin [154]. Docherty et al. [155] applied topical resveratrol cream (12.5% or 25%) to SKH1 mouse bearing HSV-1 infection. The results demonstrated that when the treatment outcome was evaluated 1 and 6 hrs after infection, both creams effectively suppressed lesion development. The creams are also advantageous to treat acyclovir-resistant HSV. No erythema, scaling, or excoriation was observed in the healthy skin which were treated by resveratrol.

Anti-HSV activity was also found in oxyresveratrol. Chuanasa et al. [156] has evaluated the therapeutic efficiency of topically applied oxyresveratrol on cutaneous HSV infection as observed in Balb/c mouse. Oxyresveratrol (50  $\mu$ g/ml) caused viral inhibitions of 26% and 33% in the infected vero cells when applied for 3 and 6 hrs respectively. The combination of resveratrol and acyclovir created a synergistic anti-HSV-1 response. Topical administration of resveratrol ointment (30%) for five times in a day delayed the development of cutaneous lesion caused by HSV-1. Yang et al. [157] investigated the antibacterial activity of pterostilbene against methicillin-resistant *S. aureus* (MRSA) and the feasibility to treat cutaneous lesion and barrier dysfunction. The minimum inhibitory concentration (MIC) assay demonstrated a superior biocidal activity of pterostilbene compared to that of resveratrol (8–16-fold) against MRSA. Pterostilbene was found to reduce MRSA biofilm thickness from 18 to 10  $\mu$ m as detected by confocal microscopy. Pterostilbene increased skin absorption by 6-fold as compared to resveratrol. Topical pterostilbene application decreased the abscess formation produced by MRSA by reducing the bacterial burden and ameliorating the skin architecture. Pterostilbene demonstrated potent anti-MRSA ability due to the involvement of various mechanisms. Firstly, it enhanced bacterial membrane leakage. Secondly, it caused downregulation of chaperone protein and upregulated ribosomal protein.

Nanovesicles were used to load resveratrol for increasing its skin delivery and antimicrobial activity. Vitonyte et al. [158] loaded both resveratrol and gallic acid in liposomes to produce vesicles with a size of around 70 nm. A further incorporation of propylene glycol or glycerin as the permeation enhancer increased the size to 170 nm. It was reported that resveratrol accumulation in the dermal layer of pig skin was greater for the glycerin-containing liposomes (1%) than that of liposomes and propylene glycol-containing liposomes (0.4%). An improvement in antimicrobial activity was shown against skin pathogens such as *S. aureus*, *S. intermedius*, *S. pyogenes* and *Candida albicans*. Table 5 summarizes the antimicrobial activity of resveratrol and its derivatives, including the design of nanocarriers.

## 5. Conclusion

The clinical application of resveratrol still poses a challenge because of its poor solubility, low bioavailability and the concern of demonstrating adverse effects. The low bioavailability of resveratrol can be due to the limited gastrointestinal absorption and its rapid metabolism. Furthermore, some systemic toxic effects such as headache, somnolence, blood electrolyte change and rash are observed after receiving high-dose resveratrol. Topical delivery of resveratrol can be used as a strategy to avoid the low oral bioavailability and other possible side effects. The topical administration is a preferable method to treat skin-related diseases as discussed in this review. Some of the resveratrol derivatives have demonstrated superior bioactivity than the parent compound while treating skin disorders. Although many resveratrol products are being developed for testing in cell- and animal-based studies, but clinical trials for skin application are still limited. This may be due to the high cost which is required to perform clinical trials and some unknown side effects that should be identified and explored before it is tested clinically. Further clinical studies are required to encourage application of resveratrol and its naturally occurring derivatives in the future.

## Conflicts of interest

The authors have no conflicts of interest.

## Acknowledgements

The authors are grateful to the financial support from Chang Gung Memorial Hospital (CMRPD1G0411-2) and Chi Mei Medical Center (108-CM-FJU-03).

## References

- [1] Cory H, Passarelli S, Szeto J, Tamez M, Mattei J. The role of polyphenols in human health and food systems: a mini-review. *Front Nutr* 2018;5:87. <https://doi.org/10.3389/fnut.2018.00087>.
- [2] Hardman WE. Diet components can suppress inflammation and reduce cancer risk. *Nutr Res Pract* 2014;8:233–40. <https://doi.org/10.4162/nrp.2014.8.3.233>.
- [3] Baur JA, Sinclair DA. Therapeutic potential of resveratrol: the in vivo evidence. *Nat Rev Drug Discov* 2006;5:493–506. <https://doi.org/10.1038/nrd2060>.
- [4] Siemann EH, Creasy LL. Concentration of the phytoalexin resveratrol in wine. *Am J Enol Vitic* 1992;43:49–52.
- [5] Kalantari H, Das Dipak K. Physiological effects of resveratrol. *Bio Factors* 2010;36:401–6. <https://doi.org/10.1002/biof.100>.
- [6] Meng X, Zhou J, Zhao CN, Gan RY, Li HB. Health benefits and molecular mechanisms of resveratrol: a narrative review. *Foods* 2020;9:E340. <https://doi.org/10.3390/foods9030340>.
- [7] Koushki M, Lakzaei M, Khodabandehloo H, Hosseini H, Meshkani R, Panahi G. Therapeutic effect of resveratrol supplementation on oxidative stress: a systematic review and meta-analysis of randomised controlled trials. *Postgrad Med J* 2020;96:197–205. <https://doi.org/10.1136/postgradmedj-2019-136415>.
- [8] Giancchetti E, Fierabracci A. Insights on the effects of resveratrol and some of its derivatives in cancer and autoimmunity: a molecule with a dual activity. *Antioxidants* 2020;9:91. <https://doi.org/10.3390/antiox9020091>.
- [9] Biasutto L, Mattarei A, Azzolini M, La Spina M, Sassi N, Romio M, Paradisi C, Zoratti M. Resveratrol derivatives as a pharmacological tool. *Ann N Y Acad Sci* 2017;1403:27–37. <https://doi.org/10.1111/nyas.13401>.
- [10] Walle T. Bioavailability of resveratrol. *Ann N Y Acad Sci* 2011;1215:9–15. <https://doi.org/10.1111/j.1749-6632.2010.05842.x>.
- [11] Francioso A, Mastromarino P, Masci A, d'Erme M, Mosca L. Chemistry, stability and bioavailability of resveratrol. *Med Chem* 2014;10:237–45. <https://doi.org/10.2174/15734064113096660053>.
- [12] Hung CF, Lin YK, Huang ZR, Fang JY. Delivery of resveratrol, a red wine polyphenol, from solutions and hydrogels via the skin. *Biol Pharm Bull* 2008;31:955–62. <https://doi.org/10.1248/bpb.31.955>.
- [13] Moyano-Mendez JR, Fabbrocini G, De Stefano D, Mazzella C, Mayol L, Scognamiglio I, Carnuccio R, Ayala F, La Rotonda MI, De Rosa G. Enhanced antioxidant effect of trans-resveratrol: potential of binary systems with polyethylene glycol and cyclodextrin. *Drug Dev Ind Pharm* 2014;40:1300–7. <https://doi.org/10.3109/03639045.2013.817416>.
- [14] Tsai MJ, Lu JJ, Fu YS, Fang YP, Huang YB, Wu PC. Nanocarriers enhance the transdermal bioavailability of resveratrol: In-vitro and in-vivo study. *Colloids Surf B Biointerfaces* 2016;148:650–6. <https://doi.org/10.1016/j.colsurfb.2016.09.045>.
- [15] Santos AC, Pereira I, Pereira-Silva M, Ferreira L, Caldas M, Collado-González M, Magalhães M, Figueiras A, Ribeiro AJ, Veiga F. Nanotechnology-based formulations for resveratrol delivery: effects on resveratrol in vivo bioavailability and bioactivity. *Colloids Surf B Biointerfaces* 2019;180:127–40. <https://doi.org/10.1016/j.colsurfb.2019.04.030>.
- [16] Summerlin N, Soo E, Thakur S, Qu Z, Jambhunkar S, Popat A. Resveratrol nanoformulations: challenges and opportunities. *Int J Pharm* 2015;479:282–90. <https://doi.org/10.1016/j.ijpharm.2015.01.003>.
- [17] Szekeres T, Fritzer-Szekeres M, Saiko P, Jäger W. Resveratrol and resveratrol analogues—structure-activity relationship. *Pharm Res* 2010;27:1042–8. <https://doi.org/10.1007/s11095-010-0090-1>.

- [18] Nawaz W, Zhou Z, Deng S, Ma X, Ma X, Li C, Shu X. Therapeutic versatility of resveratrol derivatives. *Nutrients* 2017;9:1188. <https://doi.org/10.3390/nu9111188>.
- [19] Lee HS, Kim DH, Hong JE, Lee JY, Kim EJ. Oxyresveratrol suppresses lipopolysaccharide-induced inflammatory responses in murine macrophages. *Hum Exp Toxicol* 2015;34: 808–18. <https://doi.org/10.1177/0960327114559989>.
- [20] Choi HY, Lee JH, Jegal KH, Cho IJ, Kim YW, Kim SC. Oxyresveratrol abrogates oxidative stress by activating ERK-Nrf2 pathway in the liver. *Chem Biol Interact* 2016;245: 110–21. <https://doi.org/10.1016/j.cbi.2015.06.024>.
- [21] Boo YC. Human skin lightening efficacy of resveratrol and its analogs: from in vitro studies to cosmetic applications. *Antioxidants* 2019;8:332. <https://doi.org/10.3390/antiox8090332>.
- [22] Kershaw J, Kim KH. The therapeutic potential of piceatannol, a natural stilbene, in metabolic diseases: a review. *J Med Food* 2017;20:427–38. <https://doi.org/10.1089/jmf.2017.3916>.
- [23] Tsai HY, Ho CT, Chen YK. Biological actions and molecular effects of resveratrol, pterostilbene, and 3'-hydroxypterostilbene. *J Food Drug Anal* 2017;25:134–47. <https://doi.org/10.1016/j.jfda.2016.07.004>.
- [24] Paul S, DeCastro AJ, Lee HJ, Smolarek AK, So JY, Simi B, Wang CX, Zhou R, Rimando AM, Suh N. Dietary intake of pterostilbene, a constituent of blueberries, inhibits the beta-catenin/p65 downstream signaling pathway and colon carcinogenesis in rats. *Carcinogenesis* 2010;31:1272–8. <https://doi.org/10.1093/carcin/bgq004>.
- [25] Murias M, Jäger W, Handler N, Erker T, Horvath Z, Szekeres T, Nohl H, Gille L. Antioxidant, prooxidant and cytotoxic activity of hydroxylated resveratrol analogues: structure-activity relationship. *Biochem Pharmacol* 2005;69: 903–12. <https://doi.org/10.1016/j.bcp.2004.12.001>.
- [26] Chen RJ, Lee YH, Yeh YL, Wu WS, Ho CT, Li CY, Wang BJ, Wang YJ. Autophagy-inducing effect of pterostilbene: a prospective therapeutic/preventive option for skin diseases. *J Food Drug Anal* 2017;25:125–33. <https://doi.org/10.1016/j.jfda.2016.10.022>.
- [27] Trobo-Maseda L, Orrego AH, Guisan JM, Rocha-Martín J. Coimmobilization and colocalization of a glycosyltransferase and a sucrose synthase greatly improves the recycling of UDP-glucose: glycosylation of resveratrol 3-O- $\beta$ -D-glucoside. *Int J Biol Macromol* 2020;157:510–21. <https://doi.org/10.1016/j.ijbiomac.2020.04.120>.
- [28] Şöhretöğlu D, Baran MY, Arroo R, Kuruüzüm-Uz A. Recent advances in chemistry, therapeutic properties and sources of polydatin. *Phytochem Rev* 2018;17:973–1005. <https://doi.org/10.1007/s11101-018-9574-0>.
- [29] Su D, Cheng Y, Liu M, Liu D, Cui H, Zhang B, Zhou S, Yang T, Mei Q. Comparison of piceid and resveratrol in anti-oxidation and antiproliferation activities in vitro. *PLoS One* 2013;8:e54505. <https://doi.org/10.1371/journal.pone.0054505>.
- [30] Liu WB, Hu L, Hu Q, Chen NN, Yang QS, Wang FF. New resveratrol oligomer derivatives from the roots of *Rheum lhasaense*. *Molecules* 2013;18:7093–102. <https://doi.org/10.3390/molecules18067093>.
- [31] Snyder SA, Gollner A, Chiriac MI. Regioselective reactions for programmable resveratrol oligomer synthesis. *Nature* 2011;474:461–6. <https://doi.org/10.1038/nature10197>.
- [32] Shen J, Zhou Q, Li P, Wang Z, Liu S, He C, Zhang C, Xiao P. Update on phytochemistry and pharmacology of naturally occurring resveratrol oligomers. *Molecules* 2017;22:2050. <https://doi.org/10.3390/molecules22122050>.
- [33] Meneses-Gutiérrez CL, Hernández-Damián J, Pedraza-Chaverri J, Guerrero-Legarreta I, Téllez DI, Jaramillo-Flores ME. Antioxidant capacity and cytotoxic effects of catechins and resveratrol oligomers produced by enzymatic oxidation against T24 human urinary bladder cancer cells. *Antioxidants* 2019;8:214. <https://doi.org/10.3390/antiox8070214>.
- [34] Sasikumar P, Lekshmy K, Sini S, Prabha B, Kumar NA, Sivan VV, Jithin MM, Jayamurthy P, Shibi IG, Radhakrishnan KV. Isolation and characterization of resveratrol oligomers from the stem bark of *Hopea ponga* (Dennst.) Mabb. and their antidiabetic effect by modulation of digestive enzymes, protein glycation and glucose uptake in L6 myocytes. *J Ethnopharmacol* 2019;236:196–204. <https://doi.org/10.1016/j.jep.2019.01.046>.
- [35] Ito T, Akao Y, Yi H, Ohguchi K, Matsumoto K, Tanaka T, Iinuma M, Nozawa Y. Antitumor effect of resveratrol oligomers against human cancer cell lines and the molecular mechanism of apoptosis induced by vaticanol C. *Carcinogenesis* 2003;24:1489–97. <https://doi.org/10.1093/carcin/bgg105>.
- [36] Abe N, Ito T, Ohguchi K, Nasu M, Masuda Y, Oyama M, Nozawa Y, Ito M, Iinuma M. Resveratrol oligomers from *Vatica albiramis*. *J Nat Prod* 2010;73:1499–506. <https://doi.org/10.1021/np1002675>.
- [37] Chuang SY, Lin YK, Lin CF, Wang PW, Chen EL, Fang JY. Elucidating the skin delivery of aglycone and glycoside flavonoids: how the structures affect cutaneous absorption. *Nutrients* 2017;9:1304. <https://doi.org/10.3390/nu9121304>.
- [38] Rzhetskiy AS, Guy RH, Anissimov YG. Modelling drug flux through microporated skin. *J Control Release* 2016;241: 194–9. <https://doi.org/10.1016/j.jconrel.2016.09.029>.
- [39] Karimkhani C, Dellavalle RP, Coffeng LE, Flohr C, Hay RJ, Langan SM, Nsoesie EO, Ferrari AJ, Erskine HE, Silverberg JI, Vos T, Naghavi M. Global skin disease morbidity and mortality: an update from the global burden of disease study 2013. *JAMA Dermatol* 2017;153:406–12. <https://doi.org/10.1001/jamadermatol.2016.5538>.
- [40] Hsiao CY, Yang SC, Alalaiwe A, Fang JY. Laser ablation and topical drug delivery: a review of recent advances. *Expert Opin Drug Deliv* 2019;16:937–52. <https://doi.org/10.1080/17425247.2019.1649655>.
- [41] Ratz-Lyko A, Arct J. Resveratrol as an active ingredient for cosmetic and dermatological applications: a review. *J Cosmet Laser Ther* 2019;21:84–90. <https://doi.org/10.1080/14764172.2018.1469767>.
- [42] Apalla Z, Lallas A, Sotiriou E, Lazaridou E, Ioannides D. Epidemiological trends in skin cancer. *Dermatol Pract Concept* 2017;7:1–6. <https://doi.org/10.5826/dpc.0702a01>.
- [43] Lv R, Sun Q. A network meta-analysis of non-melanoma skin cancer (NMSC) treatments: efficacy and safety assessment. *J Cell Biochem* 2017;118:3686–95. <https://doi.org/10.1002/jcb.26015>.
- [44] Costa A, Bonner MY, Arbiser JL. Use of polyphenolic compounds in dermatologic oncology. *Am J Clin Dermatol* 2016;17:369–85. <https://doi.org/10.1007/s40257-016-0193-5>.
- [45] Narayanan DL, Saladi RN, Fox JL. Ultraviolet radiation and skin cancer. *Int J Dermatol* 2010;49:978–86. <https://doi.org/10.1111/j.1365-4632.2010.04474.x>.
- [46] de Gruijl FR. UV adaptation: pigmentation and protection against overexposure. *Exp Dermatol* 2017;26:557–62. <https://doi.org/10.1111/exd.13332>.
- [47] Wagener FA, Carels CE, Lundvig DM. Targeting the redox balance in inflammatory skin conditions. *Int J Mol Sci* 2013; 14:9126–67. <https://doi.org/10.3390/ijms14059126>.
- [48] Griffiths CEM, van der Walt JM, Ashcroft DM, Flohr C, Naldi L, Nijsten T, Augustin M. The global state of psoriasis disease epidemiology: a workshop report. *Br J Dermatol* 2017;177:4–7. <https://doi.org/10.1111/bjd.15610>.
- [49] Chuang SY, Lin CH, Sung CT, Fang JY. Murine models of psoriasis and their usefulness for drug discovery. *Expert Opin Drug Discov* 2018;13:551–62. <https://doi.org/10.1080/17460441.2018.1463214>.
- [50] Helmick CG, Lee-Han H, Hirsch SC, Baird TL, Bartlett CL. Prevalence of psoriasis among adults in the U.S.: 2003–2006 and 2009–2010 National Health and Nutrition Examination Surveys. *Am J Prev Med* 2014;47:37–45. <https://doi.org/10.1016/j.amepre.2014.02.012>.
- [51] Farahnik B, Sharma D, Alban J, Sivamani RK. Topical botanical agents for the treatment of psoriasis: a systematic review. *Am J Clin Dermatol* 2017;18:451–68. <https://doi.org/10.1007/s40257-017-0266-0>.



- [52] Huang TH, Lin CF, Alalaiwe A, Yang SC, Fang JY. Apoptotic or antiproliferative activity of natural products against keratinocytes for the treatment of psoriasis. *Int J Mol Sci* 2019;20:2558. <https://doi.org/10.3390/ijms20102558>.
- [53] Shaw TE, Currie GP, Koudelka CW, Simpson EL. Eczema prevalence in the United States: data from the 2003 National Survey of Children's Health. *J. Invest Dermatol* 2011;131:67–73. <https://doi.org/10.1038/jid.2010.251>.
- [54] Nygaard U, Deleuran M, Vestergaard C. Emerging treatment options in atopic dermatitis: topical therapies. *Dermatology* 2017;233:333–43. <https://doi.org/10.1159/1000484407>.
- [55] Williams HC. Atopic dermatitis. *N Engl J Med* 2005;352:2314–24. <https://doi.org/10.1056/NEJMcp042803>.
- [56] Hajar T, Leshem YA, Hanifin JM, Nedorost ST, Lio PA, Paller AS, Block J, Simpson EL. A systematic review of topical corticosteroid withdrawal ("steroid addiction") in patients with atopic dermatitis and other dermatoses. *J Am Acad Dermatol* 2015;72:541–9. <https://doi.org/10.1016/j.jaad.2014.11.024>.
- [57] Yun Y, Kim K, Choi I, Ko SG. Topical herbal application in the management of atopic dermatitis: a review of animal studies. *Mediators Inflamm* 2014;2014:752103. <https://doi.org/10.1155/2014/752103>.
- [58] van Smeden J, Bouwstra JA. Stratum corneum lipids: their role for the skin barrier function in healthy subjects and atopic dermatitis patients. *Curr Probl Dermatol* 2016;49:8–26. <https://doi.org/10.1159/000441540>.
- [59] Ong PY. Recurrent MRSA skin infections in atopic dermatitis. *J Allergy Clin Pract* 2014;2:396–9. <https://doi.org/10.1016/j.jaip.2014.04.007>.
- [60] Shi B, Leung DYM, Taylor PA, Li H. MRSA colonization is associated with decreased skin commensal bacteria in atopic dermatitis. *J Invest Dermatol* 2018;138:1668–71. <https://doi.org/10.1016/j.jid.2018.01.022>.
- [61] Dandawate P, Padhye S, Schobert R, Biersack B. Discovery of natural products with metal-binding properties as promising antibacterial agents. *Expert Opin Drug Discov* 2019;14:563–76. <https://doi.org/10.1080/17460441.2019.1593367>.
- [62] Vestergaard M, Ingmer H. Antibacterial and antifungal properties of resveratrol. *Int J Antimicrob Agents* 2019;53:716–23. <https://doi.org/10.1016/j.ijantimicag.2019.02.015>.
- [63] Passeron T. Melasma pathogenesis and influencing factors—an overview of the latest research. *J Eur Acad Dermatol Venereol* 2013;27(Suppl. 1):5–6. <https://doi.org/10.1111/jdv.12049>.
- [64] Satooka H, Kubo I. Resveratrol as a kcat type inhibitor for tyrosinase: potentiated melanogenesis inhibitor. *Bioorg Med Chem* 2012;20:1090–9. <https://doi.org/10.1016/j.bmc.2011.11.030>.
- [65] Varoni EM, Lo Faro AF, Sharifi-Rad J, Iriti M. Anticancer molecular mechanisms of resveratrol. *Front Nutr* 2016;3:8. <https://doi.org/10.3389/fnut.2016.00008>.
- [66] Pezzuto JM. The phenomenon of resveratrol: redefining the virtues of promiscuity. *Ann N Y Acad Sci* 2011;1215:123–30. <https://doi.org/10.1111/j.1749-6632.2010.05849.x>.
- [67] Aminuddin A, Ng PY. Promising druggable target in head and neck squamous cell carcinoma: Wnt signaling. *Front Pharmacol* 2016;7:244. <https://doi.org/10.3389/fphar.2016.00244>.
- [68] Liu ZL, Li H, Liu J, Wu ML, Chen XY, Liu LH, Wang Q. Inactivated Wnt signaling in resveratrol-treated epidermal squamous cancer cells and its biological implication. *Oncol Lett* 2017;14:2239–43. <https://doi.org/10.3892/ol.2017.6458>.
- [69] Junco JJ, Mancha A, Malik G, Wei SJ, Kim DJ, Liang H, Slaga TJ. Resveratrol and P-glycoprotein inhibitors enhance the anti-skin cancer effects of ursolic acid. *Mol Cancer Res* 2013;11:1521–9. <https://doi.org/10.1158/1541-7786.MCR-13-0237>.
- [70] Junco JJ, Cho J, Mancha A, Malik G, Wei SJ, Kim DJ, Liang H, DiGiovanni J, Slaga TJ. Role of AMPK and PPAR $\alpha$  in the anti-skin cancer effects of ursolic acid. *Mol Carcinog* 2018;57:1698–706. <https://doi.org/10.1002/mc.22890>.
- [71] Kundu JK, Shin YK, Kim SH, Surh YJ. Resveratrol inhibits phorbol ester-induced expression of COX-2 and activation of NF- $\kappa$ B in mouse skin by blocking I $\kappa$ B kinase activity. *Carcinogenesis* 2006;27:1465–74. <https://doi.org/10.1093/carcin/bgi349>.
- [72] Kundu JK, Shin YK, Surh YJ. Resveratrol modulates phorbol ester-induced pro-inflammatory signal transduction pathways in mouse skin in vivo: NF- $\kappa$ B and AP-1 as prime targets. *Biochem Pharmacol* 2006;72:1506–15. <https://doi.org/10.1016/j.bcp.2006.08.005>.
- [73] Roy P, Kalra N, Prasad S, George J, Shukla Y. Chemo-preventive potential of resveratrol in mouse skin tumors through regulation of mitochondrial and PI3K/AKT signaling pathways. *Pharm Res* 2009;26:211–7. <https://doi.org/10.1007/s11095-008-9723-z>.
- [74] Heenatigala Palliyage G, Singh S, Ashby Jr CR, Tiwari AK, Chauhan H. Pharmaceutical topical delivery of poorly soluble polyphenols: potential role in prevention and treatment of melanoma. *AAPS PharmSciTech* 2019;20:250. <https://doi.org/10.1208/s12249-019-1457-1>.
- [75] Gong C, Xia H. Resveratrol suppresses melanoma growth by promoting autophagy through inhibiting the PI3K/AKT/mTOR signaling pathway. *Exp Ther Med* 2020;19:1878–86. <https://doi.org/10.3892/etm.2019.8359>.
- [76] Osmond GW, Augustine CK, Zipfel PA, Padussis J, Tyler DS. Enhancing melanoma treatment with resveratrol. *J Surg Res* 2012;172:109–15. <https://doi.org/10.1016/j.jss.2010.07.033>.
- [77] Nivellet L, Hubert J, Courtois E, Jeandet P, Aziz A, Nuzillard JM, Renault JH, Clément C, Martiny L, Delmas D, Tarpin M. Anti-cancer activity of resveratrol and derivatives produced by grapevine cell suspensions in a 14 L stirred bioreactor. *Molecules* 2017;22:474. <https://doi.org/10.3390/molecules22030474>.
- [78] Nivellet L, Aires V, Rioult D, Martiny L, Tarpin M, Delmas D. Molecular analysis of differential antiproliferative activity of resveratrol, epsilon viniferin and labruscol on melanoma cells and normal dermal cells. *Food Chem Toxicol* 2018;116:323–34. <https://doi.org/10.1016/j.fct.2018.04.043>.
- [79] Chen R, Li R, Liu Q, Bai C, Qin B, Ma Y, Han J. Ultra-deformable liposomes: a novel vesicular carrier for enhanced transdermal delivery of procyanidins: effect of surfactants on the formation, stability, and transdermal delivery. *AAPS PharmSciTech* 2017;18:1823–32. <https://doi.org/10.1208/s12249-016-0661-5>.
- [80] Cosco D, Paolino D, Maiuolo J, Marzio LD, Carafa M, Ventura CA, Fresta M. Ultradeformable liposomes as multidrug carrier of resveratrol and 5-fluorouracil for their topical delivery. *Int J Pharm* 2015;489:1–10. <https://doi.org/10.1016/j.ijpharm.2015.04.056>.
- [81] Bano S, Ahmed F, Khan F, Chaudhary SC, Samim M. Enhancement of the cancer inhibitory effect of the bioactive food component resveratrol by nanoparticle based delivery. *Food Funct* 2020;11:3213–26. <https://doi.org/10.1039/c9fo02445j>.
- [82] Kohl E, Steinbauer J, Landthaler M, Szeimies RM. Skin ageing. *J Eur Acad Dermatol Venereol* 2011;25:873–84. <https://doi.org/10.1111/j.1468-3083.2010.03963.x>.
- [83] Farage MA, Miller KW, Elsner P, Maibach HI. Intrinsic and extrinsic factors in skin ageing: a review. *Int J Cosmet Sci* 2008;30:87–95. <https://doi.org/10.1111/j.1468-2494.2007.00415.x>.
- [84] Davinelli S, Bertoglio JC, Polimeni A, Scapagnini G. Cytoprotective polyphenols against chronological skin aging and cutaneous photodamage. *Curr Pharm Des* 2018;24:99–105. <https://doi.org/10.2174/1381612823666171109102426>.
- [85] Serravallo M, Jagdeo J, Glick SA, Siegel DM, Brody NI. Sirtuins in dermatology: applications for future research and therapeutics. *Arch Dermatol Res* 2013;305:269–82. <https://doi.org/10.1007/s00403-013-1320-2>.



- [86] Truong VL, Jun M, Jeong WS. Role of resveratrol in regulation of cellular defense systems against oxidative stress. *Biofactors* 2018;44:36–49. <https://doi.org/10.1002/biof.1399>.
- [87] Alonso C, Rubio L, Touriño S, Martí M, Barba C, Fernández-Campos F, Coderch L, Parra JL. Antioxidative effects and percutaneous absorption of five polyphenols. *Free Radic Biol Med* 2014;75:149–55. <https://doi.org/10.1016/j.freeradbiomed.2014.07.014>.
- [88] Alonso C, Martí M, Barba C, Carrer V, Rubio L, Coderch L. Skin permeation and antioxidant efficacy of topically applied resveratrol. *Arch Dermatol Res* 2017;309:423–31. <https://doi.org/10.1007/s00403-017-1740-5>.
- [89] Parrado C, Mercado-Saenz S, Perez-Davo A, Gilaberte Y, Gonzalez S, Juarraz A. Environmental stressors on skin aging. Mechanistic insights. *Front Pharmacol* 2019;10:759. <https://doi.org/10.3389/fphar.2019.00759>.
- [90] Park K, Lee JH. Protective effects of resveratrol on UVB-irradiated HaCaT cells through attenuation of the caspase pathway. *Oncol Rep* 2008;19:413–7. <https://doi.org/10.3892/or.19.2.413>.
- [91] Reagan-Shaw S, Afaq F, Aziz MH, Ahmad N. Modulations of critical cell cycle regulatory events during chemoprevention of ultraviolet B-mediated responses by resveratrol in SKH-1 hairless mouse skin. *Oncogene* 2004;23:5151–60. <https://doi.org/10.1038/sj.onc.1207666>.
- [92] Aziz MH, Afaq F, Ahmad N. Prevention of ultraviolet-B radiation damage by resveratrol in mouse skin is mediated via modulation in survivin. *Photochem Photobiol* 2005;81:25–31. <https://doi.org/10.1562/2004-08-13-RA-274>.
- [93] Li H, Jiang N, Liang B, Liu Q, Zhang E, Peng L, Deng H, Li R, Li Z, Zhu H. Pterostilbene protects against UVB-induced photo-damage through a phosphatidylinositol-3-kinase-dependent Nrf2/ARE pathway in human keratinocytes. *Redox Rep* 2017;22:501–7. <https://doi.org/10.1080/13510002.2017.1329917>.
- [94] Ma Q. Role of nrf2 in oxidative stress and toxicity. *Ann Rev Pharmacol Toxicol* 2013;53:401–26. <https://doi.org/10.1146/annurev-pharmtox-011112-140320>.
- [95] Sirerol JA, Feddi F, Mena S, Rodriguez ML, Sirera P, Aupí M, Pérez S, Asensi M, Ortega A, Estrela JM. Topical treatment with pterostilbene, a natural phytoalexin, effectively protects hairless mice against UVB radiation-induced skin damage and carcinogenesis. *Free Radic Biol Med* 2015;85:1–11. <https://doi.org/10.1016/j.freeradbiomed.2015.03.027>.
- [96] He YD, Liu YT, Lin QX, Zhu J, Zhang Y, Wang LY, Ren XL, Ye XY. Polydatin suppresses ultraviolet B-induced cyclooxygenase-2 expression in vitro and in vivo via reduced production of reactive oxygen species. *Br J Dermatol* 2012;167:941–4. <https://doi.org/10.1111/j.1365-2133.2012.10951.x>.
- [97] Pittayapruet P, Meephansan J, Prapapan O, Komine M, Ohtsuki M. Role of matrix metalloproteinases in photoaging and photocarcinogenesis. *Int J Mol Sci* 2016;17:868. <https://doi.org/10.3390/ijms17060868>.
- [98] Garg V, Singh H, Bimbrawh S, Singh SK, Gulati M, Vaidya Y, Kaur P. Ethosomes and transfersomes: principles, perspectives and practices. *Curr Drug Deliv* 2017;14:613–33. <https://doi.org/10.2174/1567201813666160520114436>.
- [99] Scognamiglio I, De Stefano D, Campani V, Mayol L, Carnuccio R, Fabbrocini G, Ayala F, La Rotonda MI, De Rosa G. Nanocarriers for topical administration of resveratrol: a comparative study. *Int J Pharm* 2013;440:179–87. <https://doi.org/10.1016/j.ijpharm.2012.08.009>.
- [100] Wu PS, Li YS, Kuo YC, Tsai SJ, Lin CC. Preparation and evaluation of novel transfersomes combined with the natural antioxidant resveratrol. *Molecules* 2019;24:600. <https://doi.org/10.3390/molecules24030600>.
- [101] Wen CJ, Yen TC, Al-Suwayeh SA, Chang HW, Fang JY. In vivo real-time fluorescence visualization and brain-targeting mechanisms of lipid nanocarriers with different fatty ester:oil ratios. *Nanomedicine* 2011;6:1545–59. <https://doi.org/10.2217/nmm.11.46>.
- [102] Gokce EH, Korkmaz E, Dellera E, Sandri G, Bonferoni MC, Ozer O. Resveratrol-loaded solid lipid nanoparticles versus nanostructured lipid carriers: evaluation of antioxidant potential for dermal applications. *Int J Nanomed* 2012;7:1841–50. <https://doi.org/10.2147/IJN.S29710>.
- [103] Gu Y, Han J, Jiang C, Zhang Y. Biomarkers, oxidative stress and autophagy in skin aging. *Ageing Res Rev* 2020;59:101036. <https://doi.org/10.1016/j.arr.2020.101036>.
- [104] de Lima Cherubim DJ, Buzanello Martins CV, Oliveira Fariña L, da Silva de Lucca RA. Polyphenols as natural antioxidants in cosmetics applications. *J Cosmet Dermatol* 2020;19:33–7. <https://doi.org/10.1111/jocd.13093>.
- [105] Kato E, Tokunaga Y, Sakan F. Stilbenoids isolated from the seeds of melinjo (*Gnetum gnemon* L.) and their biological activity. *J Agric Food Chem* 2009;57:2544–9. <https://doi.org/10.1021/jf803077p>.
- [106] Watanabe K, Shibuya S, Ozawa Y, Izuo N, Shimizu T. Resveratrol derivative-rich melinjo seed extract attenuates skin atrophy in Sod1-deficient mice. *Oxid Med Cell Longev* 2015;2015:391075. <https://doi.org/10.1155/2015/391075>.
- [107] Igielska-Kalwat J, Firlej M, Lewandowska A, Biedziak B. In vivo studies of resveratrol contained in cosmetic emulsions. *Acta Biochim Pol* 2019;66:371–4. [https://doi.org/10.18388/abp.2019\\_2838](https://doi.org/10.18388/abp.2019_2838).
- [108] Buonocore D, Lazzeretti A, Tocabens P, Nobile V, Cestone E, Santin G, Bottone MG, Marzatico F. Resveratrol-procyanidin blend: nutraceutical and antiaging efficacy evaluated in a placebocontrolled, double-blind study. *Clin Cosmet Invest Dermatol* 2012;5:159–65. <https://doi.org/10.2147/CCID.S36102>.
- [109] Majeed M, Majeed S, Jain R, Mundkur L, Rajalakshmi HR, Lad PS, Neupane P. An open-label single-arm, monocentric study assessing the efficacy and safety of natural pterostilbene (*Pterocarpus marsupium*) for skin brightening and antiaging effects. *Clin Cosmet Invest Dermatol* 2020;13:105–16. <https://doi.org/10.2147/CCID.S238358>.
- [110] Pardeike J, Hommoss A, Müller RH. Lipid nanoparticles (SLN, NLC) in cosmetic and pharmaceutical dermal products. *Int J Pharm* 2009;366:170–84. <https://doi.org/10.1016/j.ijpharm.2008.10.003>.
- [111] Montenegro L, Parenti C, Turnaturi R, Pasquinnucci L. Resveratrol-loaded lipid nanocarriers: correlation between in vitro occlusion factor and in vivo skin hydrating effect. *Pharmaceutics* 2017;9:E58. <https://doi.org/10.3390/pharmaceutics9040058>.
- [112] Dainichi T, Hanakawa S, Kabashima K. Classification of inflammatory skin diseases: a proposal based on the disorders of the three-layered defense systems, barrier, innate immunity and acquired immunity. *J Dermatol Sci* 2014;76:81–9. <https://doi.org/10.1016/j.jdermsci.2014.08.010>.
- [113] Oliveira ALB, Monteiro VVS, Navegantes-Lima KC, Reis JF, Gomes RS, Rodrigues DVS, Gaspar SLF, Monteiro MC. Resveratrol role in autoimmune disease—A mini-review. *Nutrients* 2017;9:1306. <https://doi.org/10.3390/nu9121306>.
- [114] Salehi B, Mishra AP, Nigam M, Sener B, Kilic M, Sharifi-Rad M, Fokou PVT, Martins N, Sharifi-Rad J. Resveratrol: a double-edged sword in health benefits. *Biomedicines* 2018;6:91. <https://doi.org/10.3390/biomedicines6030091>.
- [115] Wu Z, Uchi H, Morino-Koga S, Shi W, Furue M. Resveratrol inhibition of human keratinocyte proliferation via SIRT1/ARNT/ERK dependent downregulation of aquaporin 3. *J Dermatol Sci* 2014;75:16–23. <https://doi.org/10.1016/j.jdermsci.2014.03.004>.
- [116] Kjør TN, Thorsen K, Jessen N, Stenderup K, Pedersen SB. Resveratrol ameliorates imiquimod-induced psoriasis-like skin inflammation in mice. *PLoS One* 2015;10:e0126599. <https://doi.org/10.1371/journal.pone.0126599>.
- [117] Madsen M, Hansen PR, Nielsen LB, Hartvigsen K, Pedersen AE, Christensen JP, Aarup A, Pedersen TX. Effect of 12-O-tetradecanoylphorbol-13-acetate-induced psoriasis-like skin lesions on systemic inflammation and atherosclerosis in hypercholesterolaemic apolipoprotein E deficient mice.

- BMC Dermatol 2016;16:9. <https://doi.org/10.1186/s12895-016-0046-1>.
- [118] Murakami I, Chaleckis R, Pluskal T, Ito K, Hori K, Ebe M, Yanagida M, Kondoh H. Metabolism of skin-absorbed resveratrol into its glucuronized form in mouse skin. *PLoS One* 2014;9:e115359. <https://doi.org/10.1371/journal.pone.0115359>.
- [119] Chung HJ, Sharma SP, Kim HJ, Baek SH, Hong ST. The resveratrol-enriched rice DJ526 boosts motor coordination and physical strength. *Sci Rep* 2016;6:23958. <https://doi.org/10.1038/srep23958>.
- [120] Kang MC, Cho K, Lee JH, Subedi L, Yumnam S, Kim SY. Effect of resveratrol-enriched rice on skin inflammation and pruritus in the NC/Nga mouse model of atopic dermatitis. *Int J Mol Sci* 2019;20:1428. <https://doi.org/10.3390/ijms20061428>.
- [121] Caglayan Sozmen S, Karaman M, Cilaker Micili S, Isik S, Arikan Ayyildiz Z, Bagriyanik A, Uzuner N, Karaman O. Resveratrol ameliorates 2,4-dinitrofluorobenzene-induced atopic dermatitis-like lesions through effects on the epithelium. *PeerJ* 2016;4:e1889. <https://doi.org/10.7717/peerj.1889>.
- [122] Shen Y, Xu J. Resveratrol exerts therapeutic effects on mice with atopic dermatitis. *Wounds* 2019;31:279–84.
- [123] Wang BJ, Chiu HW, Lee YL, Li CY, Wang YJ, Lee YH. Pterostilbene attenuates hexavalent chromium-induced allergic contact dermatitis by preventing cell apoptosis and inhibiting IL-1 $\beta$ -related NLRP3 inflammasome activation. *J Clin Med* 2018;7:489. <https://doi.org/10.3390/jcm7120489>.
- [124] Potapovich AI, Lulli D, Fidanza P, Kostyuk VA, De Luca C, Pastore S, Korkina LG. Plant polyphenols differentially modulate inflammatory responses of human keratinocytes by interfering with activation of transcription factors NF $\kappa$ B and AhR and EGFR-ERK pathway. *Toxicol Appl Pharmacol* 2011;255:138–49. <https://doi.org/10.1016/j.taap.2011.06.007>.
- [125] Pastore S, Lulli D, Fidanza P, Potapovich AI, Kostyuk VA, De Luca C, Mikhal'chik E, Korkina LG. Plant polyphenols regulate chemokine expression and tissue repair in human keratinocytes through interaction with cytoplasmic and nuclear components of epidermal growth factor receptor system. *Antioxid Redox Signal* 2012;16:314–28. <https://doi.org/10.1089/ars.2011.4053>.
- [126] Ravagnan G, De Filippis A, Carteni M, De Maria S, Cozza V, Petrazzuolo M, Tufano MA, Donnarumma G. Polydatin, a natural precursor of resveratrol, induces  $\beta$ -defensin production and reduces inflammatory response. *Inflammation* 2013;36:26–34. <https://doi.org/10.1007/s10753-012-9516-8>.
- [127] Caddeo C, Nacher A, Vassallo A, Armentano MF, Pons R, Fernández-Busquets X, Carbone C, Valenti D, Fadda AM, Manconi M. Effect of quercetin and resveratrol co-incorporated in liposomes against inflammatory/oxidative response associated with skin cancer. *Int J Pharm* 2016;513:153–63. <https://doi.org/10.1016/j.ijpharm.2016.09.014>.
- [128] Moghassemi S, Hadjizadeh A. Nano-niosomes as nanoscale drug delivery systems: an illustrated review. *J Control Release* 2014;185:22–36. <https://doi.org/10.1016/j.jconrel.2014.04.015>.
- [129] Negi P, Aggarwal M, Sharma G, Rathore C, Sharma G, Singh B, Katore OP. Niosome-based hydrogel of resveratrol for topical applications: an effective therapy for pain related disorder(s). *Biomed Pharmacother* 2017;88:480–7. <https://doi.org/10.1016/j.biopha.2017.01.083>.
- [130] Huang TH, Wang PW, Yang SC, Chou WL, Fang JY. Cosmetic and therapeutic applications of fish oil's fatty acids on the skin. *Mar Drugs* 2018;16:256. <https://doi.org/10.3390/md16080256>.
- [131] Serini S, Cassano R, Facchinetti E, Amendola G, Trombino S, Calviello G. Anti-irritant and anti-inflammatory effects of DHA encapsulated in resveratrol-based solid lipid nanoparticles in human keratinocytes. *Nutrients* 2019;11:1400. <https://doi.org/10.3390/nu11061400>.
- [132] Shrotriya SN, Ranpise NS, Vidhate BV. Skin targeting of resveratrol utilizing solid lipid nanoparticle-engrossed gel for chemically induced irritant contact dermatitis. *Drug Deliv Transl Res* 2017;7:37–52. <https://doi.org/10.1007/s13346-016-0350-7>.
- [133] Vashi NA, Wirya SA, Inyang M, Kundu RV. Facial hyperpigmentation in skin color: special considerations and treatment. *Am J Clin Dermatol* 2017;18:215–30. <https://doi.org/10.1007/s40257-016-0239-8>.
- [134] Zaidi KU, Ali SA, Ali A, Naaz I. Natural tyrosinase inhibitors: role of herbals in the treatment of hyperpigmentary disorders. *Mini Rev Med Chem* 2019;19:796–808. <https://doi.org/10.2174/1389557519666190116101039>.
- [135] Na JI, Shin JW, Choi HR, Kwon SH, Park KC. Resveratrol as a multifunctional topical hypopigmenting agent. *Int J Mol Sci* 2019;20:956. <https://doi.org/10.3390/ijms20040956>.
- [136] Park J, Boo YC. Isolation of resveratrol from *Vitis viniferae* caulis and its potent inhibition of human tyrosinase. *Evid Based Complement Alternat Med* 2013;2013:645257. <https://doi.org/10.1155/2013/645257>.
- [137] Wu Y, Jia LL, Zheng YN, Xu XG, Luo YJ, Wang B, Chen JZ, Gao XH, Chen HD, Matsui M, Li YH. Resveratrol protects human skin from damage due to repetitive ultraviolet irradiation. *J Eur Acad Dermatol Venereol* 2013;27:345–50. <https://doi.org/10.1111/j.1468-3083.2011.04414.x>.
- [138] Kim YM, Yun J, Lee CK, Lee H, Min KR, Kim Y. Oxy-resveratrol and hydroxystilbene compounds. Inhibitory effect on tyrosinase and mechanism of action. *J Biol Chem* 2002;277:16340–4. <https://doi.org/10.1074/jbc.M200678200>.
- [139] Chan EW, Lye PY, Wong SK. Phytochemistry, pharmacology, and clinical trials of *Morus alba*. *Chin J Nat Med* 2016;14:17–30. <https://doi.org/10.3724/SP.J.1009.2016.00017>.
- [140] Jeon YH, Choi SW. Isolation, identification, and quantification of tyrosinase and  $\alpha$ -glucosidase inhibitors from UVC-irradiated mulberry (*Morus alba* L.) leaves. *Prev Nutr Food Sci* 2019;24:84–94. <https://doi.org/10.3746/pnf.2019.24.1.84>.
- [141] Park J, Park JH, Suh HJ, Lee IC, Koh J, Boo YC. Effects of resveratrol, oxyresveratrol, and their acetylated derivatives on cellular melanogenesis. *Arch Dermatol Res* 2014;306:475–87. <https://doi.org/10.1007/s00403-014-1440-3>.
- [142] Yokozawa T, Kim YJ. Piceatannol inhibits melanogenesis by its antioxidative actions. *Biol Pharm Bull* 2007;30:2007–11. <https://doi.org/10.1248/bpb.30.2007>.
- [143] Jeong ET, Jin MH, Kim MS, Chang YH, Park SG. Inhibition of melanogenesis by piceid isolated from *Polygonum cuspidatum*. *Arch Pharm Res* 2010;33:1331–8. <https://doi.org/10.1007/s12272-010-0906-x>.
- [144] Uesugi D, Hamada H, Shimoda K, Kubota N, Ozaki SI, Nagatani N. Synthesis, oxygen radical absorbance capacity, and tyrosinase inhibitory activity of glycosides of resveratrol, pterostilbene, and pinostilbene. *Biosci Biotechnol Biochem* 2017;81:226–30. <https://doi.org/10.1080/09168451.2016.1240606>.
- [145] Yanagihara M, Yoshimatsu M, Inoue A, Kanno T, Tatefuji T, Hashimoto K. Inhibitory effect of gnetin C, a resveratrol dimer from melinjo (*Gnetum gnetum*), on tyrosinase activity and melanin biosynthesis. *Biol Pharm Bull* 2012;35:993–6. <https://doi.org/10.1248/bpb.35.993>.
- [146] Yun CY, Ko SM, Choi YP, Kim BJ, Lee J, Kim JM, Kim JY, Song JY, Kim SH, Hwang BY, Hong JT, Han SB, Kim Y.  $\alpha$ -Viniferin improves facial hyperpigmentation via accelerating feedback termination of cAMP/PKA-signaled phosphorylation circuit in facultative melanogenesis. *Theranostics* 2018;8:2031–43. <https://doi.org/10.7150/thno.24385>.
- [147] Lee TH, Kang JH, Seo JO, Baek SH, Moh SH, Chae JK, Park YU, Ko YT, Kim SY. Anti-melanogenic potentials of nanoparticles from calli of resveratrol-enriched rice against UVB-induced hyperpigmentation in guinea pig skin.

- Biomol Ther 2016;24:85–93. <https://doi.org/10.4062/biomolther.2015.165>.
- [148] Rigon RB, Fachinetti N, Severino P, Santana MH, Chorilli M. Skin delivery and in vitro biological evaluation of trans-resveratrol-loaded solid lipid nanoparticles for skin disorder therapies. *Molecules* 2016;21:116. <https://doi.org/10.3390/molecules21010116>.
- [149] Yeh YC, Huang TH, Yang SC, Chen CC, Fang JY. Nano-based drug delivery or targeting to eradicate bacteria for infection mitigation: a review of recent advances. *Front Chem* 2020;8:286. <https://doi.org/10.3389/fchem.2020.00286>.
- [150] Ong PY, Leung DY. Bacterial and viral infections in atopic dermatitis: a comprehensive review. *Clin Rev Allergy Immunol* 2016;51:329–37. <https://doi.org/10.1007/s12016-016-8548-5>.
- [151] Yang SC, Huang TH, Chiu CH, Chou WL, Alalaiwe A, Yeh YC, Su KW, Fang JY. The atopic dermatitis-like lesion and the associated MRSA infection and barrier dysfunction can be alleviated by 2,4-dimethoxy-6-methylbenzene-1,3-diol from *Anrodia camphorata*. *J Dermatol Sci* 2018;92:188–96. <https://doi.org/10.1016/j.jdermsci.2018.09.002>.
- [152] Chan MM. Antimicrobial effect of resveratrol on dermatophytes and bacterial pathogens of the skin. *Biochem Pharmacol* 2002;63:99–104. [https://doi.org/10.1016/s0006-2952\(01\)00886-3](https://doi.org/10.1016/s0006-2952(01)00886-3).
- [153] Mattio LM, Catinella G, Pallavalles S, Pinto A. Stilbenoids: a natural arsenal against bacterial pathogens. *Antibiotics* 2020;9:336. <https://doi.org/10.3390/antibiotics9060336>.
- [154] Annunziata G, Maisto M, Schisano C, Ciampaglia R, Narciso V, Tenore GC, Novellino E. Resveratrol as a novel anti-herpes simplex virus nutraceutical agent: an overview. *Viruses* 2018;10:473. <https://doi.org/10.3390/v10090473>.
- [155] Docherty JJ, Smith JS, Fu MM, Stoner T, Booth T. Effect of topically applied resveratrol on cutaneous herpes simplex virus infections in hairless mice. *Antiviral Res* 2004;61:19–26. <https://doi.org/10.1016/j.antiviral.2003.07.001>.
- [156] Chuanasa T, Phromjai J, Lipipun V, Likhitwitayawuid K, Suzuki M, Pramyothin P, Hattori M, Shiraki K. Anti-herpes simplex virus (HSV-1) activity of oxyresveratrol derived from Thai medicinal plant: mechanism of action and therapeutic efficacy on cutaneous HSV-1 infection in mice. *Antiviral Res* 2008;80:62–70. <https://doi.org/10.1016/j.antiviral.2008.05.002>.
- [157] Yang SC, Tseng CH, Wang PW, Lu PL, Weng YH, Yen FL, Fang JY. Pterostilbene, a methoxylated resveratrol derivative, efficiently eradicates planktonic, biofilm, and intracellular MRSA by topical application. *Front Microbiol* 2017;8:1103. <https://doi.org/10.3389/fmicb.2017.01103>.
- [158] Vitonyte J, Manca ML, Caddeo C, Valenti D, Peris JE, Usach I, Nacher A, Matos M, Gutiérrez G, Orrù G, Fernández-Busquets X, Fadda AM, Manconi M. Biofunctional viscous nanovesicles co-loaded with resveratrol and gallic acid for skin protection against microbial and oxidative injuries. *Eur J Pharm Biopharm* 2017;114:278–87. <https://doi.org/10.1016/j.ejpb.2017.02.004>.



# Stability of SARS-CoV-2 Spike G614 Variant Surpasses That of the D614 Variant after Cold Storage

 Sheng-Yu Huang,<sup>a,b</sup> Yu-An Kung,<sup>a,b</sup> Peng-Nien Huang,<sup>a,b,c</sup> Sheng-Yun Chang,<sup>a,d</sup>  Yu-Nong Gong,<sup>a,e</sup> Yi-Ju Han,<sup>a,f</sup> Huan-Jung Chiang,<sup>a,b</sup> Kuan-Ting Liu,<sup>a,f</sup>  Kuo-Ming Lee,<sup>a</sup> Chia-Yu Chang,<sup>g,h</sup> Chia-Ching Chang,<sup>g,h,i,j</sup> Chung-Guei Huang,<sup>b,e</sup>  Shin-Ru Shih<sup>a,b,e,k,l,m</sup>

<sup>a</sup>Research Center for Emerging Viral Infections, College of Medicine, Chang Gung University, Taoyuan, Taiwan

<sup>b</sup>Department of Medical Biotechnology and Laboratory Science, College of Medicine, Chang Gung University, Taoyuan, Taiwan

<sup>c</sup>Division of Infectious Diseases, Department of Pediatrics, Linkou Chang Gung Memorial Hospital, Taoyuan, Taiwan

<sup>d</sup>Bachelor Program in Artificial Intelligence, College of Engineering, Chang Gung University, Taoyuan, Taiwan

<sup>e</sup>Department of Laboratory Medicine, Linkou Chang Gung Memorial Hospital, Taoyuan, Taiwan

<sup>f</sup>Graduate Institute of Biomedical Science, Division of Biotechnology, College of Medicine, Chang Gung University, Taoyuan, Taiwan

<sup>g</sup>Department of Biological Science and Technology, College of Biological Science and Technology, National Yang Ming Chiao Tung University, Hsinchu, Taiwan

<sup>h</sup>Center for Intelligent Drug Systems and Smart Bio-devices (IDS2B), National Yang Ming Chiao Tung University, Hsinchu, Taiwan

<sup>i</sup>Department of Electrophysics, National Yang Ming Chiao Tung University, Hsinchu, Taiwan

<sup>j</sup>Institute of Physics, Academia Sinica, Nankang, Taipei, Taiwan

<sup>k</sup>Research Center for Chinese Herbal Medicine, Chang Gung University of Science and Technology, Taoyuan, Taiwan

<sup>l</sup>Research Center for Food and Cosmetic Safety, Chang Gung University of Science and Technology, Taoyuan, Taiwan

<sup>m</sup>Graduate Institute of Health Industry Technology, College of Human Ecology, Chang Gung University of Science and Technology, Taoyuan, Taiwan

Sheng-Yu Huang, Yu-An Kung, and Peng-Nien Huang contributed equally to this work; author order was decided by drawing straws.

**ABSTRACT** Severe acute respiratory syndrome coronavirus 2 (SARS-CoV-2) carrying the D614G mutation on the spike protein is the predominant circulating variant and is associated with enhanced infectivity. However, whether this dominant variant can potentially spread through the cold chain and whether the spike protein affects virus stability after cold storage remain unclear. To compare the infectivity of two SARS-CoV-2 variants, namely, SARS-CoV-2 variants with spike protein with the D614 mutation (S-D614) and G614 mutation (S-G614), after different periods of refrigeration (4°C) and freezing (−20°C). We also determined the integrity of the viral RNA and the ability of the spike protein to bind angiotensin-converting enzyme 2 (ACE2) after storage at these conditions. The results showed that SARS-CoV-2 was more stable and infectious after storage at −20°C than at 4°C. Particularly, the S-G614 variant was found to be more stable than the S-D614 variant. The spike protein of the S-G614 variant had better binding ability with the ACE2 receptor than that of the S-D614 variant after storage at −20°C for up to 30 days. Our findings revealed that SARS-CoV-2 remains stable and infectious after refrigeration or freezing, and their stability and infectivity up to 30 days depends on the spike variant. Stability and infectivity are related to each other, and the higher stability of S-G614 compared to that of S-D614 may contribute to rapid viral spread of the S-G614 variant.

**IMPORTANCE** It has been observed that variants of severe acute respiratory syndrome coronavirus 2 (SARS-CoV-2) are more stable and infectious after storage at −20°C than at 4°C. A SARS-CoV-2 S-D614G variant is currently the most dominant variant in circulation and is associated with enhanced infectivity. We compared the stability of two SARS-CoV-2 variants: the early S-D614 variant carrying the D614 spike protein and the new S-G614 variant carrying the G614 spike protein, stored at both 4°C and −20°C for different periods. We observed that SARS-CoV-2 remains stable and infectious after refrigeration or freezing, which further depends on the spike variant, that

**Citation** Huang S-Y, Kung Y-A, Huang P-N, Chang S-Y, Gong Y-N, Han Y-J, Chiang H-J, Liu K-T, Lee K-M, Chang C-Y, Chang C-C, Huang C-G, Shih S-R. 2021. Stability of SARS-CoV-2 spike G614 variant surpasses that of the D614 variant after cold storage. *mSphere* 6:e00104-21. <https://doi.org/10.1128/mSphere.00104-21>.

**Editor** Helene F. Rosenberg, National Institute of Allergy and Infectious Diseases

**Copyright** © 2021 Huang et al. This is an open-access article distributed under the terms of the [Creative Commons Attribution 4.0 International license](https://creativecommons.org/licenses/by/4.0/).

Address correspondence to Shin-Ru Shih, [srshih@mail.cgu.edu.tw](mailto:srshih@mail.cgu.edu.tw).

**Received** 3 February 2021

**Accepted** 10 March 2021

**Published** 31 March 2021



is, the ability of the spike protein to bind with the ACE2 receptor with higher efficiency. The high stability of the S-G614 variant also explains its rapid spread and infectivity. Therefore, precautions should be taken during and after handling food preserved under cold conditions.

**KEYWORDS** SARS-CoV-2, D614G mutation, spike protein, RNA integrity, temperature, ACE2, D614 variant, cold storage, stability

In 2019, a new human coronavirus, severe acute respiratory syndrome coronavirus 2 (SARS-CoV-2), emerged in Wuhan, China (1), and the disease it causes has been named coronavirus disease 2019 (COVID-19) by the World Health Organization. As of 9 March 2021, over 117 million COVID-19 cases have been recorded worldwide, causing more than 2.6 million deaths with a fatality rate of 0.8% to 14.5% (2). The estimated basic reproductive number for SARS-CoV-2 is approximately 2 to 6, whereas that for SARS-CoV is only 0.19 to 1.08 (3), which explains the rapid global spread of SARS-CoV-2 (4–7). Because COVID-19 cases are continuously increasing, the control of SARS-CoV-2 spread is of utmost importance.

Since June 2020, news reports from several countries have speculated that seafood products that are transported to the market through a cold chain may have caused the wide spread of the virus (8). Additionally, several studies have indicated that SARS-CoV-2 cannot remain viable at high temperatures (10–12), suggesting that SARS-CoV-2 could be transmitted through the cold chain. However, these studies examined only the changes in the infectious SARS-CoV-2 titer (50% tissue culture infective dose [TCID<sub>50</sub>]) of the early variant carrying spike protein with the D614 mutation (S-D614).

The SARS-CoV-2 spike protein is a receptor binding protein that is critical in its infectivity. A SARS-CoV-2 S-D614G variant emerged in February 2020 in Europe and is currently the most dominant variant in circulation (13). The reproductive number of the SARS-CoV-2 S-D614G variant increased by 31% compared with that of the wild-type SARS-CoV-2 S-D614 (14). The rapid spread of the S-D614G variant quickly garnered attention and necessitated investigations to understand its effect on SARS-CoV-2 infectivity. The S-D614G variant showed no significant association with disease severity and no change in sensitivity to neutralizing antibodies compared with the wild type (13–15). However, the titers, fitness, and transmission of S-G614-carrying SARS-CoV-2 are higher than those of the S-D614-carrying SARS-CoV-2 in hamster and human upper respiratory cells (15, 16). Although there is a clear difference in titers, the mechanism underlying these differences between the mutants remains unclear. Particularly, how mutations affect the binding ability of the virus to angiotensin-converting enzyme 2 (ACE2), an entry receptor for SARS-CoV-2, is unclear.

To compare the stability of early SARS-CoV-2 variants carrying the D614 spike protein (S-D614 variant) and new SARS-CoV-2 variant carrying the G614 spike protein (S-G614 variant), we stored both variants at 4°C and –20°C for different periods (up to 30 days). We then analyzed the effects of these temperatures on infectious viral titers, viral RNA integrity, and the ability of the virus to bind to ACE2. Our study provides insights into the differences in viral infectivity after exposure to different temperatures.

## RESULTS

**Higher infectivity of the SARS-CoV-2 S-G614 variant than that of S-D614 after cold storage.** To determine the effect of temperature on the S-D614 and S-G614 variants of SARS-CoV-2, we evaluated the titers of the two variants after cold storage. The titers of the SARS-CoV-2 S-D614 and S-G614 variants remained stable after 2.5 months of storage at –80°C compared with the baseline values (8 days of storage) (Fig. 1A). However, 14 days of storage at 4°C significantly reduced the titer of the S-D614 variant compared with storage at –20°C (Fig. 1B). The titers of the S-D614 variant were almost undetectable after 30 days of storage at 4°C but decreased by only 1 log unit relative to the baseline level (0 days of storage) when stored at –20°C. These findings indicate that the S-D614 variant is more stable at –20°C than at 4°C.

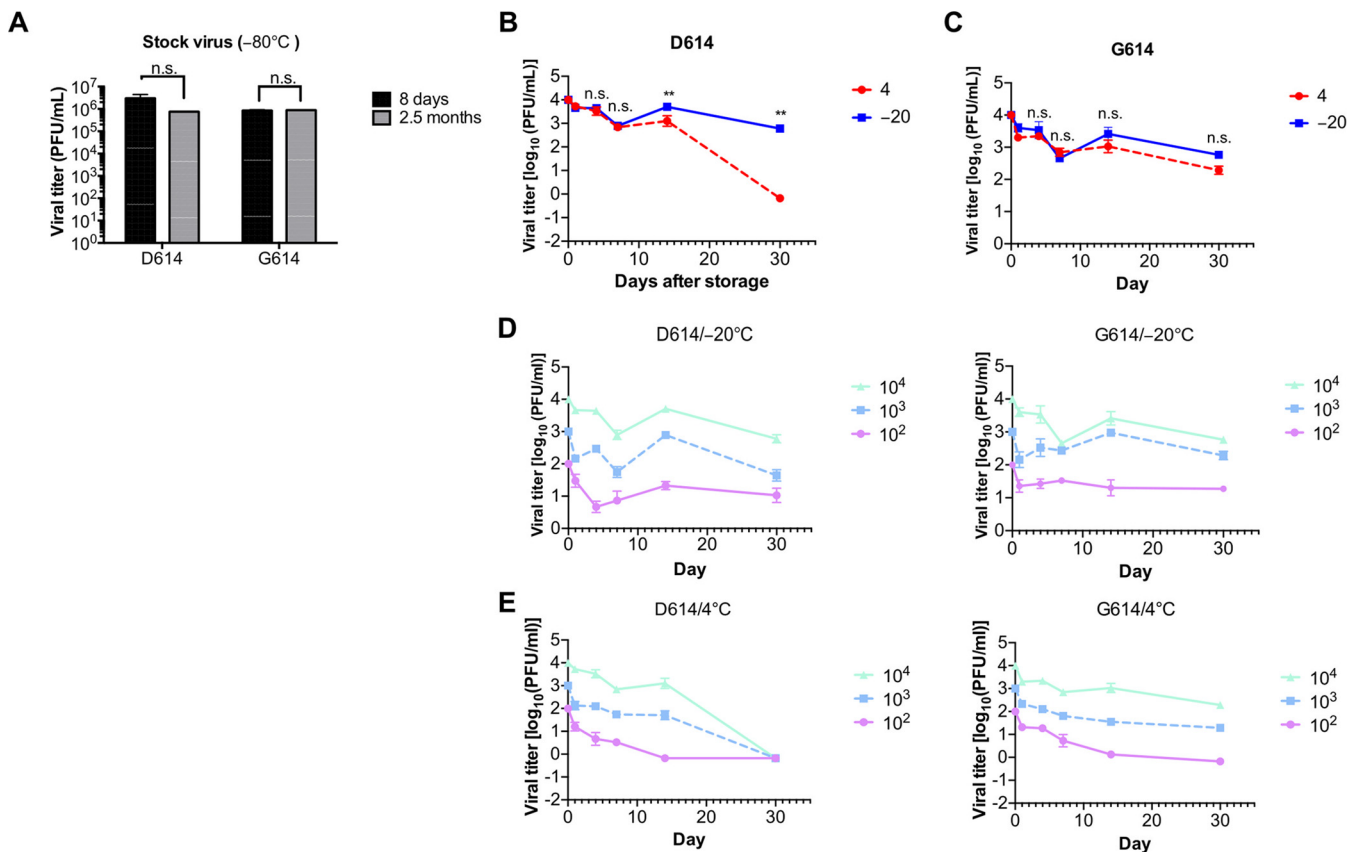


**FIG 1** Titers of severe acute respiratory syndrome coronavirus 2 (SARS-CoV-2) S-D614 and S-G614 variants after storage at  $4^{\circ}\text{C}$ ,  $-20^{\circ}\text{C}$ , and  $-80^{\circ}\text{C}$  for different durations. (A) Titers of virus stocks stored at  $-80^{\circ}\text{C}$  for 8 days and 2.5 months. (B and C) Comparison of viral titers of the S-D614 (D614) (B) and S-G614 (G614) (C) variants. The stocks of SARS-CoV-2 variants were diluted to  $10^4$  PFU/ml and stored at  $4^{\circ}\text{C}$  and  $-20^{\circ}\text{C}$  for different durations. (D) Comparison of viral titers of the S-D614 and S-G614 variants stored at  $4^{\circ}\text{C}$  and  $-20^{\circ}\text{C}$  for 30 days, with initial viral concentrations of  $10^4$  PFU/ml. (E and F) Titers of the S-D614 and S-G614 variants of SARS-CoV-2 with different initial viral concentrations stored at  $4^{\circ}\text{C}$  (E) or  $-20^{\circ}\text{C}$  (F) for different durations. Error bars represent the standard deviations (SD) of three independent experiments. Statistical significance was determined by conducting an unpaired *t* test ( $n=3$ ; \*,  $P < 0.05$ ; \*\*,  $P < 0.01$ ; ns, not significant).

Similarly, the titers of the S-G614 variant decreased approximately 1 log unit compared with the initial titer after storage at  $-20^{\circ}\text{C}$  for 30 days (Fig. 1C). Interestingly, unlike the S-D614 variant, the S-G614 variant retained a considerable degree of infectivity when stored at  $4^{\circ}\text{C}$  for 30 days (Fig. 1C), suggesting that the stability of the S-G614 variant after 30-day storage at  $4^{\circ}\text{C}$  and  $-20^{\circ}\text{C}$  is similar.

Next, we determined the stability of the variants at low initial viral titers, because the viral concentrations in the environment and on surfaces are typically not as high as that in laboratory cultures. For this purpose, we compared higher initial titers ( $10^4$ ) in Fig. 1B and C with lower initial titers ( $10^2$  and  $10^3$ ) in Fig. 1D and E. S-D614 and S-G614 with both high and low initial titers remained infectious even after 30 days of storage at  $-20^{\circ}\text{C}$  (Fig. 1D). However, the S-D614 variant exhibited higher infectivity for a longer duration at high initial viral titers ( $10^3$  and  $10^4$  PFU/ml) than low initial titers ( $10^2$  PFU/ml) at  $4^{\circ}\text{C}$  (Fig. 1E). Notably, the relatively stable S-G614 variant with high initial titers remained infectious when stored at  $4^{\circ}\text{C}$  for 30 days (Fig. 1E). These findings indicate that SARS-CoV-2 with low viral titers is less stable at  $4^{\circ}\text{C}$ .

**Higher RNA integrity of the SARS-CoV-2 S-G614 variant than that of S-D614 after cold storage.** We explored the reasons for the decrease in viral titers after storage. First, we determined whether SARS-CoV-2 RNA is degraded upon storage. The TaqMan probe system was used to quantify the expression of structural *E* and non-structural *nsp12* genes because degraded viral RNA cannot be amplified and detected (17). In both *E* and *nsp12* genes (Fig. 2), the trends in the copy numbers of viral RNA from the S-D614 and S-G614 variants were consistent with those of the infectious viral

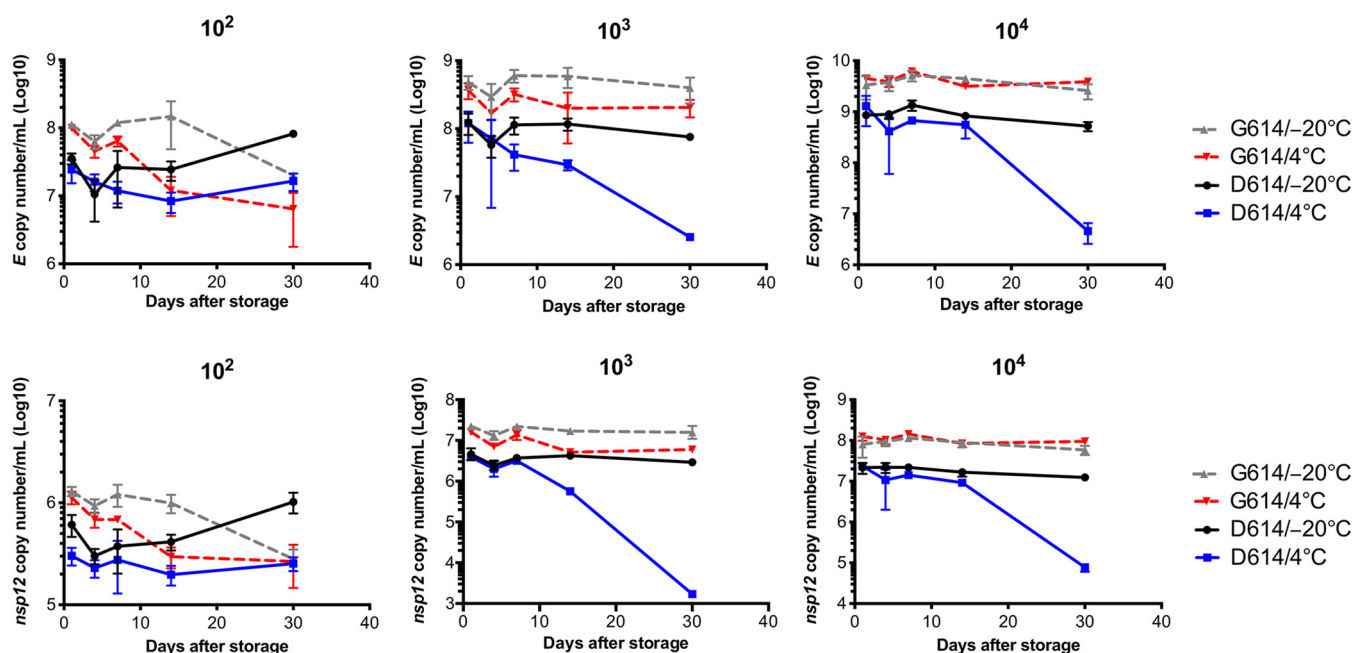


**FIG 2** Severe acute respiratory syndrome coronavirus 2 RNA copy numbers of the S-D614 and S-G614 variants stored at 4°C, –20°C, and –80°C. Virus stocks were diluted to  $10^2$ ,  $10^3$ , and  $10^4$  PFU/ml and stored at 4°C and –20°C for different durations. Viral RNA was extracted, and copy numbers were determined by targeting *E* (top) and *nsp12* (bottom) genes. Error bars represent the standard deviations (SD) derived from three independent experiments.

titers. Therefore, we speculated that the decrease in viral titer correlates with viral RNA degradation.

To confirm this hypothesis, we analyzed the integrity of SARS-CoV-2 RNA by determining the linear relationship between *nsp12* and *E* gene copies as previously described (17). The S-G614 variant showed a higher correlation between the *E* and *nsp12* genes than the S-D614 variant after storage at 4°C and –20°C (Fig. 3), indicating that the genome of the S-G614 variant is more stable. Moreover, the correlation between *E* and *nsp12* genes of the S-D614 variant was higher at –20°C than at 4°C,

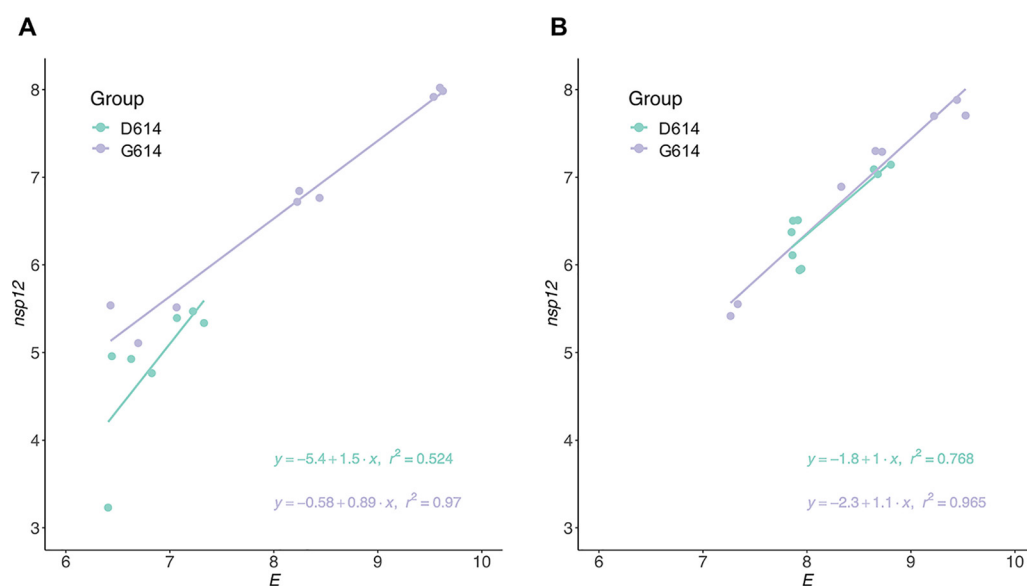


**FIG 3** Integrity of SARS-CoV-2 genomic RNA. (A and B) Correlation between the copy number of *nsp12* and *E* genes in the S-D614 and S-G614 variants of SARS-CoV-2 stored at 4°C (A) or –20°C (B) for 30 days. To increase the sample size to enable better comparison, we pooled samples of the same variant that were stored at the same temperature. The respective regression equations and  $r^2$  values are shown.

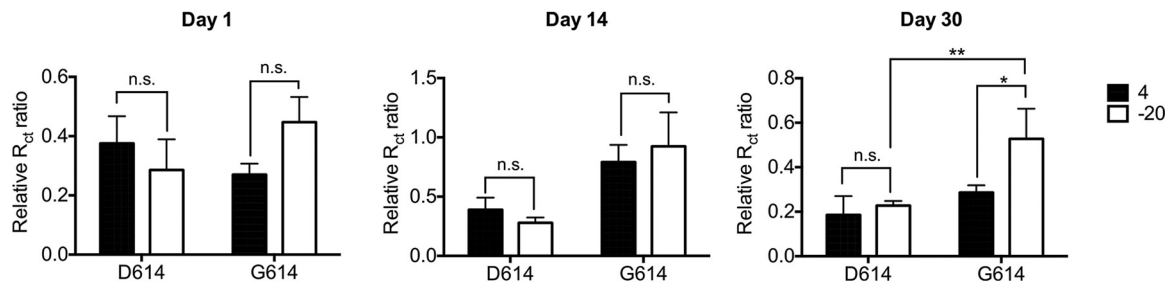


**FIG 4** Binding of the SARS-CoV-2 spike protein with recombinant human angiotensin-converting enzyme 2 (rhACE2). Pseudoviruses carrying SARS-CoV-2 S-D614 and S-G614 were stored at  $-20^{\circ}\text{C}$  or  $4^{\circ}\text{C}$  for different durations, and then added to rhACE2-coated chips. The relative  $R_{ct}$  ratio was considered proportional to the amount of spike protein bound to ACE2. Error bars represent standard deviations derived from three independent experiments. Significant differences were analyzed using the two-way ANOVA with Newman-Keuls multiple-comparison tests of data. ( $n = 3$ ; \*,  $P < 0.05$ ; \*\*,  $P < 0.01$ ; ns, not significant).

whereas that in the S-G614 variant was similar at both temperatures. These results are consistent with those observed for viral titers (Fig. 1B to E).

**Greater binding of the SARS-CoV-2 S-G614 variant to recombinant human ACE2 than that of S-D614 after cold storage.** Next, we explored the difference in the recombinant human ACE2 (rhACE2)-binding ability of the S-D614 and S-G614 variants after storage at different temperatures. We coated Pd nano-thin film polyethylene terephthalate electrodes with rhACE2 and then added either S-D614 or S-G614 pseudovirus at equal transduction unit (transduction unit [TU]/ $\mu\text{l}$ ) to the chip and observed the changes in resistance. We found no significant difference in the binding ability of the S-D614 and S-G614 pseudoviruses to rhACE2 at different temperatures on the first day (Fig. 4). Notably, the binding ability of the S-D614 pseudovirus at different temperatures did not significantly change after 30 days of storage. However, after 14 and 30 days, the binding ability of the S-G614 pseudovirus at  $-20^{\circ}\text{C}$  was significantly higher than that at  $4^{\circ}\text{C}$ . Thus, the rhACE2-binding ability of the S-G614 variant on day 30 of storage at  $-20^{\circ}\text{C}$  was significantly higher than that of the S-D614 variant. Moreover, storage at  $4^{\circ}\text{C}$  was not conducive for the maintenance of the rhACE2-binding ability of both variants, whereas storage at  $-20^{\circ}\text{C}$  better maintained the binding ability of the S-G614 variant compared with that of the S-D614 variant.

## DISCUSSION

Several studies have discussed the stability of SARS-CoV-2 at different temperatures or environmental conditions. To our knowledge, this is the first study to report the differences in viral infectivity after exposure to different temperatures by studying viral RNA integrity and binding ability of the spike protein to rhACE2, along with viral titer. Our findings also provided a possible explanation for the rapid spread of the S-G614 variant; it may be attributed to its higher stability.

The stability of viruses is affected by the concentration of the viral stock, and the viral titer present in the inoculum affects viral infectivity. The effects of temperature on SARS-CoV-2 have been previously investigated (12, 18, 19). However, the initial viral titer used was higher than  $10^6$  half-maximal tissue culture infectious dose/ml (equivalent to  $\sim 10^7$  PFU/ml). They found that the viral titer was quite stable, in contrast to our finding. We believe that the difference in the results is mainly because the initial virus concentration used is different from that in our study ( $10^2$  to  $10^4$  PFU/ml),  $3 \times 10^5$  to  $3 \times 10^3$  times higher. Our results in Fig. 1D and E show that the higher the virus concentration, the higher the stability of the virus, and the reduction in viral titer at  $4^{\circ}\text{C}$  is more significant than that at  $-20^{\circ}\text{C}$  and  $-80^{\circ}\text{C}$ . Our data, based on relatively low virus concentrations that are close to the actual concentration of viral particles in the environment, showed that the initial viral titer also affects its stability. La Scola et al. (20) reported that no virus culture was obtained from samples with cycle threshold ( $C_T$ ) values of  $\geq 34$  after the amplification of *E* gene, suggesting that patients with  $C_T$  values of  $\geq 34$  are no longer infectious and can be discharged. A  $C_T$  value of 34 for the *E* gene



is equivalent to  $6.16 \log_{10}$  copies/ml of SARS-CoV-2. Although all viral nucleic acids are not infectious viral particles, the expression of the viral RNA copies or the  $C_T$  values can provide an indication as to whether SARS-CoV-2 variants remain infectious after 1 month of storage at 4°C or −20°C. Our results indicated that SARS-CoV-2 in refrigerated or frozen foods exhibit considerable stability and infectivity even after 30 days. Notably, the aforementioned studies used the early SARS-CoV-2 S-D614 variant; in contrast, we studied both early and new variants and found that the new SARS-CoV-2 S-G614 variant is more stable than S-D614. Interestingly, the S-G614 variant we used had three other nonsynonymous mutations in the coding region and one mutation in its untranslated region. Whether these mutations contribute to the enhanced integrity of the SARS-CoV-2 G614 variant genome is unexplored. In addition, we analyzed the binding ability of the spike protein and rhACE2 through Pd nano-thin film polyethylene terephthalate electrodes. It has been shown that ACE2 undergoes glycation modification leading to integration into the plasma membrane (21). However, we conducted protein-protein interaction *in vitro*, and therefore, we believe that the expression of ACE2 without glycosylated modification through *Escherichia coli* will not affect the performance of binding ability with spike protein.

In conclusion, we found that the S-D614 variant does not remain infectious after storage at 4°C for 30 days but remains infectious after 30 days of storage at −20°C. Notably, the currently prevalent G614 mutation-harboring variant remains infectious regardless of the storage temperature for 30 days. Thus, SARS-CoV-2 may transmit through foods preserved under cold conditions. Therefore, precautions should be taken while eating and handling foods preserved under cold conditions. Moreover, although the susceptibility to serum/antibody neutralization of the S-G614 variant remains unchanged, its high stability still plays an important role in its ability to spread.

## MATERIALS AND METHODS

**Cell line.** VeroE6 (American Type Culture Collection, Manassas, VA, USA) cells were grown in Dulbecco's modified Eagle's medium (DMEM) containing 10% fetal bovine serum (FBS), 1% antibiotic/antimycotic solution, and 1% L-glutamine (Gibco, Grand Island, NY, USA). The cells were cultured at 37°C with 5% CO<sub>2</sub>.

**Viruses.** The S-D614 SARS-CoV-2/human/TWN/CGMH-CGU-01/2020 (GISAID [https://www.gisaid.org] accession number EPI\_ISL\_411915; NCBI accession number [MT192759.1](#)) and S-G614 SARS-CoV-2/human/TWN/CGMH-CGU-25/2020 (GISAID accession number EPI\_ISL\_444278; NCBI accession number [MT479227.1](#)) variants were originally isolated from a patient with COVID-19 from Chang Gung Memorial Hospital. Viral amplification and manipulation were performed in an accredited biosafety level 3 laboratory at the Chang Gung Memorial Hospital. The S-G614 variant has four synonymous and four nonsynonymous mutations in the coding region. The nonsynonymous mutations include ORF1ab-C794T(T265I), ORF1ab-C14144T(P4715L), S-A1841G(D614G), and ORF3a-G171C(Q57H). There is also a mutation in the 5' untranslated region—C241T. The SARS-CoV-2 stocks of the S-D614 and S-G614 variants were diluted in DMEM with 2% FBS at 10<sup>2</sup> to 10<sup>4</sup> PFU/ml and stored at 4°C and −20°C for different durations (1, 4, 7, 21, and 30 days). Thereafter, they were transferred to −80°C until further analyses such as titration, RNA quantification, and RNA integrity analysis. Viruses were propagated in Vero E6 cells, maintained in DMEM with 2% FBS and stored at −80°C until further study.

**Plaque assay.** VeroE6 cells were seeded into a six-well cell culture plate and grown for 18 to 24 h at 37°C. At 90% confluence, the medium was removed, and 10-fold serial viral dilutions (from 10<sup>0</sup> to 10<sup>−4</sup>) were allowed to adsorb onto the cells for 60 min. The cells were washed with phosphate-buffered saline and grown in DMEM containing 2% FBS with 0.4% of agarose for 3 days. To visualize the plaques, the cells were inactivated with 10% formalin for at least 1 h and were then stained with 0.5% crystal violet.

**Viral RNA extraction and real-time PCR (RT-PCR).** Viral RNA was extracted using the LabTurbo Viral DNA/RNAMini kit according to the manufacturer's instructions and using the LabTurbo 48 Compact System (Taigen Bioscience, Taipei, Taiwan). The *E* and *nsp12* genes were quantified as described previously (17).

**SARS-CoV-2 pseudovirus.** The SARS-CoV-2-S Luc pseudovirus (provided by the National RNAi Core Facility, Academia Sinica, Taiwan) uses pCMVdeltaR8.91 and pcDNA3.1 to express the spike protein on the viral surface. The transfer vector pLAS2w.FLuc.Ppuro carried by the virus expresses firefly luciferase.

**Recombinant expression and characterization of the human ACE2 protein.** rhACE2 was expressed in the *Escherichia coli* system as previously described (22–24). rhACE2 refolding was confirmed by Western blotting, and its interaction with the SARS-CoV-2 spike protein receptor-binding domain was confirmed by electrochemical impedance spectroscopy measurements as described below.

**Electrochemical impedance spectroscopy measurements.** The electrochemical properties of the ACE2-functionalized Pd nano-thin film polyethylene terephthalate electrodes were determined based on our previous study protocol (22, 25).

**Statistical analysis.** We used Student's *t* test to compare the results of the viral titer changes between 4°C and −20°C on the same day, presented in Fig. 1B and C. The two-way analysis of variance (ANOVA) with Newman-Keuls multiple-comparison test was used to analyze the ACE2-binding ability of the same virus variant at different temperatures and that of different variant viruses at the same temperature. Statistical analysis was performed using GraphPad Prism v9.3.3 (GraphPad Software, Inc., CA, USA). Data are presented as means ± standard errors of means. Results with a *P* value of <0.05 were considered statistically significant. Linear regression models were used to determine the correlation between genome copies of structural (*E*) and nonstructural genes (*nsp12*) with *C<sub>T</sub>* values obtained from RT-PCR, and the *R*<sup>2</sup> value was used to assess model fitness. Statistical analysis was conducted using the R software v3.6.1 (26), and the distribution of genome copies and their correlations were visualized using the R package ggplot2 as previously described (17, 27).

## ACKNOWLEDGMENTS

We thank the National RNAi Core Facility at the Academia Sinica in Taiwan for providing the SARS-CoV-2 pseudovirus, and their related services.

This work was supported by the Research Center for Emerging Viral Infections from The Featured Areas Research Center Program within the framework of the Higher Education Sprout Project by the Ministry of Education in Taiwan and the Ministry of Science and Technology, Taiwan (grant number MOST 109-2634-F-182-001), the Ministry of Science and Technology, Taiwan (grant number MOST 109-2327-B-182-002), the Chang Gung Memorial Hospital (grant number CORPD1K0011), and the National Institutes of Health USA grant U01 AI151698 for the United World Antiviral Research Network (UWARN). The funders had no role in study design, data collection and interpretation, or the decision to submit the work for publication.

## REFERENCES

- Huang C, Wang Y, Li X, Ren L, Zhao J, Hu Y, Zhang L, Fan G, Xu J, Gu X, Cheng Z, Yu T, Xia J, Wei Y, Wu W, Xie X, Yin W, Li H, Liu M, Xiao Y, Gao H, Guo L, Xie J, Wang G, Jiang R, Gao Z, Jin Q, Wang J, Cao B. 2020. Clinical features of patients infected with 2019 novel coronavirus in Wuhan, China. *Lancet* 395:497–506. [https://doi.org/10.1016/S0140-6736\(20\)30183-5](https://doi.org/10.1016/S0140-6736(20)30183-5).
- Johns Hopkins University of Medicine. 2020. Mortality analyses. Coronavirus Resource Center, Johns Hopkins University of Medicine, Baltimore, MD. <https://coronavirus.jhu.edu/data/mortality>. Accessed 29 December 2020.
- Chowell G, Castillo-Chavez C, Fenimore PW, Kribs-Zaleta CM, Arriola L, Hyman JM. 2004. Model parameters and outbreak control for SARS. *Emerg Infect Dis* 10:1258–1263. <https://doi.org/10.3201/eid1007.030647>.
- Rahman B, Sadraddin E, Porreca A. 2020. The basic reproduction number of SARS-CoV-2 in Wuhan is about to die out, how about the rest of the world? *Rev Med Virol* 30:e2111. <https://doi.org/10.1002/rmv.2111>.
- Sanche S, Lin YT, Xu C, Romero-Severson E, Hengartner N, Ke R. 2020. High contagiousness and rapid spread of severe acute respiratory syndrome coronavirus 2. *Emerg Infect Dis* 26:1470–1477. <https://doi.org/10.3201/eid2607.200282>.
- Wang L, Wang Y, Ye D, Liu Q. 2020. Review of the 2019 novel coronavirus (SARS-CoV-2) based on current evidence. *Int J Antimicrob Agents* 55:105948. <https://doi.org/10.1016/j.ijantimicag.2020.105948>.
- Lai CC, Shih TP, Ko WC, Tang HJ, Hsueh PR. 2020. Severe acute respiratory syndrome coronavirus 2 (SARS-CoV-2) and coronavirus disease-2019 (COVID-19): the epidemic and the challenges. *Int J Antimicrob Agents* 55:105924. <https://doi.org/10.1016/j.ijantimicag.2020.105924>.
- Zhao Y. 19 June 2020. China's CDC experts investigate Xinfadi market three times, announce groundbreaking virus tracing discovery. *Global Times*, Beijing, People's Republic of China. <https://www.globaltimes.cn/content/1192146.shtml>.
- Reference deleted
- Riddell S, Goldie S, Hill A, Eagles D, Drew TW. 2020. The effect of temperature on persistence of SARS-CoV-2 on common surfaces. *Virol J* 17:145. <https://doi.org/10.1186/s12985-020-01418-7>.
- Kratzel A, Steiner S, Todt D, V'kovski P, Brueggemann Y, Steinmann J, Steinmann E, Thiel V, Pfaender S. 2020. Temperature-dependent surface stability of SARS-CoV-2. *J Infect* 81:452–482. <https://doi.org/10.1016/j.jinf.2020.05.074>.
- Biryukov J, Boydston JA, Dunning RA, Yeager JJ, Wood S, Reese AL, Ferris A, Miller D, Weaver W, Zeitouni NE, Phillips A, Freeburger D, Hooper I, Ratnesar-Shumate S, Yolitz J, Krause M, Williams G, Dawson DG, Herzog A, Dabisch P, Wahl V, Hevey MC, Altamura LA. 2020. Increasing temperature and relative humidity accelerates inactivation of SARS-CoV-2 on surfaces. *mSphere* 5:e00441-20. <https://doi.org/10.1128/mSphere.00441-20>.
- Korber B, Fischer WM, Gnanakaran S, Yoon H, Theiler J, Abfalterer W, Hengartner N, Giorgi EE, Bhattacharya T, Foley B, Hastie KM, Parker MD, Partridge DG, Evans CM, Freeman TM, de Silva TI, Sheffield COVID-19 Genomics Group, McDanal C, Perez LG, Tang H, Moon-Walker A, Whelan SP, LaBranche CC, Saphire EO, Montefiori DC. 2020. Tracking changes in SARS-CoV-2 spike: evidence that D614G increases infectivity of the COVID-19 virus. *Cell* 182:812–827.e19. <https://doi.org/10.1016/j.cell.2020.06.043>.
- Leung K, Pei Y, Leung GM, Lam TT, Wu JT. 2020. Empirical transmission advantage of the D614G mutant strain of SARS-CoV-2. *medRxiv*. <https://doi.org/10.1101/2020.09.22.20199810>.
- Plante JA, Liu Y, Liu J, Xia H, Johnson BA, Lokugamage KG, Zhang X, Muruato AE, Zou J, Fontes-Garfias CR, Mirchandani D, Scharf D, Bilello JP, Ku Z, An Z, Kalveram B, Freiberg AN, Menachery VD, Xie X, Plante KS, Weaver SC, Shi PY. 2020. Spike mutation D614G alters SARS-CoV-2 fitness. *Nature*. <https://doi.org/10.1038/s41586-020-2895-3>.
- Hou YJ, Chiba S, Halfmann P, Ehre C, Kuroda M, Dinnon KH, Leist SR, Schäfer A, Nakajima N, Takahashi K, Lee RE, Mascenik TM, Graham R, Edwards CE, Tse LV, Okuda K, Markmann AJ, Bartelt L, de Silva A, Margolis DM, Boucher RC, Randell SH, Suzuki T, Gralinski LE, Kawaoka Y, Baric RS. 2020. SARS-CoV-2 D614G variant exhibits efficient replication ex vivo and transmission in vivo. *Science* 370:1464–1468. <https://doi.org/10.1126/science.abe8499>.
- Huang CG, Lee KM, Hsiao MJ, Yang SL, Huang PN, Gong YN, Hsieh TH, Huang PW, Lin YJ, Liu YC, Tsao KC, Shih SR. 2020. Culture-based virus isolation to evaluate potential infectivity of clinical specimens tested for COVID-19. *J Clin Microbiol* 58:e01068-20. <https://doi.org/10.1128/JCM.01068-20>.
- Chan KH, Sridhar S, Zhang RR, Chu H, Fung AY-F, Chan G, Chan JF-W, To KK-W, Hung IF-N, Cheng VC-C, Yuen K-Y. 2020. Factors affecting stability and infectivity of SARS-CoV-2. *J Hosp Infect* 106:226–231. <https://doi.org/10.1016/j.jhin.2020.07.009>.

19. Chin AWH, Chu JTS, Perera MRA, Hui KPY, Yen HL, Chan MCW, Peiris M, Poon LLM. 2020. Stability of SARS-CoV-2 in different environmental conditions. *Lancet Microbe* 1:e10. [https://doi.org/10.1016/S2666-5247\(20\)30003-3](https://doi.org/10.1016/S2666-5247(20)30003-3).
20. La Scola B, Le Bideau M, Andreani J, Hoang VT, Grimaldier C, Colson P, Gautret P, Raoult D. 2020. Viral RNA load as determined by cell culture as a management tool for discharge of SARS-CoV-2 patients from infectious disease wards. *Eur J Clin Microbiol Infect Dis* 39:1059–1061. <https://doi.org/10.1007/s10096-020-03913-9>.
21. Schrom E, Huber M, Aneja M, Dohmen C, Emrich D, Geiger J, Hasenpusch G, Herrmann-Janson A, Kretzschmann V, Mykhailik O, Pasewald T, Oak P, Hilgendorff A, Wohlleber D, Hoymann HG, Schaudien D, Plank C, Rudolph C, Kubisch-Dohmen R. 2017. Translation of angiotensin-converting enzyme 2 upon liver- and lung-targeted delivery of optimized chemically modified mRNA. *Mol Ther Nucleic Acids* 7:350–365. <https://doi.org/10.1016/j.omtn.2017.04.006>.
22. Chang CY, Huang YT, Chang PC, Su CH, Hsu KC, Li X, Wu CH, Chang CC. 2019. Surface active flexible palladium nano-thin-film electrode development for biosensing. *Inorg Chem Commun (Camb)* 107:107461. <https://doi.org/10.1016/j.inoche.2019.107461>.
23. Chang CC, Su YC, Cheng MS, Kan LS. 2002. Protein folding by a quasi-static-like process: a first-order state transition. *Phys Rev E Stat Nonlin Soft Matter Phys* 66:021903. <https://doi.org/10.1103/PhysRevE.66.021903>.
24. Chang CC, Cheng MS, Su YC, Kan LS. 2003. A first-order-like state transition for recombinant protein folding. *J Biomol Struct Dyn* 21:247–256. <https://doi.org/10.1080/07391102.2003.10506920>.
25. Chang CY, Chen W, Su CH, Chang PC, Huang YT, Hsu KC, Yuan CJ, Chang CC. 2019. Enhanced bioconjugation on sputtered palladium nano-thin-film electrode. *Appl Phys Lett* 114:93702. <https://doi.org/10.1063/1.5087030>.
26. R Development Core Team. 2019. R: a language and environment for statistical computing. R Foundation for Statistical Computing, Vienna, Austria.
27. Wickham H. 2016. ggplot2: elegant graphics for data analysis. Springer-Verlag, New York, NY.



OPEN

# Adverse body measurements are superior to sarcopenia-associated measurements in predicting chronic diseases

Pei-Ju Liao<sup>1</sup>, Yu-Ching Lin<sup>2</sup>, Ming-Kuo Ting<sup>3</sup>, I.-W.en Wu<sup>4</sup>, Shuo-Wei Chen<sup>5</sup>, Ning-I. Yang<sup>6</sup> & Kuang-Hung Hsu<sup>7,8,9,10,11,12</sup>✉

Few studies have demonstrated an association of sarcopenia-associated body measurements with chronic diseases through a comprehensive methodology. This study aims to examine the relationship between sarcopenia-associated body measurements and chronic diseases. This is a cohort study. We recruited 316 community dwellers, including 76 patients with sarcopenia and 240 controls, and obtained their body measurements associated with sarcopenia. We collected three-dimensional anthropometric body-surface measurements from 11,158 participants during 2000–2008 and followed up this cohort for 15 years to examine the association of these measurements with the risk of chronic diseases such as hypertension, type 2 diabetes mellitus (T2DM), heart disease, and nephrotic syndrome. Univariate analysis, canonical correlation, and Cox regression analysis were performed to explore the associations. Decreased waist width, upper left arm circumference, and left thigh circumference were significantly associated with sarcopenia. The adverse body measure score (ABMS) was derived by combining significant measurements, namely left upper arm circumference, waist width, and left thigh circumference, and used to predict the risk of hypertension, T2DM, heart diseases, and nephrotic syndrome. A positive association was observed between the ABMS and chronic diseases. Considering the first quartile of the ABMS as a reference, we determined hazard ratios of 2.259, 2.495, 1.332, and 1.595 for hypertension, T2DM, heart disease, and nephrotic syndrome, respectively, in the fourth quartile. Chronic diseases were more strongly associated with the ABMS than with sarcopenia-related body measurements alone. A high ABMS, which includes higher upper arm circumference, higher waist width, and lower thigh circumference, can significantly predict chronic diseases.

Decreased muscle mass is associated with advanced age, an inactive lifestyle, and inadequate nutrition. Sarcopenia is generally characterized by the co-occurrence of muscle reduction and dysfunction<sup>1,2</sup>. Sarcopenia results in adverse health outcomes, including increased mortality and long hospitalization, and is recognized as a systemic condition associated with metabolic syndrome, diabetes, cardiovascular disease, depression, and possibly cognitive impairment<sup>3–9</sup>. The prevalence of sarcopenia increases with age and was approximately 13%, ranging from 4.6 to 67%, in the older community-dwelling population<sup>1,10,11</sup>.

<sup>1</sup>Master Degree Program in Healthcare Industry, Chang Gung University, Taoyuan, Taiwan. <sup>2</sup>Division of Medical Imaging, Chang Gung Memorial Hospital, Keelung and Chang Gung University, Taoyuan, Taiwan. <sup>3</sup>Division of Endocrinology and Metabolism, Chang Gung Memorial Hospital, Keelung, Taiwan. <sup>4</sup>Division of Nephrology, Chang Gung Memorial Hospital, Keelung, Taiwan. <sup>5</sup>Division of Gastroenterology and Hepatology, Chang Gung Memorial Hospital, Keelung, Taiwan. <sup>6</sup>Division of Cardiology, Chang Gung Memorial Hospital, Keelung, Taiwan. <sup>7</sup>Healthy Aging Research Center, Chang Gung University, Taoyuan, Taiwan. <sup>8</sup>Laboratory for Epidemiology, Department of Health Care Management, Chang Gung University, Kwei-Shan, No. 259, Wen-Hwa 1st Road, Taoyuan 333, Taiwan. <sup>9</sup>Department of Emergency Medicine, Chang Gung Memorial Hospital, Taoyuan, Taiwan. <sup>10</sup>Department of Urology, Chang Gung Memorial Hospital, Taoyuan, Taiwan. <sup>11</sup>Research Center for Food and Cosmetic Safety, College of Human Ecology, Chang Gung University of Science and Technology, Taoyuan, Taiwan. <sup>12</sup>Department of Safety, Health and Environmental Engineering, Ming Chi University of Technology, New Taipei City, Taiwan. ✉email: khsu@mail.cgu.edu.tw



Sarcopenia can be classified into three stages: presarcopenia (low muscle mass), sarcopenia (low muscle mass along with either low muscle strength or poor physical function), and severe sarcopenia (low muscle mass, low muscle strength, and poor physical function)<sup>1</sup>. However, it is not feasible to apply the aforementioned classification criteria for sarcopenia to a large population in an epidemiological study. In addition, from a clinical perspective, the presence of an adverse body shape or a combination of body measures, including sarcopenic obesity, a large waist-to-thigh ratio, and lean lower limbs is the most concerning<sup>12,13</sup>. Specific body measurements can provide useful information for predicting adverse outcomes in the older community-dwelling population. However, limited evidence is available in this context.

Sarcopenia and sarcopenic obesity are associated with chronic diseases. Cardiovascular disease, dementia, and type II diabetes mellitus (T2DM) were reported to frequently co-occur with sarcopenia in older adults and have common risk factors such as aging, an adverse body shape, malnutrition, and an inactive lifestyle<sup>9</sup>. In addition, studies have suggested some potential consequences of sarcopenia including depression, physical dysfunction, dependency, and mortality<sup>1,9,14,15</sup>. These outcomes are correlated with body measurements such as lean lower limbs and visceral fat accumulation.

Some body measurements may be highly correlated with sarcopenia; however, obtaining body measurements is important for early prediction and prevention of this condition. Therefore, body measurements related to sarcopenia are considered crucial biomarkers of poor health outcomes. Three-dimensional techniques can be used to determine body composition at a low cost; such techniques are highly applicable in healthy individuals. Epidemiological studies have used anthropometric measurements, such as body mass index (BMI), waist circumference (WC), and waist-to-hip ratio (WHR), and have also explored different new body measurements for predicting chronic diseases. Studies have debated whether existing or innovative body measurements, such as BMI, WC, thigh circumference, WHR, and waist-to-thigh ratio, correlate better with selected diseases, such as T2DM, hypertension, dementia, and cancer<sup>12,16,17</sup>. Whether sarcopenia-related body measurements are associated with poor health outcomes is still imperfectly understood. Therefore, in the present study, we determined sarcopenia-related body measurements of community dwellers and conducted a 10-year follow-up of the cohort to investigate the causation.

## Methods

**Study participants and data collection.** All participants provided written informed consent for the procedure and the use of their data. The study protocol is in accordance with the ethical guidelines of the 1975 Declaration of Helsinki, and this study was approved by the Institutional Review Board of Chang Gung Medical Foundation (approval number: 201600934B0, 201802378B0A3, and 201801704B0). The study population was enrolled from a community located in northern Taiwan. In total, 316 community dwellers, including 76 patients with sarcopenia and 240 individuals without sarcopenia, were recruited in this study. The health consequences of sarcopenia-related body measurements were investigated using a cohort setup from 2000 onward. We recruited a total of 11,158 participants (5,872 men and 5,286 women) from the department of health examination from among those who were seeking an annual health checkup at a teaching hospital in northern Taiwan. A total of 7,797 participants without hypertension, T2DM, heart diseases, or nephrotic syndrome were included; the mean age of study participants was 49.17 (range 18–91) years. The average age of men and women was similar (49.20 and 49.13 years, respectively). Furthermore, the proportion of men (52.3%) and women (47.7%) in the study was similar. The study follow-up lasted for 17 years and 10 months, with an average of 14.55 years, from February 2000 to December 2017. The total follow-up period was 113,483.97 person-years, of which 58,170.90 person-years were for men and 55,313.07 person-years for women.

Information regarding confounders, namely age, sex, smoking, alcohol drinking, betel nut chewing, occupation, education, marriage, diet, and personal history of diseases, such as diabetes, hypertension, heart disease, renal diseases, liver cirrhosis, and chronic hepatitis, was collected using a questionnaire and confirmed through a medical chart review. T2DM, hypertension, heart disease, and nephrotic syndrome were defined based on International Classification of Diseases, Ninth Revision, Clinical Modification (ICD-9-CM) codes 250.xx (excluding 250.x1); 401–405; 390–398, 410–414, and 420–429; and 580–589, respectively. In the study population, 25.5% were smokers. The prevalence of smoking was lower in women (5.2%) than in men (44.0%). Furthermore, 26.4% of participants regularly consumed alcohol. The prevalence of alcohol drinking was lower in women (8.6%) than in men (42.6%).

**Anthropometric parameters.** Sarcopenia was assessed on the basis of muscle mass, muscle strength, and activity function. Muscle mass was evaluated using a single dual-energy fan-beam X-ray absorptiometer (DXA, GE medical system, Lunar iDXA, Madison, WI, USA). Scan modes (standard, thin, or thick) were automatically selected by the scanner software depending on body size and BMI. Scans were analyzed using enCORE Software, version 15 (GE Lunar). Muscle strength was measured on the basis of handgrip strength by using a single dynamometer. We measured the handgrip strength of the dominant hand. A walking speed of <0.8 m/s for a total distance of 4 m was defined as insufficient activity function.

According to the Asian Working Group for Sarcopenia guidelines, sarcopenia was defined as the presence of low muscle mass along with low muscle strength. Furthermore, low muscle mass without low muscle strength was defined as presarcopenia. The recommended cutoff points for low muscle mass, determined using a height-adjusted appendicular skeletal muscle index, are 7.0 kg/m<sup>2</sup> for men and 5.4 kg/m<sup>2</sup> for women. A handgrip strength of 26 and 18 kg was considered low for men and women, respectively<sup>18</sup>. Participants with presarcopenia and sarcopenia were pooled together and compared with controls to examine differences between body surface measurements.

Three-dimensional body surface measurements were performed using methods developed by the laboratory of whole-body 3D laser scanning in the study teaching hospital<sup>19</sup>. Approximately 280 standardized landmarks from the body surface were used to construct 35 body measurements for the head and neck, trunk, upper limbs, and lower limbs. In addition to body height and body weight, 35 measurements were included in this study, namely 4 measurements of the head and neck (head volume, head surface area, head circumference, and neck circumference), 11 measurements of the trunk and hip (waist profile area, WC, waist width, breast profile area, breast width, breast circumference, hip profile area, hip circumference, hip width, trunk surface area, and trunk volume), 10 measurements of the upper limbs (left arm volume, left arm surface area, left arm length, left forearm circumference, left upper arm circumference, right arm volume, right arm surface area, right arm length, right forearm circumference, and right upper arm circumference), and 10 measurements of the lower limbs (left leg volume, left leg surface area, left leg circumference, right leg volume, right leg surface area, right leg circumference, left thigh circumference, right thigh circumference, left leg length, and right leg length).

**Statistical analyses.** Numerical variables are displayed as the mean  $\pm$  standard deviation, and categorical variables are presented as the frequency and percentage. We used the two-sample independent *t* test and chi-square test to determine differences between continuous and categorical variables, respectively. Three-dimensional body surface measurements were categorized according to different body regions, including the whole body, head and neck, trunk, hip, upper limbs, and lower limbs. We performed the two-sample *t* test to examine differences in body surface measurements between cases and controls. To prevent collinearity in the regression analysis, one statistically significant body measurement ( $p < 0.05$ ) was selected from each region of the body for subsequent multivariable analyses. We performed a canonical correlation analysis to construct a linear equation of selected body measures based on the highest strength of the association with multiple chronic diseases. The linear equation of selected body measures was used as an adverse body measure score (ABMS) to validate the prediction of chronic diseases by using a prospective cohort. The sarcopenia-associated body measure score (SBMS) was constructed through the backward model selection of logistic regression by using sarcopenia as the dependent variable and selected body measures examined in the univariate analysis as independent variables. We used a Cox proportional hazards regression model to examine the strength of the association between both the body measure scores and the incidence of chronic diseases, namely T2DM, hypertension, cardiovascular disease, and renal syndrome, expressed as the hazard ratio after adjusting for the following variables: age, sex, marital status, educational level, occupation, cigarette smoking, alcohol drinking, and betel nut chewing. Statistical analysis was performed using SAS 9.4.

## Results

The basic sociodemographic, lifestyle, and disease status variables did not significantly differ between cases and controls in the study cohort. Among study participants, approximately 46% were aged  $> 60$  years, 61–70% were women, 42–35% had a senior high school education, 85–88% were employed in commerce or self-employed, 92–95% were married, 56% had low annual income ( $< US\$10,000$ ), 12–14% were smokers, 11–17% were alcohol drinkers, 2–4% were betel nut chewers, 40–53% were tea drinkers, 51–59% were coffee drinkers, 56–65% exercised regularly, 15–25% had hypertension, 9–10% had T2DM, 3–8% had heart diseases, and 6–13% had kidney diseases (Table 1).

When comparing presarcopenia and sarcopenia cases with controls, we found that all significant body measurements were negatively correlated. Three body measures, namely left upper arm circumference (odds ratio [OR] 0.683; 95% confidence interval [CI] 0.605–0.772), waist width (OR 0.713; 95% CI 0.636–0.8), and left thigh circumference (OR 0.745; 95% CI 0.681–0.816), were found to be significant in the multiple logistic regression analysis (Table 2). We performed a canonical correlation analysis to construct a linear equation of significant body measures, namely left upper arm circumference, waist width, and left thigh circumference, in relation to selected chronic diseases, namely T2DM, hypertension, heart diseases, and renal syndrome. The combination of three body measures ( $0.00365 \times \text{left upper arm circumference} + 0.33597 \times \text{waist width} - 0.10713 \times \text{left thigh circumference}$ ) was constructed as adverse body measures score (ABMS). The three body measures ( $17.3571 - 0.147 \times \text{left upper arm circumference} - 0.1595 \times \text{waist width} - 0.194 \times \text{left thigh circumference}$ ) were combined to measure the SBMS (Table 3).

We followed up this cohort for 15 years to investigate the association of both the ABMS and SBMS with the selected chronic diseases. Each increment in the ABMS was significantly associated with the hazard ratios of 1.24 (95% CI 1.17–1.30), 1.39 (95% CI 1.29–1.50), 1.09 (95% CI 1.02–1.16), and 1.12 (95% CI 0.99–1.27) for hypertension, T2DM, heart disease, and nephrotic syndrome, respectively. In addition, each increment in the SBMS was associated with the hazard ratios of 0.83 (95% CI 0.79–0.87), 0.81 (95% CI 0.76–0.87), 0.98 (95% CI 0.93–1.04), and 1.03 (95% CI 0.93–1.15) for hypertension, T2DM, heart disease, and nephrotic syndrome, respectively. Furthermore, we categorized the ABMS and SBMS into quartiles and found a dose–response relationship between the quartiles and chronic diseases. However, the strength of the association between the SBMS and chronic diseases was less significant (Fig. 1).

## Discussion

Sarcopenia is harmful to human health. Many diseases including obesity<sup>20</sup>, insulin resistance<sup>21</sup>, diabetes<sup>22</sup>, dyslipidemia<sup>23</sup>, and hypertension<sup>24</sup> are caused by sarcopenia. A study reported that an increased risk of metabolic syndrome in individuals with sarcopenia was linked to weights in upper-normal and slightly overweight ranges<sup>25</sup>. This study further confirmed the association of upper arm circumference, waist width, and thigh circumference with sarcopenia; moreover, the derived adverse body shape, which corresponds to the ABMS rather than muscular loss, results in poor health outcomes. The ABMS, a surrogate for sarcopenic obesity, includes the

| Basic sociodemographic      | Cases (n = 76) |         | Controls (n = 240) |         | Chi-square <i>p</i> value | OR    | 95% CI          |
|-----------------------------|----------------|---------|--------------------|---------|---------------------------|-------|-----------------|
|                             | n              | (%)     | n                  | (%)     |                           |       |                 |
| Age                         |                |         |                    |         |                           |       |                 |
| < 60                        | 41             | (53.95) | 129                | (53.75) | 0.976                     | 1.008 | (0.601, 1.691)  |
| > = 60                      | 35             | (46.05) | 111                | (46.25) |                           | 1.000 | –               |
| Gender                      |                |         |                    |         |                           |       |                 |
| Male                        | 29             | (38.16) | 73                 | (30.42) | 0.2639                    | 1.412 | (0.824, 2.418)  |
| Female                      | 47             | (61.84) | 167                | (69.58) |                           | 1.000 | –               |
| Education attainment        |                |         |                    |         |                           |       |                 |
| Junior high school or below | 22             | (28.95) | 83                 | (34.58) | 0.5146                    | 1.000 | –               |
| Senior high school          | 32             | (42.11) | 84                 | (35.00) |                           | 1.437 | (0.772, 2.677)  |
| College or above            | 22             | (28.95) | 70                 | (29.17) |                           | 1.186 | (0.606, 2.320)  |
| Occupation                  |                |         |                    |         |                           |       |                 |
| Government                  | 5              | (6.58)  | 21                 | (8.75)  | 0.8314                    | 1.000 | –               |
| Labor workers               | 4              | (5.26)  | 13                 | (5.42)  |                           | 1.292 | (0.292, 5.708)  |
| Commerce, self-employees    | 67             | (88.16) | 206                | (85.83) |                           | 1.366 | (0.496, 3.763)  |
| Marital status              |                |         |                    |         |                           |       |                 |
| Unmarried                   | 5              | (6.58)  | 11                 | (4.58)  | 0.5373                    | 1.481 | (0.498, 4.406)  |
| Married                     | 70             | (92.11) | 228                | (95.00) |                           | 1.000 | –               |
| Unknown                     | 1              | (1.32)  | 1                  | (0.42)  |                           | 3.257 | (0.201, 52.750) |
| Income                      |                |         |                    |         |                           |       |                 |
| < USD 10,000                | 43             | (56.58) | 135                | (56.25) | 0.7733                    | 1.000 | –               |
| USD 10,000 ~ 16,667         | 10             | (13.16) | 40                 | (16.67) |                           | 0.785 | (0.362, 1.701)  |
| USD 16,667 ~ 25,000         | 10             | (13.16) | 19                 | (7.92)  |                           | 1.652 | (0.714, 3.824)  |
| USD 25,000–33,333           | 6              | (7.89)  | 24                 | (10.00) |                           | 0.785 | (0.301, 2.046)  |
| > USD 33,333                | 3              | (3.95)  | 7                  | (2.92)  |                           | 1.346 | (0.333, 5.431)  |
| Unknown                     | 4              | (5.26)  | 13                 | (5.42)  |                           | 0.966 | (0.299, 3.119)  |
| Lifestyle variables         |                |         |                    |         |                           |       |                 |
| Cigarette smoking           |                |         |                    |         |                           |       |                 |
| No                          | 65             | (85.53) | 210                | (87.50) | 0.8023                    | 1.000 | –               |
| Yes                         | 11             | (14.47) | 30                 | (12.50) |                           | 1.185 | (0.563, 2.495)  |
| Alcohol drinking            |                |         |                    |         |                           |       |                 |
| No                          | 67             | (88.16) | 200                | (83.33) | 0.4061                    | 1.000 | –               |
| Yes                         | 9              | (11.84) | 40                 | (16.67) |                           | 0.672 | (0.310, 1.457)  |
| Betel nut chewing           |                |         |                    |         |                           |       |                 |
| No                          | 73             | (96.05) | 235                | (97.92) | 0.6294                    | 1.000 | –               |
| Yes                         | 3              | (3.95)  | 5                  | (2.08)  |                           | 1.932 | (0.451, 8.278)  |
| Tea drinking                |                |         |                    |         |                           |       |                 |
| No                          | 45             | (59.21) | 113                | (47.08) | 0.0871                    | 1.000 | –               |
| Yes                         | 31             | (40.79) | 127                | (52.92) |                           | 0.613 | (0.363, 1.034)  |
| Coffee drinking             |                |         |                    |         |                           |       |                 |
| No                          | 37             | (48.68) | 98                 | (40.83) | 0.2834                    | 1.000 | –               |
| Yes                         | 39             | (51.32) | 142                | (59.17) |                           | 0.727 | (0.433, 1.221)  |
| Exercise                    |                |         |                    |         |                           |       |                 |
| No                          | 33             | (43.42) | 83                 | (34.58) | 0.2089                    | 1.000 | –               |
| Yes                         | 43             | (56.58) | 157                | (65.42) |                           | 0.689 | (0.407, 1.165)  |
| Diseases                    |                |         |                    |         |                           |       |                 |
| Hypertension                |                |         |                    |         |                           |       |                 |
| No                          | 63             | (82.89) | 176                | (73.33) | 0.2214                    | 1.000 | –               |
| Yes                         | 12             | (15.79) | 61                 | (25.42) |                           | 0.55  | (0.278, 1.088)  |
| Unknown                     | 1              | (1.32)  | 3                  | (1.25)  |                           | 0.931 | (0.095, 9.117)  |
| Type 2 DM                   |                |         |                    |         |                           |       |                 |
| No                          | 68             | (89.47) | 212                | (88.33) | 0.9544                    | 1.000 | –               |
| Yes                         | 7              | (9.21)  | 25                 | (10.42) |                           | 0.873 | (0.362, 2.108)  |
| Unknown                     | 1              | (1.32)  | 3                  | (1.25)  |                           | 1.039 | (0.106, 10.156) |
| Heart diseases              |                |         |                    |         |                           |       |                 |
| No                          | 72             | (94.74) | 217                | (90.42) | 0.4393                    | 1.000 | –               |
| Continued                   |                |         |                    |         |                           |       |                 |

| Basic sociodemographic | Cases (n = 76) |         | Controls (n = 240) |         | Chi-square <i>p</i> value | OR    | 95% CI          |
|------------------------|----------------|---------|--------------------|---------|---------------------------|-------|-----------------|
|                        | n              | (%)     | n                  | (%)     |                           |       |                 |
| Yes                    | 3              | (3.95)  | 20                 | (8.33)  |                           | 0.452 | (0.131, 1.566)  |
| Unknown                | 1              | (1.32)  | 3                  | (1.25)  |                           | 1.005 | (0.103, 9.810)  |
| <b>Kidney diseases</b> |                |         |                    |         |                           |       |                 |
| No                     | 65             | (85.53) | 221                | (92.08) | 0.1987                    | 1.000 | –               |
| Yes                    | 10             | (13.16) | 16                 | (6.67)  |                           | 2.125 | (0.920, 4.908)  |
| Unknown                | 1              | (1.32)  | 3                  | (1.25)  |                           | 1.133 | (0.116, 11.080) |

**Table 1.** Distribution of basic characteristics between participants with sarcopenia and controls.

measurements of larger upper arm circumference and waist width and smaller thigh circumference; thus, the ABMS is superior to sarcopenia alone for predicting chronic diseases.

The results of this prospective cohort analysis indicated that upper arm circumference, waist width, and thigh circumference measurements can be used as alternative biomarkers for predicting sarcopenia-associated chronic diseases, including hypertension, T2DM, heart disease, and nephrotic syndrome, in Taiwan. Patients with sarcopenia generally have smaller measurements of almost all the limbs due to skeletal muscle loss. However, in this study, we observed that smaller measurements of the lower limbs increased the risk of diseases, whereas the smaller measurements of the upper limbs and visceral fat accumulation synergistically increased the risk of diseases. Although studies have indicated that thigh circumference is negatively associated with T2DM, dementia, and cancer<sup>12,16,17</sup>, this study confirmed that it is a long-term predictor of sarcopenia-associated chronic diseases. The present study proposes using the ABMS, which involves the use of upper arm, waist, and thigh measurements for its calculation, as a reliable biomarker for predicting sarcopenia-associated chronic diseases. Thus, the use of the ABMS as an innovative measurement is feasible in preventive medicine and epidemiological surveys in large-population communities.

The lower limbs account for approximately 70% of muscle mass. Studies have indicated that larger hip and thigh circumferences are associated with a low risk of T2DM, dementia, and internal cancers, independent of sociodemographic variables<sup>12,16,17</sup>. The soft tissue in the thigh is mostly composed of muscle mass and subcutaneous fat. The muscle of the lower limbs prevents from diseases in two aspects. First, the muscle absorbs glucose, thus regulating insulin resistance and inflammation to prevent diseases. Second, gluteofemoral body fat may secrete adipokines, including leptin, adiponectin, and inflammatory cytokines, through different actions and feedback systems to prevent diseases. Other studies have also reported an association of a large thigh circumference with a low risk of chronic diseases such as diabetes, hypertension, and heart disease<sup>26,27</sup>. Furthermore, studies have demonstrated an association of a small thigh circumference with hyperglycemia, heart disease, and premature death<sup>28,29</sup>.

WC and WHR are frequently used in current practice to estimate body fat accumulation in the trunk and are biomarkers for many metabolic disorders. A study showed that WC explains obesity-related health risk better than BMI does and that for a given WC value, people have similar health risks<sup>30</sup>. In this study, however, waist width was an indicator of abdominal fat accumulation when upper arm circumference measures were simultaneously considered. A larger upper arm circumference represents body fat accumulation in the upper trunk. Therefore, compared with using waist width alone, using a combination of waist width and upper arm circumference may better indicate upper body fat accumulation in relation to subsequent long-term adverse effects. Our previous study showed that a combination of neck circumference and waist width may be a feasible and comprehensive predictor of long-term diseases such as T2DM<sup>12</sup>. In addition, this study demonstrated that the combination was associated with multiple chronic diseases.

This study proposes that a combination of upper arm circumference, waist width, and thigh circumference is comprehensive, feasible, and superior to sarcopenia-related body measurements alone for predicting chronic diseases including hypertension, T2DM, heart disease, and nephrotic syndromes. A combination of anthropometry measurements and body fat distribution was superior to sarcopenia-related body measurements alone for predicting sarcopenia-associated diseases. Considering that muscle loss in sarcopenia results in poor health outcomes, upper body fat accumulation and lean lower limbs can be vital predictors. Therefore, the measurements proposed in this study to evaluate health outcomes could be more viable than sarcopenia-related body measurements alone in both clinical practice and preventive medicine in the future. The novelty of this study is that it proposes the ABMS as an alternative to the SBMS alone for predicting health outcomes. Clinically, two important aspects were derived from the findings. First, the measurement of lower limb circumference is vital for the identification of individuals with a high risk of chronic diseases. In addition to medications, the management of specific body measurements, including increasing the muscle content in the lower limbs, reducing abdominal fat accumulation, and reducing the fat content in the upper limbs, can be beneficial for preventing chronic diseases.

This study used a two-stage design to obtain body measurements associated with sarcopenia and related them to chronic diseases by linking a long-term follow-up cohort with a national health insurance claims database. The strengths of this study include the use of accurate disease diagnosis data, comprehensive whole-body scanning, and an adequate follow-up duration for cohort analysis. Nevertheless, this study has some limitations. First, this study used a three-dimensional surface scanning technique to obtain body measurements in which muscle mass and fat distribution could not be differentiated. Second, findings were obtained from a community population, which represents the general Taiwan population, and therefore, the findings should be cautiously



|  | Cases (n = 76)     | Controls (n = 240)    | Univariate OR(95%CI) | Multiple OR(95%CI)   |
|--|--------------------|-----------------------|----------------------|----------------------|
| <b>Whole body</b>                        |                    |                       |                      |                      |
| Height                                   | 160.69 ± 8.49      | 158.77 ± 8.01         | 1.029 (0.997, 1.062) | 1.053 (1.003, 1.106) |
| Weight                                   | 53.66 ± 9.10       | 63.36 ± 11.62         | 0.899 (0.868, 0.932) | 0.838 (0.797, 0.882) |
| BMI                                      | 20.65 ± 2.42       | 25.04 ± 3.50          | 0.545 (0.466, 0.637) | 0.480 (0.396, 0.582) |
| <b>Head and neck</b>                     |                    |                       |                      |                      |
| Head circumference (cm)                  | 57.31 ± 3.16       | 58.26 ± 2.59          | 0.884 (0.804, 0.971) | 0.854 (0.771, 0.946) |
| Head surface area (cm <sup>2</sup> )     | 1504.70 ± 481.35   | 1460.06 ± 142.79      | 1.055 (0.960, 1.160) | 1.053 (0.954, 1.161) |
| Head volume (cm <sup>3</sup> )           | 4925.16 ± 520.80   | 5094.30 ± 600.65      | 0.949 (0.905, 0.995) | 0.906 (0.855, 0.959) |
| Neck circumference (cm)                  | 37.15 ± 4.65       | 39.18 ± 4.44          | 0.902 (0.848, 0.959) | 0.853 (0.793, 0.918) |
| <b>Trunk</b>                             |                    |                       |                      |                      |
| Chest width (cm)                         | 29.72 ± 2.78       | 31.65 ± 2.89          | 0.774 (0.694, 0.864) | 0.699 (0.615, 0.795) |
| Chest circumference (cm)                 | 90.34 ± 8.85       | 98.15 ± 11.01         | 0.923 (0.894, 0.952) | 0.916 (0.886, 0.947) |
| Chest sectional area (cm <sup>2</sup> )  | 6148.49 ± 1226.19  | 6963.77 ± 1393.64     | 0.952 (0.931, 0.973) | 0.940 (0.916, 0.963) |
| Waist width (cm)                         | 28.26 ± 2.67       | 30.89 ± 3.18          | 0.740 (0.665, 0.823) | 0.713 (0.636, 0.800) |
| Waist circumference (cm)                 | 74.70 ± 7.97       | 81.02 ± 9.82          | 0.923 (0.893, 0.954) | 0.911 (0.879, 0.945) |
| Waist sectional area (cm <sup>2</sup> )  | 6039.81 ± 1283.90  | 6989.36 ± 1418.24     | 0.945 (0.924, 0.967) | 0.936 (0.913, 0.960) |
| Trunk surface area (cm <sup>2</sup> )    | 7028.05 ± 1083.28  | 11,656.68 ± 55,906.93 | 0.955 (0.933, 0.978) | 0.948 (0.924, 0.973) |
| Trunk volume (cm <sup>3</sup> )          | 37,400.9 ± 7197.27 | 45,047.98 ± 26,972.78 | 0.994 (0.991, 0.997) | 0.991 (0.988, 0.995) |
| <b>Hip</b>                               |                    |                       |                      |                      |
| Hip width (cm)                           | 32.79 ± 2.07       | 34.66 ± 2.48          | 0.684 (0.593, 0.789) | 0.671 (0.577, 0.781) |
| Hip circumference (cm)                   | 85.89 ± 5.81       | 90.63 ± 7.40          | 0.889 (0.847, 0.934) | 0.891 (0.847, 0.936) |
| Hip sectional area (cm <sup>2</sup> )    | 599.87 ± 116.49    | 718.04 ± 134.36       | 0.990 (0.986, 0.993) | 0.989 (0.986, 0.993) |
| <b>Upper limbs</b>                       |                    |                       |                      |                      |
| <b>Upper arm circumference (cm)</b>      |                    |                       |                      |                      |
| Left                                     | 27.97 ± 2.64       | 30.64 ± 3.25          | 0.73 (0.657, 0.812)  | 0.683 (0.605, 0.772) |
| Right                                    | 27.85 ± 2.85       | 30.51 ± 3.24          | 0.73 (0.655, 0.813)  | 0.672 (0.592, 0.764) |
| <b>Forearm circumference (cm)</b>        |                    |                       |                      |                      |
| Left                                     | 18.84 ± 2.36       | 20.42 ± 2.58          | 0.762 (0.676, 0.858) | 0.716 (0.625, 0.819) |
| Right                                    | 19.33 ± 2.26       | 20.80 ± 2.60          | 0.774 (0.686, 0.873) | 0.706 (0.612, 0.815) |
| <b>Arm length (cm)</b>                   |                    |                       |                      |                      |
| Left                                     | 51.63 ± 3.66       | 51.46 ± 3.62          | 1.013 (0.943, 1.088) | 1.011 (0.934, 1.094) |
| Right                                    | 51.75 ± 3.63       | 51.55 ± 3.59          | 1.015 (0.944, 1.091) | 1.014 (0.936, 1.098) |
| <b>Arm surface area (cm<sup>2</sup>)</b> |                    |                       |                      |                      |
| Left                                     | 1141.99 ± 126.66   | 1187.64 ± 128.31      | 0.997 (0.995, 0.999) | 0.996 (0.994, 0.999) |
| Right                                    | 1193.50 ± 129.95   | 1243.45 ± 132.30      | 0.997 (0.995, 0.999) | 0.996 (0.994, 0.999) |
| <b>Arm volume (cm<sup>3</sup>)</b>       |                    |                       |                      |                      |
| <b>Lower limbs</b>                       |                    |                       |                      |                      |
| Left                                     | 1887.11 ± 261.49   | 2110.50 ± 360.71      | 0.998 (0.997, 0.999) | 0.997 (0.996, 0.998) |
| Right                                    | 1901.16 ± 266.18   | 2115.20 ± 360.51      | 0.998 (0.997, 0.999) | 0.997 (0.996, 0.998) |
| <b>Thigh circumference (cm)</b>          |                    |                       |                      |                      |
| Left                                     | 47.27 ± 3.71       | 51.89 ± 4.71          | 0.763 (0.704, 0.827) | 0.745 (0.681, 0.816) |
| Right                                    | 47.24 ± 3.70       | 51.77 ± 4.70          | 0.768 (0.709, 0.832) | 0.752 (0.689, 0.822) |
| <b>Calf circumference (cm)</b>           |                    |                       |                      |                      |
| Left                                     | 26.78 ± 3.87       | 29.37 ± 4.97          | 0.841 (0.775, 0.914) | 0.840 (0.772, 0.916) |
| Right                                    | 26.80 ± 3.90       | 29.15 ± 4.43          | 0.849 (0.781, 0.922) | 0.847 (0.778, 0.922) |
| <b>Leg length (cm)</b>                   |                    |                       |                      |                      |
| Left                                     | 67.59 ± 4.78       | 66.73 ± 3.90          | 1.052 (0.987, 1.12)  | 1.069 (0.994, 1.150) |
| Right                                    | 67.48 ± 4.78       | 66.66 ± 3.92          | 1.049 (0.985, 1.117) | 1.067 (0.993, 1.147) |
| <b>Leg surface area (cm<sup>2</sup>)</b> |                    |                       |                      |                      |
| Left                                     | 2472.46 ± 319.00   | 2734.48 ± 377.75      | 0.998 (0.997, 0.999) | 0.998 (0.997, 0.999) |
| Right                                    | 2529.78 ± 304.56   | 2785.02 ± 402.93      | 0.998 (0.997, 0.999) | 0.998 (0.997, 0.999) |
| <b>Leg volume (cm<sup>3</sup>)</b>       |                    |                       |                      |                      |
| Left                                     | 5000.91 ± 882.68   | 5932.30 ± 1125.60     | 0.911 (0.883, 0.940) | 0.905 (0.874, 0.938) |
| Right                                    | 5024.09 ± 876.43   | 5960.21 ± 1091.82     | 0.903 (0.873, 0.934) | 0.893 (0.860, 0.928) |

**Table 2.** Descriptive statistics of 3D surface body measures between participants with sarcopenia/ presarcopenia and controls.

| Body measures variables      | ABMS* combination coefficient | SBMS** combination coefficient |
|------------------------------|-------------------------------|--------------------------------|
| Left upper arm circumference | 0.00365                       | -0.147                         |
| Waist width                  | 0.33597                       | -0.160                         |
| Left thigh circumference     | -0.10713                      | -0.194                         |

**Table 3.** Canonical correlation analysis between body measures and chronic diseases. ABMS adverse body measures score; SBMS sarcopenia-associated body measures score. \* Canonical correlation coefficient = 0.294476 ( $p = 0.0026$ ).  $ABMS = 0.00365 \times \text{Left upper arm circumference} + 0.33597 \times \text{Waist width} - 0.10713 \times \text{Left thigh circumference}$ . \*\* Logistic regression using backward selection method ( $p < 0.05$ ).  $SBMS = 17.3571 - 0.147 \times \text{Left upper arm circumference} - 0.1595 \times \text{Waist width} - 0.194 \times \text{Left thigh circumference}$ .

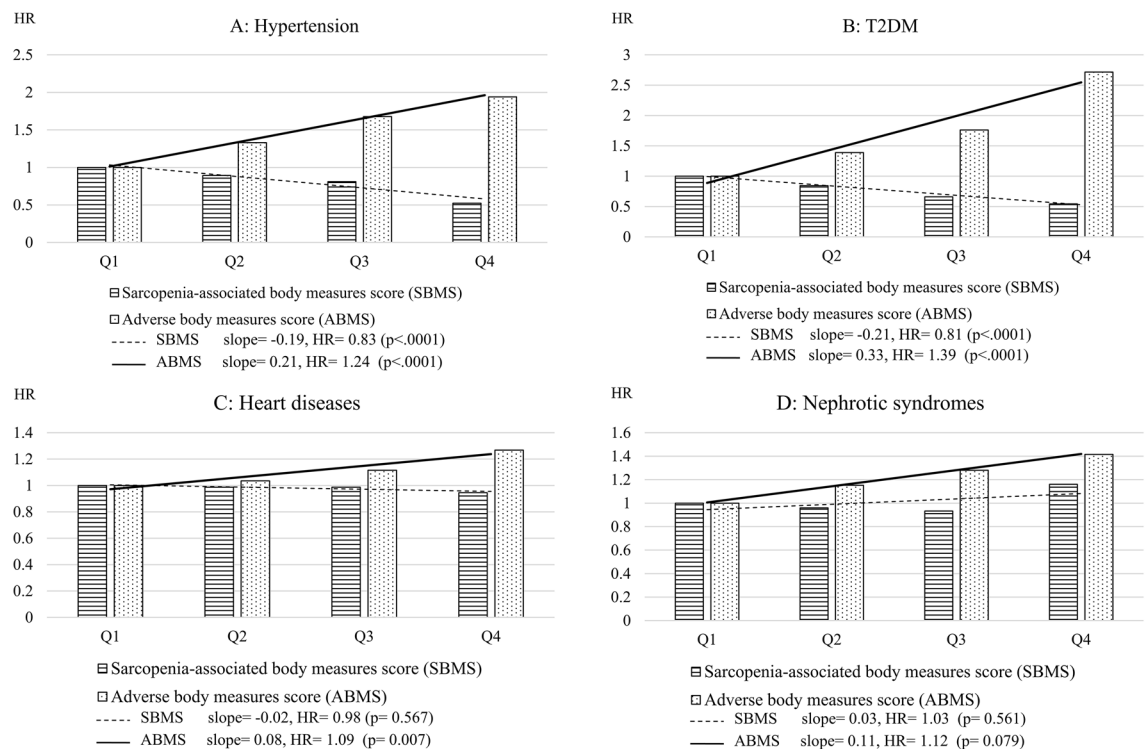


**Figure 1.** Comparison between sarcopenia-associated adverse body measures score (SBMS) and adverse body measures score (ABMS) in terms of their linear relationship with chronic diseases (the analyses were performed by Cox regression adjusted for age, sex, smoking, alcohol drinking, betel nut chewing, occupation, education, marriage, food style, and personal disease).

applied to different ethnic populations. Third, different health care systems may provide diverse intervention plans, leading to different levels of disease risk. In addition, health-seeking behavior, social support, and health literacy may change health outcomes, but nondifferential misclassification was assumed in this study. Finally, interventions such as exercise, nutrition, and medicine can modify body measurements, but obtaining data on these was not feasible in this study.

## Conclusions and implications

Adverse body shape rather than sarcopenia itself causes poor health outcomes. Sarcopenia-associated body measurements, including upper arm circumference, waist width, and thigh circumference, can be used for independently predicting the risk of chronic diseases such as T2DM, hypertension, heart disease, and nephrotic syndrome. Smaller measurements of the lower limbs and larger measurements of the upper limbs and trunk can be useful biomarkers for predicting an individual's risk of chronic diseases. The body measurements proposed in this study can be used to determine the risk of sarcopenia in clinical practice and preventive medicine.

Received: 27 August 2020; Accepted: 26 February 2021

Published online: 08 April 2021

## References

1. Cruz-Jentoft, A. *et al.* European Working Group on Sarcopenia in Older People. Sarcopenia: European consensus on definition and diagnosis: report of the European Working Group on Sarcopenia in Older People. *Age Ageing* **39**(4), 412–423 (2010).
2. Bianchi, L. *et al.* The predictive value of the EWGSOP definition of sarcopenia: results from the InCHIANTI study. *J. Gerontol. Ser. A Biomed. Sci. Med. Sci.* **71**(2), 259–264 (2016).
3. Kelley, G. A. & Kelley, K. S. Is sarcopenia associated with an increased risk of all-cause mortality and functional disability? *Exp. Gerontol.* **96**, 100–103 (2017).
4. Cerri, A. P. *et al.* Sarcopenia and malnutrition in acutely ill hospitalized elderly: prevalence and outcomes. *Clin. Nutr.* **34**(4), 745–751 (2015).
5. Zhang, H. *et al.* Association between sarcopenia and metabolic syndrome in middle-aged and older non-obese adults: a systematic review and meta-analysis. *Nutrients* **10**(3), 364 (2018).
6. Chang, K.-V. *et al.* Association between sarcopenia and cognitive impairment: a systematic review and meta-analysis. *J. Am. Med. Dir. Assoc.* **17**(12), 1164e7–1164e15 (2016).
7. Chang, K.-V. *et al.* Is sarcopenia associated with depression? A systematic review and meta-analysis of observational studies. *Age Ageing* **46**(5), 738–746 (2017).
8. Fielding, R. A. *et al.* Sarcopenia: an undiagnosed condition in older adults. Current consensus definition: prevalence, etiology, and consequences. International working group on sarcopenia. *J. Am. Med. Dir. Assoc.* **12**(4), 249–256 (2011).
9. Pacifico, J. *et al.* Prevalence of sarcopenia as a comorbid disease: a systematic review and meta-analysis. *Exp. Gerontol.* **131**, 110801 (2020).
10. Baumgartner, R. N. *et al.* Epidemiology of sarcopenia among the elderly in New Mexico. *Am. J. Epidemiol.* **147**(8), 755–763 (1998).
11. Reijnierse, E. M. *et al.* The impact of different diagnostic criteria on the prevalence of sarcopenia in healthy elderly participants and geriatric outpatients. *Gerontology* **61**(6), 491–496 (2015).
12. Ting, M.-K. *et al.* Predicting type 2 diabetes mellitus occurrence using three-dimensional anthropometric body surface scanning measurements: a prospective cohort study. *J. Diabetes Res.* <https://doi.org/10.1155/2018/6742384> (2018).
13. Lee, D.-C. *et al.* Physical activity and sarcopenic obesity: definition, assessment, prevalence and mechanism. *Fut. Sci. OA* **2**(3), FSO127 (2016).
14. Beaudart, C. *et al.* Health outcomes of sarcopenia: a systematic review and meta-analysis. *PLoS ONE* **12**(1), e0169548 (2017).
15. Janssen, I., Heymsfield, S. B. & Ross, R. Low relative skeletal muscle mass (sarcopenia) in older persons is associated with functional impairment and physical disability. *J. Am. Geriatr. Soc.* **50**(5), 889–896 (2002).
16. Hsu, K.-H., Shih, C.-P. & Liao, P.-J. Waist-to-thigh ratio is a predictor of internal organ cancers in humans: findings from a cohort study. *Ann. Epidemiol.* **23**(6), 342–348 (2013).
17. Liao, P. J. *et al.* Chest width, waist circumference, and thigh circumference are predictors of dementia. *Int. J. Geriatr. Psychiatry* **33**(8), 1019–1027 (2018).
18. Chen, L.-K. *et al.* Recent advances in sarcopenia research in Asia: 2016 update from the Asian Working Group for Sarcopenia. *J. Am. Med. Dir. Assoc.* **17**(8), 767.e1–e7 (2016).
19. Chuang, Y. C. *et al.* Waist-to-thigh ratio can also be a better indicator associated with type 2 diabetes than traditional anthropometrical measurements in Taiwan population. *Ann. Epidemiol.* **16**(5), 321–331 (2006).
20. Waters, D. L. & Baumgartner, R. N. Sarcopenia and obesity. *Clin. Geriatr. Med.* **27**(3), 401–421 (2011).
21. Abbatecola, A. M. *et al.* Discovering pathways of sarcopenia in older adults: a role for insulin resistance on mitochondria dysfunction. *J. Nutr. Health Aging* **15**(10), 890–895 (2011).
22. Khamseh, M. E. *et al.* Sarcopenia and diabetes: pathogenesis and consequences. *Br. J. Diabetes Vasc. Dis.* **11**(5), 230–234 (2011).
23. Baek, S. *et al.* Sarcopenia and sarcopenic obesity and their association with dyslipidemia in Korean elderly men: the 2008–2010 Korea National Health and Nutrition Examination Survey. *J. Endocrinol. Investig.* **37**(3), 247–260 (2014).
24. Doğan, M. *et al.* Correlations between sarcopenia and hypertensive target organ damage in a Turkish cohort. *Acta Clin. Belg.* **67**(5), 328–332 (2012).
25. St-Onge, M.-P., Janssen, I. & Heymsfield, S. B. Metabolic syndrome in normal-weight Americans: new definition of the metabolically obese, normal-weight individual. *Diabetes Care* **27**(9), 2222–2228 (2004).
26. Larsen, B. A. *et al.* Association of muscle mass, area, and strength with incident diabetes in older adults: the Health ABC Study. *J. Clin. Endocrinol. Metab.* **101**(4), 1847–1855 (2016).
27. Van Pelt, R. *et al.* Contributions of total and regional fat mass to risk for cardiovascular disease in older women. *Am. J. Physiol. Endocrinol. Metabol.* **282**(5), E1023–E1028 (2002).
28. Snijder, M. *et al.* Low subcutaneous thigh fat is a risk factor for unfavourable glucose and lipid levels, independently of high abdominal fat. The Health ABC Study. *Diabetologia* **48**(2), 301–308 (2005).
29. Heitmann, B. L. & Frederiksen, P. Thigh circumference and risk of heart disease and premature death: prospective cohort study. *BMJ* **339**, b3292 (2009).
30. Janssen, I., Katzmarzyk, P. T. & Ross, R. Waist circumference and not body mass index explains obesity-related health risk. *Am. J. Clin. Nutr.* **79**(3), 379–384 (2004).

## Acknowledgements

Authors acknowledged the supports of data linkage by Health and Welfare Data Center, Ministry of Health and Welfare in Taiwan.

## Author contributions

P.-J.L.: data collection, data analysis and interpretation, drafting. Y.-C.L.: data collection, data interpretation. M.-K.T.: data collection, data interpretation. I.-W.W.: data interpretation. S.-W.C.: data interpretation. N.-I.Y.: data interpretation. K.-H.H.: study design, data analysis and interpretation, drafting, revision.

## Funding

This work was supported by the Ministry of Science and Technology, Taiwan (108-2410-H-182-008-MY2) and a Health Aging Research Center of Chang Gung University (EMRPD1K0481). This work was also supported by the Chang Gung Medical Foundation (CORPD3J0011, CMRPD3F0021, CMRPD3F0022, CMRPD3F0023, CMRPG2F0071, CMRPG2F0072, CMRPG2F0073, CMRPG2F0081, CMRPG2F0082, CMRPG2F0083, CMRPD3G0101, CMRPD3G0102, and CMRPD3G0103) and the Wang Jhan-Yang Charitable Trust Fund (WJY 2020-HR-01, WJY 2021-HR-01).

## Competing interests

The authors declare no competing interests.

## Additional information

**Correspondence** and requests for materials should be addressed to K.-H.H.

**Reprints and permissions information** is available at [www.nature.com/reprints](http://www.nature.com/reprints).

**Publisher's note** Springer Nature remains neutral with regard to jurisdictional claims in published maps and institutional affiliations.



**Open Access** This article is licensed under a Creative Commons Attribution 4.0 International License, which permits use, sharing, adaptation, distribution and reproduction in any medium or format, as long as you give appropriate credit to the original author(s) and the source, provide a link to the Creative Commons licence, and indicate if changes were made. The images or other third party material in this article are included in the article's Creative Commons licence, unless indicated otherwise in a credit line to the material. If material is not included in the article's Creative Commons licence and your intended use is not permitted by statutory regulation or exceeds the permitted use, you will need to obtain permission directly from the copyright holder. To view a copy of this licence, visit <http://creativecommons.org/licenses/by/4.0/>.

© The Author(s) 2021





# Use of urinary hippuric acid and *o*-/*p*-/*m*-methyl hippuric acid to evaluate surgical smoke exposure in operating room healthcare personnel

Chun-Hui Chiu<sup>a,b,1</sup>, Chi-Tsung Chen<sup>c,1</sup>, Ming-Huei Cheng<sup>d,e</sup>, Li-Heng Pao<sup>a,f</sup>, Chi Wang<sup>g,h</sup>, Gwo-Hwa Wan<sup>i,j,k,l,\*</sup>

<sup>a</sup> Graduate Institute of Health Industry and Technology, Research Center for Chinese Herbal Medicine, Research Center for Food and Cosmetic Safety, College of Human Ecology, Chang Gung University of Science and Technology, Taoyuan, Taiwan

<sup>b</sup> Department of Traditional Chinese Medicine, Keelung Chang Gung Memorial Hospital, Keelung, Taiwan

<sup>c</sup> Graduate Institute of Clinical Medical Sciences, College of Medicine, Chang Gung University, Taoyuan, Taiwan

<sup>d</sup> Department of Plastic and Reconstruction Surgery, Chang Gung Memorial Hospital, Taoyuan, Taiwan

<sup>e</sup> College of Medicine, Chang Gung University, Taoyuan, Taiwan

<sup>f</sup> Department of Gastroenterology and Hepatology, Linkuo Chang Gung Memorial Hospital, Taoyuan, Taiwan

<sup>g</sup> Department of Nursing, Linkuo Chang Gung Memorial Hospital, Taoyuan, Taiwan

<sup>h</sup> School of Nursing, College of Medicine, Chang Gung University, Taoyuan, Taiwan

<sup>i</sup> Department of Respiratory Therapy, College of Medicine, Chang Gung University, Taoyuan, Taiwan

<sup>j</sup> Department of Respiratory Care, Chang Gung University of Science and Technology, Chiayi, Taiwan

<sup>k</sup> Department of Obstetrics and Gynaecology, Kaohsiung Chang Gung Memorial Hospital, Kaohsiung, Taiwan

<sup>l</sup> Center for Environmental Sustainability and Human Health, Ming Chi University of Technology, Taishan, New Taipei, Taiwan

## ARTICLE INFO

Edited by Dr. Fernando Barbosa

### Keywords:

Operating room

Surgical smoke

High-performance liquid chromatography

tandem mass spectrometry

Hippuric acid

Methylhippuric acid

## ABSTRACT

Toluene and xylene are common components of surgical smoke, whereas hippuric acid (HA) and methylhippuric acid (MHA) are the products of toluene and xylene metabolism in humans, respectively. HA and MHA can be used as indicators to evaluate the exposure hazards of toluene and xylene. In this study, we used liquid chromatography tandem mass spectrometry (LC-MS/MS) to simultaneously analyze the HA, *o*-/*m*-/*p*-MHA, and creatinine contents in the urine of healthcare personnel. Concentrations of HA and *o*-/*m*-/*p*-MHAs were normalized to those of creatinine and used to analyze urine samples of 160 operating room (OR) healthcare personnel, including administrative staff, surgical nurses, nurse anesthetists, and surgeons. The results showed that the five analytes could be accurately separated and exhibited good linearity ( $r > 0.9992$ ). The rate of recovery was between 86% and 106%, and the relative standard deviation was less than 5%. Urine from administrative staff presented the highest median concentration of hippuric acid (0.25 g/g creatinine); this was significantly higher than that found in the urine of surgeons (0.15 g/g). The concentrations of urinary *o*-/*m*-/*p*-MHAs in surgical nurses were higher than those in administrative staff, nurse anesthetists, and surgeons. Furthermore, the type, sex, and age of healthcare personnel were associated with changes in urine HA and *o*-/*m*-/*p*-MHA concentrations. Healthcare personnel should be aware of the risk of exposure to surgical smoke.

## 1. Introduction

Electrosurgical instruments such as lasers, electrosurgical units, and ultrasonic devices are used to cut human tissue and induce hemostasis during surgery; this leads to immediate release of visible and odorous surgical smoke (Ulmer, 2008). Surgical smoke is composed of 95% moisture and 5% of particulate matter or chemical substances (Ulmer,

2008). These particulates include blood (Ott et al., 1998; Heinsohn and Jewett, 1993; Jewett et al., 1992), cell debris (Fletcher et al., 1999; Nduka et al., 1998), viruses (Taravella et al., 1999; Kwak et al., 2016), and bacteria (McKinley and Ludlow, 1994; Capizzi et al., 1998), whereas the chemical substances include benzene (Zhao et al., 2013; U.S. DHHS, 1988), toluene (Zhao et al., 2013; Al Sahaf et al., 2007; Lin et al., 2010; Fitzgerald et al., 2012), xylene (Choi et al., 2014), cyclohexanone (Al

\* Correspondence to: Department of Respiratory Therapy, College of Medicine, Chang Gung University, Wen-Hwa 1st Road, Kwei-Shan, Taoyuan, Taiwan.

E-mail addresses: [chchiu@mail.cgu.edu.tw](mailto:chchiu@mail.cgu.edu.tw) (C.-H. Chiu), [jackson08036@gmail.com](mailto:jackson08036@gmail.com) (C.-T. Chen), [minghuei@cgmh.org.tw](mailto:minghuei@cgmh.org.tw) (M.-H. Cheng), [paolh@mail.cgu.edu.tw](mailto:paolh@mail.cgu.edu.tw) (L.-H. Pao), [gigy@cgmh.org.tw](mailto:gigy@cgmh.org.tw) (C. Wang), [ghwan@mail.cgu.edu.tw](mailto:ghwan@mail.cgu.edu.tw) (G.-H. Wan).

<sup>1</sup> These authors contributed equally to the study.

<https://doi.org/10.1016/j.ecoenv.2021.112231>

Received 28 October 2020; Received in revised form 29 March 2021; Accepted 1 April 2021

Available online 13 April 2021

0147-6513/© 2021 The Authors.

Published by Elsevier Inc.

This is an open access article under the CC BY-NC-ND license

(<http://creativecommons.org/licenses/by-nc-nd/4.0/>).

Sahaf et al., 2007), acrylonitrile (Zhao et al., 2013; Barrett and Garber, 2003), and furfural (Barrett and Garber, 2003). Owing to the presence of these components, exposure to surgical smoke may endanger the health of operating room (OR) healthcare personnel. Approximately 50,000 OR healthcare personnel are exposed to surgical smoke every year in the United States (OSHA, 2012).

Previous studies have primarily focused on assessing the chemical components of surgical smoke and changes in their concentrations. However, a few studies have evaluated the effects of electrocautery machine usage on the quality of air in the OR and the risk of exposing healthcare personnel to surgical smoke. Le Moual et al. (2013) found that the risk of developing severe persistent asthma was 2.48-times higher among nursing staff working in ORs than among administrative staff; surgeons ( $117 \times 10^{-6}$ ) and anesthesiologists ( $270 \times 10^{-6}$ ) had increased 70-year lifetime cancer risks due to exposure to polycyclic aromatic hydrocarbons at levels exceeding the safety level recommended by the World Health Organization (WHO;  $1 \times 10^{-6}$ ), implying that 1 out of 1,000,000 individuals may develop cancer due to polycyclic aromatic hydrocarbons (Tseng et al., 2014). Therefore, it is imperative to evaluate the exposure risk of healthcare personnel to surgical smoke. A few studies have investigated the correlation between surgical smoke exposure and changes in biomarker concentrations in humans. Dobrogowski et al. (2014) showed that urinary concentrations of benzene and toluene in patients after laparoscopic cholecystectomy were higher than those before the procedure. Cheng et al. (2019) found that the concentrations of benzene and toluene in breath specimens from healthcare personnel were slightly higher following breast and abdominal surgery than the concentrations before surgery. Furthermore, the exhaled *m*/*p*-xylene concentrations of medical staff after breast surgery were slightly higher than those before surgery (Cheng et al., 2019).

Human or animal exposure to toluene may cause central nervous system damage, sore throat, dizziness, headache, and upper respiratory tract and eye irritation (DHHS ATSDR, 2017). The American Conference of Governmental Industrial Hygienists (ACGIH) reported that humans inhale 70 ppm of toluene over 2 h; toluene can be metabolized and has a half-life of 0.5–2.7 days. Of the total quantity of inhaled toluene, 15–20% is excreted through exhalation, whereas the remaining 80% is converted to HA and excreted via urine after 7 h (ACGIH, 2013). Cytochrome P450 enzymes catalyze the conversion of toluene to benzyl alcohol and a few types of phenols in the liver. Benzyl alcohol is then converted to benzoic acid, which rapidly interacts with glycine and is excreted via urine in the form of HA (ACGIH, 1997). According to the recommendations of the ACGIH, the permissible exposure limit of urinary HA in workers after 1 day is 1.6 g/g creatinine (ACGIH, 2007). In addition to toluene exposure, urinary HA concentrations are affected by sex (Siqueira and Paiva, 2002), intake of salicylic acid-containing drugs (Pacifci et al., 1991), and intake of foods containing high amounts of benzoic acid, such as plums (Villanueva et al., 1994).

Xylene, which is composed of three isomers (*m*/*p*/*o*-xylenes), can be quickly absorbed through the skin and mucous membranes, leading to acute irritation or chronic central nervous system and auditory system toxicity (Kandiyala et al., 2010). Human exposure to 14 ppm of xylene for 8 h per day may lead to symptoms such as memory loss and anxiety (Uchida et al., 1993). Xylene is absorbed by the human body and oxidized to form methylbenzoic acids, which are subsequently conjugated with glycine to form MHA and then eliminated through urine (DHHS ATSDR, 2007). The ACGIH recommends that urinary MHA levels in workers once off-duty should be less than 1.5 g/g creatinine (ACGIH, 2007). Additionally, creatinine is a by-product of muscle metabolism, and is produced by the catabolism of phosphocreatine and mainly excreted through the kidneys. Urinary solute concentrations are easily affected by water reabsorption in the kidney; therefore, the creatinine concentration in urine is usually used to normalize the urinary concentration of metabolites (Fernández-Fernández et al., 2015).

A few studies have explored the correlation between exposure to toluene and xylene in surgical smoke and the concentrations of their

respective biomarkers, HA and MHAs. The purpose of this study was to establish an analytical method to measure the concentrations of urinary metabolites (such as HA and MHAs) and to compare their concentrations among different healthcare personnel working in ORs.

## 2. Materials and methods

### 2.1. Chemicals

Creatinine, creatinine- $d_3$ , and *o*-MHA standards were obtained from Toronto Research Chemicals Inc. (North York, Canada); *m*-MHA and *p*-MHA standards were purchased from Sigma-Aldrich Co. (St. Louis, USA), and the HA standard was purchased from Chem Service Inc. (West Chester, USA). Creatinine, *o*-MHA, *m*-MHA, and *p*-MHA were dissolved in 50% methanol at a concentration of 1000  $\mu$ g/mL. Next, creatinine and HA were diluted to 100  $\mu$ g/mL, whereas *o*-MHA, *m*-MHA, and *p*-MHA were diluted to 10  $\mu$ g/mL, using 50% methanol. Creatinine- $d_3$  was dissolved in 50% methanol, and 1  $\mu$ g/mL creatinine- $d_3$  was used as the internal standard. The standard solution was diluted to the concentration levels determined using the calibration curves (including 10 ng/mL internal standard) with 2% acetonitrile. The range of the calibration curves was 5–2000 ng/mL for creatinine, 20–2000 ng/mL for HA, and 5–200 ng/mL for *o*-MHA, *m*-MHA, and *p*-MHA.

### 2.2. Urine specimen collection

For this cross-sectional study, we recruited 160 OR healthcare personnel from the Linkuo Chang Gung Memorial Hospital in Taiwan, who had worked for at least 3 months and were not pregnant. Of these, 120 healthcare personnel from the orthopedic, colorectal, and trauma ORs (20 surgeons, 20 nurse anesthetists, and 80 surgical nurses) comprised the surgical smoke exposure group, whereas 40 administrative nurses who did not work in areas exposed to surgical smoke constituted the surgical smoke non-exposure group. Based on the half-life of toluene as reported by the ACGIH (2013), 10 mL samples of mid-stream urine were collected from the participants and immediately stored at  $-80^\circ\text{C}$  after they had worked for at least three consecutive days.

### 2.3. Sample preparation

#### 2.3.1. Pretreatment of *o*-MHA, *m*-MHA, and *p*-MHA samples

After thawing, the urine samples were centrifuged at 2100g and  $15^\circ\text{C}$  for 3 min. Then, 990  $\mu$ L of the supernatant was mixed thoroughly with 10  $\mu$ L of the internal standard (1  $\mu$ g/mL creatinine- $d_3$ ) and passed through a 0.22- $\mu$ m nylon filter before LC-MS/MS analysis.

#### 2.3.2. Pretreatment of creatinine and HA samples

An aliquot of 2 mL of 100% acetonitrile was mixed with 1 mL of the supernatant for protein precipitation. Then, deionized water was added to a final volume of 10 mL. The solution was centrifuged at 2100g for 3 min at  $15^\circ\text{C}$ , and 10  $\mu$ L of the supernatant was mixed with 980  $\mu$ L of deionized water and 10  $\mu$ L of the internal standard (1  $\mu$ g/mL creatinine- $d_3$ ). After filtration using a 0.22- $\mu$ m nylon filter, the samples were analyzed by LC-MS/MS.

#### 2.3.3. LC-MS/MS analysis

The system included a Waters Acquity UPLC equipped with a pump, column compartment, autosampler, and Waters TQS mass spectrometer (Waters, Milford, MA, USA), operated in the electrospray ion (ESI) mode. A Kinetex Biphenyl (100  $\text{\AA}$ , 1.7  $\mu$ m,  $2.1 \times 100$  mm) column was used for analysis and maintained at  $25^\circ\text{C}$  with a flow rate of 0.3 mL/min and an injection volume of 3  $\mu$ L. The mobile phase consisted of 5% (A) and 100% (B) methanol, both containing 0.01% formic acid. The linear gradient conditions were as follows: 16% B (0–13.0 min), 16–99% B (13.0–13.5 min), 99% B (13.5–15.5 min), 99–16% B (15.5–16.0 min),

and 16% B (16.0–19.0 min). The ESI parameters were set as follows: capillary voltage, 3.0 kV; desolvation temperature, 200 °C; source temperature, 150 °C; desolvation gas flow, 400 L/h; cone gas flow, 150 L/h; and nebulizer gas flow, 7.0 bar. All MS/MS data for the analytes were collected in the multiple reaction monitoring (MRM) mode, using MassLynx v4.1 software. The urine concentrations of HA and MHAs were normalized to urinary creatinine concentrations and presented as g/g creatinine and µg/g creatinine, respectively.

#### 2.4. Questionnaire

On the day of urine collection, a questionnaire was used to collect basic data and lifestyle information from the participants for the previous 3 days; these data were used as a reference to analyze changes in the urine concentrations of HA and *o*-/*m*-/*p*-MHAs. Basic data collected included sex, age, education level, job category, task in the OR, working hours, job tenure, and current residence information, whereas lifestyle information included transportation to work, eating habits, intake of salicylic acid-containing drugs, and smoking and drinking habits.

#### 2.5. Statistical analysis

All data were analyzed using SPSS version 23.0 (SPSS, Chicago, USA), and the significance level was set at 0.05. GraphPad Prism 7.0 software (GraphPad Software, San Diego, CA, USA) was used to prepare figures. The *chi*-square test was used to identify differences between groups for categorical variables. The Mann–Whitney U and Kruskal–Wallis tests were used to analyze group differences between continuous variables. A simple linear regression analysis was used to evaluate the association between HA and *o*-/*p*-/*m*-MHA concentrations in the urine and factors including healthcare personnel group, sex, age, job tenure, working hours, and bus use.

### 3. Results

#### 3.1. Analysis of urine concentrations of creatinine, HA, and *o*-/*m*-/*p*-MHAs

First, we established a platform to analyze creatinine, HA, and *o*-/*m*-/*p*-MHA concentrations in human urine, and examined the concentration distributions of toluene and xylene metabolites in the urine (i.e., HA and *o*-/*m*-/*p*-MHAs) of OR workers. Individual compounds were detected using tandem mass spectrometry in the MRM mode. The optimized MRM conditions are shown in Table 1; creatinine and creatinine-*d*<sub>3</sub> were analyzed in the positive mode, whereas the other analytes were analyzed in the negative mode. The three isomers, *o*-/*m*-/*p*-MHAs, which have the same quantitative (192 > 91 *m/z*) and qualitative (192 > 148 *m/z*) ion pairs, could be separated based on their different retention times (Fig. 1). Table 2 shows that five urinary metabolites could be efficiently separated within 14 min, with a coefficient of correlation (*r*) greater than 0.9992. The retention times of creatinine, HA, and *o*-, *m*-, and *p*-

MHAs were 0.79, 4.23, 6.56, 11.38, and 12.05 min, respectively. The rate of HA and *o*-/*m*-/*p*-MHA recovery in urine samples ranged from 86% to 106%, and the average relative standard deviation was less than 5%.

#### 3.2. Participant characteristics

As shown on Table 3, 95% of the administrative staff and nurse anesthetists and 89% of surgical nurses were female. Conversely, all the surgeons were male. The median ages of the administrative staff (48 years) and nurse anesthetists (49 years) were significantly higher than those of the surgeons (31 years, *P* < 0.01) and surgical nurses (34.0 years, *P* < 0.01). Overall, 70% of the administrative staff, 90% of the nurse anesthetists, 100% of the surgical nurses, and 100% of the surgeons were educated above the university degree level. The job tenures of the administrative staff (20.5 years) and nurse anesthetists (26 years, *P* < 0.01) were significantly higher than those of the surgeons (3.1 years, *P* < 0.01) and surgical nurses (10.5 years, *P* < 0.01). The median working hours for OR personnel were 8–8.7 h/day. Furthermore, 42.5% of the administrative staff, 40% of the nurse anesthetists, 20% of the surgical nurses, and 10% of the surgeons commuted by bus, with a significant statistical difference among the four groups (*P* = 0.041). Regarding eating habits, only 12.5% of surgeons, 3% of surgical nurses, and 20% of administrative staff did not frequently eat soy products, meat products, minced fish products, chili sauce, jam, succade, cheese products, or pickles. Moreover, 100% of surgeons, nurse anesthetists, and surgical nurses and 95% of the administrative staff were non-smokers. The remaining 5% of the administrative staff were former smokers. With regard to alcohol consumption, 35% of surgeons, 10% of nurse anesthetists, 15% of surgical nurses, and 12.5% of administrative staff had consumed an alcoholic drink within 3 days prior to sample collection. Meanwhile, 25% of surgeons, 20% of nurse anesthetists, 10% of surgical nurses, and 25% of administrative staff had not consumed soft drinks within 3 days prior to urine sample collection; 17.5% of administrative staff, 9% of surgical nurses, and 20% of nurse anesthetists took salicylic acid preparations.

#### 3.3. Urine HA and *o*-/*m*-/*p*-MHA concentrations of OR staff

Fig. 2 shows the distribution of HA and *o*-/*m*-/*p*-MHA in the urine samples of OR staff. The median concentration of HA (0.25 g/g creatinine) in the urine of administrative staff was significantly higher than that in the urine of surgeons (HA: 0.15 g/g creatinine, *P* < 0.01) and surgical nurses (HA: 0.18 g/g creatinine, *P* < 0.01).

The median concentrations of *o*-MHA (nurse anesthetists: 300.07 µg/g creatinine, *P* < 0.01; surgeons: 215.59 µg/g creatinine, *P* < 0.01; surgical nurses: 921.50 µg/g creatinine, *P* < 0.01), *m*-MHA (nurse anesthetists: 1078.67 µg/g creatinine, *P* < 0.01; surgeons: 785.52 µg/g creatinine, *P* < 0.01; surgical nurses: 3392.14 µg/g creatinine, *P* < 0.01), and *p*-MHA (nurse anesthetists: 490.77 µg/g creatinine, *P* < 0.01; surgeons: 353.94 µg/g creatinine, *P* < 0.01; surgical nurses:

**Table 1**

Optimized MRM transition and parameters for the analysis of creatinine, creatinine-*d*<sub>3</sub>, hippuric acid, and *o*-, *m*-, and *p*-methylhippuric acids.

| Compound                          | ESI | Quantitative ion pair                                    |                  |                       | Qualitative ion pair                                     |                  |                       |
|-----------------------------------|-----|--|------------------|-----------------------|--|------------------|-----------------------|
|                                   |     | Parent ions ( <i>m/z</i> ) > Product ions ( <i>m/z</i> ) | Cone voltage (V) | Collision energy (eV) | Parent ions ( <i>m/z</i> ) > Product ions ( <i>m/z</i> ) | Cone voltage (V) | Collision energy (eV) |
| Creatinine                        | +   | 114 > 44   | 34               | 30                    | 114 > 86   | 34               | 20                    |
| Creatinine- <i>d</i> <sub>3</sub> | +   | 117 > 47   | 44               | 25                    | 117 > 89   | 44               | 15                    |
| Hippuric acid                     | –   | 178 > 134  | 10               | 20                    | 178 > 77   | 10               | 30                    |
| <i>o</i> -Methylhippuric acid     | –   | 192 > 91   | 10               | 16                    | 192 > 148  | 10               | 12                    |
| <i>m</i> -Methylhippuric acid     | –   | 192 > 91   | 4                | 16                    | 192 > 148  | 4                | 12                    |
| <i>p</i> -Methylhippuric acid     | –   | 192 > 91   | 2                | 16                    | 192 > 148  | 2                | 12                    |

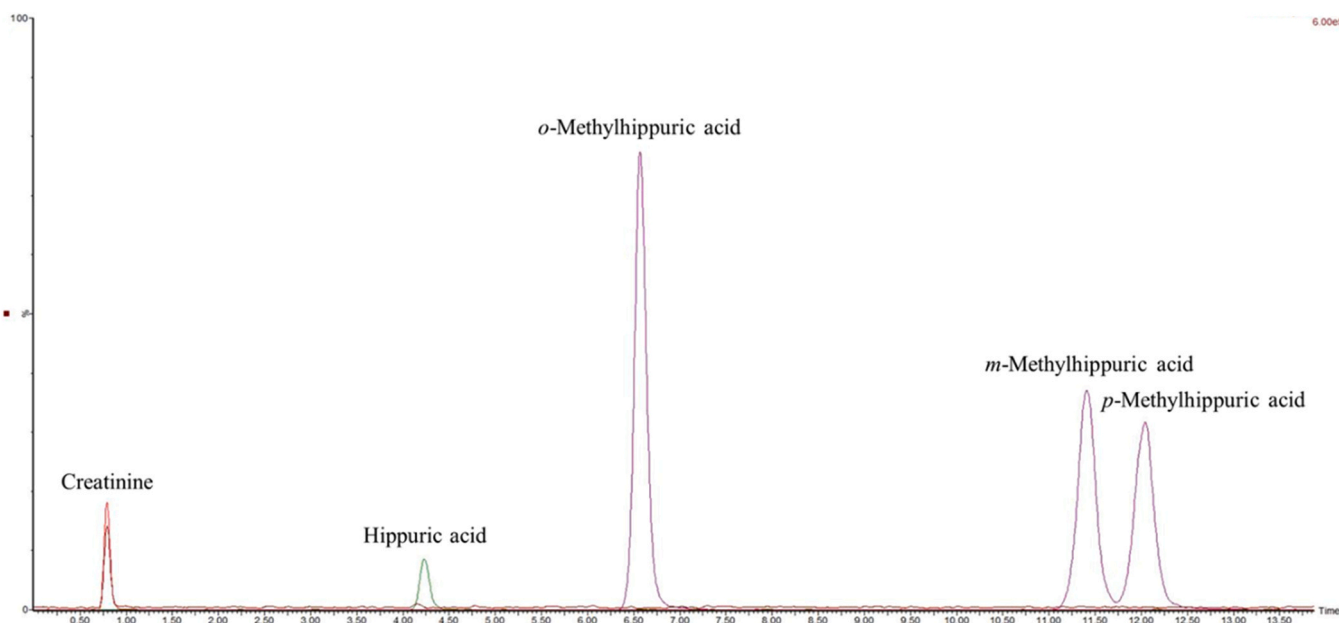


Fig. 1. LC-MS/MS analysis of creatinine, hippuric acid, and *o*-, *m*-, and *p*-MHAs.

Table 2

Calibration curves of creatinine, hippuric acid, and *o*-, *m*-, and *p*-methylhippuric acids.

| Compound                      | Retention time (min) | Calibration range (ng/mL) | <i>r</i> | Linear equation          |
|-------------------------------|----------------------|---------------------------|----------|--------------------------|
| Creatinine                    | 0.79                 | 5–2000                    | 0.9996   | $y = 0.306x + 0.059$     |
| Hippuric acid                 | 4.23                 | 20–2000                   | 0.9993   | $y = 28.910x - 173.434$  |
| <i>o</i> -Methylhippuric acid | 6.56                 | 5–200                     | 0.9999   | $y = 326.912x - 227.504$ |
| <i>m</i> -Methylhippuric acid | 11.38                | 5–200                     | 0.9992   | $y = 199.817x - 102.167$ |
| <i>p</i> -Methylhippuric acid | 12.05                | 5–200                     | 0.9993   | $y = 221.263x - 121.411$ |

1517.31 µg/g creatinine,  $P < 0.01$ ) in the urine of all surgical staff were significantly higher than those in the urine of administrative staff (*o*-MHA: 38.61 µg/g creatinine; *m*-MHA: 85.25 µg/g creatinine; *p*-MHA: 37.13 µg/g creatinine). No significant differences in urinary *o*-/*m*-/*p*-MHA levels were found between the nurse anesthetists and surgeons.

Table 4 shows that surgical nurses had significantly lower HA urine concentrations (beta coefficient [ $\beta$ ] = − 0.101, 95% confidence interval [CI] of  $\beta$  = − 0.192 to − 0.010,  $P = 0.03$ ) and higher *o*-MHA ( $\beta = 1170.135$ , 95% CI of  $\beta = 881.695$ –1458.574,  $P < 0.001$ ), *m*-MHA ( $\beta = 4341.092$ , 95% CI of  $\beta = 3281.189$ –5400.995,  $P < 0.001$ ), and *p*-MHA ( $\beta = 1945.916$ , 95% CI of  $\beta = 1471.250$ –2420.581,  $P < 0.001$ ) concentrations than administrative staff. Nurse anesthetists had higher urinary *o*-MHA ( $\beta = 441.865$ , 95% CI of  $\beta = 33.951$ –849.780,  $P = 0.034$ ), *m*-MHA ( $\beta = 1624.049$ , 95% CI of  $\beta = 125.120$ –3122.978,  $P = 0.034$ ), and *p*-MHA ( $\beta = 742.139$ , 95% CI of  $\beta = 70.861$ –1413.417,  $P = 0.03$ ) concentrations than administrative staff. Higher urinary *o*-/*m*-/*p*-MHA concentrations (*o*-MHA:  $\beta = 404.161$ , 95% CI of  $\beta = 53.993$ –754.328,  $P = 0.024$ ; *m*-MHA:  $\beta = 1475.406$ , 95% CI of  $\beta = 184.529$ –2766.282,  $P = 0.025$ ; *p*-MHA:  $\beta = 660.181$ , 95% CI of  $\beta = 82.181$ –1238.182,  $P = 0.025$ ) were positively associated with female sex. Age ( $\beta = 0.004$ , 95% CI of  $\beta = 0.001$ –0.008,  $P = 0.01$ ) and job tenure ( $\beta = 0.004$ , 95% CI of  $\beta = 0.001$ –0.008,  $P = 0.01$ ) were positively associated with urinary HA concentrations. However, age was negatively associated with urinary *o*-/*m*-/*p*-MHA concentrations (*o*-MHA:  $\beta = -15.605$ , 95% CI of  $\beta = -28.589$  to − 2.620,  $P = 0.019$ ;

*m*-MHA:  $\beta = -58.495$ , 95% CI of  $\beta = -106.318$  to − 10.672,  $P = 0.017$ ; *p*-MHA:  $\beta = -26.184$ , 95% CI of  $\beta = -47.597$  to − 4.771,  $P = 0.017$ ) of OR healthcare personnel.

#### 4. Discussion

To the best of our knowledge, only a few studies have evaluated the effects of surgical smoke exposure on human health. A study in Poland revealed that the concentrations of benzene and toluene in the urine of patients were higher after abdominal cholecystectomy than before surgery (Dobrogowski et al., 2014). A study in Taiwan showed that the concentrations of sevoflurane, dimethyl sulfide, and methyl methacrylate in breath samples from OR healthcare personnel in different departments were higher after surgery than before surgery (Cheng et al., 2019).

These results suggest that volatile organic compounds and their metabolites can be detected in urine and breath samples after exposure to surgical smoke. However, whether this exposure is hazardous to human health has not yet been confirmed. Metabolites such as HA and MHA are produced after exposure to toluene and xylene, respectively (ACGIH, 2013; Engström et al., 1978), and a positive correlation has been reported between concentrations of urinary *o*-/*m*-/*p*-MHAs and low-dose xylene exposure (< 15 ppm) (Jacobson and McLean, 2003). However, to the best of our knowledge, no study has evaluated the concentrations of HA and MHAs in the urine of OR healthcare personnel. We found that HA concentrations in the urine of administrative staff (0.04–1.58 g/g creatinine), nurse anesthetists (0.02–0.44 g/g creatinine), surgeons (0.03–1.54 g/g creatinine), and surgical nurses (0.01–1.15 g/g creatinine) were all lower than the maximum value recommended by the ACGIH (< 1.6 g/g creatinine) (ACGIH, 2007). Furthermore, the total concentrations of *o*-/*m*-/*p*-MHAs in the urine of administrative staff ( $7.92 \times 10^{-5}$  to  $1.05 \times 10^{-3}$  g/g creatinine), nurse anesthetists ( $2.68 \times 10^{-4}$  to  $1.74 \times 10^{-2}$  g/g creatinine), surgeons ( $7.15 \times 10^{-4}$  to  $4.66 \times 10^{-3}$  g/g creatinine), and surgical nurses ( $1.34 \times 10^{-3}$  to  $3.37 \times 10^{-2}$  g/g creatinine) were lower than the maximum value recommended by the ACGIH (< 1.5 g/g creatinine). The concentrations of these metabolites in the urine of OR healthcare personnel were below the maximum values recommended by the ACGIH; however, the effects of long-term exposure to low concentrations of toluene and xylene in ORs need to be further evaluated.

To date, a few studies have investigated the effects of long-term



**Table 3**  
Sociodemographic characteristics and habits of OR healthcare personnel.

| Variable                                  | Administrative staff |             | Nurse anesthetist |             | Surgeon  |                         | Surgical nurse |                            | P value |
|---|----------------------|-------------|-------------------|-------------|----------|-------------------------|----------------|----------------------------|---------|
|   | (n = 40)             |             | (n = 20)          |             | (n = 20) |                         | (n = 80)       |                            |         |
| Personal characteristics                  |                      |             |                   |             |          |                         |                |                            |         |
| Sex, n (%)                                |                      |             |                   |             |          |                         |                |                            | < 0.001 |
| Female                                    | 38                   | (95)        | 19                | (95)        | 0        | (0)                     | 71             | (89)                       |         |
| Male                                      | 2                    | (5)         | 1                 | (5)         | 20       | (100)                   | 9              | (11)                       |         |
| Age (year)                                | 48                   | (39–54)     | 49                | (43–54)     | 31       | (30–33) <sup>†‡</sup>   | 34             | (26–41) <sup>†‡</sup>      | < 0.001 |
| Education level, n (%)                    |                      |             |                   |             |          |                         |                |                            | < 0.001 |
| ≥ University degree                       | 28                   | (70)        | 18                | (90)        | 25       | (100)                   | 80             | (100)                      |         |
| < University degree                       | 12                   | (30)        | 2                 | (10)        | 0        | (0)                     | 0              | (0)                        |         |
| Job tenure, years                         | 20.5                 | (10.8–25.3) | 26.0              | (19.9–33.5) | 3.1      | (1.9–5.0) <sup>†‡</sup> | 10.5           | (3.8–20.0) <sup>†,‡§</sup> | < 0.001 |
| Working hours, h/day                      | 8                    | (8–8)       | 8.7               | (8–9.3)     | 8.5      | (7.3–12)                | 8.0            | (6.4–9.3)                  | 0.056   |
| Habits                                    |                      |             |                   |             |          |                         |                |                            |         |
| Transportation, n (%)                     |                      |             |                   |             |          |                         |                |                            |         |
| Motorcycle                                | 12                   | (30)        | 4                 | (20)        | 3        | (15)                    | 27             | (26)                       | 0.308   |
| Car                                       | 16                   | (40)        | 4                 | (20)        | 9        | (45)                    | 21             | (20)                       | 0.151   |
| Bus                                       | 17                   | (42.5)      | 8                 | (40)        | 2        | (10)                    | 21             | (20)                       | 0.041   |
| Mass rapid transit                        | 0                    | (0)         | 1                 | (5)         | 2        | (10)                    | 7              | (7)                        | 0.256   |
| Bicycle                                   | 0                    | (0)         | 0                 | (0)         | 1        | (5)                     | 1              | (1)                        | 0.386   |
| On foot                                   | 6                    | (15)        | 5                 | (25)        | 6        | (30)                    | 28             | (32)                       | 0.144   |
| Wearing mask, n (%)                       |                      |             |                   |             |          |                         |                |                            | 0.008   |
| No  | 16                   | (40)        | 13                | (65)        | 17       | (85)                    | 47             | (59)                       |         |
| Yes                                       | 24                   | (60)        | 7                 | (35)        | 3        | (15)                    | 33             | (41)                       |         |
| Dietary intake, n (%)                     |                      |             |                   |             |          |                         |                |                            |         |
| Soy product                               | 17                   | (42.5)      | 13                | (65)        | 12       | (60)                    | 47             | (25)                       | 0.264   |
| Meat product                              | 13                   | (32.5)      | 5                 | (25)        | 8        | (40)                    | 31             | (16)                       | 0.645   |
| Minced fish product                       | 12                   | (30)        | 2                 | (10)        | 4        | (20)                    | 27             | (14)                       | 0.146   |
| Chili sauce                               | 13                   | (32.5)      | 8                 | (40)        | 5        | (25)                    | 24             | (13)                       | 0.762   |
| Jam                                       | 7                    | (53.85)     | 5                 | (25)        | 0        | (0)                     | 12             | (6)                        | 0.151   |
| Succade                                   | 6                    | (15)        | 3                 | (15)        | 1        | (5)                     | 14             | (7)                        | 0.581   |
| Cheese product                            | 12                   | (30)        | 5                 | (25)        | 7        | (35)                    | 21             | (11)                       | 0.856   |
| Pickles                                   | 6                    | (15)        | 2                 | (10)        | 2        | (10)                    | 7              | (4)                        | 0.773   |
| None of the above                         | 5                    | (12.5)      | 0                 | (0)         | 4        | (20)                    | 6              | (3)                        | 0.138   |
| Soft drink consumption, n (%)             |                      |             |                   |             |          |                         |                |                            |         |
| Tea                                       | 17                   | (42.5)      | 11                | (55)        | 9        | (45)                    | 45             | (39)                       | 0.484   |
| Coffee                                    | 21                   | (50)        | 11                | (55)        | 11       | (55)                    | 42             | (37)                       | 0.995   |
| Juice                                     | 4                    | (10)        | 2                 | (10)        | 2        | (10)                    | 8              | (7)                        | 1.000   |
| Carbonated soft drink                     | 2                    | (5)         | 0                 | (0)         | 3        | (15)                    | 8              | (7)                        | 0.277   |
| None of the above                         | 10                   | (25)        | 4                 | (20)        | 5        | (25)                    | 12             | (10)                       | 0.532   |
| Use of salicylic acid preparations, n (%) |                      |             |                   |             |          |                         |                |                            | 0.105   |
| No  | 33                   | (82.5)      | 16                | (80)        | 20       | (100)                   | 73             | (91)                       |         |
| Yes                                       | 7                    | (17.5)      | 4                 | (20)        | 0        | (0)                     | 7              | (9)                        |         |
| Smoking, n (%)                            |                      |             |                   |             |          |                         |                |                            | 0.071   |
| No  | 40                   | (100)       | 20                | (100)       | 19       | (95)                    | 80             | (100)                      |         |
| Yes                                       | 0                    | (0)         | 0                 | (0)         | 0        | (0)                     | 0              | (0)                        |         |
| Former                                    | 0                    | (0)         | 0                 | (0)         | 1        | (5)                     | 0              | (0)                        |         |
| Alcohol consumption, n (%)                |                      |             |                   |             |          |                         |                |                            | 0.100   |
| No  | 35                   | (87.5)      | 18                | (90)        | 13       | (65)                    | 68             | (85)                       |         |
| Yes                                       | 5                    | (12.5)      | 2                 | (10)        | 7        | (35)                    | 12             | (15)                       |         |
| Former                                    | 0                    | (0)         | 0                 | (0)         | 0        | (0)                     | 0              | (0)                        |         |

Data are presented as n (%) or median (25–75 percentiles). †: compared to administrative staff,  $P < 0.01$ ; ‡: compared to nurse anesthetist,  $P < 0.01$ ; §: compared to surgeon,  $P < 0.01$ .

exposure to low concentrations of toluene and xylene on human health. A study in Korea (Yoon et al., 2010) showed that the concentrations of HA and MHA in the urine of people aged over 60 years with a history of long-term exposure to low concentrations of volatile organic compounds indoors (toluene:  $11.18 \mu\text{g}/\text{m}^3$ , xylene:  $5.24 \mu\text{g}/\text{m}^3$ ) and outdoors (toluene:  $6.20 \mu\text{g}/\text{m}^3$ , xylene:  $2.84 \mu\text{g}/\text{m}^3$ ) changed positively, and that exposure to low concentrations of toluene and xylene was negatively associated with lung function. A study in China (Chen et al., 2011) showed that the air concentrations of benzene, toluene, and xylene in buses were 21.3–106.4, 53.5–26.0, and 46.9–234.8  $\mu\text{g}/\text{m}^3$ , respectively, whereas the age and mileage of the buses were associated with changes in the concentrations of benzene, toluene, and xylene.

We found that the concentrations of HA in the urine of administrative staff were significantly higher than those in the urine of both surgeons and surgical nurses. This finding may be explained by the high proportion of OR administrative staff who commute by bus (42.5%) and are exposed to air pollutants during travel. Additionally, the *o*-/*m*-/*p*-MHA concentrations in the urine of surgical nurses were higher than those in

the urine of administrative staff, nurse anesthetists, and surgeons. To reduce the exposure of healthcare personnel to surgical smoke, it is recommended to use a local smoke exhaust system, strictly control overall ventilation in the OR, and provide appropriate personal protective equipment.

This study has a few limitations. The number of participants included in this study was relatively small; therefore, future studies with a larger sample size are recommended. Another limitation of this study is that exposure to toluene and xylene was from surgical smoke as well as from indoor and outdoor air pollutants. Although a questionnaire was used to collect information regarding the participants' means of transportation, some confounding factors such as commute time and the correct manner of wearing masks could not be measured in practice.

## 5. Conclusions

In this study, we successfully established a quantitative method to analyze HA and *o*-/*m*-/*p*-MHA levels in urine samples. The results

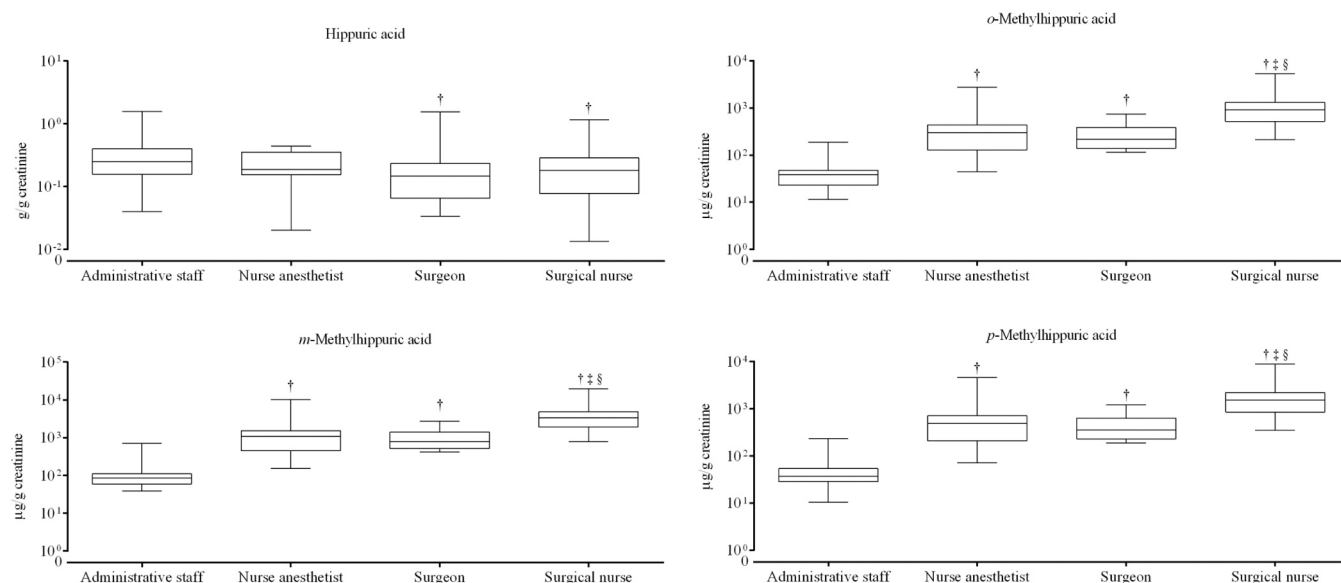


**Fig. 2.** Distribution of hippuric and *o*-/*m*-/*p*-methylhippuric acids in the urine of operating room healthcare personnel. †: compared to administrative staff,  $P < 0.01$ ; ‡: compared to nurse anesthetists,  $P < 0.01$ ; §: compared to surgeons,  $P < 0.01$ . Box-and-whisker plots show the minimum, 25<sup>th</sup> percentile, median, 75<sup>th</sup> percentile, and maximum values.

**Table 4**

Associations between sociodemographic characteristics and urinary concentrations of hippuric acid and methylhippuric acid in OR healthcare personnel.

| Independent variable                                  | $\beta$         | (95% CI of $\beta$ ) | P       | Independent variable                                  | $\beta$         | (95% CI of $\beta$ )  | P       |
|---|-----------------|----------------------|---------|---|-----------------|-----------------------|---------|
| <b>Hippuric acid, g/g creatinine</b>                  |                 |                      |         | <b>–<i>m</i>-Methylhippuric acid, µg/g creatinine</b> |                 |                       |         |
| Sex   | 0.064           | (– 0.029, 0.158)     | 0.174   | Sex   | 1475.406        | (184.529, 2766.282)   | 0.025   |
| Age, years  | 0.004           | (0.001, 0.008)       | 0.010   | Age, years  | – 58.495        | (– 106.318, – 10.672) | 0.017   |
| Job tenure, years                                     | 0.004           | (0.001, 0.008)       | 0.010   | Job tenure, years                                     | – 18.107        | (– 66.311, 30.097)    | 0.459   |
| Working hours, h/day                                  | – 0.014         | (– 0.032, 0.004)     | 0.134   | Working hours, h/day                                  | 116.795         | (– 136.492, 370.082)  | 0.364   |
| <b>Healthcare personnel group</b>                     |                 |                      |         | <b>Healthcare personnel group</b>                     |                 |                       |         |
| Administrative staff                                  | Reference group |                      |         | Administrative staff                                  | Reference group |                       |         |
| Nurse anesthetist                                     | – 0.101         | (– 0.229, 0.027)     | 0.122   | Nurse anesthetist                                     | 1624.049        | (125.120, 3122.978)   | 0.034   |
| Surgeon   | – 0.103         | (– 0.231, 0.026)     | 0.117   | Surgeon   | 930.375         | (– 568.554, 2429.304) | 0.222   |
| Surgical nurse  | – 0.101         | (– 0.192, – 0.010)   | 0.030   | Surgical nurse  | 4341.092        | (3281.189, 5400.995)  | < 0.001 |
| Bus user  | 0.034           | (– 0.048, 0.116)     | 0.412   | Bus user  | – 454.902       | (– 1597.464, 687.661) | 0.433   |
| <b>–<i>o</i>-Methylhippuric acid, µg/g creatinine</b> |                 |                      |         | <b>–<i>p</i>-Methylhippuric acid, µg/g creatinine</b> |                 |                       |         |
| Sex   | 404.161         | (53.993, 754.328)    | 0.024   | Sex   | 660.181         | (82.181, 1238.182)    | 0.025   |
| Age, years  | – 15.605        | (– 28.589, – 2.620)  | 0.019   | Age, years  | – 26.184        | (– 47.597, – 4.771)   | 0.017   |
| Job tenure, years                                     | – 4.687         | (– 17.769, 8.395)    | 0.480   | Job tenure, years                                     | – 8.052         | (– 29.636, 13.531)    | 0.462   |
| Working hours, h/day                                  | 31.433          | (– 37.298, 100.165)  | 0.368   | Working hours, h/day                                  | 52.520          | (– 60.886, 165.927)   | 0.362   |
| <b>Healthcare personnel group</b>                     |                 |                      |         | <b>Healthcare personnel group</b>                     |                 |                       |         |
| Administrative staff                                  | Reference group |                      |         | Administrative staff                                  | Reference group |                       |         |
| Nurse anesthetist                                     | 441.865         | (33.951, 849.780)    | 0.034   | Nurse anesthetist                                     | 742.139         | (70.861, 1413.417)    | 0.030   |
| Surgeon   | 245.258         | (– 162.656, 653.173) | 0.237   | Surgeon   | 422.258         | (– 249.020, 1093.536) | 0.216   |
| Surgical nurse  | 1170.135        | (881.695, 1458.574)  | < 0.001 | Surgical nurse  | 1945.916        | (1471.250, 2420.581)  | < 0.001 |
| Bus user  | – 121.711       | (– 431.759, 188.337) | 0.439   | Bus user  | – 205.870       | (– 717.429, 305.689)  | 0.428   |

Sex: reference group = male; bus user: reference group = no.

showed that the concentration of HA in the urine of administrative staff was higher than that in the urine of surgeons and surgical nurses. Surgical nurses had the highest urinary *o*-MHA, *m*-MHA, and *p*-MHA concentrations, followed by nurse anesthetists and surgeons, whereas administrative nurses had the lowest urinary concentrations of *o*-MHA, *m*-MHA, and *p*-MHA. The type of healthcare personnel, sex, age, and job tenure were all found to affect the concentration of urinary toluene and xylene metabolites.

#### CRediT authorship contribution statement

**Chun-Hui Chiu:** Formal analysis, Methodology, Visualization, Writing - original draft. **Chi-Tsung Chen:** Formal analysis, Investigation, Visualization, Writing - original draft. **Ming-Huei Cheng:** Investigation, Writing - review & editing. **Li-Heng Pao:** Writing - review &

editing. **Chi Wang:** Investigation. **Gwo-Hwa Wan:** Conceptualization, Methodology, Project administration, Funding acquisition, Writing - review & editing.

#### Declaration of Competing Interest

The authors declare that they have no known competing financial interests or personal relationships that could have appeared to influence the work reported in this paper.

#### Acknowledgements

The authors thank the Ministry of Science and Technology (107-2314-B-182-054) and Chang Gung Medical Foundation (BMRP441), Taiwan, for financially supporting this research.

## References

- Al Sahaf, O.S., Vega-Carrascal, I., Cunningham, F.O., McGrath, J.P., Bloomfield, F.J., 2007. Chemical composition of smoke produced by high-frequency electrosurgery. *Ir. J. Med. Sci.* 176 (3), 229–232.
- American Conference of Governmental Industrial Hygienists (ACGIH), 1997. Documentation of TLVs and BEIs, sixth ed. 1991581-584, BEI-169-174, BEI-187-193.
- American Conference of Governmental Industrial Hygienists (ACGIH), 2007. “TLVs® and BEI® based on the Documentation of the Threshold Limit Values for Chemical Substances and Physical Agents & Biological Exposure indices”; Cincinnati, Ohio, 104.
- American Conference of Governmental Industrial Hygienists (ACGIH), 2013. Documentation of the TLVs and BEIs with Other World Wide Occupational Exposure Values, seventh ed. CD-ROM Cincinnati, OH, 3–4.
- Barrett, W.L., Garber, S.M., 2003. Surgical smoke: a review of the literature. Is this just a lot of hot air? *Surg. Endosc.* 17 (6), 979–987.
- Capizzi, P.J., Clay, R.P., Battey, M.J., 1998. Microbiologic activity in laser resurfacing plume and debris. *Lasers Surg. Med.* 23 (3), 172–174.
- Chen, X., Zhang, G., Zhang, Q., Chen, H., 2011. Mass concentrations of BTEX inside air environment of buses in Changsha, China. *Build. Environ.* 46 (2), 421–427.
- Cheng, N.Y., Chuang, H.C., Shie, R.H., Liao, W.H., Hwang, Y.H., 2019. Pilot studies of VOC exposure profiles during surgical operations. *Ann. Work Expo. Health* 63 (2), 173–183.
- Choi, S.H., Kwon, T.G., Chung, S.K., Kim, T.H., 2014. Surgical smoke may be a biohazard to surgeons performing laparoscopic surgery. *Surg. Endosc.* 28 (8), 2374–2380.
- Department of Health and Human Services, Agency for Toxic Substances and Disease Registry, 2007. Toxicological Profile for Xylenes (Update) (PB2008-100008) p.123. (<http://www.atsdr.cdc.gov/toxprofiles/tp71.pdf>). Accessed 22 October 2019.
- Department of Health and Human Services, Agency for Toxic Substances and Disease Registry, 2017. Toxicological Profile for Toluene. (<https://www.atsdr.cdc.gov/toxprofiles/tp56.pdf>). Accessed 24 October 2019.
- Dobrogowski, M., Wesolowski, W., Kucharska, M., Sapota, A., Pomorski, L.S., 2014. Chemical composition of surgical smoke formed in the abdominal cavity during laparoscopic cholecystectomy-assessment of the risk to the patient. *Int. J. Occup. Med. Environ. Health* 27 (2), 314–325.
- Engström, K., Husman, K., Pfäffli, P., Riihimäki, V., 1978. Evaluation of occupational exposure to xylene by blood, exhaled air and urine analysis. *Scand. J. Work Environ. Health* 4 (2), 114–121.
- Fernández-Fernández, M., Rodríguez-González, P., Añón Álvarez, M.E., Rodríguez, F., Menéndez, F.V., García Alonso, J.I., 2015. Simultaneous determination of creatinine and creatine in human serum by double-spike isotope dilution liquid chromatography-tandem mass spectrometry (LC-MS/MS) and gas chromatography-mass spectrometry (GC-MS). *Anal. Chem.* 87 (7), 3755–3763.
- Fitzgerald, J.E., Malik, M., Ahmed, I., 2012. A single-blind controlled study of electrocautery and ultrasonic scalpel smoke plumes in laparoscopic surgery. *Surg. Endosc.* 26 (2), 337–342.
- Fletcher, J.N., Mew, D., DesCôteaux, J.G., 1999. Dissemination of melanoma cells within electrocautery plume. *Am. J. Surg.* 178 (1), 57–59.
- Heinsohn, P., Jewett, D.L., 1993. Exposure to blood-containing aerosols in the operating room: a preliminary study. *Am. Ind. Hyg. Assoc. J.* 54 (8), 446–453.
- Jacobson, G.A., McLean, S., 2003. Biological monitoring of low-level occupational xylene exposure and the role of recent exposure. *Ann. Occup. Hyg.* 47 (4), 331–336.
- Jewett, D.L., Heinsohn, P., Bennett, C., Rosen, A., Neuilly, C., 1992. Blood-containing aerosols generated by surgical techniques: a possible infectious hazard. *Am. Ind. Hyg. Assoc. J.* 53 (4), 228–231.
- Kandyala, R., Raghavendra, S.P., Rajasekharan, S.T., 2010. Xylene: an overview of its health hazards and preventive measures. *J. Oral Maxillofac. Pathol.* 14 (1), 1–5.
- Kwak, H.D., Kim, S.H., Seo, Y.S., Song, K.J., 2016. Detecting hepatitis B virus in surgical smoke emitted during laparoscopic surgery. *Occup. Environ. Med.* 73 (12), 857–863.
- Le Moual, N., Varraso, R., Zock, J.P., Henneberger, P., Speizer, F.E., Kauffmann, F., Camargo Jr., C.A., 2013. Are operating room nurses at higher risk of severe persistent asthma? The Nurses’ Health Study. *J. Occup. Environ. Med.* 55 (8), 973–977.
- Lin, Y.W., Fan, S.Z., Chang, K.H., Huang, C.S., Tang, C.S., 2010. A novel inspection protocol to detect volatile compounds in breast surgery electrocautery smoke. *J. Formos. Med. Assoc.* 109 (7), 511–516.
- McKinley, I.B.Jr, Ludlow, M.O., 1994. Hazards of laser smoke during endodontic therapy. *J. Endod.* 20 (11), 558–559.
- Nduka, C.C., Poland, N., Kennedy, M., Dye, J., Darzi, A., 1998. Does the ultrasonically activated scalpel release viable airborne cancer cells? *Surg. Endosc.* 12 (8), 1031–1034.
- Occupational Safety and Health Administration, Laser/Electrosurgery Plume, 2012. (<https://www.osha.gov/SLTC/laserelectrosurgeryplume/index.html>). Accessed 22 October 2019.
- Ott, D.E., Moss, E., Martinez, K., 1998. Aerosol exposure from an ultrasonically activated (Harmonic) device. *J. Am. Assoc. Gynecol. Laparosc.* 5 (1), 29–32.
- Pacifici, G.M., Mogavero, S., Giuliani, L., Rane, A., 1991. Conjugation of benzoic acid with glycine in the human fetal and adult liver and kidney. *Dev. Pharmacol. Ther.* 17 (1–2), 52–62.
- Siqueira, M.E., Paiva, M.J., 2002. Hippuric acid in urine: reference values. *Rev. Saude Publica* 36 (6), 723–727.
- Taravella, M.J., Weinberg, A., May, M., Stepp, P., 1999. Live virus survives excimer laser ablation. *Ophthalmology* 106 (8), 1498–1499.
- Tseng, H.S., Liu, S.P., Uang, S.N., Yang, L.R., Lee, S.C., Liu, Y.J., Chen, D.R., 2014. Cancer risk of incremental exposure to polycyclic aromatic hydrocarbons in electrocautery smoke for mastectomy personnel. *World J. Surg. Oncol.* 55 (8), 973–977.
- U.S. Department of Health and Human Services (DHHS), 1988. Public Health Service, Centers for Disease Control and Prevention, National Institute for Occupational Safety and Health, HETA-85-126-1932, 1–28.
- Uchida, Y., Nakatsuka, H., Ukai, H., Watanabe, T., Liu, Y.T., Huang, M.Y., Wang, Y.L., Zhu, F.Z., Yin, H., Ikeda, M., 1993. Symptoms and signs in workers exposed predominantly to xylenes. *Int. Arch. Occup. Environ. Health* 64 (8), 597–605.
- Ulmer, B.C., 2008. The hazards of surgical smoke. *AORN J.* 87 (4), 721–734.
- Villanueva, M.B., Jonai, H., Kanno, S., Takeuchi, Y., 1994. Dietary sources and background levels of hippuric acid in urine: comparison of Philippine and Japanese levels. *Ind. Health* 32 (4), 239–246.
- Yoon, H.I., Hong, Y.C., Cho, S.H., Kim, H., Kim, Y.H., Sohn, J.R., Kwon, M., Park, S.H., Cho, M.H., Cheong, H.K., 2010. Exposure to volatile organic compounds and loss of pulmonary function in the elderly. *Eur. Respir. J.* 36 (6), 1270–1276.
- Zhao, C., Kim, M.K., Kim, H.J., Lee, S.K., Chung, Y.J., Park, J.K., 2013. Comparative safety analysis of surgical smoke from transurethral resection of the bladder tumors and transurethral resection of the prostate. *Urology* 82 (3), 744.e9–744.e14 e9–e14.



## Article

# Anti-Inflammatory Principles from the Needles of *Pinus taiwanensis* Hayata and In Silico Studies of Their Potential Anti-Aging Effects

Ping-Chung Kuo <sup>1,\*</sup>, Yue-Chiun Li <sup>1,†</sup>, Anjar M. Kusuma <sup>1,†</sup>, Jason T. C. Tzen <sup>2</sup>, Tsong-Long Hwang <sup>3,4,5</sup>, Guan-Hong Ye <sup>1</sup>, Mei-Lin Yang <sup>1</sup> and Sheng-Yang Wang <sup>6</sup>

- <sup>1</sup> School of Pharmacy, College of Medicine, National Cheng Kung University, Tainan 701, Taiwan; ycli0126@gmail.com (Y.-C.L.); anjarmahardian@gmail.com (A.M.K.); elva10352@gmail.com (G.-H.Y.); l3891104@nckualumni.org.tw (M.-L.Y.)
- <sup>2</sup> Graduate Institute of Biotechnology, National Chung-Hsing University, Taichung 402, Taiwan; tctzen@dragon.nchu.edu.tw
- <sup>3</sup> Graduate Institute of Natural Products, College of Medicine, Chang Gung University, Taoyuan 333, Taiwan; htl@mail.cgu.edu.tw
- <sup>4</sup> Research Center for Chinese Herbal Medicine, Research Center for Food and Cosmetic Safety, Graduate Institute of Health Industry Technology, College of Human Ecology, Chang Gung University of Science and Technology, Taoyuan 333, Taiwan
- <sup>5</sup> Department of Anesthesiology, Chang Gung Memorial Hospital, Taoyuan 333, Taiwan
- <sup>6</sup> Department of Forestry, National Chung-Hsing University, Taichung 402, Taiwan; taiwanfir@dragon.nchu.edu.tw
- \* Correspondence: z10502016@ncku.edu.tw; Tel.: +886-6-2353535 (ext. 6806)
- † These authors contributed equally to this work.



**Citation:** Kuo, P.-C.; Li, Y.-C.; Kusuma, A.M.; Tzen, J.T.C.; Hwang, T.-L.; Ye, G.-H.; Yang, M.-L.; Wang, S.-Y. Anti-Inflammatory Principles from the Needles of *Pinus taiwanensis* Hayata and In Silico Studies of Their Potential Anti-Aging Effects. *Antioxidants* **2021**, *10*, 598. <https://doi.org/10.3390/antiox10040598>

Academic Editor: Stefania D'Angelo

Received: 23 March 2021

Accepted: 9 April 2021

Published: 13 April 2021

**Publisher's Note:** MDPI stays neutral with regard to jurisdictional claims in published maps and institutional affiliations.

**Abstract:** *Pinus* needle tea are very popular in Eastern countries such as Japan, Russia, Korea, and China. Pine needle tea is claimed to have significant anti-aging effects, but no clear evidence has supported this until now. In the present study, five undescribed compounds (1–5) as well as seventy-two known compounds were purified and characterized from the bioactive fraction of methanol extracts of *P. taiwanensis* needles. Most of the isolates were examined for their anti-inflammatory bioactivity by cellular neutrophil model and six compounds (45, 47, 48, 49, 50, and 51) exhibited a significant inhibition on superoxide anion generation and elastase release with IC<sub>50</sub> values ranging from 3.3 ± 0.9 to 8.3 ± 0.8 μM. These anti-inflammatory ingredients were subjected to docking computing to evaluate their binding affinity on the ghrelin receptor, which played an important role in regulating metabolism, with anti-aging effects. Compounds 49, 50, and 51 formed a stable complex with the ghrelin receptor via hydrogen bonds and different types of interactions. These results suggest the flavonoids are responsible for the potential anti-aging effects of pine needle tea.

**Keywords:** *Pinus taiwanensis*; Pinaceae; anti-inflammatory; superoxide anion generation; elastase release; ghrelin receptor; molecular docking



**Copyright:** © 2021 by the authors. Licensee MDPI, Basel, Switzerland. This article is an open access article distributed under the terms and conditions of the Creative Commons Attribution (CC BY) license (<https://creativecommons.org/licenses/by/4.0/>).

## 1. Introduction

*Pinus* genus (Pinaceae), comprising more than 100 species and are mainly distributed in the Northern Hemisphere, are generally evergreen trees while some are shrubs [1]. The pine wood is light and often used for furniture. However, various pharmacological effects of the needles on the pine shoots have been recorded in the ancient books of traditional Chinese medicine. In “The Divine Husbandman’s Herbal Foundation Canon”, pine needles promoted hair growth, prolonged life, and quenched thirst. In “Taiping Shenghui Fang”, it was recorded that pine needles could be cooked with alcohol and displayed an anti-aging effect. Nowadays, pine needles are processed as tea and are popular in Asia. In Korea, the constituents of the *P. densiflora* needle tea as well as its



antioxidant and anti-bacterial bioactivities were extensively investigated [2,3]. Since early last century, more than seven hundred compounds have been identified from *Pinus* needles. Most of the reported literature are related to the essential oil of *P. densiflora* [4,5], *P. halepensis* [6,7], *P. nigra* [4,8], and *P. sylvestris* [4,9]. The characterized components of *Pinus* needles are mostly benzenoids, diterpenoids, flavonoids, lignans, monoterpenoids, and sesquiterpenoids [10]. The needles of *P. densiflora* and *P. morrisonicola* have been reported for their antioxidant bioactivity [11–14]. In addition, the ethyl acetate extract of needles of *P. morrisonicola* inhibited the protein and mRNA expression of NO and iNOS in LPS-induced RAW 264.7 macrophage, exhibiting the significant anti-inflammatory bioactivity [13]. The supercritical fluid extract of *P. densiflora* needles displayed the inhibitory effect on LPS-induced NO production by downregulating the expression of iNOS, and reduced the expression of IL-6 and IL-1 $\beta$  and activation of STAT1 and STAT3 proteins in macrophages induced by LPS [15]. The ethanol extract of *P. thunbergii* needles showed a significant anti-inflammatory effect in macrophages, and suppressed arachidonic acid-induced ear edema and inhibited myeloperoxidase enzymatic activity [16]. Moreover, the fermented *P. morrisonicola* needles showed their excellent antioxidant and anti-inflammatory bioactivities through modulating the NF- $\kappa$ B signaling pathway [17].

Ghrelin is a peptide hormone consisting of twenty-eight amino acids and was originally discovered in the stomach [18,19]. It is an endogenous ligand for the growth hormone secretagogue (GHSR), which is a member of the  $\beta$ -branch in class A GPCRs (G Protein-Coupled Receptors) [18,19]. Ghrelin is the only peptide hormone that causes hunger to promote appetite [20]. Many studies have suggested that ghrelin plays an important role in regulating metabolism, energy balance, memory, cardiovascular, and gastrointestinal functions in the human body [21–23]. Ghrelin is also involved in various physiological and pathophysiological mechanisms in the human body such as aging [24,25], and it may be related to anti-inflammatory activity [26,27]. In 2014, the unique acylated flavonoid tetraglycosides named teaghrelins, were first identified in Chin-shin oolong tea by our group and demonstrated their promoting activity in growth hormone (GH) release [28]. Two other similar compounds were purified in Shy-jih-chuen oolong tea and their bioactivity on the ghrelin receptor was also verified [29]. The four teaghrelins induced hunger through the same regulatory pathway as ghrelin. Not limited to tea, compounds with similar structures or bioactivities to teaghrelins have also been explored in *Polygonum multiflorum* (Heshouwu) [30], *Ginkgo biloba* [31], *Morus alba* [32], and *Cistanche tubulosa* [33]. These results support us in the search for natural anti-aging principles by screening the teaghrelin-like compounds that possess anti-inflammatory effects. In addition to directly performing the promoting activity in growth hormone release in cellular models, molecular modeling of some potential compounds would be more efficient in exploring possible candidates [34]. Computational methods have been applied to the development and evaluation of pharmacological hypothesis. Molecular docking is one of the most commonly utilized techniques and anticipates the conformation and affinity of ligand binding to the active pocket with high accuracy [35,36]. Docking methods effectively search high-dimensional spaces for possible interaction and use a scoring function that properly ranks the candidates [37].

In 2018, three compounds were purified from the needles of *P. morrisonicola* and exhibited significant vasorelaxant activity, and among these constituents, one was reported with a teaghrelin-like structure [38]. In Taiwan, *P. taiwanensis* needles are usually dried and baked and then processed as a tea due to their famous bioactivities. *P. taiwanensis* Hayata is one of the native and endemic species in Taiwan. It is also called Taiwan red pine, or huangshan pine. There are two needles in a fascicle with 8–11 cm long and slightly stiff and straight, and it grows across the whole island from low to high altitudes and often form pure forest [39]. In a preliminary examination, the ethyl acetate layer of methanol extracts of *P. taiwanensis* needles displayed a significant inhibition on superoxide anion generation and elastase release with IC<sub>50</sub> values of  $0.8 \pm 0.2$  and  $1.0 \pm 0.1$   $\mu$ g/mL, respectively (Table S1). Therefore, in the present study, the bioactive constituents of *P. taiwanensis* needles were investigated and the purified compounds were evaluated for their anti-inflammatory

bioactivity on a cellular neutrophil model. In addition, the isolates from *P. taiwanensis* needles with anti-inflammatory bioactivities were subjected to docking computing and investigated for their interaction with the ghrelin receptor.

## 2. Materials and Methods

### 2.1. General Experimental Procedures

The melting points were recorded on a WRX-4 melting-point apparatus without correction. Optical rotations were recorded on a Jasco P-2000 digital polarimeter. The ultra violet (UV) spectra were obtained by a Hitachi U-2001 UV/V is spectrometer. The infrared (IR) spectra were examined with a Jasco FT/IR-4100 spectrophotometer.  $^1\text{H}$ -,  $^{13}\text{C}$ -, and 2D nuclear magnetic resonance (NMR) spectra were recorded on a Bruker AV-400 NMR spectrometer. Chemical shifts are shown in  $\delta$  values (ppm) with tetramethylsilane as an internal standard. The  $\delta_{\text{H}}$  and  $\delta_{\text{C}}$  values were for the chemical shifts of the signals, respectively. High resolution electrospray ionization mass spectrometry (HR-ESI-MS) was conducted with a JEOL JMS-700 spectrometer (operated in the negative-ion mode).

### 2.2. Plant Material

The needles of *P. taiwanensis* were collected in Puli, Nantou, Taiwan and identified by Prof. Sheng-Yang Wang (Department of Forestry, National Chung-Hsing University, Taichung, Taiwan). The voucher specimen (PCKuo\_2016003) was deposited in the herbarium of School of Pharmacy, National Cheng Kung University, Tainan, Taiwan.

### 2.3. Extraction and Isolation

The pine needles of *P. taiwanensis* (dried weight 2.5 kg) were powdered and extracted with methanol under reflux, the combined extracts were then concentrated in vacuo to obtain a brownish syrup (431 g). The methanol extract was partitioned between hexanes and water to remove the essential oil and produce the hexane layer (97 g) and water soluble. The water soluble part was further partitioned between ethyl acetate and water to yield the ethyl acetate layer (130 g) and water layer (204 g), respectively. The methanol extract, hexanes, ethyl acetate, and water layers were examined for their anti-inflammatory potential and only the ethyl acetate layer displayed a significant inhibition of superoxide anion generation and elastase release (see Supplementary Materials, Table S1). Therefore, the further isolation experiments were focused on this layer and the completed procedures are provided in the Supplementary Materials (Appendix A).

### 2.4. Spectral and Physical Data of 1–5

#### 2.4.1. 1-[(7'R,8'S)-7',9'-Dihydroxy-7'-(4-hydroxyphenyl)propan-8'-yloxy]benzoic Acid (1)

Colorless syrup;  $[\alpha]_{\text{D}}^{25} + 5.1$  (c 0.1, MeOH); UV (MeOH)  $\lambda_{\text{max}}$  (log  $\epsilon$ ) 248 (3.73), 228 (3.69) nm; ECD (c  $3.65 \times 10^{-4}$  M, MeOH)  $\lambda_{\text{max}}$  ( $\Delta\epsilon$ ) 301 (+0.14), 230 (+0.17), 224 (+0.15) nm; IR (neat)  $\nu_{\text{max}}$  3412, 2925, 1598, 1550, 1390, 1242  $\text{cm}^{-1}$ ;  $^1\text{H}$  and  $^{13}\text{C}$  NMR; HRESIMS  $m/z$  303.0855 ( $[\text{M} - \text{H}]^-$  calcd for  $\text{C}_{16}\text{H}_{15}\text{O}_6$ , 303.0869).

#### 2.4.2. 1-[(7'R,8'S)-7',9'-Dihydroxy-7'-(4-hydroxy-3-methoxyphenyl)propan-8'-yloxy]-2-hydroxybenzoic Acid (2)

Colorless syrup;  $[\alpha]_{\text{D}}^{25} + 5.3$  (c 0.1, MeOH); UV (MeOH)  $\lambda_{\text{max}}$  (log  $\epsilon$ ) 284 (3.59), 253 (3.80) nm; ECD (c  $3.51 \times 10^{-4}$  M, MeOH)  $\lambda_{\text{max}}$  ( $\Delta\epsilon$ ) 248 (+1.33), 224 (+1.03), 214 (+1.10) nm; IR (neat)  $\nu_{\text{max}}$  3425, 2927, 1541, 1384, 1271  $\text{cm}^{-1}$ ;  $^1\text{H}$  and  $^{13}\text{C}$  NMR; HRESIMS  $m/z$  349.0936 ( $[\text{M} - \text{H}]^-$  calcd for  $\text{C}_{17}\text{H}_{17}\text{O}_8$ , 349.0923).

#### 2.4.3. (13E,12R)-12-Hydroxyagathic Acid (3)

Colorless powder; mp: 263 °C (dec.);  $[\alpha]_{\text{D}}^{25} + 30.8$  (c 0.1, MeOH); UV (MeOH)  $\lambda_{\text{max}}$  (log  $\epsilon$ ) 225 (sh) (3.83) nm; IR (neat)  $\nu_{\text{max}}$  3450, 2937, 1648, 1252  $\text{cm}^{-1}$ ;  $^1\text{H}$ -NMR ( $\text{CD}_3\text{OD}$ , 400 MHz)  $\delta$  0.63 (3H, s,  $\text{CH}_3$ -20), 1.09 (1H, ddd,  $J = 13.6, 13.6, 3.6$  Hz, H-3a), 1.21 (3H, s,  $\text{CH}_3$ -18), 1.21 (1H, m, H-1a), 1.42 (1H, m, H-5), 1.51 (1H, m, H-2a), 1.59 (2H, m, H-11),

1.79 (1H, m, H-1b), 1.91 (1H, m, H-2b), 1.91 (1H, m, H-6a), 1.98 (1H, m, H-7a), 2.01 (1H, m, H-6b), 2.08 (3H, s, CH<sub>3</sub>-16), 2.12 (1H, m, H-9), 2.14 (1H, m, H-3b), 2.43 (1H, m, H-7b), 4.03 (1H, dd,  $J = 9.2, 2.8$  Hz, H-12), 4.53 (1H, s, H-17a), 4.91 (1H, s, H-17b), 5.88 (1H, br s, H-14); <sup>13</sup>C-NMR (CD<sub>3</sub>OD, 100 MHz)  $\delta$  13.5 (CH<sub>3</sub>-20), 14.9 (CH<sub>3</sub>-16), 21.2 (C-2), 27.6 (C-6), 29.6 (CH<sub>3</sub>-18), 31.5 (C-11), 39.4 (C-3), 40.0 (C-7), 40.3 (C-1), 41.2 (C-10), 45.3 (C-4), 53.1 (C-9), 57.6 (C-5), 75.5 (C-12), 106.9 (C-17), 117.8 (C-14), 150.2 (C-8), 159.5 (C-13), 167.2 (C-15), 181.5 (C-19); HRESIMS  $m/z$  349.2024 ([M – H]<sup>–</sup> calcd for C<sub>20</sub>H<sub>29</sub>O<sub>5</sub>, 349.2015).

#### 2.4.4. 5-Isopropyl-3-oxocyclohex-1-ene-1-carboxylic Acid (4)

Colorless tabular crystal; mp: 235 °C (dec.); [ $\alpha$ ]<sub>D</sub><sup>25</sup> + 28.6 (c 0.3, MeOH); UV (MeOH)  $\lambda_{\max}$  (log  $\epsilon$ ) 237 (sh) (3.40) nm; IR (neat)  $\nu_{\max}$  3456, 2925, 1635, 1395 cm<sup>–1</sup>; <sup>1</sup>H-NMR (CD<sub>3</sub>OD, 400 MHz) 0.88 (3H, d,  $J = 6.8$  Hz, CH<sub>3</sub>-9), 0.98 (3H, d,  $J = 6.8$  Hz, CH<sub>3</sub>-10), 1.84 (1H, m, H-4a), 2.02 (1H, m, H-4b), 2.09 (1H, m, H-5), 2.31 (1H, hept,  $J = 6.8$  Hz, H-8), 2.50 (1H, dddd,  $J = 19.2, 9.2, 4.8, 2.4$  Hz, H-6a), 2.70 (1H, dddd,  $J = 19.2, 5.2, 5.2, 1.2$  Hz, H-6b), 6.32 (1H, dd,  $J = 2.4, 1.2$  Hz, H-2); <sup>13</sup>C-NMR (CD<sub>3</sub>OD, 100 MHz)  $\delta$  19.0 (C-9), 20.9 (C-10), 24.3 (C-4), 27.0 (C-6), 27.1 (C-8), 53.7 (C-5), 128.7 (C-2), 160.6 (C-1), 174.8 (C-7), 205.7 (C-3); HRESIMS  $m/z$  181.0855 ([M – H]<sup>–</sup> calcd for C<sub>10</sub>H<sub>13</sub>O<sub>3</sub>, 181.0865).

#### 2.4.5. Styraxinolic Acid (5)

Colorless syrup; UV (MeOH)  $\lambda_{\max}$  (log  $\epsilon$ ) 308 (2.89), 237 (sh) (3.37), 222 (sh) (3.70) nm; IR (neat)  $\nu_{\max}$  3421, 2926, 1572, 1395, 1268 cm<sup>–1</sup>; <sup>1</sup>H-NMR (CD<sub>3</sub>OD, 400 MHz) 1.82 (2H, tt,  $J = 8.0, 6.8$  Hz, H-8), 2.61 (2H, t,  $J = 8.0$  Hz, H-7), 3.56 (2H, t,  $J = 6.8$  Hz, H-9), 3.83 (3H, s, OCH<sub>3</sub>-3), 6.86 (1H, d,  $J = 2.4$  Hz, H-4), 7.31 (1H, d,  $J = 2.4$  Hz, H-6); <sup>13</sup>C-NMR (CD<sub>3</sub>OD, 100 MHz)  $\delta$  32.7 (C-7), 35.6 (C-8), 56.6 (OCH<sub>3</sub>-3), 62.3 (C-9), 116.3 (C-4), 120.1 (C-1), 122.8 (C-6), 131.9 (C-5), 149.2 (C-3), 150.7 (C-2), 176.2 (C-10); HRESIMS  $m/z$  225.0767 ([M – H]<sup>–</sup> calcd for C<sub>11</sub>H<sub>13</sub>O<sub>5</sub>, 225.0763).

### 2.5. Anti-Inflammatory Bioactivity Examination

#### 2.5.1. Human Neutrophil Preparation

The study was conducted with the approval of the Institutional Review Board of Chang Gung Memorial Hospital (IRB No. 201800369A3). Blood samples were drawn from healthy human donors (20 to 30 years old), and neutrophils were isolated and purified according to the protocols described previously [40].

#### 2.5.2. Superoxide Anion Generation Measurement

The assay for measuring superoxide anion generation was based on the SOD-inhibitable reduction of ferricytochrome *c* as described previously [40].

#### 2.5.3. Elastase Release Assay

Degranulation of azurophilic granules was determined by measuring the release of elastase as previously described [40].

#### 2.5.4. Statistical Analysis

The results are expressed as mean  $\pm$  standard error of the mean (SEM). Computation of 50% inhibitory concentrations (IC<sub>50</sub>) was performed using PHARM/PCS v.4.2 software. Statistical comparisons were made between groups using the Student's *t*-test. Values of  $p < 0.05$  were considered to be statistically significant.

### 2.6. Molecular Docking Study

The *in silico* evaluation was conducted on AutoDock Vina software [41]. The crystal structure of the ghrelin receptor has been characterized [42], and a .PDB file was downloaded from the Protein Databank (PDB ID: 6KO5). The 3D structures of ligands were constructed in the Chem3D program. The hydrogen supplement, Gasteiger charge measurement for protein atoms, and selection of flexible torsions for ligands were conducted

by AutodockTools (ADT ver. 1.5.6). The size of the grid was designed at  $18.5 \text{ \AA} \times 18.5 \text{ \AA} \times 18.5 \text{ \AA}$  and a grid center at dimensions (x, y, and z, respectively): 9.7, −19.2, 14.6 was determined. The binding affinity energy was provided as docking scores and shown in kcal/mol. The best interaction was considered only the top-scoring pose. The visualization of the best docking interactions was analyzed in Biovia Discovery Studio client 2020 [43].

### 3. Results and Discussion

The pine needles were extracted with methanol and partitioned with hexanes, ethyl acetate, and water to obtain three soluble layers, respectively. The anti-inflammatory fraction, the ethyl acetate layer, was subjected to continuous conventional chromatographic technique combination, and five undescribed compounds were characterized including two new lignans, 1-[(7'R,8'S)-7',9'-dihydroxy-7'-(4-hydroxyphenyl)propan-8'-yloxy]benzoic acid (1), 1-[(7'R,8'S)-7',9'-dihydroxy-7'-(4-hydroxy-3-methoxyphenyl)-propan-8'-yloxy]-2-hydroxybenzoic acid (2), one new diterpenoid, (13E,12R)-12-hydroxyagathic acid (3), one monoterpene, 5-isopropyl-3-oxocyclohex-1-ene-1-carboxylic acid (4), and one phenylpropane, styraxinolic acid (5). The chemical structures of these new compounds were constructed with the assistance of the NMR spectral elucidation and MS spectrometric analysis. Moreover, seventy-two known compounds, comprising one steroid,  $\beta$ -sitosterol (6); one sesquiterpenoid, (-)-oplopan-4-one-10- $\alpha$ -O- $\beta$ -D-glucoside (7); one coumarin, umbelliferone (8); one alkaloid, indole-3-aldehyde (9); four diterpenoids, acrostalic acid (10), 15-hydroxy-7-oxo-8,11,13-abietatrien-18-oic acid (11), 3 $\beta$ ,13-dihydroxy- $\lambda$ -8(20),14-dien-19-oic acid (12), 12,15-dihydroxy- $\lambda$ -8(17),13-dien-19-oic acid (13); twenty-six lignans, (2S,3R)-2,3-dihydro-3-hydroxymethyl-7-methoxy-2-(4'-hydroxy-3'-methoxyphenyl)-5-benzofuranpropanol 3 $\alpha$ -O- $\alpha$ -L-rhamnopyranoside (14), (7S,8R)-dihydrodehydrodiconiferyl alcohol-9-O- $\alpha$ -L-rhamnopyranoside (15), icaraside E<sub>4</sub> (16), massonianoside B (17), (7S,8R)-dihydro-3'-hydroxy-8-hydroxymethyl-7-(4-hydroxy-3-methoxyphenyl)-1'-benzofuranpropanol (18), ( $\pm$ )-rel-(2 $\alpha$ ,3 $\beta$ )-7-O-methylcedrusin (19), cedrusinin (20), (7S,8R)-idaeusin D (21), (7S,8R)-4,9-dihydroxy-4',7'-epoxy-8',9'-dinor-8,5'-neolignan-7'-oic acid (22), 2-[4-(3-hydroxypropyl)-2-methoxyphenoxy]propane-1,3-diol (23), evofolin-B (24), (S)-3-hydroxy-1,2-bis(4-hydroxy-3-methoxyphenyl)-1-propanone (25), cupressoside A (26), 1-(4'-hydroxy-3'-methoxyphenyl)-2-[2''-hydroxy-4''-(3-O- $\alpha$ -L-rhamnopyranosyloxypropyl)phenoxy]-1,3-propanediol (27), (7R,8S)-3-methoxy-8,4'-oxyneoligna-3',4,7,9,9'-pentol (28), erythro-3-methoxy-8,4'-oxyneolignan-3',4,7,9,9'-pentol (29), pinoresinol (30), (+)-salicifoliol (31), (+)-idaeusinol A (32), schizandriside (33), (+)-isolariciresinol 2 $\alpha$ -O- $\alpha$ -L-arabinoside (34), (+)-isolariciresinol (35), secoisolariciresinol (36), secoisolariciresinol-9,9'-acetone (37), (-)-nortrachelogenin (38), (2S,3S)-2 $\alpha$ -(4''-hydroxy-3''-methoxybenzyl)-3 $\beta$ -(4'-hydroxy-3'-methoxybenzyl)- $\gamma$ -butyrolactone (39); twelve flavonoids, astragalin (40), kaempferol-3-O- $\beta$ -D-galactopyranoside (41), kaempferol-3-O- $\alpha$ -L-furanoarabinoside (42), rhamnetin 3-O- $\beta$ -D-glucopyranoside (43), apigenin (44), kaempferol-3,6-dimethyl ether (45), 5,7,8,4'-tetrahydroxy-3-methoxy-6-methylflavonol-8-O- $\beta$ -D-glucopyranoside (46), 6-methylaromadendrin (47), naringenin (48), tiliroside (49), kaempferol 3-O-(3'',6''-di-O-E-p-coumaroyl)- $\beta$ -D-glucopyranoside (50), kaempferol-3-O-(5''-O-E-p-coumaroyl)- $\alpha$ -L-arabinofuranoside (51); seven ionones, machilusoxide A (52), (+)-(S)-dehydrovomifoliol (53), isololiolide (54), (S)-(+)-abscisic acid sodium salt (55), (3S,5R,6R,7E)-3,5,6-trihydroxy-7-megastigmen-9-one (56), blumenol A (57), peltopterin B (58); nineteen benzenoids, 3,4-dihydroxybenzoic acid methyl ester (59), *p*-hydroxybenzoic acid (60), vanillic acid (61), 4-hydroxybenzaldehyde (62), methylparaben (63), 3-hydroxy-1-(4-hydroxy-3-methoxyphenyl)-1-propanone (64), 3-hydroxy-1-(4-hydroxyphenyl)-1-propanone (65), 2-(4-hydroxyphenyl)acetic acid (66), phenylacetic acid (67), isovanillic acid (68), benzoic acid (69), vanillin (70), *p*-hydroxyacetophenone (71), sodium salicylate (72), vanillic acid 4-O- $\alpha$ -L-rhamnoside (73), *trans*-ferulic acid (74), sodium *p*-coumarate (75), *p*-coumaric acid (76), *trans*-methyl *p*-coumarate (77), respectively, were identified by the examination of their physical and spectroscopic data with those previously published (references of known compounds were provided in Supplementary Materials Appendix B).



### 3.1. Structural Elucidation of Compounds 1–5

Compound **1** was isolated as an optically active colorless syrup, and the molecular formula was assigned as  $C_{16}H_{16}O_6$  by HR-ESI-MS analysis ( $[M - H]^-$ ,  $m/z$  303.0855, calcd. for  $C_{16}H_{15}O_6$ , 303.0869, Figure S1). The IR spectrum indicates the presences of a hydroxyl ( $3412\text{ cm}^{-1}$ ) and a conjugated carbonyl group ( $1598\text{ cm}^{-1}$ ). The  $^1\text{H}$ -NMR data (Figure S2) showed the signals for two *para*-substituted aromatic moieties [ $\delta_{\text{H}}$  6.72 (2H, d,  $J = 8.4\text{ Hz}$ , H-3', -5'), 6.86 (2H, d,  $J = 8.8\text{ Hz}$ , H-2, -6), 7.24 (2H, d,  $J = 8.4\text{ Hz}$ , H-2', -6'), and 7.83 (2H, d,  $J = 8.8\text{ Hz}$ , H-3, -5)], two oxygenated methines [ $\delta_{\text{H}}$  4.48 (1H, m, H-8'), and 4.85 (1H, d,  $J = 5.6\text{ Hz}$ , H-7')], and two methines [ $\delta_{\text{H}}$  3.81 (1H, dd,  $J = 12.0, 4.0\text{ Hz}$ , H-9'a), and 3.86 (1H, dd,  $J = 12.0, 5.6\text{ Hz}$ , H-9'b)]. The  $^{13}\text{C}$  and DEPT NMR spectra (Figure S3) of **1** displayed sixteen carbons, corresponding to one methylene group, two oxygenated carbons, twelve aromatic carbons, and one conjugated carbonyl (Table 1). The  $^2\text{J}$ - and  $^3\text{J}$ -HMBC correlations from H-2, -6 to C-1 and 4; from H-3, 5 to C-1 and 7; from H-2', 6' to C-4' and 7'; from H-7' to C-8' and 9'; and from H-8' to C-1, respectively, were observed in the HMBC spectrum of **1** (Figure S4). Moreover, a large coupling constant between H-7' and H-8' ( $J = 5.6\text{ Hz}$ ) supported the relative configuration of **1** at C-7'/C-8' as *threo* [44]. The absolute configurations at C-7' and C-8' of **1** were determined by electronic circular dichroism (ECD) analysis. The positive Cotton effect at 230 nm ( $\Delta\epsilon + 0.17$ ) revealed an 8S configuration for **1**, according to the published literature [37,38] and therefore 7'*R* was also determined. Other 2D spectra (Figure S5–S7) furnished the full assignment of proton and carbon signals. Accordingly, the structure of **1** was assigned as 1-[(7'*R*,8'*S*)-7',9'-dihydroxy-7'-(4-hydroxyphenyl)propan-8'-yloxy]benzoic acid as shown in Figure 1.

**Table 1.**  $^1\text{H}$  and  $^{13}\text{C}$  NMR spectroscopic data of compounds **1** and **2**.

| Position             | <b>1</b>                                  |                     | <b>2</b>                                  |                     |
|----------------------|---|---------------------|---|---------------------|
|                      | $\delta_{\text{H}}$                       | $\delta_{\text{C}}$ | $\delta_{\text{H}}$                       | $\delta_{\text{C}}$ |
| 1                    | —   | 162.1               | —   | 150.2               |
| 2                    | 6.86 (2H, d, $J = 8.8\text{ Hz}$ )        | 116.3               | —   | 148.1               |
| 3                    | 7.83 (2H, d, $J = 8.8\text{ Hz}$ )        | 132.0               | 7.45 (1H, d, $J = 2.0\text{ Hz}$ )        | 118.3               |
| 4                    | —   | 116.1               | —   | 132.4               |
| 5                    | 7.83 (2H, d, $J = 8.8\text{ Hz}$ )        | 132.0               | 7.38 (1H, dd, $J = 8.4, 2.0\text{ Hz}$ )  | 122.5               |
| 6                    | 6.86 (2H, d, $J = 8.8\text{ Hz}$ )        | 116.3               | 6.96 (1H, d, $J = 8.4\text{ Hz}$ )        | 116.5               |
| 7                    | —   | 175.4               | —   | 174.4               |
| 1'                   | —   | 133.5               | —   | 134.0               |
| 2'                   | 7.24 (2H, d, $J = 8.4\text{ Hz}$ )        | 129.2               | 7.02 (1H, d, $J = 2.0\text{ Hz}$ )        | 111.4               |
| 3'                   | 6.72 (2H, d, $J = 8.4\text{ Hz}$ )        | 115.9               | —   | 148.9               |
| 4'                   | —   | 157.9               | —   | 147.2               |
| 5'                   | 6.72 (2H, d, $J = 8.4\text{ Hz}$ )        | 115.9               | 6.74 (1H, d, $J = 8.4\text{ Hz}$ )        | 115.9               |
| 6'                   | 7.24 (2H, d, $J = 8.4\text{ Hz}$ )        | 129.2               | 6.84 (1H, dd, $J = 8.4, 2.0\text{ Hz}$ )  | 120.6               |
| 7'                   | 4.85 (1H, d, $J = 5.6\text{ Hz}$ )        | 73.8                | 4.93 (1H, d, $J = 5.2\text{ Hz}$ )        | 73.8                |
| 8'                   | 4.48 (1H, m)                              | 84.1                | 4.33 (1H, m)                              | 86.3                |
| 9'                   | 3.81 (1H, dd, $J = 12.0, 4.0\text{ Hz}$ ) | 62.0                | 3.55 (1H, dd, $J = 12.0, 5.2\text{ Hz}$ ) | 61.7                |
|                      | 3.86 (1H, dd, $J = 12.0, 5.6\text{ Hz}$ ) |                     | 3.78 (1H, dd, $J = 12.0, 4.4\text{ Hz}$ ) |                     |
| OCH <sub>3</sub> -3' | —   | —                   | 3.81 (3H, s)                              | 56.3                |

$^1\text{H}$ - and  $^{13}\text{C}$ -NMR data ( $\delta$  in ppm) were measured in  $\text{CD}_3\text{OD}$  at 400 and 100 MHz. “s”, “d”, “m”, and “dd” were for the singlet, doublet, multiplet, and doublet of doublet signals, respectively.

The molecular formula of **2** was assigned as  $C_{17}H_{18}O_8$  on the basis of HR-ESI-MS analytical data ( $m/z$  349.0936  $[M - H]^-$ , Figure S8). The absorption in the IR spectrum ( $3425$  and  $1541\text{ cm}^{-1}$ ) indicated the hydroxyl and conjugated carbonyl functionalities, respectively. Comparison of the NMR spectra of **1** and **2**, it could observe that they possessed different aromatic moieties. Two sets of ABX-coupled aromatic ring and one methoxy group could be detected in the  $^1\text{H}$ - (Figure S9) and  $^{13}\text{C}$ -NMR (Figure S10) data of **2** (Table 1), and it suggested that compound **2** possessed two trisubstituted rather than *para*-disubstituted aromatic moieties. The significant HMBC correlations (Figure S11) from

H-3 to C-1, C-5 and C-7; from H-6 to C-4; from OCH<sub>3</sub>-3' to C-3'; from H-6' to C-4' and C-7'; from H-7' to C-1', C-2', C-8' and 9'; from H-8' to C-1, respectively, established that the structure of **2** was also a neolignan skeleton. Through combination of a large coupling constant ( $J_{7,8} = 5.2$  Hz) and positive Cotton effect at 230 nm ( $\Delta\epsilon + 1.14$ ), the absolute configuration of **2** was assigned as the *threo*- and (7'*R*,8'*S*)-form, the same as **1** [44,45]. Other 2D spectra (Figure S12–S14) furnished the full assignment of proton and carbon signals. These findings concluded the structure of **2** as 1-[(7'*R*,8'*S*)-7',9'-dihydroxy-7'-(4-hydroxy-3-methoxyphenyl)propan-8'-yloxy]-2-hydroxybenzoic acid (Figure 1).

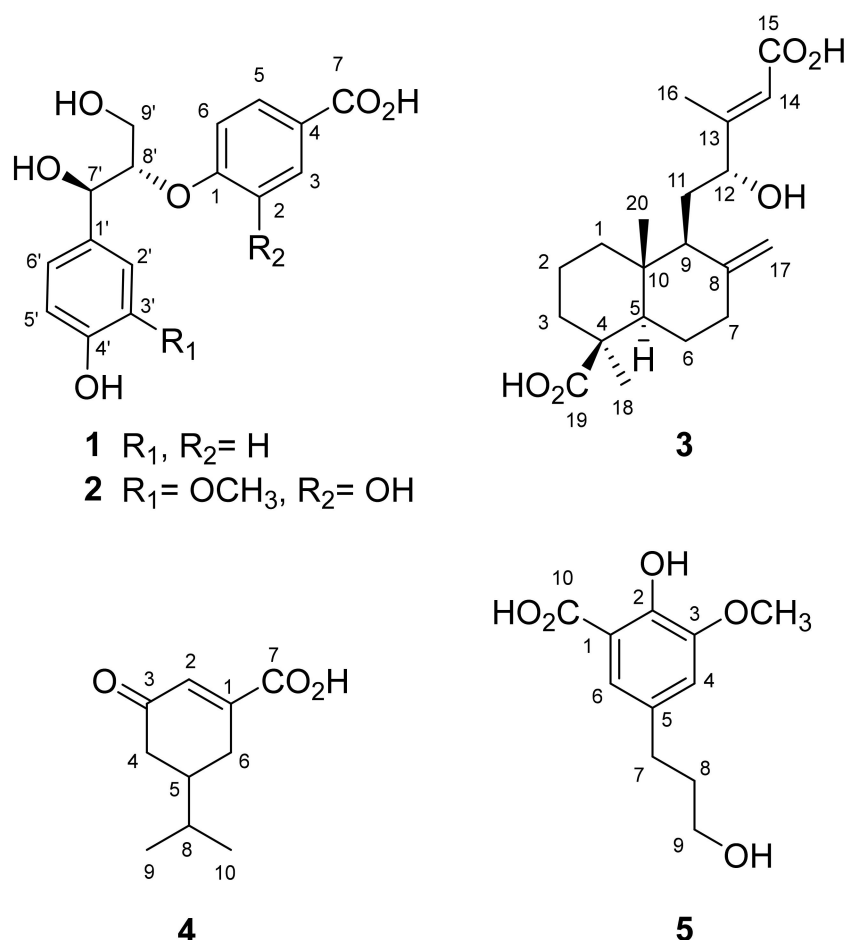


**Figure 1.** Structures of compounds **1**–**5** isolated from *P. taiwanensis*.

Compound **3** was obtained as a colorless powder and its molecular formula was assigned as C<sub>20</sub>H<sub>30</sub>O<sub>5</sub> on the basis of HR-ESI-MS analytical data ( $m/z$  349.2024 [M – H]<sup>−</sup>, Figure S15). Compound **3** showed absorption peaks at 3450 (OH), and 1648 (carboxylic acid) cm<sup>−1</sup> in its IR spectrum. It was evidenced by the <sup>13</sup>C-NMR spectrum (Figure S16) in which two carboxylic functionalities were observed at  $\delta_C$  167.2 (C-15) and 181.5 (C-19). In its <sup>1</sup>H-NMR (Figure S17), the resonances at  $\delta_H$  4.03 (1H, dd,  $J = 9.2, 2.8$  Hz, H-12) and  $\delta_C$  75.5 (C-12) indicated the presence of a secondary alcohol group. The terminal methylene group could be established due to the proton resonances at  $\delta_H$  4.53 (1H, s, H-17a) and 4.91 (1H, s, H-17b), and the carbon signals at  $\delta_C$  106.9 (C-17) and 150.2 (C-8), respectively. Two methyl groups at  $\delta_H$  0.63 (3H, s, CH<sub>3</sub>-20) and 1.21 (3H, s, CH<sub>3</sub>-18) were connected to the quarternary carbons (C-10 and C-4) evidenced by the HMBC correlations (Figure S18). The shielding effect of the carboxylic group at C-4 resulted in the upfield shift of CH<sub>3</sub>-20 ( $\delta_H$  0.63), suggesting its  $\beta$ -configuration [46]. In addition, the chemical shift of H-17a ( $\delta_H$  4.53) appeared in the upfield region, suggesting the 12*R* configuration [47]. In its HMBC spectrum, the correlations from H-12 to C-9, C-14 and C-16; from H-17 to C-7 and C-9; from CH<sub>3</sub>-16 to C-12 and C-14; from CH<sub>3</sub>-18 to C-3, C-4 and C-19; from CH<sub>3</sub>-20 to C-1, C-5,

C-9 and C-10, respectively, constructed the planar structure of **3** as previously reported for 12-hydroxyagathic acid [46]. However, the C-13 configuration of **3** was determined as *E* by the NOESY analytical data (Figure S19), which displayed the NOE effects among H-5/H-9, H-5/H-18, and H-12/H-14. Moreover, the NOE between H-14 and CH<sub>3</sub>-16, which should be recorded in 12-hydroxyagathic acid [46], was not detected in **3**. Other 2D spectra (Figure S20–S21) furnished the full assignment of proton and carbon signals. Conclusively, the structure of **3** was established as (13*E*,12*R*)-12-hydroxyagathic acid as shown (Figure 1).

The HR-ESI-MS spectrum of **4** exhibited an  $[M - H]^-$  ion peak at  $m/z$  181.0855 (Figure S22), consistent with the pseudomolecular formula of C<sub>10</sub>H<sub>13</sub>O<sub>3</sub>. The absorption peaks at 3456 and 1635 cm<sup>−1</sup> in its IR spectrum displayed hydroxyl and conjugated carbonyl groups, respectively. Two methine protons at  $\delta_H$  2.09 (1H, m, H-5) and 6.32 (1H, dd,  $J$  = 2.4, 1.2 Hz, H-2), two methylene groups at  $\delta_H$  1.84 (1H, m, H-4a), 2.02 (1H, m, H-4b), 2.50 (1H, dddd,  $J$  = 19.2, 9.2, 4.8, 2.4 Hz, H-6a) and 2.70 (1H, dddd,  $J$  = 19.2, 5.2, 5.2, 1.2 Hz, H-6b), and one set of isopropyl protons at  $\delta_H$  0.88 (3H, d,  $J$  = 6.8 Hz, CH<sub>3</sub>-9), 0.98 (3H, d,  $J$  = 6.8 Hz, CH<sub>3</sub>-10) and 2.31 (1H, hept,  $J$  = 6.8 Hz, H-8) appeared in the <sup>1</sup>H-NMR spectrum of **4** (Figure S23). In addition, one conjugated carbonyl carbon at  $\delta_C$  174.8 (C-7), and one carboxyl carbon at  $\delta_C$  205.7 (C-3) could be observed in its <sup>13</sup>C- and DEPT NMR spectra (Figure S24). The observed HMBC correlations (Figure S25) from H-2 to C-7; from H-4 to C-3; from H-6 to C-1, C-2, and C-5; from CH<sub>3</sub>-9 to C-5, and CH<sub>3</sub>-10; from CH<sub>3</sub>-10 to C-8, respectively, constructed the structure of **4** as 5-isopropyl-3-oxocyclohex-1-ene-1-carboxylic acid (Figure 1). Other 2D spectra (Figure S26–S28) furnished the full assignment of proton and carbon signals. However, the stereochemistry at C-5 remained undetermined.

Compound **5** possessed the molecular formula C<sub>11</sub>H<sub>14</sub>O<sub>5</sub> determined from a deprotonated molecular ion peak in the negative mode HR-ESI-MS analysis ( $m/z$  225.0767  $[M - H]^-$ , Figure S29). In its IR spectrum, hydroxyl (3421 cm<sup>−1</sup>) and carboxyl (1572 cm<sup>−1</sup>) functionalities could be detected. The <sup>1</sup>H-NMR spectrum (Figure S30) revealed two long-range coupling aromatic protons at  $\delta_H$  6.86 (1H, d,  $J$  = 2.4 Hz, H-4) and 7.31 (1H, d,  $J$  = 2.4 Hz, H-6), one methoxy group at  $\delta_H$  3.56 (2H, t,  $J$  = 6.8 Hz, H-9), and one set of propanol protons at  $\delta_H$  1.82 (2H, tt,  $J$  = 8.0, 6.8 Hz, H-8), 2.61 (2H, t,  $J$  = 8.0 Hz, H-7) and 3.56 (2H, t,  $J$  = 6.8 Hz, H-9). Moreover, one carboxylic group was located at  $\delta_C$  176.2 (C-10) in its <sup>13</sup>C-NMR spectrum (Figure S31). The planar structure of **5** was established by the significant HMBC correlations (Figure S32) of OCH<sub>3</sub>-3 to C-3; H-6 to C-2, C-4, C-7, and C-10; H-7 to C-4, C-5, and C-8; H-9 to C-7, and C-8, respectively. Other 2D spectra (Figure S33–S35) furnished the full assignment of proton and carbon signals. The above evidence suggests the structure of **5** as 2-hydroxy-5-(3-hydroxypropyl)-3-methoxybenzoic acid (Figure 1), which was already reported as styraxinolic acid in the previous synthetic literature [48]. Nevertheless, the present research is the first report of **5** from natural sources.

### 3.2. Anti-Inflammatory Activity

Inflammation is one of the major self-defense mechanisms stimulated by bacteria, virus, wound, or various other environmental factors. It is a first response of the immune system against infection and irritation. Neutrophils belong to an abundant kind of macrophage and play a major role in inflammation, and are usually the first lymphocytes to reach the infected region [49]. Neutrophils secrete a series of cytotoxins such as superoxide anion and elastase in response to the activation of the immune system [50]. In recent years, various human diseases have been demonstrated to be related to neutrophil overexpression [51–55]. The relationship between inflammation and cancer has been established, and the authors pointed out that the formation of cancer cells was directly related to inflammation [49]. Therefore, new anti-inflammatory compounds are worthwhile for further study on cancer treatment. Forty-three isolated compounds were evaluated for the inhibition of superoxide anion generation and elastase release by human neutrophils in response to fMLF/CB [56] (see Supplementary Materials, Table S2). The significant inhibitory results (Table 2) demonstrated that only **45**, **47**, **48**, **49**, and **50** (Figure 2) displayed

a significant inhibition of superoxide anion generation, with  $IC_{50}$  values ranging from  $3.3 \pm 0.9$  to  $7.7 \pm 0.9 \mu M$  compared with the positive control LY294002 ( $IC_{50}$   $1.1 \pm 0.3 \mu M$ ). Moreover, **48**, **50**, and **51** (Figure 2) revealed the significant inhibition of elastase release with  $IC_{50}$  values ranging from  $5.3 \pm 0.2$  to  $8.3 \pm 0.8 \mu M$  compared with the positive control LY294002 ( $IC_{50}$   $3.2 \pm 1.0 \mu M$ ) (Table 2). Compounds **48** and **50** displayed both inhibition of superoxide anion generation and elastase release, indicating their multiple anti-inflammatory bioactivities. The needles of *P. morrisonicola* have been reported to have an anti-inflammatory effect in RAW 264.7 macrophages [13]. The authors proposed that epicatechin and *p*-coumaric acid identified in *P. morrisonicola* may be the active ingredients. In the present research, all the active compounds contained the flavone backbone similar to that of epicatechin and the *p*-coumaroyl moiety could also be observed in **49**, **50**, and **51**. This indicates that the flavonoid and *p*-coumaroyl functional groups may contribute the anti-inflammatory bioactivity in the present study. These bioassay results suggest that flavonoids play key roles in *Pinus* species for anti-inflammation bioactivity.

**Table 2.** Inhibitory effects of purified compounds on superoxide anion generation and elastase release by human neutrophils in response to fMLF/CB.

| Compound              | Superoxide Anion Generation        |                     | Elastase Release      |                     |
|-----------------------|------------------------------------|---------------------|-----------------------|---------------------|
|                       | $IC_{50}$ ( $\mu M$ ) <sup>a</sup> | Inh % <sup>b</sup>  | $IC_{50}$ ( $\mu M$ ) | Inh %               |
| <b>45</b>             | $6.4 \pm 0.7$                      | $70.5 \pm 6.8$ ***  | — <sup>c</sup>        | $34.2 \pm 6.9$ **   |
| <b>47</b>             | $6.0 \pm 1.1$                      | $71.8 \pm 8.1$ ***  | —                     | $43.5 \pm 6.9$ ***  |
| <b>48</b>             | $3.3 \pm 0.9$                      | $87.5 \pm 5.4$ ***  | $5.3 \pm 0.2$         | $93.9 \pm 5.2$ ***  |
| <b>49</b>             | $7.7 \pm 0.9$                      | $60.6 \pm 3.9$ ***  | —                     | $40.3 \pm 6.0$ **   |
| <b>50</b>             | $5.3 \pm 1.1$                      | $72.9 \pm 6.3$ ***  | $5.8 \pm 0.9$         | $81.4 \pm 12.0$ *** |
| <b>51</b>             | —                                  | $45.2 \pm 5.6$ ***  | $8.3 \pm 0.8$         | $57.0 \pm 4.6$ ***  |
| LY294002 <sup>d</sup> | $1.1 \pm 0.3$                      | $100.6 \pm 1.0$ *** | $3.2 \pm 1.0$         | $76.7 \pm 6.8$ ***  |

Results are presented as mean  $\pm$  SEM ( $n = 3-5$ ). \*\*  $p < 0.01$ , \*\*\*  $p < 0.001$  compared with the control (DMSO).

<sup>a</sup> Concentration necessary for 50% inhibition ( $IC_{50}$ ). <sup>b</sup> Percentage of inhibition (Inh %) at  $10 \mu M$  concentration.

<sup>c</sup> Not determined. <sup>d</sup> A phosphatidylinositol-3-kinase inhibitor was used as a positive control.

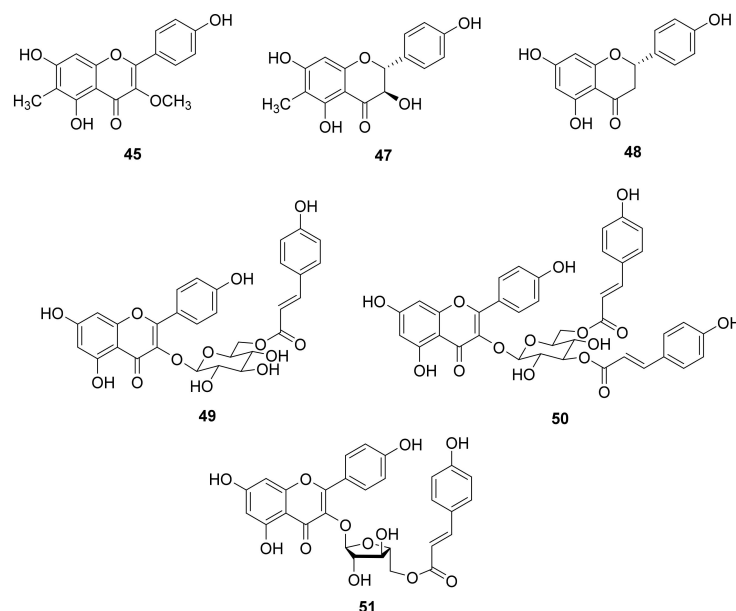


**Figure 2.** Structures of anti-inflammatory principles **45**, **47**, **48**, **49**, **50**, and **51**.

### 3.3. Molecular Docking Study

The age-related decline in GH levels is considered to be a symptom of neuroendocrine aging [57]. This phenomenon exists in several mammalian species such as humans, domestic dogs, and laboratory rodents [57]. In human, the GH levels in plasma begins to decrease

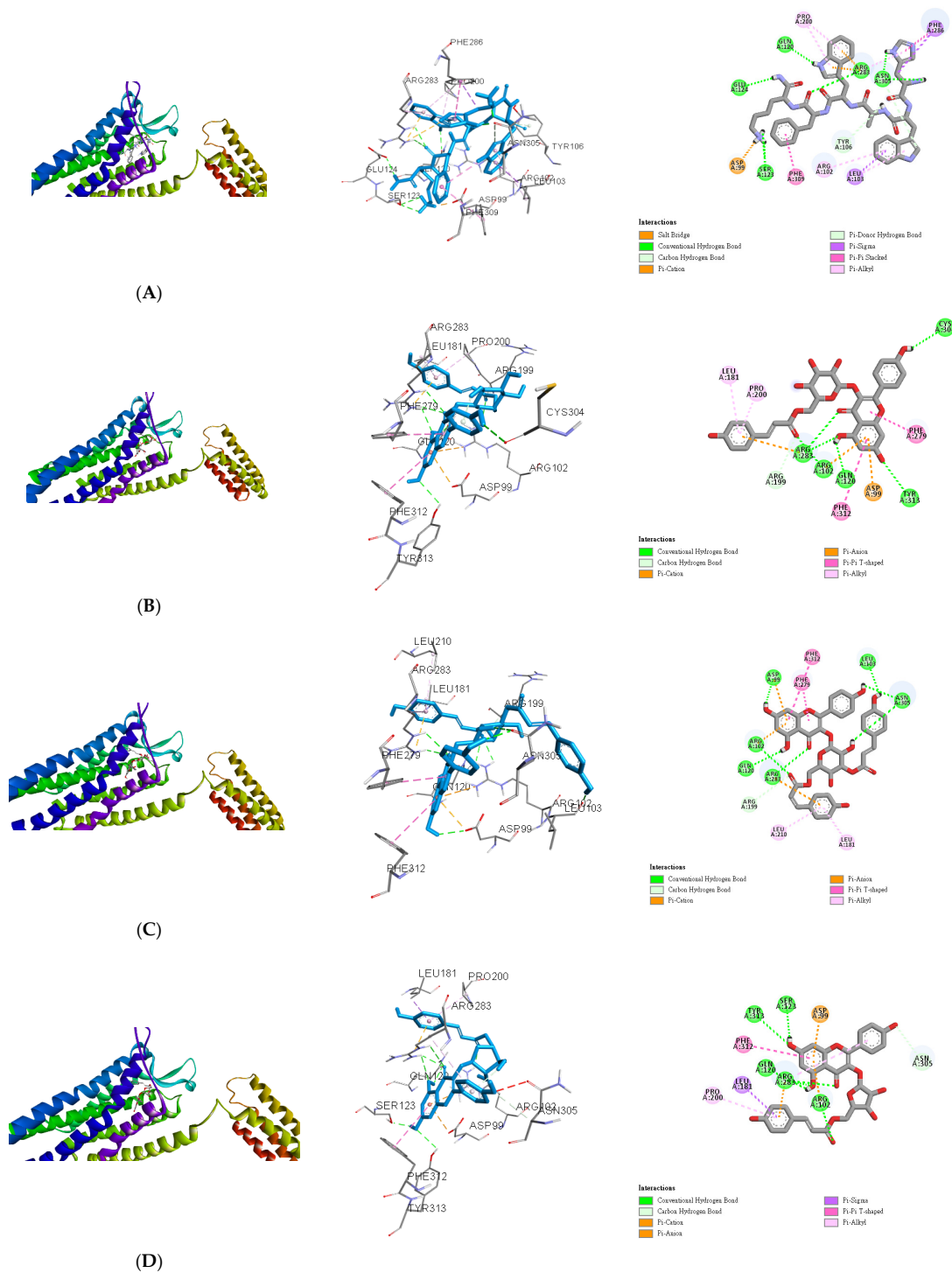


with age after full physical maturation, and continues during the decades of life [57]. Ghrelin is identified as the endogenous ligand for the GHSR and is a main regulator of GH secretion [18,19]. Ghrelin is involved in various physiological and pathophysiological mechanisms in humans such as aging [24,25]. In addition, ghrelin may be thought to be related to anti-inflammatory activity. Immune cell activation was limited by ghrelin treatment through the inhibition of NF- $\kappa$ B activation and subsequent MCP-1 secretion [26]. A synthetic ghrelin analog growth hormone-releasing peptide-2 (GHRP-2) was reported to reduce the inflammatory factors in arthritic rats, and it supports that the immune cells were mediated by the activation of ghrelin receptors [27]. Neves et al. also proposed the regulation of inflammation as an anti-aging intervention [58]. Thus, according to the anti-inflammatory bioassay experimental data, **45**, **47**, **48**, **49**, **50**, and **51** (Figure 2) showed significant inhibitory effects, and were selected to determine their binding abilities to the ghrelin receptor. Before docking simulation, the native ligand (8QX) included in the 6KO5 PDB file was re-docked for validation. The interactions between 8QX and 6KO5 and the best pose of calculated results showed high similarity and repeatability with native data (data not shown). The results indicate the high accuracy of the existing simulation system and supported the further computing.

The lowest binding energy of each ligand was considered the best conformation. The binding affinities are listed in Table 3. Growth hormone-releasing peptide 6 (GHRP-6) was used as a positive control for docking to the binding pocket of the ghrelin receptor as in our previous report. Although AutoDock Vina is not constructed for docking between peptides and proteins, several successful results have been published in previous reports [59–61]. Therefore, in this study, GHRP-6 was first computed to determine the accuracy of the present docking model and the results coincided well (Figure 3A). Compared with GHRP-6, the binding energies of **49**, **50**, and **51** were lower than  $-10.3$  kcal/mol (Table 3). This suggests that **49**, **50**, and **51** could dock into the pocket of the ghrelin receptor similar or even better than that of GHRP-6. For **49**, the hydrogen bonds could be observed between two carbonyl groups (C-4 and *p*-coumaroyl) and Arg283, C-5 hydroxyl and Gln120, C-7 hydroxyl and Tyr313, and C-4' hydroxyl and Cys304, respectively. Arg199 formed a conventional hydrogen bond with a carbonyl group of *p*-coumaroyl. In addition, **49** was linked to the Arg283, Arg102, Asp99, Phe279, Phe312, Leu181, and Pro200 residues of the ghrelin receptor via different effects such as the  $\pi$ -cation,  $\pi$ -anion,  $\pi$ - $\pi$  T-shaped, and  $\pi$ -alkyl interactions. These allowed compound **49** and protein to form a stable complex (Figure 3B). **50** was bound with Asp99, Arg102, Gln120, Arg283, Leu103, Asn305, and Arg199 through various hydrogen bonds, while other interactions ( $\pi$ -cation,  $\pi$ -anion,  $\pi$ - $\pi$  T-shaped, and  $\pi$ -alkyl) were also observed with Asp99, Arg102, Arg283, Phe279, Phe312, Leu181, and Leu210 (Figure 3C). **51** also established hydrogen or carbon hydrogen bonds with Tyr313, Ser123, Arg283, Arg102 and Asn305, together with other interactions ( $\pi$ -cation,  $\pi$ -anion,  $\pi$ -sigma,  $\pi$ - $\pi$  T-shaped, and  $\pi$ -alkyl) to link with Asp99, Arg283, Arg102, Leu181, Phe312, and Pro200 residues of ghrelin receptor could be detected (Figure 3D). Compared compounds **45**, **47**, and **48** with **49**, **50**, and **51**, the former group possessed a flavonoid skeleton only while the latter group had sugar and coumaroyl moieties. It was reported that the coumaroyl group attached on the sugar was crucial for the binding affinity to the ghrelin receptor [34]. The gap structure of GHSR interacting with the acyl acid moiety of ghrelin resulted in the transformation of the ghrelin receptor into an active configuration [43]. Moreover, the binding pocket of GHSR is bifurcated by the salt bridge between Glu124 and Arg283, and this region is rich in hydrophobic amino acids [43]. According to our data, the docking scores of **49**, **50**, and **51** were higher than those of **45**, **47**, and **48**, which suggested the better binding capability. The major structural characteristics were the coumaroyl groups rather than the sugar moieties and this could be further evidenced by examination of more compounds possessing coumaroyl functionalities. In this study, the active ingredients **49**, **50**, and **51** possessed not only anti-inflammatory bioactivity, but also the ghrelin receptor binding potential. This indicated that the claimed anti-aging effects of pine needle tea may be also based on these teaghrelin-like compounds.

**Table 3.** Binding energies of compound 45–51, and GHRP-6 calculated *in silico*.

| Compound | Affinity (kcal/mol) |
|----------|---------------------|
| 45       | −8.8                |
| 47       | −8.2                |
| 48       | −8.2                |
| 49       | −10.5               |
| 50       | −11.0               |
| 51       | −10.7               |
| GHRP-6   | −10.3               |

**Figure 3.** *In silico* modeling of (A) GHRP-6, (B) 49, (C) 50, and (D) 51 docking into the ghrelin receptor.

#### 4. Conclusions

A total of seventy-seven isolates comprising five undescribed compounds were purified from the methanol extracts of *P. taiwanensis* needles. Their structures were characterized through spectroscopic and spectrometric analyses. Forty-three purified compounds were examined for their anti-inflammatory activity by the inhibition of superoxide anion generation and elastase release on neutrophil model. The results suggest that **45**, **47**, **48**, **49**, **50**, and **51** possess significant anti-inflammatory potentials. Further molecular docking computing results supported **49**, **50**, and **51** exhibiting a binding affinity to the active pocket of the ghrelin receptor. Therefore, the crude extracts and purified constituents of *P. taiwanensis* have the potential to be developed as new anti-inflammatory lead drugs or food ingredients.

**Supplementary Materials:** The following are available online at <https://www.mdpi.com/article/10.3390/antiox10040598/s1>, Appendix A: Complete extraction and isolation procedures, Appendix B: References of known compounds, Table S1: Preliminary bioactivity screening of needles of *P. taiwanensis* on superoxide anion generation and elastase release by human neutrophils in response to fMLF/CB, Table S2: Inhibitory effects of purified compounds on superoxide anion generation and elastase release by human neutrophils in response to fMLF/CB, Figure S1–S35: HRMS and NMR spectra of new compounds 1–5.

**Author Contributions:** Conceptualization, P.-C.K. and J.T.C.T.; Methodology, P.-C.K. and T.-L.H.; Investigation, Y.-C.L., A.M.K. and M.-L.Y.; Resources, S.-Y.W.; Data curation, Y.-C.L. and G.-H.Y.; Writing—original draft preparation, P.-C.K. and Y.-C.L.; Writing—review and editing, P.-C.K. All authors have read and agreed to the published version of the manuscript.

**Funding:** This study was sponsored by the Ministry of Science and Technology, Taiwan (MOST). The research was supported in part by Higher Education Sprout Project, Ministry of Education to the Headquarters of University Advancement at National Cheng Kung University (NCKU).

**Institutional Review Board Statement:** The study was conducted with the approval of the Institutional Review Board of Chang Gung Memorial Hospital (IRB No. 201800369A3).

**Informed Consent Statement:** The statement can be provided upon request.

**Data Availability Statement:** Original data can be obtained from corresponding author upon request.

**Acknowledgments:** The authors are also thankful to Chang Gung Memorial Hospital (CMRPD1B0281~3, CMRPF1D0442~3, CMRPF1F0011~3, CMRPF1F0061~3 and BMRP450 awarded to T.-L.H.) for the partial financial support of the present research. The authors gratefully acknowledge the use of NMR equipment belonging to the Instrument Center of National Cheng Kung University.

**Conflicts of Interest:** The authors declare no conflict of interest.

#### References

1. Xie, Q.; Liu, Z.; Li, Z. Chemical composition and antioxidant activity of essential oil of six *Pinus* taxa native to China. *Molecules* **2015**, *20*, 9380–9392. [CrossRef]
2. Kim, K.Y.; Chung, H.J. Flavor compounds of pine sprout tea and pine needle tea. *J. Agric. Food Chem.* **2000**, *48*, 1269–1272. [CrossRef]
3. Park, G.; Paudyal, D.P.; Hwang, I.; Tripathi, G.R.; Yang, Y.; Cheong, H. Production of fermented needle extracts from red pine and their functional characterization. *Biotechnol. Bioprocess Eng.* **2008**, *13*, 256. [CrossRef]
4. Idžojtić, M.; Kajba, D.; Franjić, J. Differentiation of F1 hybrids *P. nigra* J. F. Arnold × *P. sylvestris* L., *P. nigra* J. F. Arnold × *P. densiflora* Siebold et Zucc., *P. nigra* J. F. Arnold × *P. thunbergiana* Franco and their parental species by needle volatile composition. *Biochem. Syst. Ecol.* **2005**, *33*, 427–439. [CrossRef]
5. Kim, Y.S.; Shin, D.H. Volatile components and antibacterial effects of pine needle (*Pinus densiflora* S. and Z.) extracts. *Food Microbiol.* **2005**, *22*, 37–45. [CrossRef]
6. Dob, T.; Berramdane, T. Essential oil composition of *Pinus halepensis* Mill. from three different regions of Algeria. *J. Essent. Oil Res.* **2007**, *19*, 40–43. [CrossRef]
7. Nam, A.M.; Tomi, F.; Gibernau, M.; Casanova, J.; Bighelli, A. Composition and chemical variability of the needle oil from *Pinus halepensis* growing in Corsica. *Chem. Biodivers.* **2016**, *13*, 380–386. [CrossRef]
8. Sezik, E.; Üstün, O.; Demirci, B.; Başer, K.H.C. Composition of the essential oils of *Pinus nigra* Arnold from Turkey. *Turk. J. Chem.* **2010**, *34*, 313–325.

9. Kupcinskiene, E.; Stikliene, A.; Judzentiene, A. The essential oil qualitative and quantitative composition in the needles of *Pinus sylvestris* L. growing along industrial transects. *Environ. Pollut.* **2008**, *155*, 481–491. [\[CrossRef\]](#) [\[PubMed\]](#)
10. Li, B.; Shen, Y.H.; He, Y.R.; Zhang, W.D. Chemical constituents and biological activities of *Pinus* species. *Chem. Biodivers.* **2013**, *10*, 2133–2160. [\[CrossRef\]](#) [\[PubMed\]](#)
11. Choi, J.H.; Kim, H.S.; Jung, M.J.; Choi, J.S. (+)-Catechin, an antioxidant principle from the leaves of *Pinus densiflora* that acts on 1,1-diphenyl-2-picrylhydrazyl radical. *Nat. Prod. Sci.* **2001**, *7*, 1–4.
12. Jung, M.J.; Chung, H.Y.; Choi, J.H.; Choi, J.S. Antioxidant principles from the needles of red pine, *Pinus densiflora*. *Phytother. Res.* **2003**, *17*, 1064–1068. [\[CrossRef\]](#) [\[PubMed\]](#)
13. Yen, G.C.; Duh, P.D.; Huang, D.W.; Hsu, C.L.; Fu, T.Y.C. Protective effect of pine (*Pinus morrisonicola* Hay.) needle on LDL oxidation and its anti-inflammatory action by modulation of iNOS and COX-2 expression in LPS-stimulated RAW 264.7 macrophages. *Food Chem. Toxicol.* **2008**, *46*, 175–185. [\[CrossRef\]](#)
14. Chen, Y.H.; Hsieh, P.C.; Mau, J.L.; Sheu, S.C. Antioxidant properties and mutagenicity of *Pinus morrisonicola* and its vinegar preparation. *LWT Food Sci. Technol.* **2011**, *44*, 1477–1481. [\[CrossRef\]](#)
15. Venkatesan, T.; Choi, Y.W.; Lee, J.; Kim, Y.K. *Pinus densiflora* needle supercritical fluid extract suppresses the expression of pro-inflammatory mediators iNOS, IL-6 and IL-1 $\beta$ , and activation of inflammatory STAT1 and STAT3 signaling proteins in bacterial lipopolysaccharide-challenged murine macrophages. *DARU J. Pharm. Sci.* **2017**, *25*, 18. [\[CrossRef\]](#)
16. Yoon, C.J.; Choi, W.S.; Kang, H.S.; Kim, H.J.; Lee, W.T.; Lee, J.S.; Lee, S.; Son, S.Y.; Lee, C.H.; Sohn, U.D.; et al. *Pinus thunbergii* Parl. extracts reduce acute inflammation by targeting oxidative stress. *Evid. Based Complement. Alternat. Med.* **2021**, *2021*, 7924645. [\[CrossRef\]](#)
17. Chiu, H.F.; Wang, H.M.; Shen, Y.C.; Venkatakrishnan, K.; Wang, C.K. Anti-inflammatory properties of fermented pine (*Pinus morrisonicola* Hay.) needle on lipopolysaccharide-induced inflammation in RAW 264.7 macrophage cells. *J. Food Biochem.* **2019**, *43*, e12994. [\[CrossRef\]](#) [\[PubMed\]](#)
18. Howard, A.D.; Feighner, S.D.; Cully, D.F.; Arena, J.P.; Liberators, P.A.; Rosenblum, C.I.; Hamelin, M.; Hreniuk, D.L.; Palyha, O.C.; Anderson, J.; et al. A receptor in pituitary and hypothalamus that functions in growth hormone release. *Science* **1996**, *273*, 974–977. [\[CrossRef\]](#)
19. Kojima, M.; Hosoda, H.; Date, Y.; Nakazato, M.; Matsuo, H.; Kangawa, K. Ghrelin is a growth-hormone-releasing acylated peptide from stomach. *Nature* **1999**, *402*, 656–660. [\[CrossRef\]](#)
20. Cui, H.; López, M.; Rahmouni, K. The cellular and molecular bases of leptin and ghrelin resistance in obesity. *Nat. Rev. Endocrinol.* **2017**, *13*, 338–351. [\[CrossRef\]](#)
21. Leidy, H.J.; Gardner, J.K.; Frye, B.R.; Snook, M.L.; Schuchert, M.K.; Richard, E.L.; Williams, N.I. Circulating ghrelin is sensitive to changes in body weight during a diet and exercise program in normal-weight young women. *J. Clin. Endocrinol. Metab.* **2004**, *89*, 2659–2664. [\[CrossRef\]](#) [\[PubMed\]](#)
22. Kojima, M.; Kangawa, K. Ghrelin: Structure and function. *Physiol. Rev.* **2005**, *85*, 495–522. [\[CrossRef\]](#)
23. Broglio, F.; Gottero, C.; Benso, A.; Prodam, F.; Destefanis, S.; Gauna, C.; Maccario, M.; Deghenghi, R.; van der Lely, A.J.; Ghigo, E. Effects of ghrelin on the insulin and glycemic responses to glucose, arginine, or free fatty acids load in humans. *J. Clin. Endocrinol. Metab.* **2003**, *88*, 4268–4272. [\[CrossRef\]](#) [\[PubMed\]](#)
24. Cheng, K.C.; Li, Y.X.; Asakawa, A.; Inui, A. The role of ghrelin in energy homeostasis and its potential clinical relevance (Review). *Int. J. Mol. Med.* **2010**, *26*, 771–778. [\[CrossRef\]](#)
25. Kaplan, R.C.; Strizich, G.; Aneke-Nash, C.; Dominguez-Islas, C.; Bužková, P.; Strickler, H.; Rohan, T.; Pollak, M.; Kuller, L.; Kizer, J.R.; et al. Insulinlike growth factor binding protein-1 and ghrelin predict health outcomes among older adults: Cardiovascular health study cohort. *J. Clin. Endocrinol. Metab.* **2017**, *102*, 267–278. [\[CrossRef\]](#)
26. Li, W.G.; Gavrila, D.; Liu, X.; Wang, L.; Gunnlaugsson, S.; Stoll, L.L.; McCormick, M.L.; Sigmund, C.D.; Tang, C.; Weintraub, N.L. Ghrelin inhibits proinflammatory responses and nuclear factor-kappaB activation in human endothelial cells. *Circulation* **2004**, *109*, 2221–2226. [\[CrossRef\]](#) [\[PubMed\]](#)
27. Granado, M.; Priego, T.; Martín, A.I.; Villanúa, M.A.; López-Calderón, A. Anti-inflammatory effect of the ghrelin agonist growth hormone-releasing peptide-2 (GHRP-2) in arthritic rats. *Am. J. Physiol. Endocrinol. Metab.* **2005**, *288*, E486–E492. [\[CrossRef\]](#)
28. Lo, Y.H.; Chen, Y.J.; Chang, C.I.; Lin, Y.W.; Chen, C.Y.; Lee, M.R.; Lee, V.S.; Tzen, J.T.C. Teaghrins, unique acylated flavonoid tetraglycosides in Chin-shin oolong tea, are putative oral agonists of the ghrelin receptor. *J. Agric. Food Chem.* **2014**, *62*, 5085–5091. [\[CrossRef\]](#)
29. Li, Y.C.; Wu, C.J.; Lin, Y.C.; Wu, R.H.; Chen, W.Y.; Kuo, P.C.; Tzen, J.T.C. Identification of two teaghrins in Shy-jih-chuen oolong tea. *J. Food Biochem.* **2019**, *43*, e12810. [\[CrossRef\]](#) [\[PubMed\]](#)
30. Lo, Y.H.; Chen, Y.J.; Chung, T.Y.; Lin, N.H.; Chen, W.Y.; Chen, C.Y.; Lee, M.R.; Chou, C.C.; Tzen, J.T.C. Emoghrelin, a unique emodin derivative in Heshouwu, stimulates growth hormone secretion via activation of the ghrelin receptor. *J. Ethnopharmacol.* **2015**, *159*, 1–8. [\[CrossRef\]](#) [\[PubMed\]](#)
31. Hsieh, S.K.; Chung, T.Y.; Li, Y.C.; Lo, Y.H.; Lin, N.H.; Kuo, P.C.; Chen, W.Y.; Tzen, J.T.C. Ginkgoghrelins, unique acylated flavonoid diglycosides in Folium Ginkgo, stimulate growth hormone secretion via activation of the ghrelin receptor. *J. Ethnopharmacol.* **2016**, *193*, 237–247. [\[CrossRef\]](#)
32. Lin, Y.C.; Wu, C.J.; Kuo, P.C.; Chen, W.Y.; Tzen, J.T.C. Quercetin 3-O-malonylglucoside in the leaves of mulberry (*Morus alba*) is a functional analog of ghrelin. *J. Food Biochem.* **2020**, *44*, e13379. [\[CrossRef\]](#) [\[PubMed\]](#)



33. Wu, C.J.; Chien, M.Y.; Lin, N.H.; Lin, Y.C.; Chen, W.Y.; Chen, C.H.; Tzen, J.T.C. Echinacoside isolated from *Cistanche tubulosa* putatively stimulates growth hormone secretion via activation of the ghrelin receptor. *Molecules* **2019**, *24*, 720. [\[CrossRef\]](#) [\[PubMed\]](#)
34. Hsieh, S.K.; Lo, Y.H.; Wu, C.C.; Chung, T.Y.; Tzen, J.T.C. Identification of biosynthetic intermediates of teaghrilins and teaghrilin-like compounds in oolong teas, and their molecular docking to the ghrelin receptor. *J. Food Drug Anal.* **2015**, *23*, 660–670. [\[CrossRef\]](#)
35. Brooijmans, N.; Kuntz, I.D. Molecular recognition and docking algorithms. *Annu. Rev. Biophys. Biomol. Struct.* **2003**, *32*, 335–373. [\[CrossRef\]](#) [\[PubMed\]](#)
36. Muegge, I.; Rarey, M. Small molecule docking and scoring. In *Reviews in Computational Chemistry*; Lipkowitz, K.B., Boyd, D.B., Eds.; Wiley: Hoboken, NJ, USA, 2001; Volume 17, pp. 1–60.
37. Halperin, I.; Ma, B.; Wolfson, H.; Nussinov, R. Principles of docking: An overview of search algorithms and a guide to scoring functions. *Proteins* **2002**, *47*, 409–443. [\[CrossRef\]](#) [\[PubMed\]](#)
38. Chen, G.H.; Li, Y.C.; Lin, N.H.; Kuo, P.C.; Tzen, J.T.C. Characterization of vasorelaxant principles from the needles of *Pinus morrissonicola* Hayata. *Molecules* **2018**, *23*, 86. [\[CrossRef\]](#) [\[PubMed\]](#)
39. Editorial Committee of Flora of Taiwan. *Flora of Taiwan*, 2nd ed.; National Science Council: Taipei, Taiwan, 1994; Volume 1, p. 571.
40. Yang, S.C.; Chung, P.J.; Ho, C.M.; Kuo, C.Y.; Hung, M.F.; Huang, Y.T.; Chang, W.Y.; Chang, Y.W.; Chan, K.H.; Hwang, T.L. Propofol inhibits superoxide production, elastase release, and chemotaxis in formyl peptide-activated human neutrophils by blocking formyl peptide receptor 1. *J. Immunol.* **2013**, *190*, 6511–6519. [\[CrossRef\]](#)
41. Trott, O.; Olson, A.J. AutoDock Vina: Improving the speed and accuracy of docking with a new scoring function, efficient optimization, and multithreading. *J. Comput. Chem.* **2010**, *31*, 455–461. [\[CrossRef\]](#)
42. Shiimura, Y.; Horita, S.; Hamamoto, A.; Asada, H.; Hirata, K.; Tanaka, M.; Mori, K.; Uemura, T.; Kobayashi, T.; Iwata, S.; et al. Structure of an antagonist-bound ghrelin receptor reveals possible ghrelin recognition mode. *Nat. Commun.* **2020**, *11*, 4160. [\[CrossRef\]](#)
43. BIOVIA; Dassault Systèmes. *Discovery Studio Client 2020*, v.20.1.0.19295; Dassault Systèmes: San Diego, CA, USA, 2019.
44. Lu, Y.; Xue, Y.; Liu, J.; Yao, G.; Li, D.; Sun, B.; Zhang, J.; Liu, Y.; Qi, C.; Xiang, M.; et al. (±)-Acortatarinowins A–F, Norlignan, Neolignan, and Lignan Enantiomers from *Acorus tatarinowii*. *J. Nat. Prod.* **2015**, *78*, 2205–2214. [\[CrossRef\]](#)
45. Huo, C.; Liang, H.; Zhao, Y.; Wang, B.; Zhang, Q. Neolignan glycosides from *Symplocos caudata*. *Phytochemistry* **2008**, *69*, 788–795. [\[CrossRef\]](#) [\[PubMed\]](#)
46. Hsieh, Y.L.; Fang, J.M.; Cheng, Y.S. Terpenoids and flavonoids from *Pseudotsuga wilsoniana*. *Phytochemistry* **1998**, *47*, 845–850. [\[CrossRef\]](#)
47. Russell, A.B.; Michael, B.G.; Vincent, Y.T. Synthesis of methyl 12S- and 12R-hydroxylabd-8(17)-en-19-oates. *Can. J. Chem.* **1975**, *53*, 2869–2873. [\[CrossRef\]](#)
48. Segal, R.; Milo-Goldzweig, I.; Sokoloff, S.; Zaitschek, D.V. A new benzofuran from the seeds of *Styrax officinalis* L. *J. Chem. Soc. C* **1967**, 2402–2404. [\[CrossRef\]](#)
49. Coussens, L.M.; Werb, Z. Inflammation and cancer. *Nature* **2002**, *420*, 860–867. [\[CrossRef\]](#)
50. Hwang, T.L.; Li, G.L.; Lan, Y.H.; Chia, Y.C.; Hsieh, P.W.; Wu, Y.H.; Wu, Y.C. Potent inhibition of superoxide anion production in activated human neutrophils by isopedicin, a bioactive component of the Chinese medicinal herb *Fissistigma Oldhamii*. *Free Radic. Biol. Med.* **2009**, *46*, 520–528. [\[CrossRef\]](#)
51. Ennis, M. Neutrophils in asthma pathophysiology. *Curr. Allergy Asthma Rep.* **2003**, *3*, 159–165. [\[CrossRef\]](#)
52. Malech, H.L.; Gallin, J.I. Neutrophils in human diseases. *N. Engl. J. Med.* **1987**, *317*, 687–694. [\[CrossRef\]](#)
53. Okajima, K.; Harada, N.; Uchiba, M. Ranitidine reduces ischemia/reperfusion-induced liver injury in rats by inhibiting neutrophil activation. *J. Pharmacol. Exp. Ther.* **2002**, *301*, 1157–1165. [\[CrossRef\]](#)
54. Vinten-Johansen, J. Involvement of neutrophils in the pathogenesis of lethal myocardial reperfusion injury. *Cardiovasc. Res.* **2004**, *61*, 481–497. [\[CrossRef\]](#)
55. Witko-Sarsat, V.; Rieu, P.; Descamps-Latscha, B.; Lesavre, P.; Halbwachs-Mecarelli, L. Neutrophils: Molecules, functions and pathophysiological aspects. *Lab. Investig.* **2000**, *80*, 617–653. [\[CrossRef\]](#)
56. Yu, H.P.; Hsieh, P.W.; Chang, Y.J.; Chung, P.J.; Kuo, L.M.; Hwang, T.L. 2-(2-Fluorobenzamido)benzoate ethyl ester (EFB-1) inhibits superoxide production by human neutrophils and attenuates hemorrhagic shock-induced organ dysfunction in rats. *Free Radic. Biol. Med.* **2011**, *50*, 1737–1748. [\[CrossRef\]](#) [\[PubMed\]](#)
57. Bartke, A. Growth hormone and aging: Updated review. *World J. Mens Health* **2019**, *37*, 19–30. [\[CrossRef\]](#) [\[PubMed\]](#)
58. Neves, J.; Sousa-Victor, P. Regulation of inflammation as an anti-aging intervention. *FEBS J.* **2020**, *287*, 43–52. [\[CrossRef\]](#)
59. Ibrahim, M.A.; Bester, M.J.; Neitz, A.W.; Gaspar, A.R.M. Rational *in silico* design of novel  $\alpha$ -glucosidase inhibitory peptides and *in vitro* evaluation of promising candidates. *Biomed. Pharmacother.* **2018**, *107*, 234–242. [\[CrossRef\]](#) [\[PubMed\]](#)
60. Jindal, H.M.; Le, C.F.; Yusof, M.Y.M.; Velayuthan, R.D.; Lee, V.S.; Zain, S.M.; Isa, D.M.; Sekaran, S.D. Antimicrobial activity of novel synthetic peptides derived from indolicidin and ranalexin against *Streptococcus pneumoniae*. *PLoS ONE* **2015**, *10*, e0128532. [\[CrossRef\]](#)
61. Kaur, K.; Kaur, P.; Mittal, A.; Nayak, S.K.; Khatik, G.L. Design and molecular docking studies of novel antimicrobial peptides using autodock molecular docking software. *Asian J. Pharm. Clin. Res.* **2017**, *10*, 28–31. [\[CrossRef\]](#)



# Photothermal treatment by PLGA–gold nanorod–isatin nanocomplexes under near-infrared irradiation for alleviating psoriasiform hyperproliferation

G.R. Nirmal<sup>a</sup>, Zih-Chan Lin<sup>a</sup>, Ming-Jun Tsai<sup>b,c,d</sup>, Shih-Chun Yang<sup>e</sup>, Ahmed Alalaiwe<sup>f</sup>, Jia-You Fang<sup>g,h,i,\*</sup>

<sup>a</sup> Graduate Institute of Biomedical Sciences, Chang Gung University, Kweishan, Taoyuan, Taiwan

<sup>b</sup> Department of Neurology, China Medical University Hospital, Taichung, Taiwan

<sup>c</sup> School of Medicine, College of Medicine, China Medical University, Taichung, Taiwan

<sup>d</sup> Department of Neurology, An-Nan Hospital, China Medical University, Tainan, Taiwan

<sup>e</sup> Department of Cosmetic Science, Providence University, Taichung, Taiwan

<sup>f</sup> Department of Pharmaceutics, College of Pharmacy, Prince Sattam Bin Abdulaziz University, Al Kharj, Saudi Arabia

<sup>g</sup> Pharmaceutics Laboratory, Graduate Institute of Natural Products, Chang Gung University, Kweishan, Taoyuan, Taiwan

<sup>h</sup> Research Center for Food and Cosmetic Safety and Research Center for Chinese Herbal Medicine, Chang Gung University of Science and Technology, Kweishan, Taoyuan, Taiwan

<sup>i</sup> Department of Anesthesiology, Chang Gung Memorial Hospital, Kweishan, Taoyuan, Taiwan

## ARTICLE INFO

Editor: Dan Peer

### Keywords:

Psoriasis  
Hyperproliferation  
Gold nanorod  
Isatin  
Nanocomplex  
Photothermal therapy

## ABSTRACT

Psoriasis is a chronic autoimmune skin disorder that involves keratinocyte hyperproliferation and inflammatory cell recruitment. A strategy to mitigate psoriatic lesions is to induce keratinocyte apoptosis for proliferation suppression. Herein we designed a nanoformulation capable of treating psoriasis via hyperthermia-induced apoptosis in response to near-infrared (NIR) irradiation. To this end, gold nanorods (GNRs) and isatin, which is an anti-inflammatory agent for synergizing antipsoriatic activity, were loaded into a poly (lactic-co-glycolic acid) (PLGA) matrix to form the nanocomplexes. The physicochemical and photothermal properties of the nanocomplexes were determined in terms of size, surface charge, NIR-absorbing feature, isatin release, keratinocyte uptake, and cytotoxicity. The nanocomplexes showed a spherical shape with an average size of about 180 nm. The GNR-loaded nanoparticles can efficiently convert NIR light at 0.42 W/cm<sup>2</sup> into heat with an increased temperature of 10 °C. When combined with NIR exposure, the nanocomplexes were internalized into keratinocyte cytoplasm with an inhibition of keratinocyte viability to about 60%. Live/dead cell assay and flow cytometry confirmed that the nanocomplexes could serve as NIR-absorbers to specifically elicit keratinocyte apoptosis through caspase and poly ADP-ribose polymerase (PARP) pathways. The in vivo psoriasiform murine model indicated that the combined nanocomplexes and NIR inhibited epidermal hyperplasia and neutrophil infiltration. The overexpressed cytokines in the lesion could be recovered to normal baseline level after the photothermal management. The subcutaneous nanocomplexes remained in the skin for at least 5 days. The nanocomposites produced a negligible toxicity in the skin or liver of healthy mice. The photothermal nano-systems, as designed in this study, shed new light on the therapeutic approach against psoriasis.

## 1. Introduction

Psoriasis is an immune-mediated inflammatory skin disease involving the interplay between keratinocytes and immune cells, which is clinically presented as skin thickening with red plaque and silvery

scales. The estimated global prevalence of psoriasis is 2%–3% [1]. Histologically, psoriasis is characterized by keratinocyte hyperproliferation and inflammatory cell infiltration in viable skin [2]. The goal of therapy to mitigate psoriasis is to suppress epidermal cell hyperproliferation and block the inflammatory pathways. The keratinocyte proliferation

\* Corresponding author at: Pharmaceutics Laboratory, Graduate Institute of Natural Products, Chang Gung University, 259 Wen-Hwa 1st Road, Kweishan, Taoyuan 333, Taiwan.

E-mail address: [fajy@mail.cgu.edu.tw](mailto:fajy@mail.cgu.edu.tw) (J.-Y. Fang).

<https://doi.org/10.1016/j.jconrel.2021.04.005>

Received 17 February 2021; Received in revised form 28 March 2021; Accepted 5 April 2021

Available online 13 April 2021

0168-3659/© 2021 Elsevier B.V. All rights reserved.

inhibition or apoptosis induction is considered as a target of the anti-psoriatic approach [3]. The prescribed antipsoriatic strategies, which include vitamin D<sub>3</sub> analogs, dithranol, methotrexate, and phototherapy, are shown to exhibit therapeutic efficiency via inhibiting hyperproliferation. However, as Vitamin D<sub>3</sub> derivatives and dithranol cause skin irritation, itching, and pain [4], and the use of methotrexate is limited by hematological suppression and hepatotoxicity [5], their use present some challenges that reduce patients' compliance. While phototherapy with UV exposure is available as narrowband UVB or psoralen plus UVA (PUVA) to produce apoptosis and immune suppression, the application of phototherapy is time consuming and only used for short-term control, as skin burning, hyperpigmentation, and the risk of carcinogenesis limit its long-term administration [6]. Photodynamic therapy (PDT) is another phototherapy that generates reactive oxygen species (ROS) in the presence of photosensitizer, near-infrared (NIR) light, and oxygen [7]. However, sole PDT is insufficient to achieve a complete treatment of diseases due to the limited oxygen generation ability and finite action distance. There is no definitive cure to control psoriasis until now.

Photothermal therapy (PTT) using photo-absorbing nanoparticles activated by light can localize heat to the target site, which results in apoptosis. PTT has been extensively studied for cancer treatment due to its minimal invasiveness and high controllability [8]. Moreover, PTT can result in minimal damage to non-targeted regions after the optimization of selecting photosensitizers and NIR energies [9]. Near-infrared (NIR) light ranging 700–1000 nm can be applied for PTT in combination with light-absorbing nanoparticles, and can achieve site-specific efficacy with reduced damage to adjacent normal tissue. Due to the low energy and precise site control [10], the pain and burn induced by NIR are negligible. However, it should be noticeable that the low NIR energy may cause the insufficient hyperthermia to induce a satisfied outcome for therapy. Gold nanoparticles are employed as an effective heat source under NIR illumination. Among the different types of gold nanoparticles, gold nanorods (GNRs) exhibit superior tunability in surface plasmon resonance, and absorb by modifying the length-breadth ratio and efficient transition of light to heat [11]. As compared to silver nanoprisms [12], GNRs show a higher NIR absorption rate than carbon nanotubes and are highly stable.

Since the combined nanoparticles and NIR are beneficial for ablating tumors via apoptotic mechanisms, it may be also useful to inhibit the hyperproliferation of psoriasis. Until now, no studies have investigated the effect of PTT on this proliferative inflammation disease. As combination therapy is a common therapeutic approach in the management of psoriasis [13], this study developed a photo-absorbing nanosystem combined with NIR for relieving psoriatic lesions. In order to complement the efficacy of PTT, this study incorporated isatin as an anti-proliferative and anti-inflammatory agent for treating psoriasis. Isatin is a heterocyclic compound found in humans and some plant species. Isatin, and its metabolites or derivatives, reveal a wide range of bio-activities, including antiviral, antitumor, anticonvulsant, and anxiolytic effects [14]. Previous studies [15,16] verified the ability of isatin to induce apoptosis in carcinoma cells, and proved the anti-inflammatory activity of isatin by using macrophages and colitis as cell and animal models, respectively [17,18]. Due to their small volume and poor loading capacity [19], gold nanoparticles are not ideal as a drug carrier. Another concern is the possible toxicity derived from GNRs. This study used poly(lactic-co-glycolic acid) (PLGA) nanoparticles to entrap both GNRs and isatins as a nanosystem to perform PTT, as PLGA has excellent biocompatibility and biodegradability, and is approved by the USFDA as a chemical of generally regarded as safe (GRAS) [20]. This work characterized the physicochemical and photothermal properties of the PLGA/GNR/isatin nanoparticles, and presented studies that assessed the nanoparticle uptake by keratinocytes, as well as the subsequent apoptosis. This study then tested the ability of the nanosystem in treating psoriasiform lesion in a murine model, and finally, examined the biodistribution of the nanoparticles after NIR irradiation.

## 2. Materials and methods

### 2.1. Materials

Cetyltrimethylammonium bromide (CTAB), HAuCl<sub>4</sub>, AgNO<sub>3</sub>, NaBH<sub>4</sub>, ascorbic acid, PLGA (lactide:glycolide = 1:1, 30–60 kDa), poly(vinyl alcohol) (PVA, 30–70 kDa), and isatin were purchased from Sigma-Aldrich; the LysoTracker, live-dead cytotoxicity kit, and DiR IR dye were purchased from Invitrogen; the Annexin V/propidium iodide (PI) apoptosis detection kit was brought from GeneDireX.

### 2.2. Synthesis of GNRs

The GNRs were synthesized by the modification of the seed-mediated growth method [21]. HAuCl<sub>4</sub> at 10 mM (0.125 ml) was added in 100 mM CTAB (3.75 ml), followed by the incorporation of 10 mM ice-cold NaBH<sub>4</sub>. This seed solution was incubated at 37 °C for 20 min. CTAB at 100 mM (47.2 ml) and HAuCl<sub>4</sub> at 10 mM (2 ml) were added into a test tube, followed by the addition of 10 mM AgNO<sub>3</sub> (0.3 ml) and 100 mM ascorbic acid (0.3 ml). The seed solution (0.21 ml) was then added, followed by incubation at 37 °C for 90 min. The solution was centrifuged at 3500 rpm and 25 °C for 15 min, followed by the centrifugation of the supernatant two times at 12,000 rpm and 25 °C for 15 min. The GNRs were obtained as a pellet deposition.

### 2.3. Preparation of PLGA/GNR/isatin nanocomplexes

The nanocarriers were fabricated by the solvent-evaporation method [22]. PLGA (50 mg) and isatin (2.5 mg) were dissolved in 4 ml dichloromethane. Then, the GNRs (0.5 ml) in 2.5% PVA (1 ml) were added into the PLGA/isatin solution. The oil/water interface was probe-sonicated for 5 min. PVA at 1% (10 ml) was included and sonicated for 5 min, followed by stirring overnight at 500 rpm. The nanoparticles were achieved by centrifugation at 4000 rpm for 3 times with water. The scheme of nanocomplex preparation is illustrated in Fig. 1a.

### 2.4. Physicochemical characterization of the nanoparticles

The GNRs or PLGA nanoparticles were positioned onto a carbon-film-coated copper grid to form a thin-film specimen and stained with 1% phosphotungstic acid. The prepared samples were imaged by transmission electron microscopy (TEM, Hitachi HT7800). The average diameter (z-average) and zeta potential of the nanoparticles were detected by a dynamic light scattering system (Malvern Nano ZS90). The dispersion was diluted 100-fold with water before determination. The chemical functional groups of the nanoparticles were examined by Fourier transform infrared spectroscopy (FTIR, Bruker Tensor 27). UV-visible spectroscopy (Hitachi U1900) was employed to understand the light absorption properties of the GNRs and nanocomplexes. The concentration of isatin in the nanocomplexes was evaluated from the standard curve drawn on the absorbance of the known concentrations of isatin at wavelength 295 nm (U2900, Hitachi). The nanocomplexes were incubated in a water bath at 60 °C for four hours followed by the absorbance measurement of the supernatant at 295 nm. From the known absorbance the concentration of isatin was calculated.

### 2.5. Isatin release from nanocomplexes

The nanocomplexes in pH 7.4 citrate-phosphate buffer were stirred for 20 min, and the supernatant was collected via centrifugation at 20,000 rpm at different time intervals. If required, NIR irradiation at 0.42 W/cm<sup>2</sup> was performed. The isatin concentration in the supernatant was analyzed by high-performance liquid chromatography (HPLC). Isatin in supernatant could be regarded as the release from nanocomplexes. A chromatogram for analyzing isatin was obtained by using a Hitachi HPLC system (7-series) with a LiChrospher C18 column (200



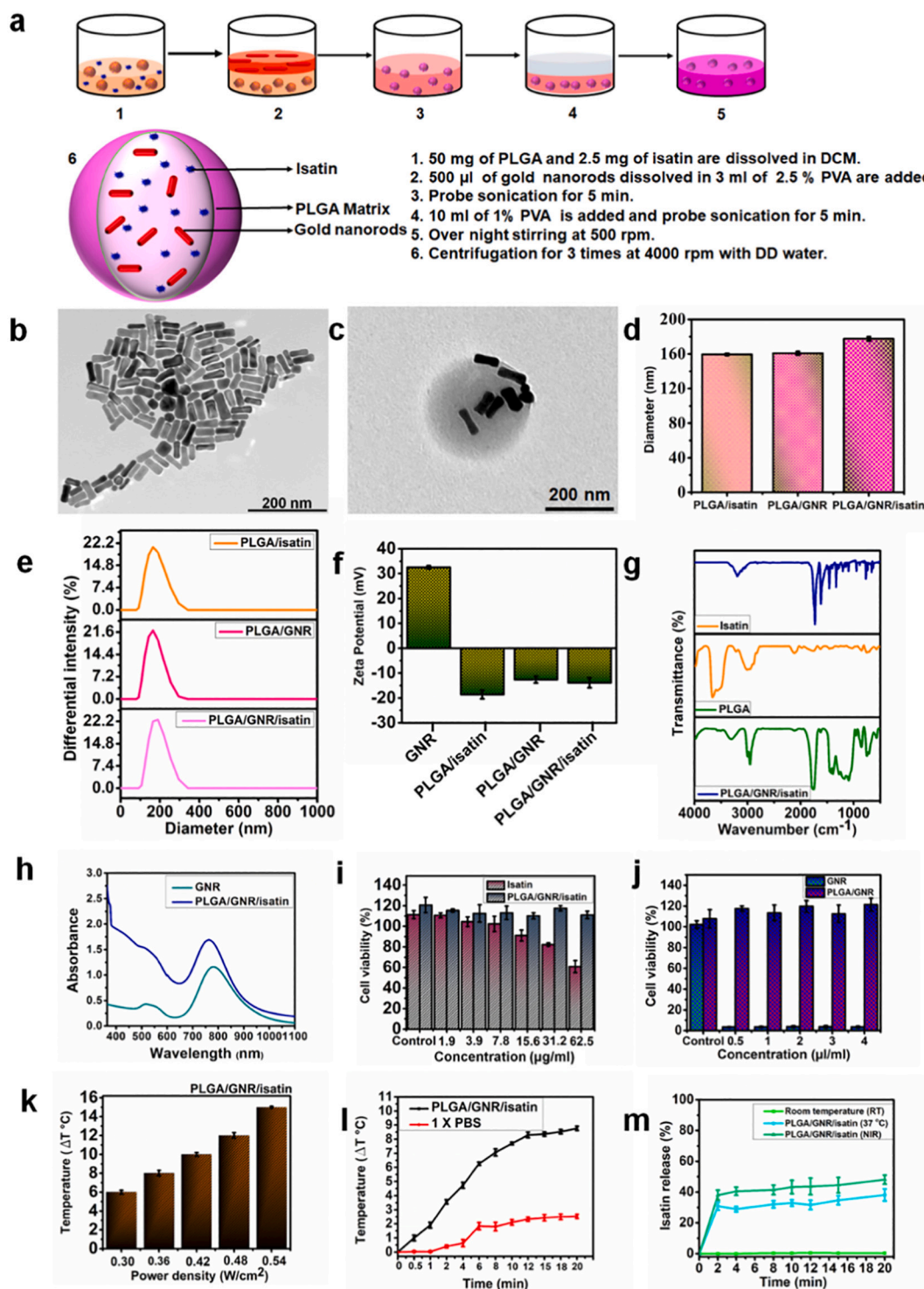


**Fig. 1.** Preparation and physicochemical characterization of the nanocomplexes: (a) The fabrication processes and schematic diagram of the nanocomplexes. (b) TEM image of the GNRs. (c) TEM image of PLGA/GNR/isatin nanocomplexes. (d) The hydrodynamic diameter of the nanoparticles. (e) The size distribution of the nanoparticles. (f) The zeta potential of the nanoparticles. (g) FTIR spectra recorded in the spectral range of 400–4000  $\text{cm}^{-1}$ . (h) UV–visible spectra recorded in the spectral range of 350–1000 nm. (i) The keratinocyte cytotoxicity of free isatin and PLGA/GNR/isatin. (j) The keratinocyte cytotoxicity of GNRs and PLGA/GNR. (k) The temperature increase of the PLGA/GNR/isatin nanocomplexes under NIR irradiation at different energies. (l) The temperature increase as a function of time of the PLGA/GNR/isatin nanocomplexes under NIR irradiation at 0.42  $\text{W/cm}^2$ . (m) Isatin release from the PLGA/GNR/isatin nanocomplexes at different temperatures or under NIR irradiation at 0.42  $\text{W/cm}^2$ . Data are expressed as mean  $\pm$  SEM ( $n = 3$ ).

$\times 4.6$  mm, Merck). The mobile phase was pH 2 double-distilled water adjusted by phosphoric acid and acetonitrile (7:3) with a flow rate of 1 ml/min. The UV–visible detection wavelength was 295 nm.

## 2.6. Cytotoxicity evaluation

The cytotoxicity of isatin and nanoparticles was studied by 3-(4,5-dimethylthiazol-2-yl)-2,5-diphenyltetrazolium bromide (MTT) analysis.



The keratinocytes (HaCaT) were cultured in DMEM with the cell density of  $1 \times 10^5$  cells/ml and incubated at 37 °C for 24 h. Subsequently, the isatin, GNRs, or the nanocomplexes at different concentrations were added into the cell suspension and incubated for 24 h. The cells with bare medium were used as the control. MTT at 0.5 mg/ml in culture medium (200  $\mu$ l) was added into the cell suspension, followed by incubation at 37 °C for 4 h. The HaCaT viability was detected by a spectrophotometer at 570 nm.

## 2.7. The photothermal property of the nanocomplexes

The photothermal effect of the nanoparticles was examined by dissolved nanoparticles in PBS with 31.2  $\mu$ g/ml isatin under NIR irradiated by NIR laser at 785 nm (B&W Tek BWF1). The temperature was detected by using a Fluke Ti32 IR thermal imager. The time-dependent increase in temperature by combined nanoparticles and NIR at 0.3–0.54 W/cm<sup>2</sup> was measured until 20 min.

## 2.8. Nanocomplex internalization by keratinocytes

Rhodamine B (1 mg) was loaded into the nanocomplexes as a dye. The keratinocyte uptake of the nanoparticles was studied through flow cytometry and fluorescence microscopy. HaCaT cells ( $1 \times 10^5$  cells/ml) were incubated with dye-loaded nanoparticles at various concentrations for 4 h, then the medium was removed and the cells were washed by PBS for 3 times to remove the non-internalized nanoparticles. The cells were dispersed in PBS for flow cytometry determination. LysoTracker (0.1%) in PBS was added to the cell suspension and incubated for 2 h to stain lysosomes. 4',6-diamidino-2-phenylindole (DAPI) was also used to stain the nuclei. The keratinocytes were washed with PBS and fixed with formaldehyde, in order to observe nanocomplex internalization using fluorescence microscopy (Leica DMI8).

## 2.9. Photothermal effect of nanocomplexes on keratinocytes

The live-dead staining of keratinocytes was carried out to examine the photothermal effect of the nanocomplexes. Isatin or nanocomplexes were incubated with HaCaT cells for 4 h. NIR laser at 0.42 W/cm<sup>2</sup> for 10 min was exposed to the cells if necessary. The live-dead kit (200  $\mu$ l) with calcein-AM and ethidium homodimer-1 was used to stain live and dead keratinocytes, respectively. After incubating the kit with cells for 15 min, the keratinocytes were fixed with formaldehyde and imaged by fluorescence microscopy. The MTT assay was used to investigate cell viability after treatment of nanoparticles with or without NIR. Neutral red staining was also performed to visualize the live cells after photothermal application [23]. The cells were monitored under an optical microscope.

## 2.10. Apoptosis of keratinocytes

The keratinocyte apoptosis induced by nanoparticles with or without NIR was examined by flow cytometry. After the addition of isatin or nanoparticles in the cell suspension, NIR treatment for 15 min was performed if necessary. The HaCaT cells were collected in the flow tube by centrifugation at 3000 rpm for 5 min. After being resuspended in the buffer, the apoptosis detection kit (5  $\mu$ l) was added. The flow cytometry was performed after kit incubation for 20 min. The treated cells were also employed to assess the level of caspase 3, caspase 9, and poly ADP-ribose polymerase (PARP) by Western blot assay. The keratinocytes were collected and pipetted into the lysis buffer. The nuclear pellets were obtained after centrifugation at 400  $\times$ g at 4 °C for 5 min. After probe sonication, the protein fraction was obtained by centrifugation at 8000  $\times$ g at 4 °C for 10 min. The protein assay dye was utilized to quantify the amount of protein, and the proteins were separated by SDS-PAGE. The proteins were treated by different primary antibodies overnight at 4 °C. Then, the membrane was washed by tris-buffered saline and

incubated with the corresponding secondary antibodies. Equal protein loading was monitored by GAPDH on the same membrane.

## 2.11. In vivo psoriasiform experiment in mice

Balb/c mice at 8 weeks old were used to establish the psoriasiform skin model. The animal experiments were conducted in strict accordance with the recommendations outlined in the guidelines of the Institutional Animal Care and Use Committee of Chang Gung University. The mouse back received a daily topical imiquimod (IMQ) cream (Aldara) at 62.5 mg for 5 days. Isatin (1 mg/ml) or nanocomplexes were subcutaneously injected into the IMQ-treated site on Day 2 ( $n = 6$ ). The NIR irradiation at 0.42 W/cm<sup>2</sup> was repeated on Day 3 and Day 4. The gross and close-up images of skin surface were taken using a digital camera and a hand-held Mini Scope-V microscope (M&T Optics), respectively. The in vivo temperature increase by the nanoparticles under NIR was monitored using thermal imager. The healthy mice without IMQ treatment was the control group.

## 2.12. Cytokine expression in skin

The cytokine level in the treated skin was quantified by enzyme-linked immunosorbent assay (ELISA). The punch biopsies from the dorsal skin were taken and incubated in 1 ml PBS with a protease inhibitor, followed by homogenization at 6500 rpm for 30 s for 3 times with a cooling process for 1 min between each repetition. The samples were centrifuged at 13,000 rpm at 4 °C for 10 min. The supernatant was collected and the protein concentration was quantified by the protein assay kit. The levels of IL-1 $\beta$ , IL-6, IL-23, and TNF- $\alpha$  were determined using the commercial kits (BioLegend), as based on the manufacturer's instruction.

## 2.13. Histological assay

The skin specimens were deposited into 10% buffered formaldehyde using ethanol, embedded in paraffin wax, and sliced at 5  $\mu$ m for hematoxylin and eosin (H&E) staining. The unstained biopsies were prepared for immunohistochemistry (IHC). The specimens were incubated with anti-mouse lymphocyte antigen 6 complex locus G6D (Ly6G), myeloperoxidase (MPO), or Ki67 antibody for 1 h, washed by 0.5% Tween 20 in saline, and then, incubated with biotinylated donkey anti-goat IgG for 20 min. All photographs of skin histology were taken by an optical microscope.

## 2.14. Biodistribution of nanocomplexes

The distribution of the subcutaneous nanoparticles in organs was studied using an in vivo imaging system (IVIS). The treatment procedure was the same as the in vivo psoriasiform experiment in mice. The DiR IR dye (0.025%) was loaded within the PLGA matrix along with GNRs and isatin, and the in vivo IR images were taken for 5 days. After sacrificing the mice on Day 5, the peripheral organs, including heart, lung, spleen, liver, and kidney, were excised for ex vivo imaging, in order to observe the biodistribution of the nanoparticles.

## 2.15. The safety of injected nanocomplexes on mouse

The control solution and nanocomplexes containing isatin (1 mg/ml) with a volume of 100  $\mu$ l were subcutaneously injected into the dorsal site of Balb/c mice ( $n = 6$ ). The skin was examined for its gross and microscopic appearances, transepidermal water loss (TEWL, TM300, Courage and Khazaka), skin surface pH (PH905, Courage and Khazaka), and erythema index (a\*, CD100, Yokogawa), and H&E-stained histology. The H&E staining was also examined for the sections of heart, lung, spleen, liver, and kidney at Day 5 post-injection.

## 2.16. Statistical analysis

The statistical differences in the data of different treatment groups were measured using the Kruskal-Wallis test, while post hoc test to check the individual differences was by Dunn's test. The levels of probability including 0.05, 0.01, and 0.001 were taken as statistically significant.

## 3. Results

### 3.1. Physicochemical characterization of the nanoparticles

The GNRs were synthesized by a seed-mediated growth method. The TEM image shows the uniform rod morphology of the developed GNRs with 50–60 nm length and 15–20 nm diameter (Fig. 1b). Spherical PLGA/GNR/isatin nanocomplexes are obtained with a size of about 250 nm under the dried condition of TEM (Fig. 1c). The GNRs were seen as dark rods dispersed in PLGA nanoparticles as a grey bed, which demonstrates the successful production of the nanocomplexes. In contrast, the hydrodynamic diameter of the PLGA/GNR/isatin nanocomplexes was 180 nm (Fig. 1d). The lack of GNRs (PLGA/isatin) or isatin (PLGA/GNR) in the PLGA nanoparticles contributed to the size reduction to about 160 nm. All the nanosystems exhibited monodispersity with narrow nanoparticle distribution, and ranged between 100 and 300 nm (Fig. 1e). The zeta potential of the GNRs was measured to be +32 mV (Fig. 1f). All the nanocomplexes were found to be negatively charged due to the inclusion of PLGA, which contained the carboxylic end moieties, and this negative surface charge indicated that GNRs were successfully covered with PLGA. The successful development of the nanocomplexes was further verified by FTIR. The presence of characteristic bands at 1760 and 3300  $\text{cm}^{-1}$  from the nanocomplexes is associated with the C=O stretching and N–H stretching of isatin (Fig. 1g). The O–H stretching of PLGA, as represented by the peak centered at 2930  $\text{cm}^{-1}$ , appeared in the spectrum of the nanocomplexes. UV/visible spectroscopy was used to characterize the optical features of GNRs and nanocomplexes. The absorption of PLGA/GNR/isatin nanosystems was observed in the range of 650–1000 nm (Fig. 1h). The nanocomplexes revealed an absorption peak at about 770 nm, which was similar to the absorption of GNRs. This spectrum has potential for efficient PTT with NIR irradiation.

### 3.2. PLGA inclusion increases biocompatibility of GNRs and isatin

The biocompatibility of isatin and nanoparticles was tested in the presence of human keratinocytes using the MTT assay. HaCaT cell viability was decreased following the concentration increase of free isatin (Fig. 1i), meaning cellular viability decreased to 60% with 62.5  $\mu\text{g}/\text{ml}$  isatin. The presence of isatin in nanocomplexes maintained complete viability, suggesting the protection of isatin by PLGA for minimizing cytotoxicity. GNRs at  $\geq 0.5 \mu\text{l}/\text{ml}$  greatly inhibit cell viability (Fig. 1j). The inclusion of GNRs by PLGA showed a viability of nearly 100%, even at GNR concentration up to 4  $\mu\text{l}/\text{ml}$ , indicating the excellent biocompatibility and non-toxicity of the nanocomplexes. Due to their high cytocompatibility, PLGA/GNR/isatin nanocomplexes containing 31.2  $\mu\text{g}/\text{ml}$  isatin (corresponding to 4  $\mu\text{l}/\text{ml}$  GNRs) were employed in the following photothermal experiments.

### 3.3. NIR can induce in vitro heating of nanocomplexes

Next, this study inspected the capability of PLGA/GNR/isatin to generate heat upon NIR irradiation. The measurement started at room temperature, followed by NIR irradiation for 20 min. The nanoparticles produced heat up to the hyperthermia temperature when exposed to NIR (Fig. 1k). The temperature of nanoparticle dispersion increased with greater NIR energy, and a significant increase in temperature from 6 to 15  $^{\circ}\text{C}$  was achieved. The nanocomplexes displayed a fast increase in temperature under NIR irradiation at 0.42  $\text{W}/\text{cm}^2$  and reached a temperature maximum after 20 min (Fig. 1l). The PBS solution showed a

mild temperature increase (about 2  $^{\circ}\text{C}$ ) under the same laser condition. Overall, the nanocomplexes were fabricated with NIR-absorbing nature, thus, the nanosystems could quickly and efficiently convert NIR energy to heat with the on-demand temperature control.

### 3.4. NIR irradiation enhances isatin release from nanocomplexes

This study examined the photothermal effect on the release of isatin from PLGA/GNR/isatin nanocarriers, and the obtained profiles show that isatin released as a function of time would exhibit an initial burst release for both 37  $^{\circ}\text{C}$  and NIR heating (about 45  $^{\circ}\text{C}$ ) (Fig. 1m). No isatin release was detected at the room temperature of about 25  $^{\circ}\text{C}$ . The cumulative release of isatin was found to be 47% after 20 min of NIR exposure, which was significantly greater than that without NIR (36%), thus, it appeared that isatin released from nanocomplexes displayed a temperature-dependent behavior.

### 3.5. The nanocomplexes can be internalized into keratinocytes

The efficacy of photothermal treatment critically depends on the nanoparticle inclusion into the target cells. In order to investigate the uptake of nanoparticles in HaCaT cells, this study loaded rhodamine B as a fluorescent dye into nanocomplexes. By using flow cytometry, a rightward shift of the peak in the histogram, as compared to the control, was observed after nanoparticle treatment (Fig. 2a), and the shift was dose-dependent, which indicates that the nanocomplexes were sufficient to be internalized by HaCaT. The nanoparticle uptake was quantitatively analyzed from flow cytometry. This study found that 47% of the cells were fluorescent after treatment of nanoparticles containing 62.5  $\mu\text{g}/\text{ml}$  isatin (Fig. 2b), and confirmed the nanocomplex uptake in keratinocytes from the fluorescence microscopic images (Fig. 2c). The nanoparticles were predominantly confined in the cytoplasm. The nuclei stained by DAPI were normal in shape, implying a negligible toxicity of the nanoparticles on HaCaT. The lysosomes were labeled by LysoTracker as a green signal. An overlay of lysosomes and nanoparticles was detected, indicating the lysosomal co-localization.

In order to examine whether the combined nanocomplexes and NIR could cause HaCaT death, the cells were stained by live-dead kit and monitored under fluorescence microscopy, where green and red signals were determined to be live and dead cell staining, respectively. Free isatin at 31.2  $\mu\text{g}/\text{ml}$  was slightly efficient to eradicate keratinocytes (Fig. 2d). There were no obvious dead cells in the treatment groups of PLGA/GNR, PLGA/GNR/isatin, and NIR alone. The viability of HaCaT treated with NIR combined with PLGA/GNR and PLGA/GNR/isatin decreased to 65% and 56%, respectively (Fig. 2e), which implies hyperthermia-induced keratinocyte death. In addition, this study used the MTT assay to further quantitatively evaluate the photothermal cytotoxicity of the nanocomplexes. Similar tendency can be confirmed between live-dead staining and MTT analysis (Fig. 2f). The result of MTT demonstrated that free isatin inhibited HaCaT cell growth with a 20% mortality rate. A significant growth inhibition effect toward HaCaT was observed upon NIR treatment on PLGA/GNR and PLGA/GNR/isatin nanoparticles. Compared with PLGA/GNR, isatin incorporated in nanoparticles exhibited stronger growth inhibition on keratinocytes. The neutral red staining also verifies the greater cytotoxicity against keratinocytes treated by combined PLGA/GNR/isatin and NIR than the other treatments (Suppl. Fig. 1). No toxicity was found from the nanoparticle treatment under dark conditions. These results suggest that nanocomplexes would be tolerated in the absence of NIR and effective to eliminate NIR-irradiated cells.

### 3.6. The combined nanocomplexes and NIR induce apoptosis in keratinocytes

This study further investigated the effect of photothermal nanocomposites on the apoptosis of HaCaT. Flow cytometric assay by

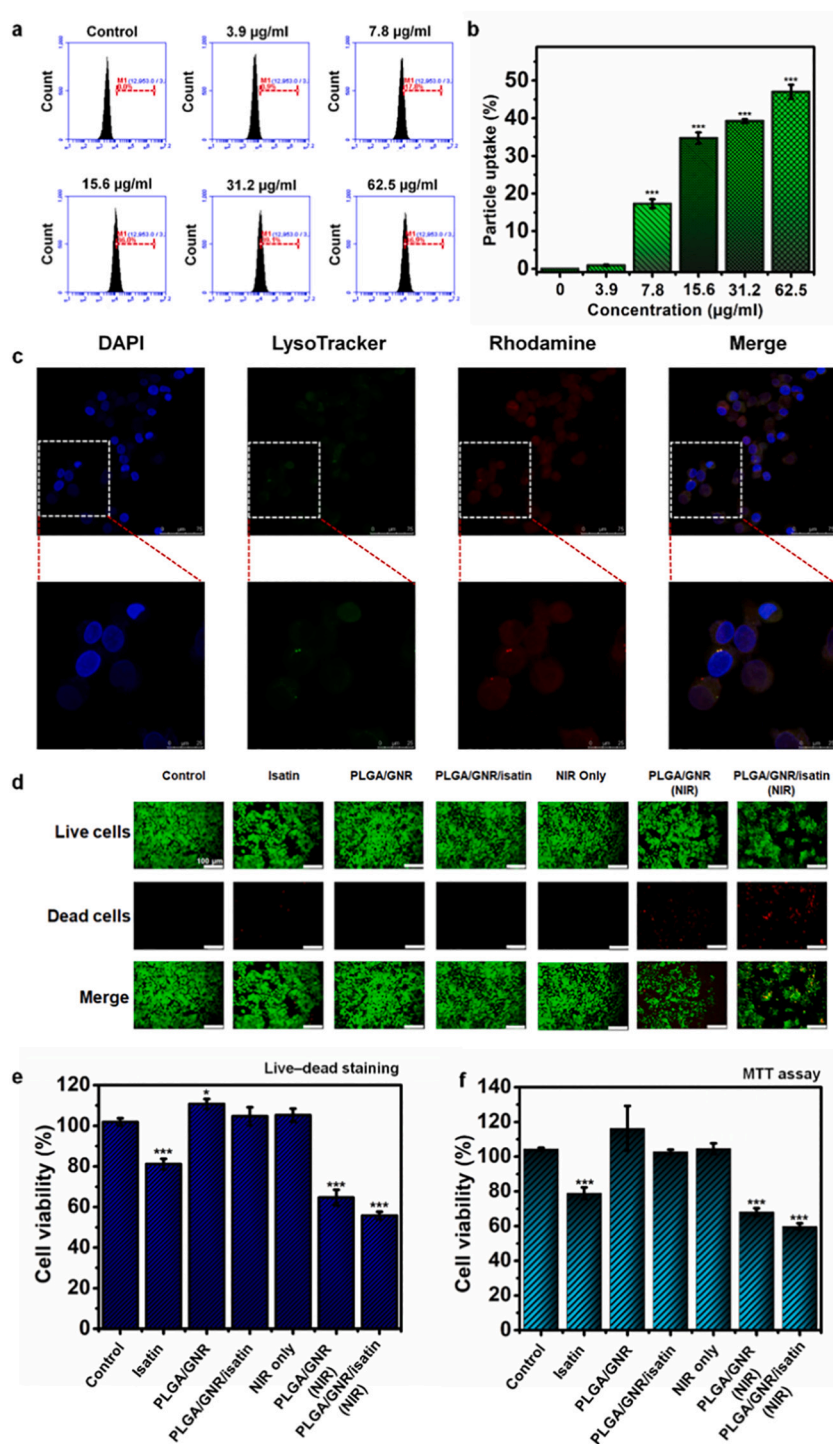


**Fig. 2.** The keratinocyte uptake and antiproliferative activity of the nanocomplexes: (a) Representative flow cytometry histogram of rhodamine B-labeled nanocomplex uptake in human keratinocytes. (b) Percentage of the cell population that has internalized rhodamine 800-labeled nanocomplexes. (c) Overlay of DAPI (blue), LysoTracker (green), and rhodamine B (red) in fluorescence microscopic images showing uptake of rhodamine 800-labeled nanocomplexes in keratinocytes. (d) The images of live-dead keratinocytes after nanocomplex treatment under fluorescence microscopy. (e) The keratinocyte viability of free isatin and nanoparticles with or without NIR irradiation determined by live-dead staining. (f) The keratinocyte viability of free isatin and nanoparticles with or without NIR irradiation determined by MTT assay. Data are expressed as mean  $\pm$  SEM ( $n = 3$ ). \*  $P < 0.05$ , \*\*\*  $P < 0.001$ , compared with control basal levels. (For interpretation of the references to colour in this figure legend, the reader is referred to the web version of this article.)

Annexin V/PI staining was determined. The distribution of viable, early apoptotic, and late apoptotic keratinocytes among the control, PLGA/GNR/isatin, and NIR alone was similar (left panel of Fig. 3a), while treatment with isatin alone significantly increased the apoptosis rate. After irradiation with NIR laser for 20 min, the apoptotic cells treated by PLGA/GNR and PLGA/GNR/isatin increased significantly, demonstrating the efficacy of PTT. The Annexin V/PI-stained keratinocytes show induction of apoptosis by PLGA/GNR/isatin with 16% apoptotic population, as compared to free isatin (8%) and PLGA/GNR (14%) (the right panel of Fig. 3a). The treatment groups with significant apoptosis effect were selected to detect the markers of apoptosis, including

caspase-3, caspase-9, and PARP, as analyzed by Western blotting. Free isatin and combined PLGA/GNR and NIR resulted in an increase in the cleavage of caspase-3 and -9, which triggered the apoptotic process (Fig. 3b and c). Further activation of cleaved caspase-3 and -9 was found for the combined PLGA/GNA/isatin and NIR, suggesting the synergistic effect of the isatin and nanoparticles. The cleaved caspase-3 and -9 in keratinocytes treated by PLGA/GNR/isatin was 2.4- and 4.3-fold higher than the nontreatment control. A similar tendency was detectable in the case of cleaved PARP (Fig. 3d).



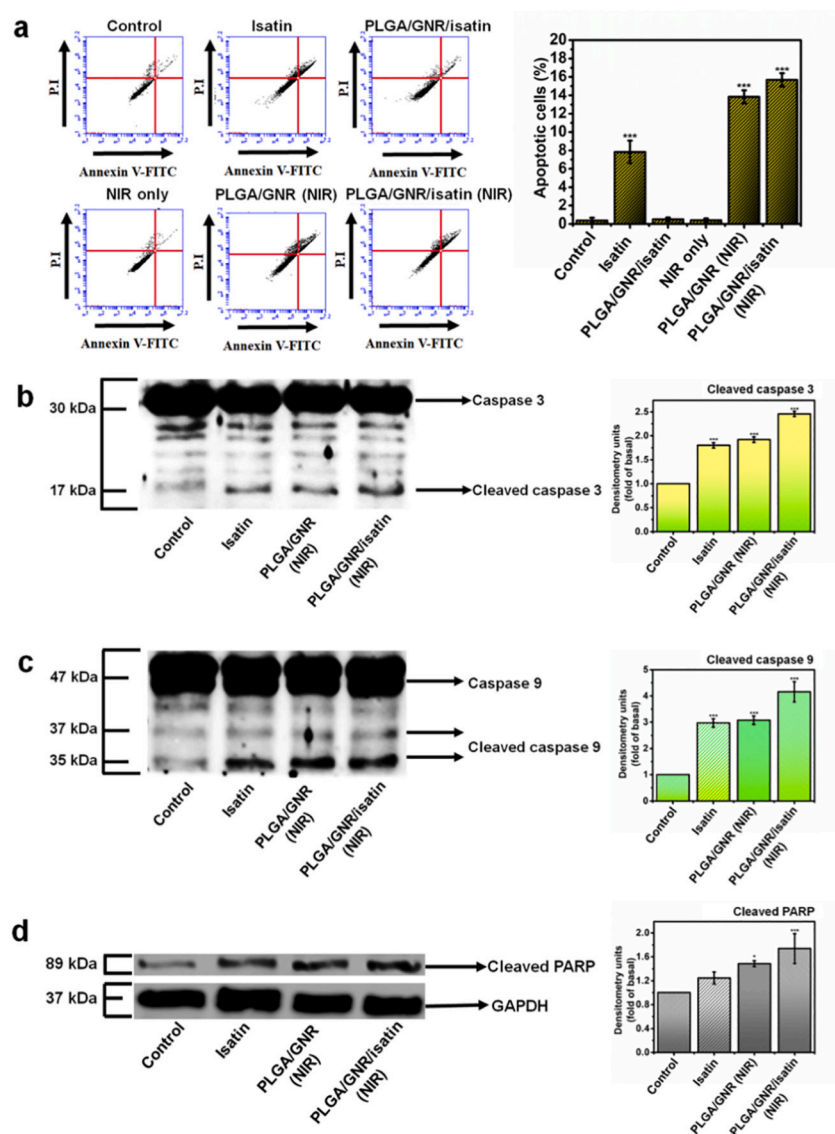


**Fig. 3.** The keratinocyte apoptosis activated by the nano-complexes: (a) Representative flow cytometry histogram of nanocomplex treatment in human keratinocytes stained by Annexin V/PI. (b) The Western blotting assay of caspase-3 in human keratinocytes after treatment of free isatin and the nanocomplexes with NIR irradiation. (c) The Western blotting assay of caspase-9 in human keratinocytes after treatment of free isatin and the nanocomplexes with NIR irradiation. (d) The Western blotting assay of PARP in human keratinocytes after treatment of free isatin and the nanocomplexes with NIR irradiation. Data are expressed as mean  $\pm$  SEM ( $n = 3$ ). \*  $P < 0.05$ , \*\*\*  $P < 0.001$ , compared with control basal levels.

### 3.7. Combined nanocomplexes and NIR mitigate psoriasiform lesion in mice

This study evaluated the antipsoriatic impact of PTT in a murine model. After initiation by IMQ to produce psoriasis-like plaque, nanocomplexes with or without NIR were subcutaneously administered into the lesion. The experimental protocol is depicted in Fig. 4a. The skin appearance, cytokines, and histology were estimated to validate the antipsoriatic efficacy. Both the phenotypic and microscopic skin surface images reveal scaling and erythema after repeated IMQ challenge (Fig. 4b and c), indicating a typical psoriasis feature. No improvement of the psoriatic signs was detected by the treatment of PLGA/GNR/isatin without NIR, whereas, according to the exterior appearance, free isatin and NIR alone could partly alleviate the symptoms. Combined PLGA/GNR/isatin and light showed a superior reduction in scaling and redness than the other treatment groups. As monitored by the IR thermal camera (Fig. 4d), the skin temperature associated with the combined nanoparticles and NIR was increased; while no significant heating effect was visualized in the treatment groups without NIR exposure. In the IMQ challenge model, a psoriasis-like lesion shows a significant increase in cytokine levels (Fig. 4e to 4h). Upon stimulation by IMQ, IL-1 $\beta$  was overexpressed by 2.3-fold as compared to the healthy control (Fig. 4e). All treatment groups alleviated IL-1 $\beta$  upregulation, and combined

nanoparticles and NIR presented the strongest suppression. A similar result is manifested in the case of IL-6 (Fig. 4f). The combined nanocomposites and NIR inhibited IL-23 to the baseline control (Fig. 4g), while the nanocomplexes or NIR alone failed to prevent TNF- $\alpha$  overexpression (Fig. 4h). A downregulatory effect of TNF- $\alpha$  by combined nanoparticles and NIR was identified. Free isatin also showed an inhibitory effect on the overexpression of TNF- $\alpha$ , although this effect did not surpass that of NIR-irradiated PLGA/GNR/isatin.

The in vivo efficacy of PTT on psoriasiform lesions was qualitatively monitored using histology. The H&E image of the control skin reveals normal morphology without damage in the epidermis or dermis (Fig. 5). As observed in the phenotypic images of the skin surface, the occurrence of epidermal hyperplasia in IMQ-treated skin highlighted the scaly plaque. The epidermal thickness was increased to about 3-fold by IMQ treatment as compared to healthy skin. The presence of an elongated rete ridge and immune cell infiltration indicated the development of a psoriasis-like status. Free isatin and PLGA/GNR/isatin without NIR could lower the epidermal thickening and immune cell accumulation. A further improvement was notable in the groups of combined nanocomplexes and NIR. The laser irradiation alone did not affect the epidermal hyperproliferation caused by IMQ. IHC staining with proliferation marker Ki67 displayed that the basal layer stained positive in the control mouse skin. Ki67 largely appeared in the stratum basale of the IMQ-



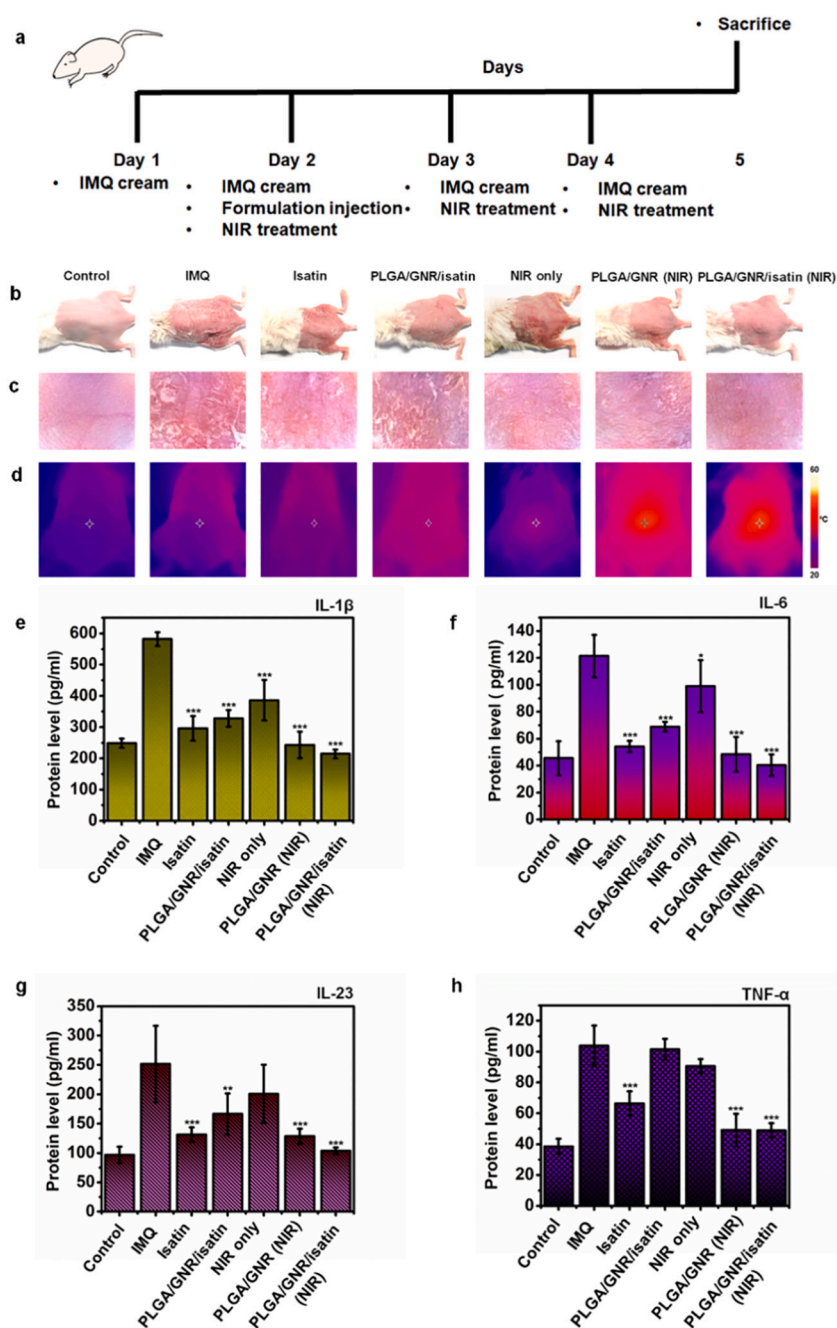


**Fig. 4.** The effect of isatin and the nanocomplexes on psoriasisiform lesion in the murine model evaluated by skin surface appearance and cytokine level: (a) The processes of the induction of psoriasisiform lesion and the administration of nanocomplexes in vivo. (b) The gross images of mouse back skin are represented on Day 5 by digital camera. (c) The close-up images by hand-held digital microscopy. (d) The temperature of skin visualized by a thermal imager. (e) The protein level of IL-1 $\beta$  in psoriasisiform mouse skin. (f) The protein level of IL-6 in psoriasisiform mouse skin. (g) The protein level of IL-23 in psoriasisiform mouse skin. (h) The protein level of TNF- $\alpha$  in psoriasisiform mouse skin. Data are expressed as mean  $\pm$  SEM ( $n = 6$ ). \*  $P < 0.05$ , \*\*  $P < 0.01$ , \*\*\*  $P < 0.001$ , compared with the IMQ treatment alone.

stimulated skin. It was observed that NIR-irradiated nanoparticle treatment showed minimum Ki67 expression among all treatment groups, suggesting a stronger inhibition on cell proliferation. The neutrophil infiltration in the dermis can be visualized by both Ly6G and MPO staining. The IHC exhibited clouds of Ly6G and MPO expression in the dermis after the IMQ challenge. Free isatin and NIR alone suppressed infiltrating neutrophil numbers in psoriasisiform plaque to a certain level. Again, combined nanoparticles and NIR were the most effective. The histological results demonstrate a reduction in the hyperproliferative epidermis and massive inflammatory dermis by PTT.

### 3.8. The photothermal effect and biodistribution of nanocomplexes in vivo

Temperature change of the mouse skin was monitored by thermal imaging after receiving NIR. With 20 min of laser application, the temperature of the PLGA/GNR- and PLGA/GNR/isatin-treated skin

gradually increased, in contrast to the NIR exposure without nanoparticle delivery (Fig. 6a). The temperature of the skin receiving nanoparticles increased 8.5 °C after NIR irradiation. Isatin inclusion did not affect the temperature rising. This result manifests that both PLGA/GNR and PLGA/GNR/isatin possess photothermal effect upon irradiation in vivo. The subcutaneous nanoparticles underwent NIR treatment for three times: immediately after injection (Day 2), 1 day after injection (Day 3), and 2 days after injection (Day 4). The temperature increment in the mouse skin was approximate on Day 2 and Day 3, and reached an increased temperature of about 8.5 °C (Fig. 6b). The PLGA/GNR/isatin nanocomplexes revealed a lower temperature increment on Day 4 than Day 2 and Day 3, which could be explained by the lower accumulation of nanoparticles in the skin after several days. The increased temperature in nanocomplex-treated skin can be recovered to the baseline control within 10 min after NIR application is stopped (Fig. 6c and Suppl. Fig. 2).

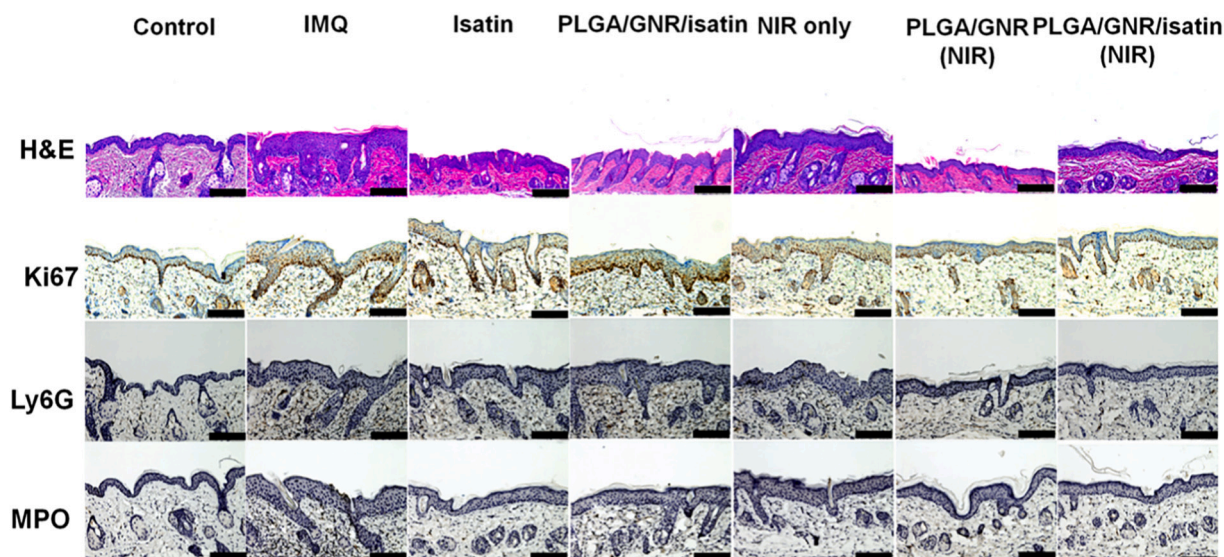


Fig. 5. The effect of isatin and the nanocomplexes on psoriasiform lesion in the murine model evaluated by histology including H&E staining, Ki67, Ly6G, and MPO.

In vivo and ex vivo bioimaging of the organs were performed after subcutaneous injection of the nanocomposites, which allowed for the investigation of biodistribution. A significant deposition of the nanoparticles in skin is observed immediately after injection (the left panel of Fig. 6d). The NIR signal derived from the DiR-loaded nanoparticles gradually faded with the increase of time from Day 2 to Day 5. The NIR intensity of nanoparticle-treated skin, as quantified from IVIS, confirms the decrease of nanoparticle distribution in skin following the time increase (the right panel of Fig. 6d). The ex vivo bioimages of the organs excised on Day 5 were also examined to achieve better insight into the biodistribution of nanoparticles. Regarding the PLGA/GNR/isatin nanocomplexes with NIR laser treatment, significantly higher accumulation was visualized in the liver, followed by the spleen (Fig. 6e), while nanoparticle deposition in the heart, lung, and kidney was negligible. The nanoparticle distribution in skin and other organs was not changed in the condition without NIR (Fig. 6f and g, Suppl. Figs. 3 and 4). This study also confirmed no auto-NIR signal in the skin or the other organs of the mice receiving NIR irradiation only (Suppl. Figs. 5 and 6).

### 3.9. The nanocomplexes show no damage on skin and organs

Since the nanoparticles exhibited some accumulation in the organs, the toxic effect of the nanocomplexes was evaluated in the healthy mice. The gross and close-up appearance of the skin surface displayed no sign of change after nanoparticle accumulation, as compared to the control (Fig. 7a and b). TEWL as the indicator of skin barrier function remained unchanged by isatin or nanoparticle treatment as compared to the vehicle control (Fig. 7c), suggesting the maintenance of the cutaneous barrier function. The pH and erythema of the recorded skin were comparable between the vehicle control and the nanoparticle-treated groups (Fig. 7d and e). This study also assessed the H&E histology of the key organs after subcutaneous administration of the isatin and nanocomplexes. No evidence of abnormal pathology is found by isatin or nanocomplex management (Fig. 7f). These results signified that the PLGA/GNR/isatin nanocomposites were well-tolerated toward normal tissues to achieve PTT.

## 4. Discussion

Excessive keratinocyte proliferation is the hallmark of lesional psoriatic skin [24]. The hyperproliferative keratinocytes respond to cytokines in the lesion to generate proinflammatory mediators for exacerbating inflammation, which caused a positive feedback loop.

Keratinocyte proliferation inhibition is a potential approach to mitigate psoriatic lesion. This study developed a novel PTT strategy to restrain hyperproliferation induced by psoriasis, and both in vitro and in vivo experiments demonstrated successful keratinocyte proliferation and hyperplasia inhibition by PLGA/GNR/isatin nanoparticles combined with NIR. As photo-absorbing materials, our nanocomplexes showed a controlled photothermal effect when irradiating the energy of 0.30–0.54 W/cm<sup>2</sup>. This heating effect of our nanoparticles was feasible since the NIR irradiation beyond 0.1 W/cm<sup>2</sup> triggered tissue hyperthermia [25]. NIR further accelerated isatin release from the nanoparticles. The GNR-loaded nanocomplexes could be served to control isatin release upon external NIR triggering, and this increased release could be attributed to the heat destabilizing PLGA matrix. PLGA undergoes a glassy-to-rubbery state transition upon NIR exposure [26], which might lead to the disassociation of intermolecular interaction between isatin and the nanocomplexes. No isatin release from the nanosystems was detected in the room temperature (25 °C). It may suggest a stable isatin residence inside the nanocarriers when storage before the administration. According to the HaCaT cytotoxicity profiles, free isatin exhibited low biocompatibility. The release result inferred that isatin remained in the PLGA at low temperature, and showed low toxicity to keratinocytes. The sudden temperature increase by NIR and the concurrent isatin release from nanocomplexes were ideal to exert the bioactivities of isatin under PTT.

Keratinocytes play a main role in triggering the early pathogenesis of psoriasis. This study used the keratinocyte cell line (HaCaT) to estimate the in vitro effect of PTT using our nanocomplexes. As it is expected that the cell internalization of photothermal materials is fundamental for PTT, the produced heat can be sufficient to induce cell death [27]. The results of this study show that PLGA/GNR/isatin nanocarriers could penetrate the keratinocyte membrane to enter into the cytoplasm. The GNRs in the cytoplasm would absorb the NIR and convert it into heat, leading to cell damage. As proved in our release experiment, the heat also triggered isatin release from the nanoparticles, and NIR-generated heat can also elevate the cellular endocytosis of the nanoparticles [28]. These effects synergistically enhanced the keratinocyte death during PTT. The nanocomposites are more effective in inhibiting the keratinocyte proliferation than free isatin, which could be due to the facile uptake of the nanoparticles.

Reduction of keratinocyte apoptosis is a specific pathogenesis in psoriasis [29]. An important strategy for treating psoriasis is to induce keratinocyte apoptosis, as the flow cytometry demonstrated an increased HaCaT apoptosis by combining nanocomplexes and NIR.

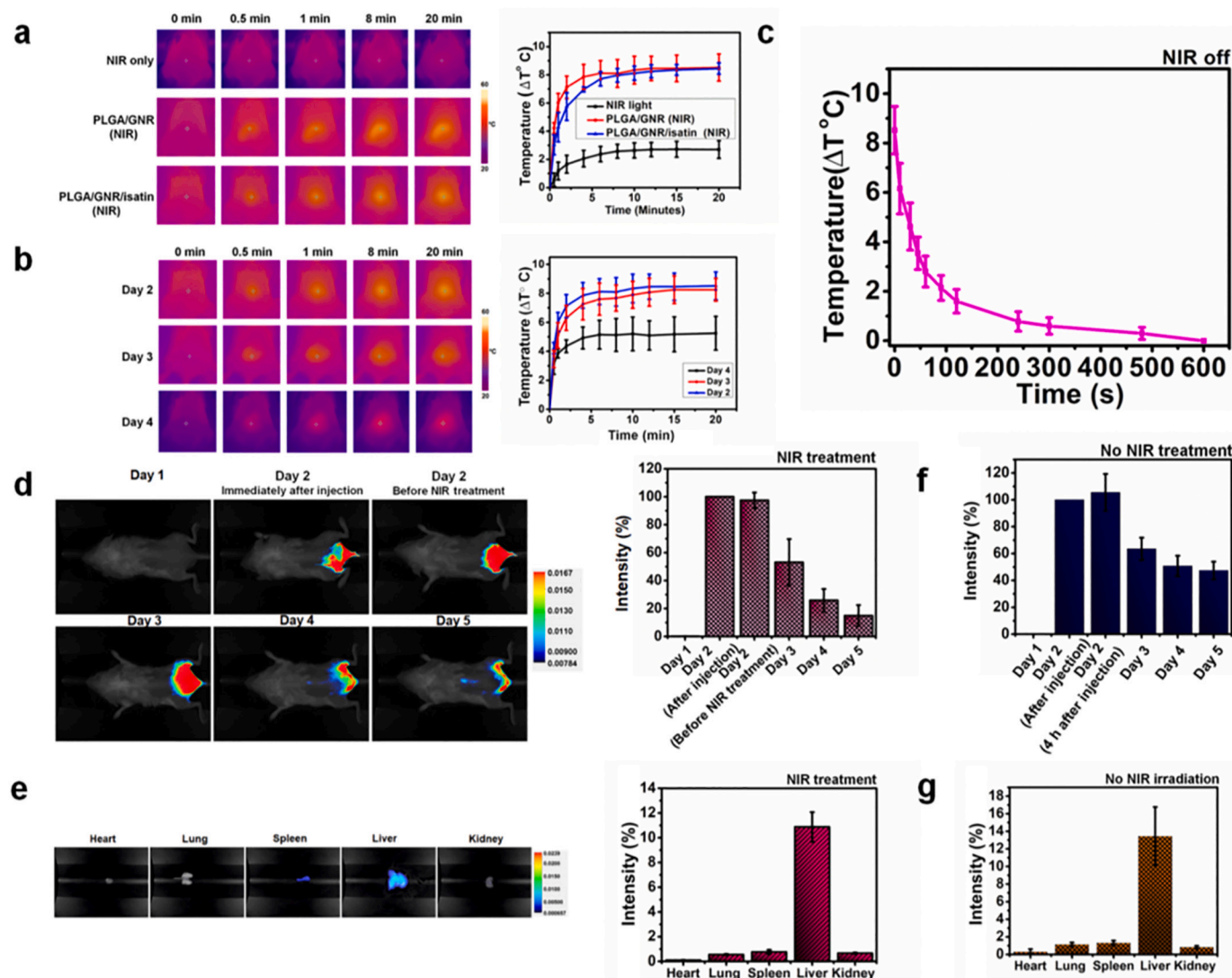


**Fig. 6.** The photothermal effect and biodistribution of the nanocomplexes under NIR irradiation: (a) The temperature of mouse skin after treatment of PLGA/GNR and PLGA/GNR/isatin under NIR irradiation monitored by a thermal imager. (b) The temperature of mouse skin after treatment of PLGA/GNR/isatin under NIR irradiation on Day 2, Day 3, AND Day 4 monitored by a thermal imager. (c) The temperature of mouse skin as a function of time after the stopping of NIR irradiation. (d) The skin distribution of DiR-labeled nanocomplexes as a function of time under NIR irradiation (from Day 1 to Day 5). (e) The organ distribution of DiR-labeled nanocomplexes under NIR irradiation on Day 5. (f) The DiR intensity in skin treated by DiR-labeled nanocomplexes as a function of time in the condition without NIR irradiation (from Day 1 to Day 5). (g) The DiR intensity in organs treated by DiR-labeled nanocomplexes in the condition without NIR irradiation on Day 5. Data are expressed as mean  $\pm$  SEM ( $n = 6$ ).

Annexin V is a marker to determine early apoptosis, as induced by the loss of membrane integrity, while PI is the fluorescent intercalating agent of late apoptosis to bind with DNA. Both markers were increased after photothermal treatment, indicating that the keratinocyte death caused by the nanocomplexes was due to both the disrupted membrane and DNA integration. The activation of caspases and PARP is known in the induction of the apoptotic process, meaning a caspase pathway was involved in the keratinocyte apoptosis evoked by photothermal nanocomposites. In cytoplasm, cytochrome *c* forms a complex with procaspase-9, and the resulting apoptosome activates caspase-9 by cleavage. Activated caspase-3 is a downstream cleavage product of cleaved caspase-9 for the execution of apoptotic keratinocyte death [30]. The evidence suggests that PLGA/GNR/isatin combined with NIR acted by inducing apoptosis of keratinocytes for antiproliferation. This mechanism of action was previously reported to demonstrate the PTT-induced apoptosis against tumors [31]. In addition, the same action occurred in the proliferative keratinocytes.

There are two biological transparency windows for NIR: one is the

wavelength of 650–950 nm (NIR-i window) and another is the wavelength of 1000–1350 nm (NIR-ii window). As NIR-ii is proved to possess deeper tissue penetration capacity [32], this study employed 785 nm as the wavelength resource, meaning there is no need for deep light penetration during skin targeting. PTT with nanocomplexes efficiently increased the mouse skin temperature by 8.5 °C. The photothermal treatment of subcutaneous nanocomplexes exerted a therapeutic effect on IMQ-induced psoriasiform lesions, with reduced scaling, erythema, and plaque thickness. The level of epidermal hyperproliferation, as determined by Ki67, was shown to be inhibited by PTT. The nanocomplexes combined with NIR led to complete regression of some cytokines in psoriatic skin. For PTT, the temperature should be raised to the hyperthermia range (3–10 °C increment) to cause cancer cell death [33], and a similar effect may be fitted for keratinocytes. Our nanocomplexes could increase the psoriasiform skin temperature within the hyperthermia range, thus, giving the potential to inhibit keratinocyte proliferation. Epidermal keratinocytes act as an integral part of the resident immune system [34], as keratinocytes release several



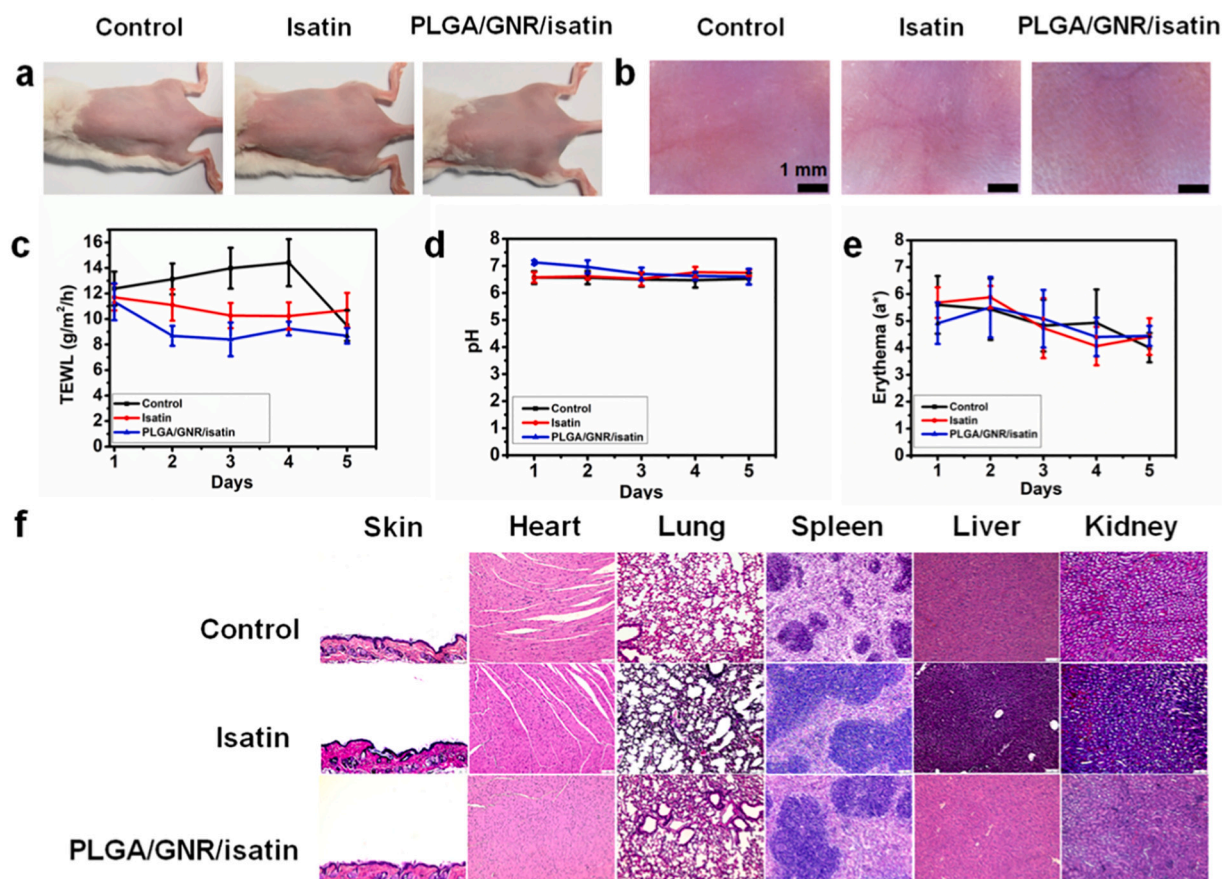


**Fig. 7.** The tolerance of free isatin and PLGA/GNR/isatin nanocomplexes on healthy mice: (a) The gross images of mouse back skin were represented on Day 5 by digital camera. (b) The close-up images by hand-held digital microscopy. (c) The TEWL of mouse back skin is represented within 5 days. (d) The pH of mouse back skin is represented within 5 days. (e) The erythema ( $a^*$ ) of mouse back skin is represented within 5 days. (f) The H&E-stained histology of the organs on Day 5. Data are expressed as mean  $\pm$  SEM ( $n = 6$ ).

proinflammatory mediators including IL-1, IL-6, IL-8, and TNF- $\alpha$  [35]. The hyperproliferative keratinocytes amplify the inflammatory response to induce chemotaxis for attracting and activating neutrophils, macrophages, and T cells [36]. The activated immune cells secrete cytokines and chemokines to stimulate keratinocytes. This positive feedback loop increases the resistance of keratinocytes to apoptosis [37]. The *in vivo* result showed that the photothermal nanocomplexes blocked epidermal hyperplasia, decreased neutrophil infiltration, and attenuated the IMQ-induced upregulation of some cytokines.

Psoriatic plaque contains high levels of IL-1 $\beta$ , IL-6, IL-23, and TNF- $\alpha$ , which are secreted by keratinocytes, neutrophils, macrophages, and mast cells [38]. Both IL-23 and TNF- $\alpha$  axis pathways involve the proliferation and cytokine formation by keratinocytes [39]. IL-1 $\beta$  and TNF- $\alpha$  are reported to link the psoriasis pathogenesis through keratinocyte hyperproliferation [40]. These proinflammatory mediators evoked by IMQ could be recovered to the baseline control by PTT developed in this study. TNF- $\alpha$  controls the proinflammatory environment in psoriasis to facilitate neutrophil recruitment in the dermis [39]. IL-6 is also known to exacerbate neutrophil activation in psoriatic lesions [41]. The IHC stained by Ly6G and MPO manifested large neutrophil accumulation in the dermis after IMQ stimulation, and this infiltration could be effectively restrained by combining nanocomposites and NIR. Free isatin showed the capability to inhibit cytokine upregulation in psoriasiform plaque. However, isatin inclusion in nanocomplexes did not further reduce the cytokine level or neutrophil migration after NIR application. Isatin is reported as an anti-inflammatory compound to suppress cytokine production, such as TNF- $\alpha$  and neutrophil infiltration [17,18]. The treatment of isatin alone for psoriasiform lesions was sufficient to inhibit

proinflammatory mediators and neutrophil accumulation to a satisfactory level, while further incorporation in the nanocomplexes showed limited efficacy to increase the anti-inflammatory activity. Another possibility could be the offset effect of the oxidative condition between the isatin and the nanocomplexes. ROS deficiency largely increases the severity of psoriasis, while the recovery of ROS generation can alleviate the symptoms [42]. Increased ROS production by phototherapy is favorable for clinical course, as the induction of keratinocyte apoptosis is usually associated in ROS-mediated pathways [43]. Since isatin can act as an antioxidant [44], the apoptosis prompted by NIR-irradiated nanocomposites was counteracted; however, further investigation is required to explore the detailed mechanisms. Although the offset effect on cytokine production occurred between the isatin and nanocomplexes, the upregulated cytokine reduction by PLGA/GNR/isatin was still stronger than that by the free isatin and PLGA/GNR. This *in vitro* cell study also demonstrated that the combination of isatin and nanocarriers further increased apoptosis and caspase cleavage. The protocol of PTT in the animal model should be optimized to accomplish the synergistic inhibition of combining isatin and PTT for psoriasiform inflammation. Although no effect was observed in the reduction of hyperplasia, NIR alone displayed some effects to restrain cytokine overexpression in psoriasiform lesions. Depending upon the selection of wavelength, energy, and irradiance [25], light irradiation within the window from UV to NIR is beneficial to treat cutaneous inflammation. NIR with low fluence shows the capability to treat psoriasis via suppressing the density of Langerhans cells and the hypersensitivity reaction in skin [45,46].

While the nanoparticles were mainly located in the psoriasiform area after subcutaneous delivery, this deposition was decreased following



NIR irradiation for three times within 3 days, which was reasonable since light-responsive nanoparticles such as GNRs undergo degradation after repeated heating [47]. A novel treatment for psoriasis that causes fewer adverse effects is desirable. Nanocomplex deposition on skin for 5 days did not produce morphological or physiological changes to healthy skin. Thus the damage to normal tissue by nanoparticles could be avoided. Some nanocomplexes were found in the liver and spleen after subcutaneous injection, indicating the distribution from the skin to the circulation system. As the histology showed no damage to the peripheral organs by the nanoparticles, the concern about the possible toxicity of nanocomplexes could be ignored.

The antipsoriatic potential of PTT was attributed to the combination of GNR-loaded nanocomplexes with NIR irradiation, coupled with the facile cell uptake and temperature-responsive release, which collectively resulted in the enhanced antiproliferation on keratinocytes. With respect to nidus targeting by the NIR laser, PTT can be advantageous for psoriasis treatment, as it leads to an effective therapy with less irritation in normal tissue. Moreover, only one injection and three NIR treatments were required to achieve successful improvement of psoriasiform signs. However, each therapeutic approach has its own advantages and drawbacks. A limitation of this present work was that IMQ-stimulated psoriasis-like plaque could not completely simulate actual human psoriasis, thus, the evidences obtained in the mouse model should be cautiously extrapolated for humans. Of course, further exploration of PTT on human psoriasis is a focus of future work. Another limitation was the subcutaneous route for delivering the nanocomplexes. This study intended to employ an injection to confirm the total delivery of the nanoparticles near the lesion. The topical administration cannot assure complete nanoparticle delivery due to the barrier feature of skin for retarding permeation, which might complicate the evaluation of the antipsoriatic effect. Nevertheless, topical application can be a suitable choice in clinical circumstances due to its convenience and non-invasiveness. Whether topical delivery is beneficial for PTT to treat psoriasis remains to be elucidated. Isatin itself could exhibit some effects to mitigate psoriasiform inflammation, especially the cytokine over-expression. The synergistic impact of combined isatin and nanocomplexes was not very significant in the *in vivo* condition. It is hypothesized that the reduction of isatin dose in the nanosystems may both exhibit a significant synergism and decreased isatin toxicity. Further studies with different treatment schedules should be carried out to improve the synergistic effect of isatin and nanocomplexes.

## 5. Conclusions

This present work investigated the antipsoriatic potential of photothermal nanocomplexes through keratinocyte apoptosis, developed a nanoformulation incorporating GNRs and isatin in a PLGA matrix. A stable nanosystem with a NIR-absorbing nature was obtained. The *in vitro* assay on HaCaT demonstrated the facile uptake of the nanocomplexes. Combined nanocomplexes and NIR efficiently produced the photothermal effect to induce keratinocyte apoptosis via caspase and PARP pathways. In the psoriasiform mouse model, the nanocomplexes could be injected subcutaneously, and then, combined with a NIR laser to successfully clear the psoriasis-like plaque. The antiproliferative effect of PTT resulted in the reduction in proinflammatory cytokines and neutrophil recruitment, and contributed to clearing the inflammatory lesions. These evidences suggest the on-demand delivery systems for mitigating psoriatic hyperproliferation. The as-prepared nanocomplexes allow for hyperthermia-induced apoptosis of keratinocytes, and serve as a promising therapy against hyperproliferation. This study provided insight regarding the potential use of PTT as a safe and effective treatment modality for psoriasis. To the best of our knowledge, this is the first paper investigating the effect of PTT on psoriasis management.

Supplementary data to this article can be found online at <https://doi.org/10.1016/j.jconrel.2021.04.005>.

## Data availability

The raw/processed data required to reproduce these findings cannot be shared at this time due to technical or time limitations.

## Acknowledgements

The authors are grateful for the financial support from Ministry of Science and Technology of Taiwan (MOST-107-2320-B-182-016-MY3) and Chang Gung Memorial Hospital (CMRPD1K0051-2).

## References

- [1] J.E. Greb, A.M. Goldminz, J.T. Elder, M.G. Lebwohl, D.D. Gladman, J.J. Wu, N. N. Mehta, A.Y. Finlay, A.B. Gottlieb, Psoriasis, *Nat. Rev. Dis. Primers* 2 (2016) 1–17.
- [2] C. Albanesi, S. Madonna, P. Gisondi, G. Girolomoni, The interplay between keratinocytes and immune cells in the pathogenesis of psoriasis, *Front. Immunol.* 9 (2018) 1549.
- [3] T.H. Huang, C.F. Lin, A. Alalaiwe, S.C. Yang, J.Y. Fang, Apoptotic or antiproliferative activity of natural products against keratinocytes for the treatment of psoriasis, *Int. J. Mol. Sci.* 20 (2019) 2558.
- [4] L. Barrea, M.C. Savanelli, C. Di Somma, M. Napolitano, M. Megna, A. Colao, S. Savastano, Vitamin D and its role in psoriasis: an overview of the dermatologist and nutritionist, *Rev. Endocr. Metab. Disord.* 18 (2017) 195–205.
- [5] D.M.W. Balak, S. Gerdes, A. Parodi, L. Salgado-Boquete, Long-term safety of oral systemic therapies for psoriasis: a comprehensive review of the literature, *Dermatol. Ther.* 10 (2020) 589–613.
- [6] L. Kemény, E. Varga, Z. Novak, Advances in phototherapy for psoriasis and atopic dermatitis, *Expert. Rev. Clin. Immunol.* 15 (2019) 1205–1214.
- [7] M. Tampa, M.I. Sarbu, C. Matei, C.I. Mitran, M.I. Mitran, C. Caruntu, C. Constantin, M. Neagu, S.R. Georgescu, Photodynamic therapy: a hot topic in dermatology, *Oncol. Lett.* 17 (2019) 4085–4093.
- [8] N. Fernandes, C.F. Rodrigues, A.F. Moreira, I.J. Correia, Overview of the application of inorganic nanomaterials in cancer photothermal therapy, *Biomater. Sci.* 8 (2020) 2990–3020.
- [9] R. Zhu, F. Gao, J.G. Piao, L. Yang, Skin-safe photothermal therapy enabled by response release of acid-activated membrane-disruptive polymer from polydopamine nanoparticle upon very low laser irradiation, *Biomater. Sci.* 5 (2017) 1596–1602.
- [10] J. Sun, L. Song, Y. Fan, L. Tian, S. Luan, S. Niu, L. Ren, W. Ming, J. Zhao, Synergistic photodynamic and photothermal antibacterial nanocomposite membrane triggered by single NIR light source, *ACS Appl. Mater. Interf.* 11 (2019) 26581–26589.
- [11] A. Onaciu, C. Braicu, A.A. Zimta, A. Moldovan, R. Stiuflu, M. Buse, C. Ciocan, S. Buduru, I. Berindan-Neagoe, Gold nanorods: from anisotropy to opportunity. An evolution update, *Nanomedicine* 14 (2019) 1203–1226.
- [12] K. Hao, Y. He, H. Lu, S. Pu, Y. Zhang, H. Dong, X. Zhang, High-sensitive surface plasmon resonance microRNA biosensor based on streptavidin functionalized gold nanorods-assisted signal amplification, *Anal. Chim. Acta* 954 (2017) 114–120.
- [13] C.J. Gustafson, C. Watkins, E. Hix, S.R. Feldman, Combination therapy is psoriasis: an evidence-based review, *Am. J. Clin. Dermatol.* 14 (2013) 9–25.
- [14] A. Medvedev, O. Buneva, V. Glover, Biological targets for isatin and its analogues: implications for therapy, *Biol. Targets Ther.* 1 (2007) 151–162.
- [15] J. Song, L. Hou, C. Ju, J. Zhang, Y. Ge, W. Yue, Isatin inhibits proliferation and induces apoptosis of SH-SY5Y neuroblastoma cells in vitro and in vivo, *Eur. J. Pharmacol.* 702 (2013) 235–241.
- [16] P. Pakravan, S. Kashanian, M.M. Khodaei, F.J. Harding, Biochemical and pharmacological characterization of isatin and its derivatives: from structure to activity, *Pharmacol. Rep.* 65 (2013) 313–335.
- [17] M.E. Matheus, F. de Almeida Vidante, S.J. Garden, A.C. Pinto, P.D. Fernandes, Isatins inhibit cyclooxygenase-2 and inducible nitric oxide synthase in a mouse macrophage cell line, *Eur. J. Pharmacol.* 556 (2007) 200–206.
- [18] E.A.R. Socca, A. Luiz-Ferreira, F.M. de Faria, A.C. de Almeida, R.J. Dunder, L. P. Manzo, A.R.M.S. Brito, Inhibition of tumor necrosis factor- $\alpha$  and cyclooxygenase-2 by isatin: a molecular mechanism of protection against TNBS-induced colitis in rats, *Chem. Biol. Interact.* 209 (2014) 48–55.
- [19] R. Agabegi, S.H. Rasta, M. Rahmati-Yamchi, R. Salehi, E. Alizadeh, Novel chemophotothermal therapy in breast cancer using methotrexate-loaded folic acid conjugated Au@SiO<sub>2</sub> nanoparticles, *Nanoscale Res. Lett.* 15 (2020) 62.
- [20] D.K. Ledezma, P.B. Balakrishnan, J. Cano-Mejia, E.E. Sweeney, M. Hadley, C. M. Bollard, A. Villagra, R. Fernandes, Indocyanine green-nexturastat A-PLGA nanoparticles combine photothermal and epigenetic therapy for melanoma, *Nanomaterials* 10 (2020) 161.
- [21] T.K. Sau, C.J. Murphy, Seeded high yield synthesis of short Au nanorods in aqueous solution, *Langmuir* 20 (2004) 6414–6420.
- [22] C.H. Chu, Y.C. Wang, L.A. Tai, L.C. Wu, C.S. Yang, Surface deformation of gold nanorod-loaded poly(dl-lactide-co-glycolide) nanoparticles after near infrared irradiation: an active and controllable drug release system, *J. Mater. Chem.* 20 (2010) 3260–3264.

- [23] R. Singh, A.S. Karakoti, W. Self, S. Seal, S. Singh, Redox-sensitive cerium oxide nanoparticles protect human keratinocytes from oxidative stress induced by glutathione depletion, *Langmuir* 32 (2016) 12202–12211.
- [24] L. Pohla, A. Ottas, B. Kaldvee, K. Abram, U. Soomets, M. Zilmer, P. Reemann, V. Jaks, K. Kingo, Hyperproliferation is the main driver of metabolomic changes in psoriasis lesional skin, *Sci. Rep.* 10 (2020) 3081.
- [25] D. Barolet, F. Christiaens, M.R. Hamblin, Infrared and skin: friend or foe, *J. Photochem. Photobiol. B Biol.* 155 (2016) 78–85.
- [26] G.K. Thirunavukkarasu, G.R. Nirmal, H. Lee, M. Lee, I. Park, J.Y. Lee, On-demand generation of heat and free radicals for dual cancer therapy using thermal initiator-and gold nanorod-embedded PLGA nanocomplexes, *J. Ind. Eng. Chem.* 69 (2019) 405–413.
- [27] S.P. Singh, S.B. Alvi, D.B. Pemmaraju, A.D. Singh, S.V. Manda, R. Srivastava, A. K. Rengan, NIR triggered liposome gold nanoparticles entrapping curcumin as in situ adjuvant for photothermal treatment of skin cancer, *Int. J. Biol. Macromol.* 110 (2018) 375–382.
- [28] S. Kang, R. Baskaran, B. Ozlu, E. Davaa, J.J. Kim, B.S. Shim, S.G. Yang, T<sub>1</sub>-positive Mn<sup>2+</sup>-doped multi-stimuli responsive poly(L-DOPA) nanoparticles for photothermal and photodynamic combination cancer therapy, *Biomedicines* 8 (2020) 417.
- [29] C.F. Mok, C.M. Xie, K.W.Y. Sham, Z.X. Lin, C.H.K. Cheng, 1,4-Dihydro-2-naphthoic acid induces apoptosis in human keratinocyte: potential application for psoriasis treatment, *Evid.-based Complement. Altern. Med.* 2013 (2013) 792840.
- [30] T. Elango, A. Thirupathi, S. Subramanian, P. Ethiraj, H. Dayalan, P. Gnanaraj, Methotrexate treatment provokes apoptosis of proliferating keratinocyte in psoriasis patients, *Clin. Exp. Med.* 17 (2017) 371–381.
- [31] M. Pérez-Hernández, P. del Pino, S.G. Mitchell, M. Moros, G. Stepien, B. Pelaz, W. J. Parak, E.M. Gálvez, J. Pardo, J.M. de la Fuente, Dissecting the molecular mechanism of apoptosis during photothermal therapy using gold nanoprisms, *ACS Nano* 9 (2015) 52–61.
- [32] R. Gan, H. Fan, Z. Wei, H. Liu, S. Lan, Q. Dai, Photothermal response of hollow gold nanorods under femtosecond laser irradiation, *Nanomaterials* 9 (2019) 711.
- [33] B. Poinard, S.Z.Y. Neo, E.L.L. Yeo, H.P.S. Heng, K.G. Neoh, J.C.Y. Kah, Polydopamine nanoparticles enhance drug release for combined photodynamic and photothermal therapy, *ACS Appl. Mater. Interfaces* 10 (2018) 21125–21136.
- [34] A. Alalaiwe, C.F. Lin, C.Y. Hsiao, E.L. Chen, C.Y. Lin, W.C. Lien, J.Y. Fang, Development of flavanone and its derivatives as topical agents against psoriasis: the prediction of therapeutic efficiency through skin permeation evaluation and cell-based assay, *Int. J. Pharm.* 581 (2020) 119256.
- [35] E. Ogawa, Y. Sato, A. Minagawa, R. Okuyama, Pathogenesis of psoriasis and development of treatment, *J. Dermatol.* 45 (2018) 264–272.
- [36] J. Gao, J. Guo, Y. Nong, W. Mo, H. Fang, J. Mi, Q. Qi, M. Yang, 18β-Glycyrrhetic acid induces human HaCaT keratinocytes apoptosis through ROS-mediated PI3K-Akt signaling pathway and ameliorates IMQ-induced psoriasis-like skin lesions in mice, *BMC Pharmacol. Toxicol.* 21 (2020) 41.
- [37] W.H. Boehncke, N.C. Brembilla, Unmet needs in the field of psoriasis: pathogenesis and treatment, *Clin. Rev. Allergy Immunol.* 55 (2018) 295–311.
- [38] G. Monteleone, F. Pallone, T.T. MacDonald, S. Chimenti, A. Costanzo, Psoriasis: from pathogenesis to novel therapeutic approaches, *Clin. Sci.* 120 (2011) 1–11.
- [39] W.H. Boehncke, M.P. Schön, Psoriasis, *Lancet* 386 (2015) 983–994.
- [40] L.M. Johnson-Huang, M.A. Lowes, J.G. Krueger, Putting together the psoriasis puzzle: an update on developing targeted therapies, *Dis. Model. Mech.* 5 (2012) 423–433.
- [41] Z.C. Lin, P.W. Hsieh, T.L. Hwang, C.Y. Chen, C.T. Sung, J.Y. Fang, Topical application of anthranilate derivatives ameliorates psoriatic inflammation in a mouse model by inhibiting keratinocyte-derived chemokine expression and neutrophil infiltration, *FASEB J.* 32 (2018) 6783–6795.
- [42] C. Mo, D. Shetti, K. Wei, Erianin inhibits proliferation and induces apoptosis of HaCaT cells via ROS-mediated JNK/c-Jun and AKT/mTOR signaling pathways, *Molecules* 24 (2019) 2727.
- [43] E. Racz, E.P. Prens, Phototherapy and photochemotherapy for psoriasis, *Dermatol. Clin.* 33 (2015) 79–89.
- [44] A. Andreani, S. Burnelli, M. Granaiola, A. Leoni, A. Locatelli, R. Morigi, M. Rambaldi, L. Varoli, M.A. Cremonini, G. Plauci, R. Cervellati, E. Greco, New isatin derivatives with antioxidant activity, *Eur. J. Med. Chem.* 45 (2010) 1374–1378.
- [45] K. Danno, N. Sugie, Effects of near-infrared radiation on the epidermal proliferation and cutaneous immune function in mice, *Photodermatol. Photoimmunol. Photomed.* 12 (1996) 233–236.
- [46] P. Zhang, M.X. Wu, A clinical review of phototherapy for psoriasis, *Lasers Med. Sci.* 33 (2018) 173–180.
- [47] A. Curcio, A.K.A. Silva, S. Cabana, A. Espinosa, B. Baptiste, N. Menguy, C. Wilhelm, A. Abou-Hassan, Iron oxide nanoflowers@CuS hybrids for cancer tri-therapy: interplay of photothermal therapy, magnetic hyperthermia and photodynamic therapy, *Theranostics* 9 (2019) 1288–1302.

UDC 615.076:615.322:581.45:581.8

DOI: 10.15587/2519-4852.2021.230288

## PHYTOCHEMICAL RESEARCH AND ANTI-INFLAMMATORY ACTIVITY OF THE DRY EXTRACTS FROM NORTHERN Highbush BLUEBERRY LEAVES

Oleksandr Stremoukhov, Oleh Koshovyi, Mykola Komisarenko, Igor Kireyev, Andriy Gudzenko, Michal Korinek, Tsong-Long Hwang, Meng-Hua Chen, Olha Mykhailenko

All over the world, non-steroidal anti-inflammatory drugs (NSAIDs) are taken annually by about three hundred million people and this figure is constantly increasing. At the same time, NSAIDs are also one of the most common causes of side effects of drug therapy. The development and implementation of new anti-inflammatory drugs, including those of plant origin, with minimal side effects is an urgent task of modern pharmaceutical science. *Vaccinium corymbosum* L. (family Ericaceae), which is gaining more and more popularity among berry crops and is successfully cultivated in Ukraine, is promising in this direction for research.

**The aim:** phytochemical analysis of dry extracts from blueberry leaves to establish the possibility of creating new drugs with anti-inflammatory activity.

**Materials and methods.** The objects of the study were dry extracts of northern highbush blueberry leaves. The content of amino acids and phenolic compounds was determined by HPLC and spectrophotometry. The prototypal activity was studied in vivo and in vitro.

**Research results.** 4 dry extracts were obtained from northern highbush blueberry leaves. In the extracts obtained by HPLC, 7 amino acids were identified, including 3 essential ones: arginine, histidine, and phenylalanine. As a result of the HPLC study, 7 phenolic compounds were identified in extracts from the leaves of northern highbush blueberry: 5 flavonoids – rutin, quercetin-3-O-glucoside, kaempferol-3-O-glucoside, quercetin and kaempferol and 2 hydroxycinnamic acids, chlorogenic and caffeic acid. For the first time, the anti-inflammatory effect of extracts from blueberry leaves was investigated. It was revealed that extract 1 at a dose of 50 mg/kg and extract 4 modified with arginine at a dose of 25 mg/kg have the highest anti-inflammatory activity.

**Conclusions.** The results of the conducted studies indicate that extracts from the leaves of northern highbush blueberry in terms of the content of biologically active substances are promising sources for the creation of new drugs and dietary supplements with anti-inflammatory activity

**Keywords:** northern highbush blueberry, dry extract, phenolic compounds, amino acid, anti-inflammatory activity

### How to cite:

Stremoukhov, O., Koshovyi, O., Komisarenko, M., Kireyev, I., Gudzenko, A., Korinek, M., Hwang, T.-L., Chen, M.-H. Mykhailenko, O. (2021). Phytochemical research and anti-inflammatory activity of the dry extracts from northern highbush blueberry leaves. ScienceRise: Pharmaceutical Science, 2 (30), 40–48. doi: <http://doi.org/10.15587/2519-4852.2021.230288>

© The Author(s) 2021

This is an open access article under the Creative Commons CC BY license

### 1. Introduction

Inflammation is a typical pathological process that underlies many diseases, is widespread, is accompanied by severe clinical manifestations and is the cause of partial or complete disability of large groups. Worldwide, non-steroidal anti-inflammatory drugs (NSAIDs) are taken by about three hundred million people annually and this number is constantly increasing [1]. At the same time, NSAIDs are also one of the most common causes of side effects of drug therapy. In the United States, NSAIDs are the 15th most common cause of death. Thus, in the United States alone, about 16,500 patients die each year from NSAID gastropathies, and in the United Kingdom - about 2,000 [2, 3]. Development and introduction of new anti-inflammatory drugs, including herbal ones, with minimal side effects is an urgent task of modern pharmaceutical science.

*Vaccinium corymbosum* L. (Ericaceae family), which is gaining more and more popularity among berry crops and is successfully cultivated in Ukraine, is promising

in this direction for research. Northern highbush blueberry is a deciduous plant [4, 5]. During the collection of fruits and pruning of bushes, a large volume of leaves remains, so the study of BAS of this raw material is relevant [6].

The main active ingredients of Northern highbush blueberry are phenols and their glycosides (hydroquinone, arbutin and methylarbutin) [7], hydroxycinnamic acids, coumarins, flavonoids (kaempferol, quercetin, astragaline, hyperoside, herbacetin, 8), luteocetin, tannins and their metabolites and terpenes ( $\alpha$ -pinene and  $\beta$ -pinene) [10, 11]. Such a rich composition of phenolic compounds creates the preconditions for the development of new raw materials from this raw material with anti-inflammatory activity.

**The aim of the work** was to conduct a phytochemical analysis of dry extracts from the leaves of Northern highbush blueberry to establish the possibility of creating new drugs with anti-inflammatory activity.

## 2. Planning (methodology) of research

Given the previous experience of creating extracts from the leaves of plants of the family Ericaceae, it is planned to obtain extracts, modify them, investigate the

phytochemical profile and anti-inflammatory activity to establish the possibility of using them as anti-inflammatory agents (Fig. 1).

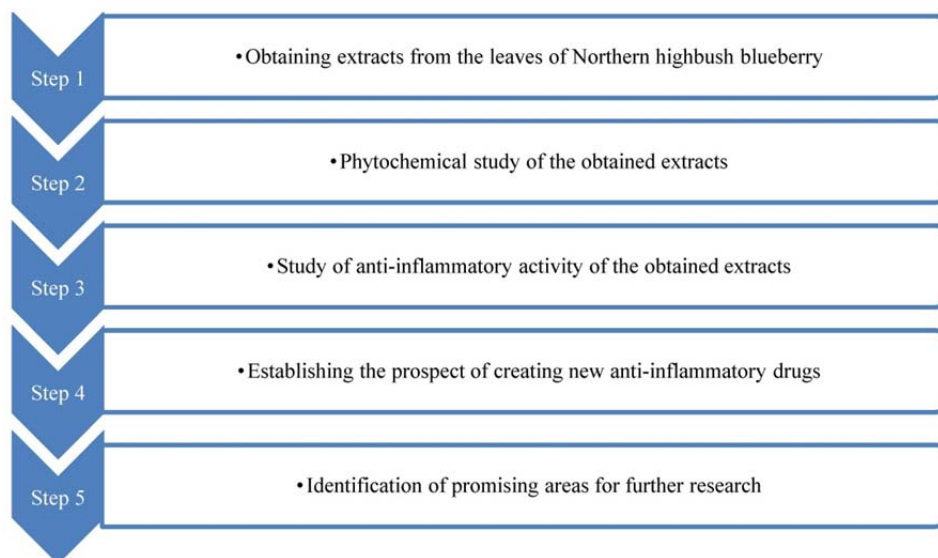


Fig. 1. Scheme of research of extracts from the leaves of Northern highbush blueberry

## 3. Materials and methods

### 3.1. Plant material

Plant raw material, *V. corymbosum* L. leaves, were collected in growing season, June-July, 2020, from Kharkov region, Ukraine області (GPS: 49°27'41.1'' N, 36°50'42.7'' E). Species identification was carried out by prof. Gontova T.M. at the Department of Botany, the National University of Pharmacy, Ukraine. Plant raw material was air-dried in darkness at room temperature. For chemical analysis, the raw material was ground to a particle size of 2–3 mm.

### 3.2. Obtaining extracts

Four extracts were obtained from Northern highbush blueberry leaves as follows: 200.0 g of Northern highbush blueberry leaves, crushed to a particle size of 2–3 mm, were placed in a flask, filled with 1000.0 ml of 50 % ethanol solution, extracted overnight at room temperature. The extraction was repeated three times with new portions of the extractant of 600.0 ml. The resulting extracts were combined, settled and filtered. The filtrate was evaporated using a rotary vacuum evaporator “Heidolph 2 WBeCo, Laborata 400 efficient” (Germany) to a dry extract (Extract 1).

Amino acids are able to form salts, conjugates, amides, etc. with other BAS (biologically active substances) extracts, while changing their bioavailability, solubility and pharmacodynamic profile [12, 13]. Depending on the conditions of amino acid addition, different products can be formed, so we proposed three ways of introducing amino acids: mechanical mixing and adding to the solution of the extract with different acidifying agents (acetic and citric acid).

To 5 g of the obtained dry extract 1 was added arginine in three times the equimolar amount relative to the total amount of phenolic compounds, which was 2.61 g.

The mixture was mixed in a mortar to a homogeneous mass (extract 2).

5 g of the obtained dry extract 1 was dissolved in 50 ml of 50 % ethanol solution, 15 % acetic acid solution was added to pH 4. 2.61 g of arginine was added to the flask with the obtained solution, followed by refluxing in a water bath until complete dissolution and left to infuse for 24 hours. After that, the solution was evaporated to dryness using a rotary vacuum evaporator (extract 3).

5 g of the obtained dry extract 1 was dissolved in 50 ml of 50 % ethanol solution, citric acid was added to pH 5 with constant stirring in a water bath. 2.61 g of arginine was added to the flask with the resulting solution, followed by refluxing in a water bath until complete dissolution and left to infuse overnight. After that, the solution was evaporated to dryness using a rotary vacuum evaporator (extract 4). Subsequently, extracts 1–4 were used for analysis.

### 3.3. Analysis of the chemical composition of extracts

#### 3.3.1. Investigation of phenolic compounds by HPLC

Separation of the sum of phenolic compounds was carried out by HPLC [14, 15] on a high-performance liquid chromatograph Agilent Technologies (model 1100), which is equipped with a flow-through vacuum degasser G1379A, a four-channel low-pressure gradient pump G13111A, an automatic injector G1313A, a column thermostat G13116A and a diode-matrix detector G1316A. A 2.1×150 mm chromatographic column filled with an octadecylsilyl sorbent with a grain size of 3.5 μm “ZORBAX-SB C-18” was used for analysis. The analysis was performed under the following conditions: thermostat temperature – 35 °C; the flow rate of the mobile phase – 0.25 ml/min; as the mobile phase used solution A (0.1 % phosphoric acid, 180 μl/l triethylna-



mine, 3 ml/l tetrahydrofuran in water) and solution B (MeOH) in a ratio of 90:10 (first 8 min), 70:30 (8 to 24 min), and from 24 min used only solution B; the working pressure of the eluent is 240–300 kPa. The following detection parameters were set during the analysis: measurement scale – 1.0; scan time – 0.5 s; spectrum removal parameters – each peak 190–600 nm [14]. Sample preparation: 50.0 mg (exact portion) of the extract was weighed in a 5.0 ml test tube and adjusted to the mark with methanol. After 30 min in an ultrasonic bath, the sample was insisted at room temperature for 3–4 hours, then the tube was again placed on an ultrasonic bath for 15 min, then the solution was filtered through a Teflon filter with a pore size of 0.45 µm in a vial for analysis. The sample volume is 2 µl. Identification of phenolic compounds was performed by the retention time of hydroxycinnamic acid and flavonoid standards and their spectral characteristics [16, 17].

### 3.3.2. Determination of the quantitative content of phenolic compounds

*Total polyphenols.* Quantitative determination of total polyphenols was carried out by spectrophotometry in terms of pyrogallol according to the pharmacopoeial method (SPhU 2.0) [18–20].

*Total flavonoids.* Determination of total flavonoids was carried out by absorption spectrophotometry in terms of rutine, which is present in the leaves in the predominant amount. (SPhU 2.0,) [19, 20, 22].

*Hydroxycinnamic acids.* Quantitative determination of hydroxycinnamic acids was carried out by the modified method of absorption spectrophotometry in terms of chlorogenic acid (SPhU 2.0) [19, 22, 23].

### 3.3.3. Investigation of amino acids compounds by HPLC

Determination of amino acid content was performed using Agilent 1260 Infinity HPLC System (degasser, binary pump, autosampler; single-quadrupole mass spectrometer Agilent 6120 with electrospray ionization (ESI); OpenLAB CDS Software. Zorbax RX-SIL column (1.8 µm, 46 mm × 50 mm, Agilent) with protective filter. Under the conditions of the HPLC study used a gradient mode using a buffer solution: A – H<sub>2</sub>O (HCOOH 0.1 %) and a solution of organic modifier: B – CH<sub>3</sub>CN (HCOOH 0.1 %). The flow rate is 0.4 ml/min. Injection volume was 10 µl. Column temperature 40 °C. MS detection conditions: ion source: API-ES; ion scan mode 50–300 m/z; mode of extraction of chromatograms by individual ions depending on molecular weight, EIS; positive polarity. The work used acetonitrile “HPLC Super gradient” (Avantor performance materials inc, Poland) and formic acid (pure, AppliChem GmbH, Darmstadt). Highly purified water (18 MΩ at 25 °C) was prepared using the Direct Q 3UV water purification system (Millipore, Molsheim, France). Amino acids (QDA qualifications) – glycine, alanine, serine, valine, threonine, methionine, histidine, phenylalanine, arginine, tryptophan [19, 24, 25].

## 3.4. Study of anti-inflammatory activity of extracts

### 3.4.1. In vivo study in a model of carrageenan edema

The study of anti-inflammatory activity of highbush blueberry extracts was conducted at the Clinical-diagnostic center of NUPh under the guidance of prof. Kireev I. V. The experimental work was performed in the scope of simple pharmacological screening. Animals were standardized for physiological and biochemical parameters and were in vivarium in accordance with sanitary and hygienic standards on a standard diet. During the experiment with animals, they behaved in accordance with the International principles of the European convention for the protection of vertebrate animals used for experiments and other scientific purposes [26].

The study of anti-inflammatory activity of highbush blueberry extracts was carried out in accordance with the guidelines “Preclinical studies of drugs” [27]. The experiments were performed on male rats weighing 180–220 g, which were divided into 6 groups of 6 animals each. The first group – control, the sixth group – intact animals. To study the effect of the obtained blueberry extracts on the course of the exudative phase of inflammation, a model of rat paw edema caused by subplanar administration of a phlogogenic agent – carrageenan solution was used. The paw volume was measured before and every hour until the time of the greatest development of edema (4 hours). For 2 h and immediately after the introduction of the phlogogenic agent, the animals were injected intraperitoneally with blueberry extracts at doses of 15, 25, 50, 75 and 100 mg/kg. The effect of blueberry extracts was evaluated on the ability to suppress swelling of the paws of rats. As a drug – a comparison with the known anti-inflammatory effect used diclofenac sodium.

### 3.4.2. Assessment of anti-inflammatory activity using in vitro assay

Blood was taken from healthy human donors using a protocol approved by the Chang Gung Memorial Hospital review board. Neutrophils were isolated according to the standard procedure described before [28]. The inhibition of superoxide anion generation was measured by the reduction of ferricytochrome C as previously described [29]. Elastase release representing the degranulation from azurophilic granules was evaluated as described before [30]. Experimental conditions have been described in detail earlier [31].

## 3.5. Statistics

Student's t-test was used to statistically test the hypothesis of the probability of differences between the indicators of different groups. Statistical processing of the results was done by calculating the arithmetic mean, the average error of the arithmetic value, the reliability of the differences between results by the methods of variation statistics (SPhU 2.0, Vol.1 – 5.3, 5.3.N1) using Statistica 6.0 program and Word Excel. The number of repetitions of experiments (n) equals 5 [19].

#### 4. Research results

The obtained extracts are brownish-yellow powders with a characteristic specific odor. The yield of dry extract 1 from the leaves of blueberries was 27.35 %. Extract 2 was brownish-yellow in color, but sometimes

had white patches of arginine, while extracts 3 and 4 were uniformly light brown in color.

Qualitative composition and quantitative content of free amino acids in blueberry leaf extracts were performed by HPLC (Table 1).

Table 1

Amino acid content (%) in extracts of highbush blueberry leaves

| Amino acid    | Extract 1 | Extract 2  | Extract 3 | Extract 4  |
|---------------|-----------|------------|-----------|------------|
| Glycine       | 1.02±0.03 | 0.63±0.06  | 0.67±0.06 | 0.81±0.04  |
| Alanine       | 0.66±0.03 | 0.66±0.03  | 0.66±0.03 | 0.65±0.02  |
| Serine        | 1.50±0.04 | 0.98±0.07  | 0.93±0.04 | 0.95±0.06  |
| Valine        | 0.53±0.04 | 0.33±0.05  | 0.35±0.02 | 0.34±0.03  |
| Histidine     | 0.22±0.01 | 0.15±0.01  | 0.15±0.02 | 0.14±0.01  |
| Phenylalanine | 0.33±0.04 | 0.23±0.02  | 0.19±0.01 | 0.21±0.03  |
| Arginine      | 1.16±0.04 | 35.09±1.18 | 32.1±0.95 | 31.82±0.76 |

Determination of the qualitative composition and quantitative content of phenolic compounds in the study objects was performed by HPLC (Table 2, Fig. 2).

Quantitative determination of the content of the

main groups of phenolic compounds (total polyphenols, flavonoids and hydroxycinnamic acids) in extracts of blueberry leaves was performed by spectrophotometry by pharmacopoeial methods (Table 3).

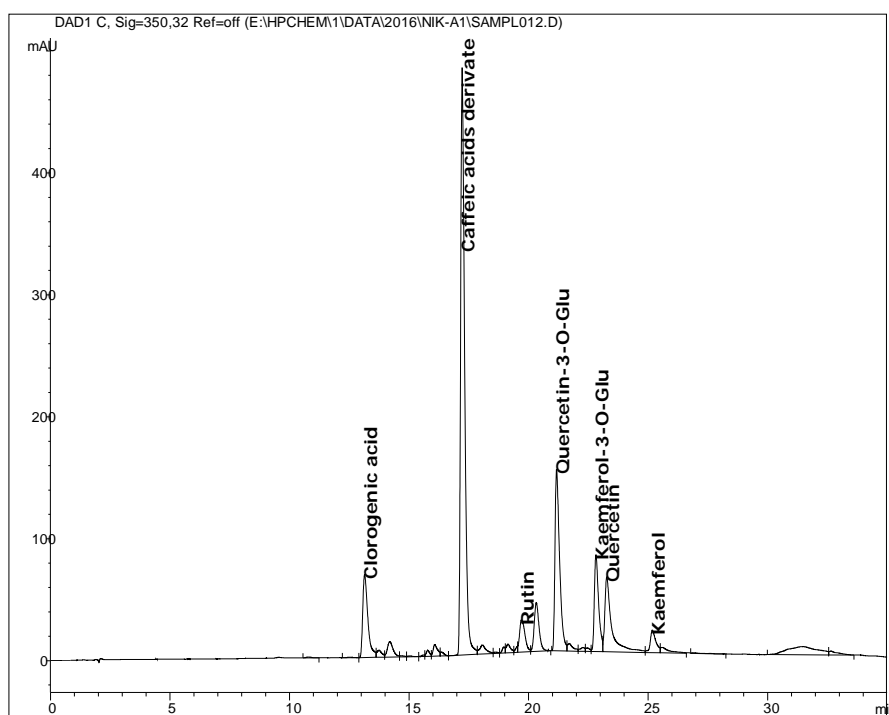


Fig. 2. Typical chromatogram of phenolic compounds of extract 1 from highbush blueberry leaves

Table 2

Quantitative content of phenolic compounds in highbush blueberry extracts

| No. | Compound                 | Retention time, min. | Content in the extract, mg/100 g |         |         |         |
|-----|--------------------------|----------------------|----------------------------------|---------|---------|---------|
|     |                          |                      | 1                                | 2       | 3       | 4       |
| 1.  | Chlorogenic acid         | 13.14                | 1217.21                          | 799.10  | 719,19  | 759,09  |
| 2.  | Caffeic acid             | 17.22                | 3124.65                          | 2051.33 | 1846,20 | 1948,63 |
| 3.  | Routine                  | 19.70                | 474.88                           | 311.76  | 280,59  | 296,15  |
| 4.  | Quercetin-3-O-glucoside  | 21.17                | 2293.65                          | 1507.05 | 1356,34 | 1431,60 |
| 5.  | Kaempferol-3-O-glucoside | 22.82                | 1136.74                          | 746.27  | 671,65  | 708,91  |
| 6.  | Quercetin                | 23.27                | 888.60                           | 583.37  | 525,03  | 554,16  |
| 7.  | Kaempferol               | 25.18                | 206.74                           | 135.73  | 122,15  | 128,93  |
| Sum |                          |                      | 9342,47                          | 6134.61 | 5521.15 | 5827.48 |

Table 3

Quantitative content of phenolic compounds in extracts of highbush blueberry leaves ( $M \pm m$ ,  $n=5$ )

| BAS group                            | The used method  | Quantitative content in the extract, % |           |            |            |
|--------------------------------------|--|--|-----------|------------|------------|
|                                      |  | 1                                      | 2         | 3          | 4          |
| Derivatives of hydroxycinnamic acids | Spectrophotometric method in terms of chlorogenic acid | 2.92±0.12                              | 1.92±0.11 | 1.9±0.12   | 1.83±0.12  |
| Flavonoids                           | Spectrophotometric method in terms of routine          | 3.03±0.11                              | 1.99±0.10 | 1.97±0.11  | 1.77±0.11  |
| Phenolic compounds                   | Spectrophotometric method in terms of pyrogallol       | 18.42±0.97                             | 12.1±0.63 | 11.97±0.62 | 11.86±0.62 |

The obtained results of experimental studies of anti-inflammatory activity of blueberry extracts in the model of carrageenan edema of the hind limb in rats are

given in Table 4. When studying extracts from highbush blueberry leaves in vitro on human blood neutrophils, only extracts 1 and 4 showed activity (Table 5).

Table 4

The effect of blueberry extracts on the development of inflammation of the hind limb in rats in a model of carrageenan edema

| Group of animals  | dose, mg/kg | Limb volume, c.u. |           |           |           |            | Antiexudative activity, % |       |       |       |
|-------------------|-------------|-------------------|-----------|-----------|-----------|------------|---------------------------|-------|-------|-------|
|                   |             | starting point    | 1 h       | 2 h       | 3 h       | 4 h        | 1 h                       | 2 h   | 3 h   | 4 h   |
| Control pathology |             | 42.5±1.47         | 57.5±1.47 | 57.5±1.47 | 62.5±1.47 | 59.5±1.47  |                           |       |       |       |
| Diclofenac sodium | 8           | 36±0.98           | 46±0.98   | 41±0.98   | 47±0.98   | 37±0.98    | 33                        | 67    | 45    | 94    |
| Extract 1         | 15          | 35.5±1.47         | 45.5±4.42 | 47.5±4.42 | 46.5±4.42 | 44±6.88    | 33                        | 20    | 45    | 50    |
|                   | 25          | 36±2.95           | 44.5±0.49 | 45.5±1.47 | 46.5±4.42 | 48.5±5.41  | 43                        | 37    | 48    | 26    |
|                   | 50          | 36.5±2.46         | 43±2.95   | 41.5±1.47 | 41.5±1.47 | 41±0.98    | 57                        | 67    | 75    | 74    |
|                   | 75          | 33±0.98           | 50.5±1.47 | 50.5±4.42 | 53.5±5.41 | 48±2.95    | 17                        | 17    | 2     | 12    |
|                   | 100         | 36±0.98           | 49±4.91   | 49.5±4.42 | 50.5±0.49 | 49.5±0.49  | 13                        | 10    | 28    | 21    |
| Extract 2         | 15          | 37.5±3.44         | 45.5±4.42 | 44.5±5.41 | 47±4.91   | 46.5±5.41  | 47                        | 53    | 53    | 47    |
|                   | 25          | 34±0.98           | 45±4.91   | 41.5±2.46 | 44±1.97   | 46±0.98    | 27                        | 50    | 50    | 29    |
|                   | 50          | 33±0.98           | 43±2.95   | 41.5±1.47 | 43.5±0.49 | 43.5±2.46  | 33                        | 43    | 48    | 38    |
|                   | 75          | 35.5±4.42         | 44±0.98   | 45±0.98   | 47.5±2.46 | 42±0.98    | 43                        | 37    | 40    | 62    |
|                   | 100         | 36±0.98           | 44.5±0.49 | 46±0.98   | 53±0.98   | 46±0.98    | 43                        | 33    | 15    | 41    |
| Extract 3         | 15          | 24.5±2.46         | 36±0.98   | 34±0.98   | 30.5±1.47 | 32±1.97    | 23                        | 37    | 70    | 56    |
|                   | 25          | 26±0.98           | 37.5±1.47 | 35±2.95   | 33±0.98   | 34±1.97    | 23                        | 40    | 65    | 53    |
|                   | 50          | 27.5±2.46         | 39.5±0.49 | 37±0.98   | 37.5±0.49 | 32.5±0.49  | 20                        | 37    | 50    | 71    |
|                   | 75          | 28±0.98           | 36±0.98   | 33±0.98   | 31.5±0.49 | 30.5±1.47  | 47                        | 67    | 83    | 85    |
|                   | 100         | 24±1.97           | 39±1.97   | 37±3.93   | 35.5±0.49 | 35±0.98    | 0                         | 13    | 43    | 35    |
| Extract 4         | 15          | 29.5±3.44         | 39±2.95   | 37±2.95   | 36±0.98   | 33±1.97    | 37                        | 50    | 68    | 79    |
|                   | 25          | 26±0.98           | 35±0.98   | 36.5±0.49 | 32.5±1.47 | 27.5±0.49  | 40                        | 30    | 68    | 91    |
|                   | 50          | 25±0.98           | 34.5±0.49 | 36±0.98   | 34±0.98   | 32±0.98    | 37                        | 27    | 55    | 59    |
|                   | 75          | 30±0.98           | 40±2.95   | 39±1.97   | 38±0.98   | 36±0.98    | 33                        | 40    | 60    | 65    |
|                   | 100         | 25±1.97           | 38±0.98   | 38±0.98   | 32.5±1.47 | 29.5±1.47  | 13                        | 13    | 63    | 74    |
| Arginine          | 15          | 42±1.97           | 48±2.95   | 60±9.83   | 59.5±9.34 | 60.5±10.32 | 60 %                      | -20 % | 13 %  | -9 %  |
|                   | 25          | 39.5±0.49         | 44±1.97   | 47±2.95   | 49±1.97   | 54.5±4.42  | 70 %                      | 50 %  | 53 %  | 12 %  |
|                   | 50          | 36±0.98           | 49.5±2.46 | 55±0.98   | 64±0.98   | 62±0.98    | 10 %                      | -27 % | -40 % | -53 % |
|                   | 75          | 41±0.98           | 50.5±5.41 | 51±0.98   | 67.5±2.46 | 63.5±3.44  | 37 %                      | 33 %  | -33 % | -32 % |
|                   | 100         | 35±0.98           | 46±0.98   | 52.5±2.46 | 57±1.97   | 61.5±8.35  | 27 %                      | -17 % | -10 % | -56 % |

Note: \* –  $p < 0.05$ , in comparison with control pathology

Table 5

Effects of samples on superoxide anion generation and elastase release in FMLP/CB-induced human neutrophils

| Extract | Superoxide anion                      |                    |                     | Elastase release                      |                     |
|---------|---------------------------------------|--------------------|---------------------|---------------------------------------|---------------------|
|         | IC <sub>50</sub> (μg/ml) <sup>a</sup> | Inh %<br>(3 μg/ml) | Inh %<br>(10 μg/ml) | IC <sub>50</sub> (μg/ml) <sup>a</sup> | Inh %<br>(10 μg/ml) |
| 1       | 3.96±0.21                             | 44.08±1.07***      | 70.39±2.39***       |                                       | b                   |
| 4       |                                       |                    | 44.12±1.73***       |                                       | 13.51±3.93*         |

Note: percentage of inhibition (Inh %) at 0.1–10 μg/ml concentration. Results are presented as mean±S.E.M. (n=3). \*  $p < 0.05$ , \*\*  $p < 0.01$ , \*\*\*  $p < 0.001$  compared with the control (fMLP/CB). BL2 and BL3 were insoluble in DMSO, water or 50 % ethanol. <sup>a</sup>Concentration necessary for 50 % inhibition (IC<sub>50</sub>). <sup>b</sup>BL1 (10 μg/ml) induced elastase release in the presence of cytochalasin B by 49.34±3.61 % \*\*\*. Results are presented as mean±S.E.M. (n=3). fMLP/CB induced cell responses were expressed as 100 %.

\*\*\*  $p < 0.001$  compared with the basal (DMSO only)

### 5. Discussion of research results

The main active ingredients of highbush blueberry leaves, which determine their pharmacological action, are phenolic compounds. The solubility of these compounds significantly affects their bioavailability and the strength of the pharmacological effect. It was previously shown that the addition of various amino acids to plant extracts led to an increase in the pharmacological effect and the emergence of new activities [12, 13], so taking into account this experience, three ways to modify highbush blueberry extract with arginine: conventional mechanical displacement and modification in acidic alcohol solution, with two acidifying agents acetic and citric acid. The choice of arginine was due to the fact that the key factor regulating the tone of the vascular endothelium is the most important physiological vasodilator – nitrogen monoxide. This mediator is formed from arginine under the action of Ca<sup>2+</sup> – dependent enzyme NO-synthase (NOS) [34, 35]. 4 dry extracts with similar organoleptic characteristics were obtained.

In the obtained extracts from highbush blueberry leaves by HPLC revealed 7 amino acids (Table 1), including 3 essential: arginine, histidine and phenylalanine. The dominant amino acids in the original extract 1 were glycine, serine and arginine. Due to the fact that when obtaining extracts 2, 3 and 4 was added arginine in significant quantities, its content increased, but not proportionally: when mechanically mixed, this proportion was maintained, but when added to the solution, the amount of free arginine was lower than added, which can be explained by the formation of conjugates of arginine with other BAS extracts. The ratio of other amino acids also changed.

As a result of HPLC, in extracts of highbush blueberry leaves were found 7 phenolic compounds (Table 2): 5 flavonoids - rutin, quercetin-3-O-glucoside, kaempferol-3-O-glucoside, quercetin and kaempferol and 2 hydroxycinnamic chlorogenic acid and caffeic acid. Among hydroxycinnamic acids, caffeic acid was dominant, the content of which was 2.6 times higher than chlorogenic acid, among flavonoids – quercetin-3-D-glucoside and kaempferol-3-D-glucoside.

In the obtained extracts from highbush blueberry leaves, the quantitative content of the main BAS groups was determined by spectrophotometry according to SPhU methods (Table 3). Because spectrophotometric methods of analysis are more accessible, easy to perform and easy to reproduce and are more convenient and appropriate in the development of methods for standardization of extracts. The results of the analysis showed the same trend as HPLC analysis of the content of the main

groups of BAS in the obtained extracts and will be used in the development of regulatory documentation for extracts. The values of spectrophotometric studies differ from HPLC analysis, which can be explained by the lower specificity of the spectrophotometric method and incomplete interpretation of substances in HPLC analysis.

Alteration is the first phase of the inflammatory process, triggers the entire cascade of inflammation, causing destructive changes in the affected tissue [36]. That is why the suppression of inflammation at the stage of its initiation is an important component of the success of anti-inflammatory therapy. The carrageenan edema model is one of the pharmacological models for assessing the anti-inflammatory activity of substances and drugs. This model in rats was used in pharmacological studies [26].

For the first time the anti-inflammatory effect of extracts from the leaves of blueberry was studied (Table 4). Extract 1 at a dose of 50 mg/kg and extract 4 modified with arginine at a dose of 25 mg/kg were found to have the highest anti-inflammatory activity. The effect of arginine on alteration was insignificant and, conversely, at a dose of 50 mg/kg and 100 mg/kg led to an increase in edema, while extracts from the leaves of blueberry had an anti-inflammatory effect. In the composition of the extract 4 available arginine, which was added in the preparation, taking into account this, in an effective dose of 25 mg/kg, the content of BAS from the leaves of blueberries is only 16.7 mg/kg, while without the addition of arginine, these BAS are effective at a dose of 50 mg/kg, indicating potentiation of the action of phenolic compounds of Northern highbush blueberry arginine. This dose (16.7 mg/kg) can relieve inflammation at the level of the comparison drug diclofenac at a dose of 8 mg/kg. Given the side effects of diclofenac sodium on the human body, we consider the use of modified extract 4 of the leaves of Northern highbush blueberry to create a new drug.

Anti-inflammatory activity of blueberry extracts against superoxide anion generation and elastase release in human neutrophils is shown in Table 5.

The major function of neutrophils include respiratory burst, degranulation and NETs formation serve as a first line of defense against pathogens and are important processes in the maintenance of human health. However, these processes need to be precisely regulated. Superoxide is a major radical produced by neutrophils while elastase belongs to major components of azurophilic granules [34] and their uncontrolled amount contributes to several acute and chronic diseases, including sepsis, ARDS, lung injury, arthritis or psoriasis [36]. These



markers of neutrophilic inflammation were shown to be affected by several plant extracts [31].

Blueberry extracts were evaluated in human neutrophils against superoxide anion generation and elastase release triggered by fMLF in CB-primed human neutrophils. According to the results the extracts of blueberry BL1 had a profound effect on superoxide anion generation with IC<sub>50</sub> 3.96 µg/ml (Table 5). Interestingly, the extracts of blueberry BL1 showed enhancing effects on elastase release by human neutrophils and thus may have immune-promoting effects related to the process of degranulation. BL4 exerted inhibitory effects on elastase release (44% at 10 µg/ml). Samples BL2 and BL3 were not tested due to low solubility in DMSO or water.

**Study limitations.** The amount of standard substances was limited during the study of plant raw materials by HPLC, so not all compounds of phenolic nature could be identified in the studied extracts. Only one model of inflammation was used in the study, which limits the ability to determine the mechanism of anti-inflammatory activity.

**Prospects for further research.** The obtained results indicate the possibility of developing drugs based on the leaves of *V. corymbosum*. The results of research can be further used to develop methods of quality control of raw materials and drugs, developed basic schemes for obtaining extracts can be the basis for the development of technology for obtaining substances in industrial conditions. According to the results of phytochemical studies, it was found that extracts from the leaves of *V. corymbosum* are promising for the development of drugs with anti-inflammatory activity.

## 6. Conclusions

From the leaves of highbush blueberry were obtained dry extracts, modified by adding argin in various ways. 7 amino acids and 7 phenolic compounds were found in the obtained extracts: 5 flavonoids - rutin, quercetin-3-O-glucoside, kaempferol-3-O-glucoside, quercetin and kaempferol and 2 hydroxycinnamic acids – chlorogenic and caffeic acids.

For the first time, the anti-inflammatory effect of highbush blueberry leaves extracts was studied in vivo and in vitro. The extract obtained with 50% ethanol solution at a dose of 50 mg/kg and the extract modified with arginine with the addition of citric acid at a dose of 25 mg/kg were found to have the greatest anti-inflammatory activity.

The results of phytochemical and pharmacological studies indicate that extracts of highbush blueberry leaves in terms of BAS are promising sources for the development of new drugs and dietary supplements with anti-inflammatory activity.

## Conflict of interests

The authors declare that they have no conflicts of interest.

## Funding

The research was funded by the Ministry of Health Care of Ukraine at the expense of the State Budget in the framework # 2301020 “Scientific and scientific-technical activity in the field of health protection” on the topic “Modern approaches to the creation of new medicines for a correction of metabolic syndrome”.

## References

- Green, G. A. (2001). Understanding NSAIDs: From aspirin to COX-2. *Clinical Cornerstone*, 3 (5), 50–59. doi: [http://doi.org/10.1016/s1098-3597\(01\)90069-9](http://doi.org/10.1016/s1098-3597(01)90069-9)
- Gislason, G. H., Rasmussen, J. N., Abildstrom, S. Z., Schramm, T. K., Hansen, M. L., Fosbøl, E. L. et. al. (2009). Increased Mortality and Cardiovascular Morbidity Associated With Use of Nonsteroidal Anti-inflammatory Drugs in Chronic Heart Failure. *Archives of Internal Medicine*, 169 (2), 141–149. doi: <http://doi.org/10.1001/archinternmed.2008.525>
- Marcus, M. B. (2011). New study links pain relievers to erectile dysfunction. *USA Today*.
- Export-oriented blueberry cultivation (2020). Available at: <https://investments.vyrashivanie-golubiki>
- Strik, B. C., Finn, C. E., Moore, P. P. (2014). Blueberry cultivars for the Pacific Northwest. *PNW*, 656, 1–13.
- Vaughan, J. G., Geissler, C. A. (2001). *Rorsliny jadalne. Pryszy gnski i Spyłka*. Warszawa
- Müller, D., Schantz, M., Richling, E. (2012). High Performance Liquid Chromatography Analysis of Anthocyanins in Bilberries (*Vaccinium myrtillus* L.), Blueberries (*Vaccinium corymbosum* L.), and Corresponding Juices. *Journal of Food Science*, 77 (4), C340–C345. doi: <http://doi.org/10.1111/j.1750-3841.2011.02605.x>
- Liu, B., Hu, T., Yan, W. (2020). Authentication of the Bilberry Extracts by an HPLC Fingerprint Method Combining Reference Standard Extracts. *Molecules*, 25 (11), 2514. doi: <http://doi.org/10.3390/molecules25112514>
- Ştefănescu (Braic), R., Imre, S., Eşianu, S., Laczko-Zold, E., Dogaru, T. M. (2019). *Vaccinium corymbosum* leaves, a potential source of polyphenolic compounds. *Romanian Biotechnological Letters*, 24 (5), 755–760. doi: <http://doi.org/10.25083/rbl/24.5/755.760>
- Wang, L.-J., Wu, J., Wang, H.-X., Li, S.-S., Zheng, X.-C., Du, H. et. al. (2015). Composition of phenolic compounds and antioxidant activity in the leaves of blueberry cultivars. *Journal of Functional Foods*, 16, 295–304. doi: <http://doi.org/10.1016/j.jff.2015.04.027>
- Becker Pertuzatti, P., Teixeira Barcia, M., Gómez-Alonso, S., Teixeira Godoy, H., Hermosin-Gutierrez, I. (2021). Phenolics profiling by HPLC-DAD-ESI-MSn aided by principal component analysis to classify Rabbiteye and Highbush blueberries. *Food Chemistry*, 340, 127958. doi: <http://doi.org/10.1016/j.foodchem.2020.127958>
- Koshovyi, O., Raal, A., Kireyev, I., Tryshchuk, N., Ilina, T., Romanenko, Y. et. al. (2021). Phytochemical and Psychotropic Research of Motherwort (*Leonurus cardiaca* L.) Modified Dry Extracts. *Plants*, 10 (2), 230. doi: <http://doi.org/10.3390/plants10020230>
- Chaika, N., Koshovyi, O., Ain, R., Kireyev, I., Zupanets, A., Odyntsova, V. (2020). Phytochemical profile and pharmacological activity of the dry extract from *Arctostaphylos uva-ursi* leaves modified with phenylalanine. *ScienceRise: Pharmaceutical Science*, 6 (28), 74–84. doi: <http://doi.org/10.15587/2519-4852.2020.222511>
- Krivoruchko, E., Markin, A., Samoilova, V., Ilina, T., Koshovyi, O. (2018). Research in the chemical composition of the bark of *sorbus aucuparia*. *Ceska a Slovenska Farmacie*, 67 (3), 113–115.

15. De Brum, T., Zadra, M., Piana, M., Boligon, A., Fröhlich, J., de Freitas, R. et. al. (2013). HPLC Analysis of Phenolics Compounds and Antioxidant Capacity of Leaves of *Vitex megapotamica* (Sprengel) Moldenke. *Molecules*, 18 (7), 8342–8357. doi: <http://doi.org/10.3390/molecules18078342>
16. Koshovyi, O., Raal, A., Kovaleva, A., Myha, M., Ilina, T., Borodina, N., Komissarenko, A. (2020). The phytochemical and chemotaxonomic study of *Salvia* spp. growing in Ukraine. *Journal of Applied Biology & Biotechnology*, 8 (3), 29–36. doi: <http://doi.org/10.7324/jabb.2020.80306>
17. Kyslychenko, V., Karpiuk, U., Diakonova, I., Abu-Darwish, M. S. (2010). Phenolic compounds and terpenes in the green parts of *glycine hispida* Advances in Environmental Biology, 4 (3), 490–494
18. Starchenko, G., Hrytsyk, A., Raal, A., Koshovyi, O. (2020). Phytochemical Profile and Pharmacological Activities of Water and Hydroethanolic Dry Extracts of *Calluna vulgaris* (L.) Hull. *Herb. Plants*, 9 (6), 751. doi: <http://doi.org/10.3390/plants9060751>
19. Derzhavna Farmakopeia Ukrainy (2008). Kharkiv: Derzhavne pidpriemstvo «Naukovo-ekspertnyi farmakopeinyi tsentr», 620.
20. Hlushchenko, A. (2014). Quantitative determination of polyphenols in extracts of *Salsola collina* L. *Zbirnyk naukovykh prats spivrobotnykiv NMAPO im. P. L. Shupyka*, 23 (4), 240–245.
21. Shinkovenko, I. L., Kashpur, N. V., Ilyina, T. V., Kovalyova, A. M., Goryacha, O. V., Koshovyi, O. M. et. al. (2018). The immunomodulatory activity of the extracts and complexes of biologically active compounds of *Galium verum* L. herb. *Ceska a Slovenska Farmacie*, 67 (1), 25–29.
22. Kislichenko, V. S., Burlaka, I. S., Karpyuk, U. V. (2013). Flavonoids from the Aerial Part of *Calamagrostis epigeios*. *Chemistry of Natural Compounds*, 49 (1), 133–134. doi: <http://doi.org/10.1007/s10600-013-0532-1>
23. Koshovyi, O. N., Vovk, G. V., Akhmedov, E. Yu., Komissarenko, A. N. (2015). The study of the chemical composition and pharmacological activity of *Salvia officinalis* leaves extracts getting by complex processing. *Azerbaijan Pharmaceutical and Pharmacotherapy Journal*, 15 (1), 30–34.
24. Karpyuk, U. V., Kislichenko, V. S., Gur'eva, I. G. (2015). HPLC Determination of Free and Bound Amino Acids in *Bryonia alba*. *Chemistry of Natural Compounds*, 51 (2), 399–400. doi: <http://doi.org/10.1007/s10600-015-1298-4>
25. Koshevoi, O. N. (2011). Amino-acid and monosaccharide compositions of *Salvia officinalis* leaves. *Chemistry of Natural Compounds*, 47 (3), 492–493. doi: <http://doi.org/10.1007/s10600-011-9976-3>
26. European Convention for the Protection of Vertebrate Animals (1986). Strasbourg. Available at: [https://zakon.rada.gov.ua/laws/show/994\\_137#Text](https://zakon.rada.gov.ua/laws/show/994_137#Text)
27. Stefanov, O. V. (Ed.) (2001). *Preclinical studies of drugs*. Kyiv, 527.
28. Boyum, A. (1968). Isolation of mononuclear cells and granulocytes from human blood. Isolation of mononuclear cells by one centrifugation, and of granulocytes by combining centrifugation and sedimentation at 1 g. *Scandinavian Journal of Clinical and Laboratory Investigation*, 97, 77–89.
29. Yang, S.-C., Chung, P.-J., Ho, C.-M., Kuo, C.-Y., Hung, M.-F., Huang, Y.-T. et. al. (2013). Propofol Inhibits Superoxide Production, Elastase Release, and Chemotaxis in Formyl Peptide–Activated Human Neutrophils by Blocking Formyl Peptide Receptor 1. *The Journal of Immunology*, 190 (12), 6511–6519. doi: <http://doi.org/10.4049/jimmunol.1202215>
30. Hwang, T.-L., Su, Y.-C., Chang, H.-L., Leu, Y.-L., Chung, P.-J., Kuo, L.-M., Chang, Y.-J. (2009). Suppression of superoxide anion and elastase release by C18 unsaturated fatty acids in human neutrophils. *Journal of Lipid Research*, 50 (7), 1395–1408. doi: <http://doi.org/10.1194/jlr.m800574-jlr200>
31. Mykhailenko, O., Korinek, M., Ivanauskas, L., Bezruk, I., Myhal, A., Petrikaitė, V. et. al. (2020). Qualitative and Quantitative Analysis of Ukrainian Iris Species: A Fresh Look on Their Antioxidant Content and Biological Activities. *Molecules*, 25 (19), 4588–4612. doi: <http://doi.org/10.3390/molecules25194588>
32. Zagayko, A. L., Voronina, L. M., Strelchenko, K. V. (2007). *Metabolic Syndrom: Mechanisms of Development and Prospects for Antioxidant Therapy*. Kharkiv: Golden Pages, 216.
33. *Metabolic syndrome*. National Heart, Lung, and Blood Institute. Available at: <https://www.nhlbi.nih.gov/health-topics/metabolic-syndrome> Last accessed: 10.02.2019
34. Gregory, J. W. (2019). Prevention of Obesity and Metabolic Syndrome in Children. *Frontiers in Endocrinology*, 10, 669. doi: <http://doi.org/10.3389/fendo.2019.00669>
35. Chiang, C.-C., Cheng, W.-J., Korinek, M., Lin, C.-Y., Hwang, T.-L. (2019). Neutrophils in Psoriasis. *Frontiers in Immunology*, 10. doi: <http://doi.org/10.3389/fimmu.2019.02376>
36. Chiang, C.-C., Korinek, M., Cheng, W.-J., Hwang, T.-L. (2020). Targeting Neutrophils to Treat Acute Respiratory Distress Syndrome in Coronavirus Disease. *Frontiers in Pharmacology*, 11. doi: <http://doi.org/10.3389/fphar.2020.572009>

Received date 02.03.2021

Accepted date 19.04.2021

Published date 30.04.2021

**Oleksandr Stremoukhov**, Postgraduate Student, Department of Pharmacognosy, National University of Pharmacy, Pushkinska str., 53, Kharkiv, Ukraine, 61002  
E-mail: [stremoukhov\\_alexander@ukr.net](mailto:stremoukhov_alexander@ukr.net)

**Oleh Koshovyi**, Doctor of Pharmaceutical Sciences, Professor, Head of Department, Department of Pharmacognosy, National University of Pharmacy, Pushkinska str., 53, Kharkiv, Ukraine, 61002  
E-mail: [oleh.koshovyi@gmail.com](mailto:oleh.koshovyi@gmail.com)

**Mykola Komisarenko**, PhD, Assistant, Department of Pharmacognosy, National University of Pharmacy, Pushkinska str., 53, Kharkiv, Ukraine, 61002  
E-mail: [a0503012358@gmail.com](mailto:a0503012358@gmail.com)

**Igor Kireyev**, MD, Professor, Director, Educational and Scientific Institute of Applied Pharmacy, National University of Pharmacy, Pushkinska str., 53, Kharkiv, Ukraine, 61002  
E-mail: ivkireev1026@gmail.com

**Andriy Gudzenko**, Doctor of Pharmaceutical Sciences, Head of Department, Department of Chemistry, Private Higher Educational Establishment «Kyiv Medical University», Boyspilska str., 2, Kyiv, Ukraine, 02099  
E-mail: ganvi75@gmail.com

**Michal Korinek**, PhD, Graduate Institute of Natural Products, College of Pharmacy, Department of Biotechnology, College of Life Science, Kaohsiung Medical University, No. 100, Shiquan 1st Road, Sanmin District, Kaohsiung City, Taiwan 80708, Graduate Institute of Natural Products, College of Medicine, Chang Gung University, No. 259, Wenhua 1st Road, Guishan District, Taoyuan City, Taiwan, 33302  
E-mail: mickorinek@hotmail.com


**Tsong-Long Hwang**, Professor, Graduate Institute of Natural Products, College of Medicine, Chang Gung University, No. 259, Wenhua 1st Road, Guishan District, Taoyuan City, Taiwan, 33302, Research Center for Chinese Herbal Medicine, Research Center for Food and Cosmetic Safety, Institute of Health Industry Technology, College of Human Ecology, Chang Gung University of Science and Technology, No. 261, Wenhua 1st Road, Guishan District, Taoyuan City, Taiwan, 33303, Department of Anesthesiology, Chang Gung Memorial Hospital, No. 5, Fuxing Street, Guishan District, Taoyuan City, Taiwan, 33305  
E-mail: htl@mail.cgu.edu.tw

**Meng-Hua Chen**, PhD, Graduate Institute of Natural Products, College of Medicine, Chang Gung University, No. 259, Wenhua 1st Road, Guishan District, Taoyuan City, Taiwan, 33302  
E-mail: menghua0418@gmail.com

**Olha Mykhailenko**, PhD, Associate Professor, Department of Pharmaceutical Chemistry, National University of Pharmacy, Pushkinska str, 53, Kharkiv, Ukraine, 61002  
E-mail: zolya85@gmail.com

## Article

# Cherbonolides M and N from a Formosan Soft Coral *Sarcophyton cherbonnieri*

Chia-Chi Peng <sup>1,†</sup>, Tzu-Yin Huang <sup>2,†</sup>, Chiung-Yao Huang <sup>1</sup>, Tsong-Long Hwang <sup>3,4,5</sup>  and Jyh-Horng Sheu <sup>1,2,6,7,\*</sup>

- <sup>1</sup> Department of Marine Biotechnology and Resources, National Sun Yat-Sen University, Kaohsiung 804, Taiwan; Chia-Chi.Peng@hki-jena.de (C.-C.P.); huangcy@mail.nsysu.edu.tw (C.-Y.H.)
  - <sup>2</sup> Doctoral Degree Program in Marine Biotechnology, National Sun Yat-Sen University, Kaohsiung 804, Taiwan; HuangTY@g-mail.nsysu.edu.tw
  - <sup>3</sup> Graduate Institute of Natural Products, College of Medicine, Chang Gung University, Taoyuan 333, Taiwan; htl@mail.cgu.edu.tw
  - <sup>4</sup> Research Center for Industry of Human Ecology and Graduate Institute of Health Industry Technology, Chang Gung University of Science and Technology, Taoyuan 333, Taiwan
  - <sup>5</sup> Department of Anesthesiology, Chang Gung Memorial Hospital, Taoyuan 333, Taiwan
  - <sup>6</sup> Graduate Institute of Natural Products, Kaohsiung Medical University, Kaohsiung 807, Taiwan
  - <sup>7</sup> Department of Medical Research, China Medical University Hospital, China Medical University, Taichung 404, Taiwan
- \* Correspondence: sheu@mail.nsysu.edu.tw; Tel.: +886-7-525-2000 (ext. 5030); Fax: +886-7-525-5020  
 † These authors contributed equally to this work.



**Citation:** Peng, C.-C.; Huang, T.-Y.; Huang, C.-Y.; Hwang, T.-L.; Sheu, J.-H. Cherbonolides M and N from a Formosan Soft Coral *Sarcophyton cherbonnieri*. *Mar. Drugs* **2021**, *19*, 260. <https://doi.org/10.3390/md19050260>

Academic Editor:  
Orazio Tagliatalata-Scafati

Received: 9 March 2021  
Accepted: 28 April 2021  
Published: 1 May 2021

**Publisher's Note:** MDPI stays neutral with regard to jurisdictional claims in published maps and institutional affiliations.



**Copyright:** © 2021 by the authors. Licensee MDPI, Basel, Switzerland. This article is an open access article distributed under the terms and conditions of the Creative Commons Attribution (CC BY) license (<https://creativecommons.org/licenses/by/4.0/>).

**Abstract:** Two new isosarcophine derivatives, cherbonolides M (1) and N (2), were further isolated from a Formosan soft coral *Sarcophyton cherbonnieri*. The planar structure and relative configuration of both compounds were established by the detailed analysis of the IR, MS, and 1D and 2D NMR data. Further, the absolute configuration of both compounds was determined by the comparison of CD spectra with that of isosarcophine (3). Notably, cherbonolide N (2) possesses the unique cembranoidal scaffold of tetrahydrooxepane with the 12,17-ether linkage fusing with a  $\gamma$ -lactone. In addition, the assay for cytotoxicity of both new compounds revealed that they showed to be noncytotoxic toward the proliferation of A549, DLD-1, and HuCCT-1 cell lines. Moreover, the anti-inflammatory activities of both metabolites were carried out by measuring the N-formyl-methionyl-leucyl-phenylalanine/cytochalasin B (fMLF/CB)-induced generation of superoxide anion and elastase release in the primary human neutrophils. Cherbonolide N (2) was found to reduce the generation of superoxide anion ( $20.6 \pm 6.8\%$ ) and the elastase release ( $30.1 \pm 3.3\%$ ) in the fMLF/CB-induced human neutrophils at a concentration of 30  $\mu$ M.

**Keywords:** isosarcophine derivatives; *Sarcophyton cherbonnieri*; tetrahydrooxepane; cytotoxicity; anti-inflammatory activity

## 1. Introduction

The chemical constituents for soft corals of the genera *Sarcophyton* have been well studied. According to the statistics, more than 500 marine natural products have been isolated from this genus during the past two decades. Among these metabolites, over 300 diterpenoids with the 14 membered cembranoidal skeleton were discovered [1]. Therefore, the *Sarcophyton* genus has been frequently considered to be an important source of the 14 membered ring diterpenoidal skeleton [2–4]. These secondary metabolites help the organisms to defend themselves against the predators and adapt to the environment stress [5]. Furthermore, some of the isolates have been demonstrated to possess various biological activities, such as cytotoxic [6–12], anti-inflammatory [6,7,13–18], neuroprotective [19], antibacterial [19], and antiviral activities [12,20]. The diversified structures and various biological applications of marine natural products thus prompt us to further explore the secondary metabolites from organisms of the *Sarcophyton* genus.



Sarcophine, the dihydrofuran-containing cembranoidal diterpene, is one of the major metabolites in the soft corals of *Sarcophyton* genera [21]. Bernstein et al. discovered this metabolite from the soft coral *Sarcophyton glaucum* in 1974 [22]. Subsequently, the absolute configuration of sarcophine was determined by Kashman et al. in 1977 [23]. Furthermore, Frincke et al. indicated that sarcophine was converted from the other 14 membered diterpene, sarcophytoxide, by auto-oxidation in 1980 [24]. Isosarcophine, an isomer of sarcophine, was proven to be converted from isosarcophytoxide via auto-oxidation and isolated from the soft coral *Sinularia mayi* by Kusumi et al. in 1990 [25]. It was found that isosarcophine showed significant cytotoxicities toward some cancer cell lines [25,26].

Our previous investigation of soft coral *Sarcophyton cherbonnieri* had contributed to the isolation of 13 new cembranoids derived from the isosarcophine [13,14]. In the present study, the continuous chemical investigation of *S. cherbonnieri* resulted in the discovery of two new isosarcophine derivatives, cherbonolides M (1) and N (2) as shown in Figure 1. The planar structures and relative configurations of both compounds were elucidated by analyzing the infrared (IR), MS, and 1D and 2D NMR data. Furthermore, to determine the absolute configurations, the circular dichroism (CD) spectra of both new compounds were measured and compared with those of isosarcophine (3). Moreover, in order to discover bioactive natural products for the development of drug leads, the cytotoxicity against human lung adenocarcinoma (A549), human colorectal adenocarcinoma (DLD-1), and human intrahepatic cholangiocarcinoma (HuCCT-1) was examined. In addition, the anti-inflammatory activity of both isolates was investigated by measuring the *N*-formyl-methionyl-leucyl-phenylalanine/cytochalasin B (fMLF/CB)-induced generation of superoxide anion and elastase release in the primary human neutrophils.

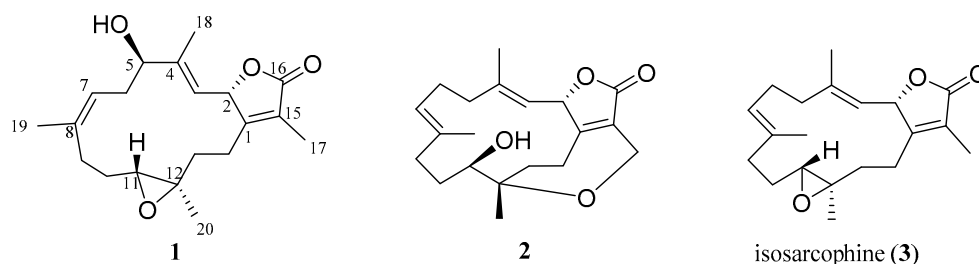


Figure 1. Marine natural products 1–3 isolated from the soft coral *S. cherbonnieri*.

## 2. Results and Discussion

The chemical structures of metabolites 1 and 2 were elucidated by analyzing the MS, IR, CD, and 1D and 2D NMR data (Supplementary Materials Figures S1–S32). Additionally, the  $^{13}\text{C}$  and  $^1\text{H}$  chemical shifts of 1 and 2 are listed in Table 1.

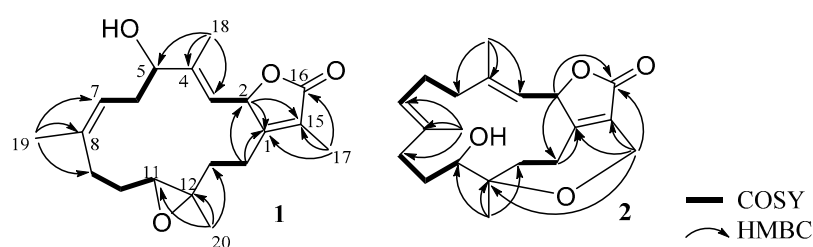
Compound 1, cherbonolide M, was isolated as a colorless oil. The molecular formula of 1 was  $\text{C}_{20}\text{H}_{28}\text{O}_4$  deduced from the pseudomolecular ion peak at  $m/z$  355.1882  $[\text{M} + \text{Na}]^+$  (calculated 355.1880,  $\text{C}_{20}\text{H}_{28}\text{O}_4\text{Na}$ ) in the high-resolution electrospray ionization mass spectrometry (HR-ESI-MS). Its IR spectrum showed the absorptions at 3445 and 1749  $\text{cm}^{-1}$ , indicating the presence of hydroxy and ester groups. The  $^{13}\text{C}$  and distortionless enhancement by polarization transfer (DEPT) spectra displayed 20 carbon signals, including four methyls, five methylenes, five methines, and six quaternary carbons.  $^1\text{H}$  and  $^{13}\text{C}$  NMR spectra showed the signals of an  $\alpha$ -methyl- $\alpha$ ,  $\beta$ -unsaturated- $\gamma$ -lactone ( $\delta_{\text{H}}$  5.64, d,  $J = 10.4$  Hz; 1.78, s;  $\delta_{\text{C}}$  174.6, C; 162.4, C; 123.5, C; 78.4, CH; 8.6,  $\text{CH}_3$ ), two trisubstituted double bonds ( $\delta_{\text{H}}$  4.98, d,  $J = 10.4$  Hz;  $\delta_{\text{C}}$  123.4, CH; 147.5, C;  $\delta_{\text{H}}$  4.98, d,  $J = 10.8$  Hz;  $\delta_{\text{C}}$  122.5, CH; 134.9, C), an oxygen-bearing methine ( $\delta_{\text{H}}$  4.21, dd,  $J = 10.8, 5.2$  Hz;  $\delta_{\text{C}}$  77.5, CH), and an epoxy groups ( $\delta_{\text{H}}$  2.45, d,  $J = 10.8$  Hz;  $\delta_{\text{C}}$  62.0, CH and 61.1, C).

**Table 1.**  $^{13}\text{C}$  and  $^1\text{H}$  NMR spectroscopic data of **1** and **2**.

| Position | <b>1</b> <sup>a</sup>   |                            | <b>1</b> <sup>b</sup>   |   | <b>2</b> <sup>c</sup>   |                                       |
|----------|-------------------------|----------------------------|-------------------------|---|-------------------------|---------------------------------------|
|          | $\delta_{\text{C}}$     | $\delta_{\text{H}}$        | $\delta_{\text{C}}$     | $\delta_{\text{H}}$                         | $\delta_{\text{C}}$     | $\delta_{\text{H}}$                   |
| 1        | 162.4 (C)               |                            | 159.9 (C)               |   | 166.1 (C)               |                                       |
| 2        | 78.4 (CH) <sup>d</sup>  | 5.64 d (10.4) <sup>e</sup> | 77.4 (CH)               | 4.99 d (10.5)                               | 79.2 (CH)               | 4.93 d (8.4)                          |
| 3        | 123.4 (CH)              | 4.98 d (10.4)              | 123.8 (CH)              | 4.55 d (10.0)                               | 120.7 (CH)              | 4.50 d (8.4)                          |
| 4        | 147.5 (C)               |                            | 145.5 (C)               |   | 139.2 (C)               |                                       |
| 5        | 77.5 (CH)               | 4.21 dd (10.8, 5.2)        | 77.3 (CH)               | 3.77 dd (10.5, 5.5)                         | 36.9 (CH <sub>2</sub> ) | 1.66 m; 1.87 m                        |
| 6        | 33.8 (CH <sub>2</sub> ) | 2.28 m; 2.52 m             | 32.8 (CH <sub>2</sub> ) | 2.23 m; 2.31 m                              | 24.3 (CH <sub>2</sub> ) | 1.77 m; 2.27 m                        |
| 7        | 122.5 (CH)              | 4.98 d (10.8)              | 121.4 (CH)              | 4.55 d (10.0)                               | 127.2 (CH)              | 4.76 d (10.4)                         |
| 8        | 134.9 (C)               |                            | 134.4 (C)               |   | 133.8 (C)               |                                       |
| 9        | 37.3 (CH <sub>2</sub> ) | 2.08 m; 2.31 m             | 36.9 (CH <sub>2</sub> ) | 1.70 m; 1.98 m                              | 36.1 (CH <sub>2</sub> ) | 1.92 m; 1.94 m                        |
| 10       | 24.5 (CH <sub>2</sub> ) | 2.07 m; 1.23 m             | 24.2 (CH <sub>2</sub> ) | 1.06 m; 1.90 m                              | 25.8 (CH <sub>2</sub> ) | 0.95 m; 1.98 m                        |
| 11       | 62.0 (CH)               | 2.45, d (10.8)             | 61.1 (CH)               | 2.28 dd (10.5, 2.5)                         | 70.7 (CH)               | 3.21 dd (10.4, 6.4)                   |
| 12       | 61.1 (C)                |                            | 59.9 (C)                |   | 79.4 (C)                |                                       |
| 13       | 37.8 (CH <sub>2</sub> ) | 2.05 m; 1.04 t (11.2)      | 37.3 (CH <sub>2</sub> ) | 0.77 td (13.5, 2.5);<br>1.61 dd (13.0, 5.5) | 29.4 (CH <sub>2</sub> ) | 1.70 m; 1.97 m                        |
| 14       | 24.7 (CH <sub>2</sub> ) | 2.02 m; 2.71 m             | 23.8 (CH <sub>2</sub> ) | 1.53 d (13.5); 1.95 m                       | 24.0 (CH <sub>2</sub> ) | 1.66 m; 2.19 m                        |
| 15       | 123.5 (C)               |                            | 123.8 (C)               |   | 128.1 (C)               |                                       |
| 16       | 174.6 (C)               |                            | 173.7 (C)               |   | 172.3 (C)               |                                       |
| 17       | 8.6 (CH <sub>3</sub> )  | 1.78 s                     | 8.7 (CH <sub>3</sub> )  | 1.67 s                                      | 55.9 (CH <sub>2</sub> ) | 4.31 dd (14.8, 1.6);<br>4.46 d (14.8) |
| 18       | 10.3 (CH <sub>3</sub> ) | 1.74 s                     | 9.8 (CH <sub>3</sub> )  | 1.33 s                                      | 18.5 (CH <sub>3</sub> ) | 1.27 s                                |
| 19       | 14.9 (CH <sub>3</sub> ) | 1.72 s                     | 14.5 (CH <sub>3</sub> ) | 1.31 s                                      | 15.2 (CH <sub>3</sub> ) | 1.36 s                                |
| 20       | 15.9 (CH <sub>3</sub> ) | 1.28 s                     | 15.9 (CH <sub>3</sub> ) | 1.02 s                                      | 22.5 (CH <sub>3</sub> ) | 1.02 s                                |

<sup>a</sup>  $^{13}\text{C}$  and  $^1\text{H}$  spectroscopic data of **1** recorded at 100 and 400 MHz in acetone- $d_6$ . <sup>b</sup>  $^{13}\text{C}$  and  $^1\text{H}$  spectroscopic data of **1** recorded at 125 and 500 MHz in  $\text{C}_6\text{D}_6$ . <sup>c</sup>  $^{13}\text{C}$  and  $^1\text{H}$  spectroscopic data of **2** recorded at 100 and 400 MHz in  $\text{C}_6\text{D}_6$ . <sup>d</sup> Attached protons were deduced from DEPT experiments. <sup>e</sup>  $J$  values (in Hz) in parentheses.

The planar structure of **1** was established according to the analysis of 2D NMR spectra as shown in Figure 2. The correlation spectroscopy (COSY) spectrum showed four partial moieties from the correlations of H-2 to H-3, H-5 via H<sub>2</sub>-6 to H-7, H<sub>2</sub>-9 via H<sub>2</sub>-10 to H-11, and H<sub>2</sub>-13 to H<sub>2</sub>-14. These partial structures were assembled by heteronuclear multiple bond correlation (HMBC) correlations from H<sub>3</sub>-17 to C-1, C-15, C-16; H<sub>3</sub>-18 to C-3, C-4, C-5; H<sub>3</sub>-19 to C-7, C-8, C-9; H<sub>3</sub>-20 to C-11, C-12, C-13; and H<sub>2</sub>-14 to C-1 and C-2. Furthermore, the NMR spectroscopic data of **1** were compared with those of the previous metabolite cherbonolide H [13] for structural elucidation. It was shown that compound **1** should possess a hydroxy group at C-5 and a 7,8-trisubstituted double bond from this NMR data comparison. According to the above evidence, the gross structure of **1** was elucidated.

**Figure 2.** COSY and selective HMBC correlations of **1** and **2**.

The relative configuration of **1** was established by analyzing the nuclear Overhauser effect spectroscopy (NOESY) spectrum, as shown in Figure 3. Assuming the  $\beta$ -orientation of H-2 ( $\delta_{\text{H}}$  5.64, d,  $J$  = 10.4 Hz), it was found the NOE correlations of H-2 with H-13 $\beta$  ( $\delta_{\text{H}}$  1.04, t,  $J$  = 11.2 Hz), H-13 $\beta$  with H-11 ( $\delta_{\text{H}}$  2.45, d,  $J$  = 10.8 Hz), and H-11 with H<sub>3</sub>-19 revealed the  $\beta$ -orientation of H-11. By contrast, H-2 did not exhibit NOE interaction with H-3, revealing the downward orientation of H-3. The NOE correlation of H-3 ( $\delta_{\text{H}}$  4.98, d,  $J$  = 10.4 Hz) with H-5 ( $\delta_{\text{H}}$  4.21, dd,  $J$  = 10.8, 5.2 Hz), H-5 with H-7 ( $\delta_{\text{H}}$  4.98, d,  $J$  = 10.8 Hz), H-7 with H-9 $\alpha$  ( $\delta_{\text{H}}$  2.08, m), and H-9 $\alpha$  with H<sub>3</sub>-20 ( $\delta_{\text{H}}$  1.28, s), suggesting the  $\alpha$ -orientation of H-5 and H<sub>3</sub>-20. Further, the  $E$  geometry of C-3/C-4 and C-7/C-8 was determined from the upfield shifted methyl groups of C-18 ( $\delta_{\text{C}}$  10.3) and C-19 ( $\delta_{\text{C}}$  14.9). The  $^3J$  values between H-2 and H-3 (10.4 Hz), H-5 and H-6 $\beta$  (10.8 Hz), and H-6 $\beta$  and H-7 (10.8 Hz) were found to be consistent with the relative configuration shown in Figure 3. In order to compare the

NMR data with those of **2** and other isosarcophine-derived metabolites measured in  $C_6D_6$  of our previous studies [13,14], the  $^1H$  and  $^{13}C$  NMR spectra of **1** were also measured, and the results (Table 1) can further confirm the structure of **1** was elucidated. The absolute configuration of **1** was determined by comparison the CD spectrum of **1** with that of isosarcophine (**3**), as shown in Figure 4. The CD spectrum of **1** showed the positive Cotton effect at 227.0 nm ( $\Delta\epsilon = +34.8$ ) for the  $\pi\text{-}\pi^*$  transition, while the negative Cotton effect at 245.5 nm ( $\Delta\epsilon = -15.6$ ) for the  $n\text{-}\pi^*$  transition. This evidence demonstrated the fact of 2*S*-configuration [27,28]. Due to the biogenesis of **1** from isosarcophine, the absolute configuration of **1** was defined as 2*S*,5*R*,11*R*,12*R*,3*E*,7*E*.

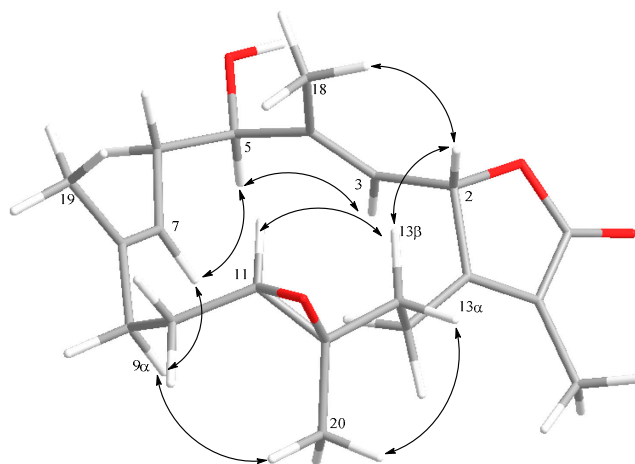


Figure 3. Selective NOE correlations of **1**.

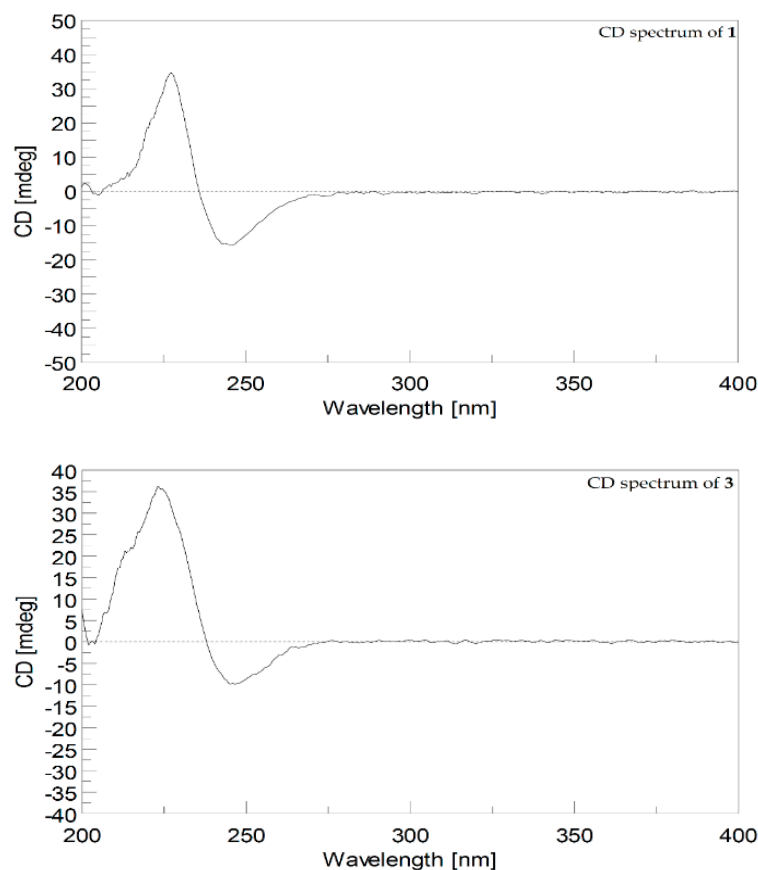
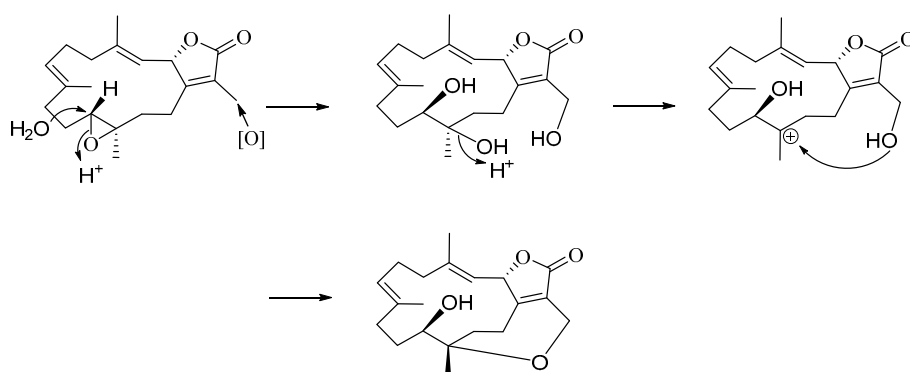


Figure 4. CD spectrum ( $1.2 \times 10^{-4}$  M, MeOH) of **1** and CD spectrum ( $1.6 \times 10^{-4}$  M, MeOH) of **3**.





In the present study, we isolated two cembranoids, cherbonolide M and N (**1** and **2**), from the soft coral *S. cherbonnieri*. Structurally, both isolates belong to the isosarcophine derivatives. By consideration of the chemical types of reported cembranoids, this is the first time to discover the cembranoidal scaffold possessing the unique tetrahydrooxepane with 12,17-ether linkage fusing with a  $\gamma$ -lactone. The plausible biosynthetic pathway was postulated, as shown in Scheme 1. Moreover, the CD spectrum of **2** (Figure 6) also revealed the positive effect at 225.0 nm ( $\Delta\epsilon = +25$ ) and the negative effect at 255.4 nm ( $\Delta\epsilon = -2.0$ ) as that of isosarcophine (**3**). Similar to compound **1**, metabolite **2** should also be biotransformed from isosarcophine and thus possessed a (2*S*,11*R*,12*S*,3*E*,7*E*) absolute configuration.



**Scheme 1.** Proposed biosynthetic pathway of cherbonolide N (**2**).

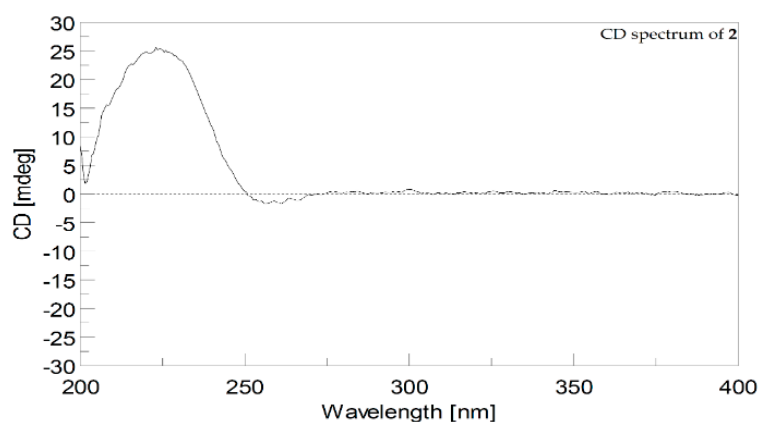


**Figure 6.** CD spectra ( $1.2 \times 10^{-4}$  M, MeOH) of **2**.

In 1990, Kusumi et al. afforded isosarcophine from the Okinawan soft coral, *Simularia mayi*, and demonstrated its moderate cytotoxicity against human colorectal carcinoma (HCT-116) cell line with the  $IC_{50}$  value of 64  $\mu\text{g/mL}$  [25]. Subsequently, in 1992, Wu et al. also isolated the same metabolite from a Formosan soft coral, *Sarcophyton trocheliophorum*, which was also found to exhibit significant cytotoxicities toward human lung epithelial cells (A549), human colon carcinoma cells (HT-29), human oral epidermoid carcinoma cells (KB), mouse lymphoid neoplasm cells (P388), and promyelocytic leukemia cells (HL-60) with the  $ED_{50}$  values of 13.3, 16.9, 24.5, 0.7, and 6.7  $\mu\text{g/mL}$ , respectively [26]. Many isosarcophine derivatives have been discovered from different marine soft corals and reported to display various biological activities [13,14,27].

For the discovery of bioactivities of new metabolites **1** and **2**, both compounds were examined according to the cytotoxic and anti-inflammatory activities. In the evaluation of cytotoxicity, both isolates were shown to be inactive against the proliferation of A549, DLD-1, and HuCCT-1 cell lines at the concentration of 30  $\mu\text{M}$ . On the other hand, in

anti-inflammatory assays at 30  $\mu$ M, metabolite **2** showed inhibition of superoxide anion generation ( $20.6 \pm 6.8\%$ ) and the elastase release ( $30.1 \pm 3.3\%$ ), while **1** only displayed  $12.9 \pm 5.7\%$  and  $16.7 \pm 5.9\%$  inhibition of superoxide anion generation and elastase release, respectively, in the fMLF/CB-induced human neutrophils.

### 3. Experimental Section

#### 3.1. General Experimental Procedures

Specific optical rotations of both compounds **1** and **2** were measured on a JASCO P-1020 polarimeter (JASCO Corporation, Tokyo, Japan), and their IR spectra were recorded on an FT/IR-4100 infrared spectrophotometer (JASCO Corporation, Tokyo, Japan). The low-resolution electrospray ionization mass spectrometry (LR-ESI-MS) and HR-ESI-MS experiments were carried out on a Bruker APEX II (Bruker, Bremen, Germany) mass spectrometer. The CD spectra of **1–3** were recorded by Jasco J-815 spectropolarimeter (JASCO, Tokyo, Japan) in MeOH. NMR spectra of **1** were acquired on a Varian Unity Inova 500 FT-NMR (Varian Inc., Palo Alto, CA, USA) at 500 MHz for  $^1\text{H}$  and 125 MHz for  $^{13}\text{C}$  in  $\text{C}_6\text{D}_6$  at room temperature (25  $^\circ\text{C}$ ). Further, NMR spectra of **1** and **2** were acquired on a Varian 400 MR FT-NMR (Varian Inc., Palo Alto, CA, USA) instrument at 400 MHz for  $^1\text{H}$  and 100 MHz for  $^{13}\text{C}$  in acetone- $d_6$  and  $\text{C}_6\text{D}_6$  at the same condition. Low-resolution electrospray ionization mass spectrometry (LRESIMS) and HRESIMS data were recorded on a Bruker APEX II (Bruker, Bremen, Germany) mass spectrometer. Normal-phase column chromatography was undertaken using silica gel (Merck, 230–400 mesh). Pre-coated silica gel plates (Merck, Kieselgel 60 F-254, 0.2 mm, Merck, Darmstadt, Germany) were used for analytical thin-layer chromatography (TLC). High-performance liquid chromatography was carried out for further purification of isolates, using a Hitachi L-2455 HPLC apparatus (Hitachi, Tokyo, Japan) with a Supelco C18 column (250  $\times$  21.2 mm, 5  $\mu\text{m}$ ; Supelco, Bellefonte, PA, USA).

#### 3.2. Animal Material

The collection and identification of the soft coral *S. cherbonnieri* were carried out as described previously [13,14].

#### 3.3. Extraction and Isolation

The soft coral *S. cherbonnieri* (wet weight: 1.2 kg) was freeze-dried to remove the water. The dried sample was sliced into small pieces for EtOAc extraction. The combined EtOAc extract was concentrated under reduced pressure to afford an oily residue (10.2 g), which was chromatographed by a normal phase column with the gradient elution of acetone in *n*-hexane (0–100%) and methanol in acetone (0–100%) to separate 19 fractions. Fraction 13, eluting with *n*-hexane-acetone (1:1), was further purified over Sephadex LH-20 column using acetone to afford five subfractions (A–E). Subfraction 13-D was further purified by reversed-phase HPLC with the elution of acetonitrile- $\text{H}_2\text{O}$  (1.6:1, 5.0 mL/min) to afford **1** (7.1 mg,  $t_{\text{R}}$  61.9 min). Subfraction 13-E was also purified by reversed-phase HPLC with the elution of acetonitrile- $\text{H}_2\text{O}$  (1.7:1, 5.0 mL/min) to afford **2** (3.6 mg,  $t_{\text{R}}$  54.5 min).

Cherbonolide M (**1**): colorless amorphous oil,  $[\alpha]_{\text{D}}^{25} +29.0$  ( $c$  1.00,  $\text{CHCl}_3$ ), IR (KBr)  $\nu_{\text{max}}$  3445, 2927, 2862, 1749, 1679, 1455, 1387, 1093, 1006, 755  $\text{cm}^{-1}$ ; CD ( $1.2 \times 10^{-4}$  M, MeOH)  $\lambda_{\text{max}}$   $\Delta\epsilon$  245.5 (−15.6), and 227.0 (+34.8) nm; for  $^{13}\text{C}$  and  $^1\text{H}$  data see Table 1; electrospray ionization mass spectrometry (ESIMS)  $m/z$  355; HRESIMS  $m/z$  355.1882  $[\text{M} + \text{Na}]^+$  (calculated for  $\text{C}_{20}\text{H}_{28}\text{O}_4\text{Na}$ : 355.1880).

Cherbonolide N (**2**): colorless amorphous oil,  $[\alpha]_{\text{D}}^{25} +15.0$  ( $c$  1.00,  $\text{CHCl}_3$ ), IR (KBr)  $\nu_{\text{max}}$  3481, 2930, 1741, 1678, 1437, 1383, 1102, 1061, 986, 754  $\text{cm}^{-1}$ ; CD ( $1.2 \times 10^{-4}$  M, MeOH)  $\lambda_{\text{max}}$   $\Delta\epsilon$  255.4 (−2.0), and 225.0 (+25.0) nm; for  $^{13}\text{C}$  and  $^1\text{H}$  data see Table 1; ESIMS  $m/z$  355; HRESIMS  $m/z$  355.1880  $[\text{M} + \text{H}]^+$  (calculated for  $\text{C}_{20}\text{H}_{28}\text{O}_4\text{Na}$ : 355.1879).

### 3.4. Cytotoxicity Testing

To measure the cytotoxicities of **1** and **2**, three different concentrations of both compounds were added to A549, DLD-1, and HuCCT-1 cell lines for 72 h. The results were detected using the Alamar Blue assay [29,30].

### 3.5. Anti-Inflammatory Assay

The generation of the superoxide anion and elastase release in the fMLF/CB-induced primary human neutrophils was screened according to the previous description [13].

## 4. Conclusions

Two new isosarcophine derivatives, cherbonolides M (**1**) and N (**2**), were isolated from the continuous investigation of the soft coral *S. cherbonnieri*. Structurally, metabolite **2** is the first cembranoid possessing the unique cembranoidal scaffold of tetrahydrooxepane with the 12,17-ether linkage fusing with a  $\gamma$ -lactone. A plausible biosynthetic pathway was postulated for compound **2**. In the anti-inflammatory assay, compound **2** was found to show moderate activity in inhibiting the generation of superoxide anion and elastase release in the fMLF/CB-induced human neutrophils. Based on the above statements and our previous discoveries [13,14], the soft coral *S. cherbonnieri* was demonstrated to be an attractive source of bioactive diterpenoids. Further, it has been proven that the soft coral *S. glaucum* existed in more than seven genetically distinct clades and led to the high structural diversification of natural products of this species [31]. Currently, over 300 cembranoids have been discovered from the *Sarcophyton* genera [1], which might also come from the same reason. According to our investigation and related studies of other research groups [13,14,32–38], the soft corals of genus *Sarcophyton* could be considered ideal organisms for discovering natural products with diversified structures and biological activities.

**Supplementary Materials:** The following are available online at <https://www.mdpi.com/article/10.3390/md19050260/s1>, Figure S1: ESIMS spectrum of **1**; Figure S2: HRESIMS spectrum of **1**; Figure S3: IR spectrum of **1**; Figure S4: CD spectrum ( $1.2 \times 10^{-4}$  M, MeOH) of **1**; Figure S5:  $^1\text{H}$  NMR spectrum of **1** in acetone- $d_6$  at 400 MHz; Figure S6:  $^1\text{H}$  NMR spectrum (from 0.9 to 2.9 ppm) of **1** in acetone- $d_6$  at 400 MHz; Figure S7:  $^{13}\text{C}$  NMR spectrum of **1** in acetone- $d_6$  at 100 MHz; Figure S8: DEPT spectrum of **1** in acetone- $d_6$ ; Figure S9: HSQC spectrum of **1** in acetone- $d_6$ ; Figure S10: COSY spectrum of **1** in acetone- $d_6$ ; Figure S11: HMBC spectrum of **1** in acetone- $d_6$ ; Figure S12: NOESY spectrum of **1** in acetone- $d_6$ ; Figure S13:  $^1\text{H}$  NMR spectrum of **1** in  $\text{C}_6\text{D}_6$  at 500 MHz; Figure S14:  $^1\text{H}$  NMR spectrum (from 0.6 to 2.5 ppm) of **1** in  $\text{C}_6\text{D}_6$  at 500 MHz; Figure S15:  $^{13}\text{C}$  NMR spectrum of **1** in  $\text{C}_6\text{D}_6$  at 125 MHz; Figure S16: DEPT spectrum of **1** in  $\text{C}_6\text{D}_6$ ; Figure S17: HSQC spectrum of **1** in  $\text{C}_6\text{D}_6$ ; Figure S18: COSY spectrum of **1** in  $\text{C}_6\text{D}_6$ ; Figure S19: HMBC spectrum of **1** in  $\text{C}_6\text{D}_6$ ; Figure S20: NOESY spectrum of **1** in  $\text{C}_6\text{D}_6$ ; Figure S21: ESIMS spectrum of **2**; Figure S22: HRESIMS spectrum of **2**; Figure S23: IR spectrum of **2**; Figure S24: CD spectrum ( $1.2 \times 10^{-4}$  M, MeOH) of **2**; Figure S25:  $^1\text{H}$  NMR spectrum of **2** in  $\text{C}_6\text{D}_6$  at 400 MHz; Figure S26:  $^1\text{H}$  NMR spectrum (from 0.8 to 3.2 ppm) of **2** in  $\text{C}_6\text{D}_6$  at 400 MHz; Figure S27:  $^{13}\text{C}$  NMR spectrum of **2** in  $\text{C}_6\text{D}_6$  at 100 MHz; Figure S28: DEPT spectrum of **2**; Figure S29: HSQC spectrum of **2**; Figure S30: COSY spectrum of **2**; Figure S31: HMBC spectrum of **2**; Figure S32: NOESY spectrum of **2**. Figure S33: CD spectrum ( $1.6 \times 10^{-4}$  M, MeOH) of isosarcophine (**3**).

**Author Contributions:** Conceptualization, J.-H.S.; investigation, C.-C.P., C.-Y.H., T.-L.H. and J.-H.S.; writing—original draft, C.-C.P., T.-Y.H. and C.-Y.H.; writing—review and editing, T.-Y.H. and J.-H.S.; bioactivity screening, C.-Y.H. and T.-L.H. All authors have read and agreed to the published version of the manuscript.

**Funding:** This study was funded mainly by the Ministry of Science and Technology of Taiwan (MOST; 104-2113-M-110-006, 104-2320-B-110-001-MY2, and 107-2320-B-110-001-MY3).

**Institutional Review Board Statement:** Not applicable.

**Informed Consent Statement:** Not applicable.

**Data Availability Statement:** Data available in a publicly accessible repository.

**Conflicts of Interest:** The authors declare no conflict of interest.

## References

- Elkhawas, Y.A.; Elissawy, A.M.; Elnaggar, M.S.; Mostafa, N.M.; Al-Sayed, E.; Bishr, M.M.; Singab, A.N.B.; Salama, O.M. Chemical diversity in species belonging to soft coral genus *Sarcophyton* and its impact on biological activity: A review. *Mar. Drugs* **2020**, *18*, 41. [\[CrossRef\]](#)
- Carroll, A.R.; Copp, B.R.; Davis, R.A.; Keyzers, R.A.; Prinsep, M.R. Marine natural products. *Nat. Prod. Rep.* **2020**, *37*, 175–223. [\[CrossRef\]](#)
- Rodrigues, I.G.; Miguel, M.G.; Mnif, W. A brief review on new naturally occurring cembranoid diterpene derivatives from the soft corals of the genera *Sarcophyton*, *Sinularia*, and *Lobophytum* since 2016. *Molecules* **2019**, *24*, 781. [\[CrossRef\]](#)
- Aratake, S.; Tomura, T.; Saitoh, S.; Yokokura, R.; Kawanishi, Y.; Shinjo, R.; Reimer, J.D.; Tanaka, J.; Maekawa, H. Soft coral *Sarcophyton* (Cnidaria: Anthozoa: Octocorallia) species diversity and chemotypes. *PLoS ONE* **2012**, *7*, e30410. [\[CrossRef\]](#) [\[PubMed\]](#)
- Wei, W.C.; Sung, P.J.; Duh, C.Y.; Chen, B.W.; Sheu, J.H.; Yang, N.S. Anti-inflammatory activities of nature products isolated from soft corals of Taiwan between 2008 and 2012. *Mar. Drugs* **2013**, *11*, 4083–4126. [\[CrossRef\]](#) [\[PubMed\]](#)
- Huang, T.Y.; Huang, C.Y.; Chen, S.R.; Weng, J.R.; Tu, T.H.; Cheng, Y.B.; Wu, S.H.; Sheu, J.H. New hydroquinone monoterpenoid and cembranoid-related metabolites from the soft coral *Sarcophyton tenuispiculatum*. *Mar. Drugs* **2021**, *19*, 8. [\[CrossRef\]](#) [\[PubMed\]](#)
- Huang, T.Y.; Huang, C.Y.; Chao, C.H.; Lin, C.C.; Dai, C.F.; Su, J.H.; Sung, P.J.; Wu, S.H.; Sheu, J.H. New biscembranoids sardigitolides A-D and known cembranoid-related compounds from *Sarcophyton digitatum*: Isolation, structure elucidation, and bioactivities. *Mar. Drugs* **2020**, *18*, 452. [\[CrossRef\]](#)
- Hegazy, M.E.F.; Mohamed, T.A.; Elshamy, A.I.; Hamed, A.R.; Ibrahim, M.A.A.; Ohta, S.; Umeyama, A.; Paré, P.W.; Efferth, T. Sarcophyton ehrenbergii D-F: Cytotoxic cembrene diterpenoids from the soft coral *Sarcophyton ehrenbergii*. *RSC Adv.* **2019**, *9*, 27183–27189. [\[CrossRef\]](#)
- Rao, C.B.; Babu, D.C.; Bharadwaj, T.V.; Srikanth, D.; Vardhan, K.S.; Raju, T.V.; Bunce, R.A.; Venkateswarlu, Y. Isolation, structural assignment and synthesis of (SE)-2-methyloctyl 3-(4-methoxyphenyl) propenoate from the marine soft coral *Sarcophyton ehrenbergii*. *Nat. Prod. Res.* **2015**, *29*, 70–76.
- Eltahawy, N.A.; Ibrahim, A.K.; Radwan, M.M.; ElSohly, M.A.; Hassanean, H.A.; Ahmed, S.A. Cytotoxic cembranoids from the Red Sea soft coral, *Sarcophyton auritum*. *Tetrahedron Lett.* **2014**, *55*, 3984–3988. [\[CrossRef\]](#)
- Elkhateeb, A.; El-Beih, A.A.; Gamal-Eldeen, A.M.; Alhammady, M.A.; Ohta, S.; Paré, P.W.; Hegazy, M.E.F. New terpenes from the Egyptian soft coral *Sarcophyton ehrenbergii*. *Mar. Drugs* **2014**, *12*, 1977–1986. [\[CrossRef\]](#) [\[PubMed\]](#)
- Wang, S.K.; Hsieh, M.K.; Duh, C.Y. New diterpenoids from soft coral *Sarcophyton ehrenbergii*. *Mar. Drugs* **2013**, *11*, 4318–4327. [\[CrossRef\]](#) [\[PubMed\]](#)
- Peng, C.C.; Huang, C.Y.; Ahmed, A.F.; Hwang, T.L.; Sheu, J.H. Anti-inflammatory cembranoids from a Formosa soft coral *Sarcophyton cherbonnieri*. *Mar. Drugs* **2020**, *18*, 573. [\[CrossRef\]](#) [\[PubMed\]](#)
- Peng, C.C.; Huang, C.Y.; Ahmed, A.F.; Hwang, T.L.; Dai, C.F.; Sheu, J.H. New cembranoids and a biscembranoid peroxide from the soft coral *Sarcophyton cherbonnieri*. *Mar. Drugs* **2018**, *16*, 276. [\[CrossRef\]](#)
- Ahmed, A.F.; Chen, Y.W.; Huang, C.Y.; Tseng, Y.J.; Lin, C.C.; Dai, C.F.; Wu, Y.C.; Sheu, J.H. Isolation and structure elucidation of cembranoids from a Dongsha Atoll soft coral *Sarcophyton stellatum*. *Mar. Drugs* **2018**, *16*, 210. [\[CrossRef\]](#)
- Li, W.; Zou, Y.H.; Ge, M.X.; Lou, L.L.; Xu, Y.S.; Ahmed, A.; Chen, Y.Y.; Zhang, J.S.; Tang, G.H.; Yin, S. Biscembranoids and cembranoids from the soft coral *Sarcophyton elegans*. *Mar. Drugs* **2017**, *15*, 85. [\[CrossRef\]](#)
- Lin, W.Y.; Chen, B.W.; Huang, C.Y.; Wen, Z.H.; Sung, P.J.; Su, J.H.; Dai, C.F.; Sheu, J.H. Bioactive cembranoids, sarcocrassocolides P–R, from the Dongsha Atoll soft coral *Sarcophyton crassocaule*. *Mar. Drugs* **2014**, *12*, 840–850. [\[CrossRef\]](#) [\[PubMed\]](#)
- Lin, W.Y.; Su, J.H.; Lu, Y.; Wen, Z.H.; Dai, C.F.; Kuo, Y.H.; Sheu, J.H. Cytotoxic and anti-inflammatory cembranoids from the Dongsha Atoll soft coral *Sarcophyton crassocaule*. *Bioorg. Med. Chem.* **2010**, *18*, 1936–1941. [\[CrossRef\]](#)
- Badria, F.A.; Guirguis, A.N.; Perovic, S.; Steffen, R.; Müller, W.E.; Schröder, H.C. Sarcophytolide: A new neuroprotective compound from the soft coral *Sarcophyton glaucum*. *Toxicology* **1998**, *131*, 133–143. [\[CrossRef\]](#)
- Liang, L.F.; Kurtán, T.; Mándi, A.; Yao, L.G.; Li, J.; Lan, L.F.; Guo, Y.W. Structural, stereochemical, and bioactive studies of cembranoids from Chinese soft coral *Sarcophyton trocheliophorum*. *Tetrahedron* **2018**, *74*, 1933–1941. [\[CrossRef\]](#)
- Farag, M.A.; Fekry, M.I.; Al-Hammady, M.A.; Khalil, M.N.; El-Seedi, H.R.; Meyer, A.; Porzel, A.; Westphal, H.; Wessjohann, L.A. Cytotoxic effects of *Sarcophyton* sp. soft coral—is there a correlation to their NMR fingerprints? *Mar. Drugs* **2017**, *15*, 211. [\[CrossRef\]](#)
- Bernstein, J.; Shmeuli, U.; Zadock, E.; Kashman, Y.; Néeman, I. Sarcophine, a new epoxy cembranolide from marine origin. *Tetrahedron* **1974**, *30*, 2817–2824. [\[CrossRef\]](#)
- Kashman, Y. *Marine Natural Products Chemistry*; Faulkner, D.J., Fenical, W.H., Eds.; Plenum Press: New York, NY, USA, 1977; pp. 17–21.
- Frincke, J.M.; McIntyre, D.E.; Faulkner, D.J. Deoxosarcophine from a soft coral, *Sarcophyton* sp. *Tetrahedron Lett.* **1980**, *21*, 735–738. [\[CrossRef\]](#)
- Kusumi, T.; Yamada, K.; Ishitsuka, M.O.; Fujita, Y.; Kakisawa, H. New cembranoids from the Okinawan soft coral *Sinularia mayi*. *Chem. Lett.* **1990**, *19*, 1315–1318. [\[CrossRef\]](#)
- Wu, Y.C.; Hsieh, P.W.; Duh, C.Y.; Wang, S.K.; Soong, K.; Fang, L.S. Studies on the Formosan soft corals I-cytotoxic cembrane diterpenes from *Sarcophyton trocheliophorum*. *J. Chin. Chem. Soc.* **1992**, *39*, 355–357. [\[CrossRef\]](#)



27. Li, S.W.; Ye, F.; Zhu, Z.D.; Huang, H.; Mao, S.C.; Guo, Y.W. Cembrane-type diterpenoids from the South China Sea soft coral *Sarcophyton mililatensis*. *Acta Pharm. Sin. B* **2018**, *8*, 944–955. [[CrossRef](#)] [[PubMed](#)]
28. Gawronski, J.K.; van Oeveren, A.; van der Deen, H.; Leung, C.W.; Feringa, B.L. Simple circular dichroic method for the determination of absolute configuration of 5-substituted 2(5H)-furanones. *J. Org. Chem.* **1996**, *61*, 1513–1517. [[CrossRef](#)]
29. Nakayama, G.R.; Caton, M.C.; Nova, M.P.; Parandoosh, Z. Assessment of the Alamar Blue assay for cellular growth and viability in vitro. *Immunol. Methods* **1997**, *204*, 205–208. [[CrossRef](#)]
30. O'Brien, J.; Wilson, I.; Orton, T.; Pognan, F. Investigation of the Alamar Blue (resazurin) fluorescent dye for the assessment of mammalian cell cytotoxicity. *Eur. J. Biochem.* **2000**, *267*, 5421–5426. [[CrossRef](#)]
31. Maloney, K.N.; Botts, R.T.; Davis, T.S.; Okada, B.K.; Maloney, E.M.; Leber, C.A.; Alvarado, O.; Brayton, C.; Caraballo-Rodríguez, A.M.; Chari, J.V.; et al. Cryptic species account for the seemingly idiosyncratic secondary metabolism of *Sarcophyton glaucum* specimens collected in Palau. *J. Nat. Prod.* **2020**, *83*, 693–705. [[CrossRef](#)]
32. Khalifa, S.A.M.; Elias, N.; Farag, M.A.; Chen, L.; Saeed, A.; Hegazy, M.E.F.; Moustafa, M.S.; El-Wahed, A.A.; Al-Mousawi, S.M.; Musharraf, S.G.; et al. Marine natural products: A source of novel anticancer drugs. *Mar. Drugs* **2019**, *17*, 491. [[CrossRef](#)] [[PubMed](#)]
33. Sang, V.T.; Dat, T.T.H.; Vinh, L.B.; Cuong, L.C.V.; Oanh, P.T.T.; Ha, H.; Kim, Y.H.; Anh, H.L.T.; Yang, S.Y. Coral and coral-associated microorganisms: A prolific source of potential bioactive natural products. *Mar. Drugs* **2019**, *17*, 468. [[CrossRef](#)] [[PubMed](#)]
34. Chao, C.H.; Li, W.L.; Huang, C.Y.; Ahmed, A.F.; Dai, C.F.; Wu, Y.C.; Lu, M.C.; Liaw, C.C.; Sheu, J.H. Isoprenoids from the soft coral *Sarcophyton glaucum*. *Mar. Drugs* **2017**, *15*, 202. [[CrossRef](#)] [[PubMed](#)]
35. Lin, K.H.; Tseng, Y.J.; Chen, B.W.; Hwang, T.L.; Chen, H.Y.; Dai, C.F.; Sheu, J.H. Tortuosenes A and B, new diterpenoid metabolites from the Formosan soft coral *Sarcophyton tortuosum*. *Org. Lett.* **2014**, *16*, 1314–1317. [[CrossRef](#)] [[PubMed](#)]
36. Huang, H.C.; Ahmed, A.F.; Su, J.H.; Chao, C.H.; Wu, Y.C.; Chiang, M.Y.; Sheu, J.H. Crassocolides A–F, cembranoids with a *trans*-fused lactone from the soft coral *Sarcophyton crassocaule*. *J. Nat. Prod.* **2006**, *69*, 1554–1559. [[CrossRef](#)] [[PubMed](#)]
37. Li, G.; Li, H.; Zhang, Q.; Yang, M.; Gu, Y.C.; Liang, L.F.; Tang, W.; Guo, Y.W. Rare cembranoids from Chinese soft coral *Sarcophyton ehrenbergi*: Structural and stereochemical studies. *J. Org. Chem.* **2019**, *84*, 5091–5098. [[CrossRef](#)] [[PubMed](#)]
38. Xi, Z.F.; Bie, W.; Chen, W.; Liu, D.; van Ofwegen, L.; Proksch, P.; Lin, W.H. Sarcophytolides G–L, new biscembranoids from the soft coral *Sarcophyton elegans*. *Helv. Chim. Acta.* **2013**, *96*, 2218–2227. [[CrossRef](#)]

# Tomatidine ameliorates obesity-induced nonalcoholic fatty liver disease in mice

Shu-Ju Wu<sup>a,b,#</sup>, Wen-Chung Huang<sup>c,d,#</sup>, Ming-Chin Yu<sup>e</sup>, Ya-Ling Chen<sup>f</sup>, Szu-Chuan Shen<sup>g</sup>, Kuo-Wei Yeh<sup>d,\*\*</sup>, Chian-Jiun Liou<sup>d,h,\*</sup>

<sup>a</sup> Department of Nutrition and Health Sciences, Research Center for Chinese Herbal Medicine, Chang Gung University of Science and Technology, Taoyuan City, Taiwan

<sup>b</sup> Aesthetic Medical Center, Department of Dermatology, Chang Gung Memorial Hospital, Taoyuan, Taiwan

<sup>c</sup> Graduate Institute of Health Industry Technology, Research Center for Food and Cosmetic Safety, Research Center for Chinese Herbal Medicine, College of Human Ecology, Chang Gung University of Science and Technology, Taoyuan City, Taiwan

<sup>d</sup> Division of Allergy, Asthma, and Rheumatology, Department of Pediatrics, Chang Gung Memorial Hospital, Taoyuan City, Taiwan

<sup>e</sup> Department of Surgery, New Taipei Municipal Tucheng Hospital, New Taipei, Taiwan

<sup>f</sup> School of Nutrition and Health Sciences, Taipei Medical University, Taipei City, Taiwan

<sup>g</sup> Graduate Program of Nutrition Science, National Taiwan Normal University, Taipei City, Taiwan

<sup>h</sup> Department of Nursing, Division of Basic Medical Sciences, Research Center for Chinese Herbal Medicine, Chang Gung University of Science and Technology, Taoyuan City, Taiwan

Received 15 April 2020; received in revised form 1 December 2020; accepted 31 December 2020

## Abstract

Tomatidine is isolated from the leaves and green fruits of some plants in the Solanaceae family, and has been reported to have anti-inflammatory and antitumor effects. Previous studies have found that tomatidine decreases hepatic lipid accumulation via regulation of vitamin D receptor and activation of AMP-activated protein kinase (AMPK) phosphorylation. However, whether tomatidine reduces weight gain and improves nonalcoholic fatty liver disease (NAFLD) remains unclear. In this study, we investigated how tomatidine ameliorates NAFLD in obese mice and evaluated the regulatory mechanism of lipogenesis in hepatocytes. Male C57BL/6 mice were fed a high-fat diet (HFD) to induce obesity and NAFLD, and treated with tomatidine via intraperitoneal injection. In vitro, FL83B hepatocytes were incubated with oleic acid and treated with tomatidine to evaluate lipid metabolism. Our results demonstrate that tomatidine significantly decreases body weight and fat weight compared to HFD-fed mice. In addition, tomatidine decreased hepatic lipid accumulation and improved hepatocyte steatosis in HFD-induced obese mice. We also found that tomatidine significantly regulated serum total cholesterol, fasting blood glucose, low-density lipoprotein, and triglyceride levels, but the serum high-density lipoprotein and adiponectin concentrations were higher than in the HFD-fed obese mice. In vivo and in vitro, tomatidine significantly suppressed the expression of fatty acid synthase and transcription factors involved in lipogenesis, and increased the expression of adipose triglyceride lipase. Tomatidine promoted the sirtuin 1 (sirt1)/AMPK signaling pathway to increase lipolysis and  $\beta$ -oxidation in fatty liver cells. These findings suggest that tomatidine potentially ameliorates obesity and acts against hepatic steatosis by regulating lipogenesis and the sirt1/AMPK pathway.

© 2021 Elsevier Inc. All rights reserved.

**Keywords:** FL83B; Lipogenesis; Lipolysis; Nonalcoholic fatty liver disease; Tomatidine.

## 1. Introduction

Obesity is a chronic inflammatory disease with abnormal metabolism and a risk factor for many chronic diseases. [1]. Long-

term intake of a high-calorie diet can cause morbid obesity, which not only leads to excessive accumulation of triglycerides (TGs) in visceral adipose tissue, but also induces liver cells to accumulate excessive TGs, causing hepatic steatosis [2]. The continuous

**Abbreviations:** ACC-1, acetyl CoA carboxylase-1; ALT, alanine aminotransferase; AMPK, AMP-activated protein kinase; AST, aspartate aminotransferase; ATGL, adipose triglyceride lipase; C/EBP, CCAAT/enhancer-binding protein; CPT-1, carnitine palmitoyltransferase 1; FAS, fatty acid synthase; HDL, high-density lipoprotein; HE, hematoxylin and eosin; HFD, high-fat diet; HSL, hormone-sensitive lipase; LDL, low-density lipoprotein; NAFL, non-alcoholic fatty liver; NAFLD, non-alcoholic fatty liver disease; NASH, non-alcoholic steatohepatitis; PAS, periodic acid-Schiff; PPAR, peroxisome proliferator-activated receptor; Sirt1, sirtuin 1; SREBP-1c, sterol regulatory element-binding protein 1c; TA, Tomatidine; TC, total cholesterol; TG, triglyceride.

\* Corresponding author at: Chian-Jiun Liou, Department of Nursing, Division of Basic Medical Sciences, Research Center for Chinese Herbal Medicine, Chang Gung University of Science and Technology, No.261, Wenhua 1st Rd., Guishan Dist., Taoyuan City 33303, Taiwan. Tel.: 886-3-2118999; fax: 886-3-2118293.

\*\* Co-corresponding author at: Kuo-Wei Yeh, Division of Allergy, Asthma, and Rheumatology, Department of Pediatrics, Chang Gung Memorial Hospital, Linkou, Guishan Dist., Taoyuan City 33303, Taiwan. Tel.: 886-3-3281200; fax: 886-3-2118293.

E-mail addresses: [kwye@cgmh.org.tw](mailto:kwye@cgmh.org.tw) (K.-W. Yeh), [ccliu@mail.cgu.edu.tw](mailto:ccliu@mail.cgu.edu.tw) (C.-J. Liou).

# Shu-Ju Wu and Wen-Chung Huang made equal contributions to the paper.

deterioration of hepatic steatosis will lead to more serious metabolic abnormalities of lipids and carbohydrates and result in nonalcoholic fatty liver disease (NAFLD). NAFLD is defined as excessive accumulation of TGs in hepatocytes, with more than 10% fatty vacuoles in the liver tissue or more than 5% fat weight in the liver, in the absence of an inducing factor such as drugs or alcohol [3]. NAFLD is a common hepatitis that is considered to be a form of hepatic dysfunction, causing liver cell damage by interfering with metabolic functions [4]. NAFLD contained the early stages of non-alcoholic fatty liver (NAFL) and the more severe nonalcoholic steatohepatitis (NASH) [5]. In NAFL, liver cells will accumulate more lipid droplets, but the hepatocytes are not damaged and apoptosis. In the NASH stage, hepatic cells will be induced persistent inflammation, which cause to steatosis and damage of hepatocytes [6]. Clinically, NAFLD will cause no symptoms in most cases. Most NAFLD patients are found that abnormal liver enzyme test and unusual liver ultrasound. Clinicians suggest that patients can reduce weight through healthy diet and exercise, which will improve the development of NAFLD [7]. However, the patient does not pay attention to diet and proper exercise, the liver's metabolic functions may gradually deteriorate, developing into severe nonalcoholic steatohepatitis and causing irreversible liver fibrosis or cirrhosis, eventually inducing liver cancer or even death [8].

Obesity is considered an important risk factor for NAFLD. In NAFLD, the hepatocytes accumulate excessive lipids, which will interfere with the metabolic function [5]. Fatty acid synthesis in the liver is regulated by several transcription factors, including sterol regulatory element binding protein 1c (SREBP-1c), CCAAT/enhancer binding protein (C/EBP), and peroxisome proliferator-activated receptor (PPAR), which regulate fatty acid synthase (FAS) expression for the synthesis of fatty acid chains [9]. Therefore, blocking these transcription factors and inhibiting FAS activation will reduce TG synthesis and improve excess lipid accumulation in the liver.

Increasing lipid breakdown to reduce accumulation is another strategy to ameliorate NAFLD. TG decomposition requires activation of lipolytic enzymes, including fatty triglyceride lipase (ATGL) and hormone sensitive lipase (HSL), which can break down TGs into free fatty acids and glycerol [10]. In addition, excess free fatty acids can be broken down by  $\beta$ -oxidation to produce energy and reduce inflammation in the liver and adipose tissue [11]. Previous studies have shown that PPAR- $\alpha$  could regulate the  $\beta$ -oxidation pathway and carnitine palmitoyltransferase I (CPT-1) expression to assist in breaking down fatty acid chains [12]. Therefore, accelerating the decomposition of lipids and the  $\beta$ -oxidation of fatty acids can improve lipid metabolism in NAFLD and return the liver to normal.

AMP-activated protein kinase (AMPK) is considered to be an important molecule for maintaining energy regulation [13]. Activated AMPK can stimulate the phosphorylation of acetyl-CoA carboxylase (ACC) and reduce the activity of FAS, which reduces the synthesis of fatty acid chains [14]. Sirtuin 1 (Sirt1) is an adenosine dinucleotide (NAD)-dependent deacetylase with a critical role in regulating intracellular NAD<sup>+</sup> levels in metabolic pathways. Sirt1 is also thought to induce AMPK phosphorylation, which assists in reducing lipid synthesis [15]. Therefore, the Sirt1/AMPK pathway is an important sensing pathway for regulating cellular energy balance.

Tomatidine is a steroidal alkaloid isolated from the leaves and unripe fruit of tomatoes or eggplant [16]. Previous studies have found that tomatidine can inhibit the proliferation and migration of lung cancer cells and liver cancer cells [17,18]. In recent years, other researchers have found that palmitate acid-induced HepG2 cells treated with tomatidine activate vitamin D receptors and reduce lipid accumulation, mainly through activation of the AMPK pathway [19]. However, whether tomatidine improves NAFLD and regulates liver lipid metabolism in obese mice is unclear.

Therefore, in the present study, we investigated tomatidine modulation of molecular mechanisms in lipid metabolism and demonstrate improved NAFLD in high-fat diet (HFD)-induced obese mice.

## 2. Material and methods

### 2.1. Animals and treatments

Four-week-old male C57BL/6 mice (National Laboratory Animal Center, Taipei, Taiwan) were used in animal experiments approved by the Laboratory Animal Care Committee of Chang Gung University of Science and Technology (IACUC approval number: 2016-023). A total of 40 mice were randomly assigned to four groups (each group,  $n=10$ ). The control group comprised mice fed standard chow diet and administered DMSO solution by intraperitoneal injection; the HFD group comprised mice fed a HFD containing 60% fat; and the TA5 and TA10 groups comprised mice fed a HFD and administered 5 or 10 mg/kg tomatidine (St. Louis, MO, USA), respectively, by intraperitoneal injection. The HFD, TA5, and TA10 groups were fed the HFD for 4 weeks and then treated with 50  $\mu$ l DMSO or tomatidine (dissolved in DMSO) twice a week for 12 weeks (Fig. 1A). Food intake was measured as the weight of consumed food in grams  $\times$  calories in the diet per day. Dietary intake was monitored each day and body weight recorded weekly.

### 2.2. Histological analysis

Mice were anesthetized with 4% isoflurane and liver and epididymal adipose tissues removed, weighed, and fixed in 10% formalin. All tissues were embedded in paraffin, cut into 6- $\mu$ m sections, and stained using hematoxylin and eosin (HE) solution as described previously [20]. Each histological slide chose a fixed field of view and counted the number of oil droplets in the liver with a light microscope (Olympus, Tokyo, Japan). Furthermore, the images of epididymal adipose tissue chose five fat cells to measure the cell area using cellSens Standard software (Olympus). Furthermore, each histological slide chose a fixed field of view and counted the number of oil droplets in the liver. Glycogen accumulation in the liver tissue was detected by periodic acid-Schiff (PAS) solution as described previously [21]. Biopsy specimens were inspected under a light microscope and NAFLD scored as described previously [22]. Briefly, NAFLD scores are based on fat vacuoles, macrophage infiltration, and lobular inflammation in liver tissue [22].

### 2.3. Immunohistochemical staining

For immunohistochemistry, the liver tissue sections were incubated with primary specific antibody (1:50) overnight, followed by secondary antibody as described previously [22]. The tissues were treated with DAB substrate solution to detect FAS and CPT-1 (Cell Signaling Technology, MA, USA) expression.

### 2.4. Biochemical analysis

Mice were anesthetized and blood collected via the orbital vascular plexus. The blood was centrifuged and serum collected to detect the levels of free fatty acids using the fatty acid quantitation kit (Sigma) according to the manufacturer's protocol. The serum levels of aspartate aminotransferase (AST), alanine aminotransferase (ALT), total TGs, total cholesterol (TC), high-density lipoprotein (HDL), and low-density lipoprotein (LDL) were detected using a biochemical analyzer (DRI-CHEM NX500, Fuji, Tokyo, Japan). Furthermore, the day before the end of the animal experiments, the mice fasted for 16 h and glucose was given by intraperitoneal injection to assay blood glucose levels using a biochemical analyzer (Fuji). Blood insulin levels were detected using the Insulin EIA Kit (Cayman, Ann Arbor, Michigan, USA). Liver glycogen was measured using the Glycogen Assay Kit (Cayman), and glycogen levels were measured using a microplate reader (Multiskan FC, Thermo, Waltham, MA, USA) based on absorbance at 570 nm.

### 2.5. Western blot analysis

Proteins were separated by 8–12% SDS-PAGE and transferred to polyvinylidene difluoride membrane. The membrane was incubated with specific antibodies (diluted at 1:1000 or 1:2000) overnight. Next, the membranes were incubated with secondary antibodies (diluted at 1:5000) and treated with luminol/enhancer solution (Millipore, Billerica, MA, USA) to detect specific protein expression by the BioSpectrum 600 system (UVP, Upland, CA, USA). The specific primary antibodies were against ATGL, HSL, phosphorylated HSL (pHSL), ACC-1, phosphorylated-ACC-1 (pACC-1), C/EBP $\alpha$ , C/EBP $\beta$ , PPAR- $\alpha$  (Abcam, Cambridge, MA, USA), AMPK $\alpha$ , phosphorylated AMPK $\alpha$  (pAMPK $\alpha$ ), CPT-1, CPT2, FAS, Serp-1c, Sirt1 (Cell Signaling Technology), and  $\beta$ -actin (Sigma).

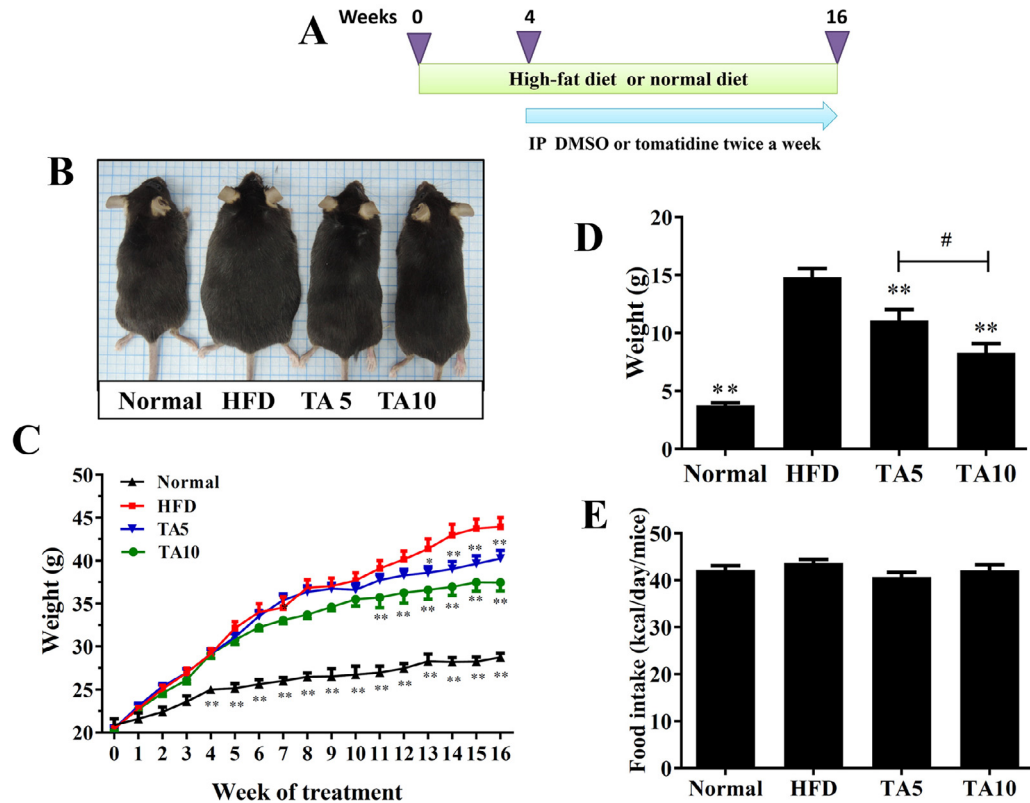


**Fig. 1.** Tomatidine (TA) decreased the body weight of mice with HFD-induced obesity. (A) Experimental procedures for obese mouse studies. The control (Normal) mice fed standard chow diet. Male mice were fed a HFD (containing 60% fat) for 16 weeks and administered DMSO and 5 mg/kg tomatidine (TA5) or 10 mg/kg tomatidine (TA10) via intraperitoneal injection (I.P.) twice a week from the 4th week to the 16th week. (B) Appearance of the mice. (C) Body weight was measured for 16 weeks. (D) Weight gain was calculated in the last week and (E) food intake was monitored each day. Data are presented as mean  $\pm$  SEM;  $n=10$ . \* $P<.05$ , \*\* $P<.01$  compared to HFD-induced obese mice. # $P<.05$  compared to the TA10 group.

## 2.6. Real-time PCR

Total RNA was extracted from liver tissues using TRIzol reagent solution (Life Technologies, Carlsbad, CA, USA). cDNA was synthesized by the cDNA synthesis kit (Bio-Rad, San Francisco, CA, USA) according to the manufacturer's protocol. Specific genes were amplified using a SYBR green master mix kit and the spectrofluorometric thermal cycler (iCycler, Bio-Rad) as described previously [23].

## 2.7. Cell culture and induced fatty liver cells

FL83B mouse hepatocyte cells were purchased from the Bioresource Collection and Research Center (BCRC, Taiwan) and cultured in F12 medium (Invitrogen-Gibco, Paisley, Scotland). For cell viability assays, tomatidine was dissolved in DMSO solution, and all cell experiments were performed using  $<0.1\%$  DMSO. FL83B cells were seeded on 96-well plates and treated with various concentrations of tomatidine for 24 h to assay cell viability using MTT solution (Sigma) as described previously [24]. The culture plate was treated with 100% isopropanol to detect absorption and evaluate cell viability at 550 nm using a microtiter plate reader (Multiskan FC). To detect lipid accumulation in hepatocytes, FL83B cells were seeded on 6-well plates and incubated with 0.5 mM oleic acid to induce lipid accumulation for 48 h. Next, vehicle (0.1% DMSO) or tomatidine (0–10  $\mu$ M) was added to cells for 24 h to investigate the molecular mechanism of lipid metabolism. In other experiments, AMPK inhibitor compound C (Sigma) was added to tomatidine-treated FL83B cells to assay molecular expression in lipid metabolism.

## 2.8. Oil Red O staining

FL83B cells were seeded on 6-well plates and incubated with 0.5 mM oleic acid for 48 h. The cells were treated with or without tomatidine (0–10  $\mu$ M) for 24 h. The plate was washed and the cells fixed with formalin solution before staining with Oil Red O solution to assay oil droplets as described previously [25]. Using an inverted microscope (Olympus), we observed the oil droplets and treated the cells with isopropanol to evaluate lipid accumulation using a microplate reader (Multiskan FC) at an absorbance of 490 nm.

## 2.9. Statistical analysis

Statistical analyses were performed using one-way analysis of variance (ANOVA) and a Dunnett post-hoc test. Data are expressed as the mean  $\pm$  SEM of a minimum of three independent experiments.  $P<.05$  was considered significant.

## 3. Results

### 3.1. Tomatidine reduced HFD-induced obesity in mice

At the end of the animal experiments, visual observation found that HFD-induced obese mice were larger than control mice, and mice in the TA5 and TA10 groups were thinner than the HFD group (Fig. 1B). In the last week of the experiment, our results demonstrated that HFD-induced obese mice treated with tomatidine had significantly decreased body weight compared to the HFD group (TA5:  $40.24 \pm 0.94$  g and TA10:  $37.46 \pm 0.97$  g vs. HFD:  $43.96 \pm 1.07$  g, both  $P<.01$ ; Fig. 1C). As HFD-induced mice were given tomatidine for 12 weeks, the weight gain in the TA5 and TA10 groups was significantly less than in the HFD group (TA5:  $11.08 \pm 0.97$  g, TA10:  $8.30 \pm 0.81$  g, HFD:  $14.81 \pm 0.74$  g;  $P<.01$ ; Fig. 1D). We also found that TA10 had significantly decreased body weight compared to the TA5 group (Fig. 1D). Interestingly, the TA5 and TA10 groups did not alter their food intake compared to the HFD group (Fig. 1E).

### 3.2. Tomatidine decreased the weight of epididymal adipose tissue in obese mice

Grossly, tomatidine significantly decreased the epididymal adipose tissue weight compared to the HFD group (Fig. 2A, B).



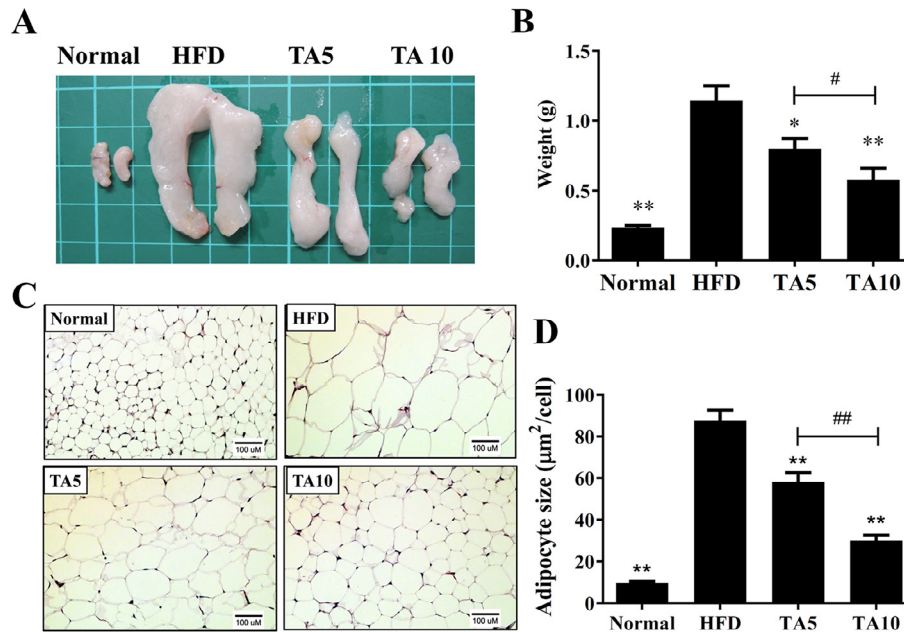


**Fig. 2.** Tomatidine (TA) reduced the epididymal adipose tissue weight in HFD-induced obese mice. The control group (Normal) mice fed standard chow diet. (A) Appearance of the epididymal adipose tissue. (B) Weight of the epididymal adipose tissue. (C) HE staining of epididymal adipose tissue (200 × magnification). (D) Adipocyte size in the epididymal adipose tissue. Data are presented as mean ± SEM; n=10. \* $P < .05$ , \*\* $P < .01$  compared to HFD-induced obese mice. # $P < .05$ , ## $P < .01$  compared to the TA10 group.

Histological staining showed that HFD-induced obese mice could significantly increase adipocyte size in the epididymal adipose tissue compared to the control group. Our results demonstrated that tomatidine significantly reduced adipocyte size in the epididymal adipose tissue compared to the HFD group (Fig. 2C, D). In addition, TA10 could significantly reduce weight and adipocyte size in the epididymal adipose tissue compared to the TA5 group (Fig. 2B, D).

### 3.3. Tomatidine attenuated liver steatosis in obese mice

The livers of control mice were dark red. In contrast, the livers of obese mice were light yellow and lackluster in color. HFD-induced obese mice treated with tomatidine could recover the dark brown-red color of the liver (Fig. 3A). Tomatidine significantly attenuated the liver weight compared to obese mice (Fig. 3B). HE staining of liver tissue demonstrated that obese mice treated with tomatidine had significantly decreased fat vacuoles, and the number of lipid droplets was significantly fewer compared to HFD-induced obese mice (Fig. 3C, D). HFD-induced obese mice treated with tomatidine had significantly decreased NAFLD scores compared to the HFD group (Fig. 3E). Furthermore, TA10 had significantly decreased the number of lipid droplets and NAFLD score compared to the TA5 group (Fig. 3D, E). PAS staining of liver tissue demonstrated that HFD mice treated with tomatidine had significantly increased glycogen accumulation compared to HFD-induced obese mice (Fig. 4A). Next, liver tissues were homogenized and the tissue solution used to detect glycogen levels. Tomatidine was found to significantly increase glycogen levels compared to HFD-induced obese mice (Fig. 4B). Moreover, tomatidine decreased TG and TC levels in the livers of HFD-induced obese mice (Fig. 4C, D). We also assayed ALT and AST levels in serum and found that tomatidine significantly decreased ALT and AST levels in treated mice compared to the HFD group (Table 1).

### 3.4. Effects of tomatidine on serum lipid metabolism

Obese mice treated with tomatidine had significantly reduced levels of serum free fatty acids, TG, TC, and LDL and significantly increased HDL levels compared to HFD-induced obese mice (Table 1). The administration of tomatidine also significantly inhibited the levels of serum glucose and insulin compared to the HFD group. The HOMA-IR value was significantly reduced in HFD-induced obese mice treated with tomatidine compared to obese mice, indicating improved insulin resistance. Obese mice treated with tomatidine also had increased adiponectin expression and significantly decreased leptin levels in serum compared to HFD-induced obese mice (Table 1).

### 3.5. Tomatidine regulated adipogenesis in liver tissue

In the liver, tomatidine significantly suppressed the gene expressions of transcription factors for lipid synthesis, including Srebp-1c and C/EBP $\beta$  (not C/EBP $\alpha$ ) compared to the HFD group (Fig. 5A–C). TA10 had significantly decreased the gene expressions of Srebp-1c and C/EBP $\beta$  compared to the TA5 group (Fig. 5A, C). Tomatidine also decreased FAS gene expression in obese mice and promoted the gene expression of ATGL and HSL for lipolysis in the liver compared to the HFD group (Fig. 5D–F). We also found that TA10 had significantly increased the gene expression of HSL compared to the TA5 group (Fig. 5F). Regarding the fatty acid  $\beta$ -oxidation signaling pathway in liver tissue, administration of tomatidine significantly increased the gene expression of PPAR- $\alpha$  and CPT-1, but not CPT-2, compared to the HFD group (Fig. 5I–L). Moreover, tomatidine treatment of HFD-induced obese mice significantly suppressed leptin and increased adiponectin and sirt1 gene expression compared to the HFD group (Fig. 5G, H, L). TA10 also significantly increased the gene expression of sirt-1 compared to the TA5 group (Fig. 5L). Immunohistochemical staining also demonstrated that increased CPT-1 and decreased FAS production

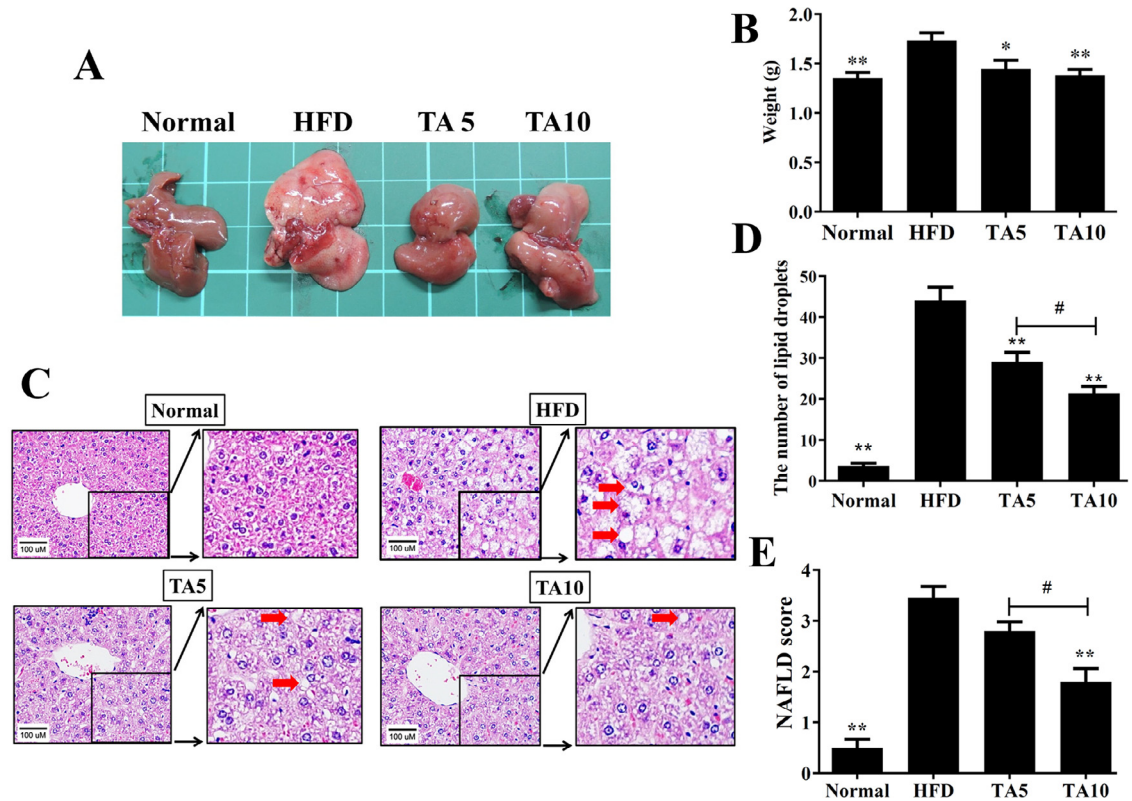


**Fig. 3.** Tomatidine (TA) ameliorated hepatic steatosis in HFD-induced obese mice. The control group (Normal) mice fed standard chow diet. (A) Appearance of the liver. (B) Liver weight. (C) HE staining of liver tissues (200 × magnification). Liver lipid droplets are indicated by arrows. Amplification sections also were shown for the indicated areas. (D) Number of lipid droplets in the liver tissue. (E) NAFLD scores in liver tissues. Data are presented as mean±SEM; n=10. \**P*<.05, \*\**P*<.01 compared to HFD-induced obese mice. #*P*<.05 compared to the TA10 group.

**Table 1**  
Serum biochemical analysis

|                           | Normal                 | HFD        | TA5                   | TA10                   |
|---------------------------|------------------------|------------|-----------------------|------------------------|
| Glucose (mmol/l)          | 8.12±0.58 <sup>†</sup> | 13.38±0.81 | 11.13±0.59            | 9.43±0.39*             |
| Insulin (mU/l)            | 2.10±0.03 <sup>†</sup> | 5.92±0.85  | 4.6±0.36*             | 3.80±0.26 <sup>†</sup> |
| HOMA-IR                   | 0.76±0.17 <sup>†</sup> | 3.52±0.9   | 2.28±0.7 <sup>†</sup> | 1.59±0.6 <sup>†</sup>  |
| Total cholesterol (mg/dl) | 105.4±7.3 <sup>†</sup> | 213.9±12.3 | 166.9±11.7*           | 157.8±8.8 <sup>†</sup> |
| Triglycerides (mg/dl)     | 78.8±6.2 <sup>†</sup>  | 134.1±11.6 | 108.4±10.3            | 97.1±9.7*              |
| HDL (mg/dl)               | 71.7±3.0 <sup>†</sup>  | 48.7±4.0   | 64.9±3.5*             | 66.0±4.8*              |
| LDL (mg/dl)               | 53.1±4.0 <sup>†</sup>  | 101.8±6.4  | 82.1±4.2*             | 73.1±4.5 <sup>†</sup>  |
| Free fatty acids (mM)     | 9.53±0.42*             | 12.34±0.64 | 11.09±0.48            | 10.03±0.42*            |
| AST (U/l)                 | 54.2±4.0 <sup>†</sup>  | 128.0±7.1  | 90.4±7.2 <sup>†</sup> | 69.9±7.2 <sup>†</sup>  |
| ALT (U/l)                 | 39.4±1.9 <sup>†</sup>  | 86.6±7.3   | 62.3±6.3*             | 53.7±5.7 <sup>†</sup>  |
| Leptin (μg/ml)            | 22.3±0.8 <sup>†</sup>  | 63.2±4.6   | 44.5±3.6 <sup>†</sup> | 39.9±4.0 <sup>†</sup>  |
| Adiponectin (mg/ml)       | 2.05±0.08 <sup>†</sup> | 1.55±0.06  | 1.94±0.06*            | 2.03±0.12 <sup>†</sup> |

\* *P*<.05.

<sup>†</sup> *P*<.01 compared to HFD-induced obese mice. Data are presented as mean±SEM.

in the liver tissue of HFD mice treated with tomatidine compared to the HFD group (Fig. 6).

### 3.6. Tomatidine suppressed lipid accumulation in FL83B cells

Next, we carefully studied whether tomatidine regulates lipid metabolism in FL83B hepatocytes in vitro. FL83B cell viability was measured by the MTT assay, and tomatidine did not significantly cause cytotoxic effects at a concentration ≤30 μM (data not shown). Thus, subsequent experiments used tomatidine at 0–10 μM. FL83B cells were stimulated with 0.5 mM oleic acid to induce

lipid accumulation and stained with Oil Red O solution. Tomatidine significantly decreased lipid droplet accumulation compared to oleic acid-induced FL83B hepatocytes (Fig. 7A). Treatment with isopropanol significantly attenuated lipid levels (Fig. 7B).

### 3.7. Tomatidine regulated lipid metabolism in hepatocytes

Tomatidine decreased Srebp-1c, C/EBPβ, and FAS expression at the protein level compared to oleic acid-induced FL83B cells (Fig. 8A, B). Tomatidine also increased ATGL and the phosphorylation of HSL in a concentration-dependent manner compared to

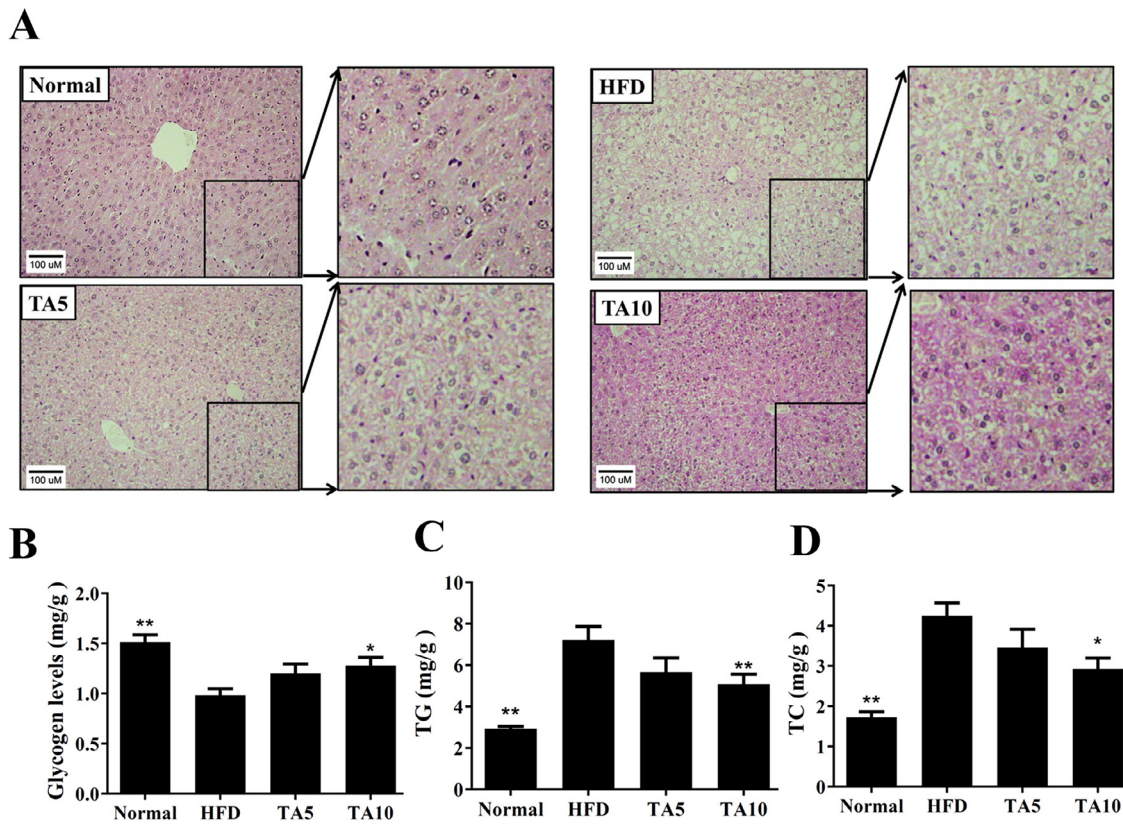


**Fig. 4.** (A) PAS staining of tomatidine (TA)-modulated glycogen distribution in the liver ( $200\times$  magnification). The control group (Normal) mice fed standard chow diet. Amplification sections also were shown for the indicated areas. (B) TA increased glycogen levels in liver tissue. (C) TA modulated triglyceride (TG) and (D) total cholesterol (TC) levels in the liver tissue. Normal: The control group mice. Three independent experiments were analyzed. The data are presented as mean $\pm$ SEM;  $n=10$ . \* $P<.05$ , \*\* $P<.01$  compared to HFD-induced obese mice.

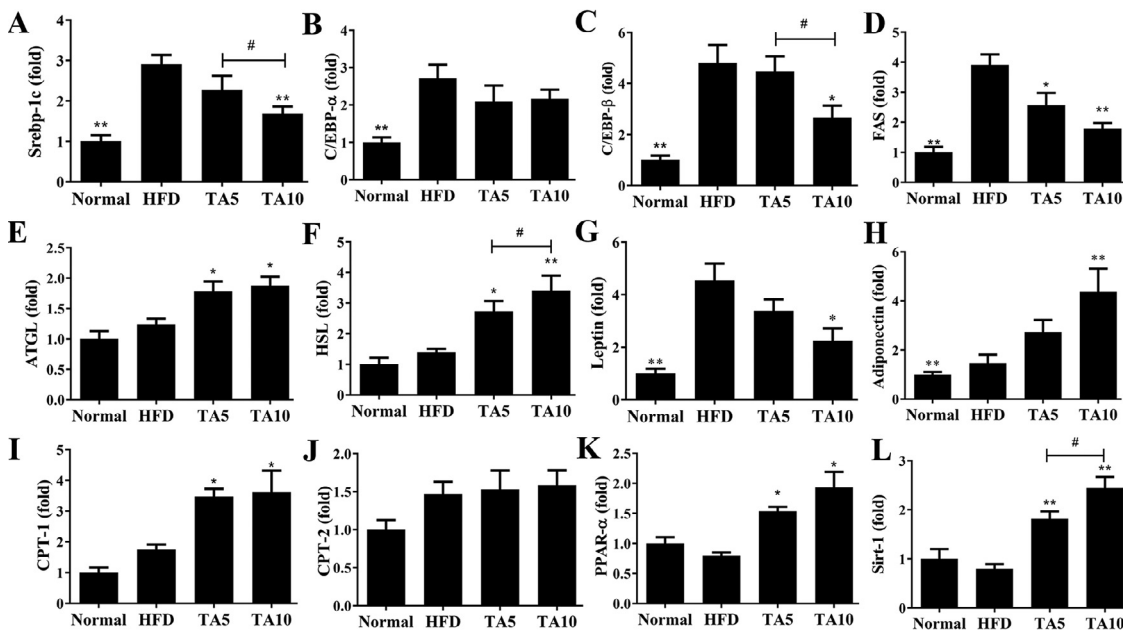


**Fig. 5.** Tomatidine (TA) modulated lipogenesis and lipolysis gene expression in liver tissue. (A) Expression levels of Srebp-1c, (B) C/EBP $\alpha$ , (C) C/EBP $\beta$ , (D) FAS, (E) ATGL, (F) HSL, (G) leptin, (H) adiponectin, (I) CPT-1, (J) CPT-2, (K) PPAR $\alpha$ , and (L) Sirt-1 as determined by real-time RT-PCR. The fold changes in expression were calculated relative to the level of  $\beta$ -actin (internal control). Three independent experiments were analyzed. The data are presented as mean $\pm$ SEM;  $n=10$ . \* $P<.05$ , \*\* $P<.01$  compared to HFD-induced obese mice. # $P<.05$  compared to the TA10 group. Normal: The control group mice.



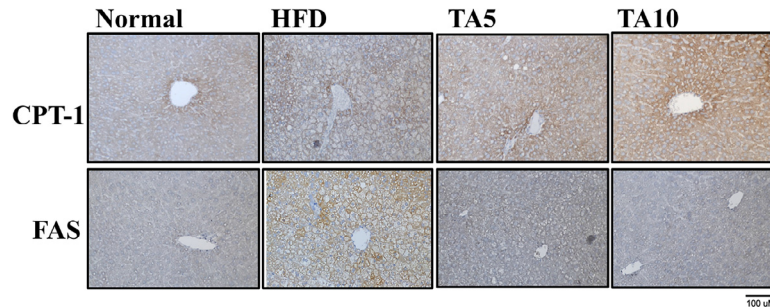


**Fig. 6.** Immunohistochemical staining of tomatidine (TA)-modulated CPT-1 and FAS expression in the liver (brown color drop). Three independent experiments were analyzed. Normal: The control group mice.

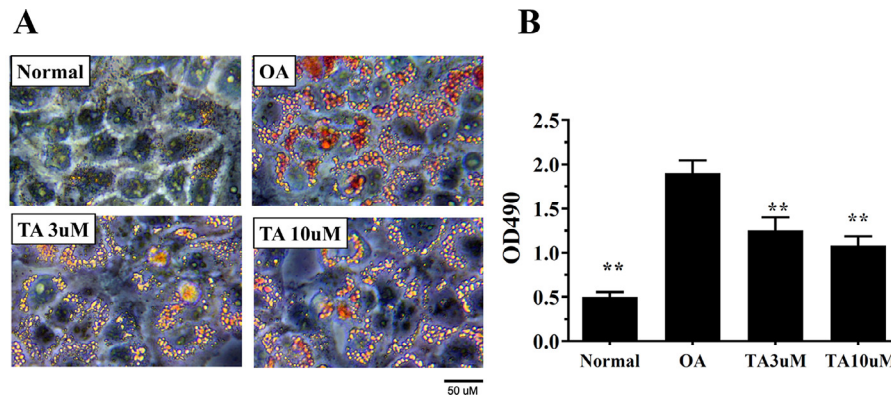


**Fig. 7.** Tomatidine (TA) reduced lipid accumulation in FL83B cells. (A) Oil Red O staining revealed lipid accumulation. (B) FL83B cells were treated with isopropanol and lipid accumulation measured by the absorbance at 490 nm (OD490). Three independent experiments were analyzed. Data are presented the mean  $\pm$  SEM. \*\* $P < .01$  compared to FL83B cells treated with oleic acid (OA).

oleic acid-induced FL83B cells (Fig. 8C, D). Regarding the fatty acid  $\beta$ -oxidation pathway, FL83B cells treated with tomatidine had significantly increased CPT-1 and PPAR $\alpha$  (but not CPT-2) expression compared to oleic acid-induced FL83B cells (Fig. 8E, F). Tomatidine also significantly enhanced Sirt1 and the phosphorylation of AMPK and ACC compared to oleic acid-induced FL83B cells (Fig. 8G, H). Surprisingly, when oleic acid-induced FL83B cells were co-treated with 10  $\mu$ M tomatidine and compound C, tomatidine could restore Sirt1, phosphorylated AMPK, phosphorylated ACC, and ATGL and more significantly reduced FAS expression (Fig. 9A, B).

#### 4. Discussion

Recent studies have found that some pure compounds from plants can reduce the body weight of obese mice and improve NAFLD. In HFD-induced obese mice, maslinic acid, licochalcone A, fisetin, and resveratrol have been shown to reduce body weight and ameliorate liver metabolic dysfunction by promoting Sirt1 and AMPK activation [21,22,26–28]. In the current study, tomatidine effectively reduced the body weight of obese mice fed HFD, the weight of epididymal adipose tissue, and the accumulation of lipid in adipocytes. Tomatidine also reduced the weight of the liver of obese mice and the accumulation of lipid in liver cells, suppressed the levels of TC and TG in the liver, and improved NAFLD in obese mice. Furthermore, we found that tomatidine can effectively inhibit lipogenesis and lipolysis in liver tissue by promoting the Sirt1/AMPK pathway, enhancing fatty acid  $\beta$ -oxidation to accelerate lipid metabolism. Our results indicate that tomatidine is an effective natural compound for improving obesity and NAFLD.

Many countries are facing a trend of a high incidence of chronic diseases caused by obesity and an overweight population. Clinical

medicine has confirmed that excessive visceral fat is closely related to the incidence of arteriosclerosis, hypertension, diabetes, hyperlipidemia, and cardiovascular disease [29,30]. Mice fed HFD clearly show that visceral fat and inguinal fat tissue have a large amount of lipid accumulation. Obese mice treated with tomatidine have significantly reduced visceral adipose tissue weight. Therefore, the body weight of these mice can also be significantly lower than that of the obese mice. We surmise that tomatidine may contribute to weight loss in persons with obesity.

A high-calorie diet high in fat and sugar will increase lipid synthesis and the carbohydrate metabolic burden in the liver, causing the liver to accumulate excessive TG and TC to induce the development of hepatic steatosis or NAFLD [31]. The NAFLD score index includes the number of fat vacuoles, blood biochemistry values, and macrophage infiltration [32]. Our experiments found that HFD-fed obese mice had higher NAFLD scores than control mice, and obese mice treated with tomatidine had significantly lower NAFLD scores than untreated obese mice. Obese mice treated with tomatidine had significantly reduced serum ALT and AST levels, which can recover liver function. Therefore, our experiments confirmed that tomatidine can improve NAFLD in obese mice.

The accumulation of TGs in the liver is related to hepatic steatosis or the formation of NAFLD. Activation of transcription factors related to lipid synthesis (including Srebp-1c, PPAR- $\gamma$ , and C/EBP $\beta$ ) and FAS would promote fatty acid chain synthesis [10]. Previous studies have used palmitic acid to induce lipid accumulation in HepG2 cells, and tomatidine has been shown to reduce Srebp-1c and FAS expression in this context [19]. However, whether tomatidine improved lipid metabolism was not examined in the obese animal experiments. In the current study, we detected lipogenesis of the liver in obese mice, and our results showed that tomatidine



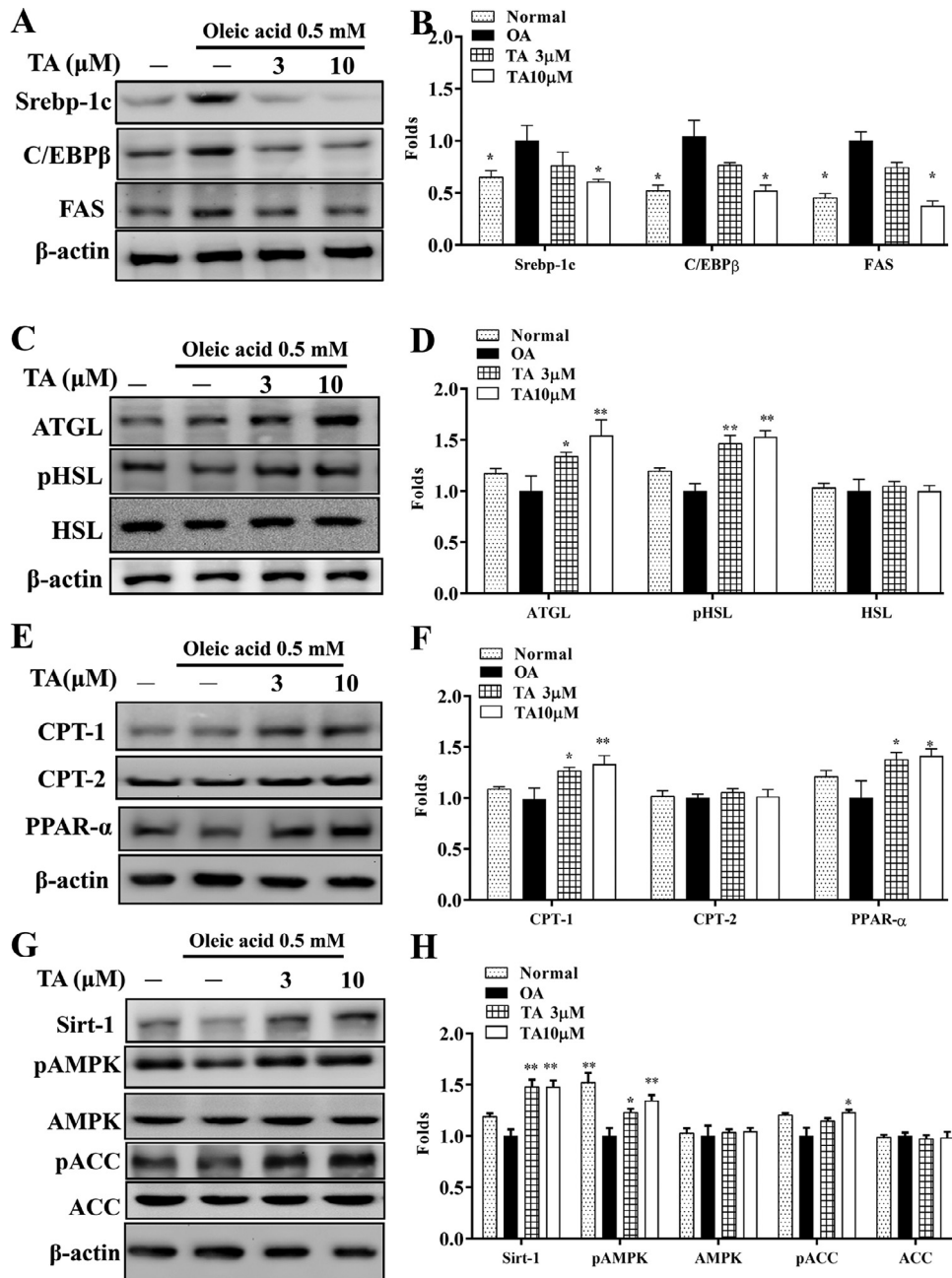


**Fig. 8.** Effects of tomatidine (TA) on lipid metabolism in FL83B cells. (A) The expression of transcription factors involved in lipogenesis and FAS were detected by Western blot. (B) The fold change in expression of the proteins in (A) relative to the expression of  $\beta$ -actin. (C) Lipolysis proteins were detected by Western blot. (D) The fold change in expression of the proteins in (C) relative to the expression of  $\beta$ -actin. (E)  $\beta$ -oxidation proteins were detected by Western blot. (F) The fold change in expression of the proteins in (E) measured relative to the expression of  $\beta$ -actin. (G) Sirt1/AMPK pathway proteins were detected by Western blot. (H) The fold change in the expression of proteins in (G) measured relative to the expression of  $\beta$ -actin. Three independent experiments were analyzed. Data are presented as mean  $\pm$  SEM. \*\* $P < .01$  compared to FL83B cells treated with oleic acid (OA).

can significantly decrease C/EBP $\beta$  and Srebp-1c, which could inhibit FAS expression in the synthesis of fatty acid chains and TGs in the liver. Thus, tomatidine could decrease the levels of TGs and TC in the liver and improve liver steatosis in obese mice. Our cellular experiments also found that tomatidine has the ability to reduce Srebp-1c, C/EBP $\beta$ , and FAS expression in oleic acid-induced FL83B cells. In addition, HE staining of liver tissue slices confirmed that tomatidine significantly improves fat vacuoles and lipid accumulation in obese mice. Therefore, we determined that tomatidine has the ability to block lipid synthesis in the liver by suppressing

the expression of transcription factors involved in lipogenesis and FAS in obese mice.

Increasing TG breakdown in fatty liver cells can also improve hepatic steatosis. Previous studies have shown that maslinic acid and licochalcone A can increase ATGL and HSL phosphorylation to accelerate lipolysis in the livers of obese mice [21,22]. In the current study, we found that tomatidine decreases ATGL and HSL gene expression in the livers of obese mice and decreases ATGL and HSL phosphorylation in oleic acid-induced FL83B cells. Moreover, in oleic acid-induced FL83B cells co-treated with tomatidine

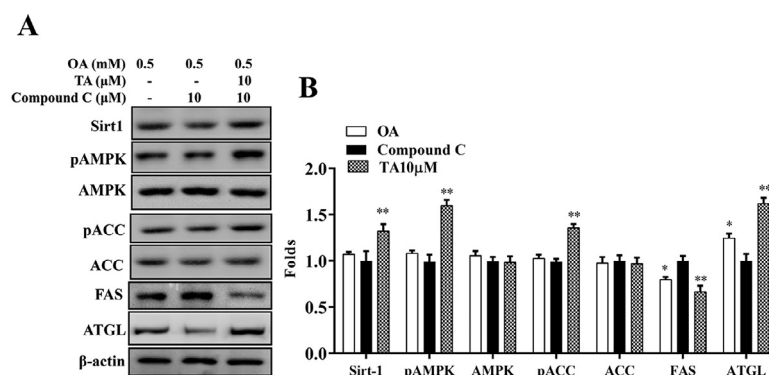


**Fig. 9.** Effects of tomatidine (TA) on the AMPK/Sirt-1 pathway in FL83B cells. (A) FL83B cells were treated with 0.5 mM oleic acid for 48 h, followed by 10  $\mu$ M tomatidine with or without an AMPK inhibitor (compound c) for 24 h. (B) The fold expression was measured relative to the expression of  $\beta$ -actin. Three independent experiments were analyzed. Data are presented as mean  $\pm$  SEM. \* $P$  < .05, \*\* $P$  < .01 compared to compound c treatment. OA, oleic acid.

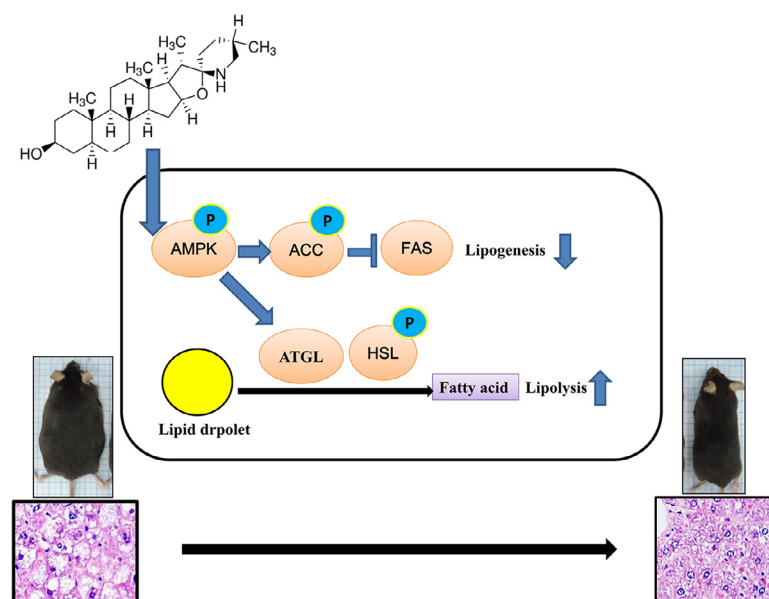


**Fig. 10.** Model explaining the mechanism for tomatidine promoted AMPK signaling pathway to increase lipolysis and decrease lipogenesis in fatty liver cells of obese mice.

and AMPK inhibitor (compound C), tomatidine significantly recovered ATGL expression. We think that tomatidine increases lipolysis in fatty liver by regulating the phosphorylation of HSL and ATGL, and AMPK expression.

The liver and adipose tissues are infiltrated by more macrophages in individuals with obesity [33]. When TGs are broken down in the liver and adipose tissue to produce excessive free fatty acids, it causes an inflammatory reaction by macrophages, and the inflamed macrophages release more  $\text{TNF-}\alpha$  to induce insulin resistance of the adipocyte and liver tissue [33]. The free fatty acids produced by TG decomposition in the liver can produce energy via  $\beta$ -oxidation of fatty acids. Long-chain fatty acids use carnitine to enter the mitochondria to generate energy through  $\beta$ -oxidation [34]. CPT-1 and CPT-2 are important enzymes for free fatty acid entry of the mitochondria of liver cells. In the cytoplasm, carnitine combines with fatty acyl-CoA, and the complex is carried by CPT-1 into mitochondria. CPT-2 assists in the separation of carnitine and fatty acyl-CoA [35], allowing fatty acid metabolism to produce energy. Our research shows that tomatidine can significantly increase CPT-1 gene expression in the livers of obese mice, and oleic acid-induced FL83B cells treated with tomatidine also exhibit enhanced CPT-1 expression.

Immunohistochemical staining in the liver also confirmed that tomatidine can increase CPT-1 protein expression in the livers of obese mice. Interestingly, animal and cell experiments have shown that tomatidine cannot regulate CPT-2 expression, but tomatidine can enhance the expression of PPAR- $\alpha$  in the liver tissue of obese mice and FL83B cells to modulate the metabolism of free fatty acids. Blood biochemical analysis has also found that tomatidine can significantly reduce serum free fatty acid levels in obese mice. Therefore, we speculate that tomatidine effectively increased the metabolism of free fatty acids by promoting the  $\beta$ -oxidation signaling pathway to reduce oxidative stress damage in fatty liver cells.

Previous research found that free fatty acids inhibit AMPK activation [36]. Lipid accumulation in the liver and adipose tissue also inhibited AMPK activity and promoted ACC activity, accelerating fatty acid synthesis and leading to excessive accumulation of TGs in the liver, inducing the development of NAFLD [36]. Other researchers have found that palmitate acid-induced HepG2 cells treated with tomatidine have enhanced expression of vitamin D receptors and blocked lipid accumulation through promotion of the AMPK signaling pathway [19]. In the current study, we confirmed that tomatidine can effectively regulate Sirt1 and phosphorylated

AMPK expression in oleic acid-induced FL83B cells. AMPK phosphorylation stimulated ACC phosphorylation, blocked FAS expression, and reduced fatty acid synthesis. Therefore, immunohistochemical staining in the liver confirmed that tomatidine reduced FAS protein expression in the livers of obese mice. In addition, tomatidine has the ability to restore AMPK phosphorylation and inhibit FAS expression in FL83B cells treated with AMPK inhibitors. Therefore, tomatidine can reduce lipid accumulation in the livers of obese mice by regulating the AMPK pathway.

Previous studies have found that the adipocyte tissues of obese mice secrete excessive leptin, which binds to leptin receptors in hypothalamic neurons, reducing appetite and regulating body weight [37]. Maslinic acid, licochalcone A, and resveratrol improve obesity and insulin resistance by reducing serum leptin levels and increasing serum adiponectin levels in obese mice [21,22,27]. Our results demonstrate a lack of significant differences in food intake between the tomatidine-treated obese mice and obese mice. However, obese mice treated with tomatidine could have significantly reduced serum leptin and increased serum adiponectin levels, without an effect on appetite. Interestingly, we found that tomatidine regulates fasting blood glucose and insulin levels. Obese mice have higher HOMA-IR values and high risk factors for insulin resistance, whereas obese mice treated with tomatidine have significantly reduced HOMA-IR values. Therefore, tomatidine may have a hypoglycemic effect and improve insulin resistance in obese mice by regulating the levels of leptin and adiponectin.

In conclusion, we demonstrated that tomatidine can improve hepatic steatosis in the livers of obese mice by promoting the Sirt1/AMPK pathway. Tomatidine also reduced the body weight and adipose tissue weight and significantly suppressed lipid accumulation in the liver (Fig. 10). Therefore, tomatidine has potential as a new anti-obesity agent for the treatment of obesity and NAFLD.

## Author Contributions

Designed the experiments: SJW, WCH, KKY, and CJL; Performed the experiments: SJW, WCH, YLC, and SCS; Analysis and interpretation of data: SJW, WCH, MCY, SCS and KKY; Drafting the manuscript: SJW, WCH, KKY, and CJL.

## Declaration of competing interest

The authors have no conflicts of interest to declare.

## Acknowledgments

This study was supported in part by grants from Chang Gung Memorial Hospital (CMRPF1J0061, CMRPF1H0043, CMRPF1K0081 and CMRPF1K0011), Chang Gung University of Science and Technology (ERRPF3J0081, ZRRPF3K0111-7, and ZRRPF3K0111-9), and the Ministry of Science and Technology in Taiwan (106-2320-B-255-007-MY3).

## References

- [1] Kolb R, Sutterwala FS, Zhang W. Obesity and cancer: inflammation bridges the two. *Curr Opin Pharmacol* 2016;29:77–89.
- [2] Kitade H, Chen G, Ni Y, Ota T. Nonalcoholic fatty liver disease and insulin resistance: new insights and potential new treatments. *Nutrients* 2017;9:387.
- [3] Drescher HK, Weiskirchen S, Weiskirchen R. Current status in testing for non-alcoholic fatty liver disease (NAFLD) and nonalcoholic steatohepatitis (NASH). *Cells* 2019;8:845.
- [4] Ma X, McKeen T, Zhang J, Ding WX. Role and mechanisms of mitophagy in liver diseases. *Cells* 2020;9:837.
- [5] Santhekadur PK, Kumar DP, Sanyal AJ. Preclinical models of non-alcoholic fatty liver disease. *J Hepatol* 2018;68:230–7.
- [6] Bedossa P. Pathology of non-alcoholic fatty liver disease. *Liver Int* 2017;37(Suppl 1):85–9.
- [7] Bellentani S. The epidemiology of non-alcoholic fatty liver disease. *Liver Int* 2017;37(Suppl 1):81–4.
- [8] Kanda T, Goto T, Hirotsu Y, Masuzaki R, Moriyama M, Omata M. Molecular mechanisms: connections between nonalcoholic fatty liver disease, steatohepatitis and hepatocellular carcinoma. *Int J Mol Sci* 2020;21:1525.
- [9] Wang Y, Viscarra J, Kim SJ, Sul HS. Transcriptional regulation of hepatic lipogenesis. *Nat Rev Mol Cell Biol* 2015;16:678–89.
- [10] Hodson L, Gunn PJ. The regulation of hepatic fatty acid synthesis and partitioning: the effect of nutritional state. *Nat Rev Endocrinol* 2019;15:689–700.
- [11] Khan RS, Bril F, Cusi K, Newsome PN. Modulation of insulin resistance in non-alcoholic fatty liver disease. *Hepatology* 2019;70:711–24.
- [12] Wang Y, Nakajima T, Gonzalez FJ, Tanaka N. PPARs as metabolic regulators in the liver: lessons from liver-specific PPAR-null mice. *Int J Mol Sci* 2020;21:2061.
- [13] Ren Y, Shen HM. Critical role of AMPK in redox regulation under glucose starvation. *Redox Biol* 2019;25:10115.
- [14] Wang Q, Liu S, Zhai A, Zhang B, Tian G. AMPK-mediated regulation of lipid metabolism by phosphorylation. *Biol Pharm Bull* 2018;41:985–93.
- [15] Karbasforooshan H, Karimi G. The role of SIRT1 in diabetic retinopathy. *Biomed Pharmacother* 2018;97:190–4.
- [16] Kuo CY, Huang WC, Liou CJ, Chen LC, Shen JJ, Kuo ML. Tomatidine attenuates airway hyperresponsiveness and inflammation by suppressing Th2 cytokines in a mouse model of asthma. *Mediators Inflamm* 2017;5261803.
- [17] Yan KH, Lee LM, Yan SH, Huang HC, Li CC, Lin HT, et al. Tomatidine inhibits invasion of human lung adenocarcinoma cell A549 by reducing matrix metalloproteinases expression. *Chem Biol Interact* 2013;203:580–7.
- [18] Friedman M, Levin CE, Lee SU, Kim HJ, Lee IS, Byun JO, et al. Tomatine-containing green tomato extracts inhibit growth of human breast, colon, liver, and stomach cancer cells. *J Agric Food Chem* 2009;57:5727–33.
- [19] Kusu H, Yoshida H, Kudo M, Okuyama M, Harada N, Tsuji-Naito K, et al. Tomatidine reduces palmitate-induced lipid accumulation by activating AMPK via vitamin D receptor-mediated signaling in human HepG2 hepatocytes. *Mol Nutr Food Res* 2019;63:e1801377.
- [20] Liou CJ, Chen YL, Yu MC, Yeh KW, Shen SC, Huang WC. Sesamol alleviates airway hyperresponsiveness and oxidative stress in asthmatic mice. *Antioxidants* 2020;9:295.
- [21] Liou CJ, Lee YK, Ting NC, Chen YL, Shen SC, Wu SJ, et al. Protective effects of licochalcone A ameliorates obesity and non-alcoholic fatty liver disease via promotion of the Sirt-1/AMPK pathway in mice fed a high-fat diet. *Cells* 2019;8:447.
- [22] Liou CJ, Dai YW, Wang CL, Fang LW, Huang WC. Maslinic acid protects against obesity-induced nonalcoholic fatty liver disease in mice through regulation of the Sirt1/AMPK signaling pathway. *FASEB J* 2019;33:11803–117910.
- [23] Huang WC, Liu CY, Shen SC, Chen LC, Yeh KW, Liu SH, et al. Protective effects of licochalcone A improve airway hyper-responsiveness and oxidative stress in a mouse model of asthma. *Cells* 2019;8:617.
- [24] Huang WC, Su HH, Fang LW, Wu SJ, Liou CJ. Licochalcone A inhibits cellular motility by suppressing E-cadherin and MAPK signaling in breast cancer. *Cells* 2019;8:218.
- [25] Huang WC, Chen YL, Liu HC, Wu SJ, Liou CJ. Ginkgolide C reduced oleic acid-induced lipid accumulation in HepG2 cells. *Saudi Pharm J* 2018;26:1178–84.
- [26] Liou CJ, Wei CH, Chen YL, Cheng CY, Wang CL, Huang WC. Fisetin protects against hepatic steatosis through regulation of the Sirt1/AMPK and fatty acid beta-oxidation signaling pathway in high-fat diet-induced obese mice. *Cell Physiol Biochem* 2018;49:1870–84.
- [27] Tiao MM, Lin YJ, Yu HR, Sheen JM, Lin IC, Lai YJ, et al. Resveratrol ameliorates maternal and post-weaning high-fat diet-induced nonalcoholic fatty liver disease via renin-angiotensin system. *Lipids Health Dis* 2018;17:018–0824.
- [28] Liou CJ, Wu SJ, Shen SC, Chen LC, Chen YL, Huang WC. Phloretin ameliorates hepatic steatosis through regulation of lipogenesis and Sirt1/AMPK signaling in obese mice. *Cell Biosci* 2020;10:114.
- [29] Divella R, De Luca R, Abbate I, Naglieri E, Daniele A. Obesity and cancer: the role of adipose tissue and adipo-cytokines-induced chronic inflammation. *J Cancer* 2016;7:2346–59.
- [30] Zhang T, Chen J, Tang X, Luo Q, Xu D, Yu B. Interaction between adipocytes and high-density lipoprotein: new insights into the mechanism of obesity-induced dyslipidemia and atherosclerosis. *Lipids Health Dis* 2019;18:223.
- [31] Liss KH, Finck BN. PPARs and nonalcoholic fatty liver disease. *Biochimie* 2016;136:65–74.
- [32] Kleiner DE, Brunt EM, Van Natta M, Behling C, Contos MJ, Cummings OW, et al. Design and validation of a histological scoring system for nonalcoholic fatty liver disease. *Hepatology* 2005;41:1313–21.
- [33] Kazankov K, Jorgensen SMD, Thomsen KL, Moller HJ, Vilstrup H, George J, et al. The role of macrophages in nonalcoholic fatty liver disease and non-alcoholic steatohepatitis. *Nat Rev Gastroenterol Hepatol* 2019;16:145–59.
- [34] Vishwanath VA. Fatty acid Beta-oxidation disorders: a brief review. *Ann Neurol* 2016;23:51–5.
- [35] Merritt JL 2nd, Norris M, Kanungo S. Fatty acid oxidation disorders. *Ann Transl Med* 2018;6:57.
- [36] Nakamura MT, Yudell BE, Loo JJ. Regulation of energy metabolism by long-chain fatty acids. *Prog Lipid Res* 2014;53:124–44.
- [37] Zhang Y, Chua S Jr. Leptin function and regulation. *Compr Physiol* 2017;8:351–69.